NUREG/CP-0142
Vol. 4
CONF-950904--Vol.4

Proceedings of the 7th International Meeting on Nuclear Reactor Thermal-Hydraulics NURETH-7

Sessions 17–24

Held at
Sheraton Hotel and Convention Center
Saratoga Springs, New York
September 10–15, 1995

Compiled by
R. C. Block, F. Feiner, ANS

Sponsored by
American Nuclear Society
American Institute of Chemical Engineers
American Society of Mechanical Engineers
Canadian Nuclear Society
European Nuclear Society
Atomic Energy Society of Japan
Japanese Society of Multiphase Flow
U.S. Nuclear Regulatory Commission

Proceedings prepared by
Northeastern New York Chapter
American Nuclear Society

AVAILABILITY NOTICE

Availability of Reference Materials Cited in NRC Publications

Most documents cited in NRC publications will be available from one of the following sources:

1. The NRC Public Document Room, 2120 L Street, NW., Lower Level, Washington, DC 20555-0001

2. The Superintendent of Documents, U.S. Government Printing Office, P. O. Box 37082, Washington, DC 20402-9328

3. The National Technical Information Service, Springfield, VA 22161-0002

Although the listing that follows represents the majority of documents cited in NRC publications, it is not intended to be exhaustive.

Referenced documents available for inspection and copying for a fee from the NRC Public Document Room include NRC correspondence and internal NRC memoranda; NRC bulletins, circulars, information notices, inspection and investigation notices; licensee event reports; vendor reports and correspondence; Commission papers; and applicant and licensee documents and correspondence.

The following documents in the NUREG series are available for purchase from the Government Printing Office: formal NRC staff and contractor reports, NRC-sponsored conference proceedings, international agreement reports, grantee reports, and NRC booklets and brochures. Also available are regulatory guides, NRC regulations in the *Code of Federal Regulations*, and *Nuclear Regulatory Commission Issuances*.

Documents available from the National Technical Information Service include NUREG-series reports and technical reports prepared by other Federal agencies and reports prepared by the Atomic Energy Commission, forerunner agency to the Nuclear Regulatory Commission.

Documents available from public and special technical libraries include all open literature items, such as books, journal articles, and transactions. *Federal Register* notices, Federal and State legislation, and congressional reports can usually be obtained from these libraries.

Documents such as theses, dissertations, foreign reports and translations, and non-NRC conference proceedings are available for purchase from the organization sponsoring the publication cited.

Single copies of NRC draft reports are available free, to the extent of supply, upon written request to the Office of Administration, Distribution and Mail Services Section, U.S. Nuclear Regulatory Commission, Washington, DC 20555-0001.

Copies of industry codes and standards used in a substantive manner in the NRC regulatory process are maintained at the NRC Library, Two White Flint North, 11545 Rockville Pike, Rockville, MD 20852-2738, for use by the public. Codes and standards are usually copyrighted and may be purchased from the originating organization or, if they are American National Standards, from the American National Standards Institute, 1430 Broadway, New York, NY 10018-3308.

DISCLAIMER NOTICE

DISCLAIMER

Conference Number: 9509 04

Do not Do Analytics on these papers

Conference 950904

7. international meeting on nuclear reactor thermal hydraulics, Saratoga, New York, 10-15 Sep 1995

Entered: 02/18/94
Changed: 09/07/95
Papers : 5
Volumes: 4
Activities: 0
Sponsors : 8
Energy Meetings: Y

Conference Paper 1 of 5

Author : Laurinat, J. E.
Report Number: WSRC-MS--94-0356
Secondary : CONF-950904--1
Trac No. SC: : M95004401
Entered : 01/26/95
Changed : 07/27/95
Description:
Note : B;Rev.1

Buoyancy-driven flow excursions in fuel assemblies

Conference Paper 2 of 5

Author : Yang, W. S.
Report Number: ANL/RA/CP--83070
Secondary : CONF-950904--2
Trac No. SC: : M95004640
Entered : 01/31/95
Changed :
Description:
Note :

Assessment of the SE2-ANL code using EBR-II temperature measurements

Conference Paper 3 of 5

Author : Boyack, B. E.
Report Number: LA-UR--95-926
Secondary : CONF-950904--3
Trac No. SC: : M95009422
Entered : 05/03/95
Changed :
Description:
Note :

Analysis of an AP600 intermediate-size loss-of-coolant accident

Conference Paper 4 of 5

Author : Sulfredge, C. D.
Report Number: CONF-950904--4
Secondary :
Trac No. SC: : M95009181
Entered : 05/04/95
Changed :
Description:
Note :

Flow excursion time scales in the Advanced Neutron Source reactor

Conference Paper 5 of 5

Author : Nourbakhsh, H. P.
Report Number: BNL-NUREG--60573
Secondary : CONF-950904--5
Trac No. SC: : M95008862
Entered : 06/27/95
Changed :
Description:
Note :

Mixing phenomena of interest to boron dilution during small break LOCAs in PWRs

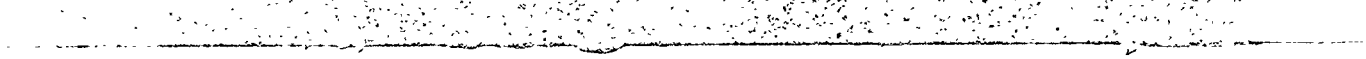

NUREG/CP-0142
Vol. 4

Proceedings of the 7th International Meeting on Nuclear Reactor Thermal-Hydraulics NURETH-7

Sessions 17-24

Held at
Sheraton Hotel and Convention Center
Saratoga Springs, New York
September 10-15, 1995

Date Published: September 1995

Compiled by:
R. C. Block, F. Feiner, ANS

Sponsored by
American Nuclear Society
555 N. Kensington Avenue
La Grange Park, IL 60525

American Institute of Chemical Engineers
345 East 47th Street
New York, NY 10017-2392

American Society of Mechanical Engineers
345 East 47th Street
New York, NY 1007-2392

Canadian Nuclear Society
144 Font Street West
Suite 725
Toronto, Ontario, Canada M5J2L7

European Nuclear Society
Secretariat: Monbijoustrasse 5
P.O. Box 5032
CH-3001 Berne, Switzerland

Atomic Energy Society of Japan
No. 1-13, 1-chome
Shimbashi, Minato-ku
Tokyo 105, Japan

Japan Society of Multiphase Flow
Prof. Akimi Serizawa
Department of Nuclear Engineering
Yoshida, Sakyo, Kycto 606-01
Japan

Division of Systems Technology
Office of Nuclear Regulatory Research
U.S. Nuclear Regulatory Commission
Washington, DC 20555-0001

Proceedings prepared by
Northeastern New York Chapter
Amrican Nuclear Society

NUREG/CP-0142, Volume 4, has been reproduced from the best available copy.

ABSTRACT

Technical papers accepted for presentation at the Seventh International Topical Meeting on Nuclear Reactor Thermal-Hydraulics are included in the present Proceedings. Except for the invited papers in the plenary session, all other papers are contributed papers. The topics of the meeting encompass all major areas of nuclear thermal-hydraulics, including analytical and experimental works on the fundamental mechanisms of fluid flow and heat transfer, the development of advanced mathematical and numerical methods, and the application of advancements in the field in the development of novel reactor concepts. Because of the complex nature of nuclear reactors and power plants, several papers deal with the combined issues of thermal-hydraulics and reactor/power-plant safety, core neutronics and/or radiation.

The participation in the conference by the authors from several countries and four continents makes the Proceedings a comprehensive review of the recent progress in the field of nuclear reactor thermal-hydraulics worldwide.

PLANNING COMMITTEE MEMBERS

General Chairman: Richard T. Lahey, Jr.

Vice-Chairman: M. Richard Mendelson

Technical Program Chairman: Michael Z. Podowski

Registration: Thomas M. Sutton

Secretary: Ray G. Gamino

Finance: Hunter B. Currin

Fund Raising: Brian Bielecki and Norman Francis

Publications: Frank Feiner and Robert C. Block

Arrangements: Robert C. Rohr

Publicity: David F. McMullan

Special Events: Jeffrey G. Hoole

Spouse Events: Ann E. Kelly

SCIENTIFIC ADVISORY COMMITTEE

K. Akagawa	Japan
G.F. Hewitt	Great Britian
Y.Y. Hsu	R.C., Taiwan
J. H. Kim	USA
S. Levy	USA
F. Mayinger	Germany
G. Matsui	Japan
U. Mueller	Germany
V. Nakoriakov	Russia
R.I. Nigmatulin	Russia
W. Rohsenow	USA
T. Sakaguchi	Japan
V.E. Schrock	USA
N. Todreas	USA
L.S. Tong	USA

TECHNICAL PROGRAM COMMITTEE

M. Akiyama	Japan	R.E. Henry	USA
K.H. Ardon	Great Britain	G. Hetsroni	Israel
S. Antal	USA	L. Hochreiter	USA
M. Aritomi	Japan	M. Ishii	USA
B. Azzopardi	Great Britain	H. Karwat	Germany
S. Banerjee	USA	G. Kojasoy	USA
F.R. Best	USA	V.S. Krishnan	Canada
B. Boyack	USA	T. K. Larson	USA
N. Brauner	Israel	H. Lemmonier	France
G.P. Celata	Italy	J. March-Leuba	USA
J.H. Cha	South Korea	M. Merilo	USA
A. Clausse	Argentina	F. Moody	USA
M.L. Corradini	USA	H. Nariai	Japan
J.M. Courtaud	France	B. Nigmatulin	Russia
M. Cumo	Italy	H. Ninokata	Japan
V.K. Dhir	USA	O. Nylund	Sweden
G.E. Dix	USA	P.F. Peterson	USA
J.J. Dorning, Jr.	USA	V. Ransom	USA
R.B. Duffey	USA	K. Rehme	Germany
F. Eltawila	USA	D.S. Rowe	USA
M. Epstein	USA	Z. Rouhani	USA
M. Erdman	USA	K. Rust	Germany
S. Ettore	USA	B.R. Sehgal	Sweden
W. Frid	Sweden	A. Serizawa	Japan
M. Golay	USA	B.S. Shiralker	USA
Y.A. Hassan	USA	L. Shotkin	USA
S. Sreepada	USA	J. Weisman	USA
A. Strupczewski	Poland	W. Wulff	USA
L. Szabados	Hungary	G. Yadigaroglu	SWITZERLAND
R. Taleyarkhan	USA	S.T. Yin	CANADA
T.G. Theofanous	USA		

SESSION ORGANIZERS

Almenas, K.
Aritomi, M.
Banerjee, S.
Baratta, A.J.
Best, F.R.
Boyack, B.
Brauner, N.
Catton, I.
Celata, G.P.
Cha, J.H.
Chabard, J.P.
Cheng, L.
Corradini, M.L.
Courtaud, J.M.
Dhir, V.K.
DiMarzo, M.
Dorning, Jr. , J.J.
Eltawila, F.
Frid, W.
Golay, M.W.
Grand, D.
Groeneveld, D.C.
Hassan, Y.A.
Hodge, S.
Hochreiter, L.
Ishii, M.
Karwat, H.
Kojasoy, G.
Krishnan, V.S.
Kurul, N.
Larson, T.K.
Lemmonier, H.
March-Leuba, J.
McMullan, D.
Merilo, M.
Modro, M.
Moody, F.
Nariai, H.
Ninokata, H.
Nylund, O.
Peterson, P.F.
Pilch, M.M.
Ransom, V.H.
Rehme, I.K.
Rouhani, Z.
Rowe, D.S.
Serizawa, A.
Shotkin, L.
Sreepada, S.
Taleyarkhan, R.
Theofanous, T.G.
Todreas, N. E.
Weisman, J.
Wilson, G.
Wright, R.W.
Wulff, W.
Yadigaroglu, G.
Yin, S. T.
Yoder, G. L.

TABLE OF CONTENTS

VOLUME I

VOLUME III

Session 12 - FUEL/COOLANT INTERACTION

VOLUME IV

Session 17 - CHF MODELING AND PREDICTIONS

Session 18 - THERMAL-HYDRAULIC COUPLING IN REACTOR SYSTEMS

Session 19 - SUBCHANNEL THERMAL-HYDRAULICS

Session 20 - THERMAL-HYDRAULICS OF REACTOR SYSTEMS AND COMPONENTS

Session 21 - THERMAL-HYDRAULICS TEST FACILITIES

Session 22 - THERMAL-HYDRAULICS AND SAFETY OF NONCOMMERCIAL REACTORS

* Paper assigned to Session 14 in the Conference Program
** Paper assigned to Session 11-3 in the Conference Program

PREFACE

Welcome to Saratoga Springs, the place of the first of the NURETH meetings, held in 1980. Since this first meeting, the NURETH series have included: Santa Barbara, California in 1983, Newport, Rhode Island in 1985, Karlsruhe, Germany in 1989, Salt Lake City, Utah in 1992 and Grenoble, France in 1993. Now, after fifteen years, the seventh of the NURETH meetings is being held again in the birth place of the series.

As you probable know, the NURETH meetings have been initiated and sponsored or co-sponsored by the Thermal-Hydraulics Division of the American Nuclear Society. The TH Division has clearly become a leader in establishing and maintaining high technical standards regarding topical meetings in the field of nuclear thermal-hydraulics, paper acceptance criteria for such meetings, and promoting international cooperation and exchange. In particular, the papers accepted for presentation at NURETH-7 and published in these volumes have been thoroughly reviewed by leading experts in their respective fields. Their work, as well as the efforts of the session organizers, are the cornerstones of the high technical quality of this meeting.

The present conference has been organized by the Northeastern New York Section of the American Nuclear Society. In addition, the following organizations have agreed to join the ANS Thermal Hydraulics Division as co-sponsors of NURETH-7: American Institute of Chemical Engineers (AIChE), American Society of Mechanical Engineers (ASME), Canadian Nuclear Society (CNS), European Nuclear Society (ENS), Japanese Nuclear Society (JNS), Japanese Society of Multiphase Flow (JSMF) and the U.S. Nuclear Regulatory Commission.

Except for the invited papers in the plenary session, all the other papers are contributed. They have been divided into twenty-four major topics. These topics cover all major areas of nuclear thermal-hydraulics.

The theme of the NURETH-7 conference is ***Thermal-Hydraulics for the 21st Century.*** This theme has been implemented in the program of the meeting through technical papers covering areas such as: progress in analytical and experimental work on the fundamentals of nuclear thermal-hydraulics, the development of advanced mathematical and numerical methods, and the application of advancements in the field in the development of novel reactor concepts. Because of the complex nature of nuclear reactors and power plants, several papers deal with the combined issues of thermal-hydraulics and reactor/power-plant safety, core neutronics and/or radiation.

I hope that both the conference participants and other future readers of this multi-volume edition of NURETH-7 Proceedings will find several new and innovative ideas as the results of the work by the authors representing an outstanding international community of experts from academia and industry.

On behalf of the organizing committee I invite you to actively participate in the conference and wish you a pleasant stay in Saratoga Springs.

Michael Z. Podowski
Technical Program Chairman

ACKNOWLEDGMENTS

The efforts of the authors of both invited and contributed papers included in this volume are gratefully acknowledged. Also acknowledged is the cooperation of the members of the Technical Program Committee and the Scientific Advisory Committee who helped to organize the technical program of the meeting and accomplish its scientific objectives. Special thanks are extended to the session organizers and paper reviewers.

Finally, appreciation is expressed to the U.S. Nuclear Regulatory Commission for their support of the publication of the Proceedings.

The Sudden Coalescence Model of the Boiling Crisis

P. M. Carrica and A. Clausse
Centro Atómico Bariloche and Instituto Balseiro
(8400) Bariloche – Argentina

Abstract

A local two–phase flow integral model of nucleate boiling and crisis is presented. The model is based on averaged balances on a control volume, yielding to a set of three nonlinear differential equations for the local void fraction, bubble number density and velocity. Boiling crisis at critical heat flux is interpreted as a dynamic transition caused by the coalescence of bubbles near the heater. The theoretical dynamic model is compared with experimental results obtained for linear power ramps in a horizontal plate heater in R–113, showing an excellent qualitative agreement.

Introduction

Boiling heat transfer is widely used in engineering applications. In nuclear power plants, local subcooled and saturated boiling are present in PWR and BWR cores and steam generators during normal operation, and in many accidental situations.

Boiling physics have been extensively studied since the pioneer work of Leidenfrost [1]. The first complete boiling curve was obtained by Nukiyama [2] and very soon researchers realized the importance of the boiling heat transfer crises. However, the comprehension of the processes involved in boiling heat transfer and crises is still today one of the most challenging problems in heat transfer technology. Despite the considerable effort devoted to this concern, many questions remain unanswered. As Lienhard [3] has pointed out, it has not been possible to derive a complete theory from first principles to predict the relation between heat flux and wall temperature for a given geometry.

The problem of the first boiling crisis or critical heat flux was always treated as a phenomenon independent of the nucleate boiling process, and almost nothing is known about their interrelation. Some authors have proposed different models that attempt to explain the critical heat flux in pool boiling. The main postulated models are:

- *Bubble coalescence*: First proposed by Rohsenow [4], this model postulates that vapor film is caused by the bubbles coalescence when bubble density increases with heat flux. Recently, breakup and coalescence models based on modern system dynamics have been presented [5].

- *Hydrodynamic theory*: Ascending bubbles coalesce in vapor jets that become unstable as the heat flux increases. When the structure collapses the vapor film covers the surface of the heater. This model was proposed by Zuber [6] and widely studied for diverse geometries and conditions [7]. The correlation obtained by Zuber is very similar to that obtained by Kutateladze [8] based on a dimensional analysis.

- *Macrolayer model*: Haramura & Katto [9] developed this model. A thin liquid layer (the macrolayer) is perforated by vapor jets and placed underneath large bubbles (vapor mushrooms). Each mushroom is fed by many vapor jets. The critical heat flux occurs when the liquid macrolayer dries out before the departure of the bubble and liquid renewal take place.

To the present, it is not clear if one or a combination of these mechanisms determine the occurrence of boiling crisis. Several investigations have been conducted to verify the hypotheses of the different models. In this direction, observations and measurements of the two–phase flow field near the heated wall have been performed in recent years. Liaw & Dhir [10] measured the void fraction along a line near a vertical plane heater in saturated water using the gamma ray attenuation technique. They observed a maximum in the void fraction near the heated wall for high heat fluxes. Bonetto et al [11] measured similar trends using local phase detection with a hot–wire anemometer over a horizontal heater immersed in saturated FC–72 refrigerant. For horizontal heaters in saturated water the same trend was measured by Shoji [12]. It has been observed that the peak in the void fraction becomes closer to the heated wall as the heat flux increases [13]. These experimental observations support the models of coalescence and macrolayer, while the hydrodynamic model would be more consistent with uniform void fraction distributions near the heater.

The knowledge of the two–phase flow parameters near the heated walls is also important in nuclear industry due to the effect of vapor distribution in neutron moderation and consequently in fission rate. This effect could be important in very compact reactors were the pitch is a few milimeters, comparable with the size of the region near the wall were the void fraction changes appreciably.

In this work a hydrodynamic model of boiling and crisis is presented. The model is based on integral momentum, energy and interfacial area density balances in a small control volume near the heated walls. The complete model is formulated in terms of three ordinary differential equations for the temporal evolution of the void fraction, number density and vapor bubble velocity. The theoretical model is compared with experimental data of void fraction and interfacial impact rate measured during power oscillations in a small horizontal heater immersed in stagnant freon R–113 at atmospheric pressure.

The model shows the same trend as the experimental data: a sudden jump to a higher void fraction is observed when the transition to film boiling occurs. The interfacial impact rate, on the other hand, experiences a pronounced drop. The transition is basically interpreted as a consequence of the sudden coalescence of all the bubbles, which causes a drastic reduction of the interfacial area in the control volume. The final state with low interfacial area density can be associated to the film boiling regime.

Boiling model

Let us assume the existence of a bubble population function $f(v)$ [14], defined as the number of bubbles per unit volume, containing gas volume between v and $v + dv$. The

number density, void fraction and interfacial area density are related to the bubble population function as:

$$n = \int_0^\infty f(v)\,dv \tag{1a}$$

$$\alpha = \int_0^\infty f(v)\,v\,dv \tag{1b}$$

$$a_i = \int_0^\infty f(v)\,a_i(v)\,dv \tag{1c}$$

where a bubble area corresponds to each bubble volume. The average bubble volume is:

$$\overline{v} = \frac{\int_0^\infty f(v)\,v\,dv}{\int_0^\infty f(v)\,dv} \tag{2}$$

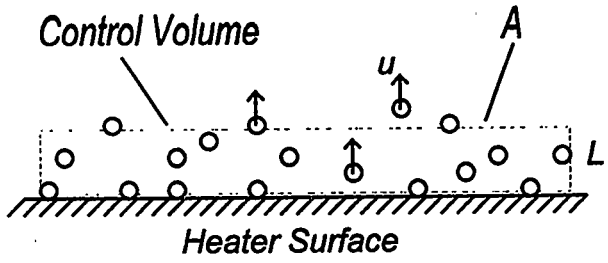

Figure 1: Diagram of the control volume and the boiling process

Let us consider a small horizontal heater providing a heat flux q'' to a pool of liquid at saturation temperature (Fig. 1). A control volume (CV) of height L is defined on top of the heated wall. The two–phase flow variables are averaged in the CV [15,16]. The following simplificative hypothesis are assumed:

- The bubbles are spherical.
- The bubbles inside the CV are identical with a volume V_b . This volume is the average volume of all the bubbles inside the CV.
- The bubble distribution is locally homogeneous, so the spatial average is valid.
- The bubble velocity is calculated as the velocity of a bubble with volume V_b .
- The heater thermal inertia is negligible.

Then the CV contains n identical bubbles per unit volume, and the void fraction, the interfacial area density and the volume of the bubbles are related by:

$$\alpha = nV_b \tag{3a}$$

$$a_i = 4\pi r_b^2 n \tag{3b}$$

$$V_b = 4/3\pi r_b^3 \tag{3c}$$

where r_b is the bubble radius.

The objective of the analysis is to find a relation between the average two–phase flow parameters in the local CV and the heat flux. The starting point are the momentum, mass and energy balances in the CV.

Vapor momentum balance

The balance of forces over a rising bubble is given by:

$$\rho_g V_b \frac{du}{dt} = g(\rho_l - \rho_g)V_b - \frac{1}{2}C_d \rho_l u^2(\pi r_b^2) - \frac{1}{2}\rho_l V_b \frac{du}{dt} \tag{4}$$

where, from left to right, the inertia, buoyancy, drag and virtual mass terms are written. The virtual mass term in vapor–liquid mixtures is discussed by Drew et al [17] and Biesheuvel & Spolestra [18].

Neglecting gas density ρ_g, compared to liquid density ρ_l, yields:

$$\frac{du}{dt} = 2g - \frac{\pi C_d u^2 r_b^2}{V_b} \tag{5}$$

combining Eqs. (3) and (5) gives

$$\frac{du}{dt} = 2g - \frac{C_d u^2 a_i}{4\alpha} \tag{6}$$

The drag coefficient C_d is calculated from the terminal velocity of the bubbles, assuming the same drag coefficient for any bubble velocity:

$$C_d = \frac{8g\alpha}{u_\infty^2 a_i} \tag{7}$$

Following Zuber & Findlay [19], the terminal velocity of bubbles can be calculated as:

$$u_\infty = C_0 j + v_\infty \tag{8}$$

where $j = u_\infty \alpha$ is the vapor superficial velocity, v_∞ is the terminal velocity of bubbles in a stagnant liquid with no gas stream (j=0) and C_0 is the spatial flow distribution parameter, which is 1 for the case of flows without spatial restrictions. The terminal velocity v_∞ is calculated from the terminal velocity of isolated bubbles $v_{\infty,i}$, corrected for the effect of void fraction [20]:

$$v_\infty = (1-\alpha) v_{\infty,i} \tag{9}$$

Combining Eqs. (8) and (9) yields:

$$u_\infty = \frac{v_\infty}{1-\alpha} = v_{\infty,i} \tag{10}$$

Eq. (10) implies that the terminal velocity of the bubbles in the CV, u_∞, is the same as the terminal velocity of isolated bubbles in a stagnant liquid $v_{\infty,i}$. The terminal velocity of the bubbles of radius r_b is then calculated using the correlations of Pebbles & Garber [21] for isolated bubbles. The drag coefficient is obtained combining Eqs. (3), (7) and (10):

$$C_d = \frac{8 g r_b}{3 v_{\infty,i}} \tag{11}$$

Vapor mass balance

The vapor mass balance in the CV can be written as:

$$\rho_g L A \frac{d\alpha}{dt} + \alpha u \rho_g A = \Gamma \tag{12}$$

where Γ is the evaporation rate inside the CV. Here the donor cell model was used, according to the hypothesis of homogeneous bubble distribution in the CV. Even when the void fraction is not constant near the wall [12,13], the differences due to this can be absorbed by the adjustable constants of the model.

Energy balance

The heat flux generated by the heater is partitioned in heat that produce vapor inside the CV and the rest which is transported by Marangoni effect, microconvection or any other mechanisms that do not produce vapor in the CV. Then the total heat flux is written as:

$$q'' A = \Gamma h_{fg} + q_{nv} \tag{13}$$

In Eq. (13) the subscript "*nv*" in the second term stands for "no vapor", and is the heat that does not produce vapor inside the CV. The modelling of q_{nv} is quite complex, and

to the present is a subject of investigation. For the purpose of the present analysis a simple model will be postulated based on logical conjectures about the physical mechanisms influencing q_{nv}. Since the different heat transfer mechanisms in the presence of bubbles without evaporation are directly related to the interfacial area density, it is postulated that in steady state we can write:

$$dq_{nv} = q_v \, k \, da_i \tag{14}$$

where q_v is the heat that generates vapor inside the CV and k is a constant coefficient. Considering that the relaxation time of the heat partition is much shorter than the remaining process we can write:

$$dq = dq_v + dq_{nv} = 0 \tag{15}$$

where q is the total heat generated by the heater. Combining Eqs. (14) and (15) gives:

$$\int_{q(1-\alpha)}^{q_v} \frac{dq_v}{q_v} = -\int_0^{a_i} k \, da_i \tag{16}$$

Notice that $q(1-\alpha)$ is the maximum amount of heat that can be used to generate vapor inside the CV, corresponding to the case when the mechanisms of microconvection, Marangoni, etc. are negligible. Combining Eqs. (13) and (16) yields:

$$\Gamma = \frac{(1-\alpha) q'' A \exp(-k a_i)}{h_{fg}} \tag{17}$$

finally, from Ecs. (12) and (17) results:

$$L \frac{d\alpha}{dt} = \frac{(1-\alpha) q'' \exp(-k a_i)}{\rho_g h_{fg}} - u\alpha \tag{18}$$

Eq. (18) will be considered valid also in the transient case, assuming that the relaxation time in the partition (15) is fast enough.

Interfacial area density

There are some correlations for the interfacial area density that where developed for small void fractions [22,23]. Recently it was suggested the idea of a conservation equation for a_i based in mechanistic models including the bubble breakup and coalescence dynamics [24]. Considering the process of bubble generation, breakup and coalescence, it is convenient to derive a conservation equation for the bubble number density n and from this calculate a_i.

The balance of bubbles in the CV is given by:

$$L A \frac{dn}{dt} = S A + \beta - \zeta - un A \tag{19}$$

where S is the bubble generation in the CV, β is the breakup source term, ζ is the loss by coalescence and the last term accounts for the leakage of bubbles through the CV surface.

The bubble source S has volumetric and superficial components [24]. Generally, S can be written as:

$$S = \phi_{ho} + \phi_{he} + \phi_c \tag{20}$$

where ϕ_{ho} and ϕ_{he} are respectively the homogeneous and heterogeneous nucleation in the liquid bulk and ϕ_c is the nucleation in the cavities in the surface of the heater. Normally the overheating present in boiling with metallic heated walls is small enough to neglect ϕ_{ho} and ϕ_{he} compared to ϕ_c [25]. Assuming that all the bubbles are generated with the same size, S results:

$$S = \frac{q_v}{A \rho_g h_{fg} V_d} \tag{21}$$

In Eq. (21) the detachment volume V_d is generally a function of the heat flux. The departure size of the bubbles depends also on surface and fluid properties, such as nucleation site density and size, contact angle, etc. [26]. Assuming that the departure frequency is constant, the dependence of V_d with the heat flux can be calculated from the dependence of the nucleation site density with the heat flux.

There is no agreement respect to the dependence of nucleation site density with heat flux in nucleate boiling. From the experiments of Zeng & Klausner [27], the nucleation site density can be written as:

$$N'' = c_1 q''^{l} \tag{22}$$

where N'' is the nucleation site density, c_1 is a constant and l varies between 1.5 and 2. Staniszewski [28] reported a value for l of about 1 and Sgheiza & Myers [29] give for l a value lower than 1. For the sake of simplicity, l will be considered here as 1, what implies that the departure size is independent of heat flux.

In two–phase flow, the turbulent coalescence kernel is assumed [30]. From this hypothesis, the coalescence term can be written as:

$$\zeta = c V_b n^2 \tag{23}$$

where c is a constant coefficient to be determined. The same equation can be obtained using the dilute media hypothesis [31].

The breakup term is modeled assuming that no breakup is possible for bubble size smaller than a critical volume V_c, while for larger bubbles breakup is more likely to occur [32]. This trend can be expressed as:

$$\beta = b\,n\,H(V_b - V_c) \tag{24}$$

and for numerical calculations the Heavyside function is approximated with:

$$H(V_b - V_c) = \frac{V_b^m}{V_b^m + V_c^m} \tag{25}$$

where m is an integer greater than 1. The critical volume is calculated following the model of Hinze [33] applied for gravity driven flows. The critical Weber number results:

$$We_c = \frac{4 r_c^2\, g\, \rho_l}{\sigma} \cong 1 \tag{26}$$

Combining Ecs. (3), (19), (21), (24) and (25) we obtain:

$$\frac{dn}{dt} = \frac{q_v}{\rho_g\, h_{fg}\, A\, L V_d} + \frac{b\,n\,\alpha^m}{\alpha^m + V_c^m\, n^m} - c\,\alpha\,n - \frac{u\,n}{L} \tag{27}$$

and combining with Eq. (18) yields:

$$\frac{dn}{dt} = \frac{1}{V_d}\frac{d\alpha}{dt} + \frac{u\,\alpha}{L}\left(\frac{1}{V_d} - \frac{1}{V_b}\right) + \frac{b\,n\,\alpha^m}{\alpha^m + V_c^m\, n^m} - c\,\alpha\,n \tag{28}$$

Dimensionless equations

Ecs. (6), (18) and (28) form a system of three ordinary differential equations which describes the dynamic of the averaged local two–phase flow variables (u, α, n) in the boiling region. The dimensionless form of these equations is:

$$\frac{d\hat{u}}{d\hat{t}} = 2 - \frac{\hat{D}\,\hat{u}^2\,\hat{a}_i}{\alpha} \tag{29a}$$

$$\hat{L}\frac{d\alpha}{d\hat{t}} = (1-\alpha)\,\hat{q}''' \exp\left(-\hat{M}\,\hat{a}_i\right) - \hat{u}\,\alpha \tag{29b}$$

$$\frac{d\hat{n}}{d\hat{t}} = \frac{1}{V_d}\frac{d\alpha}{d\hat{t}} + \frac{\hat{u}\,\alpha}{\hat{L}}\left(\frac{1}{\hat{V}_d} - \frac{1}{\hat{V}_b}\right) + \hat{C}\,\hat{n}\,\alpha\left(\frac{\hat{\alpha}_0\,\alpha^{m-1}}{\alpha^m + \hat{n}^m} - 1\right) \tag{29c}$$

where the dimensionless variables are defined as:

$$\hat{u} = \frac{u}{g^{1/2} V_c^{1/6}} \tag{30a}$$

$$\hat{n} = n V_c \tag{30b}$$

$$\hat{a}_i = a_i V_c^{1/3} \tag{30c}$$

$$\hat{t} = \frac{t g^{1/2}}{V_c^{1/6}} \tag{30d}$$

$$\hat{V}_b = \frac{V_b}{V_c} \tag{30e}$$

$$\hat{D} = \frac{C_d}{4} \tag{30f}$$

In Ecs. (29) the following dimensionless groups are introduced:

$$\hat{V}_d = \frac{V_d}{V_c} \quad \text{Dimensionless departure volume} \tag{31a}$$

$$\hat{M} = \frac{k}{V_c^{1/3}} \quad \text{Heat removal number} \tag{31b}$$

$$\hat{L} = \frac{L}{V_c^{1/3}} \quad \text{Dimensionless CV height} \tag{31c}$$

$$\hat{q}'' = \frac{q''}{\rho_g h_{fg} g^{1/2} V_c^{1/6}} \quad \text{Dimensionless heat flux} \tag{31d}$$

$$\hat{C} = \frac{c V_c^{1/6}}{g^{1/2}} \quad \text{Coalescence number} \tag{31e}$$

$$\alpha_0 = \frac{b}{c} \quad \text{Coalescence to breakup number} \tag{31f}$$

Model solutions and critical heat flux

Steady state solutions

The steady state solutions of Eqs. (29), $(\hat{u}_s, \alpha_s, \hat{n}_s)$, can be found by making zero the temporal derivatives of α, $\hat{n}$ and $\hat{u}$, which gives:

$$2\alpha_s = \hat{D}\hat{u}_s^2\,\hat{a}_{i,s} \tag{32a}$$

$$(1-\alpha_s)\hat{q}''\exp\left(-\hat{M}\,\hat{a}_{i,s}\right) = \hat{u}_s\,\alpha_s \tag{32b}$$

$$\hat{C}\alpha_s\hat{n}_s\left(1-\frac{\hat{\alpha}_0\,\alpha_s^{m-1}}{\alpha_s^m+\hat{n}_s^m}\right) = \frac{\hat{u}_s\,\alpha_s}{\hat{L}}\left(\frac{1}{\hat{V}_d}-\frac{1}{\hat{V}_b}\right) \tag{32c}$$

Combining Eqs. (32a) and (32b) yields:

$$\frac{\alpha_s}{(1-\alpha_s)^{2/3}} = \left(\frac{\hat{D}}{2}\right)^{1/3}\hat{a}_{i,s}^{1/3}\,\hat{q}''^{2/3}\exp\left(-\frac{2}{3}\hat{M}\,\hat{a}_{i,s}\right) \tag{33a}$$

and from Eqs. (32a) and (32c) results:

$$\hat{C}\alpha_s\hat{n}_s\left(1-\frac{\hat{\alpha}_0\,\alpha_s^{m-1}}{\alpha_s^m+\hat{n}_s^m}\right) = \frac{2^{1/2}\,\alpha_s^{7/6}}{(36\pi\hat{n}_s)^{1/6}\,\hat{L}\,\hat{D}^{1/2}}\left(\frac{1}{\hat{V}_d}-\frac{\hat{n}_s}{\alpha_s}\right) \tag{33b}$$

where $\hat{D}$ is a function of the bubble volume.

In order to compare the model with experimental data, the solutions will be presented in terms of the void fraction and interfacial impact rate (i. e., the number of interfaces intersecting the tip of a local phase detection probe per unit time). The interfacial impact rate can be related to the model variables as [34]:

$$f_i = \frac{u a_i}{2} \tag{34}$$

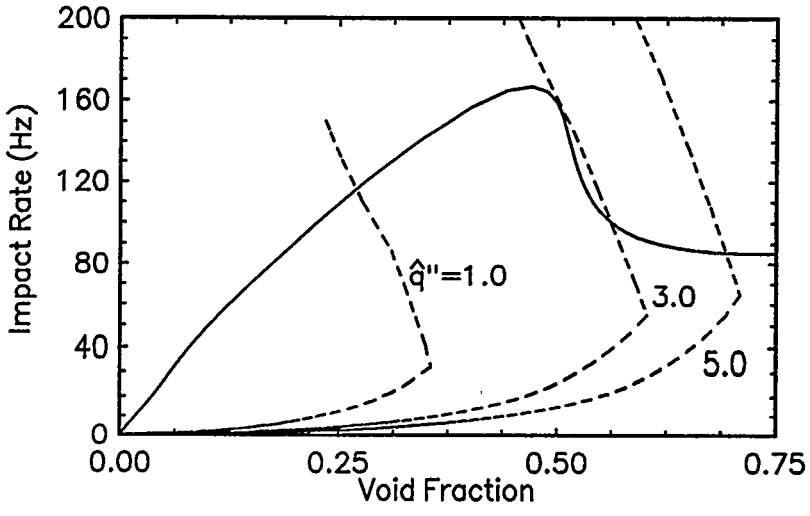

Figure 2: Steady state solutions of the model, Eqs. (33)

The steady state solutions of the model in the (α, f_i) plane are shown in Fig. 2. In order to show the behavior of the model with realistic values, the constants were calculated to represent the conditions of an experimental study on freon R–11 at atmospheric pressure [35]. The corresponding parameters are shown in Table 1. The dashed curves correspond to the solutions of Eq. (33a) for different dimensionless heat fluxes, and the full line correspond to Eq. (33b). The intersections of the curves give the values of void fraction and impact rate for a given heat flux. At low heat fluxes (see $\hat{q}'' = 1$) there is only one solution, and the void fraction and impact rate increase with heat flux. When the heat fluxes are larger than $\hat{q}'' = 3$ the system jumps to another set of solutions with lower impact rate. These two stable sets of solutions can be interpreted as the nucleate boiling and film boiling regimes, while the heat flux correspondent to the transition is associated to the critical heat flux.

$\hat{\alpha}_0$	$\hat{M}$	$\hat{C}\,\hat{L}$	L
0.3	0.3	500	2.5 *mm*

Table 1: Model parameters for Freon R–11.

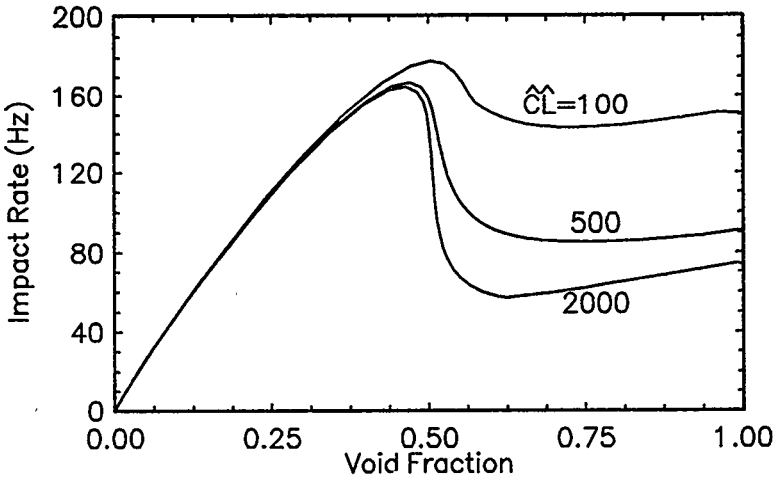

Figure 3: Effect of coalescence in Eq. (33b)

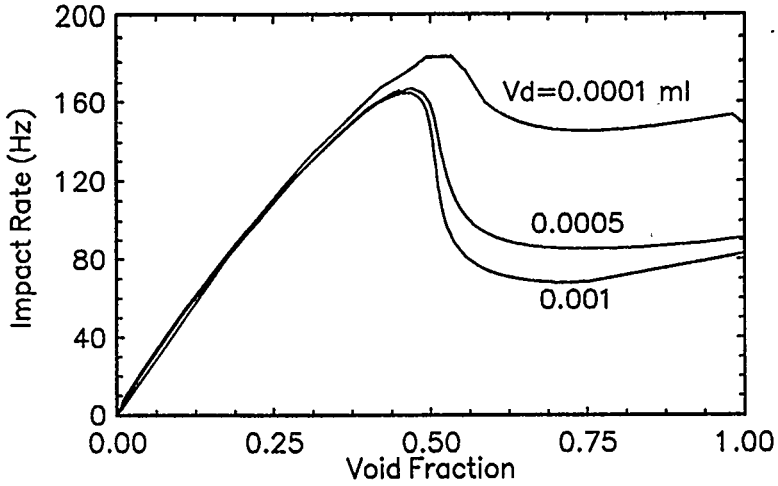

Figure 4: Effect of detachment volume in Eq. (33b)

Fig. 3 shows a parametric study of Ec. (33b) for freon R–11 with different values of $\hat{C}\,\hat{L}$. The detachment size was 0.0005 cm^3. The maximum of the curve (associated with the critical heat flux) decreases when the coalescence rate increases. Fig. 4 shows the effect of the detachment volume.

Critical heat flux relations

Ecs. (33) represent the steady state of the boiling model. The point at which these equations are tangent in the plane (α, f_i) corresponds to the critical heat flux. With some additional hypothesis it is possible to derive an analytical expression for the critical heat flux:

- The drag number value is $\hat{D} = 2/3$.
- The bubble volume at critical heat flux is $\hat{V}_b = 1$. This means that there is no breakup in the CV until critical heat flux occurs. It can be shown that this condition holds exactly when $m \to \infty$ (i. e., a Heavyside breakup probability function is assumed).

Using these conditions on Eq. (33b) yields:

$$\alpha_{chf} = \hat{\alpha}_0 + \frac{1}{\hat{\eta}}\left(\frac{1}{\hat{V}_d} - 1\right) \tag{35}$$

where the dimensionless constant $\hat{\eta}$ is proportional to the bubble coalescence number:

$$\hat{\eta} = \left(\frac{4\pi}{3}\right)^{1/6} \hat{L}\hat{C} \tag{36}$$

Combining Eqs. (3) and (30) for $\hat{V}_b = 1$ gives:

$$\hat{a}_{i,chf} = (36\pi)^{1/3}\alpha_{chf} \tag{37}$$

Combining Eqs. (37) and (33a) yields:

$$\hat{q}''_{chf} = \left(\frac{3}{4\pi}\right)^{1/6} \frac{\alpha_{chf}}{1-\alpha_{chf}} \exp\left[(36\pi)^{1/3}\hat{M}\alpha_{chf}\right] \tag{38}$$

Eq. (38) can be written in dimensional form resulting in the final relation for the critical heat flux:

$$q''_{chf} = \frac{\sqrt{2}}{2}\rho_g h_{fg}\left(\frac{g\sigma}{\rho_l}\right)^{1/4} \frac{\alpha_{chf}}{1-\alpha_{chf}} \exp\left[(36\pi)^{1/3}\hat{M}\alpha_{chf}\right] \tag{39}$$

where Eq. (35) gives the value of the void fraction at critical heat flux α_{chf}.

Eq. (39) predicts that critical heat flux must increase, in a given fluid, when α_{chf} increases. Eq. (35) shows that α_{chf} increases when the detachment volume and the coalescence rate decrease. The detachment volume can be reduced on a given fluid decreasing the contact angle between the bubbles and the heater surface. Liaw & Dhir [36] measured the relation between contact angle and critical heat flux, finding that critical heat flux increases when contact angle decreases. The same trend shows the model considering that the detachment volume decreases with the contact angle.

Eq. (39) reveals the importance of the heat that leaves the CV without producing vapor, represented by the parameter $\hat{M}$. When $\hat{M}$ increases, the critical heat flux increases. Unfortunately, at the present neither the coalescence number nor the heat removal number can be evaluated from first principles. Additional research on the subject is necessary, considering the importance of the role that these mechanisms play in the critical heat flux determination.

Comparison with experimental data

The theory is compared with experimental data of void fraction and interfacial impact rate measured during power oscillations in a small horizontal heater immersed in stagnant freon R–113 at atmospheric pressure. The heater was a thin laminated platinum foil of $5mm$ x $10mm$ x 25 μm attached to a mica substrate for downward thermal insulation. The use of a very thin heater was mandatory due to thermal inertia requirements and other experimental restrictions. The indicator function was recorded with a specifically designed high velocity acquisition card, and a sapphire optical probe located over the heater was used to detect the presence of vapor. An ensemble average method over a large number of cycles was used to obtain the temporal variation of the void fraction and interfacial impact rate. For more details related to the experimental procedure see reference [35].

The power oscillations were a triangular wave in which each period lasts 20 s following the law:

$$q''(t)\left[W/cm^2\right]=\begin{cases}30t/10 & 10\geq t\geq 0\,s\\ 60-30\ t/10 & 20\geq t\geq 10\,s\end{cases} \qquad (40)$$

The adjusted constants and model parameters used for freon R–113 are given in Table 2. L is chosen as the value at which the void fraction and impact rate were measured.

$\hat{C}\,\hat{L}$	$L(mm)$	$V_c\left(cm^3\right)$	$V_d\left(cm^3\right)$	$\hat{\alpha}_0$	$\hat{q}''_{chf}$
1000	2.5	0.0007	0.0005	0.24	2.57

Table 2: Model parameters for Freon R–113.

V_c was calculated using Eq. (26) and V_d was estimated after video recording observations of boiling R–113. $\hat{\alpha}_0$, $\hat{M}$ and $\hat{C}\hat{L}$ were adjusted to fit the experimental data. $\hat{\alpha}_0$ was adjusted to fit the void fraction at CHF and $\hat{M}$ and $\hat{C}\hat{L}$ were tuned to reproduce the experimental CHF/Leidenfrost ratio and temporal response respectively.

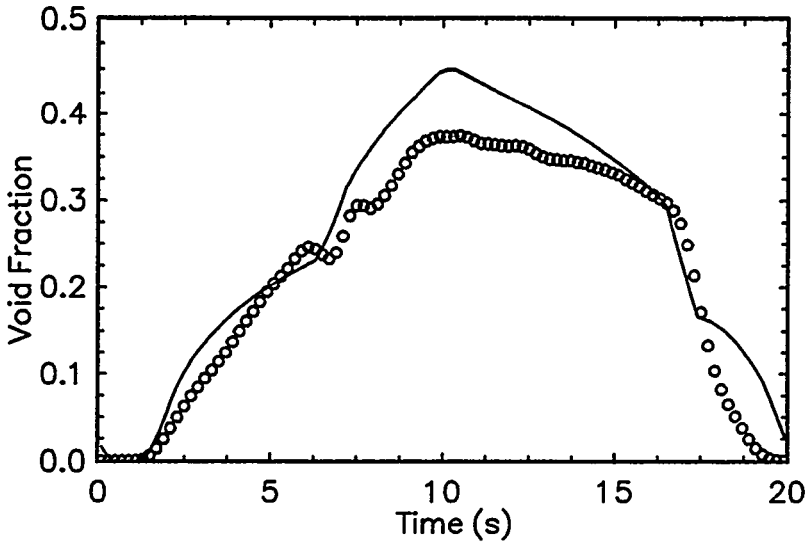

Figure 5: Comparison of the void fraction experimental data (circles) with the model (full line).

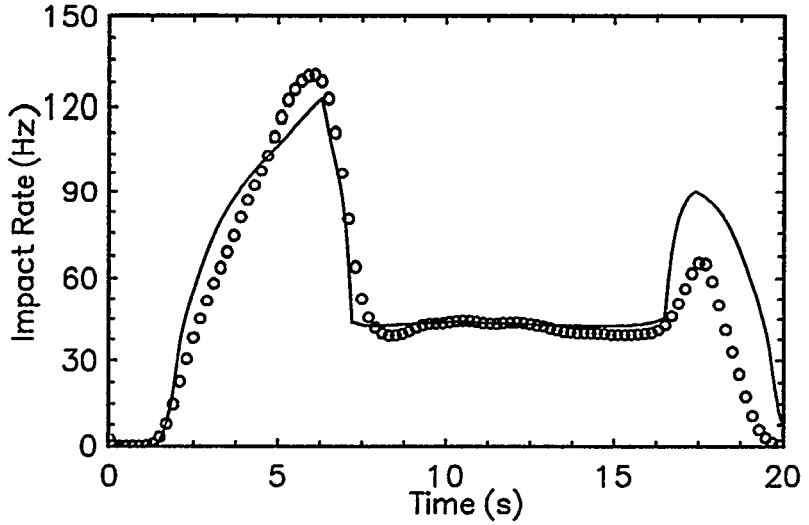

Figure 6: Comparison of the impact rate experimental data (circles) with the model (full line).

Eqs. (29) were solved numerically imposing a forcing function as defined in Eq. (40). Figure 5 shows a comparison of the void fraction experimental data with the model results. Good qualitative agreement is observed. The void fraction in film boiling is higher than in nucleate boiling, as verified experimentally. In Fig. 6 the impact rate experimental data and the model results are shown. The interfacial impact rate falls abruptly after the first boiling crisis and then increases slightly in film boiling while increasing the heat flux. In the second boiling crisis the impact rate increases yielding the second peak.

In Fig. 7 the complete cycle is shown in a three dimensional phase–space plot, where the simultaneous void fraction and the impact rate corresponding to each power level (proportional to the square of the electrical current) can be observed.

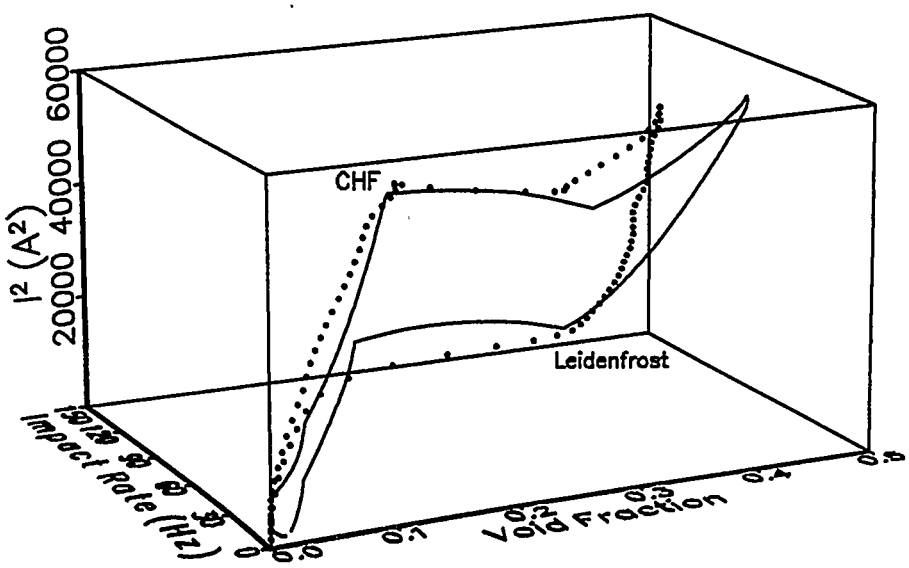

Figure 7: Comparison of the experimental data (circles) with the model (full line) in the void fraction – impact rate – I^2 space for R–113.

Conclusions

A theoretical model of boiling and crisis was presented. The differential equations governing the local boiling field state naturally undergo a sudden transition caused by the massive coalescence of bubbles in the region close to the heated wall. An analytical expression for the critical heat flux as a function of the model parameters was derived. The model predicts that the critical heat flux can be increased either reducing the coalescence rate close to the heated wall ($\hat{C}$), reducing the bubble detachment volume ($\hat{V}_d$), or increasing the sensible heat removal number ($\hat{M}$). The first two reduce the probability of coalescence delaying the crisis, while the third reduces vaporization near the wall.

The model was compared with experimental data of void fraction and interfacial impact rate during power oscillations in R–113. The comparison results in a good qualitative agreement.

Bibliography

[1] J. G. Leidenfrost, "On the fixation of water in diverse fire", translated by C. Wares, Int. J. Heat Mass Transfer 9, 1153–1166 (1966)

[2] S. Nukiyama, "Maximum and minimum values of heat transfer from metal to boiling water under atmospheric pressure", J. Soc. Mech. Eng. Japan 37, 367–374 (1934), Also reprinted in Int. J. Heat Mass Transfer 9, 367–374 (1966)

[3] J. Lienhard, "Things we don't know about boiling heat transfer", Int. Comm. Heat and Mass Transfer 15, 401–428 (1988)

[4] W. M. Rohsenow, "A method of correlating heat transfer data for surface boiling of liquids", Trans. ASME 74, 969–975 (1952)

[5] P. M. Carrica & A. Clausse "A model of boiling nonlinear dynamics and crisis", Latin American Applied Research 24, 77–87 (1994)

[6] N. Zuber, "On the stability of boiling heat transfer", ASME J. Heat Transfer 80, 711–720 (1958)

[7] J. Lienhard & L. Witte, "An Historical Review of the Hydrodynamic Theory of Boiling", Reviews in Chemical Engineering 3, 187–280 (1985)

[9] S. S. Kutateladze, "On the transition to film boiling under natural convection", Kotlo–turbostoenie 3, 10 (1948)

[9] Y. Haramura & Y. Katto, "A new hydrodynamic model of critical heat flux applicable widely to both pool and forced convection boiling on submerged bodies in saturated liquids", Int. J. Heat and Mass Transfer 26, 389–399 (1983)

[10] S. P. Liaw & V. K. Dhir, "Void fraction measurements during saturated pool boiling on partially wetted vertical surfaces", ASME J. Heat Transfer 111, 731–738 (1989)

[11] F. Bonetto, A. Clausse & J. Converti, "Two–phase flow in the localized field adjacent to a heated wall", Int. J. Heat Mass Transfer 36, 1367 (1993)

[12] M. Shoji, "Experimental Verification of Macrolayer Evaporation Model", on *Pool and External Flow Boiling*, V. K. Dhir & A. E. Bergles Editors, Engineering Foundation ASME, NYC (1992)

[13] P. M. Carrica, F. Moraga & A. Clausse, "Measurements of void fraction spatial distributions in pool boiling", Int. Comm. Heat Mass Transfer 19, 499–505 (1992)

[14] G. Guido Lavalle, "Formulación estadística de flujos bifásicos: teoría y experimentos", PHD Thesis, Instituto Balseiro, Argentina (1992)

[15] J. M. Delhaye, "Equations fondamentales des écoulements diphasiques", parts 1 and 2, CEA–R–3429, Centre d'Etudes Nucléaires de Grenoble, France (1968)

[16] M. Ishii, Thermo–fluid dynamic theory of two–phase flow, Eyrolles, Paris (1975)

[17] D. Drew, L. Cheng & R. T. Lahey, "The analysis of virtual mass effects in two–phase flow", Int. J. Multiphase Flow 5, 233–242 (1979)

[18] A. Biesheuvel & S. Spolestra, "The added mass coefficient of a dispersion of spherical gas bubbles in liquid", Int. J. Multiphase Flow 15, 911–924 (1989)

[19] N. Zuber & J. A. Findlay, "Average volumetric concentration in two–phase systems", ASME J. Heat Transfer 87, 453 (1965)

[20] G. B. Wallis, One Dimensional Two-Phase Flow, McGraw–Hill book Company, NYC, p. 253 (1969)

[21] See citation to F. N. Peebles & H. J. Garber in [20], p. 250

[22] A. Serizawa & I. Kataoka, "Phase distribution in two-phase flow", Proc. Int. Conf. Heat Mass Transfer, Dubrovnik, Yugoslavia (1987)

[23] I. Kataoka & A. Serizawa, "Interfacial area and nucleation in bubbly flows", Nucl. Eng. Des. 120, 163 (1990)

[24] G. Kocamustafaogullari & M. Ishii, "Interfacial area and nucleation site density in boiling systems", Int. J. Heat Mass Transfer 26, 1377–1387 (1983)

[25] R. Cole, "Nucleation", Boiling Phenomena, S. Van Stralen & R. Cole editors, Hemisphere Publishing Corporation, NYC, 71–151 (1979)

[26] A. K. Chesters, "Bubble sizes in nucleate pool boiling", Boiling Phenomena, S. Van Stralen & R. Cole editors, Hemisphere Publishing Corporation, NYC, 879–901 (1979)

[27] L. Zeng & J. F. Klausner "Nucleation site density in forced convection boiling", ASME J. Heat Transfer 115, 215–221 (1993)

[28] See the citation to B. E. Staniszewski in W. M. Rohsenow, Developments in Heat Transfer, MIT Press (1964), p. 199 (1952)

[29] J. E. Sgheiza & J. E. Myers "Behavior of nucleation sites in pool boiling", AIChE J. 31, 1605–1613 (1985)

[30] G. Guido Lavalle, P. M. Carrica, A. Clausse & M. K. Qazi, "A number density constitutive equation", Nucl. Eng. Des.(in press) (1994)

[31] G. Marrucci, "A theory of coalescence", Chem. Eng. Sci. 24, 975 (1969)

[32] G. I. Taylor, "The formation of emulsion in definable field of flow", Proc. Royal Soc. (London) 146, 501 (1934)

[33] J. O. Hinze, "Fundamentals of the hydrodynamical mechanisms of splitting in dispersion processes", AIChE J. 1, 289–295 (1955)

[34] L. A. Santaló, Integral Geometry and Geometric Probability, Addison–Wesley Publishing Company, Reading, Mass (1976)

[35] P. M. Carrica, S. A. Leonardi & A. Clausse, "Experimental study of the two–phase flow dynamics in nucleate and film pool boiling", Int. J. Multiphase Flow (in press) (1994)

[36] S. P. Liaw & V. K. Dhir, "Effect of surface wettability on transition boiling heat transfer from a vertical surface", Proc. 8th Int. Heat Transfer Conf. 4, 2031–2036 (1986)

Nomenclature

A	CV area	$[m^2]$
a_i	Interfacial area density	$[1/m]$
b	Constant coefficient (breakup)	$[1/\ m^3\ s]$
c	Constant coefficient (coalescence)	$[1/\ m^3\ s]$
$\hat{C}$	Coalescence number	[Dimensionless]
C_d	Drag coefficient	[Dimensionless]
$\hat{D}$	Drag number	[Dimensionless]

f_i	Interfacial impact rate	$[Hz]$
g	Gravity acceleration	$[m/s^2]$
h_{fg}	Latent vaporization heat	$[J/kg]$
k	Constant coefficient (heat removal)	$[m]$
L	Control volume height	$[m]$
$\hat{M}$	Heat removal number	[Dimensionless]
n	Bubble number density	$[1/m^3]$
N''	Nucleation site density	$[1/m^2]$
q_{nv}	Heat non producing vapor inside CV	$[W]$
q_v	Heat generating vapor inside CV	$[W]$
q''	Heat flux	$[W/m^2]$
r	Radius	$[m]$
S	Bubble source	$[1/m^2\ s]$
t	Time	$[s]$
u	Bubble velocity	$[m/s]$
u_∞	Terminal velocity	$[m/s]$
$v_{\infty,i}$	Terminal velocity, isolated bubbles	$[m/s]$
v, V	Volume	$[m^3]$
We	Weber number	[Dimensionless]
α	Void Fraction	[Dimensionless]
$\hat{\alpha}_0$	Coalescence to breakup number	[Dimensionless]
β	Breakup source term	$[Hz]$
ζ	Coalescence losses	$[Hz]$
Γ	Evaporation rate inside the CV	$[kg/s]$
$\hat{\eta}$	Constant proportional to coalescence	[Dimensionless]
ϕ	Nucleation source	$[1/m^2\ s]$
ρ	Density	$[kg/m^3]$
σ	Surface tension	$[kg/s^2]$

Superscripts

$\hat{}$	Dimensionless
$\bar{}$	Average

Subscripts

b	bubble
c	critical
chf	critical heat flux
d	detachment
g	gas
l	liquid
nv	no vapor
s	steady state
v	vapor

THE ROLE OF HEATER THERMAL RESPONSE IN REACTOR THERMAL LIMITS DURING OSCILLATORY TWO-PHASE FLOWS

A. E. Ruggles, University of Tennessee, Knoxville
A. D. Vasil'ev, Nuclear Safety Institute, Moscow
N. W. Brown, University of Tennessee, Knoxville
M. W. Wendel, Oak Ridge National Laboratory, Oak Ridge, TN

Abstract

Analytical and numerical investigations of critical heat flux (CHF) and reactor thermal limits are conducted for oscillatory two-phase flows often associated with natural circulation conditions. It is shown that the CHF and associated thermal limits depend on the amplitude of the flow oscillations, the period of the flow oscillations, and the thermal properties and dimensions of the heater. The value of the thermal limit can be much lower in unsteady flow situations than would be expected using time average flow conditions. It is also shown that the properties of the heater strongly influence the thermal limit value in unsteady flow situations, which is very important to the design of experiments to evaluate thermal limits for reactor fuel systems.

I. Introduction

The CHF used in this paper refers to the transition from nucleate boiling to transition boiling. This is the heat flux at the peak in the boiling curve corresponding to where the slope in heat flux goes from positive to negative with increasing wall superheat. In steady flow conditions, the heater surface temperature continues to rise once the transition boiling region is encountered. More of the heater surface becomes dry as the wall surface temperature rises resulting in further degredation of the heat transfer coefficient. This process continues until the heater surface is dry. The time for the transition from nucleate boiling to a dry heater surface is a function of the CHF and the heater thermal properties. Heaters with large dimensions and high thermal effusivity, $k\rho c$, transition slowly, while heaters of small dimensions and low thermal effusivity transition rapidly. This physics is easy to understand for the steady flow situation with a constant applied power and is described in many texts dealing with boiling heat transfer [1].

Unsteady two-phase flows cause the CHF value to vary in time at any given location on the heater. This allows portions of the heater to move into the transition boiling region and back to the nucleate boiling region. This behavior has been observed in experiments by Oh and Englert [2], Mishima et al. [3], Ishii and Mishima [4], and Ozawa et al. [5] amoung others. This movement into the transition boiling region and back to the nucleate boiling region results in oscillations in the wall temperature [3], [4], and [5]. The ability of the heater to return to nucleate boiling after encountering CHF causes a distinction to be necessary between CHF and the thermal limit. The term thermal limit will refer to incipient heater or fuel damage as indicated by a maximum allowable temperature.

The character of the wall temperature oscillations is controlled by the nature of the unsteady flow and the thermal properties of the heater. A thin foil heater will transition from nucleate boiling to dry surface conditions very rapidly due to low heat capacity, as discussed earlier. Therefore, a heater of this type may be damaged upon the first encounter with CHF and transition boiling conditions. A massive heater with large heat capacity and high conductivity will transition from nucleate boiling to dry surface conditions more slowly. This heater may encounter transition boiling conditions for significant periods of time and still retain wall surface temperatures low enough to allow a return to nucleate boiling when the adjacent fluid state variables allow.

If the nature of the unsteady flow is approximated by a period and amplitude, then further generalizations can be made regarding the relationship between CHF and thermal limits in unsteady flows. Flow oscillations of large amplitude and large period will allow the heater to move into the transition boiling region for an extended time. Therefore, the heater wall may become dry or exceed a temperature value

allowing for a return to nucleate boiling. Flow oscillations of short period and small amplitude allow less time for the heater temperature to rise and a return to nucleate boiling conditions may be possible.

The aforementioned physics governing the behavior of a heater in the neighborhood of the CHF is quantified in this paper. This quantification allows the scaling of thermal limit data taken with electrical heaters to reactor fuel systems. It is shown that this scaling is very important when unsteady flow conditions are present. The performance of the scaling criteria is verified by comparison with experimental data. The analytic results are also compared with a study of thermal limits performed using the RELAP5-MOD3 [6] code where the heater dimensions are varied.

II. Analytic Development

The physical development starts with the treatment of the transient conduction in the heater or nuclear fuel resulting from time varying convective boundary conditions. The time varying convective boundary condition is quantified in terms of an amplitude, period, and CHF model. These equations are then manipulated to describe the thermal limit, as determined by circumstances that do not allow the heater to return to nucleate boiling.

The temperature distribution in a single heater under transient conditions is described by the nonstationary heat conduction equation

$$\nabla(\kappa\nabla T^*) - \rho c\frac{\partial T^*}{\partial t} + E = 0, \tag{1}$$

where κ is the thermal conductivity, c is the specific heat of the heater material, ρ is density, E is volumetric energy generation of decay heat, and T^* is temperature. The variable $T = T^* - T^*_{ref}$ is defined for convience, where T_{ref} is a constant reference temperature.

Boundary conditions are applied to the equation (1) on the heater surface, S:

$$\kappa\frac{\partial T}{\partial n}\bigg|_S = q''(z,t,T_w), \tag{2}$$

where q" is the boiling heat flux. The case of cylindrical geometry requires axial symmetry of temperature. Note that the temperature gradient at the surface and boiling heat flux will be time varying despite a constant value for the volumetric energy generation in the heater, E.

The solution of equations (1) and (2) is not simple for the general case of arbitrary $q''(t, T_w)$. However, boiling heat flux oscillations with angular frequency, $\omega=2\pi/\tau$, limit consideration to temporal dependencies of a type, $\exp(in\omega t)$, where n is an arbitrary whole number and $i = \sqrt{-1}$ is imaginary unity. More general oscillations can be considered using Fourier composition techniques.

IIa: The Plane Geometry Case

First consider the one-dimensional heat conduction equation for temperature T in a slab of width 2d with temperature independent thermal conductivity, κ, and thermal diffusivity, χ. The x-axis is directed into a slab with x=0 corresponding to the wetted surface. The cases of cylindrical geometry and two-layer heater structure with a gap have been considered but are not presented here. The heat conduction equation for the plane case takes the following form:

$$\frac{\partial^2 T}{\partial x^2} - \frac{1}{\chi}\frac{\partial T}{\partial T} + \frac{E}{\kappa} = 0. \tag{3}$$

In the general case of nonsymmetrical heating of a slab, the following boundary conditions are considered:

$$\left.\frac{\partial T}{\partial x}\right|_{x=0} = \frac{q''_L(t,T_{WL})}{\kappa}, \quad \left.\frac{\partial T}{\partial x}\right|_{x=2d} = -\frac{q''_R(t,T_{WR})}{\kappa}, \tag{4}$$

where q''_L and q''_R are the heat fluxes on the left (x=0) and right (x=2d) side of the heater. Similarly, the heater left and right wall temperatures are defined by $T_{WL} = T(x=0)$ and $T_{WR} = T(x=2d)$.

Consistent with the assumption of periodic behavior for basic physical quantities, including G, p, α, and T, new non-dimensional variables are introduced

$$t = t_{old}\omega, \quad x = x_{old}/(\chi/\omega)^{1/2} \equiv x_{old}/(dN_1),$$
$$q'' = q''_{old}/(\kappa(\omega/\chi)^{1/2}\Delta T_b) \equiv q''_{old}/(q_{CHF,0}N_2), \tag{5}$$

where the amplitude of the heater wall heat flux first harmonic, $q''_{w1} \sim \kappa(\omega/\chi)^{1/2}\Delta T_b q_1/q_{CHF,0}$, is used to normalize the wall heat flux. ΔT_b is the characteristic width of the boiling heat flux curve near the CHF maximum, q''_1 is the CHF oscillation amplitude, and $q''_{CHF,0}$ is CHF at steady conditions as determined using the time average flow conditions. Note that the depth of the thermal wave penetration is $d_t \sim (\chi/\omega)^{1/2}$ [7], such that N_1 is equal to d_t/d.

Equations for temperature harmonics T_n follow from equations (3) and (4). Temperature is now represented in the form $T = \sum_{n=0}^{\infty}(T_n e^{int} + c.c.)$:

$$\frac{\partial^2 T_0}{\partial x^2} + \frac{E\chi}{\omega\kappa} = 0, \quad \frac{\partial^2 T_n}{\partial x^2} - inT_n = 0, n \geq 1;$$
$$\left.\frac{\partial T_n}{\partial x}\right|_{x=0} = \Delta T_b q^*_{Ln}, \quad -\left.\frac{\partial T_n}{\partial x}\right|_{x=2/N1} = \Delta T_b q^*_{Rn}, \tag{6}$$

where ΔT_b is the characteristic width of boiling curve near the CHF temperature and T_0 is a cycle-average temperature in the heater. Fourier harmonics of n-th order for the heat flux are given by q''_{Ln} and q''_{Rn} and c.c. denotes the complex conjugate.

The solution of the system (6) for n≥1 takes the form:

$$T_n(x) = \frac{\Delta T_b}{2k_n}\left(S_{Ln}\frac{e^{k_n x} + e^{-k_n(x-2N_1^{-1})}}{1 - e^{2k_n N_1^{-1}}} + D_{Ln}\frac{e^{k_n x} - e^{-k_n(x-2N_1^{-1})}}{1 + e^{2k_n N_1^{-1}}}\right), \tag{7}$$

$S_{Ln} = q''_{Ln} + q''_{Rn}$, $D_{Ln} = q''_{Ln} - q''_{Rn}$,

where $k_n = \sqrt{in}$. Note that in expression (7) the temperature is represented as a sum of symmetrical and antisymmetrical parts.

The zero temperature harmonic in the heater is defined by (6) as:

$$T_0(x) = T_{0L} - \frac{Ed^2N_1}{2\kappa}(N_1x^2 - 2x) + (T_{0R} - T_{0L})\frac{N_1 x}{2}, \tag{8}$$

where T_{0L} and T_{0R} are zero harmonics of the left and right heater wall respectively. The final expression for the transient one dimensional temperature profile in the heater has the form:

$$T = T_0(x) + \frac{\Delta T_b}{2}\sum_n \left(\frac{S_{Ln}}{k_n} \frac{e^{k_n x} + e^{-k_n(x-2N_1^{-1})}}{1 - e^{2k_n N_1^{-1}}} e^{int} + c.c \right) . + \tag{9}$$

$$\frac{\Delta T_b}{2}\sum_n \left(\frac{D_{Ln}}{k_n} \frac{e^{k_n x} - e^{-k_n(x-2N_1^{-1})}}{1 + e^{2k_n N_1^{-1}}} e^{int} + c.c \right) .$$

The expressions for sum and difference of heat fluxes q''_L and q''_R are obtained from (9) as:

$$\frac{q_L + q_R}{2} = \frac{Ed}{q_{CHF,0} N_2} + \sum_1^\infty (\beta_{1n} \frac{T_{Ln} + T_{Rn}}{2} e^{int} + c.c.) ,$$

$$\frac{q_L - q_R}{2} = \frac{\kappa(T_{0R} - T_{0L})}{2 q_{CHF,0} N_2 d} + \sum_1^\infty (\beta_{2n} \frac{T_{Ln} - T_{Rn}}{2} e^{int} + c.c.) , \tag{10}$$

where

$$\beta_{1n} = k_n \frac{1 - e^{2k_n N_1^{-1}}}{1 + e^{2k_n N_1^{-1}}} , \quad \beta_{2n} = k_n \frac{1 + e^{2k_n N_1^{-1}}}{1 - e^{2k_n N_1^{-1}}} .$$

The left and right heater wall temperatures are given by

$$T_L = T_{L0} + \sum_1^\infty (T_{Ln} e^{int} + c.c.) , \quad T_R = T_{R0} + \sum_1^\infty (T_{Rn} e^{int} + c.c.) . \tag{11}$$

Note that this solution is general enough to allow consideration of experimental conditions where only one side of the heater is exposed to fluid. Plate fueled research reactors would have convective boundary conditions on both sides of the fuel plate.

IIb. Modeling of Critical Heat Flux and Thermal Limit under Oscillatory Flow Conditions

The mathematical description of unsteady two-phase flow in boiling channels requires the self-consistent solution of two-phase flow thermal-hydraulic equations coupled with the heat conduction equation for the heater. The solution of these equations results in the possibility for many types of waves to exist, including waves with a period of about the characteristic transport time in the boiling channel. Note also that many types of flow oscillations can be motivated by system components outside the boiling channel that effect the boundary conditions imposed on the channel. Many reviews of types of unsteady two-phase flow have been offered to explain these phenomena in more detail with those due to Boure et al. [8] and Kakac and Veziroglu [9] offered as examples.

As a first approximation the unsteady behavior of the flow is modeled by incorporating a periodic perturbation with period τ into all physical quantities of interest for a given axial location such that,

$$F = \Sigma(F_n \exp(int) + c.c.), \tag{12}$$

where F is one of the physical parameters (α,p,G,x) and F_n are corresponding harmonics. A relationship simlar to (12) is also used for the boiling heat flux $q''=q''(\alpha,p,G,T_w)$.

The present evaluation is limited to the axial location where the thermal limit is first reached. Terms in the heat conduction equation proportional to $\partial^2 T/\partial z^2$ are neglected due to the large characteristic dimension in the axial direction. Note that the analysis presented herein identifies conditions for which a return to nucleate boiling is not possible and the heater will move to dry surface conditions. This involves wall superheat values less than

100 degrees Celsius in water systems. Therefore, the analysis is not consistent with the rewetting of very hot fuel assemblies where axial conduction terms are known to be important.

IIc: Integration of Models

The boiling heat fluxes q''_L and q''_R are represented in the following general form using Taylor series:

$$q''_L(t, T_{WL}) = q_{CHF,L}(t)\sum_0^\infty A_n (T_{WL} - T_{CHF,L}(t))^n \ ,$$

$$q''_R(t, T_{WR}) = q_{CHF,R}(t)\sum_0^\infty A_n (T_{WR} - T_{CHF,R}(t))^n \ , \qquad (13)$$

where $A_0 \equiv 1$ because $q''(t,T_w=T_{CHF})$ is the critical heat flux and $A_1 = 0$ due to extremum of function $q''(t,T_w)$ at the CHF point. A_2 is negative because this extremum point is a maximum point. Note that $|A_2| \sim (\Delta T_b)^{-2}$, which justifies the appearance of ΔT_b in equation (9) and in the nondimensional complex, N_2.

The critical heat flux values $q_{CHF,L}$ and $q_{CHF,R}$, with the periodicity expressed in equation (12), are given in the form

$$q_{CHF,L}(t) = q_{CHF,0} + \Sigma(q_{CHF,Ln}e^{int} + c.c.),$$
$$q_{CHF,R}(t) = q_{CHF,0} + \Sigma(q_{CHF,Rn}e^{int} + c.c.) \qquad (14)$$

Note that the possibility of phase shift between oscillations on the left and right of the heater (i.e., out-of-phase oscillations in parallel channels [1]) could be accepted in equations (14).

Combining equations (10), (13), and (14) gives the relationship for determination of temperature harmonics T_{Ln}, T_{Rn}, where n = 1,2,...:

$$(q_{CHF,0} + \sum(q_{CHF,Ln}e^{int} + c.c.))\sum A_n (T_{WL} - T_{CHF})^n +$$
$$(q_{CHF,0} + \sum(q_{CHF,Rn}e^{int} + c.c.))\sum A_n (T_{WR} - T_{CHF})^n =$$
$$2Ed/(q_{CHF}N_2) + \sum(\beta_{1n}(T_{Ln} + T_{Rn})e^{int} + c.c.) \ , \qquad (15)$$

$$(q_{CHF,0} + \sum(q_{CHF,Ln}e^{int} + c.c.))\sum A_n (T_{WL} - T_{CHF})^n -$$
$$(q_{CHF,0} + \sum(q_{CHF,Rn}e^{int} + c.c.))\sum A_n (T_{WR} - T_{CHF})^n =$$
$$\kappa(T_{0R} - T_{0L})/(q_{CHF}N_2 d) + \sum(\beta_{2n}(T_{Ln} - T_{Rn})e^{int} + c.c.).$$

Equation (15) requires all the terms with the same exponent, e^{int}, to equalize.

IId: CHF and Thermal Limit Models

Equation (15) has three different solutions for T_{0L}, T_{0R} in the range of parameters $q''_{min} < Ed < q''_{max}$. The nucleate boiling regime, for which T_{0L}, $T_{0R} < 0$ is the solution of (15) at $Ed < q''_{CHF,eff}$ where wall temperature does not exceed the CHF point on the boiling curve. Therefore, the first solution corresponds to wall temperature oscillations entirely in the nucleate boiling regime.

When $q''_{CHF,eff} < Ed < q''_{TL}$ the temperature solution moves into the transition boiling region and then returns to the nucleate boiling region. This cycle repeats within each flow oscillation period.

At $Ed > q''_{TL}$ the solution of equation (16) not longer exists or is unstable. Therefore, q''_{TL} is the thermal limit heat flux.

The thermal limit values obtained by this procedure have been nomalized to the steady state CHF value, $q''_{CHF,0}$, which is based on the time-average two-phase parameters at the channel exit. For example, the exit quality is determined by the relation $x_{out}=Ed(S_H/S)/(Gh_{fg})$, where S_H and S are the heater and flow areas respectively, h_{fg} is the latent heat of vaporization, and G is the mass flux.

The stability of solutions is investigated by introducing small perturbations $\delta_1 e^{(\omega+\beta)t}$+c.c. to temperature harmonics T_1. This procedure produces the following from equation (15):

$$\beta = -\frac{\chi}{\kappa d}\left.\frac{dq''}{dT}\right|_{T=T_{0L}\,or\,T=T_{0R}} . \qquad (16)$$

This indicates that when $dq''/dT>0$ (positive slope) $\beta<0$ and the solution is stable.

III. Analytical Solution within the Bounds of the Perturbation Method

For cases when the perturbation amplitude of the oscillations of the boiling curve is not large an analytic solution of equation (15) is possible. A perturbation, $\zeta=q''_1/q''_{CHF,0}$, is introduced where q''_1 is the perturbation amplitude, and $q''_{CHF,0}$ is q''_{CHF} evaluated using time-average parameters. For the case of symmetrical heating, the analytical solution of equation (15) for the thermal limit heat flux becomes

$$q_{TL} = q_{CHF,0} - \frac{2Aq_{CHF,0}q_1^2}{\left|\kappa(i\omega/\chi)^{1/2}(1-e^{2(i\omega/\chi)^{1/2}d})/(1+e^{2(i\omega/\chi)^{1/2}d})\right|^2} \qquad (17)$$

where $2A = d^2q''_{CHF,0}/dT^2$ is the second derivative of CHF at the CHF point. Note that this solution applies for small ζ and a thick heater, $N_1 < 1$ or $d_t<d$.

IV: Results

The influence of boiling instabilities on thermal limits has been evaluated experimentally for low pressure and low mass flux situations in water by Mishima et al. [3] and Ozawa et al. [5]. Unfortunately, an experimentally based characterization of the boiling curve was not found for these conditions. Griffith et al. [10] determined that the CHF value is well approximated by the pool boiling CHF value taken times the local liquid volume fraction when the mass flux is less than 200 kg/m^{2}s. A similar model is implemented in the RELAP5-MOD3 code [6] and is shown in fig. 1 for mass flux G = 20 kg/(s-m^2), pressure p = 0.10 MPa, and saturated conditions. These conditions are consistent with those of Ozawa et al. [5]. The coefficients in the Taylor series expansion of the boiling heat flux required for the model are derived from fig. 1.

Equation (15) has been solved using the packages MATHCAD and MAPLE on a PC. The wall temperature, T_w, dependence with time is shown in fig. 2 for the parameters κ=0.23W/(cm-K), χ=0.06cm^2/s, ω=1.5s^{-1}, d=0.25cm, A=0.005, $q''_{CHF,0}$=50W/cm^2,and q''_1=5W/cm^2 which are consistent with data from Ozawa et al. [5]. Note that the wall temperature in fig. 2 is normalized to the wall temperature corresponding to CHF at time average conditions. When Ed is less than thermal limit, q_{TL}, nucleate boiling persists throughout the period of oscillation and the wall temperature follows the heat flux as indicated by curve 1 in fig. 2. When Ed is just less than the thermal limit heat flux, q_{TL}, the wall temperature exhibits more complicated behavior due to the nonlinear relationship between wall superheat and boiling heat flux associated with movement into and out of the transition boiling regime.

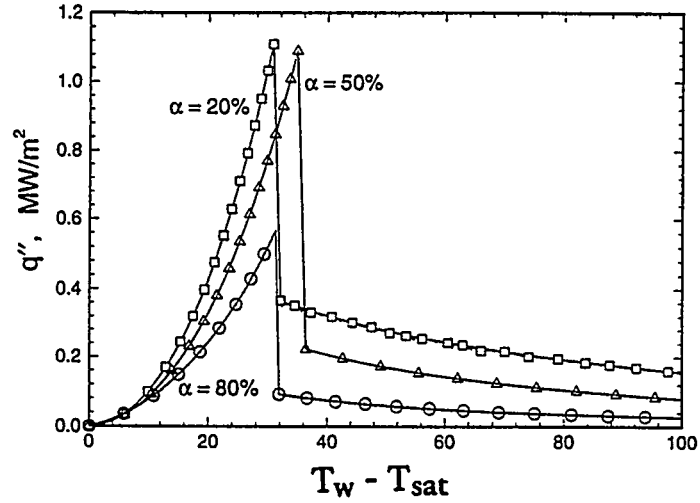

Figure 1: Heat Flux Versus Wall Temperature From RELAP5-MOD3 for G= 20 kg/(s-m^2), p = 0.10 MPa, and saturated conditions.

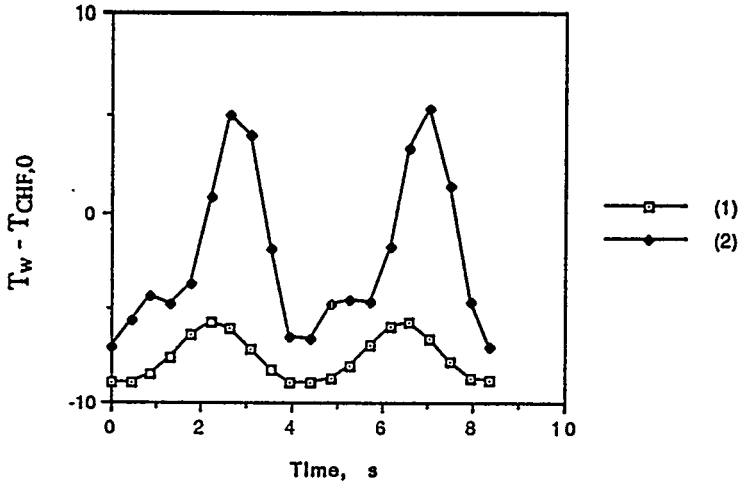

Figure 2: Wall Temperature Dependence with Time for (1) Ed=35 W/cm^2 and (2) Ed=47.2 W/cm^2

Note the phase shift between the wall temperature traces in fig. 2. The transition from nucleate boiling to transition boiling is shown by the uptum in curve two, indicating a decrease in the heat transfer coefficient. The heater then stores energy during the time it is in transition boiling. The return of the heater to nucleate boiling is delayed because the heater surface temperature must first be lowered to a value near the saturation temperature. This requires that some of the energy stored in the heater during transition boiling be discharged to the fluid. The temperature turns upward again indicating a return to transition boiling. Note that the subsequent uptum in temperature occurs somewhat before the wall temperature value corresponding to the time average CHF. This is because the heat flux is still higher than the average value at this point in the cycle due to the continued discharge of energy stored in the heater during transition boiling when the heat transfer coefficient and heat flux are low.

Analysis of expressions (10) and (13) shows that two nondimensional numbers N1 = $(\chi/\omega)^{1/2}\, d^{-1} = d_t/d$ and N2 = $\kappa(\omega/\chi)^{1/2}\Delta T_b/q''_{CHF,0} = (\kappa\rho c)^{1/2}(\omega)^{1/2}\Delta T_b/q''_{CHF,0}$ can characterize the solution. The normalized ratio, $q''_{TL}/q''_{CHF,0}$, is represented versus N1 for different N2 in fig. 3 with $q''_1/q''_{CHF,0}$=0.4. It is seen that that the major change in thermal limit takes place as N_1 moves from 0.5 to 10. This corresponds to movement from thick heaters with dimensions greater than the thermal wave penetration depth, d_t, to thin heaters with dimensions smaller than

the thermal penetration depth. Note also that as the heater thichness goes much smaller than the thermal penetration depth the heater temperature responds instantly to variations in the heat transfer coefficient and the heat flux becomes constant in time. Therefore, the thermal limit occurs when the CHF is first encountered for the case of large N1, such that $q''_{TL}=q''_{CHF,0}-q''_{1}$.

The thermal limit heat flux, q''_{TL} , approaches the steady state CHF for large N2 and small N1. The dimensionless group, N2, is proportional to the thermal effusivity, $\kappa\rho c$, to the one half power. The thermal effusivity gives a measure of the ability of the heater to store energy and move energy to the surface. A heater with large thermal effusivity and large dimensions (small N1) is therefore able to withstand periods of transition boiling without large changes in wall temperature. This allows the thermal limit heat flux, q''_{TL} , to approach the steady state CHF value.

The slight hook in curve one on fig. 3 at low N1 and high N2 is associated with high frequency behavior since N1 goes as $\omega^{-1/2}$ while N2 goes as $\omega^{1/2}$. The high frequency causes the thermal penetration depth to be small relative to the heater dimension. This limits the ability of the heater to discharge energy stored during the transition boiling part of the cycle. Note that *high frequency* is defined by the heater characteristics and the boiling curve through the definitions of N1 and N2.

The model predictions are compared with the experimental data of Ozawa et al. [5] in fig. 4. Sinusoidal inlet mass flow variations were imposed on the channel with periods of 2, 4 and 6 seconds. The comparison shows qualitative agreement between the analytical model and the experimental results.

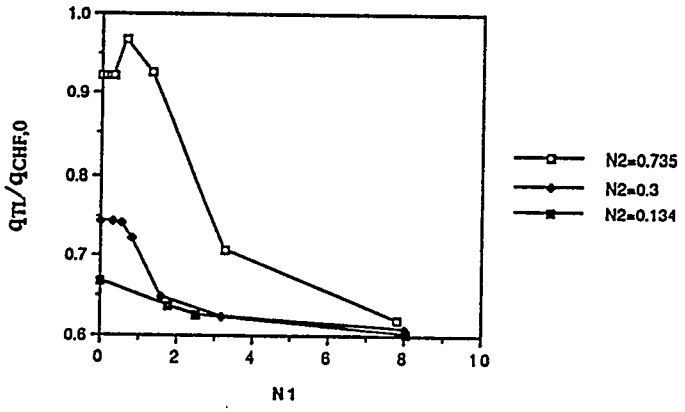

Figure 3: Dependence of Nondimensional Thermal Limit Value, $q''_{TL}/q''_{CHF,0}$, on N1 and N2.

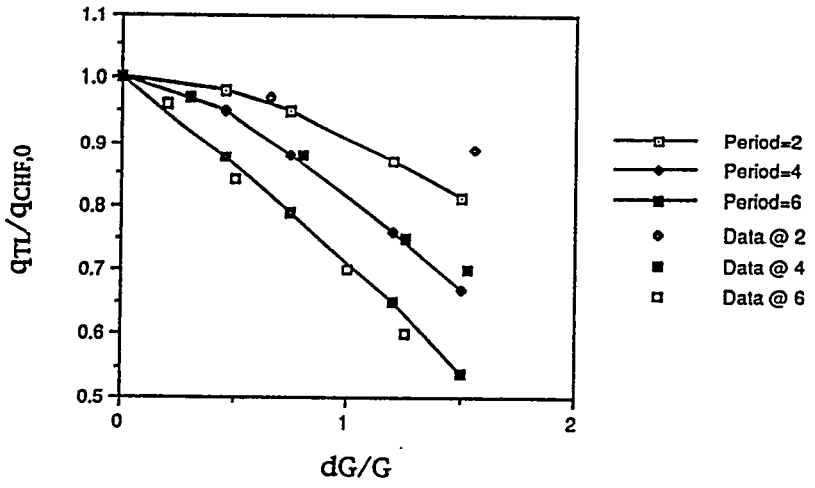

Figure 4: Comparison of the Model with Data from Ozawa et al. [5]. The model results are indicated with lines.

The RELAP5-MOD3 [6] code is a numerical representation of a two-fluid thermal-hydraulic model coupled with a one dimensional conduction model in the heater. Therefore, this code should simulate the physics required to predict the variation in thermal limit heat flux associated with unsteady flow conditions. RELAP5-MOD3 was used to simulate an experiment performed by Ishii and Mishima [4]. This simulation is an extension of work performed by Ruggles and Williams [11]. The RELAP5 code predicted unsteady flow behavior and wall temperature oscillations qualitatively consistent with those observed in the experiment. These simulations included a careful examination of the sensitivity of the results to nodalization, time step, and rate of increase in the applied heat flux. The thermal limit flux was defined as the applied heat flux when the heater back wall temperature began to rise rapidly and continued to rise for several hundred degrees Celsius. RELAP5 was run for the experimental conditions from [4] with inlet mass flow of 35 Kg/m^2s and a thermal limit flux of 72 KW/m^2 was determined. The measured thermal limit flux was 105 KW/m^2. The input file for the code was then modified to run with the heater thickness four times the original value and a thermal limit heat flux of 78 KW/m^2 was predicted. The N1 value for the experiment is 86 using an oscillation period of one second which is roughly consistent with the experiment and the simulation results. These simulations support the effect of increasing the parameter N1 on the thermal limit heat flux as indicated in fig. 3. A study with values of N1 in the range from 0.5 to 10 would likely produce more variation in the thermal limit.

V. Conclusions

Many of the experimental studies used to establish reactor thermal limits have been conducted using constant inlet mass flow conditions. However, it is the pressure drop across the fueled region that remains constant in reactor systems due to the large number of parallel cooling channels in the fuel assembly [1]. It is often assumed that thermal limits established during single channel tests with constant inlet mass flow can be used in reactor thermal limit studies. This assumption certainly holds if the flow behavior in the fuel cooling channel is identical to that recorded in the single channel experiment. However, the flow behavior and measured thermal limit can vary significantly as the applied boundary conditions are changed from those of constant inlet mass flux to those approaching constant applied pressure drop, as indicated by Mishima et al. [3].

Natural circulation flows and flows at low mass flux and low pressure are very prone to unsteady behavior. These flows are of interest in reactor safety analyses where decay heat is to be removed by natural circulation. It is generally beyond the state of the art to accurately predict the nature of flow oscillations in two-phase systems. Therefore, it is important that experiments intended to verify the performance of these systems be properly designed to produce either best estimate or conservative performance information.

The model presented herein provides a tractable and mechanistic relationship between heater properties, basic flow properties and thermal limits. These relationships allow the engineer to determine if an experiment evaluating thermal limits is likely to produce conservative, non-conservative, or best estimate results when applied to a reactor fuel assembly. However, this evaluation will require some knowledge pertaining to the nature of the unsteady flow both in the experiment and in the reactor fuel assembly.

The results of this analysis are especially important to equipment where the heat capacity of the structure in the region where the energy is generated is small and the materials used have low melting temperatures. Such systems include research reactors and production reactors which use aluminum cladding, and fusion reactors in the region of the diverter plates where copper is the primary structural material. These systems have significant heat loads after shut-down and can be damaged by dry conditions. Experiments intended to establish the thermal limits for these systems can easily produce nonconservative results if heaters of large dimensions are used.

Acknowledgements: The authors thank the National Academy of Sciences and the Nuclear Engineering Department of the University of Tennessee for supporting Dr. Vasil'ev during his visit to the United States.

Nomenclature

$A=2^{-1}d^2q''_{CHF,0}/dT^2$ $(T=T_{CHF})$ - second derivative of boiling heat flux with temperature
c - specific heat, J/kg K
d - heater thickness, m
E - volumetric energy generation, W/m^3
Ed - heater heat flux, W/m^2
G - mass flux, $kg/(m^2s)$
dG-amplitude of mass flux oscillation
h - heat transfer coefficient, $W/(m^2K)$
p - pressure, N/m^2
q" - heat flux, W/m^2
T - temperature, K
ΔT_b - characteristic boiling curve width temperature, K
x -quality; coordinate, m
z - longitudinal coordinate, m
α - void fraction
β - perturbation amplitude
τ - oscillation period, s
κ - thermal conductivity, W/mK
χ - thermal diffusivity, m^2/s
ρ - density, Kg/m^3
$\omega=2\pi/\tau$-frequency

Subscripts

ex - exit
L - left
R - right
sat - saturation
TL - thermal limit
w - wall
0 - average value
ref- reference value

Literature

1. Todreas N.E., Kazimi M.S. Nuclear Systems II: Elements of Thermal Hydraulic Design. Hemisphere, 1990, 506 p.
2. Oh C. H. and Englert S. B. Critical Heat Flux for Low Flow Boiling in Vertical Uniformly Heated Thin Rectangular Channels. Int. J. Heat Mass Transfer, 1993, v. 36, N 2, p. 325-335.
3. Mishima K., Nishihara H., Michiyoshi I. Boiling Burnout and Flow Instabilities for Water Flowing in a Round Tube under Atmospheric Pressure. Int. J. Heat Mass Transfer, 1985, v. 28, N 6, p. 1115-1129.
4. Mishima K., Ishii M. Critical Heat Flux Experiments Under Low Flow Conditions in a Vertical Annulus. 1982, NUREG/CR-2647 also ANL-82-6.
5. Ozawa M., Umekawa H., Yoshioka Y., Tomiyama A. Dryout under Oscillatory Flow Condition in Vertical and Horizontal Tubes-Experiments at Low Velocity and Pressure Conditions. Int. J. Heat Mass Transfer, 1993, v. 36, N 16, p. 4076-4078.
6. Carlson K.E. et al. RELAP5/MOD3 Code Manual. NUREG/CR-5535, 1990.
7. Carslow H.S., Jaeger J.C. Conduction of Heat in Solids, Oxford, Clarendon Press, 1959.
8. Boure J.A., Bergles A.E., Tong L.S. Review of Two-Phase Flow Instability. Nucl. Eng. and Des., 1973, v. 25, p. 165-192.
9. Kakac S. and Veziroglu T. N. A Review of Two-Phase Flow Instabilities. Advances in Two-Phase Flow and Heat Transfer Vol. 2, edited by Kakac S. and Ishii M. 1983.
10. Griffith P., Avedisian C.T., Walkush Y.P. Counter Flow Critical Heat Flux. AIChE Symp. Series, 1978, v. 74, p. 149-155.
11. Ruggles A.E., Williams P. Critical Heat Flux under Low Flow Conditions. Calculations Supporting Safety Analysis of the High Flux Isotope Reactor, ORNL Report, 1992, C-HFIR-92-026,027 and 028, also ANS Transactions, Annual Meeting Nashville, TN, June 1990, p.204-205.

NURETH7 Conference
Saratoga Springs, NY, USA, Sept. 10-15, 1995

Methodology for the Study of the Boiling Crisis in a Nuclear Fuel Bundle

F. de Crécy, D. Juhel

Commissariat à l'Energie Atomique
Reactor Thermal Hydraulics Section
CENG/DTP/STR - 17 rue des Martyrs
38054 Grenoble Cedex 9 (France)

ABSTRACT

The boiling crisis is one of the phenomena limiting the available power from a nuclear power plant. It has been widely studied for decades, and numerous data, models, correlations or tables are now available in the literature.

If we now try to obtain a general view of previous work in this field, we may note that there are several ways of tackling the subject.

The mechanistic models try to model the two-phase flow topology and the interaction between different sublayers, and must be validated by comparison with basic experiments, such as DEBORA, where we try to obtain some detailed informations on the two-phase flow pattern in a pure and simple geometry. This allows us to obtain better knowledge of the so-called "intrinsic effect".

These models are not yet acceptable for nuclear use. As the geometry of the rod bundles and grids has a tremendous importance for the Critical Heat Flux (CHF), it is mandatory to have more precise results for a given fuel rod bundle in a restricted range of parameters: this leads to the empirical approach, using empirical CHF predictors (tables, correlations, splines, etc...).

One of the key points of such a method is the obtaining local thermohydraulic values, that is to say the evaluation of the so-called "mixing effect". This is done by a subchannel analysis code or equivalent, which can be qualified on two kinds of experiments: overall flow measurements in a subchannel, such as HYDROMEL in single-phase flow or GRAZIELLA in two-phase flow, or detailed measurements inside a subchannel, such as AGATE.

Nevertheless, the final qualification of a specific nuclear fuel, i.e. the synthesis of these mechanistic and empirical approaches, intrinsic and mixing effects, etc..., must be achieved on a global test such as OMEGA. This is the strategy used in France by CEA and its partners FRAMATOME and EdF.

1. INTRODUCTION

The boiling crisis in nuclear plants is one of the phenomena limiting the available power, and must be taken into account in accidental, incidental and nominal conditions.

In accidental conditions, (more than class 2), it is necessary to have a rough estimation of the boiling crisis conditions for a very wide range of parameters. A rough but general purpose predictor, as Groeneveld's tables (1993) can be used.

In incidental (up to class 2) and nominal conditions, more precise evaluations are needed for a more narrower range of parameters. To obtain this high level of precision, one must take precisely into account the detailed rod bundle and mixing grids geometry (for example, the geometry of the vanes). The precision and the reliability of our knowledge of the boiling crisis in a given fuel design impacts directly on safety margins, available power and consequently finance.

As it is impossible to provide detailed results, which are proprietary, the purpose of this paper is to explain the French methodology used by the CEA, EdF and FRAMATOME.

2. MECHANISTIC BOILING CRISIS MODELS AND EXPERIMENTAL STUDY OF THE TWO-PHASE FLOW TOPOLOGY

This seems to be the most "physical" approach to boiling crises. Many authors have tried to model two phase flow topology, often by modelling the behavior of several sublayers and the exchanges between them. The boiling crisis occurs when a critical condition is reached on the sublayer near the heating wall.

For dry-out at rather high quality in the tubes, the Whalley model [1, 2] is well accepted. It is based on the drying of the liquid film in annular dispersed flow. A model of the exchanges between the droplets in the bulk flow, the liquid film near the wall and the vapor phase allows the prediction of the conditions in which the liquid film dries and dry-out appears.

For burn-out (lower quality), there are several families of models: the Weisman model [3, 4, 5, 6, 7, 8] proposes a mechanism by which bubbles accumulate near the wall: the boiling crisis corresponds to a critical local void fraction. On the other hand, some models such as Lee's [9] modified by Lin [10] or Katto's model [11, 12] propose a mechanism based on the drying of a thin liquid film between the wall and larger bubbles. Tong's model [13, 14, 15], based on a superheated liquid layer near the wall, a bubbly layer and the bulk flow is widely used for taking into account the non-uniformity of axial heat flux distribution.

These models are semi-empirical, that is to say that most of them have parameters adjusted using experimental data. As initial attempts at modelling were fairly simple they only applied to very simple geometries such as a circular, uniformly heated vertical tube. Subsequently, they have been adapted to more complex geometries such as rod bundles and to an extended parameter range. Recently, Katto [16] has provided a general review of the different boiling crisis models over the last decade for a wide range of parameters, geometries and conditions.

All the "mechanistic" models described above help the Progress of Science, and, consequently, must be constantly improved, mainly by simple and analytical experiments. This is one of the aims of the French Atomic Energy Commission (CEA) DEBORA facility.

In the DEBORA [17, 18] test loop, freon R12 simulates high pressure high temperature steam-water flow. For different simple test-section geometries (tube, annular space, etc), micro-thermocouples measure local fluid temperature and micro optical fiber probes (with a measuring diameter of 10 μm, using a one slice level method with a threshold at 30% of the amplitude, recording the signal during 3 mn for point) measure the phase indicator function, permitting a detailed description of the single-phase and two-phase flow patterns up to boiling crisis conditions.

From some preliminary tests performed in a tube (19.2 mm internal diameter) with pressure, mass velocity and heat flux values equivalent to the nominal conditions of a PWR, we can report some partial, provisional but interesting conclusions:

- The position of the maximum of the local time-averaged void fraction radial profile is near the wall at low mean quality and moves progressively toward the center of the tube when the mean quality increases (see, for example, figure 1).
  Assuming a velocity field and a slip model between phases, one can deduce from the optical probe signal the characteristic dimension (the diameter if we assume spherical bubbles) of the bubbles.
- The characteristic dimensions of the Freon bubbles are fairly homogeneous whatever the radial position and the mean quality, but depend on the pressure and, less, on the mass velocity.
  These dimensions are of the order of 300 μm, and a large majority of them range from 200 μm to 400 μm. There is no experimental evidence of coalescence of these bubbles in usual conditions.
- Just before the boiling crisis, a change in the two-phase flow pattern has been detected in a layer roughly 150 μm to 300 μm thick, near the wall (visible in figure 1).

These topology studies are now under way to validate the above facts and to determine their dependencies on the parameter range.

These results will be used to test the mechanistic boiling crisis models and improve basic knowledge on this phenomenon.

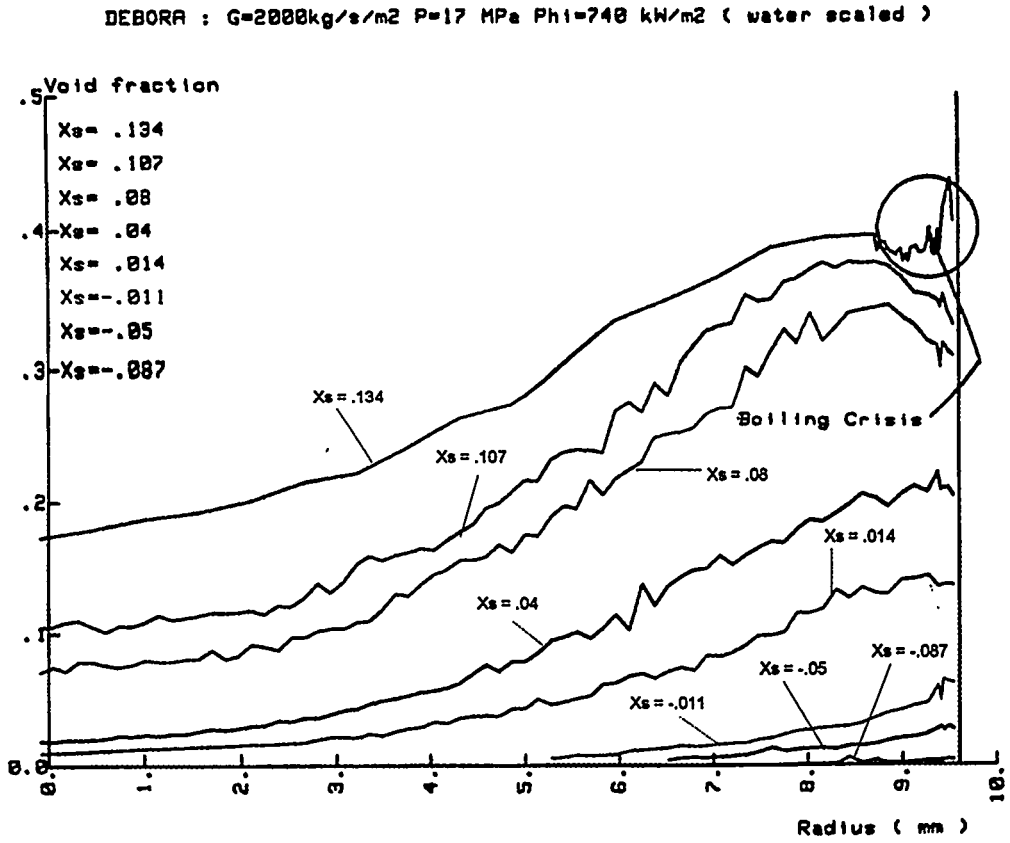

Figure 1 : Void fraction profiles measured on the DEBORA test loop
Local time-averaged void fraction plotted vs radial position of the micro-optical probe for different mean thermodynamic qualities Xs (the void fraction increases when the quality Xs increases).
The real mean freon R12 conditions are: G = 2000 kg/m²/s, P = 2.62 MPa, heat flux = 74 kW/m²

Up to now the "mechanistic" models compared to the experimental Critical Heat Flux (CHF) results have provided moderate agreement for a simple geometry (such as tubes) and poor statistical results for a more complex geometry (such as rod bundles). Most of these models are unable to take into account the complex effects of the mixing grids of a nuclear fuel rod bundle and the consequences of secondary flows. Experimentally speaking, these mixing grid effects are important.

For example, de Crecy [19] splits the **total effect** of the mixing grids and mixing vanes into a **mixing effect**, which quantifies the cross flows and determines the subchannel mean conditions and an **intrinsic effect**, which is the remaining part and represents the effect on the mixing grid and mixing vanes on the two-phase flow topology inside a subchannel. Ideally mechanistic models should describe and quantify the **intrinsic effect**. Due to the lack of understanding of local phenomena, this effect is at present quantified by empirical CHF predictors.

That is why these models, useful for the scientist and for better future knowledge of the basic phenomena, are inadequate for industrial use or safety studies of a LWR. The nuclear safety authorities do not accept the use of these mechanistic models.

3. THE EMPIRICAL APPROACH TO BOILING CRISES: THE CHF PREDICTORS

As the mechanistic models are not yet adequate for industrial use, an empirical approach is widely used. It consists in using experimental data, which is sometimes complemented with general physical considerations, to build a boiling crisis predictor such as a correlation, table, smoothing spline, neural network, etc. Usually it only applies to a specific geometry and a specific mixing grid in a given range of parameters.

According to Groeneveld [20], over 500 CHF correlations exist in the published literature and many others are proprietary; most of them deal with water-cooled tubes and have a narrow range of validity. This proliferation of CHF prediction methods illustrates the lack of understanding and consensus on the boiling crisis physical phenomena. It also demonstrates how acutely users need a means, which is both accurate and fully reliable, of estimating boiling crisis conditions in their specific geometry, parameter range and mixing grids.

These correlations are usually obtained using a least square regression method, but this approach is not really satisfactory: the scattering between measured and predicted values is significantly higher than the expected experimental uncertainties, the *a priori* given form (or, in the best cases, a limited choice between several *a priori* given forms) of the correlation seems to mean that the phenomenon has to obey this (these) form(s).

In order to use all the information from the experimental data points without adding any other hypothesis, the CEA has developed an alternative method, called PLAQUE, based on a multidimensional pseudo-cubic thin-plate type smoothing spline [21]. It uses neither physical modeling nor an *a priori* given form, but only experimental data. The only underlying hypothesis is that the phenomenon (for example, the CHF) depends in a "smooth" way on the other parameters (pressure, mass velocity, enthalpy, etc.). It does not require a normalised data base. Experimental data points may be anywhere, but of course the results will be more reliable and accurate in areas where the points are numerous.

The smoothing parameter, that is to say the strength of the smoothing or the optimal compromise between a "smooth" surface and small differences between measured and "smoothed" values, is obtained by generalized cross validation.

This smoothing spline method yields very satisfactory results, giving well validated small residual deviation and allowing statistical and uncertainty calculations. It is widely used by CEA, EDF and Framatome, for example to quantify the effects on CHF of geometric changes in mixing grids design, such as a different mixing vane angle, and reveal the parameter range in which this effect is statistically significant.

This smoothing spline can also be used to build a CHF look up table, similar to the one used by Groeneveld [20] for tubes. However, as this empirical approach using CHF predictors is mainly a way to describe and use the experimental results, one must always remember that any extrapolation from the experimental data set is doubtful, unreliable and may be dangerous: there is no physical explanation of the underlying phenomenon. This is one of the main drawbacks of the empirical approach.

4. OBTAINING "LOCAL" THERMOHYDRAULIC VALUES

Generally speaking, the use of mechanistic models requires knowledge of the local thermo-hydraulic conditions. In the same way, many CHF empirical predictors use the local thermo-hydraulic conditions, and this is the most advisable approach [22, 23].

Usually, "local" means at the scale of a subchannel, delimited by 4 (square pitch) or 3 (triangular pitch) rods; but a more precise description may be needed.

In general, only "mean" limit conditions are known: inlet temperature, average mass velocity in the whole test section, mean exit pressure, etc. A specific tool is needed to deduce local thermohydraulic conditions from the mean conditions. The problem is quite different in a real

reactor core or in a rod bundle CHF experiment (with typically a 4 × 4, 5 × 5 or 6 × 6 rod bundle). The secondary flows are not caused by the same type of heterogeneity.

In a PWR core in nominal conditions, there are some "long distance" (at the core scale) secondary flows driven by the "long distance" neutronic power heterogeneities, some "intermediate distance" secondary flows driven for example by heterogeneities between two adjacent assemblies, and some "short distance" secondary flows at the scale of adjacent subchannels driven by mixing grid heterogeneities due to the presence of guide thimbles or rod to rod differences in neutronic power.

In incidental conditions, all these long, intermediate and short distance secondary flows can be significantly modified.

In a usual rod bundle CHF experiment only "short distance" secondary flows can exist: the water proof shroud prevents intermediate and long distance cross flows. To prevent the boiling crises on the non-representative peripherical rods, the experimentors usually impose a higher heat flux radial-peaking factor in the tests than what is expected in an actual nuclear core. They also impose a rod-to-shroud gap sufficient to allow the secondary flows to pass round the peripherical rods, but this involves a larger cross-section of the subchannel to heating perimeter ratio. These two facts result in a short distance enthalpy radial-peaking factor which is higher in a CHF experiment than in a true LWR core, and, in two-phase flow, in higher quality and void fraction radial peaking factors, and, consequently in higher "short distance" secondary two-phase flows: for the same short radial distances (a few centimetres) there is usually more to mix in a CHF experiment than in an actual LWR core.

The way to use a rod bundle CHF experiment for an actual PWR core calculation may be symbolized by the following figure:

Figure 2

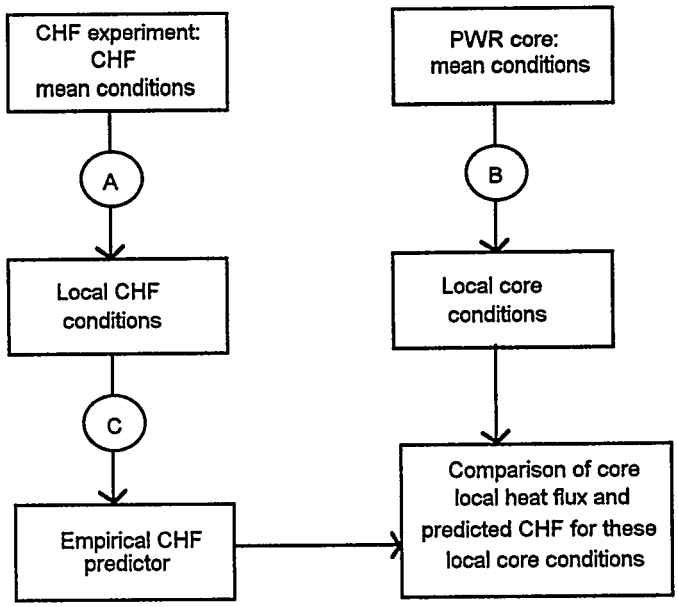

The "A" and "B" process is usually implemented with the help of subchannel analysis code such as FLICA, THYC, COBRA, etc. One of the main purposes of these codes is to model the secondary flows.

In CHF experiments, "long" and "intermediate" distance secondary flows are impossible (presence of the shroud). But, as mentionned previously, "short distance" secondary flows are enhanced. Consequently, the mixing grid effects (mainly short radial distance effects and enhancement of turbulence) have a comparatively greater influence in the "A" process than in the "B" one, because there is more to mix in "A" than "B". It is thus very important to have a reliable

description of this **mixing effect**, in order to validate the **mixing coefficient**, or equivalent, used in the subchannel analysis codes.

The CEA has two experimental facilities for studying this mixing effect: HYDROMEL in single phase flow and GRAZIELLA in two-phase flow.

In HYDROMEL, a rhodamine solution is injected into the most central subchannel of a 5 × 5 to 9 × 9 rod bundle, upstream from a mixing grid, in an adiabatic, low pressure and moderate temperature water flow. The local concentrations in each channel are measured first between the injection point and the mixing grid to quantify natural diffusion and then downstream from the mixing grid at different locations to quantify mixing effect efficiency and its variations and then adjust the mixing coefficient of FLICA code.

An interesting feature revealed by this experiment is the high asymmetry of the subchannels even a long way downstream from the mixing grid (L/Dh greater than 30).

On GRAZIELLA, isokinetic sampling is performed at the end of a 5 × 5 heating rod bundle in a freon R12 two-phase flow simulating high pressure high temperature water flow. The parameter range is characteristic of a PWR in an incidental condition, prior to the boiling crisis. 36 sampling probes can extract the totality of each subchannel to measure the sampled mass flow rate and enthalpy. The major difficulty is minimizing flow disturbance, so considerable attention is paid to the isokinecity of sampling: the exit level pressure map, precisely measured by 36 pressure taps, must remain the same with a very high stability before and during sampling. The procedure and the technology has been tested previously on FRENESIE, a 2 × 2 rod bundle.

The results are devoted to validating the description of the two-phase mixing effect in industrial subchannel analysis code such as FLICA.

5. A FINE DESCRIPTION OF THE SINGLE-PHASE MIXING EFFECT

The industrial subchannel analysis codes such as FLICA, THYC, COBRA, THINC, etc. provide overall **predictions** of the **mixing effect** and are based on a overall **description** of this mixing effect observed on experiments like HYDROMEL or GRAZIELLA.

The physics included in the code is devoted to giving **as reliable as possible an extrapolation of the experimental results** from a CHF experiment to an actual nuclear reactor for a given mixing grid. With this type of code, it is not possible to predict the effect of a new mixing grid geometry or even understand the behavior of an existing one.

As we would also like to understand mixing grid behavior, we need to determine the flow pattern at a very fine scale, ideally below the scale of the smallest structure of the flow pattern.

To progress toward this aim, two tools are used: the AGATE experiment and the TRIO code.

AGATE [24, 25] is a 3D laser Doppler anemometry test loop. It provides a precise (± 5 cm/s) and very local (the measurement volume is about 2×10^{-3} mm^3) description of the velocity and turbulence field in a 5 × 5 rod bundle, upstream and downstream from a mixing grid in an adiabatic low pressure moderate temperature single phase water flow. A two-color laser measures the two or three components of the velocities in the unshadowed area.

Figure 3 presents the areas where the 2 or 3 components of the velocities are measured in AGATE test section.

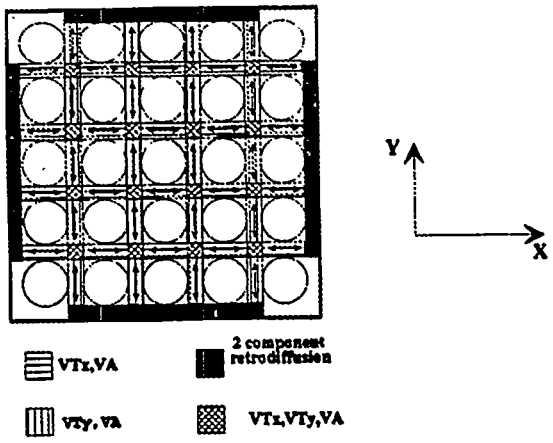

Figure 3 Two and three component velocities measured by AGATE

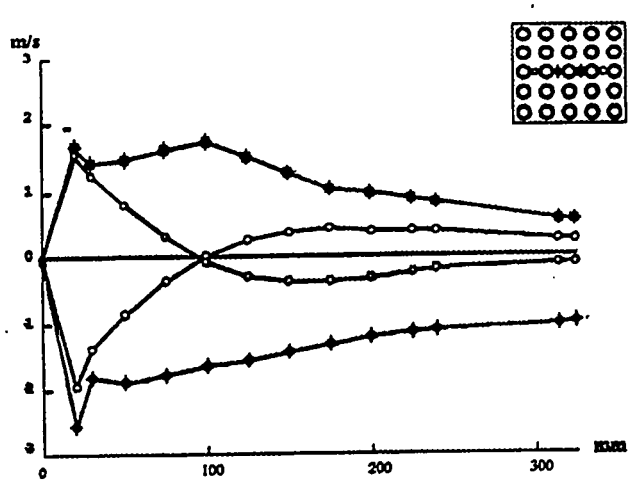

Figure 4 : AGATE - Axial evolution of transverse velocities

The numerous results reveal a complex velocity field with, for example, some inversion in cross flows. It has been observed that this flow behaviour depends strongly on the position, dimension, shape and inclination of the mixing vanes at the upper part of the mixing grid.

An example of results, the axial evolution of transverse velocities with some inversion of the flow, is presented in figure 4. This result is compared to the calculations of TRIO, a fine-meshing 3D single-phase flow computer code. We used the "natural" version of this code, with minimum closure laws but a turbulence model. The code is mainly based on local instantaneous balance equations with the usual hypotheses, such as incompressible Newtonian fluid.

The turbulence is modelled using the "large-scale simulation and sub-grid modelization" technique [26]. There is no "mixing coefficient" or equivalent. The mixing effect is only determined by a description of the geometry of the mixing vanes and mixing grids.

To obtain a satisfactory fit between the AGATE experiments and the TRIO calculations, we need a fine description of the grid and vane design and consequently a very fine meshing (the characteristic dimension of the mesh is 1 mm as an order of magnitude).

At this point, the objectives of AGATE and TRIO are:

- to facilitate the understanding of the mixing phenomenon, secondary flows, and so on,
- to allow a reliable extension of the 5 × 5 experimental results to the actual 17 × 17 nuclear fuel assembly,
- to be able to make numerical sensitivity studies on the geometry of the mixing vanes in order to optimize the geometries to be tested on AGATE.

Once the use of TRIO is well qualified on AGATE tests, it could be used as a R&D tool.

The knowledge of the flow velocity field is therefore summarized with an appropriate set of coefficients in a fast-running industrial subchannel analysis code such as FLICA.

It is obvious that the main drawback is that this approach deals only with single phase flow in the present state of the art.

Work is under way to find an equivalent fine description of the two phase mixing effect. It would involve both bringing together, in one experiment, the capabilities of AGATE and DEBORA a two phase flow version of a fine 3D code.

We hope that, in the more distant future, we may obtain a reliable description of both two phase cross-flows and two-phase flow topology. This fine two-phase description of the flow could then be used with an improved mechanistic model to obtain a reliable, physical and precise prediction of boiling crisis conditions.

6. OVERALL CHF CONDITIONS FOR INDUSTRIAL USE

With the present state of the art, a global CHF experiment with the real geometry is needed in order to obtain reliable and directly usable boiling crisis information. This is the left entry of figure 2. In our strategy, it is implemented by the OMEGA experiment: (a 5 × 5 rod bundle, 2 MPa to 17 MP, 355°C in water, 10 MW). A large number of wall thermocouples can detect the boiling crisis and its axial and azimuthal position. A wide variety of mixing-grid geometries and dispositions, axial and radial heat flux shape, diameters and pitches have been tested. It is also possible to have either an adiabatic shroud or a heating one. The measurement (in single phase) of fluid temperature maps can assess the single-phase mixing efficiency of the grids.

As explained in the left part of figure 2, the mixing effect of the grids is taken into account to obtain the local conditions from the mean boiling crisis conditions.

Then the remaining part of the total effect, that we call the intrinsic effect, is quantified by a empirical CHF predictor, usually by using the PLAQUE method (the "C" process in figure 2).

CONCLUSION

The strategy used to study the boiling crisis has been presented. We try to finalize a coherent set of methods, experimental facilities and computer codes in order to obtain:

- better knowledge and understanding of the fundamental phenomena involved,
- reliable and directly usable information on the boiling crisis, such as CHF predictors.

We emphasize the geometry and parameter range useful for PWR cores under normal and incidental conditions. Starting from very local measurements, tools are provided to transpose this basic knowledge to actual reactor conditions. This strategy is designed to help our industrial partners in their never-ending search for better performance and safety.

Acknowledgement

These CHF studies were carried out thanks to the collaboration of Electricité de France and FRAMATOME.

REFERENCES

[1] Whalley, P.B., Hutchinson, P. & Hewitt, G.F. (1974), "The calculation of critical heat flux in forced convection boiling", *Proc. 5th Int. Heat Transfer Conf.*, Versailles, vol. 4, pp. 290-294.

[2] Whalley, P.B., Hutchinson, P. & James, P.W. (1978), "The calculation of critical heat flux in complex situations using an annular flow model", *Proc. 6th Int. Heat Transfer Conf.*, Toronto, vol. 5, pp. 65-70

[3] Weisman, J. & Pei, B.S. (1983) "Prediction of critical heat flux in flow boiling at low qualities", *Int. J. Heat Mass Transfer*, vol. 26, n° 10, pp. 1463-1476

[4] Weisman, J. & Ying, S.H. (1983) "Theoretically based CHF prediction at low qualities and intermediate flows", *Trans. Am. Nucl. Soc.* , vol. 45, pp. 832-833

[5] Weisman, J. & Ying, S.H. (1985) "Theoretically based Critical Heat Flux prediction for rod bundles at PWR conditions", *Nucl. Engng Design* , vol. 85, pp. 239-250

[6] Weisman, J. & Ileslamlou, S. (1988) "Phenomenological model for prediction of critical heat flux under highly subcooled conditions", *Fusion Technology* , volume 13, pp. 654-659

[7] Lim, J.C. & Weisman, J. (1990) "A phenomenologically based prediction of the Critical Heat Flux in channels containing an unheated wall", *Int. J. Heat Mass Transfer*, vol. 33, p. 203

[8] Weisman, J. (1991) "The current status of theoretically based approaches to the prediction of the Critical Heat Flux in flow boiling", *ASME/JSME Thermal Engineering Proc.*, vol. 2

[9] Lee, C.H. & Mudawwar, I. (1988) "A mechanistic critical heat flux model for subcooled flow boiling based on local bulk conditions", *Int. J. Multiphase Flow*, vol. 14, n°6, pp. 711-721
[10] Lin, W.S., Lee, C.H. & Pei, B.S. (1989) "An improved theoretical critical heat flux model for low quality flow", *Nucl. Tech.*, vol. 88, pp. 294-306
[11] Katto, Y., (1990) "A physical approach to critical heat flux of subcooled flow boiling in round tubes", *Int. J. Heat Mass Transfer*, vol. 33, n° 4, pp. 611-620
[12] Katto, Y., (1990) "Prediction of critical heat flux of subcooled flow boiling in round tubes", *Int. J. Heat Mass Transfer*, vol. 33, n° 9, pp. 1921-1928
[13] Tong, L.S., Currin, H.B., Larsen, P.S. & Smith, O.G. (1965), "Influence of axially nonuniform heat flux on DNB", *Chem. Engng Progr. Symp. Series*, vol. 62, n° 64, pp. 35-40
[14] Tong, L.S., (1968) "Boundary layer analysis of the flow boiling crisis", *Int. J. Heat Mass Transfer*, vol. 2, pp. 1208-1211
[15] Tong, L.S., (1968) "A phenomenological study of critical heat flux", *ASME Paper 75-HT-68*
[16] Katto, Y., (1994) "Critical heat flux", *Int. J. Multiphase Flow*, vol. 20, Suppl., pp. 53-90
[17] Garnier, G., Cubizolles, G., Herer, C.(1995), "Flow pattern in boiling freon R12 simulating PWR conditions: methodology for probe design, signal processing, data acquisition and treatment", *2nd Int. Conf. on Multiphase Flow*, April 1995, Kyoto, Japan.
[18] Garnier, G., Cubizolles, (1995), "Experimental results on flow pattern in boiling freon R12 simulating PWR conditions", European Two-Phase Flow Group Meet., Nederlands, 1995.
[19] de Crécy, F (1994), "The effect of grid assembly mixing vanes on critical heat flux values and azimuthal location in fuel assemblies", *Nuclear Engng and Design*, vol. 149, pp. 233-241
[20] Groeneveld, D.C., Erbacher, F.J., Kirillov, P.L., Bobkov, V.P. & Zeggel, W. (1993), "An improved table look-up method for predicting critical heat flux", *NURETH 6*, Grenoble, France, oct. 5-8, 1993
[21] de Crécy, F (1994), "Pseudo-cubic thin-plate type spline method for analysing experimental data", *Nuclear Engineering and Design*, vol. 149, pp. 459-465
[22] Ayed, R & Bourteele, J.P. (1989), "Theoretical evaluation of currently used critical heat flux correlations", Tr*ansactions ANS*, vol. 59, Atlanta, June 1989
[23] de Crécy, F (1994), "About critical heat flux correlations using inlet conditions", *31st European Two-Phase Flow Group Meeting*, Piacenza, Italy, june 6-8, 1994.
[24] Falk, F. & Memponteil, A., (1994), "AGATE : détermination d'un champ de vitesse 3D en géométrie complexe par vélocimétrie laser à effet Doppler 2 dimensions", *4ème Congrès Francophone de Vélocimétrie Laser*, Poitiers, France, 26-29 sept. 1994.
[25] Herer, C. (1991), "3D flow measurements in nuclear fuel rod bundles using laser Doppler velocimetry", *FED*, volume 108, *Fluid Measurement and Instrumentation Forum*, ASME, Portland, USA, 1991.
[26] Metais, O., Lesieur, M. (1992), "Spectral large-eddy simulation of isotropic and stably stratified turbulence", *J. Fluid Mechanics*, vol. 239, pp. 157-194.

An Investigation of Transition Boiling Mechanisms of Subcooled Water under Forced Convective Conditions

Kwang-Won, Lee and Sang-Yong, Lee
Nuclear Power Engineering
Korea Atomic Energy Research Institute

ABSTRACT

A mechanistic model for forced convective transition boiling has been developed to investigate transition boiling mechanisms and to predict transition boiling heat flux realistically. This model is based on a postulated multi-stage boiling process occurring during the passage time of the elongated vapor blanket specified at a critical heat flux (CHF) condition. Between the departure from nucleate boiling (DNB) and the departure from film boiling (DFB)points, the boiling heat transfer is established through three boiling stages, namely, the macrolayer evaporation and dryout governed by nucleate boiling in a thin liquid film and the unstable film boiling characterized by the frequent touches of the interface and the heated wall. The total heat transfer rates after the DNB is weighted by the time fractions of each stage, which are defined as the ratio of each stage duration to the vapor blanket passage time. The model predictions are compared with some available experimental transition boiling data. The parametric effects of pressure, mass flux, inlet subcooling on the transition boiling heat transfer are also investigated. From these comparisons, it can be seen that this model can identify the crucial mechanisms of forced convective transition boiling, and that the transition boiling heat fluxes including the maximum heat flux and the minimum film boiling heat flux are well predicted at low qualities/high pressures near 10 bar. In future, this model will be improved in the unstable film boiling stage and generalized for high quality and low pressure situations.

I. INTRODUCTION

Transition boiling is an intermediate heat transfer mode where the heated surface temperature is too high to maintain nucleate boiling but too low to maintain stable film boiling. In this boiling mode, an increase in surface tempearture usually results in a decrease in surface heat flux. The transition boiling region of the boiling curve is traditionally considered to be bounded by the critical heat flux (CHF) with the corresponding CHF temperature (this point corresponds to the maximum heat flux point in the boiling curve) and by the minimum film boiling (MFB) heat flux with the corresponding MFB temperature (see figure 1). However, the transition boiling boundaries may be determined on the phenomenological basis as the points "a" and "d" rather than the points "b" and "c", as shown in Figure 1. Point "a" indicates the departure from nucleate boiling (DNB), which is characterized by the appearance of unstable local dry spots on the heating surface. Point "d" shows the departure from film boiling (DFB) characterized by the appearance of unstable local cold spots on the heating surface. Kalinin et al. [1] took notice of the fact that the transition from nucleate to film boiling with increasing the wall superheat ΔT_w (or the opposite transition with decreasing ΔT_w) is gradual and smooth, and the maximum heat flux (MHF) and MFB heat flux are interior points of the transition boiling region. To investigate the transition boiling mechanism based on the various experimental observations [1,2], this classification is considered more promising than the traditional one.

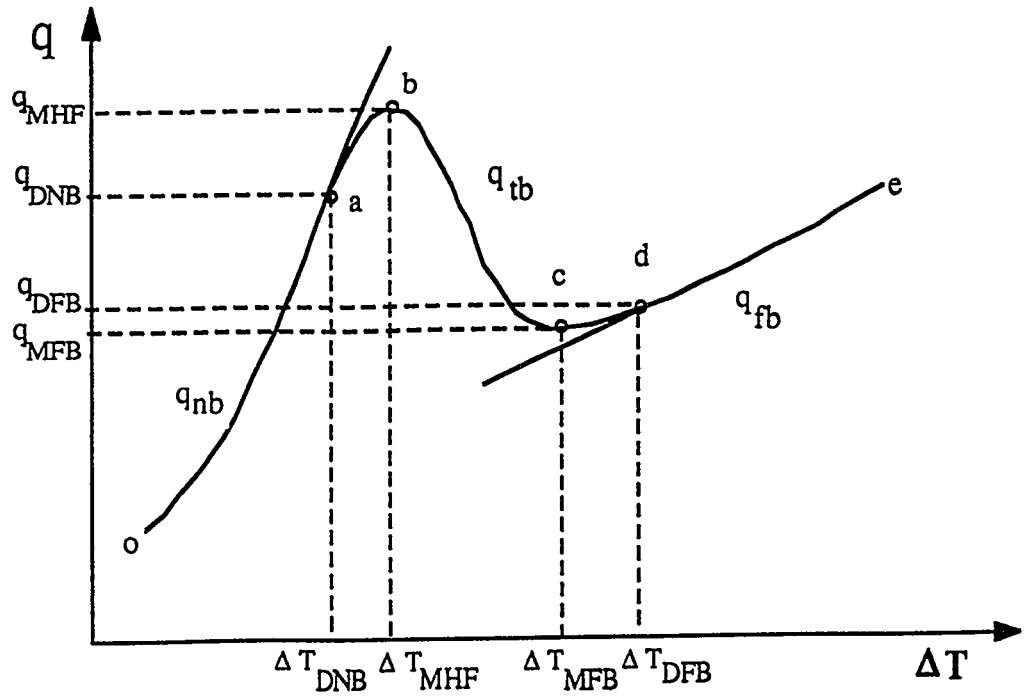

Figure 1. Schematic Diagram for Transition Boiling Boundaries. Point (a): Nucleate Boiling Instability Boundary, Point (b): Maximum Heat Flux, Point (c): Minimum Film Boiling Heat Flux, Point (d): Film Boiling Stability Boundary.

Recently, the practical interest in transition boiling has increased in connection with the safety analysis of nuclear reactors, especially with studies of hypothetical loss of coolant accidents (LOCA) as the design basis accident for light water reactors, and heat treatment of metals. Up to now, the experimental and theoretical studies have been plentifully performed for the transition boiling in pool boiling situations, but scarce in forced convective boiling situations. The comprehensive review of Kalinin et al. [1] and Auracher [2] of transition boiling shows that the present knowledge about transition boiling mechanism is plentiful only for pool boiling situations. However, the forced convective transition boiling mechanism is poorly understood due to the inherent complexity of this phenomenon and the experimental difficulties. Consequently, available prediction methods are promising in the pool boiling situations but yield large discrepancies in the forced convective boiling situations due to their limitations caused by the difficulty in accounting for the various physical mechanisms in a single correlation and the lack of reliable data base.

Most of the prediction methods for transition boiling are based on Berenson's postulate [3] that transition boiling is a combination of unstable nucleate boiling and unstable film boiling, each of which alternatively exists at any given location on the heating surface. This can be formulated as

$$q_{tb} = F_A q_l + (1 - F_A) q_v , \qquad (1)$$

where, q_l and q_v designate the average heat flux during the liquid contact and the vapor contact, respectively. F_A denotes the average statistical fraction of the wetted area on the heated wall at a given moment.. If the liquid-solid contact process can be assumed to be ergodic, the local liquid contact time fraction, F_T, is considered to be equal to the wetted area fraction, F_A.

Based on the idea of Equation (1), some phenomenological models for forced convective

transition boiling have been developed by several authors, such as Ragheb and Cheng [4], Bjornard and Griffith [5], and Kao and Weisman [6]. In the first two models, they assume that q_l and q_v are constant during the contact process, and equal to the MHF and the MFB heat flux of a boiling curve, respectively. They also assume that a linear relationship exists between the two anchor points and F_A =1 at the MHF point and F_A=0 at the MFB heat flux point, respectively. In these models, the expression of F_A becomes

$$F_A = [(T_w - T_{MFB}) / (T_{MHF} - T_{MFB})]^2. \quad (2)$$

However, Kao and Weisman [6] introduced a moving quench front model to estimate the wetted area fraction (F_A) at high quality and low flow conditions, and used a wetted heat flux curve decreasing with temperature instead of a fixed MHF and a vapor convection heat flux instead of a fixed MFB heat flux, respectively, as two anchor points. In this model, the first anchor point is not the MHF point but the DNB point in the boiling curve (see point "a" in the figure 1), thus the wetted area fraction at the MHF does not need to be unity.

In fact, the recent experimental studies [1, 2, 7-9] for the wetted area fraction show that F_A at the MHF is far below unity. Therefore, the correlations of the wetted area fraction derived from Equation (2) cannot be regarded as a reasonable estimate. Up to now, we cannot find reliable correlations for the estimation of the wetted area fraction in the forced convective boiling conditions, especially at low qualities/high flows. On the other hand, most of the recent theoretical studies on the transition boiling for pool boiling conditions, such as those of Kalinin et al. [1], Pan, Hwang, and Lin [10], and Farmer et al. [11], assumed that the liquid-solid contact process as a periodic sequence of transient conduction, nucleation and macrolayer dryout, and vapor film boiling phases on the heating surface. In these models, the wetted area fraction was evaluated by the liquid contact time fraction, assuming the contact process to be ergodic. These studies showed that the wetted area fraction at the MHF point was smaller than unity and the MHF point is much higher than the steady state CHF value as the upper limit of nucleate boiling.

In this context, we attempt to develop a mechanistic prediction model for the forced convective transition boiling of subcooled water, based on the basic idea of Pan, Hwang, and Lin (PHL) theoretical model [10] for the pool boiling. For a specific feature of forced convective transition boiling, some mechanisms and assumptions of PHL model will be modified, and their rationales will be discussed in the section of physical model and basic assumptions. The primary objective of this study is to predict the transition boiling heat flux properly, and to explain adequately the recent experimental evidence that the wetted area fraction at the MHF is smaller than unity and the liquid contact heat flux is higher than the CHF value.

II. MODEL DESCRIPTION

II.1 Physical Model and Basic Assumptions

Based on the previous investigations [10, 12-17] of the physical mechanisms of critical heat flux, transition boiling, and film boiling phenomena, the present physical model is supposed, as depicted in Figure 2. For a complete transition boiling cycle, there are four key boiling stages, namely, *approaching of vapor blanket, macrolayer evaporation, macrolayer dryout,* and *unstable film boiling* with frequent liquid-solid contacts. It is assumed that the transition boiling cycle starts when a vapor blanket approaches to a given point on the heated wall. The departure from nucleate boiling (DNB) occurs when the macrolayer dryout time is equal to the vapor blanket passage time, which is determined by dividing the vapor blanket length, L_B, by the blanket velocity, U_B, at a CHF condition. Before the DNB, the heat transfer through the macrolayer is governed by a fully developed nucleate boiling. After the DNB, the wall heat transfer is established through two boiling stages, i.e., the *macrolayer evaporation* governed by a nucleate boiling in thin liquid film and the *unstable film boiling* with alternate wet and dry periods induced by the instability of the liquid and vapor interface. The present model assumes that the total heat transfer rate during transition boiling is the sum of the heat transfer rates after the DNB weighted by the time fractions of each stages which are defined as the ratio of each stage duration to the vapor blanket passage time. The transition boiling heat

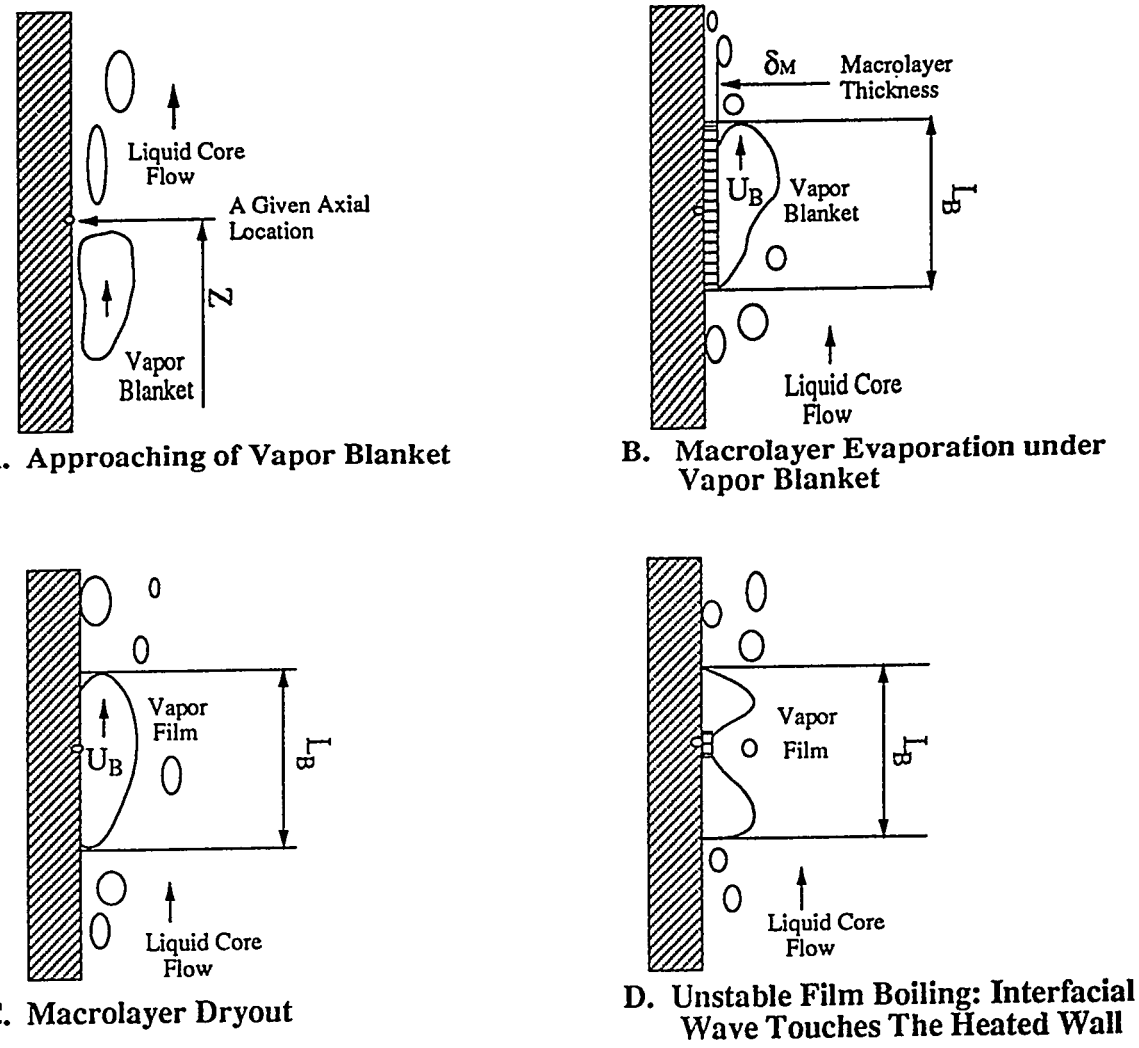

Figure 2. Illustration of the Physical Model for Each Stage of Transition Boiling Cycle

transfer is terminated when the wall superheat exceeds the DFB temperature characterized by a complete separation of the liquid-vapor interface from the wall. From the assumed ergodicity of the time sequential process during the vapor blanket passage over a given point, the transition boiling heat flux at a given axial location can be estimated.

This physical model is similar to that of PHL pool boiling model [10], but it is considerably modified to accommodate the specific feature of forced convective situations. The PHL model was based on three contributors of the transition boiling process, i.e., transient conduction, macrolayer evaporation, and vapor film boiling. In the present model, the effect of transient conduction on the forced convective transition boiling is assumed negligible and the vapor film boiling stage is replaced by the unstable film boiling stage due to the instability of the vapor-liquid interface under the forced convective boiling in the vertical tube geometry. To satisfy the ergodicity of the transition boiling process, the controlling phenomena are selected as a time sequential process occurring at a given point during the vapor blanket passage, instead of the controlling phenomena under the hovering bubble on the heated surface of PHL model. If the specified vapor blanket characteristics (its size, length, and velocity) are suitable as compared with the tube diameter and length, and the time scale including all the controlling phenomena, the ergodicity will be satisfied.

The present model is also similar to that of Katto, Yokoya, and Yasunaka (KYY) [17] for the pool transition boiling process. In the KYY proposal, the bubble departure period specified at a CHF condition does not vary during the transition boiling process and the liquid macrolayer evaporation is the same as the nucleate pool boiling. Therefore, the DNB occurs when the liquid macrolayer dryout time is equal to that for the bubble departure time, and the heat flux after the DNB is determined by multiplying the wetting time fraction by the nucleate pool boiling heat flux. In this approach, the boiling curve slope of transition boiling region is too steep. This problem is overcome in the present model by introducing a new boiling mechanism in a very thin liquid film after the DNB and considering the strong contribution of an unstable film boiling on the total transition boiling heat flux in the forced convective boiling situations.

Katto [12], Lee and Mudawwar [13], and Mudawwar et al. [14] have developed the theoretical CHF model under subcooled flow boiling based on the similar physical mechanism. They have claimed that the crucial CHF mechanism of subcooled flow boiling is a macrolayer dryout under an elongated vapor blanket. Here, the macrolayer means the thin liquid film under the elongated vapor blanket formed adjacent to the wall surface at near the CHF condition, which is distinguished from the microlayer below a fast growing bubble in nucleate boiling. According to this physical mechanism, the CHF condition reaches when the macrolayer dries out during the vapor blanket passage time (L_B / U_B). In the present model, this mechanism is used for the determination of the DNB condition.

Ueda and Kim [15] and Hino and Ueda [16] investigated heat transfer characteristics near the CHF condition in a subcooled flow boiling system. They concluded that the wall temperature excursion at the CHF condition was composed of the temperature fluctuations which accompany periodic passing of large coalescent bubbles close to the surface and a subsequent sharp temperature rise under a film boiling state. Since this heat transfer characteristics is similar to that of transition boiling, the macrolayer behaviour under the vapor blanket is also thought to be a very important heat transfer mechanism in the transition boiling process.

After the DNB condition (point "a" in Figure 1), the macrolayer dries out before the vapor blanket passage time due to the thin film boiling heat flux which is higher than the CHF. Therefore, the *macrolayer evaporation stage* can contribute to the transition boiling heat flux in proportion to the macrolayer dryout time fraction to the vapor blanket passage time. Up to the MHF, this macrolayer evaporation will be a major contributor to the total heat flux.

Just after the *macrolayer dryout*, the wall surface is covered by thin vapor film. At this time, a depression in the vapor-liquid interface occurs due to the insufficient vapor generation and it allows the interface to touch the dry wall surface if the wall temperature is below the DFB temperature (point "d" in Figure 1). This touching results in a vigorous boiling at the wall surface and then the interface is repulsed from the wall. This sequence is periodic and lasts until the vapor blanket passes a given point. Qualitatively, the frequency of this sequence is the highest near the MHF temperature and the lowest near the MFB temperature. In this model, the heat transfer characteristics of this sequence is evaluated by the simple thermomechanical model for the *unstable film boiling* proposed by Huang et al. [18]. The unstable film boiling period is determined by subtracting the macrolayer dryout time from the vapor blanket passage time.

The basic assumptions for the mathematical formulation of the physical model are listed below :

(1) The time sequential process occurring at a given point during the vapor blanket passage is ergodic.
(2) The vapor blanket passage time specified at the CHF condition remains constant with increasing wall superheat, ΔT_w.
(3) The average length and velocity of the vapor blanket during the unstable film boiling period does not vary.
(4) The thermal and physical properties at a given point are determined at the CHF condition.

II.2 Mathematical Formulations of Physical Model

A. Critical Heat Flux and Vapor Blanket Characteristics

In the present physical model, the CHF condition for forced convective boiling at low qualities is reached when the macrolayer dryout time is equal to the vapor blanket passage time. Based on the previous works of Katto [12], Lee and Mudawwar [13], and Mudawwar et al.[14], the CHF and the vapor blanket characteristics, i.e., its size, length, and velocity, are determined as follows.

From the mass balance on vapor stems in the macrolayer beneath the vapor blanket, each phase velocity is related as

$$\rho_g U_g A_g = \rho_f |U_f| (A - A_g) , \tag{3}$$

where, A and A_g denote the total surface area beneath the vapor blanket and the cross-sectional area of vapor stems, respectively. This equation simply means that there is a balance between the vapor outflow and the liquid inflow in the macrolayer. The vapor velocity is obtained by the energy balance on vapor stems as follows;

$$q_B A = \rho_g U_g A_g h_{fg} , \tag{4}$$

where, q_B, is a boiling heat flux for vaporization, which is given as

$$q_B = q_{chf} - q_{sc} . \tag{5}$$

Here, the subcooled liquid convective heat flux, q_{sc}, given by the Shah's correlation for high flux boiling conditions [20], can be expressed as

$$q_{sc} = \frac{230 q_{chf} (q_{chf} / G h_{fg})^{0.5} (T_{sat} - T_{lc})}{(230 (q_{chf} / G h_{fg})^{0.5} - 1)(T_{sat} - T_{lc}) + q_{chf} / H_{fc}} , \tag{6}$$

where, the single phase forced convective heat transfer coefficient, H_{fc}, is given by the well-known Dittus-Boelter correlation for turbulent flow. The allowable relative velocity in the vapor stem can be evaluated by the Helmholtz instability criterion as follows;

$$(U_g - |U_f|)^2 = 2 \pi \sigma (\rho_f + \rho_g) / (\rho_f \rho_g \lambda_H) . \tag{7}$$

The thickness of the macrolayer at the CHF condition is assumed by Haramura and Katto [19] as follows;

$$\delta_{chf} = \lambda_H / 4 . \tag{8}$$

From Equations (3), (4), (7), and (8), the macrolayer thickness can be rewritten as;

$$\delta_{chf} = \frac{(\pi / 2)(1 + \rho_f / \rho_g) \sigma (A_g / A)^2}{[1 + (\rho_f / \rho_g) \frac{A_g / A}{1 - A_g / A}]^2 \rho_g (\frac{q_B}{\rho_g h_{fg}})^2} , \tag{9}$$

where, A_g / A is given by Haramura and Katto's correlation [19] as follows ;

$$\begin{aligned} A_g / A &= 0.0654 [(11 \rho_f / 16 \rho_g + 1)^{3/5} / (\rho_f / \rho_g + 1)]^{1/2} \\ &\approx 0.0584 (\rho_f / \rho_g)^{0.2} \qquad \text{for} \quad \rho_f / \rho_g >> 1 . \end{aligned} \tag{10}$$

The CHF condition occurs when the liquid supply into the macrolayer from the core flow is completely vaporized and can be formulated as follows,

$$L_B q_{chf} = \rho_f (U_B - U_M)\delta_{chf} h_{fg}\{1+(h_f-h_{lc})/h_{fg}\}(1-A_g/A), \quad (11)$$

where, L_B and U_B are the length and velocity of the vapor blanket, respectively. And U_M is the macrolayer velocity, which is assumed nearly zero. The vapor blanket length can be determined by introducing Helmholtz instability criterion between the macrolayer and the vapor blanket, thus

$$L_B = 2\pi\sigma(\rho_f+\rho_g)/[\rho_f \rho_g (U_B - U_M)^2]. \quad (12)$$

Since the macrolayer velocity is negligible as compared with the vapor blanket velocity, the relative velocity can be considered equal to the vapor blanket velocity. The vapor blanket velocity can be written from the force balance between buoyancy and drag force on the vapor blanket as follows;

$$U_B = \sqrt{2L_B g(\rho_{lc}-\rho_g)/\rho_{lc}C_D} + U_{bl}, \quad (13)$$

where, U_{bl} and C_D are the liquid alone velocity (or two-phase mixture velocity) at the mass center of vapor blanket and the drag coefficient of the vapor blanket, respectively. If the liquid alone flow is turbulent, the liquid alone velocity, U_{bl}, can be obtained by the well-known Karman's three layer velocity profile. If the liquid alone flow is laminar, U_{bl} can be determined by,

$$U_{bl} = 2G/\rho_{lc}\{1-(R_o - y_B)^2/R_o^2\}. \quad (14)$$

Here, the distance of the vapor blanket center from the wall, y_B, is

$$y_B = \delta_{chf} + D_b/2. \quad (15)$$

The vapor blanket diameter is assumed equal to the bubble diameter at the bubble detachment point, D_b. The correlations for the drag coefficient, C_D, and the vapor blanket diameter, D_b, will be discussed in the section of the constitutive equations. Consequently, the CHF is obtained by Equation (11) and the vapor blanket characteristics are determined by Equations (12) and (13).

B. Macrolayer Evoparation

Before the DNB, the macrolayer thickness is larger than that for the CHF condition (δ_{chf}) and the heat transfer through the macrolayer can be evaluated by the fully developed nucleate boiling heat flux, which is estimated by the correlation of Mikic and Rohsenow [21]. Since the macrolayer beneath the vapor blanket appears to be nearly stagnant, this approach is considered reasonable. Experimentally, Fujita and Ueda [22] showed that the surface heat flux in falling liquid film approaches to a pool boiling heat flux as the wall superheating increases. From the Mikic and Rohsenow correlation for water boiling data [21], the fully developed nucleate boiling heat flux is expressed in SI units as follows:

$$q_{nb} = \frac{1.89\times10^{-14}\sqrt{g\kappa_f}(\rho_g h_{fg})^{1/8}\rho_f^{17/8}c_{pf}^{19/8}\Delta T_w^{3}}{\sigma^{9/8}(\rho_f-\rho_g)^{5/8}T_{sat}^{1/8}}. \quad (16)$$

After the DNB, the macrolayer becomes thinner than that for the CHF condition (δ_{chf}), the heat transfer through the macrolayer is changed from fully developed nucleate boiling to a thin film boiling. This thin film boiling is very different from the pool boiling or forced convective boiling. Mesler [23] suggested that the nucleate boiling heat flux in a thin liqud film might be exceptionally high because a bubble generated in the thin film can escape quickly with a very small resistance. Kopchikov et al. [24] developed a correlation for the thin film boiling heat transfer which focussed on the heat transfer through the quasi-laminar layer adjacent to the growing bubble. This correlation is expressed below;

$$q_{mb} = \frac{C\kappa_f h_{fg} \rho_g \rho_f \Delta T_w^2}{\sigma\ T_{sat}(\rho_f - \rho_g)}, \tag{17}$$

where, C is a empirical constant, which is given as 0.01 for the various fluids including water at the atmospheric and subatmospheric pressures. Kopchikov et al. [24] also explained that the boiling heat flux in a thin film boiling could increase up to the heat flux associated with the limiting temperature of the liquid superheat (i.e., Leidenfrost temperature), since in thin film boiling there are practically no hydrodynamic restrictions on the removal of the vapor and supply of the liquid.

Beattie and Lawther [25] investigated the structural change in a thin annular film as dryout is approached, and developed a more generalized thin film boiling heat flux equation based on the heat transfer through a single close-packed hexagonal layer of bubbles. If "N" bubble layers exist in the thin film, the boiling heat flux is given by

$$q_{mb} = \frac{0.0288\kappa_f h_{fg} \rho_g \rho_f \Delta T_w^2}{N\sigma\ T_{sat}(\rho_f - \rho_g)}. \tag{18}$$

It can be seen that the Beattie and Lawther correlation (Eq. 18) is equivalent to that of Kopchikov et al. if N is assumed to be 2. In the present model, the boiling heat flux in the macrolayer after the DNB is determined by Equation (18) with N=2 for the pressur below 110 kPa and N=3 for the pressure higher than 110 kPa. For the higher pressures than 110 kPa, the selection of higer N value is to consider the effect of the pressure on the packing of bubble layers in the macrolayer.

The DNB wall temperature can be determined by rearranging Equation (16) after substituting the CHF (Eq.11) for the nucleate boiling heat flux, q_{nb}. The step change in the macrolayer evaporation heat flux before and after the DNB temperature is treated as follows:

$$q_{me} = q_{nb} \quad \text{for } \Delta T_w < \Delta T_{DNB} \tag{19}$$

$$q_{me} = q_{mb}\{\Delta T_w\} + [q_{chf} - q_{mb}\{\Delta T_{DNB}\}] \text{ for } \Delta T_{DNB} < \Delta T_w < \Delta T_{DFB} \tag{20}$$

$$q_{me} = 0 \quad \text{for } \Delta T_w > \Delta T_{DFB}, \tag{21}$$

where, $q_{mb}\{\Delta T_{DNB}\}$ and $q_{mb}\{\Delta T_w\}$ denote the macrolayer boiling heat fluxes determined by Equation (18) as the functions of the wall superheats ΔT_{DNB} and ΔT_w, respectively. Equation (20) means that the macrolayer boiling heat flux after the DNB starts from the CHF value (q_{chf}) and varies with the slope of Equation (18) up to the DFB point. The macrolayer thickness, δ_{me}, during the *macrolayer evaporation stage* can be evaluated by replacing the boiling heat flux, q_B, in Equation (9) with the macrolayer evaporation heat flux, q_{me}, determined by Equations (19) to (21). This thickness is distinguished from the CHF macrolayer thickness, δ_{chf}, of Equation (9). Finally, the *macrolayer dryout time* is given by,

$$\tau_{md} = \rho_{lc}\, \delta_{me}\, h_{fg}\{1+(h_f - h_{lc})/h_{fg}\}/q_{me}, \tag{22}$$

and the contribution of the macrolayer evaporation during the macrolayer dryout timeto the total total boiling heat flux is

$$\overline{q}_{me} = q_{me}\, \tau_{md} / \tau_p, \tag{23}$$

where, τ_p, is the vapor blanket passage time, which is defined as,

$$\tau_p = L_B / U_B \ . \tag{24}$$

C. Unstable Film Boiling

Within the vapor blanket passage time, the macrolayer dries out, and then the heat transfer through a vapor film is available during the vapor film covering time. The vapor film covering time is defined as

$$\tau_{vc} = \tau_p - \tau_{md} \ . \tag{25}$$

During the vapor film coverage time, the unstable film boiling with alternate dry and wet periods is established due to the instability of the vapor-liquid interface, which is augmented by a repeating insufficient and violent vapor generations under the vapor film. Therefore, an information for the interface contact frequency, size, and time is needed to quantify the heat transfer characteristics of the unstable film boiling. Up to now, for the forced convective boiling situations, this information is unavailable in the literature.

In this model, the unstable film boiling heat transfer is simply evaluated by the thermomechanical model proposed by Huang et al. [18]. They developed an equation of the evaporation enthalpy between the wetting zone and dry zone, based on the conservation equations at the vapor-liquid interface. In their model, the wetting liquid on the highly heated wall is assumed to be at saturated state at the elevated pressure, which is defined as the saturation pressure corresponding to the wall temperature. Also, the vapor is assumed to be saturated at the system pressure of the bulk liquid. The resulting equation is

$$h_g - h_f(T_w) = 0.5\,[\,\rho_f(T_w) - \rho_g\,]\,[p_s(T_w) - p] / \rho_g\rho_f(T_w) + (q_l^* - q_v^*)/m \ , \tag{26}$$

where, $h_f(T_w)$, $\rho_f(T_w)$, and $p_s(T_w)$ designate the saturated liquid enthalpy, density, and pressure corresponding to the wall temperature, respectively. And q_l^*, q_v^*, and "m" are defined as

$$q_l^* = q_l + m\,V_l(V_g - V_i) \tag{27}$$
$$q_v^* = q_v + m\,V_g(V_g - V_i) \tag{28}$$
$$m = \rho_g(V_g - V_i) = \rho_f(V_l - V_i) \ , \tag{29}$$

where, q_l and q_v are heat fluxes from liquid phase to interface and from vapor phase to interface, respectively. V_l, V_g and V_i denote the liquid and vapor velocities normal to interface and the interface velocity, respectively. Equation (26) can be interpreted as the fact that the evaporation enthalpy is provided by both heat conduction and the mechanical energy released during the depressurization process of evaporation. Since the vapor is assumed at saturated state, q_v^* in Equation (26) must be zero to keep the vapor at the satuartion temperature. If we assume that q_l^* is negligible near the MFB temperature, Equation (26) can be rewritten by

$$h_g - h_f(T_{DFB}) = 0.5\,[\,\rho_f(T_{DFB}) - \rho_g\,]\,[p_s(T_{DFB}) - p] / \rho_g\rho_f(T_{DFB}) \tag{30}$$

As Equation (30) is used to determine the DFB temperature, this means that the evaporation enthalpy at the DFB point is supplied by the mechanical energy of depressurization alone. From the assumption that the wall heat flux during the unstable film boiling is proportional to the liquid heat flux at the interface, the following equation is derived,

$$q_{fb} = C_A q_l^* = m\,C_A\{h_g - h_f(T_w) - 0.5\,[\rho_f(T_w) - \rho_g\,]\,[p_s(T_w) - p] / \rho_g\rho_f(T_w)\} \ . \tag{31}$$

To remove the proportional coefficient, C_A, the DNB point is selected as the anchor point and then we can obtain the following equation:

$$\frac{q_{fb}}{q_{DNB}} \quad \frac{\{h_g - h_f(T_w) - 0.5\,[\rho_f(T_w) - \rho_g]\,[p_s(T_w) - p] / \rho_g\rho_f(T_w)\}}{\{h_g - h_f(T_{DNB}) - 0.5\,[\rho_f(T_{DNB}) - \rho_g]\,[p_s(T_{DNB}) - p] / \rho_g\rho_f(T_{DNB})\}} \tag{32}$$

For zero heat flux, Equation (32) reduces to Equation (30) for the DFB temperature. Finally, the contribution of the unstable film boiling to the total boiling heat flux is given as,

$$\bar{q}_{fb} = q_{fb}\, \tau_{vc} / \tau_p . \tag{33}$$

D. Boiling Curve Generation

In the present model, the boiling curve ranging from a nucleate boiling region to the DFB point can be generated. When the wall superheat is lower than the DNB temperature or the macrolayer dryout time is shorter than the vapor blanket passage time, the total boiling heat flux is

$$q_t = q_{nb} . \tag{34}$$

Between the DNB point and the MFB point, the total boiling heat flux is

$$q_t = \bar{q}_{me} + \bar{q}_{fb} . \tag{35}$$

Equation (35) involves the DNB heat flux, the MHF and the DFB heat flux in the boiling curve. If the liquid contact time during the vapor coverage period is assumed negligible, the time fraction of liquid contact is given as,

$$F_T = \tau_{md} / \tau_p . \tag{36}$$

If the liquid contact process is ergodic, the following equality can be applied,

$$F_A = F_T . \tag{37}$$

II.3 Constitutive Equations

For the determination of the CHF and the vapor blanket characteristics, the subcooled flow boiling model is required. In the subccoled flow boiling model, the subcooling at the bubble detachment point, (h_f - h_{ld}), is very important in determining the position of bubble detachment and actual quality profile. To evaluate this value, the Saha and Zuber correlation [26] is chosen as the best one for low pressure and low velocity conditions because this correlation can be applicable to laminar and turbulent flows. If the wall heat flux in the pre-CHF region is uniform, the actual quality at the CHF location is given by the profile-fit method [26] using equilibrium qualities at the bubble detachment point and the CHF location. Once the actual quality is determined, the liquid enthalpy at the CHF location is obtained as follows;

$$h_{lc} = [\, h_b - h_g x_g \,] / [\, 1 - x_g \,] , \tag{38}$$

where, the bulk enthalpy, h_b ,is defined as

$$h_b = h_{in} + 4 L_{chf} q_{chf} / GD . \tag{39}$$

The bubble diameter at the bubble detachment point is evaluated by the modified Levy's formula of Ying and Weisman [27] and expressed by

$$D_b = \frac{0.015\sqrt{\sigma D / \tau_w}}{\sqrt{1 + 0.1(\rho_l - \rho_g) g D / \tau_w}} , \tag{40}$$

where, τ_w denotes the wall shear stress. This formula can be applicable to the system that the buoyancy effect on bubble detachment is considerable as compared with the drag force effect,

such as low flow conditions.

The drag coefficient, C_D, for the vapor blanket is evaluated by the formula of Ishii and Mishima [28] for distorted bubble and expressed by

$$C_D = (2/3)D_b\sqrt{(\rho_f - \rho_g)g/\sigma}\left\{\frac{1+17.67(1-\alpha_g)^{9/7}}{18.67(1-\alpha_g)^{1.5}}\right\}^2 \quad (41)$$

From the well-known void fraction and quality relationship based on the drift flux models of Chexal et al. [29] is used to find the void fraction (or quality) when the quality (or void fraction) was known . In addition to this relationship, the flow regime map is used to identify the CHF mechanism and to validate our physical model. The flow regime map is based on Mishima and Ishii's flow transition criteria [30] .

III. RESULTS AND DISCUSSION

To investigate the prediction capability of the present model and to study the parametric effect of pressure, mass flux, and inlet subcooling on the transition boiling heat flux, the comparison of the model prediction with the available experimental data of forced convective transition boiling is performed. As the representative transient boiling curve, we choose the data of Huang et al. [31] and Cheng et al.[32]. The data of Huang et al. [31] and Weber and Johannsen [33] are selected as the representative steady-state data.

For simulation of experimental conditions, several assumptions are needed to fit the model to the experimental procedures and conditions. Since any information for the CHF condition and the post-CHF flow regime is unavailable in the experimental sources [31-33], it is assumed that transition boiling occurs in the overall heated length, and an elongated vapor blanket exists at the CHF condition whenever the inlet water flow is subcooled. The boiling curve at the mid-plane is selected as the representative boiling curve in the test section. The axial conduction due to axial temperature difference or heat flux difference is neglected in this model. The parameter ranges of the selected experimental data are listed in Table 1.

Figure 3 shows the relative contributions of macrolayer evaporation (ME) and unstable film boiling (UFB) stages to the boiling curve. In this figure, two symbolized curves designate steady-state and transient data of Huang et al., respectively. The solid line, dotted line and dashed line denote the total heat flux (given by Eq.35) and the contributions of ME (given by Eq.23) and UFB (given by Eq.33), respectively. The predicted boiling curve is well matched with the steady-state data but overestimated for the transient data whose inlet flow condition is identical with the steady-state case. From this figure, it can be seen that the contribution of macrolayer evaporation dominates before the DNB temperature but rapidly decreases after the DNB temperature, while the contribution of unstable film boiling is negligible before the DNB temperature but rapidly increase with the wall superheat after the DNB temperature. Figure 4 shows the wetted area fraction predicted by this model for the above case. The wetted area fraction decreases rapidly from unity after the DNB temperature and approaches to zero near the DFB temperature. At the MHF point, the wetted area fraction is not about 1.0 but 0.4. This result is well matched with the experimental evidence described in the section of introduction.

Figures 5 to 7 show the prediction trend for the pressure variation from 1 bar to 10 bar. In these figures, the steady-state and transient data of Huang et al. are expressed by the two symbols and the prediction is depicted by one solid line. The experimental data are well predicted in the higher pressures and the steady-state data. The large discrepancy in Figure 5 seems to be caused by the mismatch between the physical model and the real situation. At the low pressure case, the estimated diameter and length of the vapor blanket is too large to satisfy the assumed ergodicity of the controlled phenomena. Especially, the vapor blanket length predicted by the Helmholtz instability criterion is longer than the heated length of test section. For this case, a new instability

Table 1. Parameter Range of Selected Experimental Data

Source / Range	Huang et al. Data	Cheng et al. Data	Weber & Johannsen Data
Experiment Type	Steady-state & Transient	Transient	Steady-state
Pressure (MPa)	0.1 - 1.0	0.101	0.11 - 1.0
Mass Flux (Kg/m^2s)	200, 500	136, 20	100
Inlet Subcooling (K)	5, 15	28	15
Diameter (m)	0.01	0.012	0.01
Length (m)	0.05	0.0572 (Short Tube)	0.05
Mid-plane	2.46 D	2.25 D	2.46 D
Tube Material	Copper (heater) Monel (flow tube)	Copper	Copper (heater) Monel (flow tube)

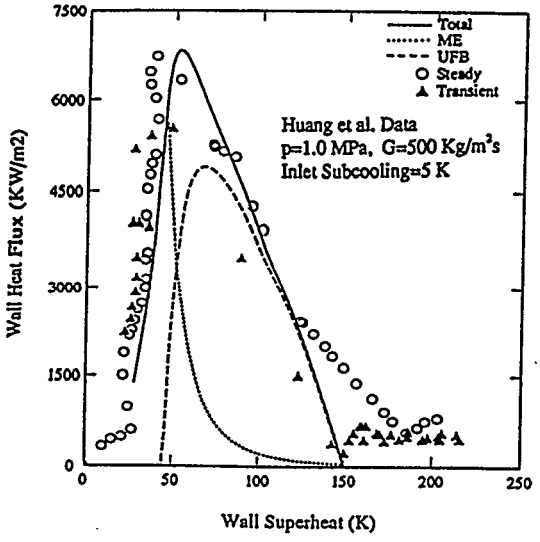

Figure 3. Relative Contributions to Transition Boiling Heat Flux

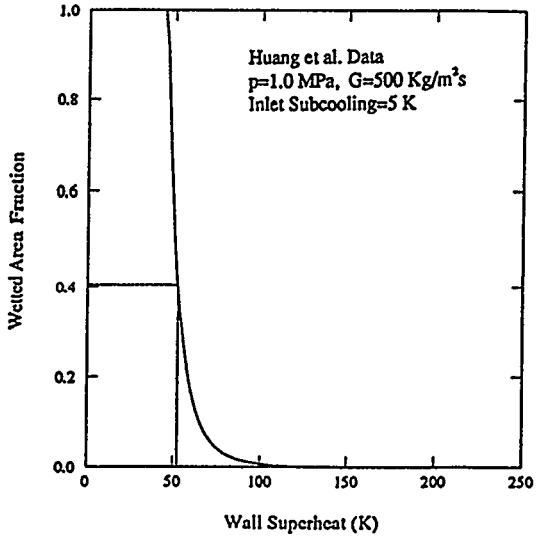

Figure 4. Predicted Wetted Area Fraction in Transition Boiling

criterion is needed to avoid this problem. It is likely that the Helmholtz instability criterion, derived for semi-infinite horizontal flow condition, is inadequate for the cases of vertical tube with low velocity and low pressure flow. Furthermore, we suppose that the flow regime just above the DFB temperature is an inverted annular flow according to our physical model. However, from the installed flow regime map, the flow regime at the CHF condition was estimated as an annular flow and thus the post-CHF flow regime is expected to be a dispersed droplet flow. Figures 7 and 8 show the parametric effect of inlet subcooling on the transition boiling in Huang et al. data. From this comparison, it can be seen that the inlet subcooling effect is not remarkable in this range.

Figure 9 shows the prediction trend for the pressure variation in Weber and Johannsen's steady-state data. The prediction is well matched with the experimental trends. However, the predictions at the low pressure cases are highly overestimated. This discrepancy can be explained by the same way as in Figure 5 case. Figure 10 shows the prediction trend for the mass flux

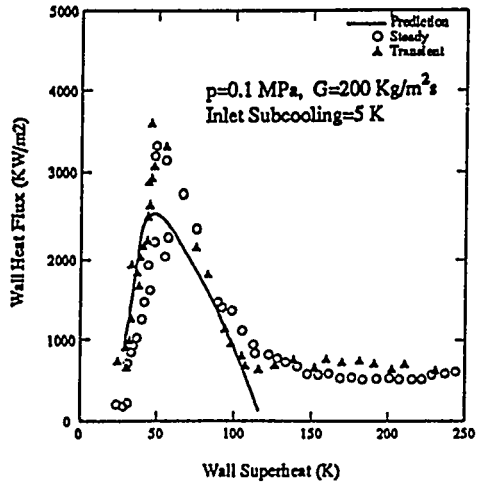

Fig.5 Comparison of Predicted Boiling Curve with Huang et al. Data

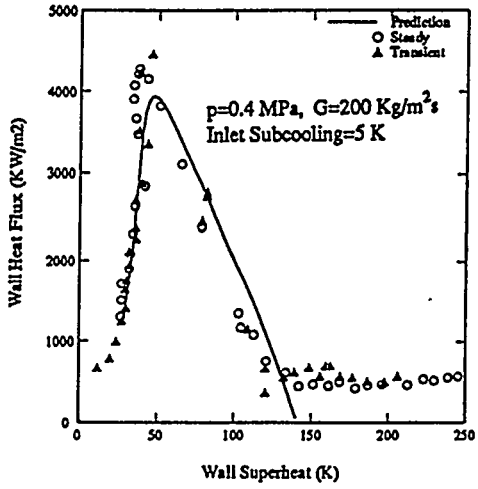

Fig.6 Comparison of Predicted Boiling Curve with Huang et al. Data

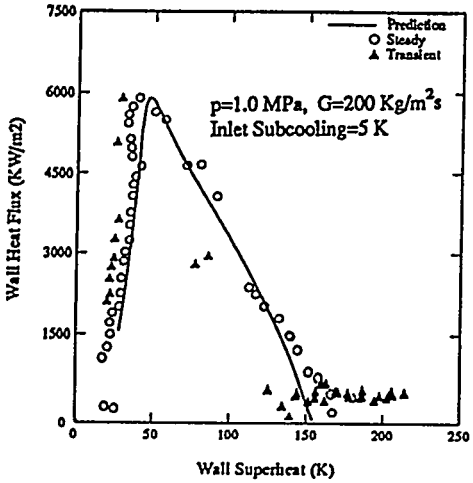

Fig.7 Comparison of Predicted Boiling Curve with Huang et al. Data

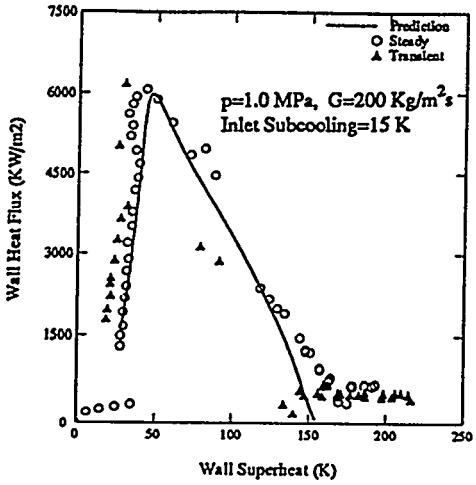

Fig.8 Comparison of Predicted Boiling Curve with Huang et al. Data

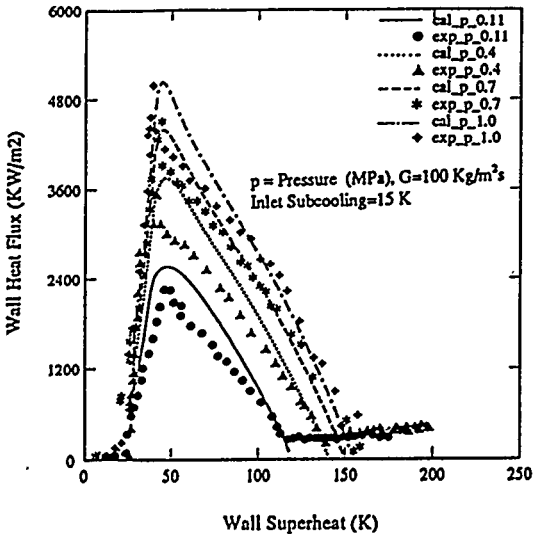

Figure 9. Comparison of Predicted Boiling Curve with Weber & Johannsen Data

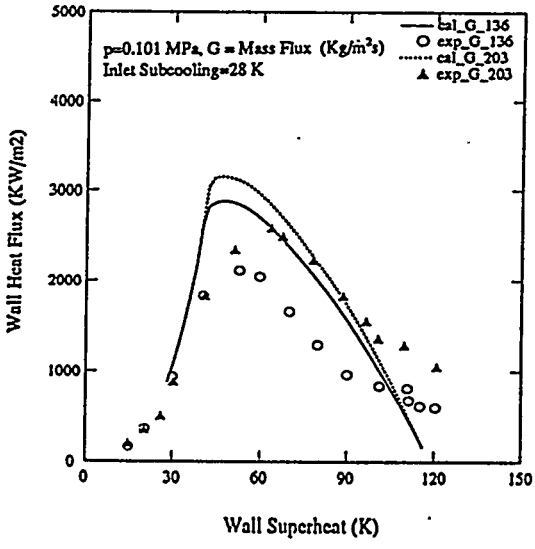

Figure 10. Comparison of Predicted Boiling Curve with Cheng et al. Data

variation in the transient data of Cheng et al. The prediction shows the same trend as in the experimental data, but remarkable mismatches are observed in the wall heat flux magnitude and the data trend near the DFB point. The overestimated heat flux seems to be caused by the inadequacy of the present physical model at low pressures (inadequacy of Helmholtz instability criterion) / high qualities (occurrence of annular flow), described above. The mismatched trendnear the DFB point is attributed to the weakpoint of the present unstable film boiling model, characterized by the fact that there is no parametric factors accounting for the mass flux and inlet subcooling effects in the prediction equations for the DFB temperature and the unstable film boiling heat flux.

From the overall comparison illustrated in Figures 3 to 10, it can be concluded that the transition boiling heat fluxes including the MHF and the MFB heat flux are well predicted at low qualities / high pressures, while a considerable discrepancy is observed at high qualites / low pressures. In future, the observed weakpoints of the present model will be overcome through an improvement of the unstable film boiling model and the development of the physical model for high quality and low pressure situations.

IV. CONCLUSION AND RECOMMENDATIONS

A mechanistic model for forced convective transition boiling has been developed to investigate transition boiling mechanisms and to predict transition boiling heat flux realistically. This model is based on a postulated multi-stage boiling process occurring during the passage time of an elongated vapor blanket.

The model predictions are compared with some available experimental transition boiling data given as the steady-state or transient boiling curves. The parametric effects of pressure, mass flux, inlet subcooling on the transition boiling heat transfer are also investigated. From these comparisons, it can be seen that this model can identify the crucial mechanisms of forced convective transition boiling at low qualities/high pressures and that the transition boiling heat fluxes including the maximum heat flux and the minimum film boiling heat flux are well predicted at low qualities/high pressures near 10 bar.

From the results of model validation, the improvement directions of the present model and further studies are recommended as follows:

(1) A new hydrodynamic instabilty criterion for the determination of the vapor blanket length at low pressure and low flow condition should be established.
(2) The generalization of the physical model for the high quality and low pressure conditions is needed.
(3) A improved model to consider the parametric effects of the mass flux and inlet subcooling on the unstable film boiling heat flux and the DFB temperature is required.
(4) A two-dimensional and transient heat conduction model is needed to simulate and evaluate realistically the experimental condition and its data.

NOMENCLATURE

A	Total Surface Area beneath Vapor Blanket (m^2)
A_g	Cross Sectional Area of Vapor Stems in Macrolayer (m^2)
c_p	Specific Heat (J / Kg ° C)
C_D	Drag Coefficient of Vapor Blanket
D	Tube Diameter (m)
D_b	Bubble Diameter at Bubble Detachment Point (m)
F_A	Average Statistical Wetted Area Fraction
F_T	Local Liquid Contact Time Fraction
g	Acceleration Due to Gravity (m/s^2)
G	Mass Flux (Kg/m^2s)
h	Enthalpy (J / Kg)
H	Heat Transfer Coefficient (W/m^2K)

h_{fg}	Latent Enthalpy of Vaporization	(J / Kg)
L_B	Vapor Blanket Length	(m)
p	Pressure	(Pa)
q	Wall Heat Flux	(W/ m^2)
R_o	Radius of Tube	(m)
T	Temperature	(° C)
ΔT_w	Wall Superheating	(K)
U,V	Velocity	(m/s)
U_M	Velocity of Macrolayer	(m/s)
U_{bl}	Liquid Velocity at the Center of Vapor Blanket	(m/s)
x_g	Actual Flow Quality	
Z	Axial Location	(m)

Greek

α_g	Void Fraction	
δ_{chf}	Macrolayer Thickness at the CHF Condition	(m)
δ_{me}	Macrolayer Thickness during Macrolayer Evaporation Stage	(m)
κ	Thermal Conductivity	(W/mK)
λ_H	Helmholtz Instability Wave Length	(m)
μ	Dynamic Viscosity	(Ns/m^2)
ρ	Density	(Kg/m^3)
σ	Surface Tension	(N/m)
τ_{md}	Macrolayer Dryout Time	(sec)
τ_p	Vapor Blanket Passage Time	(sec)
τ_{vc}	Vapor Coverage Time	(sec)
τ_w	Wall Shear Stress	(N/m^2)

Subscripts

b	Bulk
B	Vapor Blanket
chf	Critical Heat Flux Point
DFB	Departure from Film Boiling Point
DNB	Departure from Nucleate Boiling Point
f	Saturated Liquid
fb	Unstable Film Boiling Stage
g	Saturated Vapor
in	Inlet
i	Interface
lc	Subcooled Liquid at the CHF condition
me	Macrolayer Evaporation
MFB	Minimum Film Boiling Point
MHF	Maximum Heat Flux Point
SAT	Saturation
t	Total
w	Wall

REFERENCES

1. Kalinin, E.K., Berlin, I.I., and Kostiouk, V.V., 1987, " Transition Boiling Heat Transfer," Advanced Heat Transfer, vol.18, pp.241-323.
2. Auracher, H., 1990, " Transition Boiling," Proc. 9th Int. Heat Transfer Conf., vol.1, Jerusalem, Israel, KN-5.
3. Berenson, P.J., 1962, " Experiments on Pool-Boiling Heat Transfer," Int. J. Heat Mass Transfer, vol.5, pp. 985-999.
4. Ragheb, H.S. and Cheng, S.C., 1984, " Prediction of Transition Boiling Heat Transfer for

Subcooled Water at Low Flow and Atmospheric Pressure," Multi-Phase Flow and Heat Transfer III, Part A : Fundamentals, Ed. T.N. Veziroglu and A.E. Bergles, Elsevier Pub. Co., pp. 659-669.
5. Bjornard, T.A. and Griffith, P., 1977, " PWR Blowdown Heat Transfer," Symp. on Thermal and Hydraulic Aspects of Nuclear Reactor Safety, ASME, pp.17-41.
6. Kao, Y.K. and Weisman, J., 1985, "A Moving-Front Transition Boiling Model," AIChE Journal, vol.31, pp. 529-540.
7. Ragheb, H.S. and Cheng, S.C., 1979, " Surface Wetted Area during Transition Boiling in Forced Convective Flow," J. Heat Transfer, vol.101, pp.381-383.
8. Dhuga, D.S. and Winterton, R.H.S., 1985, " Measurement of Surface Contact in Transition Boiling," Int. J. Heat Mass Transfer, vol.28, pp.1869-1880.
9. Lee, L.Y.W., Chen, J.C., and Nelson, R.A., 1985, " Liquid-Solid Contact Measurements using a Surface Thermocouple Temperature Probe in Atomospheric Pool Boiling Water," Int. J. Heat Mass Transfer, vol.28, pp.1415-1423.
10. Pan, C., Hwang, J.Y., and Lin, T.L., 1989, " The Mechanism of Heat Transfer in Transition Boiling," Int. J. Heat Mass Transfer, vol.32, pp.1337-1349.
11. Farmer, M.T., Jones,G.B., and Spencer, B.W., 1987, " Analysis of Transient Contacting in the Low Temperature Film Boiling Regime, Part I and II," Proc., 24th Natl. Heat Transfer Conf., Pittsburgh, USA.
12. Katto, Y., 1990, " A Physical Approach to Critical Heat Flux of Subcooled Flow Boiling in Round Tubes," Int. J. Heat Mass Transfer, vol. 33, no.4, pp. 611-620.
13. Lee, C. H. and Mudawwar, I., 1988, " A Mechanistic Critical Heat Flux Model for Subcooled Flow Boiling Based on Local Bulk Flow Conditions," Int. J. Multiphase Flow, vol. 14, pp.711-728.
14. Mudawwar, I. A., Incropera, T.A., and Incropera, F.P., 1987, " Boiling Heat Transfer and Critical Heat Flux in Liquid Films Falling on Vertically-mounted Heat Sources," Int. J. Heat Mass Transfer, vol.30, no.10, pp.2083-2095.
15. Ueda, T. and Kim, K.K., 1986, " Heat Transfer Characteristics during the Critical Heat Flux Condition in a Subcooled Flow Boiling System," Proc., 8th Int. Heat Transfer Conf., vol.5, San Francisco, USA.
16. Hino, R. and Ueda, T., 1985, " Studies of Heat Transfer and Flow Characteristics in Subcooled Flow Boiling - Part I. Boiling Characteristics and Part II. Flow Characteristics, " Int. J. Multiphase Flow , vol.11,no.3, pp.269-297.
17. Katto, Y., Yokoya, S., and Yasunaka, 1970, " Mechanism of Boiling Crisis and Transition Boiling in Pool Boiling, " Proc. 4th Int. Heat Transfer Conf., vol. 3, B3.2.
18. Huang, X.C., Bartch,G. and Schroeder-Richter,D., 1994,"Quenching Experiments with a Circular Test Section of Medium Thermal Capacity under Forced Convection of Water," Int. J. Heat Mass Transfer, vol.37, pp. 803-818.
19. Haramura, Y. and Katto, Y., 1983, " A New Hydrodynamic Model of Critical heat Flux, Applicable Widely to Both Pool and Forced Convection Boiling on Submerged Bodies in Saturated Liquids," Int. J. Heat Mass Transfer, vol.26, no.3, pp.389-399.
20. Shah,M.M.,1977,"A General Correlation for Heat Transfer during Subcooled Boiling in Pipes and Annuli," ASHRAE Trans. vol.83, pp.202-217.
21. Mikic, B.B. and Rohsenow, W.M., 1969, " New Correlations of Pool Boiling Data Including the Effects of Heating Surface Characteristics," J. Heat Transfer, vol.91, pp.245-250.
22. Fujita, T. and Ueda, T., 1978, " Heat Transfer to Falling Liquid Films and Film Breakdown -II, Saturated Liquid Films with Nucleate Boiling," Int. J. Heat Mass Transfer, vol.21, pp.109-118.
23. Mesler, R., 1979, " Nucleate Boiling in Thin Liquid Films," Boiling Phenomena: Physicochemical & Engineering Fundamentals and Applications, vol. 2, Ed. S. Van Stralen and R. Cole, Hemisphere, WA. , pp. 813-819.
24. Kopchikov,I.A. et al., 1969,"Liquid Boiling in a Thin Film," Int. J. Heat Mass Transfer, vol.12, pp. 791-796.
25. Beattie, D.R.H. and Lawther,K.R., 1986,"An Examination of the Wall Temperature Drop Phenomena during Approach to Flow Boiling Crisis," Proc. 8th Int. Heat Transfer Conf., San Francisco, vol.4, pp.2215-2219.
26. Lahey Jr. R.T. and Moody, F., 1977, " Two-Phase Flow (Chap.5)," The Thermal-

Hydraulics of A Boiling Water Nuclear Reactor, American Nuclear Society, pp.173-248.
27. Ying, S. H. and Weisman, J., 1986, " Prediction of the CHF in Flow Boiling at Intermediate Qualities," Int. J. Heat Mass Transfer, vol.29, no.11, pp.1639-1648.
28. Ishii, M. and Mishima, K., 1984, " Two-Fluid Model and Hydrodynamic Constitutive Relations," Nucl. Engrg. Design, vol.82, pp.107-126.
29. Chexal, B. et al.,1989,"A Void Fraction Correlation for Generalized Applications," Proc. 4th Int. Topical Mtg. Nuclear Reactor Thermalhydraulics (NURETH) , Karlsruhe, pp.996-1002.
30. Mishima, K. and Ishii, M., 1984, " Flow Regime Transition Criteria for Upward Two-Phase Flow in Vertical Tubes," Int. J. Heat Mass Transfer, vol.27, pp.723-737.
31. Huang, X.C.,Weber, P. and Bartsch, G.,1993,"Comparison of Transient and Steady-State Boiling Curves for Forced Upflow of Water in a Circular Tube at Medium Pressure," Int. Comm. Heat Mass Transfer, vol.20, pp.383-392.
32. Cheng, S. C., Ng, W.W., and Heng, K.T., 1978, " Measurements of Boiling Curves of Subcooled Water under Forced Convective Conditions, " Int. J. Heat Mass Transfer, vol.21, pp.1385-1392.
33. Weber, P. and Johannsen, K., 1990, " Convective Transition Boiling of Water at Medium Pressure," Proc. 9th Int. Heat Transfer Conf., vol.6, Jerusalem, Israel, pp. 35-40.

A FORMAL APPROACH FOR THE PREDICTION OF THE CRITICAL HEAT FLUX IN SUBCOOLED WATER

C. Lombardi

Dept. of Nuclear Engineering, Polytechnic of Milan

Via Ponzio 34/3

20133 Milan, Italy

ABSTRACT

The critical heat flux (CHF) in subcooled water at high mass fluxes are not yet satisfactory correlated. For this scope a formal approach is here followed, which is based on an extension of the parameters and the correlation used for the dryout prediction for medium high quality mixtures. The obtained correlation, in spite of its simplicity and its explicit form, yields satisfactory predictions, also when applied to more conventional CHF data at low-medium mass fluxes and high pressures. Further improvements are possible, if a more complete data bank will be available. The main and general open item is the definition of a criterion, depending only on independent parameters, such as mass flux, pressure, inlet subcooling and geometry, to predict whether the heat transfer crisis will result as a DNB or a dryout phenomenon.

1. Introduction

The critical heat flux (CHF) in subcooled water at high mass fluxes is being thoroughly studied by many researchers, in view of cooling applications in thermonuclear fusion reactors. In spite of a rather wide experimental evidence, so far no fully satisfactory correlation of the data is available. However, Celata et al. of ENEA [1] recently suggested an interesting mechanistic model, which seems to yield reliable predictions.

A different approach is followed here based on a formal extension of the parameters and the correlation used for the prediction of the heat transfer crisis data in medium-high quality mixtures (the so called *dryout*).

The resulting correlation was compared with the data bank prepared by Celata and Mariani [2], which contains four different groups of data, all relevant to natural waters , round tube geometry, uniform heat flux distribution, and negative outlet quality (few positive quality data were discarded). The first group refers to high mass flux experiments (1811 CHF points), purposely obtained for fusion reactor applications (Bank 1). The second group refers to typical fission reactors conditions and is characterized of medium-low mass fluxes and high pressures (711 points, Bank 2). The other two groups of data refers to a limited number of special tests relevant to possible fusion reactor application, i.e. : i) half heated tube experiments (26 points, Bank 3), ii) half heated tube with twisted tape experiments (13 points, Bank 4).

The operating ranges covered by data banks are detailed in Table 1. These data show a rather wide scattering, which is also confirmed by the above mentioned lack of satisfactory

correlations. In particular this spread may hide the effect of relevant parameters, thus preventing the achievement of a correct physical understanding of the CHF phenomenon.

Table 1: Operating ranges of data banks with subcooled CHF (water)

Data #	Pressure [kPa]	Diameter [mm]	Length [mm]	Mass flux [kg/m^{2}s]	Inlet sub. [K]
1811	100 ÷ 8400	0.3 ÷ 25.4	2.5 ÷ 610	100 ÷ 90000	25 ÷ 255
718	1400÷21483	1.1 ÷ 37.5	35 ÷ 8490	350 ÷ 19000	13 ÷ 338
26	1960 ÷ 3700	8 - 15	150 - 300	6600÷20000	110 ÷ 190
13	2560 ÷ 3610	8 - 15	150 - 300	6900÷15000	130 ÷ 180

1: High mass flux; 2: Medium low mass fluxes and high pressures; 3: Half heated tube;
4: Half heated tube with twisted tape.

2. The dryout interpretation

The heat transfer crisis obtained in medium-high quality mixtures is commonly defined as *dryout*, because it is interpreted as the break or the dryout of the liquid film flowing along the wall. According to the CISE interpretation [3] (see fig. 1a), the heat transfer crisis is defined by a relationship between the saturation power and the saturation length, with the mass flux, the pressure and the diameter of the tube as parameters. The critical saturation power (Ws,cr) is the power supplied to the two-phase zone of the duct between the cross section where the fluid first reaches in the bulk the saturation condition (zero thermodynamic quality) and that where the crisis first occurs. The critical saturation length (Ls,cr) is the length of the region where Ws,cr is supplied.

The CISE correlation [3] is valid for steam-water mixtures flowing in round tubes, independent of axial and radial heat flux distribution, and it is written as follows:

$$\frac{W_{s,cr}}{\Gamma H_{gl}} = a(p,G)\frac{L_{s,cr}}{L_{s,cr}+b(p,G,D)} \qquad (1)$$

where Γ is the total mass flow-rate, H_{gl} is the latent heat of vaporization, and a and b are two empirical functions defined as (in SI units):

$$a = \frac{1-p/p_c}{(G/1000)^{1/3}} \qquad (2)$$

$$b = 0.2\left(p_c/p-1\right)^{0.4} D^{1.4} G \qquad (3)$$

with pressure (p), mass flux (G) and diameter (D) and p_c the pressure of the critical point of water, equal to 22120 kPa.

The correlation was successfully extended to complex geometries (rod bundles and annuli) by introducing the concept of the *rod centered* subchannel. In this context, only the round tube correlation will be used.

The left hand side of eq. (1) is the ratio between the critical saturation power to the power needed to evaporate all the saturated liquid. The asymptotic value of this quantity should be one, even though the correlation does not give this result, because in order to avoid rather complex analytical formulations it was not purposely made valid at the limit conditions ($L_{s,cr} \rightarrow \infty$, or $G \rightarrow 0$).

In the case of uniform heat flux distribution, the correlation can be transformed into the following simple form:

$$\frac{W_{cr}}{\Gamma H_{gl}} = \left(a - x_{in}\right)\frac{L}{L+b} \tag{4}$$

where W_{cr}, L, and x_{in} are the total critical power, and the total length of the channel, and the inlet quality respectively.

In this work, the pressure dependence in the function *b* was translated in terms of the steam specific volume as follows:

$$b = 2.2\left(\frac{G^2 v_g}{2}\right)^{0.5} D^{1.4} \tag{5}$$

The ratio between eqs (5) and (3) differs from one with a maximum difference of ± 13% for a pressure range of 1000 and 17000 kPa. However, the effect of this difference on critical power obtained by eq. 4 is substancially reduced, because the function *b* is to be added to the length, having in general a lower value. This modification has been suggested by the results obtained for DNB data (see below).

3. The formal appproach

The above definition of the left hand side of eq. (1) was formally extended to the subcooled CHF phenomenon. In other words, only the data for which the heat transfer crisis is obtained in the presence of subcooled liquid (thermodynamic average over the cross section) are taken into account. A parameter β is defined as the ratio of the overall test section power and the power needed to bring the inlet fluid to the saturation condition (see fig. 1b):

$$\beta = \frac{W_{cr}}{\Gamma\left(H_l - H_{in}\right)} = \frac{4\,CHF\,L}{G\left(H_l - H_{in}\right)D} \tag{6}$$

where H_l and H_{in} are the saturated and inlet liquid enthalpy respectively and CHF the critical heat flux. Because β is applied, as said above, only to the subcooled liquid conditions at the test section outlet, its asymptotic value is one. Therefore data showing β values higher than one are not used in this context. The use of β as correlating parameter reduces the data spread,

in fact when calculated for all high mass flux data it varies of a factor 23 instead of a factor 60 shown by CHF values.

The β values are plotted versus CHF in fig. 2 for data bank 1.This figure indicates a progressive convergence of β by increasing CHF, tending to a value around 0.3 for very high CHF values (> 10^5 kW/m^2). It is not clear whether this behaviour is of general meaning or only fortuitous, because the high CHF data are too few to display an actual trend. The same quantities for data bank 2 are plotted in fig. 3. In spite of a much lower maximum heat flux (roughly an order of magnitude lower) and the presence of a single set of data having β values close to 1, the trend of fig. 2 seems to be confirmed. However further verifications are undoubtly needed

In order to empirically correlate β, the same structure of eq.(1) was adopted, i.e.: the first term is substituted with β, while in the second term $L_{s,cr}$ is substituted with the overall length of the duct L; then one obtains:

$$\beta = a'(p,G)\frac{L}{L+b'(p,G,D)} \tag{7}$$

After several trials it turned out that:
- *a'* does not seem to depend on the mass flux and on the pressure; its value ranges around 1;
- *b'* results rather similar to *b*, in the sense that it is proportional to the parametric group of eq. (5), where v_l substitutes for v_g.

Summarizing, the resulting correlation can be written as:

$$\beta = \frac{L}{L+k\left(G^2 v_l/2\right)^{0.5} D^{1.4}} \tag{8}$$

where k is an empirical constant. This expression also satisfies the limiting condition of β tending to 1 for L $\rightarrow\infty$, or G $\rightarrow$ 0 (always remaining, if physically possible, in subcooled conditions).

Then CHF is as follows (see eq. 6).

$$CHF = \frac{G\left(H_l - H_{in}\right)}{4\left[L/D + k\left(G^2 v_l/2\right)^{0.5} D^{0.4}\right]} \tag{9}$$

4. Verification of the correlation

The constant k is optimized by reducing to a minimum the average error of the CHF predictions for all data of Bank 1 and Bank 2. It resulted for k a value of 1.3 (SI units). The average error (ε) and the root square error (RMS) is detailed as follows:

Data Bank	Number of data	ε [%]	**RMS**
1	1811	-1.30	20.26
2	718	3.23	19.82
1 + 2	2529	-0.01	20.14

Different kind of CHF data behave in a similar way as shown by the above values of ε and RMS. The comparison between the calculated CHF and the experimental data are shown in fig. 4 through 9 as function of different parameters. These figures, while confirming the inherent scattering of the data, do not show any clear systematic effect, apart perhaps the effect of inlet and outlet qualities, because the calculated over experimental CHF seems to increase by increasing in absolute terms both the inlet and the outlet qualities. The constant k when singly optimized on Data bank 1 or 2 does not show an appreciable difference, in spite of the different features of the two Data banks.

Fig. 10 shows a comparison among different correlations Katto [4] ENEA [1], Tong-Celata [5], and the prediction of the present correlation. The comparison refers only to data Bank 1 for which Katto and ENEA results were available in ref. [1]. The figure shows that the present correlation is better than the Katto one and worse than the ENEA one, while it is practically equivalent to the Tong-Celata one. Katto model implies that almost half of the data cannot be used. Therefore, in spite of its simplicity and its explicit form, the present correlation does not result worse than more sophisticated correlations. However, these correlations are based on a sound physical model, which is completely lacking in the present approach.

For half heated tube data (Bank 3) two different drastic hypotheses are made: i) Mixed flow; ii) Separated flow. In the first case a CHF value equal to half CHF experimental datum is assumed to be uniformly distributed along the whole circumference. Then the right hand side of equation (9) multyplied by two is adopted to predict actual CHF data. In the second case, the cross fluid mixing is assumed equal to zero and equation (9) is directly applied to the half heated channel to predict actual CHF data. The results are shown in fig. 11 in terms of calculated over experimental CHF versus mass flux. At mass flux lower than 10000 kg/m^{2}s the separated flow hypothesis yields satisfactory predictions, while the contrary is true for mass fluxes around 20000 kg/m^{2}s; in between the predictions are symmetric around 1. In fact it is reasonable to immagine that the fluid cross mixing be an increasing function of mass flux.

For half heated tube with twisted tape data (Bank 4) the same hypotheses are made; moreover the length in equation (9) is multiplied by the term

$$L = L\left(1+\frac{\pi}{2\,TTR}\right) \tag{10}$$

where TTR represents the half pitch of the twisted tape in terms of tube diameter: this in order to take into account the actual length flowed from the fluid. The results are shown in fig.12 in terms of calculated over experimental CHF versus mass flux. In this case the mixed flow hypothesis seems more able to predict the data, and this is coherent with the fact that the twisted tape determines an alternative contact between the fluid and the heated and unheated section of the tube.

Transforming eq. (9) as function of outlet quality (x_{out}) one obtains:

$$CHF = -\frac{x_{out}\,H_{gl}}{4k\left(v_l/2\right)^{0.5}D^{0.4}} \tag{11}$$

This equation implicity says that the condition of $x_{out} \rightarrow 0$ is obtained only with infinite long channel, because CHF tends to zero as well. In other words the present approach is not applicable to very small outlet qualities (on the negative side), where DNB phenomenon assumes a different character. Moreover, the above equation states that CHF vs. x_{out} trend is

linear and indipendent of mass flux while dependent on D to an exponent -0.4. This latter dependence is in agreement with other correlations. For instance Groeneveld et al. [6] suggested an exponent of -1/3, while Celata shows that its correlation foresees an exponent of -0.3 [7].

5. Concluding remarks

An approach based on a formal extrapolation of CISE dryout correlation was applied both to CHF data obtained for fusion applications and to more conventional CHF data typical of fission reactor conditions. In both cases the predictions are reasonably good and not worse than other current correlations, in spite of its simplicity and its explicit form.

The proposed correlation might be improved by taking into account the probable but not certain effect of inlet quality. For this it is advisable to refer to a more complete data bank than that used here. It is also necessary to have a further verification of the trend, which seems to indicate an asymptotic value for β (overall critical power over power needed to reach the saturation conditions) of about 0.3, by increasing the heat flux.

However, a criterion is needed to establish, on the basis of independent parameters, such as mass flux, pressure, inlet subcooling and geometry, whether the crisis will be obtained in subcooled conditions (DNB) or in the quality region (dryout). To the author's knowledge no such a criterion seems to exist in the open literature. In spite of several attempts made to this regard, no reasonable results were obtained in this research..

References

[1] G.P. Celata, M. Cumo, A: Mariani and G. Zummo, "A Mechanistic Model for the Prediction of Water Subcooled Flow Boiling CHF", 31rd Meeting of European Two.Phase Flow Group, Piacenza, Italy, June 6-8th, 1994..

[2] G.P. Celata, A. Mariani "A Data set of critical heat flux in water subcooled flow boiling" ENEA C.R.E. Casaccia Italy.

[3] S. Bertoletti, G.P Gaspari, C. Lombardi, G. Peterlongo, M. Silvestri, F.A. Tacconi. "Heat Transfer Crisis with Steam- Water Mixtures" Energia Nucleare, vol. 12, n. 3, Marzo 1965.

[4] Y. Katto "A Prediction Model of subcooled water flow boiling CHF for pressure in the range 0.1 - 20 MPa" Int. J. Heat Mass Transfer vol. 35, n. 5, pp. 1115 - 1123, 1992.

[5] G.P. Celata, M. Cumo, and A. Mariani, "Assessment of Correlations and Models for the Prediction of CHF in Subcooled Flow Boiling", Int. J. Heat Mass Transfer, vol 37, n. 2, pp 237-255, 1994.

[6] D.C. Groeneveld, S.C. Cheng and T. Doan, 1986 AECL-UO Critical Heat Flux Look-Up Table, Heat Transfer Engineering 7, 46-62 (1986).

[7] G.P. Celata, Private Communication Submitted for publication to Int. J. Heat Mass Transfer.

Nomenclature

Symbols

CHF: critical heat flux
D: diameter
G: mass flux
H: enthalpy
L: length
p: pressure
RMS: root square error
TTR: half pitch of twisted tape
v: specific volume
W: power
β: critical power over that needed to bring the inlet fluid to saturation
ε: average error
Γ: mass flow rate
x: quality

Subscripts

c:critical point of water
cr: critical
g: steam
in: inlet
l: liquid
out: outlet
s:saturation

Aknowledgments

G.P. Celata cooperation in making us available the CHF data bank on magnetic support and in giving us suggestions and comments is greatly appreciated, as well as L. Maran and R. Monzani help in preparing the computation programs and processing the data.

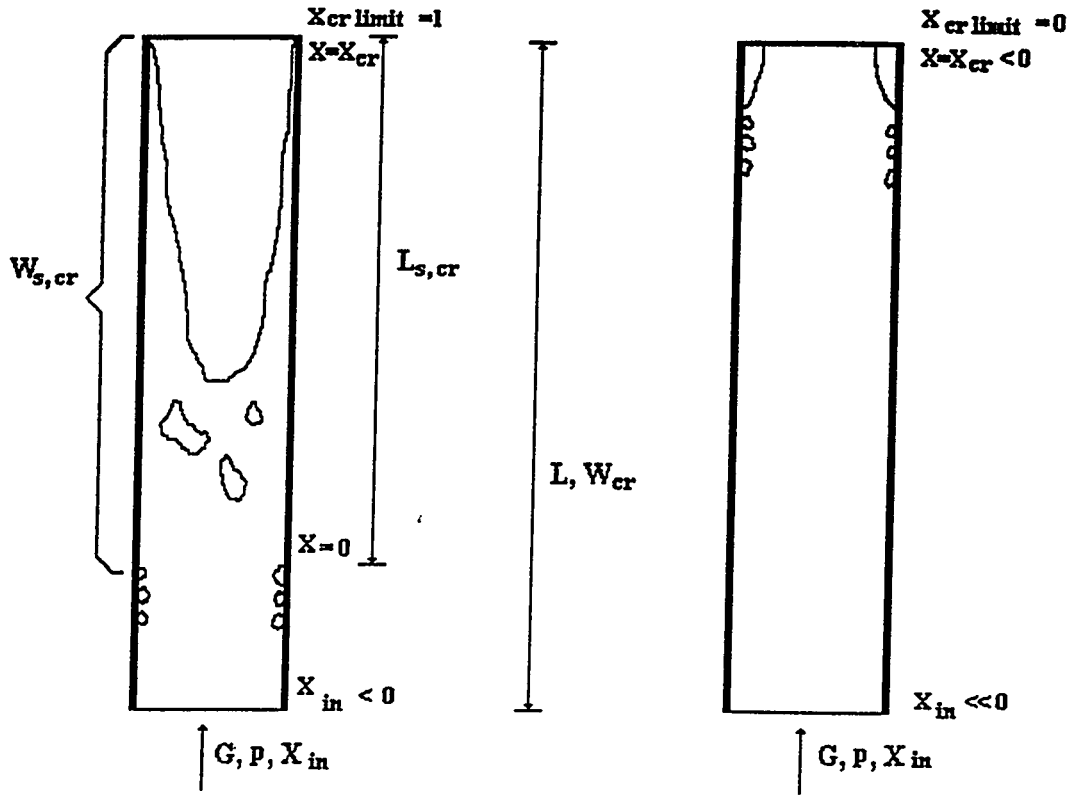

Fig. 1 a) Pictorial interpretation of the global character of the dryout phenomen
b) Subcooled CHF parameters

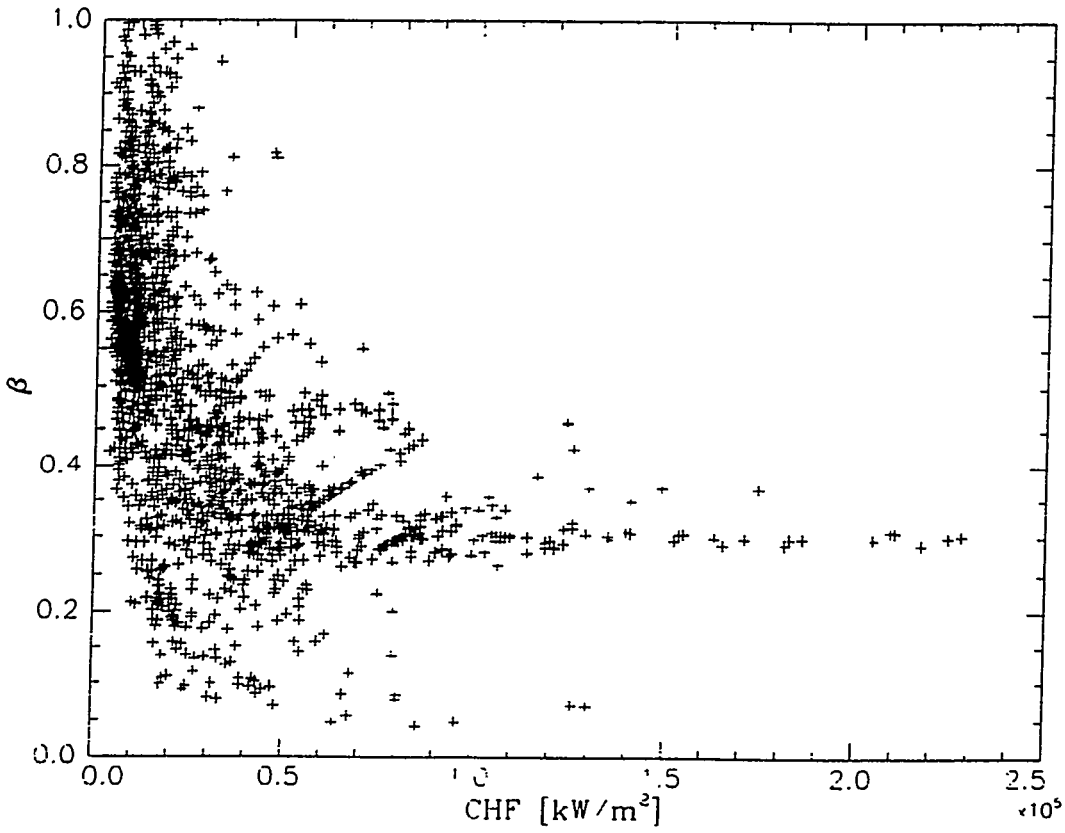

Fig. 2 Critical power over power to reach the saturation (Bank 1)

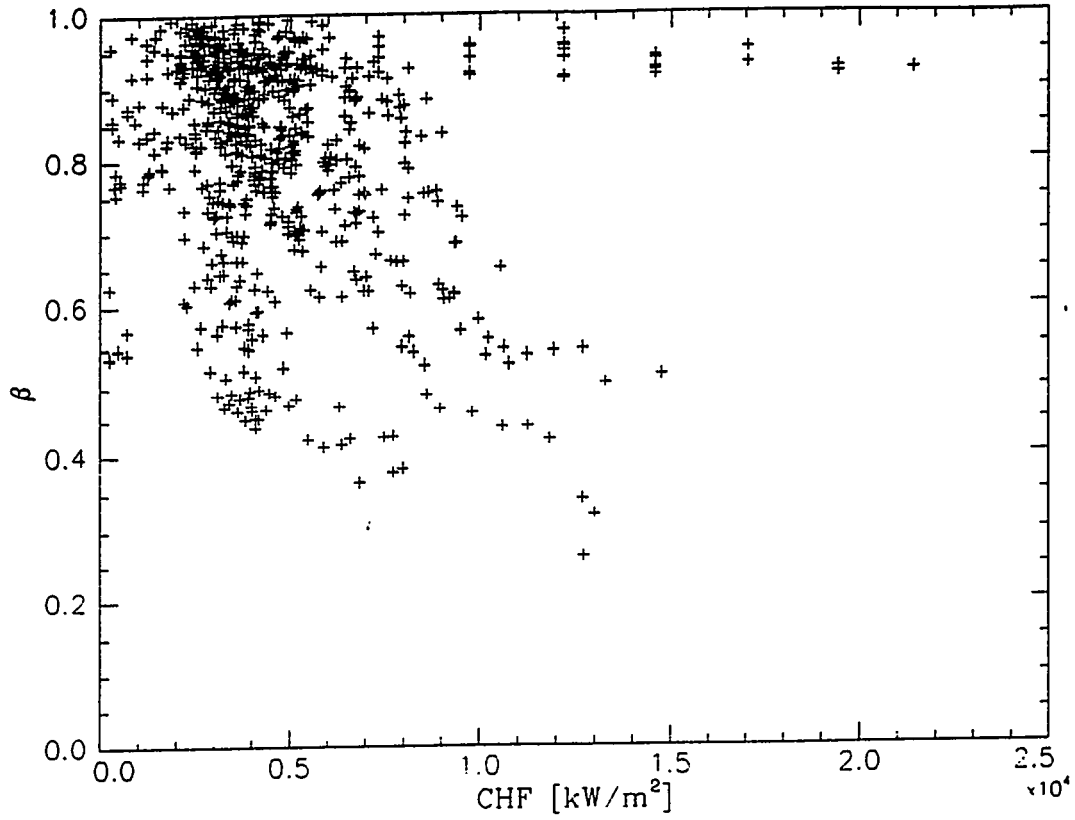

Fig. 3 Critical power over power to reach the saturation (Bank 2)

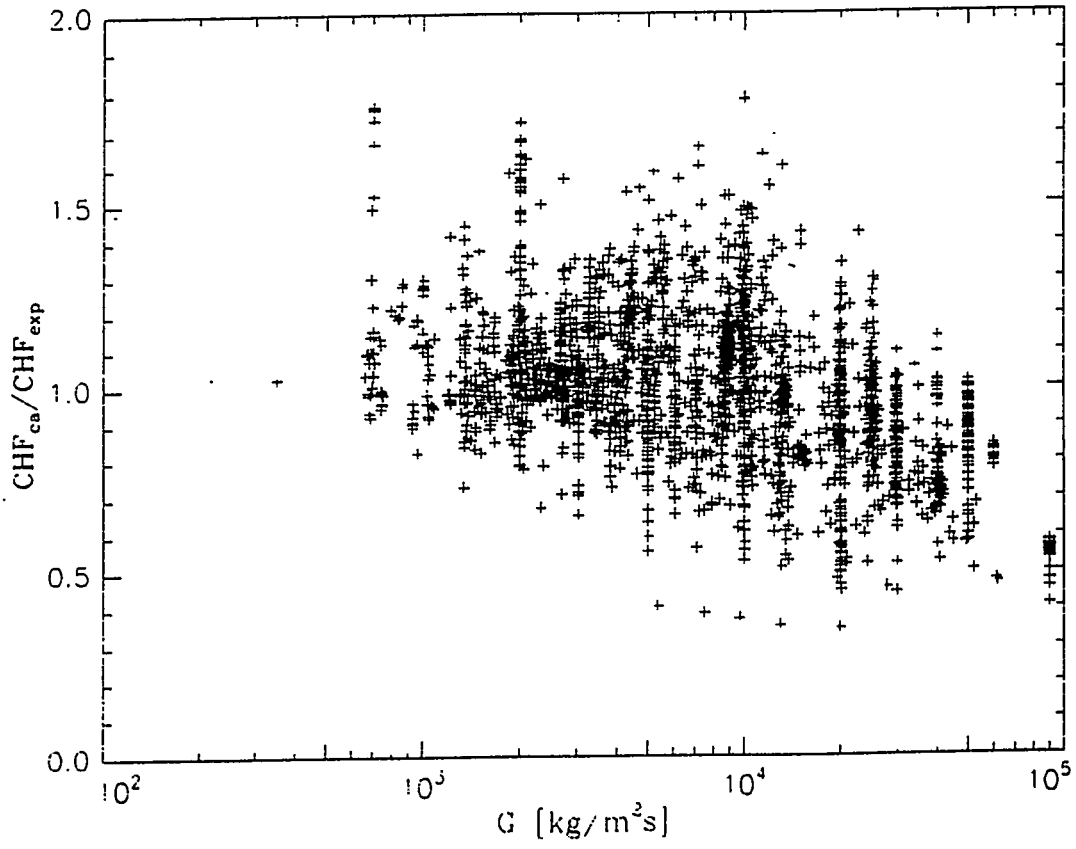

Fig. 4 Calculated over experimental CHF versus mass flux (Bank 1 + 2)

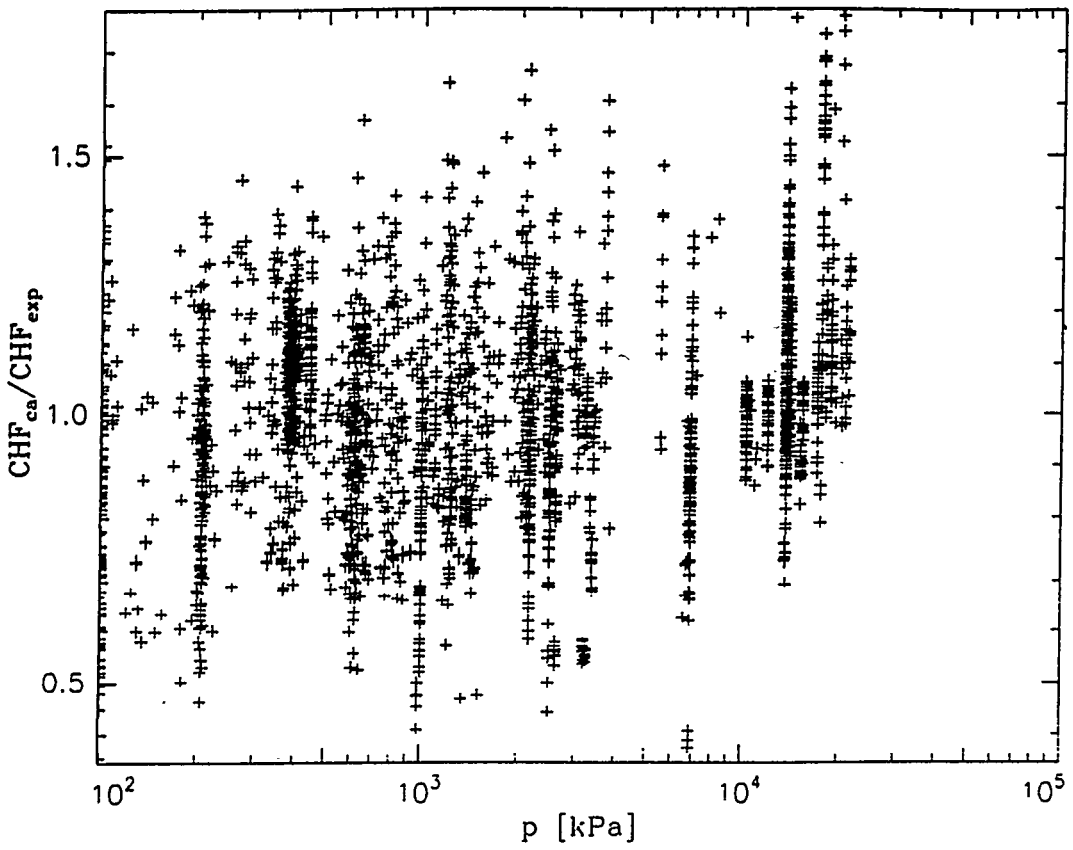

Fig. 5 Calculated over experimental CHF versus pressure (Bank 1 + 2)

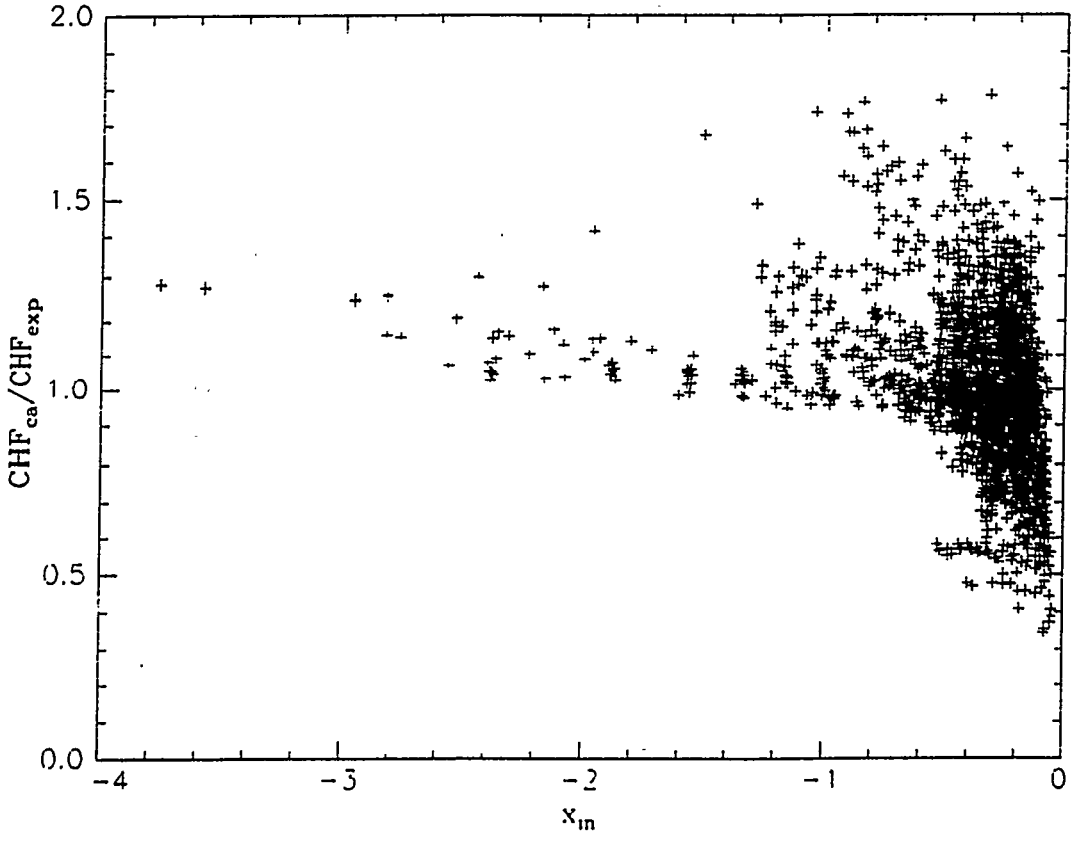

Fig. 6 Calculated over experimental CHF versus inlet quality (Bank 1 + 2)

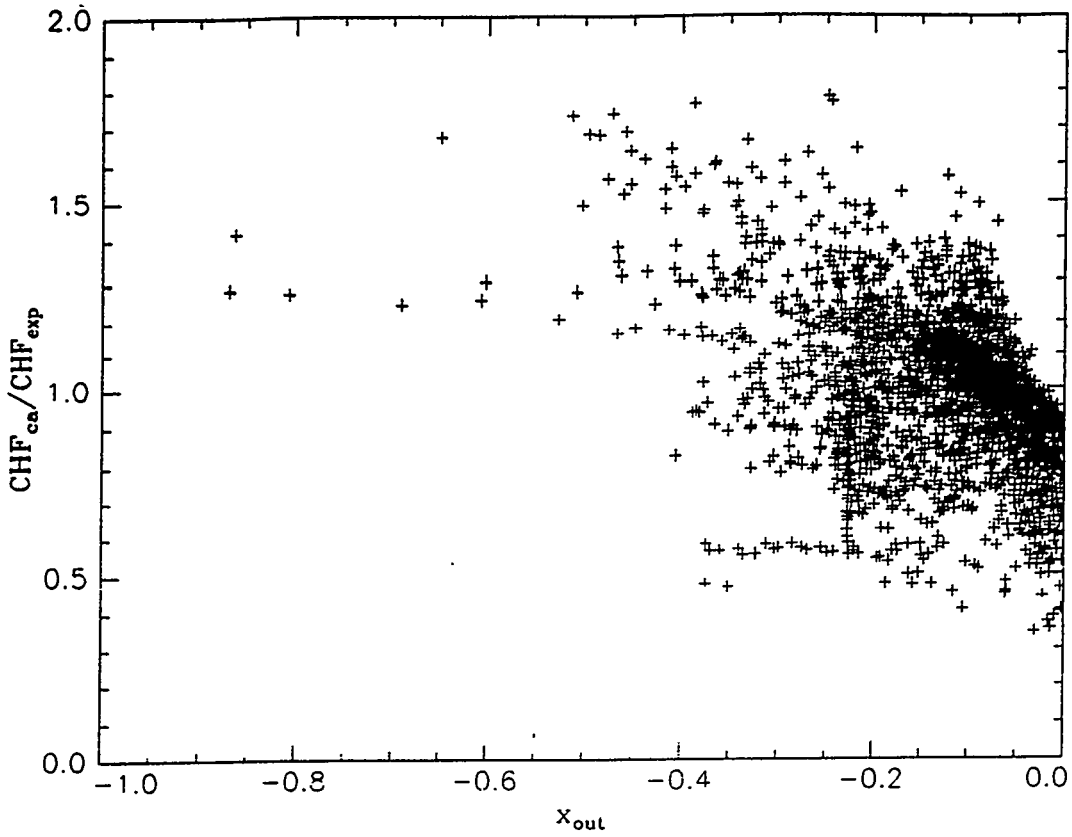

Fig. 7 Calculated over experimental CHF versus outlet quality (Bank 1 + 2)

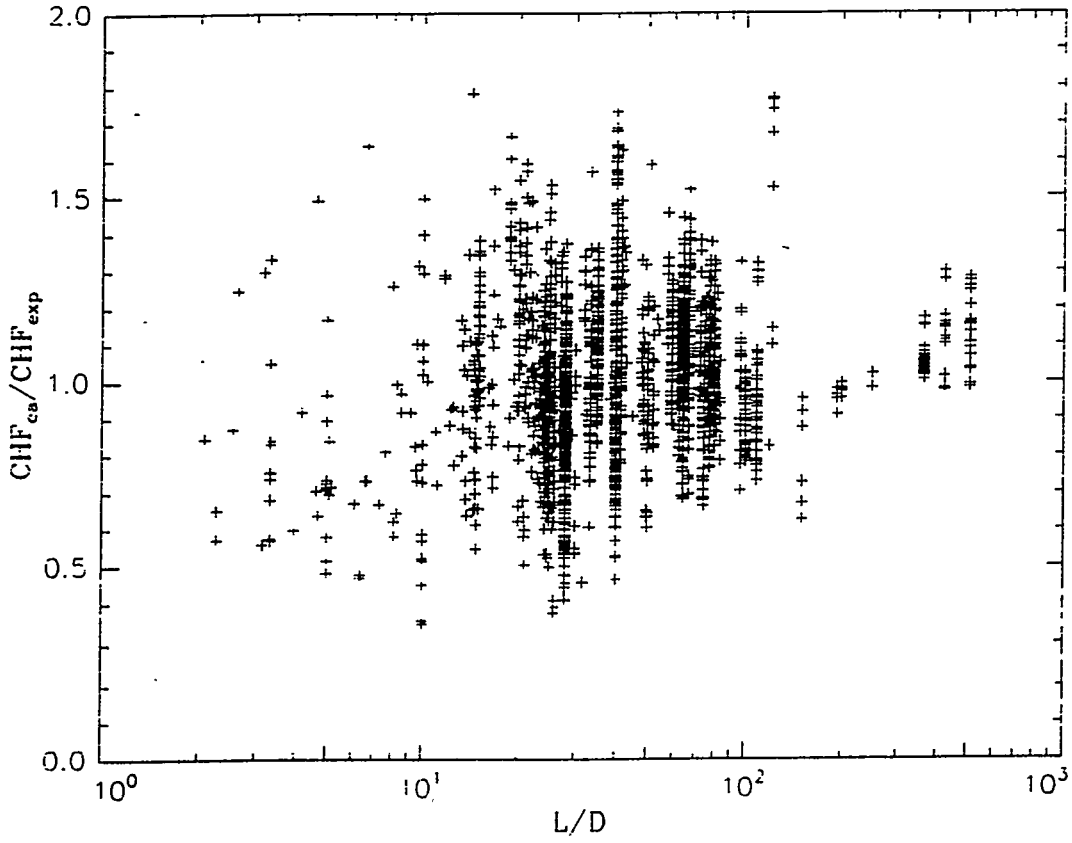

Fig. 8 Calculated over experimental CHF versus length over diameter (Bank 1 + 2)

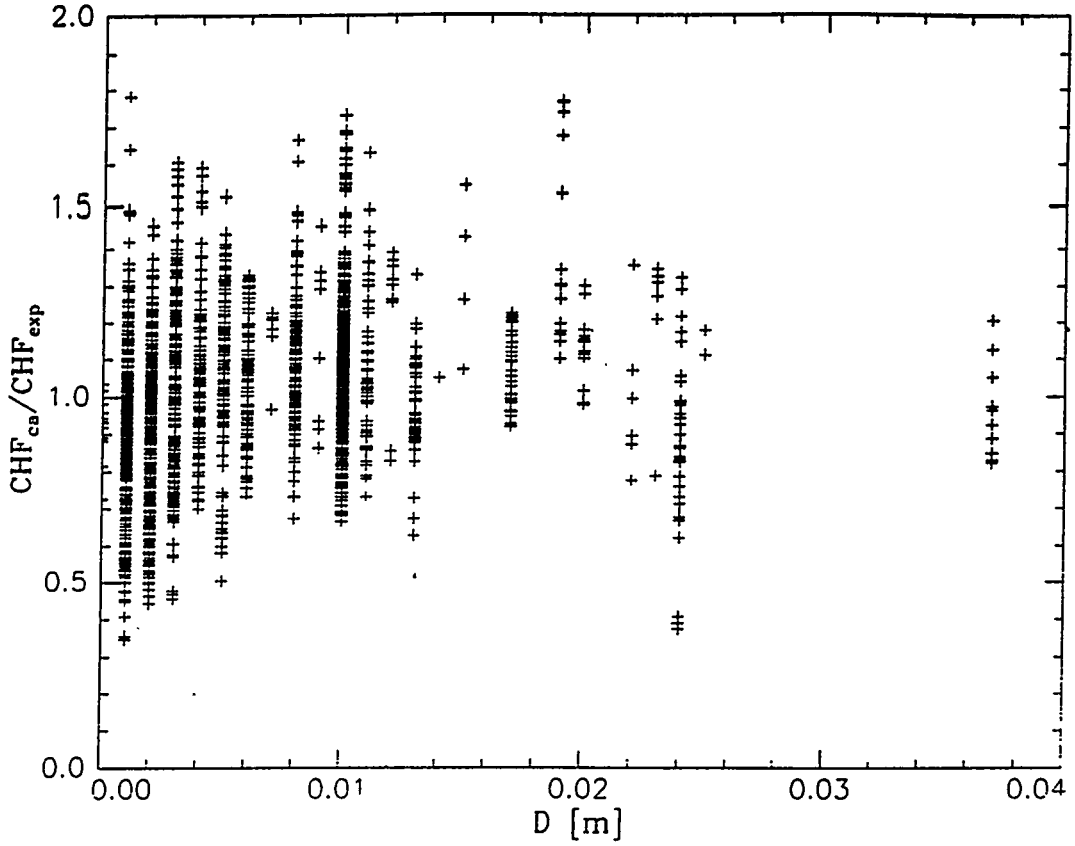

Fig. 9 Calculated over experimental CHF versus diameter (Bank 1 + 2)

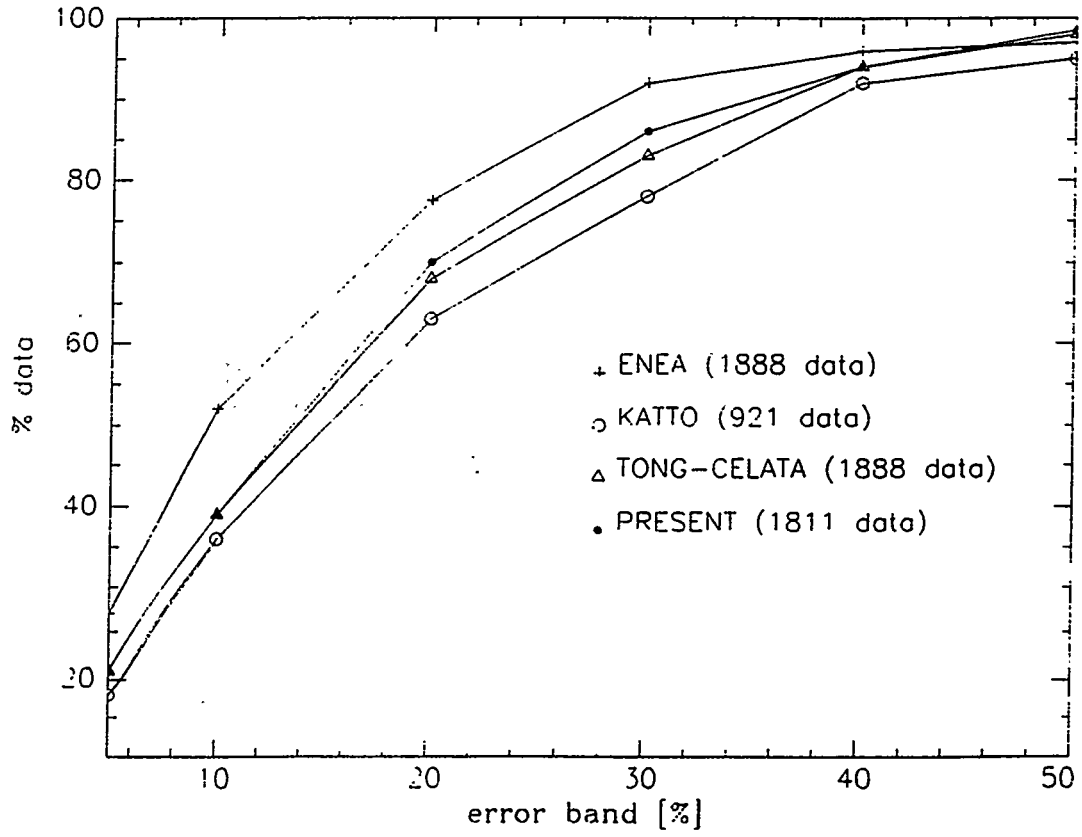

Fig. 10 Percentage of data points predicted within a given error band versus the error band for different correlations (Bank 1)

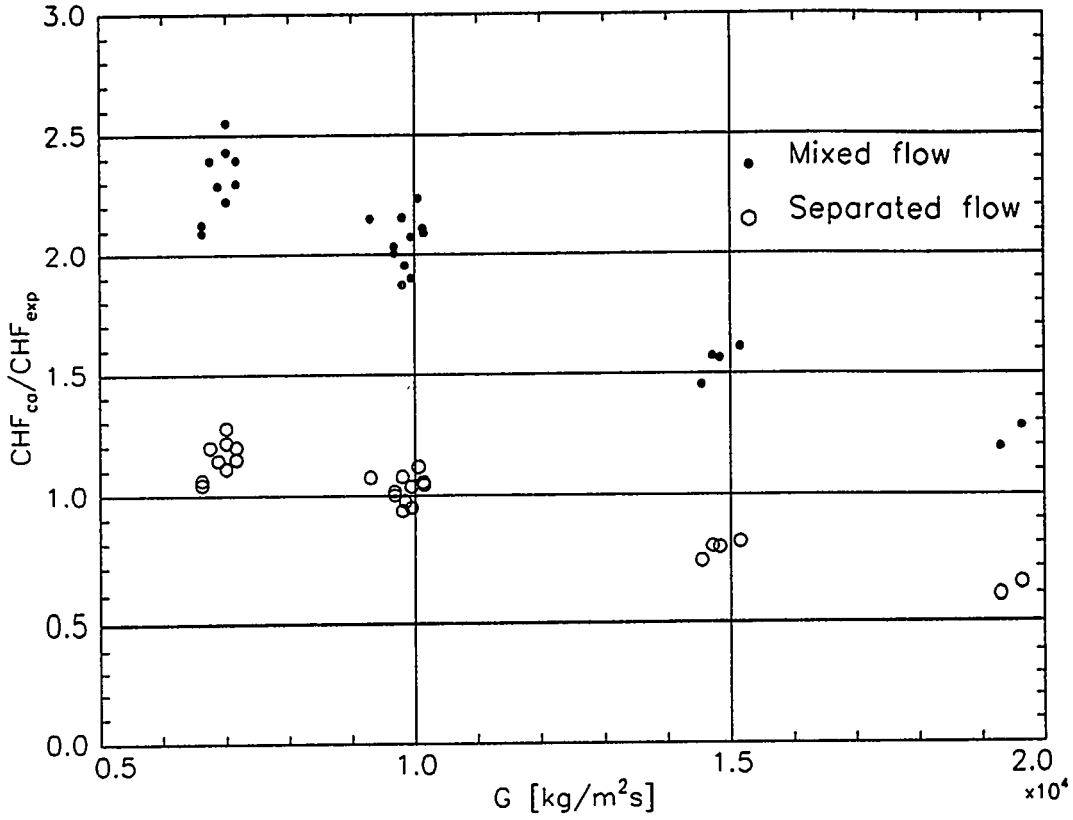

Fig. 11 Calculated over experimental CHF versus mass flux for 26 data relevant to half heated tube (Bank 3).

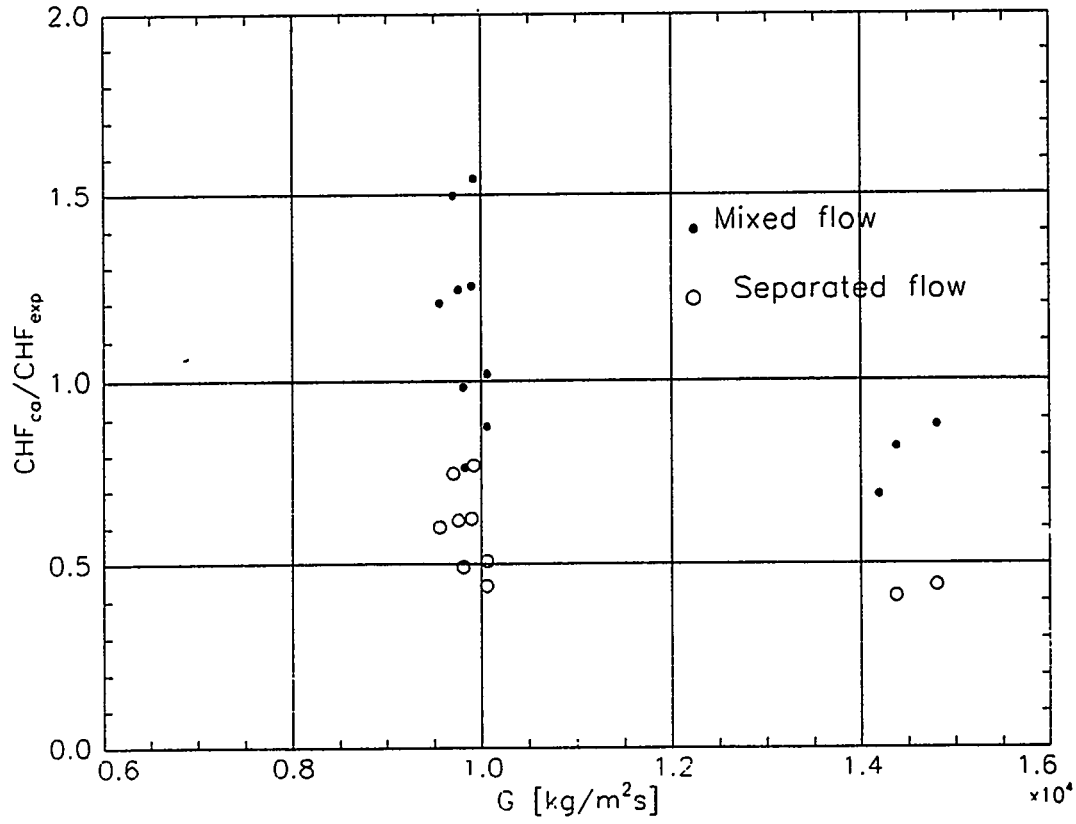

Fig. 12 Calculated over experimental CHF versus mass flux for 13 data relevant to half heated tube with twisted tape (Bank 4). Three points discarded in separated flow hypothesis having $x_{out} > 0$.

A COMPARISON OF CHF BETWEEN TUBES AND ANNULI UNDER PWR THERMAL-HYDRAULIC CONDITIONS

Ch. HERER
FRAMATOME EP/TC
BAL 1639A TOUR FIAT CEDEX 16
92084 Paris-La Défense, FRANCE
Tel.: (1) 47 96 14 84
Fax : (1) 47 96 01 48

A. SOUYRI
EdF DER/RNE/TTA
6,Quai Watier B. P. 49
78401 Chatou Cedex, FRANCE
Tel.: (1) 30 87 76 43
Fax : (1) 30 87 79 49

J. GARNIER
CEA DRN/DTP/STR/LETC
CENG 17 rue des Martyrs
38054 Grenoble Cedex 9, FRANCE
Tel.: 76 88 36 46
Fax : 76 88 52 51

Critical Heat Flux (CHF) tests were carried out in three tubes with inside diameters of 8, 13 and 19.2 mm and in two annuli with an inner tube of 9.5 mm and an outer tube of 13 or 19.2 mm. All axial heat flux distributions in the test sections were uniform. The coolant fluid was Refrigerant 12 (Freon-12) under PWR thermal-hydraulic conditions (equivalent water conditions - Pressure: 7 to 20 MPa, Mass Velocity : 1000 to 6000 kg/m2/s, Local Quality : -75% to +45%). The effect of tube diameter is correlated for qualities under 15%. The change from the tube to the annulus configuration is correctly taken into account by the equivalent hydraulic diameter. Useful information is also provided concerning the effect of a cold wall in an annulus.

0 NOMENCLATURE AND ACRONYMS

P	: Outlet pressure	MPa
W	: Mass flow rate	kg/s
G	: Mass velocity	kg/m²/s
T	: Inlet fluid temperature	°C
Q	: Total heating power	kW
M	: Measured critical heat flux	kW/m²
C	: Calculated critical heat flux	kW/m²
Φ	: Critical heat flux	kW/m²
x	: Outlet thermodynamic quality	-
d	: Tube inside diameter	mm
ϕ	: Diameter (in general)	mm
ϵ	: Exponent for correcting CHF for tube diameter	
g	: Gap between tubes in annulus	mm
d_{hy}	: channel hydraulic diameter	mm

CHF : Critical Heat Flux
CEA : Commissariat à l' Energie Atomique
CENG : Centre d' Etudes Nucléaires de Grenoble (CEA)
EdF : Electricité de France
PWR : Pressurized Water Reactor
BWR : Boiling Water Reactor
R-12 : Refrigerant 12 (Freon 12)

ID : Inside diameter
OD : Outside diameter
IT : Inner tube
OT : Outer tube
RTD : Resistance Temperature Detector
APHRODITE : EdF R-12 test loop
ENEE : 13 mm ID tube test section on APHRODITE
POSEIDON : second mockup to be tested on APHRODITE
DEBORA : CENG R-12 test loop with various test sections
AGATE : CENG LDV rod bundle test loop (no heating)
OMEGA : CENG rod bundle CHF water test loop
GRAZIELLA : CENG rod bundle CHF R-12 test loop
PLAQUEs : CENG mathematical "regression" method

g = 1/2 (ID of outer tube - OD of inner tube)
d_{hy} = 4 x flow area/wetted perimeter

I INTRODUCTION

The boiling crisis is a significant phenomenon limiting nuclear power plant operating capacities of Boiling Water Reactors (BWRs) and Pressurized Water Reactors (PWRs). It defines the limit above which correct cooling of the core is no longer assured. A sudden and large increase in the fuel clad temperature occurs, possibly leading to the loss of clad integrity and the release of fission products into the reactor coolant system. This problem is directly connected with the thermal and hydrodynamic effects of the flow and results from a rapid degradation of the heat transfer between the fuel rod and the water due to film dryout in the annular flow regime (for BWR configurations) or bubble-layer blanketing of the heating wall leading to Departure from Nucleate Boiling (DNB) in PWRs. On this subject, reliable tools, mainly based on empirical Critical Heat Flux (CHF) correlations, have been qualified to compute and predict the occurrence of boiling crisis using the CHF value. Every major nuclear plant designer and fuel assembly supplier now has an accurate CHF correlation. In fact, each correlation is designed for a specific use, i.e. for specific fuel assemblies and core configurations.

The extension of a correlation to another design or the extrapolation to larger parameter ranges has to be supported by experimental tests. One of the main reasons is that the basic CHF mechanisms, that are still not well understood (especially for DNB), are not taken into account when building a correlation. For example, some major geometry effects, such as hydraulic diameter or channel shape, are not yet correctly represented.

This paper presents a quantitative parametric analysis of CHF versus geometry and heating factors. It includes CHF tests performed both in round tubes (with inside diameters (ID) of 8, 13 and 19.2 mm) and concentric annuli (outer

tube with ID of 19.2 mm or 13 mm and inner tube with outside diameter (OD) of 9.5 mm) under normal and abnormal PWR operating conditions. These tests were conducted by Electricité de France (EdF), the Commissariat à l' Energie Atomique (CEA) and FRAMATOME as part of a larger program, briefly described below, devoted to studying the boiling crisis phenomenon.

All tests were carried out with uniform electrical heating and Refrigerant-12 (R-12) as the working fluid. R-12 is a valuable simulation fluid for water, with scaling laws to obtain equivalent water conditions, suggested, for example, by Stevens[1] or Ahmad[2].

II OBJECTIVES OF THE PROGRAM

2.1 General objectives

Better knowledge and comprehensive modeling, taking into account the basic mechanisms involved in the CHF phenomenon, would help to prepare for the nuclear plant of the future and to optimize the performance of existing reactors. In order to contribute to these objectives, two experimental programs were initiated in France:

- the APHRODITE program at EdF,
- the DEBORA program, a joint project between the CEA, EdF and FRAMATOME.

As the specific geometry of nuclear cores and the large variety of fuel assembly configurations (square or triangular fuel rod arrays, grid designs, etc.) can not be fully studied, two complementary approaches are used:

- detailled analysis and modeling of the boiling flow, up to CHF, by means of local measurements (void fraction, liquid temperature, bubble size and velocity distribution),
- quantitative analysis of CHF parameters, including among others, the geometry or heating factors like channel type, heating shape, turbulence promoters, etc.

This paper describes the first results from tests carried out in support of this latter part of the program. Tube and annulus test configurations are considered, all with uniform axial heat flux distributions.

2.2 The APHRODITE program

The APHRODITE experimental program was set up by EdF to contribute to a better understanding of the boiling crisis phenomenon. Particular attention was given to the detailled analysis of local boiling two-phase flow up to CHF, which appears to be very important for the development of a

comprehensive model of the boiling crisis. This program involved the construction of an R-12 test loop in which various mockups can be installed and tested within the following parameter ranges:

- pressure (P) :1-3.5 MPa (7-20 MPa in water),
- mass flow rate (W) : 0.03 - 12 kg/s,
- inlet temperature (T) : 25-100°C,
- electrical heating power (Q): up to 500 kW,
- height of test section : up to 6 m.

Up to now, two test sections have been designed. The first one, referred to as ENEE, consists of a single round tube. The associated experimental program is intended mainly to calibrate the experimental equipment, to permit running more complex experiments in the future (using the second mockup) and to obtain a reference CHF databank for a 13 mm ID tube for 6 and 3 meter heating lengths. This databank was used for the studies presented in this paper. The second test section (POSEIDON), is currently being designed. It is a shell side flow mockup, composed of a group of three electrically heated rods in a rectangular channel.

On the ENEE mockup, boiling crises are monitored using 168 Chromel-Alumel thermocouples (ϕ=0.3mm) welded to the outer surface of the tube wall (four thermocouples per section, at 42 heights). Souyri[3] gives more information on the test procedure. The operating parameter measurements and Instrumentation and Control (I&C) uncertainties for the test section are as follows:

Power ($\delta Q/Q$) : ± 1% ,
Mass flow rate ($\delta W/W$): ± 2% (W>0.18 kg/s), ± 1% (W<0.18)
Inlet temperature (δT): ± 0.8°C ,
Outlet pressure (δP): ± 0.008 MPa.

2.3 The DEBORA program

For several years, FRAMATOME has performed numerous CHF tests with rod bundles using water or R-12 as the coolant fluid. These tests are carried out at the CEA center in Grenoble (CENG) on the OMEGA loop (similar to the Columbia HTRF loop) and GRAZIELLA loop. The information obtained from these large loops has not been sufficient to achieve all the above-mentionned objectives. We obtain global results concerning the performance of a given fuel assembly, but without any indication of local behavior. FRAMATOME's R&D strategy has led to a comprehensive program, based on numerical simulations, experimental work using advanced mathematical tools. The experimental program, jointly performed with the CEA, involves the AGATE project (Herer[4]) for studying the hydrodynamic effects of fuel mixing grids, and the DEBORA program (CEA/

EdF/FRAMATOME) dedicated to handling all the heat transfer differences due to the specific environment of the nuclear rod bundles. DEBORA is an R-12 test loop with the following characteristics:

- pressure (P) : from 1 to 3 MPa
- mass flow rate (W) : up to 5kg/s
- inlet temperature (T) : 20°C-85°C
- heating power (Q) : up to 200kW
- height of test section : up to 4m

Heating power comes from two thyristor-type rectifiers (100 kW each). Boiling crises are monitored using 32 Chromel-Alumel thermocouples (ϕ=0.5mm) welded to the outer surface of the tube wall (at three heights). The operating parameter measurements and I&C uncertainties for the test section are as follows:

Power ($\delta Q/Q$) : ± 0.5% (CENG designed transducer),
Mass flow rate ($\delta W/W$) : ± 1% (mass flowmeter or venturi),
Inlet temperature (δT): ± 0.1°C (RTD),
Outlet pressure ($\delta P/P$): ± 0.1% (transducer).

III BASIC ELEMENTS OF THE ANALYSIS

3.1 Selected CHF databanks

A large number of CHF studies have been carried out since the 1960s, especially on simple geometries like tubes. Some authors have compiled and analyzed large tube CHF databanks from various origins. Groeneveld[5,6] has collected numerous data, these data being used to establish an international CHF look-up table for CHF in tubes. Katto[7] also used a large amount of tube data leading to a generalized correlation. Similar work was done by Hebel[8]. Most of the CHF data available does not include detailed information on the experimental procedures used, the verification tests carried out, or the accuracy of the results.

Another problem with a large databank is that it is difficult to study each parameter individually because it is hard to find two sets of data from tests run with the same parameter values except one. For example, you can have same heated lengths, pressures, and mass velocities for two tubes having different IDs, but the quality range may be different for each dataset causing difficulties in examining the effect of the tube diameter without bias.

For these reasons, each test series of our joint experimental program was carefully prepared and a quality assurance procedure based on the ISO 9001 standard was followed. Test series were defined in order to evaluate the effects of the first parameters we wanted to study, i.e. heated length (already described in our previous paper[9]),

hydraulic diameter, and cold wall. Given the absence of a heated length effect[9], at least for the range investigated here, tests series were able to be performed with various heated lengths. The analysis of the CHF data was carried out using the so-called "local conditions hypothesis", i.e. using the local thermal-hydraulic parameter values calculated at the CHF location. In our case, for all test sections, CHF location is close to the outlet because the axial flux shape is always uniform. Qualities are calculated using the ASHRAE R-12 thermodynamic tables[10].

All test series referred to in this paper are listed in Tables 1 and 2 and were carried out on the R-12 APHRODITE and DEBORA test loops with an axially uniform electrical heat flux. Even if some DEBORA tests in these tables have a relatively small (<80) L/D ratio , all DEBORA tests were carried out with a total length of about 4 m. The heated length was changed by moving the upstream electrical connector to the desired distance. In this case, we can assume that a limit of 50 for the L/D ratio is enough to avoid any inlet disturbance.

It is well known that the CHF mechanisms are very different for dryout conditions (high qualities and low heat flux densities) and DNB (low qualities and high heat flux densities). As PWRs operate with low qualities and as DNB effects are more severe than dryout effects, we will focus our attention on data with outlet qualities smaller than 0.30. This value does not correspond to the limit between DNB and dryout, which is currently not well known, but it is generally the upper limit of most of the industrial CHF correlations. In the following section, we present the general bases of our analyses performed with the usual PWR configurations and thermal-hydraulic parameters.

3.2 Comparison method

In order to obtain the "purest" and closest comparison of various CHF databanks, it is necessary to compare the CHF for exactly the same local conditions. The PLAQUEs method, as described by de Crecy[11], or any multilinear regression method allows interpolations to calculate CHF for given local conditions (pressure, mass velocity and quality), providing that calculations are made in the interpolation range. The PLAQUEs method is a non-parametric regression method with a residual standard deviation usually smaller than the one obtained from a multilinear regression method. Besides its very low standard deviation, the advantage of this method is that neither model nor mathematical relationship is needed for CHF predictions. However, a simple analytical relationship like the one obtained with a multilinear regression does not exist. In the following analyses, both types of regression have been used. The results from each method were systematically checked. One

way to compare data is to always take the same "preset" conditions. These preset conditions, constituting the reference "mesh", have the following values:

Pressure:1.5,2,2.5,3 MPa,
Mass Velocity: 2000,3000,4000,5000 kg/m²/s,
Local Quality: -.10,-.05,0.,.05,.1,.15,.2,.25 .

3.3 Error estimates

CHF and quality, the two fundamental parameters used for local analysis, are not "primary" measurements. They are calculated from the power measurement for CHF and from all the measurements for quality. They depend not only on I&C errors but also on the criteria associated with the CHF definition based on thermocouple signal analysis. In addition, the boiling crisis is, in fact, a transient phenomenon. Thus, even the most accurate (and unbiased) device can give inaccurate values. Moreover, local heat flux is a function of the local thickness of the material and of possible local electrical shunting through the thermocouple welds. Thus, it is not worth estimating the error on CHF and quality because they have no "physical" reality.

In addition, our objective was to compare CHF test series between themselves considering, on the one hand, that errors and uncertainties on raw data are very similar between each test series and, on the other hand that the regression method is always the same for all the analyses. For these reasons, and as we are not giving any reference value for CHF, error estimates were not made.

IV THE EFFECT OF DIAMETER ON CHF IN TUBES

One of the major problems still to be resolved is to know how CHF varies with hydraulic diameter. The simplest way is to know the CHF value in tubes as a function of the tube diameter. This modeling seems to be far more complicated than the literature previously supposed. Most authors have postulated that CHF varies exponentially with diameter. The power of this exponential function may be a constant or may vary with pressure, mass velocity or quality, as pointed out by Groeneveld[6] or in Czop[9]. Three different tube diameters were used. ID of tubes were 8, 13, and 19.2 mm. Tests configurations are shown in Table 1.

4.1 CHF vs. operating parameters

Using interpolated values of CHF in the mesh, the variation of CHF with pressure, mass velocity and local quality was plotted as a preliminary step, to verify the consistency of the tests. The trends are similar for each tube diameter. Two examples are given in Figures 1 & 2. In Figure 1, the

lowest pressure value (1.5 MPa) is taken. At a given local quality (0.10), CHF is the lowest for a mass velocity between 3000 and 4000 kg/m2/s. This phenomenon is related to the "Bowring point". Plotting CHF vs quality shows that the slope of the curve is higher for higher mass velocities. For two mass velocities, the two curves intersect at a point, the "Bowring point". The reason is probably that, for high qualities, high mass velocities (mostly vapor) can remove the liquid film from the wall; CHF decreases when mass velocities increases. At low qualities, higher mass velocities lead to higher CHF because of smaller enthalpy rises. CHF increases with mass velocity.

This type of phenomenon can be found again for the three tube diameter data when plotting CHF versus pressure at a given quality (Figure 2). CHF increases with pressure at a mass velocity of 4000 kg/m2/s, but decreases with pressure at a mass velocity of 2000 kg/m2/s. As for the variation of CHF with local quality at a given pressure and mass velocity, all three data sets indicate a steep slope for negative qualities and a small slope for higher qualities. During this preliminary study, the CHF behavior observed at low mass velocities (G<2000 kg/m2/s) was quite different from behaviors at higher velocities. Therefore, it was decided to consider only data obtained with mass velocities greater than or equal to 2000 kg/m2/s. The three data sets being consistent, it is now possible to compare the CHF level for the three tube diameters for the preset thermal-hydraulic parameters.

4.2 CHF in tubes of 8, 13 and 19.2 mm ID

The usual equation suggested by Doroshchuk[12,13]:

$$\Phi_{d\ mm} / \Phi_{d=\ 8\ mm} = (8/d)^{\epsilon} \quad (1)$$

gives a very convenient and easy to use relationship to relate diameters for all tube CHF data. The evaluation of ϵ permits relating all data to the single 8 mm tube data. The interpolated values of CHF are calculated in the mesh. The ratio between CHF in the 13 mm tube and CHF in the 8 mm tube appears to be almost constant ($\simeq$ 0.87) giving an average value of 0.29 for the exponent ϵ in equation (1). Thus we have:

$$\Phi_{13\ mm} / \Phi_{8mm} = 0.87 = (8/13)^{0.29}$$

In fact, the ratios are mostly in the range of 0.84 to 0.90 leading to an ϵ range of $0.36 > \epsilon > 0.22$. However, using a constant value of 0.29 gives acceptable results (Table 4). The local condition validity range for $\epsilon = 0.29$ is given in Table 3 and corresponds to the range of local conditions covered by both tests (8 & 13 mm). This value of ϵ is close

to the value suggested by Groeneveld[5] which is 0.33 for tube diameters between 4 and 16 mm. Note that in a more recent paper Groeneveld[6] suggests $\epsilon = 0.50$.

As for the 19.2 mm databank using $\epsilon = 0.29$ also gives fairly good results (Table 4). Note that the limit on the tube diameter (16 mm) suggested by Groeneveld[5] is extended to 19.2 mm. Table 4 compares the CHFs calculated using Equation (1) with the measured CHF in the 19.2 mm tube. Nevertheless, we thought that either the range of validity for ϵ or its accuracy had to be improved.

4.3 Proposed equation for ϵ

The reference mesh is no longer considered here. We first calculated a reference PLAQUEs using the 8 mm data. This allows calculating CHF at any local condition in the interpolation range. More precisely, we used the local conditions obtained in the other two tests (13 and 19.2 mm tubes) to calculate CHF in an 8 mm tube. "Experimental" values of ϵ were determine for all local conditions using :

$$\epsilon = \ln(\Phi_d/\Phi_8)/\ln(8/d) \quad d = 13 \text{ or } 19.2$$

where Φ_d is the measured CHF at given experimental local conditions for the 13 or 19.2 ID tube tests and Φ_8 is the 8mm PLAQUEs calculated CHF for the same local conditions.

We see from Figure 3 that these values change dramatically when local (outlet) qualities exceed roughly 0.1. A more precise analysis of this figure (but not directly seen on this figure) indicates that the steep slopes are strongly dependent on pressure and mass velocity. For example, the steepest slope is for 1.5 MPa and 4000-5400 kg/m2/s. It was then decided to limit our analysis to the data for local qualities below 0.15. With this restriction, it appears that even though the 8 and 13 mm data and the 8 and 19.2 mm data agree quite well, the combination of both 13 and 19.2 with 8 mm data shows some deviations. This behavior was also found by Cheng[14]. For this reason, only a slight improvement for ϵ was obtained using the following equation:

$$\epsilon = c + a_1 P + b_1 G/1000 + c_1 x + a_2 P^2 + b_2 (G/1000)^2 + c_2 x^2 \qquad (2)$$

$c = 1.087$

$a_1 = -0.526 \quad b_1 = -0.077 \quad c_1 = -0.303$

$a_2 = 0.099 \quad b_2 = 0.010 \quad c_2 = -0.910$

As shown in Table 4, this equation permits reducing the standard deviation for the 19.2 mm data from 0.063 (ϵ=0.29) to 0.049. The recommendation of Groeneveld[5] to use d=16 mm instead of the DEBORA diameter (19.2 mm) did not lead to any improvement.

We must stress the fact that the validity range for diameters is from 8 to 19.2 mm and that the upper quality limit is 0.15 and that large errors can be introduced if Equation (2) or ϵ=0.29 is used for higher qualities. The ranges of the other parameters are given in Table 3.

The variation of measured CHF (M) divided by the calculated (C) CHF (or predicted CHF) versus the local quality is given in Figure 4. Predicted values are calculated as indicated above using the PLAQUEs interpolated value of CHF for an 8 mm ID tube and equations (1) and (2). C vs M values are given in Figure 5.

A preliminary interpretation of these results, to be confirmed by some local void fraction measurements, is based on the difference between average quality and true local quality. For low qualities, the difference between local quality (at the wall) and the average calculated quality at the same height increases with the tube diameter. For the same given average local (outlet) quality in two tubes, the quality near the wall is higher in the larger tube. As DNB is a local phenomenon, CHF is then lower for the larger tube. On the contrary, for high qualities, the flow regime may be totally different and the CHF mechanism may be dryout. In which case, the above study would not be valid.

V CHF IN ANNULI

In order to extend the results in tubes into more general behaviors, we need to test other simple geometries close to the tube geometry. Annuli are the most appropriate geometries. However, this change generates secondary effects like curvature, radial heating and spacer devices etc. Spacer devices are designed to maintain the two tubes in the correct position.

Compared to CHF studies in tubes, references in annuli are far less numerous. Shah[15] used about 23 internally heated cylindrical annulus tests from 10 references to build a correlation extended to any kind of annuli with the addition of four other tests with outer or both tubes being heated. The range of tube diameters and gaps (g) is quite large. Ilic[16] presents a series of 29 annuli cooled by upflow of R-12 at an inlet pressure of 1.04 MPa with internal, external, and combined internal and external heating. The range of tube diameters is large, but gaps are small (0.8 to 3 mm). Ornatski[17] performed tests with two-side heating, the outer tube being overheated. Inner tube OD is 10 mm and the gap 1 to 2 mm. Tolubinskiy[18] used about the same geometry but with CHF occurring on the inner

tube with the inner tube being overheated. Becker[19] performed tests with a geometry close to the first DEBORA annulus, but obtained high qualities.

The first DEBORA annulus gives us three CHF annulus databanks. The annulus geometry is as follows: 19.2 mm ID for the outer tube and 9.5 mm OD for the inner tube. The choice of these dimensions was governed by the geometry of most of the 17x17 PWR fuel rod assemblies: the diameter of 9.5 mm corresponds to the fuel rod diameter and the hydraulic diameter of the annulus is 9.7 mm, which is the hydraulic diameter of a guide-tube subchannel. Spacer devices used to center the inner tube are welded on the inner tube every 300 mm, with the last one located 250 mm upstream from the end of the heated length. These spacers are designed to interfere as little as possible with the flow.

The first databank, DEBORA 13 (see Table 2), was obtained with both tubes heated by identical heat fluxes. The other two databanks were DEBORA 3, with the outer tube heated and DEBORA 4, with the inner tube heated.

5.1 One-side heating (external or internal)

Figure 6 gives a comparison of CHF in the 19.2/9.5 annulus with just one side being heated (outer tube for DEBORA 3; inner tube for DEBORA 4). CHF is greater (about 10%) when the inner tube is heated under DNB conditions ($x<0.1$).

5.2 Bilateral heating

CHF LOCATION

On DEBORA 13, power was set on each tube to try and obtain the same local heat flux densities on both tubes. In practice, as the heat fluxes are generated by two independent power supplies of 100 kW each, heat fluxes on both tubes are never strictly identical. However, the resulting heat fluxes never differed by more than 4%. Boiling crisis occurred either on the outer, the inner, or on both of tubes simultaneously. Looking at the test conditions when these three cases took place, we noted that:

- There is no relationship between the tube having the highest heat flux and the tube on which the CHF occurs.

- Pressure or mass velocity have no effect on CHF location. We found CHF occurring on either tube for the whole ranges of pressures and mass velocities.

- Local quality has an obvious effect on CHF location (see Figure 7).

For qualities greater than 0.2, almost all boiling crises occur on the inner tube (ϕ 9.5), and for qualities lower than 0.2, boiling crises occur on the outer tube (ϕ 19.2) except for very few cases. This behavior could be due to the type of boiling crisis i.e. DNB under low qualities and dryout under high qualities. This means that CHF would appear on the outer tube under DNB conditions and on the inner tube under dryout conditions. Since DNB is commonly considered to be a local phenomenon, following the conclusion of Brighton[20] that the local velocity near the wall is lower on the outer tube than on the inner tube, this could explain why the cooling is less effective on the outer tube and why CHF occurs preferentially on the outer wall. The velocity gradient, and, consequently, the shear stress can also play an important role. This preferential occurrence seems to be related more to channel geometry than to curvature of the heating surface itself, considering that the diameters and gap used in our tests are large enough.

In the references, when looking at other tests with equally heated tubes, only data under dryout conditions are available. Becker[19] found that CHF always occurred on the inner tubes (which is consistent with our observations), while Ilic[16] found that CHF occurred on both tubes. In the second case, the gaps were rather small. We believe that for small gaps, major differences can appear compared to our actual gap. This is also true for CHF in small ID tubes where other effects (like curvature) may be stronger.

When comparing CHF level for internally or externally heated annuli (Section 7.1), it seems logical that, for the same thermal-hydraulic conditions, CHF preferentially occurs on the outer tube when both tubes are heated.

CHANNEL SHAPE

Next, we looked for a relationship between the CHF in the two-side heated annulus and the CHF in a tube. What tube diameter gives about the same CHF as was obtained for the annulus? We first tried a tube diameter of 9.7 mm (hydraulic diameter of the annulus). Since we did not have any data for a 9.7 mm tube, we used either equations (1) and (2) from Chapter 6, or the PLAQUEs method to calculate the CHF for a 9.7 mm tube under the preset conditions.

Using the same method as in Section 4.3 allows the direct comparison of calculated CHF in a 9.7 mm tube and measured CHF in the annulus. Results of calculated/measured ratios are plotted in Figure 8. For qualities below about 0.1(DNB conditions), CHF in the "equivalent" 9.7 mm tube is

slightly higher (≈ 6%) than CHF in the annulus with two wall heating. In fact, the CHF in the annulus is similar to the CHF in an 11 mm tube.

Under higher qualities (dryout conditions), the effect of pressure is predominant if mass velocities are above 2000 kg/m2/s. For low pressures, CHF in the annulus can be much higher than CHF in a tube of equivalent hydraulic diameter (see Figure 8).

In conclusion, for a two-side equally heated annulus, under DNB conditions, CHF occurs on the outer tube at a value close to that found on a tube having roughly the same hydraulic diameter.

5.3 CHF on outer tube : cold wall and channel shape effects

We analyzed two annulus tests; the DEBORA 13 test for low qualities (boiling crises on the outer tube) and DEBORA 3 (inner tube not heated) and the 19.2 mm tube test (DEBORA 1 and 2). In Figure 9, a comparison of the calculated CHFs from DEBORA 13 and DEBORA 3 shows that the presence of the cold wall (inner tube not heated) tends to lower the CHF by about 10%, under DNB conditions ($x<0.1$). This result disagrees with Ornatskiy[17] who found, for gaps between 1 and 2 mm, that CHF at the external surface is independent of the heat load applied to the inner tube. But a cold wall is normally detrimental to heat transfer, since it attracts liquid which could otherwise be used to cool the heated wall. Once again, gap size seems to be important.

The next step was to compare annulus and tube. Heating tubes were the same but hydraulic diameters were different and there was a cold wall in the annulus. When the two sides of the annulus were heated, CHF was about the same as in the tube with the same hydraulic diameter. Having just the outer tube of the annulus being heated lowers the CHF by about 10% compared to both tubes being equally heated, and we found that the CHF corresponded to that of the 19.2 mm tube (Figure 10). Under DNB conditions, CHF in the outer tube heated annulus is close to the CHF in the 19.2 mm tube. The 10% cold wall penalty in a 9.7 mm hydraulic diameter annulus is compensated by a larger diameter (19.2 mm) in a tube according to Equations (1) and (2) in Section 4.3.

VI EFFECT OF HYDRAULIC DIAMETER

Lastly, a comparison has been made between the DEBORA 18 CHF data and the ENEE B&C CHF data. DEBORA 18 data is for an annulus with a 9.5 mm IT OD and a 13 mm OT ID, while ENEE is for a 13 mm tube . Since the annulus hydraulic diameter (3.5 mm) is outside the range of the tube databank (8-19.2 mm), CHF for this diameter was not calculated.

The only remark we can make is that the behavior of the data would lead to completely different conclusions from the conclusions drawn from the above comparison between annulus and tube. We lack enough data to continue this investigation, but we can assume that this difference is probably due to the fact that the flow and heat transfer characteristics are not the same for such a small hydraulic diameter.

VII CONCLUSION

The first observation we can make is that CHF can exhibit dramatically different behaviors under dryout conditions and for DNB. These behaviors have been precisely establish with the help of an advanced spline method.

Limiting our conclusions to DNB conditions, we found, for CHF in a round tube, that the variation with the tube diameter followed the recommended equation and initial exponent value of Groeneveld[5], although the exponent value was slightly modified. But a more recent exponent value proposed by Groeneveld[6] gives less satisfactory results. Nevertheless, we impose an upper limit (0.15) for local qualities, although Groeneveld[5,6] indicates no upper limit. Respecting this limit allows comparing the CHF in an annulus (with both walls heated equally) with the CHF in a tube having the same hydraulic diameter.

Concerning the externally heated annulus, still under DNB conditions, the results seem comparable for tubes having the same diameter as the outer tube of the annulus.

Also, internally heated annuli can reach higher CHF than externally heated annuli, under the same DNB conditions.

Small tube diameters and small gaps can totally change these conclusions.

Nevertheless, the need for more research is evident if we want to assess and generalize these results. Also further work has to be done to expand our analysis to rod bundles. It seems that for low qualities, good accuracy can be achieved, but for higher qualities, we need to improve the phenomenological approach to the boiling crisis phenomenon.

0 REFERENCES

[1] STEVENS G.F., ELIOTT D.F., WOOD R.W. *"An experimental investigation into forced convection burnout in Freon, with reference to burnout in water. Uniformly heated round tubes with vertical upflow."* AEEW-R237 (1964)

[2] AHMAD S.Y. *"Fluid to fluid modeling of critical heat flux: a compensated distortion model"* Int. J. Heat Mass Transfer,16,641-661 (1973)

[3] SOUYRI A., CONAN S., PORTESSE A., TREMBLAY D. *"The Aphrodite Program. Analysis of the first CHF tests performed on a vertical tube"* NURETH6 meeting Grenoble France (1993)

[4] HERER C. *"3D flow measurement in nuclear fuel rod bundles using laser Doppler velocimetry"* FED, vol 108, Fluid Meas. & Inst. Forum, ASME, Portland USA (1991)

[5] GROENEVELD D.C., CHENG S.C., DOAN T. *"1986 AECL-UO critical heat flux lookup table"* Heat Transfer Eng.,7,nos1-2,46-62 (1986)

[6] GROENEVELD D.C., LEUNG L.K.H., KIRILLOV P.L., BOBKOV V.P., ERBACHER F.J., ZEGGEL W. *"An improved table look-up method for predicting critical heat flux"* NURETH6 meeting Grenoble France (1993)

[7] KATTO Y. *"Critical heat flux of forced convection boiling in uniformly heated vertical tubes"* Int. J. Heat Mass Transfer,23,1573-1580 (1980)

[8] HEBEL W., DETAVERNIER W., DECRETON M., *"A contribution to the hydrodynamics of boiling crisis in a forced flow of water"* Nucl. Eng. & Design,64,433-445 (1981)

[9] CZOP V., HERER C., SOUYRI A., GARNIER J., *"Analysis of in R12 CHF data: influence of hydraulic diameter and heating length; preliminary test of Weisman theoretical boiling crisis model"* European Two-Phase Flow Group Meeting, paper F3, Hannover Germany (1993)

[10] STEWART R.B., JACOBSEN R.T., PENONCELLO S.G. *"ASHRAE Thermodynamic Properties of Refrigerants"* American Soc. of Heating Refrigerants & Air Conditioning Eng., Inc. (1986)

[11] de CRECY F. *"Pseudo-cubic thin-plate type spline method for analyzing experimental data"* Nucl. Eng. & Design,149,459-465 (1994)

[12] DOROSHCHUK V.E., LEVITAN L.L., LANTZMAN F.P. *"Recommendations for calculating burnout in a round tube with uniform heat release"* Teploenergetika,22,66-70 (1975)

[13] DOROSHCHUK V.E., LEVITAN L.L., LANTZMAN F.P. *"Investigations into burnout in uniformly heated tubes"* ASME Paper 75-WA/HT-22 (1975)

[14] CHENG X., ERBACHER F.J., STARON E., ZEGGEL W. *"Critical Heat Flux in circular tubes at high pressures and high mass fluxes"* NURETH5 meeting Salt Lake City USA (1992)

[15] SHAH M.M. *"A general correlation for CHF in annuli"* Int. J. Heat Mass Transfer,23,225-234 (1980)

[16] ILIC V. *"Burnout data from annuli cooled by upflow of Freon-12"* AAEC/E323 (1974)

[17] ORNATSKIY A.P., GLUSHCHENKO L.F., KICHIGIN A. M. *"Burnout in annular channels with two-sided heating"* HEAT TRANSFER - Soviet Research,1,12-16 (1969)

[18] TOLUBINSKIY V.I. *"Heat transfer crisis at the inward surface of annuli heated from both sides"* HEAT TRANSFER-Soviet Research,5,93-96 (1973)

[19] BECKER K.M., LETZTER A. *"burnout measurements for flow of water in an annulus with two-sided heating"* KTH-NEL-23 presented at the European Two-Phase Flow Group Meeting, Haifa, Israel (1975)

[20] BRIGHTON J.A., JONES J.B. *"Fully developed turbulent flow in annuli"* J. Basic Eng. , Trans. ASME, 835-844 (1964)

TABLE 1 : CHF TESTS IN TUBE DESCRIPTION OF TESTS CONFIGURATIONS

TEST SECTION	TEST #	Heated length(m)	ID (mm)	OD (mm)	# of tests	Pressure (MPa)		Mass Vel. (Kg/m2/s		Quality (%)		Flux (kW/m2)	
						Min	Max	Min	Max	Min	Max	Min	Max
DEBORA	20	1.5	8.0	12.0	75	1.44	3.03	1007	5102	−21	+44	53	435
DEBORA	21	0.68	8.0	12.0	45	1.44	3.02	955	5073	−51	+32	70	650
ENEE	B	6.0	13.0	14.0	97	1.24	3.51	2660	5380	−11	+37	60	232
ENEE	C	3.5	13.0	14.0	197	1.03	3.47	1775	5432	−33	+38	53	344
DEBORA	1	3.5	19.2	21.2	146	1.43	3.03	960	5017	−30	+39	59	415
DEBORA	2	1.0	19.2	21.2	35	1.45	3.02	1007	5015	−74	+19	108	663

TABLE 2 : CHF TESTS IN ANNULI DESCRIPTION OF TESTS CONFIGURATIONS (DEBORA LOOP)

TEST #	Heated length (m)	Inner Tube OD (mm)	Outer Tube ID (mm)	# of tests	Pressure (MPa)		Mass Vel. (Kg/m2/s		Quality (%)		Inner tube Flux (kW/m2)		Outer tube Flux (kW/m2)	
					Min	Max	Min	Max	Min	Max	Min	Max	Min	Max
3	3.5	9.5	19.2	120	1.46	3.01	976	5038	−20	+41	0	0	44	356
4	3.5	9.5	19.2	101	1.46	3.01	991	5024	−34	+19	67	522	0	0
13 (*)	3.5	9.5	19.2	33	1.46	3.01	1012	5020	−2	+30	50.7	261.3	52.6	260.0
14 (*)	3.5	9.5	19.2	39	1.46	3.01	991	4998	+20	+34	30.6	141.7	29.4	144.5
18	3.5	9.5	13.0	30	1.46	3.01	2022	5040	+2	+41	0	0	34	177
19	3.5	9.5	13.0	27	1.46	3.01	2031	5021	−7	+23	35	224	0	0

(*) DEBORA 13 concerns CHF detected on the outer tube
(*) DEBORA 14 is the same CHF test series as DEBORA 13 but concerns CHF detected on the inner tube
All test series carried out on the DEBORA loop

TABLE 3 : VALIDITY RANGES

	Limited Range	Extended Range	All Data
Pressure (MPa)	1.5 3	1.5 3.5	1.0 3.5
Mass Vel. (kg/m2/s)	2000 5000	2000 5400	1000 5400
Quality (%)	−5 +15	−60 +15	−74 +44

Limited Range : for e (epsilon) constant = 0.29
Extended Range : for e (epsilon) using Equation (2)

TABLE 4 : STATISTICS OF M/C

epsilon = 0.29	Limited Range	Extended Range	All Data	
ENEE B & C	1.035	1.023	1.29	average
TUBE	0.052	0.069	0.57	std
13 mm ID	48	131	294	data
DEBORA 1 & 2	0979	0.996	1.05	average
TUBE	0.062	0.063	0.13	std
19.2 mm ID	92	129	181	data

epsilon = EQ. (2)	Limited Range	Extended Range	All Data	
ENEE A & B	1.021	1.012	1.26	average
TUBE	0.048	0.064	0.58	std
13 mm ID	48	131	294	data
DEBORA 1 & 2	0975	0.996	1.05	average
TUBE	0.060	0.049	0.12	std
19.2 mm ID	92	129	181	data

M is the measured CHF
P is the calculated CHF using the 8 mm ID tube data and Equation (1) with epsilon constant (0.29) or varying according to Equation (2).

FIGURE 1 : CHF vs Mass velocity

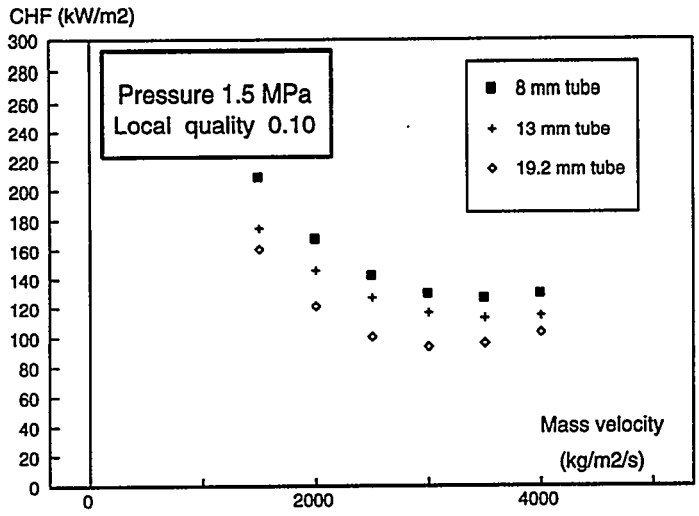

FIGURE 2 : CHF vs Pressure

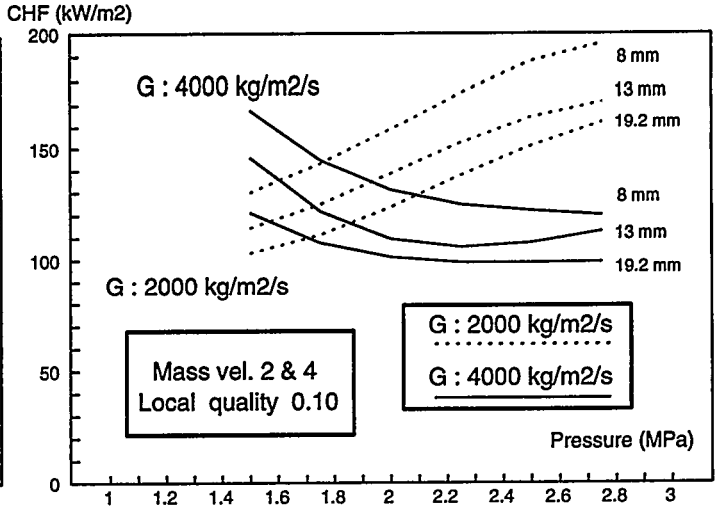

FIGURE 3 : "EXPERIMENTAL" VALUES OF EPSILON

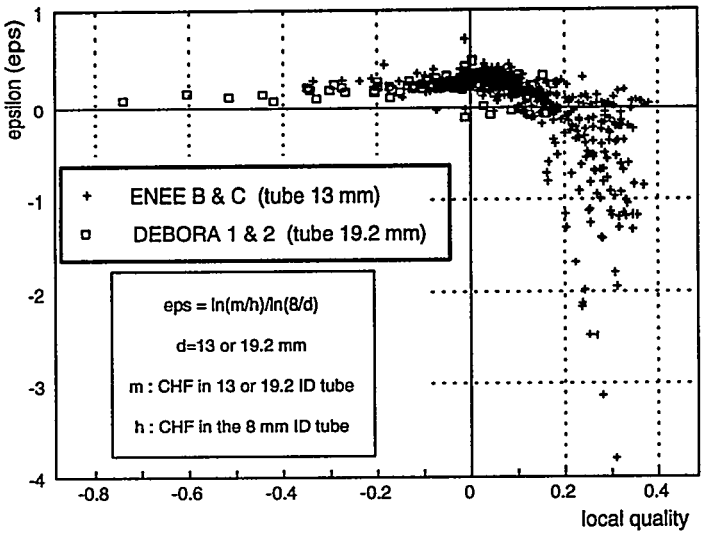

FIGURE 4a : M/C ENEE B&C (13 mm)

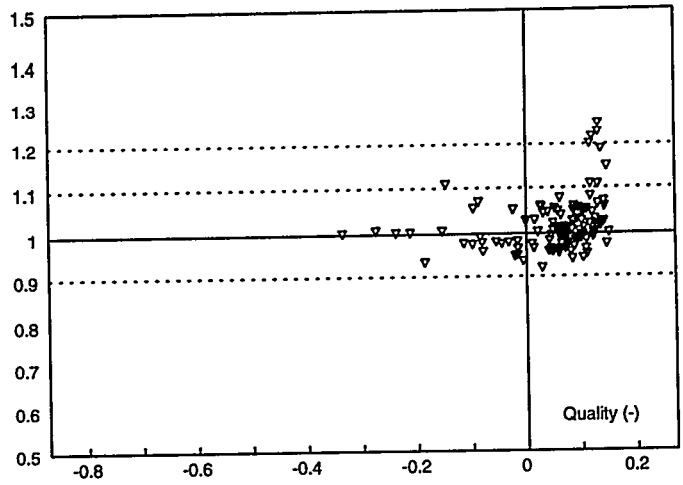

FIGURE 4b : M/C DEBORA 1&2 (19.2 mm)

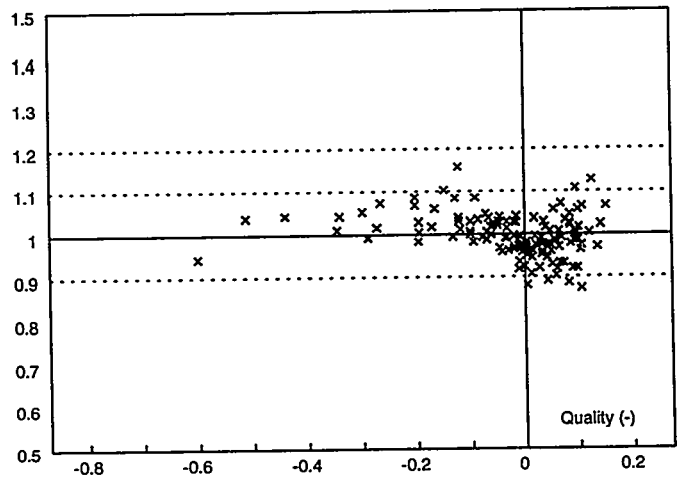

FIGURE 5a : C vs M ENEE B&C (13 mm)

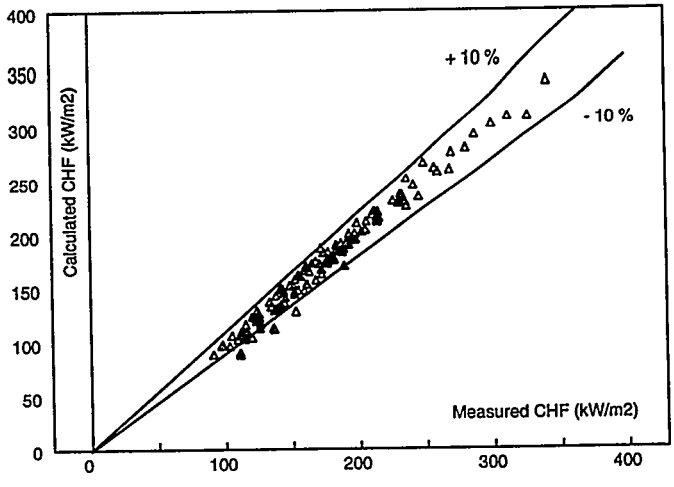

FIGURE 5b : C vs M DEBORA 1&2 (19.2 mm tube)

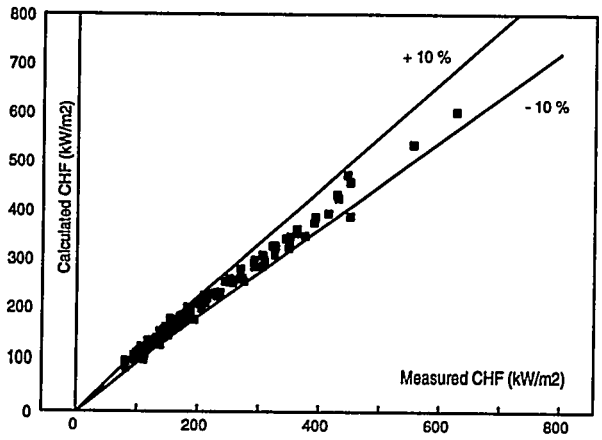

FIGURE 6 : CHF IN ONE-SIDE HEATED ANNULI

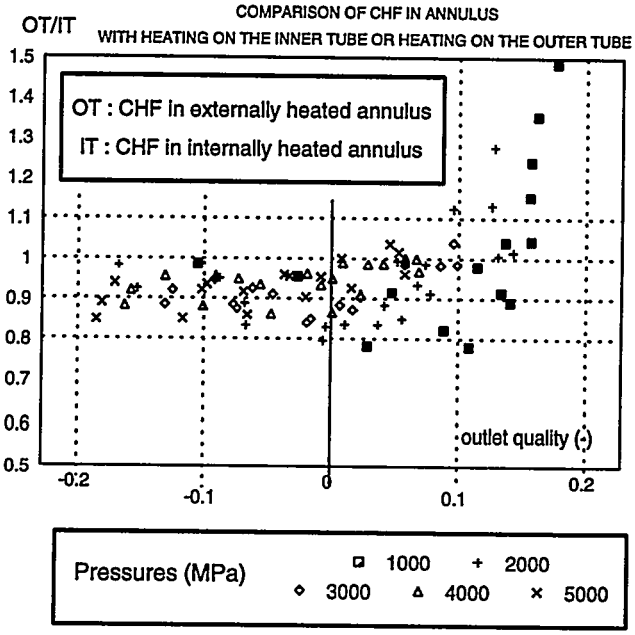

FIGURE 7 : CHF IN A TWO-SIDE EQUALLY HEATED ANNULUS

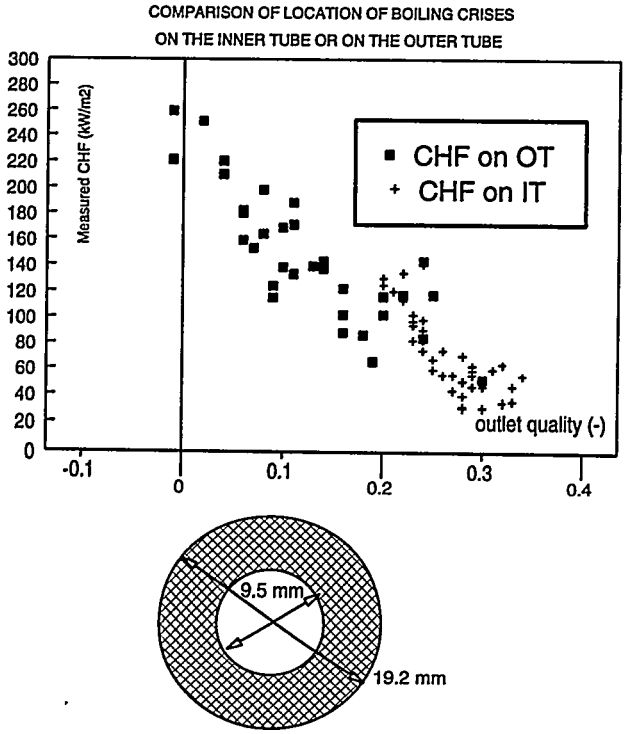

FIGURE 8 : COMPARISON OF CHF IN A TUBE AND CHF IN A TWO-SIDE EQUALLY HEATED ANNULUS HAVING THE SAME HYDRAULIC DIAMETER

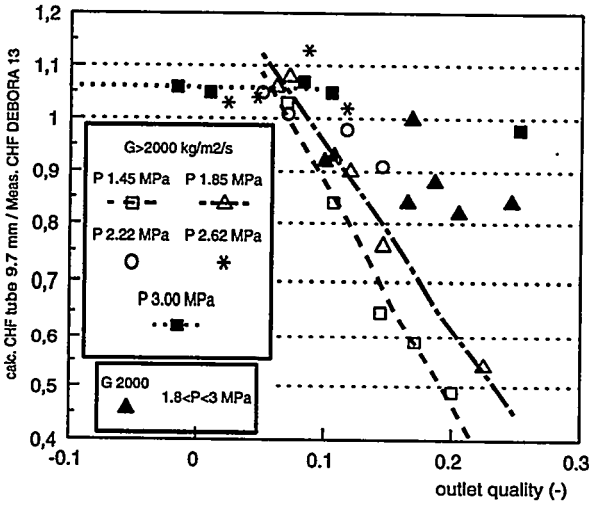

FIGURE 9 : COMPARISON OF CHF IN A TWO-SIDE EQUALLY HEATED ANNULUS OR IN AN EXTERNALLY HEATED ANNULUS

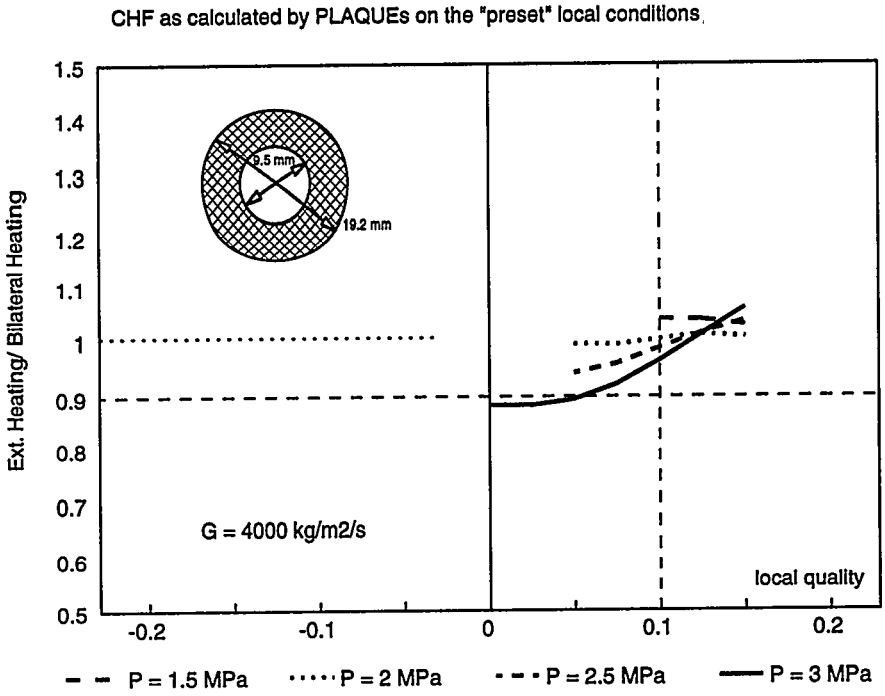

FIGURE 10 : COMPARISON OF CHF IN AN EXTERNALLY HEATED ANNULUS AND IN A TUBE WITH THE SAME DIAMETER AS THE OUTER TUBE OF THE ANNULUS

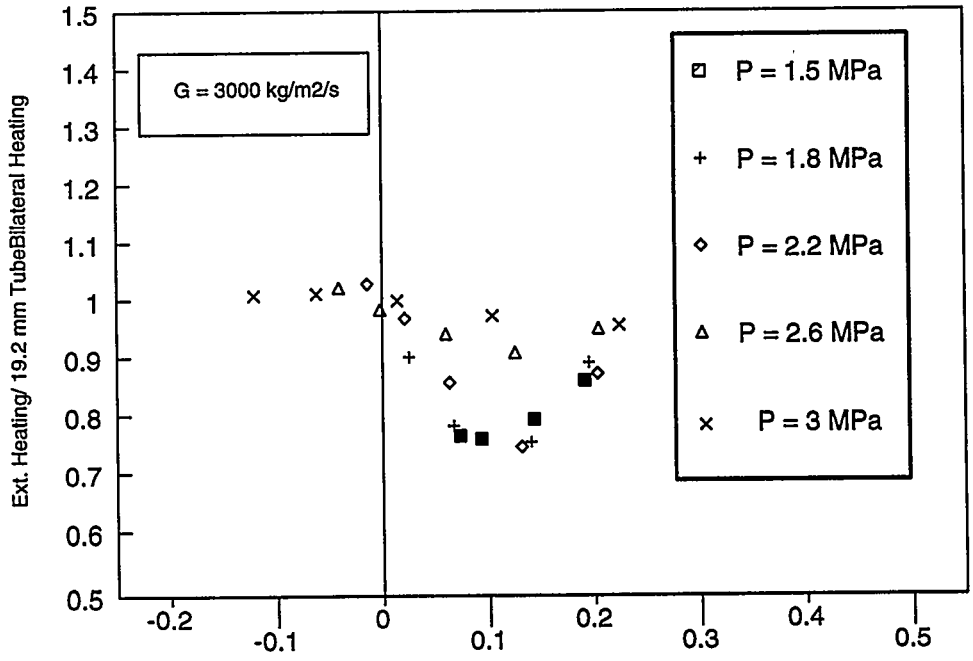

New Model for Burnout Prediction in Channels of Various Cross-Section

Bobkov V.P., Kozina N.V., Vinogradov V.N., Zyatnina O.A.

State Scientific Center,
Institute of Physics and Power Engineering
Bondarenko Sq. 1, 249020 Obninsk,
Kaluga Region, Russian Federation
Telex: 911509 URAN SU
Fax: (095)883-3112

Abstract.

The model developed to predict a critical heat flux (CHF) in various channels is presented together with the results of data analysis. A model is the realization of relative method of CHF describing based on the data for round tube and on the system of correction factors. The results of data description presented here are for rectangular and triangular channels, annuli and rod bundles.

Table of Nomenclature.

C_o curvature of thermal boundary layer;
D tube diameter, m;
D_{he} heated equivalent diameter, m;
F flow area, m^2;
G mass flow rate, $kg/(m^2 s)$;
K_{et} parameter of effective thermoconductivity of fuel rod;
L length, m;
L_h heated length, mm;
L_o relative extension of elementary thermal cell flow area;
P pressure, MPa;
P_{cr} pressure, critical value, MPa;
P_h heated perimeter, m;
Q heat flux (also critical), MWt/m^2;
Q_D heat flux in tube with diameter D, MWt/m^2;
Q_8 heat flux in tube with diameter 8 mm, MWt/m^2;
Q_t heat flux in tube, MWt/m^2;
R radius, m;
R_h radius of heated surface, m;
X steam quality;
X_o steam quality, modelling value;
ΔX value of X biasing;
Y_t model parameter, a thickness of thermal boundary layer, m;
secondary parameters $Y_{t,min}$, $Y_{t,av}$ and Y_o;
indexes: 1 - for internal surface of annulus;
2 - for external surface of annulus.

1.Introduction.

The report contains the analysis of specific features of critical heat flux (CHF) for water flowing in channels of various non-round cross-section and the results of CHF description in such channels. The method used here is a relative one which can be considered to be analogous to ones being used in another fields of thermohydraulics. The relative model means here the using of recommendations for CHF in round tubes in order to predict CHF values in more complex channels. The examples of investigations based on similar approach can be found in [1,2].

The authors of [1] have elaborated the corrections to skeleton (look-up) table on CHF in round tubes with uniform heating which have been used to predict CHF in rod bundles. These corrections describe the effects of cross-section geometry, heated length, minimum gap, curvature of heated surface, spacers, distribution of heat flux along heated perimeter. The authors have considered their results as preliminary and awaiting for improvement. They have not presented the estimates of data fitting accuracy and the ranges of applicability.

The authors of [2] have checked directly (without any corrections) the possibility of using of CHF values in tubes for prediction CHF in spaced 7-rods bundles. The cases explored have yielded satisfactory results.

2. Special features of CHF in complex channels.

When deriving the model of relative CHF description one should define the conditions of comparation of CHF in various channels. It seems that the main conditions are connected with pressure, P, mass flux, G, and steam quality, X. Others will be considered later.

The complex channels with special features of CHF can be divided to two types: 1) isolated channels of complex cross-section (annuli, rectangular or triangular channels, simulators of rod bundle cells); 2) rod bundles which, in contrast to isolated channels, should be considered as systems of parallel channels.

Let's look at first at CHF in isolated channels with respect to CHF in round tube.

1. Having in mind the dependence of CHF in tubes on cross-section scale (diameter) we should choose the proper scaling factor for other channels. We guess that we can use the heated equivalent diameter, D_{he}, as proper one.

2. An overheating of fluid is inevitable in the narrowest place of channel with nonuniform gap of flow area along heated perimeter. Therefore the CHF in such channel depends on such parameters of cross-section geometry as variation of gap value and its relative extent. The last factor affects heat transfer efficiency along heated perimeter and consequently overheating degree and CHF value.

3. We assume that thermoconductivity and thickness of heated channel wall affect CHF in such channels because an efficiency of transverse heat transfer depends on these factors.

4. Having in mind the fact that CHF differs in annuli with internal and external heating with the same main parameters (P, G, D_{he}, X, L) we should assume that CHF depends on the type of heated surface curvature (either convex or concave) - see also [3-5].

5. It seems also that CHF depends on conditions of heating along perimeter in isolated channels of complex profile. The example is the flat channel or annuli with unilateral and bilateral heating. A presence or absence of heat flux on opposite surface affects strongly CHF value. There is no steam generation on nonheated surface (a liquid film is retained) that leads to displacment of flow regimes and to variation in CHF. It had been mentioned in [6].

The specific features of CHF in various rod bundles include features presented above for isolated channels. But we have here additional factors due to the fact that rod bundle is the system of parallel connected channels of complex profile. It leads to considerable complication of experimental methods and phenomena description. These additional factors are:

1. The problem of thermohydraulic non-equivalence of bundle cells (subchannels) is connected with difference of central and peripheral zones of bundle and also with possible presence of technological distortions of bundle geometry. It leads to nonuniform distribution of mass and heat flow and to dispersion of such parameters as G, X and, maybe, P along cross-section. The crisis occurs in the cell featured by most adverse conditions.

2. The transverse heat and mass transfer between cells can decrease or suppress the effect of non-equivalence of central and peripheral cells.

3. The additional turbulization of flow by spacers leads usually to an increase of CHF value.

The main difficulty of CHF description in rod bundles is how to define the values of main local parameters in crisis locality - both operating (P, G) and geometrical.

3. New model.

This new model of CHF description in channels of complex cross-section including rod bundles is based on CHF features presented above and on following assumptions [7,8].

1. The main dependencies of CHF on main parameters (P, G, X, D_{he}) are defined by the case of round tube of D=8 mm with correction factor for another values of diameter. We use here the look-up table method for calculation of CHF in tube - see, for example, [9,10].

2. The model is valid for the smooth channels with arbitrary cross-section which is uniform along length. We assume that the local values of main parameters (P, G, X, D_{he}) are known and the heat flux is uniform along length.

3. The whole cross-section of channel is divided to "elementary thermal cells" (ETC). Its definition ([7,8]) is presented below.
4. We take the heated equivalent diameter $D_{he}=4F/P_h$ (F is a flow area of ETC, P_h is its heated perimeter of ETC) as the typical scaling factor for cross-section. It is used to correct the CHF value for tube diameter. This factor can help to take into account a type of heat flux cross-distribution and the constancy of derivative of enthalpy with respect to length.
5. The CHF value for ETC can be found from value for tube with the same P and G, $D=D_{he}$:

$$Q(P,G,D_{he},X)/Q_t(P,G,D,X_o)=f(C_i), \qquad (1)$$

where C_i is the system of correction factors contained mainly geometrical factors and effective thermoconductivity of fuel rod. The definition of function X_o is presented below.

4. Definitions.

The elementary thermal cell (ETC) is the part of channel cross-section which contains the part of fuel rod or its simulator and adjacent thermal boundary layer - flow area section which is responsible for removing of heat from heated surface of ETC. The ETC can be defined by following borderlines (see Fig.1).
1) Lines dividing ETCs along normal to heated surface (lines N1, N2, N3 and N4 on Fig.1a). It is assumed that heat transfer across these lines is absent. We call them "the lines of zero transfer" (LZT). With these lines been defined properly the heating of heat agent inside the ETC is equal to the subchannel mean value.

In the case of bundle with *uniform radial heating* these lines for internal (closed) ETC coincide with the lines of symmetry (line N1 on Fig.1a) and the surface of barrel gives the LZT (N3, N4) for peripheral (open) ETC (ETCs of types 3 and 4). We take the N2 as LZT for ETC of type 2.

The case of bundle with *nonuniform radial heating* is more complicated one. We assume that the first step of analysis should be done by using of proper method of subchannel analysis to define local parameters values of most "dangerous" cell (subchannel). Then this last should be divided to a number of ETCs. Such a complicated case is a subject of further investigation which will lead to more grounded method of CHF calculation.

In general, each LZT is the geometric locus of points whose distances from nearest heated surfaces along normals are *proportional to corresponding values of heat flux*.
2) Lines dividing the neighboring ETCs along heated perimeter (lines L4 of Fig.1,a). In the case of uniform heating these lines are also defined by symmetry and in general can be defined after building the LZTs.

The exact definition of ETC's borderlines demands checking the relation derived from heat balance equation:

$$Q_i * P_{h,i}/F_i = \Sigma(Q_j * P_{h,j}) \ / \ \Sigma(F_j), \qquad (2)$$

where index i stands for given ETC, the sums are over all ETCs included into the subchannel of commonly accepted division (for example, one consists of two ETCs of type 3 plus two of type 2).

The thermal boundary layer (TBL) of ETC is its flow area closed by heated perimeter and LZT.

The thickness of TBL (Y_t) is a distance from heated surface to LZT (see Fig. 1b). The nonuniform ETC has Y_t which varies along perimeter with definite minimum value, $Y_{t,min}$. It is important that Y_t varies monotonically along heated perimeter. We use also the average value of Y_t, $Y_{t,av}$:

$$Y_{t,av} = (1/P_h) * \int_{P_h} Y_t * dP_h \qquad (3)$$

and such parameter of ETC's nonuniformity as $Y_o = Y_{t,min}/Y_{t,av}$.

The curvature of TBL (C_o) is the ratio $C_o = Y_{t,av}/R_h$, where R_h is a radius of heated surface. We have: for tube - $R_h = D/2$, $C_o = -1$; for annulus with external heating - $-1 < C_o < 0$; for annulus with internal heating - $C_o > 0$; for flat channel - $C_o = 0$. For all channels which we deal with C_o varies from -1 to 1. By the way, the parameter C_o in annuli has also meaning of undimensional mean gap value.

The relative extension of ETC's cross section (L_o) is the ratio $L_o = P_h/Y_{t,av}$.

The modelling value of steam quality (X_o) in tube is defined by a relation of biasing $X_o = X + \Delta X$, where X is the value in given channel and ΔX depends on other parameters (see below).

The thermohydraulic nonuniformity of ETC is caused by different heating of heat agent in narrow and wide parts of its flow area (see definition of parameter Y_o). It leads to a heat transfer along heating perimeter both in flow area and in a body of fuel rod (or its simulator). In the last case the value of heat transfer depends on thickness and thermoconductivity of a simulator wall. So we should insert the parameter of effective thermoconductivity of fuel rod or its simulator, K_{et}. It is well defined for case of convective single-phase heat transfer [11] but additional investigations are needed to define it for burnout phenomena. We estimate this parameter here phenomenologically.

So we have such a system of model parameters: thickness of thermal boundary layer, Y_t, with minimum value, $Y_{t,min}$; parameter of nonuniformity of TBL, Y_o; curvature of TBL, C_o; relative extension of TBL, L_o; parameter of effective thermoconductivity of fuel rod or its simulator, K_{et}.

5. Results for isolated channels.

The data used were chosen from HEMATIC's (Heat and Mass Transfer Information Center, IPPE, Obninsk) data bank on CHF in various isolated channels. The correction factors have been derived from the data for concentric and eccentric annuli with uni- and bilateral heating in such form:

$$Q(P,G,D_{he},X)/Q_t(P,G,D=D_{he},X_o)=1-K*(1-Y_o)^n \quad (4)$$

where

$$K=K1*K2*K3*K4*K5 \quad (5)$$

The recommended data for tubes used to derive coefficients in (4-5) were (here and below) in the form of look-up table [9], with diameter effect $Q_D/Q_8=(8/D)^{0.5}$.

Let's begin with the relation between X and $X_o=X+\Delta X$. The typical case of this biasing for annulus can be seen on Fig.2. Fig.3 shows the dependence of biasing ΔX on C_o obtained after analysis of experimental data on CHF in concentric annuli. With $C_o=-1$ (round tube) ΔX is equal to 0. Let's imagine the nonheated rod inside the tube with both diameters (D_1 and D_2) being increased so that D_{he} is being retained constant. When D_1/D_2 varies from 0 to 1 the value of C_o is increased from -1 to 0 and that of ΔX - from 0 to some definite value (our estimate is approximately 0.05). A changing over $C_o=0$ to positive values means the changing of heating from external to internal surface. The positive increasing of C_o (decreasing of D_1/D_2) leads to further insreasing of biasing ΔX.

What are the reasons of this curvature effect? Here we can only give the hypothesis. Analysing the data on CHF in concentric annuli we see that 1) CHF biasing along X-axis is greater at internal heating ($C_o>0$); 2) the values of ΔX are approximately the same at all values of X for given C_o. This means that the reasons of curvature effect on ΔX value are the same at film boiling, transition and dispersed-annular regimes and result in better water supplying of an external (concave) surface. We guess that the reasons are connected with turbulent pulsations of velocity along curved isotachs. These pulsations lead to a rise of massive forces acting on each elementary volume of flow. These forces being proportional to density push the heavy phase (water) to an external (concave) surface more effectively than light phase (steam).

The phenomenological relation for ΔX is (see Fig.3):

$$X_o=X+\Delta X, \quad (6)$$

where

$$\Delta X=0.05*(C_o+1)^2*(1-0.4*P/P_{cr}), \quad (7)$$

P_{cr} is the critical value of pressure.

The correction for Y_o in (4) have been derived after analysis of data on CHF in eccentric annuli:

$$n=0.5+0.0015*G*C_o^2, \quad (8)$$

where G is in kg/(m^2s). The typical plots of CHF dependencies on Y_o are presented on Fig.4. The greater is the nonuniformity of ETC's cross-section (eccentric annulus) the greater is difference between CHF in this ETC and in ETC with uniform cross-section (concentric annulus). When Y_o=1 (uniform cross-section of ETC, for example, concentric annulus) the correction factor $(1-Y_o)^n$ equals to 0, when Y_o=0 (maximum nonuniformity, minimum gap value equals to zero) this factor equals to 1. The dependence of exponent n on G and $|C_o|$ (modulus of C_o) extracted from data can be seen on Fig.5.

In (4) K1 is the correction for relative extension, L_o, which have been derived from the data in eccentric annuli:

$$K1=K(L_o)=0.077*L_o \quad (9)$$

The correction for both mass flux, G, and C_o have been derived using the relation from [5]:

$$K2=K(G,|C_o|)=G^{**}(-0.37*|C_o|^{0.5}), \quad (10)$$

where G is in kg/(m^2*s), ** - raising to a power..

The correction for both C_o and heated length, L_h, mm, is:

$$K3=K(L_h,|C_o|)=L_h^{**}[(0.29*|C_o|)^{0.33}] \quad (11)$$

The correction for steam quality is (see [5]):

$$K4=K(X)=1-0.3*X \quad (12)$$

The correction for assumed parameter K_{et} have been defined from the data for annuli as phenomenological constant.

$$K5=K(K_{et})=0.4 \quad (13)$$

This value is valid for tubular simulator of fuel rod made from stainless steel, with wall thickness being in range 1-1.5 mm.

So, we can describe now the CHF in concentric annulus. We have the given values of P, G, X, heat fluxes Q_1 and Q_2, diameters D_1 and D_2. Here we have Y_o=1, the right part of (4) equals to 1 and the correction is connected only with biasing Δ X.

We should define on which surface the crisis arises. We have for annulus:

$$D_{he,i}=4F_i/P_{h,i}, \quad (14)$$

$$C_{o,i}=Y_{t,i}/R_i, \quad (15)$$

where i=1 - internal and i=2 - external surface.

To define the value of D_{he} we should calculate the diameter D_o of LZH dividing both TBLs - near internal and external

surfaces (see Fig.1c). This value can be defined as sufficient approximation using condition: $F_1/F_2=Q_1*P_{h,1}/(Q_2*P_{h,2})$. It leads to relation

$$D_o^2=(Q_1*D_1*D_2^2+Q_2*D_2*D_1^2)/(Q_1*D_1+Q_2*D_2) \quad (16)$$

Then we have for internal surface:

$$D_{he,1}=(D_o^2-D_1^2)/D_1, \quad (17)$$

$$Y_{t,1}=(D_o-D_1)/2, \quad (18)$$

$$C_{o,1}=(D_o-D_1)/D_1, \quad (19)$$

and for external one:

$$D_{he,2}=(D_2^2-D_o^2)/D_2, \quad (20)$$

$$Y_{t,2}=(D_2-D_o)/2, \quad (21)$$

$$C_{o,2}=(D_o-D_2)/D_2 \quad (22)$$

Note that C_o in (22) is negative.

The calculated values of CHF, $Q_{cr,1}$ and $Q_{cr,2}$, for both surfaces are equal to the values, $Q_{t,1}$ and $Q_{t,2}$, for equivalent tube with given parameter values: internal - P, G, $D=D_{he,1}$, $X_o=X+\Delta X_1$, external - P, G, $D=D_{he,2}$, $X_o=X+\Delta X_2$. These values should be compared with real values of heat flux on each surface. If $Q_1<Q_{cr,1}$ and $Q_2<Q_{cr,2}$ then the crisis had not arose. Otherwise we easily define the critical surface and the value of CHF.

To define the CHF in <u>eccentric annulus</u> we should calculate additionally the parameters $Y_{o,i}$ and $L_{o,i}$ and use the phenomenological value K5=0.4. With $R_o=D_o/2$, $R_1=D_1/2$, $R_2=D_2/2$ we have ($Y_{o,1}=Y_{o,2}$ by definition)

$$Y_{o,1}=(R_2-R_1-E)/(R_2-R_1), \quad (23)$$

$$Y_{o,2}=(R_2-R_1-E)/(R_2-R_1), \quad (24)$$

$$L_{o,1}=3.14*R_1/(R_o-R_1), \quad (25)$$

$$L_{o,2}=3.14*R_2/(R_2-R_o), \quad (26)$$

where E is the eccentricity in meters. The values of D_o, $D_{he,1}$, $D_{he,2}$, $C_{o,1}$ and $C_{o,2}$ should be defined in the same way as for concentric annulus (Fig.1c).

Statistical results of description CHF data in annuli with uniform heating are presented in Table 1. The data used have been taken from HEMATIC's data bank [3]. The notations in Table 1 are: M is mean value of relative residues, RMS is relative root mean

square error (non-biasing estimate of scattering around the mean value M).

The Table 1 contains also the results for CHF in rectangular and triangular channel [17].

So, we've got the correction functions system in a rather general form which helps to predict CHF in isolated channels of various cross-section. It can be done with given values of main parameters: pressure, mass flux, steam quality, cross-section geometry, features of fuel rod or its simulator. It should be noted that the accuracy of description of data for isolated channels equals approximately to that for tubes, but the discrepancies between the data sets of different authors and/or for different test-sections are greater. The maximum value of this discrepancy for annuli is about 40%.

6. Results for spaced rod bundles.

The data used were for triangular bundle geometry, hexagonal nonheated barrel, with the number of rods from 3 to 37. The parametric ranges of 2100 points were: pressure - from 3 to 19.9 MPa, mass flux - from 500 to 4130 kg/m^2, steam quality - from -0.5 to 0.7, thermal diameter - from 5.8 to 12.45 mm, pitch/diameter ratio T_{pd} - from 1.22 to 1.4.

The thermohydraulic non-equivalence of internal and peripheral cells means the difference of local values of system parameters (P, G, X). The crisis takes place always *in internal cell* for the cases under consideration. To be sure that the local values of system parameters differ little from the mean ones across channel we use the criterion

$$K_{thd}=dH(c)/dH(b) \qquad (27)$$

Here dH is a variation of mean enthalpy in cell ("c" - cell) and in channel ("b" - bundle) as the result of heating. With neglecting of intercell exchange this relation can be simplified:

$$K_{thd}=(D_{he,b}/D_{he,c})*(D_{hy,b}/D_{hy,c})^{0.5}, \qquad (28)$$

where subscript "he" means "heated equivalent" and "hy" means "hydraulic equivalent".

We use the data with the vaues of K_{thd} from 0.85 to 1.15. The relation (28) gives rather upper limit of criterion because of the transverse intercell mixing. After that we don't use the subchannel analysis which is needed for more detailed development.

The use of spacers inside the channel body helps to turbulize the flow and to increase CHF. To account for this effect we use the relation [1]

$$K_{sp}=1+1.5*K_o^{0.5}*G^{0.2}*\exp(-0.1*L_{sp}/D_{hy,c}), \qquad (29)$$

where K_o is the spacer loss coefficient, G is in $Mg/(m^2s)$, Lsp is the distance from top to nearest spacer.

The main relations of geometric parameters for internal ETC are: $D_{he}=D_r*(1.103*T_{pd}^2-1)$, $C_o=1.047*T_{pd}-1$, $Y_o=T_{pd}/C_o$, $L_o=0.5236/C_o$, where D_r is rod diameter.

So, we assume that the main features of CHF in spaced rod bundles are described by the function $\Delta X(P,C_o)$ (7). The further data analysis has shown that we have here the residual dependence of CHF on P, G and X. After data fitting this dependence is

$$Q_{rb}(P,G,X,D_{he})/[Q_t(P,G,X_o,D_{he})*K_{sp}]=N(P,G,X), \quad (30)$$

where

$$N(P,G,X)=(0.091+1.02*P*G-0.0575*P^2*G^3)*(1+0.536*X) \quad (31)$$

Finally, the relation (30, 31) fit 2105 data points with M= -4.7% and RMS=22.8%. The ranges of values of M and RMS for various data sets are: M - 60%, RMS - from 8.3% to 29%. The Figures 6-10 display several plots of CHF (data and calculated values) versus Xcr.

The data show, just as in the cases of other channels, the noticeable discrepancies between data sets of different authors. These data sets differ often by parametric regions so one meet the danger *to overestimate* the residual parametric trends when fitting forcely mentioned discrepancies. Our compromise has been grounded by the analysis of residual error distribution function for each data set - we have demanded them to be approximately normal.

7. Results for tighted rod bundles.

The description of CHF in tighted rod bundles is made difficult by the fact that this case has the features both of isolated and bonded channels. Another difficulty is the lack of data available with all of them being for $D_{he}<4$ mm.

Having this in mind we have dealt with a special case of problem - to check the accuracy of relation

$$Q_{rb}(P,G,X,D_{he})/Q_t(P,G,X_o,D_{he})=[1-K*(1-Y_o)^n]*K_{sp}*N(P,G,X) \quad (32)$$

against the data for tighted rod bundles.

We have two data sets available: 41 points for $T_{pd}=1.02$ and 49 points for $T_{pd}=1.05$. The parametric ranges are: pressure - from 8.2 to 13.8 MPa, mass flux - from 650 to 5550 kg/m^2s, quality - from 0 to 0.77, heated equivalent diameter - 2.4 and 2.8 mm. The best fit is for K5=0.6 - see (13), with this value being equal to that for triangular channel [17]. It should be noted that these experiments have had the aim to simulate the crisis in tighted rod bundle. Also, the best fit is for diameter correction $Q_D/Q_8=(8/D)^{1/3}$. This fact recalls the conclusion of

D.C.Groeneveld [1] that the degree value of 1/3 helps to fit better the data on CHF in tubes with D<4 mm.

Finally, the statistical results are: M=15% and RMS=22% for first data set (Tpd=1.02), M=7% and RMS=22% for second one.

8. Conclusions.

1. CHF in channel differing from tubular one can be predicted by using reliable recommendations for tube and correction functions system. This last must include the corrections for geometry, heating conditions, details of fuel rod design or its simulator and thermoconductivity of its body.
2. The approximations for CHF in isolated channels presented here are based on the model which allows to derive such system of corrections which are workable for channels of various cross-section. The data for annuli and triangular and rectangular channels have been used to determine the phenomenological coefficients.
3. The nucleus of model is the concept of "elementary thermal cell" (ETC) which helps to analyse the general features of CHF in various channels. It is geometric and thermohydraulic non-uniformity of ETC that can result in decreasing of CHF in non-tubular channel.
4. The model gives a quite reasonable description of CHF in rod bundles. The residual parametric trends have been been revealed which are important mainly for low values of pressure and/or mass flux.
5. The use of subchannel analysis can help to improve the description of CHF in rod bundles.
6. Up to now we don't success to determine accurately the corrections to internal properties of fuel rod. The reason is the lack of appropriate data and the absence of suitable theory. Instead, we have got the phenomenological values for corrections.
7. The authors hope that the results presented here can be used to improve the methods of CHF calculations in channels of nuclear reactors.

Acknoledgements.

This investigation was financially supported by Ministry of Atomic Energy, Ministry of Science, Russia, and, partly, by Atomic Energy of Canada, Ltd. The authors would like to express their thanks to Professors D.C.Groeneveld (Chalk River, Canada), P.L.Kirillov (Obninsk, Russia), Yu.A.Zeigarnik (Moscow, Russia) and Dr. I.P.Smogalev (Obninsk, Russia) for constructive discussions.

References.

1.D.C.Groeneveld, K.Joober, S.Doefler, W.Wong, L.K.H.Leung, S.C.Cheng, "The Effect of Fuel Subchannel Geometry on CHF," Thesis of Report to NURETH-5 (1992).
2.W.Zeggel, F.J.Erbacher, S.Bethke, X.Cheng, H.J.Neitzel, "CHF-Measurement in a Hexagonal Tight Lattice and CHF-Table

Prediction," Proc. of Seminar "Thermophysics-90", Obninsk, Russia (1990).
3.O.A.Sudnitsin, P.L.Kirillov, V.P.Bobkov et al, "The Review of Experimental Data on CHF in Concentric and Eccentric Annuli," Preprint IPPE-2318, Obninsk, Russia (1993) - in Russian.
4.A.P.Ornatsky, V.A.Tchernobay, N.A.Lazarev, V.S.Furaev, "An Investigation of Eccentricity Effect to CHF in Annuli", Teploenergetika, v.16, #7, 74-77 (1969) - in Russian.
5.V.I.Tolubinsky, E.D.Domashev, "Boiling Burnout in Annuli", Voprosi Atomnoy Nauki i Tekhniki, ser. "Fizika i Tekhnika Yadernikh Reaktorov", v.1, #30, 58-68 (1983) - in Russian.
6.P.L.Kirillov, I.P.Smogalev, "Prediction of Burnout for Water-Steam Mixture in Annuli at Annular Dispersed Regime", Preprint IPPE-297, Obninsk (1972) - in Russian.
7.V.P.Bobkov, "Boiling Burnout in Channels of Various Cross-Section. Description Model," Preprint IPPE-2313, Obninsk (1993) - in Russian.
8.V.P.Bobkov, O.A.Zyatnina, N.V.Kozina, O.A.Sudnitsin, "Boiling Burnout in Channels of Various Cross-Section. Model and Results of Statistical Analysis" Preprint IPPE-2314, Obninsk (1993) - in Russian.
9.P.L.Kirillov, V.P.Bobkov, E.A.Boltenko, V.N.Vinogradov, A.A.Ivashkevitch, I.B.Katan, I.P.Smogalev, "A Method of the Development of Standard CHF Data for Tubes with Uniform Heat Flux", Preprint IPPE-2030, Obninsk (1989) - in Russian.
10.D.C.Groeneveld, L.K.H.Leung, P.L.Kirillov, V.P.Bobkov, F.J.Erbacher, W.Zeggel, "An Improved Look-Up Table Method for Predicting the Critical Heat Flux", Report on NURETH-6, Grenobl, 1993.
11.P.A.Ushakov, "Approximate Thermal Simulation of Fuel Rods," In book "Liquid Metals", Moscow, Atomizdat (1967) - in Russian.
12."A Research Program in Two-Phase Flow", Centro Informazione Studi Esperience (CISE), Italy (1963).
13.S.Levy, E.F.Polomic, C.N.Swan, W.McKinney, "Eccentric Rod Burnout at 1000 lbf/in2 with Net Steam Generation," Int. J. Heat Mass Transfer, v.5, 595-614 (1962).
14.S.I.Green, E.F.Sladna, B.W.Letourneau, P.S.Sherba, "Critical Heat Flux Test on a Cooolant Channel, Simulating a Closely Spaced Lattice of Rodes," Proc. of ASME Winter Meeting, 72-80 (1969).
15.P.S.Anderson, A.Jensen, G.Mannov, A.Olsen, "Burnout Circumferential Film Flow Distribution and Pressure Drop for Eccentric Annulus with Heated Rod," Int. J. Multiphase Flow, v.1, 585-600 (1974).
16.V.I.Tolubinsky, A.K.Litovtchenko, E.D.Domashev et al, "Critical Heat Flux in Eccentric Annuli," Teploenergetika, v.18, #6, 64-66 (1971).
17.V.I.Subbotin, B.A.Zenkevitch, O.V.Remizov, "On Effect of Channel Geometry on CHF with Forced Water Flow," Teploenergetika, v.7, 81-83 (1962) - in Russian.

Table 1. The statistical results for isolated channels, the data are from HEMATIC's data bank. The first column features a data sample (all data, inside the scattering range of 100% and 50%)

Sample	N	P	G ranges	X	Gap mm	M %	RMSP %
Concentric annuli.							
Unilateral uniform heating							
All	3359	3:20	500:5600	-0.50:0.85	1.0:5	0.1	34.7
100%	3293	-	-	-	-	-2.6	28.9
50%	3028	-	-	-	-	-5.3	22.0
Internal uniform heating							
All	1737	3:20	500:5600	-0.5:0.85	1:5	-4.5	38.4
100%	1689	-	-	-	-	-8.4	30.1
50%	1539	-	-	-	-	-10.7	22.5
External uniform heating							
All	1622	3:20	500:4100	-0.5:0.7	1:5	5	29.3
100%	1604	-	-	-	-	3.5	26.2
50%	1489	-	-	-	-	0.3	20.1
Bilateral uniform heating							
All	296	6:20	500:4500	-0.3:0.8	2.1	-6.2	30
50%	260	-	-	-	-	-5.3	23
Eccentric annuli (relative eccentricities were 0.25 and 0.5)							
All	82	9:20	500:1000	-0.35:0.35	0.5:1	-15.6	15.2
Rectangular channel							
All	47	6:15	620:3500	-0.2:0	0	0.8	8.2
Triangular channel							
All	40	6:17	500:3700	-0.2:0	0	2.3	16.8

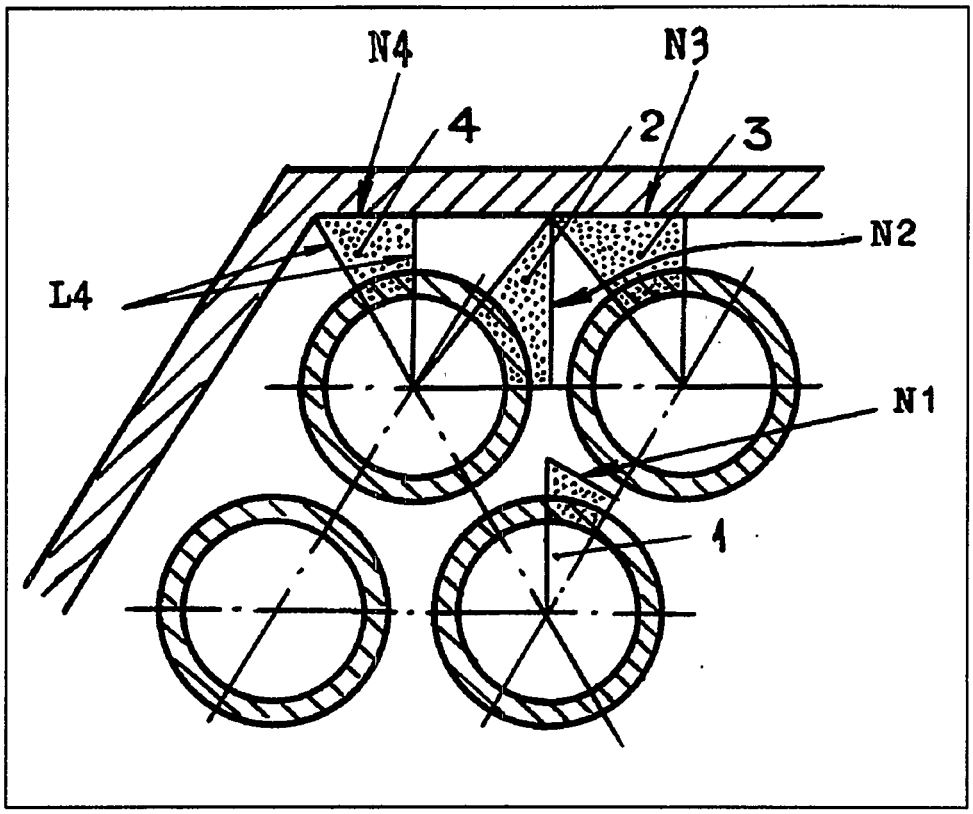

a

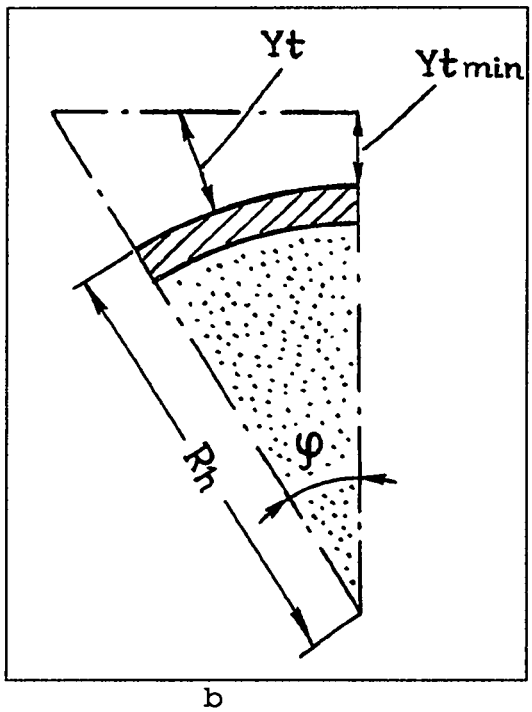

b

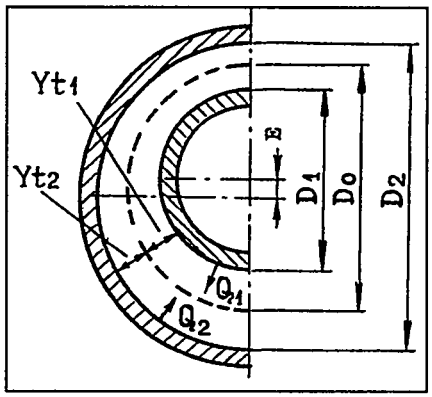

c

Fig.1 The schemes of typical ETCs: a) for rod bundle; b) internal ETC of type 1 for subchannel; c) for eccentric annulus.

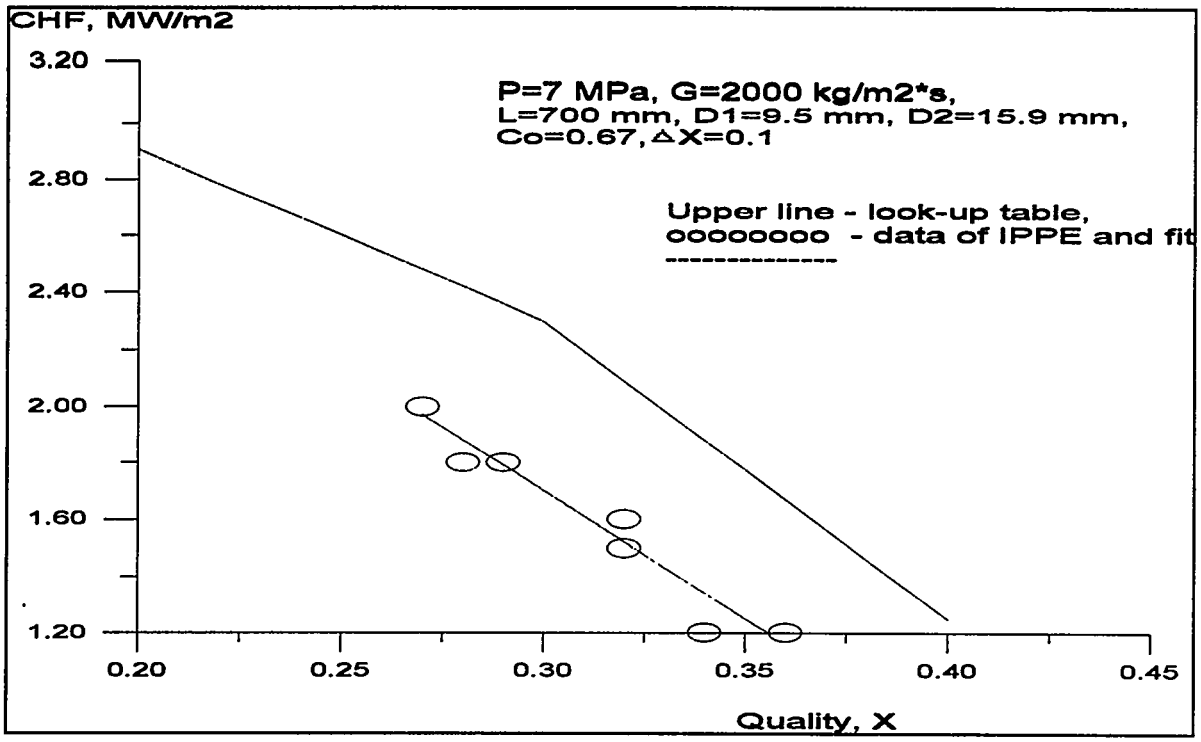

Fig.2 The example of X-biasing (ΔX), data in annulus.

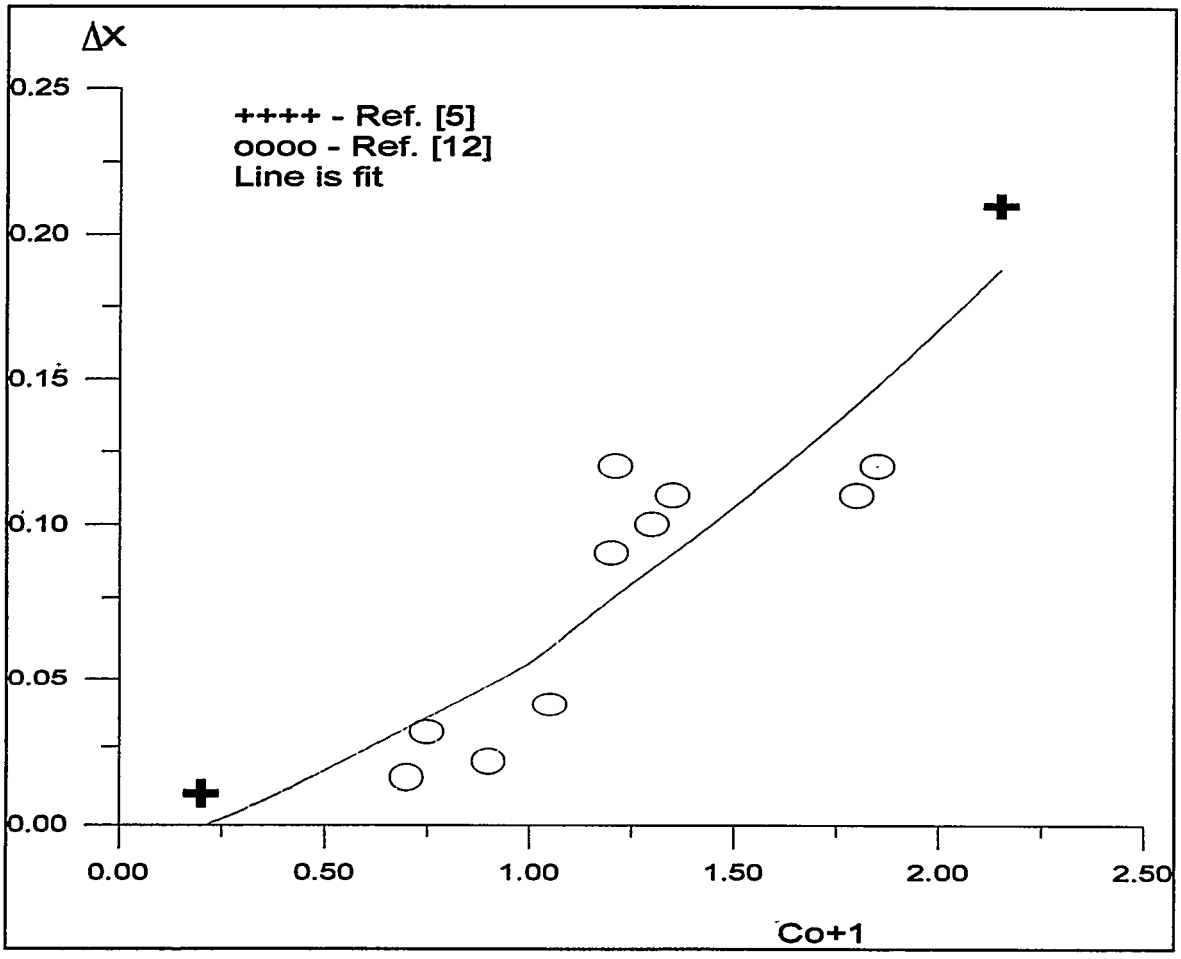

Fig.3 Dependence of ΔX on curvature (C_o+1)

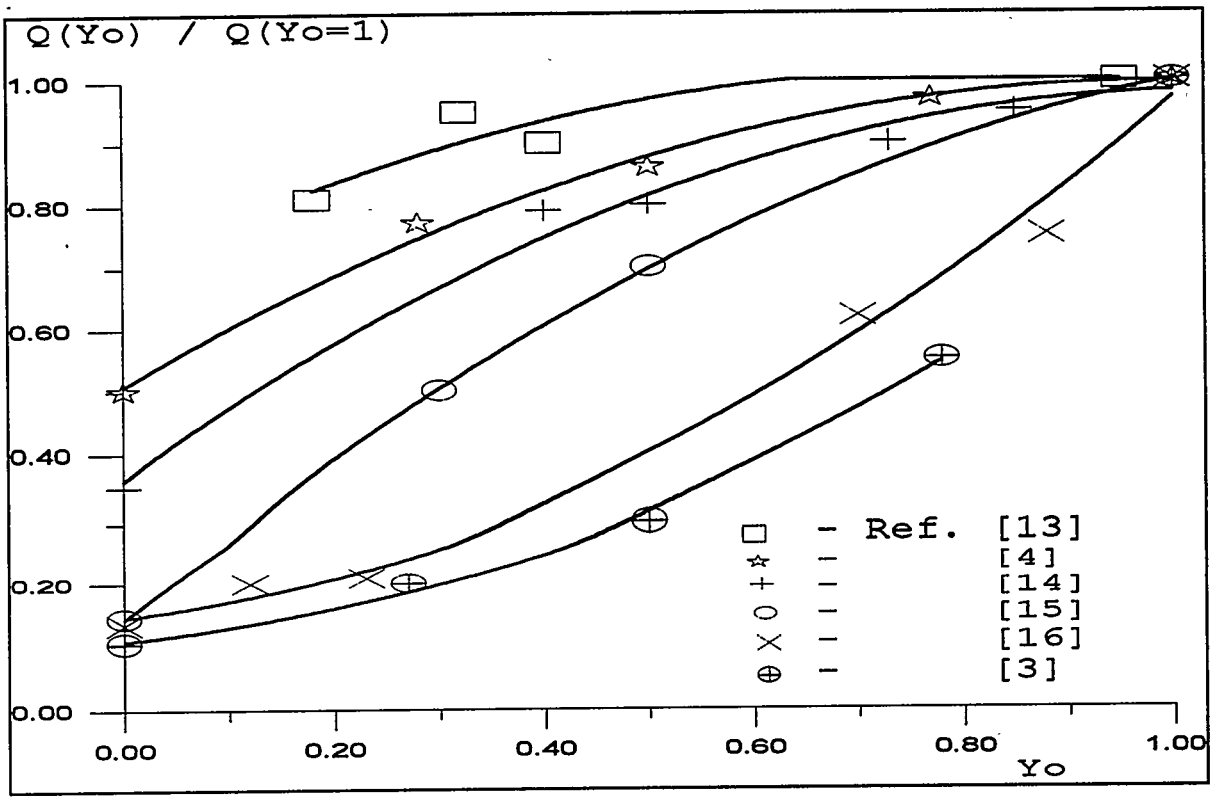

Fig.4 Experimental dependence of CHF on parameter Y_o.

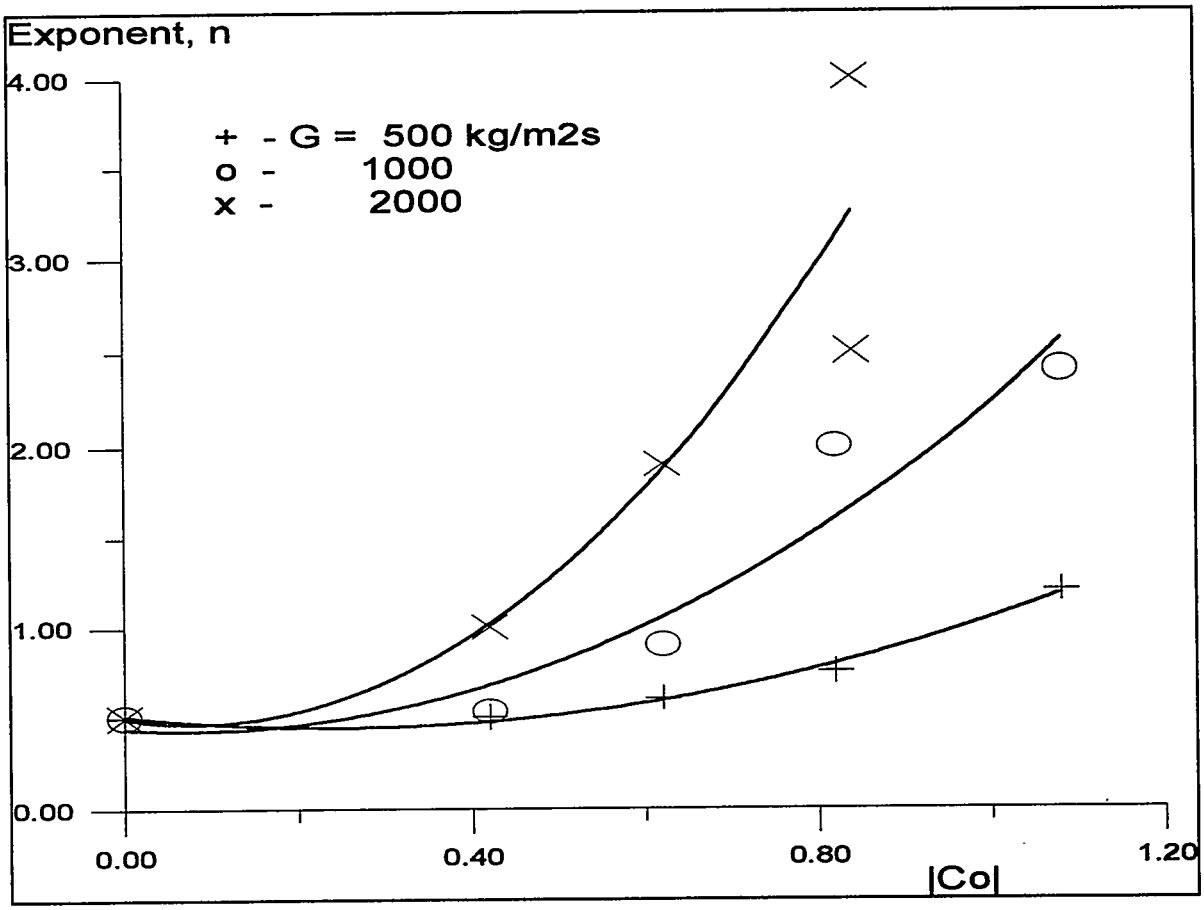

Fig.5 Dependence of exponent n on $|C_o|$ G [4], lines are fits.

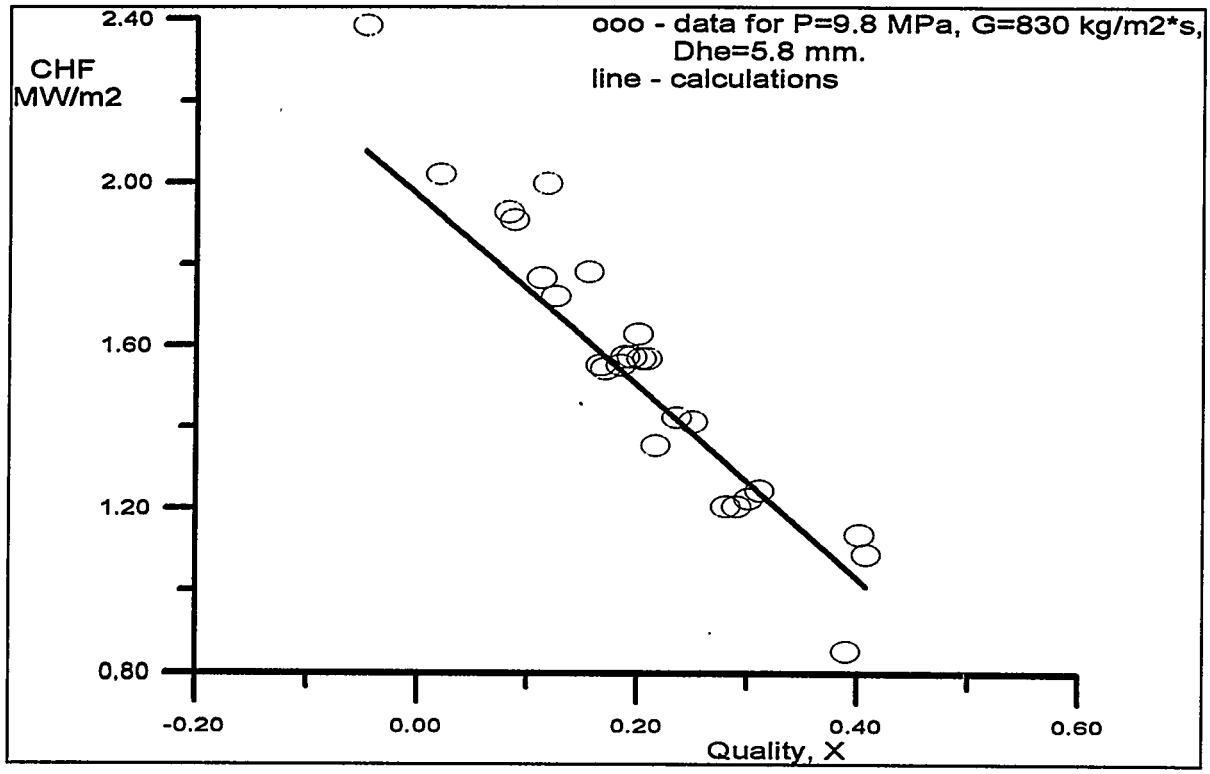

Fig.6 The data versus calculation, CHF in rod bundles.

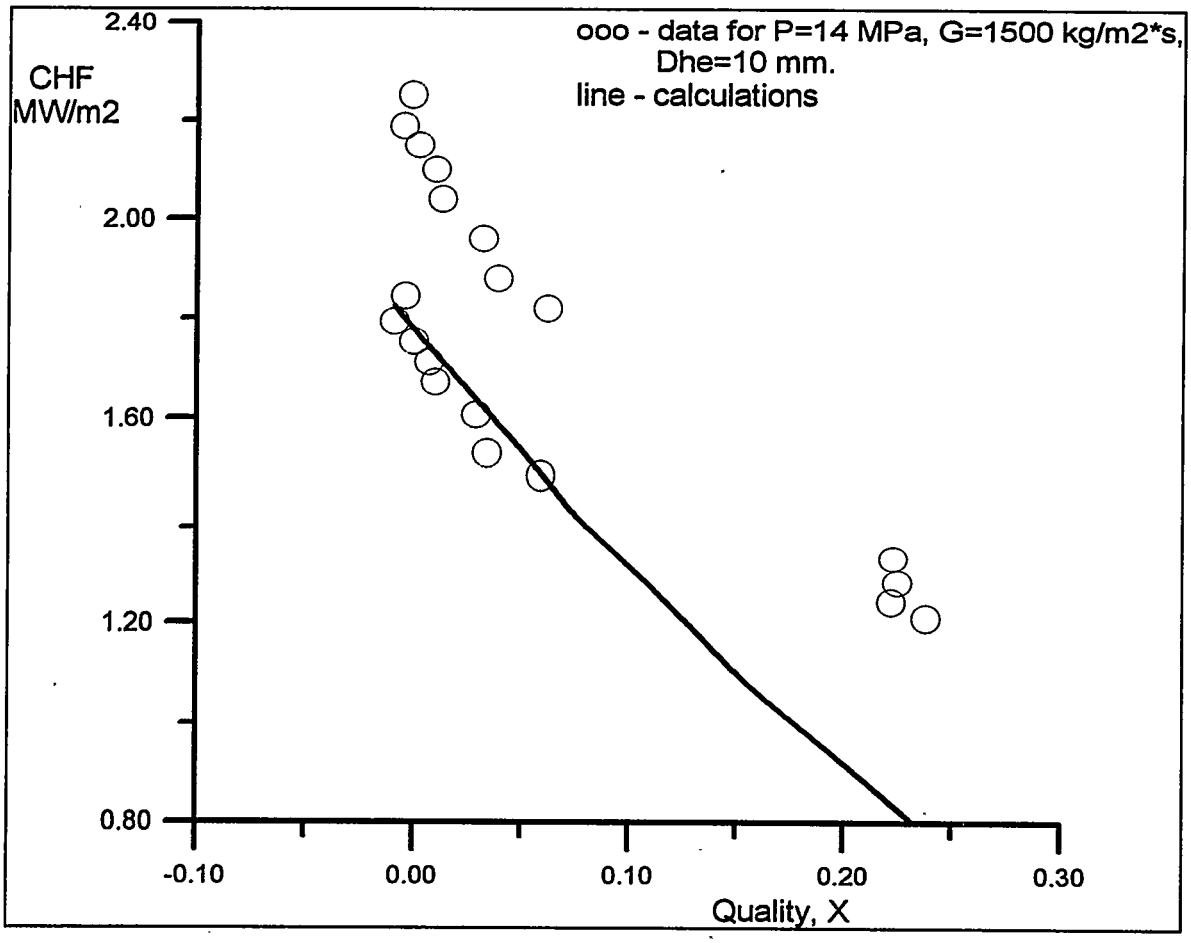

Fig.7. The data versus calculation, CHF in rod bundles. One can see two different data sets.

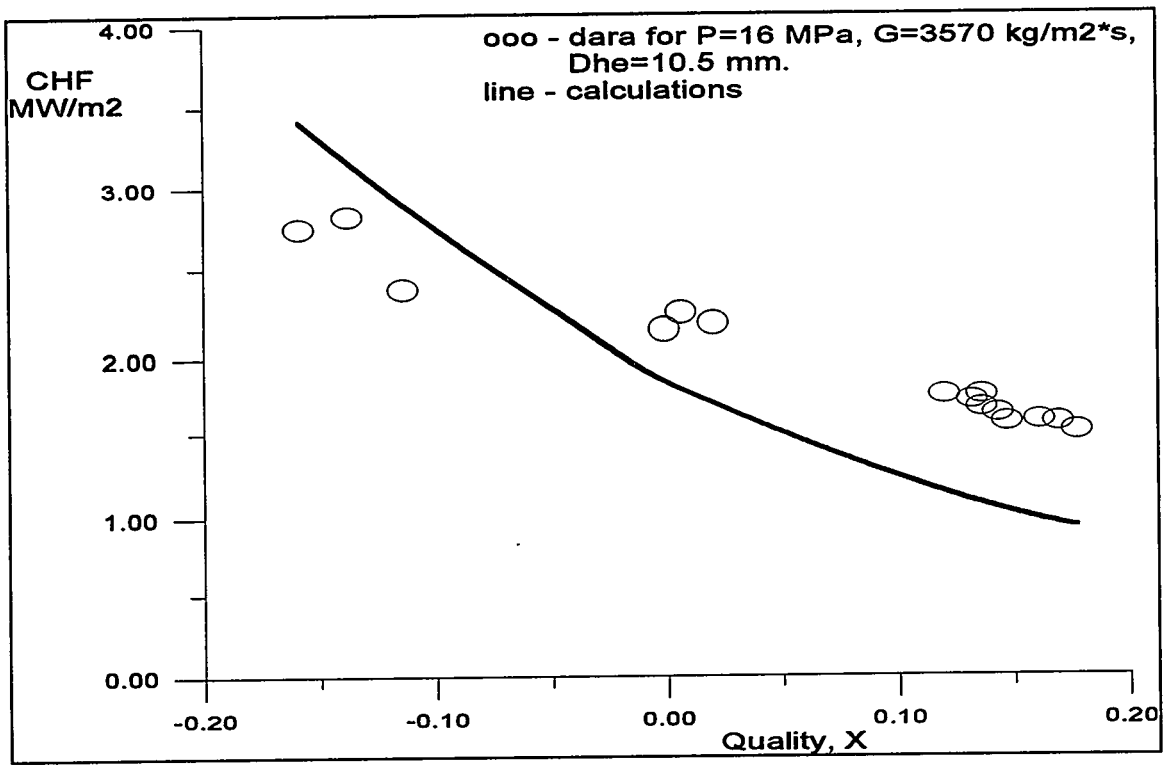

Fig.8 The data versus calculation, CHF in rod bundles.

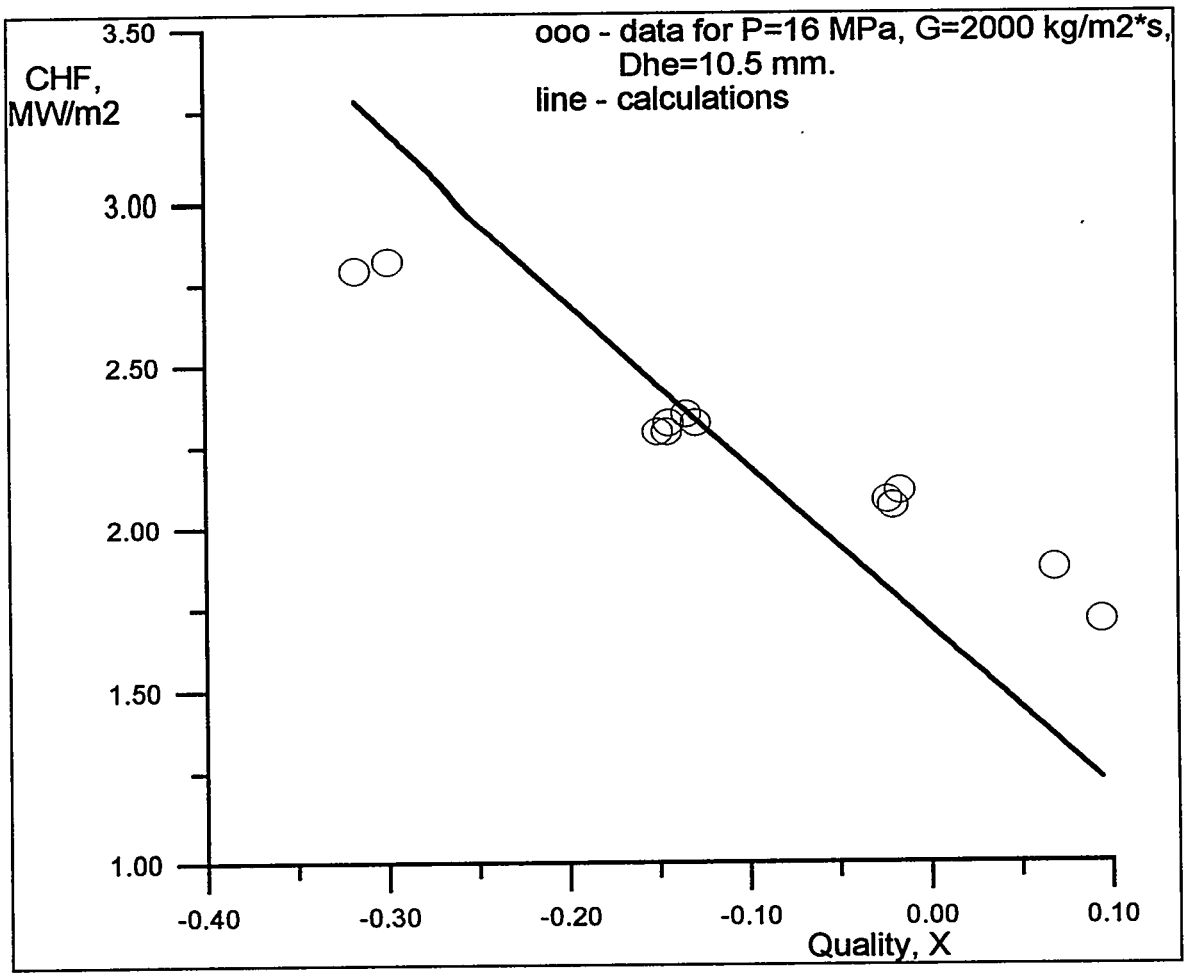

Fig.9. The data versus calculation, CHF in rod bundles.

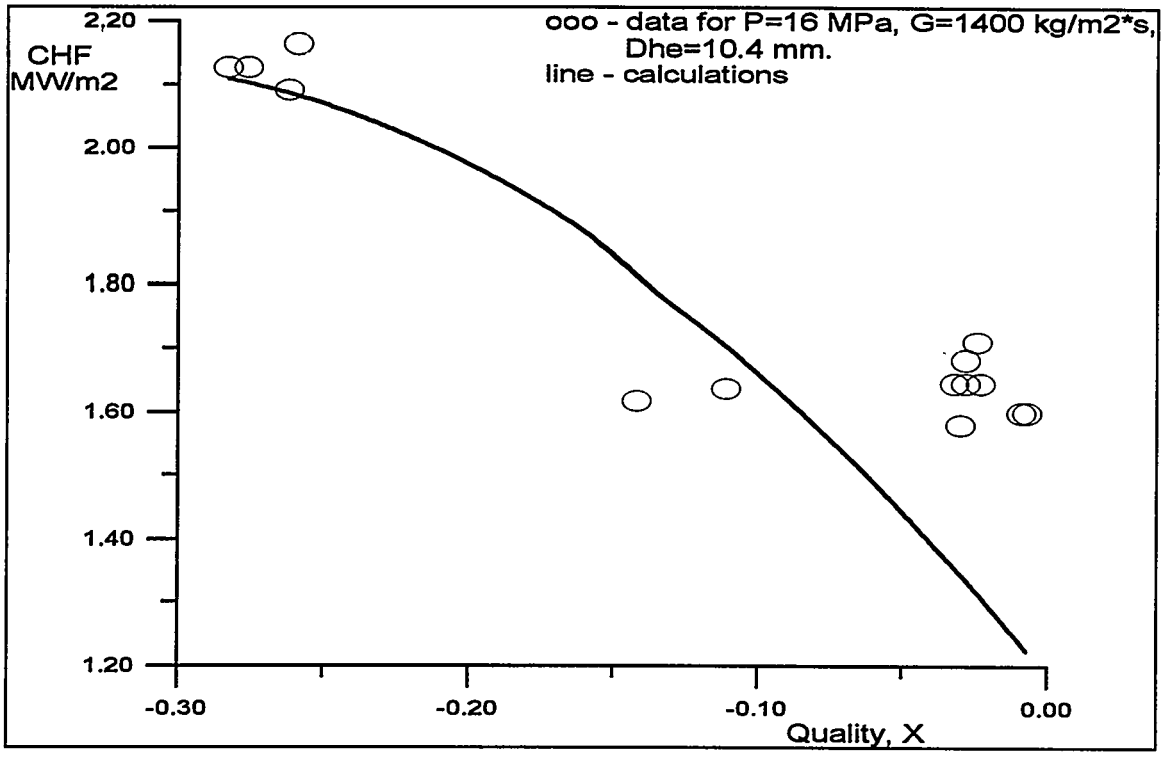

Fig.10 The data versus calcularion, CHF in rod bundles

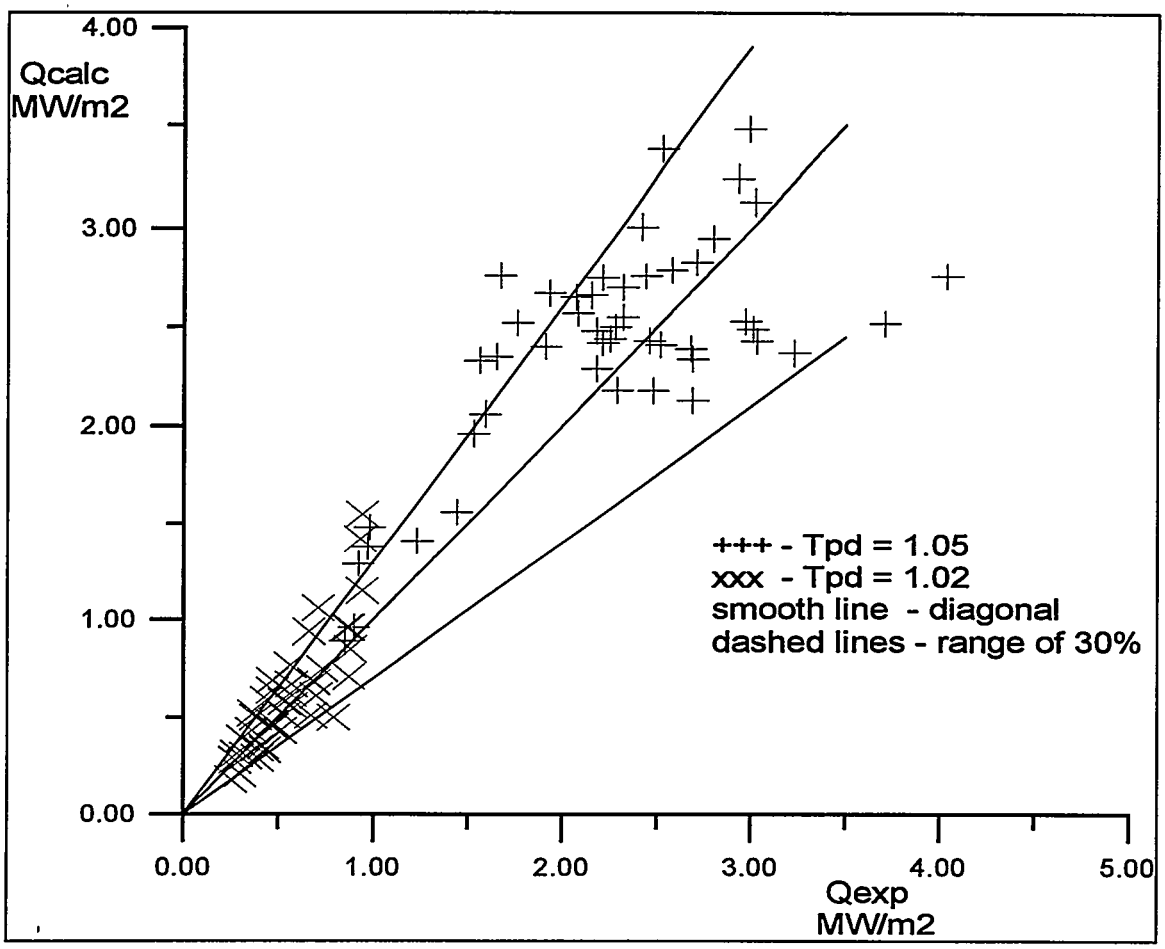

Fig.11 Data versus calculation, CHF in tighted rod bundles.

ON THE LOOK-UP TABLES FOR THE CRITICAL HEAT FLUX IN TUBES (HISTORY AND PROBLEMS).

P.L.Kirillov, I.P.Smogalev.
National Research Center, Institute of Physics and Power Engineering (IPPE), Thermophysical Department

249020 Obninsk, Kaluga Region, Russia
Fax: 7(095)230 2326, 883 3112

Abstract.

The complication of critical heat flux (CHF) problem for boiling in channels is caused by the large number of variable factors and the variety of two-phase flows. The existence of several hundreds of correlations for the prediction of CHF demonstrates the unsatisfactory state of this problem. The phenomenological CHF models can provide only the qualitative predictions of CHF primarily in annular-dispersed flow.

The CHF look-up tables covered the results of numerous experiments received more recognition in the last 15 years. These tables are based on the statistical averaging of CHF values for each range of pressure, mass flux and quality. The CHF values for regions, where no experimental data is available, are obtained by extrapolation.

The correction of these tables to account for the diameter effect is a complicated problem.There are ranges of conditions where the simple correlations cannot produce the reliable results. Therefore, diameter effect on CHF needs additional study.

The modification of look-up table data for CHF in tubes to predict CHF in rod bundles must include a method which to take into account the nonuniformity of quality in a rod bundle cross section.

1. Outline of history of CHF look-up tables derivation and relevant publications up to 1989

The idea of derivation of CHF look-up tables was first proposed by Doroschuk V.E. whose publications initiated this study [1,2]. The first version of look-up table then available was based on a relatively small experimental data base and a number of subjective approaches in the form of quality function of CHF. The Section of Heat and Mass Transfer of the USSR Academy of Science has formed a commission to generate new recomendations. The activity of this commission was based on the method of expert evaluations presented by four research organizations such as VTI+, IVTAN#, RDIPE*, IPPE. As a result the edition of "Recomendations for Prediction of CHF" [3] and the publication in the journal [4] have been performed. The procedure to calculate CHF values formulated in terms of an approximated correlations and based on the CHF look-up table of Smolin et al. was published [5]. Doroschuk et al. have reported the new look-up tables [6]. The next version of look-up tables derived by the experts of the commission was published in the paper of the IVTAN [7]. They have been distributed as "The Tables of the USSR Academy of Science".

However, there were disagreements between the data from the look-up table of the commission [4] and the data from the look-up table in [6]. Therefore, initiated by the IPPE a series of control experiments to elucidate the cause of these differences was carried out during 1981-1983. Nine organizations in Russia were invited to accomplish these experiments. But not all organizations have taken part in this study. Besides, the others have not completely carried it out.

+ VTI - All-Russian Thermotechnical Institute (Moscow)

IVTAN - Institute of High Temperatures, Academy of Science, Russian Federation (Moscow)

* RDIPE - Research & Design Institute of Power Engineering(Moscow)

In each organization the experiments were carried out using their own procedure and test facilities, but on the same 12x2 mm tube under the agreed range of conditions: P=7,10,14, 18 MPa; G=0.5, 1, 2, 4 Mg/(m^2s); L=1, 3, 6 m. The results of their control experiments have shown that the data of four organisations presented in q_{cr} versus x_{cr} coordinates practically agreed. The data of ITTF++ and KPI** were lower.The data of VTI were a much higher. There is a brief publication about this control experiment - Ref.[8]. The possible reason of data disagreements may be caused by the difference in the"hydraulic stiffness" of circulation loops. The hydraulic stability of flow (the degree of "hydraulic stiffness") is dependent on the flow throtting value in front of an inlet. When the flow throtting is absent at the boiling initiation ("soft" conditions), then the oscillations of flow rate, pressure, coolant temperature in a loop occur due to reverse flow rate.

Unfortunately, no CHF measurements have been conducted using the available test rigs neither at that time, nor at present. In 1980 the Heat and Mass Transfer Information Center(HEMATIC) was founded at the IPPE. Among other problems, the problems of derivation of up-to-date CHF look-up tables has been set before the HEMATIC. At the same time the related study was fulfilled at the Chalk River Laboratory, Canada. In 1986 Groeneveld et al. [9] published the first version of look-up tables used in computer codes such as RELAP 5/Mod.3, CATHARE and others. The procedure used in this study was based on the formalized matrix approach to statistical elimination of experimental data through the three dimensional space with parametric directions P-G-X_{cr}. During the data estimation the values which overcome more than 50% the average mean have been excluded. For G -> 0 the results of prediction of CHF under pool boiling were used. And for X_{cr}-> 1 the CHF value is taken equal to zero. However, these extrapolations were

++ ITTF - Institute of Technical Thermophysics (Kiev)

** KPI - Kiev Polytechnical Institute

not proved.The CHF look-up tables with slight corrections were published in Ref.[10].

2. Improvement of CHF look-up tables.

The IPPE CHF data bank (see Table 1) covers the results of all known publications, the RDIPE data base, the Chalk River data base and a number of other data.The four approaches used to develop the CHF look-up tables on the base of this data bank were as follows:

- The separation of the range of quality (P=const, G=const) into regions corresponding different two-phase flow patterns and the description of each region by polynomial function [11];
- The analysis of the available look-up tables to determine the form of function and to calculate the optimal values of exponents of the polynomial expressed as [12]:

$$q_{cr} = \mathrm{Sum}(a_i \cdot P_i^n \cdot X_{cr,i}^k \cdot G_i^m)$$

- The regression analysis procedure based on the division of the data array for P and G into two zones and on the description of each zone with a following relationship:

$$q_{cr} = K_r \cdot (X_i - X_{cr}) / X_i$$

Where K_r and X_i are the functions of P and G ;

- The model which takes into account the initiation of intensive quality growth or void fraction.

Furthermore, when the differences between the result of above evaluations were within 15%, the data of these four approaches were averaged with equal weight. If there were disagreements between the results, the data of other CHF look-up tables [7,10] were used and then the averaging of all these values were performed. The results of research were published in 1989 [13,14]. In the following years further improvement of CHF look-up tables took place [15,16].

The availability in the literature of two or more CHF

look-up tables raises the question of agreement among them and the production of an unified reference data. Such study was started in 1993 by the specialists of Russia, Canada and Germany [17,18]. To date (1994), the project of CHF look-up tables has taken into account the different approaches and aimed to evaluate data and to eliminate disagreement between different versions of CHF look-up tables. The final results of study can be summarized as follows:

1. The additional amount of data in the regions where they are already sufficient data does not improve the accuracy (see Table 1).

2. There are limited data in the regions of low mass fluxes, low pressures and X < 0. It should be pointed out that the use of only three parameters (P, G, X) is insufficient to generate a CHF look-up table for these regions. The inaccuracies in these regions were still considerable.Most data were collected in small diameter and short heated length where the effect of diameter and length on CHF is strong. Although the use of pressure, mass flux and dryout quality as parameters may not be sufficient to characterize CHF at subcooled conditions, they are also the primary parameters used in the bubble-crowding or vapor-blanketing type of subcooled burnout models and seems to provide good prediction accuracy.

3. The diameter effect on the CHF values is not yet well clarified. It is not clear whether the use of complex correlations provides a better agreement between the data for different diameters.

4.In perspective, it is possible to develop CHF look-up tables using a dimensionless criterion. A dimensionless CHF look-up table has been derived by Groeneveld and his co-worker for non-aqueous fluid.

3. Effect of some factors on CHF.

3.1. Effect of tube diameter on CHF.

The diameter effect on CHF has been studied by many researchers over almost 30 years. However, to date the

contradictions were not eliminated. In deriving the look-up table a correction factor for CHF based on the diameter ratio to the some power has been used:

$$q_{cr}\ (\ d\ )\ /\ q_{cr}(8) = (\ d\ /\ 8\ )^{n} \qquad (1)$$

Doroschuk et al. [16] suggested a value of -1/2 for the exponent. Groeneveld et al. [9] pointed out that different researchers recommended an exponent within the range (-1/10) ÷ (-1/2). An exponent value of -1/3 for d = (2 ÷ 16)mm has been used in the first version of the look-up table. A correction factor equal to 0.79 was acceppted for d > 16mm. Similar values were also recommended by Smith [42] suggested the exponent: -1/3 for d < 32mm and 0.63 for d >32mm. In the last version of the look-up table [18] an exponent of -1/2 has been used and for d > 25 mm the correction factor 0.6 was accepted. It is noted that for d < 8 mm the diameter effect is better described with the above law with n=1/3 (see Fig.1).

Becker and Soderquist [19] suggested the diameter correction factor given in tabular form (see Table 2). These values disagree with other data.

The complex correlations were suggested by Muller-Menzel and Zeggel [20], and also by the IPPE [21]. In practical calculations their application presents difficulties. Moreover, the physical nature of these correlations remains to be understood. Besides, the above suggestions disagree with each other (see Figs.2,3).

An effort to analyse the diameter effect on CHF was performed by Bethke [22], but there are no conclusions.

Boltenko and Pomet'ko [23] observed that increasing the diameter increases the CHF at nucleate boiling and the reverse situation occures at the annular-dispersed flow conditions for freon (see Fig.4a). The same results were also observed for water(see Figs.4b and 4c) at high pressures. The following has been proposed to explain these trends:

"At nucleate boiling an increase of diameter enhances the mass exchange between the flow core and the two-phase layer

near the wall. Consequently, the bubble removal is enhanced which, in turn, increases q_{cr}."

In an annular-dispersed flow the fraction of the liquid in the flow core increases with increasing diameter and causes a decrease in q_{cr}. This observation is qualitatively confirmed by the "entraintment curve" [24] given in Fig.5 as well as by the measurements carried out by other researchers [25,26]. The similar results were obtained by Celata et al. [4] at high mass flux.

Erbacher et al. [26] pointed out that the exponent in the equation (1) depends on the quality. Although the numerical values of n obtained (see Fig.6) in the recent investigations [11, 23, 27] were different the dependence of the exponent on the quality seemed to be similar.

To clearly establish the quality effect on $q_{cr}(d)/q_{cr}(8)= = f(d)$, we compared the data obtained by different authors specified in Table 4 on freon and water. A typical example of such comparison is shown in Fig.7. Unfortunately, there is no sufficient amount of data for the large diameters and $X \leq 0$.

Since in Fig.7 the data for different pressures and mass fluxes have been used, it has only an illustrative character and demonstrates the complex character of the diameter effect. The results of the investigations for which deviations from the equation (1) are observed are shown in Figs.8(a -d).

The question is then: why does the simple power dependence given in the equation (1) provide reasonable results in deriving the look-up tables. The fact is that the most data used to develop the look-up tables were obtained for quality $X > 0$ and the contribution of data obtained for $X < 0$ is small. This argument is supported by Fig.9 reproduced from [18].

The look-up tables provide the best results when the geometrical characteristics of channel and the flow parameters are located in the center of the "points galaxy"; when they are brought to the periphery of the "galaxy", the accuracy decreases. This concerns, especially, subcooled water, small diameter tubes, low pressures and low mass

fluxes. It is not apparently the only reason of deviations from the equation (1) as indicated by Figs. 8c, 8d.

Despite the data scattering for the dependence of q_{cr} on "d", one can draw the following qualitative conclusions:

1. For high qualities X>>0, pressures and mass fluxes, q_{cr} decreases with increasing diameter according to the equation (1).

2. For X<0, the diameter effect on q_{cr} is more complex. The dependence of q_{cr} on "d" can be directly or inversly proportional. The experimental data sets for water do not agree. There is a direct effect of diameter for long tubes (l>1m). Celata [41] observed an inverse effect of diameter for short tubes (l≤0.1m) which is consistent with the equation (1). The data for freon are also ambiguous. The experiments of Erbacher [27] have shown an inverse effect of diameter at high pressure (2.3-3 MPa). The results of Boltenko [21] for a pressure of 1.08 MPa have shown a direct effect of diameter. The qualitative character of the dependence of q_{cr} on "d" as confirmed by the experiments (see Figs.8(a-d)) is shown in Fig.10.

3. It should be supposed that the current conditions and the structure of two-phase flow have an effect on the function $q_{cr}(d)$. The refinement of the equation (1) should be carried out by conducting systematic researches.

3.2. Gas content effect.

The use of gas pressurizers in NPP experiments results in the saturation of the water by gas due to a contact between them. As the water temperature increases, the gas solubility decreases. Therefore, the gas liberation and accumulation in the flow near heat transfer surfaces can initiate an early CHF.

The investigations dealing with the determination of effect of gas content in water on heat transfer and CHF are rare, and the results presented are contradictory. Subbotin et al. [31] have not found a variation in the CHF value for nitrogen content in water of 1500 ncm^3/kg under subcooled boiling

conditions. However, approximately with the same parameters Fisenko et al. [32] have observed the q_{cr} reduction by 10% under subcooling conditions; under saturated conditions and with gas content of 3500 ncm^3 /kg they established that the q_{cr} decreases by 30%. The similar effect was also observed by Bertoletti [33].

In order to establish the causes of data disagreement, the verification experiments were carried out by Lozhkin et al. in the IPPE [34] and Smolin in the RDIPE [35]. Different techniques of gas dissolution in water and various sampling methods were tested. The gas distribution over the tube cross-section was determined by using an isokinetic probe.

For qualities > 0, pressures between 10 and 18 MPa, mass fluxes between 1000 and 3700 kg/(m^2s) and gas concentrations up to 4100 ncm^3 /kg, the CHF was not found to be reduced within the experimental accuracy (Table 3).

In the region of subcooled water, within the same range of parameters and gas concentrations above 2000 ncm^3/kg, a reduction in the CHF has been observed up to 20% at c = 4100 ncm^3/kg) (Fig.11,12).

These results were confirmed by the gas content variation measurements in a liquid film flowing along the wall. For X<0, the gas content in the liquid layers near to the wall corresponds to the mean content of the flow. For X>0, the film turns out to be completely degassed.

4. Application of data of look-up tables for prediction of CHF in rod bunles.

With the advent of look-up tables for the prediction of CHF in uniformly heated tubes, their use in the computer codes, instead of rod bundles correlations, is recommended. One of the reasons is that the look-up tables are based on a wider range of parameters as compared with the correlations. These tables are also important for calculations under transient and abnormal operating conditions.

The first step in this direction was made by Groeneveld

[9,36]. His procedure involves the introduction of eight empirical coefficients to correct the data of look-up tables with respect to the data for rod bundles.

The other approach was reported by Bobkov [37,38], who made an effort to derive universal correlations independent of the geometry of the channel.

Currently, some objections against the use of such approaches have been raised [39]. It is the author's opinion "that since the tubes and rod bundles have different relationships between q_{cr} and G the transition procedure from a tube to a rod bundle could be quite complicated".

This argument can be supported confirm by the data of Smolin [40] (shown in Figs. 13a, 13b). However, such a direct comparison is not right because the experiments with rod bundles were carried out with few rods only 7 and 19. It should be believed that the use of the function q_{cr} (X_{avr}) for a such small number of rods is incorrect.

For a small number of rods the average quality in a bundle is considerably less than the local quality where the crisis takes place. Therefore, it is incorrect to perform the direct comparison between the results of experiments in tubes and rod bundles in forms of similar average parameters.

It is more adequate to make the comparison using the coordinate transform:

$$X_{cr,b} = X_{cr,t} - a(P,G)$$
$$q_{cr,b} = q_{cr,t} - b(P,G)$$

Where $X_{cr,t}$; $q_{cr,t}$ - for tubes,

$X_{cr,b}$; $q_{cr,b}$ - for bundles.

Figure 14 illustrates as the data on diagrams Figs. 13a, 13b agree better in this specific case. Only under these conditions (the given bundle and the pressure 7.4-7.8 MPa) there are a=0,23G and b=1,55-0,7G, where G in $Mg/(m^2 \cdot s)$; q_{cr} in MW/m^2.

5. Conclusions.

The results of study could be summarized as follows:

1. The additional amount of data in the regions where they are already sufficient data does not lead to an improvement of the look-up table accuracy (see Table 4).
2. There is a lack of data for low mass fluxes, low pressures, high qualities and, especially, in the subcooled boiling region. In this region the use of only three parameters (P,G,X) to develop the look-up table does not seem to be sufficient. The inaccuraccies in these regions are still considerable.
3. The diameter effect for qualities X>0 may be represented by the law: $q_{cr} \cdot d^n = const$, where n=0,5.

For X<0, low pressures and low mass fluxes, the dependence of q_{cr} on "d" is more complex and no relationship has been obtained. There is a need to perform systematic researches in the shaded regions shown in Fig.9.

4. It is possible to use the data of look-up tables for the prediction of CHF in rod bundles if the rules of data correction are refined. The determination of generalized correlations for this purpose represents an interesting avenue for further development.

Acknowlegements.

This research was carried out due to the support of the Ministry of Science of the Russian Federation, the contract 6356.5. The authors are thankful for this support.

Table 1.

DATA BANK THERMOPHYSICAL CENTER IPPE

(D-inner diameter, Dt-heated diameter, Del- gap size annuli, L-length, P-pressure, G-mass flux).

Form channel	Geometry		Parameters		No.of Data
	D,mm	L,mm	P,MPa	G,Mg/m² s	
Tubes, uniform heated	0.1-44.7	2-20000	0.1-21	0.01-90	27825
Tubes, nonuniform heated	6-22	100-6000	0.28-20.6	0.25-9.97	8330
Annuli, uniform heated	Del 0.5-11.1	40-2740	0.45-20.6	0.05-8.4	13000
Rectangle, uniform heated	Dt 8.3	200	6-15	0.6-3.5	47
Triangle, uniform heated	Dt 4.8	200	6-17	0.5-3.6	40
Rod bundle, uniform and nonuniform heated	S/D= =1.01-2.22 D=5-19		0.28-19.6	0.02-7.48	24227

Table 2.

Correction Factors for Diameter Effect on CHF [19].

d, mm	3.930	6.010	7.85	10	13.06	17.49	19.93	24.95	36.0
$q_{cr}(d)/q_{cr}(10)$	1.176	1.193	1.11	1	0.965	0.941	0.926	0.905	0.915

Table 3.

CHF in tube D=9 mm, by different content of gas dissolution in water.

G, kg/(m^{2}s)	P, MPa	C, ncm^3/kg	q_{cr}, MW/m^2	X_{cr}
1000	10	53	2.21	0.404
		1350	2.17	0.792
	14	590	1.81	0.226
		1350	1.84	0.218
	18	53	1.78	0.079
		1350	1.71	0.074
2000	10	53	2.53	0.145
		1350	2.52	0.146
	14	127	2.27	0.002
		1470	2.25	0.002
	18	95	2.33	-0.190
		1440	2.37	-0.184
3000	10	29	2.81	0.069
		1510	2.93	0.068
	14	29	3.18	-0.025
		750	3.10	-0.039
	18	29	3.44	-0.170
		1630	3.38	-0.180

Table 4.

ASSESSMENT OF VARIOUS CHF TABLE (From [17]).

Table	Ref.	No of Data	Error %	
			Avg.	Rms.
Doroschuk et.al. Table 1993	6	3705 3741	-3.00 -1.18	12.27 4.42
Recommendation Table 1993	7	4901 4926	10.56 -1.32	9.78 4.61
Groeneveld et.al. Table 1993	9	21710 21724	1.54 1.01	8.07 7.44
Kirillov et.al. Table 1993	13	12129 12131	2.32 0.81	9.97 7.14
Kirillov et.al. Table 1993	15	13300 13259	0.67 1.14	8.76 7.59
Kirillov et.al. Table 1993	16	16900 16881	1.53 1.17	9.49 7.68

References.

[1] V.E.Doroshuk. " CHF in Tubes", Thesis (1966), (R)*.

[2] V.E.Doroshuk." CHF in Boiling Water in Tubes", Energia, Moscow (1970), (R).

[3] Recommendation. "On CHF in Tubes", 1-ed., Akad. Nauk USSR, Moscow (1975), (R).

[4] Recommendation. "Tabular Data for Calculating Burnout Boiling Water in Uniforming Heated Round Tubes(Standard)", Teploenergetika (9) 90-92 (1976), (R).

[5] V.N.Smolin, S.V.Shpansky, V.I.Esikov, T.K.Sedova "Method of CHF Calculation in Tubes at Water and Steam-water Mixtures Cooling", Teploenergetika (12) 30-35 (1977), (R).

[6] V.E.Doroschuk, L.L.Levitan, F.P.Lantsman "Recommendtions for Calculating Burnout in Round Tubes", Teploenergetika (12) 66-70 (1975), (R); ASME-Paper 75-WA/HT-22 (1975).

[7] Recommendation. "On CHF in Tubes", 2-ed., Preprint IVTAN-1-57, Akad. Nauk USSR, Moscow (1980), (R).

[8] P.L.Kirillov, O.L.Peskov, N.P.Serdun " Bench-mark Experiment on Burnout with Water Flowing in Tubes", Atomnaia energia 57(6) 422-423 (1984), (R).

[9] D.C.Groeneveld, S.C.Cheng, T.Doan "1986 AECL-UO Critical Heat Flux Look-Up Table", Heat Transfer Eng. 7(1-2) 46-62 (1986).

[10] D.C.Groeneveld, L.K.H.Leung "Tabular Approach for Predicting CHF and Post-dryout Heat Transfer", Proc. NURETH-4 Topical Meeting, 1, 109-114 (1989).

[11] E.A.Boltenko, I.B.Katan, O.A.Ziatnina "The Method of CHF Calculation in Tubes at Uniformly Heat Flux Distribution", Preprint FEI-2037 (1989), (R).

[12] P.L.Kirillov, V.P.Bobkov, V.N.Vinogradov, A.A.Ivashkevich, O.L.Peskov, I.P.Smogalev "The Recommendation on CHF in Tubes", Atomnaia energia 59, 3-8 (1985),(R).

* (R) - in Russian

[13] P.L.Kirillov, V.P.Bobkov, E.A.Boltenko, V.N.Vinigradov, A.A.Ivashkevich, I.B.Katan, I.P.Smogalev "The Method of Elaboration Standarg Data CHF in Tubes by Uniform Heat Flux", Preprint FEI-2030 (1989), (R).

[14] P.L.Kirillov, V.P.Bobkov, V.N.Vinogradov, A.A.Ivashkevich, I.P.Smogalev " On Standard CHF Data for Round Tubes", Proc. NURETH-4 Topical Meeting, 1, 103-107 (1989), (R).

[15] P.L.Kirillov, V.P.Bobkov, E.A.Boltenko, V.N.Vinogradov, I.B.Katan, I.P.Smogalev " The Tables of Burnout Heat Flux ", Atomnaia energia 71(1) 18-21 (1991), (R).

[16] P.L.Kirillov, V.P.Bobkov, E.A.Boltenko, V.N.Vinogradov, I.B.Katan, I.P.Smogalev " New CHF Table for Water in Round Tubes", Proc. NURETH-5 Topical Meeting, 2, 511-518 (1992).

[17] D.C.Groeneveld, L.K.H.Leung, P.L.Kirillov, V.P.Bobkov, F.I.Erbacher, W.Zeggel "An Improved Table Look-up Method for Prediction the CHF", Proc. NURETH-6 Topical Meeting 1, 223-230 (1993).

[18] D.C.Groeneveld, L.K.H.Leung, P.L.Kirillov, V.P.Bobkov, I.P.Smogalev, V.N.Vinogradov, X.C.Huang, E.Royer " The 1994 Look-up Table for CHF in Tubes",Nucl.Eng.Des.(in printed).

[19] K.M.Becker, Soderquist.B "Assessment of Round Tube CHF Tables", Paper presented at the European Two-Phase flow Group Meeting, Stockholm, June 1-3(1992)(also KTH-NEL-55).

[20] T.Muller-Menzel, W.Zeggel "CHF in Parameter Range of APWR Cores", Nucl.Eng.Des. 99, 265-273 (1987).

[21] E.A.Boltenko, V.N.Vinogradov, I.B.Katan, R.S.Pometko " Effect of Tube Diameter on CHF at Different Flow Regime", Preprint FEI-1889 (1988), (R).

[22] S.Bethke "Darstellung Kritischer Siederzustande in Stabbundeln", Dissertation, Techn. Univ. Braunschweig (1992).

[23] E.A.Boltenko, R.S.Pometko, I.B.Katan, O.A.Ziatnina "Effect of Tube Diameter on CHF", Proc.Intern.Symposium "Thermophysics-90 - Thermophysical Aspects of VVER Safety ", 2, 400-403 (1991),(R).

[24] M.Jshic, K.Mishima " Droplet Entrainment Correlation in Annular Two-Phase Flow", Int.J.Heat Mass Transfer, 32, (10), 1835-1846 (1989).

[25] V.E.Doroschuk, F.P.Lantsman " Effect of Tube Diameter on CHF", Teploenergetika 8, 73-76 (1963), (R).
[26] L.L.Levitan, F.P.Lantsman, E.I.Dedneva " Influence the Diameter of Tube on CHF at Dryout", Teploenergetika 7, 40-44 (1981), (R).
[27] F.I.Erbacher, X.Cheng, U.Martin, W.Zeggel " CHF in Circular Tubes at High Pressure and High Mass Fluxes", Int. Working Group Meeting on CHF Fundamentals, Braunschweig (1993).
[28] X.Cheng, F.I.Erbacher, E.Staron, W.Zeggel "CHF in Circular Tubes at High Pressure and High Mass Fluxes", Proc. NURETH-5 Topical Meeting 3, 832-838 (1992).
[29] D.C.Groeneveld, D.Blumenroehr, S.C.Cheng, X.Cheng, S.Doerffer, F.I.Erbacher, R.M.Tain, W.Zeggel "CHF Fluid-to Fluid Modeling Studies in Three Laboratories Using Different Modelling Fluids", Proc. NURETH-5, 531-538, Salt Lake City, (1992).
[30] G.P.Celata, M.Cumo, A.Mariani, H.Nariai, F.Inasaka "Influence of Channel Diameter on Subcooled Flow Boiling Burnout at High Heat Fluxes", Int.J.Heat Mass Transfer, 36, (13) 3407-3410 (1993).
[31] V.I.Subbotin, B.A.Zenkevich, O.A.Sudnitsyn, N.D Sergeev, A.A.Ivashkevich, O.L.Peskov "CHF Boiling Water in Tubes", Coll. Papers " Heat Transfer Research to Steam and Boiling Water", Publ. Atomizdat, Moscow (1985), (R).
[32] V.Z.Fisenko, Yu.D.Katkov, A.P.Lastochkin, V.I.Maksimov " Effect Dissolved Gas in Water", Atomnaia energia, 48(5) 327-328 (1980), (R).
[33] S.Bertoletti, G.P.Gaspari, C.Lombardi, G.Peterlongo, M.Silvestri, F.A.Tacconi "Heat Transfer Crisis with Steam-Water Mixtures", Energia Nucleare, 12(3) 121-171 (1965).
[34] V.V.Lozhkin, Yu.A.Smirnov, R.V.Shumsky, Yu.Yu.Stein "Effect Dissolved Gas on CHF", Atomnaia energia, 53(4) 234-237 (1982), (R).
[35] V.N.Smolin, L.G.Ezhova, V.K.Poljakov, R.E.Poljakov "Effect Dissoved Gas on Heat Transfer and CHF", Proc.7th Heat and Mass Transfer Conf. 4(pt1) 63-67, Minsk (1984), (R).

[36] D.C.Groeneveld, K.Joober, D.Doeffer, W.Wong, L.K.H.Leung, S.C.Cheng "The Effect of Fuel Subchannel Geometry on CHF",Proc. NURETH-5 Topical Meating 3, 683-690 (1992).
[37] V.P.Bobkov, N.V.Kozina, V.N.Vinogradov, O.A.Ziatnina "CHF in Channels of Various Geometry", Preprint FEI-2314 (1993),(R).
[38] V.P.Bobkov, N.V.Kozina, V.N.Vinogradov, O.A.Ziatnina "The New Model of Burnout Prediction in Channels of Various Cross Section", Proc. NURETH-7 Topical Meeting (1993).
[39] Yu.M.Zhukov "The Problem Used CHF Look-up Table in Round Tube for Safety Analysis Water Cooled NPP", Atomnaia energia, 77(2) 108-111 (1994), (R).
[40] V.N.Smolin, V.K.Poljakov " The Heat Transfer Enhancement in Rod Bundles", In.Proc. Seminar TF-74, 307-312 (1974),(R).
[41] G.P.Celata, M.Cumo, A.Mariani " Recent Achievements in Subcooled Water DNB at Very High Heat Fluxes", Russia Jour. of Sng. Thermophysics, 4(1) 83-104 (1994).
[42] R. A. Smith "Boiling Inside Tubes: Critical Heat Flux for Upward Flow in Uniformly Heated Tubes", ESDU Data N86032, 1986. (Cit. by AECL Report).

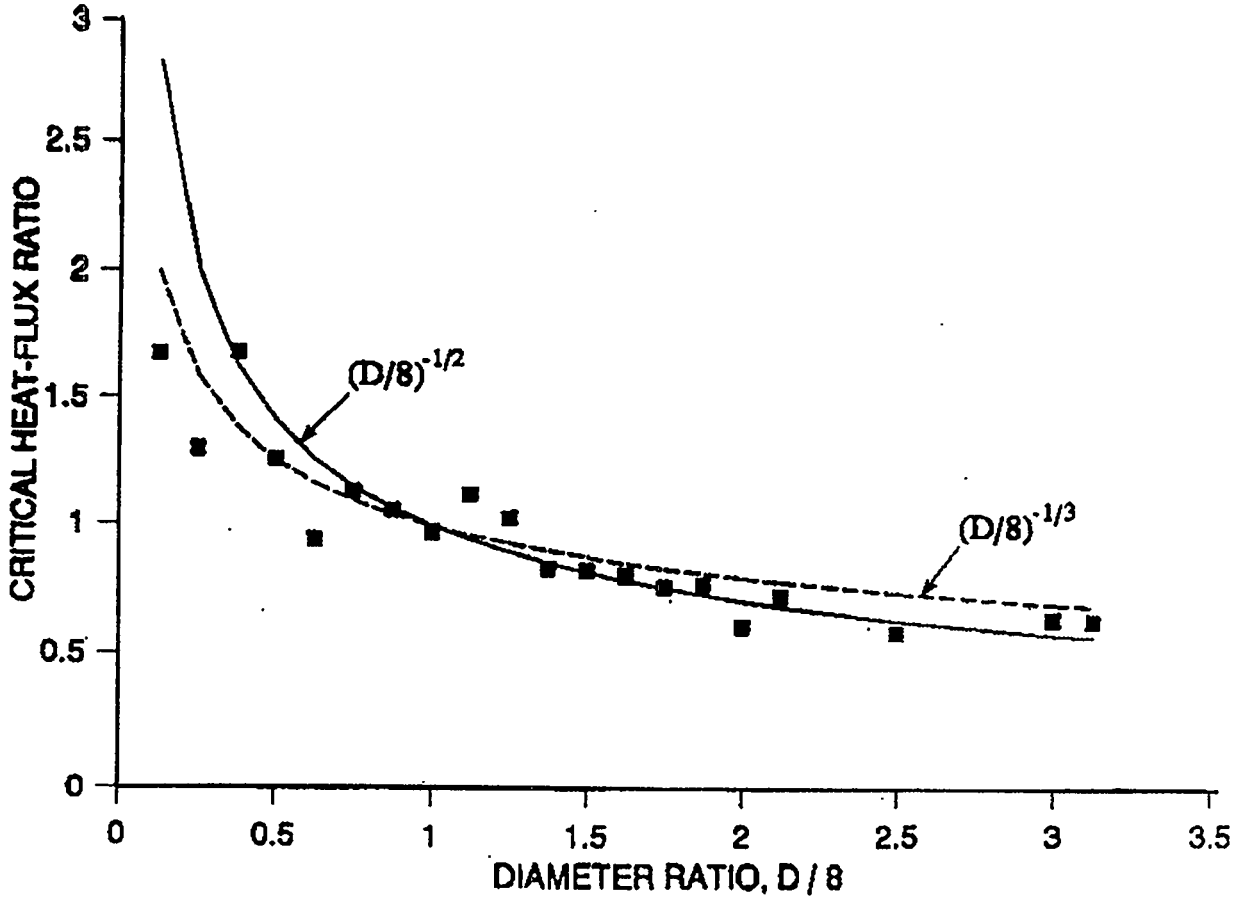

Fig. 1. CHF ratios for tubes of various diameter values.

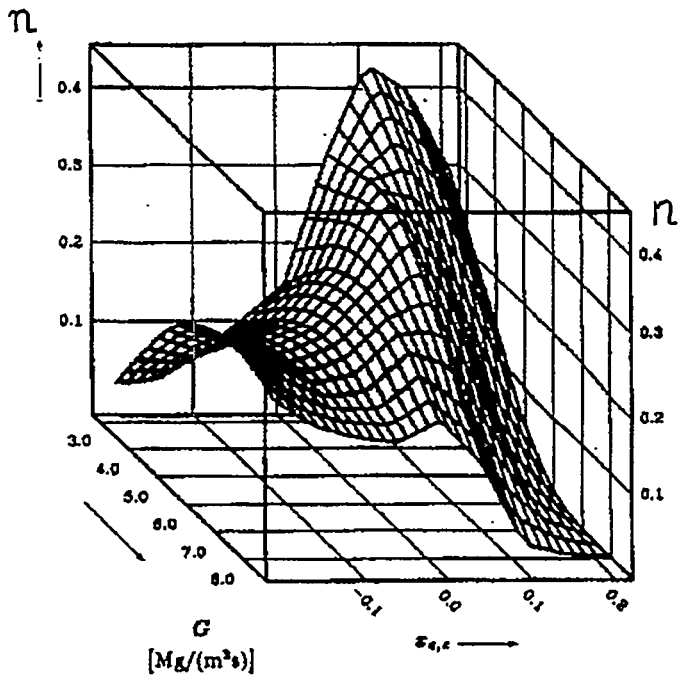

Fig. 2. Exponent "n" as recommended by Muller-Menzel and Zeggel [20] (cit. from [22]).

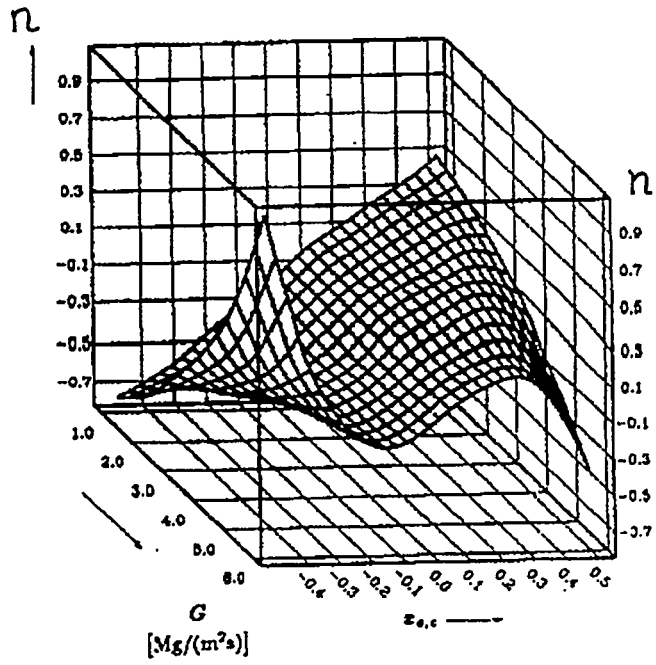

Fig. 3. Exponent "n" as recommended by Boltenko etal. [21, 23] (cit. from [22])

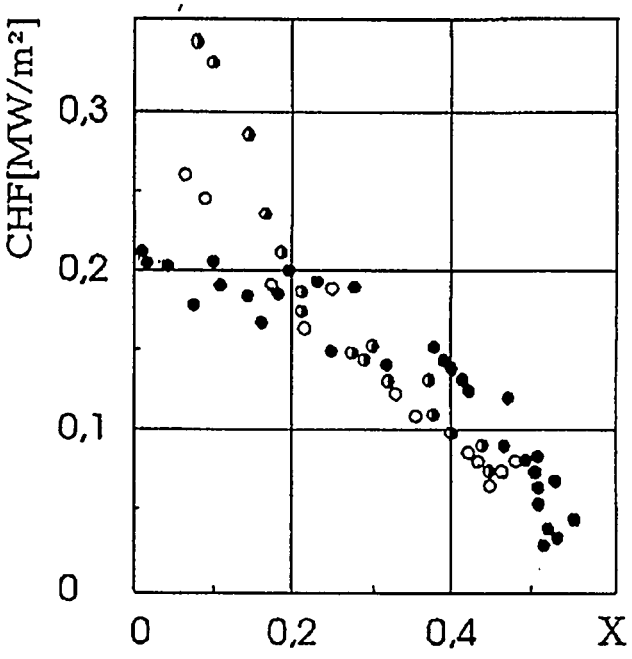

Fig. 4a. CHF by various diameters. Freon-12 [23]. P=1,06 MPa, G=1 Mg/(m^{2}s) d, mm ● - 8, o - 16, ◐ - 20.

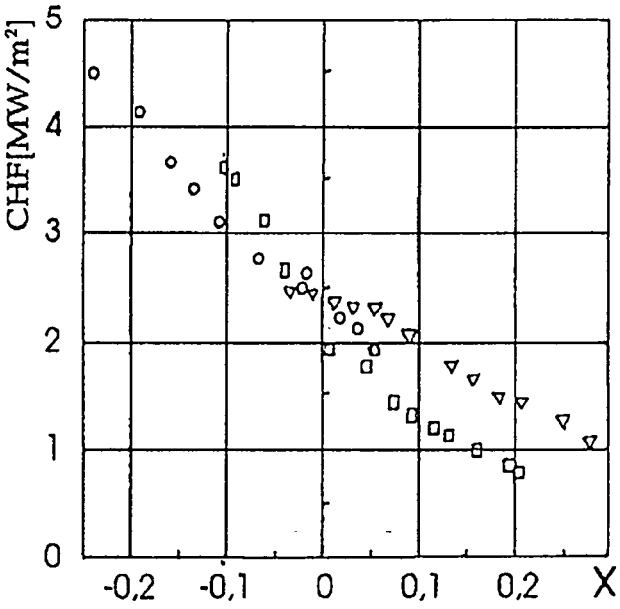

Fig. 4c. CHF by various diameter. Water P=14,71 MPa, G=1,5 Mg/(m^{2}s) d, mm ▽-5,81, o-7,82, □-10,8

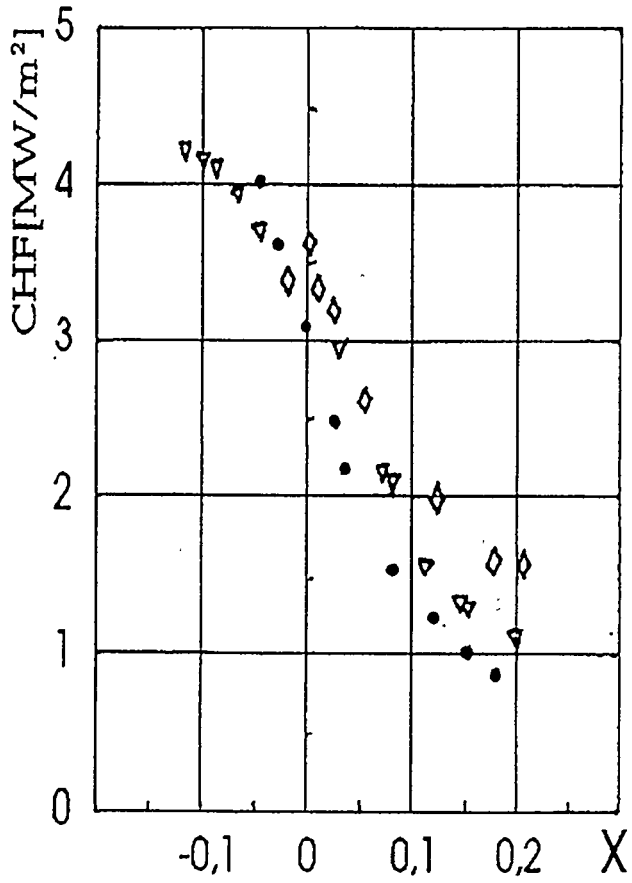

Fig. 4b. CHF by various diameter. Water P=13,72 MPa, G=3,3Mg/(m^{2}s). d, mm ◊-4,75, ▽-5,81, ●-8,05

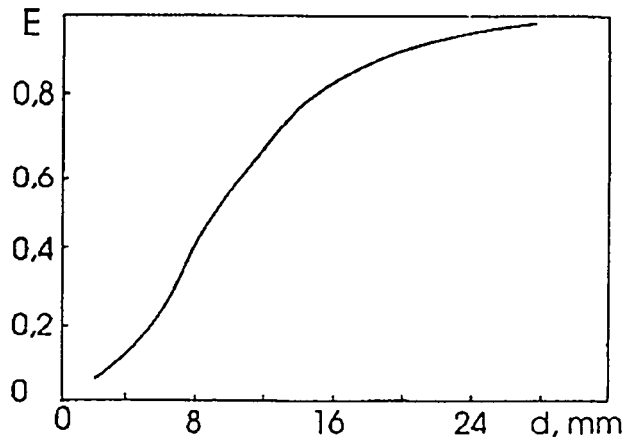

Fig. 5. Entrainment diagram [24] P=1,05 MPa, G=3 Mg/(m^{2}s), x=0,1

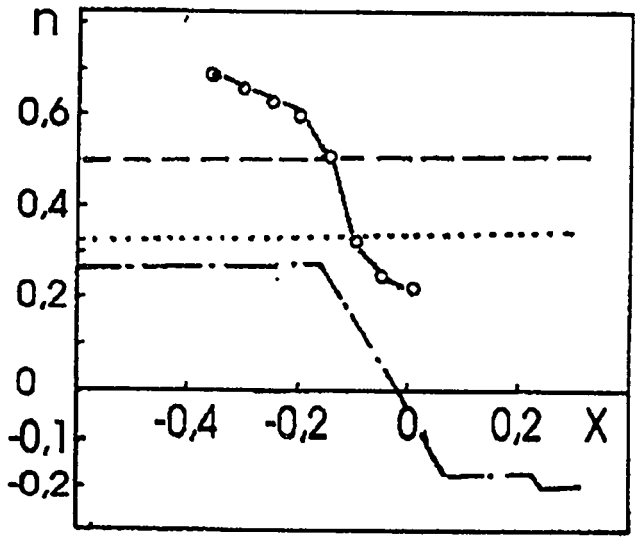

Fig. 6. Exponent "n" as recommended various authors:
—o— Erbacher et al [27] (1993)
— — — Doroschuk et al [6] (1975)
····· Groeneveld et al [18] (1994)
—·— Boltenko et al [11] (1989)

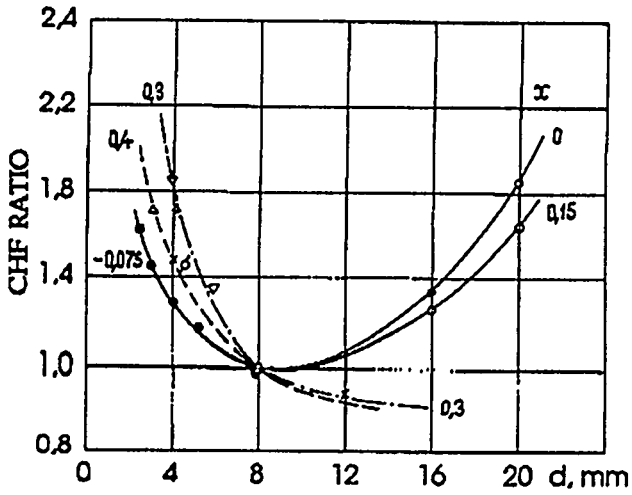

Fig. 7. CHF ratio for tubes of various diameter values.
——— x - o
—•— x - 0,3
— — x - 0,4

Data is used for Fig. 7.

	Author	Ref.	Coolant	P, MPa	G, Mg/m²s	x
o	Boltenko et al.	23	F-12	1,06	1	0; 0,15
×	Cheng et al.	28	F-12	2,3	4	-0,4
⌀	Groeneveld et al.	29	F-12	1,34	2	0,3
Δ	Doroschuk et al.	25	Water	8,0	2,86	0,3
•	Celata et al.	30	Water	0,8	1	-0,075
▽	Levitan et al.	26	Water	9,8	3	0,3

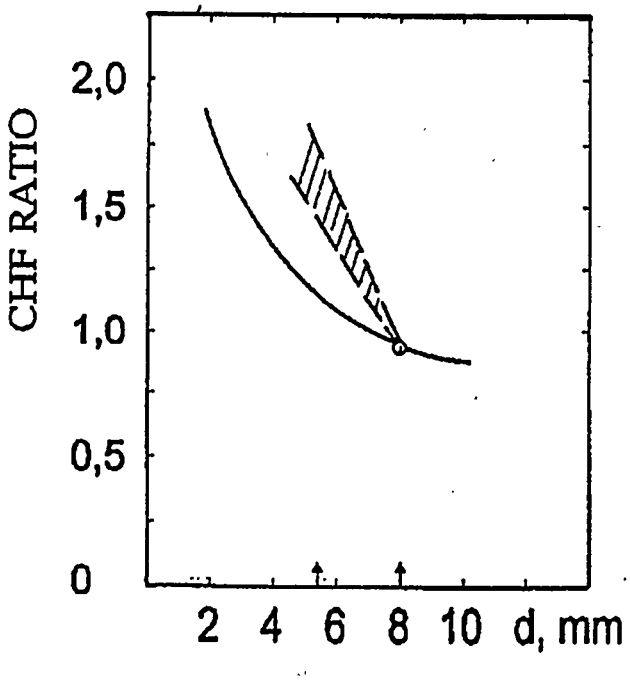

Fig. 8a. CHF ratio for tubes of various diameter values.
F. J. Erbacher [27] F-12, P=2,7 MPa
G=1-6 Mg/(m^{2}s). x=-0,6-0.

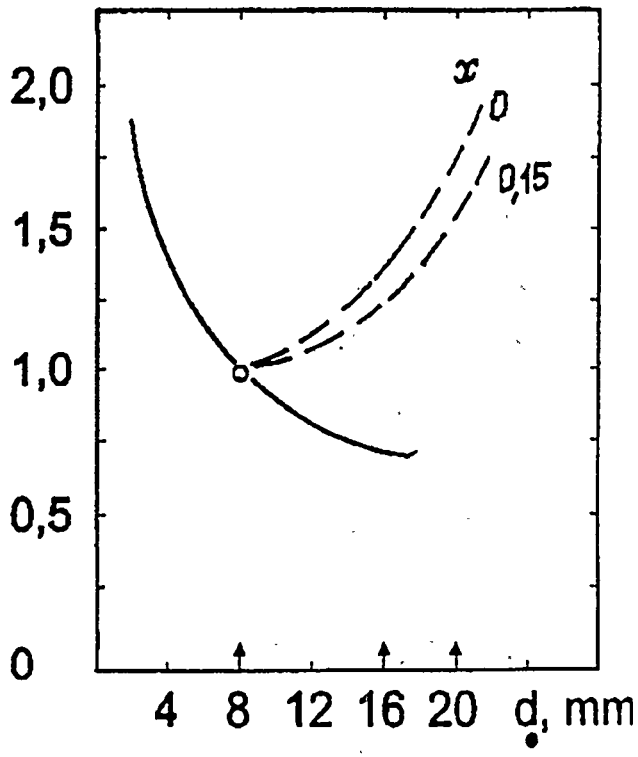

Fig. 8b. CHF ratio. E. A. Boltenko [21, 23]
F-12, P=1,06 MPa, G=1 Mg/(m^{2}s).

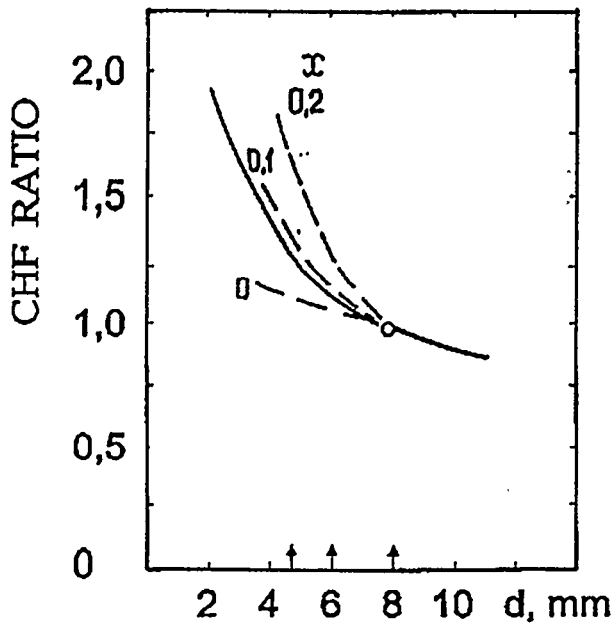

Fig. 8c. CHF ratio. Data bank IPPE,
Water, P=13,72 MPa, G=3,3 Mg/(m^{2}s).

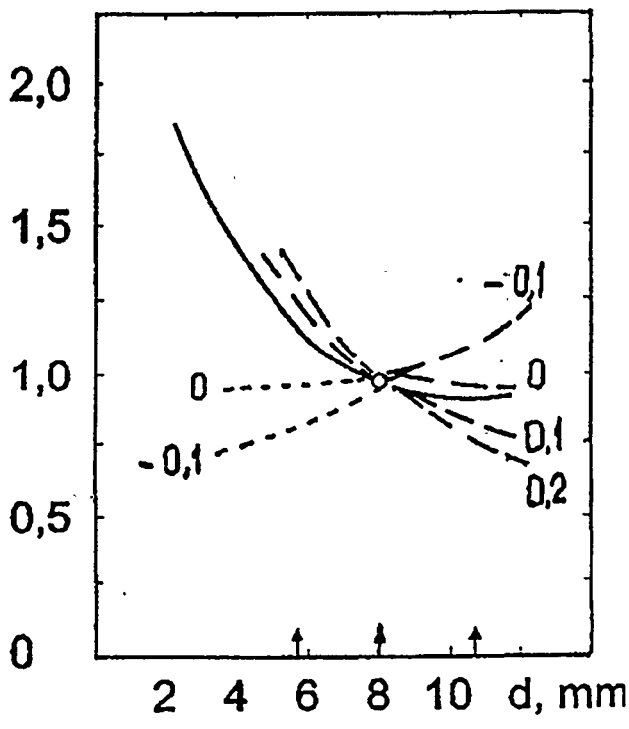

Fig. 8d. CHF ratio. Data bank IPPE
Water, P=14,71 MPa, G=1,5 Mg/(m^{2}s)

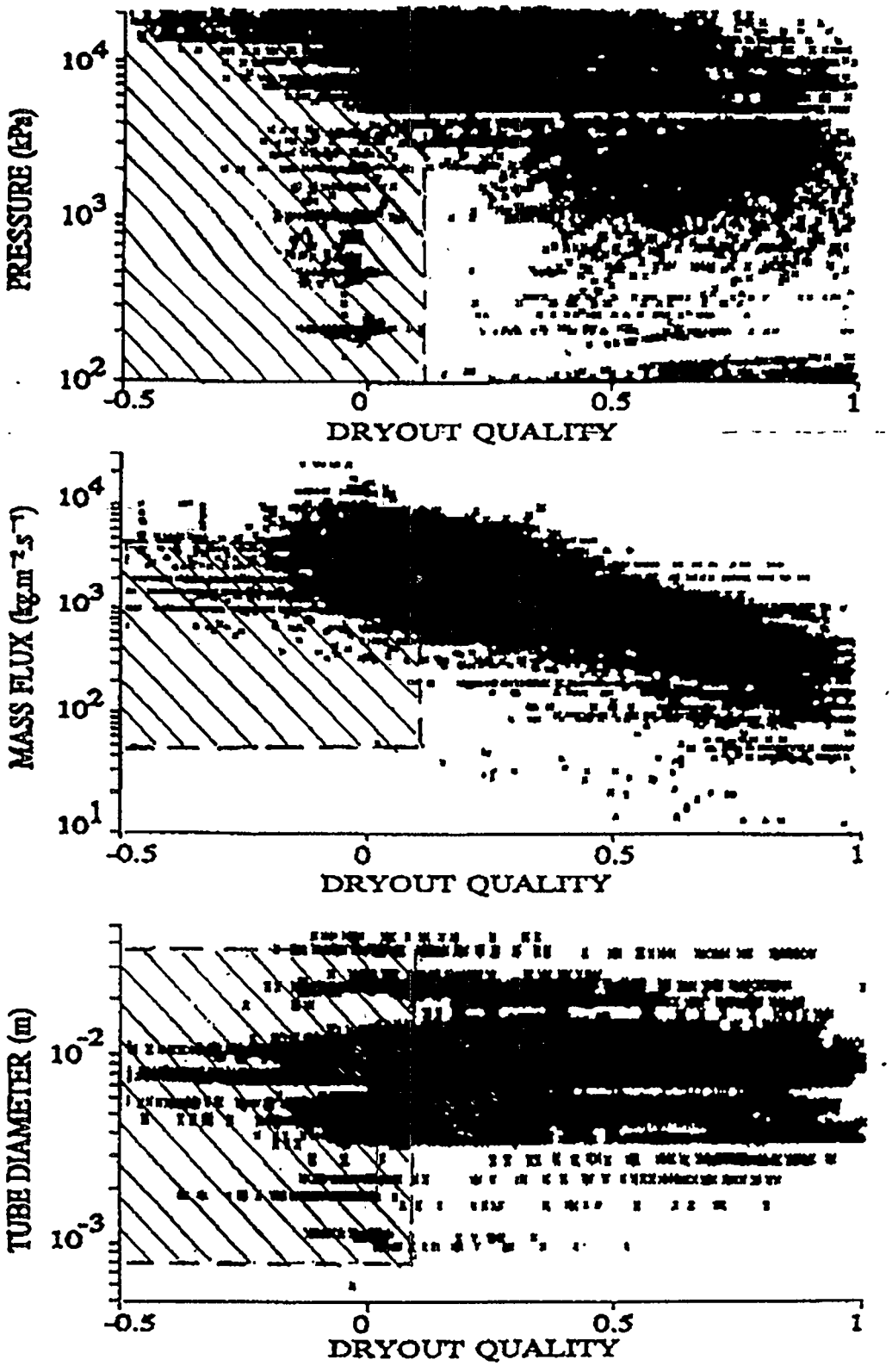

Fig. 9. Range of conditions covered by combined AECL-IPPE world data bank

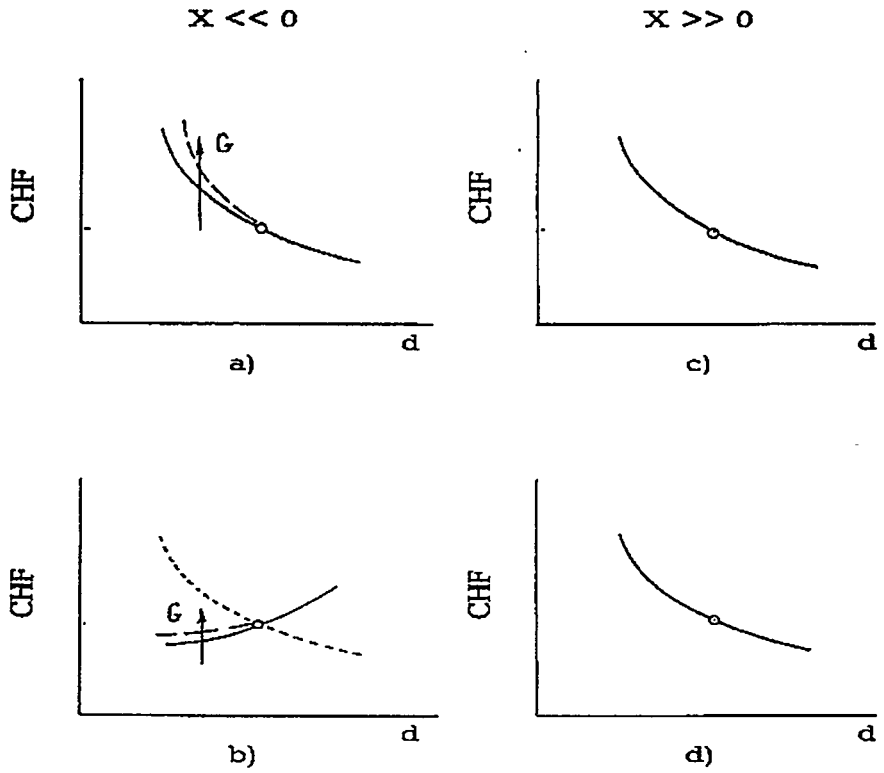

Fig.10. CHF ratios for tubes of various diameter by various pressure and quality. Cf.10b correspond to 8b; 10c-8c; 10d-8d.

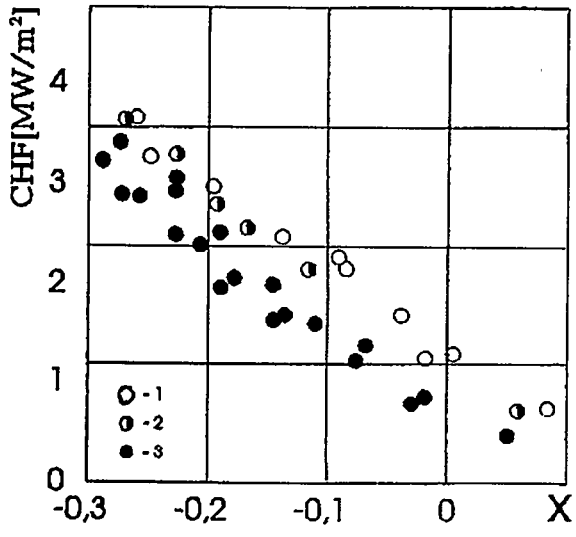

Fig.11. Gas content effect at P=16,71 MPa, G=2,1 Mg/(m2s), c-ncm3/kg: 1-50; 2-1900; 3-(3800-4000) [34].

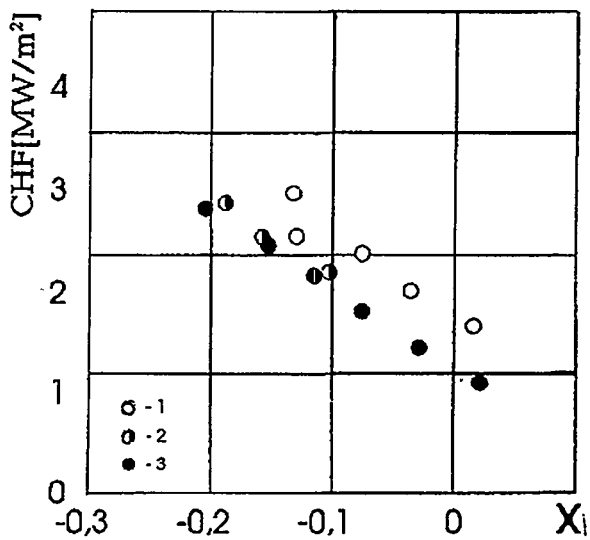

Fig.12. Gas content effect at P=17 MPa, G=2 Mg/(m2s), c-ncm3/kg: 1-50; 2-2000; 3-3000 [34].

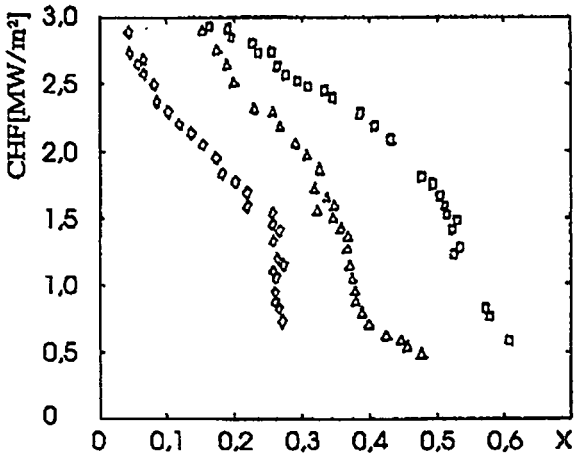

Fig.13a. CHF for tube 8mm, P=78 bar G Mg/(m²s): □-1; △-1,6; ◇-2,7. [40].

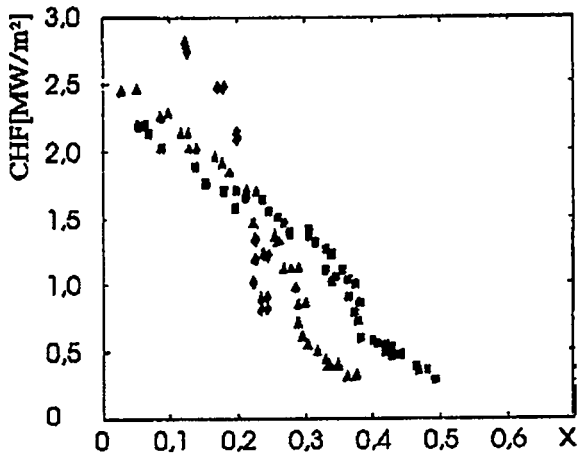

Fig.13b. CHF for rod bundle, P=74 bar G Mg/(m²s): ■-1; ▲-1,5; ◆-2,5. [40].

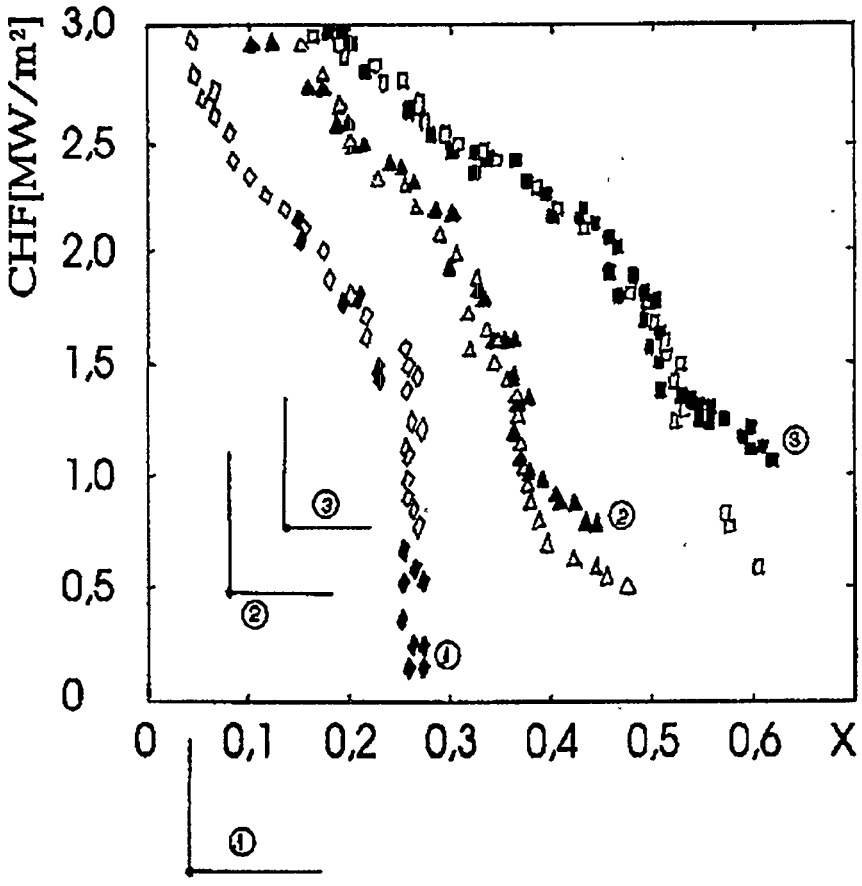

Fig.14. Comparision CHF tubes $[q_{c,t}(x_t)]$ and rod bundle $[q_{c,b}(x_b)]$ P=74-78 bar, G Mg/(m²s): □■ -1; △▲ -1,5-1,6; ◇◆ -2,5-2,7.

A COMPARISON OF CRITICAL HEAT FLUX IN TUBES AND BILATERALLY HEATED ANNULI

by

S. Doerffer[+], D.C. Groeneveld[+] and S.C. Cheng

University of Ottawa, Department of Mechanical Engineering
Ottawa, Ontario, K1N 6N5, Canada

ABSTRACT

This paper examines the critical heat flux (CHF) behaviour for annular flow in bilaterally heated annuli and compares it to that in tubes and unilaterally heated annuli. It was found that the differences in CHF between bilaterally and unilaterally heated annuli or tubes strongly depend on pressure and quality. The CHF in bilaterally heated annuli can be predicted by tube CHF prediction methods for the simultaneous CHF occurrence at both surfaces, and the following flow conditions: pressure 7-10 MPa, mass flux 0.5-4.0 Mg/m^{2}s and critical quality 0.23-0.9.

The effect on CHF of the outer-to-inner surface heat flux ratio, was also examined. The prediction of CHF for bilaterally heated annuli was based on the droplet-diffusion model proposed by Kirillov and Smogalev [1,2]. While their model refers only to CHF occurrence at the inner surface, we extended it to cases where CHF occurs at the outer surface, and simultaneously at both surfaces, thus covering all cases of CHF occurrence in bilaterally heated annuli. From the annuli CHF data of Becker and Letzter [3], we derived empirical functions required by the model. The proposed equations provide good accuracy for the CHF data used in this study. Moreover, the equations can predict conditions at which CHF occurs simultaneously at both surfaces. Also, this method can be used for cases with only one heated surface.

1. INTRODUCTION

Current methods to predict critical heat flux (CHF) in subchannel codes are often based on empirical CHF correlations derived from tube data, which ignore the influence of bundle-specific parameters such as element-element gap size, heated surface curvature, and the presence of unheated surfaces. The paper presented by Doerffer et al. [4] at NURETH-6 systematically examined the differences between CHF in tubes and internally heated annuli by accounting for the differences in geometric parameters. One of the methods, accounting for the effect of eccentricity, was applied recently at Chalk River Laboratories (CRL) to the analysis of CHF data obtained from a full-scale bundle simulator contained in a pressure tube with a variable diametral creep, resembling an internally heated annulus with an eccentricity. It was found that the relative effect on CHF is approximately the same in a bundle-pressure tube system with and without diametral creep, as it is between an eccentric and concentric internally heated annulus. This successful extrapolation of a prediction method for a simple flow geometry to a more complex geometry demonstrates the relevance of studying subchannel-specific separate effects in simpler geometries.

This paper is an extension of Doerffer et al. [4] previous CHF study on concentric and eccentric annuli. The objectives of the current paper are: (i) to examine the CHF behaviour in bilaterally heated annuli and compare it with that in tubes and unilaterally heated annuli, and (ii) to develop a CHF prediction method for bilaterally heated annuli. Both studies are directed towards improving the CHF prediction accuracy in geometries having bilateral heating, such as subchannels in a fuel bundle.

[+]Mailing address: Chalk River Laboratories, AECL Research
Chalk River, Ontario, Canada K0J 1J0

2. EXPERIMENTAL OBSERVATIONS AND COMPARISON AGAINST TUBE DATA

In general, the literature on CHF in bilaterally heated annuli is very scarce, compared to that of CHF in unilaterally heated annuli. The few available sources apply to concentric annuli, and of these only the experimental data of Becker and Letzter [3] and Becker et al. [5] are available and well documented. The Becker and Letzter data [3] were chosen as a reference data base since: (i) their parameter ranges cover conditions of interest (i.e., P > 3 MPa, G > 1 Mg/m^{2}s and the critical quality range corresponds to the dryout-type CHF in water), and (ii) their data base includes also CHF data obtained in the same annulus with only internal and only external heating. Their ranges of parameters and geometric dimensions are given in Table 1.

The initial location of CHF occurrence in bilaterally heated annuli was found to depend primarily on the heat flux ratio, R, between the outer and inner surfaces. At low R values the CHF occurs preferentially at the inner surface; at R value somewhat between 1.2 and 2.2 CHF could occur simultaneously at both surfaces; and for higher R values CHF occurs only at the outer surface of an annulus. At simultaneous CHF occurrence the dryout quality reaches its maximum value (during the experiments, the inlet quality remains constant). To assess the effect of bilateral heating on CHF these three cases were considered individually and compared against a reference tube CHF prediction method (the standard 8-mm tube CHF look-up table of Groeneveld et al. [6]), and the prediction method for annuli with unilateral heating (Doerffer et al. [4]) at the same dryout conditions (i.e., P, G and x_e).

Table 1: Conditions of Water CHF Data for Annulus with Bilateral Heating

Parameter	Range
P [MPa]	2.96 - 10.0
G [Mg/(m^{2}s)]	0.24 - 3.98
x_{in} [-]	-0.03 - -0.06
x_e [-]	0.15 - 0.89
L [m]	3.0
δ [mm]	4.65
D_i [mm]	12.0
D_o [mm]	21.3
D_{he} [mm]	9.3
D_{hy} [mm]	9.3
L/D_{he}	322.6
No. of CHF	240

2.1 Bilateral Heating with CHF Occurring Only at Inner Surface

The data of Becker and Letzter [3], representing the CHF occurring at the inner annulus surface, CHF_i, were compared with the predicted CHF values: (i) for a tube of ID = 8 mm, $CHF_{D=8}$, and (ii) for internally heated annuli (using correlation (1) of Doerffer et al., [4]), CHF_{ii}.

For the same dryout conditions it was observed that CHF_i is larger than CHF_{ii}. This difference, in general, increases with an increase in q''_o and R, and pressure (see Figures 1 and 2). The corresponding $CHF_{D=8}$ is always larger than that in an annulus, but its value decreases with pressure.

Moreover, at constant inlet conditions CHF_i decreases, regardless of pressure and mass flux, with increasing heat flux applied to the outer surface, q''_o, (e.g., Figure 3). At a certain value of q''_o, significantly higher than q''_i, the CHF occurs simultaneously at both surfaces of an annulus (at R = 2.17, for conditions shown in Figure 3). Figure 3 also shows the CHF_{ii} values corresponding to CHF_i values, which decrease at higher rate than the CHF_i with increasing x_e.

The fact that heating both inner and outer surfaces results in an increase of the inner surface CHF, compared with that of the inner surface heating only, was also confirmed in other studies. Kirillov and Smogalev [2], Becker at el. [5], Jensen and Mannov [7] and Alekseev et al. [8] observed that in the annular geometry, while Collier et al.

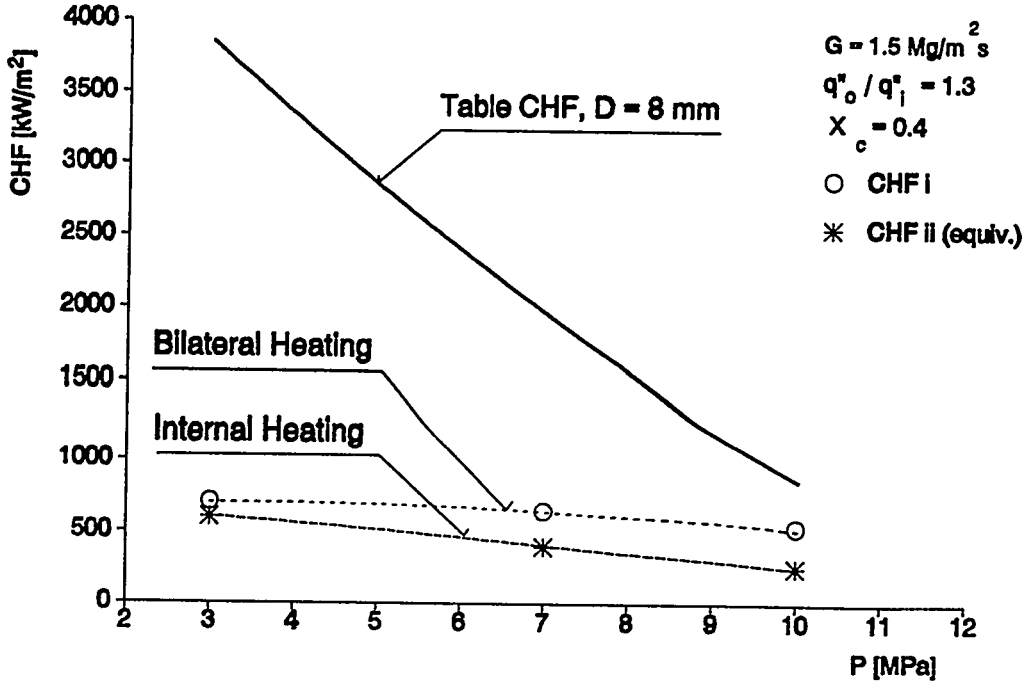

Figure 1: Comparison at Various Pressures of Experimental CHF_i Data with Predicted $CHF_{D=8}$ for Tube and CHF_{ii} for Internally Heated Annulus, at G = 1.5 Mg/m^2s, R = 1.3 and x_c = 0.4.

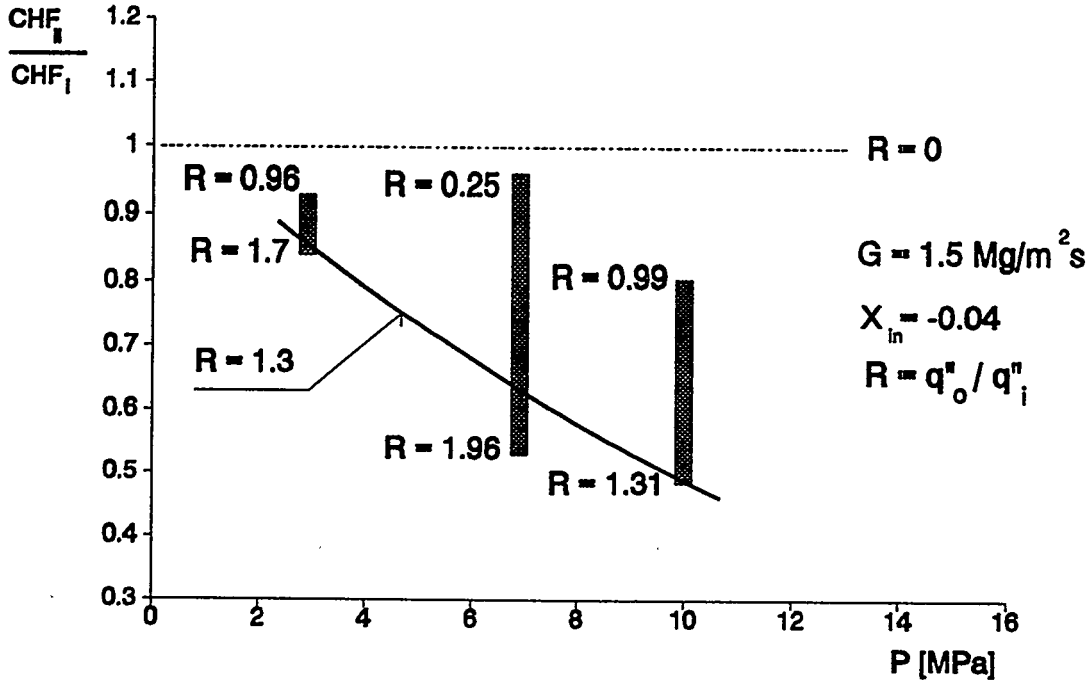

Figure 2: CHF_{ii} /CHF_i Ratio at Various Pressures, G = 1.5 Mg/m^2s and x_{in} = -0.04. Shaded Areas Cover Experimental Data Range of Becker and Letzter [3] of Different Outer-to-Inner Surface Heat Flux Ratio, R.

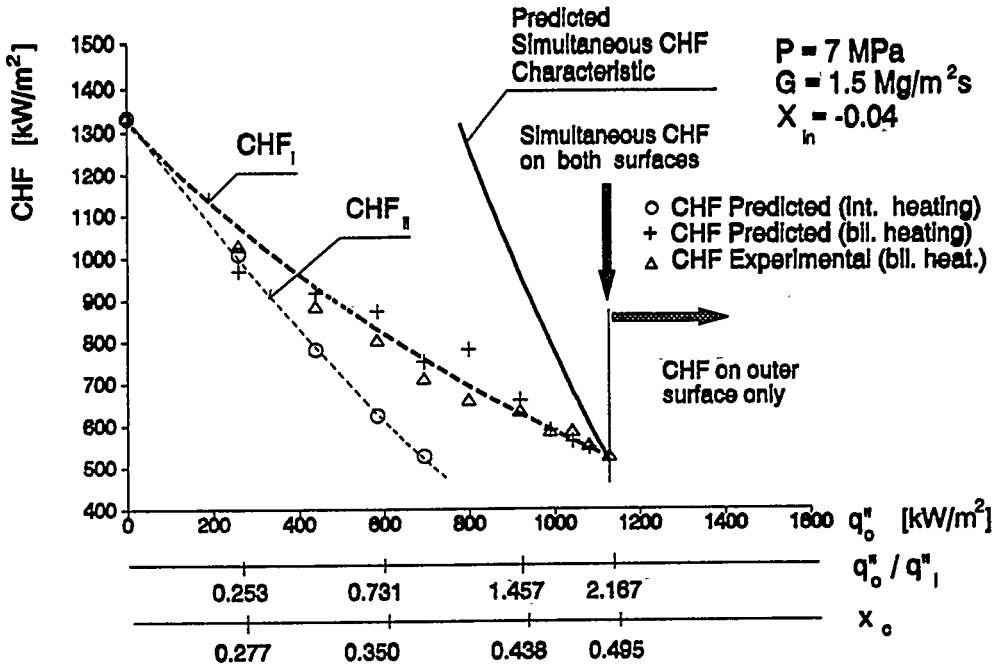

Figure 3: CHF_i vs. Outer Surface Heat Flux, q''_o. Comparison of Experimental CHF_i Data with Their Prediction by Equation (29) and with Corresponding CHF_{ii} Values. Determination of Simultaneous CHF Occurrence by Equation (45).

[9] found it in an annulus with irregular outer surface, and Tippets [10] in a rectangular channel with either one or both long sides heated. These observations refer only to the dryout-type CHF. A situation during the DNB-type CHF is different.

Tolubinskiy et al. [11] and Ornatskiy et al. [12] investigated the effect of bilateral heating on CHF at very high pressure (15-20 MPa) and very high subcoolings resulting in DNB-type CHF. They concluded that the presence of a heat flux at the outer surface does not affect the CHF at the inner surface, and vice versa. In addition, they found that the CHF at the inner surface is always higher than that at the outer surface. This is opposite to the CHF behaviour during dryout.

2.2 Simultaneous CHF at Both Surfaces

Figure 4 shows an example of the experimental data (i.e., CHF_o and CHF_i), obtained during simultaneous CHF occurrence at both surfaces of an annulus, as a function of mass flux for two pressures (7 and 10 MPa) and one inlet quality (-4%). It was observed that: (i) the CHF_o value is always much higher than the CHF_i value, (ii) at a given pressure, with an increase in mass flux, both CHF_o and CHF_i increase monotonically, (iii) the ratio $R = CHF_o/CHF_i$ decreases with pressure regardless of the mass flux (Figure 4), but CHF_o decreases at a much higher rate with pressure than CHF_i (compare Figures 4 and 5; when pressure increases from 7 to 10 MPa, CHF_o drops by 43% while CHF_i does not drop at all at $G = 1.5$ Mg/m²s).

When comparing for the same exit qualities CHF_o vs. CHF_{oo} and CHF_i vs. CHF_{ii}, the values obtained during bilateral heating are larger than those of unilateral heating. The $CHF_{D=8}$ values in a tube are larger than those of CHF_o and CHF_i, but are closer to the CHF_o values. For CHF_{oo} the following equation was used (Doerffer and Cheng [13]):

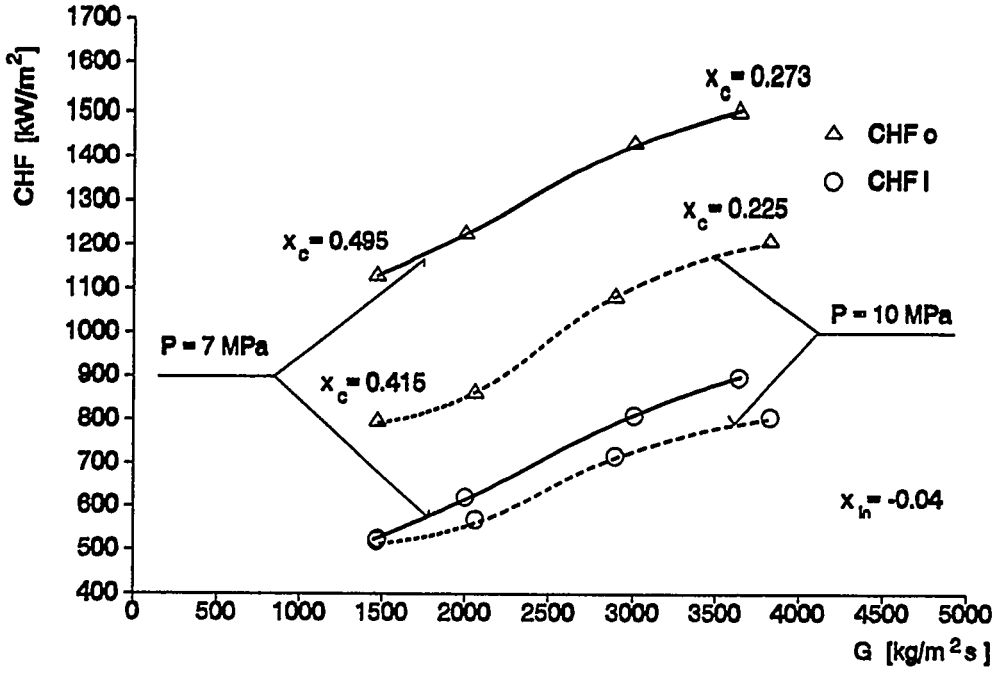

Figure 4: Effects of Mass Flux and Pressure on CHF at Inner and Outer Surfaces of Annulus During Simultaneous CHF Occurrence (Data of Becker & Letzter [3]).

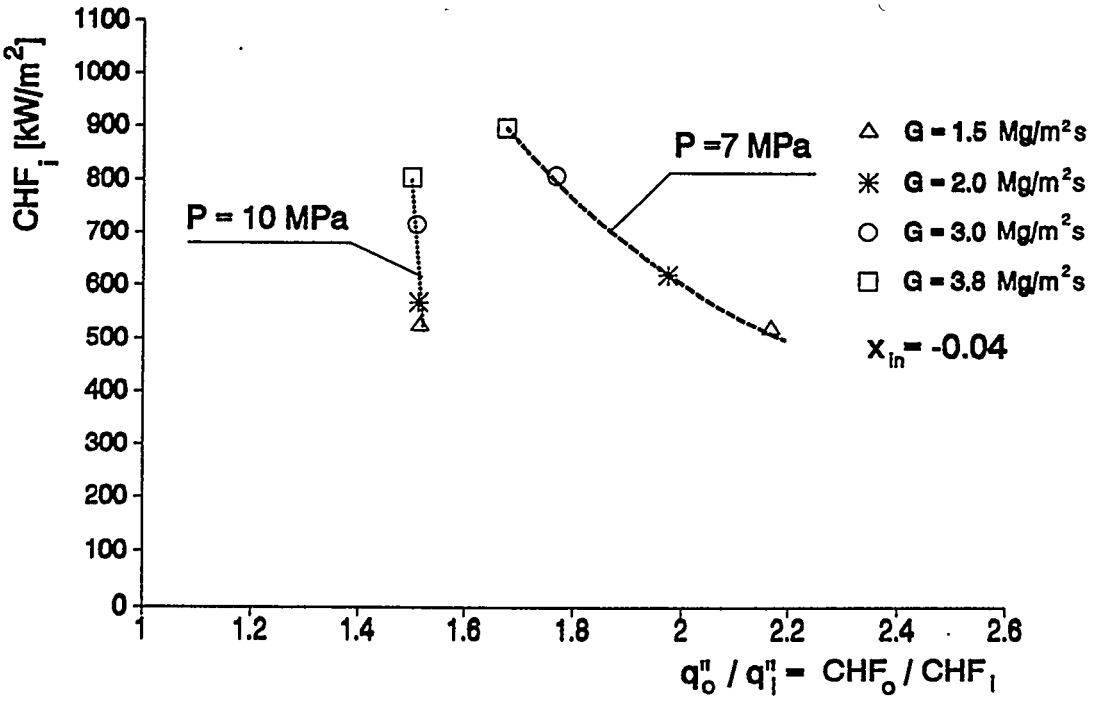

Figure 5: Relation Between CHF_i and Ratio $q''_o/q''_i = CHF_o/CHF_i$ as Function of Pressure and Mass Flux During Simultaneous CHF Occurrence in Annulus (Data of Becker & Letzter [3]).

$$CHF_{oe} = CHF_{ii} * \frac{r_i}{r_o} + \frac{r_i + r_o}{r_o} * (K_a \, H_{fg} \, \rho_g \, B) * (C_{oi} - C_{ie}) * f(P,G) \quad (1)$$

where $f = 0.0102*G^{0.887} - 0.0035$ for P = 5 MPa, $f = 0.012*G^{0.893} - 0.00315$ for P = 7 MPa, $f = 0.00782*G^{1.79} + 0.0035$ for P = 10 MPa, G is in Mg/m^2s, and other parameters are specified in chapter 4.

2.3 Bilateral Heating with CHF Occurring Only at Outer Surface

When at given pressure and mass flux, the ratio R exceeds a value of the CHF_o/CHF_i ratio corresponding to the simultaneous CHF at both surfaces, then CHF occurs only at the outer surface of an annulus. At constant inlet conditions it appears that CHF_o is almost insensitive to q''_i at the inner surface (i.e., CHF_o slightly decreases with heat input to the inner surface, q''_i, as shown in Figure 6), and the predicted CHF_{oe} values corresponding to CHF_o values are lower and decrease at higher rate than the CHF_o with increasing x_c, similarly as in the case of CHF occurrence at the inner surface.

At the same P, G and x_c, the corresponding $CHF_{D=8}$ values are also higher than CHF_o, but very close to each other at pressure 7 to 10 MPa.

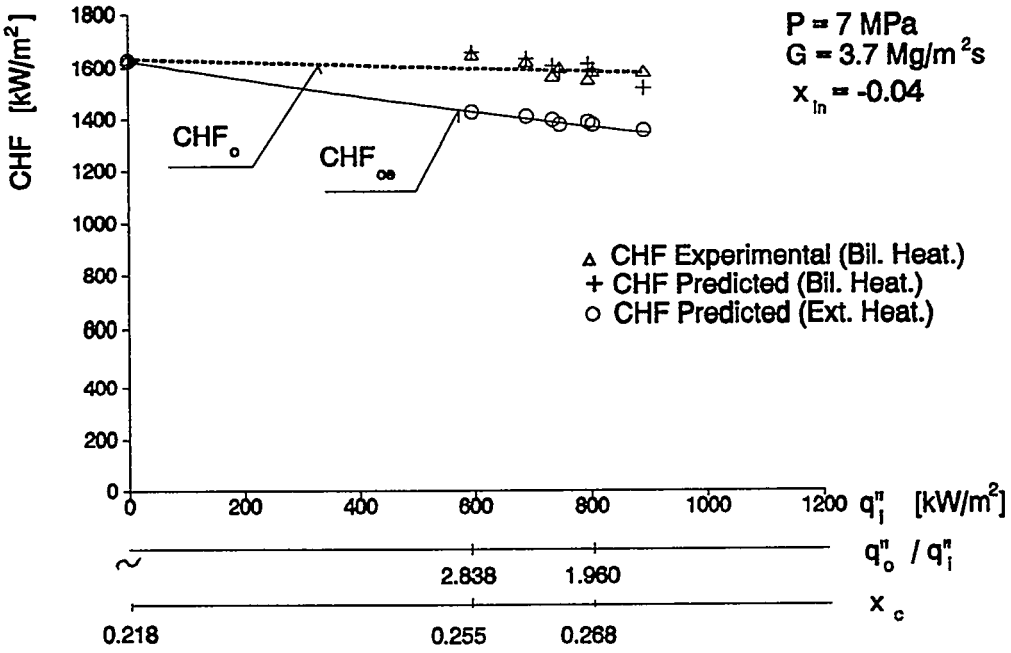

Figure 6: CHF_o Occurring at Outer Annulus Surface During Bilateral Heating vs. Inner Surface Heat Flux, q''_i, at P = 7 MPa and G = 3.7 Mg/m^2s. Comparison of CHF_o with Their Prediction by Equation (42), and with Corresponding CHF_{oe} Values.

2.4 Comparison with Tube CHF Data

When comparing the tube CHF to an annulus CHF, an equivalent diameter must be chosen. The following possibilities are available D_{he}, D_{hy}, D_o and D = 8 mm (for convenience only). Strictly speaking, $D_{he} = D_{hy}$, even if there is only very small heat flux present on the lower heat flux surface. An alternative D_{he} could be based on a heated perimeter $p = p_{dryout\ surf.} + p_{opp.\ surf.} * q''_{opp.\ surf.} / q''_{CHF}$.

The ratios CHF_o/CHF_D for $D = D_o$ (21.3 mm), $D = D_{he}$ (9.3 mm) and D = 8 mm for the simultaneous CHF occurrence are shown in Figure 7. Each point in the figure represents an average value of the experimental CHF_o to the predicted CHF_D ratio over the given range of mass flux and exit quality. Both for $D = D_{he}$ and D = 8 mm the tube CHF values appear to agree well with the CHF_o for simultaneous CHF, from 7 to 10 MPa. Note that in all other cases either for bilateral heating or unilateral heating, or simultaneous CHF at lower pressure, CHF_D is higher than the CHF in an annulus.

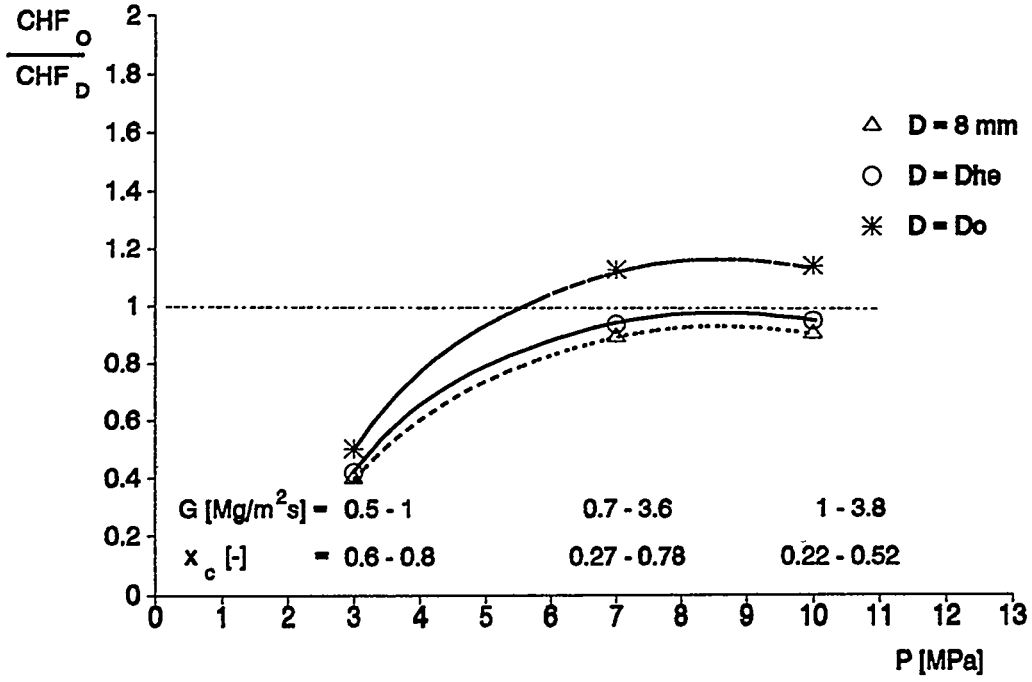

Figure 7: Comparison of CHF_o Data at Outer Surface in Bilaterally Heated Annulus During Simultaneous CHF Occurrence with Corresponding CHF_D Values Predicted for Tubes of Various Diameters as Function of Pressure. Points Represents Average Values Over Given Ranges of Mass Flux and Exit Quality.

3. CHF MECHANISMS IN BILATERALLY AND UNILATERALLY HEATED ANNULI

The physical phenomena responsible for CHF in annuli are more complex than those in tubes. The following interacting phenomena control the dryout type of CHF in annuli: (i) the shear stresses and their distribution between the surfaces, (ii) the distribution of the droplet deposition between the surfaces (the droplet deposition is assumed to be affected by the vapour flow normal to a heated wall, the droplet concentration, pressure and fluid properties), and (iii) differences in entrainment rates from liquid films flowing along concave and convex surfaces. Each of them will be discussed separately:

- Shear stress distribution: In single-phase flow, both in the laminar and turbulent flow regimes $\tau_i > \tau_o$ (e.g., Knudsen and Katz [14], Brighton and Jones [15]). This is also assumed to be true in two-phase annular flow at the vapour-liquid films interfaces.

- Deposition rates D^*: Deposition rate $D^* = f(C, K)$, where the deposition coefficient $K = f(P, q'', \text{view factor})$. At the same P and q": $K_o > K_i$, because of the difference in so-called view factor, which is larger for the outer surface than for the inner one, hence $D_o^* > D_i^*$. The view factor quantifies chances of reaching a given surface by the droplets entrained in the vapour core. It can be defined differently (e.g., Equation (5) in the Kirillov and Smogalev [2] model presented below, or Equation (4.10) of Doerffer and Cheng [13]). In general, K decreases with an increase in P; moreover, for a given surface, K decreases with an increase in q" supplied to this surface (Kirillov and Smogalev [2]) due to the vapour counterflow generated by q". Saito et al. [16] concluded also that $D_o^* > D_i^*$.

- Film thickness: For the same heat fluxes on both surfaces $\delta_o > \delta_i$ due to $\tau_i > \tau_o$ and $D_o^* > D_i^*$. For this reason $CHF_o > CHF_i$.

- Entrainment rate: $E = f(\delta, \tau, q'')$. The thicker liquid film, δ, the more wavy surface and greater E. It is difficult to quantify at which surface E is higher, because the higher δ_o may compensate for lower τ_o. The q" effect on E is probably small.

Compared to unilateral heating ($q''_o = 0$), the presence of q''_o decreases the film thickness δ_o, increases C and hence enhances K_i; therefore CHF_i is always higher than the corresponding CHF_{ii} (at internal heating, as shown in Figure 3). When $q''_i = q''_o$ then $\delta_o > \delta_i$ due to $\tau_i > \tau_o$, and $D_o^* > D_i^*$. All these effects are favourable to enhance the CHF_o at the outer surface, and that is why CHF_o is always observed larger than CHF_i. A change in q''_i has a less significant effect on CHF_o comparing to the effect of q''_o on CHF_i (see Figures 6 and 3), and this is presumably due to the smaller impact of a change in δ_i on C. Still, the presence of q''_i enhances K_o, therefore CHF_o is higher than the corresponding CHF_{oe} (at external heating, see Figure 6).

In general, the CHF_D in tubes is always higher than that in annuli, regardless of a mode of heat supply to the annulus surfaces (although in bilaterally heated annuli the ratio of the heated perimeter to the total wetted perimeter is one, like in tubes). But CHF in annuli strongly depends on the ratio of the perimeter of the wall where CHF occurs, to the total perimeter. The discrepancy between CHF_D and CHF_{An} is the largest when CHF occurs at the inner surface (where this ratio is minimum), and it is the smallest when CHF occurs simultaneously at both surfaces (where this ratio is maximum = 1). The differences in the shear stress distribution and the shape of the flow area can partially explain the differences in CHF behaviour between these two flow geometries. Even though the heated equivalent diameter of an annulus is close the tube diameter, the gap in the annulus is only 4.65 mm. At the same exit conditions the average velocity of two-phase mixture is the same in both geometries, but the maximum velocity and the velocity gradients at the walls are much larger in the narrow gap of an annulus than at the tube wall. Because these gradients control entrainment and the thickness of the liquid films, therefore they lower CHF in annuli compared with that in tubes.

Moreover, the deposition of droplets in tubes is uniform around the whole perimeter and entirely reaches the heated perimeter where CHF occurs, while in annuli always one heated wall, where CHF occurs, experiences a lower deposition rate due to the parasitic effect of the opposite wall. This fact contributes to the lower CHF values in annuli than in tubes. Therefore the ratio CHF_{An}/CHF_D is smaller at a low pressure, where the deposition coefficient is high and the parasitic effect on CHF of the opposite wall in an annulus is more pronounced than at a high pressure (see Figures 1 and 7).

However, for DNB-type CHF behaviour opposite trends have been observed by Tolubinskiy et al. [11] and Ornatskiy et al. [12]. The fact that $\tau_i > \tau_o$ explains that $CHF_i > CHF_o$ during the DNB. A higher τ_i causes more effective cooling of a heated surface by bubble removal from that surface, and prevents the formation of a thick bubbly layer near the surface and thus increases CHF_i. Since the DNB type of CHF is a very local phenomenon, therefore the presence of a heat flux at the opposite surface does not affect the CHF at a given surface.

4. DERIVATION OF PHENOMENOLOGICAL CHF EQUATIONS FOR BILATERALLY HEATED ANNULI

Saito et al. [16] formulated a four-fluid model to analyze flow characteristics and CHF in the annular flow regime in annuli. This very complex model, involving numerous constitutive relationships, was solved numerically, and was tested against CHF data obtained in a bilaterally heated annulus. The model was able to predict a general CHF trend, but overestimated CHF occurring at the inner rod, underestimated CHF at the outer rod, and failed to predict simultaneous CHF occurrence at both annulus surfaces. It was concluded that "the deposition coefficient for the outer tube should be larger than that for the inner rod. No direct experimental data are available to verify this observation".

No empirical correlations or analytical equations to predict the CHF and its location in bilaterally heated annulus have been found in the literature. Only Kirillov and Smogalev [2] proposed an analytical model to predict CHF at the inner surface. This model, which takes into account the differences in deposition rates on the inner and outer surfaces, and the effect of the normal vapour flow on the droplet deposition, has been applied to bilateral heating with simultaneous CHF occurrence, or CHF occurrence at the outer surface of the annulus. The results have been adopted to the experimental data used in this study.

4.1 Description of the Kirillov and Smogalev Model

An analytical droplet-diffusion model describing the dryout-type CHF in tubes (Kirillov and Smogalev [1]) introduced the new parameter x_n, the quality at which droplet deposition from the core stream onto the channel wall deteriorates markedly or ceases completely, for adiabatic two-phase flow. This approach was subsequently used to developed a CHF prediction model for annuli (Kirillov and Smogalev [2]). Due to restricted availability of reference [2], this model will be summarized below.

4.1.1 CHF in Internally Heated Annulus

To develop a CHF model for bilateral heating, Kirillov and Smogalev [2] first derived the model for internally heated annuli. Figure 8 shows that a formation of annular flow takes place between 1 to 2. Between 2 to 3 droplets from the wavy liquid films become entrained in the vapour core as a result of interaction between the films and the core flow. At 3 liquid entrainment ceases and a fairly smooth liquid films begin. In the region from 3 to 4 (i.e, to the section, where CHF occurs) the core flow consists of the vapour and the liquid droplets. If the effect of the vapour thrust velocity (due to the film evaporation) on droplet deposition is neglected, then deposition will continue until the liquid mass flow rate in the core flow reaches its minimum value Γ_n^c (corresponding to the quality x_n).

The mass flow rate of deposited droplets in this region is

$$\Gamma_{dep} = \Gamma_{\Delta P}^c - \Gamma_n^c \tag{2}$$

Deposition on the inner (heated) surface is

$$\Gamma_{i,\,dep} = n_i\,\Gamma_{dep} \tag{3}$$

and on the outer (unheated) surface is

$$\Gamma_{o,\,dep} = n_o\,\Gamma_{dep} \tag{4}$$

where

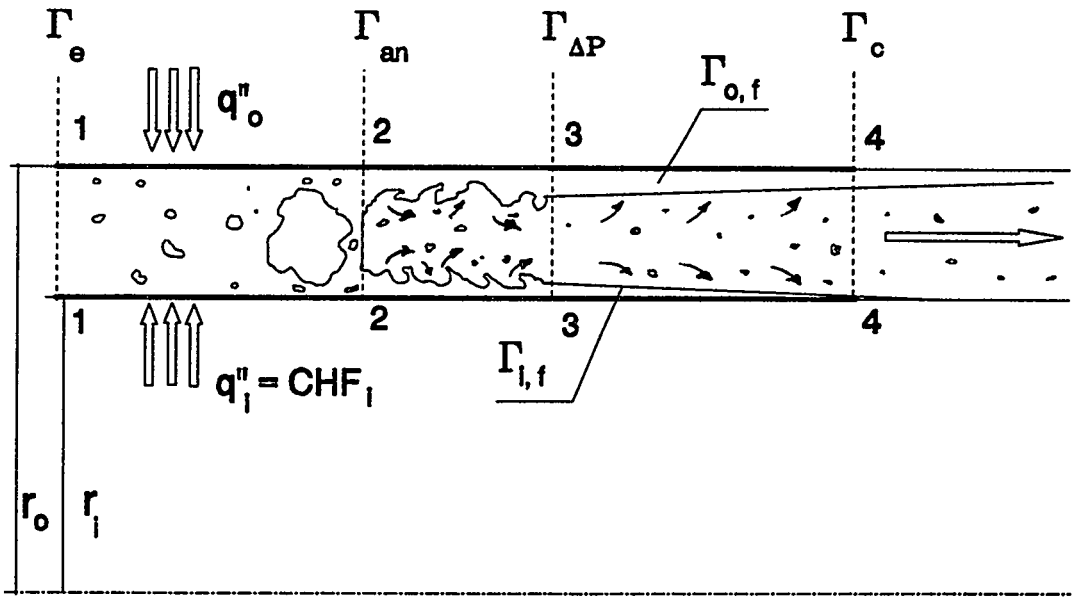

Figure 8: Schematic of Flow Patterns in Annulus for Kirillov and Smogalev's Model [2]

$$n_l = \frac{r_l}{r_l + r_o} \quad and \quad n_o = \frac{r_o}{r_l + r_o} \tag{5}$$

A normal component of the vapour flow, $q_l''/(H_{fg}\rho_g)$, decreases the droplet deposition onto the inner surface in the ratio K_q/K_a as follows:

$$\Gamma_{l,\,dep} = n_l\,\Gamma_{dep}\,\frac{K_q}{K_a} \tag{6}$$

Consequently, the mass flow rate of droplets in the core flow, at which their mass transfer toward the wall deteriorates, is increased by the amount:

$$\Delta\Gamma_n^c = n_l\,\Gamma_{dep}\left(1 - \frac{K_q}{K_a}\right) \tag{7}$$

The droplets mass flow rate in the core stream, at which mass transfer deteriorates, is

$$\Gamma_{nq}^c = \Gamma_n^c + n_l\,\Gamma_{dep}\left(1 - \frac{K_q}{K_a}\right) \tag{8}$$

In this case, the liquid mass flow rate at any section in the region is

$$\Gamma = \Gamma_{nq}^{c} + (\Gamma E - \Gamma_{nq}^{c}) + \Gamma_{i,f} + \Gamma_{o,f} \tag{9}$$

For the onset of CHF it is necessary that:

$$\Gamma E = \Gamma_{nq}^{c} \quad and \quad \Gamma_{i,f} = 0 \tag{10}$$

so that

$$\Gamma_{c} = \Gamma_{nq}^{c} + \Gamma_{o,f} \tag{11}$$

Equations (2) and (8) with the following relation

$$\Gamma_{\Delta P}^{c} = \Gamma_{\Delta P} E_{\Delta P} \tag{12}$$

and the assumption

$$K_{q} = K_{a} - \frac{q_{i}''}{H_{fg}\rho_{g}} \tag{13}$$

introduced to Equation (11), which divided by the total mass flow rate, Γ_T, yields

$$x_{c} = x_{n} - n_{i}\left[(1 - x_{\Delta P})\, E_{\Delta P} - 1 + x_{n}\right] \frac{q_{i}''}{K_{a} H_{fg} \rho_{g}} - \frac{\Gamma_{o,f}}{\Gamma_{T}} \tag{14}$$

where $\Gamma_c/\Gamma_T = 1 - x_c$, $\Gamma_n^c/\Gamma_T = 1 - x_n$ and $\Gamma_{\Delta P}/\Gamma_T = 1 - x_{\Delta P}$. The liquid mass flow rate in the film on the outer surface is

$$\Gamma_{o,f} = 2\pi\, r_{o}\, \delta_{o}\, \rho_{f}\, v_{f} \tag{15}$$

The stable film thickness, δ_o, is assessed from the Tippets formula [17]

$$\delta_{o} = \frac{C_{3} C_{4} \sigma \left(1 + \dfrac{\rho_{f}}{\rho_{g}}\right)}{\tau_{o} \left(1 + \left(\dfrac{\rho_{f}}{\rho_{g}}\right)^{0.5}\right)^{2}} \tag{16}$$

where the shear stress at the outer surface was assumed after Knudsen and Katz [14] for single-phase flow as also valid for the annular flow regime

$$\tau_{o} = \frac{4\, \mu_{g}\, v_{g}\, (r_{o}^{2} - r_{m}^{2})}{r_{o}\, (r_{o}^{2} + r_{I}^{2} - 2 r_{m}^{2})} \tag{17}$$

and

$$r_m = \sqrt{(r_o^2 - r_i^2) / (2\ln\frac{r_o}{r_i})} \tag{18}$$

To replace the average vapour velocity, v_g, in Equation (17), by the average liquid velocity, v_f, the following slip ratio equation is assumed to be valid:

$$S = \frac{v_g}{v_f} = \left(\frac{\rho_f}{\rho_g}\right)^{\frac{1}{2}} \tag{19}$$

Then, the fraction of liquid in the film at the outer surface can be expressed as follows:

$$\phi_{ol} = \frac{\Gamma_{o,f}}{\Gamma_T} = A_{ol} * B * C_{ol} \tag{20}$$

where

$$B = \frac{\sigma\rho_f\left(\frac{\rho_g}{\rho_f}\right)^{0.5}\left(1+\frac{\rho_f}{\rho_g}\right)}{2\mu_g G\left(1+\left(\frac{\rho_f}{\rho_g}\right)^{0.5}\right)^2}, \tag{21}$$

and

$$C_{ol} = \frac{r_o^2 (r_o^2 + r_i^2 - 2r_m^2)}{(r_o^2 - r_i^2)(r_o^2 - r_m^2)} \tag{22}$$

Rearrangement of Equation (14) with an assumption $E_{\Delta P} = 1$, yields this equation the following form:

$$CHF_{ll} = \frac{r_i + r_o}{r_i} * \frac{K_a H_{fg}\rho_g}{x_{nl}} * (x_n - \phi_{ol} - x_c) \tag{23}$$

where $x_{nl} = x_n - x_{\Delta P}$, and the heat flux q''_i becomes the CHF in an internally heated annulus.

4.1.2 CHF at Inner Surface During Bilateral Heating

Due to evaporation of the outer film, the normal component of the vapour velocity, $q_o''/(H_{fg}\rho_g)$, attenuates droplet deposition on this surface, and thus increases the liquid mass flow rate in the core flow, Γ_n^c, by the amount

$$\Delta\Gamma_n^c = n_o \Gamma_{dep}\left(1 - \frac{K_q}{K_a}\right) = n_o (\Gamma_{\Delta P}^c - \Gamma_n^c)\frac{q_o''}{K_a H_{fg}\rho_g} \tag{24}$$

Therefore, the liquid balance equation at the CHF section with bilateral heating is

$$\Gamma_c = \Gamma_n^c + (\Gamma_{\Delta P}^c - \Gamma_n^c)\left(n_l \frac{CHF_l}{K_a H_{fg} \rho_g} + n_o \frac{q_o''}{K_a H_{fg} \rho_g}\right) + \Gamma_{o,f} \tag{25}$$

Also, due to evaporation the liquid film thickness at the outer surface decreases in the direction of flow at the rate

$$\frac{d\delta_o}{dl} = - \frac{q_o''}{H_{fg}\, \rho_f\, v_f} \tag{26}$$

Then, the film thickness at the CHF section can be determined as

$$\delta_{oq} = \delta_o - \Delta\delta_o \tag{27}$$

where $\Delta\delta_o$ is obtained from integration of Equation (26) over the distance $(L - L_{\Delta P})$. Using Equation (15), where δ_o is replaced by δ_{oq}, the fraction of liquid flowing along the outer (now also heated) surface is

$$\phi_o = \phi_{ol} - \frac{2 r_o q_o'' (L - L_{\Delta P})}{G H_{fg} (r_o^2 - r_i^2)} = \phi_{ol} - \Delta\phi_o \tag{28}$$

Dividing Equation (25) by the total flow rate, and using Equations (12) and (28) the equation for CHF at the inner surface during bilateral heating is obtained

$$CHF_i = \frac{r_i + r_o}{r_i} * \frac{K_a H_{fg} \rho_g}{x_{nl}} * (x_n - \phi_o - x_c) - \frac{r_o}{r_i} q_o'' \tag{29}$$

Kirillov and Smogalev assumed this method to be valid for: (i) $L \geq 1$ m, (ii) $n_i \geq 0.17$, (iii) $7 \leq P \leq 20$ MPa, (iv) $2 \leq G \leq 5.5$ Mg/m^{2}s, and (v) $x_n/2 \leq x_c \leq x_n$.

4.2 Extension of the Kirillov and Smogalev Model

Applying the same methodology as Kirillov and Smogalev [2], we extended their method to bilaterally heated annuli where: (i) CHF occurs at the outer surface only, and (ii) CHF occurs simultaneously CHF at both surfaces. To obtain the equation for case (i), first the equation for CHF for external heating has to be derived.

4.2.1 CHF in Externally Heated Annuli

If evaporation at the outer surface only takes place, then a normal component of the vapour flow, $q_o''/(H_{fg}\rho_g)$, decreases the droplet deposition onto this surface in the ratio K_q/K_a as follows:

$$\Gamma_{o,\,dep} = n_o\, \Gamma_{dep}\, \frac{K_q}{K_a} \tag{30}$$

Consequently, the mass flow rate of droplets in the core flow is increased by the amount:

$$\Delta\Gamma_n^c = n_o\, \Gamma_{dep} \left(1 - \frac{K_q}{K_a}\right) \tag{31}$$

The droplets mass flow rate in the core flow, at which mass transfer deteriorates, is

$$\Gamma_{nq}^{c} = \Gamma_{n}^{c} + n_o \, \Gamma_{dep} \left(1 - \frac{K_q}{K_a}\right) \tag{32}$$

In this case, the liquid mass flow rate at any section in the region is given also by Equation (9). For the onset of CHF at the outer surface it is necessary that:

$$\Gamma E = \Gamma_{nq}^{c} \quad and \quad \Gamma_{o,f} = 0 \tag{33}$$

so that

$$\Gamma_c = \Gamma_{nq}^{c} + \Gamma_{i,f} \tag{34}$$

Applying the same approach as to Equation (11), Equation (34) takes the form

$$x_c = x_n - n_o \left[(1 - x_{\Delta P}) \, E_{\Delta P} - 1 + x_n\right] \frac{q_o''}{K_a H_{fg} \rho_g} - \frac{\Gamma_{i,f}}{\Gamma_T} \tag{35}$$

The liquid mass flow rate in the film on the inner surface, $\Gamma_{i,f}$, and the stable film thickness, δ_i, are obtained similarly as before, using Equations (15) and (16), where the quantities with the index "o" are replaced by those with the index "i". The required shear stress at the inner surface we calculated from the force balance in the annular flow, which results in

$$\tau_i = \tau_o \frac{r_o(r_m^2 - r_i^2)}{r_i(r_o^2 - r_m^2)} \tag{36}$$

where τ_o is given by Equation (17).

Taking into account Equations (18) and (19), and modified Equations (15), (16) and (36) the fraction of liquid in the film at the inner surface can be expressed as follows:

$$\phi_{ie} = \frac{\Gamma_{i,f}}{\Gamma} = A_{ie} * B * C_{ie} \tag{37}$$

where

$$C_{ie} = \frac{r_i^2 \, (r_o^2 + r_i^2 - 2r_m^2)}{(r_o^2 - r_i^2)(r_m^2 - r_i^2)} \tag{38}$$

Finally, the equation for CHF in externally heated annulus takes the form

$$CHF_{oe} = \frac{r_i + r_o}{r_o} * \frac{K_a \, H_{fg} \, \rho_g}{x_{n1}} * (x_n - \phi_{ie} - x_c) \tag{39}$$

4.2.2 CHF at Outer Surface During Bilateral Heating

The similar considerations apply in this case as those in Section 4.1.2, but now the liquid film in question is that on the inner surface, which decreases its thickness due to the heat flux, q''_i, and its evaporation attenuates the droplet deposition onto this surface.

The liquid balance equation at the CHF section with bilateral heating can be written as

$$\Gamma_c = \Gamma_n^c + (\Gamma_{\Delta P}^c - \Gamma_n^c)\left(n_i \frac{q_i''}{K_a H_{fg} \rho_g} + n_o \frac{CHF_o}{K_a H_{fg} \rho_g}\right) + \Gamma_{i,f} \tag{40}$$

In this case, the fraction of liquid flowing along the inner (now also heated) surface is

$$\phi_i = \frac{\Gamma_{i,f}}{\Gamma_T} = \phi_{ie} - \frac{2 r_i q_i'' (L - L_{\Delta P})}{G H_{fg} (r_o^2 - r_i^2)} = \phi_{ie} - \Delta\phi_i \tag{41}$$

The CHF at the outer surface during bilateral heating is given by

$$CHF_o = \frac{r_i + r_o}{r_o} * \frac{K_a H_{fg} \rho_g}{x_{nl}} * (x_n - \phi_i - x_c) - \frac{r_i}{r_o} q_i'' \tag{42}$$

4.2.3 Simultaneous CHF at Both Annulus Surfaces

If CHF occurs simultaneously at both surfaces, then at the CHF section both liquid films disappear. So, for the onset of CHF it is necessary that $\Gamma_{i,f} = 0$ and $\Gamma_{o,f} = 0$. For this case the liquid balance equation at the CHF section is

$$\Gamma_c = \Gamma_n^c + (\Gamma_{\Delta P}^c - \Gamma_n^c)\left(n_i \frac{q_i''}{K_a H_{fg} \rho_g} + n_o \frac{q_o''}{K_a H_{fg} \rho_g}\right) \tag{43}$$

and this equation yields the following equation for the critical quality

$$x_c = x_n - \frac{x_{nl}}{K_a H_{fg} \rho_g} * \frac{r_i q_i'' + r_o q_o''}{r_i + r_o} \tag{44}$$

where the heat flux at each surface is the critical one (i.e., $q_i'' = CHF_i$ and $q_o'' = CHF_o$). Rearrangement of Equation (44) allows to relate the CHF_i to the critical heat flux ratio q_o''/q_i as follows:

$$CHF_i = \frac{K_a H_{fg} \rho_g}{x_{nl}} * (x_n - x_c) * \frac{r_i + r_o}{r_i + r_o * (q_o''/q_i'')} \tag{45}$$

5. APPLICATION OF MODEL TO EXPERIMENTAL CONDITIONS

In this chapter we will apply the above derived CHF equations to predict the CHF in bilaterally heated annulus. The basis for this application will be the data of Becker and Letzter [3].

5.1 Development of Working Equations

Once the values of K_a, ϕ_o, ϕ_i, x_n and x_{n1} in Equations (29), (42) and (45) are known then the CHF can be predicted for all above cases. Unfortunately, not all of these values are known, and have to be derived from the experimental data [3]. Kirillov and Smogalev [2] suggested that the term $x_{n1} = x_n - x_{\Delta P}$ is independent of mass flux and constant at a given pressure (based on their Figure 2b, but from this figure x_{n1} can be assessed only at P = 14.3 MPa). On the other hand, this term can be equal to x_n (Kirillov and Smogalev [1]). Both approaches were tested (Doerffer and Cheng [13]), but the assumption $x_{n1} = x_n$ seems to work better and will be presented in this paper.

5.1.1 Prediction of simultaneous CHF at both surfaces

Kirillov and Smogalev [2] provided in a graphical form (Figures 6a and 6b in [2]): (i) K_a as a function of pressure (7 to 20 MPa), and (ii) x_n as a function of mass flux (< 2.2 Mg/m^{2}s) and pressure (7 to 20 MPa), both obtained from tube CHF data. The function K_a can be approximated by

$$K_a = 0.15869 + 3.5917*10^{-5}*P^{2.5} - 0.047*P^{0.5} + 1.7591*P^{-2} \qquad (46)$$

Thus only Equation (45), for the simultaneous CHF occurrence, may be directly used and tested within the given range of the parameters. A comparison of the CHF prediction by the equation with the corresponding experimental data (seven CHF points) is very good as shown in Table 2. This indicates an applicability of tube CHF data to CHF prediction in annuli. (N.B. A comparison based on the inlet conditions is required as these are the independent parameters; a comparison based on x_e is frequently used, as x_e is specified in the prediction method, but x_e is not an independent parameter. Both comparisons are given in Table 2).

Table 2: Accuracy of CHF Prediction Methods for Bilaterally Heated Annuli

Correlation	Error [%]				Number of CHF Data
	Inlet Conditions		Exit Conditions		
	Rms	Avg	Rms	Avg	
Equation (45) (simult. CHF - predicted by [2])	3.61	0.63	6.85	1.43	7
Equation (45) (simult. CHF - our prediction)	2.93	0.22	5.53	0.64	15
Equation (23) (internal heating only)	3.32	0.49	11.27	0.78	146
Equation (29) (CHF at inner surface)	3.55	0.36	14.56	1.28	62
Equation (39) (external heating only)	0.55	-0.03	1.94	0.0	17
Equation (42) (CHF at outer surface)	1.52	-0.07	7.20	0.01	47

Due to very limited mass flux range of x_n, given by Kirillov and Smogalev [2], we extended this range using all the data of simultaneous CHF occurrence as follows. Converting Equation (45) into the form

$$x_n = x_c * \frac{K_a H_{fg} \rho_g (r_i + r_o)}{K_a H_{fg} \rho_g (r_i + r_o) - (r_i q_i'' + r_o q_o'')} \tag{47}$$

we found:

- for P ≈ 7 MPa and 0.57 < G < 4 Mg/m²s

$$x_n = 0.302686 + 0.323285 * G^{-1} - 0.061864 * G^{-2} + 0.61698 * e^{-G} \tag{48}$$

- for P ≈ 10 MPa and 0.5 < G < 4 Mg/m²s

$$x_n = 0.323236 + 0.201339 * G^{-1.5} + 0.051459 * G^{-2} * Ln(G) + 0.38443 * e^{-G} \tag{49}$$

where G is in Mg/m²s. For the G values lower than indicated above x_n=1 was assumed. These x_n results are shown in Figure 9 together with the curves obtained by Kirillov and Smogalev [2].

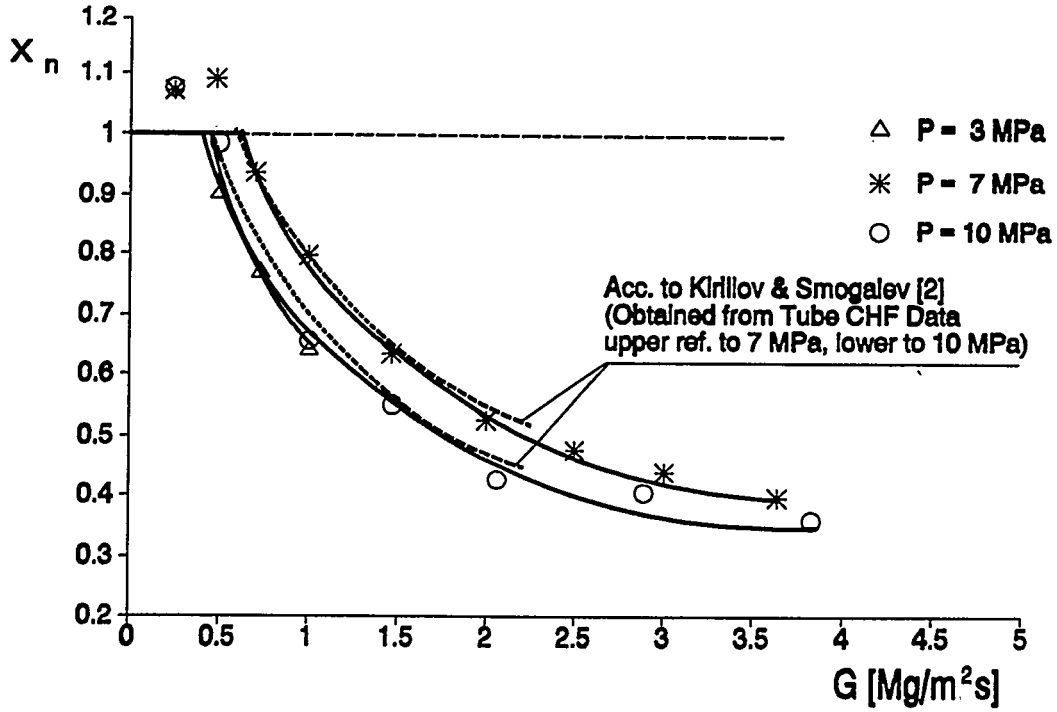

Figure 9: Comparison of Quality x_n Obtained from CHF Data of Bilaterally Heated Annulus with those Obtained by Kirillov & Smogalev [2] from Tube CHF Data, as Function of Mass Flux.

5.1.2 Prediction of CHF at the inner surface

Equation (29) defines CHF_i occurring at the inner surface, while the heat flux q''_o is supplied to the outer surface.

To use this equation first the quantity ϕ_o has to be determined. It can be done in two steps: (i) the quantity ϕ_{oi} (i.e., Equation (20)) can be retrieved from the CHF data obtained in internally heated annuli using Equation (23), and (ii) the unknown term $\Delta\phi_o$ of Equation (28) may be defined from the CHF data in bilaterally heated annuli for CHF occurrence at the inner surface.

The first step yields the unknown quantity A_{oi} in the form

$$A_{oi} = \left(x_n - x_c - \frac{CHF_i\, r_i\, x_n}{(r_i+r_o)K_a\, H_{fg}\, \rho_g}\right) * \frac{2\mu_g G\left(1+\left(\frac{\rho_f}{\rho_g}\right)^{0.5}\right)^2}{C_{oi}\sigma\rho_f\left(\frac{\rho_g}{\rho_f}\right)^{0.5}\left(1+\frac{\rho_f}{\rho_g}\right)} \tag{50}$$

This analysis is limited to pressures of 7 and 10 MPa due to limitation of the x_n characteristics. Among 1547 CHF data for concentric annuli with internal heating (Table 1 of Doerffer et al. [4]) there are 138 and 8 CHF points meeting conditions with respect to Equations (48) and (49). We found that:

- for P = 6.9 to 7.1 MPa and 0.57 < G < 4 Mg/m^{2}s

$$A_{oi} = 0.022174 + 0.000638*G^{2.5} - 0.008031*G^{-1.5} + 0.00272*G^{-2} \tag{51}$$

- for P = 9.8 to 10.2 MPa and 0.5 < G < 4 Mg/m^{2}s

$$A_{oi} = 0.066306 + 0.01678*(\ln G)^2 - 0.02709*G^{0.5} - 0.019618*G^{-1} \tag{52}$$

and are valid for the quality range $0.05 < x_e < 0.35$ (G is in Mg/m^{2}s). Having defined A_{oi} and thus ϕ_{oi} the CHF in internally heated annuli can be predicted using Equation (23).

To determine $\Delta\phi_o$ Equations (29) and (28) were rearranged and yield

$$\Delta\phi_o = \phi_{oi} - x_n + x_c + \frac{\left(CHF_i + \frac{r_o q_o''}{r_i}\right) r_i\, x_n}{(r_o + r_i)\, K_a H_{fg} \rho_g} \tag{53}$$

The functions $\Delta\phi_o$ of a general form

$$\Delta\phi_o = a\,(q_o'')^b\left(G^c + dG + eq_o''\right) \tag{54}$$

of mass flux and the outer surface heat flux, were found with the following coefficients:

- for P = 6.9 to 7.1 MPa and 0.5 < G < 4 Mg/m^{2}s

a = 0.467855,
b = 1.237649,
c = -0.999684,
d = 0.055746, and
e = -0.109612, (55)

- for P = 9.8 to 10.2 MPa and 0.5 < G < 4 Mg/m^{2}s

a = 0.586847,
b = 1.417714,
c = -1.307195,
d = 0.011097, and
e = 0.022094, (56)

where G is in Mg/m^2s and q''_o is in MW/m^2. Finally, having defined $\Delta\phi_o$, ϕ_o (Equation (28)) is determined and so the CHF_i at the inner surface in bilaterally heated annuli (Equation (29)).

5.1.3 Prediction of CHF at the outer surface

Following the same steps as in Section 4.2.2, the unknown quantities A_{ie} and $\Delta\phi_i$ are derived. The functions A_{ie} derived from the CHF experimental data of Becker and Letzter [3] for externally heated annuli are:

- for P = 6.9 to 7.1 MPa and $0.5 < G < 4$ Mg/m^2s

$$A_{ie} = 0.037945 + 0.3151*G^{-0.5} - 0.35825*G^{-1}*lnG - 0.34439*G^{-1.5} \quad (57)$$

- for P = 9.8 to 10.2 MPa and $0.5 < G < 4$ Mg/m^2s

$$A_{ie} = 0.04615 - 0.1258*G^{-1} + 0.09118*G^{-1.5} + 0.014224*G^{-2}*\ln G \quad (58)$$

and are valid for the quality range $0.22 < x_e < 0.65$ (G is in Mg/m^2s). A_{ie} and thus ϕ_{ie} allows the CHF prediction in externally heated annuli using Equation (39).

The functions for $\Delta\phi_i$ of the form (54), where q_o'' was replaced by q_i'', were found with the following coefficients:

- for P = 6.9 to 7.1 MPa and $0.5 < G < 3.8$ Mg/m^2s

a = 0.399263,
b = 1.464061,
c = -0.974858,
d = 0.070029, and
e = -0.339141, (59)

- for P = 9.8 to 10.2 MPa and $0.7 < G < 4$ Mg/m^2s

a = 0.228416,
b = 1.538116,
c = -2.354578,
d = -0.104088, and
e = 0.96837, (60)

where G is in Mg/m^2s and q''_i is in MW/m^2. Now, having defined $\Delta\phi_i$, Equation (42) can be used to predict CHF_o at the outer surface in bilaterally heated annuli.

5.2 Comparison of Model Results with Experimental Results and Discussion

A direct use of K_a and x_n functions, obtained by Kirillov and Smogalev [2] from tube CHF data, allowed the CHF prediction in bilaterally heated annulus only for simultaneous CHF occurrence at both surfaces at known ratio R.

The agreement with the experimental data is very good as shown in Table 2 (seven CHF points). Our extension of x_n function, obtained from annulus CHF data, allows CHF prediction over wider range of mass flux also with good accuracy (Table 2, 15 CHF points).

The good agreement between Kirillov's and our x_n functions (see Figure 9), strongly suggests similar physical mechanism governing the dryout-type CHF in tubes and annuli, especially in bilaterally heated annuli with simultaneous CHF occurrence at both surfaces.

An agreement between the CHF data and the corresponding predicted values for internal and external heating, and for CHF at the inner and outer surfaces during bilateral heating is also very good as shown in Table 2, and in Figures 3 and 7. Figure 3 illustrates this comparison for CHF_i at P = 7 MPa and G = 1.5 Mg/m^2s with increasing the heat flux applied to the outer surface, q''_o (or increasing the ratio q''_o/q''_i). The predicted characteristic for the simultaneous CHF at both surfaces (Equation (45)) is also shown. The intersection of these two characteristics determines the simultaneous CHF occurrence. It can served as a criterion defining the simultaneous CHF occurrence. Beyond this point CHF can occur only at the outer surface.

To make above predictions possible empirical functions such as ϕ_{oi}, ϕ_{ie}, $\Delta\phi_o$ and $\Delta\phi_i$ were derived form the data of Becker and Letzter [3]. Unfortunately, the limited range of the data limits the range of the functions' application.

Some interesting observations can be drawn from Equations (28) and (29), particularly the effect of the term $\Delta\phi_o$, which describes a contribution of vapour generation at the outer surface due to the heat flux, q''_o, to the critical quality as shown in Figure 10. The experimental CHF_i data show a linear dependence between this term and the critical quality for a given mass flux with the heat flux, q''_o, as a parameter. The higher q''_o the higher increase of the term and the higher x_e at a given mass flux. On the other hand, the higher mass flux the lower critical quality and the lower contribution of the term.

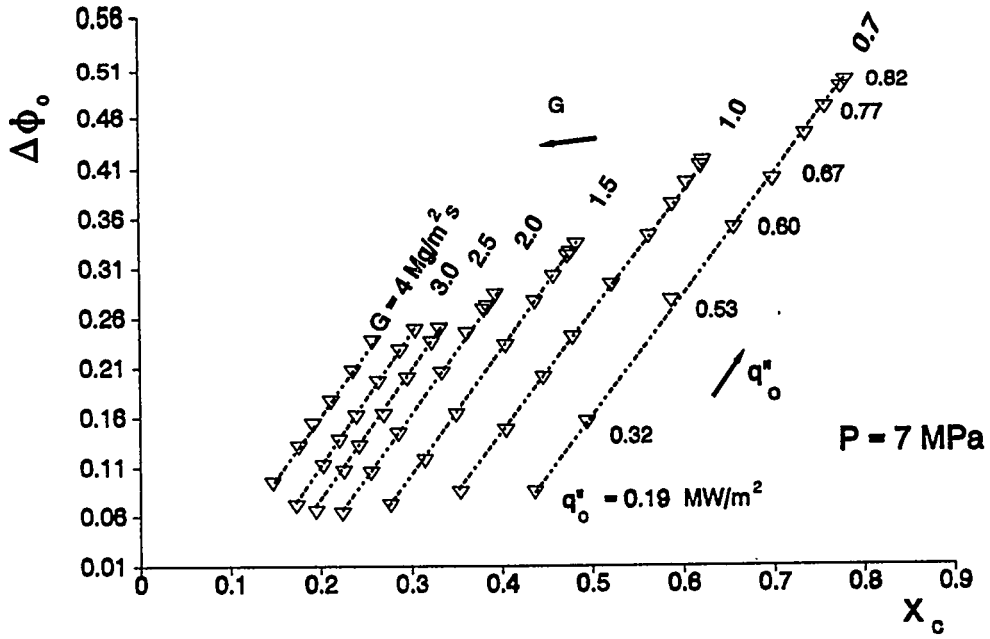

Figure 10: Contribution of Heat Flux at Outer Surface, q''_o, in Bilaterally Heated Annulus to Changes in Critical Quality while CHF Occurs Only at Inner Surface.

An extension of every line in Figure 10 up to the intersection with the axis x_e defines the x_e value at $q''_o = 0$ (i.e., at internal heating, where flowing liquid film at the outer surface does not evaporate or change the critical quality). A comparison of the x_e values obtained from these extrapolations with those from Becker and Letzter's [3]

experiments in internally heated annulus confirms this observation (e.g., at P = 7 MPa, G = 1 Mg/m^{2}s those values are 0.29 and 0.296, respectively).

Similarly, the effect of $\Delta\phi_i$ on the critical quality x_c when CHF occurs at the outer surface is shown in Figure 11. An extension of every line in Figure 11 up to the intersection with the axis x_c defines the value of x_c at $q''_i = 0$ (i.e., at external heating), and these values are almost identical to those of the Becker and Letzter [3] data obtained in the externally heated annulus.

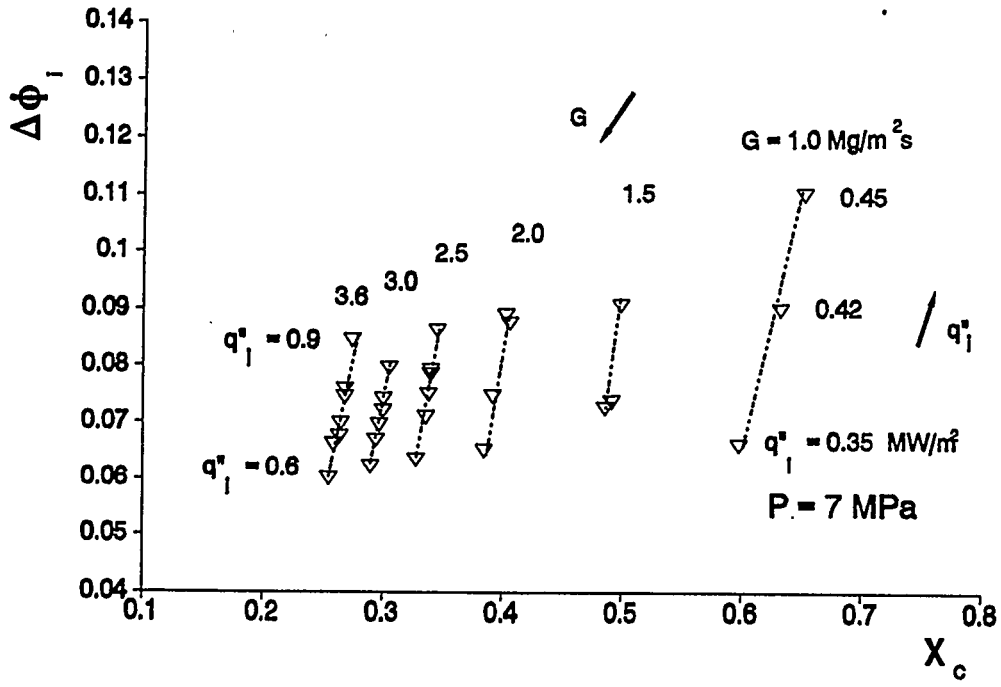

Figure 11: Contribution of Heat Flux at Inner Surface, q'$_i$, in Bilaterally Heated Annulus to Changes in Critical Quality while CHF Occurs Only at Outer Surface.

A comparison of both terms, $\Delta\phi_o$ and $\Delta\phi_i$, indicates that for the CHF occurrence at the inner surface the heat flux applied to the outer surface, q''_o, generates much more vapour and increases the critical quality much more (demonstrated by a smaller slope of the curves in Figure 10) than for the case of Figure 11, where the curves are steeper and the values of the term $\Delta\phi_i$ are much lower.

In addition, a qualitative analysis of general Equations (29), (42) and (45) shows agreement between the trends predicted by these equations with those of the experimental data. Equation (29) reflects correctly the effect of the heat flux q''_o on CHF_i (compare with Figure 3). Equation (42) shows a much weaker effect of q''_i on CHF_o than the effect of q''_o on CHF_i (compare Figures 3 and 6; and also compare the last terms in Equations (29) and (42)). Finally, Equation (45) predicts the correct relation between CHF_i and the ratio $q''_o/q''_i = CHF_o/CHF_i$ during simultaneous CHF at both surfaces (the equivalent trend is shown in Figure 5).

6. CONCLUSIONS AND FINAL REMARKS

This paper investigates the effect of bilateral heating on CHF of the dryout type in annuli and compares it with that in tubes and unilaterally heated annuli. Also, it provides the CHF prediction method for bilaterally heated annuli. It was found that the predicted CHF trends agree well with those observed from the experiments, especially:

- The heat addition to one surface of an annulus (where CHF does not occur) enhances CHF at the other surface (due to an enhancement of droplet deposition). Therefore, the corresponding CHF values in unilaterally heated annuli are always lower than those in bilaterally heated annuli.

- The CHF occurring at the outer annulus surface is less sensitive to the heat addition to the inner surface than that in the opposite case.

- During simultaneous CHF occurrence at both annulus surfaces, the CHF_o is always larger than the CHF_i, and this difference is a strong function of pressure.

- The q''_o/q''_i ratio determines the location of CHF occurrence in bilaterally heated annuli.

In addition, the corresponding CHF value in a tube is always larger than that in an annulus regardless of a mode of heat supply to the annulus. The CHF_o value can be predicted from the tube CHF prediction method within the ranges of pressure 7-10 MPa, mass flux 0.5-4.0 Mg/m^2s and critical quality 0.23-0.9, when CHF occurs simultaneously at both surfaces and D_{he} is the characteristic dimension.

As CHF was primarily obtained at conditions far away from the spacers (i.e., the most downstream spacer plane was located 630 mm from the CHF location, or $L_{SP}/D_{he} = 68$, in the Becker and Letzter [3] experiments), the effect of spacers on CHF is considered to be minimal. However, in fuel designs with short axial spacings between spacer planes (i.e., $L_{SP}/D_{he} < 40$) the results will be affected by spacer-generated turbulence, which may reduce the CHF differences between two adjacent heated surfaces.

For the first time a CHF prediction method is proposed to cover all cases of CHF occurrence in bilaterally heated annuli for annular flow type dryout, including a prediction of the radial location of dryout.

It is also the first practical application of the Kirillov and Smogalev droplet-diffusion model [2] for CHF occurrence at the inner annulus surface, and our further development of their method for CHF occurrence at the outer surface and for simultaneous CHF occurrence at both surfaces.

We noted, that the quantity x_n is almost identical in tubes and annuli. It suggests the similarity in CHF mechanisms for both geometries. In this study we extended the range of x_n beyond that of Kirillov and Smogalev [2].

Presently, this successful application is limited to the data range used in this study, due to a limited range of validity of the empirical functions derived from the data. Especially, the functions $\Delta\phi_i$ and $\Delta\phi_o$, which depend on the upstream flow history, should be developed for wider range of conditions, or derived from theoretical considerations.

The results presented in this paper suggest a further refinement of the mechanistic model of Kirillov and Smogalev [1,2]. This should eventually lead to a general analytical CHF prediction method valid not only for bilaterally heated annuli but also for similar flow geometries such as rectangular channel, a rod surrounded by a channel of irregular shape, and finally for a fuel bundle.

7. REFERENCES

[1] P.L. Kirillov and I.P. Smogalev, "Calculating the Heat Exchange Crisis for a Vapour-Liquid Mixture on the Basis of a Droplet-Diffusion Model", Institute of Physics and Power, Obninsk, USSR, Report No. FEI-181 (1969).

[2] P.L. Kirillov and I.P. Smogalev, "Calculation of Heat-Transfer Crisis for Annular Two-Phase Flow of a Steam-Liquid Mixture Through an Annular Channel", translation from Report FEI-297 of the Physics and Power-Engineering Institute, Obninsk, USSR (1972), as Report AECL-4752 of Chalk River Laboratories (1974).

[3] K.M. Becker and A. Letzter, "Burnout Measurements for Flow of Water in Annulus with Two-Sided Heating",

Paper presented at the European Two-Phase Flow Group Meeting in Haifa, Israel (1975).

[4] S. Doerffer, D.C. Groeneveld, S.C. Cheng and K.F. Rudzinski, "A Comparison of Critical Heat Flux in Tubes and Annuli", Proc. NURETH-6, Grenoble, France, 1, pp. 707-714 (1993), and extended version in Nucl. Engrg. Des., 149, pp. 167-175 (1994).

[5] K.M. Becker, G. Hernborg, M. Bode and O. Eriksson, "Burnout Data of Boiling water in Vertical Round Ducts, Annuli and Rod Clusters", Report AE-177 of Heat Engineering Laboratory, AB, Atomenergi, Sweden (1965).

[6] D.C. Groeneveld, S.C. Cheng and T. Doan, "1986 AECL-UO Critical Heat Flux Lookup Table", Heat Transfer Engineering, vol. 7, nos 1-2, pp. 46-62 (1986).

[7] A. Jansen and G. Mannov, "Burnout, Film Flow, Film Thickness and Pressure Drop in a Concentric Annulus 3500 x 26 x 17 With Heated Rod and Tube", Danish Atomic Energy Commission, SDS-77 (1974).

[8] G.V. Alekseev, O.L. Peskov, O.V. Remizov, B.A. Zenkevich and V.I. Subbotin, "Critical Heat Flux Densities with Forced Flow of water", Teploenergetika, vol. 12, No. 3, pp. 47-51 (1965).

[9] J.G. Collier, P.M.C. Lacey and D.J. Pulling, "Heat Transfer to Two-Phase Gas-Liquid Systems Part 3, The Effects of proximity of Other Heated Surfaces", AERE-R-3960 (1964).

[10] F.E. Tippets, "Critical Heat Fluxes and Flow Patterns in High Pressure Boiling water Flows", ASME Winter Annual Meeting, Paper 62-WA-162, New York (1962).

[11] V.I. Tolubinskiy, A.K. Litoshenko, YE.D. Damashev, A.S. Kravchenko and D.A. Chirov, "Heat Transfer Crisis at the Inward Surface of Annuli Heated from Both Sides", Heat Transfer-Soviet Research, vol. 5, No. 3, pp. 93-96 (1973).

[12] A.P. Ornatskiy, L.F. Glushchenko and A.M. Kichigin, "Burnout in Annular Channel with Two-Sided Heating", Heat Transfer-Soviet Research, Vol. 1, No. 6, pp. 12-16 (1969).

[13] S. Doerffer and S.C. Cheng, "The Effect of Flow Cross-Section on the Critical Heat Flux - CHF Characteristics in Concentric and Eccentric Annuli with Uni- and Bilateral Heating", Report of University of Ottawa, Dept. of Mech. Engrg. (1994).

[14] J.G. Knudsen and D.L. Katz, Fluid Dynamics and Heat Transfer, McGraw-Hill Book Co., Inc., N.Y., p. 186 (1958).

[15] J.A. Brighton and J.B. Jones, "Fully Developed Turbulent Flow in Annuli", Transactions of the ASME, Journal of Basic Engineering, December, pp. 835-844 (1964).

[16] T. Saito, E.D. Hughes and M.W. Carbon, "Multi-Fluid Modelling of Annular Two-Phase Flow", Nuclear Engineering and Design, vol. 50, pp. 225-271 (1978).

[17] F.E. Tippets, "Analysis of the Critical Heat-Flux Conditions in High-Pressure Boiling Water Flows", Trans.of ASME, J. Heat Transfer, vol. 86, series C, No. 1, pp. 23-38 (1964).

8. NOMENCLATURE

A - function defined by Equation (50),
avg - average error [%],
B,C - auxiliary functions defined by Equations (21, 22 and 38),

C - concentration of droplets [kg/m^3],
CHF - critical heat flux [kW/m^2],
D - diameter [mm],
D* - deposition rate [kg/m^2.s],
E - fraction of liquid entrained [-],
error - (predicted CHF - experimental CHF)/ experimental CHF,
G - mass flux [Mg/m^2.s],
H - enthalpy [kJ/kg],
K_a - deposition coefficient in adiabatic conditions, defined by Equation (46) [m/s],
K_q - deposition coefficient in diabatic conditions [m/s],
L - heated length [m],
$L_{\Delta P}$ - distance from tube inlet to point at which entrainment ceases [m],
n - fraction of deposition rate on a given surface [-],
P - pressure [MPa],
p - perimeter [m],
q" - heat flux [kW/m^2],
R - outer-to-inner surface heat flux ratio, $q"_o/q"_i$, [-],
S - slip ratio [-],
r - radius [m],
rms - root mean square error [%],
v - average velocity [m/s],
x - quality [-],
x_n - quality at which deposition ceases [-],
x_{nl} - difference of qualities x_n and $x_{\Delta P}$ [-],
$x_{\Delta P}$ - quality at which entrainment ceases [-],
Γ - liquid flow rate [kg/s],
Δx - quality shift [-],
Δ - change,
δ - liquid film thickness [m],
μ - dynamic viscosity [kg/m.s],
Φ - fraction of liquid flowing as a film [-],
ρ - density [kg/m^3],
σ - surface tension [N/m],
τ - shear stress [N/m^2],

Subscripts

an - section at which annular flow regime begins,
An - annulus,
c - critical, at CHF location,
dep - deposition,
D - refers to tube of a given ID,
e - entry of test section,
f - saturated liquid; liquid film,
g - saturated vapour,
fg - latent heat,
he - heated equivalent diameter of annulus,
hy - hydraulic equivalent diameter of annulus,
i - on inner surface for to bilateral heating,
ie - on inner surface for external heating,
ii - on inner surface for internal heating,
m - corresponds to radius of maximum flow velocity,
n - corresponds to minimum liquid in the core for adiabatic conditions,
nq - corresponds to minimum liquid in the core at CHF section in diabatic conditions,

o - on outer surface for bilateral heating,
oe - on outer surface for external heating,
oi - on outer surface for internal heating,
SP - spacer plane; spacer pitch,
T - total flow (liquid + vapour),

Superscripts:

c - core flow.

Experience Using Individually Supplied Heater Rods in Critical Power Testing of Advanced BWR Fuel

by

M. Majed, G. Norback, P. Wiman
ABB Atom AB
S–721 63 Vasteras, Sweden
Telephone: +46 (21) 347000
Telefax: +46 (21) 147862

G.I. Hadaller, R.C. Hayes, F. Stern
Stern Laboratories Inc.
1590 Burlington Street East
Hamilton, Ontario, Canada L8H 3L3
Telephone: +1 (905) 548-5300
Telefax: +1 (905) 545-5399

Abstract

The ABB Atom FRIGG loop located in Vasteras Sweden has during the last six years given a large experience of critical power measurements for BWR fuel designs using indirectly heated rods with individual power supply. The loop was built in the sixties and designed for maximum 100 bar pressure. Testing up to the mid eighties was performed with directly heated rods using a 9 MW, 80 kA power supply.

Providing test data to develop critical power correlations for BWR fuel assemblies requires testing with many radial power distributions over the full range of hydraulic conditions. Indirectly heated rods give large advantages for the testing procedure, particularly convenient for variation of individual rod power. A test method being used at Stern Laboratories (formerly Westinghouse Canada) since the early sixties, allows one fuel assembly to simulate all required radial power distributions. This technique requires reliable indirectly heated rods with independently controlled power supplies and uses insulated electric fuel rod simulators with built–in instrumentation.

The FRIGG loop was adapted to this system in 1987. A 4 MW power supply with 10 individual units was then installed, and has since been used for testing 24 and 25 rod bundles simulating one subbundle of SVEA–96/100 type fuel assemblies. The experience with the system is very good, as being presented, and it is selected also for a planned upgrading of the facility to 15 MW.

FRIGG Loop History and Description

The FRIGG loop was built in 1965 for full scale thermal–hydraulic testing of simulated BHWR and BWR fuel assemblies [1]. It is still in extensive use and a major upgrading is even underway. Although the general layout of the loop is unchanged (Figure 1), numerous modifications have taken place over the years, in particular with regard to control and instrumentation systems, and power supply. It is interesting to note that the carbon steel piping and pressure vessels are still in very good condition, thanks to careful water chemistry control and preservation measures.

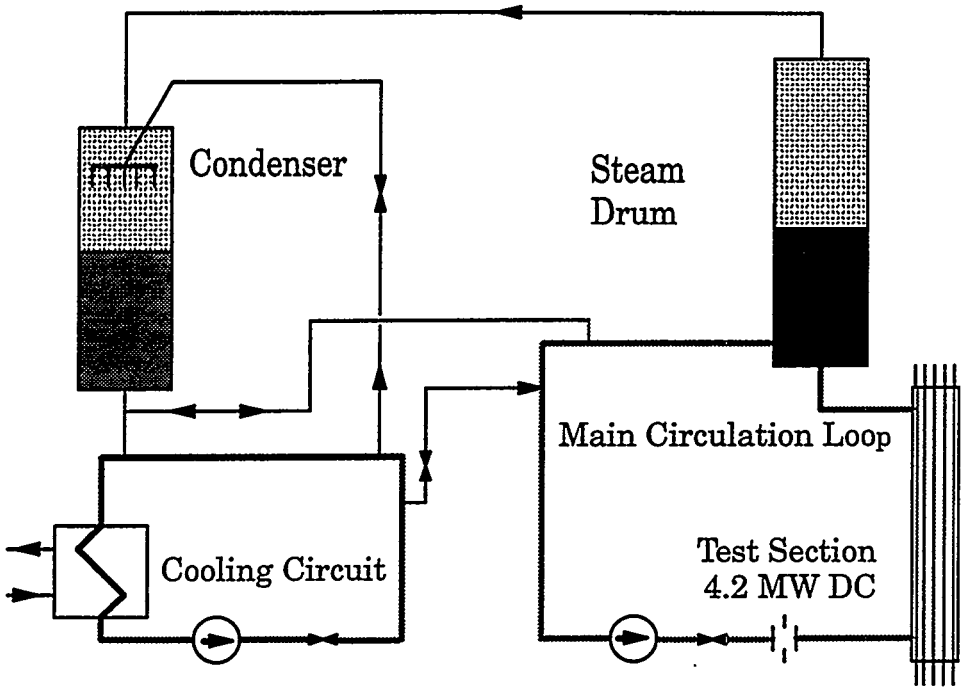

Figure 1. Schematic of FRIGG Loop

A major change in experimental technique took place in 1987, when the use of directly heated rods was abandoned in favour of indirectly heated. Such rods were previously used also in the FRIGG loop for LOCA testing but were up to then not considered mature for critical power testing.

The use of indirectly heated rods offers several important advantages:

- Low electromagnetic forces between rods because of high voltage and thus low currents with a helical current path.
- No electrical insulation of the channel needed.
- Radial power distribution can be easily changed during the experiment.
- Thermocouples are at ground potential.

The change to indirectly heated rods was tied to the development of new multirod fuel versions, SVEA–96 and SVEA–100 (Figure 2). Low electromagnetic forces were considered essential for testing with the relatively slim rods of those designs. The requirement for the detailed investigations of the effect of the radial power distribution was another strong driver. The existing 9 MW low voltage power supply was replaced by a new 4 MW high voltage power supply consisting of ten individually controlled rectifier units. The lower total power was chosen as being adequate for testing one SVEA–96/100 sub–bundle with 24 or 25 rods.

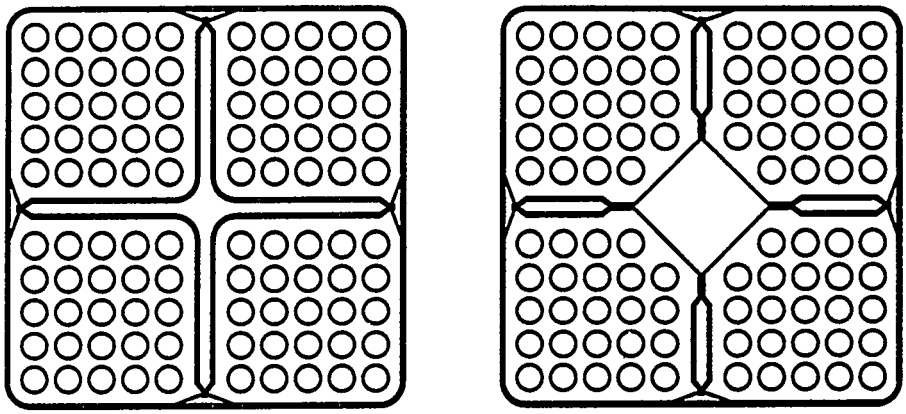

SVEA–100 SVEA–96

Figure 2. SVEA–5x5 Design Versions and Simulated Geometries

The new power supply has a maximum voltage of 400 V. Six rectifiers have a maximum current of 800 A and four 1600 A. The rods are grouped with one to four rods on each rectifier. To optimize the radial power distribution and to test the sensitivity of individual rods, grouping may have to be altered several times during an experiment.

A detailed description of the development and manufacturing of the rods is given below. The principle design of a test section consisting of a pressure vessel with the flow channel and the rods is shown in Figure 3. The rods are supplied with up to eight themocouples at different axial positions where dryout is expected to occur, generally upstream of spacers and at the end of heated length. The flow channel is cut out and rewelded from an actual full assembly Zircaloy channel. The indirectly heated rods enable this to be used without electrical insulation. Along the channel are pressure taps for detailed single– and two–phase pressure drop measurements.

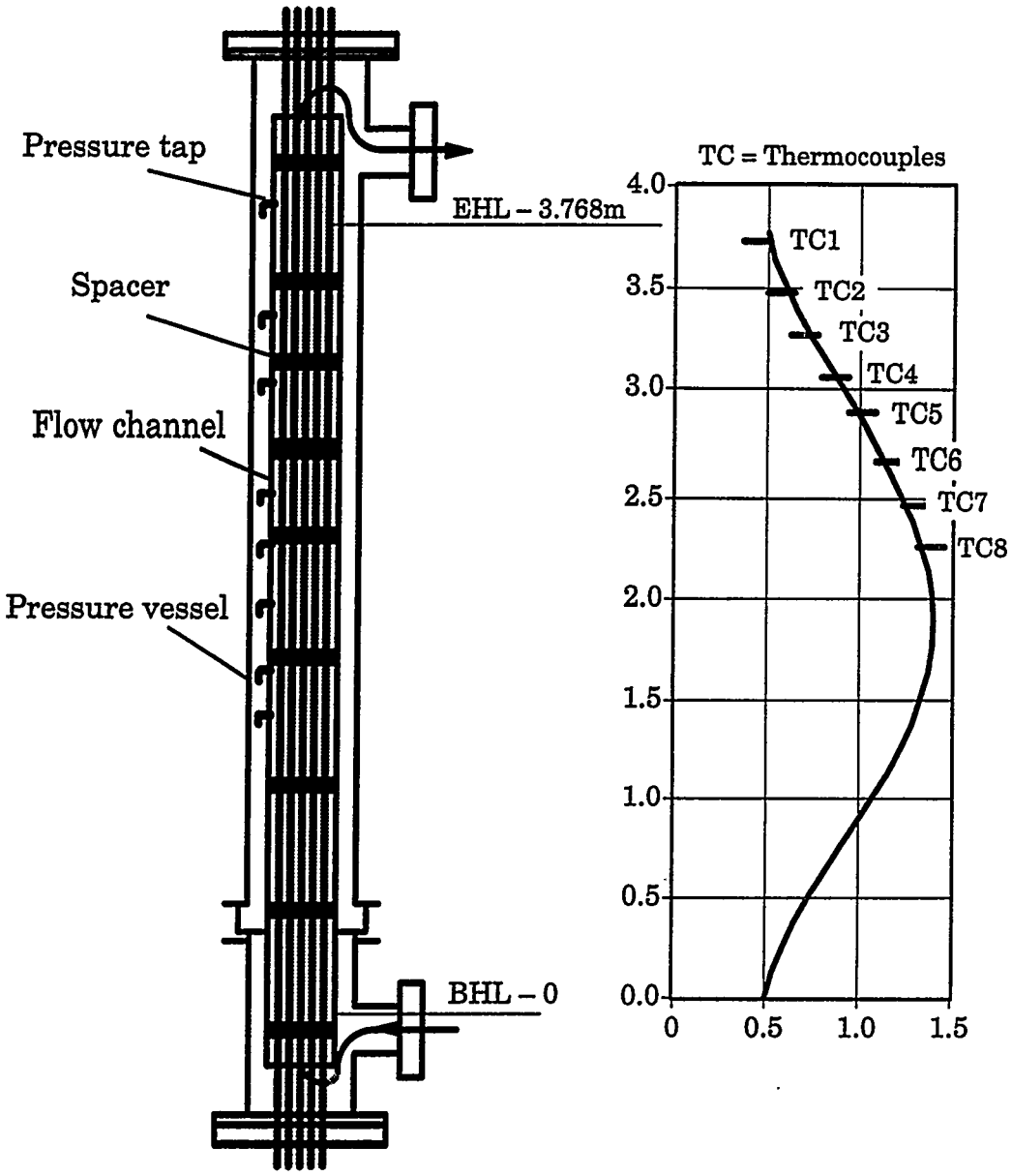

Figure 3. Axial Geometry and Power Distribution of the Test Section

The results of early SVEA–96/100 tests with this system were presented in [2]. Since then, a lot more experience has been gained during continued testing in support of the fuel development. It is the objective of this paper to discuss some of this experience with emphasis on the experimental technique.

History of Development and Manufacturing of the Rods

Development of electrically heated fuel simulators started at what is now Stern Laboratories in the early 1960's [3]. For these early heaters, the filaments were made by winding uniform width Kanthal or Nichrome ribbon in a helix, and welding this to steel electrodes. Electrical insulation was

provided by magnesia powder and thermocouples were placed in external grooves in the thick walled stainless steel sheaths.

These heaters were built by Stern Lab. Inc. for use in their laboratory, and their many weaknesses soon became apparent, as did the significant cost associated with unreliable heaters. Over the thirty years since then, the problems have been eliminated one by one, and the design and manufacturing techniques have been continuously refined to improve all aspects of heater performance. Apart from heaters designed for Critical Heat Flux experiments, which operate typically at external sheath temperatures no higher than 350°C, but at heat fluxes up to 350 W/cm^2, many heaters have been designed and built for Loss of Emergency Core Cooling experiments. These have to perform reliably at much higher temperatures (1100°C) but at much lower fluxes.

The most common type of failures encountered by Stern Lab. Inc. with the early indirect heaters were due to failure of the termination weld, i.e. the weld joining the filament ribbon to the electrode at the end of the heated length, and arcing from the filament to the sheath. In both cases, the heat generated locally by the arc quickly cuts through the sheath wall, resulting in damage to neighboring heaters. This necessitates rebuilding of the fuel assembly with several replacement heaters, usually a very expensive disruption of the program.

The current design has eliminated the termination failure problem by making the filament from a seamless tube, which is laser cut into a helix on a numerically controlled machine. Figure 4 shows a schematic of a completed heater used in the FRIGG tests and illustrates how the termination weld has been eliminated. The cut simply does not go all the way to the end of the tube but leaves a short length of intact tube for welding to the electrode. Laser cutting from tubing also eliminates the curling up of the edges of the ribbon due to the deformation caused by winding. This allows the average distance between the sheath and the filament to be reduced, and thereby permits an increase in heat flux without exceeding the filament temperature limit. It also, because of the narrow, uniform gap between turns, achieved even with non–uniform axial heat flux profiles, practically eliminates the valleys seen in the longitudinal heat flux with wound filaments at the gap between turns. Replacement of the powder filled magnesium dioxide insulation by hot pressed boron nitride (BN) sleeves addresses the problem of filament to sheath arcing by ensuring excellent concentricity and hence excellent circumferential uniformity in the surface heat flux. The BN also has better thermal conductivity, resulting in lower internal temperatures, as well as having greater thermal stability, enabling post CHF temperature determination without significant risk of heater failure.

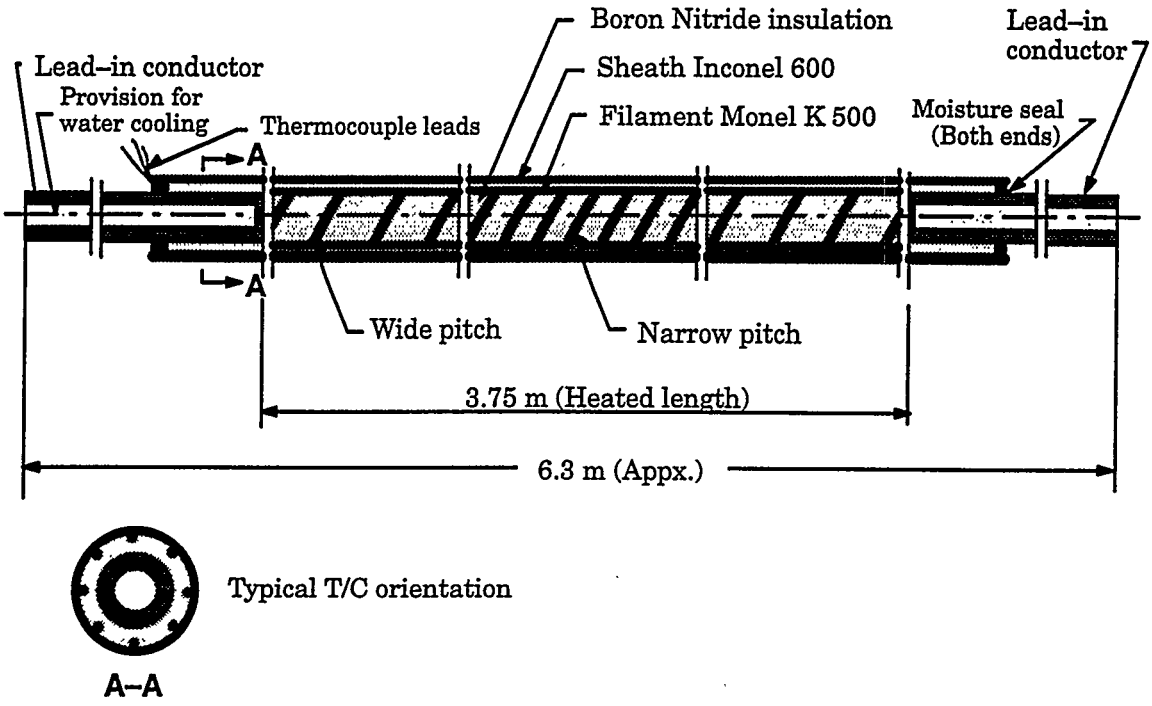

Figure 4. Heater Rod Design

Stern Lab. continues to use their fuel simulators with great success in their own loop facilities, and consider the cost of producing them of secondary importance, because of the very considerable cost of the failure of just one heater of inferior design during loop operation.

Each heater is custom designed usually starting with a specified operating voltage, total power, heated length, axial power distribution and finished diameter. The heater filament diameter and wall thickness are chosen to provide at least 0.7 mm of BN below the thermocouple groove and provide the appropriate resistance to match the specified supply voltage and power. Generally the wall thickness is also adjusted to provide a pitch to diameter ratio in the filament of one or greater at the peak power location. Custom software is used to compute the angular rotation required for each cut step to match the required axial power profile. Adjustments are made to the cut filament length to account for the increase that occurs during final swaging while achieving the required finished resistance. The maximum filament temperature is calculated and adjustments are made to component thickness to ensure that this does not exceed a limiting value, based on the melting point of the filament material.

The present heaters have filaments laser cut from Monel or Inconel tubing and can be provided with axial power profiles having a peak to average ratio of up to 1.6. The filaments are precision cut in steps of constant pitch, where the number of steps is at the customer's discretion, usually between 200 to 500. The heaters used here had 248 steps or 70 steps per meter

having a peak to average ratio of up to 1.6. The filaments are precision cut in steps of constant pitch, where the number of steps is at the customer's discretion, usually between 200 to 500. The heaters used here had 248 steps or 70 steps per meter of heated length. After the internal space is filled with cylindrical slugs of BN, the uncut ends are welded to short nickel transition electrodes, which in turn are brazed to copper electrodes. The gaps between turns are packed with BN powder, and BN sleeves with 100 % x–ray inspection are assembled over the full length to be sheathed.

With the BN sleeves held tightly in place, round bottomed grooves are cut longitudinally in the sleeves to accommodate the thermocouple instrumentation. This is then placed in the grooves with the junction at the specified location, and the whole subassembly is inserted into the oversized sheath and thoroughly dried by heating in a vacuum and back–filling with helium when cold. The assembly is then swaged for a number of passes, until the specified outside diameter and degree of compaction are reached. The sheath is cut to length and heater resistance and insulation resistance are measured and the sheath to electrode ends are sealed with a room temperature vulcanizing (RTV) compound. The locations of the thermocouple junctions are determined by flux probing with a soldering iron, and each location is marked on the exterior of the sheath.

For high power, small diameter components such as the ones used in the present experiments, the heat generated in the "unheated length" outside the test section pressure boundary, by I^2R losses in the electrodes, presents a problem. This has been solved by making copper electrodes from thick walled tubing, and inserting a small hypodermic style tube into this to form a re–entrant path for water cooling.

This particular design of fuel simulator with a Zircaloy sheath was used for the Quad +/SVEA–C test program conducted at Stern Lab in Hamilton both with uniform axial and symmetric cosine power distributions. With the use of indirect heaters and six power zones 38 different radial power distributions were tested. Changes between distributions were made by a combination of cable reconnections or by simple changes in the relative input from each power zone by adjusting constants in the computer software. In total about 3000 data points were taken with this arrangement. Some problems developed at high powers with the cosine profile after about 1000 test points when heater failures began occurring. It was discovered that the heater sheaths were increasing in diameter due to creeping of the Zircaloy cladding. A light swage of the sheath eliminated this failure mode and allowed for completion of the program. This problem has not been observed with stronger Inconel sheaths used in the FRIGG tests.

FRIGG Loop Applications

Twenty–seven critical power experiments performed during the years 1988–1994 in the FRIGG loop have given the experience of more than 13000 critical power data points, making successful improvements of the critical power performance of the SVEA–96/100 fuel possible. The large amount of data is due to the convenience of independent power supply and indirectly heated rods.

Due to the indirect heating of the rods, the radial power distribution can be modified within less than five minutes, unless rectifier connection modification is necessary. The convenience of altering the radial power distribution is a large advantage for collecting the sufficiently large amounts of relevant data needed to develop accurate CPR correlations and to investigate critical power performances of certain rods.

Further advantages discovered during the experience of individually controlled heater rods are the possibilities to investigate the impact of the radial void distribution on two–phase pressure drop and stability.

The experience of the heater rod reliability is very good. Some of the heater rods from the first delivery from Stern Lab. Inc. (December 1987) have been used in all of these experiments. Some problems have occurred due to corrosion in thermocouple leads under the fiberglass sleeving (Figure 4), occurring after a large amount of experiments. To prevent these corrosion problems, an electric fan heater has been used to keep the connections dry. The heater rod connection polarity has also been altered. Even if the usage of the fan heater inhibits the corrosion procedure it does not eliminate them. Some rods with corroded thermocouple leads have been sent to Stern Lab. Inc., and most of these rods have been successfully repaired.

Once, due to water leakage at the test section's inlet (lower) part, a flash–over occurred during one of the many experiments, causing damage to the heater rod connections. However, after a rather simple reparation of the connections no malfunction of the heater rods was detected.

The FRIGG loop will be upgraded during summer 1995 to allow measurements on a full SVEA fuel bundle. The capacity of the power supply will be increased from 4 MW to 15 MW. Due to the very good experience of the indirectly heated rods, the same heater rod design and the same type of power supply system will be used.

In most cases, a so called fuel development experiment is performed to investigate the impacts of design alterings, e.g. spacer design, axial spacer positioning or numbers of spacers

on the critical power performance. During a fuel development experiment different radial power distributions are tested, generally only at 70 bar pressure and 10 K subcooling, but each radial power distribution at mass fluxes from 500 to 2000 kg/m^2s to obtain critical powers for uniform and optimized radial power distributions. The so called optimized radial power distribution is obtained when dryout occurs on most of the rods, and the bundle critical power is maximized. In the described experiment type, the number of radial power distributions generally is within the range 20–45, and the experiment lasts about one and a half week, within 16 hours of testing per workday.

Larger experiments are performed to verify thermal–hydraulic performance of a new fuel design.

Development and verification of CPR correlations

To determine CPR correlations, testing with a large amount of different radial power distributions at different pressure (25–85 bar) and subcooling (5–40 K) are required. More than 1300 critical power data points, covering 115 radial power distributions, were obtained at the SVEA–96+ [4] design experiments. The large amount of radial power distributions is necessary to investigate local dryout performance for each rod, and to create a sufficient correlation development data base. Such an experiment lasts 3–4 weeks.

The SVEA–96+ fuel type assembly, used as an example, is a further developed SVEA–96 fuel type assembly. The number of spacers are increased from 6 to 7 to increase the critical power. The spacer frame has been designed for minimum flow obstruction and maximum ability to shave off the coolant film from the channel walls. The upper portion of the frame has been given features to divert the water towards the fuel rods, favouring particularly the corner rods.

In the SVEA–96+ design, the spacer distance in the upper part of the fuel bundle is 2/3 of the spacer distance at the corresponding region in the SVEA–96 design. By improving the spacer design, increasing of the numbers of spacers from 6 to 7, and by reducing the spacer distance in the upper part of the fuel bundle,the critical power improved by about 12% compared with the original SVEA–96 fuel design, as shown in Figure 5.

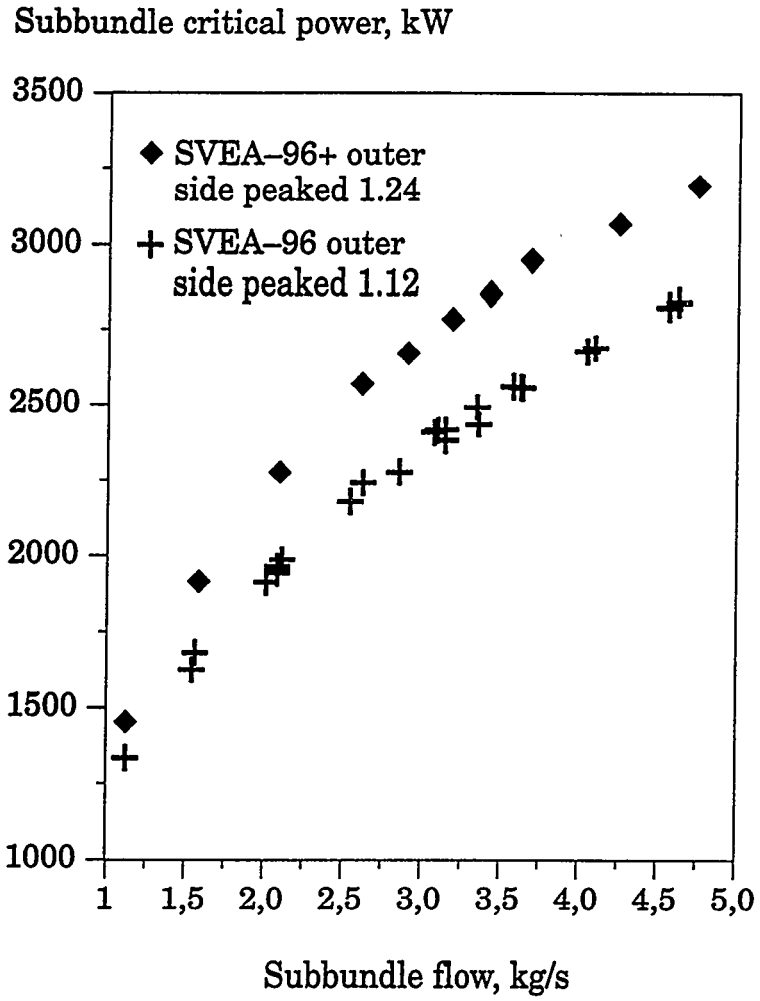

Figure 5. SVEA–96+ and SVEA–96 critical power comparison

Of historical reasons two types of CPR correlations are used by ABB Atom for the SVEA fuel designs:

- local type (for SVEA–100 fuel in ABB designed BWR:s)
  $\phi_{crit} = f(x,G,D_{heat},p)$
- boiling length type (for SVEA–96 and SVEA–96+ fuels in BWR:s from other vendors)
  $x_{crit} = f(L_B,G, D_{heat},p)$

where

ϕ_{crit} = critical heat flux
x_{crit} = critical steam quality
x = steam quality
G = mass flux
D_{heat} = heated diameter ($4 \times A_{flow}/U_{heat}$)
A_{flow} = flow area
U_{heat} = heated perimeter
p = pressure
L_B = boiling length

A weighting factor model is used to take into account the impact of local power distribution on CPR and corresponding additive constants for different fuel designs are used in this model.

The base CPR correlation (boiling length type) with new correction multipliers for mass flux, pressure and boiling length was developed by ABB Atom for SVEA–96+ fuel design and named XL–96+.

The XL–96+ CPR correlation is based on 1393 data items, and the obtained mean error is –0.014, and the standard deviation is 1.737. The XL–96+ CPR correlation is valid within the following ranges:

Pressure:	25 – 85 bar
Mass flux:	341 – 2090 kg/(m^2,s)
Subcooling:	4 – 49 K

As illustrated in Figure 6, the data obtained from the measurements and the accuracy of the CPR correlation for SVEA–96+ type fuel assembly are very good, most of the error of the dryout points are in between ±3.5%, even if it covers 115 different radial power distributions.

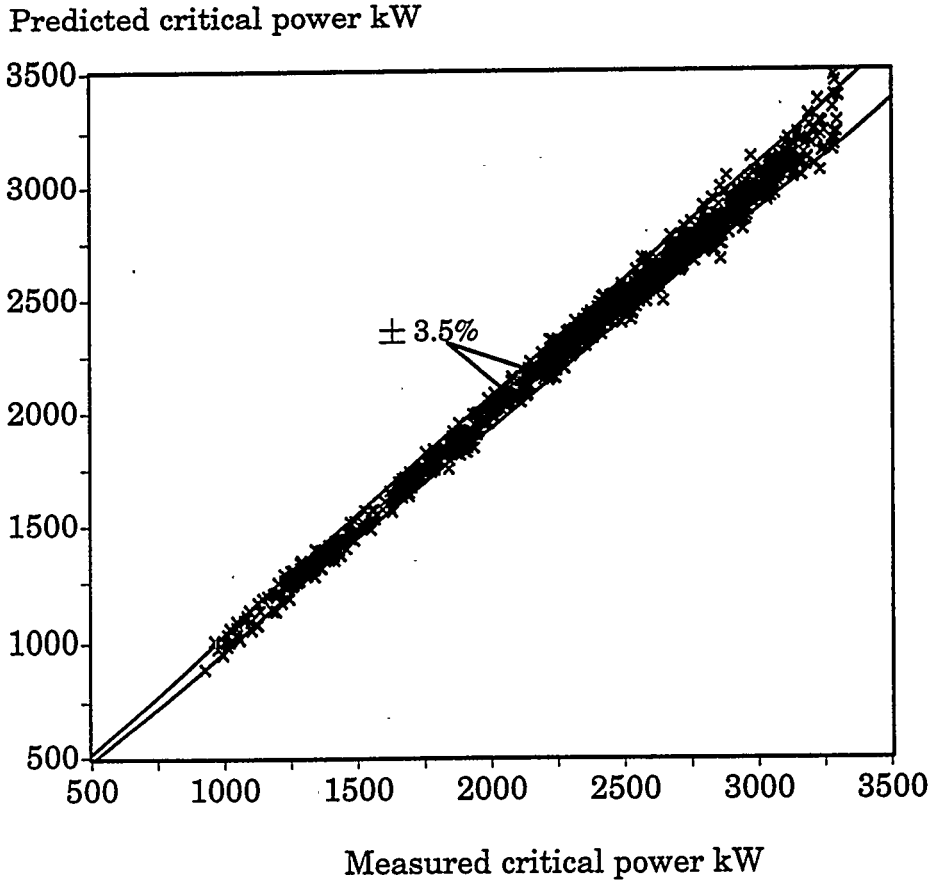

Figure 6. Predicted critical power from XL–96+ dryout correlation versus measured critical power

Figures 7–10 show the errors in dryout power plotted versus pressure, mass flux, subcooling and boiling length respectively. As can be seen, there are no biases depending on pressure, mass flux, subcooling or boiling length.

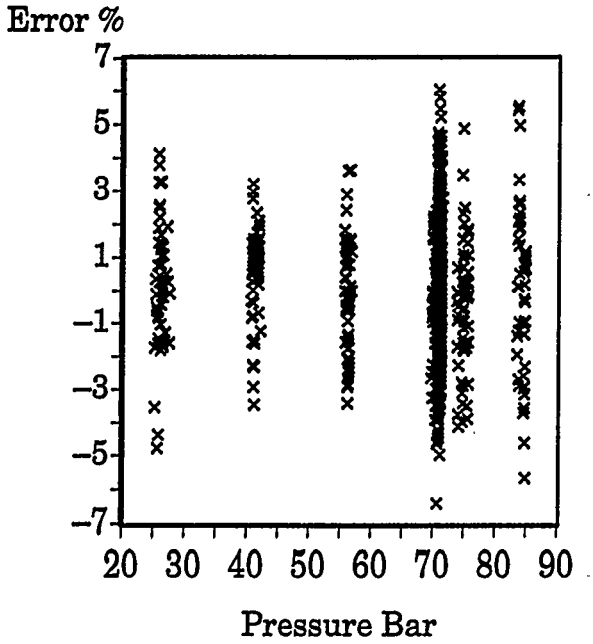

Figure 7 Error in the XL–96+ dryout correlation plotted versus pressure

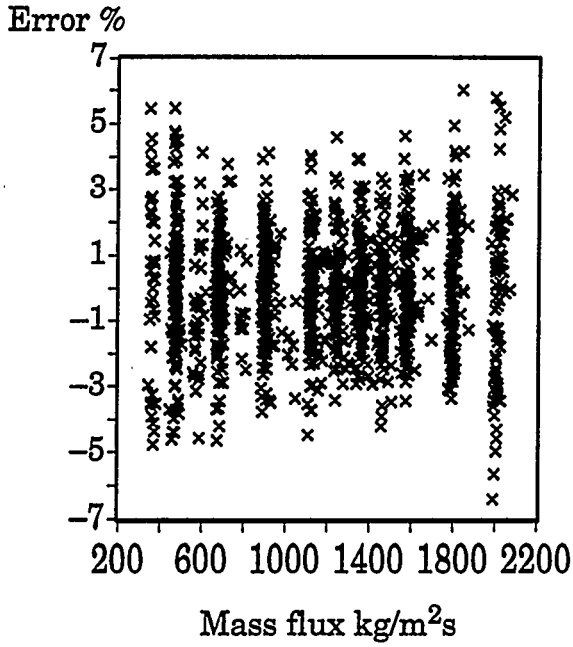

Figure 8 Error in the XL–96+ dryout correlation plotted versus mass flux

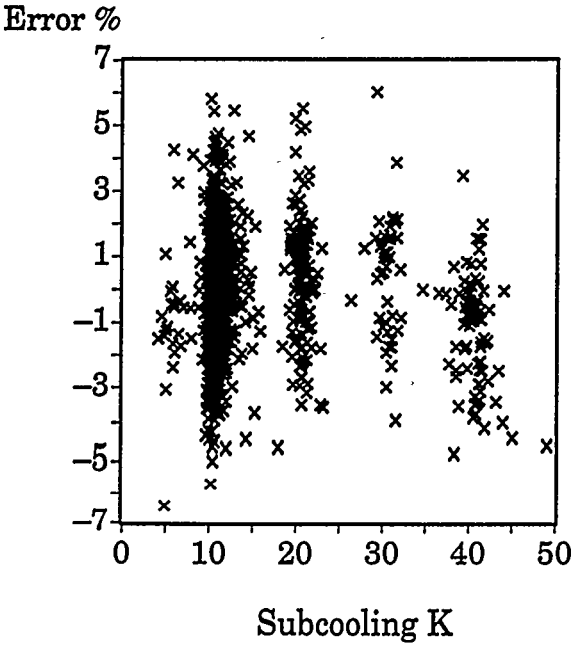

Figure 9 Error in the XL–96+ dryout correlation plotted versus subcooling

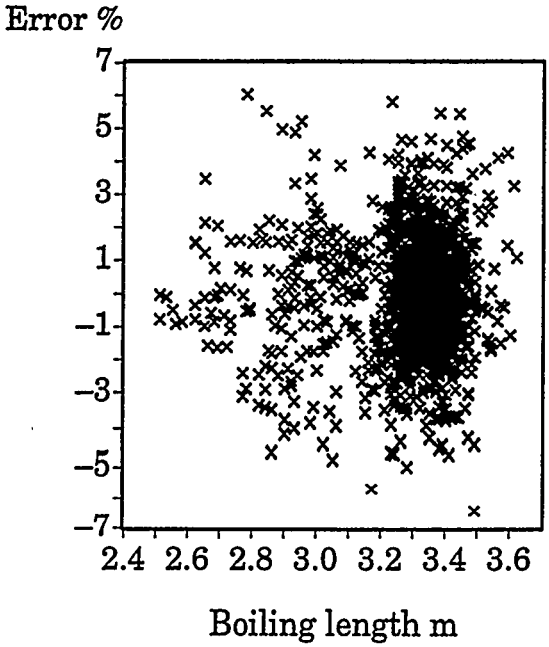

Figure 10 Error in the XL–96+ dryout correlation plotted versus boiling length

Conclusions

Applications of indirectly heated rods in the FRIGG loop have implied several advantages. Due to high voltage and low current, the electromagnetic forces are kept at a low level. Electric insulation of the flow channel is not needed, and the radial power distribution can be easily changed during the experiments, where critical power performances of individual rods are investigated. The latter advantage makes it possible to provide large data bases within relatively short time, enabling development of critical power correlations with good accuracy.

The indirectly heated rods have turned out to be very reliable, a consequence of manufacturing experience and refining by Stern Lab. Inc. since the early 1960's, e.g. the improved insulation system and filaments cut from tubing by laser. The latter permits a very uniform circumferencial heat flux with heaters having a non–uniform axial heat flux profile, improved filament to electrode terminations and a higher maximum heat flux. The 25 heater rods first delivered for the FRIGG loop have experienced more than 13000 dryout measurements without malfunction.

The significant impact of the spacer distance on the critical power has conveniently been verified and quantified.

Even with a large amount of critical power measurement points have been used as input for CPR correlation development, remarkably small standard deviation and mean error have been obtained for e.g. the XL–96+ CPR correlation.

References

[1] O. Nylund, "Full–scale Loop Studies of BHWR and BWR Fuel Assemblies", ASEA Research, Vol 10, 63–125 (1969)

[2] R. Eklund, M. Majed, O. Nylund and B. Schölin, "Thermal–Hydraulic Verification of SVEA 5x5 Fuel", NURETH–4 Vol. 1, 572–578 (1989)

[3] E. M. Moeck, F. Stern, G. A. Wikhammer and R. T. Dempster, "Dryout in a 19 Rod Bundle Cooled by Steam/Water Fog at 515 psia", ASME 65–HT–50

[4] S. Helmersson, T. Gustavsson, O. Nylund, M. Majed, "Second Generation SVEA–96S/+ BWR Fuel Assembly", Jahrestagung Kerntechnik '94, 327–330 (1994)

CHF Considerations for Highly Moderated 100% MOX Fueled PWRs. [1]

D. Saphier and P. Raymond

CEA Saclay, DMT/SERMA/LETR,
91191 GIF-sur-YVETTE, CEDEX France

Abstract

A feasibility study on using 100% MOX fuel in a PWR with increased moderating ratio, RMA[2], was initiated [1]. In the proposed design all the parameters were chosen identical to the French 1450MW PWR, except the fuel pin diameter which was reduced to achieve higher moderating ratios, V_M/V_F, where V_M and V_F are the moderator and fuel volume respectively. Moderating ratios from 2 to 4 were considered. In the present study the thermal-hydraulic feasibility of using fuel assemblies with smaller diameter fuel pins was investigated. The major design constrain in this study was the critical heat flux (CHF). In order to maintain the fuel pin integrity under nominal operating and transient conditions, the minimum DNBR, (Departure from Nucleate Boiling Ratio given by CHF/q"$_{local}$, where q"$_{local}$ is the local heat flux), has to be above a given value. The limitations of the existing CHF correlations for the present study are outlined. Two designs based on the conventional 17x17 fuel assembly and on the advanced 19x19 assembly meeting the MDNBR criteria and satisfying the control margin requirements, are proposed.

Introduction

Large stockpiles of plutonium from water moderated reactors are expensive to maintain, and therefore, in addition to the problem of safeguarding, there is a strong economic incentive to consume as large a quantity of Pu as possible. Since 1987 several French plants have been using up to 30% MOX fuel loading. However, even with this loading, more Pu will be produced than consumed. In a conventional PWR it is impossible to increase the MOX load above 30%, since the resulting spectrum hardening reduces significantly the efficiency of the control rods and the soluble boron. Calculations performed by Nisan et al. [1] and [2] have shown that using 100% MOX in a conventional PWR reduces the control rod value to one half, and the boron efficiency to one third. The required shutdown margin therefore precludes the use of more than 30% MOX fuel. In addition, the negative moderator temperature coefficient increases significantly, generating a major concern in case of reactor cool down accidents. By increasing the V_M/V_F the neutron spectrum is softened again and the recycling of Pu in 100% MOX fueled PWR becomes feasible.

From the thermal-hydraulic (T-H) point of view, reducing the fuel pin diameter affects

[1] Paper submitted to the NURETH-7 Meeting, Sept 10-15, 95, Saratoga N.Y., (pap171)
[2] RMA stands for Reacteurs a Moderation Accrue

the core performance parameters - assuming that flow and power remain unchanged - in the following manner:

1. Heat transfer area decreases
2. Heat flux increases
3. Flow cross section area increases
4. Flow velocity decreases
5. Heat transfer coefficient decreases

Calculations have shown, that one of the consequence of the above changes in the core T-H parameters is a reduction in the predicted critical heat flux, CHF, while the local heat flux increases. The direct result is a significant reduction in the DNBR. One of the most stringent constrains in the T-H design of a PWR core is to keep the minimum DNBR, (MDNBR), above a certain value, (1.3 in the N4-PWR when using the W3-CHF [3] correlation) under predefined transient limiting conditions. It became obvious that some additional modifications are needed in addition to the diameter reduction in order to maintain the above design limit.

The purpose of the present investigation is to find a PWR fuel assembly design, and core operating conditions with a moderating ratio of 3 which will have the same MDNBR as the N4 reference design.

Operating Conditions

The nominal operating conditions of the FRAMATOME 1450MWe (4250MWt) PWR were used in the present study. The calculations in the present study were limited to steady state conditions. The ultimate requirement for the reactor safety analysis is to show that for a given set of predetermined transients and accidents, the fuel pin integrity is maintained. However, at this stage of the project, only steady state calculations were performed. These calculations were performed for nominal and for limiting conditions. These conditions are defined in the safety analysis report (SAR) [4] and include the setpoints which operational transients can achieve and which will trip the reactor shutdown system. These conditions are defined in table 1.

The Calculational Model

The FLICA-4 [5] code was used in the present study. This code has a full three dimensional thermal hydraulic model that can be used for steady state and transient analysis of a PWR core. The flow of the fluid through the core is described by a set of four balance equations

Parameter	Units	Nominal Conditions	Added uncertainties		Transient limiting cond	
Power	Mw	4250	+2%	4335	+18%	5115
Flow	kg/s	18527	-3.2%	17934	-20%	14347
Pressure	MPa	15.6	-0.21	15.39		15.39
Inlet Temp	°C	292	+2.2	294.2		294.2

Table 1: Limiting conditions for which DNBR was calculated.

for each discrete volume element. These equations include the conservation of the total mass, conservation of the total momentum, conservation of the total energy, and a mass conservation equation for the vapor phase. The drift velocity between the vapor and the liquid are obtained from algebraic relations. Closure equations, given in the form of various correlations and equations of state are used to describe the following phenomena:

- Wall vaporization - Subcooled boiling
- Bulk condensation
- Turbulent mass diffusivity
- Pressure drop due to wall friction, mixing grids and other singularities
- Drift velocity between the liquid and vapor
- Eddy viscosity
- Eddy diffusivity
- Heat transfer between wall and coolant

A three dimensional finite difference scheme is used and several levels of discretization are possible, ranging from very detailed scheme centered around a fuel pin, up to the coarse mesh where the fuel assembly is a single mesh in the horizontal direction. Because of the symmetrical power distribution it was sufficient to model in the present study one eighth of the core, using the scheme shown in Fig. 1. The FLICA4 and FLICA3 codes were partially verified, by reproducing several CHF experiments performed at Columbia University [15] The numerical scheme [6] is based on an approximate Rieman solver for the discretized inviscid fluid terms and a central difference scheme for the diffusive terms, (see full details in ref [5] and [6]).

Applying the CHF correlations

A recent literature search revealed the existence of tens of thousands CHF measured points, several tens of correlations to estimate the CHF and more then a thousand publications.

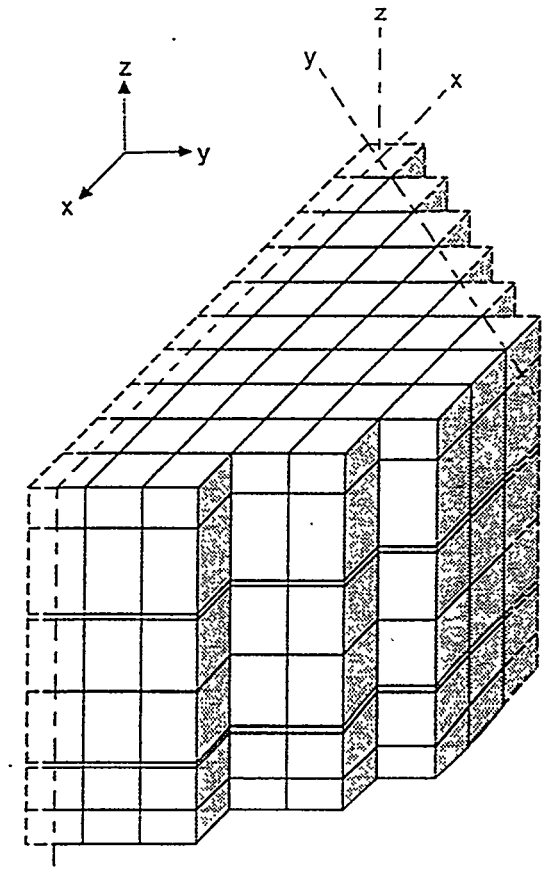

Figure 1: Discretization scheme of 1/8 core used in the FLICA-4 thermal hydraulic model.

This is only to stress the importance of the CHF prediction for the reactor safety analysis. Since CHF limits the maximum power extractable from a nuclear reactor, and because there is a strong commercial interest to extract as much power as possible, the CHF is a continuous subject of theoretical and experimental studies. Most of the measurements were performed in tubes for a wide range of flows, heat fluxes, pressures, T-H conditions and diameters. However, there exist today a large body of data from rod bundle measurements, and correction factors were applied to tube data to extend their applicability to rod bundles. An excellent recent review and comparison of various correlations was prepared by Lellouche [7] while an older review describing also the theoretical modeling efforts was prepared by Marinelly [8].

Some of the correlations, such as a recent Siemens ERB-3 [9] and the Westinghouse WRB-1 [10] correlations, claiming excellent agreement to measured rod bundle data, and claiming significantly lower statistical deviations, are still proprietary. Several table look up techniques based on a large volume of experimental data, such as the standard Russian tabulations by Doroshchuk [11] and the recent tables by Groeneveld [12] made for flow in pipes, are also available. Recently deCrecy [13] proposed the pseudo-cubic thin-plate type spline method for the analysis of CHF measurements indicating that a significantly smaller standard deviation can be obtained than with algebraic correlations based on the same set of data. The technique was applied to rod bundle measurements performed at Grenoble in the Omega and Betsy loops. Tables based on this methodology to calculate CHF for given conditions were included in the FLICA-4 code.

The problem of evaluating the CHF and the MDNBR in the present study was therefore

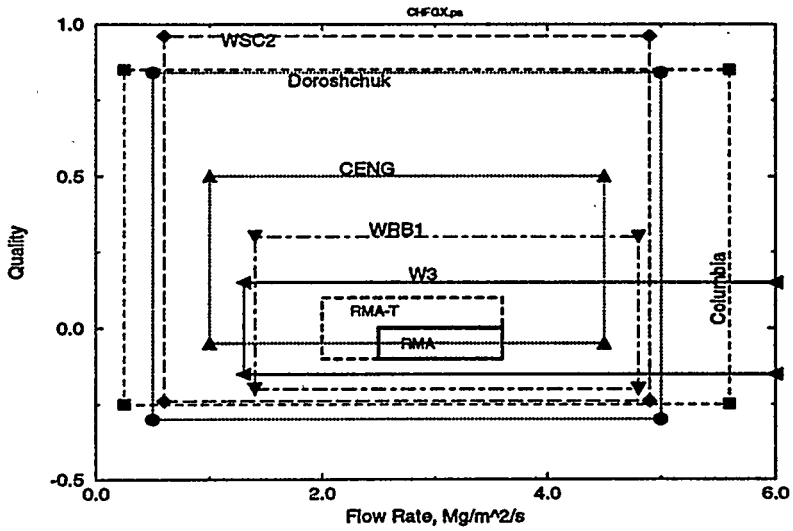

Figure 2: Validity range of some CHF correlations and tables w.r. to flow and quality, (CHFGX).

fourfold: some of the correlations were not applicable to fuel assembly calculations; others were not within the range of interest; some are still proprietary; and others are not yet part of the FLICA-4 database. Consequently - only a small part of the available correlations were used in this study. In the near future the CHF data base in the code will be expanded.

The Range of the CHF Correlations

Each CHF correlation and look-up table is valid for a certain range of T-H parameters. Although the correlations are often used beyond their explicit range of applicability, this usage can only be justified when approached with great caution and reserve.

Some computer codes have already introduced a mapping technique rather than using a single CHF correlation. Inside these programs, the local thermodynamic conditions are evaluated and the most appropriate location in the CHF map is then identified. If necessary averages or interpolations of several values can be made to achieve the best CHF value.

It is of interest to map the various correlations and look-up tables, together with the predicted range of parameters of interest in the present study to obtain a graphical view of the applicability of the various correlations.

In Fig. 2 some correlations and look-up tables are mapped in the quality-flow area. As can be seen from the figure all the correlations and tables presented cover the range of interest with respect to the quality and flow rate for the RMA-S (RMA nominal steady

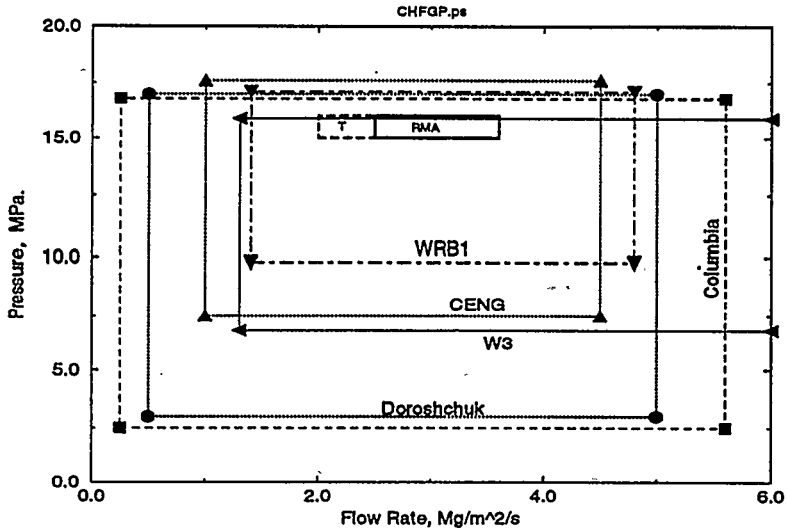

Figure 3: Validity range of some CHF correlations and tables w.r. to flow and pressure, (CHFGP).

state calculations) and for the RMA-T (RMA transient operating conditions). The CENG measurements have no values below the quality of -5%, but were extrapolated by deCrecy [13] into this range when the look-up tables were prepared. For accident conditions, where low flow and high quality can be expected the W3 and WRB1 might not be sufficient and other correlations or tables have to be introduced into the FLICA-4 code.

In Fig. 3 some correlations and look-up tables are mapped in the pressure-flow area. As can be seen from the figure all the correlations and tables presented cover the range of interest with respect to the pressure and flow rate. The W3 correlation upper pressure limit is just on the upper boundary of the required range.

The major difficulty in using the available CHF correlations can be observed from Fig. 4 and Fig. 5. These figures present the range of validity for the fuel-channel heated diameter and for the fuel pin diameter. As can be seen, there is no correlation shown in these two figures that covers the range of smaller fuel pin diameters. In this study, therefore, extrapolations were used, but their validity can not be verified, since no bundle experiments exist for this range. The deCrecy look-up tables can be only used for the 9.5mm fuel pin since no measurements with smaller fuel pin diameters were performed. Although extrapolation tables were prepared their quality is not known.

The Doroshchuk tables seem to cover the whole range of interest with respect to hydraulic diameters and so do the Groeneveld tables. These tables were prepared for uniformly heated smooth 8mm tubes and their validity for nonuniformly heated rod bundles with mixing grids is unknown. At the present time only the W3, the Columbia, and two modes of look up tables based on the Grenoble CHF data by deCrecy [13] are present

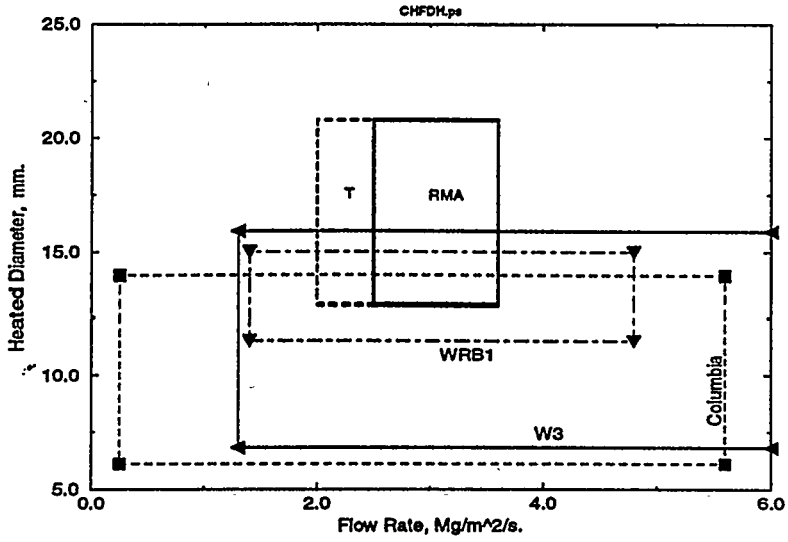

Figure 4: Validity range of some CHF correlations and tables w.r. to flow and heated diameter, (CHFDH).

in the FLICA-4 code. Some proprietary correlations are also included and additional correlations and look up tables are in the process of being added to the code.

The Effect of Decreasing the Fuel Pin Diameter on DNBR

As indicated, the simplest way of increasing the moderating ratio in a given assembly geometry is to reduce the fuel pin radius. This reduction increases the heat flux and reduces flow velocity. The combined effect on the MDNBR is shown in Fig. 6. As expected, the MDNBR increases with the fuel pin diameter. On the same figure the moderating ratio is plotted as a function of the fuel diameter, and as can be seen it increases with reducing the fuel pin diameter.

The purpose of the present investigation is to find the appropriate technique by which the fuel diameter can be decreased to increase the V_M/V_F while keeping the DNBR at nominal conditions.

The Effect of Increasing the Number of Mixing Grids

Grid spacers with mixing vanes increase the mixing of the coolant, thus enhancing heat transfer. Decreasing the distance between the mixing grids will increase the CHF. Several formulas are available in the literature (see for example ref. [14]). Most formulas are presented in the form of a correction factor, Fs, to the CHF correlation. The value of

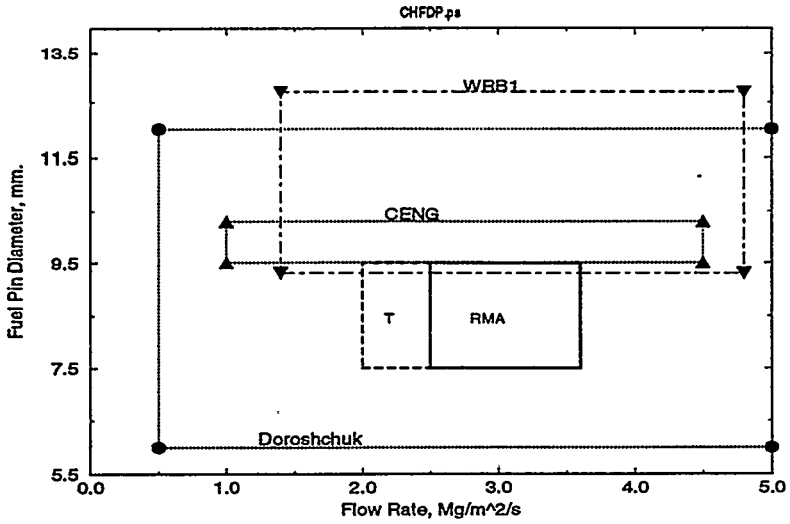

Figure 5: Validity range of some CHF correlations and tables w.r. to flow and fuel pin diameter, (CHFDP).

Fs increases with decreasing the distance between grids. For consistency we have used Tong's formulation [10], extrapolating his Ks - axial grid spacing coefficient whenever needed for smaller grid spacings. The effect of increasing the number of mixing grids, that is, reducing the distance between the grids, for a 17x17 assembly with 9.5mm fuel pins under nominal operating conditions, is shown in Fig. 7. With decreasing the distance between the mixing grids the MDNBR increases as expected. The rate of change decreases, however, significantly going from a grid spacing of 501 to 270mm.

With increasing the number of grids, the pressure drop across the core also increases, however this is offset by the increase in the flow cross section area when the fuel pin diameter is decreased.

The number of mixing grids was varied from 8 to 16 which corresponds to a distance of 501 to 270mm. The maximum number of mixing grids considered were 16. Having a larger number of grids was not considered practical, and there are some indications, as can be seen from Fig. 7 that there will be very little gain in the MDNBR with smaller grid spacing.

The Effect of "Water Holes"

The number of guide thimbles or "water holes" desired in a fuel assembly is determined by the requirements of the control system. In the N4 reactor having a 17x17 fuel assembly, there are 24, guide thimbles and one instrumentation tube. Obviously increasing the number of "water holes" will increase the moderating ratio, and reduce the DNBR, since

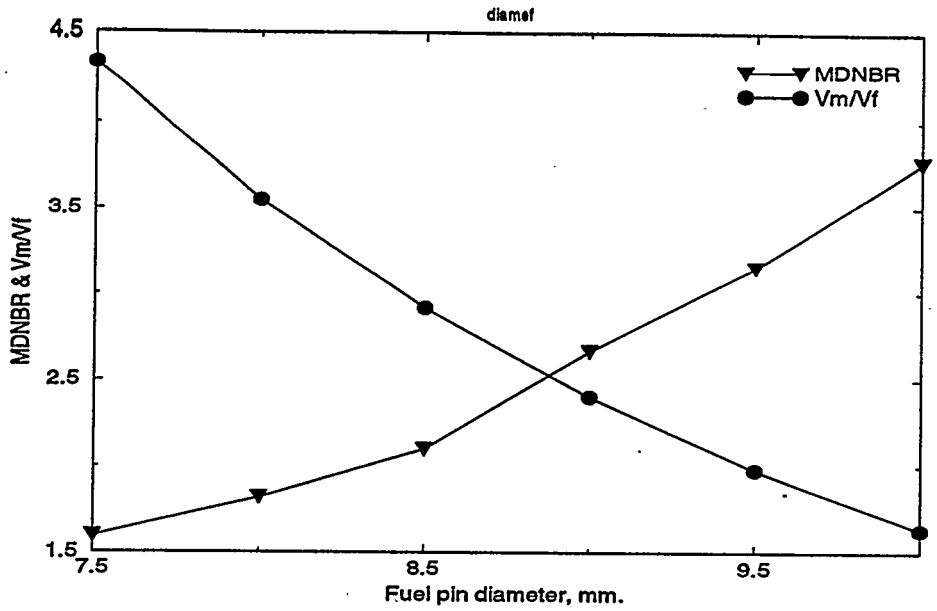

Figure 6: The effect of the decrease of the fuel pin diameter on MDNBR and the moderating ratio, (diamef).

the same power is produced in a smaller number of fuel pins.

If, however, the Vm/Vf ratio is kept constant, increasing the number of guide tubes, requires a corresponding increase in the fuel pin diameter. The resulting DNBR as a function of the number of guide tubes is shown in Fig. 8. The calculations were performed for a 19x19 assembly, and the Vm/Vf was set to 3. In the figure the corresponding change in the fuel pin radius is also shown. As can be seen from the figure, the DNBR changes very little in the range of 29 to 101 "water holes". As a consequence of this behavior, it is concluded that from thermal hydraulic considerations the exact number of "water holes" or guide thimbles is not important and their number can be determined by neutronic considerations, in particular according to the control system requirement and the desire to minimize local assembly power peaking.

Results of the Study

The purpose of the many calculations performed in this study was to identify the conditions for which the same CHF and MDNBR can be obtained as for the reference PWR during normal operating and upset conditions, while trying to achieve the highest possible moderating ratio. Two basic designs were considered. Design A, with the presently used 17x17 fuel assembly, and design B, with an advanced 19x19 assembly. For the nominal 17x17 PWR fuel assembly this can be achieved by reducing the fuel pin diameter by

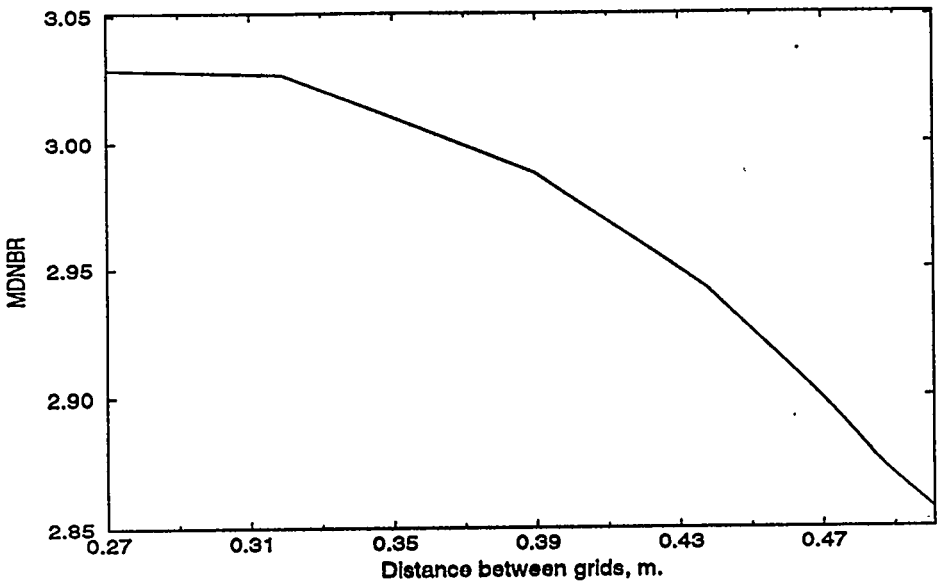

Figure 7: Effect of the spacing between mixing grids on the MDNBR, (gridef)

0.9mm, that is to 8.6mm and by using additional 6 mixing grids. The moderating ratio achieved from this reduction of the fuel pin diameter is 3, which is the desired value to achieve sufficient reactivity shutdown margin. The details of the design are presented in Table 2. The number of "water holes" was increased to 41. This core when operated at 90% of nominal power will achieve the same DNBR as the reference core. The heat flux and the CHF are presented in Fig. 9 and the resulting DNBR is shown in Fig. 10 along the core hot channel.

The major advantage of this design is, that except for the fuel pin diameter and additional mixing grids, the core and assembly design, as well as the control system, are identical to the N4 design. Using an advanced fuel assembly having a 19x19 grid instead of the original 17x17, additional flexibility is introduced into the design. This design has a smaller diameter fuel-pin and a smaller pitch, both of which affect the CHF. The fuel pin pitch decreases from 12.624 to 11.274 and the number of fuel elements increases from 239 to 336, (assuming 25 guide tubes). Although the fuel diameter is smaller, the surface area increases and more design flexibility is permitted. To achieve a moderating ratio of three, the fuel pin radius has to be reduced to 7.7mm. The optimal number of guide tubes under these conditions is 41. With this design and nominal power the same DNBR is achieved as in the nominal core. The heat flux and the CHF are presented in Fig. 11 and the resulting DNBR is shown in Fig. 12 along the core hot channel.

As can be seen from Table 3, due to the increased heat transfer area, the average heat flux is reduced by 18%, however, the flow rate is also reduced by 12% due to the increase in the flow cross-section area. From the T-H considerations there is a significant freedom

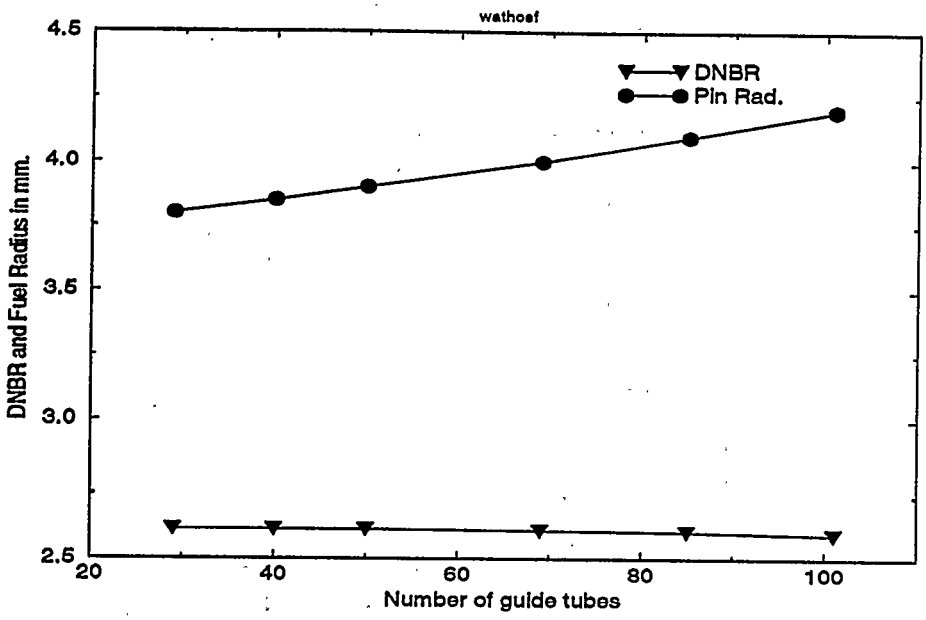

Figure 8: The effect of changing the number of "water holes" on MDNBR in a 19x19 assembly and on the fuel pin radius, (wathoef).

to choose the number of guide tubes. These can be, therefore, determined according to the neutronic considerations, such as core controllability, local intra-assembly radial power peaking. A significant radial peak in the assembly due to "water holes", will again affect the T-H design. There might be also mechanical constraint on the control assembly structure and the number of permissible rods in the assembly.

Conclusions

From the results it can be concluded that a 19x19 fuel assembly can be designed with the T-H conditions similar to the reference design. Using this assembly the MDNBR is the same as in the reference 4250MWt PWR.

Keeping the original 17x17 design, a moderating ratio of 3 can be achieved if a fuel pin of 8.6mm is used and the power is reduced to 90% of its nominal value while maintaining a 100% flow rate. All proposed designs required an increase in the number grids with mixing vanes.

Further improvements in the CHF data and correlations are necessary to improve the design of the RMA cores using small diameter fuel pins which is equivalent to larger hydraulic and heated diameters. Most of the tables and correlations are not parametrized with respect to the grid spacing distance. They relay mostly on som previously published correction factors. This too has to be corrected since in this study the mixing grids with

		Proposed	Nominal
1.	Assembly	17x17	17x17
2.	Fuel Pin D, mm	8.6	9.516
3.	Fuel Pellet D, mm	7.33	8.19
4.	Cladding dR, mm	0.571	0.571
5.	Fuel Pin Pitch, mm	12.624	12.624
6.	Assembly Pitch, m	0.2161	0.2161
7.	Core height, m	4.681	4.681
8.	Core active length, m	4.295	4.295
9.	Moderating Ratio	3.02	1.98
10.	Mixing Grids	14	8
11.	Flow, $kg/m^2/s$	3180	3598
12.	Core ΔP,bar	2.77	2.83
13.	Heat Flux MW/m^2	.651	.612
14.	Minimum DNBR	2.23	2.23
15.	Water Holes	40+1	24+1
16.	Power MW (%)	3850(90)	4250
17.	Peak to Av Power	1.490	1.490
18.	Case No.	708 (3G)	28

Table 2: Design A: based on the N4 core with 205 assemblies of 17x17 pins, the same minimum DNBR as N4, with the moderating ratio increased from 2 to 3, (designA).

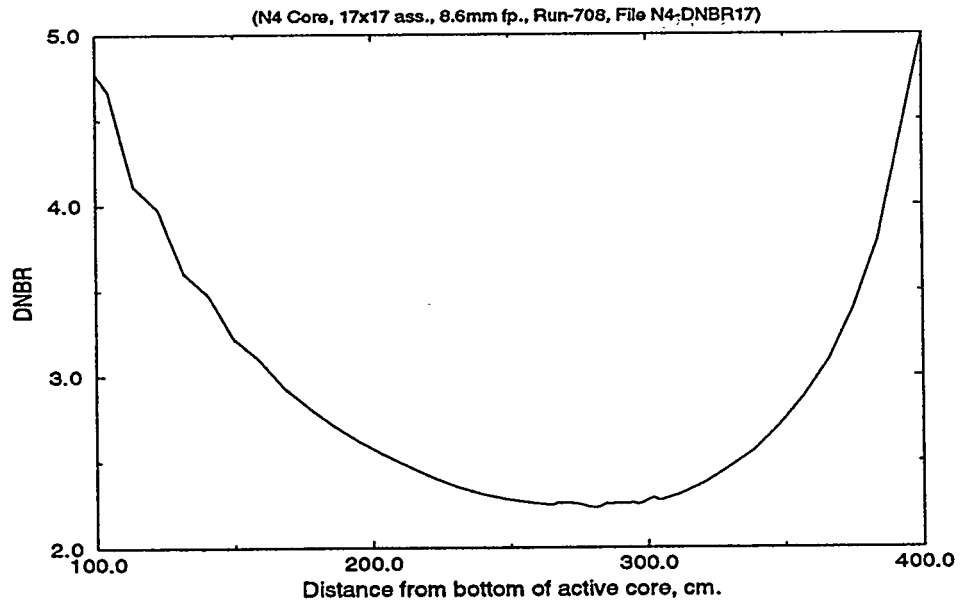

Figure 10: DNBR along the hot channel of design A, (N4-DNBR17).

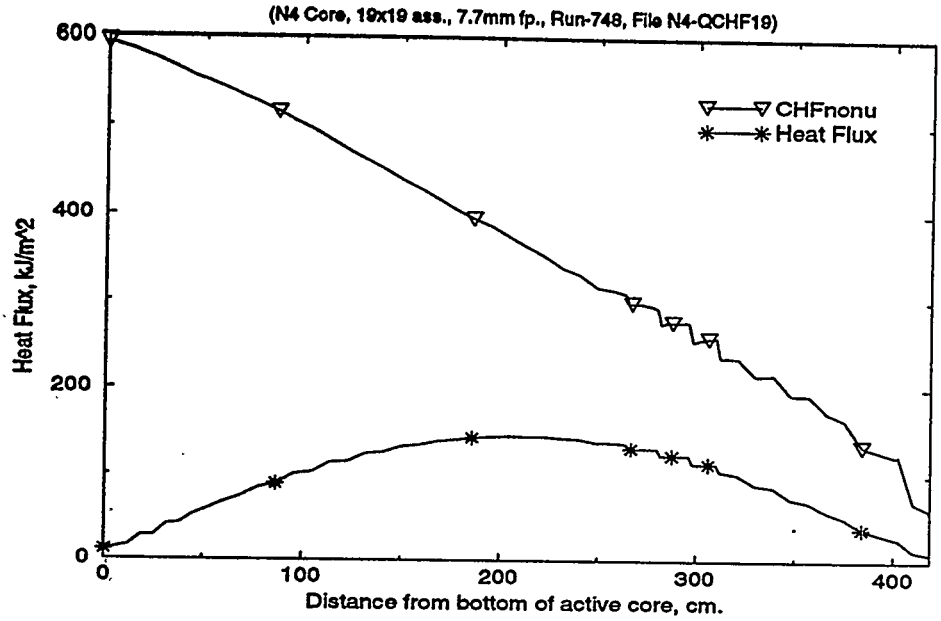

Figure 11: CHF and heat flux distribution for design B, (N4-QCHF19).

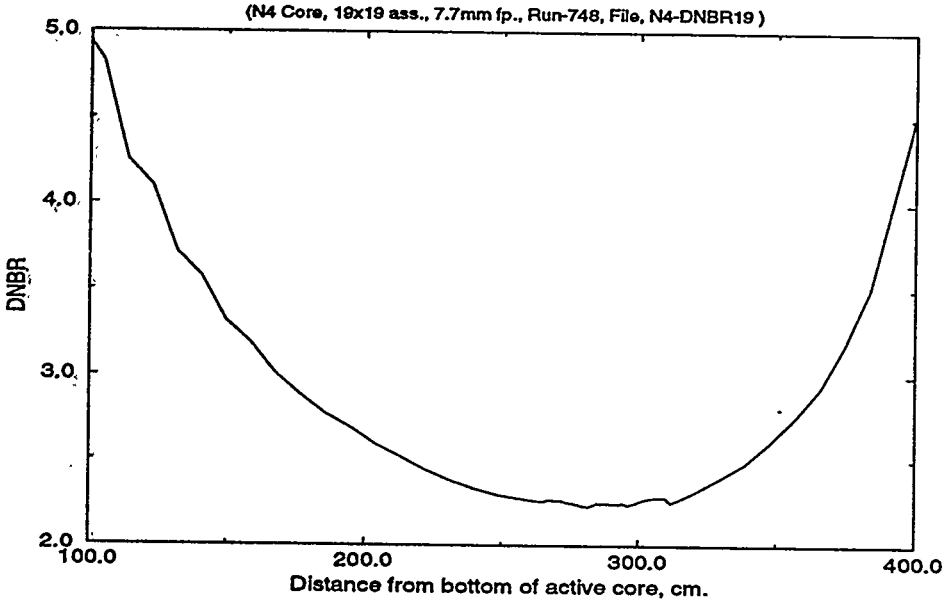

Figure 12: DNBR along the hot channel of design B, (N4-DNBR19).

		Proposed	Nominal
1.	Assembly	19x19	17x17
2.	Fuel Pin D, mm	7.7	9.516
3.	Fuel Pellet D, mm	6.414	8.19
4.	Cladding dR, mm	0.571	0.571
5.	Fuel Pin Pitch, mm	11.274	12.624
6.	Assembly Pitch, m	0.2161	0.2161
7.	Core height, m	4.681	4.681
8.	Core active length, m	4.295	4.295
9.	Moderating Ratio	3.02	1.98
10.	Mixing Grids	14	8
11.	Flow, $kg/m^2/s$	3215	3598
12.	Core ΔP,bar	2.73	2.83
13.	Heat Flux MW/m^2	.519	.612
14.	Minimum DNBR	2.23	2.23
15.	Water Holes	40+1	24+1
16.	Power MW (%)	4250	4250
17.	Peak to Av Power	1.490	1.490
18.	Case No.	748 (3J)	28

Table 3: Design B: based on the N4 core with 205 assemblies of 19x19 pins, the same minimum DNBR as N4, with the moderating ratio increased from 2 to 3, (designB).

mixing vanes are of major importance.

References

[1] S. Nisan, G. Manent, C. Girard, *Bilan des études de faisabilite des coeurs REP a 100% MOX*, Raport DER/SIS (et DER/SPRC/LEDC) No. 93/001, (1993)

[2] S. Nisan, Ph. Dubiau, Ph. Bergeronneau, *Neutron Physical Aspects of Core Design Optimization in MOX Fueled APWRs*, ANS Topical Meeting, Pittsburgh (1991)

[3] L. S. Tong, *Prediction of Departure from nucleate Boiling for an Axially Nonuniform Heat Flux Distribution*, J. of Nucl. En. 21, (1967), pp 241-248.

[4] Electricite de France *Centrales Nucleaires du Palier 1400 MWe - N4.* Report Preliminaire de Surete, Electricite de France (1991)

[5] I. Toumi, *FLICA-4, Manuel de référence de la méthod numérique* CEA/DRN/DMT/SERMA-DMT/93/434 (1994)

[6] P. Raymond, I. Toumi, *Numerical Method for three Dimensional Steady-State Two-Phase Flow Calculations.* ANS Proceedings of NURETH-5 Salt Lake City, (1992)

[7] G.S. Lellouche, *The Boiling Transition Analysis and Data Comparison.* Nucl. Eng. and Design 116 (1989) 117-133

[8] V. Marinnelli, *Critical Heat Flux: A Review of Recent Publications*, Nucl. Tech. 34, (1976) pp135-171.

[9] K. Meistelberg, C. Vogel, G. Ulrych, *The Correlation ERB3 for Critical Heat Flux in PWR Rod Bundles.* Kerntechnik, 57 (1992) 42

[10] L.S. Tong, *Thermal Analysis of PWR.* ANS Publication (1972)

[11] V.E. Doroshchuck, L.L. Levitan, F.P. Lantzman, *Recommendations for Calculating Burnout in a Round Tube with Uniform Heat Release.* Teploenergetika, 22 (1975) 66-70

[12] D.C. Groeneveld et.al., *An Improved Table Look-up Method for Predicting Critical Heat Flux.* ANS Proceedings of NURETH-6, Grenoble, France(1993)

[13] F. de Crecy, *Pseudo-Cubic Thin-Plate Spline Method for Analyzing Experimental Data*, ANS Proceedings of NURETH-6, Grenoble, France (1993)

[14] Wen-Shan Lin, Bai-Shei Pei, Chien-Hsiung Lee, *Bundles Critical power Predictions Under Normal and Abnormal Conditions in PWR.* Nucl. Tech. 98 (1992) 354

[15] D. Caruge, *FLICA-4, Dosier de Validation, Comparison des rapports d' echauffement critique, calculé à l'aide des codes FLICA3F et FLICA4(V1.1)* Raport DMT 92/613 (1994)

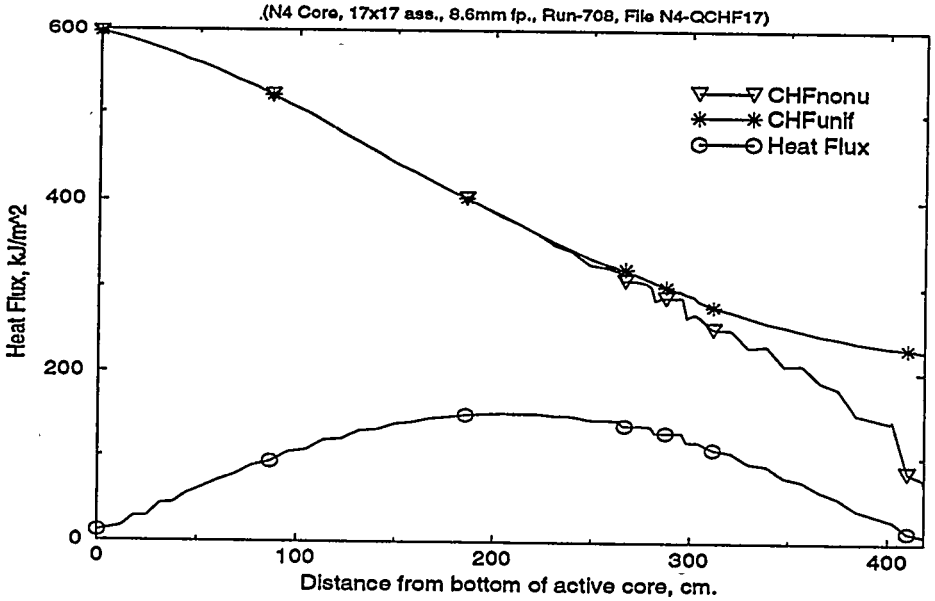

Figure 9: CHF and heat flux distribution for design A. CHFnonu indicates the nonuniform heat flux correction was included (N4-QCHF17).

GENERAL CORRELATION FOR PREDICTION OF CRITICAL HEAT FLUX RATIO IN WATER COOLED CHANNELS

Rostislav PERNICA, Jiri CIZEK
Nuclear Research Institute plc, 250 68 Rez, Czech Republic
Tel: (+422)6857068/Fax: (+422)6857567

ABSTRACT

The paper presents the general empirical Critical Heat Flux Ratio (CHFR) correlation which is valid for vertical water upflow through tubes, internally heated concentric annuli and rod bundles geometries with both wide and very tight square and triangular rod lattices. The proposed general PG correlation directly predicts the CHFR, it comprises axial and radial non-uniform heating, and is valid in a wider range of thermal hydraulic conditions than previously published critical heat flux correlations. The PG correlation has been developed using the critical heat flux Czech data bank which includes more than 9500 experimental data on tubes, 7600 data on rod bundles and 713 data on internally heated concentric annuli. Accuracy of the CHFR prediction, statistically assessed by the constant dryout conditions approach, is characterized by the mean value nearing 1.00 and the standard deviation less than 0.06 . Moreover, a subchannel form of the PG correlation is statistically verified on Westinghouse and Combustion Engineering rod bundle data bases, i.e. more than 7000 experimental CHF points of Columbia University data bank were used.

INTRODUCTION

Critical heat flux phenomenon is one of technical problems, physical description of which has been so far unsuccessful. Many Critical Heat Flux (CHF) correlations have been proposed for water cooled heated rod clusters and tubes. However, a majority of these correlations is limited to a narrow range of thermal hydraulic conditions and geometric parameters. Several CHF correlations are usually involved to predict CHF over a wide range of conditions by advance computer codes currently used for Light Water Reactor modeling. However, a combination of various correlations predicting CHF over a wide range of conditions often results in a discontinuity of computed CHF or physically inadequate dependence in the certain range of coolant flow conditions. Shortcomings of the above mentioned procedures and lack of sufficiently suitable correlations employed for prediction of the CHF over a wide range of thermal hydraulic conditions in various rod bundle geometries led to the use of existing CHF correlations valid for water cooled tubes,

and - to the development of tabular prediction methods for CHF in rod bundles, based on CHF values for water cooled tubes. The present Critical Heat Flux Ratio (CHFR) correlation [1], which we call PG, is valid in a wide range of tube, rod bundle and annulus geometries, as well as - for a wide range of thermal hydraulic conditions, and shows excellent statistical characteristics.

The value of CHFR, i.e. the ratio of predicted and experimental CHF, is used to compare the CHF correlations with experimental results - it is understood as a statistical random quantity (denoted R in this paper) which fixes the boiling crisis probability. The approach used until now assumed only a simple inverse proportion of the random quantity R to a local heat flux. The proposed PG correlation of CHFR uses a more complex dependence on the local heat flux and thus - determines a value of the quantity R as a direct result. This should be one of the reasons, why description of CHF conditions by means of the PG correlation gives very good results, the other one - can be an appropriate choice of correlating parameters. The PG correlation respects mixing between rod bundle subchannels as described in the subchannel codes. That is another significant difference between this and previously published CHF correlations [2,3] which were developed for the isolated subchannel model in a rod bundle.

CHF EXPERIMENTAL DATA

The CHFR PG correlation is developed with the critical heat flux Czech data bank [4] which comprises the boiling crisis experimental data for vertical water upflow in tubes, internally heated concentric annuli and hexagonal or square or circular rod bundles for the range of coolant flow and geometric parameters, and the non-uniform power distributions as shown in TABLE I.

The CHF data of Czech data bank were compiled from 40 literary sources. These data were obtained by different experimental research facilities and measuring equipment. Thus, 173 tube and 23 annulus test geometries and 153 different rod bundle test sections, which involve different types of spacers, are included in Czech data bank which were used to introduce the PG correlation. It is obvious that the description of experimental facilities, measuring equipment, test sections and uncertainties of CHF data is hardly possible in such a paper. Nevertheless, very favourable statistical results of the PG correlation on Westinghouse and Combustion Engineering rod bundle data bases, i.e. more than 7000 CHF experimental points of Columbia University data bank [5] are presented below. Description of the Heat Transfer Research Facility of Columbia University and CHF data points is known and/or accessible to the readers.

To the correlation parameters belongs the reduced pressure:

$$P_r = p/p_{crit}$$

here p_{crit} = 22.115 MPa is the critical pressure.

The equivalent diameter of a tube or an annulus or a rod bundle subchannel d (m):

TABLE I

Range of Experimental Data Used for Development of the PG Correlation
Rod Bundle Geometry: Hexagonal, Rectangular, Circular - Czech Data Bank

Data Base			Tube	Rod Bundle	Annulus
No. of Test Geometries			173	153	23
Total No. of Data Points			9547	7616	713
p	MPa	Exit pressure	0.26 17.95	0.28 18.73	6.89 6.89
G	kg/m^2s	Local mass flux	102.3 7491	34.1 7478	189.87 6740
x_i		Inlet quality	-1.73 0.	-1.14 0.44	-0.63 0.
x		Local quality	-0.49 0.99	-0.34 1.	-0.23 0.61
q_e	MW/m^2	Measured CHF	0.07 7.	0.12 6.	0.49 8.96
L	m	Heated length	0.22 6.05	0.4 7.	0.61 2.74
d	m	Equivalent diameter of subchannel or tube	0.00384 0.03747	0.00241 0.07813	0.00322 0.02223
L/d		Ratio of heated length to equivalent diameter	20.06 756.25	12.29 1422.36	36.9 584.5
D	m	Rod diameter	- -	0.005 0.01905	0.00952 0.09647
t		Relative pitch - pitch to rod diameter ratio	- -	1.02 2.48	- -
k_a		Peak to axial average heat flux ratio	1. 3.1	1. 1.9	1. 1.
k_r		Maximum to radial average rod power ratio	- -	1. 1.95	- -

$$d = \frac{4\,A}{\sum_i r_i} \quad , \qquad (1)$$

where A is the flow area and r_i's are perimeters adjacent to the (sub-)channel. The factor of the radial heat flux distribution is:

$$T_r = q(y)\ \frac{\sum_i r_i}{\sum_i r_i q_i(y)} \quad , \qquad (2)$$

i.e. the ratio of local heat flux through the given perimeter to average heat flux through perimeters adjacent to the rod bundle subchannel or the annulus at the axial coordinate y (m). It is obvious that for the tubes $T_r = 1$.

To derive other forms of the PG correlation, which will be fully applicable for the closed channels, i.e. tubes and annuli, let us introduce the factor of the axial heat flux shape at the axial coordinate y:

$$T_a = \frac{1}{y}\ \frac{\sum_i r_i \int_0^y q_i(z)\,dz}{\sum_i r_i q_i(y)} \quad , \qquad (3)$$

For a rod bundle with the identical axial heat flux shape along heated perimeters as that of the subchannel (it is fulfilled for all CHF experimental data points [4]) as well as for the tubes, the following products, obtained by combining Eqs.(1) and (2), and from Eq.(3) respectively, are used as the correlation parameters:

$$d\,T_r = 4\,A\ \frac{q}{\sum_i r_i q_i} \quad , \qquad (4)$$

$$y\,T_a = \frac{1}{q(y)} \int_0^y q(z)dz \quad . \qquad (5)$$

GENERAL CHFR CORRELATION

The common correlation functions can be expressed as:

$$f(P_r, G) = G^{\,0.126 + 0.22\,P_r} \quad , \qquad (6)$$

$$f(P_r, x_i) = 1.9 + 8\,P_r^{10} - P_r - x_i \quad . \qquad (7)$$

Although the PG correlation is called general, there are characteristics related to different geometric forms (tube, annulus or rod bundle) given by constant values k_1, k_2 and pressure function $f(P_r)$. All of these are

TABLE II

Correlation Constants k_1, k_2 and Pressure Function $f(P_r)$ Depending on Geometric Form and Indication of Developed Correlations

Geometry	Correlation	k_1	k_2	$f(P_r)$	F_g
Tube	PG-T	70.9	0.15	$0.17 + P_r + 1.82\,P_r^2 + 17.7\,P_r^{12}$	1.
Annulus	PG-A	102.1			1.
Rod Bundle:					
Subchannel Code	PG-S	105.3	0.04	$0.2 + P_r + 1.2\,P_r^2 + 14.4\,P_r^{11}$	
Isolated Subchannel Model	PG-I	109.8			

introduced in TABLE II. For rod bundles the value of the constant k_1 depends on the thermal hydraulic method used for the determination of the subchannel local fluid conditions.

CHFR PG Correlation

The original form of the PG correlation [1] which determines the CHFR is:

$$R = f(P_r, G, x_i, x, q, d\,T_r, F_g) =$$

$$= \frac{k_1 \quad F_g}{f(P_r)\ (d\,T_r)^{k_2}} \cdot \frac{f(P_r,G)\ f(P_r,x_i)}{f_a} \quad , \qquad (8)$$

where F_g is the rod bundle factor. This factor allows us simple transformation of the general PG correlation to ad hoc form on the basis of CHF experiments on rod bundle test section. By default, or for tubes and annuli, $F_g = 1$. The alternative function f_a which in closed channel can be described by different forms may be written as:

$$f_a = f_x\ f(q,f_x)\ f(P_r,f_x)\ f(P_r,x_i,x) \quad , \qquad (9)$$

where

$$f_x = \frac{G\,h_{fg}}{4}\ (x - x_i) \quad , \qquad (10)$$

and h_{fg} is the latent heat of vaporization (MJ/kg). Other functions are expressed as:

$$f(q,f_x) = \left(1+ \frac{40}{30 + \frac{f_x}{q}}\right) \quad , \tag{11}$$

$$f(P_r,f_x) = \left(1+ \frac{400 + \frac{10}{0.016 + P_r^{1.8}}}{30 + f_x}\right) \quad , \tag{12}$$

$$f(P_r,x_i,x) = \left(1+ \frac{1.8}{1.6 + 4\,P_r - x}\right)\left(1+ \frac{0.001}{0.006 + (x - x_i)^3}\right) \quad . \tag{13}$$

The original form of the PG correlation is very convenient for a number of applications. The following correlation parameters are used: the product ($d\,T_r$) described by Eq.(4), inlet quality x_i, the local heat flux q and local fluid conditions at the CHFR point. The coolant flow history and mixing between rod bundle subchannels are both represented by the difference between the local and inlet quality.

The original form of the PG correlation for tubes and internally heated concentric annuli is denoted PG-T and PG-A, respectively. For the subchannel codes, which respect mixing between subchannels of a rod bundle, the original form is denoted PG-S, it is denoted PG-I if the isolated subchannel model is used.

CLOSED CHANNEL APPLICATION

For a closed channel, i.e. tubes and annuli, we can derive other forms of PG correlation with help of the energy equation. The same is possible also for the rod bundle geometry, if the isolated subchannel model is applied. In this case the rod bundle average mass flux is used to determine the local subchannel quality at the point of CHFR. The energy equation applied to an isolated subchannel at the axial coordinate y is:

$$(x-x_i)\,h_{fg}\,G\,A = \sum_i r_i \int_0^y q_i(z)\,dz \quad . \tag{14}$$

From Eqs.(1), (2), (3) and Eq.(14) we get the quality x along the subchannel:

$$x = x_i + \frac{1}{G\,h_{fg}}\,\frac{1}{A}\sum_i r_i \int_0^y q_i(z)\,dz = x_i + \frac{4}{G\,h_{fg}}\,f_g\,q \quad , \tag{15}$$

where

$$f_g = \frac{y\ T_a}{d\ T_r} \quad . \tag{16}$$

By combining Eqs.(10), (15) and (16) we obtain the following relation:

$$f_x = f_g\ q \quad . \tag{17}$$

Results of the statistical analysis of the CHFR PG correlation transformed forms are identical to those obtained for the original form.

CHFR PG-.g Correlation

The PG-.g is the geometric form of the PG correlation which differs from the original form by the alternative function only:

$$f_a = f_{ag} = f_x\ f(f_g)\ f(P_r, f_x)\ f(P_r, x_i, x) \quad , \tag{18}$$

where Eq. (17) is applied to transfer Eq.(9) into Eq.(18) and then:

$$f(f_g) = \left(1 + \frac{40}{30 + f_g}\right) \quad . \tag{19}$$

The local heat flux q as a correlation parameter is replaced by the parameter ($y\ T_a$) - see Eqs.(16) and (19). The PG-.g correlation is expressed as the function:

$$R = f(P_r,\ G,\ x_i,\ x,\ y\ T_a,\ d\ T_r,\ F_g) \quad .$$

The PG-.g correlation for tubes and annuli is denoted PG-Tg and PG-Ag, respectively. For an isolated subchannel model in rod bundle it is denoted PG-Ig.

CHFR PG-.f Correlation

The PG-.f is the flux form of the PG correlation which differs from the original form by the alternative function only:

$$f_a = f_{af} = q\ f_g\ f(f_g)\ f(P_r, q\ f_g)\ f\left(P_r, x_i, q\ \frac{f_g}{G\ h_{fg}}\right) \quad , \tag{20}$$

where Eqs.(15) and (17) are applied to transfer Eq.(9) into Eq.(20), then:

$$f(P_r, q\ f_g) = \left(1 + \frac{400 + \dfrac{10}{0.016 + P_r^{1.8}}}{30 + q\ f_g}\right) \quad , \tag{21}$$

$$f(P_r, x_i, q \frac{f_g}{G\, h_{fg}}) = \left[1 + \frac{1.8}{1.6 + 4\, P_r - x_i - \frac{4}{G\, h_{fg}}\, q\, f_g}\right] \left[1 + \frac{0.001}{0.006 + \left(\frac{4}{G\, h_{fg}}\, q\, f_g\right)^3}\right] \quad . \qquad (22)$$

The local quality x as a correlation parameter is replaced by the parameter ($y\, T_a$) - see Eqs.(16) and (19). The PG-.f correlation is expressed as the function:

$$R = f(P_r,\ G,\ x_i,\ q,\ y\, T_a,\ d\, T_r,\ F_g) \quad .$$

The PG-.f correlation for tubes and annuli is denoted PG-Tf and PG-Af, respectively. For the isolated subchannel model in rod bundle the correlation is denoted PG-If.

Comment. The PG-.f correlation is based on the inlet fluid conditions, i.e. pressure, mass flux and inlet quality. This correlation form determines the CHFR without analyzing local thermal hydraulic conditions. The use of the PG-.f, same as of the power PG-.p correlation (introduced in the next paragraph), is not convenient for such transients in which the time frequency of any parameter is either comparable or lower than the coolant transport time in a channel.

CHF PG-.p Correlation

The last form of the general correlation which predicts the CHF is that the PG-.p power form, that can be derived from the flux form PG-.f . The f_c function representing predicted critical heat flux can be expressed as:

$$f_c = q\, R(P_r,\ G,\ x_i,\ q,\ y\, T_a,\ d\, T_r,\ F_g) =$$

$$= \frac{k_1\ \ F_g}{f(P_r)\ (d\, T_r)^{k_2}}\ \ \frac{f(P_r, G)\, f(P_r, x_i)}{f_p(q)} \quad , \qquad (23)$$

then using Eq.(20) we obtain:

$$f_p(q) = \frac{f_{af}}{q} = f_g\, f(f_g)\, f(P_r, q\, f_g)\, f(P_r, x_i, q \frac{f_g}{G\, h_{fg}}) \quad . \qquad (24)$$

The terms on the right-hand side of Eq.(24) are described by Eqs.(16), (19), (21) and (22), respectively.

The PG-.p power form is applicable to a tube, an annulus or an isolated subchannel in the rod bundle. It is obtained by replacing the heat flux q in the right hand side of Eq.(23) and Eq.(24) by the predicted critical heat flux q_c. Then the PG-.p correlation is described by the non-linear constitutive equation for q_c (MW/m^2) as follows:

$$q_c = f_c(P_r,\ G,\ x_i,\ q_c,\ y\ T_a,\ d\ T_r,\ F_g) \quad . \tag{25}$$

The random statistical variable describing CHFR is:

$$R = \frac{q_c}{q_e} \quad , \tag{26}$$

where q_e is the measured CHF. Results of the statistical analysis of the PG-.p correlation differ from that for the previous CHFR correlations. The PG-.p correlation is based on the inlet conditions. Value of CHF calculated by Eq.(25) represents the critical heat power and enables us to determine the critical power ratio.

CORRECTION FACTORS

Rod Bundle Factor

Effects of the spacer types and spacers location in a rod bundle are important. Values of local fluid parameters in a rod bundle, especially that of quality and mass flux which are determined with help of a thermal hydraulic model implemented in the subchannel computer code, depend also on the computer code and influence the CHFR prediction results. It is recommended to assess these effects together, using results of the statistical analysis of the correlation obtained with the help of the subchannel code and the CHF experimental data on the examined rod bundle test section. The rod bundle factor characterizes statistical population, and for the PG correlation is given by:

$$F_g = \frac{1}{\bar{R}} \quad , \tag{27}$$

where $\bar{R}$ is the mean value of the random dimensionless variable R - it represents the CHFR computed with the PG correlation using $F_g = 1$. When the value of the rod bundle factor determined by Eq.(27) is used in the PG correlations, the mean $\bar{R}$ for the rod bundle is 1.00, and the corresponding standard deviation is denoted S_g. If the user lacks CHF experimental data on the rod bundle under discussion, we recommend to use $F_g = 1$.

It should be emphasized that the value of rod bundle factor can not be determined by applying the CHF correlation power form PG-.p . The rod bundle factor value determined by the PG correlation should be used in the PG-.p form. The described procedure of determining the rod bundle factor value F_g enables us a simple transformation of the PG correlation to the ad hoc correlation form based on the test section CHF experiments - i.e. the PG correlation is applicable as the design equation for CHF prediction in a rod bundle.

Cold Wall Factor

The effect on the CHF of the cold wall in a subchannel is respected by the product ($d T_r$) in the PG correlation. If on the surfaces adjacent to a subchannel there are constant and zero heat flux only, then the product ($d T_r$) describes heated diameter of the subchannel - see Eq.(4).

Low Mass Flux

If the PG correlations are used in computer codes for transients, and low or negative mass flux are expected, it is recommended to replace the quantity G by max(50,|G|).

STATISTICAL CHARACTERISTICS OF THE CORRELATIONS

In the statistical evaluation of the correlations the constant dryout conditions approach is applied. This approach requires a prior knowledge of the correlation parameters, only.

Statistical evaluation of the correlations is performed with the random dimensionless variable R which represents the CHFR value computed by the PG correlations, or the ratio of the CHF predicted by the PG-.p power form and the experimental CHF. The statistical characteristics used are: mean $\bar{R}$, standard deviation S_R and root mean square S_1. For non-uniform axial heat flux shapes the random dimensionless variable R is defined as:

$$R = R(y_c) = \min_y R(y) \qquad (28)$$

The predicted axial coordinate of CHF location y_c satisfies Eq.(28). The differences between the predicted axial coordinate of CHF location y_c and the experimentally determined coordinate y_e are also examined. The dimensionless random variable

$$Y = \frac{y_c - y_e}{L} \qquad (29)$$

is introduced.

The mean $\bar{Y}$ and the root mean square, defined as:

$$S_{YO} = \left(\frac{1}{n-1} \sum_{i=1}^{n} Y_i^2 \right)^{0.5} , \qquad (30)$$

are determined (n is the number of experimental points).

To compare the PG correlation with experimental results the CHF data of Czech data bank [4] are used - see TABLE I. Results of the statistical analysis of the original PG form, the PG-.g geometric form and the PG-.f flux form are in a closed channel identical. Statistical evaluation of the correlation power form PG-.p, which predicts CHF, gives different results. The

statistical results presented below do not involve favourable influence of the rod bundle factor; $F_g = 1$ was used in statistical analyses.

Tubes

TABLE III summarizes results of the statistical analysis of the PG-T tube correlation and its PG-Tp power form for various tube data bases. Correlation limit of CHFR, which corresponds to the probability value of 0.95 that CHF does not occur, is 1.096 for the tube correlation PG-T (PG-Tg, PG-Tf) and - 1.181 for the power correlation PG-Tp.

Annuli

Results of the statistical analysis data of the annulus correlations for the annulus data base (n = 713) are $\bar{R} = 0.998$, $S_R = 0.052$ - for the PG-A (PG-Ag, PG-Af) and $\bar{R} = 0.999$, $S_R = 0.071$ - for the power form PG-Ap. Experimental data of the same pressure 6.89 MPa were used.

Rod bundles

The fluid flow conditions in rod bundles subchannels are predicted with the help of a subchannel code. The code CALOPEA [6] is used for the CHF test data evaluation to determine local flow conditions. The CALOPEA thermal hydraulic computer code for Light Water Reactor analysis predicts the three-dimensional velocity, pressure, end thermal-energy fields and fuel temperatures for both single and two-phase flow. The basic computational philosophy comes from COBRA IIIC. Both codes use the subchannel analysis approach where the reactor core or fuel bundle is divided into a number of

TABLE III

Statistical Analysis Results of the Tube Correlations PG-T, PG-Tg, PG-Tf and the Power Correlation PG-Tp for Tube Data Bases

Axial Heat Flux	n	Correlation			
		PG-T PG-Tg, PG-Tf		PG-Tp	
		$\bar{R}$	S_1	$\bar{R}$	S_1
General	9547	1.001	0.056	1.003	0.103
Uniform	5589	1.001	0.058	1.008	0.106
Non-uniform	3958	0.999	0.053	0.997	0.099
Non-uniform		$\bar{Y}$	S_{Y0}	$\bar{Y}$	S_{Y0}
		0.01	0.084	-0.002	0.081

quasi-one dimensional channels that communicate laterally by crossflow and turbulent mixing. The flow field is assumed to be incompressible and homogeneous, although models are added to reflect subcooled boiling and liquid/vapor slip. The CALOPEA verification and comparison calculations are provided in the reference [7].

The CALOPEA modeling of CHF test sections is summarized as follows: uniform bundle outlet pressure; crossflow resistance is an uniform value; turbulent mixing factor TDC = 0.0064 ; Levy's subcooled void model; Madsen's bulk void relations; Armand's correlation for two-phase friction multiplier.

The PG-S subchannel correlation is compared with the rod bundle experimental CHF data, and the results of statistical analysis are summarized in TABLE IV for the various data bases. CHFR correlation limit which corresponds to the PG-S statistical characteristics (n = 7577) is 1.096 .

The isolated subchannel model does not take mixing among subchannels. Although the statistical results [2,3] can be good and applicable in the hot channel method, it is obvious that their use is limited and depends on the acceptance of the assumption on no mixing in a test section. Results of the statistical analysis (n = 7616) are $\bar{R}$ = 0.987, S_R = 0.081, S^g = 0.043 - for the PG-I (PG-Ig, PG-If) correlation, and $\bar{R}$ = 0.993, S^R_R = 0.145, S^g = 0.086 - for the power form PG-Ip. CHFR correlation limit of the PG-I (PG-Ig, PG-If) and the PG-Ip correlations which correspond to the statistical results are 1.126 and 1.248, respectively.

Columbia Rod Bundle Data. The subchannel correlation PG-S is also verified on Westinghouse and Combustion Engineering rod bundle data bases, i.e. on more than 7000 experimental data points of Columbia University data bank [5]. Results of the statistical analysis are presented in the TABLE V. The PG-S correlation shows very good statistical results for both data bases.

From mean CHFR of Westinghouse, i.e. $\bar{R}$ = 0.972, which is lower than 1.00 it can be concluded that the design of Westinghouse test sections (mixing grids) increases measured CHF values compared with others. The rod bundle factor $F_g = 1/\bar{R} = 1/0.972 = 1.029$ calculated with the Westinghouse data would change mean CHFR to 1.00 . Uncertainty of the CHF point prediction, characterized by root mean square S_{YO}, may be caused by mixing grids of test sections.

Results of the calculations with Combustion Engineering data base are also good, the higher standard deviation value 0.073 can be due to the fact that a guide tube thimble geometry is present. Better mixing model of the subchannel code could decrease the standard deviation, since local fluid conditions in the adjacent subchannels are significantly different.

Comment on Statistical Results and Correlations Comparison

The statistical characteristics of the PG correlation described in TABLES III, IV and V are comparable with each other, i.e. for tube and different rod bundle data bases, and show the high accuracy of the new correlation. Comparison of the PG correlation with several other prior correlations or CHF Table is presented below.

TABLE IV

Statistical Analysis Results of the PG-S Subchannel Correlation for the Data Bases - Czech Rod Bundle Data Base

Select Data Base	Radial Heat Flux		
	General	Uniform	Non-Uniform
Axial Heat Flux	n $\bar{R}$ S_R S_1 S_g	n $\bar{R}$ S_R S_1 S_g	n $\bar{R}$ S_R S_1 S_g
General	7577 1.005 0.054 0.054 0.037	5225 1.006 0.049 0.049 0.036	2352 1.004 0.064 0.064 0.04
Uniform	6529 1.005 0.054 0.054 0.038	4520 1.004 0.047 0.047 0.037	2009 1.007 0.067 0.067 0.042
Non-uniform	1048 1.009 0.054 0.055 0.03	705 1.019 0.057 0.06 0.03	343 0.988 0.041 0.043 0.028
Non-uniform	$\bar{Y}$ S_{YO}	$\bar{Y}$ S_{YO}	$\bar{Y}$ S_{YO}
	-0.032 0.099	-0.035 0.086	-0.025 0.122

TABLE V

Statistical Analysis Results of the Subchannel Correlation PG-S for Westinghouse and Combustion Engineering Data Bases Columbia University Rod Bundle Data Bank

Data Base	Westinghouse				Combustion Engineering			
Axial Heat Flux	n	$\bar{R}$	S_R	S_1	S_g	n	$\bar{R}$	S_R	S_1	S_g
General	2485	0.972	0.052	0.06	0.038	4655	1.007	0.073	0.073	0.057
Uniform	668	0.954	0.048	0.067	0.037	3910	1.009	0.075	0.076	0.059
Non-uniform	1817	0.978	0.053	0.058	0.039	755	1.	0.06	0.06	0.048
Non-uniform	$\bar{Y}$		S_{YO}			$\bar{Y}$		S_{YO}		
	0.058		0.119			-0.041		0.08		

The 1986 AECL-UO CHF look-up table [8] is evaluated by comparing with the tube data base of Czech data bank for uniform axial heat flux (n = 5589). Obtained statistical characteristics are the mean $\bar{R}$ = 1.05 and the standard deviation S_R = 0.284 (the PG-T correlation statistical characteristics are $\bar{R}$ = 1.00 and S_R = 0.058 - see TABLE III). Results of the 1993 CHF look-up table compared with the combined tube data base of AECL and IPPE (n = 21781), based on the constant inlet subcooling approach, are the average error of 0.0099 and the root mean square error of 0.075 - it is from the reference [9]. However, the constant inlet subcooling approach gives more favourable statistical characteristics than the constant dryout quality approach which is consistently applied in this paper analyses. As an example the results from the reference [8] are used: the CHF data predicted by the 1986 AECL-UO CHF look-up table within ±10% error bounds based on the constant inlet subcooling approach and the constant dryout quality approach are 87.4% and 40.6%, respectively.

Subchannel correlations respecting mixing among rod bundles subchannels are compared with Westinghouse data base of Columbia University data bank. The subchannel correlation PG-S gives statistical results which are presented in TABLE V. If the rod bundle factor, which respects effects of the rod bundle spacers and the influence of thermal hydraulic model implemented in the

subchannel computer code, is used (F_g = 1.029) then the statistical characteristics of the PG-S correlation are $\bar{R}$ = 1.00 and S_R = 0.053 (n = 2485). The correlations ERB3 and WRB-1 show the higher standard deviations - see the reference [10]: $\bar{R}$ = 0.994, S_R = 0.096 and $\bar{R}$ = 1.004, S_R = 0.087, respectively (n = 1147). Coefficients of these correlations were not published and were determined with help of Westinghouse rod bundle data base, i.e. for the specific geometry and restricted range of thermal hydraulic conditions.

The adequacy of CHF correlations [11,12,13] was evaluated previously by applying isolated subchannel model. Statistical results of the comparison of the CHF correlations with CHF data are described in the reference [2].

Favourable statistical characteristics of the PG correlation and a simple determination of the spacer types and location effects, i.e. rod bundle design specific features, on CHF, by means of only one correlation coefficient (rod bundle factor F_g), make the PG correlation convenient for the application as the design equation for CHF prediction in the rod bundles. This has been proved statistically for the PG-S correlation on Westinghouse and Combustion Engineering rod bundle data bases. We consider that the applicability of the PG correlation as the design equation for CHF prediction in newly designed rod bundle may be regarded as a valuable contribution of this paper.

CONCLUSIONS

Developed general correlation combines a simple analytical form and a wide range of applicability with the excellent accuracy of CHFR prediction.

The CHFR PG-S correlation respects mixing among rod bundle subchannels and gives the best results for the rod bundle geometry. The effect of spacer's type and their spacing, and the subchannel method used for the determination of local fluid conditions in a rod bundle are taken into account by including the rod bundle factor, which enables a simple transformation of the correlation to ad hoc form - on the basis of CHF experimental data of the examined rod bundle test section.

The CHFR PG-.f correlation and the CHF PG-.p correlation require as parameters inlet conditions only. The PG-.p correlation requires few iterations (approx. 4), and the value of the calculated CHF represents the critical power.

The correlation uses the lowest reasonable number of correlating parameters and shows the well-balanced means in various data bases. It has also a wide range of validity for flow conditions, it includes axial non-uniform heating, and for the rod bundle - also radial non-uniform heating.

The correlation is verified in tube geometries on more than 9500 CHF data and in rod bundle geometries on more than 14790 data, representative for both triangular and square rod bundle geometries. For internally heated concentric annuli 713 experimental data of the same pressure were available.

The correlation is applicable for thermal hydraulic analysis purposes, for tubes and water cooled rod bundles representing both typical pressurized water reactor or boiling water reactor and high conversion pressure water reactor geometries.

NOMENCLATURE

A	= flow area of (sub-)channel, i.e. tube or annulus or rod bundle subchannel (m^2)
CHF	= Critical Heat Flux
CHFR	= Critical Heat Flux Ratio
D	= rod diameter (m)
d	= equivalent diameter of (sub-)channel (m)
G	= mass flux (kg/m^2s)
F_g	= rod bundle factor: F_g = 1 or is defined by user - value depends on rod bundle grid and the mixing model used in subchannel code
h_{fg}	= latent heat of vaporization (MJ/kg)
k_a	= peak to axial average heat flux ratio
k_r	= maximum to radial average rod power ratio
L	= heated length (m)
n	= number of experimental points
P_r	= reduced pressure, ratio of pressure to critical pressure
p	= pressure (MPa)
q	= local heat flux (MW/m^2)
q_c	= predicted CHF (MW/m^2)
q_e	= measured CHF (MW/m^2)
R	= statistical random variable representing CHFR, i.e. the predicted CHF to measured CHF ratio
$\bar{R}$	= mean of variable R
r	= perimeter adjacent to a subchannel (m)
S_1	= root mean square of the variable R
S_R	= standard deviation of the variable R
S_{YO}	= root mean square of the variable Y
S_g	= standard deviation of the variable R when rod bundle factors F_g determined for test sections are used in the statistical evaluation of correlation
T_a	= factor of the axial heat flux shape
T_r	= factor of the radial heat flux distribution
t	= pitch to rod diameter ratio
x	= local quality
x_i	= inlet quality
Y	= $(y_c - y_e)/ L$

$\bar{Y}$ = mean of variable Y

y = distance from the channel inlet to the predicted CHF point (m)

y_c = CHF predicted axial coordinate (m)

y_e = CHF experimentally determined axial coordinate (m)

REFERENCES

1. R. Pernica, J. Cizek, "PG general correlation of CHFR and statistical evaluation results", UJV-10156-T, Rez, Czech Republic (1994)

2. R. Pernica, J. Cizek, "PI correlations for prediction of critical heat flux in LWR fuel assemblies", Proceedings of the Fifth International Topical Meeting on Reactor Thermal Hydraulics, NURETH-5, Vol. I, 227-234, Salt Lake City, Utah (1992)

3. R. Pernica, J. Cizek, "Critical heat flux correlations for rod bundles over a wide range of conditions", Proceedings of the International Topical Meeting on Safety of Thermal Reactors, 712-719, Portland, Oregon (1991)

4. J. Cizek, "CHF data bank - the 3rd generation", SVUSS-93-05001, Prague, Czech Republic (1993)

5. C.F. Fighetti, D.G. Reddy, "Parametric study of CHF data, Vol.3, Part 2: Critical heat flux data", EPRI-NP-2609, Columbia University, Research project 813, Final report, N.Y. (1982)

6. J. Cizek, J. Chum, "CALOPEA - CMP1IN, CMO1IN, CMYAZ1IN", Program versions for AT PCs, SVUSS-91-05302, Prague, Czech Republic (1991)

7. Y. Sung, T.Q. Nguyen, J. Cizek, "VIPRE modelling of VVER reactor core for DNB analysis", Seventh International Meeting on Nuclear Reactor Thermal-Hydraulics, NURETH-7, Saratoga Springs, N.Y. (1995)

8. D.C. Groeneveld, S.C. Cheng and T. Doan, "1986 AECL-UO critical heat flux look-up table" Heat Transfer Engineering 7, 46-62 (1986)

9. D.C. Groeneveld, L.K.H. Leung, P.L. Kirillov, V.P. Bobkov, F.J. Erbacher, W. Zeggel, "An improved table look-up method for predicting critical heat flux", Proceedings Sixth International Topical Meeting on Nuclear Reactor Thermal Hydraulics, NURETH-6, Vol. I, 223-230, Grenoble, France, (1993)

10. K. Mistelberger, C. Vogel, G. Ulrych, "The correlation ERB3 for critical heat flux in pressurized water reactor rod bundles", Kerntechnik 57, 42-48 (1992)

11. D.G. Reddy, C.F. Fighetti, "Parametric study of CHF data, Vol.2: Generalized subchannel CHF correlation for PWR and BWR fuel assemblies", EPRI-NP-2609, Palo Alto (1983)

12. G.P. Gaspari, A. Hassid, F. Lucchini, "A rod-centered subchannel analysis with turbulent (enthalpy) mixing for critical heat flux prediction in rod clusters cooled by boiling water", Fifth International Heat Transfer Conference, 295-306, Tokyo (1974)

13. R.W. Bowring, "WSC-2: A subchannel dryout correlation for water - cooled clusters over the pressure range 3.4 - 15.9 MPa", AEEW-R 983, Winfrith (1979)

A STUDY OF THE EFFECT OF SPACE-DEPENDENT NEUTRONICS ON STOCHASTICALLY-INDUCED BIFURCATIONS IN BWR DYNAMICS[1]

G. Th. Analytis

Laboratory for Thermal Hydraulics,
Paul Scherrer Institute (PSI),
CH-5232 Villigen PSI, Switzerland
Tel: 56-99-21-11 / Fax: 56-99-21-99

ABSTRACT

A non-linear one-group space-dependent neutronic model for a finite one-dimensional core is coupled with a simple BWR feed-back model. In agreement with results obtained by the authors who originally developed the point-kinetics version of this model, we shall show numerically that stochastic reactivity excitations may result in limit-cycles and eventually in a chaotic behaviour, depending on the magnitude of the feed-back coefficient K. In the framework of this simple space-dependent model, the effect of the non-linearities on the different spatial harmonics is studied and the importance of the space-dependent effects is exemplified and assessed in terms of the importance of the higher harmonics. It is shown that under certain conditions, when the limit-cycle-type develop, the neutron spectra may exhibit strong space-dependent effects.

1. INTRODUCTION

In the fields of rector physics and thermohydraulics, non-linearities and their effect on the behaviour and stability of nuclear reactors have acquired great importance during the last decade. Though, the problem of the effect of random **parametric** excitations on the stability of early BWRs and in particular, on the observed random bursts (large-amplitude fluctuations which could cause a reactor scram) has attracted the attention of a number of workers in the field as early as 1961 [1 - 3] and is still a subject of interest under study by a number of researchers [4 - 6].

A simple phenomenological non-linear reduced-order dynamical BWR model was developed and reported in a series of works [7 - 9]. This model was based on point-kinetics neutronics and predicted stable limit-cycles for BWRs above a certain value of the void-feedback reactivity coefficient (bifurcation parameter) K and the appearance of higher harmonics of the resonance associated with the void reactivity feed-back in the neutronic Auto-Power Spectral Densities (APSDs). It also predicted the transition to chaos above a certain value of the feed-back coefficient. The measurements at the Swedish BWR plant Forsmark during limit-cycle oscillations [10] have confirmed the appearance of these higher harmonics in the neutronic APSDs. Similar (but more complicated) results are to be found in Ref 11 (see also Ref. 12) in which measurements of Decay Rations (DRs) at the Ringhals-1 Swedish BWR plant were presented. In these measurements, while at some radial position in the core there was only one resonance appearing in the neutron spectrum, in other positions there were two [13], indicating the existence of strong space-dependent effects and regional oscillations different

[1]This work has been privately pursued and is not related to the present activities of the author at PSI.

DR's. These strong space-dependent effects were due to the way that the control rods and fuel boxes were radially distributed in the core [12,14], resulting in a double-hump radial power profile. Due to this, the two radial segments behaved like a "loosely coupled core", with the first higher flux harmonic in the transient neutronic equations (which reflects such an azimuthal shape) being excited by the particular "double-hump" radial power distribution in the core. Recently [15], a theoretical study on the problem of out-of-phase core oscillations has also been reported. In general, measurements in different BWRs during limit cycle oscillations have shown that while some times the whole core oscillates "in-phase", there are cases in which this is not the case (Parmegiani et al., 1984) and the oscillations are 180° out-of-phase. This will certainly depend on the static radial flux shape which in turn will determine which one of the azimuthal harmonics will dominate. Consequently, ([11], one cannot always associate a unique DR to the system, but rather there are different local DR's.

In this work, we shall extend the model of Ref. 7 - 9 by including explicit space-dependent neutronics, but only giving a simple "ad hoc" phenomenological space dependence to the other equations of the model (eg avoiding any **direct** modeling of the axial dependence of the transport of the coolant). After writing down the non-linear space-dependent neutron kinetics modified one-group diffusion equation for a homogeneous core which is finite in the x- direction, we shall assume that the system is stochastically excited by a distributed random source. We shall then separate the independent variables into their deterministic and fluctuating parts and expand their space-dependent fluctuating components (both of the independent variables and of the space-dependent random source) in a series of time-dependent coefficients and orthogonal spatial eigenfunctions of the Helmholtz equation [3]. The resulting infinite set (due to the coupling of each harmonic to all other harmonics) of non-linear equations for the time-dependent coefficients we shall solve numerically after truncating them at a certain harmonic. Finally, the complete space-dependent solution (up to the n^{th} spatial harmonic considered) is constructed, from which one can compute the APSDs, CPSDs or assess the importance of the different spatial harmonics. In particular, we shall show that depending on the assumptions made about the magnitude of the different harmonics of the feed-back coefficients and the random excitation source, when the limit-cycle-type oscillations develop, there may be 180° out-of-phase neutronic oscillations in the two halves of the core and also, strong spatial dependence of the neutronic APSDs. In this work, we shall not investigate the actual hydraulic mechanism which is responsible for inducing the instabilities and the power oscillations; instead, we shall assume the simple reactivity feed-back (with a simple space-dependence) as formulated in Ref. 7 - 9. A more in-depth analysis of this problem and a subsequent association of model parameters with reactor parameters would be a worth-while task.

2. THE COUPLED NEUTRONICS-THERMOHYDRAULICS MODEL

We shall first write down the equations of the model of Ref. 7 - 9. Though, in contrast to the point-kinetics approach followed by these authors, we shall assume one-group space-dependent neutronics in the diffusion approximation and a spatially finite and homogeneous core (we shall perform the calculations only for the one-dimensional case) in which the random perturbations are spatially smeared. Then, the neutronic and the coupled thermo-hydraulic equations can readily be written for the general case; we shall have the following system of non-linear differential equations

$$\frac{\partial N(\mathbf{r},t)}{\partial t} = \frac{M^2}{l}\nabla^2 N(\mathbf{r},t) + \frac{(\rho(\mathbf{r},t) - \beta)}{l} N(\mathbf{r},t) + \lambda C(\mathbf{r},t), \qquad (2.1a)$$

$$\frac{\partial C(\mathbf{r},t)}{\partial t} = \frac{N(\mathbf{r},t)\beta}{l} - \lambda C(\mathbf{r},t), \qquad (2.1b)$$

$$\frac{\partial T(\mathbf{r},t)}{\partial t} = K\,[N(\mathbf{r},t) + \sigma\xi f(\mathbf{r},t)] - a_3 T(\mathbf{r},t), \qquad (2.1c)$$

$$\frac{\partial^2 \rho(\mathbf{r},t)}{\partial t^2} + a_2 \frac{\partial \rho(\mathbf{r},t)}{\partial t} + a_1 \rho(\mathbf{r},t) = T(\mathbf{r},t). \qquad (2.1d)$$

Equation (2.1d) above is derived by utilizing the void propagation equation for void fluctuations with the fluctuations in the coolant heat absorption rate $\delta Q(z,t)$ as the source (this equations results after linearizing the mixture mass and energy continuity equations)

$$\frac{\partial \delta\alpha(z,t)}{\partial t} + V_\alpha \frac{\partial \delta\alpha(z,t)}{\partial z} = \frac{\delta Q(z,t)}{h_0} \qquad (2.1e)$$

(where the void propagation velocity V_α and h_0 are functions of the phasic enthalpies and densities), Laplace transforming the equation, solving it, expressing the reactivity fluctuations in terms of the void fluctuations by integrating over the core height and taking the inverse Laplace transform, after approximating an exponential. In doing this, separability of the fluctuations of the heat transferred to the coolant in space (in the axial direction) and time is assumed i.e. point kinetics. An equation similar to (2.1d) was used as early as 1961 by Akcasu [1] (see also Ref 3), who studied the origin of large-amplitude fluctuations (random power bursts) which were randomly occurring in the early BWRs. Notice that apart from the neutronic equations for which we have explicitly used the modified one-group space-dependent model, we have assumed for the thermohydraulic (and reactivity) equations a "naive" straightforward space-dependent extension of the corresponding equations of the model of Ref. 7 - 9. In eqs (2.1a) - (2.1d), M^2 , l, λ and β are the migration area, the prompt neutron life time, the delayed neutron time constant and the delayed neutron fraction, respectively. K is the adjustable feed-back coefficient, $f(\mathbf{r},t)$ is a Gaussian noise (not necessarily white) by which we shall excite the dynamical system parametrically, σ is the standard deviation and ξ is, for the time being, a constant which we shall later set equal to either 0 or 1, in order to assess the importance of the different axial harmonics to the final result. a_1 and a_2 are constants related to some thermohydraulic parameters in the core [7 - 9]; in principle, one could actually generalize this and assume that they are also random functions, consisting of an average and a fluctuating part ($a_i(t) = a_i + \delta a_i(t)$) [1,3]. In general, one can assume that $\xi(\mathbf{r},t)$ satisfies a random differential equation of the form

$$\frac{df(\mathbf{r},t)}{dt} = -bf(\mathbf{r},t) + \sigma_w w(\mathbf{r},t) \qquad (2.1f)$$

where b is a constant, σ_w is the standard deviation, and $w(\mathbf{r},t)$ is a temporally white noise which, similarly to $f(\mathbf{r},t)$, can be expanded in an infinite series of orthogonal spatial eigenfunctions multiplied by temporally white random coefficients. In this work, we shall assume that $f(\mathbf{r},t)$ itself is temporally white. We shall now proceed and separate all variables in eqs (2.1a) - (2.1d) into their steady-state and fluctuating components, but we shall keep the second-order non-linear term in the prompt neutron equation. The neutronic equations for example can be written by separating $N(\mathbf{r},t)$, $C(\mathbf{r},t)$ and $\rho(\mathbf{r},t)$ into averaged and fluctuating parts [3], but avoiding any linearization of the resulting equations. After some straight-forward algebra, it can readily be shown that eq. (2.1a) can be written as

$$\frac{\partial \delta n(\mathbf{r},t)}{\partial t} = \frac{M^2}{l} \nabla^2 \delta n(\mathbf{r},t) + \frac{M^2}{l} \nabla^2 N(\mathbf{r}) + \frac{(\rho_0 - \beta)}{l} N(\mathbf{r}) + \frac{(\delta\rho(\mathbf{r},t) - \beta)}{l} \delta n(\mathbf{r},t) + \frac{\delta\rho(\mathbf{r},t)}{l} N(\mathbf{r}) + \lambda \delta c(\mathbf{r},t), \qquad (2.2)$$

where now

$$\delta n(\mathbf{r},t) \;=\; N(\mathbf{r},t) \;-\; N(\mathbf{r}), \tag{2.3a}$$

$$\delta c(\mathbf{r},t) \;=\; C(\mathbf{r},t) \;-\; C(\mathbf{r}), \tag{2.3b}$$

$$\delta \rho(\mathbf{r},t) \;=\; \rho(\mathbf{r},t) \;-\; \rho_0 \tag{2.3c}$$

and $N(\mathbf{r})$, $C(\mathbf{r})$ and ρ_0 are the corresponding steady-state values.

Finally, if one notices that $N(\mathbf{r})$ satisfies the steady-state equation, eq. (2.2) simplifies to

$$\frac{\partial \delta n(\mathbf{r},t)}{\partial t} \;=\; \frac{M^2}{l}\,\nabla^2\,\delta n(\mathbf{r},t) \;+\; \frac{(\delta\rho(\mathbf{r},t) \;-\; \beta)}{l}\,\delta n(\mathbf{r},t) \;+\; \frac{\delta\rho(\mathbf{r},t)}{l}\,N(\mathbf{r}) \;+\; \lambda\delta c(\mathbf{r},t), \tag{2.4}$$

It can readily be shown that eq. (2.4) above together with eqs. (2.1b) - (2.1d) (after also assuming that $T(\mathbf{r},t) \;=\; T(\mathbf{r}) \;+\; \delta T(\mathbf{r},t)$ and re-writing eq. (2.1d) as two first-order differential equations) can be written in the following form

$$\frac{\partial \delta \mathbf{Y}_i(\mathbf{r},t)}{\partial t} \;=\; \mathbf{M}_{ij}(\nabla^2,\mathbf{r},t)\;\delta\mathbf{Y}_j(\mathbf{r},t) \;+\; \Big(\delta\mathbf{Y}_i(\mathbf{r},t)\;\delta\mathbf{Y}_j(\mathbf{r},t)\Big)\;\delta_{i1}\;\delta_{j4} \;+\; (K\;\xi\;f_i(\mathbf{r},t))\;\delta_{i3} \tag{2.5a}$$

where $\mathbf{M}_{ij}(\nabla^2,\mathbf{r},t)$ is a **5X5** matrix, $\mathbf{Y}_i(\mathbf{r},t)$ is a (column) vector with components

$$\mathbf{Y}_i(\mathbf{r},t) \;=\; (\delta n(\mathbf{r},t),\; \delta c(\mathbf{r},t),\; \delta T(\mathbf{r},t), d\delta\rho(\mathbf{r},t)\;/\;dt,\; \delta\rho(\mathbf{r},t)) \tag{2.5b}$$

and δ_{ij} is equal to 0 if $i \neq j$ and 1 otherwise. Eq. (2.5a) above is a non-linear space-dependent Langevin's equation [3]. The second term on the RHS of the above matrix equation is the non-linear term which we shall retain (and which is ignored in the linearized approach as being of second-order), while the third term is the random source function.

We shall now expand the vector $\delta\mathbf{Y}_i(\mathbf{r},t)$ the source $f(\mathbf{r},t)_i$ and each term in the product $(\delta\mathbf{Y}_i(\mathbf{r},t)\;\delta\mathbf{Y}_j(\mathbf{r},t))$ (which in fact is $(\delta\rho(\mathbf{r},t)\;\delta n(\mathbf{r},t))$) in a series of eigenfunctions of the Helmholtz equation; neglecting for notational convenience the subscript "i" we shall have

$$\nabla^2 N_\mu(\mathbf{r}) \;+\; B_\mu^2\;N_\mu(\mathbf{r}) \;=\; 0 \tag{2.6a}$$

satisfying

$$\int_{-\infty}^{\infty} d\mathbf{r}\;N_\mu(\mathbf{r})\;N_\nu(\mathbf{r}) \;=\; \delta_{\mu\nu} \tag{2.6b}$$

where $\delta_{\mu\nu}$ is the Kronecker delta, in the following way:

$$\delta \mathbf{Y}(\mathbf{r},t) \;=\; \sum_{\mu=1}^{\mu=\infty} \mathbf{Y}_{\mu}(t)\; N_{\mu}(\mathbf{r}), \tag{2.7a}$$

and

$$(\xi f(\mathbf{r},t)) \;=\; \sum_{\mu=1}^{\mu=\infty} \xi_{\mu}\; f_{\mu}(t)\; N_{\mu}(\mathbf{r}). \tag{2.7b}$$

where now we shall assume that ξ_{μ} is either 1 or 0. For the sake of simplicity, we shall assume orthogonal rectangular coordinates and for computational convenience, we shall assume that the core is finite only in the x-direction; hence,

$$N_k(x) = \left(\frac{2}{H}\right) \sin(B_{k,x}x) \qquad (B_{k,x} = \frac{k\,\pi}{H},\; k = 1,2,3.....) \tag{2.8}$$

and $B^2_{1,x}$ is the geometrical buckling in the x-direction. Notice that we could have easily assumed that the core is cylindrical (which would have been a much better approximation with more realistic space-dependent effects, as well as preserving the radial two-dimensionality of the problem); though, we tried to simplify the problem by avoiding dealing with Bessel functions, hence keeping the algebra as simple as possible. We shall now insert the eqs (2.7a), (2.7b) and (2.8) into eq (2.4) multiply both sides by $N^*(x)$ (which is the adjoint; in the one-group case, it is identical to the normal one) and integrate from 0 to H (we denote by H the core "length" in the x-direction); the equation(s) satisfied by the expansion coefficients $n_n(t)$ of the fluctuations $\delta n(x,t)$ for the n^{th} harmonic will be

$$\begin{aligned}
\frac{dn_{n'}(t)}{dt} \;&=\; -\,\frac{M^2}{l}\, B^2_{n',x}\, n_{n'}(t) \\
&+\; \frac{4}{lH^2} \sum_{m=1}^{m=\infty} \rho_m(t) \sum_{n=1}^{n=\infty} n_n(t) I(n'\,;\,m\,,\,n) \\
&-\; \frac{\beta}{l}\, n_{n'}(t) \;+\; \frac{4}{lH^2} \sum_{n=1}^{n=\infty} \rho_n(t) I(n'\,;\,1\,,\,n) \\
&+\; \lambda c_{n'}(t)
\end{aligned} \tag{2.9a}$$

and the "tensor" $I_{n'mn}$ is defined by

$$\begin{aligned}
I_{n'mn} \;&=\; I(n'\,;\,m\,,\,n) \\
&=\; \int_0^H dx\; N_m(x)\; N_n(x) N_{n'}(x).
\end{aligned} \tag{2.9b}$$

It can readily be shown after some straight-forward algebra that with the simple assumption of sinusoidal harmonics as defined above, we shall have

$$I(n^{'}\,;\,m\,,\,n) \;=\; I_{n'mn} \;=$$
$$-\frac{H}{4\pi}\left(\frac{\cos(m+n-n^{'})\pi \;-\; 1}{m+n-n^{'}} \;+\; \frac{\cos(m-n+n^{'})\pi \;-\; 1}{m-n+n^{'}}\right.$$
$$\left. -\;\frac{\cos(m+n+n^{'})\pi \;-\; 1}{m+n+n^{'}} \;-\; \frac{\cos(m-n-n^{'})\pi \;-\; 1}{m-n-n^{'}}\right) \tag{2.10}$$

Eq. (2.9) constitutes in fact an infinite number of non-linear equations for the time-dependent coefficients $n_{n'}(t)$. This infinite hierarchy of equations for the time-dependent coefficients is typical for non-linear problems, but also for problems with feed-back in which each harmonic is coupled to all the other harmonics. Hence, we cannot completely neglect the cross-couplings between the harmonics, since if we were to do this, we would probably be neglecting important non-linearities. As an example, for $n^{'} \;=\; 1$, if we only keep the first three harmonics, we shall explicitly have

$$\begin{aligned}\frac{dn_1(t)}{dt} \;&=\; -\,\frac{M^2}{l}\,B_{1,x}^2\,n_1(t) \;-\; \frac{\beta}{l}\,n_1(t) \;+\; \lambda c_1(t)\\
&+\; \frac{4}{H^2 l}\Big(\rho_1(t)\;(n_1(t)I_{111} \;+\; n_2(t)I_{112} \;+\; n_3(t)I_{113})\\
&+\; \rho_2(t)\;(n_1(t)I_{121} \;+\; n_2(t)I_{122} \;+\; n_3(t)I_{123})\\
&+\; \rho_3(t)\;(n_1(t)I_{131} \;+\; n_2(t)I_{132} \;+\; n_3(t)I_{133})\Big)\\
&+\; \frac{4}{H^2 l}\left(\rho_1(t)I_{111} \;+\; \rho_2(t)I_{112} \;+\; \rho_3(t)I_{113}\right)\end{aligned} \tag{2.11a}$$

with similar equations for $n_2(t)$ and $n_3(t)$, while for the other equations ($n \;=\; 1,2,3$),

$$\frac{dc_n(t)}{dt} \;=\; \frac{\beta}{l}n_n(t) \;-\; \lambda c_n(t), \tag{2.11b}$$

$$\frac{dT_n(t)}{dt} \;=\; K_n\,[n_n(t) \;+\; \sigma\xi_n f_n(t)] \;-\; a_3 T_n(t), \tag{2.11c}$$

$$\frac{d^2\rho_n(t)}{dt^2} \;+\; a_2\frac{d\rho_n(t)}{dt} \;+\; a_1\rho_n(t) \;=\; T_n(t). \tag{2.11d}$$

In writing down the above equations, we have assumed that the feed-back coefficient K is in fact different for different harmonics. Within the framework of our simple homogeneous model, it is not easy to justify this assumption. Though,we shall see in due course that this is a basic requirement for predicting strong space-dependent neutronic APSDs from the model. The system of non-linear neutronic and "hydraulic" differential equations for the time-dependent coefficients can be solved efficiently by one of the IMSL ordinary non-linear differential equations solvers based on the Runge-Kutta or Gear methods (eq. (2.11d) must

first be written as two first-order differential equations). Subsequently, the time-dependent coefficients are substituted back into eqs. (2.7a), and the space-dependent solution is obtained. Though, since a large number of points is needed when the spectral functions are calculated, the running time increases dramatically as the number of harmonics increases, since clearly, the number of equations to be solved if one wants to keep up to and including the N^{th} harmonic will be $5N$. Concluding this section, we should say that a very important problem which we shall not tackle in this work is the establishment of rigorous convergence criteria for the "infinite" sums above and hence, the minimum number of harmonics one should retain to achieve convergence. Due to the non-linearities of the problem, this is not a straight-forward task. Instead, in this work, we shall follow a "non-rigorous" approach and try, for one particular case, to get a feeling of the differences between the model predictions, depending on the number of spatial harmonics retained in the series expansions.

3. NUMERICAL EXAMPLES

In this section, we shall evaluate the model numerically and try to assess the importance of the different spatial harmonics to the final results. Additionally, we shall show that under certain conditions, the model can predict strong space-dependent effects, which manifest themselves in the neutronic APSDs [11,12].

We shall assume that the core is finite in the x-direction and that its "length" is given by $H = 2.8\ m$. The nuclear constants which we shall use in the neutronic equations will be typical for a BWR [7] and are given by $\beta = 0.0056$, $\lambda = 0.08\ s^{-1}$, $l = 4.5\ 10^{-5}\ s$ and $M^2 = 0.0056\ m^2$. The coefficients a_1, a_2 and a_3 in the thermohydraulic equations were also taken from the aforementioned reference and are given by $a_1 = 6.8166$, $a_3 = 2.2494$ and $a_3 = 0.2325$. Finally, we shall assume that $\xi_1 = 0$ and $\xi_2 = \xi_3 = 1$, while we shall keep the feed-back coefficients K_n as open parameters and, as we have already mentioned before, we shall assume that generally, are different for different spatial harmonics. By choosing these values for the factors ξ_n's multiplying the expansion coefficients of the random spatially distributed sources (cf. eq. (2.7b)) we have completely suppressed the contribution from the fundamental spatial mode of the random source. We shall see in due course that although this is necessary for the appearance of space-dependent effects, it leads to a divergent solution some time after the appearance of limit-cycle-type oscillations. Similarly, in the present work, in order to magnify the contribution from the second spatial harmonic, we shall assume that K_2 is always much higher than the other K_n's. Finally, we shall assume that there are three neutron detectors are located at $x = 0.7\ m$, $x = 1.4\ m$ and $x = 1.85\ m$, and a temporally white noise source excites the system parametrically, with $\sigma = 0.001$. Other non-white sources have been considered (cf eq. (2.11e)) and the final results do, to some extent, depend on it. In this work, we shall not elaborate further on this point. The system of differential equations (2.9a), (2.11b - c) was solved by an IMSL ordinary non-linear differential equations solver based on the Runge-Kutta-Verner fifth-order method; the white noise-source $f_n(t)$ in eq. (2.11c) was generated also by an IMSL routine.

In Fig. 1, we show the predicted neutronic responses (A) and APSDs (B) (also computed by an IMSL routine from the signals generated by the solution of the system of non-linear differential equations), respectively, at $x = 0.7\ m$, $x = 1.4\ m$ and $x = 1.85\ m$ after the limit-cycle-type oscillations are initiated. For all the calculations, 2000 neutronic "measurement" points were used from the solution of the non-linear differential equations at intervals of $0.1\ s$ and the spectra were evaluated by utilizing the predicted neutronic fluctuations between $t = 200\ s$ and $t = 400\ s$. In these calculations, three spatial harmonics were originally considered (ie a system of 15 simultaneous non-linear differential equations was solved), and $K_2 = 2.65$, $K_1 = K_3 = 0.72$, $\xi_1 = 0$, $\xi_2 = \xi_3 = 1$ was assumed. Clearly, one can see that under the aforementioned assumptions, the neutronic response at $x = 1.4\ m$ exhibits a double-frequency behaviour when compared to the neutronic response at $x = 0.7\ m$, and that this is clearly reflected on the computed neutronic APSDs: At $x = 0.7\ m$, the

APSD exhibits two resonances at approximately 0.433 and 0.865 Hz, respectively, with the resonance at 0.46 being the dominant one, while at $x = 1.4\ m$, the APSD exhibits only one resonance at 0.865 Hz. The appearance of these multiple resonances when the limit-cycle oscillations develop was first predicted in Ref. 7 - 9 who used the point-kinetics neutronic model, and has since been verified by measurements [10]. In the same figure, one can see that although the APSD at $x = 1.85\ m$ is almost identical to the APSD at $x = 0.7\ m$, the neutronic response is 180° out-of-phase with respect to the one at $x = 0.7\ m$. The reason for this is clear: Due to the assumed dominance of the first higher harmonic, the neutronic responses in the two different sides of the core will be out-of-phase. In Fig. 2, we show the predicted Cross-Power Spectral Density (CPSD) (A) and phase (B) between $x = 0.7\ m$ and $x = 1.4\ m$, also computed in the same way. The two neutronic APSDs at the two different locations are different and exhibit a strong space-dependence; though, these differences are extremely sensitive and are strongly dependent on the assumed values of K_n's and ξ_n's. As an example of this, we show in Fig. 3 the computed neutronic responses (A) and APSDs (B) at the same spatial locations as above, but with $K_2 = 2.65$, $K_1 = K_3 = 0.77$. If one compares the APSDs with the ones shown in Fig. 1, the APSD at $x = 1.4\ m$ exhibit now a second peak while again, at $x = 0.7\ m$ the APSD is almost identical to the one at $x = 1.85\ m$. Furthermore, one can clearly see in the same figure that while the neutronic response at $x = 1.4\ m$ also exhibits this second frequency, in this case, the neutronic oscillations consist of a superposition of two signals with different amplitudes. At $x = 1.85\ m$, the neutronic signals are also 180° out-of-phase with respect to the ones at $x = 0.7\ m$. Finally, we show in Fig. 4 the trajectories in the n(t) - T(t) plane at $x = 0.7\ m$ (A) and $x = 1.4\ m$ (B), respectively. One can clearly see the different behaviour of these trajectories at the two different spatial positions. Clearly, full limit-cycle oscillations have not yet been established within the time period of 400 s considered in this work, as can also be seen from the predicted neutronic signals whose amplitude is still increasing.

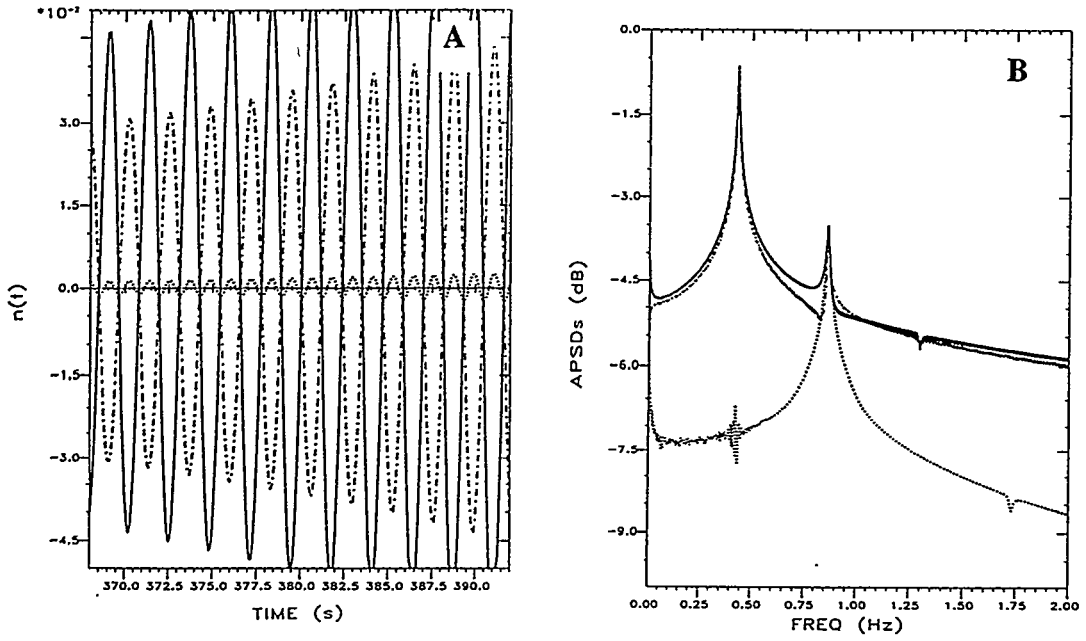

Fig. 1 Predicted neutronic responses (A) and APSDs (B) at $x = 0.7\ m$ (—), $x = 1.4\ m$ (....) and $x = 1.85\ m$ (-.-.) after initiation of limit-cycle-type oscillations; 3 spatial harmonics retained. $K_2 = 2.65$, $K_1 = K_3 = 0.72$, $\xi_1 = 0$, $\xi_2 = \xi_3 = 1$.

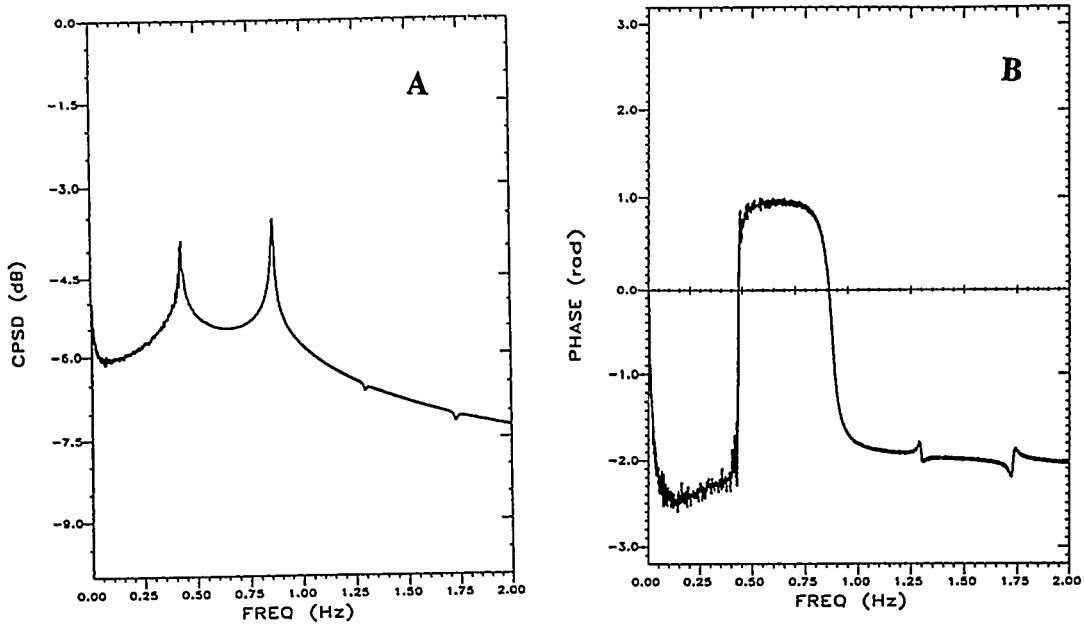

Fig. 2 Predicted CPSD (A) and phase (B) between $x = 0.7\ m$ and $x = 1.4\ m$ after initiation of limit-cycle-type oscillations; 3 spatial harmonics considered. $K_2 = 2.65$, $K_1 = K_3 = 0.72$, $\xi_1 = 0$, $\xi_2 = \xi_3 = 1$.

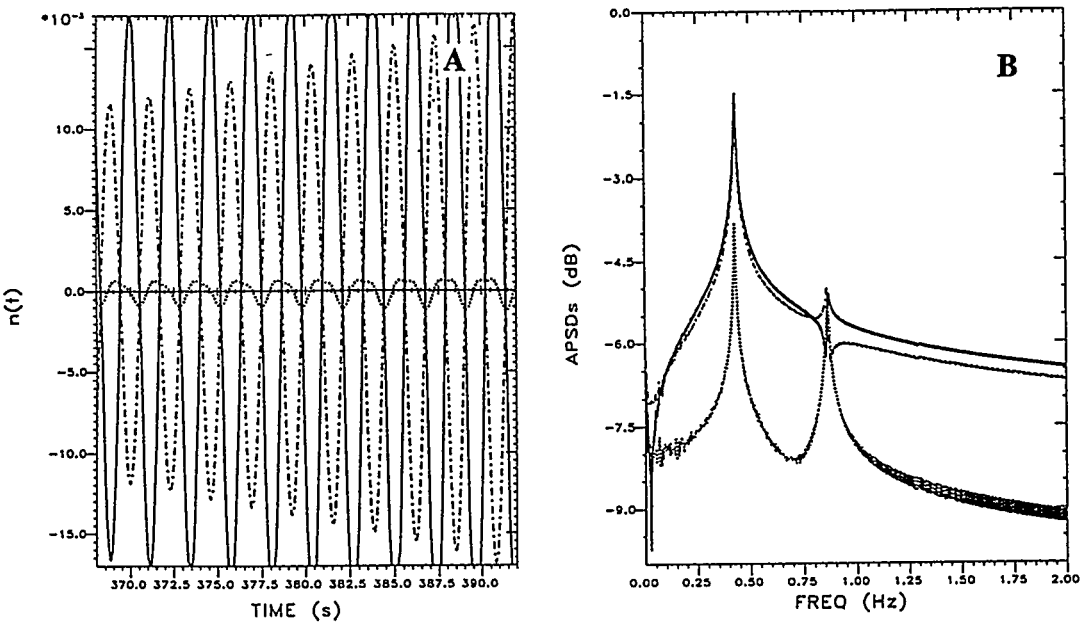

Fig. 3 Predicted neutronic responses (A) and APSDs (B) at $x = 0.7\ m$ (—), $x = 1.4\ m$ (....) and $x = 1.85\ m$ (-.-.) after initiation of limit-cycle-type oscillations; 3 spatial harmonics considered. $\xi_1 = 0$, $\xi_2 = \xi_3 = 1$ and $K_2 = 2.65$, $K_1 = K_3 = 0.77$.

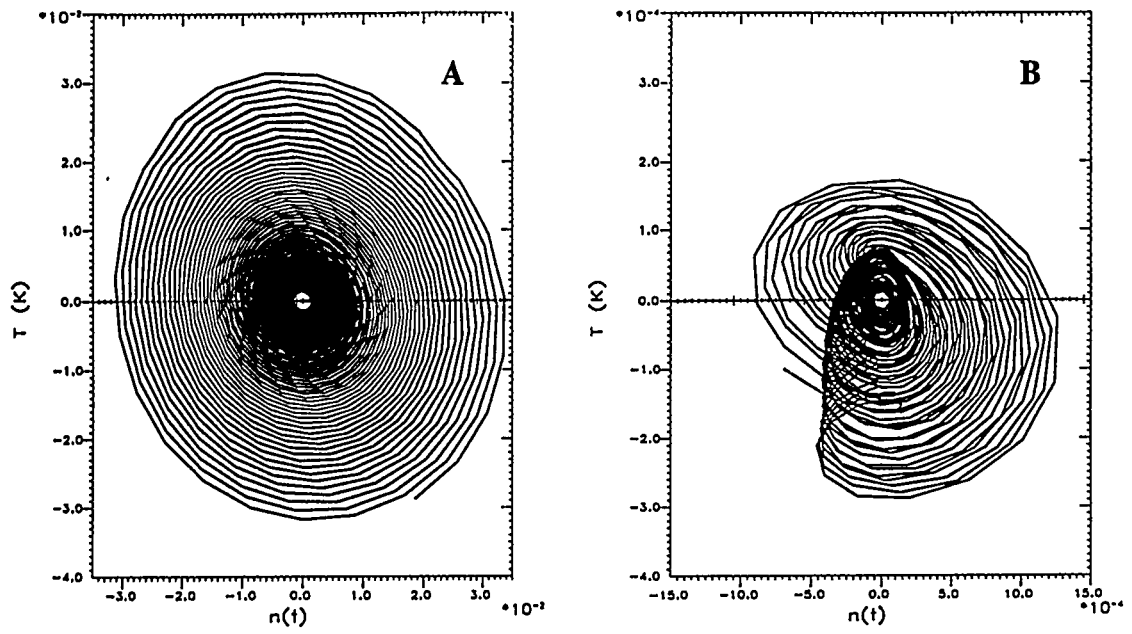

Fig. 4 Predicted trajectories on the n(t) - T(t) plane at $x = 0.7\ m$ (—) and $x = 1.4\ m$ (....). 3 spatial harmonics considered. $\xi_1 = 0$, $\xi_2 = \xi_3 = 1$ and $K_2 = 2.65$, $K_1 = K_3 = 0.77$.

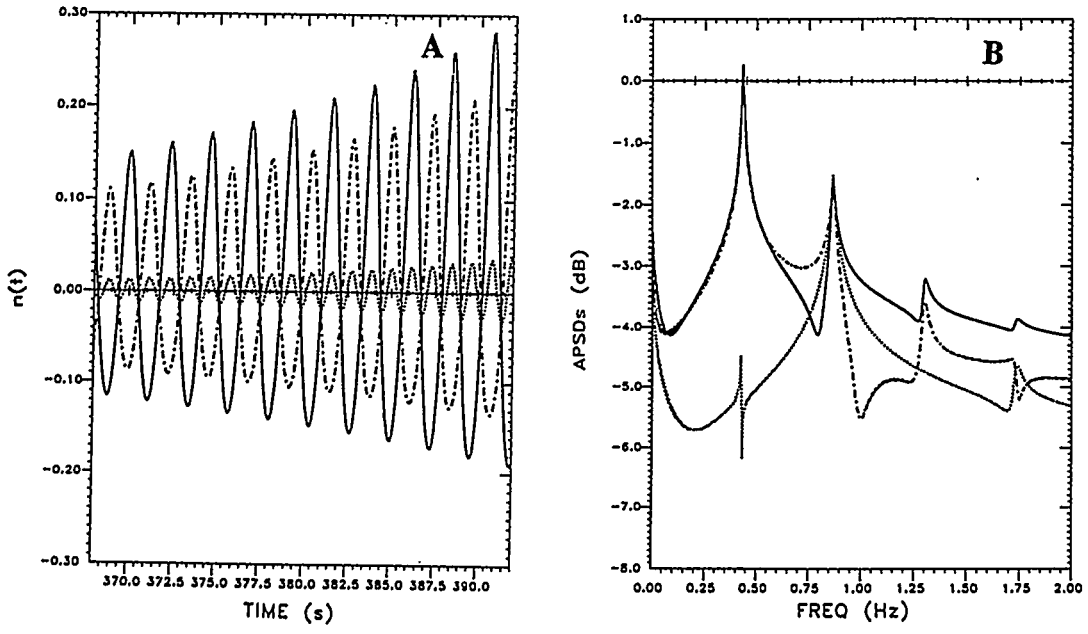

Fig. 5 Predicted neutronic responses (A) and APSDs (B) at $x = 0.7\ m$ (—), $x = 1.4\ m$ (....) and $x = 1.85\ m$ (-.-.); 4 spatial harmonics retained. $K_2 = 2.65$, $K_1 = K_3 = K_4 = 0.77$, $\xi_1 = 0$, $\xi_2 = \xi_3 = \xi_4 = 1$.

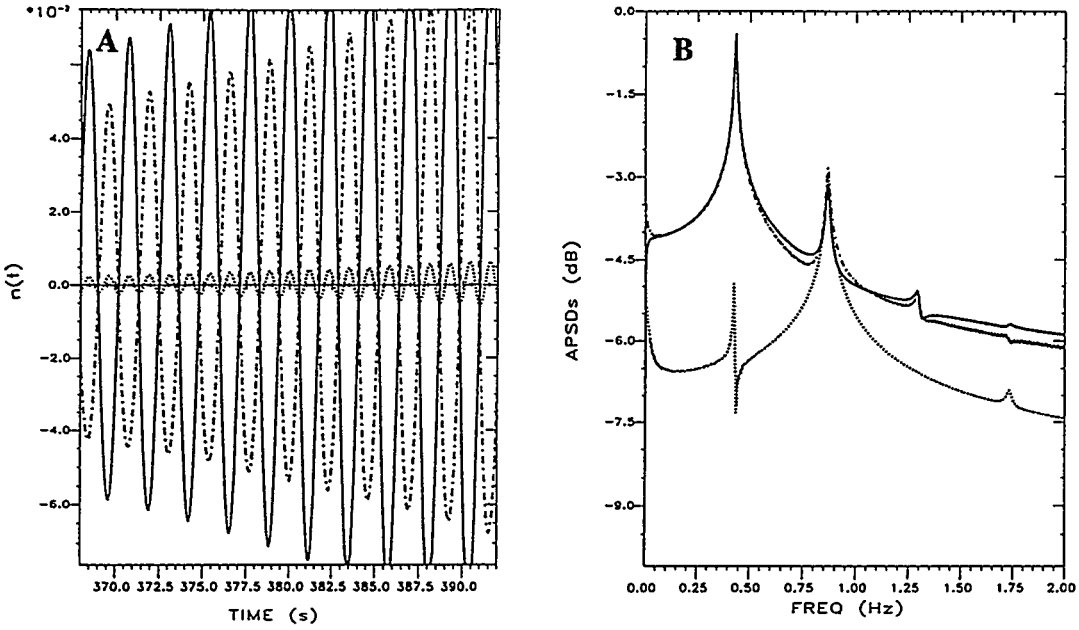

Fig. 6 Predicted neutronic responses (A) and APSDs (B) at $x = 0.7\ m$ (—), $x = 1.4\ m$ (....) and $x = 1.85\ m$ (-.-.); 5 spatial harmonics retained. $K_2 = 2.65$, $K_1 = K_3 = K_4 = K_5 = 0.77$, $\xi_1 = 0$, $\xi_2 = \xi_3 = \xi_4 = \xi_5 = 1$.

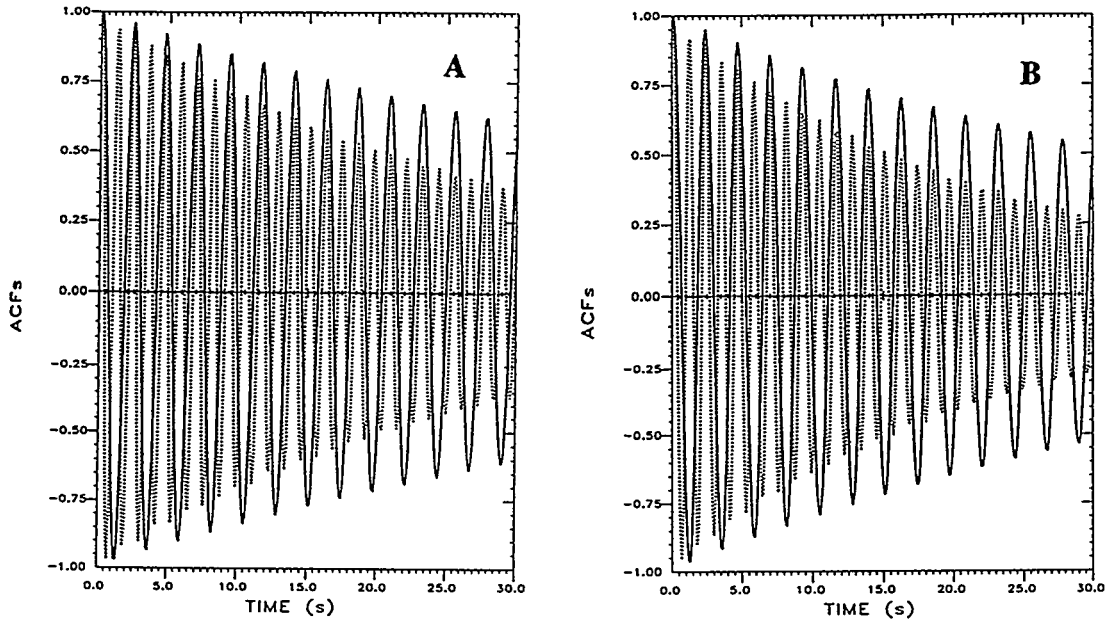

Fig. 7 Predicted ACFs at $x = 0.7\ m$ (—) and $x = 1.4\ m$ (....). $K_2 = 2.65$, $K_1 = K_3 = K_4 = K_5 = 0.77$, $\xi_1 = 0$, $\xi_2 = \xi_3 = \xi_4 = \xi_5 = 1$. Calculations performed with 3 (A) and 5 (B) harmonics retained.

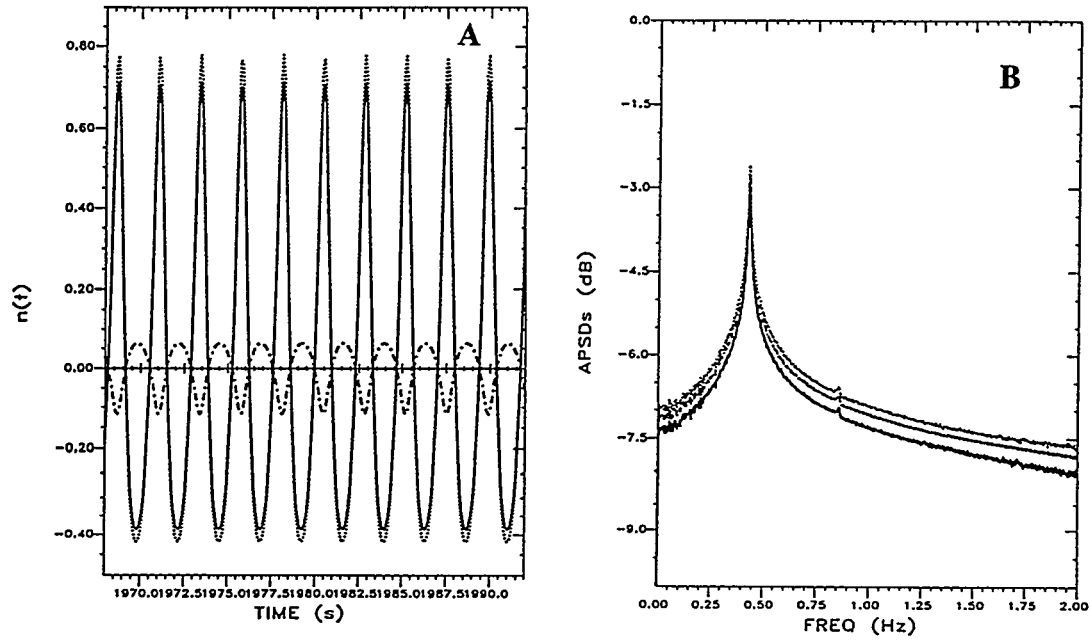

Fig. 8 Predicted neutronic responses (A) and APSDs (B) at $x = 0.7\ m$ (—), $x = 1.4\ m$ (....) and $x = 1.85\ m$ (-.-.); 3 spatial harmonics retained. $K_2 = 3.00$, $K_1 = K_3 = 0.78$, $\xi_1 = 1$, $\xi_2 = \xi_3 = 0$.

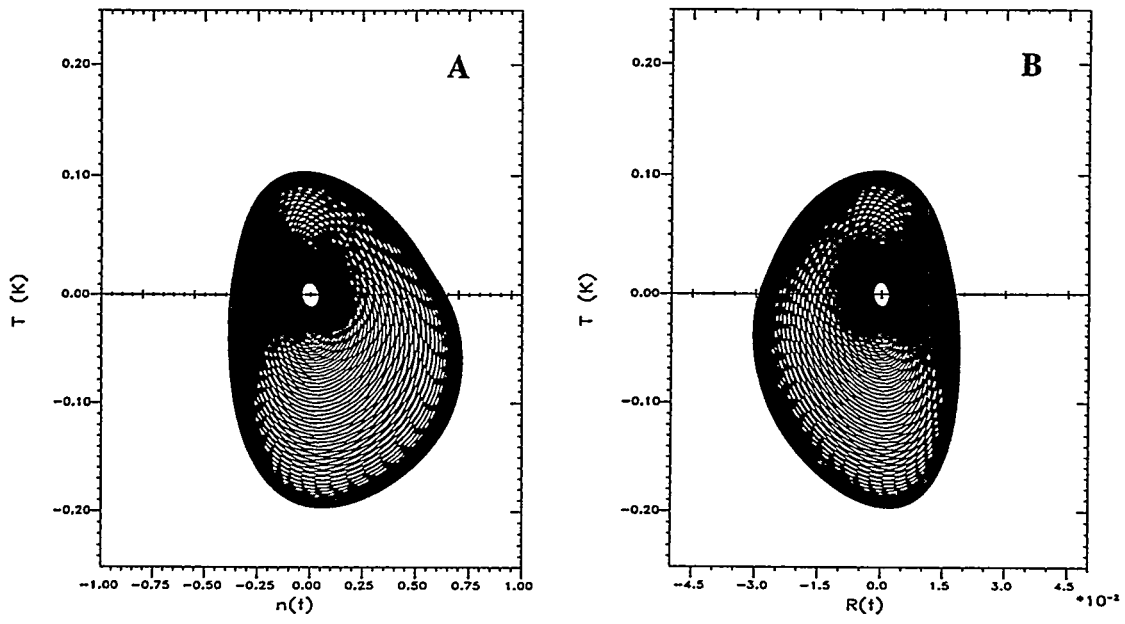

Fig. 9 Predicted trajectories on the n(t) - T(t) (A) and on the $\rho(t)$ - T(t) planes (B) at $x = 0.7\ m$; 3 spatial harmonics considered. $\xi_1 = 1$, $\xi_2 = \xi_3 = 0$ and $K_2 = 3.0$, $K_1 = K_3 = 0.78$.

In order to try to assess the sensitivity of the series expansions used in this work to the number of spatial harmonics retained, we show in Fig. 5 and 6 the predicted neutronic responses (A) and APSDs (B) at locations $x = 0.7\ m$, $x = 1.4\ m$ and $x = 1.85\ m$ by retaining 4 and 5 harmonics, respectively (solving 21 and 26 non-linear differential equations, respectively) with $K_1 = 2.65$, $K_n = 0.77, (n = 1, ...5)$, and with the same values for ξ_n's (a case similar to the one shown in Fig. 3). If one compares the APSDs shown in these figures with the corresponding APSDs of the case depicted in Fig. 3 (in which only 3 spatial harmonics were retained in the analysis), one can see that their general shapes are very similar, although for the case in which 4 spatial harmonics were retained (Fig. 5), they have started developing rather pronounced resonances at integral multiples of the fundamental resonance of the system (as predicted also by the point-model [7]). For both cases, the neutronic responses at $x = 1.85\ m$ are also 180° out-of-phase with respect to the ones at $x = 0.7\ m$ while at $x = 1.40\ m$, they exhibit a double-frequency, consistent with the frequency of the dominant resonances in the corresponding APSDs. In general, if one looks at at Figs. 3 and 5 - 6, one can say that at least for this particular case, the model predictions are relatively insensitive to the number of spatial harmonics retained; though, our argument is qualitative and this conclusion is by no means one of general validity since we only demonstrated it for a particular case.

Finally, in Fig. 7, we show the Auto-Correlation functions (ACCF(t)) at $x = 0.7\ m$ and $x = 1.4\ m$ for the same case depicted in figures 3 - 5, computed by retaining 3 (A) and 5 (B) harmonics. Notice that for our case, at $x = 1.4m$, the ACFs exhibit a double-frequency; the DRs are estimated in Fig. 7(A) to be 0.96 and 0.935, while in Fig. 7(B) are estimated 0.95 and 0.914, respectively. Hence, there is a small difference between the DRS of the two oscillation modes (and this can be seen directly from the figures) which, at least in our case, increases when the number of harmonics retained in the calculations increases. Generally, in our model, the mode associated with the second resonance in the spectrum is a little more stable than the one associated with the first.

Before concluding this section, we should elaborate on a problem which cannot be easily realized from the results presented until now. As it is well-known [7-9], if only the fundamental spatial mode is retained in the series expansions (equivalent to point-model), the system develops typical limit-cycle oscillations after some time greater then 400 s. Though, within the framework of our model and with the particular assumptions made about the spatial distibution of the random sources and the values assumed for the ξ_n (cf. eq. (2.7b)), this is not the case if higher harmonics are retained. In this case, the "limit-cycle-type" oscillations shown in the previous figures start growing without bound (as can be seen both from the neutronic signals and the trajectories on the n(t) - T(t) plane which diverge) and after some time, the numerical solution scheme breaks-down. Analysis of the same cases by assuming that the only spatial mode of the random source $f(x,t)$ in eq. (2.1c) is the fundamental (ie assuming that $\xi_1 = 1$ and all other ξ_n are equal to 0) did not exhibit this behaviour. In Fig. 8, we show the neutronic signals (A) and APSDs (B) for a case in which 3 spatial harmonics are retained, at the spatial locations $x_1 = 0.7\ m$, $x_2 = 1.4\ m$ and $x_3 = 1.85\ m$, but with $\xi_1 = 1$, $\xi_2 = \xi_3 = 0$, and with $K_2 = 3.0$ and $K_1 = K_3 = 0.78$. In Fig. 9, we show the trajectories on the n(t) - T(t) (A) and $\rho(t)$ - T(t) (B) planes at $x_1 = 0.7\ m$. For this case, the transient was run until 2000 s and the limit-cycle oscillations were established at approximately 630 s. The trajectories shown in Fig. 9 are plotted from $t = 400\ s$ until $t = 2000\ s$ and after $t = 630\ s$, they converge to a limit-cycle. One can now see that although all three APSDs are almost identical and the neutronic signals at $x_1 = 0.7\ m$ and $x_2 = 1.4\ m$ are in phase, the neutronic signals at $x_3 = 1.85\ m$ are 180° out-of-phase. Similarly, one can see from Fig. 9 that limit-cylce oscillations have developed. Clearly, the solution now remains bounded, but although the neutronic signals exhibit space-dependence, the APSDs do not exhibit the strong space-dependence shown in the previous cases. Hence, we conclude that the reason of the pathological divergent behaviour is the assumed form of the spatial distribution of the random source.

4. CONCLUSIONS

By employing the model developed by March-Leuba et al. ([7] - [9]) but with space-dependent neutronics and assumed uniformly distributed stochastic perturbations, similarly to the conclusions reached in these works, we showed that for a finite (in the x-direction) BWR core excited by small inherent stochastic perturbations, the magnitude of the feed-back coefficient will determine the stability of the system and the subsequent bifurcations and development of limit-cycle-type oscillations; in the point-model, this will lead to a transition to a chaotic behaviour which will occur above a certain value of the feed-back coefficient K [7 - 9]. Additionally, we showed that within the framework of our model, under certain conditions which include the dominance of the higher spatial harmonics of the stochastic source as well as a feed-back coefficient associated with the first higher spatial harmonic which is higher than the one associated with the other harmonics, the model can predict strong space-dependent effects which, when the limit-cycle-type oscillations develop, manifest themselves by the appearance of resonances in the neutronic APSD whose frequency depends on the position in the core. These effects are manifesting themselves only over a relatively narrow band of values of the feed-back coefficient(s) K_n and outside this band, they almost disappear. On the other hand, if one assumes that all the K_n's are the same and that all ξ_n's are equal to 1, no significant space-dependent effects can be seen. With the aforementioned special spatial distribution of the random sources from which the first spatial mode is missing (a necessary assumption for exciting space-dependent effects), limit-cycle-type oscillations do appear above certain values of the feed-back coefficients K_n's but after some time, the solution suddenly diverges. The typical limit-cycle oscillations appear only if one assumes that the random source is spatially distributed proportionally to the sinusoidal static flux (ie assuming that $f(x,t) = f(t)sinBx$). For this case, there are still significant space-dependent effects and out-of-phase neutronic fluctuations; though, there is no strong space-dependence of the APSDs as in the previous cases.

As far as the convergence of the model is concerned, for one particular case, we showed that the model predictions are converging, and are not so strongly dependent on the number of harmonics retained. This we showed in a heuristic and non-rigorous fashion, by retaining different number of harmonics. Finally, due to the one-dimensional character of the model, in this work, we could not investigate the importance of the axial harmonics on the predictions.

Concluding, we should say that the simple analytical model developed in this work shows that under certain conditions, strong space-dependent effects **can** become important during limit-cycle-type oscillations of a BWR. Clearly, a more detailed analysis of this problem may reveal that other effects of thermohydraulic origin are also important for explaining observed space-dependent effects; hence, we consider the value of this model more didactical and qualitative than predictive and quantitative, and should not be considered as a substitute for detailed calculations with a suitable code like RAMONA.

Acknowledgements

We would like to thank Imre Pázsit, Chalmers University of Technology, Göteborg, Sweden and Dieter Hennig, PSI, for some discussions and for providing us with some important references and Oddbjörn Sandervag, Swedish Nuclear Power Inspectorate (SKI), for some information.

References

[1] AKCASU Z., *Nucl. Sci. Engng*, **10**, 337 (1961).

[2] ANALYTIS G. TH., The Spatial Dependence of Noise in Power Reactors, Ph.D. Thesis, Queen Mary College, London (1979).

[3] WILLIAMS M. M. R., Random Processes in Nuclear Reactors, Pergammon Press (1974).

[4] NOMURA T., TSUNODA T. and KANEMOTO S., *Progr. Nucl. Energy*, **21**, 299 (1988).

[5] KONO H., HAYASHI K. and SHINOHARA Y., *Ann. Nucl. Energy*, **17**, 317 (1990).

[6] KONO H., Space-dependent nonlinear nuclear stochastic theory, A Symposium on Nuclear Reactor Surveillance and Diagnostics, SMORN VI, May 19 - 24, 1991, Gatlinburg, Tennessee, USA, paper 8.01 (1991).

[7] MARCH-LEUBA J. and PEREZ R. B., *Trans. Amer. Nucl. Soc.*, **44**, 523 (1983)

[8] MARCH-LEUBA J., CACUCI D. G. and PEREZ R. B., *Nucl. Sci. Engng*, **86**, 401 (1984).

[9] MARCH-LEUBA J., CACUCI D. G. and PEREZ R. B., *Nucl. Sci. Engng*, **93**, 111 (1986).

[10] BERGDAHL B. G., REISCH F., OGUMA R., LORENZEN J. and AKERHIELM F., *Ann. Nucl. Energy*, **16**, 509 (1989).

[11] van der HAGEN T. H. J. J., PÁZSIT I., THOMPSON O. and MELKERSSON B., *Nuclear Technology*, **107**, 193 (1994).

[12] GIUST F. D. and MOBERG L., RAMONA Stability Analysis on Ringhals-1: Model Qualification. SCANPOWER report Nr. TR1/42.83.06 (1991).

[13] HENNIG D., Private communication (1995).

[14] SADERVAG O., Private communication (1994).

[15] MARCH-LEUBA J. and BLACKEMAN E. D., *Nucl. Sci. Engng*, **107**, 173 (1990)

ANALYSIS OF THE RETURN TO POWER SCENARIO FOLLOWING A LBLOCA IN A PWR

Rafael Macian, Trevor N. Tyler, John H. Mahaffy

Department of Nuclear Engineering
The Pennsylvania State University
University Park,PA 16802

ABSTRACT

The risk of reactivity accidents has been considered an important safety issue since the beginning of the nuclear power industry. In particular, several events leading to such scenarios for PWR's have been recognized and studied to assess the potential risk of fuel damage. The present paper analyzes one such event: the possible return to power during the reflooding phase following a LBLOCA.

TRAC-PF1/MOD2 coupled with a three-dimensional neutronic model of the core based on the Nodal Expansion Method (NEM) was used to perform the analysis. The system computer model contains a detailed representation of a complete typical 4-loop PWR. Thus, the simulation can follow complex system interactions during reflooding, which may influence the neutronics feedback in the core.

Analyses were made with core models based on cross sections generated by LEOPARD. A standard and a potentially more limiting case, with increased pressurizer and accumulator inventories, were run. In both simulations, the reactor reaches a stable state after the reflooding is completed. The lower core region, filled with cold water, generates enough power to boil part of the incoming liquid, thus preventing the core average liquid fraction from reaching a value high enough to cause a return to power. At the same time, the mass flow rate through the core is adequate to maintain the rod temperature well below the fuel damage limit.

1. Introduction

Several events leading to reactivity accidents in PWRs have been recognized and studied to assess the potential risk of fuel damage. In most of such events, the injection of cold water with low boron content into the core inserts a large positive reactivity. Thus, depending on the thermal-hydraulic conditions during the injection, there exists the potential for a return to criticality, which could lead to a dangerous power excursion and severe fuel damage.

Some studies have been performed to analyze reactivity accidents during local dilution transients[1] and SBLOCAs[2]. These analyses have identified the necessity of detailed three-dimensional thermal-hydraulic and a three-dimensional neutronic core models to better describe the transient evolutions. A first step in this direction has been taken with an analysis of a LBLOCA without SCRAM using TRAC-PF1/MOD2, coupled to a 3D transient kinetics model[3]. That study was an extension of LBLOCA analyses made by Los Alamos[4,5] using a modified version of TRAC-PF1/MOD2v5.3. In the LANL studies, a reactor SCRAM was assumed, and the potential for recriticality was thus averted. Tyler's work and analysis[3] described in that paper used a similar plant model, but two major differences were introduced: no SCRAM was simulated and a full three-dimensional neutronic core model replaced the classic point-kinetics model. The close thermal-hydraulic and neutronic coupling allowed a refined study of the core power evolution as the transient progressed, and could predict a return to a critical state, should it occur during the reflooding phase. Tyler's original work included the standard "conservative" assumption of minimum pressurizer and accumulator inventory. That calculation also included the further conservative assumption that no boron entered with the ECCS flow. Since recriticality in this case depends on the amount of liquid reentering the core, we have reversed the original minimum inventory assumption to study the consequences of maximum pressurizer and accumulator initial inventories. This paper first presents the system model together with the assumptions involved in its development, especially in the neutronics modeling. Then the computational process is described and the results of the steady state presented. Finally, a description of the transient is followed by the computational results and the conclusions.

2. Computer Model Description

2.1. Thermal-hydraulic Model

The thermal-hydraulic plant model used in this study was developed as part of the international safety research effort known as the 2D/3D Refill/Reflood Program. The model describes a typical US/Japan PWR with four loops and contains 949 fluid cells. The nitrogen in the accumulators was allowed to penetrate into the system and modeled by TRAC with an additional mass transport equation. Therefore, its effect on condensation rates within the primary side components is taken into account.

The four loops of the primary side are identical, except for the cold leg of the loop 3, where the 200% guillotine break occurs between the cold leg nozzle and the ECCS injection point. The containment backpressure is simulated by breaks whose pressure histories depend on a pressure vs. time table. From an initial atmospheric pressure (0.1 MPa), the containment pressure reaches a peak of 0.341 MPa at 25.0 seconds, finally dropping to 0.242 MPa at 300 seconds.

The vessel component was divided into 544 hydrodynamic cells representing 17 axial levels, 4 radial rings and 8 azimuthal sectors. Most of the vessel internals were included in the model. Leakage paths between the hot leg nozzles and core barrel nozzles were also included. The core region within the vessel is contained in the inner two rings and between axial levels five to nine.

The balance of plant was simulated by feedwater FILLs and steam outlet BREAKS attached to the steam generator's secondary sides, with appropriate values for the boundary conditions.

The differences between the base study and the modified run with higher primary inventory can be found in the initial pressurizer's and accumulators' inventories. According to the minimum requirement by technical specifications in a PWR, the pressurizer in the standard run had the water level set to 2.7 m (13.53 m^3 of liquid), whereas in the modified case this volume was increased to 30.58 m^3 (60% of total pressurizer's volume). The standard accumulator's inventory of 14.15 m^3 per unit was also increased in the modified run to 27.90 m^3 according to the minimum acceptable gas volume of 10.3 m^3. It was expected that an increase in the primary water inventory would result in a larger final core liquid content, thus increasing the potential for recriticality.

2.2. Neutronic Core Model

The core contains 193 15x15 fuel assemblies with three different enrichments: 65 of 2.2 w/o (weight percentage), 64 of 2.7 w/o and 64 of 3.2 w/o. The model is completed by 64 water reflector assemblies surrounding the fuel region.

The power evolution during the transient is computed by a two group three-dimensional neutron kinetics core model. The TRAC-PF1/MOD2 version used in this study contains a full three-dimensional neutronics module developed by Bandini[6] based on the Nodal Expansion Method (NEM)[7] capable of handling both steady state and transient situations with several energy groups. This method was shown to provide accurate results for a variety of benchmark problems[8].

The coupling between the neutronic and the thermal-hydraulic core is described in detail by Tyler[3]. Each Cartesian neutronic node is mapped onto one thermal-hydraulic node according to its location in the core. The first coupling stage takes place at the end of the thermal-hydraulic solution for a given time step. Values of fuel temperature and moderator density are assigned to each neutronic node according to the mapping described above. These values are used to compute the neutronic parameters for the neutronic node. The three-dimensional neutronic solution is then calculated and the relative power level for each neutronic node obtained. Since the number of neutronic nodes is usually much larger than that of thermal-hydraulic ones, each thermal-hydraulic node can receive power from several neutronic nodes mapped onto it. In the second coupling stage, the sum of all these powers results in the total power being transferred to the coolant, through the fuel rods, to each thermal-hydraulic node. The power coupling yields an axial power shape determined by the three-dimensional neutronic calculation. The power is then used as input to evaluate the new thermal-hydraulic solution the next time step. It is important to note that the solution procedures for each problem, neutronic and thermal-hydraulic, are independent from each other once the needed information has been transferred during the two coupling stages described above for each time step. Such procedure allows for different geometries to be used when solving each problem. Special care was put into selecting a core neutronic noding scheme that, once mapped onto the thermal-hydraulic model, resulted in a symmetrical steady state power mapping consistent with the core power distribution of a typical PWR (see Tyler[3]).

3. Calculation Procedure

3.1. Cross Section Calculation

The original polynomial fitting procedure used by Bandini's NEM implementation to compute the cross sections and diffusion coefficients proved to lack the robustness required to handle the rigors of LBLOCA and post-LOCA conditions in the core. In order to solve this problem, an interpolatory method based in cross section tables was devised and implemented. The tables cover the widest range of core conditions expected after a LBLOCA, and only two independent variables were chosen to model the two most important reactivity feedback mechanisms expected to control the neutronic behavior in a post-LBLOCA environment: i.e. the fuel temperature, responsible for the Doppler feedback, and the moderator density (water temperature and void fraction included), which determines the moderation efficiency, thus controlling the neutron spectrum surrounding the fuel elements. The detailed three-dimensional core model requires the appropriate consideration of this effect since the likely process leading to recriticality is based on the high density moderator flowing up into a rather dry post-blowdown core. Nodes located in different parts of the core, even at the same axial level, can be surrounded by different void fractions, thus presenting a different neutronic behavior. Dependence on boron concentration was not included because only the base operating concentration (780 ppm) is permitted during the calculation as a conservative assumption.

The fuel temperature range spanned from 450 K (350 °F) to 2033 K (3200 °F) and the moderator density covered void fractions from 0.0 to 0.6 at 572 K (570.1 °F) (operating temperature) and 0.0 at 378 K (220.0 °F) (expected reflooding temperature). It is important to note that in case of a LBLOCA, the core void fraction ranges from 0.0 to almost 1.0 at the end of blowdown, to decrease again after reflooding starts. Therefore, the moderator temperature is not as important as the void fraction in controlling the moderator density values. Void fractions larger than 0.6, however, were not considered for two reasons: first, the code selected to calculate the cross sections, LEOPARD[9], could not handle accurately void fractions larger than 0.6, and second, it was found that such large void fractions would yield very low moderation and could be neglected if compared to the moderating power of the high density reflooding front flowing into the core. As mentioned above, the three-dimensional analysis can resolve the contribution of each neutronic node to the total neutron population in the core. Therefore, this description is able to account for the much greater influence that nodes coupled with low void fraction cells will have in the overall core neutronic behavior, as compared to those nodes coupled to high void fraction regions.

The LEOPARD runs depleted the fuel down to Xe equilibrium conditions with a soluble boron equilibrium concentration of 780 ppm.

The core model represented a first load core with burnable poison rods in some of the fuel assemblies. LEOPARD cannot include discrete highly absorbing rods into the fuel assembly model it uses. To overcome this problem, the effect of the burnable poison rods was accounted for by including an equivalent boron volume fraction in the clad region that would yield the same number density as that in the actual burnable poison rods for the corresponding fuel assembly. This value was further modified by a factor which decreased the boron concentration to simulate the self-shielding effect on the neutron flux that a highly absorbing material produces. The same value was used for all fuel assemblies. The final value for this parameter was obtained by running several TRAC steady-state runs based on cross section tables generated with different self-shielding factors until K_{eff} was close enough to one.

The homogenization of the burnable poison rods is a conservative assumption from the point of view of the maximum clad and fuel temperature reached by the fuel rods. The burnable poison rods are located in the mid-core and in the highest enrichment fuel assemblies. The homogenization process reduces the boron poison concentration in these assemblies, which results in a higher assembly power peak being predicted than if the poison were heterogeneously distributed. The power that those assemblies transfer to the ROD components coupled to them (the assemblies correspond actually to NEM nodes) is also higher, and this increases maximum values predicted for the clad and fuel centerline temperatures.

3.2. LBLOCA Simulation

The study was initiated with a steady state run, whose main system parameters are displayed in Table 1. They correspond to actual plant values observed in a typical US/Japan PWR Plant.

From a system steady state configuration, the transient run was started with a complete double-ended (200%) guillotine break located in the largest pipe of the reactor cooling system (RCS). The break was simulated in the cold leg of loop #3, 2.70 m from

Table 1. Steady State Main Parameters

PARAMETER	VALUE
Core Power	3315 MW
Keff	0.9906
Pressurizer Pressure	15.720 MPa
RCS loop flow	4.637E+3 Kg/s
Reactor Flow	1.855E+4 Kg/s
Core Flow	1.771E+4 Kg/s
Core Bypass Flow	4.5 %
Core Inlet Temperature	551.4 K
Core Outlet Temp.	586.0 K
S.G. Secondary Flow	4.493E+2Kg/s
S.G. Steam Pressure	4.964 MPa
S.G. Steam Temperat.	536.6 K
S.G. Feedwater Temp.	493.4 K

the end of the cold leg nozzle (between the vessel injection nozzle and the ECCS injection point). The pressure history for the containment was described by pressure vs. time tables as mentioned above. After the break, a pressurizer low-pressure signal tripped the recirculation pumps. The steam generator isolation was accomplished by closing the feedwater fills and the steam outlet valves connected to the secondary sides. Low pressure readings in the cold leg (4.23 MPa) opened the accumulator's check valves, thus initiating the emergency cooling water injection. The ECCS (HPIS/LPIS), modeled as pressure dependent fills, was tripped at 12.5 MPa in the cold legs with a 25 second delay to account for the inertia of the fluid and the pumps in the ECCS.

Regarding the core power evolution, three major conservative assumptions were made. First, the steady state power was set to 102% of the nominal power, that is 3315MW; second, no SCRAM was activated after the LBLOCA took place; and third, no credit was given to the strong negative effect that the highly borated water from the accumulators and ECCS has in the core reactivity. Under such conditions, the core power level depends mainly on the moderating capacity of the coolant present in the core (liquid fraction), and on the Doppler feedback resulting from the increase of the fuel rod temperatures. Finally, the decay heat was calculated by the standard TRAC decay heat model: ANS 79[10] with a one-dimensional axial distribution according to the steady state axial power shape.

The transient run was extended up to 250 seconds, since a stable oscillation was observed in the core and downcomer inventories for more than 100 seconds.

4. Description and Analysis of Results

After the transient begins with the double ended guillotine break in loop 3 at time 0.0 seconds, the vessel depressurizes rapidly as the vessel inventory is lost through the break (Figs. 1 and 2).

The fast vessel inventory depletion results in almost total core uncovery at 2.3 seconds (Fig. 3); the core void fraction is 0.99. As a result, the clad temperature rises sharply and reaches a maximum below 1000.0 K in the base and the modified runs. (see Fig. 5). The maximum value is limited because of a partial core refill following the initial inventory depletion. The water for this refill comes from the liquid in the cold legs and downcomer, and from the pump coastdown. The pumps, tripped at 3.5 s because of a low primary side pressure signal and keep on pumping coolant into the cold legs until their stored inertia vanishes. The partial refill stops at 5.5 s after which the core liquid inventory is reduced again because the reactor coolant is being lost through the break, and no other coolant source is yet available. By 30 s, the core is empty and the clad temperature raises a second time, but this peak is lower than the first one. In both cases the peak value is well below the limit of 1475 K (2195°F).

When comparing the behavior of each run during this first stage of the LBLOCA, one can see differences in the rod temperature and power curves (Fig. 5, 6 and 7). These discrepancies are probably caused by the differences in core inventory. The modified run, with a slightly lower rate of depressurization during the initial seconds, does not lose as much liquid as the standard run which limits the rod temperature rise. When the partial refill starts at 3 seconds, the liquid rushes up into the core, and this time it is the standard run, with a slightly lower core pressure, the one with a larger core inventory. It is at this point that one of the advantages of employing a three-dimensional neutronic core shows. The increase in lower core inventory enhances the moderation of the neutronic population from the

neutron precursors, thus increasing the fission rates in the lower core. The result is a first peak in the reactor power (see Fig. 7).

Although not clear in the figure, the increase in power observed in the modified run, whose inventory at this point is lower than that of the standard run, is also lower (300 vs. 335 MW). This peak in power is partly responsible for the peak in clad temperature and increase in fuel centerline temperatures observed in both runs at this time. The lower power peak of the modified run results in lower rod temperatures, as expected.

The different hydraulic behavior exhibited by the modified run may be traced to the larger pressurizer inventory. The increased inertia added to the primary inventory may influence the depressurization rate and the rate of the first core refill.

Fig. 3 shows how, after the first refill, the core inventory drops again during the second part of the blowdown, when the pressure decreases more slowly (see Fig. 1) and the accumulators start the coolant injection into the cold legs at 13.5 s. The liquid, however, does not flow immediately into the core, but it fills the downcomer, whose liquid volume fraction increases as the water from the accumulators is injected into the vessel. Eventually, the core dries out at 30 seconds. This situation is a result of the downcomer bypass phenomenon, simulated by TRAC due to its three-dimensional vessel model. The differences observed between both runs are probably due to the different interfacial drag computed by the code. The modified run downcomer liquid fraction (see Fig. 3) reaches a larger value because of the higher accumulators' inventories, and remains high longer than in the standard run. The retention of liquid in the downcomer results in more water being discharged through the break (see Fig. 2). and increases the time that the core is empty, which in turn, delays the reflood of the first core level (see Fig. 5). In both runs, the downcomer liquid fraction drops sharply after 30 seconds, and the liquid is pushed into the core, but its inventory is not large enough for a return to criticality in any case (see Fig. 7). By this time, the ECCS injection has already started (at 28.6 seconds), and the surge of water from the ECCS into the vessel fills up the downcomer again. Since the downcomer bypass is not as important now that the system pressure is much closer to the break containment backpressure, the reflooding of the core begins.

Once the ECCS injection stabilizes, the core and downcomer water contents in both runs grow steadily, with some oscillations which translate into power peaks, never larger than 500 MW (15% nominal). Peaks appear when the core liquid volume fraction increases suddenly. The increase in power evaporates part of this liquid, and the system returns to low power again. This is a direct result of the local neutronic-thermalhydraulic coupling used in this work. In no case, however, does the core inventory reach a value high enough to drive the core into a critical configuration, which would be identified by a sudden power increase of over 100% nominal power.

The core quench is completed at 154 s for the standard run and 141 s for the modified run. At this point, the reactor pressure has reached a stable value around 0.30 MPa in equilibrium with the containment pressure.

During the reflooding process the reactor power remains low as shown in Fig. 7. The rod temperatures (Fig. 5 and 6) show no sign of increase that would be expected in an eventual return to criticality, especially in the case of the center line values. The core and downcomer liquid inventories grow slowly because of the ECCS injection. The modified run shows a slightly higher downcomer and core inventories after the first 50 seconds until the end of the transient.

Figure 3 shows the stabilization of the liquid content in the core around 170 s. Since the ECCS injects liquid water into the vessel during the entire transient, the stabilization of the core inventory around 0.4 may be linked to enhanced vaporization by the power generated in the lower core. The total power is about 5% larger than expected from decay heat sources alone (see Fig. 8) in both runs. This additional power is released in the lower core region. According to Fig. 6, the fuel center line temperature in the lower core regions (Bottom level) remains higher than the upper regions (Top Level), and equal for most of the transient to the mid-plane region, after the quenching has been completed. This can be explained considering the environment surrounding the fuel rods in the lower core. Liquid water fills up to 40% of the core (see Fig. 3) with the void fraction in the core increasing rapidly along the axial direction. This fact alone would support a different picture of the axial temperature profiles were decay heat the only source of power. The higher cooler liquid content in the lower core should enhance the heat transfer and cool down the fuel more effectively than in the upper core, where a larger void fraction would make the heat transfer less effective. As mentioned above, however, this is not what Fig. 6 shows.

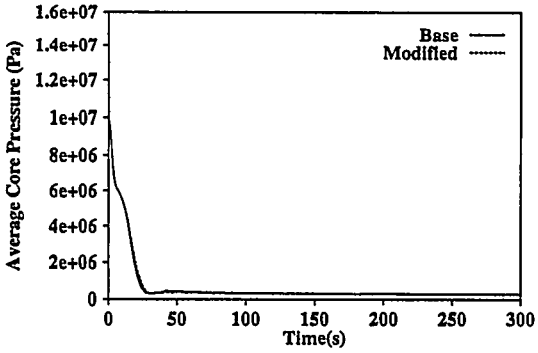

Figure 1. Vessel Pressure during Transient

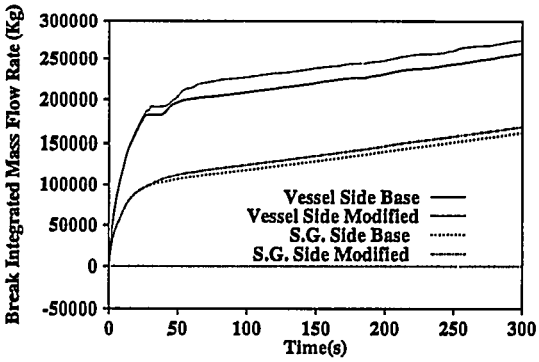

Figure 4. Integrated Mass Flow Rate through the Break

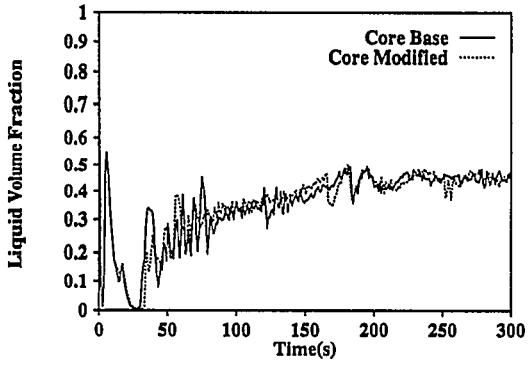

Figure 2. Liquid Volume Fraction in Downcomer and Core

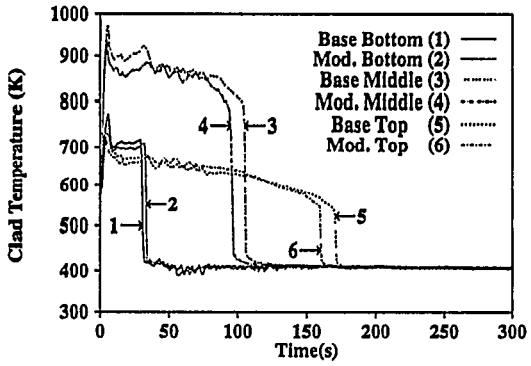

Figure 5. Clad Temperature for Average Rod

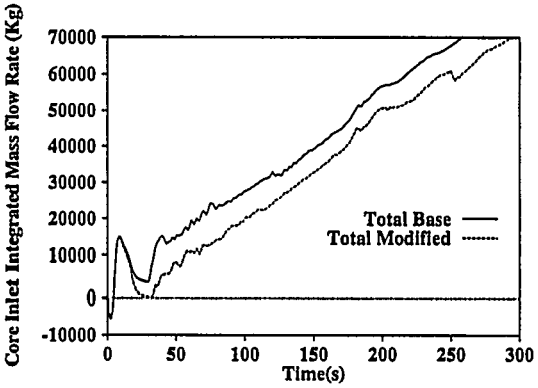

Figure 3. Total Coolant Mass Injected in the Core

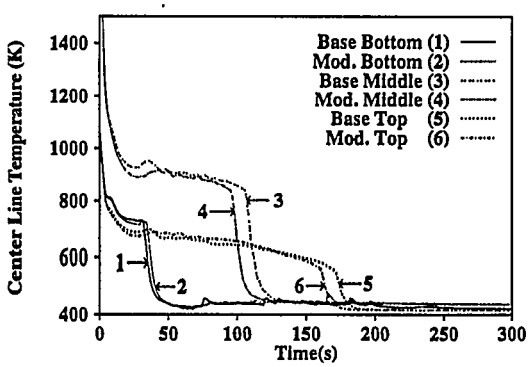

Figure 6. Fuel Center Line Temperature for Average Rod

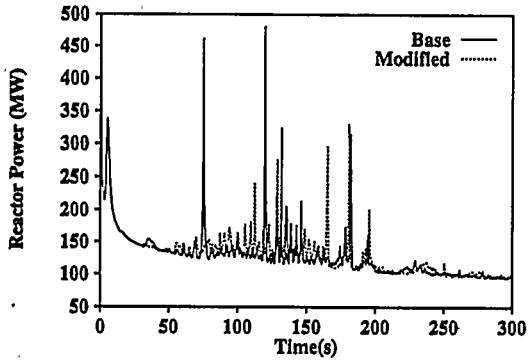

Figure 7. Reactor Power Behavior during Transient

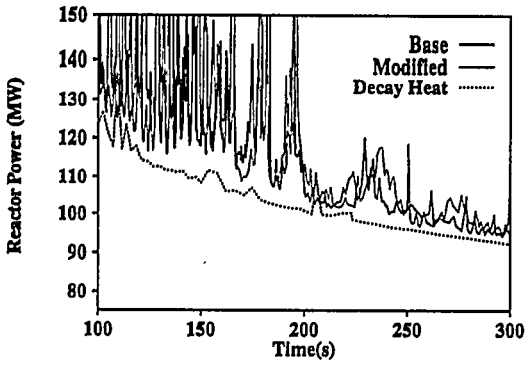

Figure 8. Reactor Power compared to Decay Heat

The increase in power generation in the lower core shows that the neutronic model is able to deal with local thermal-hydraulic feedback effects based on the conditions surrounding the neutronic nodes. Such detailed analysis is not possible with a point kinetics.

The three-dimensional calculation describes the lower core based on the mostly liquid environment surrounding the fuel rods. These conditions effectively enhance moderation of the fast neutron flux from precursor decay (computed also in the model) resulting in a higher fission rate (and power production), which results in a higher thermal flux available for fission in the fuel in a subcritical environment.

In both runs, the power generated in the lower core seems to boil off enough incoming liquid to keep the average core liquid fraction constant and below the value necessary to drive the core into a critical state.

5. Conclusions

The main objective of the analysis described in this paper was to investigate the possible return to criticality during the reflooding phase of the LBLOCA. This possibility could not be ruled out performing studies based on a quasi-static neutronic analysis of the core, which obtain the thermal-hydraulic coupling from the state of the core at a given time into the transient, but cannot close the coupling loop, that is, the neutronics calculation had no effect on the thermal-hydraulic one. As a result, these previous studies do not usually take into account the dynamic behavior of the whole primary system, nor can they simulate the self-limiting negative feedback that an eventual rise of reactor power would produce as a result of the increase in void fraction. This mechanism is especially important in the kind of analysis described above. The return to criticality, if possible, should result from a slow reflooding rate that would eventually fill the core with liquid water, increasing its moderation power and, ultimately, yielding a critical configuration. The rate of reflooding and the power generation in the lower core (from the decay power and from the increase in fissions caused by the increase in moderation) become, therefore, the key control mechanisms to determine the future outcome of the transient. The analysis of the results presented in section 4 has shown that, after the reflooding is practically completed (quenching of the full rod length), a return to criticality was not observed in either run. The reactor power remains at a level higher than decay heat (Fig. 8), and is high enough to evaporate enough additional incoming liquid to keep the average core liquid fraction stable around 0.40. This value is, according to the power evolution plots (Fig. 7), and to the fuel rod temperature plots (Figs. 5 and 6), below the threshold for achieving a core critical configuration. The stability of this situation is maintained by the continuing ECCS water injection which keeps a constant flow through the core, assuring an adequate cooling of the fuel rods and preventing fuel damage.

It is also important to note that one of the main conservative assumptions in this study neglected the boron injection from the accumulators and ECCS system, a highly improbable event. The tracking of the boron field by TRAC showed that the core reached a high boron concentration roughly 35 seconds into the transient. According to this result, and since no sign of power increase was observed up to 300 seconds in either run, we can conclude that,

under the circumstances and assumptions covered in this analysis, TRAC-PF1/MOD2 coupled with the 3D-NEM neutronics method predicts that the core will not reach a critical state during the reflooding phase of a LBLOCA.

The analysis described in this paper tried to overcome the limitations reported when using quasi-static coupling approaches[1,11] by employing the capabilities offered by TRAC-PF1/MOD2 coupled to the 3D-NEM transient neutronics method. They allowed us to closely simulate the coupled dynamic response of both the complete primary side and the neutronic core at each time step during the transient. The result showed a less severe scenario than an eventual return to criticality would produce.

6. References

[1] S. Jacobson, "Risk Evaluation of LOCA Dilution Transients in a Pressurized Water Reactor", Thesis 5-58183. Linkoping University, 1992.

[2] J. Hyvarinen, "An Inherent Boron Dilution Mechanism in Pressurized Water Reactors", Finnish Centre for Radiation and Nuclear Safety, Helsinki. 1992.

[3] T. N. Tyler, "Large Break Loss of Coolant Accident Analysis of a PWR using TRAC and Three-Dimensional Kinetics", M.S. Thesis. Penn State University, 1994.

[4] J. C. Lin and F. Motley,"TRAC-PF1/MOD2 Analysis of a Minimum Safeguards Large Break LOCA in a US/Japan PWR with Four Loops and 15x15 Fuel", LA-LP-92-58. Los Alamos National Lab. 1992.

[5] P. R. Shire and J. W. Spore, "TRAC-PF1/MOD2 Analysis of a Minimum Safeguards Large Break LOCA in a US/Japan PWR with Four Loops and 15x15 Fuel", LA-CB-87-61. Los Alamos National Lab. 1987.

[6] B. R. Bandini, "A Three Dimensional Transient Neutronics Routine for the TRAC-PF1 Reactor Thermal Hydraulic Computer Code". Ph. D. Thesis, Penn State University. 1990.

[7] H. Finneman, et al. "Interface Current Technique for Multidimensional Reactor Calculations", Atomkernenergie, 30, p.123. 1977.

[8] B. R. Bandini, et al., "Verification of the Three-dimensional Nodal Transient Neutronics Routine for the TRAC-PF1/MOD2 Thermal-hydraulic System Analysis Code", LA-UR-92-1210. Los Alamos National Lab. 1992.

[9] S. H. Levine and S. S. Kim, "PSU-LEOPARD User's Manual", The Pennsylvania State University. 1987.

[10] V. E. Schrock, "A Revised ANS Standard for Decay Heat from Fission Products", Nuclear Technology ,46, p. 323. 1979. and ANSI/ANS-5.1-1979: "Decay Heat Power in Light Water Reactors". Hinsdale, IL. American Nuclear Society. 1979.

[11] P. Hyun-Jons and P. Raymond, "Pressurized Water Reactor Steam Line Break Analysis by Means of Coupled 3-Dimensional Neutronic, 3-Dimensional Core Thermalhydraulic, and Fast Running System Codes", Nuclear Technology, 107, p.103. 1994.

Stability Analysis of BWR Nuclear-Coupled Thermal-Hydraulics Using a Simple Model*

Atul A. Karve, Rizwan-uddin† and J.J. Dorning†,✚
Department of Mechanical, Aerospace and Nuclear Engineering
University of Virginia
Charlottesville, VA 22903

Abstract

A simple mathematical model is developed to describe the dynamics of the nuclear-coupled thermal-hydraulics in a boiling water reactor (BWR) core. The model, which incorporates the essential features of neutron kinetics, and single-phase and two-phase thermal-hydraulics, leads to a simple dynamical system comprised of a set of nonlinear ordinary differential equations (ODEs). The stability boundary is determined and plotted in the inlet-subcooling-number(enthalpy)/external-reactivity operating parameter plane. The eigenvalues of the Jacobian matrix of the dynamical system also are calculated at various steady-states (fixed points); the results are consistent with those of the direct stability analysis and indicate that a Hopf bifurcation occurs as the stability boundary in the operating parameter plane is crossed. Numerical simulations of the time-dependent, nonlinear ODEs are carried out for selected points in the operating parameter plane to obtain the actual damped and growing oscillations in the neutron number density, the channel inlet flow velocity, and the other phase variables. These indicate that the Hopf bifurcation is *subcritical*, hence, density wave oscillations with *growing* amplitude could result from a finite perturbation of the system even when it is being operated in the parameter region *thought* to be safe, i.e., where the steady-state is stable. Finally, the power-flow map, frequently used by reactor operators during start-up and shut-down operation of a BWR, is mapped to the inlet-subcooling-number/neutron-density (operating-parameter/phase-variable) plane, and then related to the stability boundaries for different fixed inlet velocities corresponding to selected points on the flow-control line. Also, the stability boundaries for different fixed inlet subcooling numbers corresponding to those selected points, are plotted in the neutron-density/inlet-velocity phase variable plane and then the points on the flow-control line are related to their respective stability boundaries in this plane. The relationship of the operating points on the flow-control line to their respective stability boundaries in these two planes provides insight into the instability observed in BWRs during low-flow/high-power operating conditions. It also shows that the normal operating point of a BWR is very stable in comparison with other possible operating points on the power-flow map.

Introduction

Following several incidents of density-wave oscillations (DWOs) during operational transients in BWRs, the study of this instability from an operational and a safety point of view, has become very relevant and important. Over the past several years, many mathematical models and computational codes have been developed, and tests have been carried out, to investigate this problem. In the work done so far, stability analyses usually have been carried out by evaluating the decay ratios and studying the effect of certain parameters on BWR stability. Numerical simulations have been done to study the time evolution of certain phase variables. The results of some of these stability analyses and numerical simulations have been compared with test results or data collected from actual BWR

*This research was supported in part by the US NRC under grant No. NRC-04-90-113 and in part by the US DOE under grant No. DE-FG05-92ER75788. The opinions, findings, conclusions, and recommendations expressed herein are those of the authors and do not necessarily reflect the views of the NRC or DOE.

†Also: Engineering Physics Program
✚Also: Department of Applied Mathematics

instability incidents, and the overall agreement has been reasonably good. However, in the various models and codes developed, either no attempt has been made to determine the stability boundary in an operating parameter plane, or the models and codes are mathematically and computationally so complex that only a few points approximating the stability boundary are computed. It has thus been the purpose of the research reported here to develop a model that is simple and yet retains the essential physical dynamics of BWR thermal-hydraulics and neutron kinetics, and therefore can be used both to carry out extensive stability analyses and to provide a starting point for a more complete, yet simple, model for the nonlinear dynamics of a BWR.

Belblidia, Weaver and Carlson [1] carried out a nodal analysis of DWOs in BWRs. They showed that the point kinetics model representation of the BWR neutronics yields conservative results, although for better assessment of BWR core stability radial coupling effects should be included. The mass-flux/pressure-drop results predicted by their model compared well with production codes such as FIBWR and COBRA-III. Peng et al. [2] developed a linear frequency domain computer code NUFREQ-NP for BWR stability analysis under conditions of either forced or natural circulation. That code is based on a one-dimensional drift flux model for the two-phase flow and takes into account subcooled boiling, arbitrary nonuniform axial and radial power shapes, distributed local losses, detailed fuel element dynamics, and system pressure perturbation. Peng et al. [2] compared stability results they obtained using it with experimental data from Peach Bottom-2 stability tests and found good agreement. March-Leuba, Cacuci and Perez [3] developed a phenomenological model to simulate the "qualitative" behavior of BWRs. They also developed a detailed nodalized (numerically discretized) physical model to simulate the dynamic behavior of the Vermont Yankee BWR over a broad operating range by varying the power and flow [4]. Their analysis led to the conclusion that for a wide range of oscillation amplitudes, no significant effect on the integrity of the fuel is expected. However, in order to keep their model simple, they assumed that the coolant enters the core at saturation enthalpy (not as a subcooled liquid), i.e., that the boiling boundary always is at the bottom of the core channels. Valtonen [5] validated the RAMONA-3B and TRAB BWR transient codes using DWO data from an oscillation incident that occurred at the TVO-1 BWR. It was shown that both spatially out-of-phase and spatially in-phase oscillations are possible in BWRs, and that decreasing the fuel gas gap conductance has a destabilizing effect. Bergdhal et al. [6] investigated the BWR stability at Forsmark-1 and showed that the decay ratio ranged considerably higher than that expected based on code calculations. Rizwan-uddin and Dorning [7] studied the effects of unheated riser sections that are added to enhance natural circulation in advanced and simple BWRs. They found that, for a fixed flow rate, the addition of the riser sections makes the system less stable. They also showed that the feedback recirculation loop plays an important role in reactor stability, and if omitted from the model, can lead to nonconservative conclusions. Wulff et al. [8] simulated the instability that occurred at the LaSalle-2 power plant (and several other BWR transients) using the Brookhaven National Laboratory Engineering Plant Analyzer (EPA) in order to determine the causes that lead to the observed magnitudes of power, flow and temperature oscillations. They found it to be a powerful tool for scoping calculations and for supporting accident management. Although very valuable in many contexts, production codes such as EPA are not very useful for thorough stability analyses or extensive parameter studies in general, because of their complexity and large computer running times. Ward and Lee [9] developed a simplified BWR core model — where they described the neutronics by the point kinetics equation without any delayed precursor group, had a single node representation of the fuel rod temperature dynamics, and simplified the thermal hydraulics representation of the two phases in the flow channel by omitting the temporal acceleration term in the momentum equations — and by singular perturbation analysis, presented extensive results on limit-cycle behavior in neutronics-coupled DWOs. While all the works cited above on stability analysis of BWRs were performed either using a time-domain (nonlinear, numerical) approach or a frequency-domain (linear) approach, Tsuji, Nishio, and Narita [10] developed a simple BWR core model as a dynamical system comprised of a set of nonlinear ODEs and used *bifurcation theory* to investigate the dependencies of the fixed point (steady-state) on the parameters — such as the inlet pressure loss coefficient, the inlet subcooling, the gap conductivity between the fuel and cladding, the system pressure, and the void reactivity feedback coefficient — which have a large influence on the stability of BWRs. They also showed that loss of stability took place at low-flow/high-power conditions and that sustained limit-cycle in-phase power oscillations observed in BWR instabilities were not directly excited by the subcritical Hopf bifurcation that resulted from their model.

Accurate models for the study of the stability of boiling flow *without* nuclear coupling also have been developed. Achard, Drew and Lahey [11] developed one, starting from the homogeneous equilibrium model for the two-phase flow, which led to two functional differential equations (FDEs) with complicated nonlinear delay multiple integral operators. Rizwan-uddin and Dorning [12] extended that model by starting from the drift-flux equations to

represent the two-phase flow, and not surprisingly arrived at considerably more complicated FDEs, which they analyzed. However, by starting from the homogeneous equilibrium model and introducing some simplifying assumptions, Clausse and Lahey [13] developed a simple model for the boiling flow problem that yields a rich variety of nonlinear phenomena, many of which are similar to those that result from the much more complicated FDE models [11,12] and also are similar to those observed experimentally.

Following Clausse and Lahey [13], and motivated by the desire to represent a BWR as a simple dynamical system, we have extended their model by including neutron kinetics and heat conduction in the fuel rods to develop a basic model for the dynamics of BWR along the lines of those developed in Refs. 9 and 10, and we have used it to carry out stability analyses and to do numerical simulations. This model is simple in that the dynamical system that results is comprised of a set of nonlinear ODEs rather than complicated FDEs, yet it incorporates the essential features of neutron kinetics, fuel rod dynamics, and single- and two-phase flow thermal-hydraulics. Most previous ODE-based models developed to represent BWR dynamics (such as those reported in Refs. 4 and 10) are based on approaches in which the phase variables are discretized via finite-difference approximations, or by "nodalization" procedures in which they are discretized along vertical segments of the coolant channel length by approximating them as spatially constant (but time-dependent) within these segments or nodes. Rather, we follow the weighted-residual-like approach introduced by Clausse and Lahey [13] in their simple linear approximations of the space dependence of the enthalpies in the single-phase region and the two-phase region. These approximations lead to three ODEs for the single- and two-phase flow, which are combined here with the ODEs of point neutron kinetics and the ODEs of heat conduction in the fuel rod obtained by reducing the heat conduction PDE to ODEs using two approaches — a simple eigenfunction expansion method and a variational method. The resulting set of ODEs can be analyzed straightforwardly using standard techniques of bifurcation theory to determine the DWO stability boundaries in various parameter planes. This was done and the results are presented in the most relevant parameter plane — the inlet-subcooling-number (enthalpy)/external-reactivity operating parameter plane. Although the mass flow rate (proportional to the core inlet velocity) and the power (proportional to the neutron density) are phase variables (unknowns) and not parameters of the dynamical system, they are the coordinates of the power-flow map used during start-up and shut-down operations of a BWR, and the mass flow rate actually is used as the practical control variable during these operations. Thus, it is useful to relate operating points on a typical BWR power-flow map to the stability boundaries in operating-parameter/phase-variable planes. Hence, the stability boundaries are also calculated and presented in the inlet-subcooling-number/neutron-density (operating-parameter/phase-variable) plane and the neutron-density/inlet-velocity phase variable plane. Selected points on the flow-control line are then related to their respective stability boundaries in these two planes to qualitatively explain the instabilities observed during operation of BWRs at low-flow/high-power operating conditions and also to show that the normal operating point of a BWR is very stable in comparison with other possible operating points on the power-flow map. Direct numerical integration of the set of nonlinear ODEs are consistent with the results of the stability analysis, and further indicate the nature of the bifurcation.

Description of the Model

In this section we first describe the physical model developed and employed, and then present the dynamical system that results, i.e., the set of final nonlinear ODEs. Details of the model development procedure are given in the following section. A BWR lattice cell is represented as a vertical fuel-centered boiling flow channel. The core neutronics are described by the point kinetics equations with one delayed neutron precursor group. The reactivity in the point kinetics equation depends upon the spatially averaged, time-dependent void fraction and the spatially averaged, time-dependent fuel temperature; hence, it couples the core neutronics with the thermal-hydraulics. An ODE for the boiling boundary is obtained by spatially integrating the single-phase energy equation from the channel inlet to the boiling boundary by introducing a spatially linear but time-dependent temperature profile (equivalent to the spatially linear single-phase enthalpy profile used by Clausse and Lahey [13]). The homogeneous equilibrium model, in which no-slip flow and thermal equilibrium between the two-phases is assumed, is used to represent the two-phase thermal-hydraulics in the boiling channel. This heated channel model has been shown to lead to conservative results with respect to DWO instabilities [12]. The void propagation equation in the two-phase region is rewritten in terms of the quality by using the homogeneous equilibrium model relationship between the void fraction and the two-phase quality. This equation is then reduced to an ODE for the slope of the quality by

introducing a spatially linear but time-dependent two-phase quality profile (equivalent to the spatially linear two-phase enthalpy profile used by Clausse and Lahey [13]). Pressure drops in the single-phase and two-phase regions are calculated by integrating the momentum equations for the respective regions. An ODE for the inlet velocity is obtained by equating the sum of the pressure drops in the single-phase region, in the two-phase region, and those due to the channel inlet and the channel exit, to the externally imposed pressure drop. Assuming only radial conduction, the PDE for heat conduction in the fuel rod is reduced to a set of ODEs using two approaches — a standard eigenfunction expansion method is used in version 1, and in version 2 a variational method is used. Version 1 leads to a converging solution of the time-dependent heat conduction equation as the number of eigenfunctions retained in the expansion is increased. However, this approach is inefficient since a large number of eigenfunctions (hence, ODEs) is required in order to obtain a reasonably accurate solution. Version 2 on the other hand, yields results comparable to the converged solution for version 1 with far fewer ODEs, thereby keeping the number of ODEs required to represent the fuel rod dynamics small and retaining the simplicity of the overall BWR model.

The phase variables, which are dimensionless, are the neutron density $n(t)$, the average delayed neutron precursor concentration $c(t)$, the boiling boundary $\mu(t)$, the slope $s(t)$ of the spatially linear representation of the two-phase quality as a function of the distance above the boiling boundary, the inlet velocity $\mathrm{v}(t)$, and finally, the fuel temperature coefficients in the single-phase region, $T_{i,1\phi}(t)$, and in the two-phase region, $T_{i,2\phi}(t)$. In version 1, $T_{i,1\phi}(t)$ and $T_{i,2\phi}(t)$ are the time-dependent coefficients in the eigenfunction expansions for the fuel temperature in the single- and two-phase regions, and in version 2, they are the time-dependent coefficients of the space-dependent functions in the space- and time-dependent trial function used in the variational method. The operating parameters are the control-rod-induced external reactivity ρ_{ext}, the inlet subcooling number N_{sub}, and the external pressure drop ΔP_{ext}. The Roman and Greek symbols are defined in the nomenclature section, and the details of the nondimensionalization of the variables and parameters are given in Appendix A.

The dynamical system that results from the model is of the form

$$\dot{\underline{X}}(t) = \underline{F}(\underline{X};\ \underline{\gamma},\ \underline{\kappa}) \tag{1}$$

where $\underline{X}(t)$ is the vector of phase variables

$$\underline{X}(t) = (n(t),\ c(t),\ \mu(t),\ s(t),\ \mathrm{v}(t),\ T_{i,1\phi}(t),\ T_{i,2\phi}(t))^T, \tag{2}$$

$\underline{\gamma}$ is the vector of system operating parameters

$$\underline{\gamma} = (\rho_{ext},\ N_{sub},\ \Delta P_{ext})^T, \tag{3}$$

and $\underline{\kappa}$, the vector of design parameters

$$\begin{aligned}\underline{\kappa} = (&Bi,\ Fr,\ G_g,\ N_{f1},\ N_{f2},\ N_{pch},\ N_r,\ N_{sbo},\ N_\rho,\\ &T_{sat},\ c_1,\ c_2,\ c_q,\ k_{exit},\ k_{inlet},\ r_1,\ \Lambda,\ \alpha_s,\ \beta,\ \lambda)^T\end{aligned} \tag{4}$$

is suppressed throughout the rest of the paper for brevity.

More explicitly, the dimensionless system of ODEs that forms this dynamical system is

$$\frac{dn(t)}{dt} = \frac{\rho(t) - \beta}{\Lambda} n(t) + \lambda c(t) \tag{5}$$

$$\frac{dc(t)}{dt} = \frac{\beta}{\Lambda} n(t) - \lambda c(t) \tag{6}$$

$$\frac{d\mu(t)}{dt} = 2\ \mathrm{v}(t) - 2\ \mu(t) \frac{N_{pch,1\phi}}{N_{sub}} \left[T_{s,1\phi}(t) - T_{sat} + N_{sub} N_{sbo}\right] \equiv f_1(t) \tag{7}$$

$$\frac{ds(t)}{dt} = \frac{g_1(t) + s(t)f_1(t)}{g_2(t)} \tag{8}$$

$$\frac{dv(t)}{dt} = \frac{g_3(t) + g_4(t) + g_5(t)f_1(t)}{g_6(t)} \tag{9}$$

For version 1, the ODEs that represent the fuel rod dynamics are

$$\frac{dT_{i,j\phi}(t)}{dt} = -\frac{\omega_{i,j\phi}^2 \alpha_s}{r_1^2} T_{i,j\phi}(t) + \frac{2\alpha_s c_q Bi_{j\phi}}{(\omega_{i,j\phi}^2 + Bi_{j\phi}^2) J_0(\omega_{i,j\phi})} \Delta n(t), \quad \begin{matrix} i = 1,2,\ldots,N \\ j = 1,2 \end{matrix} \tag{10}$$

and for version 2 they are

$$\frac{dT_{i,j\phi}(t)}{dt} = l_{1,i,j\phi} T_{1,j\phi}(t) + l_{2,i,j\phi} T_{2,j\phi}(t) + l_{3,i,j\phi} \Delta n(t), \quad \begin{matrix} i = 1,2 \\ j = 1,2 \end{matrix} \tag{11}$$

In Eq. (5), $\rho(t)$ is the reactivity given by

$$\rho(t) = \rho_{ext} + c_1 \Delta\alpha(t) + c_2 \Delta T_{avg}(t) \tag{12}$$

where the external reactivity ρ_{ext} is the reactivity that results from the displacement of the control rods from their positions during normal operation of a reference BWR at 100% power. $\alpha(t)$ is the void fraction spatially averaged over the two-phase region, and $T_{avg}(t)$ is the fuel temperature averaged over the rod cross-sectional area and the rod length (both the part in the single-phase region and the part in the two-phase region). Both $\Delta\alpha(t)$ and $\Delta T_{avg}(t)$ are then the changes measured from α_o and $T_{avg,o}$, their respective steady-state values at normal operation of a reference BWR at 100% power. In Eq. (7), $N_{pch,1\phi}$ is the phase change number in the single-phase defined in terms of a reference temperature T_o^*, taken here as T_{sat}^*. The temperature $T_{s,1\phi}(t)$ in that equation is the surface temperature of the fuel rod in the single-phase region, and N_{sbo} is a dimensionless number given in Appendix A. The quantities $g_1(t), \ldots, g_6(t)$ in Eqs. (8) and (9) are defined in the next section in the equations that arise in the development of the model. The index j in Eqs. (10) and (11) is 1 for the single-phase region and 2 for the two-phase region, and $\Delta n(t) = n(t) - \bar{n}$, where $\bar{n}$ is the steady-state (fixed point) value of the neutron density at a given set of system operating parameters $\underline{\gamma}$. The quantities r_1, $\omega_{i,j\phi}$, α_s, c_q, $Bi_{j\phi}$, and J_0 in Eq. (10) are the fuel rod radius, the eigenvalues of the fuel-rod heat-conduction equation, the thermal diffusivity of the fuel, the ratio of the volumetric heat generation rate in the fuel rod to the average BWR core neutron density, the Biot number in phase j, and the Bessel function of the first kind of order 0, respectively. The number of ODEs in Eq. (10), N, corresponds to the number of terms retained in the eigenfunction expansion for the fuel temperature in the two axial regions. In Eq. (11), $l_{1,i,j\phi}$, $l_{2,i,j\phi}$ and $l_{3,i,j\phi}$ are the constants that result when the heat conduction equation is integrated after substituting the trial function used in the variational method.

Development of the Model

The point kinetics equations, Eqs. (5) and (6) in the dynamical system above, are well known, and a description of the remaining ODEs follows.

Equation (7)

Equation (7) is obtained from the single-phase energy equation

$$\rho_f^* c_f^* \frac{\partial T^*(z^*,t^*)}{\partial t^*} + \rho_f^* c_f^* v^*(t^*) \frac{\partial T^*(z^*,t^*)}{\partial z^*} = \frac{q''^*_{1\phi}(t^*)\xi^*}{A^*} \tag{13}$$

where $q''^*_{1\phi}(t^*) = h^*_{1\phi}\,[T^*_{s,1\phi}(t^*) - (T^*_{sat} + T^*_{inlet})/2]$ is the wall heat flux in the single-phase region. A spatially linear but time-dependent temperature profile $T^*_{1\phi}(z^*,t^*) = T^*_{inlet} + (T^*_{sat} - T^*_{inlet})z^*/\mu^*(t^*)$ is introduced (this is equivalent to that assumed for the single-phase enthalpy by Clausse and Lahey [13]), and the above equation is reduced to Eq. (7) by integrating from the inlet $z^* = 0$ to the boiling boundary $z^* = \mu^*(t^*)$.

Equation (8)

Equation (8) is developed from the mixture-density equation which in dimensionless form is [12]

$$\frac{\partial \rho_m(z,t)}{\partial t} + v_m(z,t)\frac{\partial \rho_m(z,t)}{\partial z} = - N_{pch,2\phi}(t)\rho_m(z,t)\ , \tag{14}$$

where $\rho_m(z,t)$ is the mixture-density and $v_m(z,t)$ is the mixture velocity given by [12]

$$v_m(z,t) = v(t) + N_{pch,2\phi}(t)\,[z - \mu(t)]\ . \tag{15}$$

Here the time-dependent dimensionless phase change number in the two-phase region is given by $N_{pch,2\phi}(t) = \Gamma_g(t)/N_r$, where $\Gamma_g(t)$ is the vapor generation rate proportional to $q''^*_{2\phi}(t^*)$ — the wall heat flux in the two-phase region, here given by the Jens-Lottes correlation (for e.g, see Todreas and Kazimi [14]). The vapor generation rate rewritten in terms of this correlation in SI units is

$$\Gamma_g(t) = G_g\,(T_{s,2\phi}(t) - T_{sat})^4 \tag{16}$$

where G_g is a dimensionless number that depends on the system pressure p^*, and $T_{s,2\phi}(t)$ is the fuel rod surface temperature in the two-phase region. A spatially linear but time-dependent quality profile $x(z,t) = s(t)[z - \mu(t)]$ is introduced. This is equivalent to that assumed for the enthalpy by Clausse and Lahey [13] and leads to the following expression for the mixture density.

$$\rho_m(z,t) = \frac{1}{1 + s(t)\,[z - \mu(t)]/(N_\rho N_r)} \tag{17}$$

Equation (17) is substituted into Eq. (14) for the mixture density which then is integrated from $z = \mu(t)$ to 1 to reduce it to Eq. (8), an ODE for the slope $s(t)$ of the spatially linear quality. The quantities $g_1(t)$ and $g_2(t)$ in Eq. (8) are given by

$$g_1(t) = \Gamma_g(t)N_\rho - v(t)s(t) \tag{18}$$

$$g_2(t) = \frac{\{1 + [1 - \mu(t)]s(t)/(N_\rho N_r)\}\,\log\{1 + [1 - \mu(t)]s(t)/(N_\rho N_r)\}}{[1 - \mu(t)]s^2(t)/(N_\rho N_r)^2} - \frac{1}{s(t)/(N_\rho N_r)} \tag{19}$$

Equation (9)

The dimensionless single-phase and two-phase momentum equations [12]

$$- \frac{\partial p_{1\phi}}{\partial z} = \frac{dv(t)}{dt} + N_{f1}v^2(t) + Fr^{-1} \tag{20}$$

$$- \frac{\partial p_{2\phi}}{\partial z} = \rho_m(z,t)\left[\frac{\partial v_m(z,t)}{\partial t} + v_m(z,t)\,\frac{\partial v_m(z,t)}{\partial z} + N_{f2}v_m^2(z,t) + Fr^{-1}\right] \tag{21}$$

are used to obtain Eq. (9), the ODE for the inlet velocity v(t). The single-phase momentum equation, Eq. (20), is

integrated from $z = 0$ to $\mu(t)$ to give the single-phase region pressure drop, and the two-phase momentum equation, Eq. (21), is integrated from $z = \mu(t)$ to 1 to obtain the two-phase region pressure drop. These pressure drops are summed along with the inlet and exit form pressure drops, and then equated to the external pressure drop ΔP_{ext} to arrive at Eq. (9). The functions $g_3(t)$, $g_4(t)$, $g_5(t)$, and $g_6(t)$ that appear in Eq. (9) are given by

$$g_3(t) = \Delta P_{ext} - \Delta P_{inlet}(t) - \Delta P_{exit}(t) - \Delta P_{fric,1\phi}(t) - \Delta P_{grav,1\phi}(t) - \Delta P_{acc,2\phi}(t) - \Delta P_{fric,2\phi}(t) - \Delta P_{grav,2\phi}(t) \tag{22}$$

where explicit expressions for the seven internal channel pressure drops are given in Appendix B,

$$g_4(t) = -\frac{M_2(t)}{N_r} 4G_g(T_{s,2\phi}(t) - T_{sat})^3 g_7(t) \tag{23}$$

$$g_5(t) = \frac{1}{N_r} \Gamma_g(t) Q_1(t) \tag{24}$$

and

$$g_6(t) = \mu(t) + Q_1(t) \tag{25}$$

where $M_2(t)$ and $Q_1(t)$ are defined in Appendix B. The expression for $g_7(t)$ — which is equivalent to the time derivative of the two-phase region fuel surface temperature — is quite long and complex. Its detailed derivation is given below after the heat conduction equation is introduced and the fuel rod surface temperature in the two-phase region, $T_{s,2\phi}(t)$, is defined.

Equations (10) and (11)

Equations (10) and (11) are developed from the heat conduction equation for the fuel rod which in this simple model is taken as a single region, i.e., both the clad and the gap between the pin and the clad are omitted. That heat equation in cylindrical coordinates with conduction in the radial direction only, and with a time-dependent spatially-uniform volumetric heat generation rate $q'''^*(t^*)$ [which is directly proportional to the neutron density, $q'''^*(t^*) = c_q^* n^*(t^*)$]

$$\frac{\rho^* c_p^*}{k_d^*} \frac{\partial T_{j\phi}^*(r^*,t^*)}{\partial t^*} = \frac{\partial^2 T_{j\phi}^*(r^*,t^*)}{\partial r^{*2}} + \frac{1}{r^*} \frac{\partial T_{j\phi}^*(r^*,t^*)}{\partial r^*} + \frac{q'''^*(t^*)}{k_d^*}, \quad j = 1,2 \tag{26}$$

must be solved with boundary conditions

$$|T_{j\phi}^*(0,t^*)| < \infty \text{ , and } -k_d^* \frac{\partial T_{j\phi}^*(r_1^*,t^*)}{\partial r^*} = h_{j\phi}^*(T_{j\phi}^*(r_1^*,t^*) - T_{b,j\phi}^*), \quad j = 1,2 \tag{27}$$

where $T_{j\phi}^*(r^*,t^*)$ — the fuel rod temperature in the single-phase region for $j = 1$ and in the two-phase region for $j = 2$ — are treated separately in the regions below and above the moving boiling boundary and the solutions are not required to be continuous at the interface between these two regions. The single-phase heat transfer coefficient $h_{1\phi}^*$ is estimated by the Dittus-Boelter correlation, and the two-phase heat transfer coefficient $h_{2\phi}^*$ is estimated using the Jens-Lottes correlation (e.g., see Todreas and Kazimi, [14]). In Eq. (27), $T_{b,1\phi}^* = (T_{sat}^* + T_{inlet}^*)/2$ and $T_{b,2\phi}^* = T_{sat}^*$ are the bulk fluid temperatures in the single-phase region and the two-phase region, respectively.

Equation (26) is made dimensionless by using the dimensionless quantities $T_{j\phi}$, α_s, c_q, r_1 and $Bi_{j\phi}$ given in Appendix A. The steady-state solution of the heat conduction equation $\tilde{T}_{j\phi}(r)$ subject to the boundary conditions [Eq. (27)], then is

$$\tilde{T}_{j\phi}(r) = c_q \tilde{n} \left(\frac{r_1^2}{2\, Bi_{j\phi}} + \frac{r_1^2 - r^2}{4} \right) + T_{b,j\phi}, \quad j = 1,2 \tag{28}$$

where $T_{b,1\phi} = T_{sat} - N_{sub} N_{sbo}$ and $T_{b,2\phi} = T_{sat}$. Now, by introducing the variable

$$\theta_{j\phi}(r,t) = T_{j\phi}(r,t) - \tilde{T}_{j\phi}(r), \quad j = 1,2 \tag{29}$$

the dimensionless heat conduction equation becomes

$$\frac{1}{\alpha_s} \frac{\partial \theta_{j\phi}(r,t)}{\partial t} = \frac{\partial^2 \theta_{j\phi}(r,t)}{\partial r^2} + \frac{1}{r} \frac{\partial \theta_{j\phi}(r,t)}{\partial r} + c_q \Delta n(t), \quad j = 1,2 \tag{30}$$

with boundary conditions

$$\begin{aligned} \frac{\partial \theta_{j\phi}(0,t)}{\partial r} &= 0 \\ \frac{\partial \theta_{j\phi}(r_1,t)}{\partial r} &= - \frac{Bi_{j\phi}}{r_1} \theta_{j\phi}(r_1,t) \end{aligned}, \quad j = 1,2 \tag{31}$$

Equation (30) with the boundary conditions, Eq. (31), is solved using two approaches — version 1 is a standard eigenfunction expansion method that leads to Eq. (10) and version 2 is a variational method that leads to Eq. (11). For version 1, a standard eigenfunction expansion

$$\theta_{j\phi}(r,t) = \sum_{i=1}^{N} T_{i,j\phi}(t) J_0\left(\frac{\omega_{i,j\phi} r}{r_1} \right), \quad j = 1,2 \tag{32}$$

is introduced where $\omega_{i,j\phi}$ are the eigenvalues given by the transcendental equation

$$\omega_{i,j\phi}\, J_1(\omega_{i,j\phi}) = Bi_{j\phi} J_0(\omega_{i,j\phi}), \quad \begin{matrix} i = 1,2,\ldots,N \\ j = 1,2 \end{matrix} \tag{33}$$

Substituting Eq. (32) into Eq. (30) and after using the orthogonality of the Bessel functions

$$\int_0^{r_1} J_0\left(\frac{\omega_{i,j\phi} r}{r_1} \right) J_0\left(\frac{\omega_{k,j\phi} r}{r_1} \right) r dr = \begin{cases} \dfrac{r_1^2}{2} J_1^2(\omega_{i,j\phi}) \left(1 + \dfrac{\omega_{i,j\phi}^2}{Bi_{j\phi}^2} \right) & , i = k \\ 0 & , i \neq k \end{cases}, \quad j = 1,2 \tag{34}$$

etc., we arrive at the ODEs for the time-dependent coefficients $T_{i,j\phi}(t)$ given by Eq. (10) above.

For version 2, Eq. (30) can be written as $H\theta = f$ where the operator $H = \nabla^2$ is in cylindrical coordinates and $f = 1/\alpha_s \partial\theta/\partial t - c_q \Delta n(t)$. Here and throughout the application of the variational method, for simplicity of notation we have omitted the subscript $j\phi$ from all the terms with an understanding that the analysis is either for the single-phase region ($j = 1$), or for the two-phase region ($j = 2$). We introduce a general functional $\mathcal{F}(\varphi)$ that accommodates discontinuous trial functions $\varphi(r,t)$, that need not satisfy the boundary conditions [Eq. (31)]

$$\begin{aligned} \mathcal{F}(\varphi) = (\varphi, H\varphi) - 2(\varphi, f) &+ \left[\frac{r_1^2}{2\, Bi} \left(\frac{\partial \varphi}{\partial r} \right)^2 - \frac{Bi}{2} \varphi^2 \right]_{r=r_1} \\ &- \left[\frac{r_1^2}{2} \left(\frac{\partial \varphi}{\partial r} \right)^2 \right]_{r=0} + r_d \left[\varphi_l \frac{\partial \varphi_r}{\partial r} - \varphi_r \frac{\partial \varphi_l}{\partial r} \right]_{r=r_d} \end{aligned} \tag{35}$$

where the notation (a,b) indicates the inner product of a and b given by

$$(a,b) = \int_0^{r_1} a(r)\, b(r)\, r\, dr\ , \tag{36}$$

r_d is the point of discontinuity, and the subscripts l and r stand for the value of the function at the left and right of the discontinuity, respectively. The function that minimizes this functional is the solution $\varphi = \theta$ that satisfies $H\theta = f$ subject to the boundary conditions [Eq. (31)]. The procedure for constructing this functional can be found in references [16,17], and is not elaborated here.

We follow the Rayleigh-Ritz procedure [16,17] to approximately minimize the functional in Eq. (35) and arrive at the ODEs in Eq. (11). To do this, we substitute a two-piecewise quadratic trial function

$$\begin{aligned} \theta(r,t) &= T_1(t)v_{1a}(r) + T_2(t)v_{1b}(r), \quad 0 < r < r_d \\ &= T_1(t)v_{2a}(r) + T_2(t)v_{2b}(r), \quad r_d < r < r_1 \end{aligned} \tag{37}$$

into the functional $\mathcal{F}(\varphi)$ and adjust $T_1(t)$ and $T_2(t)$ so as to minimize $\mathcal{F}$. This is accomplished by setting $\delta\mathcal{F}/\delta T_1 = 0$ and $\delta\mathcal{F}/\delta T_2 = 0$. The resulting two equations can be solved simultaneously to arrive at the ODEs in Eq. (11) above. The quadratic functions $v_{1a}(r)$, $v_{1b}(r)$, $v_{2a}(r)$, and $v_{2b}(r)$ used in the final calculations actually reported here are such that the trial function $\theta(r,t)$ satisfies the boundary conditions [Eq. (31)] and is continuous and smooth at r_d. The details of the derivation of these quadratic functions are given in Appendix C. The details that lead to the expressions for $l_{1,i,j\phi}$, $l_{2,i,j\phi}$ and $l_{3,i,j\phi}$ in Eq. (11) are given in Appendix D.

Equation (12)

Though Eq. (12) is trivial, it involves $\Delta\alpha(t)$ ($\equiv \alpha(t) - \alpha_o$) and $\Delta T_{avg}(t)$ ($\equiv T_{avg}(t) - T_{avg,o}$) which must be expressed in terms of the other phase variables. The average void fraction in the channel $\alpha(t)$ is

$$\begin{aligned} \alpha(t) &= \frac{1}{[1 - \mu(t)]} \int_{\mu(t)}^{1} \alpha(z,t)dz \\ &= \frac{1}{[1 - \mu(t)]} \int_{\mu(t)}^{1} N_r \frac{x(z,t)}{N_\rho N_r + x(z,t)} dz = N_r \left\{ 1 - \frac{Q_1(t)}{[1 - \mu(t)]} \right\} \end{aligned} \tag{38}$$

and the average fuel temperature $T_{avg}(t)$ is given by

$$T_{avg}(t) = \mu(t)\, T_{avg,1\phi}(t) + [1 - \mu(t)]\, T_{avg,2\phi}(t) \tag{39}$$

where $T_{avg,j\phi}(t)$ is given by Eq. (40) below.

This completes the formal development of the set of equations, Eqs. (5)-(12). To be able to carry out the stability analyses and numerical simulations, the intermediate variables, the average temperature in the fuel rod, $T_{avg,j\phi}(t)$, the fuel rod surface temperature, $T_{s,j\phi}(t)$, and $g_7(t)$ ($\equiv dT_{s,2\phi}(t)/dt$) that arise in Eqs. (7), (16), (23), and (39) of the model, must be appropriately defined in terms of the phase variables $T_{i,j\phi}(t)$. In fact, Eqs (5)-(9) of the dynamical system are related to Eqs. (10) and (11) only through these intermediate variables. First, by multiplying each term in Eq. (29) with $2r/r_1^2$ and then integrating that equation from 0 to r_1 gives $T_{avg,j\phi}(t)$ as

$$\begin{aligned} T_{avg,j\phi}(t) &= \theta_{avg,j\phi}(t) + \tilde{T}_{avg,j\phi}\ , \quad j = 1,2 \\ T_{avg,j\phi}(t) &= \frac{2}{r_1^2} \int_0^{r_1} T_{j\phi}(r,t) r dr \quad \text{, and} \quad \theta_{avg,j\phi}(t) = \frac{2}{r_1^2} \int_0^{r_1} \theta_{j\phi}(r,t) r dr \end{aligned} \tag{40}$$

where the $T_{i,j\phi}(t)$ dependence in the above equation enters through $\theta_{j\phi}(r,t)$, taken from Eq. (32) for version 1 and

Eq. (37) for version 2. The steady-state average temperature, $\tilde{T}_{avgj\phi}$, in the above equation is obtained from Eq. (28)

$$\tilde{T}_{avgj\phi} = \frac{2}{r_1^2}\int_0^{r_1}\tilde{T}_{j\phi}(r)rdr = c_q\tilde{n}r_1^2\left(\frac{1}{2\,Bi_{j\phi}} + \frac{1}{8}\right) + T_{bj\phi}\ ,\ \ j = 1,2 \tag{41}$$

Now, evaluating Eq. (29) at r_1 gives $T_{sj\phi}(t)$ as

$$T_{sj\phi}(t) = T_{j\phi}(r_1,t) = \theta_{sj\phi}(t) + \tilde{T}_{sj\phi}\ ,\ \ j = 1,2 \tag{42}$$

where the steady-state surface temperature, $\tilde{T}_{sj\phi} = \tilde{T}_{j\phi}(r_1)$ is obtained from Eq. (28). The surface temperature $\theta_{sj\phi}(t) = \theta_{j\phi}(r_1,t)$ can be defined in two ways — either directly from Eqs. (32) or (37), or by relating it to the average quantity defined in Eq. (40). For example, $\theta_{sj\phi}(t)$ obtained for version 1 by using Eq. (32) can be written as

$$\theta_{sj\phi}(t) = \theta_{j\phi}(r_1,t) = \sum_{i=1}^{N} T_{ij\phi}(t)J_0(\omega_{ij\phi})\ \ j = 1,2 \tag{43}$$

and for version 2 by using Eq. (37)

$$\theta_{sj\phi}(t) = T_1(t)v_{2a}(r_1) + T_2(t)v_{2b}(r_1) \tag{44}$$

where the subscript $j\phi$ has been omitted from the terms on the right side of the equation. For both versions, version 1 and 2, $\theta_{sj\phi}(t)$ can also be defined by relating it to the average quantity defined in Eq. (40). This relationship is obtained by multiplying each term in Eq. (30) with $2r/r_1^2$ and then integrating that equation from 0 to r_1, which yields

$$\theta_{sj\phi}(t) = \frac{r_1^2}{2\,Bi_{j\phi}}\left[c_q\Delta n(t) - \frac{1}{\alpha_s}\frac{d\theta_{avgj\phi}(t)}{dt}\right],\ \ j = 1,2 \tag{45}$$

Based on these two definitions for $\theta_{sj\phi}(t)$, we subdivide version 1 (based on the eigenfunction expansion approach) into two subdivisions: version 1a based on Eq. (43), and version 1b based on Eq. (45). Equation (44) for version 2, which is equivalent to Eq. (43) for version 1, is however not used because, as explained in the next paragraph, Eq. (45) yielded better results than Eq. (43) for version 1. Hence, we do not subdivide version 2, and only use the definition of $\theta_{sj\phi}(t)$ given by Eq. (45) for the variational approach. Finally, expressions for the term $g_7(t)$ ($\equiv dT_{s,2\phi}(t)/dt$) in Eq. (23) now can be straightforwardly derived from Eq. (43) and Eq. (45) for versions 1a and 1b, respectively, and from Eq. (45) for version 2. These expressions are algebraically very complicated, and hence not given here explicitly.

In the next section we shall compare the stability boundaries in the N_{sub}-ρ_{ext} operating parameter plane that result from versions 1a and 1b and version 2, for a fixed ΔP_{ext} — the pressure drop at normal operation of a reference BWR at 100% power. We shall show that for version 1a, the convergence of the stability boundary in the operating parameter plane with respect to N — the number of ODEs retained in Eq. (10) of the dynamical system — is very slow. For version 1b on the other hand, the convergence is much faster, indicating that version 1b can accurately represent the fuel rod dynamics with fewer ODEs, and hence, is better and simpler than version 1a. Further, we shall show that version 2 is comprised of the least number of ODEs by far, and accurately represents the fuel rod dynamics, thereby making it the simplest of the three models developed here.

Although version 2 is by far the simplest model, it became so only after the most suitable or the "best" trial function given by Eq. (37), was determined — and determining such a function is a major disadvantage of the variational method. Before selecting the function in Eq. (37) as the most suitable trial function, various other trial

functions were tried and in each case, the resulting stability boundary in the N_{sub}-ρ_{ext} operating parameter plane for a fixed ΔP_{ext} was compared to a reference stability boundary — taken here as the one from version 1b with $N = 32$. First, trial functions with one time-dependent coefficient were tried. The spatial dependence of the trial function in this category was a constant that did not satisfy the boundary conditions and a quadratic function that did satisfy the boundary conditions. However, in both these cases, the resulting stability boundary agreed rather poorly with the reference stability boundary. The next step was to try trial functions with two time-dependent coefficients. In this category, two-piecewise constants were tried which also did not do well. Finally, a two-piecewise quadratic trial function [Eq. (37)] that satisfied the boundary conditions and was continuous and smooth at r_d was tried. The resulting stability boundary agreed well with the reference stability boundary. For this case, the respective sizes of the two sub-divisions as determined by r_d ($0 < r_d < r_1$), must be decided *a priori*. For this purpose, stability boundaries were determined for several values of the ratio r_d/r_1 and ΔP_{ext}, and compared with reference stability boundaries. For ΔP_{ext} values of practical interest, it was determined that the ratio $r_d/r_1 = 0.83$ was best. This value subsequently was used in all the calculations reported here.

Stability Analyses and Numerical Simulations

Stability analyses and numerical simulations were carried out using the simple dynamical system $\dot{\underline{X}}(t) = \underline{F}(\underline{X}; \underline{\gamma})$, developed in the previous section, and given by Eqs. (5)-(11). The stability analyses were done using two approaches. In the first approach, the stability boundary in an operating parameter plane was generated directly by perturbing the vector of phase variables $\underline{X}$ about a fixed point $\tilde{\underline{X}}$ (where tilde indicates the steady-state) as $\underline{X}(t) = \tilde{\underline{X}}(\underline{\gamma}) + \delta\underline{X}\, e^{i\omega t}$, and then linearizing the dynamical system, which is then reduced to a set of two transcendental equations that involve the phase variables at the fixed point, the design and operating parameters, and the oscillation frequency ω. The entire stability boundary in an operating parameter plane was generated by varying ω, and solving these two equations directly for the two operating parameters. This approach, of course, corresponds to the case in which a complex conjugate pair of eigenvalues of the Jacobian matrix $\underline{F}_{\underline{X}}(\tilde{\underline{X}}(\underline{\gamma}); \underline{\gamma})$ evaluated at the fixed point $\tilde{\underline{X}}(\underline{\gamma})$ have a zero real part and imaginary parts $\pm i\omega$, and suggests that a Hopf bifurcation occurs when the stability boundary in the parameter plane is crossed. In the second approach, the eigenvalues of the Jacobian matrix $\underline{F}_{\underline{X}}(\tilde{\underline{X}}(\underline{\gamma}); \underline{\gamma})$ at the fixed point $\tilde{\underline{X}}(\underline{\gamma})$ were calculated. Any eigenvalue with a positive real part indicates that the corresponding fixed point is unstable, and when — with all the other eigenvalues in the left half of the complex plane — a complex conjugate pair crosses the imaginary axis as a parameter is varied, a Hopf bifurcation is signaled. The special case in which the parameter values are such that the complex conjugate pair is on the imaginary axis, corresponds to the direct calculation (first approach) of the stability boundary. Finally, simulations were carried out by numerically integrating the full nonlinear ODEs in time. The results obtained via the direct calculation of the stability boundary, the calculation of the eigenvalues of the Jacobian matrix for various parameter values, and the full numerical simulations based on the time-dependent nonlinear ODEs are mutually consistent.

Typical design parameters and thermal-hydraulics data for operating conditions of a BWR [14], and the neutronics data for the point kinetics equations [3,15], are given in Appendix E. All the data are for the conditions at normal operation of a reference BWR at 100% power. Data for some design parameters such as k_{inlet} and k_{exit} had to be adjusted to lump the spacer pressure losses in the channel at the inlet and the exit.

Version 1 is represented by Eqs. (5)-(10), and it is further subdivided into two alternatives, versions 1a and 1b, based on the expressions used for the fuel rod surface temperature. For version 1a the fuel rod surface temperature is given by Eq. (43) and for version 1b it is given by Eq. (45). Version 2 is represented by Eqs. (5)-(9) and (11) and is not further subdivided; the fuel rod surface temperature is given by Eq. (45) only. Fig. 1a shows the stability boundaries obtained using model versions 1a and 1b for various values of N plotted in the N_{sub}-ρ_{ext} parameter plane for a fixed ΔP_{ext} — the core pressure drop at normal operation of a reference BWR at 100% power.

As N is increased from 4 to 64, the stability boundaries for version 1a converge from left to right in the parameter plane and those for version 1b converge from right to left. Moreover, for increasing N, the stability boundaries for versions 1a and 1b do not cross each other, but tend to converge to a single limit from opposite sides. This indicates that version 1a gives a lower bound and 1b gives an upper bound on the stability boundary. Further, for version 1b there is no perceptible shift in the stability boundary as N is increased above 32, indicating that the solution has reasonably well converged for $N = 32$. However, this is not so for version 1a — even when N is increased from 32 to 64. Hence, version 1b (in which the surface temperature was expressed in terms of the average temperature) is simpler than version 1a (in which the surface temperature was determined directly from the explicit expression for the temperature), since N is smaller for it, thereby resulting in a lower dimensionality of the dynamical system that is given by $(2N + 5)$. We take the stability boundary for version 1b for $N = 32$ as a reference stability boundary and compare the results for version 2 with it in Fig. 1b. It is clear from this figure that the stability boundary for version 2 with just two ODEs representing the fuel rod dynamics in each phase region agrees well with the reference stability boundary over most of the parameter plane, and it lies within a lower bound given by version 1a for $N = 32$. Furthermore, considering that the stability boundary given by version 2 with only nine equations in the dynamical system is comparable in accuracy to the stability boundary given by version 1b for $N = 8$ that has a total of 21 equations, shows that the variational method approach is a reasonable compromise between retaining the simplicity of the model and the accuracy of the results. Hence, in the remainder of this paper, we carry out the stability analyses and numerical simulations using only version 2 of the model.

The stability boundary for version 2 replotted in the N_{sub}- ρ_{ext} parameter plane for a fixed ΔP_{ext} (= 33.88) was calculated directly using the first approach described above, and is shown in Fig. 2. This boundary divides the operating parameter plane into the stable region, where the fixed point $\underline{\tilde{X}}(\underline{\gamma})$ of the dynamical system at each $\underline{\gamma} = (N_{sub}, \rho_{ext}, \Delta P_{ext})$ is stable, and the unstable region where the fixed point is unstable. The normal operating point of a BWR, for which $\rho_{ext} = 0$, $N_{sub} = 0.66$, and $\Delta P_{ext} = 33.88$, also is shown in Fig. 2. Clearly, this point lies well within the stable region in the operating parameter plane. It is interesting to note that — above a certain critical $\rho^c_{ext} = 0.02096$ — while increasing N_{sub} from an initially small value (for fixed ρ_{ext}) makes the system unstable, further increasing it eventually leads to a stable system again. As expected, for a fixed N_{sub}, increasing ρ_{ext} (which corresponds physically to moving the control rods out of the core) leads the system from a stable to an unstable state.

The results of the direct calculation of the stability boundary summarized above were checked by calculating the eigenvalues of the Jacobian matrix evaluated at the fixed point for various points in the N_{sub}- ρ_{ext} parameter plane. The need to check the results of the direct calculation arises because, though there is a pair of complex conjugate eigenvalues with zero real part for parameter values *on* the stability boundary, there is no guarantee that there are no eigenvalues with positive real part for these parameter values. Moreover, it is also necessary to ensure that the complex conjugate pair of eigenvalues *cross* the imaginary axis as the parameters are varied, since this is a *necessary* condition for Hopf bifurcation. The computed eigenvalues yielded the same stable and unstable regions. For example, all the eigenvalues at the point A in the unstable region of Fig. 2 — where the parameter values $(N_{sub}, \rho_{ext}) = (1.50, 0.02258)$ (and $\Delta P_{ext} = 33.88$) and the phase variables at the corresponding fixed point $(\tilde{n}, \tilde{c}, \tilde{\mu}, \tilde{s}, \tilde{v}) = (1.69, 2950, 0.23, 0.35, 0.88)$ — there is a complex conjugate pair with positive real part and all the other eigenvalues have negative real parts; and for the parameter values at the point B in the stable region of Fig. 2 — where $(N_{sub}, \rho_{ext}) = (1.50, 0.02058)$ (and $\Delta P_{ext} = 33.88$) and the phase variables at the corresponding fixed point $(\tilde{n}, \tilde{c}, \tilde{\mu}, \tilde{s}, \tilde{v}) = (1.64, 2863, 0.25, 0.33, 0.90)$ — all the eigenvalues have negative real parts. Hence, the steady-state or fixed point is unstable for the parameter values corresponding to point A in the N_{sub}- ρ_{ext} parameter plane and stable for those corresponding to point B. At the point C — where $(N_{sub}, \rho_{ext}) = (1.50, 0.02158)$ — which lies *on* the stability boundary in Fig. 2, there is a complex conjugate pair with zero real part and non-zero imaginary part $\pm i\omega$ with $\omega = 13.48$ (or, $\omega^* = 1.5$ Hz); all the other eigenvalues have negative real parts. Points A and B in Fig. 2 are very close to point C. Hence, as the parameter ρ_{ext} is decreased through its value on the stability boundary, a complex conjugate pair of eigenvalues of $\underline{F}_{\underline{X}}(\underline{\tilde{X}}(\underline{\gamma}),\underline{\gamma})$ crosses the imaginary axis indicating

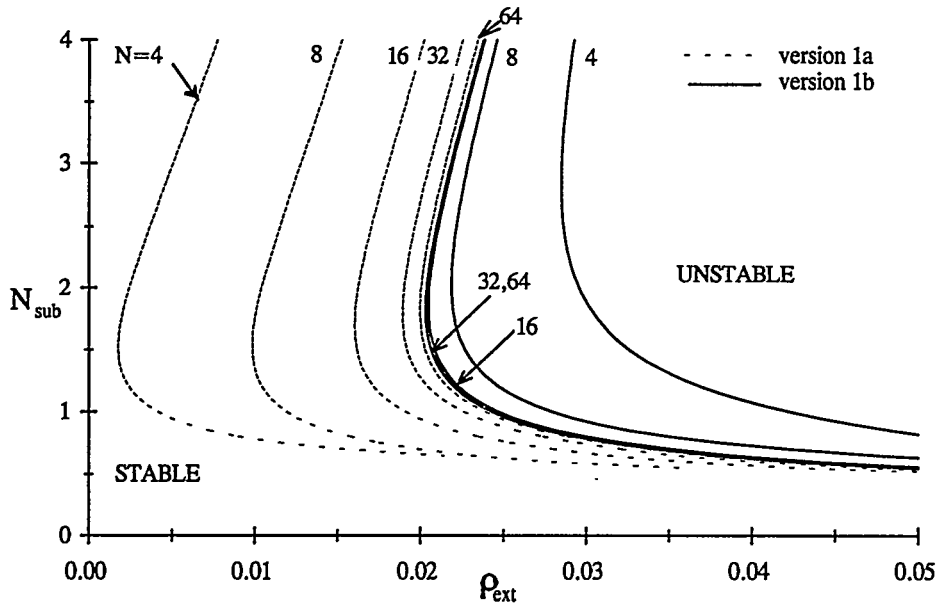

Fig. 1a: Sensitivity of the stability boundaries for model versions 1a and 1b in the N_{sub}-ρ_{ext} parameter plane (ΔP_{ext} = 33.88) to N — the number of terms in the eigenfunction expansion of the fuel rod temperature.

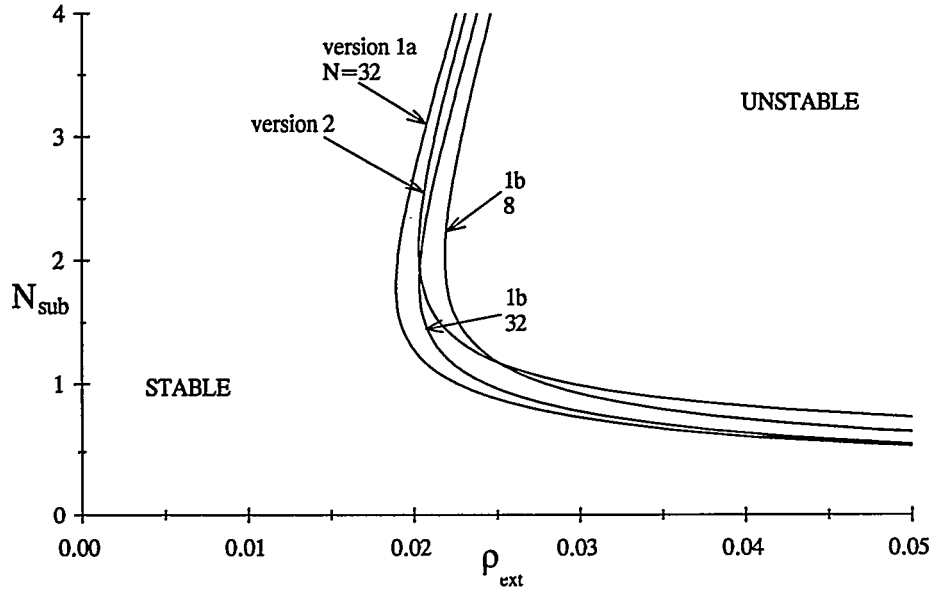

Fig. 1b: Comparison of the stability boundary in the N_{sub}-ρ_{ext} parameter plane (ΔP_{ext} = 33.88) of model version 2 with those for model version 1a for N = 32, and model version 1b for N = 8 and 32.

that the system does indeed undergo a Hopf bifurcation [18,19]. The fixed point is completely specified only by the fixed point values of *all* the phase variables, i.e. $\underline{\tilde{X}}(\gamma) = (\tilde{n}, \tilde{c}, \tilde{\mu}, \tilde{s}, \tilde{v}, \tilde{T}_{1,1\phi}, \tilde{T}_{2,1\phi}, \tilde{T}_{1,2\phi}, \tilde{T}_{2,2\phi})$. However, only the first five are given above, because $\tilde{T}_{i,j\phi}$ $i = 1,2$ $j = 1,2$ are always zero at a fixed point (because in Eq. (11), $\Delta n = 0$, and in general, $l_{1,1,j\phi} l_{2,2,j\phi} \neq l_{2,1,j\phi} l_{1,2,j\phi}$ at the fixed point) and therefore, we have not indicated them in the fixed point.

Finally, numerical simulations were carried out for several points in the operating parameter plane to study the nonlinear effects not captured by the local bifurcation and stability analyses. For initial conditions only "slightly" away from the fixed points, the results of the numerical simulations always agreed with those of the stability analyses, i.e., growing oscillations resulted for points on the unstable side of the stability boundary in the parameter plane and decaying oscillations (back to the fixed point) resulted for points on the stable side. Shown in Figs. 3 through 6 are the results of the numerical simulations carried out at point A (in the unstable region) and at point B (in the stable region) in Fig. 2. The time evolution of the neutron density $n(t)$ and the inlet velocity v(t), when the system parameters are at point A, starting from initial condition $(n(0), c(0), \mu(0), s(0), v(0)) = (1.60, 2950, 0.23, 0.35, 0.80)$ and $T_{i,j\phi}(0) = 0$, $i = 1,2$ $j = 1,2$ nearby the fixed point, is shown in Fig. 3. As expected on the basis of the stability analyses, the oscillation amplitudes grow, and the system moves away from the unstable fixed point. The time evolution of $n(t)$ and v(t) for parameter values at point B, starting from initial condition $(n(0), c(0), \mu(0), s(0), v(0)) = (2.50, 2863, 0.23, 0.33, 1.00)$ and all $T(0)$'s $= 0$ close to the fixed point, is shown in Fig. 4. Also as expected from the stability results, the oscillations decay in this case and the system evolves to the stable fixed point. However, when the initial condition for the numerical simulation is taken farther away from the fixed point corresponding to point B in Fig. 2, i.e., $(n(0), c(0), \mu(0), s(0), v(0)) = (3.00, 2863, 0.20, 0.33, 1.10)$ and all $T(0)$'s $= 0$, the system moves away from the fixed point. The time evolution of the neutron density and the inlet velocity for this case is shown in Fig. 5, where the oscillation amplitude of the phase variables now grows in time. The time evolutions of $n(t)$ and v(t) in Figs. 4 and 5 are plotted in Fig. 6 as phase-portraits projected onto the n-v phase plane. The trajectory that emanates from the initial conditions used in Fig. 4, moves towards the stable fixed point, whereas the one that emanates from the initial conditions used in Fig. 5, evolves away from the fixed point. These two phase portraits, shown in Fig. 6, indicate that there exists an *unstable limit cycle* in the phase space nearby the *stable fixed point* when the parameter values are at point B, and thus that the Hopf bifurcation that occurs as the stability boundary in Fig. 2 is crossed is a *subcritical* Hopf bifurcation, not a supercritical Hopf bifurcation. This is consistent with the fact that the growing oscillations, that result from the simulation done for parameter values at point A, do not saturate at a stable limit cycle which would indicate that the Hopf bifurcation is supercritical. Hence, when the system is operated at the allegedly "safe" parameter values corresponding to point B, for which the fixed point is stable, an initial condition that could result due to a finite perturbation from that fixed point would lead to growing oscillations, not oscillations that would die away and evolve to the fixed point. Thus, although the steady-state or the fixed point corresponding to the point B in Fig. 2 is *stable*, it may not be a safe point at which to operate the BWR since a small but finite perturbation could lead to growing nuclear-coupled density-wave oscillations as indeed the simulation (Figs. 5 and 6) shows. This, of course, typically is the case when a *subcritical* Hopf bifurcation occurs. These results are consistent with the results reported by Tsuji et al. [10] who also showed in the stability analysis of their model that a subcritical Hopf bifurcation occurred as the stability boundary was crossed.

The frequencies of oscillations obtained from the numerical simulations were compared with those evaluated via the eigenvalue calculations. The points A and B in Fig. 2 are very close to the point C which is on the stability boundary. Hence, the damped and growing oscillations, that occur for parameter values at A and B, respectively, following initial conditions very close to the corresponding fixed point values, should have frequencies very close to the imaginary part of the eigenvalues — the complex conjugate pair that has zero real part — of the Jacobian matrix for parameter values at point C. Indeed, the growing and damped neutron densities and inlet velocities shown in Figs. 3 and 4 for parameter values at points A and B respectively, oscillate with frequency 1.5 Hz, consistent with the eigenvalues of the Jacobian matrix corresponding to the point C.

The stability results just described can be related to the operating regimes on the power-flow map familiar to BWR plant engineers. A typical power-flow map for a BWR [8] is shown in Fig. 7. This power-flow map also

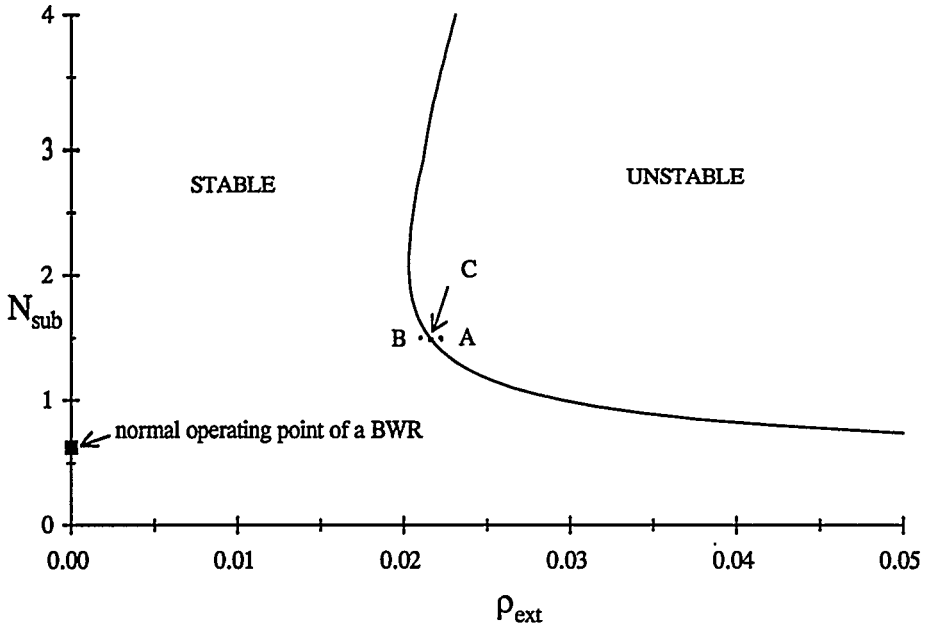

Fig. 2: The stability boundary of model version 2 in the N_{sub}-ρ_{ext} parameter plane (ΔP_{ext} = 33.88).

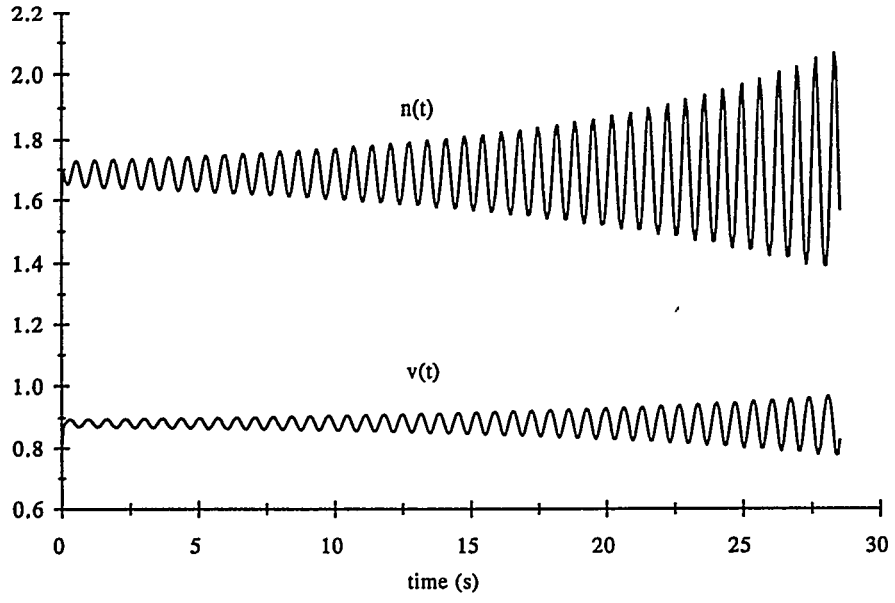

Fig. 3: Time evolution of phase variables for parameter values at point A in Fig. 2. Initial condition, (n(0), c(0), μ(0), s(0), v(0)) = (1.60, 2950, 0.23, 0.35, 0.80) and all T(0)'s = 0, is nearby the unstable fixed point ($\bar{n}$, $\bar{c}$, $\bar{\mu}$, $\bar{s}$, $\bar{v}$) = (1.69, 2950, 0.23, 0.35, 0.88).

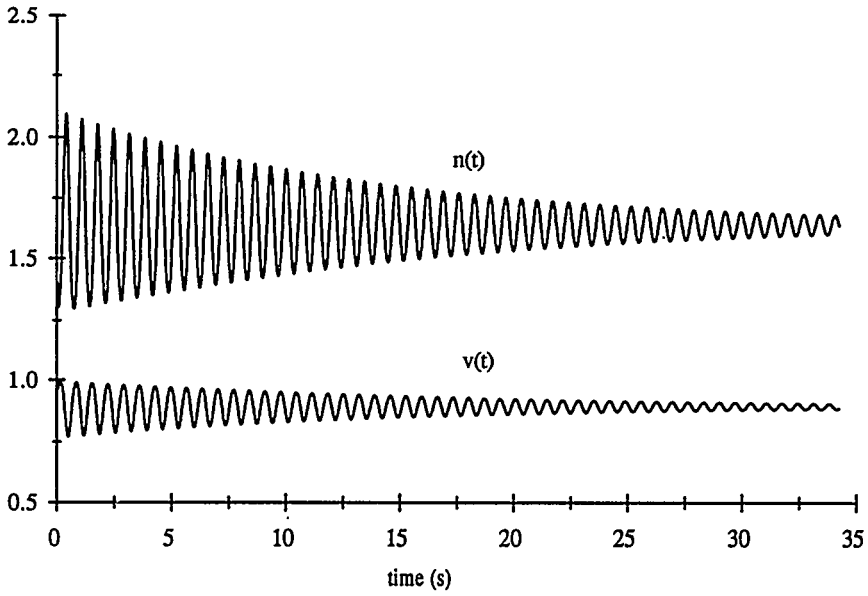

Fig. 4: Time evolution of phase variables for parameter values at point B in Fig. 2. Initial condition, ($n(0)$, $c(0)$, $\mu(0)$, $s(0)$, v(0)) = (2.50, 2863, 0.23, 0.33, 1.00) and all $T(0)$'s = 0, is nearby the stable fixed point ($\tilde{n}$, $\tilde{c}$, $\tilde{\mu}$, $\tilde{s}$, $\tilde{v}$) = (1.64, 2863, 0.25, 0.33, 0.90).

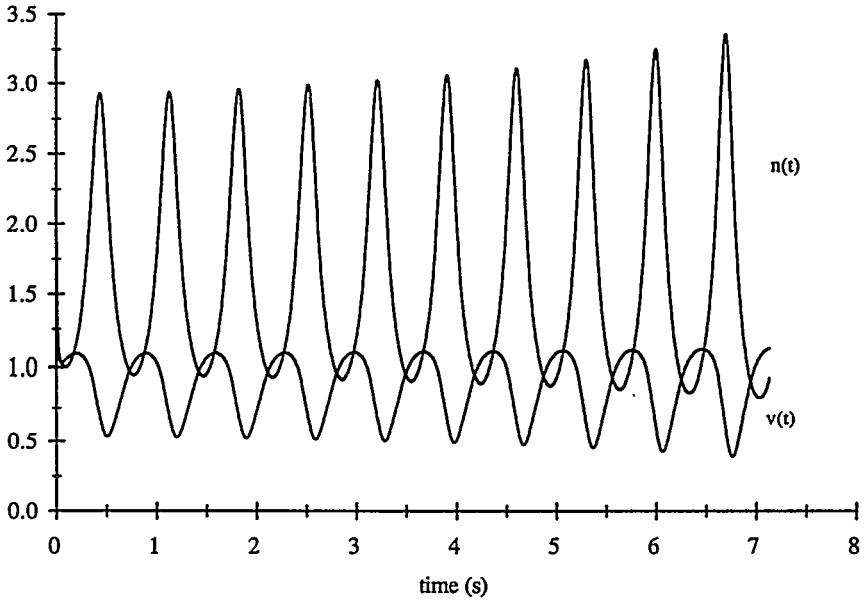

Fig. 5: Time evolution of phase variables for parameter values at point B in Fig. 2. Initial condition, ($n(0)$, $c(0)$, $\mu(0)$, $s(0)$, v(0)) = (3.00, 2863, 0.20, 0.33, 1.10) and all $T(0)$'s = 0, is some distance away from the stable fixed point ($\tilde{n}$, $\tilde{c}$, $\tilde{\mu}$, $\tilde{s}$, $\tilde{v}$) = (1.64, 2863, 0.25, 0.33, 0.90).

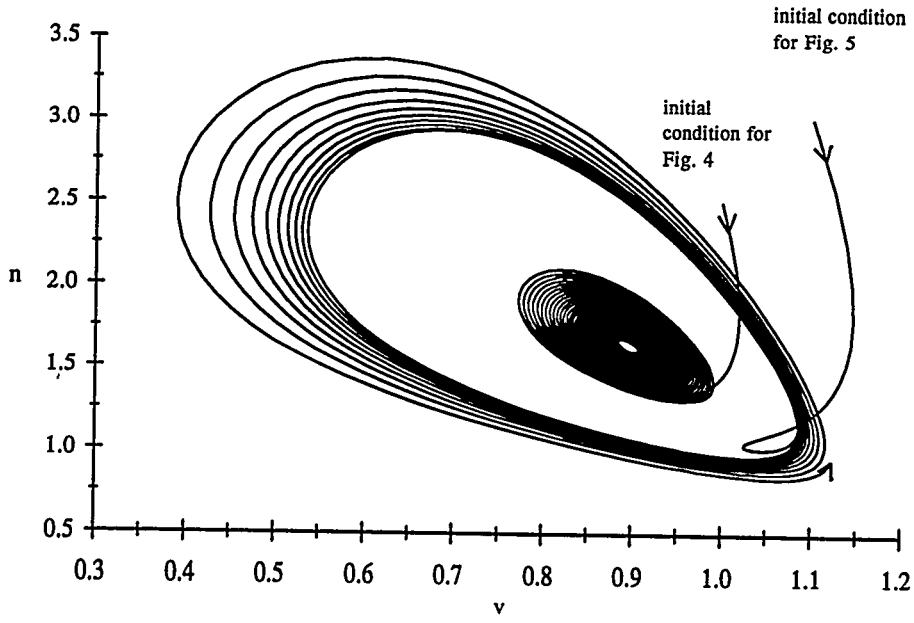

Fig. 6: Phase portrait. Evolution of the phase space trajectories in the projection of the phase space onto the *n*-v plane for parameter values at point B in Fig. 2 for two different sets of initial conditions.

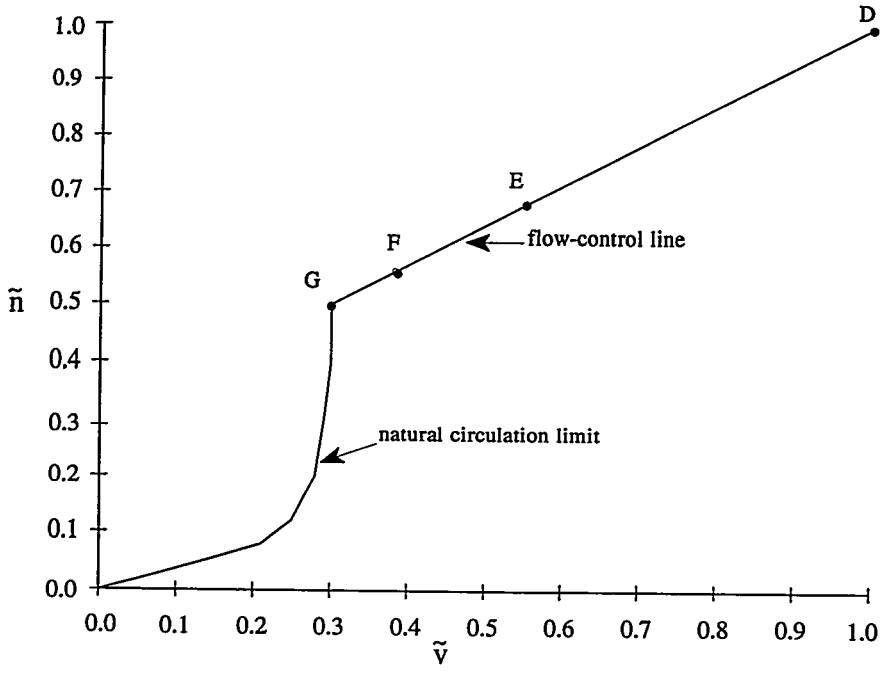

Fig. 7: A typical power-flow map for a BWR [8].

can be referred to as an $\tilde{n}$-$\tilde{v}$ map (as is done in Fig. 7) since the power can be related directly to the steady-state (fixed point) neutron density $\tilde{n}$ and the flow rate can be related directly to the steady-state inlet velocity $\tilde{v}$. The map is generated from the natural circulation limit and the forced-convection flow-control line of a BWR. For most operational transients, flow-control is used to follow BWR load changes. This method of load-following ensures that the system pressure is essentially constant and reduces the need for control rod action on the flow-control line. Point D on this line in Fig. 7 is the normal operating point of a BWR , points E and F correspond to operating conditions with 20 K and 30 K subcooling respectively, and point G is known to correspond to the least stable BWR operating conditions [4]. This line D-G is the flow-control line used to follow load changes.

Keeping in mind both that the model developed and analyzed here is a very simple BWR core model and that not all design and operating parameters are available for an actual BWR, we do not attempt a detailed quantitative comparison with all possible operating points on the power-flow map. Rather, we use the results of the stability analyses and numerical simulations described above to explain qualitatively the change in stability between the normal BWR operating point, point D, and the least stable operating point, point G, in the power-flow map shown in Fig. 7. The flow-control line, D-G in Fig. 7 is mapped to the N_{sub}-$\tilde{n}$ operating-parameter/phase-variable plane in Fig. 8. Unlike previous stability boundaries generated directly in an operating parameter plane by keeping the third operating parameter fixed, the stability boundary for a fixed inlet velocity was first generated in the N_{sub}-ρ_{ext} parameter plane by keeping the steady-state inlet velocity $\tilde{v}$ fixed and allowing the third operating parameter ΔP_{ext} to vary. This stability boundary was then mapped to the N_{sub}-$\tilde{n}$ plane and is shown in Fig. 8. Since operating points D, E , F, and G have different fixed-point inlet velocities — $\tilde{v}$ = 1.0, 0.55, 0.39, and 0.3, respectively — there are correspondingly different stability boundaries for them. The operating point D in Fig. 8 is related to the $\tilde{v}$ = 1.0 stability boundary, and clearly lies well within the stable region defined by that boundary. The operating point E in Fig. 8 is related to the $\tilde{v}$ = 0.55 stability boundary and we observe that point E is closer to that boundary than point D is to the $\tilde{v}$ = 1.0 stability boundary. Hence, although the point E is stable, it is less stable than D in the sense that it would be more easily susceptible to diverging oscillations when the initial conditions are not near the fixed point. Such diverging oscillations for a fixed point on the stable side of the stability boundary were indeed demonstrated for the point B in Fig. 2. The decreasing stability of the operating points continues as they are moved down the flow-control line to point F which is related to the $\tilde{v}$ = 0.39 stability boundary, and finally to point G which is related to the $\tilde{v}$ = 0.3 stability boundary. Point G is the closest point to its stability boundary; hence, it is clear that among all the operating points on the flow-control line, point G is the least stable operating point, and point D is the most stable since it is farthest from its stability boundary. We reiterate here that this explanation is very qualitative, limited not only by the simplicity of the model, but also by the unavailability of accurate data for design and operating parameters. For example, the stability boundaries that were shown to be sensitive to design parameters such as the pressure loss coefficients, friction factors, feedback coefficients, etc., by Tsuji et al. [10], shift appreciably when these parameters are varied. Depending on the values of these parameters, according to our calculations the point G could be on the unstable side of the stability boundary for $\tilde{v}$ = 0.3 which corresponds to it, clearly making it an unstable operating point; or, the point G could be a little further into the stable region of the N_{sub}-$\tilde{n}$ plane. In either case, the overall trend of decreasing stability of operating points on the flow-control line as the flow rate is reduced, will continue to be exhibited in Fig. 8, and that is what we have attempted to establish here as quantitatively as possible in the absence of proprietary design data (and a complicated detailed engineering model).

The decreasing stability of the operating points on the flow-control line as the flow rate is reduced, can also be observed from Fig. 9, where the stability boundaries are plotted for four fixed values of N_{sub} = 0.66, 1.33, 1.99, and 2.71, corresponding to the inlet subcooling at points D, E, F and G, respectively, in Fig. 7. These stability boundaries were first generated directly in the ΔP_{ext}-ρ_{ext} operating parameter plane by keeping the third operating parameter, N_{sub}, fixed. They then were mapped on to the $\tilde{n}$-$\tilde{v}$ plane and are shown in Fig. 9. Operating point D can now be related to the N_{sub} = 0.66 stability boundary and we observe that it is very stable. Points E, F, and G can be related to their respective stability boundaries, and we observe that the corresponding stability boundaries move closer to the operating points as we move along the flow-control line from E to F and finally to G. This again demonstrates the decreasing stability of the operating points as we move down the flow-control line. It is interesting to observe that the stability boundary for fixed N_{sub} in this plane passes through a minimum as N_{sub} is increased from

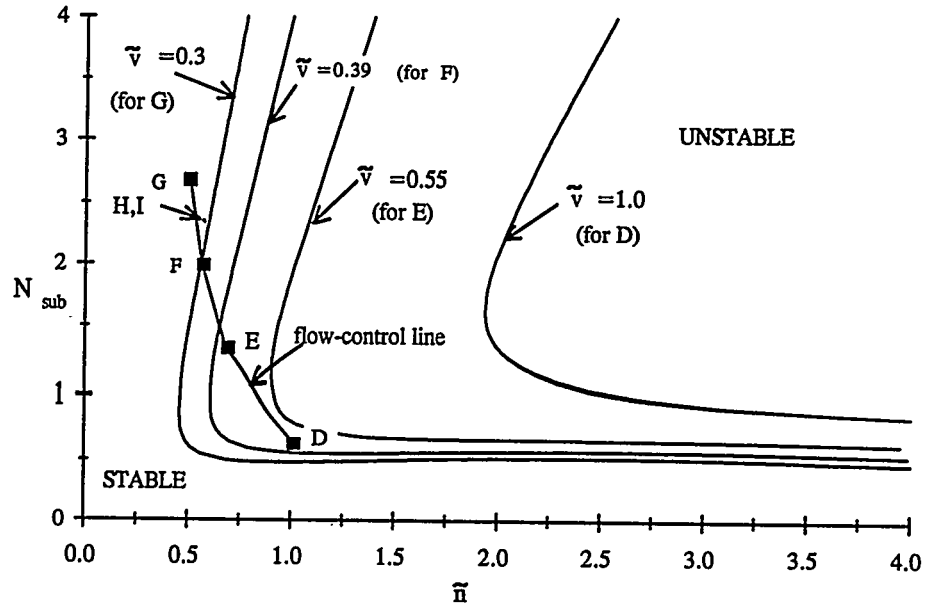

Fig. 8: Stability boundaries in the N_{sub}-$\tilde{n}$ operating-parameter/phase-variable plane for four fixed values of the inlet velocity — each value corresponds to a point on the flow-control line (points D, E, F and G in Fig. 7). Points H and I are essentially indistinguishable on the scale used here.

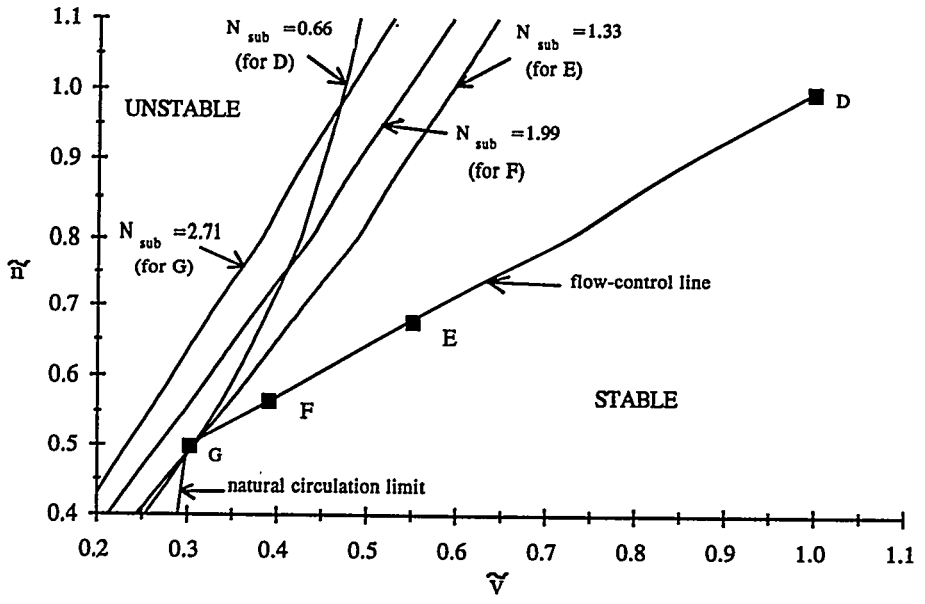

Fig. 9: Stability boundaries in the $\tilde{n}$-$\tilde{v}$ phase-variable plane for four fixed values of the inlet subcooling — each value corresponds to a point on the flow-control line.

its value at the point D — the stability boundary moves to the right as N_{sub} is increased from 0.66 to 1.33 and then starts moving back to the left as N_{sub} is increased further to 2.71.

One of the possible consequences of subcritical Hopf bifurcation was illustrated in Figs. 4 through 6, which showed that for the same set of operating parameters values that correspond to a stable fixed point, transients initiating from two different initial conditions may lead either to oscillations decaying to the stable fixed point, or more importantly, to oscillations with growing amplitude diverging away from the stable fixed point. From a BWR operations perspective, another important consequence of the subcritical Hopf bifurcation is that by changing the operating parameters from a point in the stable region to two operating points that are nearby each other and closer to the stability boundary — but both in the stable region — may lead to oscillations that converge to the stable fixed point in one case, and to oscillations that diverge from the second nearby stable fixed point in the other. As an illustration, Fig. 10 shows the time evolution of the neutron density $n(t)$ initiated from the phase variables corresponding to the fixed point values at point G (with a 20% reduction in the initial boiling boundary, $\mu(0)$, that was necessary to prevent the inlet velocity from becoming negative during the initial transient oscillations rendering the model developed and used here irrelevant), as operating parameters are changed at t = 0 to a point H in Fig. 8 defined by the new set of operating parameters, $(\rho_{ext}, N_{sub}, \Delta P_{ext}) = (0.011011, 2.205, 6.4421)$. Clearly, the transient is converging to the stable fixed point corresponding to point H given by $N_{sub} = 2.205$ and $(\tilde{n}, \tilde{v}) = (0.55388, 0.3)$. Also shown in Fig. 10 is the time evolution of the neutron density $n(t)$ initiated from the same initial conditions as before, i.e., from point G (with a 20% reduction in the initial boiling boundary, $\mu(0)$), as operating parameters at t = 0 are changed to a point I in the parameter space defined by $(\rho_{ext}, N_{sub}, \Delta P_{ext}) = (0.011011, 2.2, 6.4407)$, that also is in the stable region very close to the point H. The oscillations in this case diverge from the the new stable fixed point corresponding to point I, given by $N_{sub} = 2.2$ and $(\tilde{n}, \tilde{v}) = (0.55346, 0.3)$. The converging and diverging transients which start from the same initial conditions and result from a change from the same operating point to two operating points very close to each other (both in the stable region), also are shown as phase plane trajectories in Fig. 11, in which the phase portraits projected onto the n-v phase plane are shown for parameter values corresponding to the points H and I.

Summary and Conclusions

A simple model, that led to a representation of a BWR core as a low-dimensional dynamical system comprised of a set of nonlinear ODEs, has been developed for stability analyses and transient simulations. A BWR (fuel) lattice cell was represented as a vertical fuel-centered boiling flow channel. The neutronics was modeled by the point kinetics equations with one precursor group, and the two-phase region thermal-hydraulics in the channel was represented by the homogeneous equilibrium model. The equations for the single-phase temperature and the two-phase quality were reduced to ODEs by approximating these quantities by spatially linear but time-dependent functions in a weighted-residual-like approach with weighing functions of unity. Finally, the PDE for heat conduction in the fuel rod was reduced to a set of ODEs using two approaches — version 1 was based on an eigenfunction expansion method and version 2 was based on a variational method. These two approaches were compared in terms of stability boundaries plotted in the N_{sub}- ρ_{ext} operating parameter plane for a fixed ΔP_{ext}. Based on conflicting objectives of improving the stability boundary accuracy and reducing the number of equations in the dynamical system, the variational method was determined to be the best choice; therefore, only the dynamical system with the heat conduction PDE reduced to a set of ODEs via the variational method, was used for the main stability analyses and numerical simulations.

The stability boundary was calculated directly and plotted in the N_{sub}- ρ_{ext} operating parameter plane for a fixed ΔP_{ext}. The eigenvalues of the Jacobian matrix of the dynamical system were computed at the fixed points corresponding to various points in that N_{sub}- ρ_{ext} operating parameter plane. The results of these eigenvalue calculations were consistent with the stability analysis, and indicated that a Hopf bifurcation occurs as the stability boundary is crossed. Also, time-dependent numerical simulations of the nonlinear equations were carried out for points on both sides of this stability boundary, and the results were consistent with those of the stability analysis.

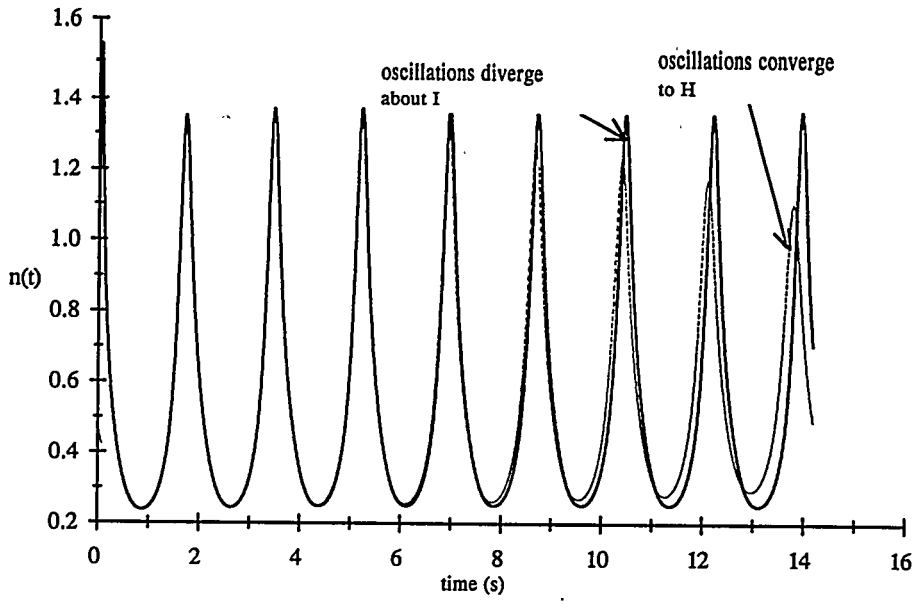

Fig. 10: The converging oscillations (to the fixed point corresponding to point H in Fig. 8) and the diverging oscillations (about the fixed point corresponding to point I in Fig. 8) of $n(t)$ that are initiated by changing the operating parameters from point G to points H and I in Fig. 8.

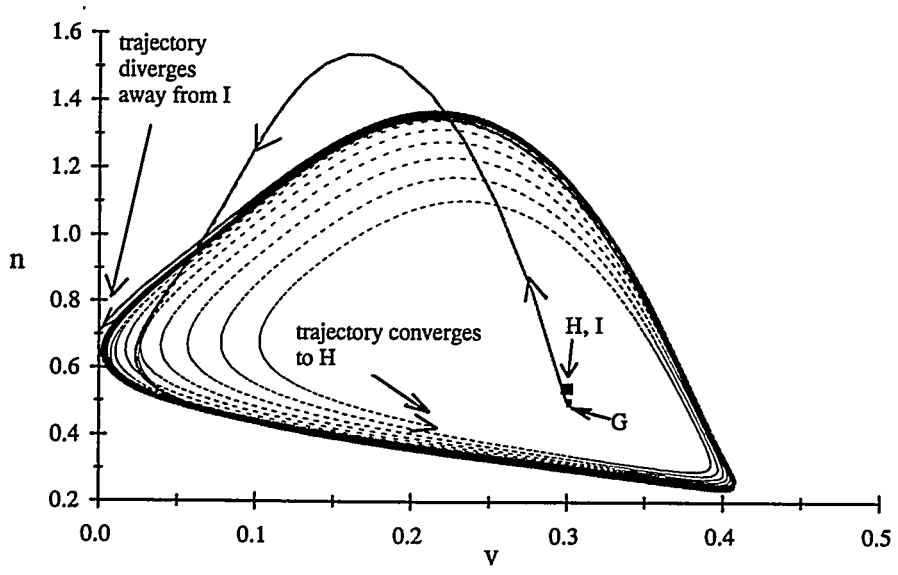

Fig. 11: Phase portrait. Evolution of the phase space trajectories in the projection of the phase space onto the n-v plane for parameter values at point H (converging to the corresponding fixed point) and for those at point I (diverging from the corresponding fixed point) for the same initial condition — the fixed point corresponding to the point G in Fig. 8.

Further numerical simulations with different initial conditions indicated that the Hopf bifurcation is subcritical, and that an unstable limit cycle exists along with the stable fixed point (steady-state) for parameter values in the stable region nearby the stability boundary. The practical implications thus could be important because when the system is operated on the allegedly "safe" (stable) side of the stability boundary, but near it, notwithstanding the fact that the fixed point is stable, a finite perturbation from it could lead to DWOs with growing amplitudes — which indeed occurred for the simple model studied here. Although a subcritical Hopf bifurcation observed here supports the fact that no sustained oscillations were observed in stability tests at low-flow/high-power operating conditions performed at several operating plants [9], we may also conclude that the stable limit cycle oscillations observed at other operating plants [9] are not excited directly by this subcritical Hopf bifurcation.

Finally, the flow-control line was mapped to N_{sub}- $\tilde{n}$ operating-parameter/phase-variable plane. The decreasing stability of the operating points on the flow-control line as the flow rate is reduced was shown by comparing the mapped curve with stability boundaries plotted for four fixed inlet velocities in that operating-parameter/phase-variable plane. Stability boundaries also were plotted in the $\tilde{n}$–$\tilde{v}$ phase variable plane for four fixed inlet subcooling numbers corresponding to four operating points on the flow-control line, and the decreasing stability of the operating points on the flow-control line as the flow rate is reduced was then shown by relating those points to their respective stability boundaries. Thus operating points on the power-flow map were related to the stability boundaries in an operating-parameter/phase-variable plane and in a phase variable plane, and a qualitative explanation was given for the instabilities observed at the least stable operating point on the flow-control line of the power-flow map. It was also shown that the normal operating point of a BWR at 100% power is very stable in comparison with other operating points on the power flow map.

Appendix A

The dimensionless variables and parameters used in the BWR model are listed below. The asterisks indicate the original dimensional quantities.

$$Bi_{j\phi} = \frac{h^*_{j\phi} r^*_1}{k^*_d}, \quad j = 1,2 \qquad Fr = \frac{v^{*2}_o}{g^* L^*} \qquad G_g = \frac{2.56 e^{4p^*/16.2*10^6} \xi^* T^*_o L^*}{\Delta h^*_{fg} A^* v^*_o \rho^*_g}$$

$$N_{fj} = \frac{f_{j\phi} L^*}{2 D^*_h}, \quad j = 1,2 \qquad N_{pch,1\phi} = \frac{h^*_{1\phi} T^*_o \xi^* L^* \Delta\rho^*}{A^* \Delta h^*_{fg} \rho^*_g \rho^*_f v^*_o} \qquad N_r = \frac{\rho^*_f}{\Delta\rho^*}$$

$$N_{sbo} = \frac{\Delta h^*_{fg} \rho^*_g}{2 c^*_f T^*_o \Delta\rho^*} \qquad N_{sub} = \frac{c^*_f (T^*_{sat} - T^*_{inlet}) \Delta\rho^*}{\Delta h^*_{fg} \rho^*_g} \qquad N_\rho = \frac{\rho^*_g}{\rho^*_f}$$

$$T_{i,j\phi} = \frac{T^*_{i,j\phi}}{T^*_o}, \quad i = s,avg,1,2 \quad j = 1,2 \qquad T_{j\phi}(r,t) = \frac{T^*_{j\phi}(r^*,t^*)}{T^*_o}, \quad j = 1,2 \qquad T_{sat} = \frac{T^*_{sat}}{T^*_o}$$

$$c = \frac{c^*}{n^*_o} \qquad c_2 = c^*_2 T^*_o$$

$$c_q = \frac{c^*_q L^{*2} n^*_o}{k^*_d T^*_o} \qquad n = \frac{n^*}{n^*_o} \qquad r_1 = \frac{r^*_1}{L^*}$$

$$s = s^* L^* \qquad t = \frac{t^* v^*_o}{L^*} \qquad v = \frac{v^*}{v^*_o}$$

$$\Gamma_g(t) = \frac{q''^*_{2\phi}(t^*) \xi^* L^*}{A^* \Delta h^*_{fg} v^*_o \rho^*_g} \qquad \Delta P_{ext} = \frac{\Delta P^*_{ext}}{\rho^*_f v^{*2}_o} \qquad \Lambda = \frac{\Lambda^* v^*_o}{L^*}$$

$$\alpha_s = \frac{\alpha^*_s}{v^*_o L^*} \qquad \lambda = \frac{\lambda^* L^*}{v^*_o} \qquad \mu = \frac{\mu^*}{L^*}$$

Appendix B

The expressions for the seven internal pressure drops that appear in Eq. (22) are

$$\Delta P_{inlet}(t) = k_{inlet} v^2(t) \tag{B-1}$$

$$\Delta P_{exit}(t) = k_{exit} \frac{1}{1 + [(1 - \mu(t)]s(t)/(N_\rho N_r)]} \left\{v(t) + N_{pch,2\phi}(t)[1 - \mu(t)]\right\}^2 \tag{B-2}$$

$$\Delta P_{fric,1\phi}(t) = N_{f1} v^2(t)\mu(t) \tag{B-3}$$

$$\Delta P_{grav,1\phi}(t) = \frac{\mu(t)}{Fr} \tag{B-4}$$

$$\Delta P_{acc,2\phi}(t) = N_{pch,2\phi}(t)\ [v(t)Q_1(t) + N_{pch,2\phi}(t)\ M_2(t)] \tag{B-5}$$

$$\Delta P_{fric,2\phi}(t) = N_{f2}[v^2(t)Q_1(t) + 2N_{pch,2\phi}(t)v(t)M_2(t) + N^2_{pch,2\phi}(t)M_3(t)] \tag{B-6}$$

$$\Delta P_{grav,2\phi}(t) = \frac{Q_1(t)}{Fr} \tag{B-7}$$

where $Q_1(t)$, $M_2(t)$, and $M_3(t)$ are defined as

$$Q_1(t) = \int_{\mu(t)}^{1} \rho_m(z,t)dz = \frac{1}{s(t)/(N_\rho N_r)} \log\left\{1 + [1 - \mu(t)]\ [s(t)/(N_\rho N_r)]\right\} \tag{B-8}$$

$$M_2(t) = \int_{\mu(t)}^{1} \rho_m(z,t)[z - \mu(t)]dz = \frac{1}{s(t)/(N_\rho N_r)} \left\{[1 - \mu(t)] - Q_1(t)\right\} \tag{B-9}$$

$$M_3(t) = \frac{1}{s(t)/(N_\rho N_r)} \left[\frac{[1 - \mu(t)]^2}{2} - M_2(t)\right] \tag{B-10}$$

and the subscripts *fric, grav,* and *acc* indicate that these pressure drops are due respectively to friction, gravity and the acceleration associated with the convective term in the substantial derivative.

Appendix C

The most general form of the quadratic expressions for $v_{1a}(r)$, $v_{1b}(r)$, $v_{2a}(r)$, and $v_{2b}(r)$ in Eq. (37) can be simplified using the appropriate boundary conditions on domain boundaries and using continuity and smoothness (continuity of first derivatives) conditions at the interface between sub-domains. For simplicity of notation, the subscript $j\phi$ on all the terms indicating the phase is omitted with an understanding that the analysis is either for the single-phase region ($j = 1$), or the two-phase region ($j = 2$). The function $\theta(r,t)$ in Eq. (37) is written as a two-piecewise quadratic function

$$\begin{aligned}\theta(r,t) &= T_1(t) + a_1(t)r + a_2(t)r^2 , \quad 0 \le r \le r_d \\ &= T_2(t) + b_1(t)r + b_2(t)r^2 , \quad r_d \le r \le r_1\end{aligned} \tag{C-1}$$

where T_1, a_1, a_2, T_2, b_1, and b_2 are the time-dependent coefficients. The function $\theta(r,t)$ in Eq. (C-1) satisfies the following four conditions

$$\partial\theta(0,t)/\partial r = 0 \tag{C-2}$$

$$\partial\theta(r_1,t)/\partial r = -(Bi/r_1)\,\theta(r_1,t) \tag{C-3}$$

$$\theta_l(r_d,t) = \theta_r(r_d,t) \tag{C-4}$$

$$\partial\theta_l(r_d,t)/\partial r = \partial\theta_r(r_d,t)/\partial r \tag{C-5}$$

where Eqs. (C-4) and (C-5) are respectively the continuity and smoothness conditions at $r = r_d$, and the subscripts l and r indicate the limits from the left and right, respectively. Application of Eq. (C-2) gives $a_1(t) = 0$. Using Eqs. (C-3)-(C-5), the quantities a_2, b_1, and b_2 in Eq. (C-1) are eliminated in terms of T_1 and T_2 as

$$\begin{aligned}a_2(t) &= a_{2a}T_1(t) + a_{2b}T_2(t) \\ b_1(t) &= b_{1a}T_1(t) + b_{1b}T_2(t) \\ b_2(t) &= b_{2a}T_1(t) + b_{2b}T_2(t)\end{aligned} \tag{C-6}$$

where, a_{2a}, a_{2b}, b_{1a}, b_{1b}, b_{2a}, and b_{2b} are constants. Substituting Eq. (C-6) into (C-1) and comparing it with Eq. (37) gives

$$\begin{aligned}v_{1a}(r) &= 1 + a_{2a}r^2 \\ v_{1b}(r) &= a_{2b}r^2 \\ v_{2a}(r) &= b_{1a}r + b_{2a}r^2 \\ v_{2b}(r) &= 1 + b_{1b}r + b_{2b}r^2\end{aligned} \tag{C-7}$$

Explicit expressions for the constants a_{2a}, a_{2b}, b_{1a}, b_{1b}, b_{2a}, and b_{2b} are algebraically very complicated; hence, they are not given here. Following the procedure described above, they can easily be obtained from symbolic manipulation packages such as Mathematica or Maple, as was done in the research reported here.

Appendix D

The detailed derivation of Eq. (11) — the ODEs for fuel rod dynamics for version 2 of the model, obtained using the variational method to solve the heat conduction equation — is presented below. For simplicity of notation, the subscript $j\phi$ on all the terms indicating the phase is omitted with an understanding that the analysis is either for the single-phase region ($j = 1$), or the two-phase region ($j = 2$).

Following the Rayleigh-Ritz procedure [16,17], the variations $\delta\mathcal{F}/\delta T_1$ and $\delta\mathcal{F}/\delta T_2$ for the functional in Eq. (35) are set equal to zero to obtain the following two ODEs [note that although f in Eq. (35) includes the term $\partial\theta/\partial t$, it is treated as a constant when taking the variations]

$$\begin{aligned}m_1\frac{dT_1(t)}{dt} + m_2\frac{dT_2(t)}{dt} &= m_3T_1(t) + m_4T_2(t) + m_5c_q\Delta n(t) \\ n_1\frac{dT_1(t)}{dt} + n_2\frac{dT_2(t)}{dt} &= n_3T_1(t) + n_4T_2(t) + n_5c_q\Delta n(t)\end{aligned} \tag{D-1}$$

where

$$m_1 \equiv (v_{1aa}+v_{2aa})/\alpha_s, \qquad m_2 \equiv (v_{1ab}+v_{2ab})/\alpha_s, \qquad m_3 \equiv v_{1aHa}+v_{2aHa},$$
$$m_4 \equiv v_{1aHb}+v_{2aHb}, \qquad m_5 \equiv c_q\Delta n(t)(v_{1aI}+v_{2aI}),$$
$$n_1 \equiv (v_{1ba}+v_{2ba})/\alpha_s, \qquad n_2 \equiv (v_{1bb}+v_{2bb})/\alpha_s, \qquad n_3 \equiv v_{1bHa}+v_{2bHa},$$
$$n_4 \equiv v_{1bHb}+v_{2bHb}, \text{ and} \qquad n_5 \equiv c_q\Delta n(t)(v_{1bI}+v_{2bI}). \tag{D-2}$$

The shortened notations for the inner products used in the above equation are given by

$$v_{1aHa} = (v_{1a}, Hv_{1a}), \quad v_{1aHb} = (v_{1a}, Hv_{1b}), \quad v_{2aHa} = (v_{2a}, Hv_{2a}),$$
$$v_{1aa} = (v_{1a}, v_{1a}), \quad v_{2ab} = (v_{2a}, v_{2b}), \quad v_{1aI} = (v_{1a}, 1), \text{ etc.} \tag{D-3}$$

where the first subscript indicates the domain of integration in the inner product; 1 for the inner sub-domain from 0 to r_d, and 2 for the outer sub-domain from r_d to r_1.

Equations (D-1) can be solved simultaneously to arrive at Eq. (11) — the ODEs for version 2— where

$$l_{1,i} = (- m_k n_3 + n_k m_3)/\Delta$$
$$l_{2,i} = (- m_k n_4 + n_k m_4)/\Delta$$
$$l_{3,i} = (- m_k n_5 + n_k m_5)/\Delta$$
$$\Delta = m_1 n_2 - n_1 m_2$$
$$\text{and } k = 2 \text{ when } i = 1$$
$$= 1 \text{ when } i = 2 \tag{D-4}$$

It should be noted that since the operator $H = \nabla^2$ is self-adjoint, and the final trial function used here [Eq. (37)] satisfies the boundary conditions [Eq. (31)] and is smooth at r_d, the Rayleigh-Ritz method becomes identical to the Bubnov-Galerkin method [16,17].

Appendix E

In this paper, the following typical BWR design and operating parameters [3,14,15] were used:

A^*	$= 1.442\times10^{-4}$ m^2	k_{inlet}	$= 15$
L^*	$= 3.81$ m	p^*	$= 7.2\times10^{6}$ Nm^{-2}
T^*_{inlet}	$= 551$ K	r_1^*	$= 6.135\times10^{-3}$ m
T_o^*	$= 561$ K	v_o^*	$= 2.67$ ms^{-1}
T^*_{sat}	$= 561$ K	Δh^*_{fg}	$= 1494.2\times10^{3}$ Jkg^{-1}
c_1	$= -0.15$	ΔP^*_{ext}	$= 177.88\times10^{3}$ Nm^{-2}
c_2^*	$= -2.0\times10^{-5}$ K^{-1}	Λ^*	$= 4.0\times10^{-5}$ s
c_f^*	$= 5.307\times10^{3}$ Jkg^{-1}K^{-1}	α_s^*	$= 1.398\times10^{-6}$ m^{2}s^{-1}
c_q^*	$= 3.148\times10^{-6}$ Wm^{-3}cm^{2}s	β	$= 0.0056$
$f_{1\phi}$	$= 0.01467$	λ^*	$= 0.08$ s^{-1}
$f_{2\phi}$	$= 0.01467$	μ_f^*	$= 9.750\times10^{-5}$ Nm^{-2}s
k_d^*	$= 3.6$ Wm^{-1}K^{-1}	ξ^*	$= 3.855\times10^{-2}$ m
k_{exit}	$= 2.5$	ρ_f^*	$= 736.49$ kgm^{-3}
k_f^*	$= 5.740\times10^{-1}$ Wm^{-1}K^{-1}	ρ_g^*	$= 37.71$ kgm^{-3}

Nomenclature

A	cross sectional flow area
Bi	Biot number
D_h	diameter = $4A/\xi$
Fr	Froude number
J_0	Bessel function of first kind order 0
J_1	Bessel function of first kind order 1
L	channel length
N	number of ODEs in Eq. (10)
N_f	friction number
N_{pch}	phase change number
N_{sub}	subcooling number
P	pressure
T	temperature
c	precursor concentration
c_1	void reactivity coefficient
c_2	fuel temperature coefficient
c_f	liquid specific heat
c_q	$q'''^*(t^*) \equiv c_q^* n^*(t^*)$
f	friction factor
g	gravitational constant
h	heat transfer coefficient
h_f	liquid enthalpy
h_g	vapor enthalpy
k_d	fuel conductivity
k_{exit}	exit pressure loss coefficient
k_f	liquid conductivity
k_{inlet}	inlet pressure loss coefficient
n	neutron density
p	system pressure
q''	wall heat flux
q'''	volumetric heat generation rate
r_1	fuel rod radius
s	quality slope
v	velocity
x	quality
Γ_g	vapor generation rate
Δh_{fg}	enthalpy difference, $h_g - h_f$
Δn	neutron density difference, $n - \tilde{n}$
$\Delta\rho$	density difference, $\rho_f - \rho_g$
Λ	delayed neutron generation time
α	void fraction
α_s	thermal diffusivity = $k_d/(\rho c_p)_{fuel}$
β	delayed neutron fraction
θ	temperature difference, $T - \tilde{T}$
λ	precursor decay constant
μ	boiling boundary
μ_f	liquid viscosity
ξ	heated perimeter
ρ	reactivity
ρ_f	liquid density
ρ_g	vapor density
ω	frequency
$\omega_{i,j\phi}$	eigenvalues

Subscripts

1ϕ	single-phase
2ϕ	two-phase
avg	average
b	bulk
ext	external
f	liquid
g	vapor
l	left
m	mixture
o	reference
r	right
s	surface
sat	saturation

Superscripts

~	steady-state (fixed point)
*	dimensional quantity

References

[1] L.A. Belblidia, L.E. Weaver and R.W. Carlson, "Nodal analysis of density-wave oscillations in boiling water nuclear reactors," Ann. Nucl. Energy 10, No. 10, 505-534 (1983).

[2] S.J. Peng, M.Z. Podowski, R.T. Lahey and M. Becker, "NUFREQ-NP: A computer code for the stability analysis of boiling water nuclear reactors," Nucl. Sci. Eng. 88, 404-411 (1984).

[3] J. March-Leuba, D.G. Cacuci and R.B. Perez , "Nonlinear dynamics and stability of boiling water reactors: Part I-Qualitative analysis," Nucl. Sci. Eng. 93, 111-123 (1986).

[4] J. March-Leuba, D.G. Cacuci and R.B. Perez, "Nonlinear dynamics and stability of boiling water reactors: Part II-Quantitative analysis," Nucl. Sci. Eng. 93, 124-136 (1986).

[5] K. Valtonen, "BWR stability analysis," Finnish Center for Radiation and Nuclear Safety, Helsinki (1989).

[6] B.G. Bergdahl, F. Reisch, R. Oguma, J. Lorenzen and F. Akerhielm, "BWR stability investigation at Forsmark-1," Ann. Nucl. Energy 16, No. 10, 509-520 (1989).

[7] Rizwan-uddin and J.J. Dorning, "Density-wave instabilities in advanced boiling water reactors," ANS Proc. National Heat Transfer Conference, HTC Vol. 6, 161-170 (1992)

[8] W. Wulff, H.S. Cheng, A.N. Mallen and U.S. Rohatgi, "BWR stability analysis with the BNL engineering plant analyzer," BNL-NUREG-52312 (1992).

[9] M.E. Ward and J.C. Lee, "Singular perturbation analysis of limit cycle behavior in nuclear-coupled density-wave oscillations," Nucl. Sci. Eng. 97, 190-202 (1987).

[10] M. Tsuji, K. Nishio and M. Narita, "Stability analysis of BWRs using bifurcation theory," J. Nuc. Sci. and Tech. 30[11], 1107-1119 (1993).

[11] Jean-Luc Achard, D.A. Drew and R. Lahey, "The analysis of nonlinear density-wave oscillations in boiling channels," J. Fluid Mech. 155, 213-232 (1985).

[12] Rizwan-uddin and J.J. Dorning, "Some nonlinear dynamics of a heated channel," Nucl. Eng. Des. 93, 1-14 (1986).

[13] A. Clausse and R.T. Lahey, "The analysis of periodic and strange attractors during density-wave oscillations in boiling flows," Chaos, Solitons, and Fractals 1, No. 2 , 167-178 (1991).

[14] N.E. Todreas and M.S. Kazimi, Nuclear Systems I-Thermal Hydraulics Fundamentals, Hemisphere, New York (1990).

[15] J.J. Duderstadt and L.J. Hamilton, Nuclear Reactor Analysis, John Wiley, New York (1976).

[16] L.V. Kantorovich and V. I. Krylov, Approximate Methods of Higher Analysis, Interscience, New York (1964).

[17] I. Stackgold, Boundary Value Problems of Mathematical Physics-II, Macmillan, New York (1968).

[18] J.K. Hale and H. Kocak, Dynamics and Bifurcations, Springer-Verlag, New York (1991).

[19] B.D. Hassard, N.D. Kazarinoff and Y.H. Wan, Theory and Applications of Hopf Bifurcation, Cambridge University Press, New York (1981).

COUPLED CALCULATION OF THE RADIOLOGICAL RELEASE AND THE THERMAL-HYDRAULIC BEHAVIOR OF A 3-LOOP PWR AFTER A SGTR BY MEANS OF THE CODE RELAP5

W. Van Hove, K. Van Laeken, L. Bartsoen, B. Centner, L. Vanhoenacker
Belgatom, Avenue Ariane 7, B-1200 Brussels, Belgium

ABSTRACT

To enable a more realistic and accurate calculation of the radiological consequences of a SGTR, a fission product transport model was developed. As the radiological releases strongly depend on the thermal-hydraulic transient, the model was included in the RELAP5 input decks of the Belgian NPPs. This enables the coupled calculation of the thermal-hydraulic transient and the radiological release.

The fission product transport model tracks the concentration of the fission products in the primary circuit, in each of the SGs as well as in the condenser. This leads to a system of 6 coupled, first order ordinary differential equations with time dependent coefficients. Flashing, scrubbing, atomisation and dry out of the break flow are accounted for. Coupling with the thermal-hydraulic calculation and correct modelling of the break position enables an accurate calculation of the mixture level above the break. Pre- and post-accident spiking in the primary circuit are introduced. The transport times in the FW-system and the SG blowdown system are also taken into account, as is the decontaminating effect of the primary make-up system and of the SG blowdown system. Physical input parameters such as the partition coefficients, half life times and spiking coefficients are explicitly introduced so that the same model can be used for iodine, caesium and noble gases.

1. INTRODUCTION

A Steam Generator Tube Rupture (SGTR) is one of the accidents that must be analysed within the framework of the Safety Analysis Report (SAR) of a PWR to verify compliance with the criteria for radiological releases. Although it is an infrequent fault, a number of instances have occurred on operating plants due to corrosion related problems. The Belgian Safety Authorities have therefore, based on an increased probability of occurrence, reclassified the accident from class 4 to class 3 which has more restricting release limits.

To enable a more realistic and more accurate calculation of the radiological consequences of a SGTR, a fission product transport model was developed. As the radiological releases strongly depend on the thermal-hydraulic transient, the model was included in the RELAP5 input deck of the Belgian Nuclear Power Plants. This enables the coupled calculation of the thermal-hydraulic transient and the radiological release without introducing the excessively conservative assumptions needed for an uncoupled calculation, but still providing a conservative result for licensing purpose. A realistic evaluation is also possible with this model.

The SGTR accident is analysed with the best-estimate code RELAP5/MOD2 [11]. At Belgatom a methodology has been developed to avoid the tedious and time consuming effort of evaluating the uncertainty related to the use of best-estimate codes for licensing. This methodology is described in reference [1] and provides a bounding analysis for a given transient using a best-estimate code. Without quantification of the uncertainty, the margin between the realistic and the licensing analysis is however not known.

The methodology is based on the definition of an unambiguous licensing parameter, the value of which must be compared with a licensing limit. The margin between both values is the licensing margin. In the case of a SGTR, the licensing parameter is the total infant thyroid dose, which has to remain below the legal limit.

In the calculation of the licensing parameter, limiting values are imposed for all initial and boundary conditions. These limiting values must cover all operational limits within the Technical Specifications and operational uncertainties of the plant. Code uncertainties and code deficiencies are covered by limiting values for certain input parameters or by special modelling techniques.

The coupling of the fission product transport model with the thermal-hydraulic calculation creates the possibility to analyse the sensitivity of the licensing parameter to the limiting values of the initial and boundary conditions.

The model was developed for the calculation of the iodine-isotope release. Nevertheless, the general form of the equations makes it also suitable for the evaluation of releases of noble gases and caesium

2. RADIOLOGICAL MODEL

2.1 Physical phenomena

A comprehensive description of the phenomena involved in the production, retention and release of iodine during a SGTR accident is given in [2,3].

2.1.1 Flashing

If the reactor coolant water is superheated with respect to secondary side saturation temperature, part of the break flow will flash into steam. This flashing process will cause part of the iodine in the break flow to be evaporated.

The flashing fraction, x, is determined by means of an isenthalpic expansion from primary to secondary conditions. The iodine mass partition coefficient between liquid and vapour is set to 1 [2].

2.1.2 Atomisation

Due to hydrodynamic forces and due to flashing, the liquid part of the break flow will break up into droplets. If the rupture location is above the liquid level or in a region of high void, the smaller droplets are likely to be entrained by the steam flow. This phenomenon will lead to a primary liquid bypass.

For the calculation of the bypass fraction, the model of ref [4] is used. Bypass of primary liquid occurs when the Net Liquid Height (NLH), i.e. the collapsed liquid level above the rupture location, drops below a limit level. The bypass fraction depends on the steam flow and the type of steam separators. The model has been validated with experimental data and yields conservative high values for the bypass fraction [4].

2.1.3 Scrubbing

If the break is submerged in secondary water, the primary steam bubbles produced on flashing will rise through the overlying secondary water. Primary droplets in the steam bubbles may deposit on the bubble walls, so transferring activity to the secondary water. Activity may also partition between primary steam and secondary liquid.

Since the calculation (§.6 & §.7) shows that atomisation is the most important release mechanism, the most restrictive rupture location for radiological release is the tube bundle apex and thus scrubbing has not been introduced in the radiological model.

2.1.4 Boil off

Partially volatile species such as iodine present in the secondary water will partition into the vapour phase to an extent which depends on the value of the partition coefficient under the existing conditions (i.e. temperature and pH).

The conservative value of 100 is used for the mass partition coefficient as recommended by the SRP 15.6.3 [5].

2.1.5 Carry over

The steam produced by evaporation in the SG still contains a small amount of secondary liquid droplets at the outlet of the steam dryers. The warranted moisture carryover of 0.25% covers all SG conditions encountered during a SGTR transient [3].

Reference [6] proves that a mass partition coefficient of 272 is the minimum value that can occur during a SGTR. The conservative value of 100 for the mass partition coefficient for evaporation in the SG, recommended by [5], is thus sufficiently conservative to include the effect of a moisture carryover of 0.25%.

2.1.6 Dry out

When the liquid inventory in the faulty SG (i.e. the SG with the broken tube) decreases due to insufficient water supply to make up for the steaming rate, recirculation in the SG ceases and the tube bundle may uncover. If at the same time the primary average temperature remains higher than the secondary saturation temperature, the dry part of the tube bundle becomes superheated with respect to secondary saturation temperature. This situation can occur when a concurrent secondary side break or stuck open secondary relief valve must be considered.

For a rupture location at the tube bundle apex, the break liquid droplets not entrained by the steam flow possibly drain on the tube bundle outer surface. In case the rupture location is inside the U-bend region, most of the break liquid will impact on the neighbouring tubes [3].

On this dry, superheated tube surface, the liquid part of the break flow may evaporate before mixing with the remaining secondary liquid is possible. Due to the lack of experimental data, it is conservatively assumed that the liquid part of the break flow completely evaporates as soon as sufficient tube surface is available. The latter is calculated using the available primary-to-secondary temperature difference and a pool boiling correlation. All activity contained in the liquid part of the break flow is in this case transferred to the vapour phase and released to the environment.

2.1.7 Plate out

When dry out of the break flow occurs, a certain amount of the iodine isotopes in the break flow will deposit on the tube outer surface. Independently of this dry out, a certain amount of the iodine in the steam flow can deposit on the SG internal structures, especially on the large surface offered by the steam dryers.

Due to lack of reliable data on both mechanisms, the conservative assumption of no iodine deposition is used.

2.1.8 Overfill

In case an overfill of the faulty SG occurs, secondary liquid is discharged directly to the environment.

The conservative initial and boundary conditions leading to overfill, are however completely different from the bounding conditions that favour radiological release by atomisation and dry-out. Therefore the potential for overfill must be the subject of a different methodology, where it has to be shown either that overfill does not occur or that the radiological consequences are less severe. Overfill is therefore not included in the model.

2.2 Fission product transport model

The fission product transport model tracks the concentration of fission products in the primary circuit, in the pressuriser, in each of the SGs as well as in the condenser (fig.1). This leads to a system of 6 coupled linear first order ordinary differential equations with time dependent coefficients which are given in appendix A.

The equations in appendix A contain only one break flow, but in practice the two sides of the break are treated as two independent breaks because of a possible different flashing behaviour. Since both break flows can change direction during the transient, the following convention is used for each break flow:

$$\begin{cases} Q_{b,out} = Q_b \quad \text{if } Q_b > 0 \; ; Q_{b,out} = 0 \quad \text{if } Q_b < 0 \\ Q_{b,in} = -Q_b \quad \text{if } Q_b < 0 \; ; \; Q_{b,in} = 0 \quad \text{if } Q_b > 0 \end{cases}$$ (positive direction, see figure 1).

The same convention is used for the surge line flow, that can also change direction during the transient.

The maximum allowable Technical Specification leakage is postulated in one of the intact SGs (i.e. SGs not affected by the tube rupture). This primary-to-secondary leak flow (Q_l) is cooled to the secondary temperature in the leak path so that neither flashing nor atomisation of the leak flow occurs [2].

In order to evaluate the radiological releases, one may distinguish four different phases:

- the period prior to the rupture of the tube. Following the SRP 15.6.3 [5], one of the intact SGs must be considered affected by the maximum allowable steady state primary-to-secondary leak. The Belgian Safety Authorities also request to consider a pre-spiking event, that has brought the primary activity to the maximum value allowed by the Technical Specifications for a limited period (typically 12h). During this steady-state operation, the liquid masses remain constant and the flow rates are either zero or constant. The steady-state solution of the equations yields in this case the initial values of the activities in the SGs and in the condenser at the start of the transient.

- the period from the rupture of the tube until scram. Primary activity enters the secondary system through the ruptured tube. The secondary pressure remains stable, the plant continues to operate at full power and the contamination spreads from the faulty SG to the intact SGs through the condenser and the feed water system.

- the period from scram until break reversal. A post-spiking must be assumed following reactor trip. Duration and release rate of the post-spiking are introduced via input data. After the turbine trip and the feed water isolation, one may consider the three steam generators as being uncoupled in terms of contamination. The probability to uncover the top of the bundle is most likely during this period. The bulk of the radiological release to the environment is produced during this period and comes from the faulty SG.

- the period from zero break flow to cold shutdown. During this phase, both primary and secondary circuits are cooled through steam discharge from the intact SGs. As these SGs were contaminated during the previous phases, a small amount of radiological release occurs during this period.

Note that equation (A.6) for the condenser activity is not valid during the third and fourth period. However, this has no impact as during this period the turbine is tripped, the feed water is isolated and the condenser is uncoupled in terms of contamination from the SGs.

The coupled calculation covers the period from break opening until break cancellation. Since the fourth period only contains negligible radiological releases, it is usually not included in the RELAP5 calculation.

For a SGTR accident with a stuck open SG safety valve (SOSV), the third and fourth period cannot be distinguished and the coupled calculation must be continued until cold shutdown conditions are reached.

2.3 Fission product releases

After the tube rupture and before the turbine trip and feed water isolation, iodine is released only via the condenser vacuum pumps or air ejectors (see nomenclature for symbols):

$$RI_c = \frac{1}{DF_c} \int a_c . Q_c . \frac{1}{PC_c} . dt \qquad (1)$$

However, those releases occur via the plant stack and are monitored. Therefore there contribution to the total release is negligible.

Following turbine trip and with the steam dump to the condenser assumed not available, the SG relief valves and/or safety valves will open to control the secondary pressure. This will result in a severe situation since it constitutes a direct path to the environment.

Equation (2), which gives the total integrated release from the faulty SG, includes three important release mechanisms:

$$RI_{sg,G} = \int \left(Q_{b,out} . a_{p,i} . x + Q_{b,out} . a_{p,i} . y . (1-x) + \left(Q_{v,G} - x . Q_{b,out} \right) . \frac{a_{sg,G}}{PC_{sg}} \right) dt \quad (2)$$

flashing *atomisation* *boil off*

(2)

In case dry out occurs in the faulty SG, x is set equal to one.

From the intact SGs, there is only a small contribution due to boil off of secondary liquid:

$$RI_{sg,R} = \int Q_{v,R} . \frac{a_{sg,R}}{PC_{sg}} dt \quad (3)$$

$$RI_{sg,B} = \int Q_{v,B} . \frac{a_{sg,B}}{PC_{sg}} . dt \quad (4)$$

2.4 Solution

The equations in appendix A are of the form

$$\frac{dm(t)}{dt} + a(t) . m(t) = b(t) \quad (5)$$

The differential equations are solved using the general method:

$$m(t) = \frac{1}{\mu(t)} \left(\int b(s) . \mu(s) ds + C \right) \quad (6)$$

$$\mu(t) = \exp\left(\int a(t) dt \right)$$

with C a constant, defined from the initial conditions.

This method uses only integrators and avoids the need to calculate derivatives, which introduces noise in the calculation and leads to instability and error accumulation.

The complete model, including the solution of the equations in appendix A, the evaluation of the integrals in §.2.3 and the calculation of all auxiliary variables needed in the model, is introduced in the RELAP input deck by means of the in-house developed TROPIC [7] pre-processor under the form of RELAP control variables, in a way similar to the modelling of a control system. In this way the radiological equations are integrated with the same time step as the thermal-hydraulic equations. This allows a once-through calculation of the radiological releases which is very cost effective to perform sensitivity studies.

2.5 Validation of the model

2.5.1 Stability and accuracy of the solution

A first test has been performed in order to verify that RELAP5 is able to provide, via control variables, the solution of a first order ordinary differential equation with time dependent coefficients.

For testing purpose, specific, oscillating functions were used in eq.(5) for a(t) and b(t), functions that permit an analytical solution for eq.(5). Figure 2 shows the comparison between the analytical result and the RELAP5 calculation with the second order accurate integration scheme of eq.(6). There is no cumulated error in the numerical solution.

2.5.2 Introduction of the model in the RELAP5 input deck

Since the previous test gave confidence in the process, the complete model was developed and introduced in the RELAP5 input deck .

The response of this complex model has been checked by uncoupling the radiological release model from the thermal-hydraulic calculation and introducing simplified boundary conditions by means of tables for all the thermal-hydraulic parameters which are used as input parameters in the model. A hand calculation could be performed and the results compared to these obtained with the RELAP model.

The deviations between the RELAP5 values and the manually calculated values vary, for the integrated releases, between 0.5% and 1.5%. The deviations observed are caused by the approximations required for the hand calculation.

2.5.3 Models and constants

The radiological release model is entirely based on the isotope mass balance equations. The correct solution of the equations by RELAP has been verified. The equations contain however a number of modelling parameters. According to the type of analysis, either best-estimate or conservative values can be introduced for these parameters.

For the atomisation, the model of reference [4] is used. The model has been validated against experimental data and yields conservative high bypass fractions for Westinghouse type SGs. More realistic data or data for other types of SGs can however be used if available.

The calculation reported in this paper was carried out with a SG iodine mass partition coefficient of 100, as recommended by the S.R.P. [5]. Comparison with experimental data in [6] shows that this value is sufficiently conservative to cover the effect of moisture carry-over of secondary liquid. More realistic values for the SG iodine mass partition coefficient can however be introduced.

Likewise the iodine mass partition coefficient for the flashing break flow was set to 1 in the calculation reported in this paper. This value maximises the radiological consequences of flashing. Again more realistic values can be introduced if available.

For the decontamination factors of the primary make-up system or the secondary blowdown system, either minimum warranted values or realistic values can be introduced.

Both a pre-accident and a post-accident iodine spiking can be introduced. Each spiking is characterised by a steady-state iodine release rate and a spiking factor. Either conservative, bounding values or realistic values based on operating experience can be introduced. The calculation reported in this paper starts from a constant primary activity equal to the maximum Technical Specification limit and considers only a post-accident spiking with conservative high spiking factor.

2.5.4 Thermal-hydraulic transient

All initial and boundary conditions for the transient and certain input parameters and code options are chosen such that the calculation of the SGTR transient with RELAP5/MOD2 yields a bounding value for the total radiological release. This is the subject of a specific methodology report to be presented to the Safety Authorities.

3. THERMAL-HYDRAULIC MODEL

3.1 The 3 loop PWR plant model

The RELAP5 model of the plant (fig.3) explicitly models the reactor vessel, all primary loops, the pressuriser with expansion line, the pressuriser spray lines and the SGs. The FW lines are modelled starting at the isolation valves. The steam lines are modelled up to the turbine stop valves. Safety valves, relief valves and safeguard systems are modelled as boundary conditions. Control and protection systems are modelled using the control variables specific to RELAP.

The plant model (fig.3) is a detailed and realistic standard plant nodalisation built on user guidelines without reference to any specific accident. This standard nodalisation is based on experience from various small scale test facilities and on full scale plant transients. The data in the input deck are extensively reviewed and documented in a plant specific data base.

3.2 Broken SG tube

The broken SG tube is explicitly modelled with the correct length up to the rupture location. Both parts of the broken tube are divided in several volumes in order to realistically model pressure losses and void formation inside the tube. Due to the flashing definition, both break mass flows must be treated separately.

The break flow is calculated using the RELAP critical flow model. To cover uncertainties on the break flow calculation, the pressure losses inside the tube are reduced by 20% and the tube outlet discharge coefficient is set at 1.20.

The most penalising rupture location for the radiological consequences is a rupture at the tube bundle apex. The uncover time is maximum, the discharge coming from the inlet header will be two-phase for some period but the break mass flow is minimum. However, for the overfill case the most limiting break is located near the outlet header, since the break mass flow is then maximum.

In SGTR analyses, the break flow is often calculated using correlation's for the critical flow of a subcooled liquid through an orifice. These correlation's yield larger break mass flows than a correct modelling of the broken tube, taking pressure losses and void formation in account. Provided a maximum break flow is the conservative option, the use of these correlation's gives conservative results. But an overestimation of the break mass flow may lead to a higher liquid inventory in the SG and a shorter period of break uncover, resulting in less severe radiological consequences.

3.3 Net Liquid Height

The criterion for submersion of the rupture is defined based on the Net Liquid Height (NLH) instead of the collapsed level in the riser:

$$NLH = \int_{\text{rupture location}}^{\text{top riser}} (1-\alpha).dz$$

A known deficiency of RELAP5/MOD2 is the inter phase drag model for bubbly/slug flow regime, that is inappropriate for rod bundles [8]. This results in an overestimation of the void fraction in low flooding rate reflood or slow boil off conditions. The latter condition is typical for the faulty SG after reactor trip. Even when applying the recommendations of Kukita et al. [9] (increase of the tube bundle outer hydraulic diameter by a factor of 10), the code overpredicts the void fraction. For a given liquid mass inventory, this results in an overprediction of the NLH above the rupture location.

Applicable experimental data to assess the uncertainty of the void fraction prediction are the high pressure, low flow data from the ORNL level swell tests and the TLTA boil off tests, app. B of ref. [10]. To the authors knowledge there is unfortunately no systematic quantification of the uncertainty of the RELAP5/MOD2 code with respect to these data available in the literature.

The nodalisation of the SG is a second source of uncertainty. The RELAP volumes have a constant section, but the corresponding real volume may have a variable section over the height of the volume. For a given liquid inventory in the volume, the RELAP collapsed level could show an error with respect to the real collapsed level.

The uncertainty due to the inter phase drag model has been assessed using the ORNL and TLTA data. The uncertainty due to the nodalisation is calculated based on the real geometry of the volumes. The total uncertainty on the NLH calculation with RELAP5/MOD2 amounts to approximately 1m (3 ft). This uncertainty is systematic in nature as RELAP5/MOD2 consistently overevaluates the NLH. The uncertainty is therefore added to the criterion for the onset of atomisation. The value of this uncertainty has little impact on the results reported in paragraph 6. Reducing the uncertainty from 1 m to 0.5 m (provided it could be demonstrated that the latter value is still a bounding value for the total uncertainty) would reduce the calculated total radiological release by only 13%.

4. INITIAL AND BOUNDARY CONDITIONS

To demonstrate the capabilities of the radiological release model, a SGTR accident has been analysed for a typical 3 loop PWR.

The initiating event is the double ended guillotine rupture of one tube. The rupture location is at the tube bundle apex. The plant is at full power at the moment of the break.

A pre-spiking event must be assumed and the initial primary activity at the start of the transient is equal to 37 MBq/kg (1 Ci/t). The initial secondary activity is obtained from an equilibrium situation for the maximum allowable primary-to-secondary leak rate in one of the intact SGs.

Following reactor trip, a post-spiking occurs. For this calculation the Spiking Factor is 70 and the steady-state iodine release rate from the fuel is calculated from a continuous operation primary activity of 5.55 MBq/kg (0.15 Ci/t).

The most restrictive single failure is the failure of the auxiliary feed water (AFW) turbo pump. This leads to minimum liquid inventory in the faulty steam generator and consequently to a maximum rupture uncover period.

As a general rule for licensing calculations, control systems cannot be considered if their operation is favourable for the consequences of the accident. The steam dump to the condenser is consequently assumed unavailable.

For the other initial and boundary conditions, limiting values are imposed that maximise the total radiological release.

5. OPERATOR ACTIONS

The reactor protection system is designed to preserve core integrity and no automatic action exists to stop radiological releases to the environment. A SGTR analysis must therefore necessarily consider operator actions according to the plant specific procedures.

As a number of SGTRs have occurred world-wide, today operators are intensively trained to cope with a SGTR accident. In Belgium, each operator has, at least once a year, a refresher course, including a SGTR accident, on a full scope plant simulator.

In the sample calculation, an increase of secondary activity rapidly warns the operator that a SGTR has occurred and the operator is requested to take the appropriate actions. If the instrumentation to monitor secondary activity is qualified, this early warning can be considered in a licensing study.

6. RESULTS

The sequence of events is given in table 1. The course of the accident is illustrated in (fig.4 to 10).

The tube rupture occurs after 400 s in the calculation. The initial total break flow is 17.5 kg/s, (fig.5).

Alarms on high condenser activity direct the operator to the 'SGTR without safety injection' procedure.

At 640 s or 4 min. after break occurrence, the operator has diagnosed the accident. He isolates the letdown and starts a second charging pump in an attempt to compensate the break flow and to avoid safety injection signal. As a result, the primary pressure, (fig.4), increases again.

Table 1 : sequence of events

time (s)	event (#:operator action)
0	start of calculation
400	double ended guillotine rupture of 1 tube at tube bundle apex
460	alarm high activity in condenser start of alarm procedure
520	alarm identified start of procedure 'SGTR without safety injection signal'
640	diagnosis confirmed # start additional charging pump # letdown isolation # minimum SG blowdown flow
940	operators attempt load reduction program - reactor trip - turbine trip and loss of condenser (no steam dump) - FW isolation (main valve)
941	SG atmospheric relief valves start to open
960	SG safety valves open for 15 s
1030	FW isolation (bypass valves) AFW start, but turbo pump fails to start (single failure)
1060	operator initiates primary depressurisation # pressuriser spray valves completely open
1350	# pressuriser spray flow reduced to maintain 30°C subcooling
1540	chemist has identified the faulty SG by blowdown activity # MSIV closure on faulty SG # start primary cool down at 28 °C/h with intact SGs # control intact SG narrow range level with AFW
1670	atmospheric relief valve closes on faulty SG end of radiological release from faulty SG
1700	end of calculation

Next the operator is requested to bring the plant to hot shutdown by reducing the plant power output in a controlled way. As control systems cannot be considered in a licensing study if their operation is favourable, it must be assumed that the attempt fails and that a reactor trip occurs. This reactor trip is postulated to occur at 940 s or 9 min. after break occurrence.

Reactor trip leads to turbine trip, feed water isolation and AFW start. Following turbine trip, the secondary pressure increases sharply and the SG safety valves open briefly to limit the secondary pressure, (fig.6). But very soon the atmospheric relief valves are able to control the secondary pressure, which is maintained around 7.3 MPa.

The safety injection signal is effectively not reached and the operator stays in the same procedure. Next the operator is requested to stop the break flow. This is accomplished by cooling and depressurising the primary circuit until the primary pressure is equal to the pressure in the faulty SG.

At 1060 s or 11 min. after break occurrence the operator opens the pressuriser spray valves and depressurises the primary circuit to reduce the break flow, (fig.4 and 5). The spray flow is controlled to maintain a minimum subcooling of 30 °C in the primary circuit.

Lacking a qualified activity measurement on each SG separately, the chemist must make a local activity measurement on the SG blowdown flows. At 1540 s or 19 min. after break occurrence, the faulty SG is identified. The operator isolates the faulty SG, but maintains AFW to the faulty SG to recover a visible narrow range level.

Next the operator initiates a plant cooldown at 28 °C/h with the atmospheric relief valves of the intact SGs, (fig.7). Some 130 s later, the relief valve on the faulty SG closes and the radiological releases from the faulty SG are stopped. As the total release from the intact SGs is at least an order of magnitude smaller than from the faulty SG, (fig.10), the analysis was stopped at this point.

During the period from 400 to 1700 s, a total of 780 GBq (21 Ci) has flowed into the faulty SG through the break, (fig.8). The activity of the secondary liquid has risen to 15.5 MBq/kg (0.42 Ci/t) in the same period, (fig.9).

Except for a short period when the safety valves are open, the NLH remains below the criterion. The most important mechanism of radiological release is therefore the atomisation or bypass of primary liquid out of the faulty SG. The contributions of the different mechanisms in the total release from the faulty SG are given in table 2 and illustrated in fig.11.

The tube bundle remains covered and dry out does not occur in this calculation.

The total retention factor (ratio of integrated break activity to the activity released) for the period considered is 10, which means that only 10% of the break flow activity is released to the environment.

Using the site specific dose conversion factors, this total release can be converted in an infant thyroid dose. This dose must remain below the legal limit for class III accidents. Reversibly, this comparison can determine the maximum allowable limits for the primary activity in the Technical Specifications of the plant.

7. HAND CALCULATION

The radiological consequences of an accident are often evaluated by hand calculation, using the results of the thermal-hydraulic calculation as input data.

To make a hand calculation possible, the duration of the accident is split in a number of periods, during which the relevant thermal-hydraulic input data are more or less constant. Bounding, constant values are then used for these input data for each period considered. Introduction of some supplementary simplifying assumptions reduces the equations to linear first order differential equations with constant coefficients, which can than be integrated analytically.

The results of such a hand calculation, using 4 periods from reactor trip till relief valve closure on the faulty SG, are compared with the RELAP results in table 1.

table 2: Radioactive release (iodine-131) from faulty SG

	RELAP		*HAND*	
	GBq	%	GBq	%
boil off + carryover	2.0	2.6	2.4	2.1
flashing	1.7	2.2	1.0	0.8
atomisation	73.4	95.2	113.0	97.1
total	77.1	100.0	116.4	100.0

8. COMPARISON BETWEEN RELAP AND HAND CALCULATION

Comparing the hand calculation with the RELAP calculation in table 1 shows that in both cases atomisation is the major contribution to the radiological release from the faulty SG. The reasons are the break position at the tube bundle apex and the conservative initial and boundary conditions leading to minimal SG liquid inventory.

The coupled calculation of the thermal hydraulic transient and the radiological release with RELAP gives a 1/3 reduction of the total radiological release with respect to the hand calculation, while still providing a conservative, bounding value for this licensing parameter. This reduction makes additional operational margin available.

But the hand calculation does not necessarily give conservative values for each release mechanism. Table 1 shows that the radiological release due to flashing is underestimated in the hand calculation. The reason is that the flashed fraction of the break is very sensitive to small enthalpy differences and only a coupled calculation can provide the correct flashing fraction during the course of the accident.

Another problem is the strong interaction between the different phenomena involved in the radiological release. An overly conservative calculation of one release mechanism may adversely affect the other mechanism. In the sample calculation used in this paper, the overestimation of the atomisation in the hand calculation leads to a lower secondary liquid activity (12.4 GBq/kg for the hand calculation versus 15.5 GBq/kg for the RELAP calculation at the end of the transient), which reduces the radiological release by boil off. Another example is the fact that in the thermal-hydraulic calculation without coupled radiological model, the liquid fraction leaving the faulty SG through atomisation (roughly 2.5 ton of liquid in the hand calculation) is not accounted for, leading to higher SG liquid inventory and a possible reduction of the atomisation period.

9. CONCLUSIONS

- Taking into account such novel phenomena as atomisation and dry-out, may lead to much larger radiological releases to the environment following a SGTR. Depending on the imposed initial and boundary conditions (licensing versus realistic), these releases may lead to violation of the criteria. In the sample calculation presented, the most important release mechanism is atomisation. But under conditions where most of the SG secondary inventory is lost, dry-out may lead to very large radiological releases.

- The different phenomena responsible for radiological releases manifest a strong interaction, which can only be properly accounted for by a suitable isotope transport model like the one presented here.

- The reactor coolant is the main vehicle for the transport of the isotopes. Hence, a more precise evaluation of the radiological releases requires a instantaneous coupling of the thermal-hydraulic parameters with the fission product transport model. Only such a coupled calculation correctly accounts for the interaction between thermal-hydraulics and radiological releases.

- The coupled calculation of the thermal-hydraulic transient and the radiological releases also allows parametric studies to be performed in a cost effective manner.

- Programming a mathematical model involving differential equations into the powerful control variable package of RELAP, is normally a very tedious effort. The TROPIC pre-processor is an extremely useful tool in this respect, making the programming much more user friendly.

- The coupled calculation shows an important benefit in terms of total radiological releases over the hand calculation, while still able to provide a conservative value. This enables one to make additional operational margin available.

- Iodine is responsible for the largest contribution to the total effective dose. Therefore only iodine releases were calculated in this paper. Nevertheless, the model is also suitable for the evaluation of releases of noble gases and caesium.

10. NOMENCLATURE

parameter	*unit*	*symbol*	*index*	
Pressure	Pa	p	p	primary
Temperature	K	T	s	main steam
Enthalpy	J/kg	H	c	condenser
Mass flow rate	kg/s	Q	sg	steam generator
Water mass	kg	M	pr	pressuriser
Density	kg/m^3	ρ	l	leak
Mass activity	Bq/kg	a	cv	primary make-up system
Integrated release	Bq	RI	f	feed water
Decontamination factor for iodine	-	DF	s	mean steam
Decay constant of isotope i	s^{-1}	λ_i	af	auxiliary feed water
Partition coefficient	$\frac{Bq/kg}{Bq/kg}$	PC	b	break
Spiking factor	-	SF	v	safety and/or relief valve on SG
Void fraction	-	α	pv	PORV on the pressuriser
Steam quality	-	x	bd	blow down
Atomisation fraction	-	y	i	isotope
Time	s	t	spr	spray
Time delay	s	Δt	sc	scram
Activity release rate from the fuel	Bq/s	R	in/out	flow direction

11. REFERENCES

[1] M. Callaert, Y. Crommelynck, P. Deschutter, E. Stubbe, L. Vanhoenacker, 'The Belgatom methodology for licensing of non loca transients by means of the best estimate code RELAP5/MOD2', Paper presented at the A.I.E.A. technical committee meeting on comparison of best estimate methods for judging design margins of advanced water-cooled reactors, Lyon, France, (1994)

[2] A.K. Postma, P.S. Tam, 'Iodine behaviour in a PWR cooling system following a postulated SGTR accident, NUREG-0409, (1978)

[3] L.M.C. Dutton, C. Smedley, B.J. Handy, S.R. Herdlhofer, 'Realistic methods for calculating radioactivity release following a steam generator tube rupture accident', NNC Report C9008/PWR/REP/001 issue A, (1993)

[4] O.J. Mendler, 'The effect of steam generator tube uncovery on radioiodine release', WCAP-13132, (1992)

[5] USNRC Standard Review Plan, NUREG-0800, (1981)

[6] James P. Adams, 'Iodine release during a steam generator tube rupture', Nucl. Techn. Vol.109 (Feb.1995)

[7] F.J. Bastenaire, L.A. Vanhoenacker, 'TROPIC: an interactive preprocessor for RELAP5',paper presented at the 1990 Joint RELAP5 TRAC-BWR International User Seminar, (1990).

[8] R.R. Schultz, International code assessment and applications program: summary of code assessment studies concerning RELAP5/MOD2, RELAP5/MOD3 and TRAC-B', NUREG/IA-0088,(1992).

[9] Y. Kukita, Y. Anoda, H. Nakamura, K. Tasaka, 'Assessment and improvement of RELAP5/MOD2 code interphase drag models', AIChE Symposium Series,Heat Transfer - Pittsburgh, No. 257, Volume 83, (1987)

[10] B. Chexal, J. Horowitz, G. Lellouche, 'An assessment of Eight Void Fraction Models for Vertical Flows', NSAC-107, (1986)

[11] V.H.Ransom, et al., 'RELAP5/MOD2 Code Manuel', NUREG/CR-4312

APPENDIX A: Fission product activity balances

Based on figure 1, we can write the activity balances down:

primary circuit without pressuriser

$$\frac{d(M_p.a_p)}{dt} = R_i + Q_{pr,in}.a_{pr} + (Q_{b,in,cold} + Q_{b,in,hot}).a_{sg,G} - (Q_l + Q_{b,out,cold} + Q_{b,out,hot} + Q_{spr} + Q_{pr,out} + \lambda_{pi}.M_p).a_p \quad (A.1)$$

with $\lambda_{pi} = \lambda_i + \frac{Q_{cv}}{M_p}\left(1 - \frac{1}{DF_{cv}}\right)$

pressuriser

$$\frac{d(M_{pr}.a_{pr})}{dt} = (Q_{spr}.(t-\Delta t_{spr}) + Q_{pr,out}).a_p - (Q_{pr,in} + Q_{pv} + \lambda_i.M_{pr}).a_{pr} \quad (A.2)$$

SG with break (SG G)

$$\frac{d(M_{sg,G}.a_{sg,G})}{dt} = ((1-x_{cold} - y.(1-x_{cold})).Q_{b,out,cold} + (1-x_{hot} - y.(1-x_{hot})).Q_{b,out,hot}).a_p - \left(\frac{Q_{s,G}}{PC_{sg}} + Q_{bd,G} + \frac{Q_{v,G} - (x_{cold}.Q_{b,out,cold} + x_{hot}.Q_{b,out,hot})}{PC_{sg}} + Q_{b,in,cold} + Q_{b,in,hot} + \lambda_i.M_{sg,G}\right).a_{sg,G} + Q_{f,G}.a_c.(t-\Delta t_f) + Q_{af,G}.a_c(t_{sc} - \Delta t_f) \quad (A.3)$$

SG with leak (SG R)

$$\frac{d(M_{sg,R}.a_{sg,R})}{dt} = Q_l.a_p - \left(\frac{Q_{s,R}}{PC_{sg}} + Q_{bd,R} + \frac{Q_{v,R}}{PC_{sg}} + \lambda_i.M_{sg,R}\right).a_{sg,R} + Q_{f,R}.a_c.(t-\Delta t_f) + Q_{af,R}.a_c(t_{sc} - \Delta t_f) \quad (A.4)$$

intact SG (SG B)

$$\frac{d(M_{sg,B}.a_{sg,B})}{dt} = Q_{f,B}.a_c.(t-\Delta t_f) - \left(\frac{Q_{s,B}}{PC_{sg}} + Q_{bd,B} + \frac{Q_{v,B}}{PC_{sg}} + \lambda_i.M_{sg,B}\right).a_{sg,B} + Q_{af,B}.a_c(t_{sc} - \Delta t_f) \quad (A.5)$$

condenser

$$\frac{d(M_c.a_c)}{dt} = ((x_{cold} + (1-x_{cold}).y).Q_{b,out,cold} + (x_{hot} + (1-x_{hot}).y).Q_{b,out,hot}).a_p + \frac{Q_{bd,G}}{DF_{bd}}.a_{sg,G}(t-\Delta t_{bd}) + \frac{Q_{s,G} - (x_{cold}.Q_{b,out,cold} + x_{hot}.Q_{b,out,hot})}{PC_{sg}}.a_{sg,G} + \frac{Q_{bd,R}}{DF_{bd}}.a_{sg,R}(t-\Delta t_{bd}) + \frac{Q_{s,R}}{PC_{sg}}.a_{sg,R} + \frac{Q_{bd,B}}{DF_{bd}}.a_{sg,B}(t-\Delta t_{bd}) + \frac{Q_{s,B}}{PC_{sg}}.a_{sg,B} - (Q_{f,G} + Q_{f,R} + Q_{f,B}).a_c - \left(\lambda_i.M_c + \frac{Q_c}{PC_c}\right).a_c \quad (A.6)$$

Figure1: Schematic presentation of the mean parameters of the Fission Products Transport Model

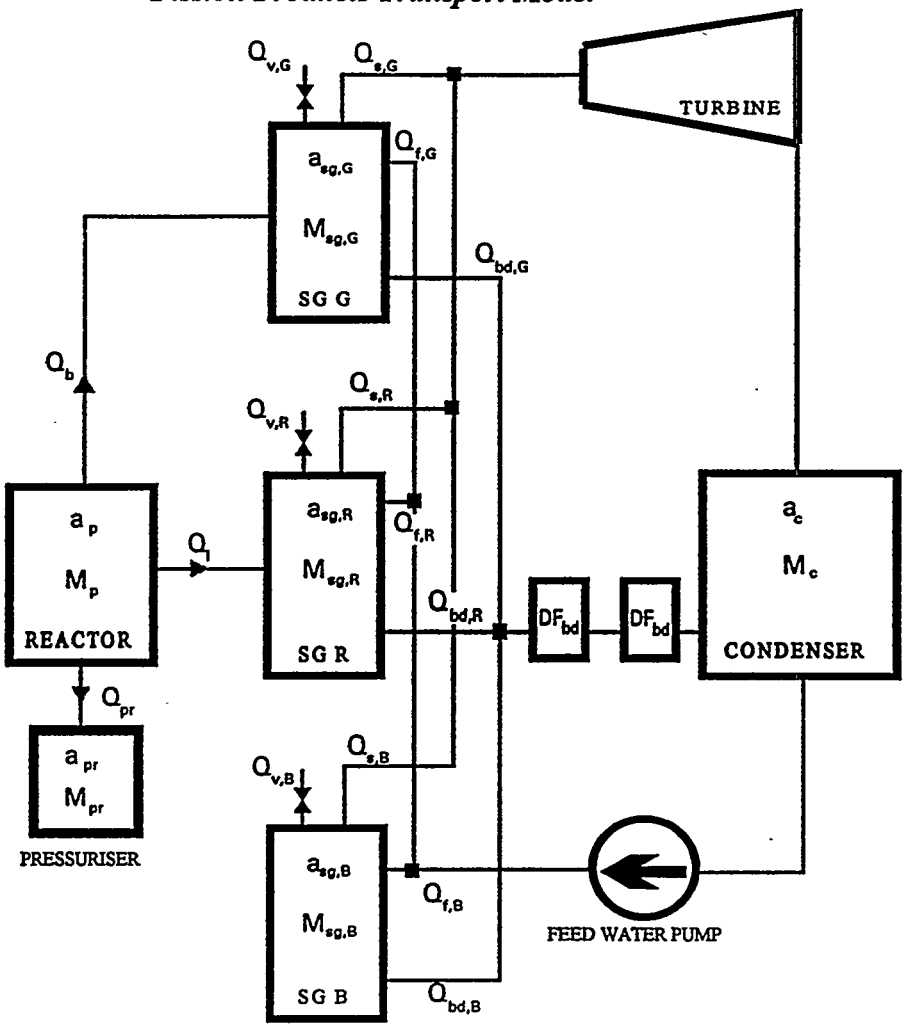

Figure 2: Comparison between the analytical solution and the RELAP evolution obtained by the model

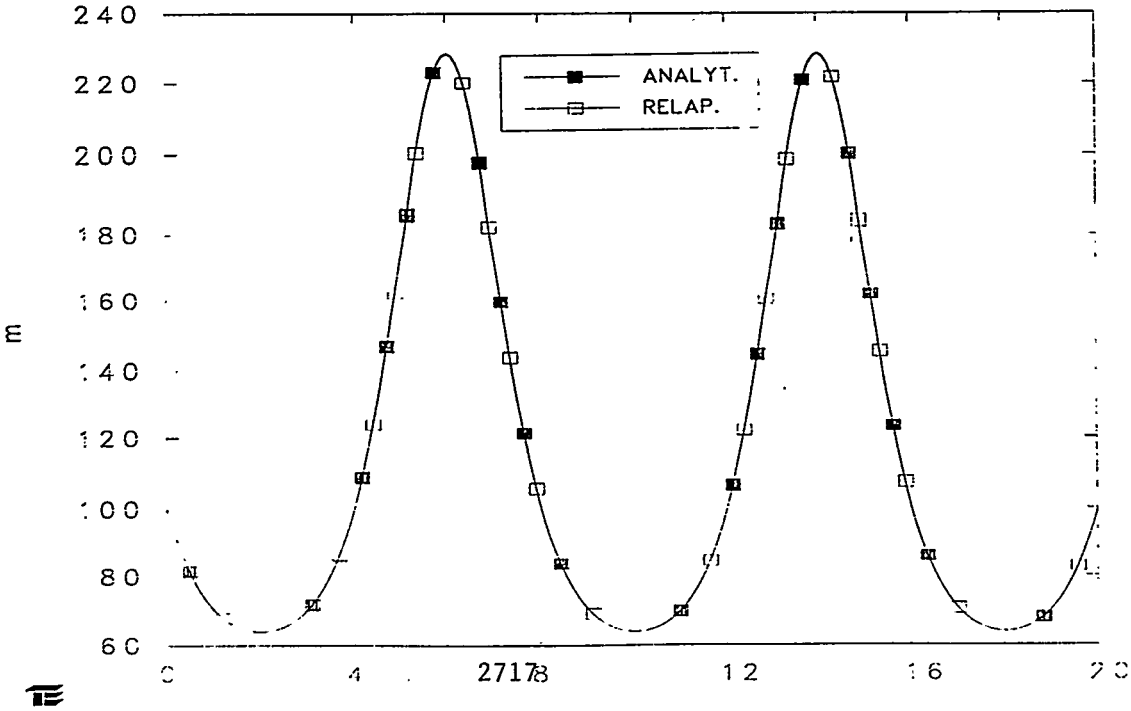

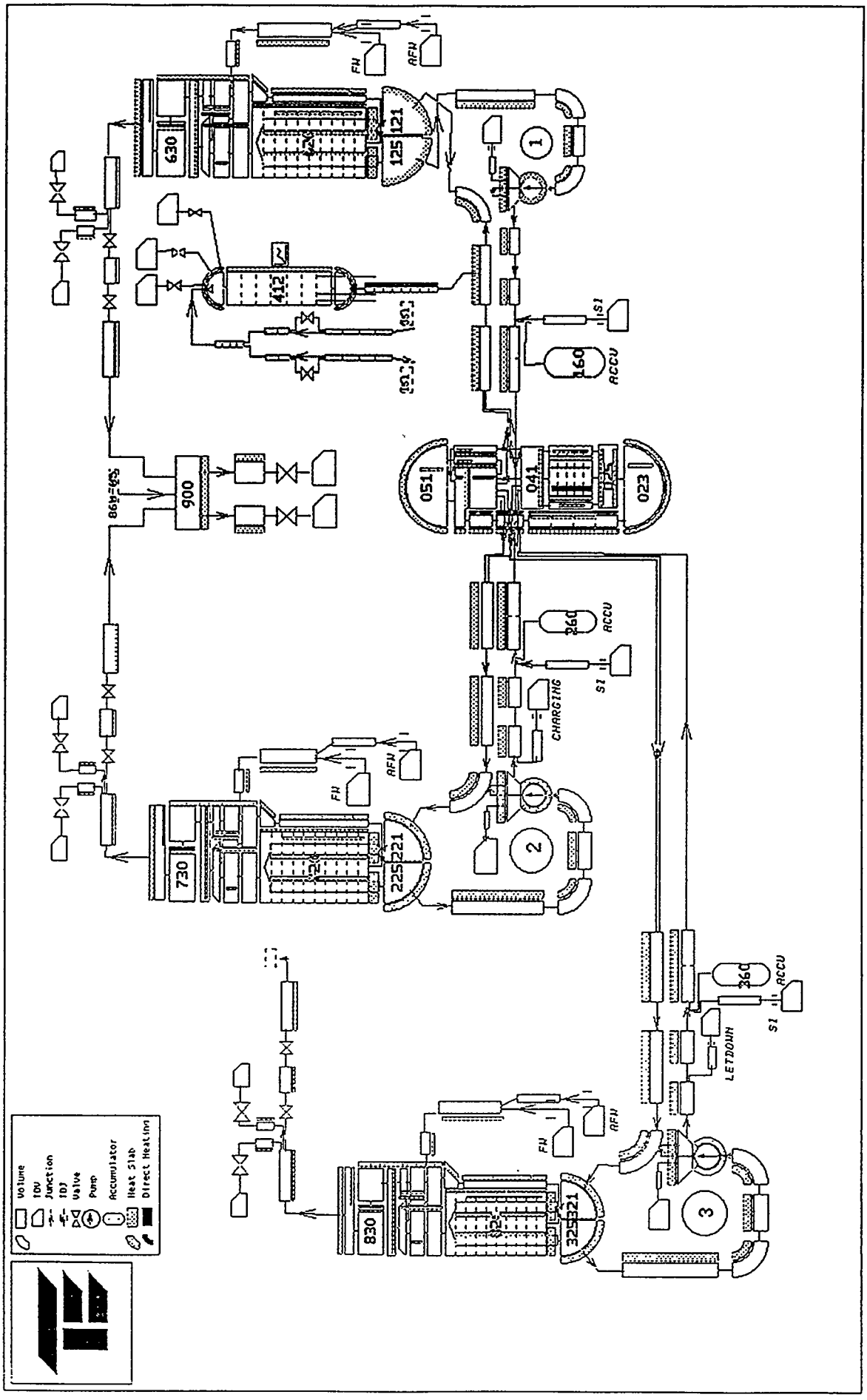

Figure 3: Plant nodalisation

FIG. 4 : Pressurizer Pressure

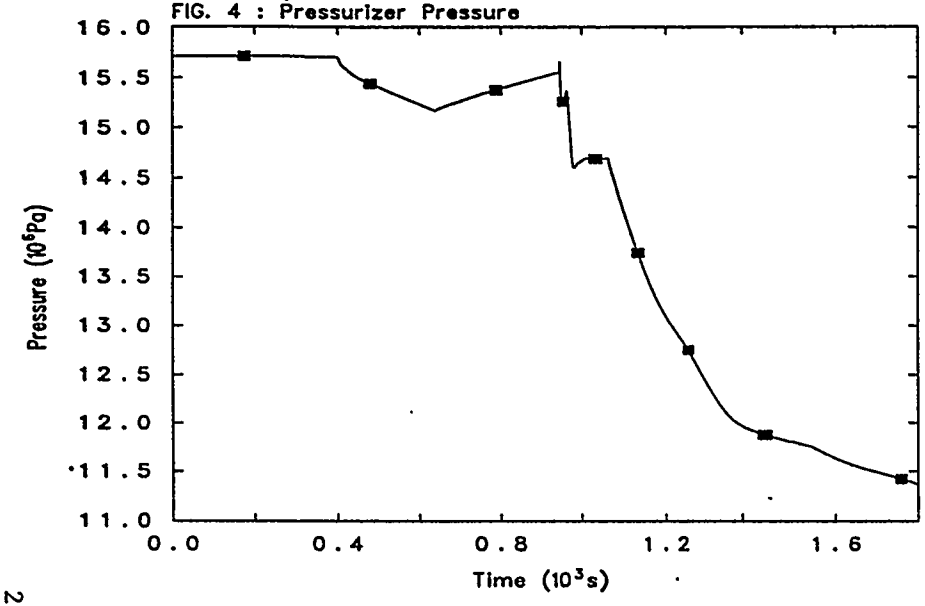

FIG. 5 : Break Mass Flow

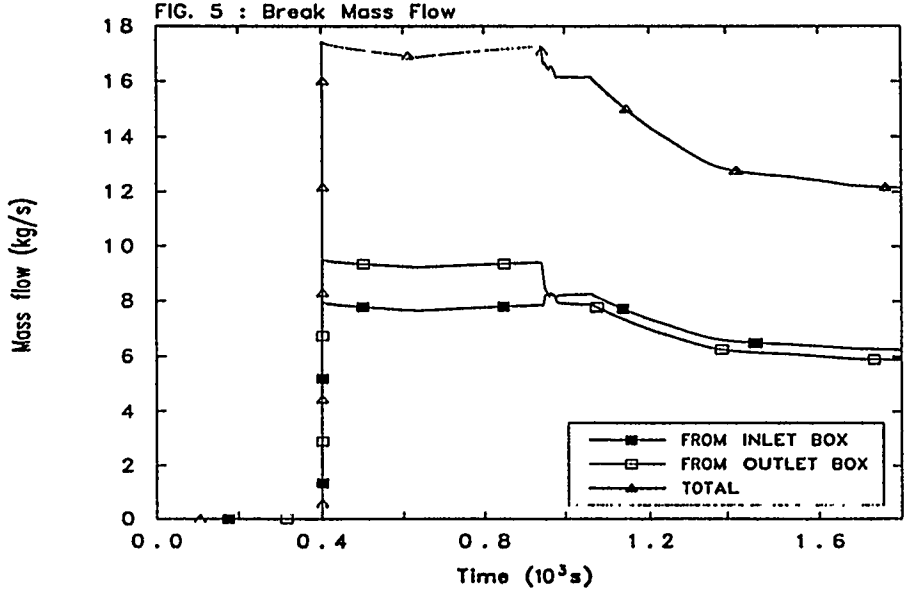

FIG. 6 : Steam Generator Pressure

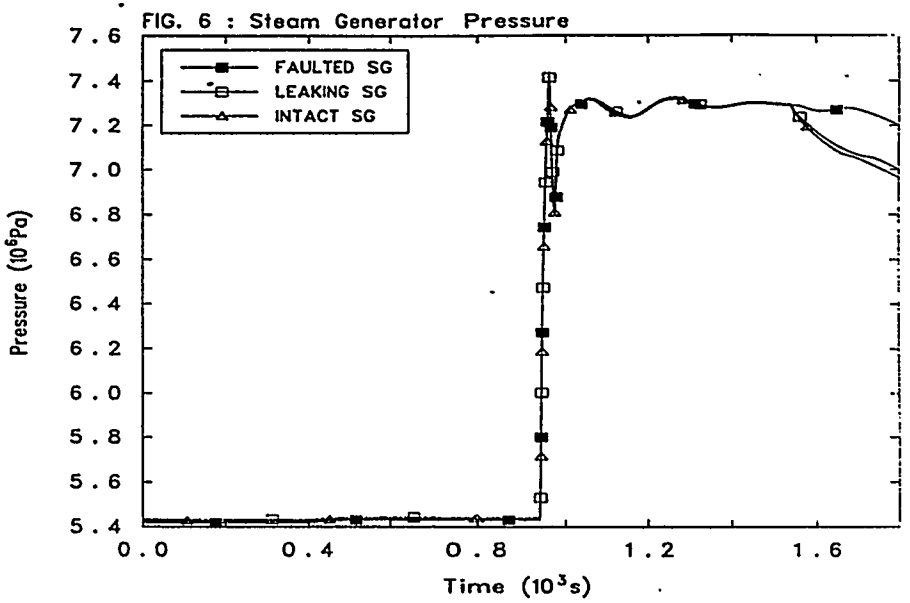

FIG. 7 : SG Relief Valve Steam Flow

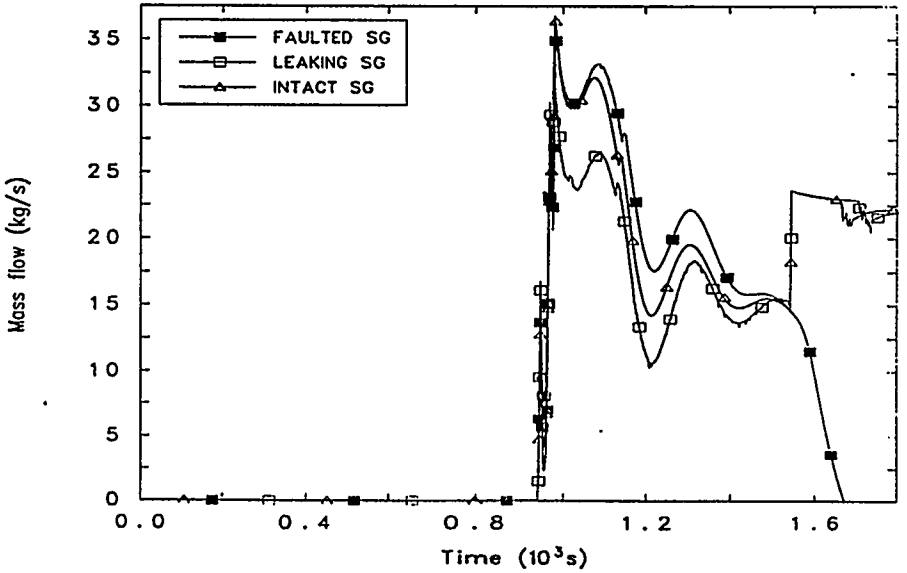

FIG. 8 : Integrated Break Activity

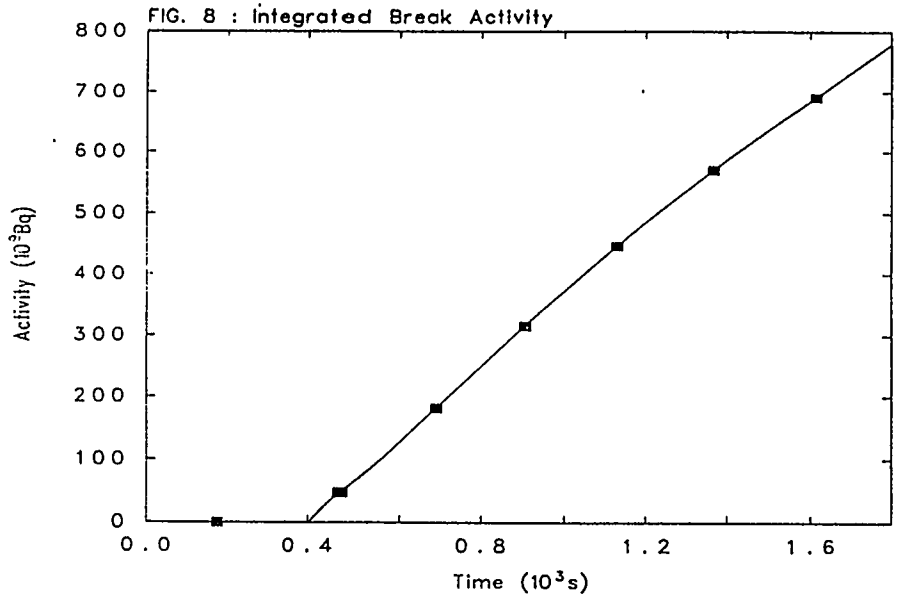

FIG. 9 : Steam Generator Liquid Activity

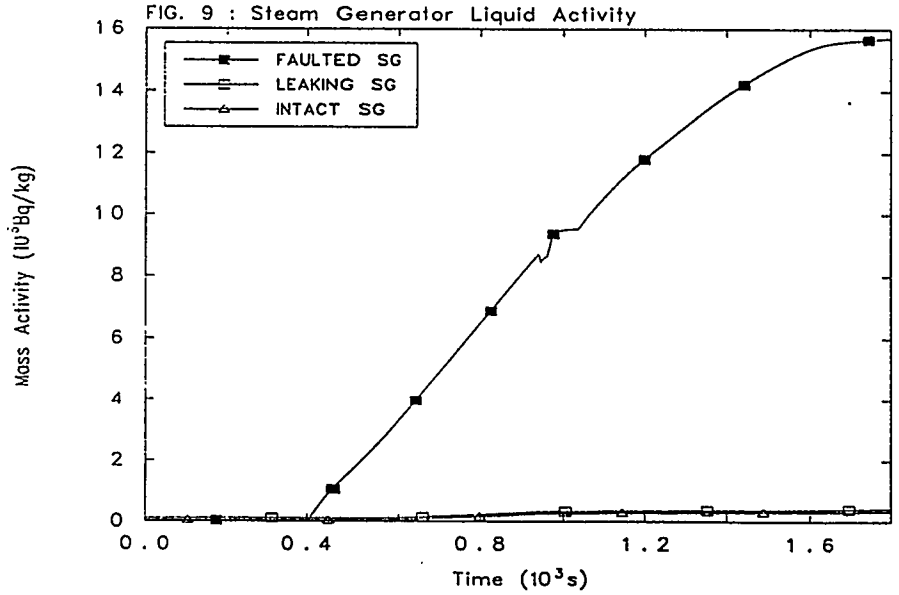

FIG. 10 : Total Release from each SG

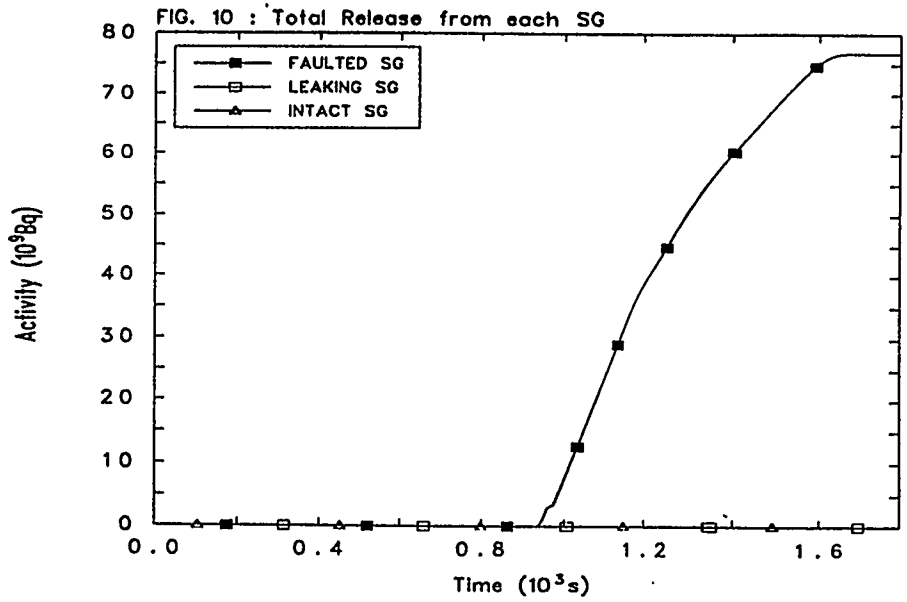

FIG. 11 : Activity Release from Faulted SG

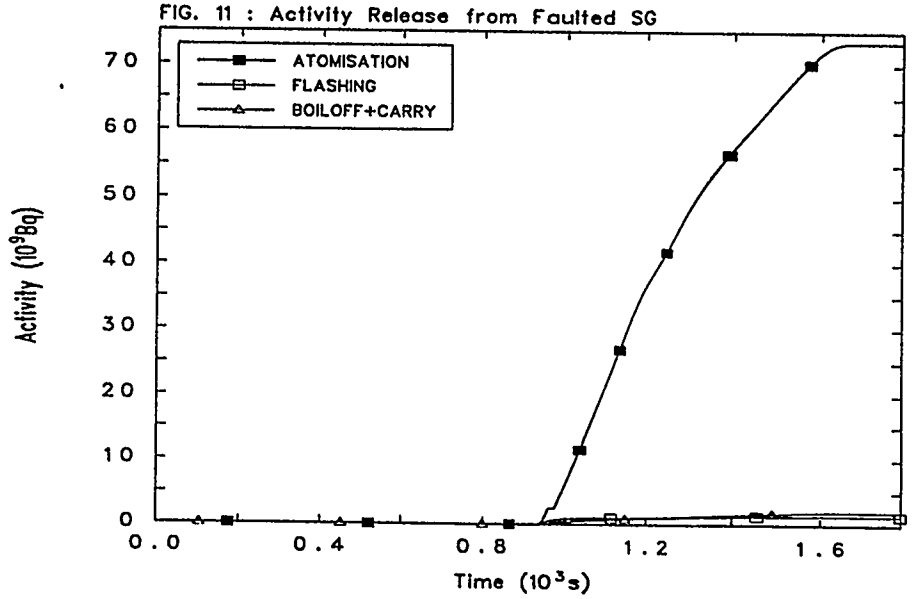

Analysis of Two-Phase Flow Inter-Subchannel Mass and Momentum Exchanges by the Two-Fluid Model Approach

H. Ninokata, A. Deguchi* and A. Kawahara**

Research Laboratory for Nuclear Reactors, Tokyo Institute of Technology
2-12-1 O-okayama, Meguro-ku, Tokyo 152 Japan

* ENO Mathematical Analysis
2-7-12 Arai, Nakano-ku, Tokyo 165 Japan

** Department of Mechanical Engineering, Kumamoto University
2-39-1 Kurokami, Kumamoto 860 Japan

Abstract

A new void drift model for the subchannel analysis method is presented for the thermohydraulics calculation of two-phase flows in rod bundles where the flow model uses a two-fluid formulation for the conservation of mass, momentum and energy. A void drift model is constructed based on the experimental data obtained in a geometrically simple inter-connected two circular channel test sections using air-water as working fluids. The void drift force is assumed to be an origin of void drift velocity components of the two-phase cross-flow in a gap area between two adjacent rods and to overcome the momentum exchanges at the phase interface and wall-fluid interface. This void drift force is implemented in the cross flow momentum equations. Computational results have been successfully compared to experimental data available including 3x3 rod bundle data.

1. Introduction

The subchannel analysis method has long been established since the pioneering work made, for example, by Rowe [1] and is being fully used in thermal hydraulics design of the nuclear reactor fuel assemblies as well as in safety evaluation. In the BWR subchannel analysis, current efforts are placed on developing the capabilities of analyzing transient two-phase flow phenomena starting from, for instance, flow coast down triggered by a pump trip, boiling transition (BT) up to post BT phenomena including re-wetting. A trend of the basic subchannel code framework has been based on the two-fluid multi-field description, differentiating basically three fields of liquid film, vapor core and droplet flows. In the formulation, of vital importance is the mechanistic approach to the constitutive relationships that are the result of the integration process of a set of local instantaneous flow conservation equations over subchannel control volumes. Three major physical processes are identified that require us to elaborate on experimental endeavors to make the mechanistic modeling possible: 1) turbulent inter-subchannel mixing and void drift; 2) spacer effects on the flow characteristics; and 3) re-wetting phenomena after BT.

Three fundamental mechanisms are considered in connection to the two-phase flow inter-subchannel exchanges: i) turbulent mixing that results in non-directional exchanges, ii) cross-flow

convection (diversion cross-flow) and iii) void drift[2, 3]. We assume that these three mechanisms can be dealt with independently and modeled on the basis of experimental results obtained in an air-water system using inter-connected two channel test sections. In this paper we focus our interest on modeling inter-subchannel exchanges, in particular, on the void drift phenomena.

Briefly, for the turbulent mixing of momentum and energy of two phase flows in a rod bundle the equal mass exchange model between two adjacent subchannels i and j is adopted in our calculations:

$$s_{ij}\left(\frac{\varepsilon}{l}\right)_{TP}\alpha_{gap}[(\rho\xi)_i - (\rho\xi)_j] \qquad (1)$$

where s_{ij} is the gap spacing; ε and l are the eddy diffusivity and Prandtl mixing length and $(\varepsilon/l)_{TP}$ indicates an extension of the single-phase flow concept to two-phase flow, e.g., with a help of Beus's two-phase multiplier[4]. ρ is the fluid density and ξ the transport property; α_{gap} is the void fraction at the gap. Axial momentum mixing is given by Eq. (1) with $\xi = w$ (axial velocity component) and likewise $\xi = h$ (enthalpy) for the energy mixing. Note that Eq. (1) with $\xi = 1$ corresponds to the turbulent mixing in the mass conservation equations and leads to net zero mass transfer between two subchannels. Also the forced mixing should be considered that is caused by such flow obstacles as spacer grids; however, this is out of scope in this paper and not discussed.

For the void drift phenomena, we identify the magnitude of the force that induces the phenomena and propose a new model to be included in the lateral momentum equations. By solving these lateral momentum equations with a newly added void drift force term, we obtain the cross-flow velocity that already includes the void drift contribution. Because the other two-fluid equations of mass, axial momentum and energy conservation are solved simultaneously, where this cross-flow component is incorporated in all the convection terms, the void drift contribution is accounted for in the calculated mass, momentum and energy distributions inside a bundle. Several comparisons will be made between calculation and experiment including the void redistribution in simple inter-connected two channel test sections [5] and in a GE3x3 rod bundle [6]. Overall it has been confirmed that the above driving force model can well reproduce most of the experimental results.

2. Void Drift Model

2.1. Void Drift Force

We assume that the void drift phenomena are a result of a net cross-flow occurring in the non-equilibrium flow without the lateral pressure difference as suggested by Sadatomi, et al.[5] Based

on this assumption, an attempt is made to identify the force that induces the void drift velocity. Further, because the void drift is predominant in churn-turbulent flow regime [5], we assume throughout in this paper that the void drift effect can be neglected in the other two-phase flow regime.

Let us consider first the steady-state lateral momentum conservation equation in the two-fluid six-equation description:

$$\frac{\partial}{\partial x}(\alpha_k \rho_k u_k u_k) + \frac{\partial}{\partial z}(\alpha_k \rho_k u_k w_k) = -\alpha_k \frac{\partial p}{\partial x} - F_{W,k}(u_k) - F_{I,k}(u_{fg}) - F_{\Gamma,k}, \qquad (2a)$$

where x and z are the lateral and axial coordinates; u and w are the lateral and axial components of the flow velocity in a gap and in a subchannel, respectively; α and ρ are the volume fraction and density; p is the pressure; the subscript k refers to the k-th phase (i.e., k = g: gas or vapor phase; k = f: liquid phase); $F_W(u_k)$ and $F_I(u_{fg})$ are the momentum exchanges between fluid and wall (W) as a function of u_k, and between two phases (I) as a function of the relative velocity between two phases, i.e., $u_{fg} = u_f - u_g$, respectively; and F_Γ is the momentum exchange due to evaporation /condensation (Γ). u_k in Eq. (2a) is the diversion cross-flow component due to the lateral pressure difference between subchannels. It is noted that $u_k = 0$ when $\partial p/\partial x = 0$ and $F_{\Gamma,k} = 0$ in Eq. (2a).

Considering that the void drift phenomena are a result of a cross-flow occurring in the non-equilibrium flow without the lateral pressure difference, we introduce the driving force of void drift F_{VD} and the void drift velocity u_{VD} that satisfy the steady-state lateral momentum equation (2a) but without pressure gradient term $\alpha_k \partial p/\partial x$ and $F_{\Gamma,k}$:

$$\frac{\partial}{\partial x}(\alpha_k \rho_k u_{VD,k} u_{VD,k}) + \frac{\partial}{\partial z}(\alpha_k \rho_k u_{VD,k} w_k) = F_{VD,k} - F_{W,VD,k}(u_{VD,k}) - F_{I,VD,k}(u_{VD,fg}), \quad (3a)$$

or rearranging Eq. (3a):

$$F_{VD,k} = \frac{\partial}{\partial x}(\alpha_k \rho_k u_{VD,k} u_{VD,k}) + \frac{\partial}{\partial z}(\alpha_k \rho_k u_{VD,k} w_k) + F_{W,VD,k}(u_{VD,k}) + F_{I,VD,k}(u_{VD,fg}), \quad (3b)$$

where $F_{VD,k}$ is the void drift force on the phase k; u_{VD} is the void drift velocity; and $u_{VD,fg}$ is the relative velocity between two phases, i.e., $u_{VD,fg} = u_{VD,f} - u_{VD,g}$. $F_{W,VD}$ and $F_{I,VD}$ are interpreted as the components that balance with the wall and interface friction. It is our assumption that the complete form of the steady-state lateral momentum equation is given, instead of Eq. (2a), by:

$$\frac{\partial}{\partial x}[\alpha_k\rho_k(u_k+u_{VD,k})(u_k+u_{VD,k})] + \frac{\partial}{\partial z}[\alpha_k\rho_k(u_k+u_{VD,k})w_k] =$$

$$-\alpha_k\frac{\partial p}{\partial x} + F_{VD,k}(u_{VD,k}) - F_{W,VD,k}(u_k+u_{VD,k}) - F_{I,VD,k}(u_{fg}+u_{VD,fg}) - F_{\Gamma,k}. \qquad (2b)$$

Note that a total of the diversion cross-flow and void drift components $u_k+u_{VD,k}$ is treated as one component, i.e., the cross-flow component, in actual computations.

The question is to find $F_{VD,f}$ and $F_{VD,g}$ in terms of subchannel-averaged two-phase flow quantities. This attempt will be made in the following section 2.3. By subtracting Eq. (2a) from Eq. (2b) on both hand-sides, we relate $F_{VD,f}$ and $F_{VD,g}$ to the wall friction term F_W and the interface friction term F_I in the following:

$$F_{VD,f} = (\text{convection terms}) + [F_{W,f}(u_f+u_{VD,f}) - F_{W,f}(u_f)] + [F_{I,f}(u_{fg}+u_{VD,fg}) - F_{I,f}(u_{fg})] \qquad (4a)$$

$$\cong (\text{convection terms}) + \left[\frac{\partial F_{W,f}}{\partial u_f}u_{VD,f} + \frac{1}{2}\frac{\partial^2 F_{W,f}}{\partial u_f^2}(u_{VD,f})^2 + \ldots\right] + \left[\frac{\partial F_{I,f}}{\partial u_{fg}}u_{VD,fg} + \frac{1}{2}\frac{\partial^2 F_{I,f}}{\partial u_{fg}^2}(u_{VD,fg})^2 + \ldots\right] \qquad (4b)$$

$$F_{VD,g} = (\text{convection terms}) + [F_{I,g}(u_{fg}+u_{VD,fg}) - F_{I,g}(u_{fg})] \qquad (5a)$$

$$\cong (\text{convection terms}) + \frac{\partial F_{I,g}}{\partial u_{fg}}u_{VD,fg} + \frac{1}{2}\frac{\partial^2 F_{I,g}}{\partial u_{fg}^2}(u_{VD,fg})^2 + \ldots \qquad (5b)$$

where the 'convection terms' is given by:

$$\frac{\partial}{\partial x}(\alpha_k\rho_k[(u_k+u_{VD,k})(u_k+u_{VD,k}) - u_k u_k]) + \frac{\partial}{\partial z}(\alpha_k\rho_k[(u_k+u_{VD,k})w_k - u_k w_k])$$

$$\approx 2\frac{\partial}{\partial x}(\alpha_k\rho_k u_{VD,k}u_k) + \frac{\partial}{\partial z}(\alpha_k\rho_k u_{VD,k}w_k),$$

with the subscript k being f for Eq. (4) and g for Eq. (5). In Eq. (5), the force corresponding to the wall friction $F_{W,VD,g}$ is neglected for the gas-phase because the interface friction force is considered to dominate. F_W and F_I in Eqs. (4) and (5) are usually expressed as:

$$F_{W,k}(u_k) = \frac{f_W}{2D_h}\rho_k u_k^2 \ , \qquad (6)$$

where f_W could be given, e.g., by the Gunther-Shaw correlation [7] for cross flow pressure drop across the tube bank and D_h is the equivalent hydraulic diameter of the subchannel gap; and

$$F_{I,k}(u_{fg}) = \frac{f_I(\rho_k, \alpha_k, ..)}{2D_h}\rho_g u_{fg}^2 \ , \qquad (7)$$

where the interface friction factor f_I is dependent also on the phase-interface area, sauter radius of bubbles, etc. A detailed description of this model is found in [8].

2.2. Experimental Data Analysis

The void drift data subject to analysis in this paper was obtained in the churn-turbulent flow regime at Kumamoto University [5] using two simple inter-connected two channel test sections: one with two circular subchannels of different diameters (Ch.E-F in Fig. 1) and the other with two identical circular subchannels (Ch.F-F in Fig. 1). Working fluids are water and air under the atmospheric pressure condition. Flow redistribution along the channel axis without diversion cross-flow was obtained by realizing the following conditions: (1) pressure gradient in the axial direction to be the same at the entry section ; and (2) the time averaged pressures in both subchannels to be identical at the inlet and at the exit for Ch.E-F and Ch.F-F test sections. Thus no lateral pressure gradient was established on a time-averaged basis, where no diversion cross-flow is judged to take place: i.e., $u_k = 0$. Under these conditions the mass flux redistribution of both phases, i.e., $\alpha_k\rho_k w_k$ (k = g, f), along the axial length of each subchannel was measured for various inlet mass flow rates. Sadatomi et al. [5] gave the air volume fraction redistribution α_k through Smith's correlation[9]. Also the equilibrium void fractions $\alpha_{k,EQ,E}$ and $\alpha_{k,EQ,F}$ (with the subscripts E and F referring to the subchannels E and F) were evaluated by substituting the measured flow rates of both phases in each subchannel into Smith's correlation.

The void drift velocity of the k-th phase $u_{VD,k}(z)$ can be defined by the mass balance over a flow control volume for either one subchannel i or the other j of two subchannels with known $\rho_k(z)$, $\alpha_k(z)$ and $w_k(z)$:

$$(\rho_k\alpha_k w_k)_{i,\ z+\Delta z} - (\rho_k\alpha_k w_k)_{i,\ z} + \frac{s_{ij}\Delta z}{A_i}(\rho_k\alpha_k u_{VD,k})_{i\to j,\ z+1/2\Delta z} = 0 \qquad (8\,a)$$

or

$$(\rho_k\alpha_k w_k)_{j,\ z+\Delta z} - (\rho_k\alpha_k w_k)_{j,\ z} - \frac{s_{ij}\Delta z}{A_j}(\rho_k\alpha_k u_{VD,k})_{i\to j,\ z+1/2\Delta z} = 0 \qquad (8\,b)$$

where Δz is the axial spacing of the control volume; s_{ij} is the gap spacing; and $i\to j$ indicates the void drift direction from subchannel i to j. We can select Δz complying with the axial locations of measurement. A_i and A_j are the flow area of subchannel i and j. From Eqs. (8a) and (8b), we obtain:

$$u_{VD,k} = \frac{1}{2\,s_{ij}\Delta z\,(\rho_k\alpha_k)_{av}}\{[G_{k,j}\,A_j - G_{k,i}\,A_i]_{z+\Delta z} - [G_{k,j}\,A_j - G_{k,i}\,A_i]_z\} \qquad (9a)$$

with $G_k(z) = \rho_k(z)\alpha_k(z)w_k(z)$ and A is the flow area. The subscript av refers to the gap quantity, represented by an average between channel i and j. If we select Δz to allow the flow to be fully developed at $z+\Delta z$, Eq. (9a) could be rewritten as:

$$u_{VD,k} = \frac{1}{2\, s_{ij}\Delta z\, (\rho_k\alpha_k)_{av}}\{[G_{k,i}\, A_i - G_{k,j}\, A_j]_{EQ} - [G_{k,i}\, A_i - G_{k,j}\, A_j]_z\} \qquad (9b)$$

where the subscript EQ refers to the equilibrium flow.

Thus, having $u_{VD,k}(z)$, we evaluate $F_{VD,f}$ and $F_{VD,g}$ by Eqs. (4)-(7) along the axial length of the E-F and F-F test sections with u_f and u_g, hence u_{fg}, being zero (no diversion cross-flows in the experiments). It is also worthwhile to note here that contributions of convection terms in Eqs. (4) and (5) are found much smaller than from the remaining $F_{W,VD}$ and $F_{I,VD}$ terms. Therefore in the following model construction, we neglect the convection for simplicity.

2.3. New Void Drift Model

$F_{VD,g}$ and $F_{VD,f}$ in the preceding section 2.1 must be correlated, in the absence of the diversion cross-flow ($u_f = u_g = 0$), in terms of subchannel averaged two-phase flow quantities except for $u_{VD,k}$ which should be regarded now as the unknown variable, and flow geometry data. Looking at the equations (5b) and (7), we could well assume, first for $F_{VD,g}$, the following:

$$|F_{VD,g}| \propto \rho_g (u_{VD,fg})^2 \qquad (10)$$

since the coefficient of first order term becomes zero with $u_{fg} = 0$ in Eq. (5b). Equation (9b) is simplified by assuming constant density as:

$$u_{VD,k} \approx \frac{A_{av}}{2\, s_{ij}\Delta z\, \alpha_{k,av}}\{[\alpha_{k,i}w_{k,i} - \alpha_{k,j}w_{k,j}] - [\alpha_{k,i}w_{k,i} - \alpha_{k,j}w_{k,j}]_{EQ}\} \qquad (9c)$$

where A_{av} is equal to $(A_i+A_j)/2$. From Eq. (9c), we get $u_{VD,fg}$ $(= u_{VD,f} - u_{VD,g})$ as:

$$\begin{aligned} u_{VD,fg} &\approx \frac{A_{av}}{2\, s_{ij}\Delta z}\left[\{[w^*_{f,i} - w^*_{f,j}] - [w^*_{f,i} - w^*_{f,j}]_{EQ}\} - \{[w^*_{g,i} - w^*_{g,j}] - [w^*_{g,i} - w^*_{g,j}]_{EQ}\}\right] \\ &= \frac{A_{av}}{2\, s_{ij}\Delta z}\{[w^*_{fg,i} - w^*_{fg,j}] - [w^*_{fg,i} - w^*_{fg,j}]_{EQ}\} \end{aligned} \qquad (9d)$$

where we have introduced w_k^* just for convenience as:

$$w^*_{f,i} \equiv \left(\frac{\alpha_{f,i}}{\alpha_{f,av}}\right) w_{f.i} \text{ and } w^*_g \equiv \left(\frac{\alpha_{g,i}}{\alpha_{g,av}}\right) w_{g,i} \text{ , ..., etc.}$$

and $w_{fg}^* = w_f^* - w_g^*$. Substituting Eq. (9d) into Eq. (10), finally we get:

$$|F_{VD,g}| \propto \rho_g \left(\frac{A_{av}}{2s_{ij}\Delta z}\right)^2 \left\{\left[w^*_{fg,i} - w^*_{fg,j}\right] - \left[w^*_{fg,i} - w^*_{fg,j}\right]_{EQ}\right\}^2 . \quad (11a)$$

or in a more approximated form with a proportionality constant $K_{VD,g}$:

$$|F_{VD,g}| \approx K_{VD,g} \left\{\left[w^*_{fg,i} - w^*_{fg,j}\right] - \left[w^*_{fg,i} - w^*_{fg,j}\right]_{EQ}\right\}^2 . \quad (11b)$$

Noting the magnitude of $F_{VD,f} + F_{VD,g}$ to be equal to that of wall friction $F_{W,f}$, which is a result from Eqs. (4b) and (5b) with $F_{I,f} + F_{I,g} = 0$, we try to model $|F_{VD,f} + F_{VD,g}|$ next. Following the same procedure as $|F_{VD,g}|$, we could assume $|F_{VD,f} + F_{VD,g}| \propto \rho_f (u_{VD,f})^2$ as suggested by Eq. (6). However, this assumption has lead to rather scattered representation of the experimental data. This is considered to be due to the fact that the form of cross-flow pressure drop model $F_{W,f}$ given by Eq. (6) still involves much uncertainty. As a consequence, there is no reason to deny that the Taylor expansion first order term does not vanish, i.e., $|F_{VD,f} + F_{VD,g}| \propto \rho_f |u_{VD,f}|$ $(= \rho_f (u_{VD,f})^2 / |u_{VD,f}|)$. This means the momentum exchange between fluid and rod wall, i.e., the cross-flow wall friction and form loss, could be represented by a combination of $\rho_f |u_{VD,f}|$ and $\rho_f (u_{VD,f})^2$ instead of Eq. (6). Finally proposed model is given by:

$$|F_{VD,f} + F_{VD,g}| \propto \left(\frac{A_{av}}{2 s_{ij}\Delta z}\right) \left|\rho_f \left(\left[w^*_{f,i} - w^*_{f,j}\right] - \left[w^*_{f,i} - w^*_{f,j}\right]_{EQ}\right)\right| \quad (12a)$$

or in a simpler form with $K_{VD,f}$ proportionality constant:

$$|F_{VD,f} + F_{VD,g}| \approx K_{VD,f} \left|\left[w^*_{f,i} - w^*_{f,j}\right] - \left[w^*_{f,i} - w^*_{f,j}\right]_{EQ}\right| . \quad (12b)$$

Still we need an expression for α_{EQ} and w_{EQ}. In this regard, we employ Rowe's model [10] for the equilibrium void distribution α_{EQ}:

$$\alpha_{EQ,i} = \overline{\alpha} + (1 - \overline{\alpha}) K_2 \left(1 - \frac{\overline{D_h}}{D_{h,i}}\right) \quad (13)$$

where K_2 is constant and equal to 1.0; over-bar quantities refer to those of bundle cross-section average. With α_{EQ} at z+Δz plane and α_k, w_k, $F_{W,f}$, ρ_k, $\partial p/\partial z$, etc. at z-plane as known quantities, equilibrium velocity w_{EQ} can be obtained by solving iteratively a set of non-linear phasic balance equations of momentum and mass between z and z+Δz planes per each subchannel.

This procedure is necessary for all computational meshes and constitutes of large part of computational efforts in this work.

3. Computational Results and Discussions

3.1 Evaluation of the Void Drift Force Model

This section describes a result of analysis in 2.1 - 2.3. Six sets of experimental data are evaluated and Table 1 shows their experimental conditions. Experimental data are reduced to $|F_{VD,g}|$ through Eqs. (5a), (7) and (9a) and to $|F_{VD,f} + F_{VD,g}|$ through Eqs. (4a), (5a), (6) and (9a) as described in 2.1 and 2.2, and are plotted against the prediction of Eqs. (11b) and (12b) in Figs. 2 and 3, respectively. The use of Smith's correlation [9] has been made for the void fraction distribution, as shown in 2.2, to obtain the experimental values of $|F_{VD,g}|$ and $|F_{VD,g} + F_{VD,f}|$, while the prediction is based on the void fraction distribution directly from the two-fluid calculation. It is worthwhile to note here that the results have been found insensitive to void fraction correlations.

In evaluating Eq. (11b), we used the equilibrium volume fraction α_{EQ} that was provided by Sadatomi et al. [5] and the constant $K_{VD,g}$ equal to be 1,250. Figure 2 shows a comparison of prediction by Eq. (11b) and experiment with respect to the void drift force exerted on the gas phase (air) $F_{VD,g}$. On both axis, $F_{VD,g}$ is normalized by 1,250 $Kg/m^2/s^2$. It is shown that the void drift force could be predicted by Eq. (11) within accuracy of 5 - 7%.

Likewise, Figure 3 displays a comparison between prediction and experiment with respect to the void drift force exerted on both gas and liquid phases $|F_{VD,g} + F_{VD,f}|$, which is plotted after being normalized by 2,800 $Kg/m^2/s^2$. In the prediction, Eq. (12b) is used with the constant $K_{VD,f}$ = 9.3. It is noted that the zero void drift force is attained normally far beyond the exit of the test section where the equilibrium condition is reached. Therefore in both figures, as the location of evaluation along the axis approaches the exit, the void drift lines tend to converge to zero; or conversely as the measurement point approaches the entry region the void drift force increases.

In general the relation $|F_{VD,f}| > |F_{VD,g}|$ is valid. This implies that not only the spatial non-uniformity of vapor velocity distribution but also that of the liquid-phase at subchannel control volume boundaries, which are caused by uneven inter-phase turbulent momentum transfer and wall shear, is considered to be related closely to void drift phenomena. More mechanistic modeling of such void drift phenomena would be possible if we look into a detail of microscopic wall-fluid and inter-phase momentum transfer phenomena and complicated structure of the two-phase flow in the slug to churn-turbulent flow regime.

3.2 Inter-Connected Two Channel Flow Redistribution

We have implemented Eqs. (11b) and (12b) into the cross-flow momentum equations and Eq. (13) together with the iteration scheme to obtain the equilibrium mass flux distribution in a two-fluid model subchannel analysis code [11]. Using this code we have carried out calculation in an attempt to reproduce the experimental results for flow redistribution in the churn-turbulent flow regime. The boundary conditions include subchannel inlet volumetric flux distribution and exit pressure; a total length of 2m is divided into 40 meshes.

Typical results are illustrated in Fig. 4 for Run EF2 and in Fig. 5 for Run EF6 (see Table 1 for the run number). In the both figures, a comparison is made for the ratio of the volumetric flow Q_{kE} in E-channel to the total volumetric flow $Q_{kE}+Q_{kF}$ (k = g and f) along the axial elevation from the entry (z = 0 m) to exit (z = 2 m). Figure 5 shows good agreement of calculated results with experiment, while Fig. 4 shows a slight discrepancy in the gas-phase redistribution near the exit region. This discrepancy is considered to be due to a direct result from disagreement of the calculated α_{EQ} by Eq. (13) with the experimental value. In fact if we use the experimental value for α_{EQ}, we get excellent agreement with experiment as shown Fig. 6. This fact suggests that the α_{EQ} prediction plays a key role in calculating overall flow re-distributions and also that the approach based on the void drift force concept has been justified.

For example, although Rowe's correlation is found to be good for $\alpha>0.5$ when compared with the Kumamoto University data [4], it does not represent well experimental data for lower void fraction flow, e.g. $\alpha<0.5$ on a bundle average basis. Also it is pointed out that Eq. (13) leads to non-zero $\alpha_{EQ,i}$ even if the bundle average void fraction is zero. When the model is applied to low void fraction experiments of the GE3x3 bundle experiment as will be shown in the following, the α_{EQ} frequently becomes negative, which must be corrected to zero. In this regard it is pointed out that model improvement in the equilibrium flow prediction is important as a next step.

3.3. 3x3 Bundle Flow Redistribution

The proposed void drift model is evaluated by the GE3x3 rod bundle data where subchannel flow and enthalpy has been measured in rod bundles relevant to BWR conditions. Again the two-fluid model subchannel analysis code is used in the same manner as in 3.2 with the same constants, e.g., $K_{VD,g}$ = 1,250 and $K_{VD,f}$ = 9.3. In this calculation, two modifications are introduced to the models described in 2.3 for better agreement:

1) K_2 in Eq. (13) is set 0.5.

2) Eqs. (11b) and (12b) are further multiplied by the following weighting factor C_{VD}:

(I)	For $\alpha_{av} < 0.1$	$C_{VD} = 0.0$;
(II)	$0.1 \leq \alpha_{av} < 0.5$	$C_{VD} = (\alpha_{av} - 0.1)/0.4$;
(III)	$0.5 \leq \alpha_{av} < 0.8$	$C_{VD} = 1.0 - (\alpha_{av} - 0.5)/0.3$; and
(IV)	$0.8 \leq \alpha_{av}$	$C_{VD} = 0.0$.

The second modification is to take into account that the void drift phenomena are less important in bubbly and annular flow regime and are maximum when α_{av} is about 0.5. Also it was found that without C_{VD}, two-phase flow computation became less stable possibly because the void drift forces were over-estimated.

Figure 7 shows an exit quality distribution in terms of bundle average quality where a comparison is shown between the calculation with the new void drift model and the experiment. Figure 8 shows the same comparison but the calculation is made without void drift model in the code.

Figure 9 shows an exit mass flux distribution both in terms of bundle average quality where the comparison is between the calculation with the new void drift model and the experiment. The calculational result in Fig. 10 is obtained without void drift model. In general agreement of the calculational results (Figs. 7 and 9) with the experiment is considered to be good over the range of quality $x > 0.03$.

By comparing Fig. 7 with 8, and Fig. 9 with 10, it is apparent that the void drift model reproduces well the trend of two-phase flow re-distribution phenomena in rod bundles. In particular the comparisons for the corner subchannel are consistent with the comparisons for side and interior subchannels. However, our void drift model is constructed based on the air/water data under low pressure conditions, applicability of the model to actual BWR conditions remains subject to further investigation.

4. Conclusions

A new void drift model for the subchannel analysis method is presented for the thermohydraulics calculation of two-phase flows in rod bundles where the flow model uses a two-fluid formulation for the conservation of mass, momentum and energy.

The void drift driving force is assumed to be an origin of void drift velocity components of the two-phase cross-flow in a gap area and its magnitude equal to that which surmounts the momentum exchanges at the phase interface and wall-fluid interface resulting in uni-directional flows. On the basis of this assumption, a void drift model has been derived and constructed using

the experimental data obtained in geometrically simple inter-connected two circular channel test sections using air-water as working fluids.

Assessment of the model has revealed that the void drift force exists and induces the void drift phenomena. The void drift force, Eqs. (11b) and (12b), are recommended to be used with the constants $K_{VD,g}$ and $K_{VD,f}$ of 1,250 and 9.3, respectively and with the weighting factor C_{VD} that emphasize the importance of the void drift in the churn-turbulent flow regime. Extensive two-channel data analysis has shown that the two-fluid model prediction of the void drift force, Eqs. (11b) and (12b), is in good agreement with a body of the data experimentally obtained. It is noted that the void drift force reduced from the experimental channel flow data is rather insensitive to void fraction correlation. Also it has been shown that the two-fluid subchannel analysis code with the new void drift model being implemented in the cross-flow momentum equation can produce results consistent with the typical subchannel data including 3x3 rod bundle data. Calculational results have been compared to experiments with good agreement provided that the equilibrium flow distribution is correctly predicted.

Acknowledgment

This work was carried out in the framework of the BWR subchannel analysis code development program supported by Tokyo Electric Power Co., Tohoku Electric Power Co., Chubu Electric Power Co., Hokuriku Electric Power Co., Chugoku Electric Power Co. and Japan Atomic Power Co.

Nomenclatures

A	flow area
Ch.E	subchannel E of the test section
Ch.F	subchannel F of the test section
C_{VD}	flow regime weighting factor to be multiplied with Eqs. (11b) and (12b)
D_h	equivalent hydraulic diameter
F_I	inter-phase momentum exchange between two phases
F_{VD}	void drift force
F_W	cross-flow momentum exchange between flow and wall
F_Γ	force due to mass exchange
G	mass flow rate
$K_{VD,k}$	constant used in Eqs. (11b) and (12b)
p	pressure
Q	volume flow rate
s_{ij}	gap spacing between subchannels i and j
u	cross-flow component of the fluid velocity
u_k	diversion cross-flow component of the k-th phase

u_{fg}	relative velocity between two phases
$u_{VD,k}$	void drift cross-flow component of the k-th phase
$u_{VD,fg}$	relative velocity of void drift cross-flow components ($= u_{VD,f} - u_{VD,g}$)
w	axial flow component of the fluid velocity
w_k^*	superficial velocity divided by the average volume fraction of the k-th phase
x	lateral coordinate
z	axial coordinate
α_k	volume fraction of the k-th phase
α_{av}	subchannel average void fraction
ρ	density
Δz	axial mesh spacing

Subscripts

av	average between two subchannels or average in one subchannel
EQ	equilibrium
f	liquid phase
fg	relative value between liquid and gas phases
g	gas or vapor phase
I	inter-phase quantity
i	subchannel i
j	subchannel j
k	k-th phase
VD	void drift
W	wall
Γ	mass exchange (evaporation/condensation)

References

[1] D.S. Rowe, "COBRA-IIIC: A digital computer program for steady state and transient thermal-hydraulic analysis of rod bundle nuclear fuel elements," Pacific Northwest Laboratory, BNWL-1695 (1973).

[2] R.T. Lahey and F.J. Moody, The Thermal Hydraulics of a Boiling Water Nuclear Reactor, Monograph Series on Nuclear Science and Technology, ANS, 122-138 (1977).

[3] N.E. Todreas and M.S. Kazimi, Nuclear Systems II, Hemisphere Publishing Co., p. 265 (1990).

[4] S.G. Beus, "A two-phase turbulent mixing model for flow in rod bundles," WAPD-TM-2438 (1971).

[5] M. Sadatomi, A. Kawahara and Y. Sato, "Flow redistribution due to void drift in two-phase flow in a multiple channel consisting of two subchannels," Nucl. Eng. Des. 148, 463-474 (1994).

[6] R.T. Lahey, B.S. Shiralkar and D.W. Radcliffe, "Mass flux and enthalpy distribution in a rod bundle for single- and two-phase flow conditions," J. Heat Transfer 93, 197-209 (1971).

[7] A.Y. Gunter and W.A. Shaw, "A general correlation of friction factors for various types of surfaces in crossflow," ASME Trans. 57 (1945).

[8] V.H. Ransom et al., "RELAP5/Mod2 code manual, Vol.1: Code structure, system models and solution methods," NUREG/CR-4312, EG&G-2796 (1985).

[9] S.L. Smith, "Void fractions in two-phase flow: a correlation based upon an equal velocity head model," Proc. Inst. Mech. Eng. 184, 647-664 (1969-70).

[10] D.S. Rowe, R.B. Macduff and R.E. Collingham, Thermal hydraulic subchannel model based on void drift, Proc. Nat. Heat Transfer Conf., Vol.1, 401-406 (1990).

[11] H. Ninokata and M. Aritomi, "An overview of the BWR subchannel analysis code development and experiments for Japanese utilities," Proc. 2nd Int. Seminar on Subchannel Analysis, EPRI TR-103188, 15-1~17 (1993).

Table 1. Experimental conditions

Run No.	Channel (see Fig. 1)	j_f (m s^{-1})	j_g (m s^{-1})	$Q_{f,E(0)}/Q_{f,tot}$	$Q_{g,E(0)}/Q_{g,tot}$
EF2	E-F	1.0	3.0	0.751	0.2
EF4	E-F	1.0	3.0	0.612	0.9
EF5	E-F	1.0	5.0	0.683	0.518
EF6	E-F	1.5	4.0	0.69	0.5
FF12	F-F	1.0	3.3	0.417	0.7
FF13	F-F	1.5	4.0	0.405	0.7

j_f and j_g are the volumetric fluxes of liquid and gas for the whole channel;
$Q_{f,E}(0)/Q_{f,tot}$ is the ratio of volume flow rate of the liquid phase in subchannel E (or in subchannel F to the left of Ch F-F in Fig. 1) to that in the whole channel at the inlet of the test section and $Q_{g,E}(0)/Q_{g,tot}$ is the same ratio of the gas phase.

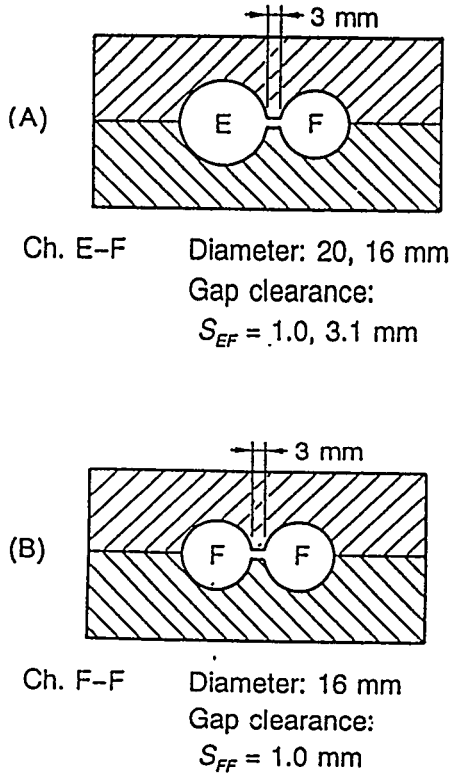

Fig. 1 Cross-section of the test channels

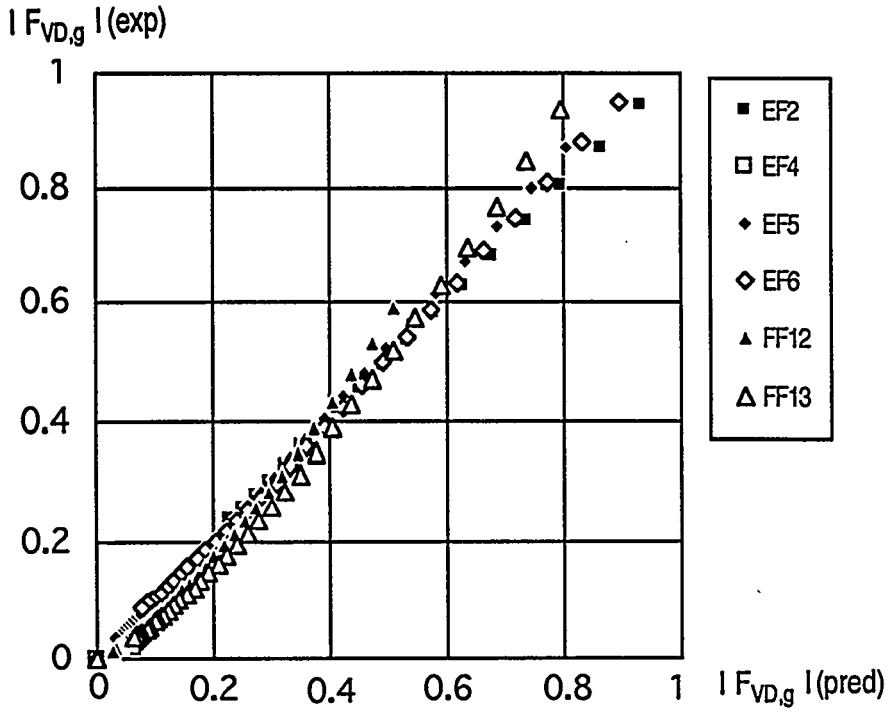

Fig. 2 Comparison of prediction by Eq.(11) and experimental data for the void drift force exerted on vapor phase $F_{VD,g}$

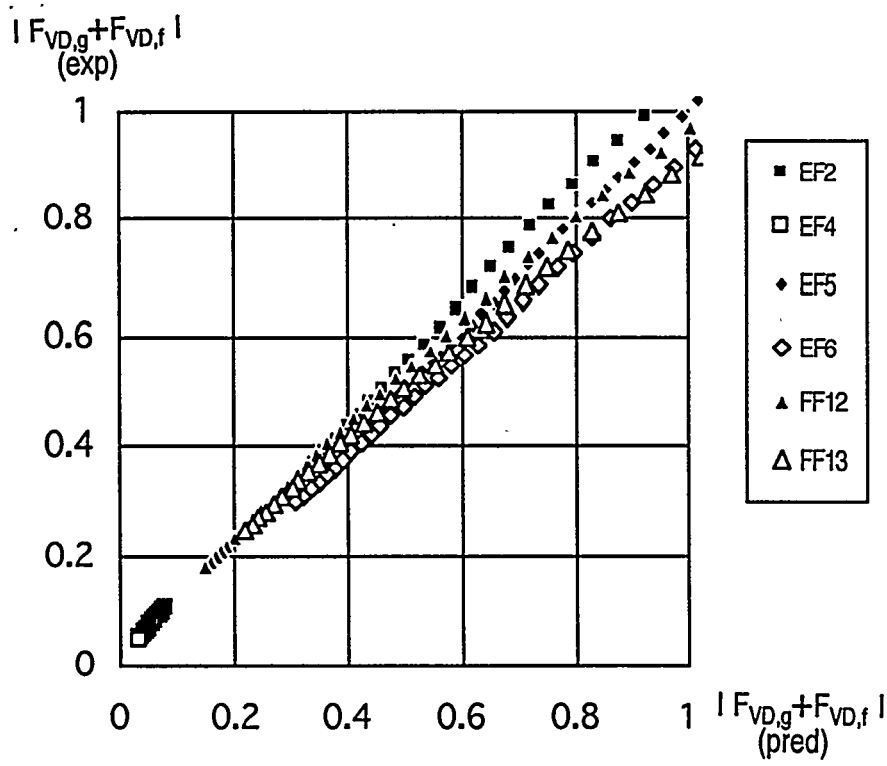

Fig. 3 Comparison of prediction by Eq.(12) and experimental data for the void drift force exerted on both liquid and vapor phases $F_{VD,g} + F_{VD,f}$

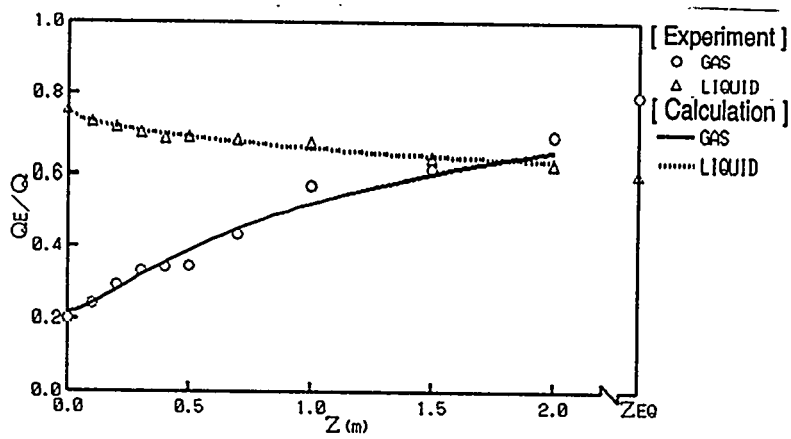

Fig. 4 Comparison of the calculation with experiment: Run EF2 flow redistributions of gas and liquid phases due to void drift in Channel E of the Ch.E-F test section.

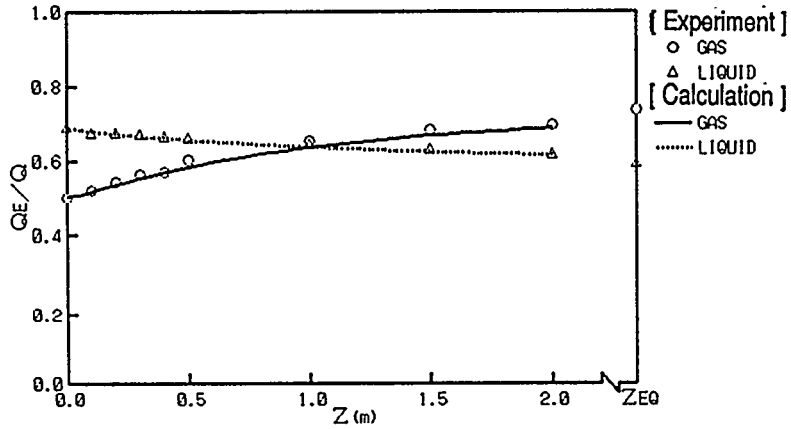

Fig. 5 Comparison of the calculation with experiment: Run EF6 flow redistributions of gas and liquid phases due to void drift in Channel E of the Ch.E-F test section.

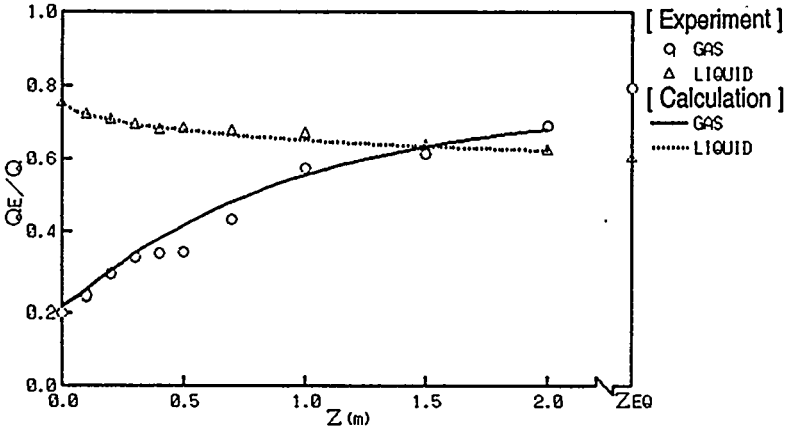

Fig. 6 Comparison of the calculation with experiment: Run EF2 flow redistributions in Channel E (α_{EQ} provided from the experimental data)

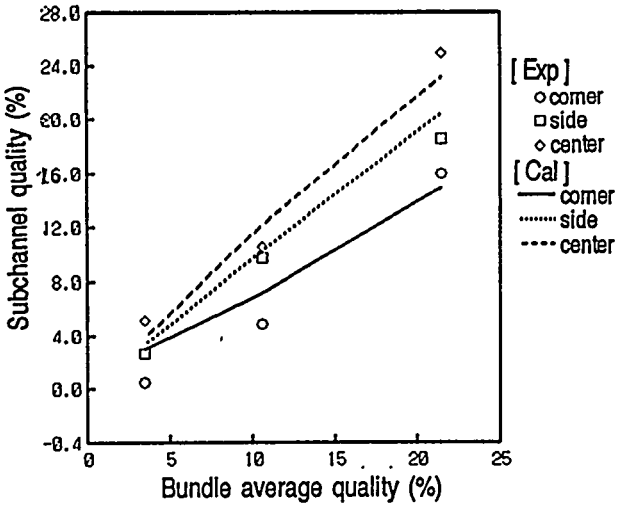

Fig. 7 Comparison of predicted and measured subchannel qualities: prediction with void drift model, GE3x3 bundle data (Ref.6)

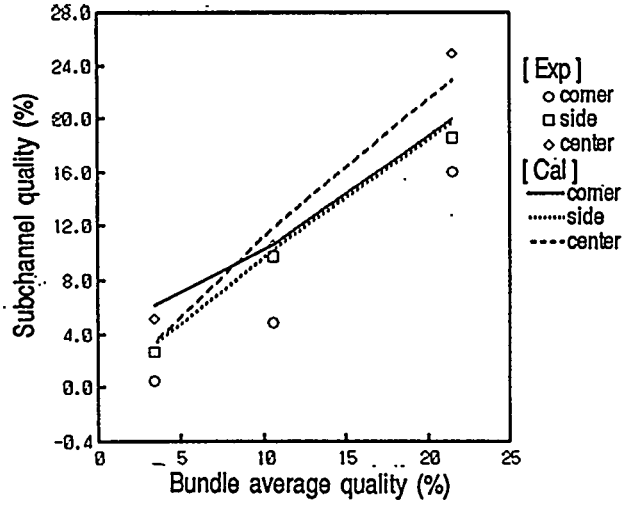

Fig. 8 Comparison of predicted and measured subchannel qualities: prediction without void drift model, GE3x3 bundle data (Ref.6)

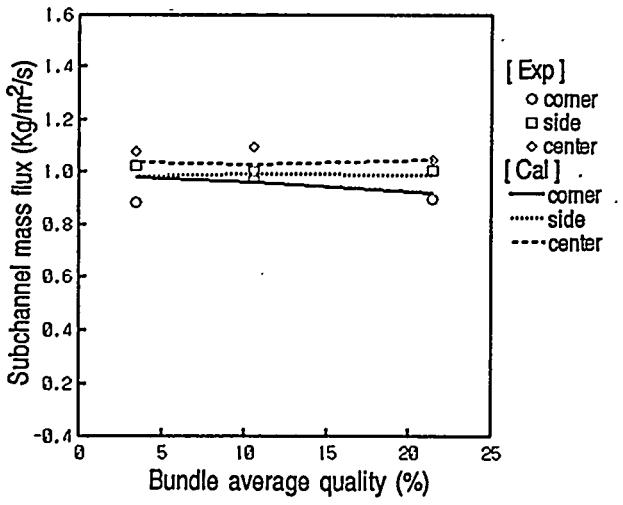

Fig. 9 Comparison of predicted and measured subchannel mass flux: prediction with void drift model, GE3x3 bundle data (Ref.6)

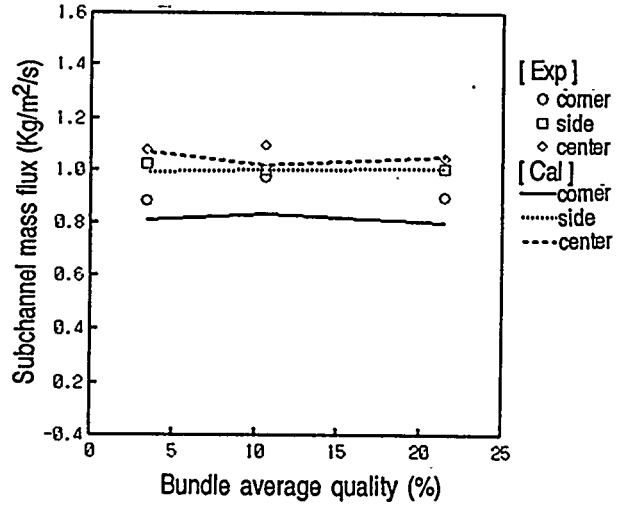

Fig. 10 Comparison of predicted and measured subchannel mass flux: prediction without void drift model, GE3x3 bundle data (Ref.6)

Large-Scale Transport Across Narrow Gaps in Rod Bundles

M.S. Guellouz and S. Tavoularis
Department of Mechanical Engineering, University of Ottawa
Ottawa, Canada K1N 6N5

Abstract

Flow visualization and hot-wire anemometry were used to investigate the velocity field in a rectangular channel containing a single cylindrical rod, which could be traversed on the centreplane to form gaps of different widths with the plane wall. The presence of large-scale, quasi-periodic structures in the vicinity of the gap has been demonstrated through flow visualization, spectral analysis and space-time correlation measurements. These structures are seen to exist even for relatively large gaps, at least up to W/D=1.350 (W is the sum of the rod diameter, D, and the gap width). The above measurements appear to be compatible with the field of a street of three-dimensional, counter-rotating vortices, whose detailed structure, however, remains to be determined. The convection speed and the streamwise spacing of these vortices have been determined as functions of the gap size.

1. Introduction

One of the main tasks of nuclear reactor thermal-hydraulic analyses is to predict heat transfer in rod bundle channel flows, which are commonly encountered in reactor cores. A well known but still puzzling phenomenon in such configurations is that the local friction factor and the local heat transfer coefficient in narrow gaps between adjacent fuel rods or a rod and the pressure vessel wall are rather insensitive to the gap width, even for relatively small widths. Among the various hypotheses that were put forward to explain this insensitivity, the most likely one appears to be the enhancement of cross-subchannel mixing due to large-scale, quasi-periodic pulsations, which transport fluid across the gap much more efficiently than small-scale turbulence does.

The existence of such flow pulsations in rod bundle flows was first detected by Rowe et al [1], who observed significant periodicity in the axial velocity autocorrelation function, measured in the region between the gap and the subchannel centre for a pitch-to-diameter ratio $P/D = 1.125$. No significant periodicity was seen for larger gap spacing but the reduction of the gap width led to stronger periodic flow pulsations in the region adjacent to the rod gap. The next relevant experiments were those by Tapucu [2] and Tapucu and Merilo [3] in a channel consisting of two parallel square subchannels, interconnected by a long lateral slot, thus modelling adjacent rod bundle subchannels. These authors observed a systematic waviness in the mean pressure variation along each subchannel, as well as flow pulsations across the slot, visualized by injecting tiny PVC beads. Tapucu and Merilo [3] noted that the wavelength of the pulsations seemed to increase with increasing gap clearance but they could not reach a conclusive description of either the pulsation wavelength or its amplitude.

The first systematic studies of flow pulsations across rod bundle gaps were performed by Hooper [4] and Hooper and Rehme [5], who confirmed their presence and observed that their frequency was proportional to the Reynolds number and that the periodic component of the momentum exchange became more dominant as the gap width was reduced. The above authors explained these flow pulsations by a parallel-channel instability mechanism, which produces vortex-like structures in the gap region. Rehme's [6,7,8] measurements, as well as those by Wu and Trupp [9], concurred with the above findings. Rehme [6] also speculated that the flow pulsations were caused by a static pressure instability between the subchannels. Quasi-periodic momentum transport was observed (Rehme [8]) to exist even for the relatively large value of the ratio W/D=1.30 (W is the sum of the rod diameter and gap width).

Möller [10] continued the work of Hooper and Rehme in order to determine experimentally the origin of the flow pulsations observed earlier and their dependency on the bundle geometry and Reynolds number. His power spectra of the azimuthal velocity components showed a very pronounced peak, at a location where the azimuthal turbulence intensity had a local maximum, and a weaker peak at the same frequency at a location 1.76 gap-widths away from the gap (W/D=1.072). The spectra of the pressure difference (measured with two microphones placed symmetrically on the two sides of the gap) showed an even more pronounced peak at the same frequency as the peak in the velocity fluctuation spectra. The frequency of the flow pulsations was found to increase with increasing Reynolds number and diminishing gap width. Möller [10] defined a Strouhal number as

$$Str = \frac{fD}{u^*} \qquad (1)$$

where f represents the peak frequency in the spectra, D is the rod diameter and u^* is the friction velocity, and found it to be inversely proportional to the gap width and independent of the Reynolds

number. Möller's [10] correlation analysis confirmed the findings of Hooper and Rehme, by showing flow pulsations to propagate over a large region of the subchannel. Based on the above results and the distribution of the vorticity normal to the wall, he proposed a model, according to which the flow pulsations were generated by the turbulent motion itself and are particular to the geometry of rod bundles. Möller concluded that the turbulence structure in the gap region was a coherent structure and that it is this motion that would be mainly responsible for the mass exchange between the subchannels of rod bundles.

The important contribution of the large-scale pulsations to the inter-subchannel mixing was demonstrated by Rehme [11] and Möller [12], who attempted to integrate the pulsation effects into the "lumped parameter" type of analyses of rod bundle flows. Most recently, Meyer and Rehme [13] presented some very relevant measurements in compound channels formed by two rectangular subchannels interconnected by a lateral slot. They documented in detail the formation of strong, large-scale, quasi-periodic flow pulsations in the slot region, and correlated their frequency with the slot geometry and the bulk velocity.

The above studies have demonstrated beyond doubt the presence and importance of quasi-periodic flow structures in rod bundles, however, they have not yet produced a complete description of all features of these structures, neither their relationship on the geometrical and dynamic flow parameters. The present work is aimed at further characterizing such structures, particularly those forming in outer subchannel gaps, with the ultimate objective to incorporate their effects in analytical and computational models of rod-bundle flows.

2. Flow Facility and Instrumentation

The flow facility (Figure 1) consists of an open-discharge wind tunnel, whose test section consists of a rectangular channel containing a suspended, traversable aluminum pipe ("rod") with a diameter of D = 101 mm. The hydraulic diameter and the length of the test section were, respectively, 1.59D and 54.0D. The channel was supplied with air produced by a blower through a pressure box with a cross section 9.4 times larger than the open test section area. A woven screen was stretched across the entrance of the channel to enhance the full development of the flow.

The rod was suspended at both ends as well as at a third location, placed at approximately 20D downstream of the tunnel entrance. Dial gauges provided accurate positioning of the rod. The plexiglass base of the channel contained an array of machined circular ports, which could be fitted with special plugs containing pressure taps or measuring probes. In addition to these, the channel base had a sliding plexiglass plate, 2.8D upstream of the exit end of the tunnel, which could be used for transverse traversing of the probes.

Measurements of wall shear stress were conducted with the use of a Preston tube and a flush-mounted hot-film probe. The Preston tube had an outer diameter of 0.72 mm and an inner to outer diameter ratio of 0.57; the wall shear stress was computed from the pressure difference using Patel's [14] procedure. The hot-film probe consisted of a miniature, flush-mounted sensor element (TSI 1268, platinum hot-film), with length and width of 1.5 mm and 0.5 mm, respectively. The hot-film was deposited on a quartz cylinder, which was fitted, through a teflon sleeve, to a plexiglass plug. The hot-film probe was calibrated *in situ* versus the Preston tube reading.

Cross-sensor probes were used for the measurement of the velocity components. Two types of probes were available. The first one was a cross-wire probe (TSI, model 1248), inserted into the flow from the exit end of the channel and mounted on a mechanism permitting accurate traversing

azimuthally, radially and longitudinally with respect to the rod. The second probe was a boundary layer type, cross-film probe (TSI, model 1249) that measures the streamwise and parallel-to-the-wall velocity components. This probe was inserted through the plexiglass base of the channel and was traversed normal to it.

For the measurement of the mean and turbulence statistics, the probes were calibrated versus a Pitot tube, using standard procedures. For the measurement of two-point correlations, however, a simpler approach was followed, by which the overheat ratios of the two sensors in each probe were adjusted to provide nearly equal velocity sensitivities; then, the streamwise velocity fluctuation was computed from the sum of the two digitized signals and the transverse fluctuation from their difference. As a test of this method, it was found that the voltage difference of the two sensors changed by less than 4% of the corresponding rms values over the entire velocity range of interest.

The hot-wire and hot film signals were low pass filtered at 380 Hz (3dB point) and discretized at a frequency of 1 kHz. 50 records, each containing 4096 points and separated by 1 s, were recorded at each position.

3. Measurements

3.1 The flow in the wall subchannel

Measurements of the centerline static pressure distribution in the streamwise direction, for several rod-wall gap sizes, indicated that the pressure gradient was essentially constant in the downstream end of the channel, inferring that the velocity profile was essentially fully developed. Further manipulation of the flow in the pressure box resulted in reducing the flow asymmetry in the test section to less than 1% of the corresponding averages.

The bulk velocity, defined in the region bounded by the rod surface and the surrounding line of maximum velocity (Ouma and Tavoularis [15]), as

$$U_b = \frac{1}{A}\int_0^{\pi}\int_0^{y_o} U(r,\phi)\, r\, dr\, d\phi \qquad (2)$$

was found to be essentially independent of the rod-wall gap size. In the present tests, U_b = 10.1 m/s ±2%, for 1.050 < W/D < 1.250. The Reynolds number, Re_h, based on the bulk velocity and the hydraulic diameter of the entire channel, was approximately equal to 140,000.

A few typical isotachs (i.e. contours of constant axial mean velocity) and isocontours of the axial, u', and azimuthal, u_ϕ', rms turbulent velocities, for the W/D = 1.100 configuration are shown in Figure 2.

The variation of the mean local wall shear stress, τ_w, normalized by the bulk dynamic pressure, $\frac{1}{2}\rho U_b^2$, , measured around the periphery of the rod and along the channel bottom wall, is presented in Figure 3. This coefficient varied only slightly for 1.100 < W/D < 1.250, but, for smaller gaps, it presented increasingly lower minima on the symmetry plane. In addition to the mean, the fluctuations of the wall shear stress along the bottom wall were also measured, using the hot-film probe. These fluctuations were quite strong, with rms values typically about 7% of the corresponding local means. The profiles of the dimensionless rms wall shear stress, shown in Figure 3, appear to be similar to the corresponding mean profiles.

3.2 *Flow visualization*

Flow visualization was performed by injecting smoke through a thin tube inserted in the gap and illuminating the gap with a transverse thin sheet of light produced by passing a 100 mW laser beam through a cylindrical lens. The visualized flow was recorded by a video camera, which had a minimum exposure time of 0.001 sec per frame and a fixed speed of 30 frames per sec. For clarity of the pictures, the latter were taken at relatively low velocities, typically at Re_h = 16,000, and, usually, with an exposure time of 0.004 sec. At higher velocities, the general appearance of the pictures was essentially the same, however, the obtained pictures were blurred. For presentation here, sections of the video tape were digitized, frame by frame. A typical sequence of digitized frames of the video film (not consecutive ones) is presented in Figure 4.

The visualization clearly showed the presence of large-scale pulsations, which occurred almost periodically across the gap. Turbulent diffusion was also visible, but it was obviously much weaker than the large-scale transport. Such pulsations were visible over the entire range of Reynolds numbers possible in the present setup, including laminar flows (this range remains to be documented) and highly turbulent flows, and persisted even for gap sizes as small as 0.025D. The flow pulsations were not perfectly periodic at any Reynolds number, but displayed some perceptible frequency irregularities and occasional jittering. The lateral excursions of the smoke reached beyond the projection of the rod for relatively narrow gaps but they appeared to diminish progressively to about $D/8$ (on each side of the axis) as the gap widened to W/D=1.200. At first glance, this diminishing of the smoke streak amplitude may seem to indicate a decrease of the cross-sectional area of the vortices. However, the same effect could be caused by a weakening of the vortex strength and/or the increasing local convection speed at wider gaps. Therefore, although useful in confirming the presence of pulsations, smoke streaks cannot provide conclusive information about the size and strength of the presumed vortices.

3.3 *Velocity fluctuation patterns*

The structure of possible coherent motions was first investigated qualitatively by inspection of the velocity signals, samples of which are shown in Figure 5. This approach generally confirmed the presence of quasi-periodic flow pulsations across the gap, in conformity with the flow visualization results and previous studies. The highest degree of regularity was exhibited by the w component on the centreplane of the channel and at nearby locations, while, at larger distances from the centreplane, the fluctuations of the same component appeared both to decrease in amplitude and to lose their periodic character. The u component also exhibited a quasi-periodic variation, which was most noticeable at intermediate distances from the centreplane and weakened on the centreplane as well as at relatively large distances from it. The velocity time series provided by a fixed probe can be viewed as streamwise profiles across a structure convected downstream by some constant convection speed, while not changing substantially during that time. The present velocity signals have patterns which are generally compatible with the velocity field of an array of convected parallel vortices, distorted by small-scale turbulence and by occasional vortex interactions. Although the typical fluctuation patterns corresponding to the passage of a vortex are easily recognized by eye, they also exhibit substantial cycle-to-cycle variation and frequent phase shifts, which would obscure the statistical representation of these structures. This can be seen by considering typical spectra of selected, quasi-periodic, velocity signals (see Figure 6). Although these spectra generally exhibit

distinct peaks, presumably corresponding to the most likely convection frequency of these structures, the peaks are fairly wide and tend to be obscured at locations where the effects of these vortices are either weak or not well represented by the selected signal. In conclusion, it is clear that the proper identification of the statistical features of these vortical structures is not an easy matter and would likely require the use of sophisticated methods, such as conditional sampling and pattern recognition techniques. The application of such an approach to the present flow is currently in progress, but its results are still too tentative for presentation here.

3.4 Two-point measurements

The complete mapping of the instantaneous flow structure would require the simultaneous measurement of the velocity vectors throughout a flow region. This was not possible with the available means, but, instead, an approximate mapping was attempted by conducting two-point velocity measurements with the use of two cross-wire probes. The first probe was fixed at a position (x,y,z) and the other one was traversed to a distance $(\Delta x,\Delta y,\Delta z)$ from the fixed probe. As the present channel flow was fully developed, all statistics should be independent of the streamwise position, x (this was verified by correlation measurements performed at different x positions near the exit end of the channel). Furthermore, for the present work, both probes were always positioned at the same distance, y, from the bottom wall, so that $\Delta y = 0$. Therefore, all measured statistical properties would only be functions of $z,\Delta x,\Delta z$ and the time difference, Δt. For example, the measured two-point, space-time correlation of the streamwise velocity fluctuation would be

$$R_{uu}(z,\Delta x,\Delta z,\Delta t) = \frac{\overline{u(z,t)\, u(z+\Delta z,\Delta x,t+\Delta t)}}{u'(z)\, u'(z+\Delta z,\Delta x)} \qquad (3)$$

From the above definition, one could recover the single-point autocorrelation by letting $\Delta x = \Delta z = 0$, and the two-point, space correlation by letting $\Delta t = 0$.

A set of measurements were taken with the fixed probe at the centre of the gap and the traversed probe at a distance from the bottom wall equal to half the gap width. Figure 7 presents the two-point correlations R_{uu} and R_{ww}, measured for several gap widths with the two probes aligned on the symmetry plane of the test section. The corresponding correlations R_{uw} and R_{wu}, not presented here, attained very low values for these probe positions. The correlations in Figure 7 show clear oscillations, which can be interpreted as evidence of spatial periodicity, only for the smaller gap widths and mostly for the transverse velocity component. In view of other evidence for the existence of quasi-periodic flow pulsations at all considered gaps, one feels compelled to search for an explanation for the non-oscillatory appearance of most correlations in Figure 7. First of all, it has already been observed in the flow visualisation images and the velocity signals that the repeating patterns ("coherent structures") vary substantially among themselves and that their regular sequence is often interrupted by other, distinct events. In particular, the latter events, which could represent structure breakdowns or mergings, introduce shifts in the spacing of consecutive structures and, thus, obscure their periodicity. The increasing intensity of small-scale turbulence at larger gaps further weakens the periodic appearance of velocity correlations. The differences in the appearance of the u and w correlations is compatible with the velocity pattern in the field of a sequence of vortices, centred at or near the symmetry plane. The above limitations notwithstanding, the spatial correlations in Figure 7 had a striking feature: they remained high over a relatively long distance, much longer than

the expected size of typical turbulent eddies.

The presence of convected, organized structures is better seen in the space-time correlations presented in Figure 8, in which both probes were also located on the centreplane. The R_{ww}, in particular, exhibited correlation peaks larger than 0.90, which essentially did not decay with streamwise probe separation as large as $\Delta x/D \approx 6$, in contrast with similar measurements in non-coherent turbulent shear flows (e.g. see Tavoularis and Corrsin [16]). A measurable correlation peak of about 0.20 was observed even for a probe separation of 43 D, with the upstream probe at 10 D from the channel entrance. These results seem to indicate that coherent structures formed close to the channel entrance and were convected downstream, often with relatively small change in their features over the entire channel length. The average convection speed, U_c, of these structures can be estimated from the above space-time correlations as the ratio $\Delta x/\Delta t_{max}$ of the streamwise probe separation over the time delay corresponding to the maximum correlation. A typical plot of Δt_{max} vs. Δx, shown in Figure 9, justifies this approach, as it clearly shows that these quantities were proportional. The use of a convection speed permits the estimation of streamwise, two-point, space correlations from corresponding single-point, time correlations, which are easier to measure. This is achieved by multiplying the time shift in the single-point, time correlations by the convection speed to obtain the streamwise separation. The accuracy of these estimates is demonstrated in Figure 7.

The above results will be further analysed and discussed in the following section. Another set of measurements that appeared to be useful was the measurement of space-time correlations with the probes separated in the transverse as well as the streamwise direction. A summary of such results, obtained with the fixed probe on the centreplane, and making use of the convection speed to supplement the two-point measurements, is shown in the form of iso-correlation contours in Figure 10. The increment in the transverse spacing of the probes was $\Delta z = 0.1D$, while the streamwise increment, based on the convection speed $U_c = 7.9$ m/s, was $\Delta x = 0.078D$. These results clearly prove the symmetry of the flow about the centreplane. In addition, the R_{ww} contours seem to indicate the presence of at least two structures with similar features, with an average streamwise spacing of about 2.1 D, for the case presented in that Figure. Additional two-point, space-time correlations were taken with the fixed probe positioned off-centre. For example, Figure 11 shows that R_{uu} correlations peaked at time differences consistent with the concept of convected structures. The main peaks were positive or negative depending on the position of the fixed probe and the transverse spacing of the probes. One may be tempted to use these results, in conjunction with a physical model of the dominant structures, in order to estimate the spatial features of these structures. At the same time, it must be recognized that correlation results could actually mask the distinct features of individual structures, as they are produced by indiscriminate averaging of all events.

4. Analysis of the Results and Discussion

The present measurements have further documented the already known fact that organized, quasi-periodic, vortical structures form in the vicinity of the narrow gap between a circular rod and a plane wall as well as in a variety of similar configurations. For an incorporation of the effects of these structures into a practical model, one should like to estimate their shapes, strengths, orientations and lateral extents and their dependence on the channel geometry and the Reynolds number. This task, however, may be much more difficult than it appears to be at first glance. First of all, because of the narrowness of the passage, these structures would have a strongly three-dimensional character: although it is likely that, near the gap centre, their axes could be parallel to the centreplane, these

same axes must turn as they approach the flat wall or the rod surface and continue into the neighbouring subchannels. Furthermore, the cross-sections of these structures are likely to be non-axisymmetric and non-planar. Although certain features of the present results and previous measurements appear to point to an array of alternating, counter-rotating structures, it is not clear how consecutive structures are connected. Therefore, the following discussion must be treated as preliminary and quite tentative.

The only features of the structures that can be estimated with relative confidence are their average convection speed, U_c, and their average streamwise spacing, λ. U_c, computed from the peaks of space-time correlations, decreased significantly with diminishing gap width (Figure 12) and approached an asymptote at $W/D > 1.25$. For rough purposes, one may approximate its variation by a fitted exponential curve. The convection speed had a value intermediate between the maximum mean speed in the neighbouring open subchannel and the mean speed in the gap centre. The streamwise spacing between two consecutive structures could be estimated as half the "wavelength" of the oscillations in the spatial velocity correlations or, alternatively, as

$$\lambda = \frac{U_c}{f} \tag{4}$$

where f is the frequency of the oscillations, estimated from the peak in the measured power spectra. Both approaches became increasingly uncertain as the gap width increased. The vortex spacing obtained in this manner seems to vary linearly with gap width (Figure 13), in agreement with Möller's [10] findings. In the above analysis, it has been implicitly assumed, by analogy to two dimensional wakes and mixing layers, that the vortex spacing is independent of the Reynolds number, at least within the ranges of the available rod bundle experiments. The validity of this assumption will be tested in the future.

To help interpret the experimental results, we have examined the fields of various arrays of two-dimensional vortices, for example a street of counter-rotating, "potential" vortices being convected with a constant velocity, U_c. Both the case with the axes of consecutive vortices on the centreplane and the case with these axes symmetrically located with respect to the gap centreplane were considered. Each of these fields produced certain correlations that were similar to the measured ones but also correlations that were incompatible with the measurements. In conclusion, we have so far been unable to formulate a physical model of coherent structures that is consistent in all its features with the measurements. Additional measurements and analysis are in progress to further clarify this issue.

5. Conclusions

The presence of large-scale, quasi-periodic structures in the gap formed by a single rod suspended in a rectangular channel has been demonstrated through flow visualization and space-time correlation measurements. These structures are seen to exist even for relatively large gaps, at least up to W/D=1.350. The above measurements appear to be compatible with the field of a street of three-dimensional, counter-rotating vortices, whose detailed structure, however, remains to be determined. The convection speed and the streamwise spacing of these vortices have been determined as functions of the gap size.

Acknowledgement

Financial support for this work was provided by the Natural Sciences and Engineering Research Council of Canada and by the Atomic Energy of Canada Ltd.

Nomenclature

A area of the region bounded by the rod surface and the line of maximum velocity
D rod diameter
E_{ww} Power spectral density of w
f frequency
P rod pitch
r radial distance from the rod surface
Re_h Reynolds number based on the bulk velocity and hydraulic diameter of the channel
R_{uu}, R_{ww} two-point velocity correlation coefficients; the first subscript corresponds to the fixed probe and the second subscript to the moving probe
Str Strouhal number
t time
U velocity
U_b bulk velocity
U_c convection speed
u, u_r, u_ϕ velocity fluctuations in cylindrical coordinates
u, v, w velocity fluctuations in Cartesian coordinates
u^* friction velocity
W wall subchannel width
x streamwise coordinate
y vertical distance from the bottom wall
y_o radial distance from the rod surface to the measured line of maximum velocity
z transverse distance from the line of symmetry of the test section

Greek symbols

Δt time delay
Δx probe separation in the streamwise direction
Δz probe separation in the transverse direction
λ wavelength of oscillations
ρ fluid density
τ_w wall shear stress
ϕ peripheral coordinate

Subscripts and superscripts

$( )'$ root mean square

References

[1] D.S. Rowe, B.M. Johnson and J.G. Knudsen, "Implications concerning rod bundle crossflow mixing based on measurements of turbulent flow structure", Int. J. Heat Mass Transfer 17, 407-419 (1974).

[2] A. Tapucu, "Studies on diversion cross-flow between two parallel channels communicating by a lateral slot. I: transverse flow resistance coefficient", Nucl. Eng. Des. 42, 297-306 (1977).

[3] A. Tapucu and M. Merilo, "Studies on diversion cross-flow between two parallel channels communicating by a lateral slot. II: axial pressure variations", Nucl. Eng. Des. 42, 307-318 (1977).

[4] J.D. Hooper, "The development of a large structure in the rod gap region for turbulent in line flow through closely spaced rod arrays", Proc. 4th Symp. Turb. Shear Flows, Karlsruhe, 1.23-1.27 (1983).

[5] J.D. Hooper and K. Rehme, "Large-scale structural effects in developed turbulent flow through closely-spaced rod arrays", J. Fluid Mech. 145, 305-337 (1984).

[6] K. Rehme, "The structure of turbulent flow through rod bundles", Nucl. Eng. Des. 99, 141-154 (1987).

[7] K. Rehme, "Turbulent flow through two asymmetric rod bundles", Heat Technol. 5, 19-37 (1987).

[8] K. Rehme, "The structure of turbulence in wall subchannels of a rod bundle", Atomkernenergie Kerntechnik 49, 145-150 (1987).

[9] X. Wu and A.C. Trupp, "Experimental study on the unusual turbulence intensity distributions in rod-to-wall gap regions", Exper. Therm. Fluid Sci. 6, 360-370 (1993).

[10] S.V. Möller, "On phenomena of turbulent flow through rod bundles", Exper. Therm. Fluid Sci. 4, 25-35 (1991).

[11] K. Rehme, "The structure of turbulence in rod bundles and the implications on natural mixing between the subchannels", Int. J. Heat Mass Transfer 35, 567-581 (1992).

[12] S.V. Möller, "Single-phase turbulent mixing in rod bundles", Exper. Therm. Fluid Sci. 5, 26-33 (1992).

[13] L. Meyer and K. Rehme, "Large-scale turbulence phenomena in compound rectangular channels", Exper. Therm. Fluid Sci. 8, 286-304 (1994).

[14] V.C. Patel, "Calibration of the Preston tube and limitations on its use in Pressure gradients", J. Fluid Mech. 23, 185-208 (1965).

[15] B.H. Ouma and S. Tavoularis, "Flow measurements in rod bundle subchannels with varying rod-wall proximity", Nucl. Eng. Des. 131, 193-208 (1991).

[16] S. Tavoularis and S. Corrsin, "Experiments in nearly homogeneous turbulent shear flow with uniform mean temperature gradient; Part1", J. Fluid Mech. 104, 311-347 (1981).

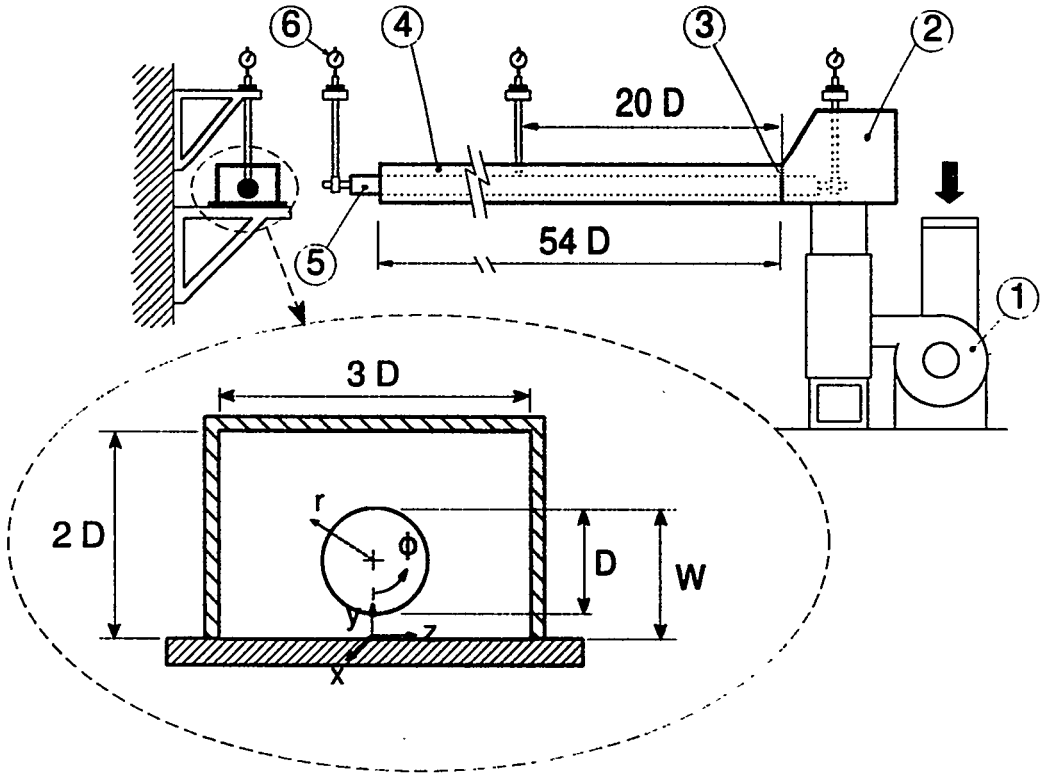

Figure 1: Sketch of the flow facility showing the fan (1), the pressure box (2), the woven screen (3), the flow section (4), the rod (5) and the micrometers and rod supports (6).

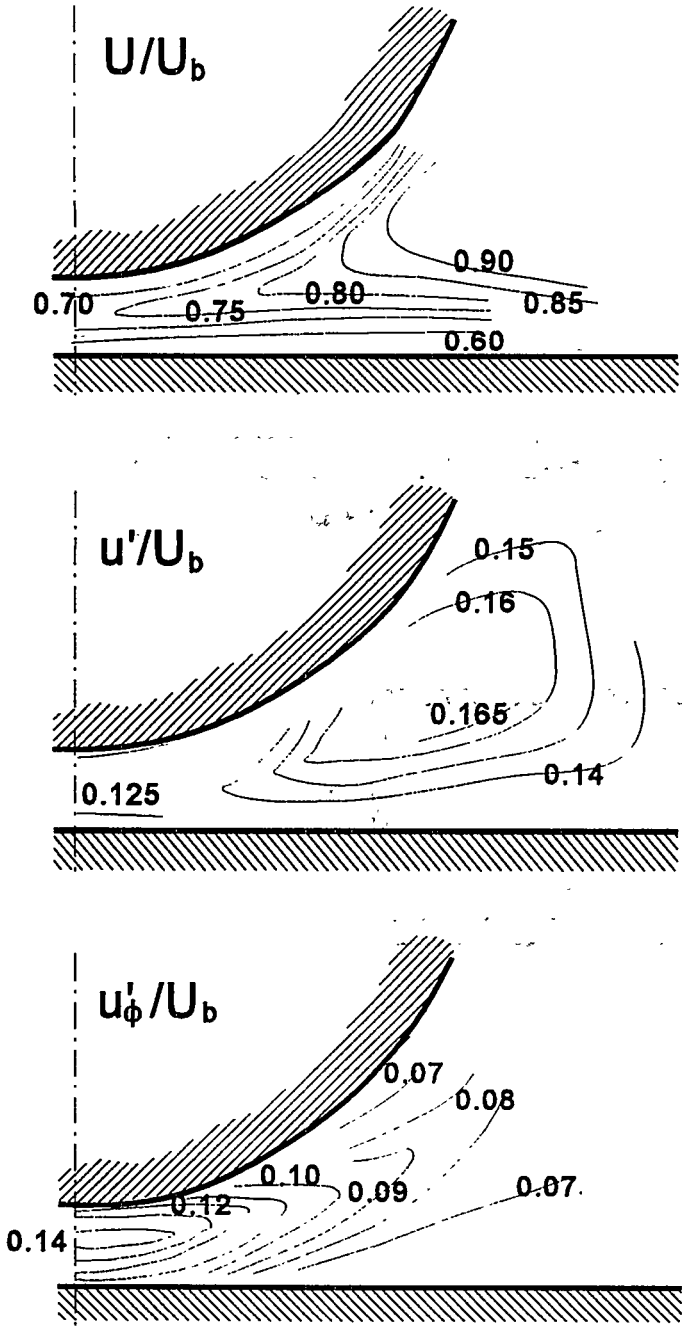

Figure 2: Isotachs (contours of constant U/U_b) and contours of constant axial and azimuthal turbulent intensities (u'/U_b and u_ϕ'/U_b) in the rod-wall gap region for W/D=1.100.

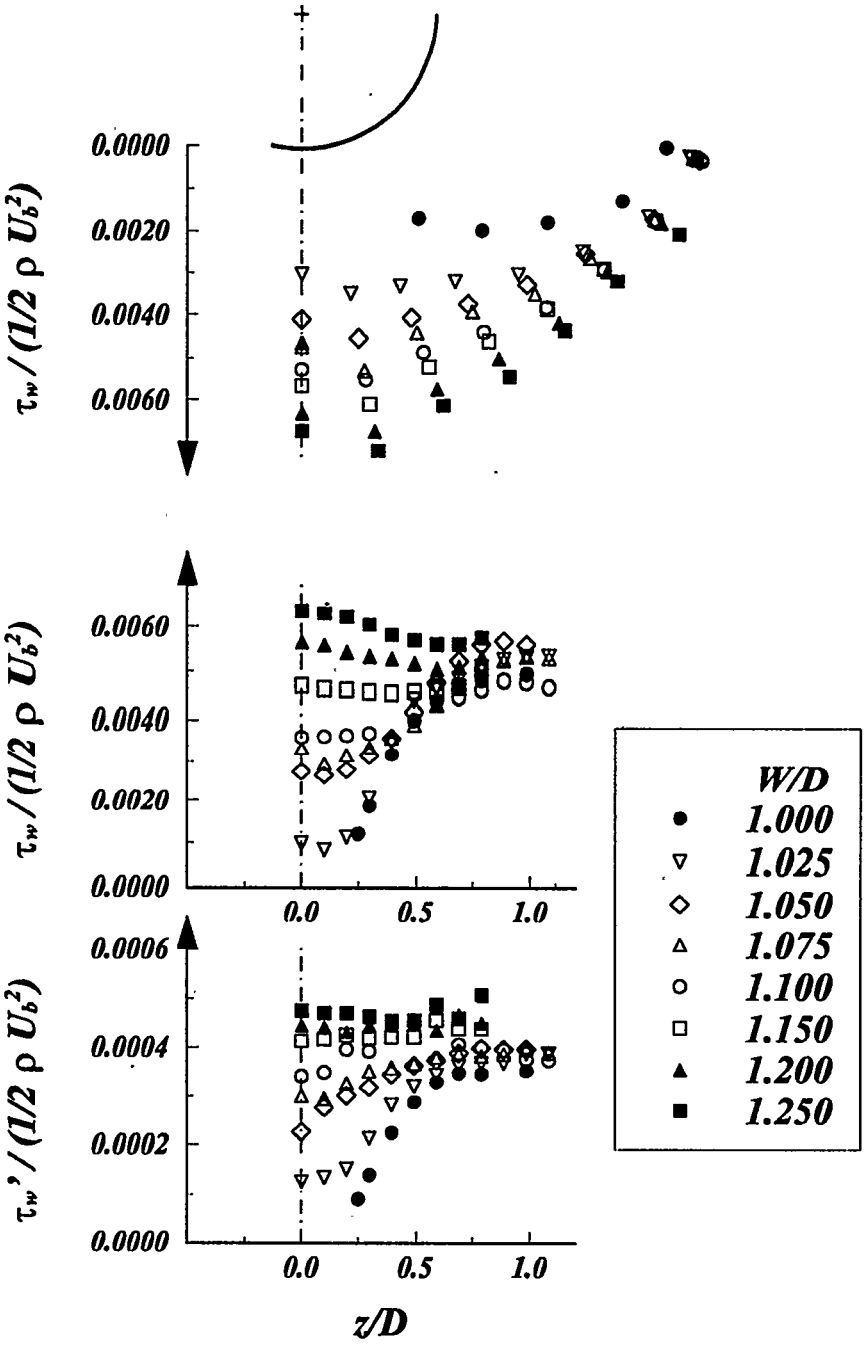

Figure 3: Mean wall shear stress around the rod (top; polar coordinates) and along the bottom wall (middle) of the channel; rms wall shear stress along the bottom wall (bottom) of the channel.

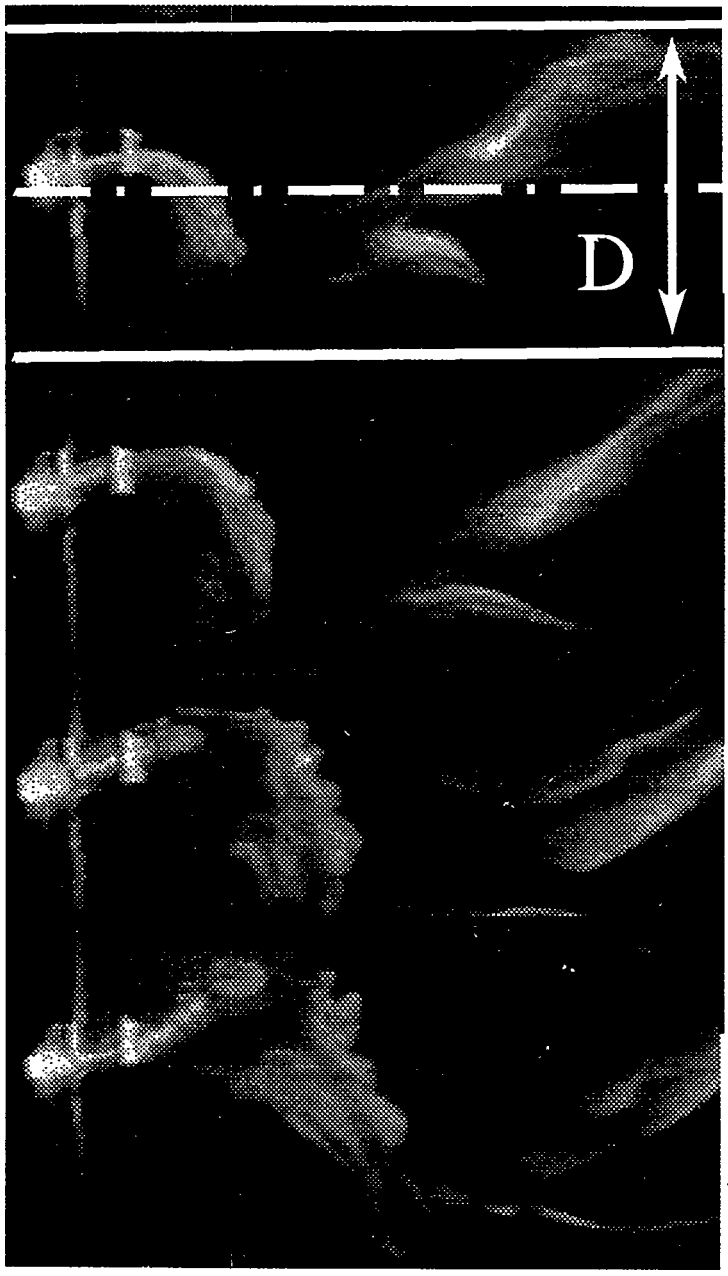

Figure 4: Sample of flow visualization images from the videotape; time interval between frames equal to 0.10 s.

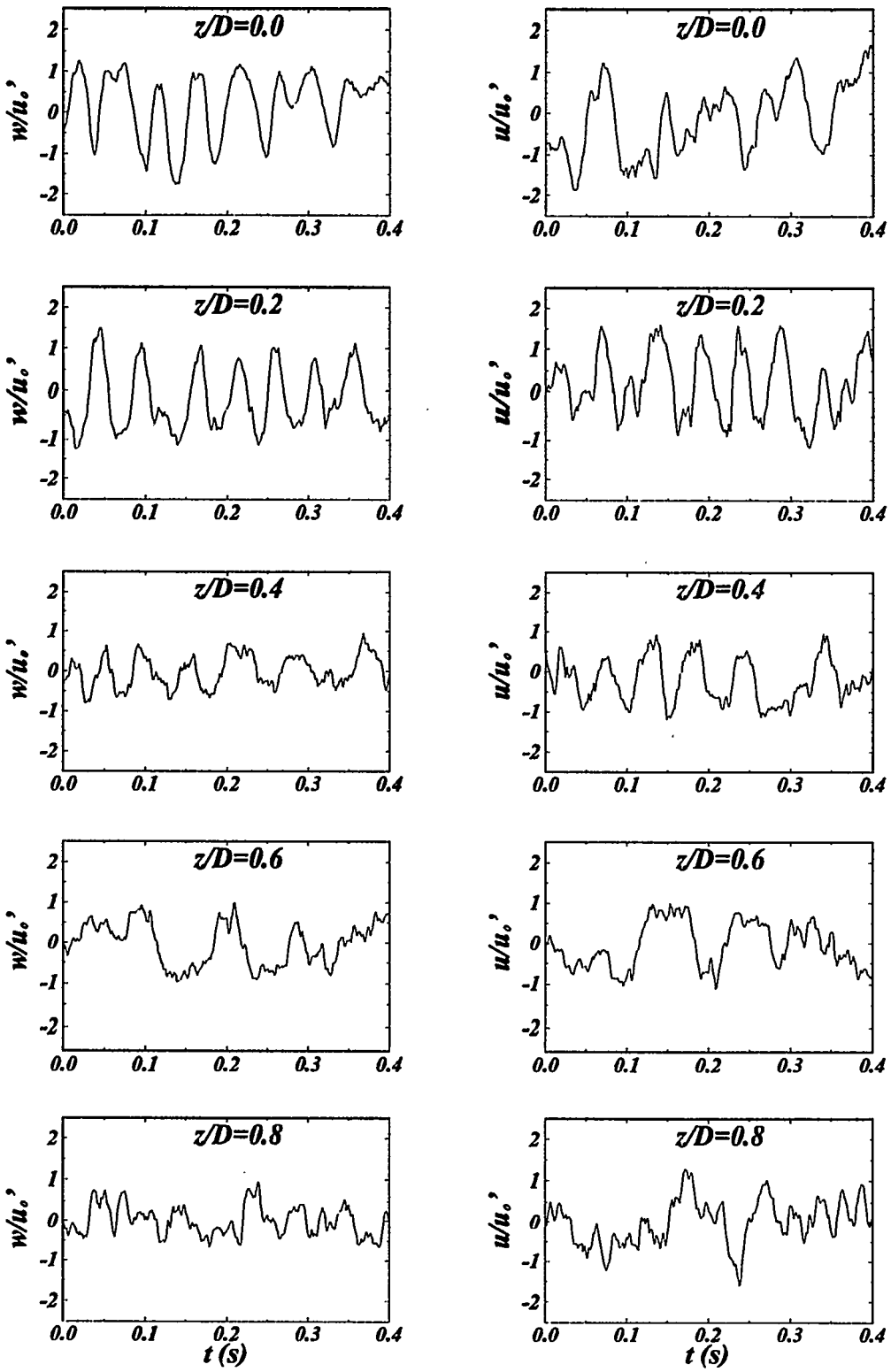

Figure 5: Transverse and streamwise velocity traces at several transverse positions, normalized by the rms streamwise velocity, u_o', at z/D=0.0 (W/D=1.100 and y/D=0.050).

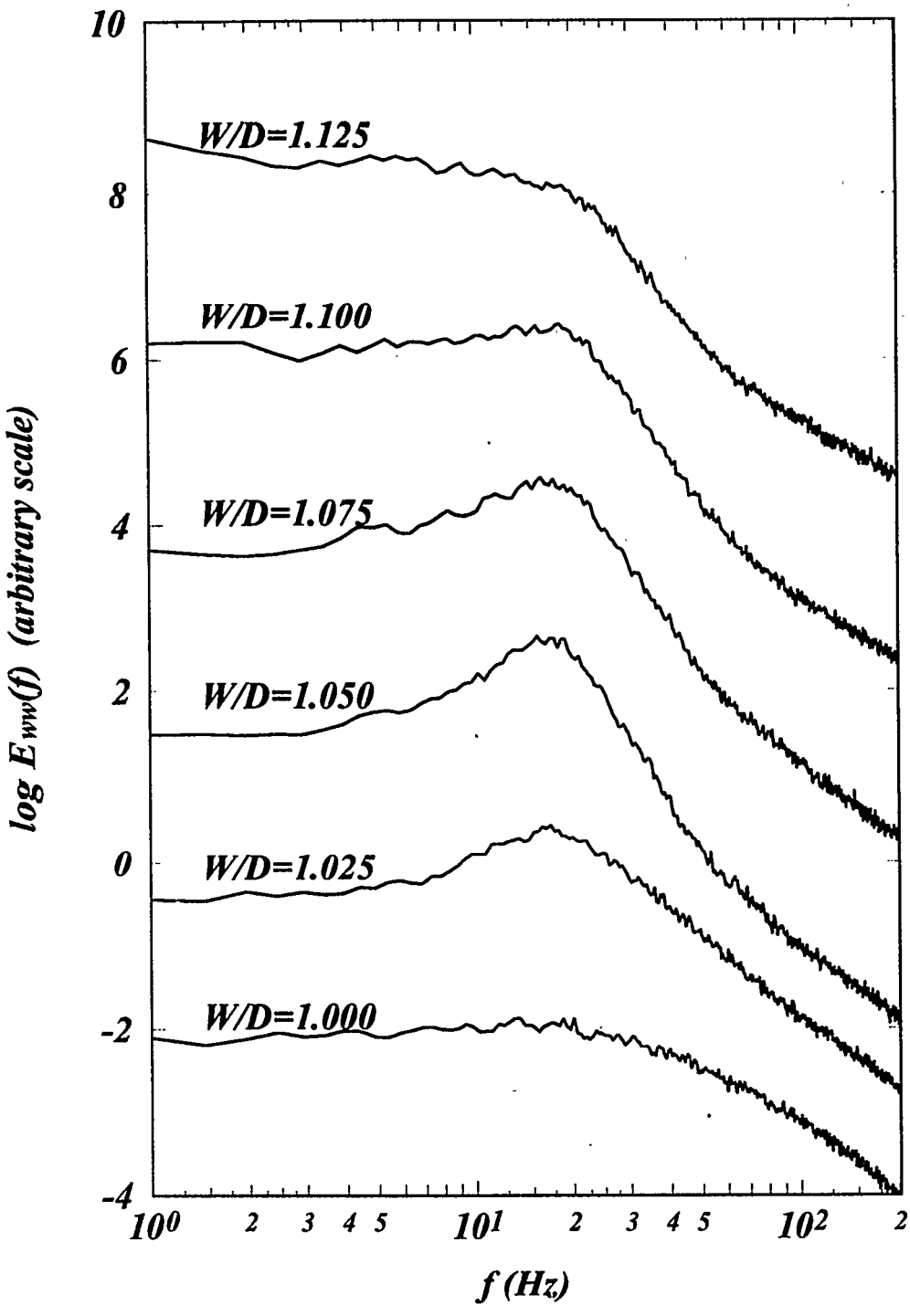

Figure 6: Power spectra of the transverse velocity component at the center of the gap, except for the cases with W/D=1.000 and 1.025, for which z/D=0.25 (arbitrary scale; different spectra have been staggered by two decades).

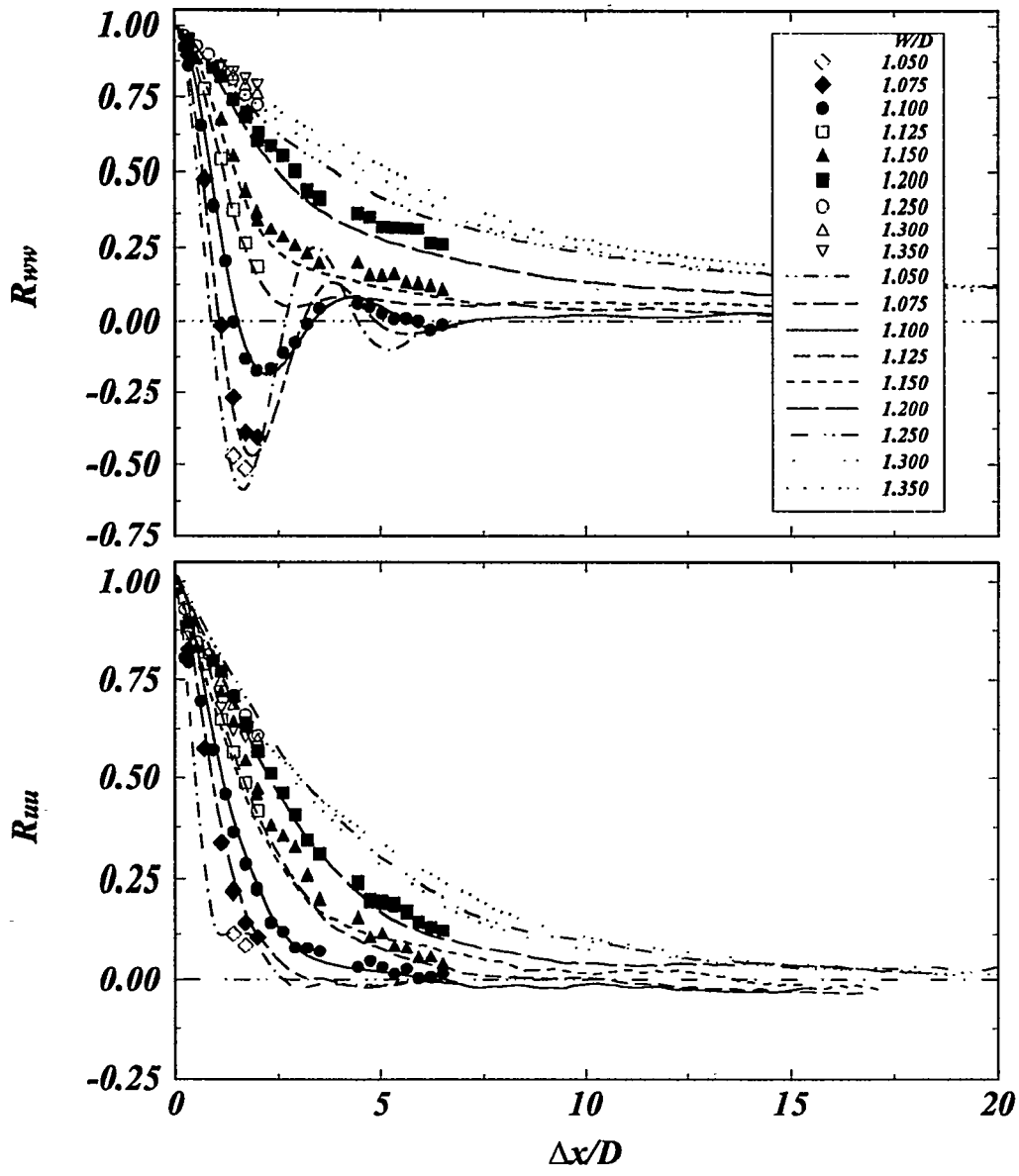

Figure 7: Two-point velocity correlations measured for several gap widths with the two probes aligned on the symmetry plane of the test section. Symbols represent actual measurements, while lines are estimates from corresponding single-point time correlations.

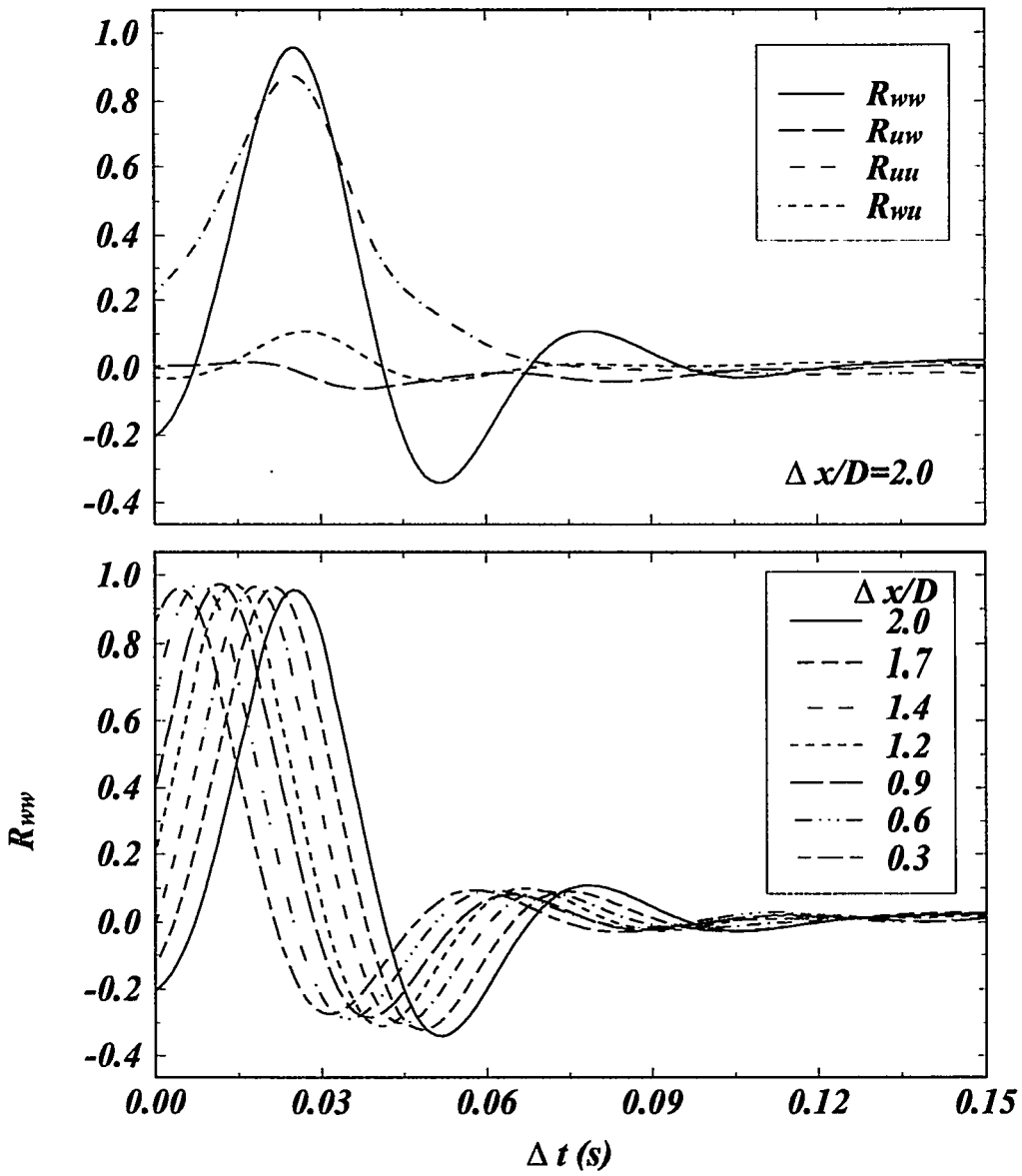

Figure 8: Space-time correlations with both probes located on the centreplane (W/D=1.100).

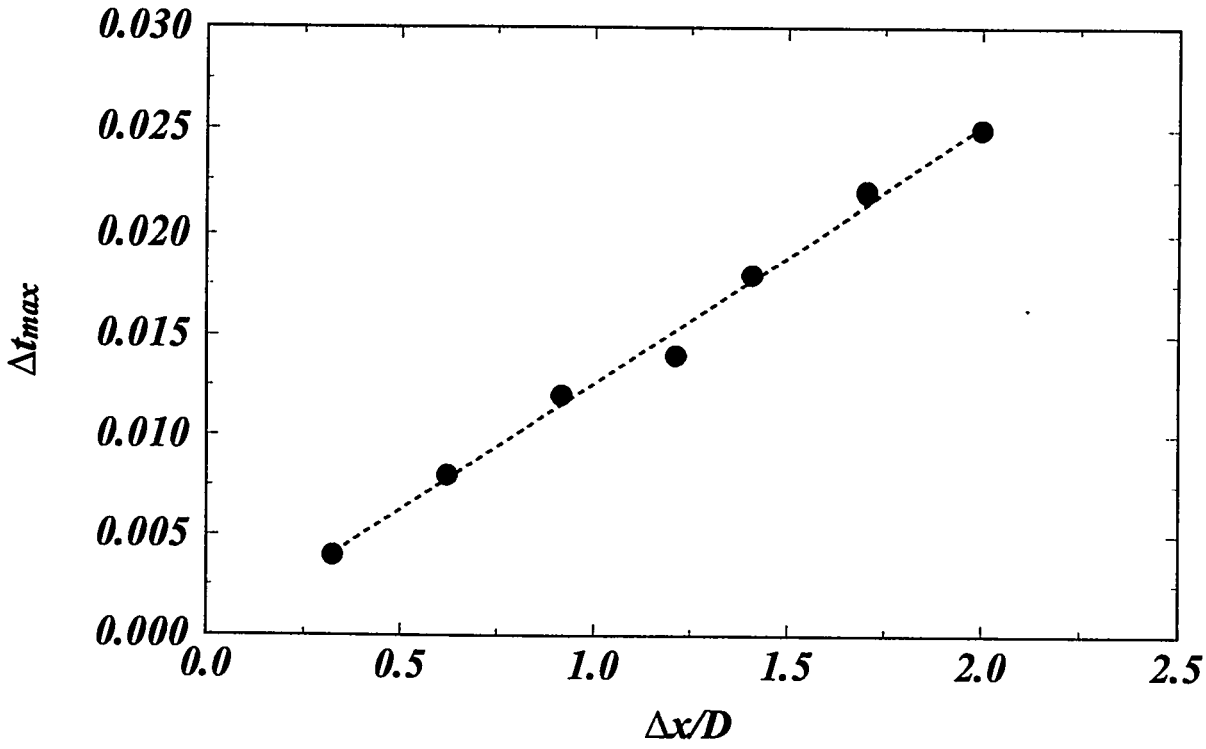

Figure 9: Time delay corresponding to the maximum correlation, R_{uu}, as a function of streamwise probe separation (W/D=1.100).

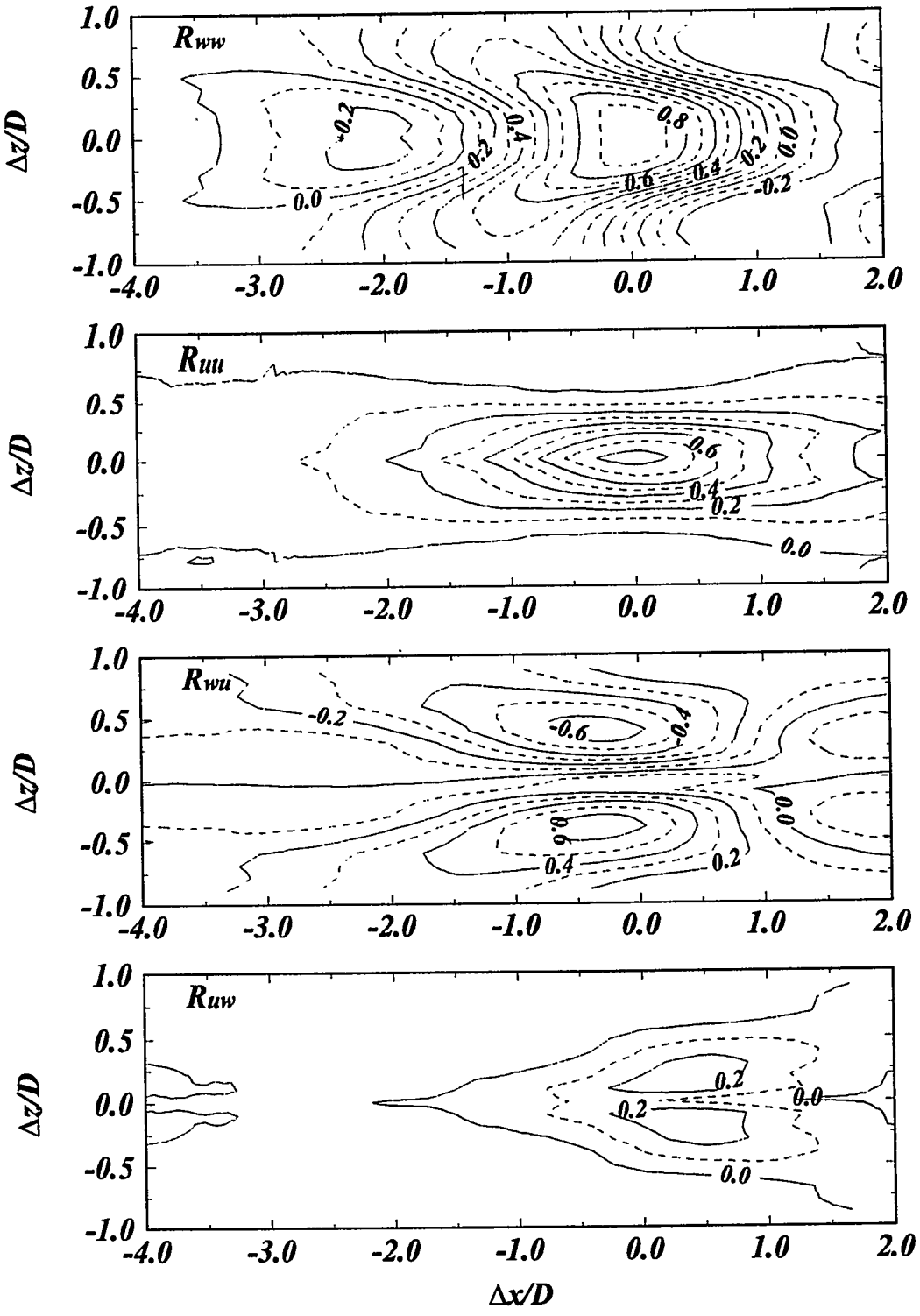

Figure 10: Iso-correlation contours for W/D=1.100.

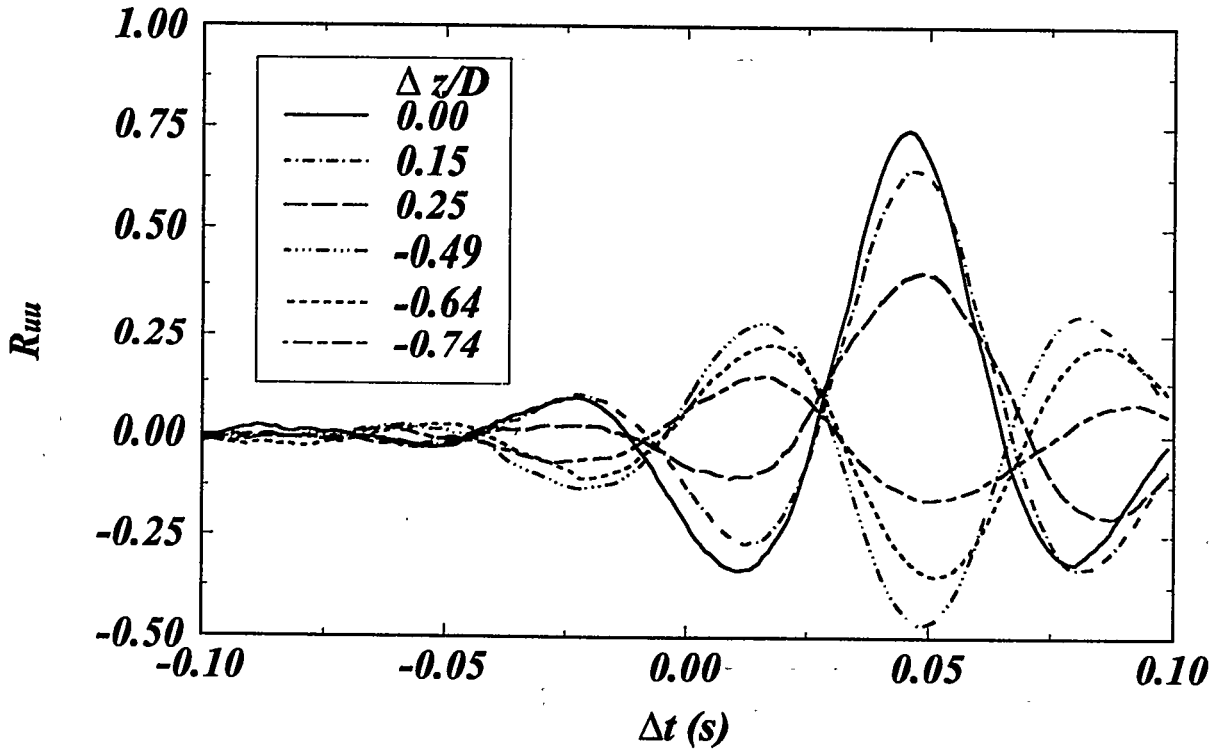

Figure 11: Space-time correlations R_{uu} (z/D=0.25; $\Delta x/D$=2.0; W/D=1.025).

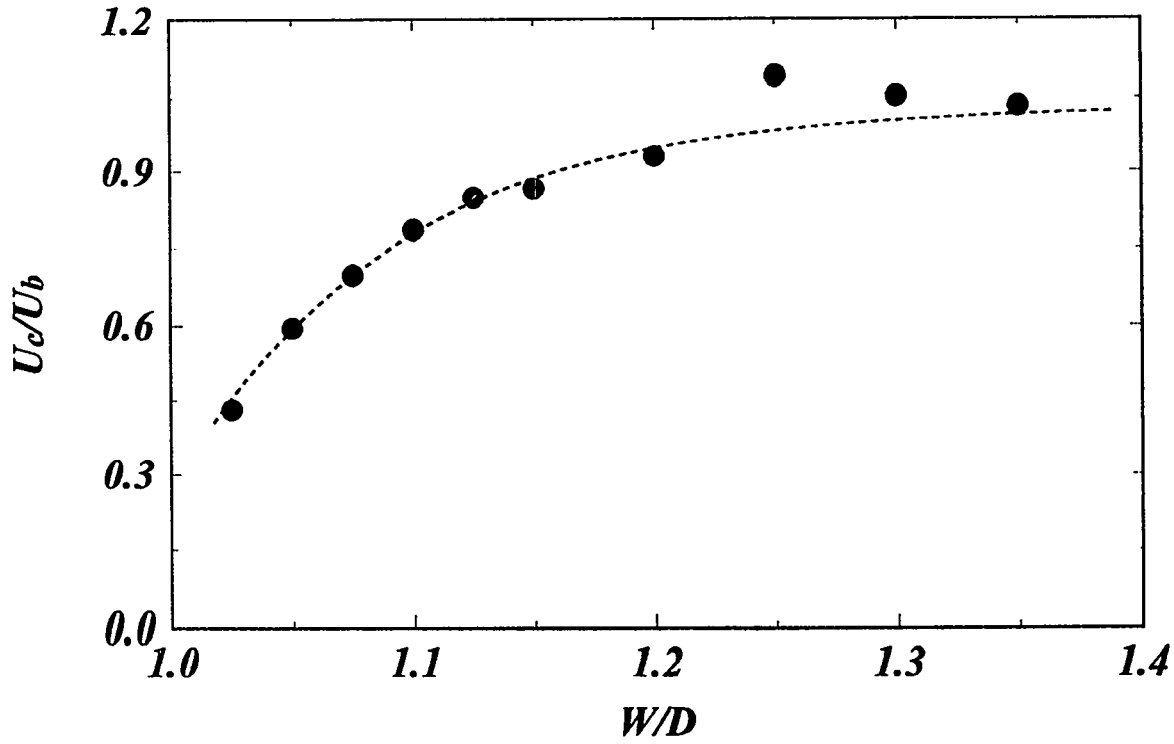

Figure 12: Average convective speed of the structures as a function of the wall subchannel width.

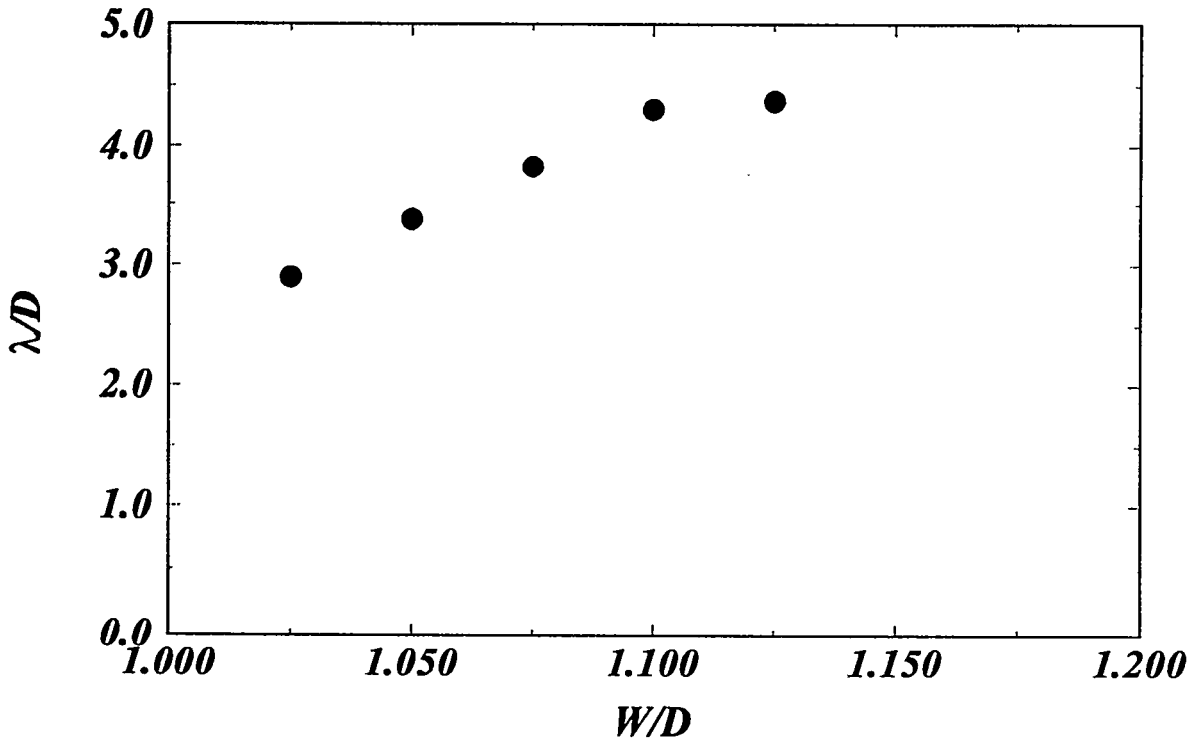

Figure 13: Spacing of the structures as a function of the wall subchannel width.

VOID FRACTION DISTRIBUTION IN A HEATED ROD BUNDLE UNDER FLOW STAGNATION CONDITIONS

V. A. Herrero, G. Guido-Lavalle and A. Clausse
Centro Atómico Bariloche and Instituto Balseiro
8400 Bariloche, Argentina

ABSTRACT

An experimental study was performed to determine the axial void fraction distribution along a heated rod bundle under flow stagnation conditions. The development of the flow pattern was investigated for different heat flow rates. It was found that in general the void fraction is overestimated by the Zuber & Findlay model while the Chexal-Lellouche correlation produces a better prediction.

KEYWORDS:

Two-phase flow, flow pattern transition, rod bundle

Nomenclature

A = flow area [m^2]
C_0= distribution parameter [-]
U_∞= terminal bubble velocity [m/s]
j = superficial velocity [$(m^3/s)/m^2$]
j_v = vapor superficial velocity [$(m^3/s)/m^2$]
ε = void fraction [-]
σ_ε= standard deviation of void fraction [-]
h_{fg}= heat of vaporization [j/Kg]
ρ_l = density [kg/m^3]
Z= axial position [m]
L= heated length [m]
$\dot{Q}$ = heat flow rate [W]

1. INTRODUCTION

The determination of the void fraction in a gas-liquid flow with given phase fluxes, fluid properties and boundary conditions is a problem that researchers have dealt with since many decades. An important step forward was achieved in the sixties with the development of the drift-flux model by Zuber and coworkers [1,2] and the contributions of other authors such as Wallis [3] and Bankoff [4]. Nowadays the major part of the resources is devoted to the development of the so-called two-fluid models. However the task is so complicated -as recently pointed out by Wallis [5]- that a great amount of empiricism is generally required, rules-of-thumb and *ad-hoc* approaches.

Within this scenario the most challenging problems and the main difficulties are concerned with phase distribution phenomena related, in particular, to flow-pattern transitions and lateral phase distribution. To complete this picture we should mention the urgent need for experimental data to develop closure laws for two-fluid models.

The present paper is related to a typical problem of two-phase flow which has applications in many industrial systems: the determination of the two-phase mixture level under low-flow conditions. This issue, which in principle is easy to treat using the drift-flux model [1], proved to be quite complicated by the potential occurrence of different flow patterns [6,8]

In the following, we present the results of measurements of the void fraction distribution along a channel containing a heated rod bundle under flow stagnation conditions. The subject is of interest in nuclear safety and boiling heat transfer equipments.

2. EXPERIMENTAL SETUP

2. 1 Experimental apparatus

A schematic diagram of the experimental rig is shown in Fig. 1. It consist of a test section, a constant head tank and instrumentation. Basically it is an open U type loop with the test section on one end and a constant head tank on the other. Both ends are open to the atmosphere. Water from the tank

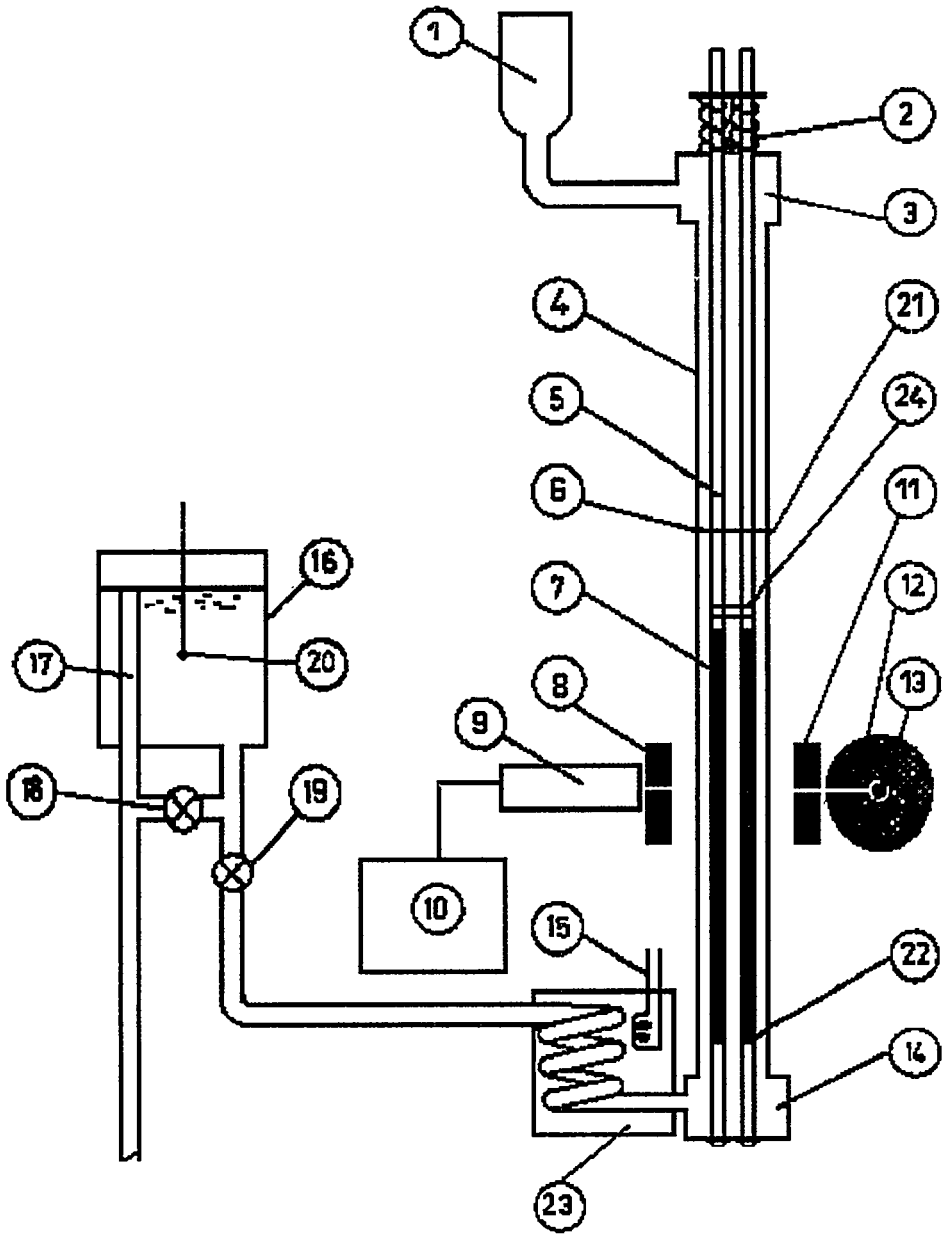

Figure 1. Schematic diagram of the experimental facility. 1: funnel, 2: springs, 3: top plenum, 4: test section tube, 5: unheated rod, 6: collapsed liquid level, 7: heated rod, 8: detector collimator, 9: detector, 10: instrumentation, 11: source collimator, 12: shielding, 13: γ-source, 14: bottom plenum, 15: preheater, 16: insulated tank, 17: tank overflow, 18: drain valve, 19: valve, 20, 21 and 22: thermocouples, 23: intermediate tank, 24: separator.

enters the test section through its bottom and the vapor leaves through the top.

The test section is a vertical glass tube of 40 mm i. d. and 200 cm in height. An array of four cylindrical heaters (9.5 mm diameter each) is located inside the tube in a square configuration, as shown in Fig. 2. The lower 100 cm of the rods are electrically heated by means of a DC power supply. The upper part of the bundle remains unheated while maintaining the cross section geometry along the channel. The heater assembly is fixed at the bottom plate of the test section and is free to expand axially through the top plate. To avoid bowing due to thermal expansion, the rods are axially tensed by means of springs located at the top plate. The test section tube is surrounded with another transparent tube. In order to minimize thermal losses the annular gap between the tubes (7.5 mm) is filled with air.

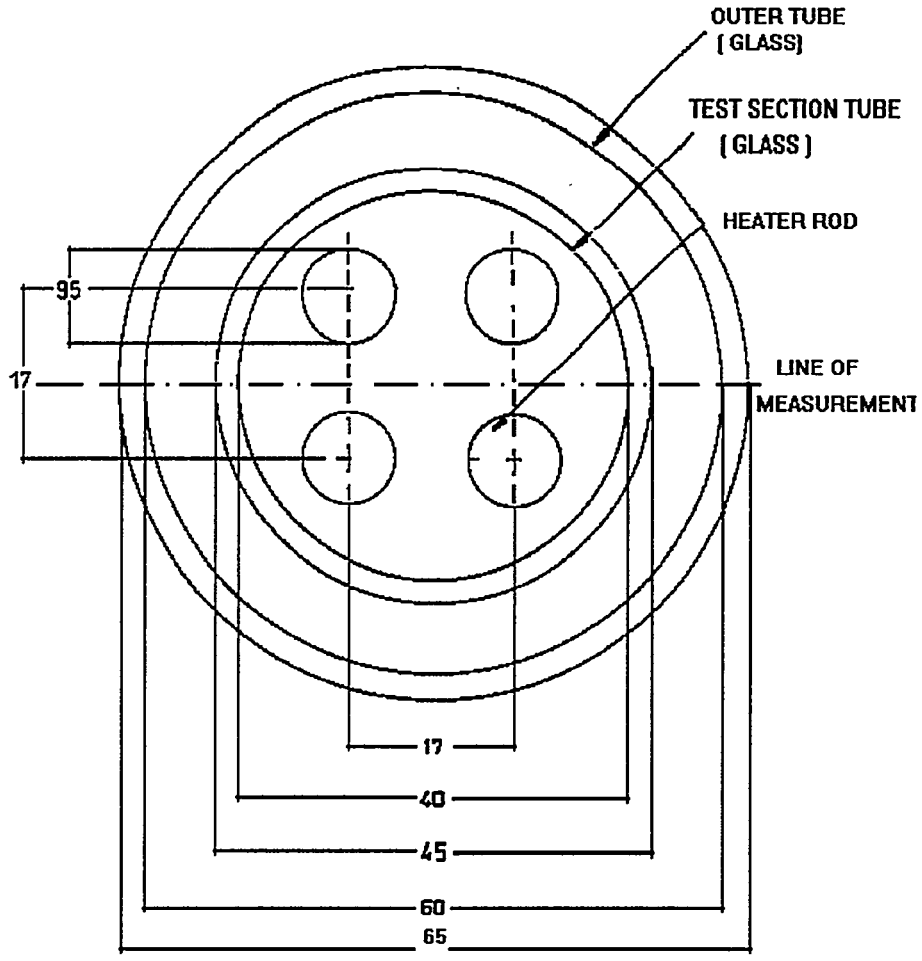

Figure 2. Cross-sectional view of the test section.

The bottom of the test section is connected to a 20 liters tank. The hydrostatic pressure in the tank is maintained constant by allowing the excess of water entering the tank to overflow. The inlet temperature is maintained at the saturation temperature by means of an intermediate preheater and associated controller. In all the measurements the liquid level in case of no heating was located 10 cm above the end of the heated section.

2. 2. Instrumentation

A standard γ-ray attenuation technique has been applied to measure the chordal void fraction along the tube diameter. A 100 mCi Cs^{137} source has been used in conjunction with a NaI (Tl) detector. The γ-ray densitometer is able to move in the vertical direction in order to scan the entire length of the test section. The densitometer was calibrated before and after each set of measurements in the liquid filled and gas filled tube.

Steady-state void fraction measurements have been carried out at 10 locations along the channel length for different heat flow rates. The static error of the void fraction (*i.e.*, the error due to the statistical nature of the γ-ray technique) had a typical value of 1.2 %, and a maximum of 1.5 % at very low void fractions. The dynamic error, due to void fraction variations in intermittent flow patterns, was negligible in most cases.

Chromel-alumel thermocouples were located and moved along the channel and in the inlet section to measure temperature distributions. Voltage drop across the heaters and across a calibrated shunt were measured to calculate the power input. The power to the heaters was provided by a DC power supply. The electrical current was controlled by a personal computer, which was also used to acquire the data of the densitometer electronics and to store them on magnetic media for off-line analysis.

3. EXPERIMENTAL RESULTS AND DISCUSSION

3.1. Axial void fraction distribution

Figure 3 shows typical plots of the void fraction as a function of the heat flow rate measured at different locations. As expected, the void fraction increases monotonously with the power input at all locations

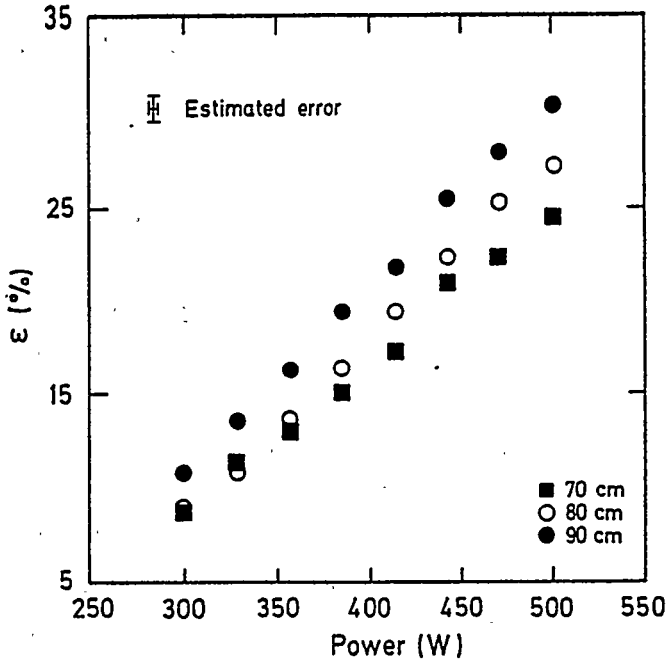

Figure 3. Void fraction as a function of heat flow rate at different locations within the heated region.

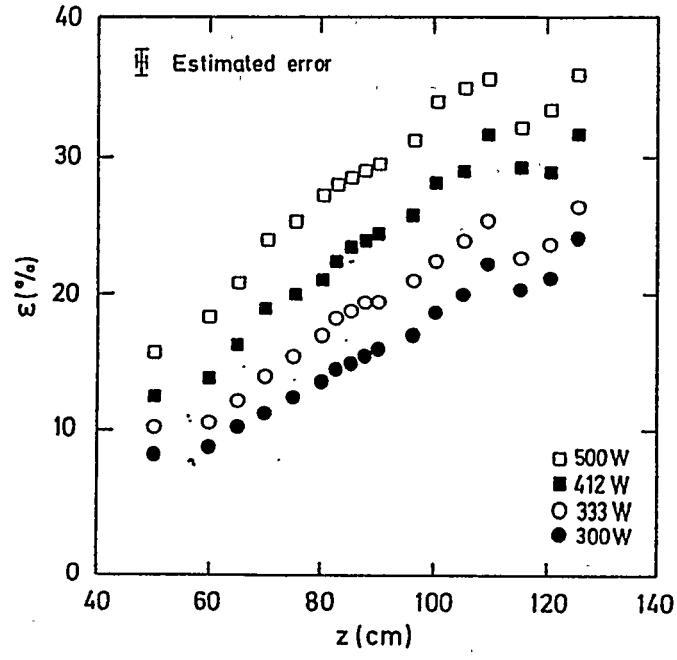

Figure 4. Axial void fraction distribution at different heat flow rates.

The void fraction variations along the axis of the test section are shown in Fig 4, for different values of the heat flow rate. The beginning of the heated section corresponds to 0 cm on the scale and the end to 100 cm on the scale. It can be seen that the void fraction increases with the axial position due to the incorporation of the vapor phase generated at the heated rod. The measurements at positions lower than 40 cm presented large dispersions due to the high error at low void fractions.

The fact that the void fraction increases beyond Z = 100 cm, even though this part is unheated, is an indication of non-equilibrium conditions (i.e. the liquid is superheated). At Z=110 cm, the void fraction presents a sudden drop. However, this effect does not correspond to a local reduction of the amount of vapor, but is primarily due to the transversal redistribution of the dispersed phase caused by the turbulence induced by the rod separators. Consequently the chordal measurements performed in the wake of the separators reveal the mixing action of the secondary flows which redistribute the vapor across the flow area.

3.2 Comparison with standard correlations

The drift-flux model by Zuber and Findlay [1] predicts the void fraction as a function of the volumetric flux, with two parameters: the terminal velocity of a single bubble, U_∞, and the distribution parameter C_0. The model was compared with the experimental data, assuming that the chordal void fraction represents the cross sectional averaged void fraction (which is true if radial variations are not significant). The vapor superficial velocity, j_2, is calculated by:

$$j_2 = \left[\frac{\dot{Q}}{h_{fg}\rho_g A}\right]\frac{z}{L} \qquad (1)$$

since the inlet subcooling is very small.

In general the theory results in overestimations of the local void fraction. Figure 5 shows comparison of the Zuber & Findlay model with the data corresponding to 500 W. A better agreement was obtained with a recent correlation by Chexal & Lellouche [7].

3.3 Local relation of the flow parameters

In order to search for the reason of the poor performance of both well-known correlations, the results are plotted in the plane originally proposed by Zuber & Findlay ; *i.e.*, $\frac{j_2}{\varepsilon}$ *vs.* j which is shown in Fig. 6.

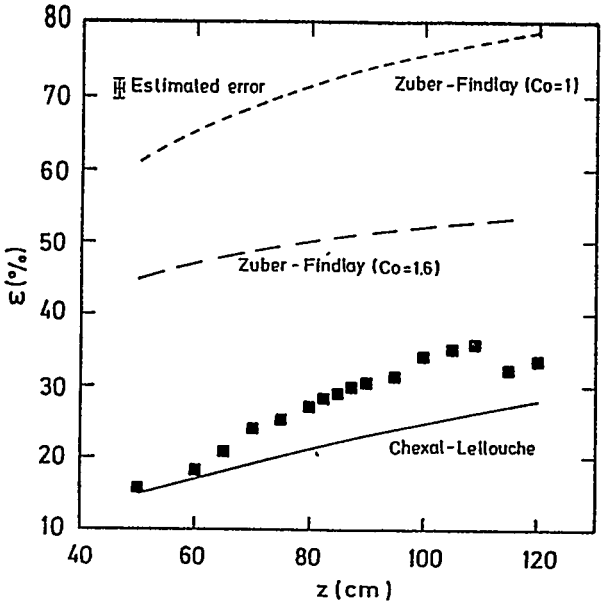

Figure 5. Comparison of the axial void fraction distribution with drift-flux correlation for 500 W.

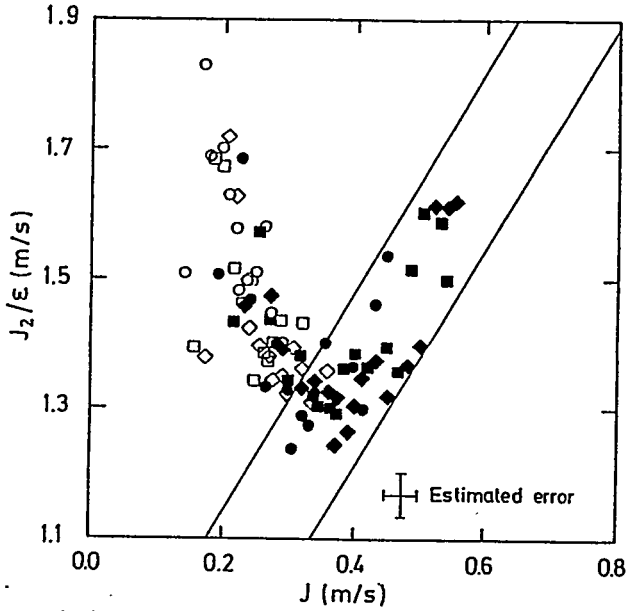

Figure 6. Data plotted .in the plane (j_2/ε, j). O 300 W, □ 333 W, ✧ 366 W, ● 412 W, ■, 472 W, ◆ 500 W.

We should remember that a major finding of these authors was the linear relationship between the two quantities, that is:

$$\frac{j_2}{\varepsilon} = C_o\, j + U_\infty \qquad (2)$$

Recent correlations, such as the one due to Chexal & Lellouche make use of a more general interpretation of the distribution parameter, C_0, and the terminal velocity, U_∞ , allowing them to depend on the phase fluxes. Nevertheless the corresponding curve in the (j_2/ε , j) plane is still approximately linear.

The strip shown in Fig 6 represents a family of lines generated by Eq. (2) with C_o=1.6 and U_∞ between 0.7 m/s and 0.4 m/s, assuming $j_1 = 0$. This value of C_0 is in agreement with the Chexal-Lellouche correlation. It can be seen that for values of j larger than 0.3 m/sec the data is well represented by Eq. (2), whereas for lower vapor superficial velocities the slope followed by the experimental data is negative.

An interesting feature which contributes to the understanding of the reasons for the deviation of the experimental data from Eq. (2) is shown in Fig. 7. Here the normalized standard deviation of the void fraction measurements, $\frac{\sigma_\varepsilon}{\varepsilon}$, is plotted as a function of j at a fixed position.

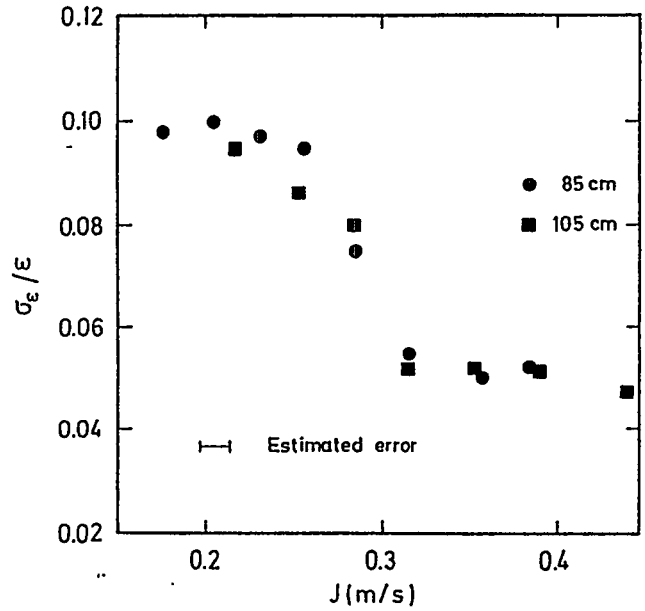

Figure 7. Relative standard deviation of the void fraction as a function of the superficial velocity j

It can be seen that there is a clear transition around j =0.3 m/s, which is in coincidence with the minimum value of j for which the data is well described by Eq. (2). Moreover our visual observations using slow motion video indicate that when j is higher than 0.3 m/s slug flow pattern is observed, characterized by long bubbles separated by liquid slugs filled with small satellite bubbles. On the contrary, at the locations where j is lower than 0.3 m/s, the boiling field is characterized by separated bubbles describing turbulent trajectories due to the interaction with liquid eddies.

4. CONCLUSIONS

An experimental study was performed to determine the axial void fraction distribution along a heated rod bundle under flow stagnation conditions. The development of the flow pattern was investigated for different heat flow rates.

It was found that in general the void fraction is overestimated by the Zuber & Findlay model while the Chexal-Lellouche correlation produces a better prediction. However, none of them is adequate to deal with situations where flow pattern transitions are taking place. The results appear to indicate that the bubbly flow pattern at incipient boiling stages switches to slug flow before the lateral development is completed.

It is expected that the results presented herein incentive the research in simple experiments which isolate particular mechanisms, providing an excellent tool for testing theoretical models.

REFERENCES

[1] Zuber, N., and Findlay, J. A., Average volumetric concentration in two-phase flow systems, J. Heat Transfer 1965, 87, 453-468.

[2] Zuber, N., On the variable-Density Single-Fluid Model for Two-Phase Flow, J. Heat Transfer 1960,82, 255-258.

[3] Wallis, G. B., One dimensional two-phase flow, Mc-Graw-Hill, 1969

[4] Bankoff, S. G., A Variable Density Single-Fluid Model for Two-Phase Flow With Particular Reference to Steam-Water Flow, J. Heat Transfer 1960, 82, 265-272.

[5] Wallis, G. B., Review-Theoretical Models of Gas-Liquid Flows, J. of Fluid Engineering, 1982, 104, 279-283

[6] Taitel, Y., and Bornea, D., Dukler A. E., Modeling Flow Pattern Transitions for Upward Gas-Liquid Flow in Vertical Tubes, AIChE J. 1980, 26, 345-354.

[7] Chexal, B., Lellouche, G., Horowitz, J., Healzer, J. and Oh, S., The Chexal-Lellouche Void Fraction Correlation for Generalized Applications, Report NSAC-139, 1991.

[8] Venkateswararao, Semiat and Dukler, Flow Pattern Transition for gas-liquid flows in a vertical rod bundle, Int. Journal of Multiphase Flow 1982, 8, 509-524.

Numerical Determination of Lateral Loss Coefficients for Subchannel Analysis in Nuclear Fuel Bundles

Sin Kim and Goon-Cherl Park
Department of Nuclear Engineering
Seoul National University
Seoul, 151-742 Korea
Tel. (02) 880-7210; Fax (02) 889-2688

Abstract

An accurate prediction of cross-flow based on detailed knowledge of the velocity field in subchannels of a nuclear fuel assembly is of importance in nuclear fuel performance analysis. In this study, the low-Reynolds number k-ε turbulence model has been adopted in two adjacent subchannels with cross-flow. The secondary flow is estimated accurately by the anisotropic algebraic Reynolds stress model. This model was numerically calculated by the finite element method and has been verified successfully through comparison with existing experimental data. Finally, with the numerical analysis of the velocity field in such subchannel domain, an analytical correlation of the lateral loss coefficient is obtained to predict the cross-flow rate in subchannel analysis codes. The correlation is expressed as a function of the ratio of the lateral flow velocity to the donor subchannel axial velocity, recipient channel Reynolds number and pitch-to-diameter.

I. Introduction

In the design and safety analysis of nuclear reactors, it is very important to verify that DNBR does not exceed the safety limit. For this purpose, accurate subchannel analysis for nuclear fuel rod bundles is required. However, the thermal-hydraulic phenomena in such geometries as rod bundles are complex due to geometrical complexity and high turbulence. Also, between subchannels in the rod bundle, there exist the interchanges of physical quantities such as mass, momentum and energy. Especially, the cross-flow can induce fuel rod vibrations through vortex shedding or turbulent mechanisms. Therefore, to accurately predict the nuclear fuel performance, the knowledge on such interchanges including the turbulent effects is essential.

Coolant mixing between subchannels in rod bundles is classified into four mechanisms as follows[1]: (1) turbulent interchange, (2) diversion cross-flow, (3) flow scattering, and (4) flow sweeping. The first two mechanisms are natural mixing effects which always occur in rod bundles and the last two are forced mixing effects due to mechanical means. Turbulent interchange is natural eddy diffusion between subchannels which can be characterized by eddy diffusivities. Diversion cross-flow is a directed flow between subchannels caused by radial pressure gradients between adjacent subchannels. Flow scattering and sweeping are non-directional mixing associated with the presence of grid spacers and directed cross-flow due to mixing vanes on grid spacers, respectively.

One of the important intersubchannel interaction is the mass transfer by diversion cross-flow, which is due to the lateral pressure difference. The diversion cross-flow carries the momentum and energy and thus affects the velocity and temperature profiles in the rod bundle. This quantity is calculated in commercial computer codes with the lateral pressure loss coefficient, which correlates the cross-flow rate with the lateral pressure difference.

In COBRA-II code, the lateral pressure loss coefficient was evaluated on the basis of the frictional resistance which would be observed for given lateral flow velocities in the absence of an axial flow component. This approach does not agree with the data for lateral flow through orifices in the presence of substantial axial flows. Hence, Weisman[2] pointed out that the analysis of the lateral flow between two rod bundles should recognize the strong inertial effect of axial flow on the lateral flow. Thus, using the subchannel approach, he derived the expression for the

lateral pressure loss coefficient between assemblies and established a correlation using experimental data. His correlation indicates that the inertial effect is the main parameter in describing lateral pressure losses, and the frictional losses are negligible.

Tapucu's experiment[3], on the diversion cross-flow between two parallel channels communicating by a lateral slot, has shown that the lateral pressure loss coefficient is mainly a function of the ratio of the lateral flow velocity to the donor channel axial velocity, the recipient channel axial velocity, and the gap clearance and thickness of the slot. On the basis of Tapucu's experiments, Tapucu-Merilo[4] derived the axial pressure variations in terms of two new parameters for donor and recipient channels. These parameters include the combined effect of fluid transferred and drag force brought by the connection gap, and are functions of the velocities and the geometrical parameters of the slot.

Baytas[5] determined that the axial velocity in the gap region influences the cross-flow, by comparing the numerical predictions with Tapucu's experimental data. He expressed the axial velocity in the gap region in terms of the axial velocity of the adjacent channels and a new parameter, which was found by numerical optimization.

Brown et. al.[6] found that, with a constant width control volume of gap region in the subchannel approach, the results for blockage conditions could not be satisfactory. They suggested that a variable width control volume should be used to analyze the cross-flow behind the blockage.

Gencay et. al.[7] conducted the experiments for the hydraulic behavior of two laterally interconnected channels with blockages in one of them. They observed that in the upstream region of the blockage the diversion cross-flow takes place over a relatively short distance and in the downstream of the blockage the recovery of the diverted flow by the blocked channel is a slow process and the rate of this recovery decreases with increasing blockage severity. By comparing with experimental data, Tapucu et. al.[8] concluded that COBRA-IIIC may not be adequate to describe the hydrodynamic behavior of two-interconnected channels with plate type blockages much higher than 30% severity in one of them.

Gencay-Tapucu[9] defined new momentum parameters for the axial momentum equation to investigate the hydrodynamic behavior of two interconnected parallel channels when one of them had a high blockage fraction, and studied the lateral resistance between two channels by taking into account the convective contribution of transverse momentum due to axial and transverse velocities. These parameters are expressed as a function of the square of the ratio of cross-flow velocity to the donor channel velocity.

As mentioned above, many works have been performed to analyze the cross-flow mixing phenomena and develop a suitable correlation for the loss coefficient, experimentally or numerically. However, most experiments were conducted on two parallel flow channels coupled by small holes or slots, or on blowing and sucking manifolds. These seem to be quite irrelevant to nuclear fuel bundles. Also, numerical predictions are normally based on the subchannel approaches which are derived by the lumped parameter concept in the subchannel of nuclear fuel assemblies. Hence, it is required to analyze the cross-flow phenomena in more realistic situations.

In this study, a turbulent flow field analysis code in subchannels is developed, accounting for the secondary flow caused by the anisotropic feature of Reynolds stress. The numerical scheme adopted in this code is the Galerkin weighted finite element method. The code has been verified by comparing with available experimental data. Finally, using the same code, a correlation for the lateral loss coefficient between subchannels is numerically obtained in terms of the ratio of the lateral flow velocity to the donor subchannel axial velocity, recipient channel Reynolds number, and pitch-to-diameter.

II. Turbulence Model

1. Secondary Flow and Anisotropic Model

Turbulent flow in non-circular ducts is characterized by secondary motions in a plane perpendicular to the streamwise direction. In general, the secondary motion is caused by two different mechanisms. The pressure-induced secondary motion (of Prandtl's first kind) exists in curved ducts and its magnitude can be quite large,

say of the order of 20-30% of the streamwise mean velocity. On the contrary, the secondary motion encountered in straight non-circular ducts is caused by the turbulence and thus this secondary flow can be present even under fully-developed conditions. Although the magnitude of turbulence-driven secondary motion (of Prandtl's second kind) is smaller than the root-mean-square value of turbulent intensity, this motion distorts the streamwise mean velocity and temperature contours towards the corners.

From the experimental investigations, Brundrett-Baines[10] have shown that the turbulence-driven secondary flows in non-circular ducts result from the anisotropy of Reynolds stress in the cross-sectional plane. Thus, the anisotropic Reynolds stress model should be adopted for more accurate description of the secondary flow.

The importance of anisotropic effect on the flow field in rod bundles has been confirmed by several investigations. There may be two possible ways to include the anisotropic effect in turbulence models. One is the anisotropic eddy viscosity model which accounts for the anisotropic eddy diffusion, and the other is the anisotropic algebraic Reynolds stress model which accounts for the secondary flow.

Trupp-Aly[11] analyzed the anisotropic effect in a triangular-arrayed rod bundle by introducing a constant anisotropic factor as the ratio of eddy viscosities.

Slagter[12] developed a new form of the one-equation turbulence model allowing for the effect of anisotropic eddy viscosities. Slagter's anisotropic model is based on anisotropic length scale expressions of Carajilescov-Todreas and on Wolfshtein's length scale model which includes the damping effects near the wall and, thus, is applicable up to the wall.

Launder-Ying[13] derived the relations between the Reynolds stresses under some reasonable approximations. Using the results of order of magnitude analysis, Baker [14] established the leading terms of the Reynolds stresses which are essentially equivalent to those of the Launder-Ying model.

Myong-Kasagi[15] added some complex correction terms of second order to the isotropic Reynolds stress to describe the anisotropy and its behavior at low Reynolds number near the wall.

2. Low-Reynolds Number Model

Most of the turbulence models are devised for high Reynolds number and fully turbulent flows far from the wall. Thus the success of the prediction of wall-bounded shear flows depends, to a large extent, on the use of the appropriate wall functions that relate surface boundary conditions to points in the fluid away from the boundaries and thereby avoid the problem of modeling the direct influence of viscosity. However, in some cases such as subchannel analysis where the ultimate purpose is to find the rod surface temperature and information on the flow field in the immediate vicinity of the wall is essential, the low-Reynolds number model is required.

Many low-Reynolds number models combined with widely used k-ε model were proposed[16]; Lam-Bremhorst and Launder-Sharma were the most successful in using this approach. Especially, the Lam-Bremhorst model has the advantage in that it does not require additional terms to the standard k-ε model.

III. Mathematical Model

In this study, a two-dimensional turbulent model including the secondary flow calculation has been established to obtain an analytical correlation of the lateral pressure loss coefficient between subchannels based on detailed knowledge of the velocity field in such domain. In the analysis, instead of the lumped parameter concept, the field equations are solved directly. In order to obtain the amount of cross-flow between square-arrayed sub-channels, mass and momentum conservation equations were written under the steady state and fully-developed conditions.

The low-Reynolds number k-ε model suggested by Lam-Bremhorst[17] is used to describe the complex turbulent phenomena near the wall. Thus, instead of the wall function, the no-slip wall boundary condition is used. This means that with this approach the velocity and the temperature profiles, even in the vicinity of the wall, can be calculated. The anisotropic Reynolds stress model of Launder-Ying is adopted

for more accurate description on the secondary flow. Although the Launder-Ying model was developed for the fully turbulent region and the constants were adjusted to the square duct geometry, Lee et. al.[18] applied this model up to the wall successfully for the closely-packed rod array (P/D = 1.123). However, it was found that the larger pitch-to-diameter, the more discrepancy between the predicted values and the experimental data resulted. Therefore, in this study, the model constant was modified to take into consideration the aspect ratio (pitch-to-diameter) through a numerical optimization.

The continuity equation and transverse direction momentum equations are transformed into vorticity and stream functions to construct the convenient and efficient numerical scheme. The Galerkin weighted residual finite element method is used to solve the governing equations effectively.

1. Governing Equations

The governing equations for the analysis of the flow field in subchannels are established as follows and, for simplicity, the Cartesian tensor notations are used; the subscripts i and j denote lateral coordinates 1 and 2, respectively.

- Stream function

$$U_1 = \frac{\partial \Psi}{\partial x_2} , \qquad U_2 = -\frac{\partial \Psi}{\partial x_1} \tag{1}$$

- Axial vorticity

$$\Omega = \frac{\partial U_2}{\partial x_1} - \frac{\partial U_1}{\partial x_2} \tag{2}$$

- Stream function equation

$$\frac{\partial^2 \Psi}{\partial x_j \partial x_j} = -\Omega \tag{3}$$

- Axial momentum equation

$$U_j \frac{\partial U_3}{\partial x_j} - \frac{\partial}{\partial x_j}\left((\nu + \nu_T) \frac{\partial U_3}{\partial x_j} \right) = -\frac{1}{\rho} \frac{\partial P}{\partial x_3} \tag{4}$$

- Axial vorticity equation

$$\frac{\partial}{\partial x_j}\left(\Omega U_j + \overline{\omega u_j} - \nu \frac{\partial \Omega}{\partial x_j} \right) = 0 \tag{5}$$

- Turbulent kinetic energy equation (k equation)

$$U_j \frac{\partial k}{\partial x_j} - \frac{\partial}{\partial x_j}\left((\nu + \nu_T/\sigma_k) \frac{\partial k}{\partial x_j} \right) = P_k - \varepsilon , \tag{6}$$

$$P_k = -\overline{u_1 u_3} \frac{\partial U_3}{\partial x_1} - \overline{u_2 u_3} \frac{\partial U_3}{\partial x_2} ,$$

$$\nu_T = C_\mu f_\mu \frac{k^2}{\varepsilon} ,$$

$$f_\mu = (1 - \exp(-B_\mu R))^2 (1 + \frac{D_\mu}{R_t}) ,$$

$$R = \frac{k^{1/2} x_l}{\nu} , \qquad R_t = \frac{k^2}{\varepsilon \nu}$$

where

$$\sigma_k = 1.0 \quad B_\mu = 0.0165 \quad C_\mu = 0.09 \quad D_\mu = 20.5$$

- Turbulent kinetic energy dissipation rate equation (ε equation)

$$U_j \frac{\partial \varepsilon}{\partial x_j} - \frac{\partial}{\partial x_j}\left((\nu + \nu_T/\sigma_\varepsilon) \frac{\partial \varepsilon}{\partial x_j} \right) = C_{\varepsilon 1} f_{\varepsilon 1} \frac{\varepsilon}{k} P_k - C_{\varepsilon 2} f_{\varepsilon 2} \frac{\varepsilon^2}{k} , \tag{7}$$

$$f_{\varepsilon 1} = 1 + (\frac{A_{\varepsilon 1}}{f_\mu})^3 , \qquad f_{\varepsilon 2} = 1 - \exp(-R_t^2)$$

where

$$\sigma_\varepsilon = 1.3 \quad A_{\varepsilon 1} = 0.05 \quad C_{\varepsilon 1} = 1.44 \quad C_{\varepsilon 2} = 1.92$$

- Pressure equation

$$\frac{\partial^2}{\partial x_i \partial x_j}\left(U_i U_j + \overline{u_i u_j} + \frac{P}{\rho}\delta_{ij} \right) = 0 \tag{8}$$

- Anisotropic algebraic Reynolds stresses

$$-\overline{u_i u_3} = \nu_T \frac{\partial U_3}{\partial x_i} \tag{9}$$

$$-\overline{u_i u_j} = C_3 k\, \delta_{ij} - C\frac{k^3}{\varepsilon^2}\frac{\partial U_3}{\partial x_i}\frac{\partial U_3}{\partial x_j} \tag{10}$$

where $C = -0.00237(P/D - 1) + 0.000871$ and $C_3 = 0.562$

As mentioned above, the model constant C was adjusted satisfy both equilateral triangular and square-arrayed rod bundle geometries.

2. Boundary Conditions

The boundaries of the subject domain consist of rod surface, symmetry boundary, and inflow and outflow boundaries, which permit flow-in and flow-out causing the cross-flow between adjacent two subchannels. Thus, three types of boundary conditions are needed: no-slip condition on the rod surface, symmetry condition on the symmetry boundary, and inlet and outlet conditions on the inflow and outflow boundaries.

On the rod surface, all components of the velocities and turbulent kinetic energy are zero from the no-slip condition and the stream functions can also be set to zero. However, for the axial vorticity and dissipation rate of turbulent kinetic energy, the boundary conditions are neither exact nor simple. Furthermore, some of them, even used commonly, are likely to cause the divergence of solutions especially at high Reynolds number[19]. Thus, in this study, new types of wall conditions of third order are derived, with the Taylor expansion and the near wall behavior of turbulence and under the assumption that the length of the first and the second grid are equal, as follows:

$$\Omega_w = \frac{\Psi_{w+1}}{0.5\,\Psi_{w+2} - \Psi_{w+1}}\,\Omega_{w+1} , \tag{11}$$

$$\varepsilon_w = \frac{3\,k_{w+1}}{k_{w+2} - k_{w+1}}\,\varepsilon_{w+1} . \tag{12}$$

On the symmetry boundaries, the normal gradients of axial velocity, turbulent kinetic energy and its dissipation rate and vorticity are set to zero. On the other hand, the stream function is equal to zero on the stream line containing the rod surface and on other symmetry lines it can be calculated from the inlet and outlet flowrates.

If it is assumed that the normal fluxes of all physical quantities of the inflow and outflow are zero, the normal gradients of these quantities are zero along the inlet and outlet boundaries. And, the stream function and axial vorticity can be calculated from the velocity distribution along these boundaries.

3. Numerical Scheme

The governing equations were formulated numerically by the Galerkin weighted residual finite element method using bilinear cardinal bases satisfying the C^0

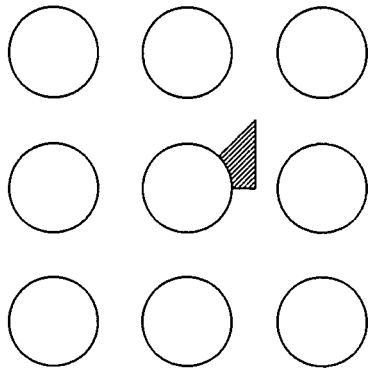

Fig. 1 Unit subchannel of square rod bundle array

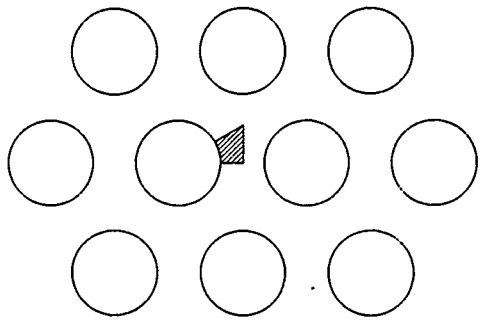

Fig. 2 Unit subchannel of triangular rod bundle array

continuity. The two dimensional calculation domain was discretized into square finite elements.

In general, numerical analyses on turbulent flows suffer from severe non-linearity and numerical instability. Thus, the initial guesses of dependent variables, mesh spacing and iteration scheme must be determined carefully. Initial profiles of the axial velocity, turbulent kinetic energy and its dissipation rate were obtained by universal profiles. The universal velocity profile was also used to determine the mesh spacing. To filter the oscillatory behavior of numerical solutions, the guessed values for the next iteration were obtained by using the geometric mean of the value of the previous iteration step and the calculated value with an under-relaxation factor.

The convergence criteria used was that the maximum individual relative error should be below 10^{-3}, except for the stream function and axial vorticity, for which the criteria recommended by Gosman et. al.[20] was applied.

All of the governing equations were not solved simultaneously, but segregatedly. The equations were divided into two groups: the first consisted of the axial momentum, turbulent kinetic energy and its dissipation rate equation and the second included the axial vorticity and stream function equations. Each group formed an independent iteration set, in which each equation was solved by an inner iteration procedure. The pressure distribution was found after the solutions of the five dependent variables met the convergence criteria.

IV. Results and Discussion

The calculations of the flow field in domains such as shown in Figs. 1 and 2 have been implemented using the turbulent model described above. In order to validate this model, the predicted distributions of axial velocities and stream functions under various geometrical and hydraulical conditions were compared with well-known experimental data.

Figs. 3 and 5 show the comparison of the computed axial velocity contours with experimental results on a triangular array[21] of P/D = 1.123 and Re = 27,000 and on a square array[22] of P/D = 1.25 and Re = 100,000, respectively. The first result shows a good agreement but the second deviates from the experimental data slightly. However, the difference is within 5% on the basis of maximum velocity. Predictions without secondary flow are shown in Fig. 4. It shows that the secondary flow makes flow field uniform with convective transport from the core to the gap region. Fig. 6 shows that the wall shear stress distribution in triangular array.

Carajilescov-Todreas[21] failed to measure the secondary flow velocities in the equilateral triangular arrays but predicted the result of the existence of two swirls in a unit cell. They pointed out that the weaker swirl has almost vanished for P/D = 1.217. However, Trupp-Aly[11] found a single swirl of secondary flow from the numerical analysis. Vonka[23] measured the secondary flow velocities successfully and

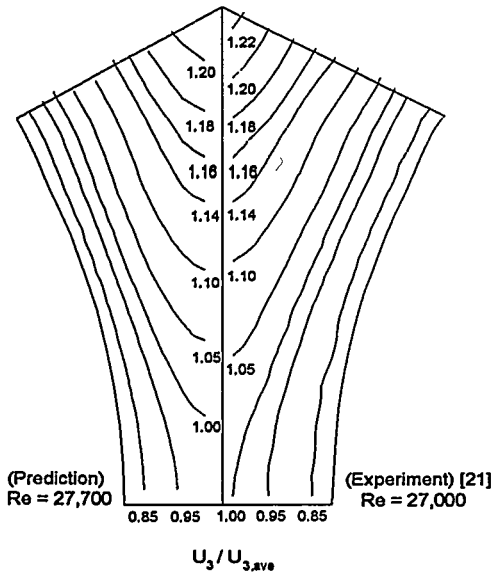

Fig. 3 Axial velocity contour with secondary flow in a triangular subchannel (P/D = 1.123)

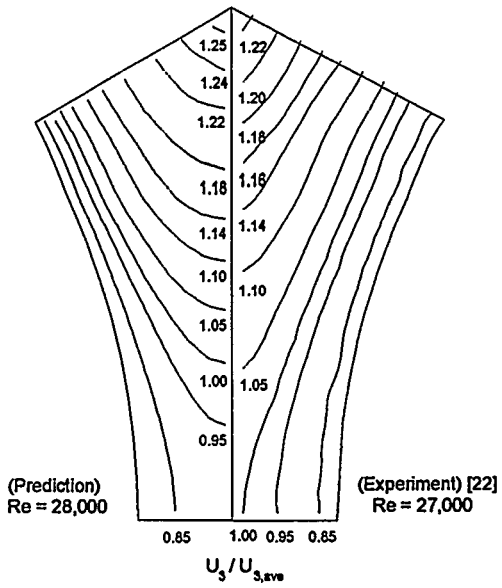

Fig. 4 Axial velocity contour without secondary flow in a triangular subchannel (P/D = 1.123)

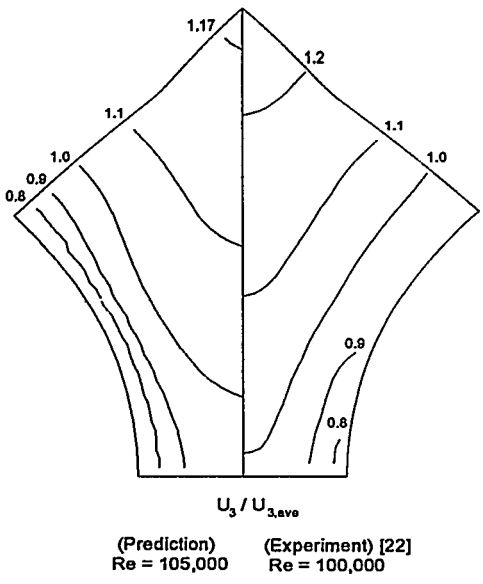

Fig. 5 Axial velocity contour in a square subchannel (P/D = 1.25)

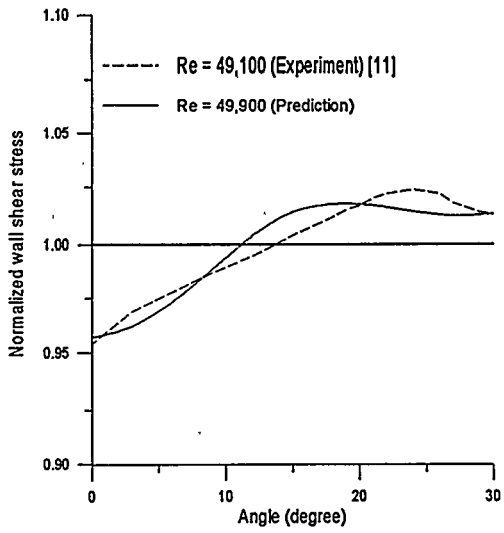

Fig. 6 Wall shear stress distribution of a triangular subchannel (P/D = 1.2)

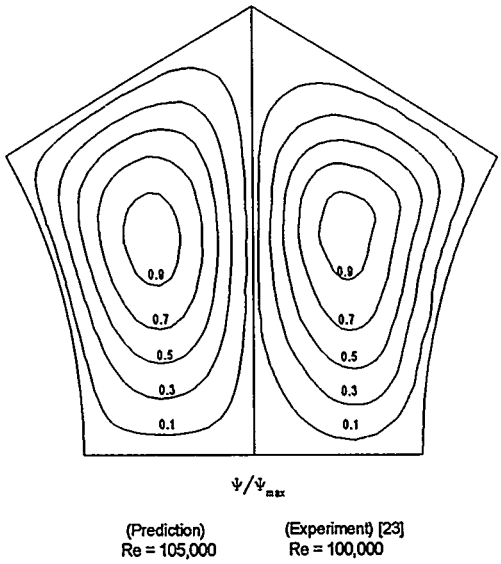

Fig. 7 Streamline in a triangular subchannel (P/D = 1.30)

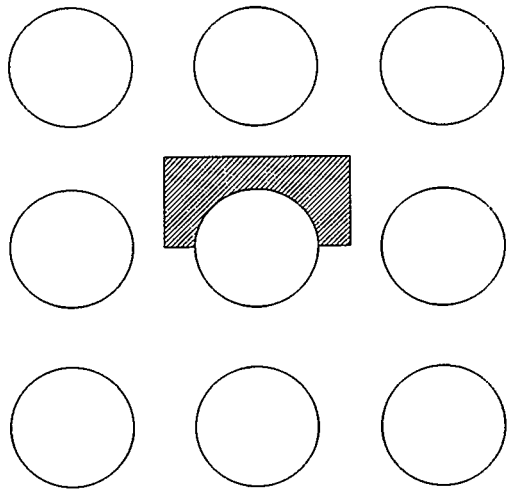

Fig. 8 Calculation domain for cross-flow in square rod bundle array

observed only a single swirl. In this analysis, a single swirl was obtained not only for the equilateral triangular array but also for the square array. Fig. 7 shows the predicted and experimentally measured stream lines under the condition of P/D = 1.30 and Re = 100,000 for the equilateral triangular array.

For the analysis of the cross-flow, the next step is to calculate the flow field composed of 4 unit cells such as Fig. 8 with the verified model. The upper and lower boundaries are assumed to be symmetrical. The left and right are flow-inlet and outlet, respectively; equal amounts of mass flow in and out cause the cross-flow, without violation of the fully-developed condition.

Predictions of the streamlines under the various inlet flowrate conditions are shown in Fig. 9. This figure shows that the swirl of the secondary flow almost vanishes when the ratio of the inlet flow velocity to the axial velocity is greater than 1%. To construct the correlation, many calculations were performed, varying P/D = 1.15 - 1.30, Re = 50,000 - 100,000 and the ratio of cross-flow velocity to axial velocity up to 5.4%. Once the distributions of flow variables such as velocity and pressure in the flow field are determined through the numerical analysis, the lateral loss coefficient K can be obtained,

$$K = \frac{\Delta P}{\frac{1}{2}\rho U_{cross}^2} , \tag{13}$$

where the difference between channel- averaged pressures can be calculated from the pressure distribution in each channel. Fig. 10 shows the distribution of lateral loss coefficients, which are decreasing exponentially as the ratio of the cross-flow velocity to the axial velocity of donor subchannel, U_{cross}/U_{don}, increases. It also implies that the ratio of U_{cross}/U_{don} is a cruicial parameter on the lateral loss coefficient. On the other hand, for P/D smaller than about 1.23, K decreases with P/D. However, for larger P/D, K increases.

A correlation for K was constructed in terms of U_{cross}/U_{don}, Reynolds number based on the axial velocity of recipient subchannel, Re_{rec}, and P/D according to the proposition of Tapucu[3]:

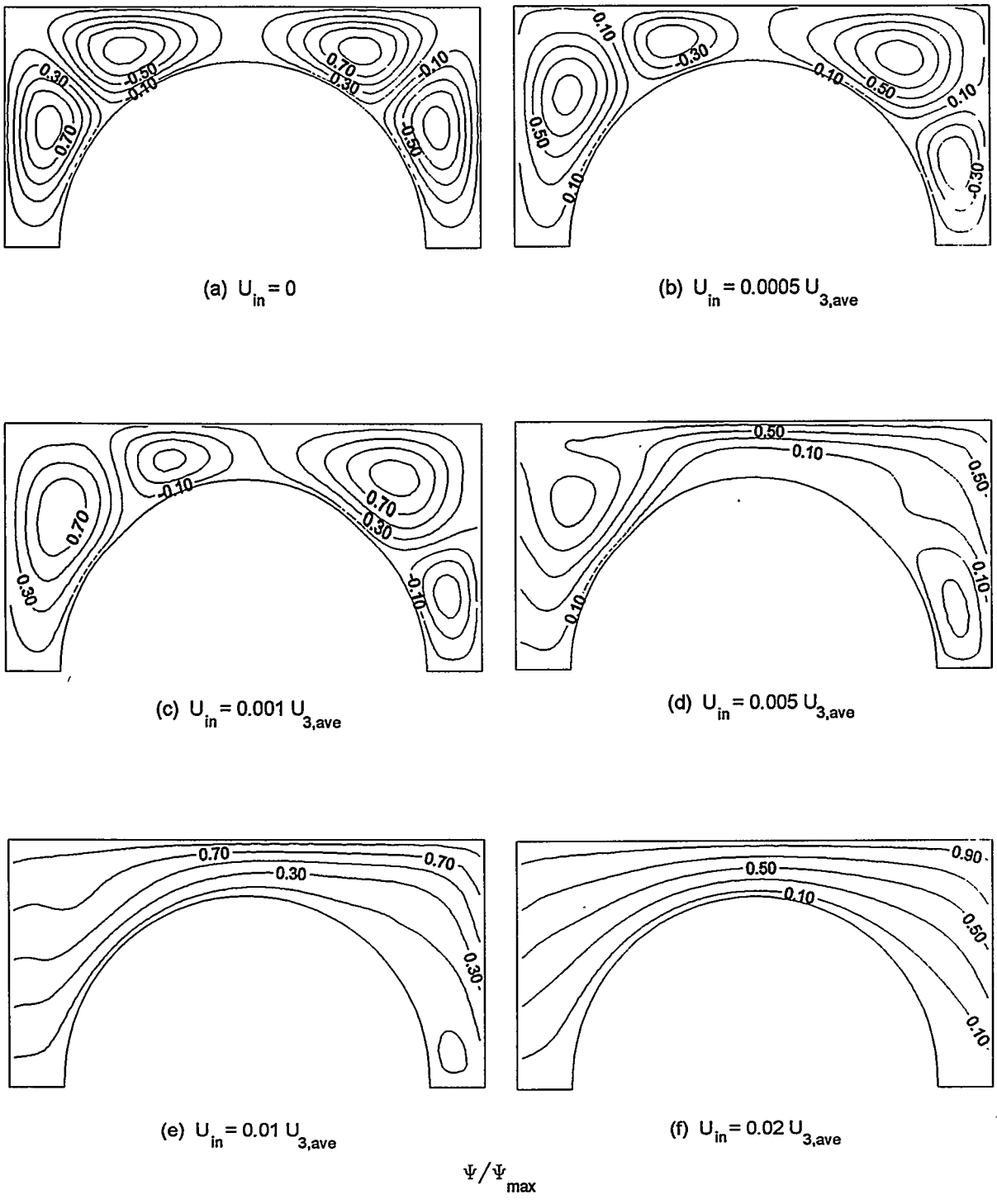

Fig. 9 Cross-flow streamline variations (P/D = 1.30, Re = 100,000)

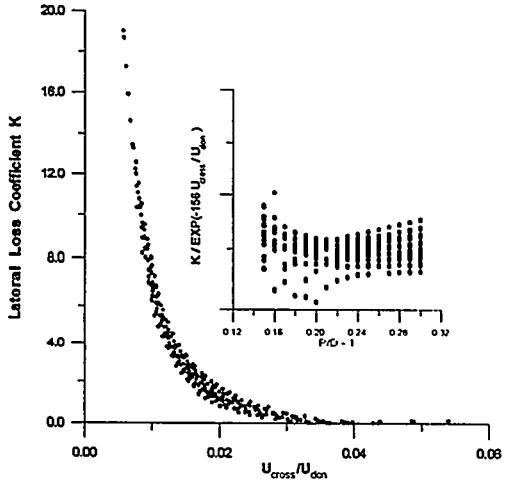

Fig. 10 Distribution of the calculated lateral loss cefficients

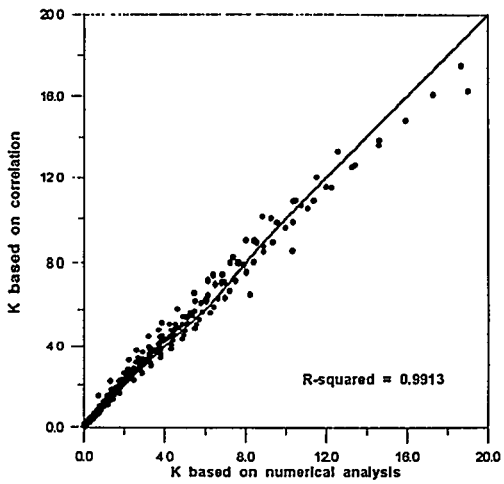

Fig. 11 Correlation diagram of lateral loss coefficient

$$K = 32.8\ K_{P/D} K_{rec} \exp(-156 \frac{U_{cross}}{U_{don}}) \tag{14}$$

where

$$K_{P/D} = 32.4(P/D-1)^2 - 15.1(P/D-1) + 2.68\ ,$$

$$K_{rec} = 1.79 - 1.03 \frac{Re_{rec}}{10^5}\ .$$

Fig. 11 shows the correlation diagram.

There are some available experimental data for lateral loss coefficient in the rod bundle geometries, but they were obtained without axial flow[24] or for rod assemblies[2][25]. These conditions are quite different from the situation considered in this study. Therefore the correlation developed in this work was not compared with experimental data. However, it may be expected that the loss coefficient between subchannels with axial inertia be greater than that of without axial inertia, and smaller than that of between assemblies.

V. Conclusions

The nuclear subchannel analysis codes such as COBRA and TORC for reactor design and safety analysis use the lateral pressure loss coefficient to predict the cross-flow between subchannels. In this study, a computer code for two-dimensional fully-developed turbulent flow fields was developed to predict the analytical lateral loss coefficient correlation. The model in the code includes the secondary flow, anisotropic algebraic Reynolds stress of Lander-Ying and low-Reynolds number k-ε model. Launder-Ying's model constant was also modified through the numerical optimization to be suitable to the rod bundle geometry.

For the code verification, the numerical results for a unit cell were compared with experimental data and the predictions were shown to be in satisfactory agreements. A large number of calculations were performed under the various geometrical and hydraulical conditions to find the lateral loss coefficients; a numerical correlation was also determined. This correlation is in the form of a function of the ratio of the lateral flow velocity to the donor subchannel axial velocity, recipient channel Reynolds number, and pitch-to-diameter. In addition, it is expected that the model developed in this study, which can predict an accurate velocity field in subchannels, may be applied in the future to calculate the temperature distribution and other subchannel parameters analytically.

Table of Nomenclature

k	turbulent kinetic energy (= $\overline{u_i u_i}/2$)
K	lateral pressure loss coefficient
P	pressure
P/D	pitch-to-diameter
Re	Reynolds number
U_i	mean velocity of i direction
u_i	velocity fluctuation of i direction
$\overline{u_i u_j}$	Reynolds stress
x_i	coordinate of i direction
x_l	normal distance from the wall
δ_{ij}	Kronecker delta
ε	dissipation rate of turbulent kinetic energy
ν	molecular kinematic viscosity
ν_T	eddy viscosity
ρ	density
Ψ	stream function
Ω	mean axial vorticity
ω	axial vorticity fluctuation
$\overline{\omega u_i}$	correlation between axial vorticity fluctuation and velocity fluctuation

Subscript

ave	average value
i,j	Cartesian index (3 for axial direction)
cross	cross-flow
don	donor channel
rec	recipient channel
w	wall

References

[1] J.H. Rust, Nuclear Power Plant Engineering, Haralson Publishing Company (1979).

[2] J. Weisman, "Cross flow resistance in rod bundle cores," Nucl. Tech. 15, 465-469 (1972).

[3] A. Tapucu, "Studies on diversion cross-flow between two parallel channels communicating by a lateral slot I : Transverse flow resistance coefficient," Nucl. Engrg. Des. 42, 297-306 (1977).

[4] A. Tapucu and M. Merilo, "Studies on diversion cross-flow between two parallel channels communicating by a lateral slot II : Axial pressure variations," Nucl. Engrg. Des. 42, 307-318 (1977).

[5] A.C. Baytas, "A comparison of prediction and Tapucu experimental data for determination of the axial velocity in the gap region," Nucl. Tech. 90, 417-425 (1990).

[6] W.D. Brown, E.U. Khan, and N.E. Todreas, "Prediction of cross flow due to coolant channel blockage," Nucl. Sci. Eng. 57, 164-174 (1975).

[7] S. Gencay, A. Tapucu, N. Troche, and M. Merilo, "Experimental study of the diversion crossflow caused by subchannel blockages. Part I : Experimental procedure and mass flow rates in the channels," J. Fluids Eng. 106, 435-440 (1984).

[8] A. Tapucu, S. Gencay, N. Troche, and M. Merilo, "Experimental study of the diversion crossflow caused by subchannel blockages. Part II : Pressures on the channels and the comparison of the COBRA-IIIC predictions with experimental data," J. Fluids Engrg. 106, 441-447 (1984).

[9] S. Gencay and A. Tapucu, "Cross-flow between identical subchannels caused by severe blockage," Nucl. Engrg. Des. 127, 33-45 (1991).

[10] E. Brundrett and W.D. Baines, "The Production and diffusion of vorticity in duct flow," J. Fluid Mech. 19, 375-394 (1964).
[11] A.C. Trupp and A.M.M. Aly, "Predicted secondary flows in triangular array rod bundles," J. Fluids Engrg. 101, 354-363 (1979).
[12] W. Slagter, "Finite element solution of axial turbulent flow in a bare rod bundle using a one-equation turbulence model," Nucl. Sci. Eng. 82, 243-259 (1982).
[13] B.E. Launder and W.M. Ying, "Prediction of flow and heat transfer in ducts of square cross-section," Proc. Instn. Mech. Engrs. 187, 455-461 (1973).
[14] A.J. Baker, Finite Element Computational Fluid Mechanics, McGraw Hill Book Company (1985).
[15] H.K. Myong and N. Kasagi, "Prediction of the near-wall turbulence with an anisotropic low-Reynolds-number k-ε turbulence model," J. Fluids Engrg. 112, 521-524 (1990).
[16] V.C. Patel, W. Rodi, and G. Scheuerer, "Turbulence models for near-wall and low Reynolds number flow : A review," AIAA J. 23, 1308-1319 (1984).
[17] C.K.G. Lam and K. Bremhorst, "A modified form of the k-ε model for predicting wall turbulence," J. Fluids Engrg. 103, 456-460 (1981).
[18] K.B. Lee, H.C. Jang, and S.K. Lee, "Study of the secondary flow effect on the turbulent flow characteristics in fuel rod bundles," J. KNS 26, 345-354 (1994).
[19] P.J. Roache, Computational Fluid Dynamics, Hermosa Publishers (1972).
[20] A.D. Gosman, W.M. Pun, A.K. Runchal, D.B. Spalding, and M. Wolfshtein, Heat and Mass Transfer in Recirculating Flows, Academic Press (1969).
[21] P. Carajilescov and N.E. Todreas, "Experimental and analytical study of axial turbulent flows in an interior subchannel of a bare rod bundle," J. Heat Transfer 93, 262-268 (1976).
[22] A.S. Yang and C.C. Chieng, "Turbulent heat and momentum transports in an infinite rod array," J. Heat Transfer 109, 599-605 (1987).
[23] V. Vonka, "Measurement of secondary flow vortices in a rod bundle," Nucl. Engrg. Des. 106, 191-207 (1988).
[24] I.E. Idelchik, Handbook of Hydraulic Resistance, 2nd ed., Hemisphere Publishing Corporation (1986).
[25] G. Hetsroni, "Use of hydraulic models in nuclear reactor design," Nucl. Sci. Eng. 28, 1-11 (1967).

THE LOW-POWER LOW-PRESSURE FLOW RESONANCE IN A NATURAL CIRCULATION COOLED BOILING WATER REACTOR

T.H.J.J. van der Hagen and **A.J.C. Stekelenburg**
Interfaculty Reactor Institute, Delft University of Technology
Mekelweg 15, 2629 JB Delft, The Netherlands

ABSTRACT

The last few years the possibility of flow resonances during the start-up phase of natural circulation cooled BWRs has been put forward by several authors. The present paper reports on actual oscillations observed at the Dodewaard reactor, the world's only operating BWR cooled by natural circulation. In addition, results of a parameter study performed by means of a simple theoretical model are presented. The influence of relevant parameters on the resonance characteristics, being the decay ratio and the resonance frequency, is investigated and explained.

INTRODUCTION

Natural circulation is a keyword in the design of modern safe boiling water reactors (BWRs). A striking example is the SBWR-design of General Electric [1]. The Netherlands is fortunate enough to operate the only existing BWR that uses natural circulation to drive the coolant through the core: the Dodewaard BWR. This reactor has been in operation since 1969. Some authors claim that a disadvantage of natural circulation cooled reactors is that they are more susceptible to unstable behavior than forced-circulation cooled reactors [2]. During the last decade a lot of international effort has been put in determining, monitoring and predicting the characteristics of BWRs as to the so-called reactor-kinetic and the density-wave stability. The last few years, it has been put forward that additional stability problems may arise during the start-up phase, when the pressure and the power are very low [2-5].

The present paper focuses on the stability characteristics of natural circulation reactors in that region of operation. It presents results of measurements taken during the start-up phase of the Dodewaard reactor and a parameter study made by means of a simple theoretical model.

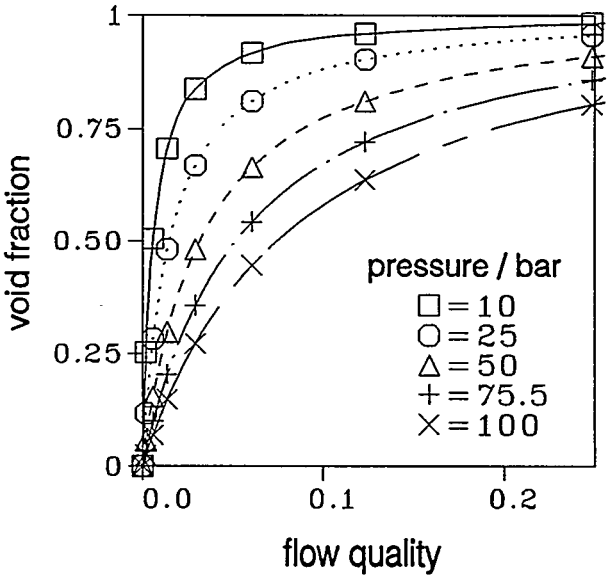

Fig. 1. Void-quality relationship according to the homogeneous equilibrium model [6].

THE FLOW RESONANCE IN ESSENCE

Usually two phenomena related to unstable behavior at start-up conditions are distinguished: geysering and flow resonance. The latter has its origin in the fact that the void-quality relation is considerably different at low power and low pressure than at nominal conditions (see Fig. 1). The lower steam density at low pressure leads to a higher gain from flow quality to void fraction at low quality, i.e. at low power.

The essence of the flow resonance will be discussed on the basis of the simplified block diagram as presented in Fig. 2. For sake of clearness, inlet subcooling, water level, reactor pressure and reactor power are considered to be constant and carry under (i.e. steam dragged into the downcomer) is neglected. Although variations of these quantities in a reactor complicate matters considerably [7], they are not important for describing and understanding the crux of the matter.

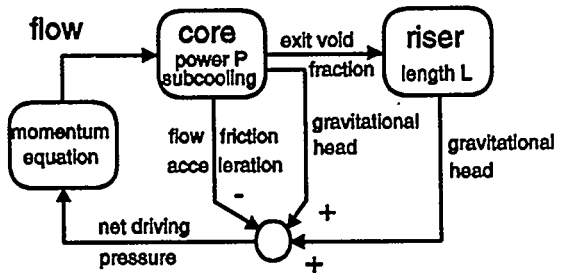

Fig. 2. Simplified block diagram of natural circulation flow dynamics.

A fluctuation in circulation flow rate causes a fluctuation in flow quality. For instance, a flow increase leads to a lower quality. At low power and low pressure, this results in a large decrease of the void fraction (both in the core and in the riser), which diminishes the gravitational head. In turn, the driving pressure is decreased (less friction and acceleration make a positive but smaller contribution to the driving pressure). Finally, the feedback loop is closed via the momentum equation, which couples up the driving pressure and the flow rate. In this manner a negative feedback loop with large gain is established.

Flow resonances of this type have been observed under specific unfavorable conditions in experimental set-ups [2-5] and in the Dodewaard reactor [7,8].

THE DODEWAARD REACTOR

Figure 3 shows a cut-away view of the reactor vessel of the Dodewaard reactor. Table I lists the main characteristics of the full-power conditions. The reactor has been subjected to research on its static and dynamic behavior for many years. During the measurements, use is made of the noise signals from neutron and gamma detectors, thermocouples, pressure sensors and flow meters and of the readings of the power plant's process computer, which provides general information on the operating condition, like, for example, neutron flux levels, vessel pressure, thermal power, and steam and feedwater flow rates.

The circulation flow rate, however, cannot be measured by simple means. It is measured indirectly through application of the cross-correlation flow measurement technique to the noise signals of axially displaced thermocouples in the downcomer flow [7].

This measurement technique was calibrated with the use of a set of numerical simulations of heat transport in turbulent flow [9].

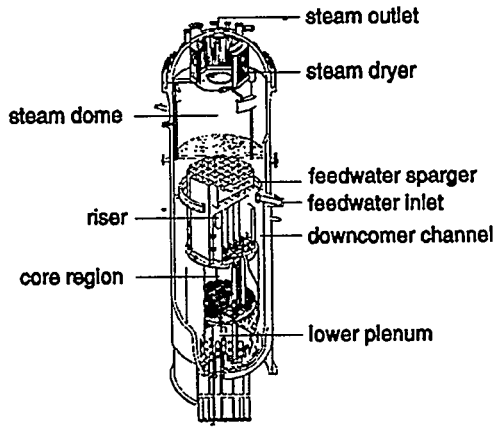

Fig. 3. Cut-away view of the Dodewaard BWR vessel.

A device is installed to measure the subcooling of the flow in the downcomer next to the core [10].

The carry under is calculated from an enthalpy balance, in which the measured circulation flow rate, feedwater flow rate and temperature, the measured subcooling and properties of water and steam appear.

Table I
Full-power conditions of the Dodewaard BWR

electric power	60 MW
thermal power	183 MW
pressure	75.5 bar
saturation temperature	563 K
circulation flow rate	approx. 1300 kg/s
feedwater flow rate	81 kg/s
feedwater temperature	408 K
collapsed water level (at hot stand-by)	55 cm above the top of the chimney
core-averaged outlet flow quality	approx. 8 %
core-averaged outlet void fraction	approx. 62 %
flow quality in the downcomer above the feedwater sparger	approx. 2 %

MEASUREMENTS DURING START-UP

In order to investigate the circulation flow dynamics at the Dodewaard reactor at the unfavorable conditions mentioned earlier, measurements were performed in the beginning of the start-up phase of cycle 24 (early 1993, [11]; see Stekelenburg *et al.* [8] for the most relevant results) and of cycle 25 (1994, [12]).

Unfortunately, possible circulation flow oscillations cannot be measured by the before-mentioned correlation technique since its response time is too large. Flow fluctuations, however, can be monitored from the neutron noise signals, as a change in flow will affect the power: the negative reactivity of voids causes the power to change.

Figure 4 presents the noise signal of an ex-vessel neutron detector during several phases of the start-up procedure. The position of the graphs is in accordance with the vessel pressure (horizontal position) and the estimated thermal power (vertical position). The power values are not very accurate as they are derived from the neutron flux level, a method that is calibrated for usage at nominal power. The noisy like behavior of the signals is due to the continuous in-core process of steam formation, transport and collapse, which gives rise to reactivity and thus power disturbances. These ever present fluctuations enable the noise specialist to extract much information about the characteristics of the reactor. Here, we will concentrate on the low frequent fluctuations as shown in some of the graphs (cases 1, 2, 4 and 6), that are not present during normal reactor operation. By cross-correlating the neutron noise signals with the noise component of the feedwater flow and temperature, the pressure and the downcomer water temperature, it was found that these fluctuations of the neutron detector noise signal are not caused by fluctuations of the before mentioned quantities, which leaves fluctuations of the circulation flow rate as being responsible. The noise signals of the two other neutron detectors present at the Dodewaard reactor (not shown here) show a very high coherence (close to unity) and a zero phase change with the noise signals of Fig. 5. This corresponds to the fact that the detectors are measuring a more or less core averaged neutron flux, which is representative for the core power.

At intermediate power (approximately 5 MW) the amplitude of the low-frequency oscillation is less than 0.5% at 3 bar, but it is around 4 times as large at 4.5 bar.

A better impression of the stability is given by taking the auto-correlation function (ACF) of the time signal. The ACFs are displayed in Fig. 5. At the lowest power and pressure, only a very slow oscillation occurs; at these conditions only single-phase flow is present and circulation flow has just started. Increasing the power yields a very low flow quality and sets the flow resonance to start. The decay ratio (defined as the ratio between two consecutive maxima) is smaller than 0.5 for the first 25 s, but considerably larger for longer times. The fact that the decay ratio is not constant throughout the ACF

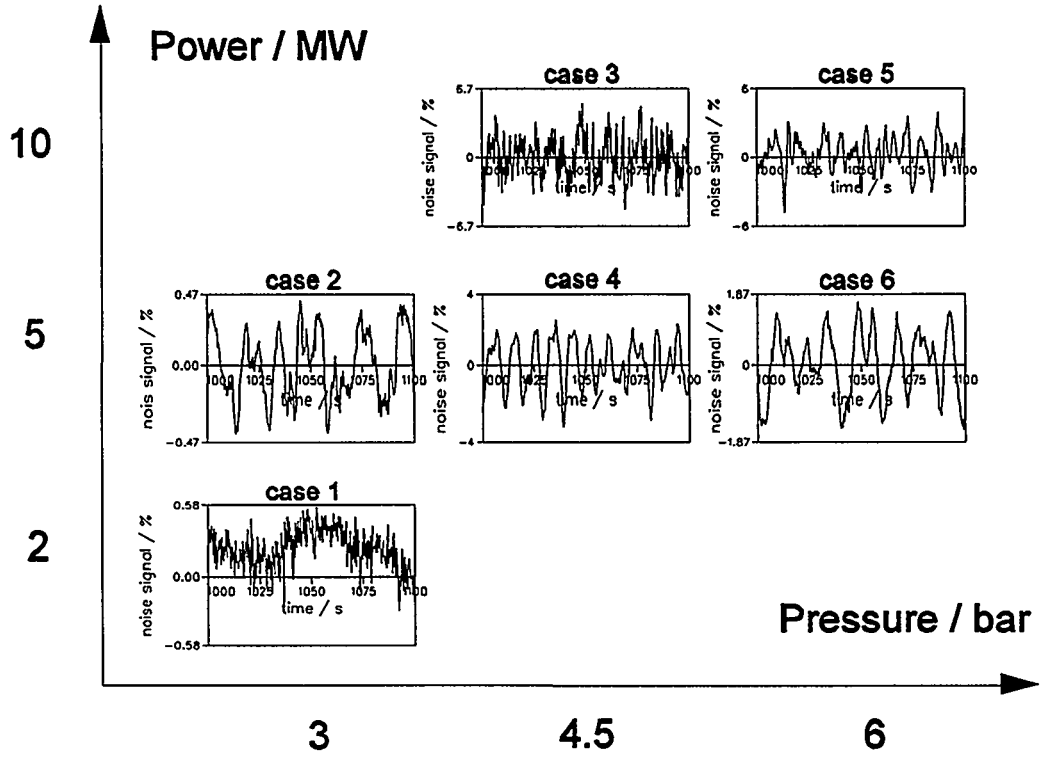

Fig. 4. Ex-vessel neutron noise as measured during start-up of the Dodewaard BWR (horizontal axes: 1000 - 1100 s).

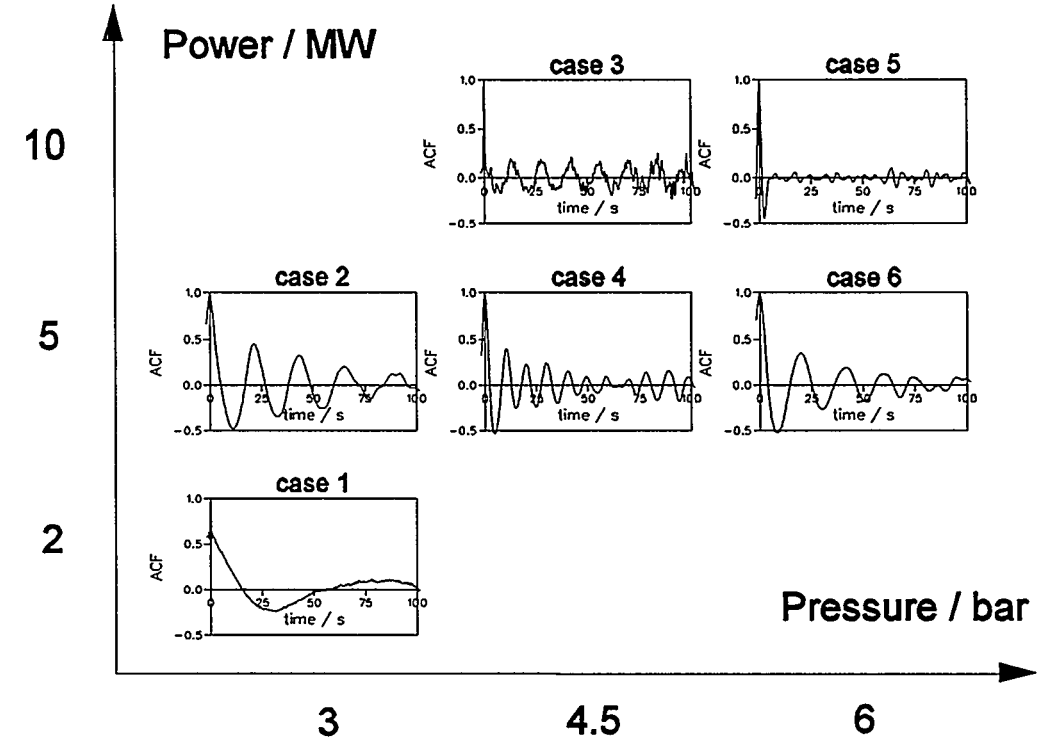

Fig. 5. Auto-correlation functions of neutron noise signals measured in the Dodewaard BWR (horizontal axes: 0 - 100 s; vertical axes: -0.5 - 1).

points to a system that is not of the 2nd-order type. The damping is approximately the same in all three 5-MW cases. It is interesting to note that the resonance frequency at 4.5 bar is approximately twice that at 3 and 6 bar: 0.1 Hz and 0.05 Hz, respectively.

The beating visible in the three graphs at 5 MW might be a result of the combined contribution of different fuel bundles with different flow qualities and thus different resonance frequencies.

Increasing the power to 10 MW gives a non-damped oscillation (hardly visible in the time signal !) with a frequency of 0.07 Hz at a pressure of 4.5 bar and no resonance at 6 bar.

The thermal-hydraulic state of the core during start-up is influenced by many parameters and devices, such as the control rod cooling flow and temperature, the reactor water clean up system and the reactor shut-down cooling system [13]. This impedes a thorough lumped parameter characterization, let alone a space dependent description, such as needed to explain the phenomena measured. Table II presents three important quantities that give some insight into the thermal-hydraulic state of the core: the measured circulation flow, the measured inlet subcooling and the calculated exit equilibrium quality for the six cases. The latter is calculated from power, flow, inlet subcooling and water/steam properties, assuming a flat power and flow profile over the core. From this approach, it can be seen that the exit equilibrium quality is positive for only one case, in other cases core void can only appear through subcooled boiling. Although a radially flat power and flow profile is unlikely, this demonstrates that the core flow quality is low, that perhaps only the hottest channels drive the coolant flow and that flashing (evaporation in the riser due to the lower pressure at higher elevations) and single-phase density differences can play an important role. Notice that the flow at 2-MW/3-bar is larger than the flow at 5-MW/3-bar since friction increases significantly when going from one-phase (case 1) to two-phase flow (case 2). Additional complications arise from possible changes in feedwater flow, leading to changes in water level, and the influence of carry under. Also, reactivity feedback might be of importance to the flow dynamics.

Table II

Circulation flow (kg/s, upper values), inlet subcooling (K, middlemost values) and exit equilibrium quality (%, lower values) for the six Dodewaard cases

power / MW			
10		870 4 -0.3	600 2.5 0.3
5	370 8 -1.0	470 3 -0.1	400 3 -0.03
2	400 8.5 -1.5		
	3	4.5	6

pressure / bar

It is clear that a detailed thermal-hydraulic analysis is needed for a complete description of the six cases.

THEORETICAL MODEL

To study the influence of system parameters (power, pressure, subcooling and so on) on the resonance characteristics (decay ratio and resonance frequency) a simple theoretical model was established. The idea is that this model incorporates the physics essential to the flow dynamics as displayed by the block diagram of Fig. 2. It is expected

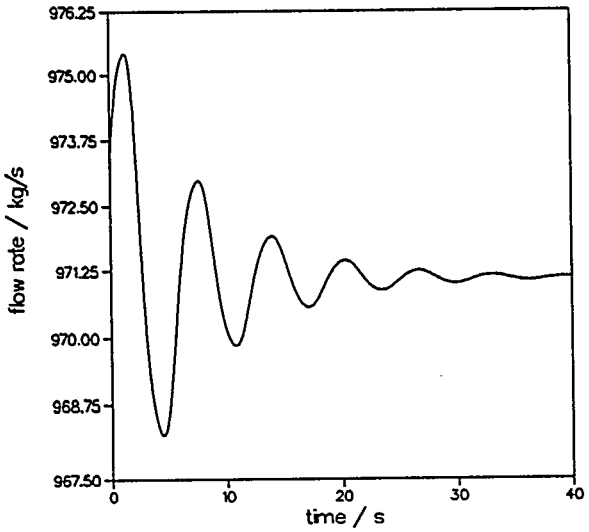

Fig. 6. Simulated flow rate response to a small perturbation at 2 bar, 2 MW, 0.3 K inlet subcooling.

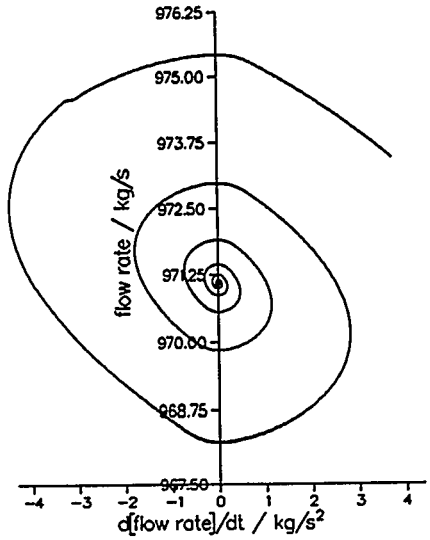

Fig. 7. State space trajectory for the same response as shown in Fig. 6.

that it is too simplified to permit the attachment of great value to the absolute values of the resonance characteristics derived.

The 1-D model uses a constant axially uniform core power and a constant flow inlet specific enthalpy (i.e. a constant subcooling). The core boiling boundary is calculated, whereafter the boiling and non-boiling nodes are treated separately. The axial void fraction distribution is calculated from the flow quality and phase densities using the homogeneous equilibrium model of two-phase flow [6]. Frictional pressure drop in the non-boiling region is calculated; friction in the boiling region is related to the single-phase friction using the Martinelli-Nelson two-phase friction multiplier. The accelerational pressure drop in the boiling region is treated explicitly [6]. The exit void fraction is transported with a delay (depending on the flow rate) to the 1-node riser. Friction in the riser and in the downcomer is neglected. Carry under is neglected, which means that the downcomer flow is purely single phase. The net driving pressure is constituted as the difference between the gravitational head in the downcomer and that in the core and the riser minus frictional and accelerational pressure losses. Finally, a momentum equation relates the driving pressure to a change in flow rate, taking into account masses and volumes of the flowing material in the core, the riser, the upper plenum, the downcomer and the lower plenum. The Dodewaard full-core, riser, downcomer, upper- and lower-plenum dimensions are used in the model (see Stekelenburg, [7]).

SIMULATIONS

With the theoretical model, the flow rate as a function of time was calculated. Flow resonance characteristics were calculated by firstly calculating stationary conditions of flow rate, flow quality and void fraction, thereafter perturbing the flow rate slightly and observing the time response. The decay ratio was taken as the ratio of two

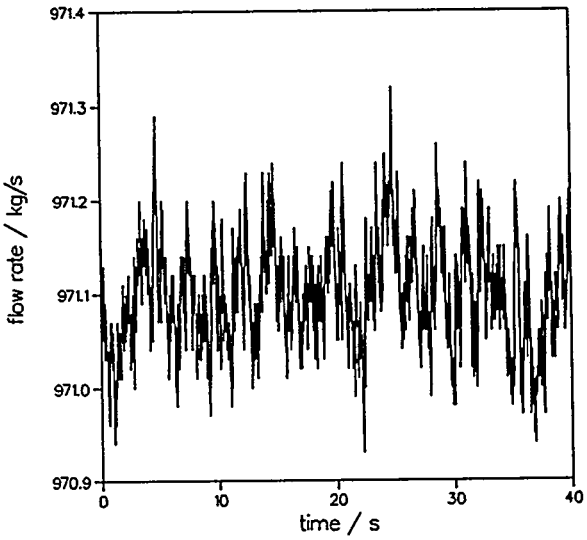

Fig. 8. Simulated flow fluctuations as a result of 0.1 % power fluctuations at 2 bar, 2 MW, 0.3 K inlet subcooling.

consecutive maxima of the response at longer times, where only the least damped component remains. A typical example is shown in Fig. 6. The corresponding state space diagram is shown in Fig. 7. Clearly, the flow shows an oscillatory response, in this case with a decay ratio of approximately 0.45 and a resonance frequency of approximately 0.15 Hz. Another means of exciting the system is by putting some artificial noise on the reactor power. Figure 8 gives such a simulation, where the noise term had a uniform distribution from -0.1 to 0.1%.

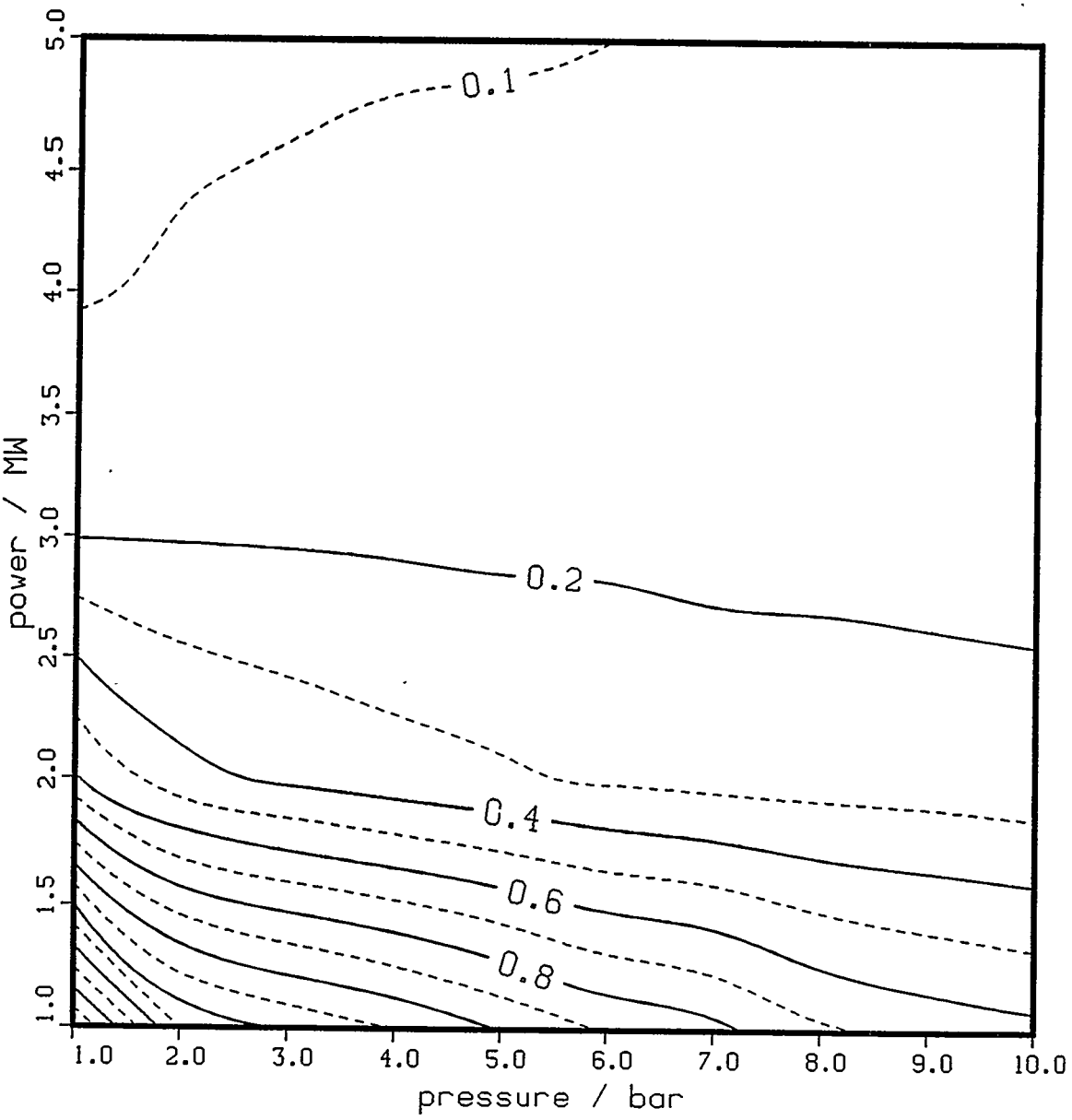

Fig. 9. Contour map of the decay ratio as function of pressure and power obtained from simulations.

The influence of several model parameters was investigated from the flow perturbation response. Figures 9 and 10 give a pressure-power contour map of the decay ratio and the resonance frequency, respectively. The inlet subcooling was 0.3 K in all cases. It can be seen that the decay is large (pointing to a small stability margin) at low pressure and low power, as expected. In this region, both increasing power and increasing pressure have a stabilizing effect. The influence of the pressure, however, on the decay ratio is not very strong. Notice that the model predicts an unstable situation

(decay ratio >1) for very low pressures and powers. In a reactor the situation at extremely low powers is expected to be different, since single-phase density differences will set the circulation flow to start at lower powers than in the model. It is interesting to see that at powers larger than 3 MW (with a decay ratio smaller than 0.2) the decay ratio increases with pressure. This corresponds to the slope of the void-fraction flow-quality relation (Fig. 1), which is increasing with pressure for qualities larger than say 0.1 (whereas it is decreasing with pressure for smaller qualities). The resonance frequency increases with power and decreases with pressure, which has its origin in the higher flow rate and thus smaller transit time of the mixture at higher void fractions.

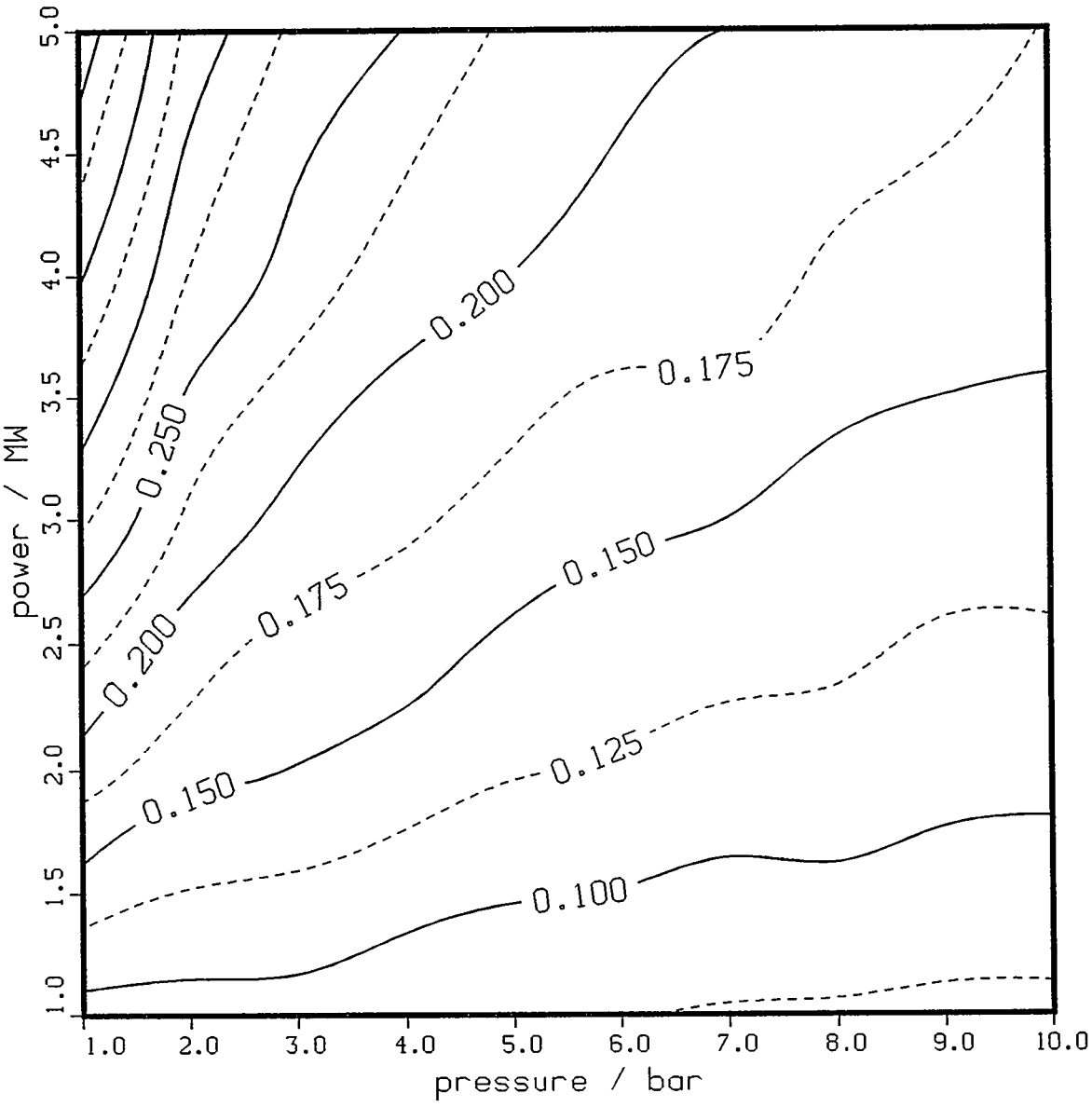

Fig. 10. Contour map of the resonance frequency as function of pressure and power obtained from simulations.

The influence of the inlet subcooling is shown in Fig. 11. More subcooling leads to a higher decay ratio, i.e. a lower stability margin. This effect can be understood by real izing that the flow quality decreases with increasing subcooling, leading to a larger gradient of the void-quality relation. Please notice that the curves corresponding to the same power cross each other at a small subcooling value: the curve for the higher pressure gives the highest decay ratio at small subcooling values, i.e. relatively large

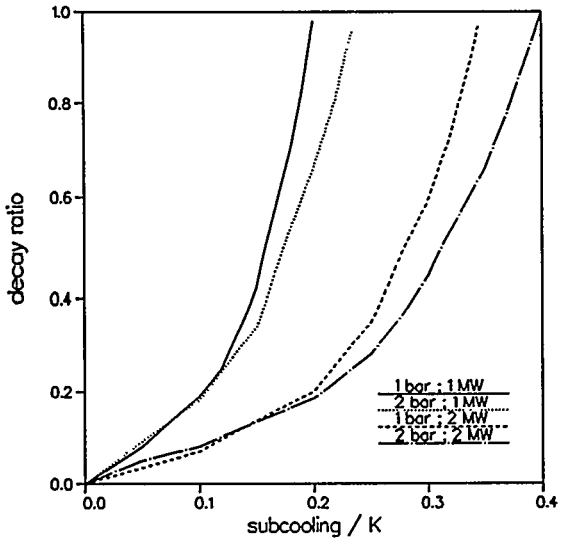

Fig. 11. Decay ratio from simulated flow response as a function of inlet subcooling at several powers and pressures.

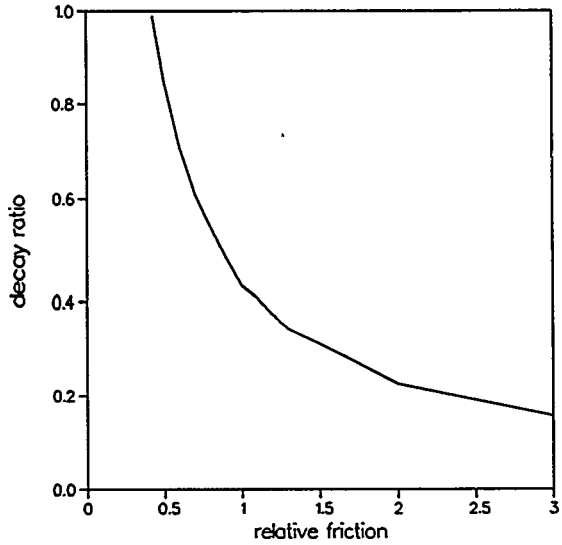

Fig. 12. Decay ratio from simulated flow response as a function of relative flow friction (1 = normal) at 2 bar, 2 MW, 0.3 K inlet subcooling.

qualities. This finding corresponds to the gradient of the void-fraction flow-quality relation mentioned before.

As expected, increasing the flow friction has a stabilizing effect (Fig. 12). Increasing the riser length destabilizes the system, as is shown in Fig. 13. This effect, which is in correspondence with the findings of Wang *et al.* [14], is due to an increased gain in the feedback loop: the difference in gravitational head between riser and downcomer increases with increasing riser length. The resonance frequency is decreasing with riser length (see Fig. 14), because a longer riser leads to a larger transit time of the flowing mixture (the increase in flow rate is not enough to compensate the increase in travelling length).

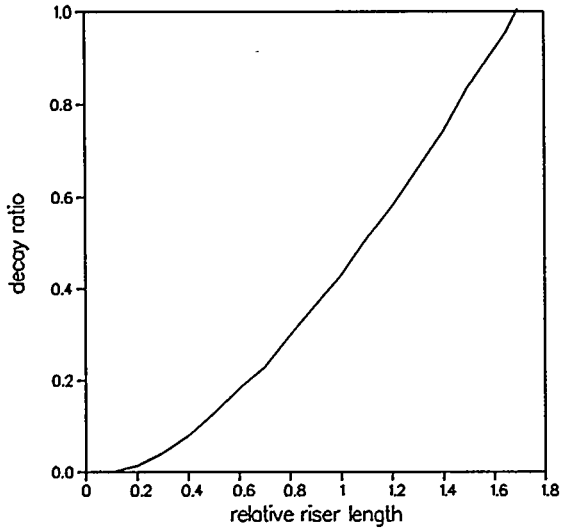

Fig. 13. Decay ratio from simulated flow response as a function of the relative riser length (1 corresponds to 3.06 m) at 2 bar, 2 MW, 0.3 K inlet subcooling.

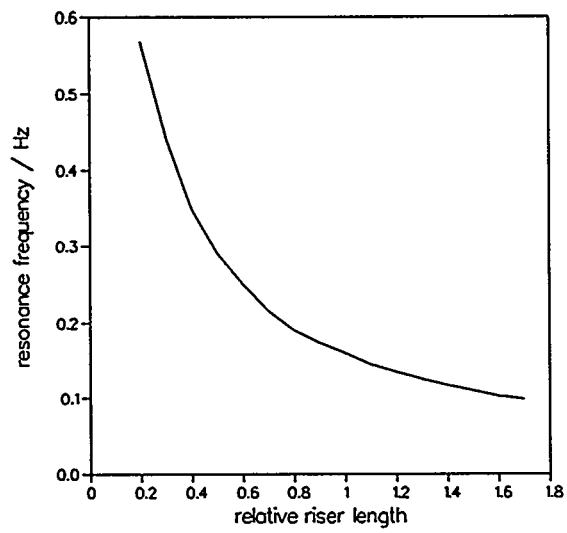

Fig. 14. Resonance frequency from simulated flow response as a function of the relative riser length (1 corresponds to 3.06 m) at 2 bar, 2 MW, 0.3 K inlet subcooling.

CONCLUSIONS AND EVALUATION

As several researchers have put forward the possibility of flow resonances during the start-up phase of a natural circulation cooled BWR, special attention has been paid to this phenomenon at the start-up of the Dodewaard reactor in 1993 and in 1994. Indeed, oscillations in the ex-vessel neutron flux (with a top-top value of some percents) point to flow oscillations at some specific conditions (low power and low pressure). It is felt that the power oscillations are of no concern for safety aspects, because:

a) they occur only at low power;
b) they occur only at low qualities where the in-core void fraction is low or even zero; in the latter case the circulation flow is mainly driven by the two-phase mixture in the riser (where the steam is formed by flashing).

The decay ratio and the frequency of the oscillations seem to depend on at least the vessel pressure, the reactor power and the inlet subcooling. Other factors probably of importance are the power distribution over the core, possible changes in the feedwater flow and temperature, void reactivity feedback, carry under and the vessel water level. More research as to this aspect is needed and will be performed.

With the aid of a simple theoretical model the trend in decay ratio and resonance frequency as function of the value of relevant parameters could be predicted. Parameters varied in this study are the vessel pressure, the reactor power, the inlet subcooling, the flow friction and the riser length.

In summary:

A stabilizing effect has:
- increasing pressure at low flow qualities;
- decreasing pressure at higher qualities;
- increasing power;
- decreasing inlet subcooling;
- increasing flow friction;
- decreasing the riser length.

The resonance frequency is decreased by:
- increasing pressure;
- decreasing power;
- increasing the riser length.

All of these findings can be explained from physical principles.

It is shown that the simple model incorporates the essential thermal-hydraulic ingredients for a qualitatively correct simulation of the relevant effects. For a quantitatively reliable simulation, the model could be extended with inclusion of the neutronic part, a slip model (it was found that an increase in slip has a stabilizing effect, due to the decrease in void fraction) and perhaps a subcooled boiling model.

REFERENCES

[1] R.J. McCandless and J.R. Redding, "Simplicity: the key to improved safety, performance and economics," Nucl. Engrg. Int. 34(424), 20-24 (1989).

[2] M. Aritomi, J.H. Chiang, T. Nakahashi, M. Wataru and M. Mori, "Fundamental study on thermo-hydraulics during start-up in natural circulation boiling water reactors (I), thermo-hydraulic instabilities", J. Nucl. Sci. Technol. 29(7), 631-641 (1992).

[3] S.R. Wu, M.S. Yao, D.Z. Wang, K. Hofer and E. Knogliner, "An Experimental Study on Hydrodynamic Stability of Low Quality Two-Phase Flow with Natural

Circulation," Proc. First World Conf. Experimental Heat Transfer, Fluid Mechanics and Thermodynamics, Sep. 4-9. 1988, Dubrovnik, Yugoslavia, 1120-1127 (1988).

[4] J.H. Chiang, M. Aritomi, R. Inoue and M. Mori, "Thermo-hydraulics during start-up in natural circulation boiling water reactors," Proc. Int. Topical Meeting on Reactor Thermal Hydraulics, NURETH-5, Sep. 21-24, 1992, Salt Lake City, UT, USA, Vol. I, 119-126 (1992).

[5] J.H. Chiang, M. Aritomi and M. Mori, "Fundamental study on thermo-hydraulics during start-up in natural circulation boiling water reactors (II), natural circulation oscillation induced by hydrostatic head fluctuation" J. Nucl. Sci. Technol. 30(3), 203-211 (1993).

[6] N.E. Todreas and M.S. Kazimi, Nuclear Systems I: Thermal Hydraulic Fundamentals, Hemisphere Publ. Inc., New York (1990).

[7] A.J.C. Stekelenburg, Statics and dynamics of a natural circulation cooled boiling water reactor, PhD thesis, Delft University of Technology, Delft, The Netherlands, (1994).

[8] A.J.C. Stekelenburg and T.H.J.J. van der Hagen, "Low Frequency Dynamics of a Natural Circulation Cooled Boiling Water Reactor," Proc. New Trends in Nuclear System Thermohydraulics, May 30 - June 2, 1994 Pisa, Italy, Vol. I, 205-217 (1994).

[9] A.J.C. Stekelenburg T.H.J.J. van der Hagen and H.E.A. van den Akker, "Numerical simulation of turbulent flow for calibration of cross-correlation flow measurements," Int. J. Num. Methods for Heat and Fluid Flow 4(2), 143-158 (1994).

[10] J.A.A. Wouters, F.J. van der Kaa and W.H.M. Nissen, "Measurements on the thermal hydraulics and reactor physics of the Dodewaard natural circulation BWR," Proc. Specialists' Meeting In-core Instrumentation and Reactor Core Assessment, 1-4 October, 1991, Pittsburg, USA, NEA-OECD, Paris (1992).

[11] T.H.J.J. van der Hagen, F.J. van der Kaa, J. Karuza, W.H.M. Nissen, A.J.C. Stekelenburg and J.A.A. Wouters - to be published (1995).

[12] T.H.J.J. van der Hagen, F.J. van der Kaa, J. Karuza, W.H.M. Nissen, A.J.C. Stekelenburg and J.A.A. Wouters - to be published (1995).

[13] W.H.M. Nissen, J. van der Voet and J. Karuza, "The startup of the Dodewaard natural circulation boiling water reactor - experiences," Nucl. Techn. 107, 93-102 (1994).

[14] F.S. Wang, L.W. Hu and C. Pan, "Thermal and stability analysis of a two-phase natural circulation loop," Nucl. Sci. Engrg. 117, 33-46 (1994).

FLOW CHARACTERISTICS OF KOREA MULTI-PURPOSE RESEARCH REACTOR

Heonil Kim, Hee Taek Chae, Byung Jin Jun, and Ji Bok Lee
Korea Atomic Energy Research Institute
P.O.Box 7, Daeduk-danji, Taejon, Korea
Tel: 042-868-8490

ABSTRACT

The construction of Korea Multi-purpose Research Reactor (KMRR), a 30 MW_{th} open-tank-in-pool type, is completed. Various thermal-hydraulic experiments have been conducted to verify the design characteristics of the KMRR. This paper describes the commissioning experiments to determine the flow distribution of KMRR core and the flow characteristics inside the chimney which stands on top of the core. The core flow is distributed to within ±6% of the averge values, which is sufficiently flat in the sense that the design velocity in the fueled region is satisfied. The role of core bypass flow to confine the activated core coolant in the chimney structure is confirmed.

1. Introduction

The KMRR is designed to be operated at low pressure (3 bars) and temperature (40℃)[1]. The reactor is submerged at the bottom of the reactor pool. A schematic diagram of the reactor and the primary cooling system is given in Fig.1. Sitting on top of the reactor core is the hexagon-shaped chimney. The chimney provides a driving way for the control absorber rods(CAR) and the shutoff rods(SOR). It also acts as a flow path of the downward bypass flow. Two outlet pipes are attached at two opposite sides of the chimney. The reactor coolant from the core exits through the two outlet nozzles. Each outlet pipe is connected to a 400 hp pump, a 14 MW plate-type heat exchanger and a check valve which is designed to close at backward flow. The coolant flow of 780kg/sec passing through the pumps and heat exchangers directs to the reactor core. On returning to the reactor core 10% of the flow is branched to the bottom of the reactor pool, and 90% of

the flow enters via 16inch tube into the inlet plenum, which is 2meters(diameter) x 0.6meters(height)[2]. The core coolant then is distributed into 39 flow channels after passing through a column which is 0.76meters (dia) x 0.3meters(height). The coolant temperature in the core inlet is 35℃ and that in the core exit is 45℃. Meanwhile, the bypass flow slowly rises in the pool. At the top of the chimney the coolant flows down to the core. This downward flow suppresses the upward flowing, activated core coolant and prevents it from escaping to the pool surface.

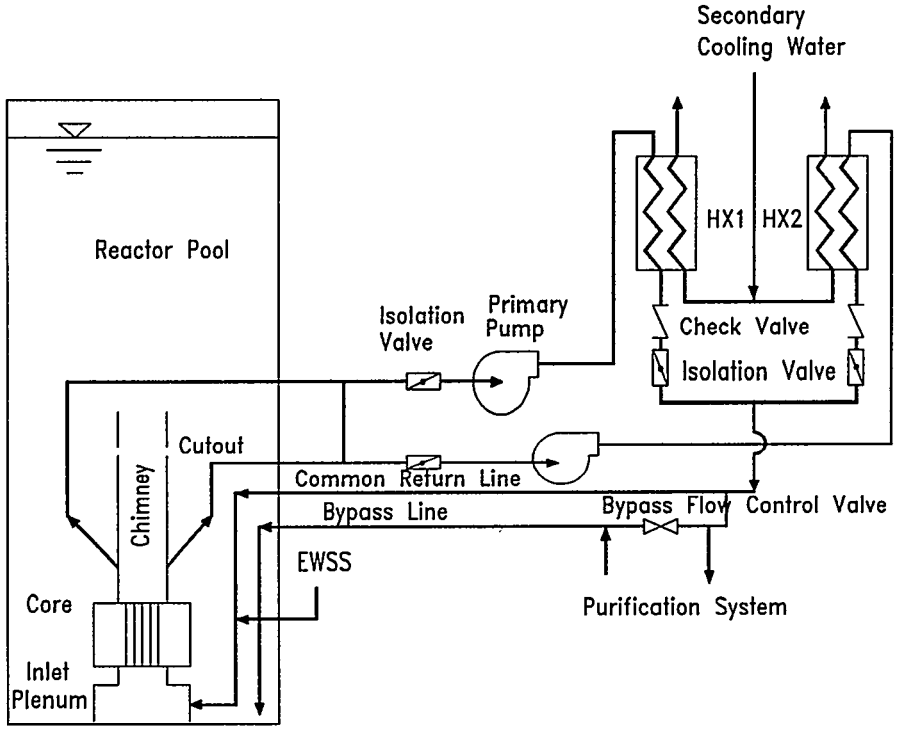

Fig.1 A Schematic Diagram of the Reactor and the Primary Cooling System

The core consists of 23 hexagonal flow tubes (20 fuellable sites) and 16 cylindrical flow tubes (12 fuellable sites). Of the 16 cylindrical flow tubes, eight are located in the heavy water reflector tank outside the core, which is called the outer core or OR sites. Fig.2 shows the plane view of the reactor core. Control absorber rods and shutoff rods are designated as C and S. CT and IR stand for central trap and irradiation hole respectively. The hexagonal and cylindrical flow tubes house the 36 element hexagonal and 18 element cylindrical fuel assemblies respectively. The nominal coolant flow-rate through the hexagonal flow tube is 19.6kg/sec and that through the cylindrical

flow tube is 12.7kg/sec. A fuel assembly is composed of a central support rod, two end plates, three spacers, and 36 or 18 fuel elements. During the fuel loading, the bottom end of the central support rod is locked at the receptacle which is welded on the reactor grid plate. The core is designed to have a pressure drop of 2 bars with a nominal flow-rate. Orifice plates for adjusting core ΔP are installed at the receptacles. In the non-fuellable sites KMRR dummy fuel assemblies, irradiation capsules or separate experimental loops can be loaded. Dummy fuel assemblies are exactly the same as the real fuel assemblies but with no uranium.

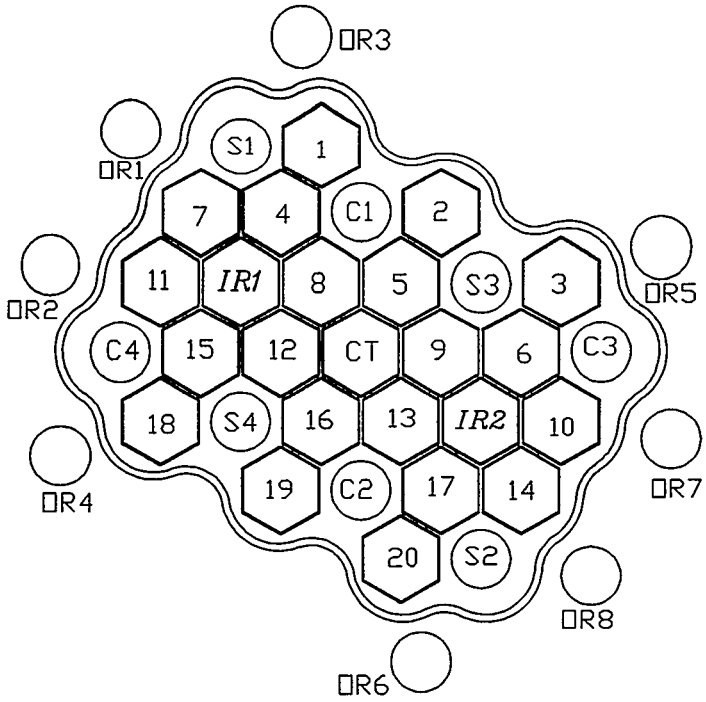

Fig.2 Plane View of KMRR Reactor Core

Commissioning tests start as soon as all dummy fuel assemblies are installed. Of the many tests a couple of important hydraulic tests, channel flow-rate measurement and chimney flow-field survey, are described. Section 2 explains the experimental procedure and apparatus for the two tests and results are summarized in the following section.

2. Commissioning Tests

2.1 Channel Flow-Rate Measurement

To measure the flow-rate of individual flow channel we devised instrumented dummy fuel assemblies where, two pressure taps are installed in the central support rod of the fuel assemblies and two pressure tubings are connected to the tapped holes. Once we know the relationships between ΔP and mass flow-rate they can be used to measure the mass flow-rate. To minimize the flow obstruction the two pressure tubings(1.6mm) are inserted in the grooves along the central support rod. The pressure tubings coming out from the upper part of the fuel assemblies are then connected to the 3.2mm stainless steel tubings via the Swagelok fittings which are welded onto the bundle structure. The instumented dummy fuel assemblies are calibrated in the outcore test loop, where real flow tubes are used to achieve the best result. Three hexagonal instrumented dummy fuel assemblies and three cylindrical instrumented dummy fuel assemblies are tested. In this outcore test, we obtained the characteristic differential pressure curve(ΔP .vs. Mass Flow-Rate) for each instrumented dummy fuel assembly.

During commissioning test, we install the instrumented dummy fuel assemblies in KMRR core. For each run we load only three instrumented dummy fuel assemblies for ease of handling the fuel assemblies and the pressure tubings. The 3.2mm pressure tubings from the reactor core are connected to three differential pressure transmitters (Rosemount 3051 Model CD3A) which are located on the reactor hall floor whose elevation is lower than the core. The accuracy of the differential pressure transmitter is ±0.1%. The calibration equations for the voltage versus the differential pressure are obtained by a conventional pressure calibrator. Data acquisition is done by an A/D board and PC system. The voltage signal is obtained at the rate of 20Hz. For one flow channel we record 20 data points which are already averaged for 10 seconds. After pump operation the pressure tubing lines are completely vented to avoid errors due to air in the piping system. The ambient coolant temperature is controlled by using secondary cooling system intermittently.

2.2 Chimney Flow-Field Survey

The majority of coolant coming out from the core is sucked away through the two exit nozzles at the lower chimney wall. Some coolant, however, is directed upward through the control shroud tubes and the shutoff shroud tubes because these tubes encompass the cylindrical flow tubes. This injected upward flow to the chimney loses its momentum mainly because of the downward bypass flow from the chimney top.

To get the idea of the flow behavior in the chimney, we measure the vertical velocity components. Hot film anemometer system (TSI Model IFA100&200) is used. To hold the hot film anemometer probe in the reactor pool we prepare a 12 meter pipe which is made up with four 3 meter pipes. A coaxial cable from the probe is routed inside the pipe and connected to the anemometer. The pipe is hung at the manbridge hoist which is used to move the fuel assemblies and can move to any direction with the manbridge control. Since the pipe is very long, a support structure is necessary during the velocity measurement. To do this we make a wire net with several guide holes. This wire net is temporarily mounted on top of the chimney. The pipe with the probe is inserted through the guide holes and the wire net supports it.

A meter scale is engraved in the pipe to indicate the axial probe location. To read the scale we use a laser pointer which sits on the manbridge guard.

In the commissioning test we check two things. First, downward velocities are measured to ascertain the downward bypass flow from the top of the chimney. To get the flow behavior of the upcoming jet from the cylindrical flow tubes which are guided by control and shutoff shroud tubes, upward velocities are measured. The signal is obtained at the rate of 100Hz and averaged for 60 seconds.

3. Results

3.1 Channel Flow-Rate Measurement

Figure 3 shows the differential pressures versus the mass flow-rates for the instrumented dummy fuel assemblies; the hexagonal dummy fuel assemblies are designated by DH002~DH004 and the cylindrical dummy fuel assemblies are DC002~DC004. The fitting correlations are obtained using a regression analysis and are applied in the channel flow measurement. The correlations predict the measured data within ±1.7%. The discrepancies between the individual instrumented dummy fuel assemblies are believed to be occurred due to the manufacturing variation of the pressure tap holes in the central support rods. This discrepancy does not weaken the function of the individual instrumented dummy fuel assembly as a flowmeter.

Since the calibration of the instrumented dummy fuel assemblies was done at the water temperature of 20℃ and incore measurement was done at 30℃, we corrected the incore test results using the temperature compensation curve which shows ΔP-mass flow-rates with coolant temperatures(Fig.4). The differential pressure increases with the decreasing water temperature mainly due to the increased water viscosity.

Figure 5 shows the relative mass flow-rates of all flow channels. The flow channels with mass flow-rate less than 99% of the average flow are indicated by shades. The minimum flow channels are identified as shown in Fig.5. Generally the mass flow-rates of outer core channels show smaller values compared to those of inner core. The channels near to the core inlet pipe and outlet pipes also show somewhat lower mass flow-rates. This trend had been confirmed in the half-core full-scale test performed in the AECL[3].

3.2 Chimney Flow-Field Survey

Due to a turbulent nature of the flow the measurement uncertainties are significant (10 to 80%, depending on the measuring location), enen though the accuracy is less than ±10% accoding to the measuring system manufacturer data. For the purpose of flow-field survey, however, the hot film anemometer system is adequate.

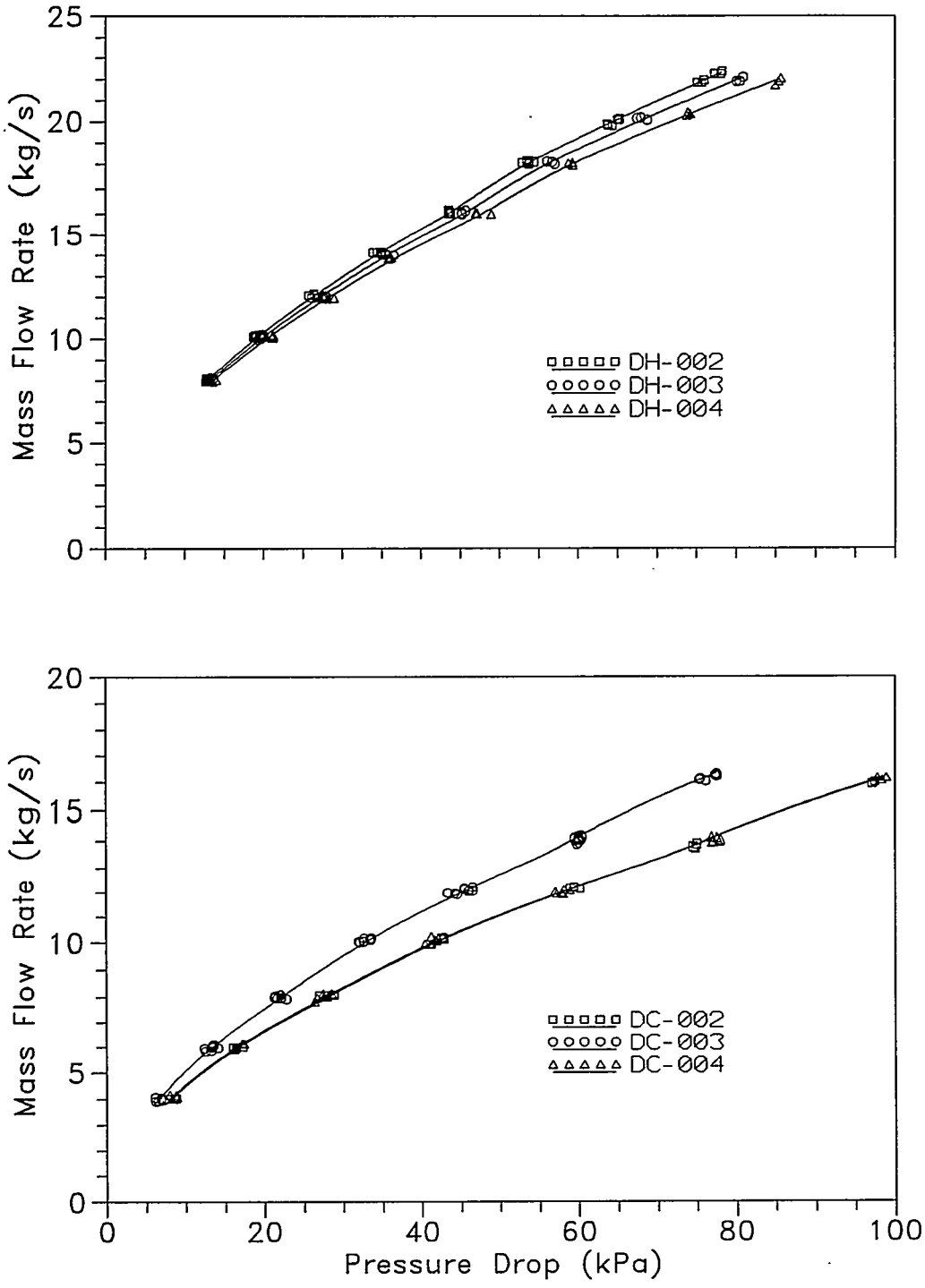

Fig.3 ΔP .vs. Mass Flow-Rate for the Instrumented Dummy Fuel Assemblies

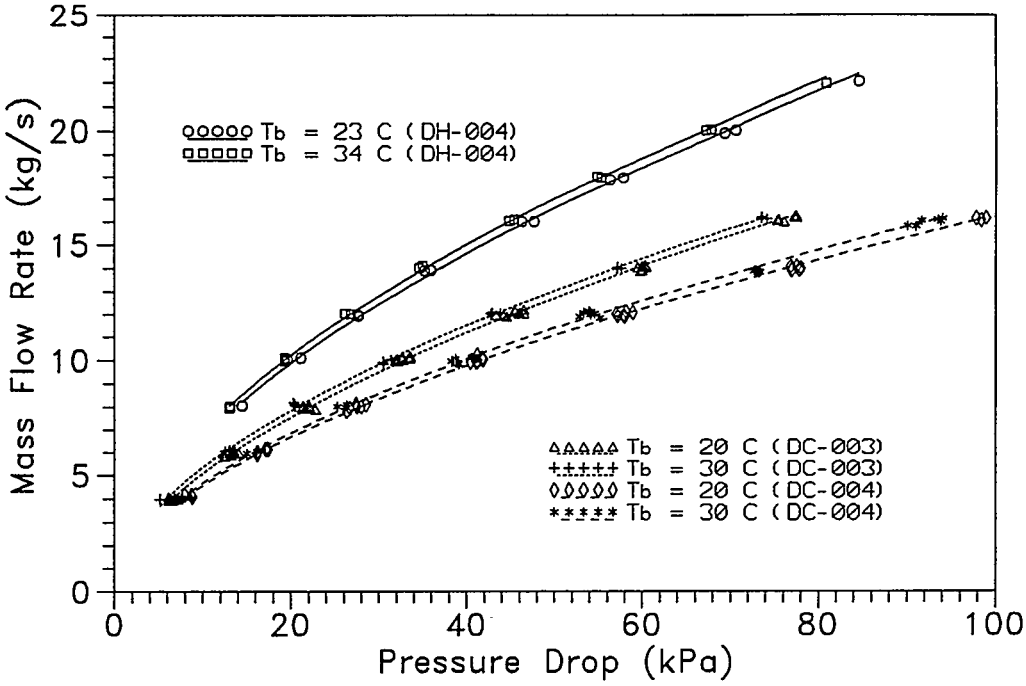

Fig.4 Effect of Water Temperature on the ΔP .vs. Mass Flow-Rate

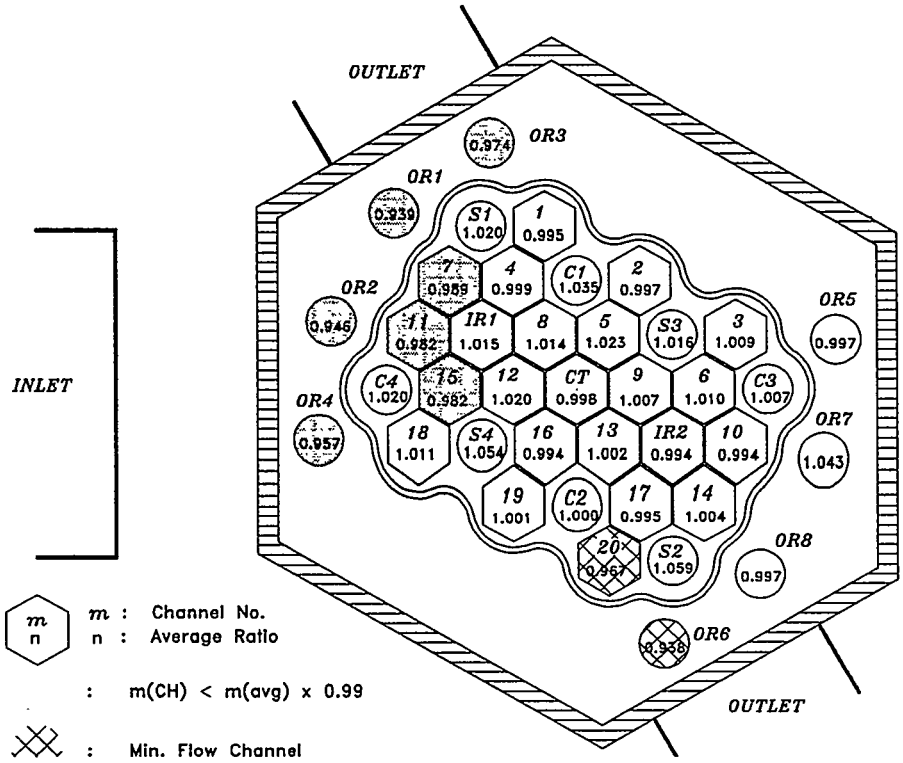

Fig.5 Core Flow Distribution

Downward velocities are measured at two horizontal planes, 30centimeters apart from the chimney cutout openings, which are the rectangular holes at the upper chimney wall for provision of natural circulation path during the longterm core cooling phase. The bypass flow goes down both through the top of the chimney and through the cutout openings. The downward velocities at the plane in between the chimney top and the cutout openings range from 8 to 15cm/sec. The downward velocities at the plane 30cm below the chimney cutout openings range from 17 to 27cm/sec, which agree with the calculated chimney down flow velocity(22cm/sec) by taking into account the measured bypass flow-rate and the cross-sectional area of the chimney. This indicates that the bypass flow coming into the chimney through the cutout openings merge into the bypass flow from the top of the chimney.

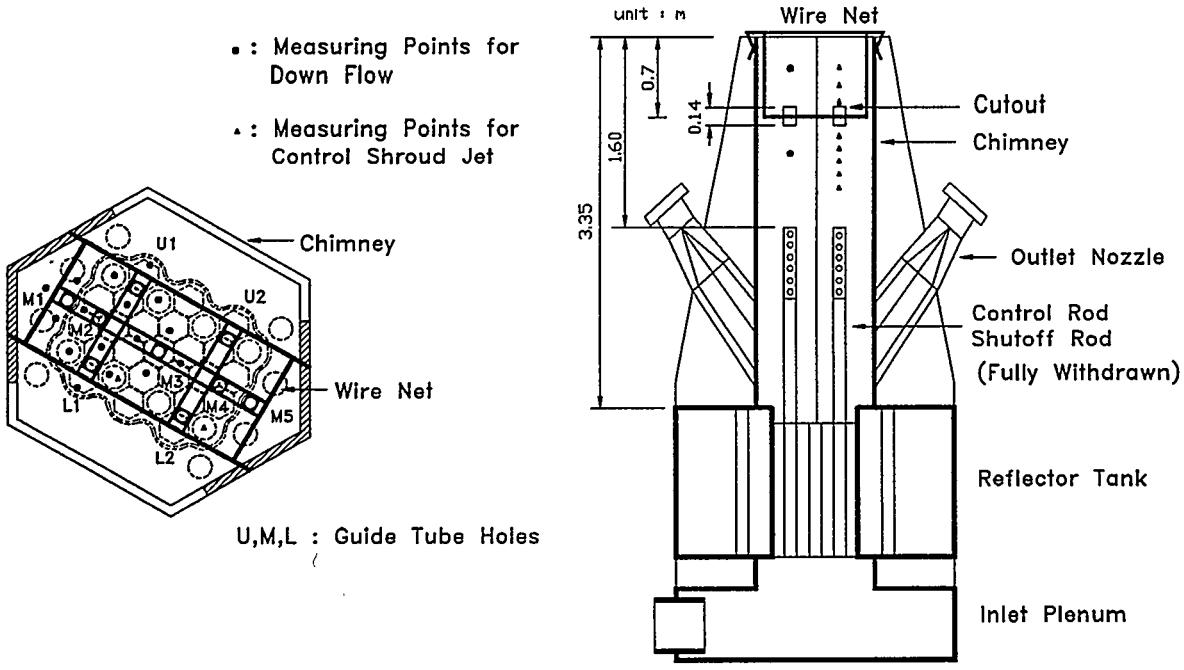

Fig.6 Horizontal and Vertical View of Velocity Measuring Location

The upward coolant jet from control(or shutoff) shroud tube is supposed to be suppressed due to the downward bypass flow. The jet velocities are measured to observe the suppression. Figure 6 shows the measuring location. Since the bypass flow is fixed, the net flow in any horizontal plane in the chimney is also invariant. The chracteristic velocity scale in the chimney can be decided by the net flow in the chimney. Therefore, we let the velocity of

22cm/sec be the representative velocity scale in the chimney. Figure 7 shows the velocities of coolant jet. The SOR#2 and SOR#4 are depicted as S2 and S4 in the Fig.5. As seen in the Fig.7, jet velocities become less than 22cm/sec 60 ~70cm above the shroud tube openings. From this result we conclude that the jet loses its momentum after ejecting about 70cm to the chimney. The jet seems to be suppressed at this height and confined within the chimney.

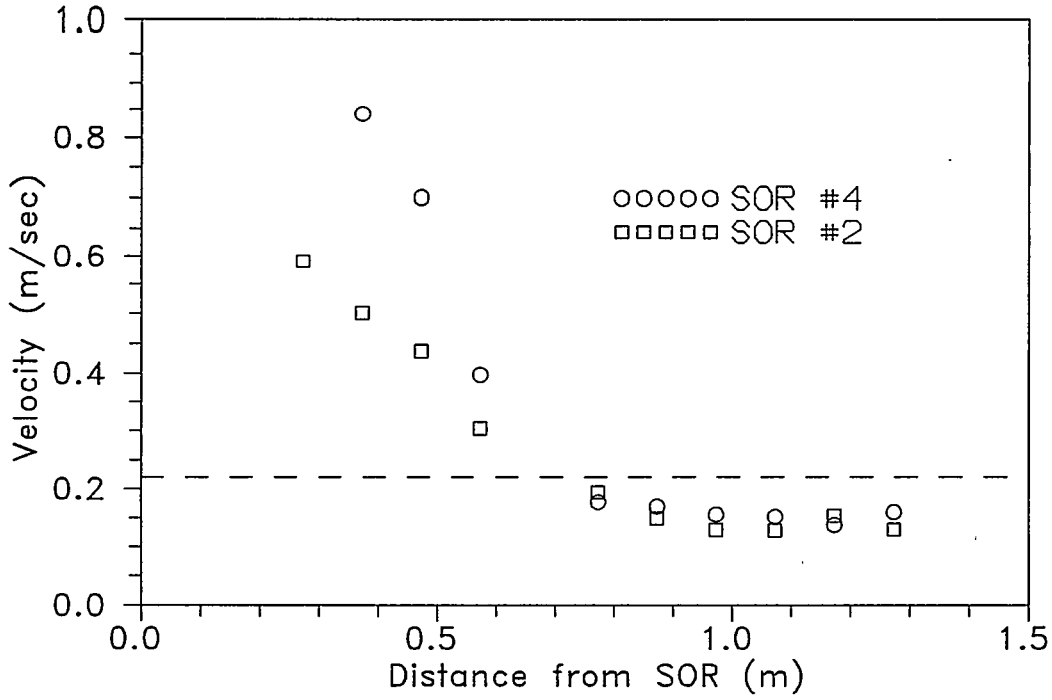

Fig.7 The Velocity of SOR Shroud Jet

4. Concluding Remarks

In order to measure the flow-rates of all flow channels in KMRR core, six instrumented dummy fuel assemblies are devised. Each instrumented dummy fuel assembly is calibrated and can measure the channel flow-rate within ± 1.7%. The flow distribution map shows a flat profile with a maximum deviation of 6% in one of the outer core flow channels near to the core outlet. The downward bypass flow from the reactor pool to the core through the chimney is confirmed. The coolant jet through the reactivity control devices is believed to be suppressed and confined within the chimney.

References

[1] H. Kim, et.al, "Korea Multi-purpose Research Reactor, A Prominence of New Korean Nuclear R&D Era", The 8th PBNC, Taipei, 1992 Apr.

[2] Wan, P.T., et.al., "Experimental Investigation of Core Flow Jet Confined in a MAPLE Flow Test Facility", 8th Annual Conference of Canadian Nuclear Society, Saint John, 1987 June.

[3] W.E. Bishop and J.C. Garbutt, "MAPLE-X10 Reactor Full-Scale Hydraulic Test Rig", AECL-10512, 1991 Nov.

ANALYSIS OF STEAM GENERATOR LOSS-OF-FEEDWATER EXPERIMENTS WITH APROS AND RELAP5/MOD3.1 COMPUTER CODES

E. Virtanen, T. Haapalehto
Lappeenranta University of Technology
P.O.Box 20, FIN-53851 Lappeenranta, Finland

J. Kouhia
VTT Energy, Nuclear Energy
P.O.Box 20, FIN-53851 Lappeenranta, Finland

Three experiments were conducted to study the behaviour of the new horizontal steam generator construction of the PACTEL test facility. In the experiments the secondary side coolant level was reduced stepwise. The experiments were calculated with two computer codes RELAP5/MOD3.1 and APROS version 2.11. A similar nodalization scheme was used for both codes so that the results may be compared. Only the steam generator was modelled and the rest of the facility was given as a boundary condition. The results show that both codes calculate well the behaviour of the primary side of the steam generator. On the secondary side both codes calculate lower steam temperatures in the upper part of the heat exchange tube bundle than was measured in the experiments.

1. INTRODUCTION

Compared to the Western PWRs the Russian design VVER-reactors have a special feature: horizontal steam generators. This type of steam generator (SG) has two vertical collectors and horizontal U-shaped heat exchange tubes. The behaviour of the horizontal SG is very different compared to the western type vertical SG. For example, the secondary side of a horizontal SG contains much more water. Hence, all the loss-of-feedwater transients are slower. During a total station black-out accident a vertical SG dries in some tens of minutes but a horizontal SG in some hours.

During normal operation all the heat exchange tubes of a horizontal SG are covered with water, but in the case of loss-of-feedwater accident the secondary side water level starts to decrease. When the level falls below the highest tube rows the heat transfer from primary to secondary side starts to deteriorate and primary coolant temperature begins to rise. If the heat transfer decreases more rapidly than the decay heat produced in the core, the primary circuit pressure rises up to the opening pressure of the pressurizer relief valve. The primary coolant leaks out of the system and as a result the reactor core may be damaged.

The Western thermal-hydraulic system codes, like RELAP5 [1] and CATHARE2 [2], are developed and validated to model the phenomena in the vertical SG's. But the differences between vertical and horizontal steam generators are so important that the calculational models developed for the vertical SG's are not directly applicable for the horizontal SG's. The PACTEL loss-of-feedwater experiments have been performed to study the overall behaviour of the horizontal steam generators and especially to produce experimental results for code assessment. The work presented here has been done at Lappeenranta University of Technology.

2. FACILITY DESCRIPTION

PACTEL (Parallel Channel Test Loop) [3] is a volumetrically scaled (1:305) out-of-pile model of the Russian design VVER-440 reactors used in Finland. The facility is an integral test facility and it includes all the main components of the primary circuit of the reference reactor. The reactor vessel is simulated by a U-tube construction consisting of separate core and downcomer sections. The core is comprised of 144 electrically heated fuel rod simulators. The geometry and the pitch of the rods are the same as in the reference reactor. The rods are divided into three roughly triangular shaped parallel channels, which represent the intersection of the corners of three hexagonal VVER rod bundles. The maximum total core power is 1 MW, or 22% of the scaled nominal power. The maximum primary pressure is 8.0 MPa compared to 12.3 MPa of the reference reactor.

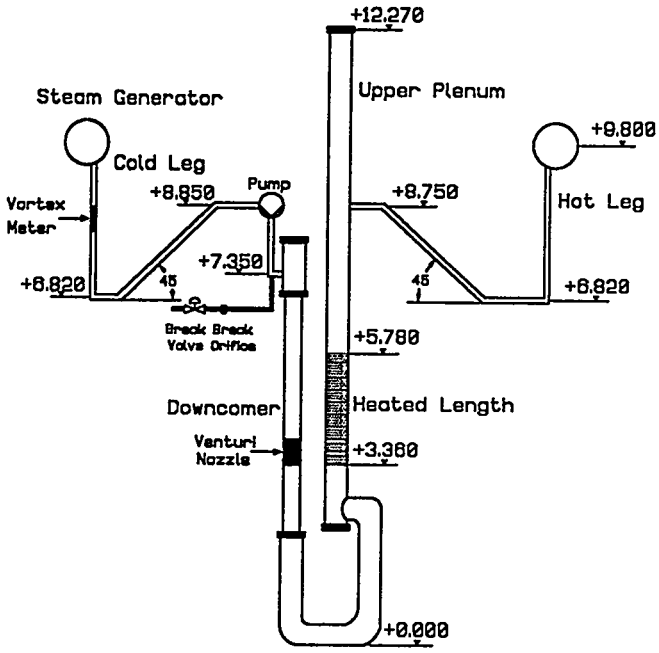

Fig. 1. Geometry of the PACTEL facility.

The component heights and the relative elevations correspond to those of the full scale reactor to match the natural circulation pressure heads in the reference system. The hot and cold leg elevations of the power plant have been reproduced. This is particularly important for the loop seals. Unlike other PWRs VVER-440 has a loop seal also in the hot leg. This is a consequence of the steam generator location, which is almost at the same height as the hot leg connection to the upper plenum. The primary collector of the steam generator is connected to the hot leg at the bottom of the steam generator, hence a roughly U-shaped pipe is needed to complete the connection. The cold leg loop seal is formed by the elevation difference of the inlet and outlet of the reactor coolant pump. Fig. 1 shows how the geometry of the loop seals are modelled in the PACTEL facility.

2.1. Steam generator description

The number of the loops has been reduced from six of the reference system to three in PACTEL, thus one PACTEL steam generator corresponds to two in the power plant. The original steam generator of PACTEL has full-length heat exchange tubes and the same tube bundle geometry as in the power plant steam generator. The tube bundle height is less than 15% of the height of the reference steam generator. This fact limits the use of the original PACTEL steam generator, when for example the effects of the decrease of the secondary side level are studied.

The new steam generator (Fig. 2), installed in one loop, has vertical primary collectors and horizontal heat exchange tubes. The 118 U-shaped heat exchange tubes are arranged in 14 layers and 9 vertical columns. The average length of the tubes (2.8 m) is about one third of that in the full scale steam generator (9.0 m). The outer diameter of the tubes is 16 mm, corresponding to the reference system, and the inner diameter is 13 mm (in the power plant 13.2 mm). In order to have a higher tube bundle, the pitch in the vertical direction has been doubled (48 mm) compared to the reference steam generator. The pitch in the horizontal direction has been maintained. The longer pitch in the vertical direction may cause differences especially for the heat transfer but also for pressure losses and swelling. However, under loss-of-feedwater conditions a relatively large error in the estimation of boiling heat transfer coefficient has only a small effect on the total heat transfer coefficient, because the boiling heat transfer coefficient is very large compared to the convective coefficient on the primary side.

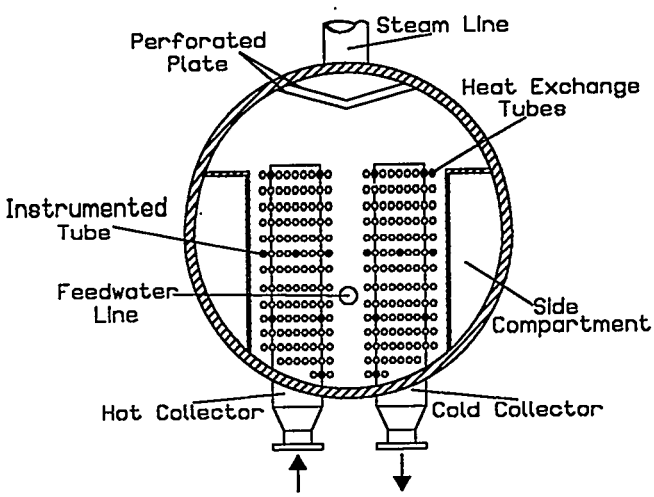

Fig. 2. New steam generator of PACTEL.

The outer diameter of the shell is 1.0 m (in the power plant 3.34 m). Because of the higher vertical pitch, the secondary side is larger than the scaled down secondary volume. This distorts the time scale of secondary side transients. Two compartments have been constructed on each side of the steam generator to decrease the mass of water directly involved in the primary to secondary heat transfer process. The compartments are not totally isolated from the rest of the secondary side, but the coolant has several flow paths in and out of the compartments.

The instrumentation of the steam generator contains mainly temperature measurements. The primary and secondary side temperatures are measured in eight tubes in three or four different locations in each tube. The inlet and outlet temperature of the primary coolant, the primary mass flow rate, the mass flow rate of the feedwater and the differential pressure on the secondary side are measured as well. The measured collapsed level is based on the differential pressure measurement.

3. EXPERIMENTS

Three experiments, SG-2, SG-3 and SG-4, were conducted to study the behaviour of the new steam generator construction of PACTEL facility. The experiments were like the loss-of-feedwater experiments but instead of reducing the secondary level continuously it was reduced in steps.

In these experiments only one loop with the new steam generator was in operation. The primary coolant pump was operating during the whole experiment. Primary and secondary side pressures were different from one experiment to the other (Table 1).

In the beginning of each experiment the core power was set as high as possible and it was kept constant until a steady state was reached. The collapsed level of the secondary side was then reduced stepwise. Feedwater injection was stopped and when the secondary level had dropped 50 mm the injection was started again. In Fig. 3 the measured feedwater mass flow rate in experiment SG-3 is shown. The system was allowed to settle down for 30 minutes between each step. When the secondary side coolant level had dropped below the highest heat exchange tube row the heat transfer from primary to secondary side began to decrease. The temperature in the outlet of the cold collector as well as in the inlet of the hot collector began to rise. In order to keep the coolant temperature in the inlet of the hot collector constant the core power was reduced. Also the feedwater mass flow rate was changed to correspond to the evaporation rate and to keep the collapsed level constant during the settling down period.

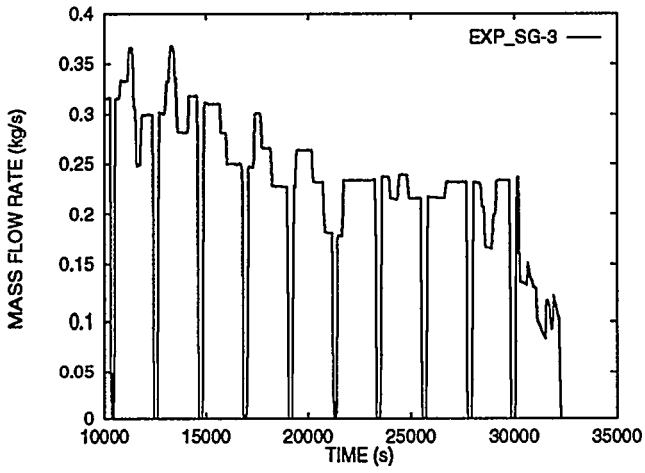

Fig. 3 Measured feedwater mass flow rate in experiment SG-3

The results of the different loss-of-feedwater experiments are similar. Naturally, both primary and secondary temperatures are different because the pressures are different. The only clear difference is that the behavior is more stable when the secondary pressure is higher. This is because the collapsed level is near the swell level and the transition zone where the highest tubes start to dry out is shorter.

Table 1 Primary and secondary pressures in the experiments

EXPERIMENT	PRIMARY PRESSURE	SECONDARY PRESSURE
SG-2	3.0 MPa	0.7 MPa
SG-3	1.2 MPa	0.3 MPa
SG-4	7.5 MPa	4.2 MPa

4. CALCULATIONS

4.1. Computer codes used in the calculations

Two computer codes, RELAP5/MOD3.1 and APROS version 2.11, were used in the calculation of the experiments. RELAP5 is a thermal-hydraulic system code developed at the Idaho National Engineering Laboratory (INEL) for best-estimate transient simulation of light water reactor coolant systems. RELAP5/MOD3.1 is the latest version based on a nonhomogeneous and nonequilibrium (six-equation) model for the two-phase system. APROS (Advanced Process Simulator) [4] code is developed in Finland by VTT and Imatran Voima Oy (IVO). The APROS simulation environment contains a database, graphics and physical models for the simulation of nuclear and conventional power plants and chemical processes. The database includes several predefined process components, like tanks, steam generators, pumps and valves, which makes it easier to create a new simulation model. The thermal-hydraulics of APROS include single-phase and three- five- and six-equation two-phase flow models.

4.2. Nodalization

Only the steam generator part of the facility has been modelled, the rest of the facility has been given as a boundary condition. The same nodalization scheme has been used for both computer codes although some code dependent alterations had to be made.

The nodalization for RELAP5/MOD3.1 is shown in Fig. 4. Hot and cold legs are modelled with large time dependent volumes where the pressure and temperature are controllable. A time dependent junction connects the volume modelling the hot leg to the hot collector. The vertical hot and cold collectors are modelled with eight nodes. The heat exchange tubes are lumped into seven pipe components (numbers 705 - 735 in Fig. 4). The lowest component models the three lowest tube rows, the next five components two tube rows each and the highest component models the highest tube row. All the pipe components are divided horizontally into five nodes.

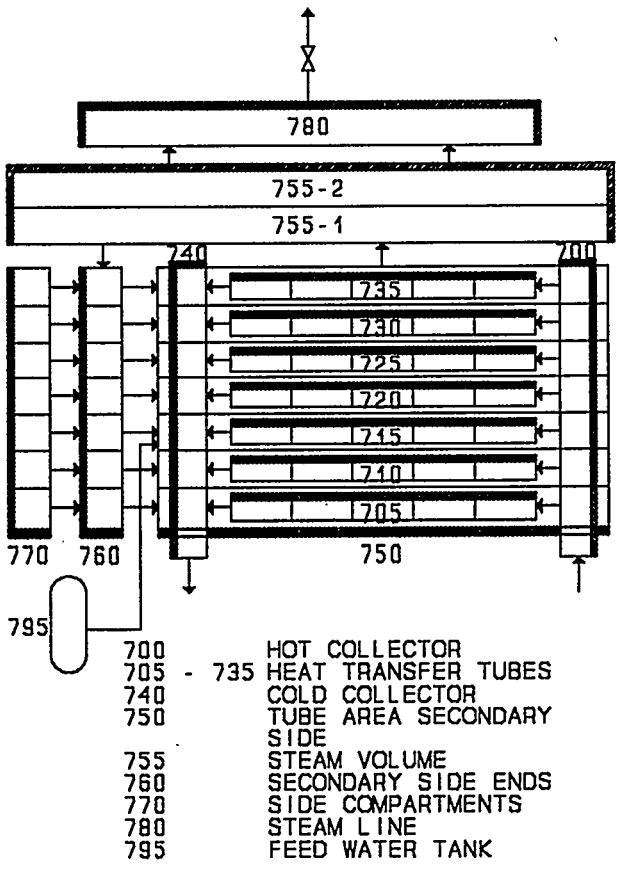

Fig. 4 Nodalization of the new steam generator for RELAP5/MOD3.1

On the secondary side of the steam generator the heat exchange tube area is modelled with seven nodes and the vapor volume above the heat exchange tubes with two nodes. The steam generator ends as well as the side compartments are modelled with separate components. From the side compartments (number 770 in Fig. 4) there are only cross flow junctions to the steam generator ends (number 760 in Fig. 4), which in turn are connected to the tube bundle area and also to the vapour volume. This construction allows vertical internal recirculation typically associated with horizontal steam generators. Feedwater is injected into the third lowest node in the heat exchange tube area. The outlet of steam is modelled with a time dependent volume as a mass sink and a control valve connecting the steam line (number 780 in Fig. 4) to the sink.

All heat structures except the thin plates between the heat exchange tube area and the side compartments are modelled. The material properties have been obtained from the manufacturers. Heat losses to the environment are taken into account in the simulation. A constant heat transfer coefficient together with a constant environment temperature is used as a boundary condition.

In APROS there are certain predefined process components like tanks, pumps and valves. The predefined steam generator model was not used in this study, but a new model was constructed using five-equation calculation level modules e.g. nodes and branches. Basically it is the same model as was used with the RELAP5 code. Because APROS does not have the same kind of time dependent components as RELAP5, two control valves had to be added, one to control the primary mass flow rate and another to control the secondary feedwater mass flow rate. Otherwise, the same input information was given for the APROS code as for RELAP5.

During a steady state run the secondary side collapsed level is controlled with a control system in both codes. In the start of the transient this system is excluded from the simulation. Another control system is used to keep the secondary side pressure constant during the whole calculation.

Primary side pressure, coolant mass flow rate and hot leg temperature as well as secondary side pressure and feedwater mass flow rate were given as a boundary condition. The values were obtained from the measurement data of each experiment.

4.3. Results of the simulations

From the point of view of the safety analysis of a nuclear reactor the interesting parameter is the amount of heat transferred form the primary side to the secondary side. The transferred power is a function of the temperature difference between the hot and cold collector. Because most of the heat transfer occurs through the heat exchange tubes, the ability of a code to calculate overall heat transfer can be evaluated by observing the inlet and outlet temperatures of the heat exchange tubes.

Fig. 5 shows the measured primary temperatures from one instrumented heat exchange tube together with the

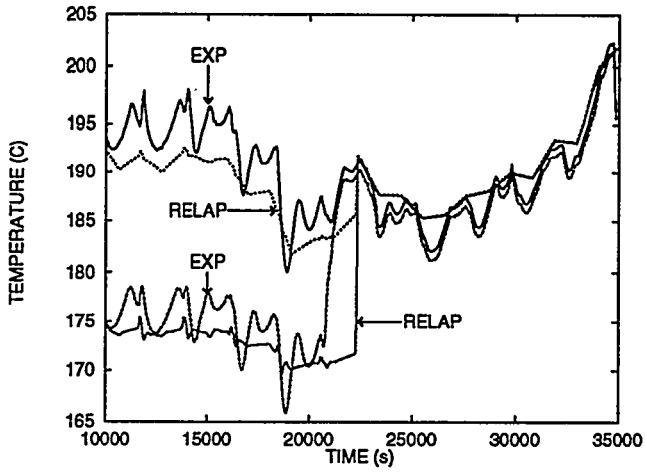

Fig. 5 Primary temperatures in one tube from experiment SG-2 and from RELAP5 calculation

corresponding temperatures calculated with RELAP5/MOD3.1. The measurement locations are 200 mm from the hot collector and 500 mm from the cold collector, and the calculation nodes are 279 mm from both collectors. This causes a small difference between the measured and calculated values. The oscillations in the measured temperatures were not well reproduced because the boundary condition values for the hot leg temperature are based on the averaged measurement data. In Fig. 6 the same measured temperatures and temperatures calculated with the APROS code are presented. The uncovering of the tube can clearly be seen around 20500 seconds in the experiment and around 22500 seconds in the RELAP5 calculation. APROS calculates the uncovering of the tube to occur a little later. The time difference between experiment and calculation results is mainly caused by the nodalization. In nodalization two heat exchange tube rows are lumped together. The scalar values, like temperature, are calculated in the middle of the node. The corresponding temperature measurements are located in the uppermost tube row. The difference in elevation between the measurement point and the middle of the node is 24 mm corresponding to around 1000 seconds of experimental time.

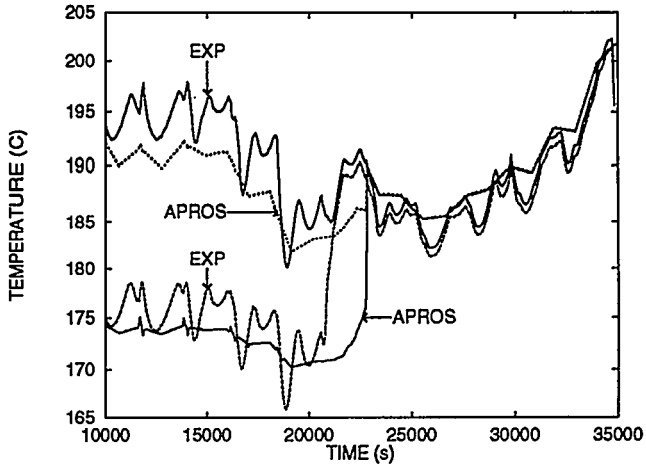

Fig. 6 Primary temperatures in one tube from experiment SG-2 and from APROS calculation

In the experiment, steam superheating was observed after the highest heat exchange tubes were uncovered. In Fig. 7 the measured secondary side temperatures in the highest tube layer together with the temperatures from the RELAP5/MOD3.1 calculation are shown. In Fig. 8 the same measured temperatures with temperatures from two different APROS calculations are shown. Both codes underestimate the steam superheating. In APROS calculations it was observed that the hydraulic diameter of the secondary nodes has a significant influence on the calculated steam temperature. If the hydraulic diameter is not given for the code the code calculates it based on the given flow area of the node, Eq. 1.

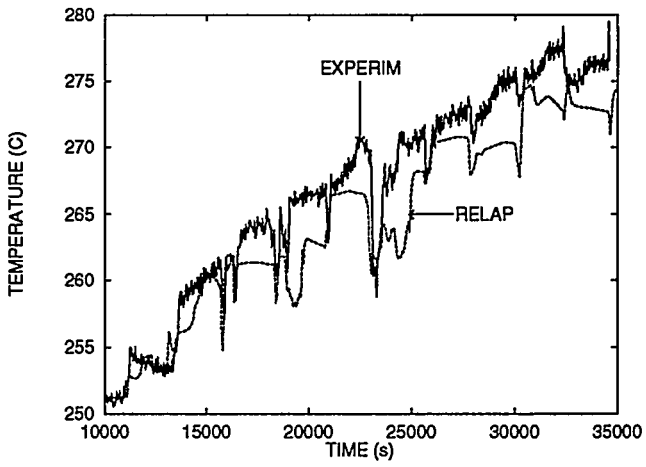

Fig. 7 Secondary temperatures in the highest tube layer from experiment SG-4 and from RELAP5 calculation

$$D_h = \sqrt{\frac{4 \cdot A_f}{\pi}} \qquad (1)$$

$$D_h = \frac{4 \cdot A_f}{P_w} \qquad (2)$$

where A_f is the flow area and P_w is the wetted perimeter. In Fig. 8 APROS refers to the result from the calculation where the code was allowed to calculate the hydraulic diameter itself. In the other calculation presented here (APROS_1 in Fig. 8) the hydraulic diameter was calculated using Eq. 2 and it was given to the code. The value is the same which was used in the RELAP5 calculations. When calculated from Eq. 1 the hydraulic diameter for a tube bundle area secondary side node is 1.002 m, and calculated from Eq. 2 it is 50 mm. As can be seen, the calculated steam temperature using the hydraulic diameter of 50 mm (APROS_1) is nearer the measured values. Even though the difference between measured and calculated steam temperatures was around 15 K in some cases the effect on the overall heat transfer was negligible because the heat transfer to single-phase steam is small compared to the heat transfer to steam-water mixture.

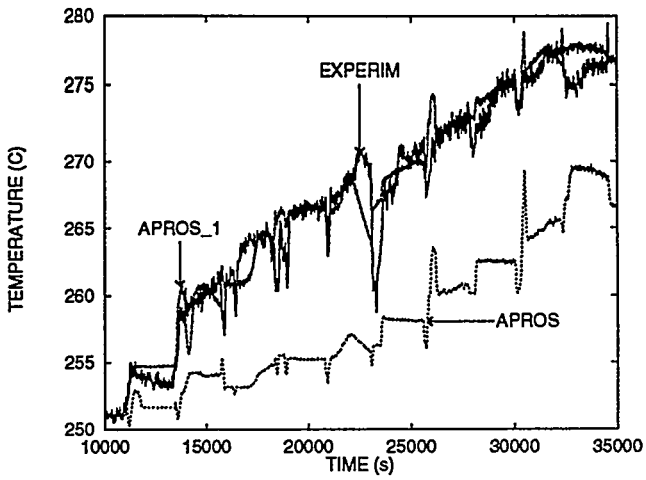

Fig. 8 Secondary temperatures in the highest tube layer from experiment SG-4 and from APROS calculations with imposed (APROS_1) hydraulic diameter and with D_h calculated by the code

In the experiment the temperature of steam in the steam line was a little lower than in the highest tube layer. Both codes calculated significantly lower steam temperatures in the steam line. The heat transfer mode, that RELAP5 uses on the inner surface of the heat structure describing the upper part of the steam generator shell, was found to be condensation. In this mode the calculated heat transfer is more efficient than heat transfer from single-phase vapor to the wall. As a sensitivity calculation the whole steam dome was modeled in one RELAP5 calculation with only one node. In this case the heat transfer mode was conduction and the steam temperature was nearer the measured value.

5. CONCLUSIONS

Three PACTEL loss-of-feedwater experiments have been calculated using the APROS version 2.11 and RELAP5/MOD3.1 computer codes. The main parameter to be compared was the temperature difference between hot and cold collectors, e.g. the total power transferred from primary to secondary side. In all the calculations the results obtained were acceptable. Some differences were caused by the rather rapid changes in the experimental boundary conditions, which were not completely reproduced. When the results were compared more in detail, some differences were observed. Especially the steam temperature above the heat exchange tube bundle

was in most of the calculations lower than in the experiments. Even though the difference between measured and calculated steam temperatures is relatively large it does not affect the overall heat transfer.

The assessment calculations presented here are not sufficient to validate the codes used, but they show that the APROS and RELAP5 codes are able to model the overall behaviour of the horizontal steam generators. Even with quite a simple secondary side model, for example without recirculation, it is possible to simulate reasonably well the heat transfer from the primary to the secondary side under loss-of-feedwater conditions. However, some problems seem to exist in their capabilities to model the phenomena on the secondary side. In order to validate or improve the models new experiments are needed, because in the experiments performed the boundary conditions were too complex. Also some parameters were not measured, like steam flow rate and heat exchange tube surface temperatures, limiting the usefulness of the experiments used for comparison.

REFERENCES

[1] Carlson,K. E., Riemke, R. A., Rouhani, S. Z., Shumway, R. W., Weawer, W. L., "RELAP5/MOD3 CODE MANUAL, Volume 1: Code structure, System Models and Solution Methods", EG&G Idaho, Inc., Idaho Falls, Idaho, USA. June 1990.

[2] Barre, F., Bernard M., The CATHARE code strategy and assessment. Nuclear Engineering and Design, 124, 1990. pp. 257-284.

[3] Raussi, P., Munther, R., Kalli, H., Kouhia, J., Puustinen, M., "Experimental VVER Safety Studies in Finland", Trans. of ENC'94, Int. Nuclear Congress, Lyon, France, October 2-6, 1994.

[4] Porkholm, K., Hänninen, M., Puska, E. K., Ylijoki, J., "APROS Code for the Analysis of Nuclear Power Plant Thermal-Hydraulic transients", Eight Proceedings of Nuclear Thermal-Hydraulics, ANS Winter Meeting, Chicago, Illinois, November 15-20, 1992.

HORIZONTAL STEAM GENERATOR THERMAL-HYDRAULICS

Olga Ubra
SKODA Praha Company
Prague, Czech Republic

Michael Doubek
Czech Technical University
Prague, Czech Republic

ABSTRACT

Horizontal steam generators are typical components of nuclear power plants with pressure water reactor type VVER. Thermal-hydraulic behavior of horizontal steam generators is very different from the vertical U-tube steam generator, which has been extensively studied for several years. To contribute to the understanding of the horizontal steam generator thermal-hydraulics a computer program for 3-D steady state analysis of the PGV-1000 steam generator has been developed. By means of this computer program, a detailed thermal-hydraulic and thermodynamic study of the horizontal steam generator PGV-1000 has been carried out and a set of important steam generator characteristics has been obtained. The 3-D distribution of the void fraction and 3-D level profile as functions of load and secondary side pressure have been investigated and secondary side volumes and masses as functions of load and pressure have been evaluated. Some of the interesting results of calculations are presented in the paper.

1. INTRODUCTION

Horizontal steam generators are typical parts of nuclear power plants with Russian designed pressure water reactor - type VVER. Currently 46 VVER reactors (VVER 440, VVER 1000) are under operation or under construction in Central and Eastern European countries, mostly in Ukraine and Russia, and in Finland. All these countries have made a decision to modernize VVER nuclear power plants and their main activities are focused on VVER safety enhancement. The impact of the horizontal steam generator on the integrity of the VVER reactor coolant system and on nuclear power plant safety is significant. At the IAEA Consultants Meeting on "The Safety of VVER Nuclear Power Plants", the problem of VVER-1000 steam generator integrity was identified as an important issue of safety concern [1]. Within the framework of IAEA "Extrabudgetary Program of the Safety of VVER-1000 NPP", a group of international experts has been created to analyze

information on the horizontal steam generators operating experience, deficiencies and corrective measures.

The first VVER-1000 nuclear power plant was put into operation in 1980 and there are currently 19 units operating with 76 steam generators PGV-1000 (1000 MW) and two nuclear power plants with 8 PGV-1000 are under construction in the Czech Republic. In the period from 1986 to 1991, serious deficiencies on 24 horizontal steam generators at six VVER 1000 nuclear power plants were detected. The identification of the causes of deficiencies has shown that secondary side fluid flow, primarily flow influence on the mineral distribution, plays important role in the damage processes. In order to optimize flow distribution on the secondary side and to minimize mineral concentration in failure sensitive areas the multidimensional thermal-hydraulics phenomena in the steam generator secondary side should be analyzed in detail.

More information on steam generator thermal-hydraulics is also needed for safety analyses of VVER reactor concept that has a fundamental importance for the licensing procedure of VVER units. Currently safety analyses are to be performed by means of the thermal-hydraulic codes RELAP 5/MOD 2, CATHARE or ATHLET that have a large international assessment base regarding western PWR. To adapt these codes to VVER type power plants requires a substitution of a vertical steam generator model by a horizontal steam generator model and verification of the adapted code for VVER typical phenomena. A nodalization scheme of the horizontal steam generator secondary side should be rough but realistic and sufficient for Non LOCA analysis. Several different approaches for modelling horizontal steam generator were presented at the first, second and third International Seminars of Horizontal Steam Generator Modelling that were held in Lappearanta in 1991, 1992 and 1994 [2], [3], [4]. One of the conclusions of the seminars was that the modelling of the horizontal steam generator has not been established yet and the final solution of modelling with international plant codes has not yet been found. Clearly to develop a realistic nodalization scheme of the horizontal steam generator is not possible without understanding all key phenomena in both the primary and the secondary side of the steam generators.

Thermal-hydraulic behavior of horizontal steam generator is very different from the vertical U-tube steam generator which has been extensively studied for many years. Only limited experimental data on the behavior of horizontal steam generators is available and particularly on the natural circulation in the secondary side. Thus more information is needed. The study in this field proceeds in both directions - experimental and theoretical using mathematical modelling. Experimental tests using experimental facilities have been performed in Finland (PACTEL facility) and in Hungary (PMK-2 facility), experimental tests at operating nuclear power plant units in Russia [2], [4], [5]. Detailed mathematical models for the study of the horizontal steam generators behavior have been developed in Russia and in the Czech Republic [4], [6]. Design principles of the Czech computer program for steady state thermal-hydraulic analysis of the horizontal steam generator PGV-1000, the verification of this program and some interesting results of calculations will be discussed

in this paper.

2. A COMPUTER PROGRAM FOR THERMAL HYDRAULIC ANALYSES OF THE STEAM GENERATOR PGV-1000

The general view of the horizontal steam generator is in the Fig.1. The heat exchanger, consisting of 11000 horizontal U-tubes, is in a large water pool where the fluid is under conditions of natural circulation. The feed-water injection is located above the hot side of the tubes in order to diminish the level swelling close to the hot collector. A perforated sheet is located above the tubes. Its rim, more than 500 mm long, is directed downwards. The louvers moisture separator system is located in the top part of the steam generator. The steam flow from the moisture separator proceeds to the short steam lines connecting the steam dome with the steam collector.

The secondary side flow pattern is difficult to define. It is supposed, that the flow pattern includes two major circulations and a number of minor circulations. Two-phase mass flow rises up through the shell side of the heat exchanger and the separated water mixed with feed water flows down through the peripheral zone and in the open portion between the tube bundles. The minor circulations complete the major circulation like in the turbulent flow field.

The horizontal steam generator water level and water inventory determination are complicated because of a 3-D distribution of the heat flux and void fraction that depends on the steam generator power and the secondary side pressure. Water level measurement has two scales - a wide range and a narrow range. Level control is based on the narrow range and the protection system on the wide range measurement.

2.1. Computer Program Capabilities

The developed computer program is capable to analyze :

1. *Steam generator primary side hydraulics*
   - primary side flow distribution in tube bundles;
   - velocity distribution in collectors;
   - pressure drop distribution on the primary side and the total primary side pressure drop.
2. *Heat exchanger behavior*
   - heat transfer for various situations in the tube and shell side (low level and the effect of tube bundle uncovery is taken into account);
   - multidimensional heat flux distribution, total heat flux transferred through heat exchanger tubes (steam generator heat power);

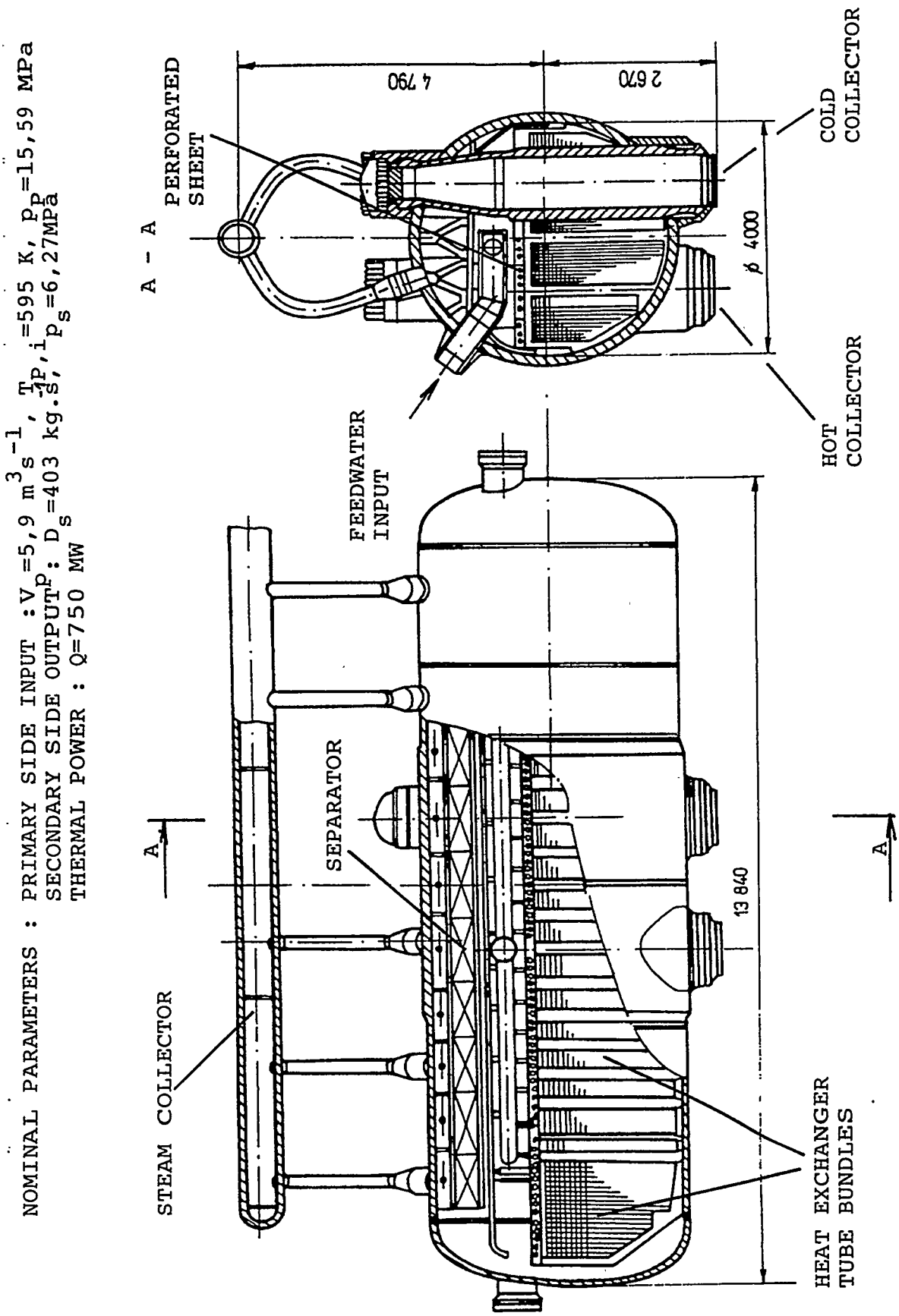

Figure 1: **PGV-1000 Steam Generator. Dimension [mm]**

- primary side fluid temperature distribution - temperature profile along the tubes;
- outlet mixed mean temperature of the primary side fluid;
- steam outlet temperature and the temperature of the steam-water mixture at the shell side;
- steam generator tube temperature profile.

3. *Steam generator secondary side thermal-hydraulics and thermodynamics*
   - average circulation rate for the cases with the level above the top of the tube bundles;
   - 3-D void fraction distribution in the shell side;
   - steam and water volumes under the level, steam generator water mass inventory;
   - mass redistribution under the perforated sheet (for the cases with level above the perforated sheet);
   - minimal thickness of the steam layer under the perforated sheet (for the cases with the level above the top tube bundles);
   - secondary side pressure (for the plant operation in Mode that maintains a constant mean coolant temperature in the primary system);
   - steam flow rate;
   - secondary side pressure drops between the perforated sheet and outlet of the steam collector, the total secondary side pressure drop.

2.2. Nodalization

For the mathematical simulation the steam generator is divided into three main regions.

1. The area between the bottom of the steam generator and upper tubes of the heat exchanger (the top of the tube bundles).
   This region is subdivided into horizontal and vertical directions as shown in Fig.2 and Fig.3. The heat exchanger is divided into two bundle groups - inner and outer. Both bundle groups and their corresponding secondary volumes are subdivided in the vertical direction into layers, the inner group into four layers and the outer one into three layers. Every tube is divided into eleven nodes in the axial tube direction.

2. The region between the top of the tube bundles and the steam generator level. The nodalization of this area is derived from the division of the submerged perforated sheet shown in Fig.4.
3. The steam region between steam generator level and the outlet of the steam collector - steam dome with moisture separator and steam line.

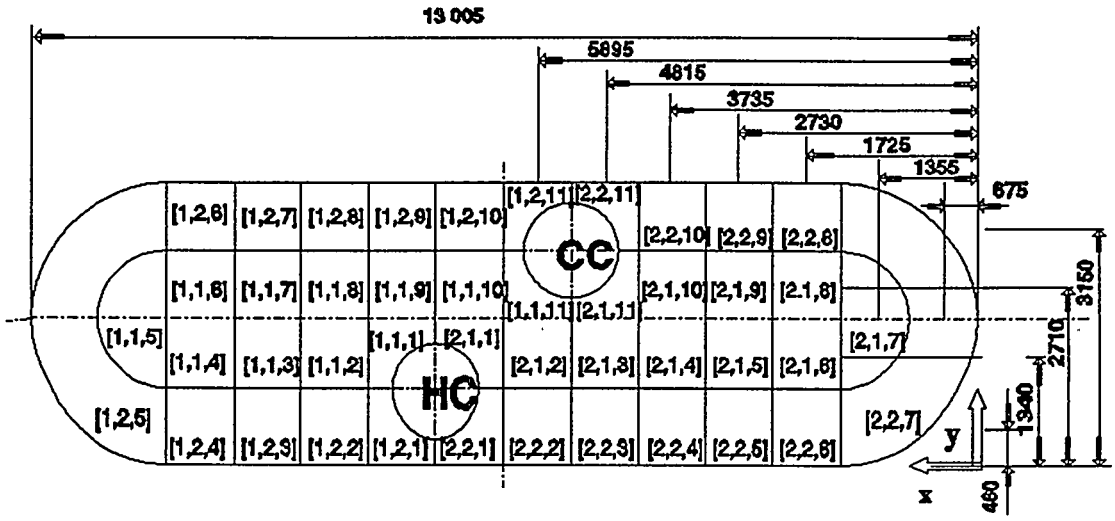

Figure 2: **Tube Bundles Nodalization [horizontal direction]. Dimension [mm].**

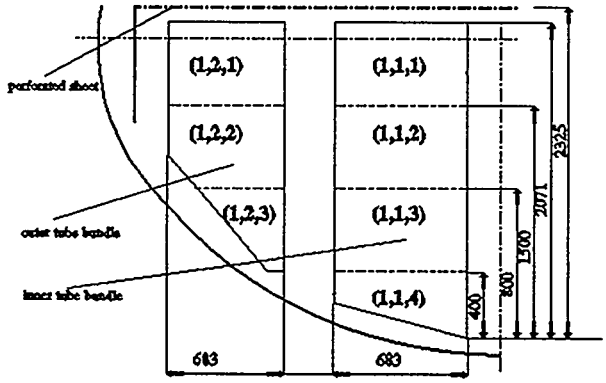

Figure 3: **Tube Bundles Nodalization [vertical direction]. Dimension [mm].**

2.3. Simulation Methods

The physical backgrounds applied in the model will be only summarized in this paper. They are shortly described in [7] and fully in [6].

A computer program for steady state calculations of steam generator primary side hydraulics yields :

- primary flow distribution in the tubes,
- pressure losses over steam generator primary side.

For the calculation of primary side flow distribution, the heat exchanger is divided into groups of tubes, as shown in Fig.3. Average flow velocity is evaluated for each group. The

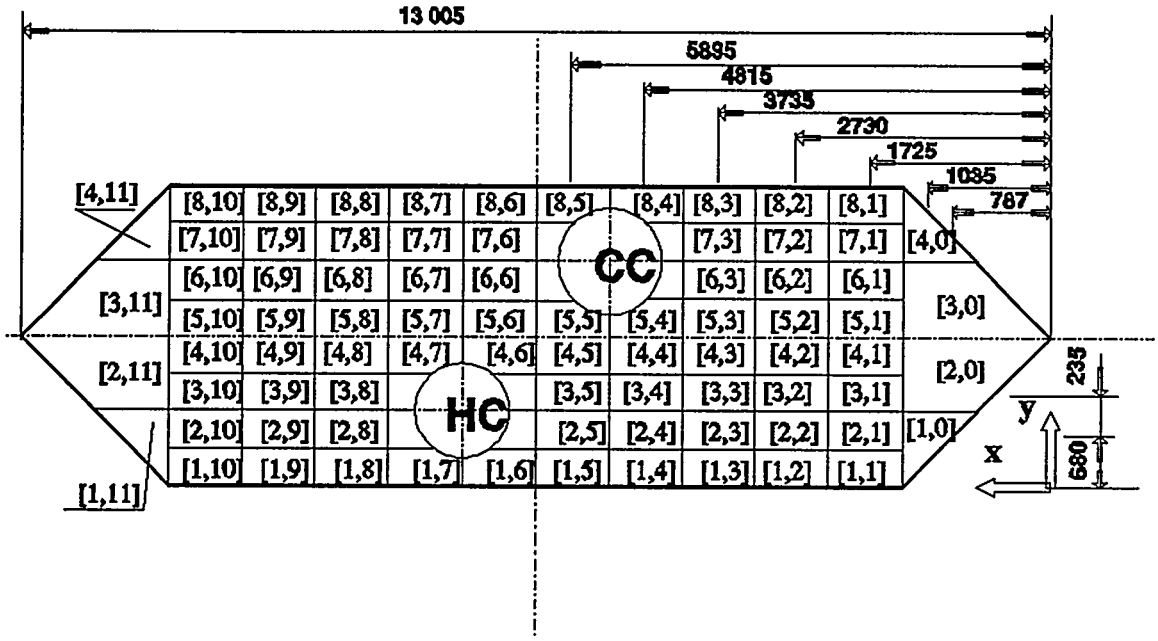

Figure 4: **Perforated Sheet Division. Dimension [mm].**

primary results of the calculation are the velocity distribution in the header and the flow velocities in the tubes.

The flow distribution is described by two differential equations:

$$A \cdot \rho_2 \cdot v_2 \cdot \frac{dv_2}{dx} - E \cdot \rho_1 \cdot v_1 \cdot \frac{dv_1}{dx} = \xi_t \cdot \rho_1 \cdot w_1 \cdot \frac{dw_1}{dx} + (\rho_1 - \rho_2) \cdot g \qquad (1)$$

$$\frac{dw_1}{dx} = -L \cdot \frac{S_1}{n \cdot s} \cdot \frac{d^2 v_1}{dx^2} \qquad (2)$$

Model representation of the primary side pressure drops takes into account pressure drops in the inlet and outlet of the tubes connecting the steam generator with the hot and cold legs of the circulation loops, in both collectors and in the heat exchanger tubes.

The nodalization of the heat exchanger tube bundles for steady state thermal analysis corresponds to that shown in Figs.2 and 3. The iterative method of calculation is based on thermal balance. The calculation is performed for every node separately and a global thermal balance is checked. The main result is the heat flux distribution in the steam generator shell side. The global heat flux is the essential parameter for the assessment of secondary side pressure and steam output. The program takes into consideration two possibilities - the steam generator level is above the top of tube bundles and the steam generator level is under the top of tube bundles with some tube uncovered.

For the arbitrary node [i,j,k] the following system of equations is used :

$$Q^{*}_{i,j,k,l}=G_{j,k}\cdot[i(p,T_{i-1,j,k,l}) - i(p,T_{i,j,k,l})] \tag{3}$$

$$Q_{i,j,k,l} = F_{i,j,k,l}\cdot\overline{q_{i,j,k,l}} \tag{4}$$

For tubes under SG level:

$$\overline{q_{i,j,k,l}}=k_{i,j,k,l}\left(\frac{T_{i,j,k,l} + T_{i-1,j,k,l}}{2}-T_s\right) \tag{5}$$

For tubes above SG level (uncovered tubes):

$$\overline{q_{i,j,k,l}}=k_{i,j,k,l}\cdot\frac{(T^{p}_{i,j,k,l} - T^{s}_{i-1,j,k,l}) - (T^{p}_{i-1,j,k,l} - T^{s}_{i,j,k,l})}{\log\frac{T^{p}_{i,j,k,l} - T^{s}_{i-1,j,k,l}}{T^{p}_{i-1,j,k,l} - T^{s}_{i,j,k,l}}} \tag{6}$$

$$k_{i,j,k,l} = \frac{1}{\frac{d_o}{d_j\cdot\alpha^{p}_{i,j,k,l}}+R_W+\frac{1}{\alpha^{s}_{i,j,k,l}}} \tag{7}$$

$$G_{j,k} = \rho_j\cdot n_{j,k}\cdot W_j\cdot S_j \tag{8}$$

where subscripts specify :

i = 1,2,..11	number of the node in axial tube direction;
j = 1,2,4.../5/	number of the group of tubes in vertical direction;
k = 1,2	inner and outer tube bundles;
l = 1,2	left or right side of the heat exchanger.

Correlations used for the assessment of the heat-transfer coefficients on the outside and inside of the tubes are presented for various operating conditions in [6].

A computer program for steady state thermal hydraulic analysis of the steam generator secondary side provides the capability to determine the average circulation rate for the cases with the level above the top of the tube bundles, void fraction distribution in the region between the steam generator bottom and upper rows of heat exchanger bundles, mass redistribution in the area between the upper part of the tube bundles and the submerged perforated sheet, and the steam generator level profile.

To determine the average value of the circulation rate, a simple flow diagram is assumed. Two phase mixture rises up through the area in tube bundles. The steam and water are separated above the tube bundles . The water flows back in the downcomer and

in the free space between the tube bundles. The average value of the circulation rate is determined through the iteration method based on the pressure balance in the upflow section with heat exchanger tubes and in downflow section, free of tubes. The applied method builds on the theory of industrial steam boilers with natural circulation [8].

For the assessment of void fraction distribution, the region between steam generator bottom and upper tube rows of heat exchanger is divided in vertical direction into layers of equal height of 50 mm. The heat flux into an arbitrary volume is obtained from the heat exchanger calculation. The feedwater distribution is taken into account. The calculation of the void fraction begins in the bottom of the steam generator and proceeds step by step over the layers to the top of the region. Two different methods have been developed for this calculation. The first method is based on the circulation rate assessment and it is applied to cases where the average level is above the top tube bundles. The void fraction in the elementary volume in n-th of the [i,k,l] element layer is described by the following equations :

$$\varphi_n = C_n \cdot \beta_n \tag{9}$$

$$\beta_n = \frac{V_n''}{V_n' + V_n''} = \frac{G_n'' \cdot \rho'}{G_n \cdot \rho'' + G_n'' \cdot (\rho' - \rho'')} \tag{10}$$

$$G_n = G_{n-1} + \overline{w_2} \cdot \rho \cdot (S_n^* - S_{n-1}^*) \tag{11}$$

$$G_n'' = G_{n-1}'' + \frac{Q_n}{r} \tag{12}$$

$$C_n = f(p, w_n) \tag{13}$$

where the average velocity in the bundle w_2 is a function of circulation rate, the cross sections S_n, S_{n-1} depend on the arrangement of the tube bundles, the parameter C_n is given as a function of medium pressure and velocity in nomograms published in [8].

The second method is based on the theory of free bubbles rising through liquid by buoyancy [9] and it is used for all cases with the level under the top of tube bundles. On the basis of mass and energy conservation laws, considering some acceptable assumptions, the problem is described by two following differential equations :

$$(1 - C)\cdot\frac{d\varphi}{dH} - \varphi\cdot\frac{dC}{dH} = 1 - \varphi \qquad (14)$$

$$(1 - \varphi)\cdot\frac{dC}{dH} - C\cdot\frac{d\varphi}{dH} = \frac{\rho''}{\rho'}(1 - \varphi) \qquad (15)$$

where $C = c_o/w$, w.....vapour velocity;
c_o....downward water flow velocity;

$H = h\cdot\frac{\rho'}{\rho''}\cdot\frac{Q}{w\cdot T''}$ h.....height from the bottom.

The second method of void fraction assessment does not take into consideration the circulation of the fluid. In comparison with the first one, the second method gives slightly higher void fraction, especially in the close vicinity of the hot collector.

For the cases with the level above the top tube bundle, the effect of perforated sheet is simulated. Hydrodynamic processes in the region between upper rows of the tube bundles and submerged perforated sheet depend on perforated sheet design, especially on the degree of the perforation and on the height of the perforated sheet rim. The goal of the simulation is to assess the steam flow rate from more loaded zones to the less loaded regions and to determine the thickness of the steam layer in different locations bellow the perforated sheet. The nodalization of this region corresponds to the perforated sheet division, which is shown in Fig.4. The iterative method which is used for mass redistribution assessment is based on different hydrostatic pressure in neighboring elements.

The effect of submerged perforated sheet is described by following equations:

$$\delta\cdot(\overline{\rho_3} - \rho'')\cdot g = \xi\cdot\frac{w^2}{2}\cdot\rho'' + 2\cdot\frac{\sigma}{R} + \Delta P_1 + \Delta P_3 - H_1\cdot(\overline{\rho_3} - \overline{\rho_1})\cdot g - H_2'\cdot(\overline{\rho_3} - \overline{\rho_2})\cdot g \qquad (17)$$

$$d\delta_{r,s} = \frac{G_{v,r,s} - G_{PS,r,s} - (G_{p,r-1,s} + G_{p,r+1,s} + G_{p,r,s-1} + G_{p,r,s+1})}{\rho''\cdot S_{r,s}} \qquad (18)$$

R defines a critical value of steam bubble radius. Steam flow rate $G_{v,r,s}$ is given by the calculation of the first region (heat exchanger shell side). Steam flow rate over the perforated sheet $G_{PS,r,s}$ is given by the equation:

$$G^2_{PS,r,s} = \frac{2 \cdot S^2_{PS,r,s} \cdot (p_{r,s} - p_4) \cdot \rho''}{1 + \xi_{PS}} \tag{19}$$

and steam flow rate between neighboring elements $G_{P,r,s+1}$ by the equation:

$$G^2_{P,r,s+1} = \frac{2 \cdot S^2_{r,s+1} \cdot (p_{r,s} - p_{r,s+1}) \cdot \rho''}{1 + \xi_{r,s+1}} \tag{20}$$

For the determination of the local value of steam generator level height and for assessment of the steam generator level profile two different method are used, one for the cases with the level above the perforated sheet, and the second one for the level under the perforated sheet.

For the determination of the shape of steam generator level above the perforated sheet, the zone above the perforated sheet should be analyzed. The nodalization is derived from the perforated sheet division. In every node, the void fraction, water volume and finally the height of the steam generator level are calculated.

For the assessment of void fraction in the zone above perforated sheet a method published in [10] has been adopted. Average value of void fraction is given by the relation:

$$\overline{\varphi_{r,s}} = 0.26 \left[\frac{w''^2_{o,r,s}}{\sqrt{\frac{g \cdot \sigma}{(\rho' - \rho'')}}} \right]^{0.36} \left(\frac{\rho''}{\rho' - \rho''} \right)^{0.12} \tag{21}$$

where $w''_{o,r,s}$ is a local steam velocity above the perforated sheet. The height of the steam-water mixture level may be determined from equation:

$$H_{r,s} = \frac{V_{w,r,s}}{1 - \overline{\varphi_{r,s}}} \cdot \frac{1}{S_{r,s}} \tag{22}$$

where $S_{r,s}$ is the cross section for vertical vapour flow area.

The determination of the level profile in the area between the steam generator bottom and the perforated sheet is based only on the calculation of void fraction. The height of the steam generator level in an arbitrary element [i,k,l] is described by the equation:

$$H_{i,k,l} = \overline{H} + \sum_{m=1}^{n} V_m \cdot \varphi_m \cdot \left(1 - \frac{\rho''}{\rho'} \right) \cdot S_{i,k,l} \qquad (23)$$

The complete mathematical model for the steam generator PGV-1000 thermal-hydraulic study is formulated in [6].

3. COMPUTER PROGRAM VERIFICATION

Only a partial verification of the model could be performed. Some results of void fraction calculations were compared with experimental data obtained by Russian organization Gidropress. The comparisons of the void fraction could be made only in the downcomer areas and above the tube bundle (just below the perforated sheet), because there are no data available inside the tube bundles. The results of comparisons between measured void fraction closely below the perforated sheet near the hot collector [5] and calculated void fraction at the output from the tube bundle in elements [1,1,1], [2,1,2], [2,2,8], [2,1,6] and [2,1,9] as a function of load are shown in Fig.5 (the notation of the tube bundles corresponds to Fig.2.). Note, that the higher measured value of void fraction is caused by a function of perforated sheet which creates the vapour layer below the perforated sheet. Therefore, the results of calculations show a good agreement with experimental results.

Similar results of the measurement of the void fraction have been published in [11]. There is no significant disagreement between experimental data and calculations results. It may be noted that the presented model of the steam generator PGV 1000 reproduces the void fraction distribution reasonably well.

4. STEAM GENERATOR PGV 1000 THERMAL HYDRAULIC STUDY

By means of the developed computer program, a detailed thermal-hydraulic and thermodynamic study of the PGV-1000 horizontal steam generator for the Czech nuclear power plant Temelin has been carried out.

About one hundred calculations have been performed and a great amount of interesting information has been obtained. The special attention has been paid to the secondary side analysis, primarily to the mixture level profile, 3-D void fraction distribution and to the distribution of the heat flux transferred to the secondary medium under different operation conditions.

Some important steam generator characteristic parameters have been investigated, for example:

- secondary side water and steam volumes and masses as functions of load

at constant pressure;

- 3-D distribution of the void fraction as a function of load at constant pressure and as a function of pressure at constant load;
- the steam generator level profile as a function of load and a function of pressure;
- the average void fraction as a function of steam generator load and secondary pressure;
- the average level as a function of load for constant pressure and as a function of pressure for constant load;
- the perforated sheet pressure drop as a function of load.

Some results of the PGV 1000 thermal-hydraulic investigations are given in Figures 6 to 13.

In the first group of presented calculations the values of parameters as volumetric flow rate, primary side pressure, the feed-water flow rate, feed water temperature and the steam generator level correspond to nominal operating conditions (Figure 6 to 13). Under these conditions the vapour volume V'' and the water volume V' under steam generator level as functions of the heat power Q (steam generator load) are shown in Figures 6,7. As evident from Figure 7, the vapour volume V'' is proportional to Q for a given (fixed) pressure p. The increase is higher for the low pressure than for the high pressure. The water volume V' in Figure 6 decreases proportionally with increasing Q.

The vapour volume V'' and the water volume V' under the steam generator level as functions of secondary side pressure are given in Figures 8,9. It can be observed from Figure 8 that the vapour volume V'' decreases with increasing pressure p for fixed heat power Q. The decrease is higher for higher heat power. The water volume V' in Figure 9 increases with increasing of pressure. It is evident that the vapour volume - power relationship has twice as high influence than the relationship between the vapour volume and pressure. This fact should be taken into consideration when setting the steam generator measurement and control system is carried out.

The water mass inventory M' which is one of the most important parameters of the steam generator is shown as a function of load in Figure 10 and as a function of secondary side pressure in Figure 12. The water inventory in the horizontal steam generator is higher than in the vertical one. This is important with respect to steam generator dynamic behavior and water level fluctuation during normal operation. The effect of the steam generator water inventory is one of the factors influencing the steam generator operational reliability and plant safety.

The vapour mass M' under the steam generator level as a function of total heat power Q and secondary side pressure p is given in Figures 11 and 13.

For illustration the heat flux profiles and the tube temperature profiles for the tube bundles [1,1,1], [1,1,3] and [1,1,4] under three different secondary side pressures and reduced level (1.9m) are shown in Figures 14,16 and 18. It can be observed that the reduced level affects to the heat flux profile and the tube temperature profile in tube

horizontal tube bundle section [1,1,1]. The notation of the tube bundles corresponds to that given in Figure 3. The void fraction profiles in vertical direction obtained for the same input data in the elements close to the hot and cold collectors [1,1,1], [1,1,5], [1,1,7], [1,1,11], [1,2,3] and [1,2,10] are presented in Figures 15,17 and 19. The effects of both the SG power level and secondary side pressure on the void fraction behavior has been investigated. It can be observed that the effects of the both these parameters are more pronouncedin the vicinity of the hot collector. The void fraction profiles for two different thermal power and nominal steam generator level (2.55m) are shown in Figures 20 and 21. The void fraction distribution has been calculated by method based on the circulation rate assessment. The notation of the tube bundles corresponds to that in Figure 3.

5. SUMMARY

The presented work is a contribution to the investigation of the thermal-hydraulic behavior of the horizontal steam generator for VVER nuclear power plants. The developed computer program provides the capability to determine overall behavior of the steam generator in steady state under various load and pressure conditions and to provide more detailed information about multidimensional two-phase flow in the steam generator shell side. This includes void fractions, circulation flow rates and the dynamics of the heat transfer and swelled level. The detailed knowledge of these parameters may provide information needed for the efficient nodalization of the horizontal steam generator in safety analysis codes and for the safety enhancement of the VVER nuclear power plants.

6. NOMENCLATURE

A	-	Hot collector characteristic value
C	-	Circulation rate
d	m	Tube diameter
D	$kg.s^{-1}$	Steam flow rate
E	-	Cold collector characteristic value
G	$kg.s^{-1}$	Mass flow rate
H	m	Geometric height
i	$J.kg^{-1}$	Enthalpy
g	$m.s^{-2}$	Gravitational constant
k	$W.m^{-2}.K^{-1}$	Overall heat transfer coefficient
L	m	Collector length
n	-	Number of tubes in tube bundle
p	Pa	Pressure
Q	W	Heat flux
q	$W.m^{-2}$	Specific heat flux
R	m	Critical bubble radius

R_w	$K.m^2.W^{-1}$	Thermal resistance
S	m^2	Flow area
T	K	Temperature
V	m^3	Volume
V_n	$m^3.s^{-1}$	Volumetric flow rate in n-th layer
v	$m.s^{-1}$	Flow velocity
w	$m.s^{-1}$	Flow velocity
w''	$m.s^{-1}$	Vapour flow velocity
α	$W.m^{-2}.K^{-1}$	Heat transfer coefficient
β	-	Vapour volumetric flow ratio
φ	-	Void fraction
δ	m	Vapour layer thickness
λ	$W.m^{-1}.K^{-1}$	Thermal conductivity
ξ	-	Flow resistance coefficient
ϱ	$kg.m^{-3}$	Density
σ	$N.m^{-1}$	Surface tension

Subscripts and superscripts

1/2	Refers to inlet/outlet collector
i/o	Refers to inner/outer value
PS	Refers to perforated sheet
P/S	Refers to primary/secondary side of steam generator
'/''	Refers to liquid/vapour phase

7. REFERENCE

[1] Lin, Ch., Strupczewski, A.: ***Steam Generator Collector Integrity of WWER-1000 Reactors***, Proc. 3th Int.Seminar on Horizontal Steam Generators, 14, (1994).

[2] ***International Seminar on Horizontal Steam Generator Modelling, Vol.I., Vol.II.***, Proc., Lappearanta University of Technology, Finland, (1991).

[3] ***Second International Seminar on Horizontal Steam Generator Modelling***, Proc., Lappearanta University of Technology, Finland, (1993).

[4] ***Third International Seminar on Horizontal Steam Generator Modelling***, Proc., Lappearanta University of Technology, Finland, (1994).

[5] Vasiljeva, A.G.,Dmitrijev, A.I.: ***Issledovanije gidrodinamiky parogeneratora PGV-1000***, Elektriceskije Stanciji 6, Pg.19-23, Fig.2, (1987). (in Russian)

[6] Doubek,M., Ubra,O.: ***Steam Generator PGV-1000, Steady State***, CTU Report, Z-490, CTU, Dept.of Thermal and Nuclear Power Plants, Prague, (1994).

[7] Doubek,M., Ubra,O.: ***Computer Program for Horizontal Steam Generator Thermal-hydraulic Analysis***, Proc. New Trends in Nuclear System Thermohydraulics, Vol.I., 751-760, Italy (1994).

[8] Lokshin,V.A., Peterson,D.F.: ***Gidravliceskij rozcot kotelnych agregatov (Normativnyj method)***, Energia, Moskva, (1978). (in Russian)

[9] Avdeev,A.A., Avdeeva,A.A.: ***Kipenije zidkosti pri sbrose davlenija***, Teploenergetika 8, 53-57, (1980). (in Russian)

[10] Sterman,L.S., Stjushin, N.G., Kuthepov, A.M.: Gidrodinamika i teploobmem dlja paroobrozovanii, Vyschaja Skola, Moskva, (1977). (in Russian)

[11] Logvinov,S.A., Dmitrijev,A.I., Trunov,N.B., Tarankov,G.A., Titov,V.F.: ***Thermal-and-Hydraulic Characteristic of Water Volume of PGV-1000 Steam Generator Under Stationary Conditions***, 2-17, Figs.3,8b, International Seminar on Horizontal Steam Generator Modelling, Vol.I., Vol.II., Proc., Lappearanta University of Technology, Finland, (1991).

8. FIGURES

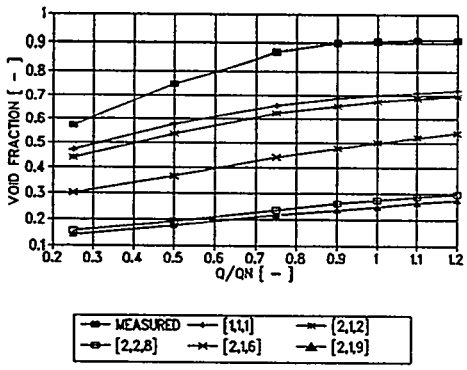

Figure 5 :
Void fraction at the outlet of the tube bundle as a function of load
(nominal heat power QN = 750 MW)

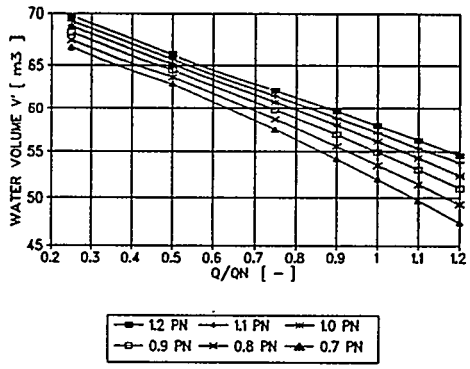

Figure 6 :
Water volume under steam generator level as a function of load
(nominal heat power QN = 750 MW)

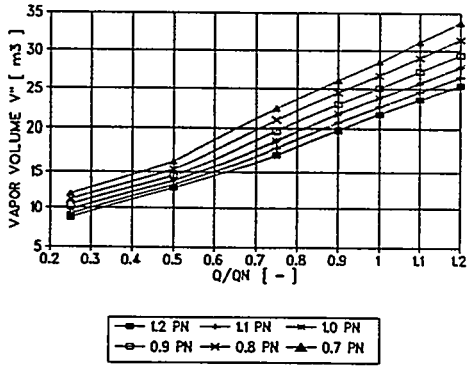

Figure 7 :
Vapour volume under steam generator level as a function of load
(nominal heat power QN = 750 MW)

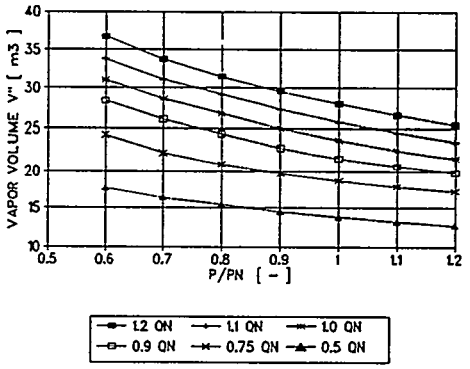

Figure 8 :
Vapour volume under steam generator level as a function of secondary side pressure
(nominal pressure PN = 6,27 MPa)

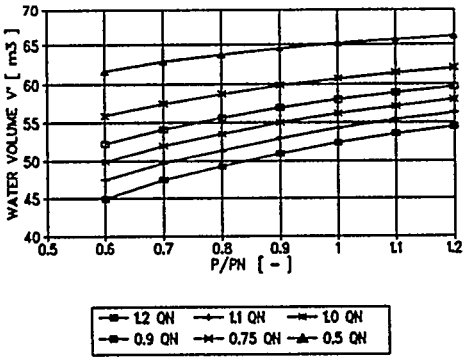

Figure 9 :
Water volume under steam generator level as a function of secondary side pressure
(nominal pressure PN = 6,27 MPa)

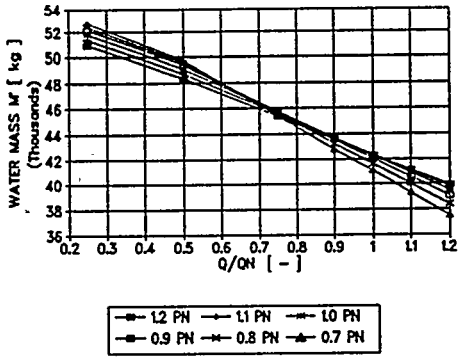

Figure 10 :
Steam generator water inventory as a function of load
(for 6 different secondary side pressure)

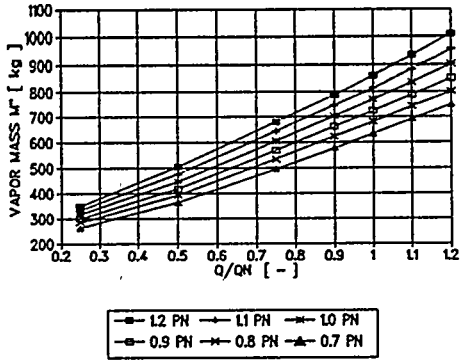

Figure 11 :
Vapour mass under steam generator level as a function of load
(nominal heat power QN = 750 MW)

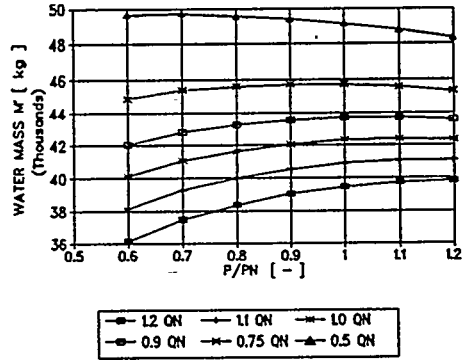

Figure 12 :
Steam generator water inventory as a function of secondary side pressure
(nominal pressure PN = 6,27 MPa)

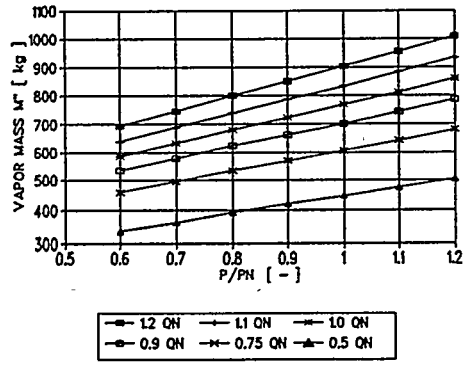

Figure 13 :
Vapour mass under steam generator level as a function of secondary side pressure
(nominal pressure PN = 6,27 MPa)

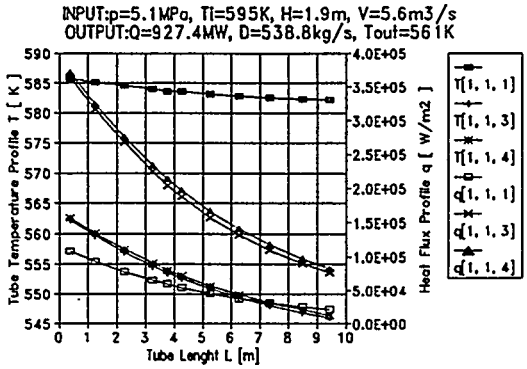

Figure 14 :
Heat flux and tube temperature profiles

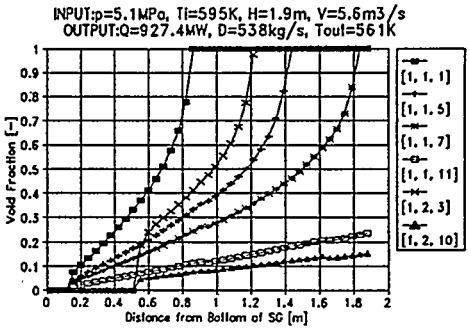

Figure 15 :
The void fraction profiles in vertical direction

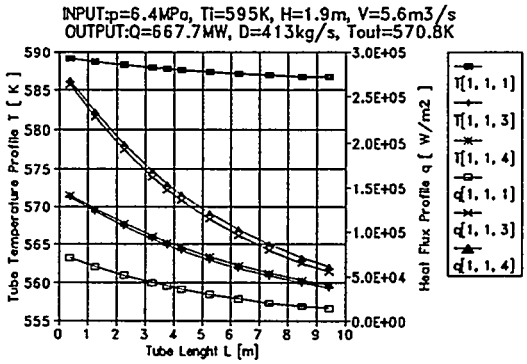

Figure 16 :
The heat flux and the tube temperature profiles

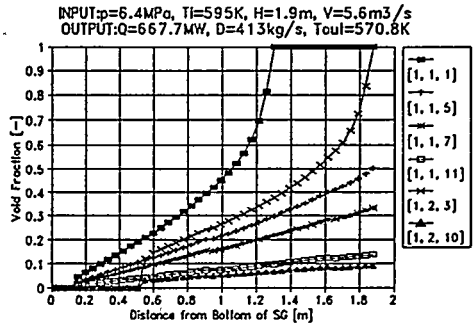

Figure 17 :
The void fraction profiles in vertical direction

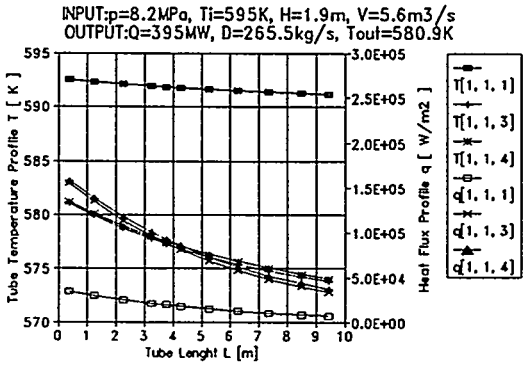

Figure 18 :
The heat flux and tube temperature profiles

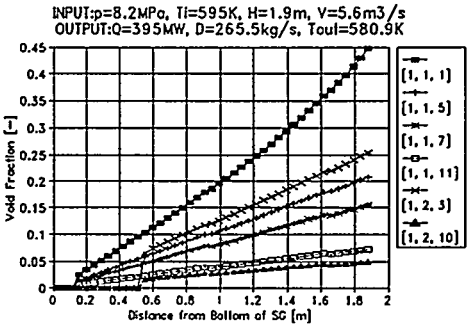

Figure 19 :
The void fraction profiles in vertical direction

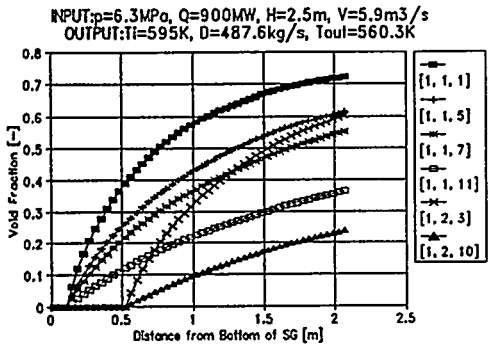

Figure 20 :
The void fraction profiles in vertical direction

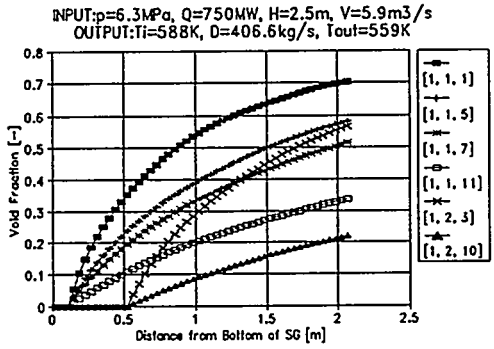

Figure 21 :
The void fraction profiles in vertical direction

ISP33 STANDARD PROBLEM ON THE PACTEL FACILITY

H. Purhonen[1], J. Kouhia[1], H. Kalli[2]

[1]VTT Energy, Nuclear Energy
P.O.Box 20, FIN 53851 Lappeenranta
[2]Lappeenranta University of Technology
Department of Energy Technology
P.O.Box 20, FIN 53851 Lappeenranta

ABSTRACT

ISP33 is the first OECD/NEA/CSNI standard problem related to VVER type of pressurized water reactors. The reference reactor of the PACTEL test facility, which was used to carry out the ISP33 experiment, is the VVER-440 reactor, two of which are located near the Finnish city of Loviisa.

The objective of the ISP33 test was to study the natural circulation behaviour of VVER-440 reactors at different coolant inventories. Natural circulation was considered as a suitable phenomenon to focus on by the first VVER related ISP due to its importance in most accidents and transients. The behaviour of the natural circulation was expected to be different compared to Western type of PWRs as a result of the effect of horizontal steam generators and the hot leg loop seals. This ISP was conducted as a blind problem.

The experiment was started at full coolant inventory. Single-phase natural circulation transported the energy from the core to the steam generators. The inventory was then reduced stepwise at about 900 s intervals draining 60 kg each time from the bottom of the downcomer. The core power was about 3.7 % of the nominal value. The test was terminated after the cladding temperatures began to rise. ATHLET, CATHARE, RELAP5 (MODs 3, 2.5 and 2), RELAP4/MOD6, DINAMIKA and TECH-M4 codes were used in 21 pre- and 20 posttest calculations submitted for the ISP33.

FACILITY DESCRIPTION

PACTEL is a volumetrically scaled (1:305), out of pile model of Russian design VVER-440 pressurized water reactors used in Finland, Figure 1, [1]. The maximum operating pressures on the primary and secondary sides are 8 MPa and 4.6 MPa respectively, while the corresponding

values in VVER-440 are 12.3 MPa and 4.6 MPa. The reactor vessel is simulated with a U-tube construction including separate downcomer and core sections. The core itself consists of 144 full-height, electrically heated fuel rod simulators with a chopped cosine axial power distribution and a maximum total power output of 1 MW, 22 % of scaled full power.

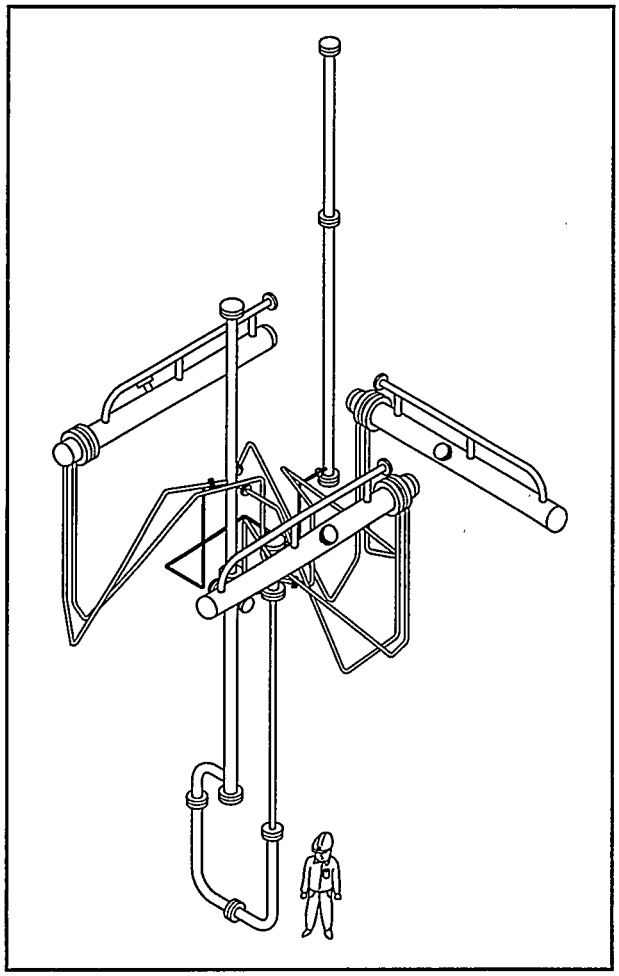

Figure 1. PACTEL facility.

Component heights and relative elevations correspond to those of the full-scale reactor to match the natural circulation gravitational heads in the reference system. The hot leg loop seals are a result of the steam generator locations, which are at roughly the same elevation as the hot leg connections to the upper plenum. The hot and cold leg connections to the steam generators are at the bottom of each collector, and a U-shaped pipe must be used. The cold leg loop seals result from the elevation difference between the inlet and outlet of the reactor coolant pumps, as in other PWRs.

For practical reasons, the total hot and cold leg pipe lengths of the reference plant were not maintained in the PACTEL facility, but were shortened by almost a factor of two. As a result, the pipe cross-sectional area was increased to preserve the volume scaling factor used for the remainder of the facility and preserve the time scale for energy transport from the heat source to the sinks. As a consequence of the increased cross-sections the Froude number in the loop seals becomes closer to that of the full-scale plant.

Three coolant loops with double capacity steam generators are used to model the six loops of the reference power plant. The U-tube lengths and diameters of the PACTEL steam generators correspond to those of the full-scale design, but the overall height is smaller. The horizontal orientation of these steam generators is one of the unique features of the VVER design. One consequence of this geometry is a reduced driving head for natural circulation. Another notable feature is the relatively large secondary side water inventory, which tends to slow down the progression of transients.

The facility includes a pressurizer, high and low pressure emergency core cooling systems, and an accumulator. No primary pumps were available in any of the ISP experiments. The pumps were installed later in the beginning of 1993.

There are about 400 channels available for instrumentation in the data acquisition system of the facility. The instrumentation consists of temperature, pressure, differential pressure and flow measurements. The core power is measured with a built-in instrument of power supply.

EXPERIMENT DESCRIPTION

In a typical standard problem an expected accident scenario of the reference plant is simulated as a complete transient. The VVER-440 type reactor is addressed for the first time by a CSNI international standard problem. That is why a natural circulation experiment was considered particularly suitable. In a typical LOCA event the transitions between different two-phase flow natural circulation modes are continuous and dominate the scenarios [2].

The main goal of ISP33 and the corresponding experiment was to study natural circulation in a VVER plant including various single- and two-phase natural circulation modes. The heat generated in the core is transported by the coolant to the steam generator. The primary coolant mass was reduced stepwise in the liquid form, and the amount of the drained water was given as a boundary condition. The expected periods were single-phase natural circulation, two-phase natural circulation with continuous liquid flow, natural circulation of reflux boiling type and cooling of the uncovered core with partially superheated steam.

SUMMARY OF EXPERIMENTAL RESULTS

The ISP33 experiment was performed to investigate natural circulation flow behaviour under quasi-steady state conditions at several different primary side inventory levels. Core power level of 3.7% of the scaled nominal power was selected for this test. Before the experiment the facility was heated until it reached the selected temperature and pressure, and a steady state was established at these conditions. The primary coolant was drained from the lower plenum in several steps, allowing the system to restabilize for 900 seconds between each step. For the duration of the test, the secondary side conditions were maintained near the nominal full power operating conditions of the reference plant.

The effect of the first draining was a rapid decrease of the primary pressure until saturated conditions were reached at the core outlet. Almost all the water in the pressurizer flowed into the hot leg of loop one. The fluid temperature in the hot leg decreased temporarily when the subcooled water slug from the pressurizer surge line reached the hot leg. Vapour started to accumulate at the top of the upper plenum. The flow in the downcomer remained single-phase with a nearly constant flow rate.

During the second draining the amount of vapour in the upper plenum increased rapidly. The loop and the downcomer mass flow rates increased. When the swell level in the upper plenum fell below the hot leg nozzles, voiding also began in the hot legs. The flow rate dropped and became stagnant. The loop seals prevented the vapour from reaching the steam generators. This flow stagnation was observed in all three loops simultaneously. The system pressure rose sharply

since energy transfer to the steam generators was interrupted. Temperature rise was noticed in the upper plenum, hot legs and at the core outlet.

When the pressure increased, water flowed back into the pressurizer. After about two minutes of flow stagnation and a continued increase in the pressurizer water level, all three loop seals cleared and a surge of two-phase flow into the steam generators reduced the pressure. As the pressure dropped, a fraction of the water in the pressurizer returned to the loop and the flow stagnated again initiating another system pressure increase. This was repeated two additional times, with the peak water level in the pressurizer decreasing with each cycle. During the highest pressure peaks approximately 10 kg of coolant escaped through the safety valve leak at the top of the upper plenum.

During the next draining the primary pressure dropped quickly. Temperatures in the upper plenum followed the saturation temperatures. The pressurizer was depleted again and primary mass flow rates increased. When the draining stopped a relatively steady two-phase flow was established between 3000 s and 4000 s. The bulk of this flow took place through one loop, though none of the loops was totally stagnant. The two loops with low flow rates had partially filled hot leg loop seals while the third loop seal was clear.

As the inventory was reduced further the water level in the two filled loop seals dropped and the flow rates continued to decline, finally becoming nearly stagnant. The heat transfer mechanism from primary to secondary changed to a boiler-condenser mode. Steam was condensed in the steam generators, collected in the cold legs, and returned to the core via the downcomer. The downcomer flow rate was quite low although the energy was transferred efficiently. Reflux condensation was not observed because of the steam generator and hot leg loop seal geometries. Condensation took place in the horizontal U-tubes, but there was no driving force for back flow towards the hot leg and the upper plenum. Moreover, it is apparent that a steady flow of condensate back into the hot leg would eventually fill the loop seal and block the steam flow.

It is noted that the ability of the steam generator to retain significant amounts of condensate has a tendency to shorten the time available before the core heat-up starts.

CALCULATIONS

The blind calculations were carried out using the data from the characterizing test to tune the models and initial conditions. In general the initial conditions were in good agreement with the experimental results in both blind and posttest calculations. As a calculation exercise the results of the blind calculations give a realistic estimate on the capabilities of the codes and the users to predict the given transient. The posttest calculations give an oppurtunity to fix obvious mistakes and then to try different ways to improve the results. The variations of primary pressures in blind and posttest calculations are presented as shaded area in Figures 2 and 3.

The main discrepancies were noticed in predicting stagnations and pressure peaks after the second draining and in the timing of the core heat-up at the end of the experiment. In the blind

calculations other reasons for differences could be observed. The posttest results indicated that these two differences were still present in the most of the calculations.

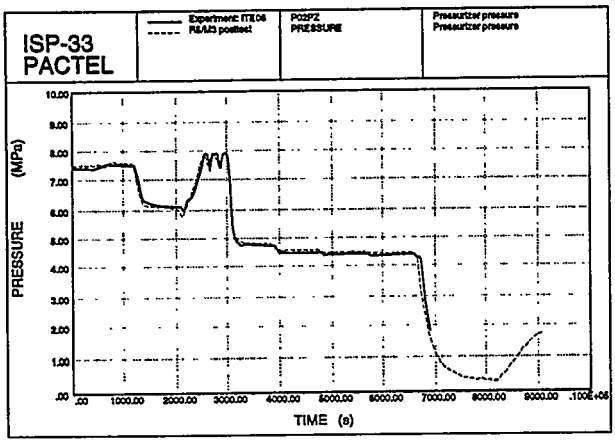

Figure 2. Variation of primary pressure in blind calculations. (RELAP4/MOD6 not included)

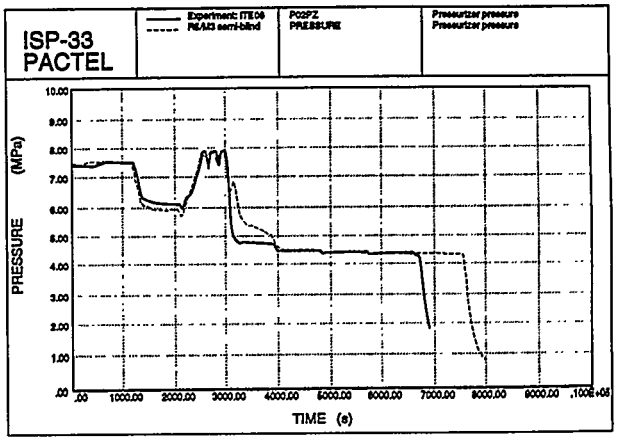

Figure 3. Variation of primary pressure in posttest calculations.

EXAMPLE CALCULATION

As an example of a successful total analysis of ISP33, the blind and posttest calculations of Nuclear Research Institute in Rez, Czech Republic (NRI) by P. Král with RELAP5 code are shortly described here. The blind calculation was performed using RELAP5/MOD2.5/SRL code. The input of the transient model included 273 volumes, 310 junctions, 360 heat structures and 209 control components. The correlations used in constitutive relations are mostly automatically determined according to the flow regime and related models. The horizontal stratification model was expected to cause problems, because RELAP5/MOD2.5 does not permit horizontal stratification for volume with inclination higher than 15 degrees.The different phases of the analysis are described here by using the primary pressure behaviour as a measure of the quality of the results. Figure 4 illustrates the primary pressure behaviour in blind calculations using RELAP5/MOD2.5. The re-pressurizing after the second draining is late and the core heat-up occurs after one additional draining

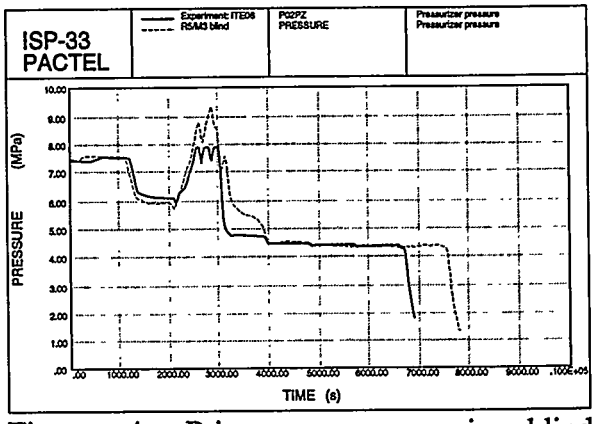

Figure 4. Primary pressure in blind calculation using RELAP5/MOD2.5.

After releasing the experimental results similar calculations using RELAP5/MOD3 were conducted. The effect of allowing the horizontal stratification in the hot leg loop seals can be observed during flow stagnation and system re-

pressurizing after the second draining, Figure 5. The late heat-up of the core is visible.

The modifications after the blind calculations included the modelling of the small leakage of the safety valve during the highest pressure peaks, updated drainages and updated core power. The effects of these and other minor modifications can be seen in Figure 6. The transient behaviour up to the third drainage is very close to the experimental results.

In the final calculation steam generator tubing nodalization was modified by inclining the tubes to allow the accumulation of condensate in the tubes. The differences in the primary pressure have been minimized after these modifications, Figure 7.

The results of the blind calculations of standard problems form a base for the analysis capabilities of the codes and the posttest analysis gives experience for the analyst, which is needed in the future work. Both phases of the analysis give new information for the code developers of the features of the code to be improved.

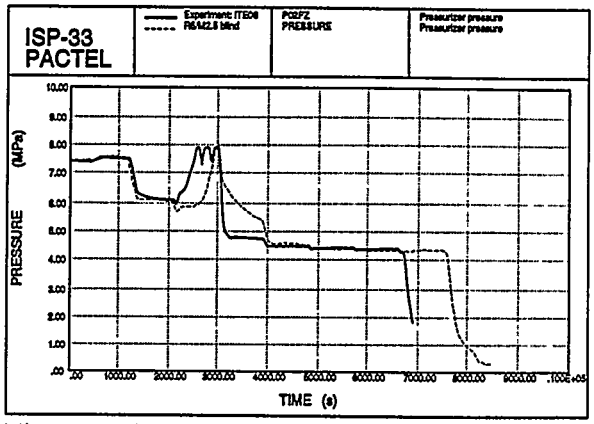

Figure 5. Primary pressure in blind calculation using RELAP5/MOD3.

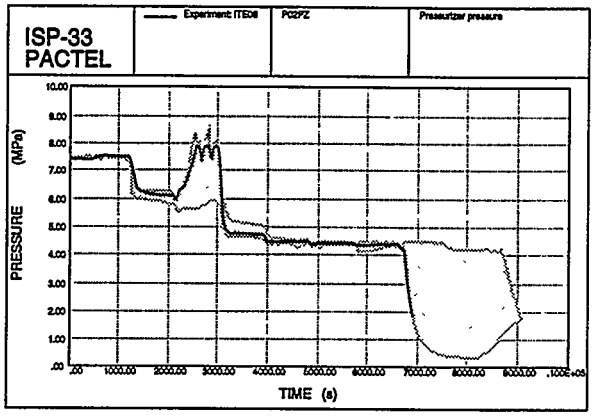

Figure 6. Primary pressure in semi-blind calculation using RELAP5/MOD3.

CONCLUSIONS

The objective of the ISP33 test was to study the natural circulation behaviour of VVER-440 reactors at different coolant inventories. This ISP was conducted as a double-blind problem.

The experiment was started with single-phase liquid flow at full coolant inventory. The inventory was reduced stepwise. The test was terminated soon after the cladding temperatures began to rise.

The overall transient was reasonably well calculated by all codes except by RELAP4/MOD6 indicating the limitations of the

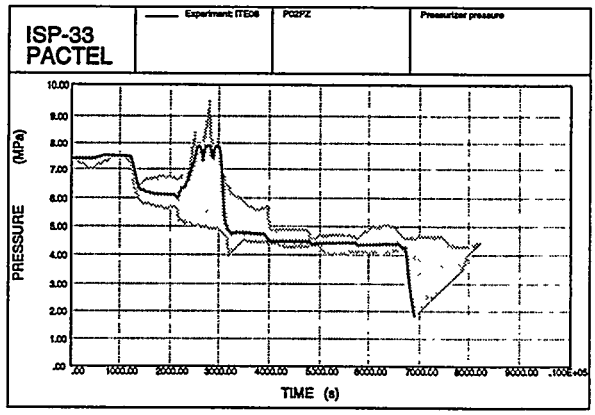

Figure 7. Primary pressure in posttest calculation using RELAP5/MOD3.

old conservative codes. However, some shortcomings were also encountered with respect the capabilities of the advanced best-estimate codes.

The main discrepancies were noticed in the prediction of the flow stagnations and the three pressure peaks after the second draining, and the time of the core heat-up at the end of the test. The heat-up was calculated to occur later than in the experiment. These problems were mainly due to the inability to calculate accurately the behaviour of the hot leg loop seals and the accumulation of water in the horizontal steam generator tubes. The two-phase natural circulation flow rate and the refilling rate of the pressurizer at the end of the test were generally overpredicted.

Compared to the blind calculations the results of open calculation were naturally improved. Some of the posttest calculations can be considered excellent. Only a few problem areas remain.

The input modifications for the posttest calculations included addition of a model for the safety valve and allowing for a leak through it, increase of the power from 155 kW to 165 kW, decrease of the pressurizer heat losses and corrections to the coolant mass, the pressure losses etc.

In addition, there were some artificial changes. The Nuclear Research Institute, Czech Republic, tilted the steam generator tubes in order to investigate whether the assumption of accumulation of water in the steam generator tubes was a proper one. Two participants added a circulation in the pressurizer. Several participants used a circulation in the upper plenum in both blind and open calculations.

The remaining problems had to do with the accurate calculation of the loop seal behaviour and accumulation of water inside the steam generators leading to a too late core heat-up. Also, the codes tend to overpredict two-phase natural circulation flow rate in case of small gravitational driving heads.

In summary, despite of some inaccuracies in the original specifications ISP33 proved to be a successful and valuable exercise with a wider than expected participation. The reasons for the observed discrepancies were easier to investigate than in most ISPs, because the experiment was not excessively complicated.

REFERENCES

[1] J. Miettinen, and H. Purhonen, "PACTEL - Parallel Channel Test Loop, General Description for ISP", Technical Research Centre of Finland, Technical Report No. PROPA-9/91 (1991).

[2] H. Purhonen, J. Kouhia and H. Holmström, ISP33 OECD/NEA/CSNI International Standard Problem No. 33. PACTEL Natural Circulation Stepwise Coolant Inventory Reduction Experiment. Comparison Report, NEA/CSNI/R (1994) 24, Vol I and II, Paris (1994).

SPES-2, an experimental program to support the AP600 development.

M. Tarantini
ENEA, Nuclear Fission Branch
Via Martiri di Monte Sole,5
40129 Bologna

C. Medich
SIET S.p.A.
Via Nino Bixio, 27
29100 Piacenza

Abstract.

In support of the development of the AP600 reactor, ENEA, ENEL, ANSALDO and Westinghouse have signed a research agreement. In the framework of this agreement a complex Full Height Full Pressure (FHFP) integral system testing program has been planned on SPES-2 facility.
The main purpose of this paper is to point out the status of the test program ; describe the hot pre-operational test performed and the complete test matrix, giving all the necessary references on the work already published.
Two identical Small Break LOCA transients, performed with Pressurizer to Core Make-up Tank (PRZ-CMT) balance line (Test S00203) and without PRZ-CMT balance line (Test S00303) are then compared, to show how the SPES-2 facility can contribute in confirming the new AP600 reactor design choices and can give useful indications to designers.
Altough the detailed analysis of test data has not been completed, some consideration on the analytical tools utilized and on the SPES-2 capability to simulate the reference plant is then drawn.

Introduction.

In the last few years Italian organizations involved in nuclear activities focused on the available economical and technical resources for research on advanced nuclear reactors. Cooperative research agreements were signed with the nuclear vendors that planned the development of advanced nuclear reactor concepts (Westinghouse, General Electric, ABB).
A particularly important research agreement was signed among ENEA, the Italian Agency for New Technologies, Energy and the Environment; ENEL, the national electrical utility; ANSALDO, the Italian nuclear industry and Westinghouse to support AP600 development.
The planned activities included testing of innovative AP600 systems such as the Automatic Depressurization System valves (ADS, tested in VAPORE facility- ENEA, Italy) and an integral systems testing program (SPES-2 facility -SIET, Italy). The funding was provided by Westinghouse, ENEA and ENEL.
The Full Height Full Pressure (FHFP) integral systems testing was awarded to SIET (Italian Society for Development and Qualification of Thermo-mechanical Components) that already had extensive experience in designing and conducting similar test facilities.
The pretest analyses, assigned to the Nuclear Division of ANSALDO, were performed using the RELAP5/mod3 code.
The main purpose of the integral FHFP integral system test was to validate the thermalhydraulic codes used by Westinghouse in the AP600 Standard Safety Analysis Report.
The purposes of the involved Italian organizations included the necessity to gain a better knowledge of all phenomena related to the passive systems and to evaluate the performances of independent thermalhydraulic codes such as RELAP5.

Status of the test program.

The preliminary design activities on SPES-2 facility started in 1990 when ENEA/SIET sponsored evaluations of the advanced nuclear reactor performance. Because of the SIET's experience in building and conducting the original SPES facility test program, a Full Height, Full Pressure, volume/power scaling approach was used. Since the actual design of SPES-2 facility was begun in 1992 several major components of the existing facility such as power channel, steam generators and pressurizer were utilized. This imposed the choice of some facility parameters such as the power and volume ratio of 1/395 to the AP600.

The scaling approach adopted for SPES-2 facility is described in Ref. [1,2]. A facility schematic is shown in Fig. 1.

The RELAP5/mod3 code was utilized throughout the experimental program for scaling simulation analysis, to perform pretest calculations and support the definition of the tests operating procedures. A typical SPES-2 nodalization is shown in Fig.2. Identical AP600 and SPES-2 transient calculations were performed by ANSALDO to improve the facility simulation capability; determine the facility limitations; address specific concerns of the organizations involved and aid in sizing specific components such as the ADS fourth stage flowpath. In these analyses an AP600 input deck independently developed by EG&G (Idaho National Engineering Laboratory-INEL) under USNRC contract and a SPES-2 input deck developed by ANSALDO were utilized.

RELAP5 analyses included parametric evaluations for optimizing the compensation of SPES-2 heat losses in steady state conditions and of metal heat release during the depressurization phase of the transients. In fact, due to the higher surface-to-volume ratio of the facility compared to the reference reactor, the heat losses and the metal heat release are larger than needed.

Particular studies were made on critical components such as pressurizer and downcomer for improving the RELAP5/mod3 input deck simulation capability and supporting the scaling choices.

The SPES-2 pressurizer is shorter than the AP600 one (about 60%), because it was scaled using the Wilson bubble rise model and an existing component was utilized. A parametric sensitivity study was therefore performed for verifying the impact of the pressurizer height on the overall facility behavior. The results of the calculations have been published in Ref. [2].

The annular and tubular part of the SPES-2 downcomer (Fig. 3 and 4) was analyzed by CFDS FLOW3D, a three dimensional code developed by the Harwell laboratories to support the RELAP5/mod3 nodalization choices and to assess the coolant flow field and temperature distribution . The problems faced consist of determining the annular downcomer form losses, due to the obstruction caused by hot legs and the Passive Safety Systems flow distribution between the tubular part of the downcomer and the break location.

As a result of these analyses, a quasi 2-D RELAP5/mod3 nodalization was chosen for SPES-2 annular and tubular downcomer simulation (Ref.[3]).

The experimental results confirmed the RELAP5 predictions of the timing of the main events and of the overall transients behavior [4].

The CMTs and In-containment Refueling Water Storage Tank (IRWST) nodalization utilized in the first pretests were also improved by comparison with the experimental results, trying to overcome the code limitations.

The facility modifications began in May 1992 and continued until the end of 1993. The final facility configuration is described in Ref. [5]. As part of the test program, cold and hot shakedown tests have been performed .

The purpose of cold shakedown tests was to characterize the facility and verify that the piping pressure losses and flowrates were properly scaled to match the AP600. Due to the SPES-2 primary loop configuration, which uses one RCP per loop, special care was taken in characterizing the cold leg friction losses in normal and reverse flow. Instrumentation and control system calibration and functionality were also verified as a part of these tests.

The hot shakedown tests completed the facility characterization at full pressure and full temperature, verifying safe facility operation and the data acquisition system capability.
Hot preoperational tests included steady state heat losses and facility heat capacity measurement, due to the importance of these characteristics in a FHFP scaled facility.
The complete set of the hot shakedown tests performed is shown in Table 1.
Table 2 shows the SPES-2 matrix tests.
The tests performed included three AP600 major design basis transients : Small Break Loss of Coolant Accident (SBLOCA), Steam Generator Tube Rupture (SGTR) and Main Steam Line Break (MSLB). Pre-test calculations were performed before each test on the facility and, for the most part of the transients, on the reference plant and the results were compared.
In addition, some tests were repeated with a system configuration change, in order to be able to compare the impact of the change on transients.
For example, the two inch cold leg break test was performed with and without the PRZ-CMT balance line. A comparison of the two transients is shown in the next section.
Other tests were performed with one PRHR Hx tube or three PRHR Hx tubes as recommended by USNRC for observing the effect of additional cooldown in a MSLB and in a SBLOCA transient.
The original test program was completed in October 1994. Two new tests (tests S01613 and S01703) were performed to verify the facility repeatability and the effect of a more severe cooldown caused by a three-tube simulated PRHR Hx in a 1" cold leg break transient.
To date, the Westinghouse sponsored testing program has concluded and at the moment no further testing is planned. However the facility will be kept operational by ENEA.

Effects of balance line suppression on a 2" cold leg break transient.

The two inch Cold Leg (CL) break test was performed in two different configurations, with and without PRZ-CMT balance line (respectively test S00203 and S00303).
The tests were performed with the facility operating at full pressure and simulated power and flow. A scaled 2" break was initiated in loop B, at the bottom of the Cold Leg number two (CL B2) between the CL-CMT balance line and the PC vessel; all the passive safety systems (ADS valves, PRHR Hx, CMTs, ACCs, IRWST) were in operating condition .
The Control Volume and Chemical System (CVCS), the Normal Residual Heat Removal System (NRHR) and the Startup Feedwater System (SFW) were not operated throughout the entire transient.
The test was carried out simulating the failure of one of the two 4th stage ADS valves on loop B.
The facility initial conditions of both tests are shown in Table 3.
The main difference between the two tests initial conditions, was the higher secondary system pressure in test S00303. In this test the Steam Generators pressure was intentionally increased to keep the average hot leg and the core inlet temperatures within the specified allowable range; in fact, in test S00203, the average hot leg temperature before the test initiation was slightly below the specified range. This change was judged to have an acceptable impact on the test purpose.
Fig.5 shows the CMT A instrumentation arrangement. (ref. [6] for details on CMT design). The CMT A fluid temperature is monitored by means of 20 thermocouples; 12 wall thermocouples measure the temperature of the primary and secondary tank; two thermocouples measure the temperature of the air gap between the two tanks.
The particular double tank design was chosen to preserve the same metal /water volume ratio as the AP600, to avoiding any large distortion in CMT water temperature or steam condensation on tank walls.

A steam distributor was installed on the CMT inlet pipe, for minimizing the steam jet induced CMT water heat-up.
Fig. 6 is representative of the general behavior of the primary system pressure in the transient. The system depressurization was very similar in the two tests; after pump trip and before ADS actuation the primary system pressure was slightly higher in test S00203. This is probably due to the higher steam generator pressure and temperature that provides higher HL temperature and higher primary system saturation pressure. The impact of the PRZ-CMT balance line elimination on the overall system depressurization was negligible.
The sequence of the events for both tests is shown in Table 4.
The sequence of the events is nearly identical; in S00303 the accumulator injection is sooner due to the lower primary system pressure.
Fig. 7 shows CMTs injection flowrate for both tests. At about 400 s the transition from natural recirculation to steam displacement mode is very evident for the CMT connected to the broken cold leg. In S00203 the transition is sooner by about 30 s because the CL-CMT balance lines reach the saturation temperature earlier than for S00303 (fig 8) due to steam mixing from the PRZ via Balance Line. In test S00303 with no PRZ to CMT Balance Line the transition is later.
Fig. 9 shows the pressure losses between the pressurizer and the CMTs in test S00203. After the opening of CMTs isolation valves, steam flows from pressurizer to CMT, as measured from the PRZ-CMT balance line pressure losses.
Because a small length of the CL-CMT balance line that is included between the DP-A28P/DP-B28P taps, the measured pressure losses decrease when two phase flow is observed in the CL-CMT balance line. The PRZ-CMT steam flow completely stops when ADS is actuated. The check valve on PRZ-CMT balance line prevents reverse flow from occurring .
Fig. 10 shows the CMT A fluid temperature distribution.
The initial water temperature at the top of the CMTs as measured by T-A401E and T-B401E was lower for S00203 than for S00303 by approximately 6 °C. After CMT actuation, the temperature at the top of the CMTs was higher for S00203 than for S00303 by approximately 20 °C; this is due to the steam at higher temperature flowing from pressurizer.
A similar behavior is observed in the CMT wall temperature distribution (Fig 11).

Conclusions.

At this point of the experimental program some considerations on the facility and on the analytical tools utilized can be drawn:

- The comparison of the S00203 and S00303 data confirms that the PRZ-CMT balance line does not affect the CMT drain time and therefore the ADS actuation and the overall timing of the transient. The only remarkable effect of the PRZ-CMT balance line elimination was a lower heat-up of the CMT fluid before initiating the CMT draindown; this is a positive result because cooler water means an higher hydraulic head available to initiate the CMT natural circulation. This is of some importance in case of transients with smaller breaks, in which the CMT draindown is delayed and the CMT natural recirculation mode lasts longer.

-The RELAP5/mod3 input deck developed by Ansaldo was sufficient to predict the overall system response, to reasonably reproduce the timing of the transients and the interactions between the safety systems.
The expected phenomena and the synergistic effects between passive safety systems were often reproduced not only in a qualitative but also in a quantitative way.
Naturally some improvements are needed.
In the ANSALDO input deck, developed for the mod3 version, the CMTs were simulated with 60 volumes to improve the prediction of the fluid level behavior; the

new code version with the level tracking model should simplify the nodalization requirements.
A systematic RELAP5 overestimate of the fluid temperature at the PRHR Hx outlet was observed in all tests, due to an underestimation of the heat exchange coefficient between the PRHR Hx C-shaped tubes and the IRWST water; this had a particular importance in long transients like the one inch cold leg break, in which the heat removed by PRHR Hx is significant. A two dimensional nodalization adopted for IRWST in recent pretest analyses improved the PRHR Hx outlet temperature prediction, simulating the natural circulation flow path taking place in IRWST and estimating more realistically the IRWST water temperature and heat exchange coefficient [3].
Sensitivity analyses, sponsored by ENEL, will be performed by a Pisa University team to have an independent review of two different SPES-2 input decks; improve the transient simulation and further investigate code limitations.
The new RELAP5 code versions, with enhanced models of passive safety systems will be compared to the experimental data.

-Analyses performed by Ansaldo using RELAP5/mod3 code on AP600 and SPES-2 identical transients showed good agreement between the reference plant and the facility system response (Ref. [7]). All the phenomena taking place in the plant transients are also reproduced in the facility. All the pretests performed for cold leg breaks and steam generator tube ruptures match the experimental results (Ref. [3,5,6]). This confirms the scaling approach and the facility capability to simulate the AP600 system behavior in small break LOCA and SGTR transients.

- Because of the distortions inherent in any scaled integral test facility, the data generated in these facilities cannot be considered a precise indicator of full scale plant response. An analytical interpretation of the data is always necessary.
The FHFP scaling approach has been applied many times in different facilities and its strength and typical distortions are now well known; it permits minimal analysis effort to extrapolate facility experimental data to the actual plant.
Moreover, due to the large test matrix and the considerable number of analyses performed on SPES-2, the facility response is now characterized over a wide range of AP600 transients improving the confidence in the experimental results.
Therefore, the facility could provide useful indications to designers and utilities to investigate accident mitigation procedures, effectiveness of operator actions, as well as confirm any future developments in passive system designs.
The scaling ratio of the facility permits easy and inexpensive modifications in order to test new system configurations or to permit parametric studies on components (e.g. PRHR, passive depressurization systems, ...).
This is of particular interest in view of the development of a 900 MW passive nuclear plant with "European" safety requirements .

Acknowledgments.

The authors wish to thank Westinghouse Safety Analysis and Test Engineering team (Gene Piplica, Larry Conway and Larry Hochreiter) for the useful discussions in conducting this work.
The authors also acknowledge the positive and continuous contribution of Ansaldo analysis team (Alessandro Alemberti, Gerardo Graziosi and Cesare Frepoli).

Nomenclature.

ACC	Accumulators
ADS	Automatic Depressurization System
CMT	Core Makeup Tank
CL	Cold Leg

CVCS	Control Volume and Chemical System
DC	Downcomer
ECCS	Emergency Core Cooling Systems
FHFP	Full Height Full Pressure
HL	Hot Leg
IRWST	In-containment Refueling Water Storage Tank
I.V.	Isolation valve
MSL	Main Steam Line
MSLB	Main Steam Line Break
NRHR	Normal Residual Heat Removal
OSU	Oregon State University
PC	Power Channel
PRHR Hx	Passive Residual Heat Removal Exchanger
PRZ	Pressurizer
RCP	Reactor Coolant Pump
SBLOCA	Small break LOCA
SFW	Startup Feedwater
SGTR	Steam Generator Tube Rupture
SSAR	Standard Safety Analysis Report
UH	Upper Head

References.

[1] Hochreiter L. E., Fanto S. V., Conway L. E., Lau L. K. "Integral testing of the AP600 passive emergency core cooling systems" Proc. ARS 1994 International Topical meeting on Advanced Reactors Safety 2, 991-1002 (1994) Pittsburgh, PA

[2] Alemberti A. Frepoli C., Graziosi G. "SPES-2 cold leg break experiments: Scaling approach for decay power, heat losses compensation and metal heat release" Proc. New trends in Nuclear System Thermohydraulics 1, 679-687 (1994) - Pisa, (Italy)

[3] Alemberti A., Frepoli C., Graziosi G. "SPES-2 RELAP5/mod3 noding and 1" cold leg break test S00401" 22nd Water Reactor Safety Information Meeting (1994) Washington DC

[4] Tarantini M., Medich C. "An overview of SPES-2 test program" Proc. ICONE-3 The third international Conference on Nuclear Engineering (To be published) Kyoto (1994)

[5] Bacchiani M., Medich C., Rigamonti M. "SPES-2 AP600 Integral System Test: Inadvertent ADS opening and Cold Leg Break Transients" ARS 1994 International Topical meeting on Advanced Reactors Safety April 17-21 Pittsburgh, PA

[6] Bacchiani M., Medich C., Rigamonti M., Vescovi O., Alemberti A, Conway L.E. "SPES-2, AP600 Integral System Test S00706: DEG break of DVI" Proc. ICONE-3 The third international Conference on Nuclear Engineering (To be published) Kyoto (1994)

[7] Alemberti A., Frepoli C., Graziosi G. "Comparison of the SPES-2 pretest prediction and AP600 calculations using RELAP5/mod3" Proc. New trends in Nuclear System Thermohydraulics 1 689-698 (1994) - Pisa (Italy)

TEST	TEST DESCRIPTION	TEST PURPOSE	COMMENTS
H-01	The facility was heated and held at four constant temperatures.	Determine the heat losses vs. temperatures of the main component	The test included measurements with and without pressurizer internal heaters. Verified heat loss compensation for future tests.
H-02	This test was performed concurrent with H-01 test.	Quantified the water and metal heat capacity of the facility.	Temperature and measurements was performed with RCP's running.
H-03	The facility was operated at normal full pressure, temperature and power.	Verified the proper operation of all components and instrumentation.	
H-04	The facility was transitioned from about 1 MW power operating conditions to a hot shutdown/natural circulation mode of operation.	Verified proper transition of heater rod bundle power and SFW flow to decay heat power level; characterized the loop, PRHR heat exchanger and CMT natural circulation flows; confirmed PRHR heat removal rate.	
H-05	The facility was depressurized from approximately 27 bar using ADS with CMT draindown and ACC injection.	Verified the proper safety system actuation at low pressure; the initial conditions had been the same as OSU.	Provided full height vs. 1/4 height comparison to verify OSU scaling. No intervention of ADS 4th stage and of non-safety systems.
H-06	The test was performed from full power conditions and initiated by opening the first stage of the ADS.	Verified the actuation and performance of the safety systems including IRWST delivery.	Similar to inadvertent ADS SSAR analysis. No intervention of ADS 4th stage and of non-safety systems.

Table 1 SPES-2 hot shakedown tests.

IDENTIFICATION	PERFORMANCE DATE	TYPE	DESCRIPTION	STATUS OF NON SAFETY SYSTEMS	STATUS OF PRHR	SINGLE FAILURES	NOTES
S00103	Feb 5, 1994	SBLOCA	2 inch CL break	CVCS, NRHR and SFW off.	On	ADS 4th stage B.	Sharp orifice at the break.
S00203	April 9, 1994	SBLOCA	2 inch CL break	CVCS, NRHR and SFW off.	On	1 of two ADS 4th stage B valves.	Smooth orifice at the break
S00303	April 30, 1994	SBLOCA	2 inch CL break	CVCS, NRHR and SFW off.	On	1 of two ADS 4th stage B valves.	As above without PR balance line.
S00401	May 5, 1994	SBLOCA	1 inch CL break	CVCS, NRHR and SFW off.	On	1 of two ADS 4th stage B valves.	/
S00504	May 18, 1994	SBLOCA	2 inch CL break	CVCS, NRHR and SFW on.	On	No effect.	/
S00605	May 27, 1994	SBLOCA	2 inch DVI break	CVCS, NRHR and SFW off.	On	1 of two ADS 4th stage B valves.	/
S00706	June 10, 1994	SBLOCA	DEG break of DVI	CVCS, NRHR and SFW off.	On	1 of two ADS 1st and 3rd stage valves.	/
S00908	June 23, 1994	SBLOCA	DEG break of a CMT balance line	CVCS, NRHR and SFW off.	On	1 of two ADS 1st and 3rd stage valves.	Blind test.
S01007	July 7,1994	SBLOCA	2 inch CMT balance line break	CVCS, NRHR and SFW off.	On	1 of two ADS 4th stage B valves.	/
S01110	July 14, 1994	SGTR	SG tube rupture (1 tube)	CVCS, NRHR and SFW off.	On	No effect.	/
S01211	Sept 9, 1994	SGTR	SG tube rupture (1 tube)	CVCS, NRHR and SFW off.	On	1 of two ADS 4th stage B valves	Inadvertent ADS opening. Blind test.
S01309	Sept 22, 1994	SGTR	SG tube rupture (1 tube)	CVCS, SFW on; NRHR off.	On	No effect	Operator action to isolate SG, subcool primary system.
S01512	Oct 11, 1994	SLB	Large steam line break	CVCS, NRHR and SFW off.	(3 tubes)	/	Maximum PRHR cooldown. No return to power simulation.
S01613	Oct 15, 1994	SBLOCA	1 inch CL break	CVCS, NRHR and SFW off.	On (3 tubes)	1 of four ADS 4th stages valves	Small break with maximum PRHR cooling
S01703	Nov 12, 1994	SBLOCA	2 inch CL break	CVCS, NRHR and SFW off.	On (1tube)	1 of four ADS 4th stages valves	Repeat of S00303 to show facility repeatability

Table 2 - SPES-2 tests matrix.

Quantity	Test S00203	Test S00303
Heated rod power [MW]	4.99	4.98
Pressurizer pressure [MPa]	15.48	15.44
Average HL temperature [°C]	317.4	320.3
Core inlet temperature [°C]	274.9	284.3
Core flowrate [kg/s]	23.4	23.4
Cold leg flowrate [kg/s]	5.85	5.87
DC-UH bypass flowrate [kg/s]	0.18	0.17
Pressurizer level [m]	3.85	3.85
Accumulator level [m]	2.3	2.3
Accumulator water temperature [°C]	20.6	15.8
Accumulator pressure [MPa]	4.9	4.9
IRWST level [m]	8.5	8.5
IRWST temperature [°C]	23.7	17.7
PRHR supply line temperature [°C]	97.8	92.3
UH average temperature [°C]	271	276
CL-CMT balance line temp. [°C]	220	228
CMT level [m]	full	full
CMT temperature [°C]	21	15.3
SG's level [m]	1.25	1.2
SG's MFW temp. [°C]	230	229.9
SG's pressure [MPa]	4.8	5.1

Table 3. Initial conditions for S00203 and S00303 tests.

EVENTS	Test S00203	Test S00303
	PRZ-CMT bal.line	No PRZ-CMT bal.line
Break opens	0	0
Scram initiation	56	56
MSL I.V. closed	58	59
MFW I.V. closed	66	67
CMT I.V. open	67	68
PRHR I.V. open	67	68
PCP trip	80	83
ADS 1 opening	879	896
ADS 2 opening	974	992
ADS 3 opening	1095	1111
ADS 4 opening	1940	1940
Accumulators injection start	830	750
Accumulator empty	1300(A) 1302(B)	1307(A) 1327(B)
CMTs empty	2291	3069
IRWST injection	2000	2000

Table 4. Sequence of the events for S00203 and S00303 tests.

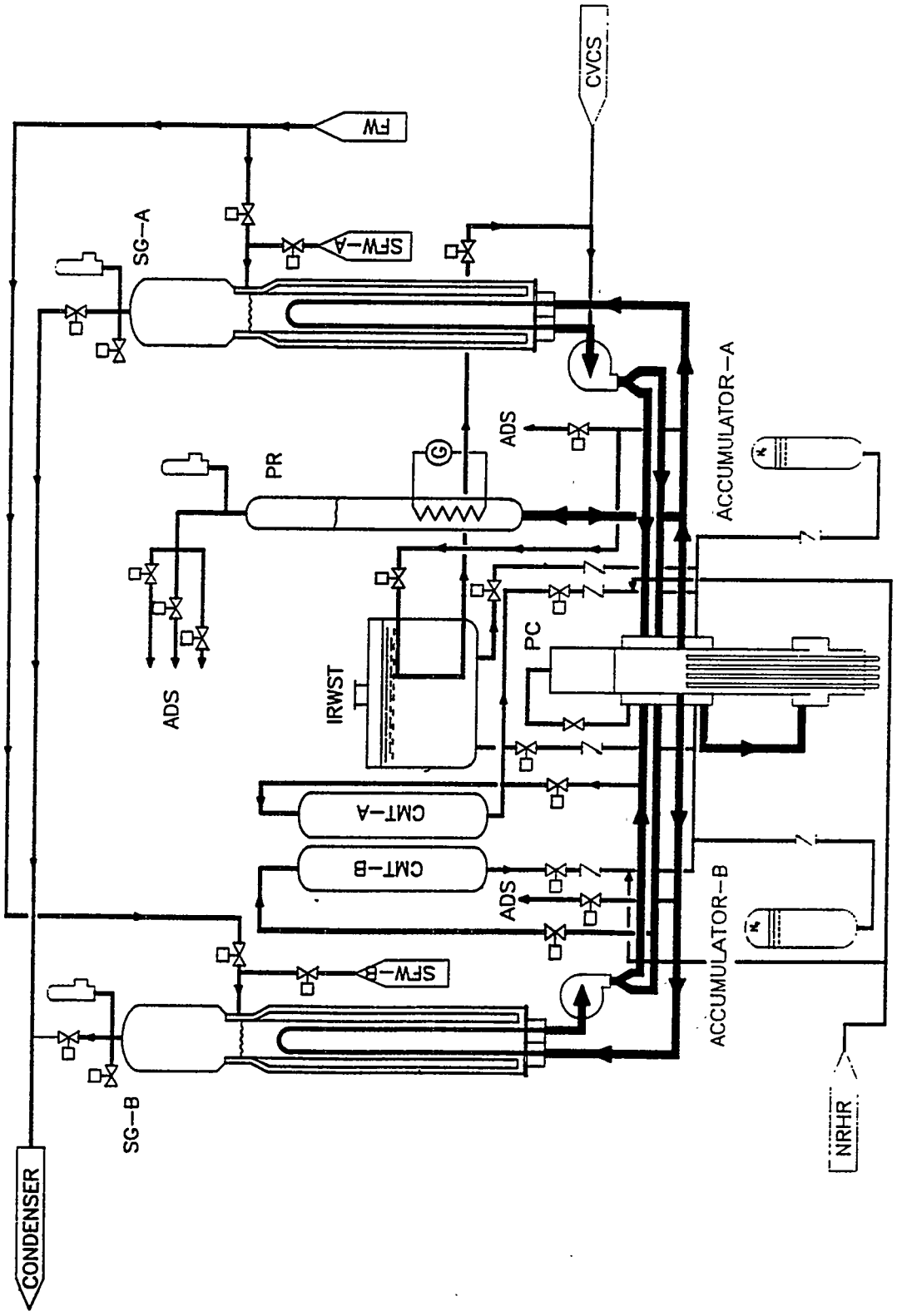

Fig.1 SPES-2 Facility schematic.

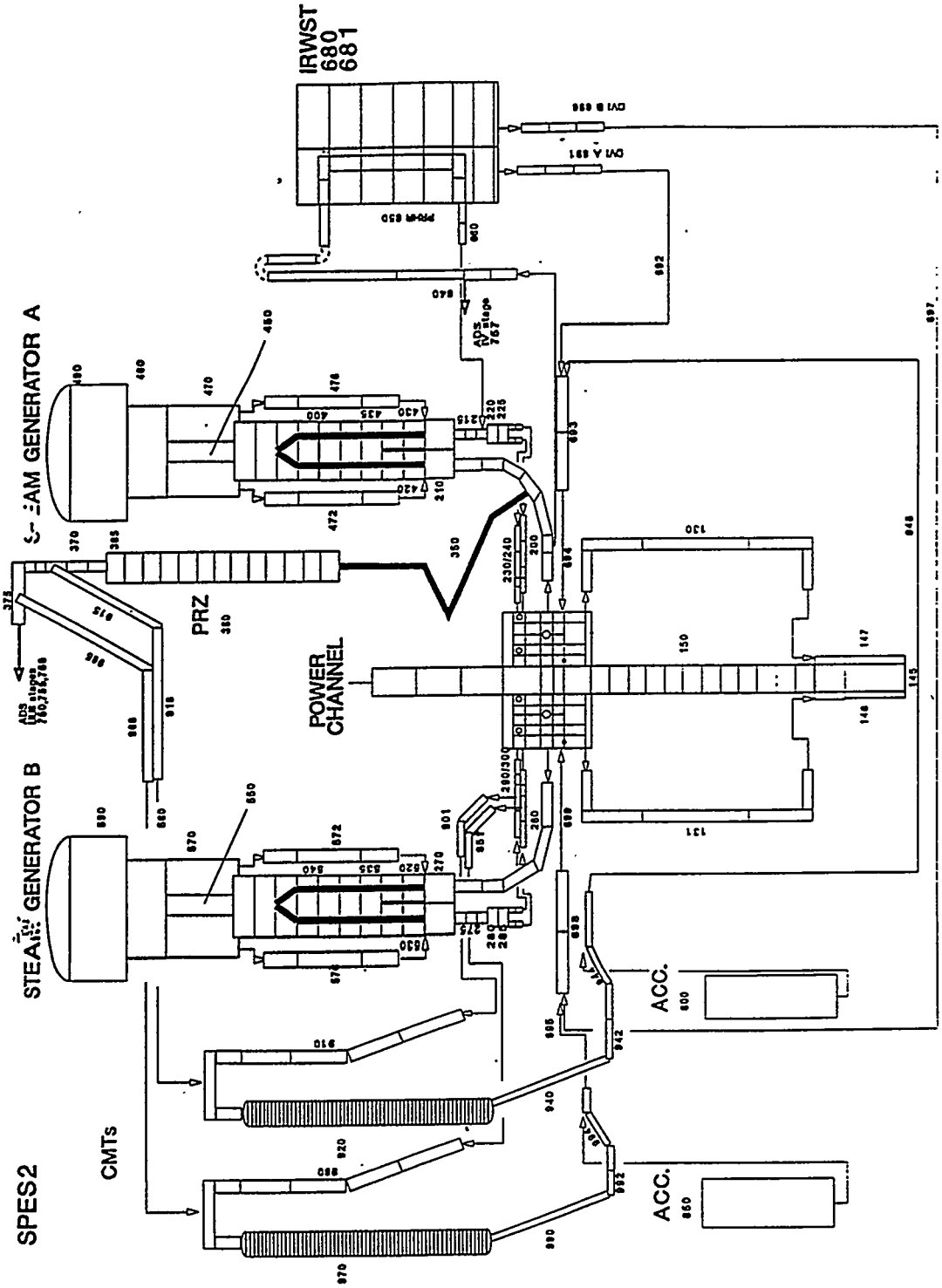

Fig.2 SPES-2 RELAP5/mod3 nodalization.

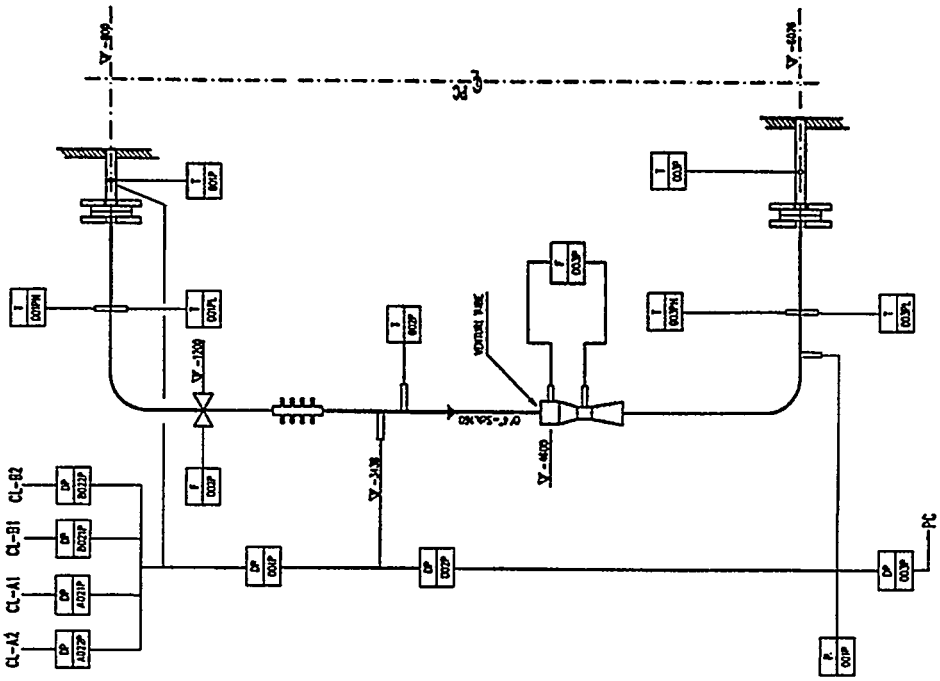

Fig. 4 SPES-2 tubular downcomer schematic.

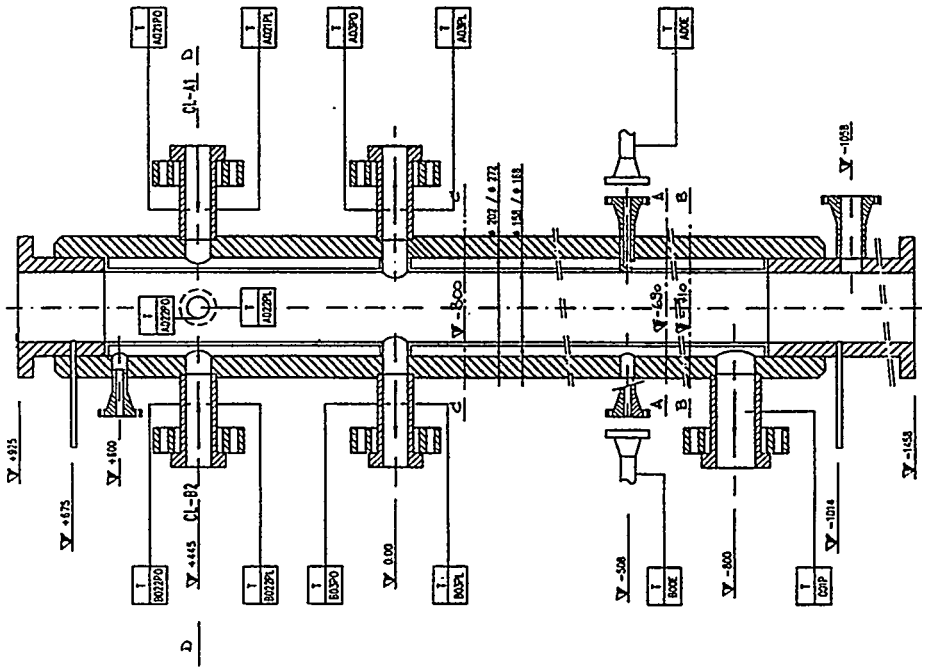

Fig. 3 SPES-2 annular downcomer vertical section.

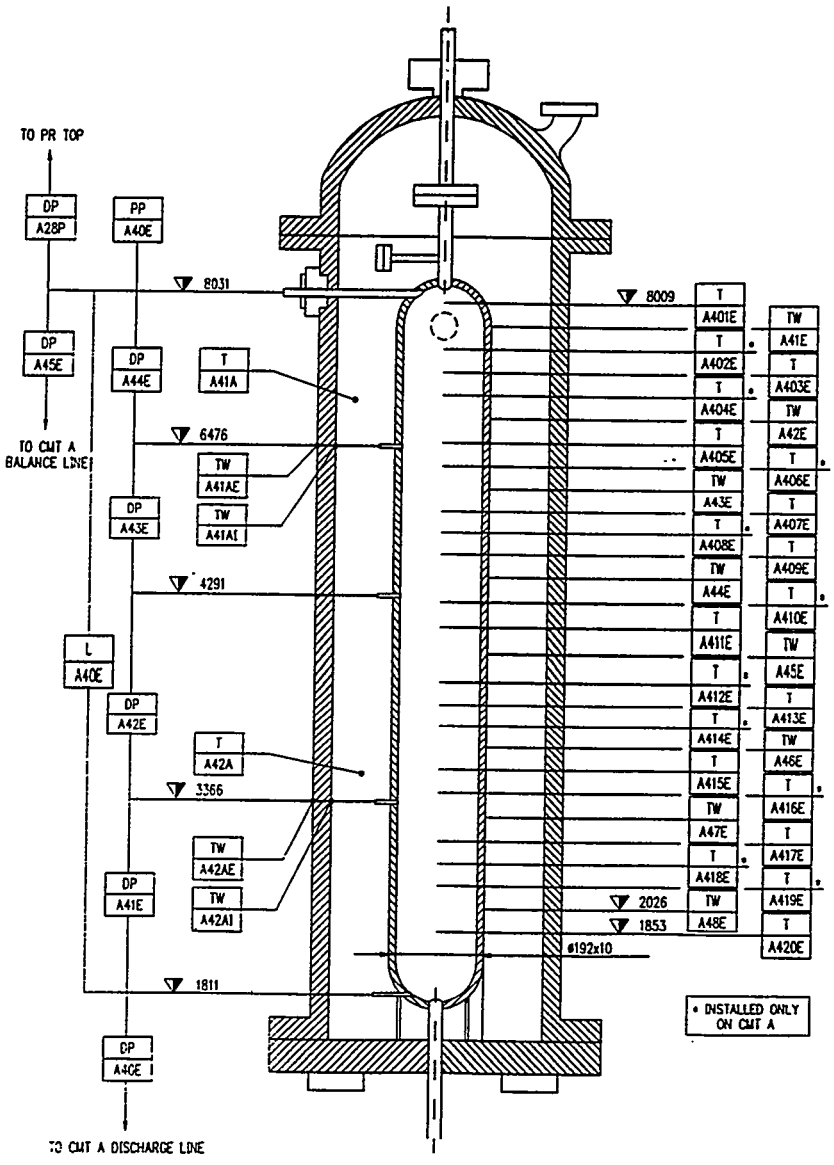

Fig.5 CMT A instrumentation arrangement.

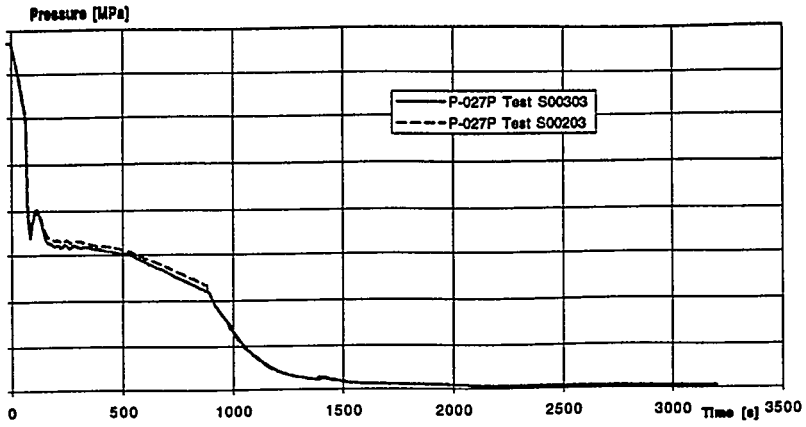

Fig.6 Pressurizer pressure.

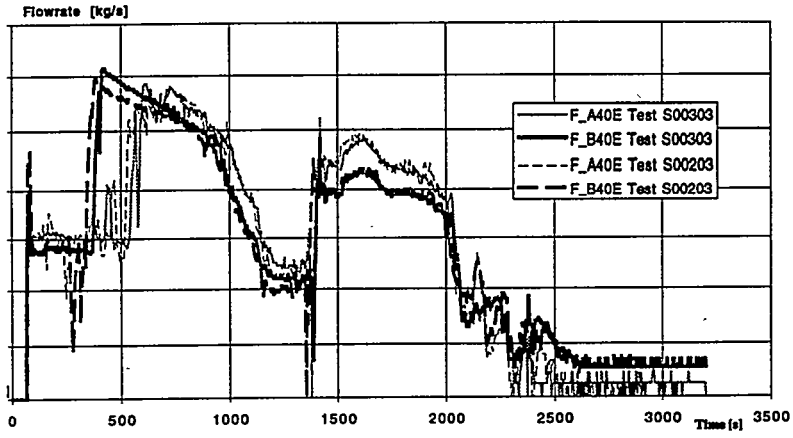

Fig.7 CMTs injection flowrate.

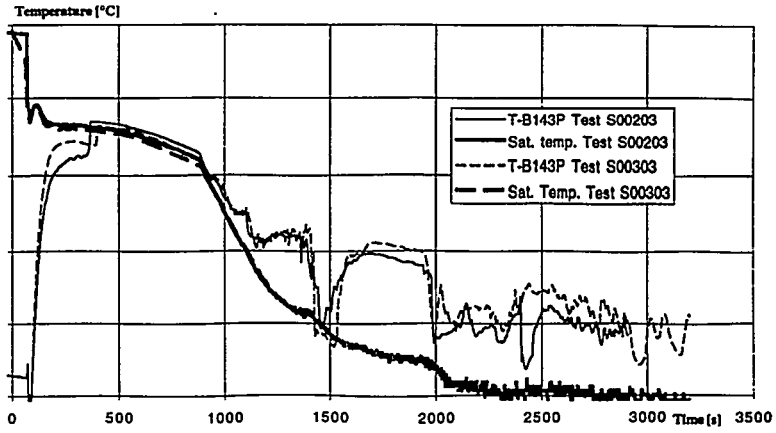

Fig.8 CL-CMT B balance line temperature compared to saturation temperature calculated at CMT pressure.

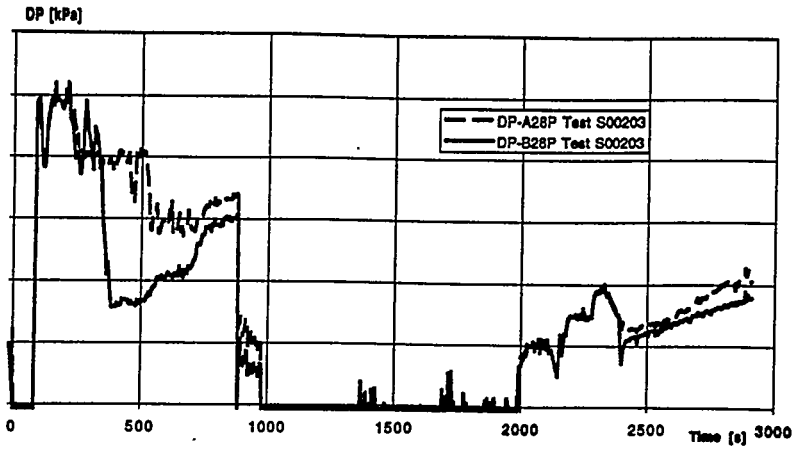

Fig. 9 PRZ-CMT balance lines pressure losses for S00203 test.

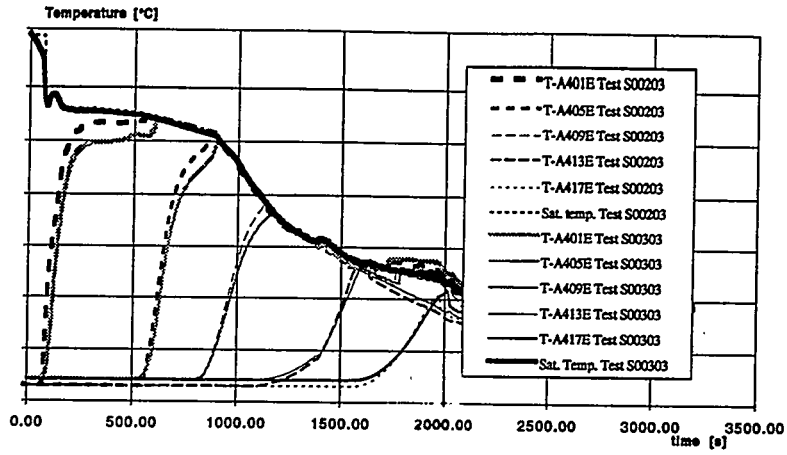

Fig.10 CMT A fluid temperature compared to fluid saturation temperature calculated at CMT pressure (see Fig. 5 for thermocouples position).

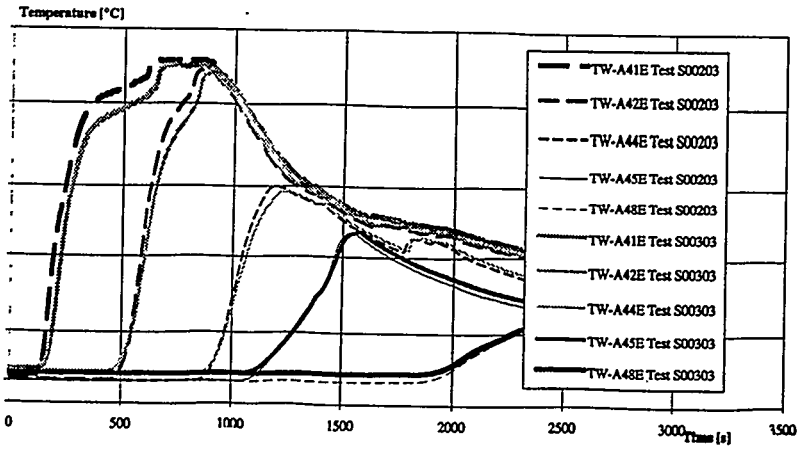

Fig.11 CMT A wall temperatures for S00203 and S00303 tests (see Fig. 5 for thermocouples position).

PWR-Related Integral Safety Experiments in the PKL III Test Facility SBLOCA Under Beyond-Design-Basis Accident Conditions

P. Weber, K. J. Umminger, B. Schoen
Siemens AG, Power Generation Group (KWU)
Freyeslebenstr. 1, 91058 Erlangen, FRG
FAX 0049-9131-182779

ABSTRACT

The thermal hydraulic behaviour of a PWR during beyond-design-basis accident scenarios is of vital interest for the verification and optimization of accident management procedures. Within the scope of the German reactor safety research program experiments were performed in the volumetrically scaled PKL III test facility by Siemens/KWU. This highly instrumented test rig simulates a KWU-design PWR (1300 MWe). In particular, the latest tests performed related to a SBLOCA with additional system failures, e.g. nitrogen entering the primary system.

In the case of a SBLOCA, it is the goal of the operator to put the plant in a condition where the decay heat can be removed first using the low pressure emergency core cooling system and then the residual heat removal system. The experimental investigation presented assumed the following beyond-design-basis accident conditions: 0.5 % break in a cold leg, 2 of 4 steam generators (SGs) isolated on the secondary side (feedwater- and steam line-valves closed), filled with steam on the primary side, cooldown of the primary system using the remaining two steam generators, high pressure injection system only in the two loops with intact steam generators, if possible no operator actions to reach the conditions for residual heat removal system activation. Furthermore, it was postulated that 2 of the 4 hot leg accumulators had a reduced initial water inventory (increased nitrogen inventory), allowing nitrogen to enter the primary system at a pressure of 15 bar and nearly preventing the heat transfer in the SGs ("passivating" U-tubes). Due to this the heat transfer regime in the intact steam generators changed remarkably. The primary system showed self-regulating system effects and heat transfer improved again (reflux-condenser mode in the U-tube inlet region). Additionally a secondary bleed of one steam generator was initiated after approx. 30 min, which resulted in reducing primary side pressure below 10 bar, allowing the low pressure injection system and the residual heat removal system to be successfully activated. By this long term core cooling was secured.

1. INTRODUCTION

The PKL III project (research programs PKL III A, B and C), which started in 1986, with the support of the German Utilities (VDEW) and the Federal Ministry for Education and Research (BMBF) addresses the thermal hydraulic behaviour of a PWR during cooldown procedures under design-basis accident (DBA) and beyond-design-basis accident (BDBA) conditions and aims at experimentally investigating transients with and without

loss of coolant [1]. The main topic of the current PKL III C program which was started in 1991 is the confirmation of accident management (AM) procedures in transients related to small breaks and steam generator (SG) U-tube ruptures with additional system failures.

One experiment in this program dealt with the thermal hydraulic response of the PWR under transient SBLOCA conditions with postulated additional failures, resulting in nitrogen from two accumulators (ACCs) entering the primary system (test C6.1). Systematic investigations under well controlled boundary conditions related to the different regimes of heat transfer in the presence of nitrogen in the primary system have already been performed in the PKL III B program [2], giving encouraging results. These experiments, with respect to SBLOCAs, demonstrated that even under considerably aggravated boundary conditions the PWR can effectively be cooled down and the primary pressure controlled, even if unrealistically high quantities of nitrogen are fed into the primary system.

Some of the transients where presence of nitrogen must be assumed are listed below:

- Small or medium size LOCAs cause depressurization of the primary system; on reaching a preset pressure ACC water is injected. Failure to close an ACC isolation valve at low-inventory signal and primary pressure < 10 bar can lead to significant amounts of nitrogen entering the primary system.

- Assuming a reduced initial water inventory level in some ACCs, resulting in an increased amount of nitrogen in these ACCs with the consequence, that nitrogen would enter the primary system at a pressure level higher than the operational pressure of the low pressure injection system (LPIS) (background of the presented paper).

The presence of non-condensible gas in the primary system affects the regime of heat transfer from the core to the heat sinks (SGs). The natural circulation in the loops with intact SG is interrupted, by the nitrogen blocking the U-tubes in these SGs. The detailed description of this experiment is the subject of this paper. Special attention is given to the analyses of the N_2 effects on heat removal and primary system behaviour. Furthermore, it was investigated in the test whether the LPIS and the residual heat removal system (RHRS) could be activated with or without additional operator actions, e.g. the possibility of reducing the primary pressure below to 10 bar.

It has to be stated, that there is little information available on transient PWR system behaviour in the presence of non-condensibles, e.g. interaction between the four loops and the core and the prevailing heat transfer regimes. Some related experimental investigations were performed in the BETHSY integral test facility, see test 7.2c [3] and test 6.9d [4]. Relevant details will be discussed in chapter 4.1.

2. TEST FACILITY DESCRIPTION

A. Primary Side: The PKL III test facility was designed to investigate a wide range of DBA and BDBA scenarios. The scaling in volume and power of this extensively used test rig is 1:145, (Fig. 1). The elevations are fixed at 1:1. The ratio between the number

of heater rods in the core simulator to the number of fuel rods in the reactor is identical to the scaling factor of 1:145. The maximum pressure on the primary side is limited to 45 bar (reduced pressure); the maximum core power of 2.5 MWe is equivalent to 10 % of the nominal rate.

The PKL test facility is the only large-scale test facility with 4 loops symmetrically arranged around the reactor pressure vessel (RPV) and 4 reactor coolant pumps (RCP). All relevant engineered safety and auxiliary systems are simulated, e.g. high pressure injection system (HPIS), ACCs, LPIS and RHRS, volume control system and pressurizer pressure control system (heating and spraying).

B. Secondary Side: The volumetric scaling factor of the PKL III test facility for the SGs is also 1:145. The number of U-tubes as compared to the original plant is reduced by the same scaling factor. The SG-tubes (material, length, wall thickness) are identical to those used in a KWU-PWR steam generator. Allowance has been made for the differing elevations between the U-tubes with the smallest and largest bending radius. These different elevations may affect the natural circulation behaviour (flow stagnation, transition to reflux-condensation) as well as the distribution of nitrogen entering the U-tube bundle.

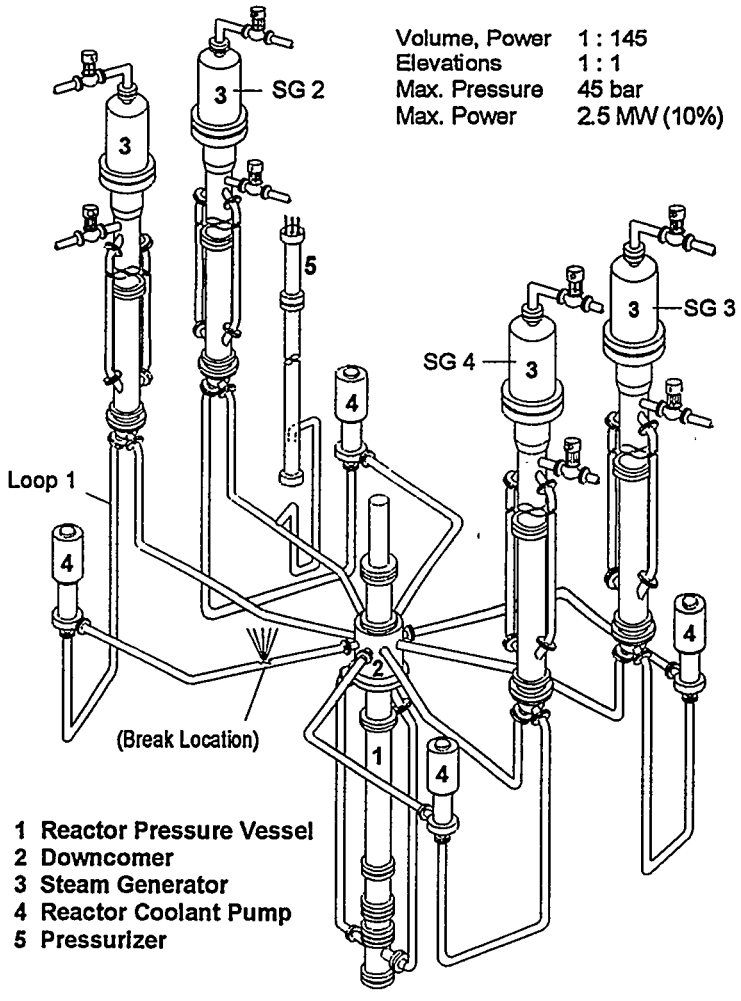

Fig. 1: PKL III test facility

Since the secondary side is the main and in many accident scenarios the only heat sink temporarily available, special care has been taken to correctly simulate the steam generators and their relevant systems connected. This includes the feedwater system and the main steam lines.
The turbine and the condenser are not simulated; the outflowing steam is dumped via silencers to the atmosphere.

C. Instrumentation: There are more than 1300 measuring points in the test facility; the data acquisition system scans 990 selected data channels. The relative accuracy of the measured collapsed levels (by pressure difference transducers) is better than 1 % of the end value of the parameters' range. The fluid temperature

thermocouples are selected ones (high-quality charge), the amplifiers are calibrated; so the water or steam temperatures have an absolute accuracy of ± 1.5 K.
D. Effect of Reduced Facility Pressure: Caused by the limited pressure of the PKL components (45 bar on the primary side) not all kinds of postulated PWR transients can be completely simulated. The presented experiment "enters" the postulated PWR transient at a pressure level of 40 bar (approx. 30 min after the start of the BDBA). The initial and boundary conditions were set up using a code calculation (RELAP5/MOD2) of the PWR transient in question (e.g. 0.5 % SBLOCA, PWR geometry).

The main part of the simulated scenario (pressure decreases below 40 bar) is covered by the PKL experiment (Fig. 2). The relevant physical phenomena observed in the test take place in the SGs. Here the geometry - the SG-tubing - is identical to the PWR. Due to this the test results can be qualitatively and within some limits quantitatively extrapolated to the PWR.

3. DESCRIPTION OF THE EXPERIMENT

The detailed boundary conditions of the experiment are given in table 1. The relevant part of the test (after adjusting the initial conditions in accordance with the RELAP5 PWR calculation) started by opening the simulated 0.5 % leakage in the cold leg (CL) of loop 1 (Fig. 1). The core power was controlled (decay heat simulation), the HPIS pumps of loops 1 and 3 (hot legs (HLs) only) switched on and the facility cooled down at 100 K/h using both intact SGs 1 and 3, see Fig. 2. The SGs 2 and 4 (Fig. 1 and 2) were assumed to be isolated on the secondary side and filled with steam on the primary side (no heat transfer).

	Test PKL III C 6.1
Leakage	(0.5 %) 24 cm² (1/145 *); cold leg
Pressure at BoE **	37 bar ("entering" the PWR transient)
Inventory at BoE	~ 80 %; RPV head and two isolated SGs filled with steam
Safety Injection System	2 HPIS pumps; 2 LPIS pumps; 4 ACCs
Additional Condition	Cooldown of primary side with 2 SGs; rate 100 K/h
Extreme Conditions	Reduced water inventory in 2 ACCs ⇒ Nitrogen enters primary system

(* PKL Scaling Factor)
(** BoE: Beginning of Experiment)

Table 1: Boundary conditions of SBLOCA test with N_2 entering the primary system

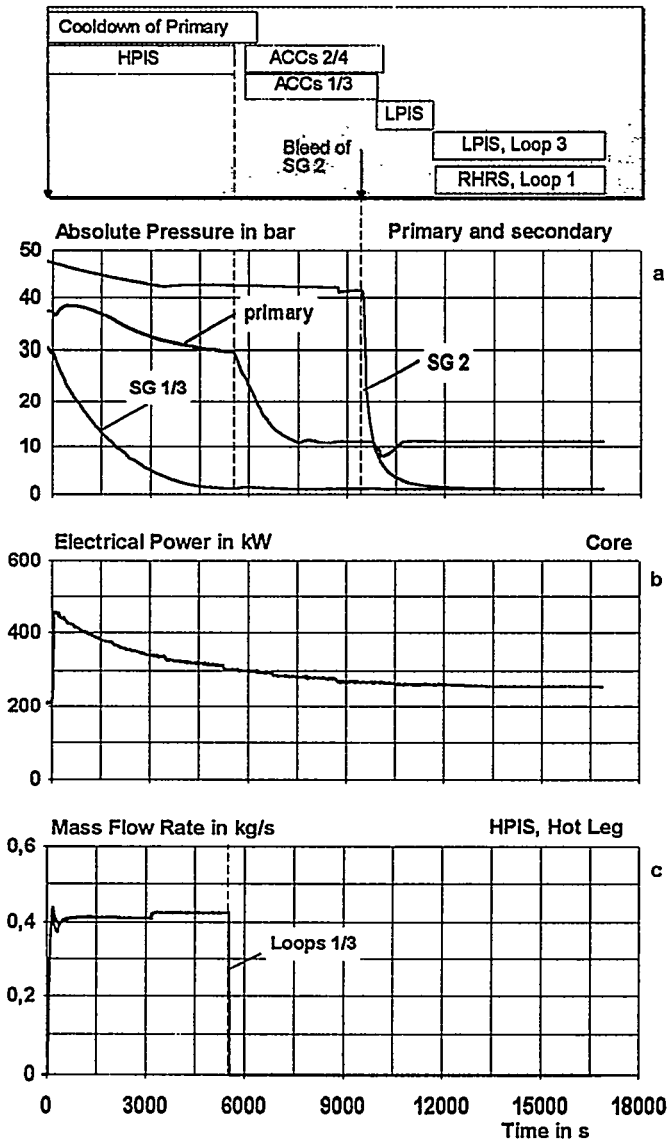

Fig. 2: Experimental results (full test)

During the period of HPIS operation (2 systems in the HLs) the primary system reached an equilibrium state at a pressure of approx. 30 bar. When the borated water storage tank was assumed to be empty and the HPIS pumps switched off (Fig. 2c, and distribution of inventory given in Fig. 3), the primary pressure decreased (due to the leakage rate), see Fig. 4a, and the accumulators passively pushed water into the primary system (Fig. 5a,b). Before the criterion for activating the LPIS was reached, nitrogen from 2 of the 4 accumulators had entered the primary system (1.0 m^3 at STP each, Fig. 5c). This resulted in the prevention of heat transfer in the remaining two intact SGs 1 and 3 (interruption of natural circulation, blocking U-tubes with N_2/steam mixture, see Fig. 4b).

The heat transfer regime in the N_2/steam mixture filled intact SGs 1 and 3 changed to a special form of reflux-condenser mode in the inlet region of the SG U-tubes, see Fig. 6.

The primary pressure stabilized self-regulating at a level of 11.2 bar (Fig. 5a). The leakage rate was not compensated, resulting in a continuously decreasing inventory on the primary side.

Facing this situation (SBLOCA without the possibility to operate the LPIS), a secondary side depressurization (bleed) of one SG (SG 2) was initiated after approx. 30 min (Fig. 5a), which resulted in reducing primary side pressure below 10 bar due to condensation, allowing the LPIS to be successfully activated (Fig. 5a). The injected water filled up the U-tubes of the depressurized SG 2, and subcooled single-phase natural circulation began in this loop (Fig. 7). The SG now acted as a heat sink. Later the transition to "combined" recirculation/RHR mode of operation (one loop with LP injection, one with RHR) was performed whereby further cooldown of the primary side was assured at a primary pressure level of 11 bar (inventory distribution of primary side shown in Fig. 8).

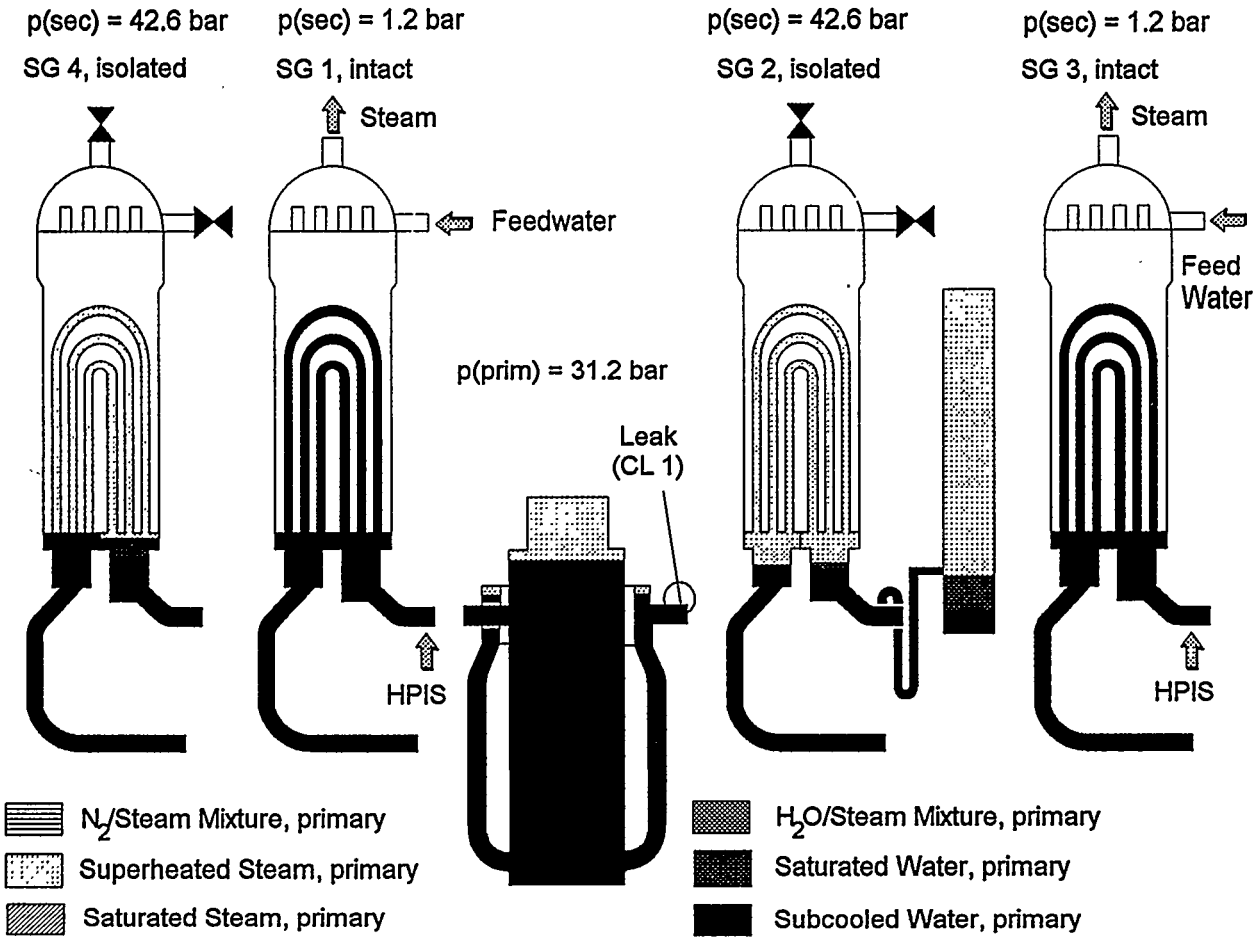

Fig. 3: Distribution of inventory at 5500 s after test initiation (prior to switching off the HPIS)

4. SELECTED TEST RESULTS AND OBSERVED PHENOMENA

4.1 Reflux-Condenser Mode in the Presence of Nitrogen

One essential part of the test is the phase with ACC feeding in which the flow and heat transfer mechanism in the intact SGs changed from natural circulation to reflux-condenser mode with N_2-blocked U-tubes (Fig. 6).

In this test phase the following processes are of particular interest:

- distribution of the injected nitrogen in the primary system
- influence of nitrogen on heat transfer regime in the intact SGs
- influence of the entering nitrogen on the thermal hydraulic behaviour of the primary system.

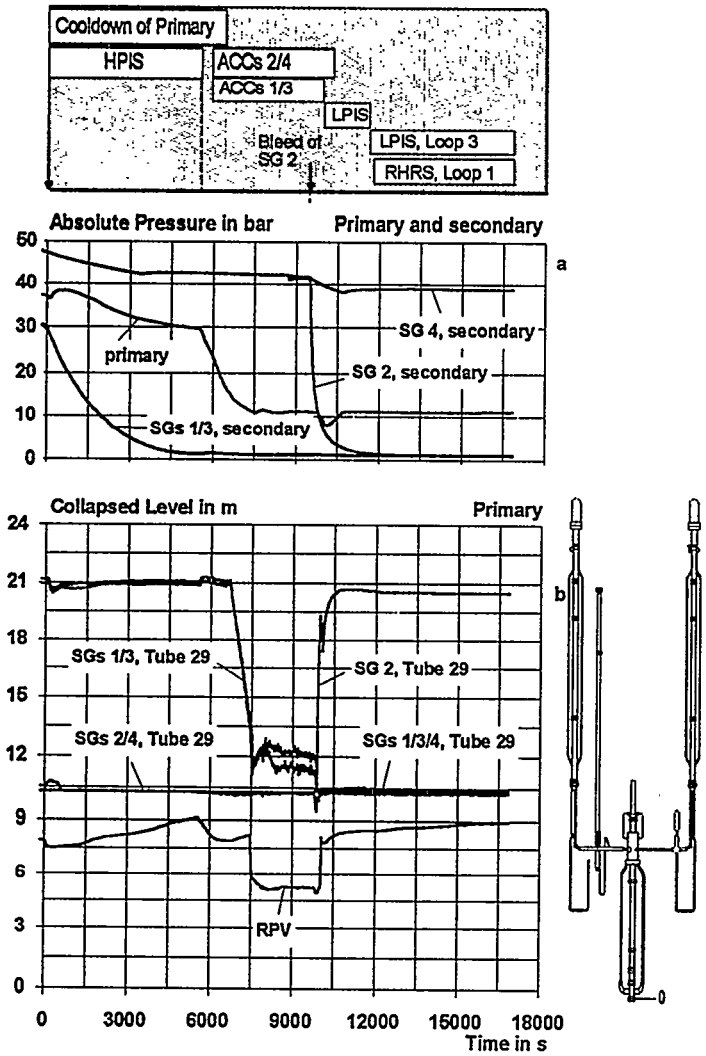

Fig. 4: Pressure and inventory during the experiment

According to the postulated scenario, the water in ACCs 1 and 3 was already completely exhausted after the primary pressure had reached a value of 15 bar, so that the nitrogen from these ACCs entered the primary system (Fig. 5). The gas continued to be fed into the primary system, until the primary pressure stabilized itself. The nitrogen injected into the hot legs was transported in the direction of the corresponding SGs due to the single-phase natural circulation and buoyancy effects of the non-condensible gas in water. Having reached the SGs the nitrogen accumulated in the U-tubes, thereby displacing water (Fig. 4b) and stopping the natural circulation in all tubes of the intact SGs 1 and 3. The pressure on the primary side stabilized at a level of 11.2 bar (see explanation below). Up to this situation the ACCs 1 and 3 had each fed 1.0 m³ of nitrogen (at STP) into the primary system (Fig. 5c). In relation to the PWR this corresponds to the content of nitrogen of about two ACCs filled under normal operational conditions.

Analyzing the temperature distribution in the tubes of the affected SGs (not shown here) it could be concluded, that there was a continuous nitrogen/steam mixture in the SGs (temperature identical to the secondary side), and that nearly all non-condensible gas had accumulated in the tubing of the respective SGs.

The proportion of steam in this mixture reduced as the steam condensed on the tube walls, until the partial pressure of the steam corresponded to that of the secondary side. The region with nitrogen/steam mixture became "passive" and no further heat transfer took place. The partial pressure of the nitrogen then corresponded to the difference between the primary and secondary pressure (Dalton's Law):

$$p_{prim} = p_{H_2O} + p_{N_2} \quad , \quad \text{with} \quad p_{H_2O} = p_{sat,\sec} \qquad (1)$$

Caused by the seriously reduced ability of the intact SGs to act further as a heat sink, the decay power from the core could no longer be fully removed from the primary side and the core temperature rose until saturation conditions were reached, resulting in production of steam in the core. This stopped the primary pressure decrease. A continuous two-phase region developed, which extended from the core into the U-tubes (Fig. 6).

The steam condensed very intensively in the inlet region of the U-tubes in the reflux-condenser mode, thereby transmitting heat from the primary to the secondary side. The resulting condensate formed a counter-current flow pattern from the inlet region of the U-tubes back to the core via the hot leg.

By means of the leak flow rate and the above mentioned heat transfer mechanism the decay power was completely removed from the primary side. The primary pressure stabilized at a level of 11.2 bar, which resulted in a (necessary) temperature difference of 80 K between the primary and secondary side to balance the decay power.

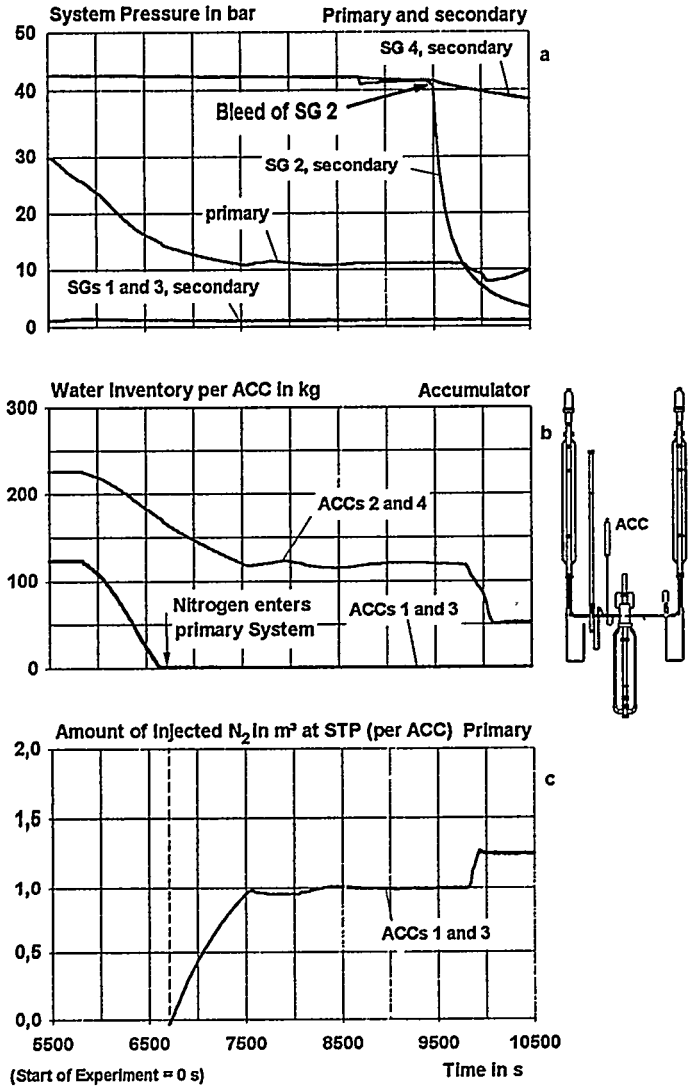

Fig. 5: System pressure and ACC injection

The water level reading in the U-tubes of the intact SGs indicated another interesting phenomenon: there was a swell level approx. 2 m high in the inlet region of the instrumented U-tubes. Therefore a situation existed whereby a stable - but oscillating - subcooled water column had formed above the two-phase mixture in the inlet of the U-tubes (Fig. 4b and 6). This phenomenon was maintained in a pseudo-steady state condition during the complete test phase with reflux-condenser mode, because the flow impulse of the rising steam did not permit the column of subcooled water to descend inside the U-tubes. Additionally, the pressure in the nitrogen/steam region of the U-tubes would decrease with the downward movement of the water column thus "supporting" this effect.

The above mentioned BETHSY experiments [3, 4] showed a similar reflux-condenser mode

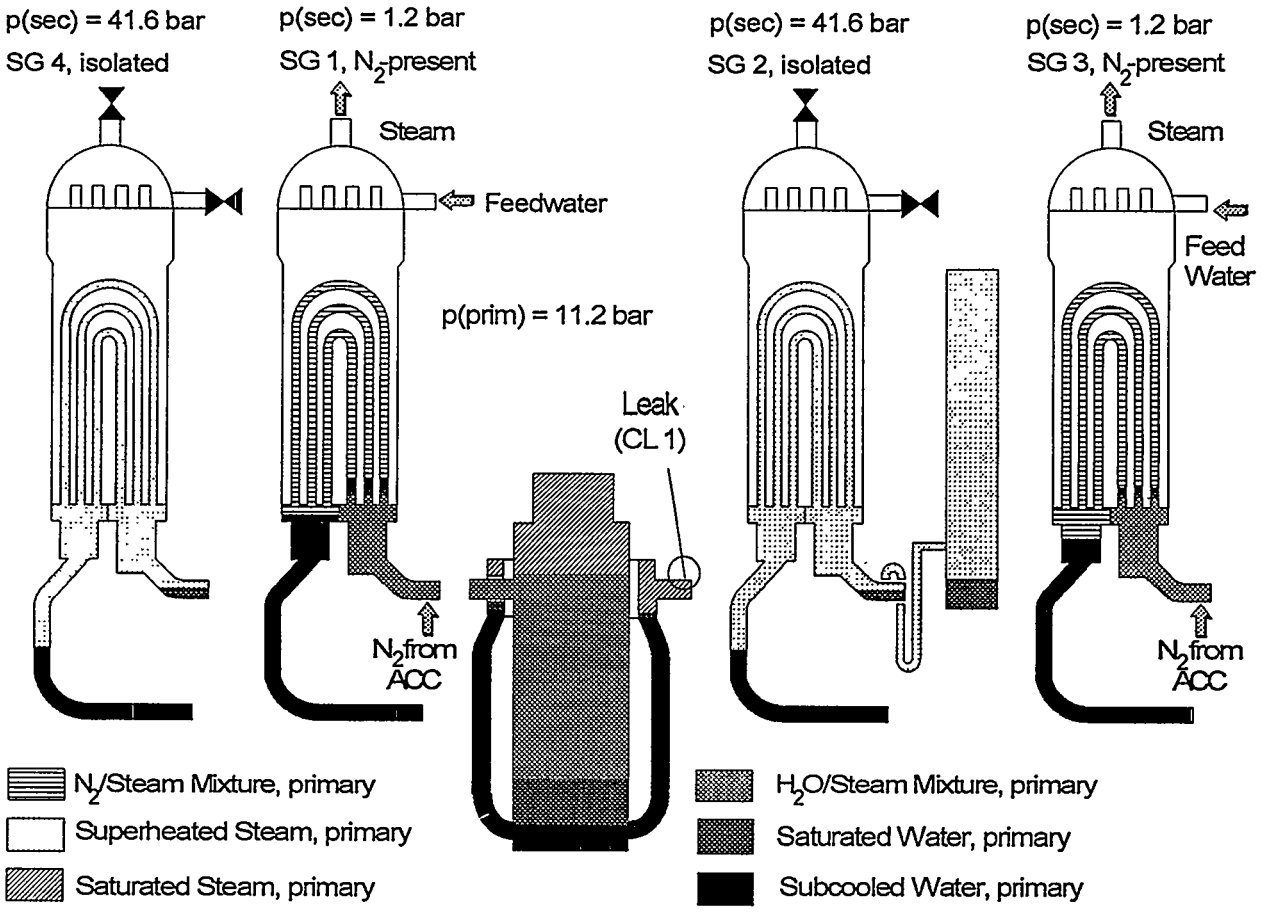

Fig. 6: Distribution of inventory at 9000 s after test initiation (reflux-condenser mode)

with heat transfer in the presence of nitrogen. At elevated pressure conditions the examination of the fluid temperatures in the U-tubes of the intact SG (all 34 tubes instrumented at the inlet) demonstrated that all the tubes were active in the lower part of the tubing (filmwise condensation of pure steam). Above this zone another section (transition zone) filled with nitrogen was present, followed by a passive region where no condensation took place. In this zone a thermal and fluid-mechanical equilibrium existed between the steam and the non-condensible gas.
During the PKL experiment this pseudo-steady state condition was maintained and observed for nearly 30 min. The primary pressure did not show any tendency to decrease further, resulting in a situation, where the heat removal from the core was secured, but no possibility existed to put the LPIS (or RHRS) in operation. Due to this additional operator procedures had to be performed.

4.2 Secondary Side Depressurization and Transition to RHRS Operation

As described in chapter 4.1 the primary pressure stabilized self-regulating after the nitrogen entered the primary system at a level of 11.2 bar. To compensate for the continuous loss of coolant in the CL of loop 1, the LPIS had to be put in operation. Caused

by the prevailing pressure greater than 10 bar, an additional operator procedure was necessary to reach the pressure-operation conditions for starting the LPIS and later the RHRS.

As an AM procedure the secondary side depressurization (bleed) of one SG (SG 2, Fig. 5a) was performed. This SG was isolated from the beginning of the experiment and had a liquid level of 12.1 m on the secondary side. Caused by the sharply decreasing secondary saturation temperature, condensation of steam in the U-tubes of SG 2 was induced (Fig. 7c). The condensation began when the temperature of the secondary side had fallen short of the steam temperature in the primary side tubing. As a consequence the water inventory in the primary system was shifted in the U-tubes of the depressurized SG (Fig. 7a). Due to flashing of saturated water the void in the core increased (indicated by the decreasing collapsed level, Fig 4b), but the heater rods were always covered by water or a two-phase mixture during the experiment.

Another effect of decreasing pressure was the renewed feeding of nitrogen from the ACCs 1 and 3 and the water-feeding from the ACCs 2 and 4 (Fig. 5) in the primary system. This water compensated some of the steam production in the RPV by flowing - because of the missing circulation in the loops - directly in the upper plenum, sinking in the core and improving the cooling of the heater rods.

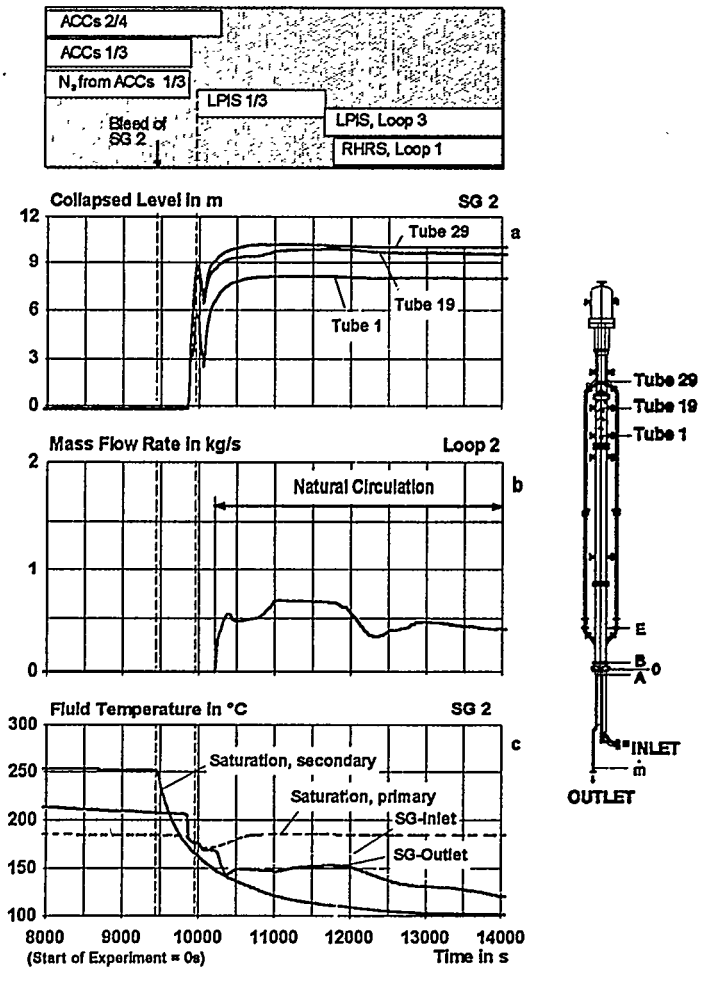

Fig. 7: Effects of secondary side bleed on the primary side

Thus approximately 530 s after starting the secondary side depressurization the primary pressure reached a level of 9.4 bar. The LPIS was switched on in the loops 1 and 3 (hot and cold legs). The injection rate of the pumps resulted in reaching a new equilibrium state with the leakage rate at a pressure of approx. 11 bar. The U-tubes of the SG 2 were filled completely with water and the subcooled natural circulation heat transfer regime in loop 2 was established (Fig. 7a and 7b).

The decay heat of the core was completely compensated in this phase by the subcooling of the injected water, the heat sink in SG 2 and the flow rate of subcooled liquid through the leak. The injected subcooled water of the LPIS in the hot legs of the loops 1 and 3 reached the

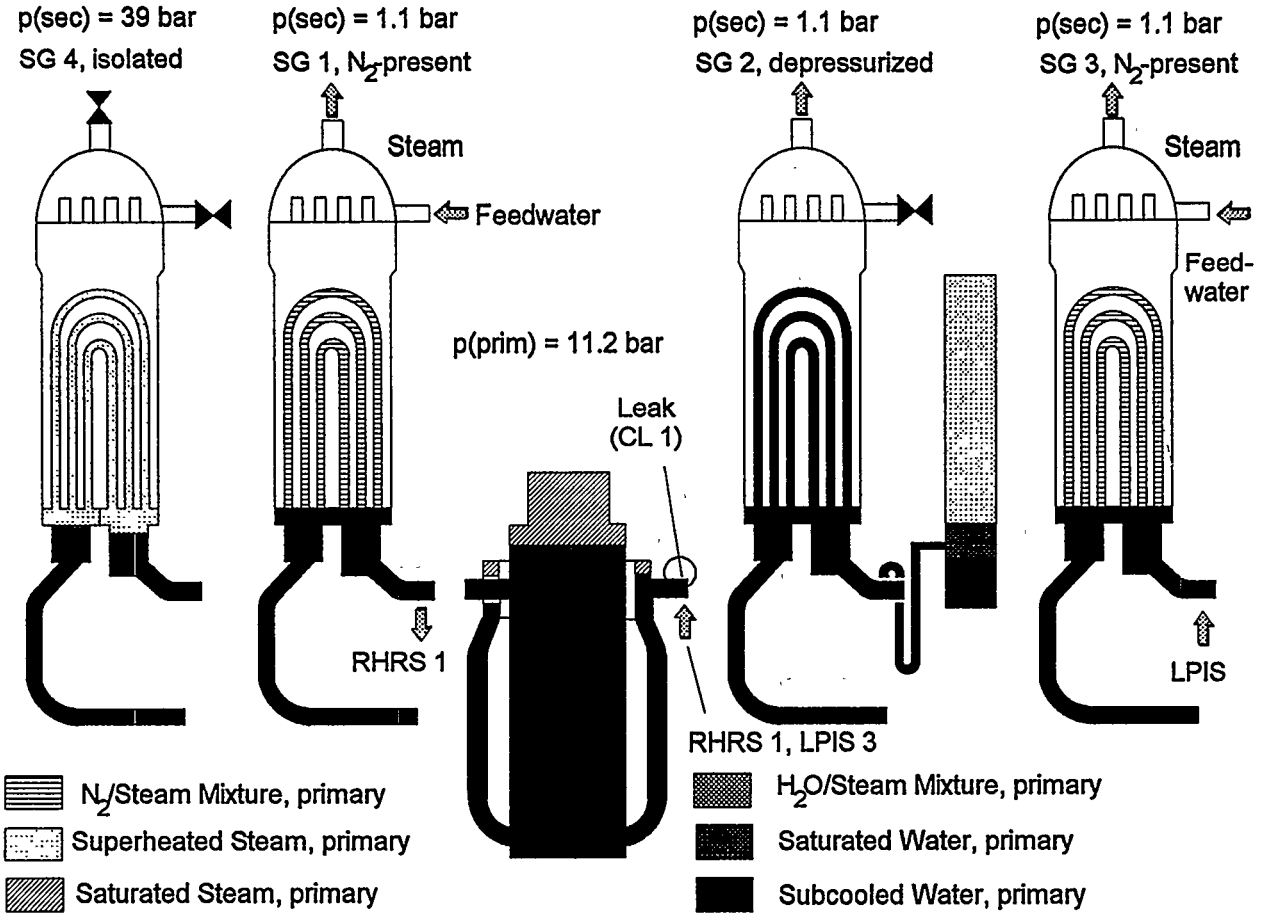

Fig. 8: Safe plant conditions; combined recirculation/RHR mode

upper plenum and resulted in an increasing subcooling at the core outlet and an increased collapsed level in the RPV (Fig. 4b).

Approx. 30 min after the start of the LPIS the transition to combined recirculation/RHR mode of operation was performed. The hot and cold legs of loop 1 were already filled with subcooled water, hence the operation conditions for the RHRS were succesfully adjusted. The loss of coolant through the break was compensated for by the LP injection into loop 3. With this mode of operation, long-term core cooling, i.e. the dissipation of the decay heat, was finally secured.

5. CONCLUSIONS

The PKL experiment showed that, despite the assumed extreme SBLOCA scenario (beyond-design-basis accident conditions, injection of unrealistically large amounts of N_2 into the primary system via two ACCs), the loss of natural circulation in the two loops with intact SGs, caused by the accumulation of N_2 in these SGs, did not result in loss of heat transfer to the secondary side. The primary system adjusted to the very effective reflux-condenser mode. The system stabilized self-regulating at a constant

pressure and temperature level and consequently the removal of the decay core power was secured. Under these conditions, the primary water inventory was nearly 48 % of the total mass in the primary system (without pressurizer and surge line) and the system reached an equilibrium at a primary pressure of 11.2 bar, with a temperature difference of 80 K between the primary and secondary side.

The secondary side depressurization of one SG allowed the LP injection pumps (10 bar) to come into operation. After the transition to the combined recirculation/RHR mode of operation long-term core cooling and further cooldown of the primary side were secured.

6. TABLE OF NOMENCLATURE

Abbreviations

ACC	accumulator
AM	accident management
BDBA	beyond-design-basis accident
BMBF	Federal Ministry for Education and Research, FRG
CL	cold leg
HL	hot leg
HPIS	high pressure injection system
LPIS	low pressure injection system
N_2	nitrogen
PKL	Primärkreisläufe, test facility operated by Siemens AG/KWU, Erlangen, FRG
PWR	pressurized water reactor
RCP	reactor coolant pump
RPV	reactor pressure vessel
SBLOCA	small break loss of coolant accident
SG	steam generator
STP	standard temperature and pressure
UP	upper plenum
VDEW	German Utilities

Latin symbols

p	[bar]	pressure

Subscripts

H_2O	water
N_2	nitrogen
prim	primary
sec	secondary
sat	saturation

7. REFERENCES

[1] K. J. Umminger, W. Kastner, R. M. Mandl, P. Weber
"Thermal Hydraulic Behaviour of a PWR Under Beyond-Design-Basis Accident Conditions - Conclusions from an Experimental Program in a 4-Loop Test Facility (PKL) "
ICONE-2, San Francisco, California USA, March 21-24, 1993

[2] K. J. Umminger, R. M. Mandl
"Thermal Hydraulic Response of a PWR to Nitrogen Entering the Primary - Experimental Investigation in a 4-Loop Test Facility (PKL) "
NURETH-5, Salt Lake City, USA, September 21-24, 1992

[3] B. Noel, R. Deruaz
"Reflux-Condenser Mode with Non-Condensible Gas: Assessment of CATHARE against BETHSY Test 7.2c"
NURETH-6, Grenoble, France, October 5-8, 1993

[4] D. Dumont, G. Lavaille, B. Noel, R. Deruaz
"Loss of Residual Heat Removal During Mid-Loop Operation: BETHSY Experiments"
NURETH-6, Grenoble, France, October 5-8, 1993

SPES-2, AP600 Integral System Test S01007 2" CL to Core Make-up Tank Pressure Balance Line Break

M. Bacchiani, C. Medich
M. Rigamonti, O. Vescovi
SIET S.p.A.
Piacenza, Italy

A. Alemberti
ANSALDO Nuclear Division
Genova, Italy

L. E. Conway
Westinghouse Electric Co.
Pittsburgh, Pa - USA

ABSTRACT

The SPES-2 is a full height, full pressure experimental test facility reproducing the Westinghouse AP600 reactor with a scaling factor of 1/395. The experimental plant, designed and operated by SIET in Piacenza, consists of a full simulation of the AP600 primary core cooling system including all the passive and active safety systems. In 1992, Westinghouse, in cooperation with ENEL (Ente Nazionale per l' Energia Elettrica), ENEA (Ente per le Nuove Tecnologie,l' Energia e l' Ambiente), SIET (Società Informazioni Esperienze Termoidrauliche) and ANSALDO developed an experimental program to test the integrated behaviour of the AP600 passive safety systems. The SPES-2 test matrix, concluded in November '94 (see Table 1), has examined the AP600 passive safety system response for a range of small break LOCAs at different locations on the primary system and on the passive system lines; single steam generator tube ruptures with passive and active safety systems and a main steam line break transient to demonstrate the boration capability of passive safety systems for rapid cooldown. Each of the tests has provided detailed experimental results for verification of the capability of the analysis methods to predict the integrated passive safety system behaviour. Cold and hot shakedown tests have been performed on the facility to check the characteristics of the plant before starting the experimental campaign.

The paper first presents a description of the SPES-2 test facility then the main results of S01007 test "2" Cold Leg (CL) to Core Make-up Tank (CMT) pressure balance line break" are reported and compared with predictions performed using RELAP5/mod3/80 obtained by ANSALDO through agreement with U.S.N.R.C. (U. S. Nuclear Regulatory Commission). The SPES-2 nodalization and all the calculations here presented were performed by ANSALDO and sponsored by ENEL as a part of pre-test predictions for SPES-2.

INTRODUCTION

Westinghouse Electric Corporation, in conjunction with the U.S. Department of Energy and the Electric Power Research Institute, has developed an advanced light water reactor design, known as AP600. AP600 is a 1940 MWt, 600MWe two-loop pressurized water reactor (PWR) that utilizes passive safety systems and modular design and construction techniques to reduce the capital costs, construction time and operational and maintenance cost.
The AP600 primary system utilizes a four-cold-leg, two-hot-leg onfiguration with canned-motor primary reactor coolant pumps. The pressurizer used in the AP600 design has a volume which is 30% larger than any operating two-loop PWR. The larger

pressurizer allows the unit to tolerate operational transients with increased margin. The average power has been reduced by 20%, the lower power density provides additional critical heat flux (DNB) margins for postulated design basis accident such as the large-break loss-of-coolant accident (LOCA). The primary loop design also results in smaller cold legs for AP600 compared to a current PWR. As a result, the break flow is reduced for the postulated large LOCAs resulting in an increased margin for AP600. Also, injection flow is injected directly into the reactor vessel downcomer so that less cooling water is lost through the break, making the passive safety systems more effective. The most significant unique features of the AP600 are the use of a safety grade passive core cooling system (PXS) and a passive containment cooling system (PCS) to mitigate the consequences of postulated accidents.
The passive safety systems are comprised of:

- two full pressure Core Make-up Tanks (CMT) providing borated makeup water to the primary system in the event of a loss of reactor coolant as reactor cooldown;
- two accumulators discharging water at high flow rates into the core in the event of a large loss of reactor coolant;
- a set of valves connected to the pressurizer steam space and on the two hot legs, constituting the ADS which provides a controlled depressurization;
- an In-Containment Refuelling Water storage Tank (IRWST) that is the long term gravity fed core cooling water reservoir and in which the ADS from the pressurizer are discharged;
- a Passive Residual Heat Removal System (PRHR) supplied with a C shaped heat exchanger submerged inside the IRWST that removes decay heat during loss of steam generator inventory.

A comprehensive test and analysis program [1] has been developed to confirm the passive safety features of the AP600 design. The program includes large-scale separate effects tests on the major components and two integral system experimental campaigns: the experimental results obtained at SPES-2 facility are to be used in conjunction with one-quarter scale, low pressure Oregon State University facility to obtain the final design approval of the AP600 and to verify the capability of the analysis methods to predict the integrated passive safety systems behaviour.

SYSTEM DESCRIPTION [2]

A schematic flow sheet of SPES-2 facility is shown in Figure 1.

Scaling criteria

The facility simulates the AP600:

. primary circuit;
. secondary circuit up to the steam isolation valve;
. all the passive safety systems: CMT, IRWST, PRHR, ADS;
. the non safety systems: CVCS (Chemical Volume Control System), NRHRS (Normal Residual Heat Removal) and Startup Feedwater (SFW).

The following general scaling criteria have been applied to the design of the SPES-2 test facility:

- conservation of thermodynamic conditions (pressure and temperature);
- power over volume ratio conservation in each component;
- power over mass flowrate conservation;
- fluid transit time preservation (as a consequence of 1, 2, 3);
- heat flux conservation in heat transfer components (core and steam generator);
- elevations maintained in lines and components;

- preservation of Froude number in the primary circuit loop piping (hot leg and cold legs) in order to preserve the flow regime transition to a stratified flow that would be expected for small break LOCA situations in horizontal piping.

Further specific scaling criteria have been applied to some components or lines to better duplicate the AP600 behavior.
The overall scaling factor of the facility is 1/395, the main characteristics are:

. process fluid	water
. number of loops	2
. number of reactor coolant pumps	2
. primary design pressure, MPa	20
. secondary design pressure, MPa	20
. primary design temperature, °C	365
. secondary design temperature, °C	310
. max power, Mw	9
. elevation scaling	1/1

Primary piping

The primary piping consists of two loops each one including one hot leg and two cold legs. The hot leg, connecting the reactor vessel to a steam generator, duplicates the AP600 up to the pressurizer surge line nozzle by maintaining the AP600 L/D in the horizontal section and the same 55° angle in the inclined section.
The AP600 two cold legs per loop design, is duplicated, however, they detach from a single coolant pump vertical discharge. The split from the single pump discharge into the two cold legs is positioned at the elevation of the AP600 SG channel head in order to preserve the same geodetic flow path that the fluid must take from the unbroken cold leg to the broken one during a cold leg break transient .
Due to the great importance of surge line during ADS depressurization the line has been designed preserving the friction pressure drops.

Rod bundle

The rod bundle is electrically heated and consists of 97 skin heated inconel rods reproducing, in the active zone, the same geometry (rod pitch, rod diameter and length) as the AP600 bundle. The axial power profile is uniform for all the rods, radially the profile is also uniform with the exception of two rods with a peaking factor of 1.19. The heater rods are single ended and are connected to a ground bus at the top of the bundle at the upper core plate elevation. The maximum power is 9 Mw and the maximum current is 70 kA. The scaled full power used for the AP600 transients is 4.89 MW (x 1.02)

Power channel downcomer

The downcomer is composed of an annular section in which the four cold legs and two direct vessel injection (DVI) nozzles for safety injection enter. Below these nozzles a pipe connects this annular downcomer section to the lower plenum. In this fashion, the four cold legs/two hot legs characteristic of the AP600 can be preserved along with the downcomer injection features.
The annular and the tubular downcomer sections have the same friction pressure drops. The circumferential pressure drop of the annulus has been equalized to the AP600. There are turning devices to direct the ECC injection flow downward in the annular downcomer as in the AP600. The total volume is scaled by the scaling factor. The annular downcomer sketch is shown in Fig. 2.

Pressurizer

The pressurizer controls primary system pressure during normal and transient plant operation and consists of a cylindrical flanged vessel equipped with 2 immersion type heaters each having a maximum controlled power of 16 kw and 6 external heaters each generating 3 kW. The pressurizer volume is scaled and the bottom elevation is preserved. The level swelling is preserved by ensuring that the average void fraction in the test is equal to AP600 for similar thermo-hydraulics conditions using the Wilson bubble rise models. Ad hoc RELAP5 calculations performed by ANSALDO indicated that this was a proper scaling approach.

Pumps

Two primary pumps (one per loop) drive primary coolant into the PC (Power Channel) downcomer to remove the generated heat. The pumps are centrifugal-single stage-horizontal shaft type, the suction line is horizontal while the delivery is directed downwards discharging in a 3" pipe common to the two cold legs. A flywheel is provided to have an inertia closer to the AP600. The rotational speed can be controlled in the range +/- 190% of the nominal value and the speed variations can be programmed by a means of a motor driven regulator.

Steam Generators

The facility has two identical generators to transfer thermal power from the primary to the secondary circuit. The steam generator primary side consists of a tube bundle and inlet/outlet plena. The SG bundle includes 13 inconel 600 U-tubes assembled in a square array.
The secondary side volumes are scaled by 1/395, and all the vertical elevations are preserved up to the top of the steam separator (the steam dome has no influence on the natural circulation phenomena).

Passive safety systems

- The Core Make up Tanks (CMTs) design is unique and has been developed by SIET engineers so that the CMT metal mass is scaled to the AP600 CMT. The CMT design uses a thin-walled vessel inside a thicker pressure vessel with the space between the two vessel pressurized with air at 70 bar. In this manner the rate of steam condensation on the walls is preserved. Since the CMTs are full height and operate at full pressure, the surface area to volume and total metal mass of a single pressure vessel would have been excessive resulting in very large wall steam condensation effects.
- two Accumulators with volume scaled;
- one Passive Residual Heat Removal (PRHR) with a full height C shaped heat exchanger with friction pressure drops maintained and the heat transfer area is scaled such that the natural circulation behaviour of the AP600 PRHR is simulated (i.e.:one tube).
- In-containment Refuelling Water Storage Tank (IRWST) at atmospheric pressure with water volume scaled and elevation maintained;
- four stages of Automatic Depressurization System (ADS) simulated by means of ball valves (one per stage) with an orifice in series to achieve the proper scaled flow area. The two sets of piping connected to the steam space of the pressurizer in the AP600 are combined into a single set with the first, second and third stage valves in SPES-2. The three ADS valves share a common discharge line to a condenser and a collection tank that has load cells to measure the mass accumulation. A similar

measuring arrangement is also used for the ADS four stage, which is located on the hot legs of the primary piping.

The injection capability of the AP600 non safety systems such as CVCS, NRHR and SFW is provided in order to illustrate any safety/non safety system interaction. The friction pressure drops of all the connecting lines are maintained. Small breaks are simulated using a spool piece which contains a break orifice and quick opening valve. The break, ADS and secondary relief valve discharges are collected into different catch tanks with load cells to measure the mass accumulation.

2" BREAK OF A COLD LEG TO CMT PRESSURE BALANCE LINE.

Test description

This test simulated a 2" break in one of the two cold legs to CMT pressure balance lines to investigate the asymmetric CMT performance following the break. Only the passive safety systems for accident mitigation were used.
This test was performed by quickly opening the break valve connected to the cold leg side of the balance line isolation valve.
The break was connected to a separate condenser and a weigh tank in order to measure break flow versus time.
The transient was initiated from a full power condition (see Table 3) by opening the break valve. All other actuations were performed automatically by the SPES-2 data acquisition and control systems according to the following procedure.
After opening the break, when reactor trip "R" signal condition (PRZ pressure = 12.41 MPa) is achieved the heater rod power is controlled to match the scaled AP600 decay heat and 2 s after the SG's MSIV are closed. When "S" signal condition (PRZ pressure = 11.72 MPa) is reached, 2 s after the CMTIVs (Core Makeup Tank Isolation Valves) are opened and the MFWIVs (Main Feed Water Isolation Valves) closed, and 16.2 s after the RCP's (Reactor Coolant Pumps) coastdown is initiated. The PRHR (Passive Residual Heat Removal) isolation valve is opened by the Protection System signals (2 s after S-signal or either SG's low narrow range level - 0.15 m - plus a delay time of 60 s). The ADS valves are opened versus either CMT's level (volume) with a corresponding delay time, that is:

- ADS 1 CMT vol.= 67% + 30 s
- ADS 2 CMT vol. =67% + 125 s
- ADS 3 CMT vol. =67% + 245 s
- ADS 4a/b CMT vol. =20% + 60 s

The accumulator starts to inject water into DVI when primary pressure was lower than 4.9 MPa.
The IRWST discharges water by gravity into DVI when primary pressure is lower than 0.18 MPa.
The actual times recorded are reported in Tab.2.

- TABLE 2- SEQUENCE OF EVENTS

Event	Signal	Time (s)
Break opens	/	0
Reactor trip signal "R"	P=12.41 MPa	60
MSLIV	R signal +2s	62
Safety Inj. signal "S"	P=11.72 MPa	69
MFWIV closure	S signal + 2s	71
CMT IV opening	S signal +2s	72
RCP trip	S signal +16.2s	87
PRHR HX actuation	S signal + 2s	72
ADS 1 opening	CMT lev. 67% + 30s	1072
Accumulators A on	/	1074
Accumulator B on	/	1074
ADS 2 opening	CMT lev. 67% + 125s	1167
ADS 3 opening	CMT lev. 67% + 245s	1286
ADS 4 opening	CMT lev. 20% + 60s	2090
IRWST IV opening	/	2189

- TABLE 3 - INITIAL CONDITIONS

Quantity	Specified	Actual
Rod power	4.99±.1 MW	4.915 MW
Pressurizer pressure	15.51±.2 MPa	15.4 MPa
Average HL temperature	315.5±5 °C	318.4 °C
Core inlet temperature	276.4±5 °C	283 °C
Core flowrate	23.2±.25 kg/s	23.3 kg/s
Cold leg flowrate	5.86±.1 kg/s	5.8 kg/s
DC-UH bypass flowrate	.18±.05 kg/s	.19 kg/s
Pressurizer level	3.78±.38 m	3.7 m
Accumulator pressure	4.9±.1 MPa	4.9 MPa
IRWST level	8.5±.1m	8.5 m
PRHR supply line temp.	>100 °C	107 °C
UH average temperature	296±5 °C	269 °C
Balance line temperature	>165 °C	255 °C
CMT level	full	full
CMT temperature	20±5 °C	28.35 °C
SG level	1.48±.15m	1.3 m
SG pressure	4.9±.2 MPa	5.05 MPa
SG MFW temperature	226±7 °C	233 °C

Experimental results

The response of the facility is discussed below and is compared with pre-test analysis which were performed by ANSALDO using RELAP5/mod3/80 [3] in Figures 3 to 13. The SPES-2 input noding is shown in Fig. 14. The above initial conditions and automatic actuations in the sequence of events simulate the AP600 full power conditions and safety actuation signal setpoints.

The results of this test are very similar to the 2" cold leg and the 2" direct vessel injection breaks with only the passive safety systems operating, but for the behaviour of the CMT connected to the broken balance line as discussed below.
This transient is characterized by the following main characteristics/events which are shown in the attached figures:

- Reactor coolant system (RCS) pressure rapidly decreased, due to the mass loss out the break, to the saturation pressure corresponding to the primary system fluid temperature, while pressurizer emptied;
- Reactor trip and safety system "S" signal actuation occurred soon after transient initiation (60 and 69 sec respectively);
- Soon after "S" signal actuation, the intact CMT begins to provide cold water injection via natural circulation; it drains at about 400 seconds transitioning from natural circulation operation to steam displacement.
  The broken CMT injection starts when the break mass flow is sufficiently low with consequent sufficiently low pressure drop in the balance line (i.e.; when two phase flow conditions are reached in the broken balance line at about 400 seconds): at these conditions the presence of two phase flow in the broken balance line causes an unstable natural recirculation (i.e. broken CMT level does not decrease) due to steam condensation at CMT inlet, until ADS 1 opens.
  At this time, primary system depressurization becomes more rapid increasing the presence of steam in the system and causing the broken CMT to drain for steam displacement.
  From ADS 1 opening on, the behaviour of broken CMT injection is very similar to the intact CMT: only its flow is a bit higher as the intact CMT head decreased as it had already begun to drain:
- Primary pressure remains relatively constant due to the SG stored energy, until the first stage of ADS is opened (about 1072 seconds);
- Pressurizer level increases after ADS 1 opening due to the high depressurization entrainment. The same phenomenon is shown for ADS 2 and 3 opening;
- accumulators injection initiates soon after ADS 1 opened. Accumulator flow increases after both second and third stage ADS actuations, while CMT flow is reduced due to high accumulator delivery;
- IRWST flow begins just after ADS 4 actuation and prior to CMT flow termination.

Comparison between experimental data and pre-test calculations

The 2" CL-CMT balance line break pre-test predictions performed by ANSALDO agree with the experimental data from the SPES-2 facility.
The primary fast depressurization transient in the first part of the test reproduces the facility behaviour while a small mismatch of the primary pressure behaviour is present when subcooled blowdown ends and when primary pressure reaches secondary one. Intact CMT level well compares with experimental level and obviously its flow is reproduced by the code. Less agreement is found in the broken CMT level behaviour, some mismatch is present in its flow although the overall phenomenologies of the broken CMT are correct.
The accumulator injection flow rates well compare with experimental data. The overall pressurizer behaviour is well predicted by the code but for an overestimated value after accumulator stops injecting.
Power channel temperature are well followed by the code.
IRWST injection timing and flows are well predicted by the code for both sides of the DVI's.

From a phenomenological point of view the code captures all the behaviours taking place during the transient, often quantitatively the predictions of the code were in good agreement with the experimental results.

ACKNOWLEDGEMENTS

SIET acknowledges the Westinghouse Electric Corp. (Dr. L.E. Hochreiter) for his continuing advise on the overall conduct of this project.
SIET also acknowledges the contributions of G. Graziosi and C. Frepoli of Ansaldo for their diligent and timely pre-test analyses which were used to provide guidance in both the design of the SPES-2 facility and in preparation of the test procedures.

REFERENCES

[1] L.E. Conway, "AP600 FHFP Integral System Test Specification", Westinghouse report, *September 1994.*

[2] M. Rigamonti, "SPES-2 Facility Description", SIET report, *April 1994.*

[3] A. Alemberti, G. Graziosi, "SPES-2 Test Matrix; final RELAP5/Mod3 pre-test analysis", ANSALDO report, *November 1994.*

TABLE 1-MATRIX TESTS PERFORMED ON SPES-2

TAG	TEST DATE	TYPE	DESCRIPTION	STATUS OF NON SAFETY SYSTEMS	PRHR STATUS	SINGLE FAILURES	NOTES
S00103	Feb 5, 1994	SBLOCA	2 inch CL break	CVCS, NRHR,SFW off.	On	ADS 4th stage B.	Sharp orifice at the break.
S00203	April 9, 1994	SBLOCA	2 inch CL break	CVCS, NRHR,SFW off..	On	1 of 2 ADS 4th stage B valves.	Smooth orifice at the break.
S00303	April 30, 1994	SBLOCA	2 inch CL break	CVCS, NRHR,SFW off.	On	1 of 2 ADS 4th stage B valves.	As above without PR balance line. Reference CL break.
S00401	May 5, 1994	SBLOCA	1 inch CL break	CVCS, NRHR,SFW off.	On	1 of 2 ADS 4th stage B valves.	Maximize CMT heatup prior to ADS actuation.
S00504	May 18, 1994	SBLOCA	2 inch CL break	CVCS, NRHR,SFW on.	On	No effect. No 4th stage actuation expected.	Non safety/passive system interaction.
S00605	May 27, 1994	SBLOCA	2 inch DVI break	CVCS, NRHR,SFW off.	On	1 of 2 ADS 4th stage B valves.	Asymmetric CMT performance.
S00706	June 10, 1994	SBLOCA	DEG break of DVI	CVCS, NRHR,SFW off..	On	1 of two ADS 1st and 3rd stage valves.	Complete loss of one-of-two PXS subsystems.
S00908	June 23, 1994	SBLOCA	CMT BL DEG break	CVCS, NRHR,SFW off.	On	1 of 2 ADS 1st and 3rd stage valves.	No delivery from faulted CMT . Blind test.
S01007	July 7, 1994	SBLOCA	2 inch CMT BL break	CVCS, NRHR,SFW off.	On	1 of 2 ADS 4th stage B valves.	Examine effect on CMT draindown.
S01110	July 14, 1994	SGTR	SG tube rupture (1 tube)	CVCS, NRHR,SFW off..	On	No effect.	No operator actions.
S01211	Sept 9, 1994	SGTR	SG tube rupture (1 tube)	CVCS, NRHR,SFW off.	On	1 of 2 ADS 4th stage B valves	Inadvertent ADS opening. Blind test.
S01309	Sept 22, 1994	SGTR	SG tube rupture (1 tube)	NRHR off. SFW, CVCS on.	On	No effect	Operator action to isolate SG, subcool and depressurize primary system.
S01512	Oct 11, 1994	SLB	SG A steam line break	CVCS, NRHR,SFW off.	On (3 tubes)	SFW not isolated on T cold signal	Maximum PRHR cooldown. CMT's do not drain and no ADS actuation occurs.
S01613	Oct 15, 1994	SBLOCA	1 inch CL break	CVCS, NRHR,SFW off.	On (3 tubes)	1 of 2 ADS 4th stage B valves.	Show effect of 2 PRHR HX's on cold leg temperature.
S01703	Nov. 12, 1994	SBLOCA	2 inch CL break	CVCS, NRHR,SFW off.	On	1 of 2 ADS 4th stage B valves.	Reference CL break repeatability test.

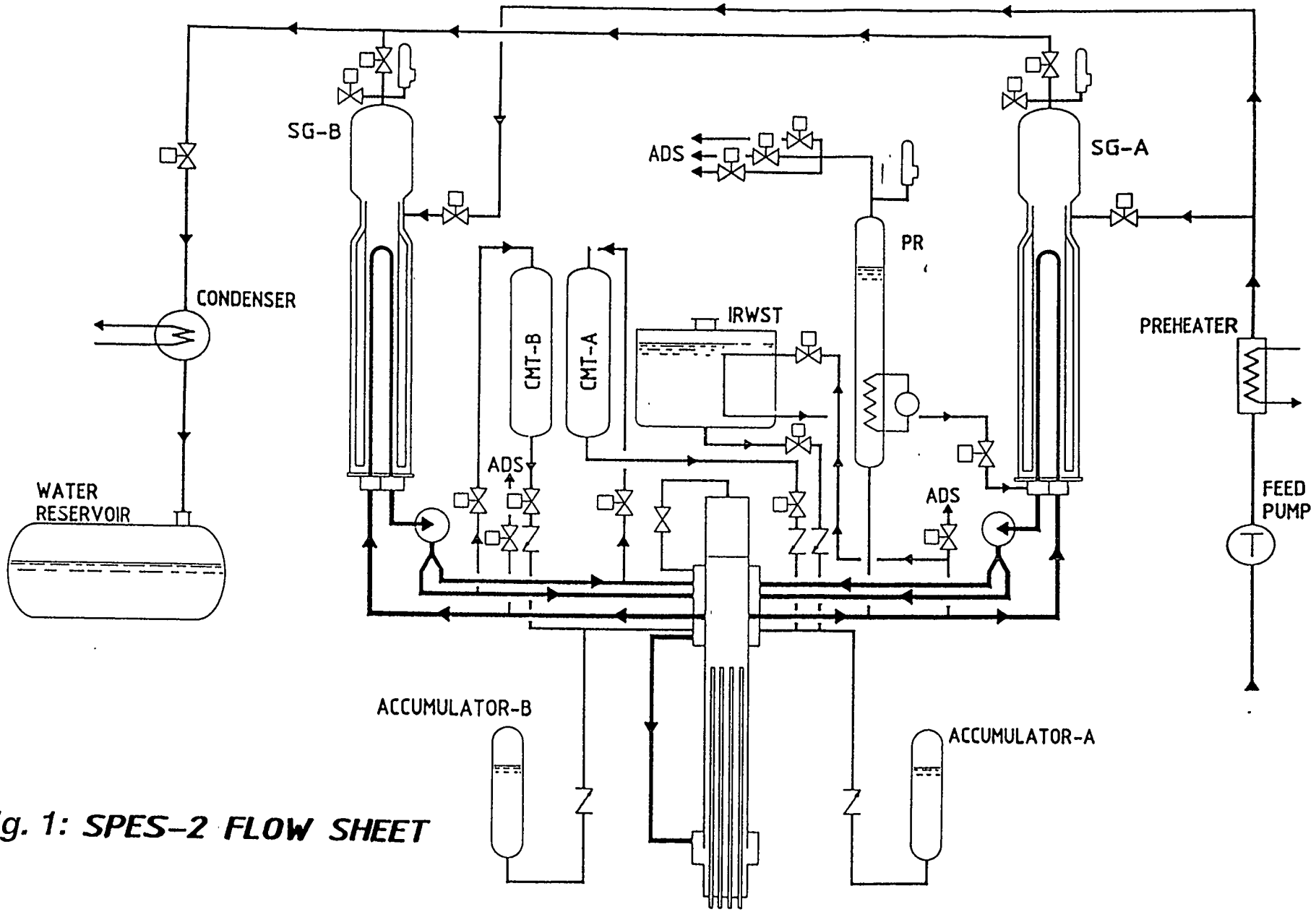

2878

Fig. 1: SPES-2 FLOW SHEET

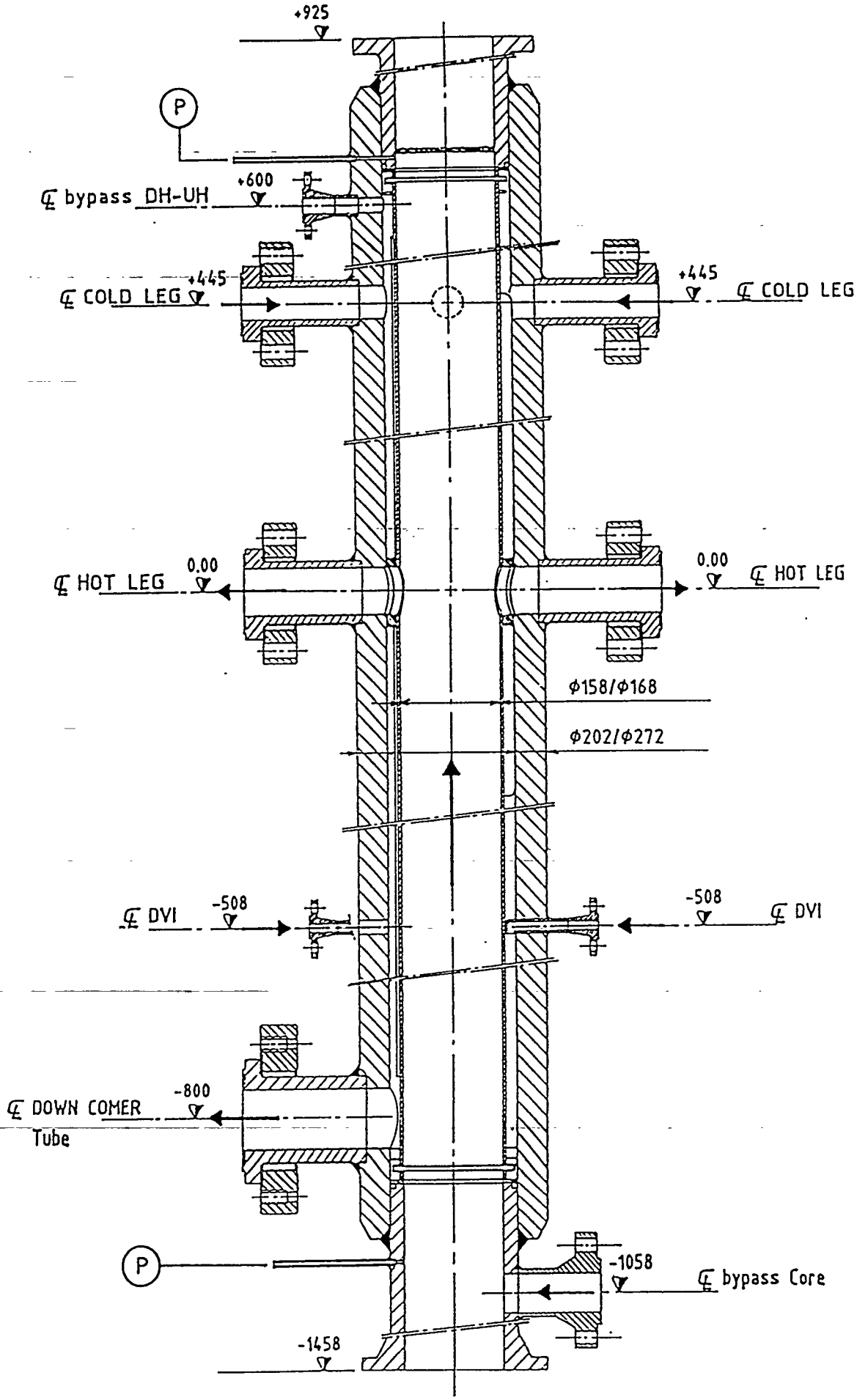

Fig. 2 Power channel: annular downcomer and upper riser

Fig. 3: Primary pressure

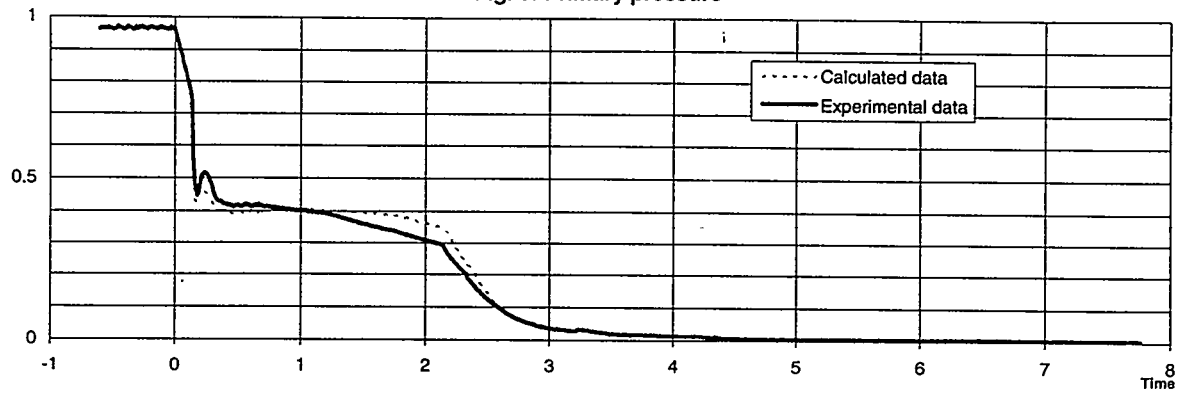

Fig. 4: Pressurizer level

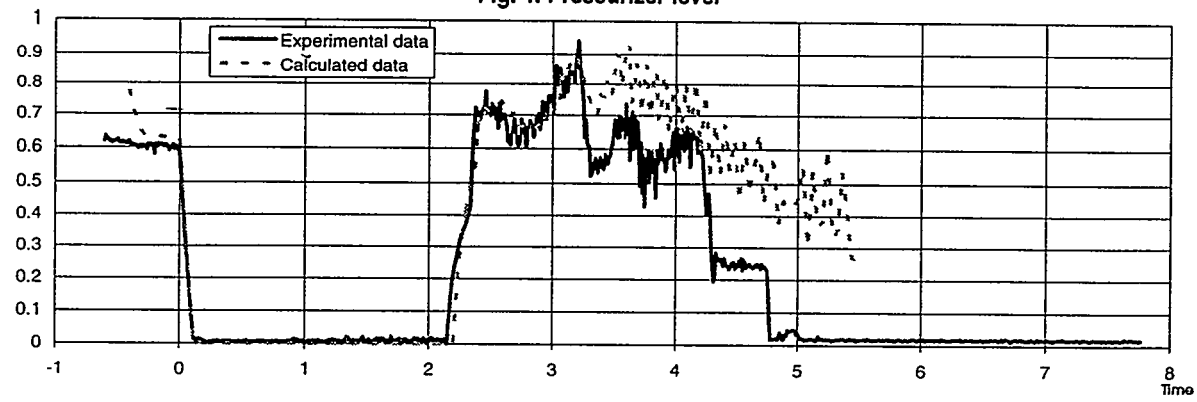

Fig. 5: Intact CMT level

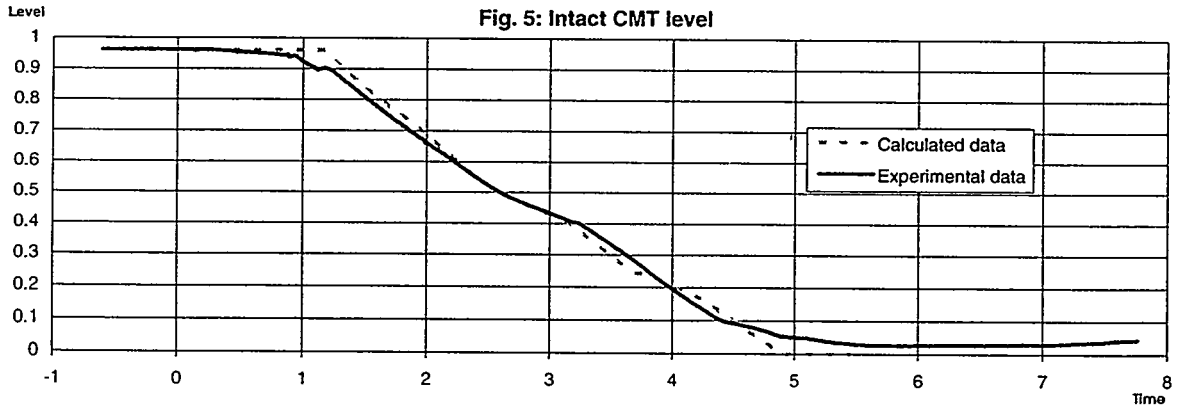

Fig. 6: Faulted CMT level

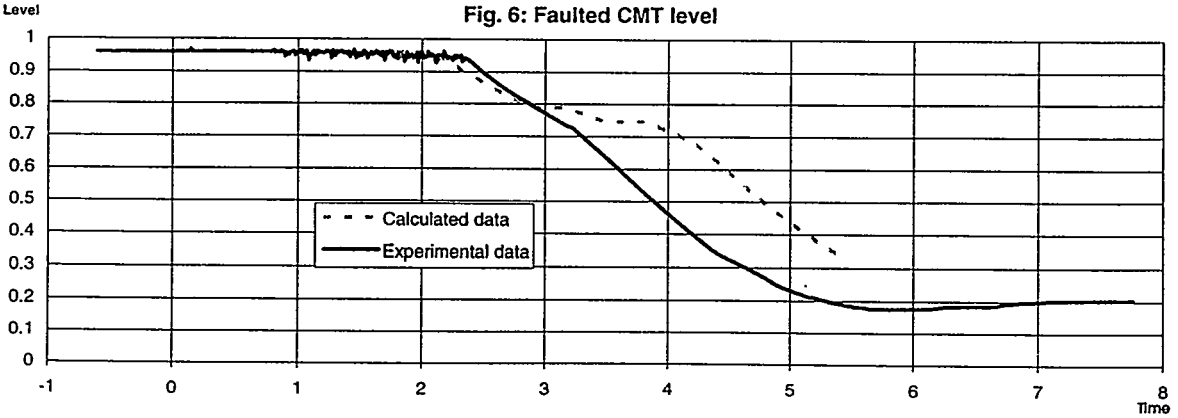

All the scales are normalized: Y-axes are normalized over the maximum value of plot scales, while time-axes are divided by a constant value.

Fig. 7: Intact CMT flow

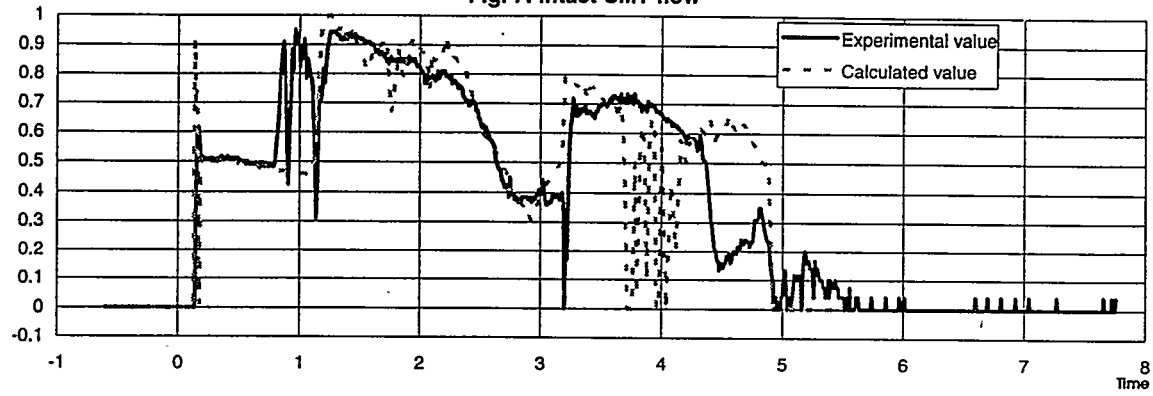

Fig. 8: Faulted CMT flow

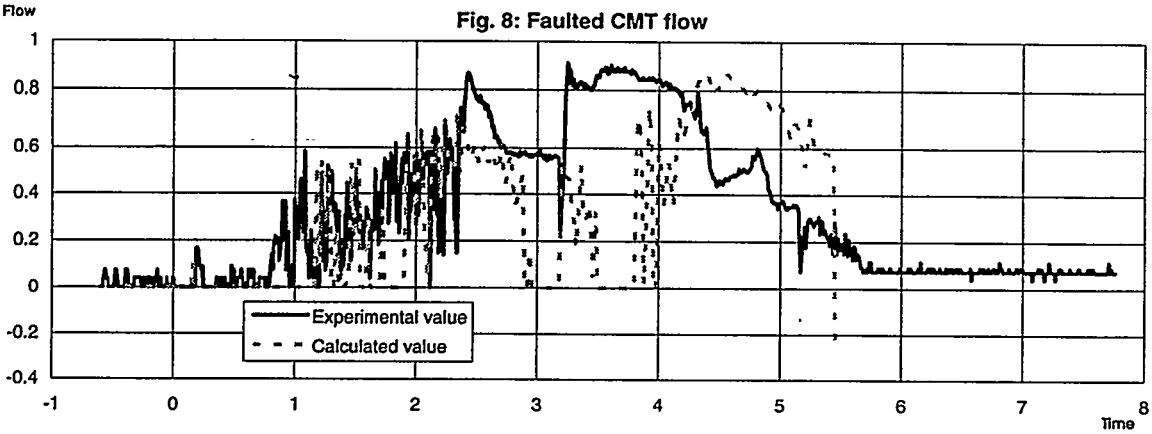

Fig. 9: Intact accumulator flow

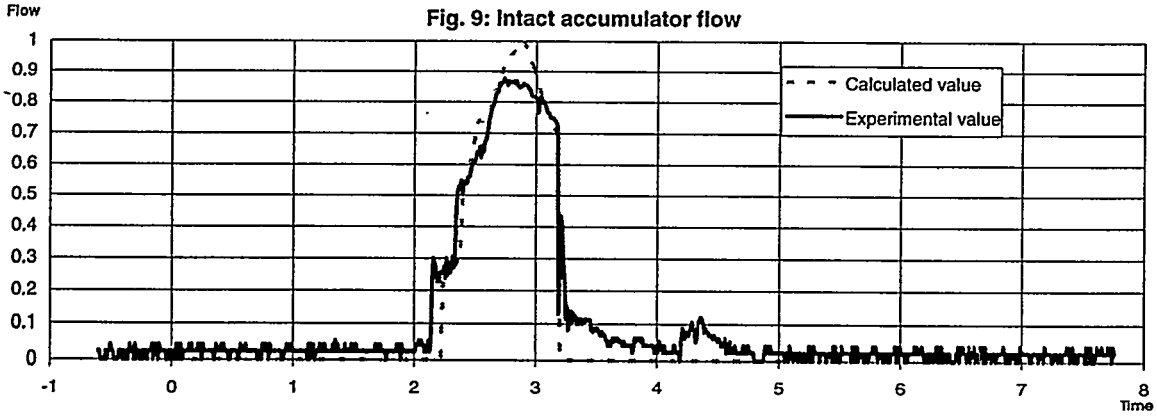

Fig. 10: Faulted accumulator flow

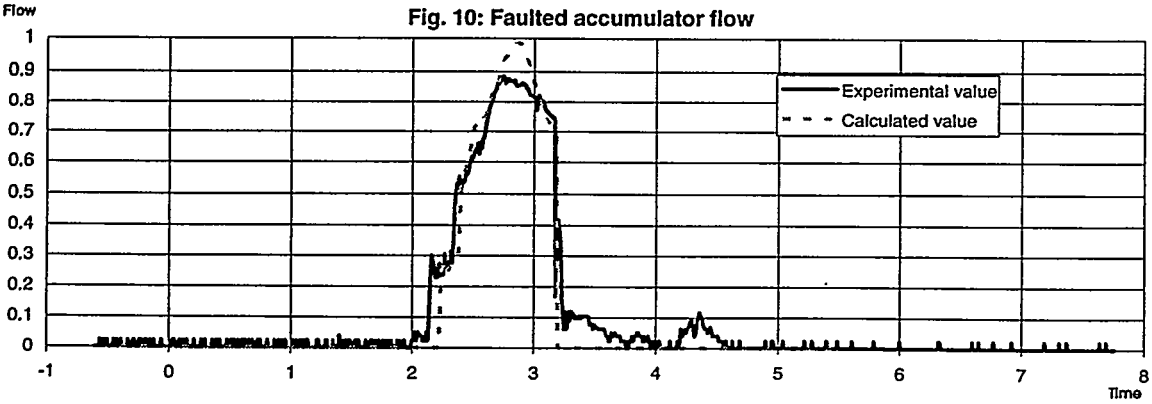

All the scales are normalized: Y-axes are normalized over the maximum value of plot scales, while time-axes are divided by a constant value.

Fig. 11: Intact IRWST flow

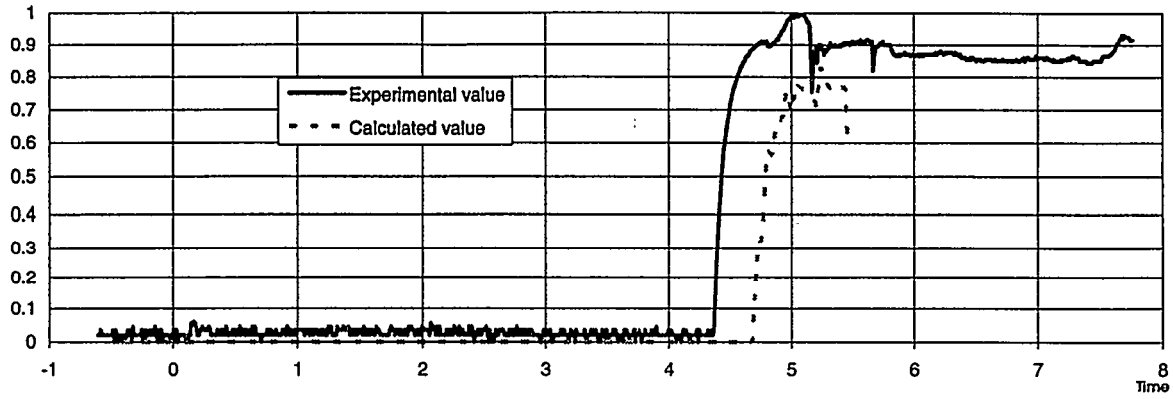

Fig. 12: Faulted IRWST flow

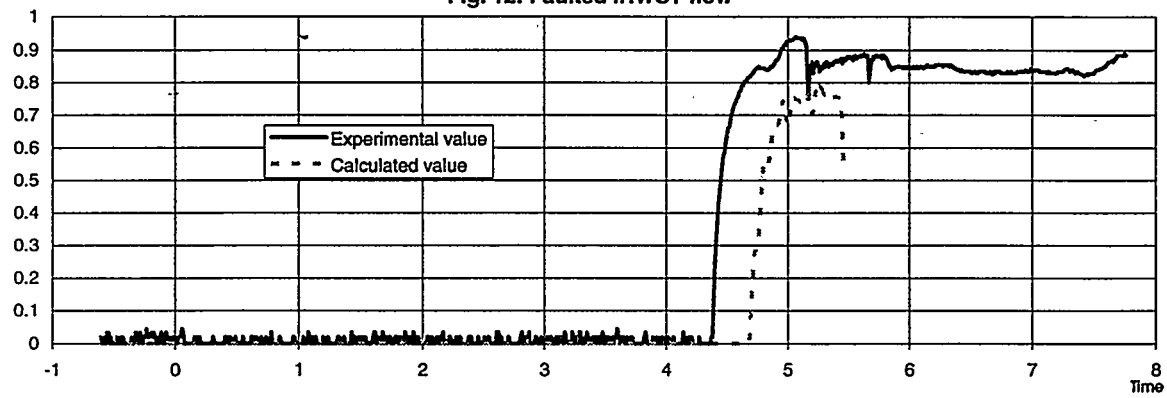

Fig. 13: Power channel temperature

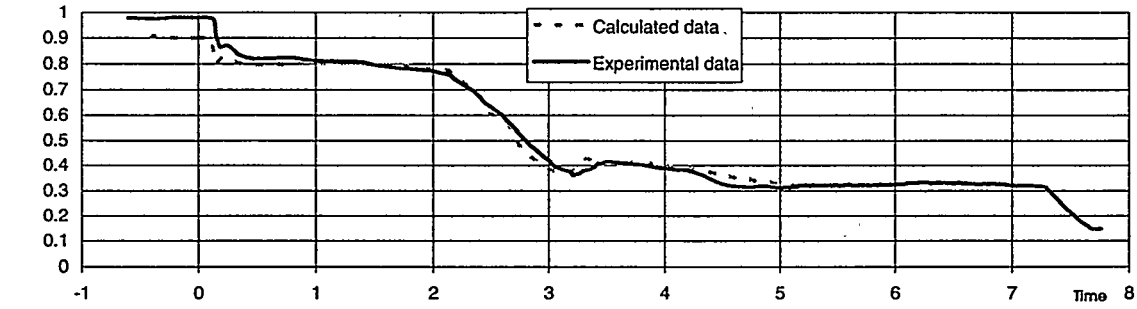

All the scales are normalized: Y-axes are normalized over the maximum value of plot scales, while time-axes are divided by a constant value.

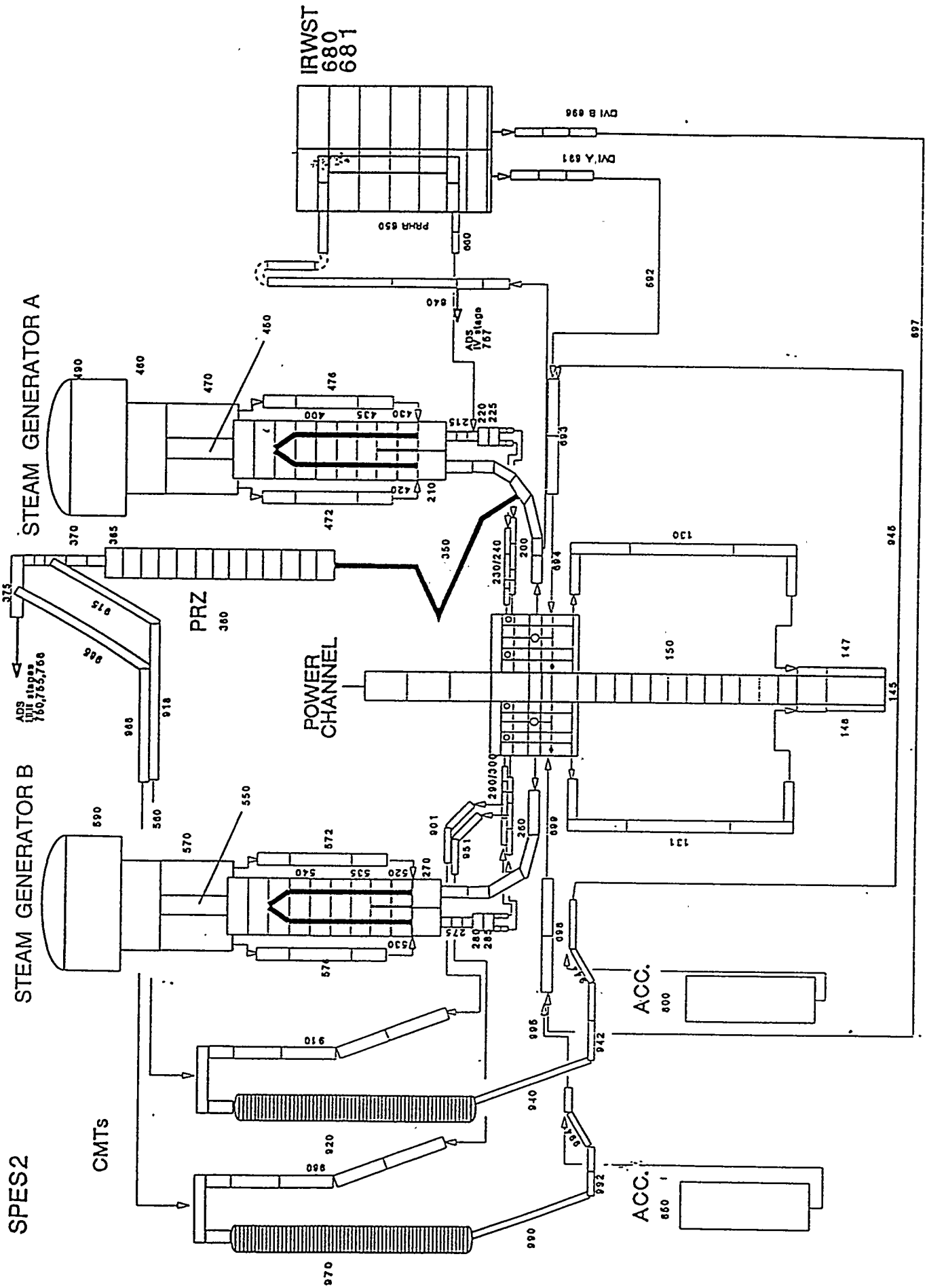

Fig. 14 - SPES-2 RELAP5/Mod3 noding

Investigations on the thermal-hydraulics of a natural circulation cooled BWR fuel assembly

H.V. Kok, T.H.J.J. van der Hagen
Interfaculty Reactor Institute, Delft University of Technology
Mekelweg 15, 2629 JB Delft, The Netherlands

and

R.F. Mudde
Kramers Laboratorium voor Fysische Technologie, Delft University of Technology
Prins Bernhardlaan 6, 2628 BW Delft, The Netherlands

Abstract

A scaled natural circulation loop facility has been built after the Dodewaard Boiling Water Reactor, which is the only operating natural circulation cooled BWR in the world. The loop comprises one fuel assembly, a riser with a downcomer and a condenser with a cooling system. Freon-12 is used as a scaling liquid. This paper reports on the first measurements done with this facility. Quantities like the circulation flow, carry-under and the void-fraction have been measured as a function of power, pressure, liquid level, riser length, condensate temperature and friction factors. The behavior of the circulation flow can be understood by considering the driving force. Special attention has been paid to the carry-under, which has been shown to have a very important impact on the dynamics of a natural circulation cooled BWR.

I. INTRODUCTION

Natural circulation is a keyword in the design of modern safe boiling water reactors (BWRs). A striking example can be found in the SBWR-design of General Electric. The attraction of natural circulation lies in its technical simplicity and its safety, at the cost of the physical complexity of the natural circulation. In order for this balance to tilt in favor of the technical simplicity the phenomena surrounding natural circulation must be well understood.

The Netherlands is fortunate enough to operate the only existing BWR that uses natural circulation to drive the coolant: the Dodewaard BWR. This reactor has been in operation since 1969. Although it has been subject to extensive measurements, questions remain as to the detailed behavior of the two-phase flow through the fuel assemblies and the effect of this behavior on the natural circulation flow rate. The flow rate cannot be measured directly in the Dodewaard reactor, and to date only indirect methods (such as correlations between thermocouple signals [1]) have given an indication of its value. This exemplifies the difficulties in performing research on the Dodewaard reactor, namely the limited presence of measuring devices. Another important point is of course the limit on the operating conditions of a real reactor. Accident conditions for example cannot be studied. Finally, it is not possible to measure local parameters, for example in one fuel assembly or a subchannel.

For these reasons it was decided to build an electrically heated scaled model consisting of the most important parts that govern the natural circulation of the Dodewaard BWR: a fuel assembly, a riser and a downcomer. This facility is called SIDAS (SImulated Dodewaard ASsembly).

Each of the above mentioned parts plays its own role in the behavior of the natural circulation flow. In the fuel assembly a large role is given to the flow patterns, which influence the two-phase friction and the driving force, as well as the heat transfer from fuel to coolant and the moderation. Because flow patterns are very sensitive to geometry, special attention was paid to the constituting parts of the fuel assembly, such as spacers (an exact scaled copy was made) and fuel rods (cosine axial power

distribution). Furthermore each fuel rod can be connected to any one of six power supplies making many radial power distributions possible.

The role of the riser together with the downcomer is to provide additional driving force for the natural circulation flow. In the riser there is a high void-fraction, while the flow in the downcomer is one-phase, except for the so-called carry-under. This difference in void-fraction leads to a difference in density which provides the driving force. In principle it is possible to maintain a natural circulation flow without the riser, because in the fuel assembly itself there is also void-fraction present. Adding a riser can greatly increase the driving force because the friction of the riser is low compared to the friction in the fuel assembly.

When designing a scaled model it is not possible to predict exactly the driving force and friction. In order to be able to match these exactly with Dodewaard a riser of variable length was made. This in addition to a valve to control friction allows us to change both the driving force and friction, and so to tune the natural circulation flow.

The main complication of natural circulation compared to forced circulation is that the flow not only influences, but is also influenced by various parameters. Because in a natural circulation flow many phenomena are intimately related it can be difficult to study these effects independently. This is another reason for using a riser of variable length. This creates an extra degree of freedom with which we can separate and study different aspects of natural circulation.

At the design stage of the scaled model decisions had to be made concerning the scale, modelling fluid etc. [2,3]. It is not possible to scale all two-phase flow characteristics in one model because of the large number of thermal-hydraulic similarity groups. Depending on the importance one attaches to various flow phenomena different scaling rules result [2,3] (see appendix). In SIDAS major attention was paid to the flow quality and void-fraction because these are the primary factors controlling the thermal-hydraulic behavior. As a scaling liquid Freon-12 (CF_2Cl_2) was chosen, which has the advantage of a low heat of evaporation, thus reducing the power needed from 2 MW to 40 kW. This fluid led to a scaling in dimensions of a factor of 0.46. The appendix gives an outline of the scaling study. In table 1 the different conditions are given for the Dodewaard BWR and SIDAS.

	Dodewaard assembly (water)	SIDAS (Freon-12)
Power (kW)		
average	1116	22.3
maximum	2000	40
Pressure (bar)	75.5	11.6
T_{sat} (°C)	291	48
Assembly (cm)	13x13	6x6
l_{rod} (m)	1.8	0.83
d_{rod} (mm)	13.5	6.23
$\dot{m}''$ (kg/m^2· s)	1006	1137
ΔT_{sub} (°C)	5	2

Table 1. Dodewaard BWR and SIDAS parameters.

II THE SIDAS FACILITY

In figure 1 a schematic view of the SIDAS loop is given showing the instrumentation. The fuel assembly has a rectangular cross-section with sides of 6 cm and is 83 cm long. The riser has a fixed part of 1 meter and a telescopic part of also 1 meter. It is made of glass, so both the flows in the riser and in the downcomer can be inspected visually through viewing ports in the downcomer wall. The riser has a rectangular cross-section of 36 cm^2 and the downcomer of 51 cm^2. The vapor is condensed in a condenser and the condensed liquid can be cooled down to -10 °C via a heat exchanger connected to a cooling system. The liquid level is controlled by an automatic valve in the feedwater line. The Dodewaard fuel assembly consists of 35 fuel rods and one water rod arranged in a square lattice. In SIDAS the assembly consists of 35 fuel rods and 1 instrumentation rod.

As can be seen in the figure the downcomer flow is diverted away from the fuel assembly through four downcomer tubes. This is done to give an unobstructed view of the fuel assembly for visual inspection and gamma-transmission void-fraction measurement techniques. The length and diameter of the tubes have been designed to give the same circulation time as in Dodewaard, which is important for the dynamics of the loop. The friction factor can be tuned by valves.

SIDAS can be operated with forced circulation as well. In this case the flow is diverted to a circulation pump (not shown in the figure). The flow can then easily be controlled by valves.

SIDAS is fully equipped with thermocouples, vortex flowmeters, pressure sensors, a level gauge and a γ-ray densitometer. In the near future a γ-transmission tomographic technique will be used for measurement of local void-fractions. There are viewing-ports in the assembly (4 pairs), in the downcomer (2 pairs) and in the section above the riser exit (2 pairs). One of the viewing-ports is located in the range of the riser exit.

Figure 2 shows the section of the loop at the riser exit, where several mass-flows have been defined. We distinguish the following flows: the circulation flow (Φ_{cir}), the downcomer flow (Φ_d), the liquid part of the downcomer flow (Φ_l), the vapor part of the downcomer flow or carry-under (Φ_{cu}), the vapor or outlet flow (Φ_v) and the feedwater flow (Φ_f). The circulation flow is the flow that passes through the fuel assembly. In the fuel assembly part of this flow is turned into vapor. Most of this vapor passes into the condenser loop and in turn becomes the feedwater flow. In a steady state condition $\Phi_f = \Phi_v$ holds. The remaining part of the circulation flow flows into the downcomer and is called the downcomer flow. This downcomer flow partly consists of entrapped vapor, which is called the carry-under flow. At the feedwater sparger the cold feedwater is injected. Here the carry-under is condensed.

The following balances can be applied to the flows at the feedwater sparger:

$$\Phi_{cir} = \Phi_d + \Phi_f \qquad (1)$$

$$h_{cir}\Phi_{cir} = h_d\Phi_d + h_f\Phi_f$$

in which the h are enthalpies and h_{cir} is the enthalpy of the circulation flow before it enters the fuel assembly.

The circulation flow and feedwater flow are measured directly by vortex flowmeters with an accuracy of better than 1%. The downcomer flow follows from the mass-balance (eq. 1). The carry-under flow cannot be measured directly but can be calculated using the energy balance (eq. 1). In this balance h_{cir} and h_f follow directly from their

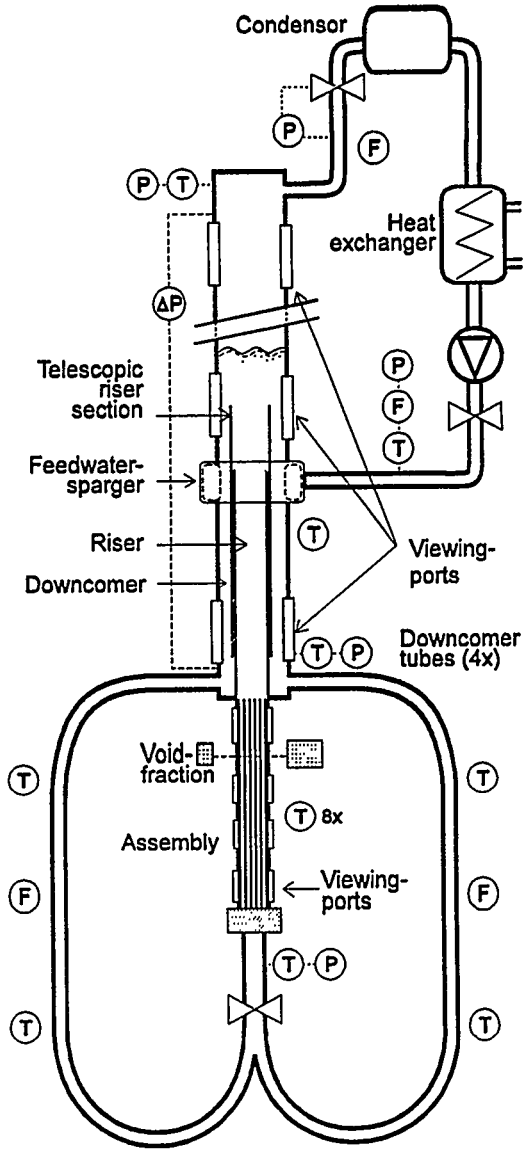

Figure 1. A schematic view of the SIDAS facility. (Not to scale) T=thermocouples, p=pressure sensors, F=flow meters, ΔP = level gauge.

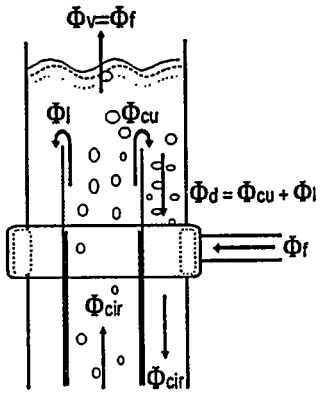

Figure 2. Definition of various flows.

temperatures, which are measured. From this h_d follows, and via the definitions of Φ_d, Φ_l, Φ_{cu} :

$$\Phi_d = \Phi_l + \Phi_{cu}$$
$$h_d\Phi_d = h_l\Phi_l + h_v\Phi_{cu} \qquad (2)$$

the carry-under can be calculated. (h_l and h_v follow from the temperature, which is the saturation temperature).

This can only be done if all carry-under is condensed by the cold feedwater, otherwise the enthalpy of the circulation flow below the feedwater sparger cannot be determined by its temperature (normally it will be subcooled). Besides checking the subcooling to see if the calculations are valid the flow can be inspected visually for traces of vapor in the downcomer below the feedwater sparger.

III EXPERIMENTAL RESULTS

a) Natural circulation

The experimental results given in this paper all concern stationary conditions. Figures 3 and 4 show the circulation flow as a function of power for different pressures and friction factors respectively. Notice that 20 kW SIDAS-power corresponds to the average nominal Dodewaard assembly power (1 MW). As can be seen the flow rises quickly at first and then saturates. This can be understood by considering the loop momentum balance. This reads [4]

$$\frac{d\phi}{dt} = \frac{\Delta p_d(t) - \Delta p_{loss}(t)}{\sum_l \frac{l_l}{A_l}}$$

where the summation runs over the length-to-area ratios of all sections of the flow loop.

The pressure losses Δp_{loss} consist of frictional and accelerational losses. The driving pressure Δp_d is linear with the density difference between the riser+assembly and the downcomer, which is linear with the void fraction:

$$\Delta p_d = \int_{downcomer} \rho_l g \, dh - \int_{riser+assembly} (1-\alpha(h))\rho_l g \, dh \qquad (3)$$

where the carry-under and the mass of the vapor

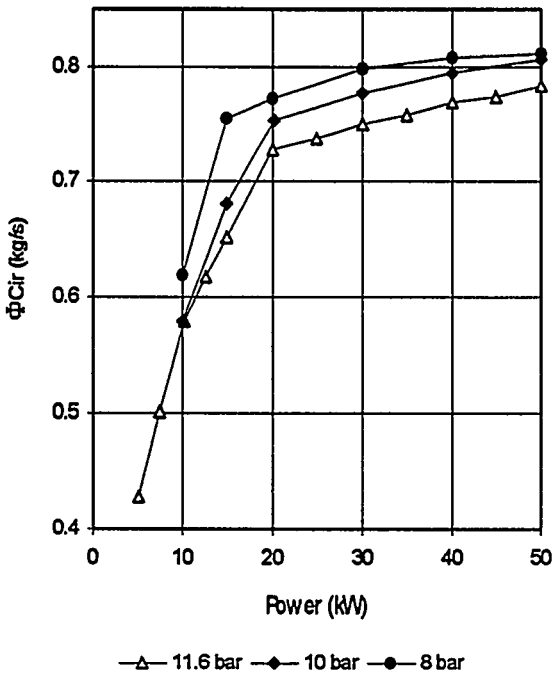

Figure 3. Circulation flow as a function of power at different pressures.

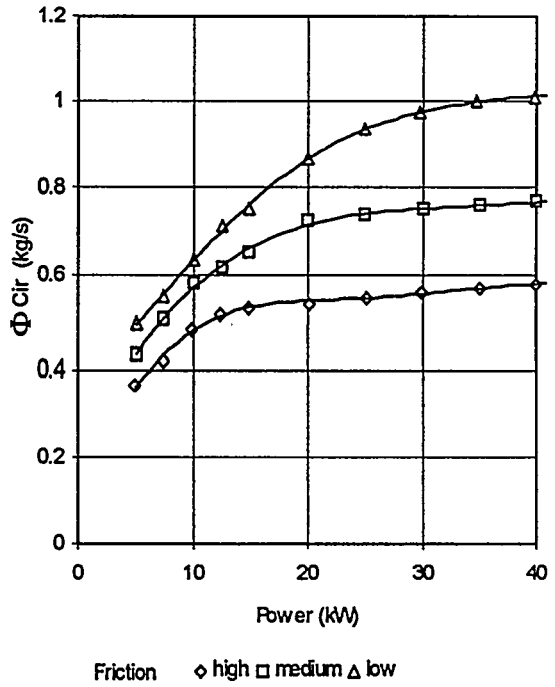

Figure 4. Circulation flow as function of power for different valve settings controlling friction.

have been neglected. The relation between void-fraction and quality however is not linear:

$$\frac{1-x}{x} = \frac{v_l}{v_g}\frac{\rho_l}{\rho_g}\frac{1-\alpha}{\alpha} \qquad (4)$$

with x the quality and v_l and v_g the speed of the liquid and the gaseous phase respectively.

At low power, and thus low quality a given increase in quality gives a relatively large increase in void-fraction and so in the driving force. At high power and high quality however the void-fraction changes very little with the quality. The friction does not scale with the void-fraction but with the quality. This explains the saturation of the flow at high powers. At lower pressure the void-fraction is higher for a given quality (see also figure 6) so the driving force is greater. This results in a higher circulation.

In figure 5 the measured chordal void-fraction at 63% of the length of the fuel assembly is shown for these measurements, and in figure 6 the void-quality relationship measured is compared with the theoretical curve of equation 4 for a slipfactor of 1 (v_l=v_g). The accuracy of the measured void-fraction is estimated at 5%. Identical symbols in figures 3-6 denote the same measurements. The measurements follow the theoretical curve very closely, even though the different measurements span a wide range of operating conditions. Although there are still uncertainties in the local void-fraction (only a chordal void-fraction is measured at this time) this suggests that the slipfactor is close to 1.

In figure 7 the circulation flow is given as a function of the collapsed liquid level. Two regions can be distinguished in this figure. Above a certain point (80 cm) the flow rises slowly with the level. Below this point the flow rises sharply. This transition point corresponds to the liquid level reaching the riser exit.

Again this behavior can be understood by considering the driving force. If the liquid level falls below the riser exit the first integral in equation 3 should not be taken over the complete riser length but only up to the liquid level. This means that the driving force is linear with the liquid level, and the flow should scale approximately as the square root of the liquid level. This behavior can indeed be seen in figure 7. It is because we have expressed the flow as a

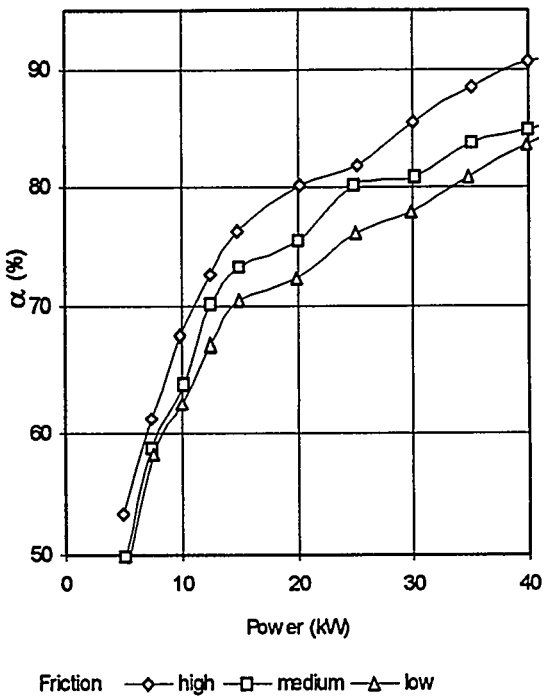

Figure 5. Void-fraction as a function of power for different valve settings controlling friction.

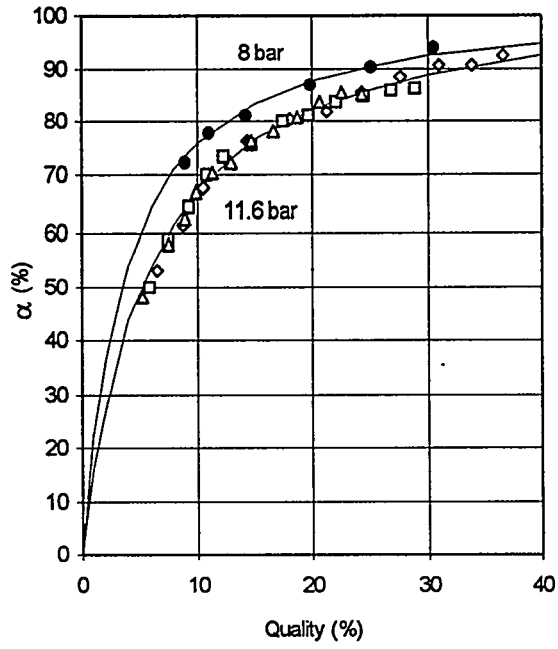

Figure 6. Void-quality relationship for two pressures.

function of collapsed liquid level instead of the actual liquid level that this is possible. For our Δp liquid level gauge in effect directly measures the first integral in equation 3, which means that the carry-under will not affect this analysis. Of course the carry-under will affect the position of the transition point, because this point occurs where the actual liquid level reaches the riser exit.

An additional remark needs to be made on the second integral in equation 3. As the circulation flow changes the quality of the flow in the riser and the downcomer also changes. Also the subcooling can change and have an effect on the quality. However, at high powers, the void-fraction will not change much thanks to the void-quality relation in equation 4. This means that the second integral does not change appreciably.

The slow rise of the circulation flow for higher levels is caused by the decrease of the carry-under. This effect will be investigated further in the next section.

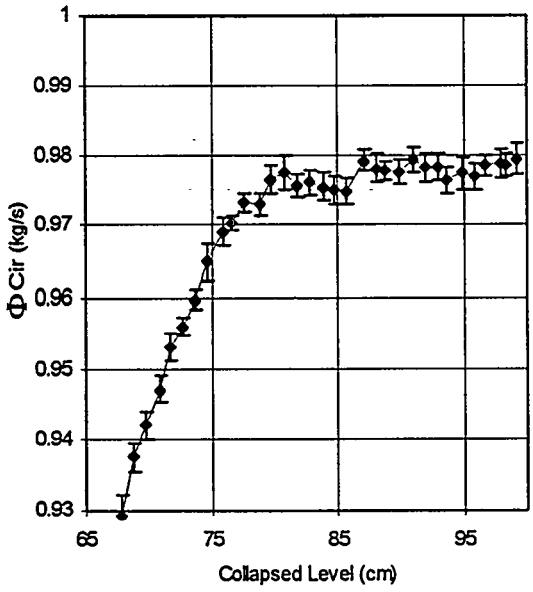

Figure 7. Circulation flow as a function of the collapsed liquid level.

The circulation flow as a function of the riser length is shown in figure 8. The liquid level in this experiment was set well above the riser exit, in the slowly changing part of figure 7. It can be clearly seen that the circulation flow decreases with increasing riser length. This is somewhat surprising since the function of the riser is to increase the circulation. Apparently our assumptions underlying equation 3 have broken down. This is caused by the carry-under, which is the subject of the next section.

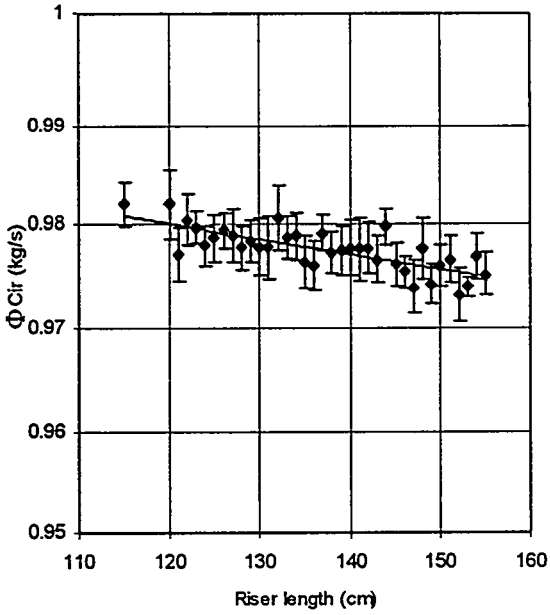

Figure 8. Circulation flow as a function of the riser length.

b) The carry-under

The carry-under plays a very important role in both the dynamics [5] and the statics of the natural circulation. In particular in SIDAS it determined the operating range of the loop (see also section IIIa). If the carry-under is not completely condensed, the vapor will be dragged down through the downcomer and into the downcomer tubes. This destroys most of the driving head of the natural circulation flow and gives a different flow regime in the fuel assembly. Unfortunately, under scaled nominal Dodewaard conditions the carry-under in SIDAS turned out to be too large to be condensed by the feedwater. By decreasing the circulation flow the carry-under could be reduced until it could be totally condensed. At this point the circulation flow was

about half that of the nominal value, which means that the void-fraction and flow patterns in the fuel assembly are not representative of Dodewaard.

This unfortunate situation calls for a better understanding of the factors that determine the carry-under. In fact, it is to eliminate this unknown factor, the carry-under, that General Electric has placed steam separators above the riser in its SBWR design, despite the added costs and complexity. The effect of carry-under in a reactor without steam-water separators emphasizes the importance of the feedwater pump on reactor safety: a feedwater pump trip will stop the condensation of carry-under in the downcomer whereafter the circulation flow will decrease. In our case it will be necessary to modify the geometry at the riser exit to reduce the carry-under and use the loop at its full potential.

At a given power and pressure the circulation flow is the most important factor determining the carry-under in SIDAS. The circulation flow can be influenced by changing the friction in the downcomer tubes. So the circulation flow can be set to any desired value under particular conditions. However, when performing measurements in which one of the parameters is continuously changed (very slowly, to operate in a quasi-steady-state condition) the circulation flow will in general also change.

Actually it is not the circulation flow but the downcomer flow that is important for the carry-under because this determines the speed of the flow where it rounds the corner from the riser into the downcomer. For powers of 25, 30 and 40 kW the carry-under as a function of downcomer flow is shown in figure 9. The carry-under is approximately linear with the flow. This suggests a constant downcomer flow quality. A higher downcomer flow means higher horizontal velocities of the flow, which means that vapor has less chance to escape to the surface. Visual inspection shows the flow in the downcomer channel just below the riser exit to be highly turbulent and consisting of a foamlike bubbly flow dragging along larger sluglike bubbles. A higher power produces a higher carry-under. This will be caused by a higher void-fraction at the riser exit, which in turn gives higher horizontal velocities.

The idea that the carry-under is determined by the downcomer flow rather than the circulation flow can be tested by changing the feedwater flow.

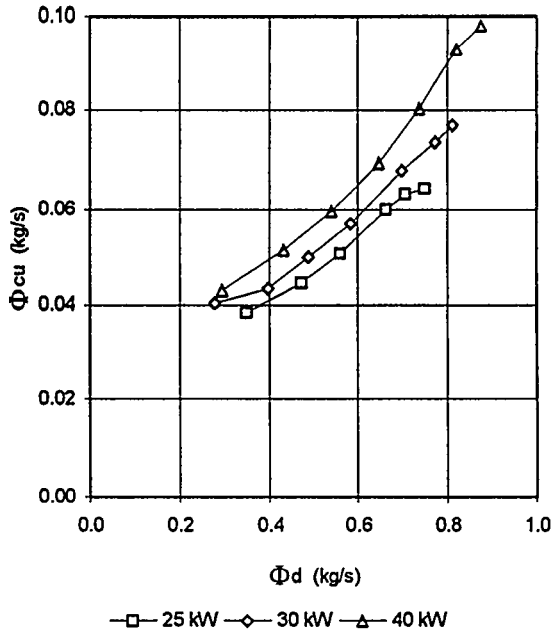

Figure 9. Carry-under as a function of downcomer flow at different powers.

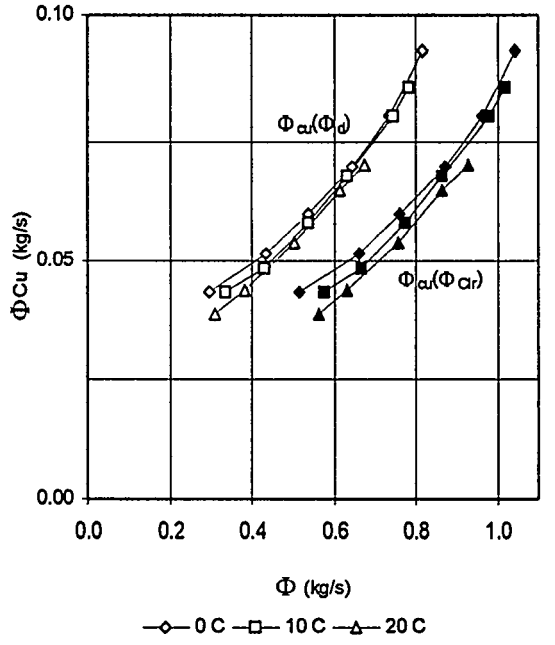

Figure 10. Carry-under as a function of the circulation and downcomer flow.

In stationary conditions this can only be done by changing the feedwater temperature because the product of feedwater flow and enthalpy must be constant (because $(h_v-h_f)\Phi_f = Power$). In figure 10 the carry-under is shown as a function of both the circulation flow and the downcomer flow for three different feedwater temperatures. Expressed as a function of downcomer flow it can be seen the carry-under is independent of the feedwater temperature and thus of the feedwater flow.

Besides the dependence on the downcomer flow, the carry-under also depends on the liquid level above the riser. In figure 11 the carry-under is shown as a function of the (collapsed) liquid level in the downcomer above the top of the fuel assembly. Above a certain level the carry-under decreases slowly and linearly with the level. Below this level the carry-under decreases sharply. As in the measurement of the circulation flow this is the point at which the liquid level reaches the riser exit. Above this point the horizontal velocities will decrease as the level rises, so the carry-under will decrease.

As to for the sharp drop in carry-under at low liquid levels two effects might be of importance: i) As the falling liquid in the downcomer gains a greater momentum while the liquid level drops it is able to trap more vapor. ii) As the liquid level gets closer to the feedwater sparger bubbles that would otherwise have escaped, might now be condensed and thus contribute to the carry-under flow. These two effects can be separated by changing both the liquid level and the riser length (the feedwater sparger is fixed). This will be done in the near future.

As we have seen in figure 7 the circulation flow also changes with level change. Since the carry-under, and thus the void-fraction in the downcomer decreases with increasing level we expect the circulation flow to increase which is indeed the case. From figure 9 it follows that an increasing circulation flow leads to an increasing carry-under, thus the change in circulation flow provides a negative feedback in the change of carry-under. If we want to study the carry-under locally, at the exit of the riser, we need to know the carry-under as a function of liquid level at a constant circulation flow. This can be estimated by considering the circulation flow as a perturbation and linearising:

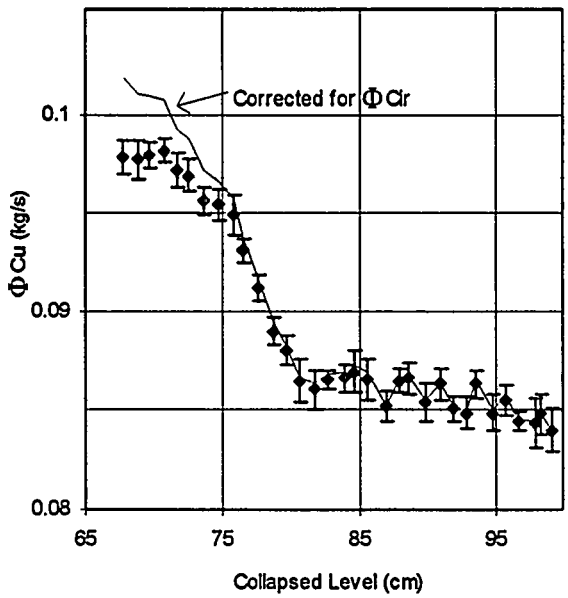

Figure 11. The carry-under as a function of the collapsed liquid level.

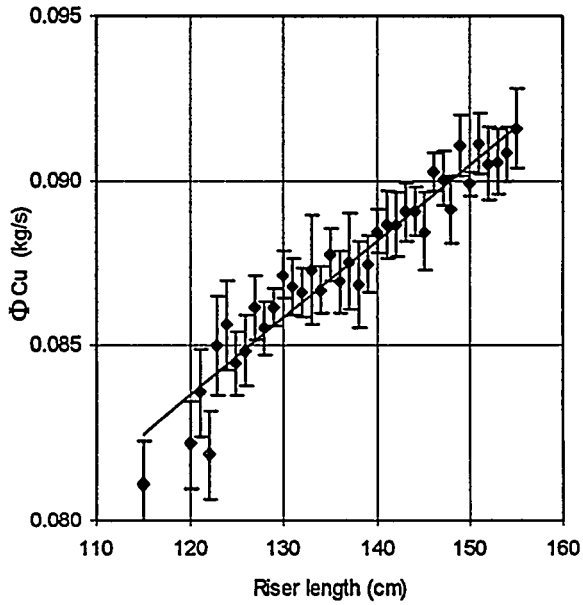

Figure 12. Carry-under as a function of the riser length.

$$\Phi_{cu} = \Phi_{cu}|_{\Phi_{cir}=\Phi_0} + \frac{\partial \Phi_{cu}}{\partial \Phi_{cir}} (\Phi_{cir} - \Phi_0) \quad (5)$$

in which Φ_0 is the 'setpoint' for the circulation flow. The partial differential is given by the slope in figure 9. In figure 11 the corrected carry-under is shown as well as the measured carry-under. For Φ_0 the flow at the maximum level was used.

A somewhat surprising result is given by the variation of the riser length. In figure 12 the carry-under is shown as a function of the riser length. It can be clearly seen that the carry-under increases with riser length. Several remarks can be made on this measurement. Firstly, because the circulation flow changes only slightly (figure 8) the difference between the corrected and uncorrected flow (via equation 5) is very small. Secondly the change in carry-under has a seemingly natural explanation: as the riser is elongated the liquid level comes closer to the riser exit, and as we have seen in the previous measurement the carry-under increases with a decreasing liquid level above the riser exit. To compare these two measurements we must know the relationship between the collapsed liquid level and the actual liquid level. This depends on the void-fraction in the downcomer above the feedwater sparger which is estimated to be about 80%. Thus a change of 1 cm in the collapsed liquid level corresponds to a change of 5 cm in the actual liquid level. In terms of the true liquid level the carry-under changes with 0.002 (kg/s)/m in the liquid level experiment and 0.025 (kg/s)/m in the riser length experiment. This means that the decreasing liquid level above the riser as it is elongated is not enough to explain the rise in the carry-under.

Now we can also attempt to explain why the circulation flow decreases with increasing riser length. It is caused by the large carry-under, which causes a large void-fraction in the downcomer. Because the slipfactor in the riser is greater than 1 and in the downcomer smaller than 1 it is possible for the void-fraction in the downcomer to be as large as in the riser even if the quality in the downcomer is smaller than in the riser (see equation 4). This situation will be different once the riser and downcomer have been adapted to yield a smaller carry-under.

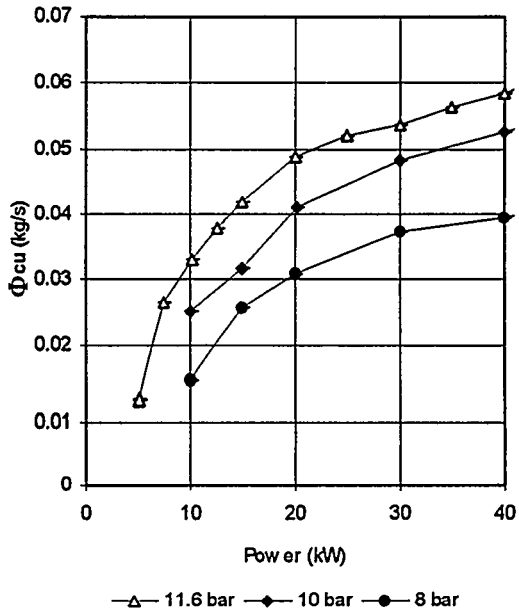

Figure 13. Carry-under as a function of power at different pressures.

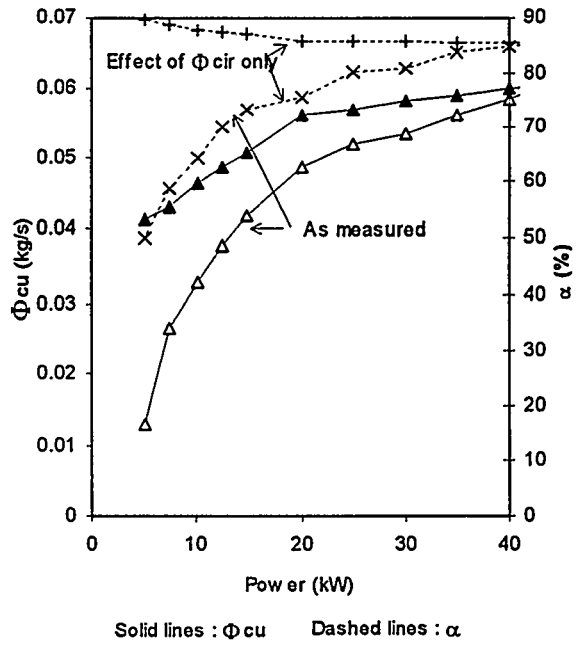

Figure 14. Carry-under and void fraction as a function of power compared with the case that only the circulation flow changes.

In figure 13 the carry-under as function of power is given for different working pressures. (Again identical symbols in figures 13-14 denote the same experiments as in figures 3-6.) At lower pressures the density of the vapor is lower. The density difference between liquid and vapor does not change appreciably, so the forces acting on the bubbles change only little. Thus we expect that the number and size of the bubbles dragged into the downcomer is roughly independent of the pressure. But the mass of the vapor in these bubbles is lower for low pressures, so the carry-under decreases with decreasing pressure.

The increase of the carry-under in SIDAS with the power is probably caused by at least two things: the increase in void-fraction at the riser exit, and the increase of circulation flow with power (as in figure 3). The relative importance of these two effects can be estimated by calculating what the carry-under would be if only the circulation flow would change and the void-fraction would remain constant. This measurement is not available, but the void-fraction when varying the circulation flow (figure 3) changes much less than when varying the power, so we will use this measurement. For the case of 11.6 bar the carry-under and void-fraction are shown in figure 14 for the experiment in which the power changes and as calculated for the corresponding change in circulation flow at constant power. The difference between the dashed lines is the additional void-fraction that the change in power gives above the change resulting from a different circulation flow. This additional change in void-fraction should be discernible in the difference between the two solid lines, which is indeed the case. Because the power in figure 3 was 50 kW the curves come together at this power.

At lower power we see that in SIDAS about half of the change in carry-under is caused by the decrease of the circulation flow and half by the additional change in void-fraction in the riser.

IV CONCLUSIONS

The first measurements on the natural circulation scaled loop facility SIDAS have shown the feasibility of measuring accurately such parameters as the circulation flow, carry-under and void-fractions as a function of many different parameters. The behavior of the circulation flow can be understood by considering the driving force, that is, the void fraction in the assembly, riser and downcomer. The circulation flow increased with increasing power. At high power the flow saturates. The flow decreases with increasing pressure. The effect of the liquid level can be separated into two regions. The transition point between these regions occurs when the level reaches the riser exit. Below this point the circulation flow rises strongly with the liquid level. Above this point it increases slowly. Surprisingly, the circulation decreases with increasing riser length. This is caused by the large carry-under in SIDAS.

The carry-under was shown to have an important effect on the natural circulation. It is mainly determined by the circulation flow, the power and pressure. The carry-under in the facility turned out to be too large to enable operation under scaled Dodewaard conditions. In the future the geometry at the riser exit will be changed to decrease the carry-under. Preferably this will be a variable geometry so the carry-under can be tuned during operation. This together with the variable riser length should provide a useful tool for the study of the carry-under and its effect on the statics and dynamics of the natural circulation.

APPENDIX SCALING GROUPS

A full derivation of the scaling laws used and the dimensionless groups obtained is given in [2] and [3]. This section gives a short overview of the results of the scaling.

In scaling the loop emphasis was put on a correct scaling of flow pattern distribution and local void fractions [3]. In the Dodewaard reactor different flow regimes are present, from subcooled boiling to a flow with void fractions as high as 70 %.

Correct scaling of the flow quality in the subcooled boiling region is obtained if the following groups are kept the same for Dodewaard and SIDAS:

$$N_{pch} = \left(\frac{q''}{\dot{m}''r}\right)\left(\frac{4l}{D_h}\right)$$

$$N_s = \frac{h_l^{sat} - h_{inl}}{r}$$

with N_{pch} the phase change number and N_s the subcooling number.

Above the subcooled region the flow is in thermal equilibrium. Ishii e.a. [6,7] give scaling criteria for two-phase flow loops, derived from the conservation equations of the drift-flux model. Besides N_{pch} the following dimensionless numbers are important for the proper scaling of the flow in thermal equilibrium:

$$N_\rho = \frac{\rho_v}{\rho_l}$$

$$N_g = \frac{D_h}{l}$$

$$N_{Fr} = \frac{(\dot{m}'')^2}{\rho_l^2 l g}$$

$$N_d = \frac{\rho_l (C_0 - 1)\gamma}{\dot{m}''} + \rho_l \frac{\bar{v}_{gj}}{\dot{m}''}$$

with N_ρ the ratio of vapor and liquid densities, N_g the geometry number, N_{Fr} the Froude number and N_d the drift-flux number. Modelling C_o and $\bar{v}_{gj}$ (which appear in N_d) for different flow regimes gives rise to an artificial Weber number, which should also be properly scaled:

$$N_{We} = \frac{\dot{m}'' D_h}{\rho_l \sigma}$$

Application of these dimensionless numbers for Freon-12 to water scaling leads to the values given in table 2. Notice that the size, pressure and power have to be reduced considerately when using Freon-12 instead of water

Group	System-parameter (X)	X_{Sidas}/X_{Do}
N_ρ	pressure	0.15
$(N_{We}N_g)/N_{Fr}$	size	0.46
N_{Fr}	mass flux	1.135
N_{pch}	power	0.020
N_s	inlet temp.	0.4

Table 2. The first column gives the used scaling groups and the second column the variable which is tuned to obtain the same values of the scaling group for Dodewaard and SIDAS. Finally the last column gives the relative values of the system parameters thus obtained.

Nomenclature

A_i	Cross sectional area of loop section
C_o	distribution parameter
D_h	hydraulic diameter (m)
g	gravitational acceleration (m s^{-2})
h_{inl}	enthalpy of the liquid at the inlet of the assembly (J kg^{-1})
h_l^{sat}	liquid saturation enthalpy (J kg^{-1})
l	fuel rod length (m)
l_i	length of loop section
$\dot{m}''$	mass flux (kg m^{-2} s^{-1})
N_d	drift flux number
N_{Fr}	Froude number
N_g	geometry number
N_{pch}	phase change number
N_s	subcooling number
N_{We}	Weber number
N_ρ	density ratio number
p	pressure (Pa)
q''	wall heat flux (W m^{-2})
r	latent heat of evaporation (J kg^{-1})
v	velocity (m s^{-1})
$\bar{v}_{gj}$	weighted mean drift velocity (m s^{-1})
x	flow quality
α	void fraction
γ	mixture volumetric flux (m s^{-1})
ρ	density (kg m^{-3})
σ	surface tension (N m^{-1})
Φ	mass flow

Subscripts

cir	circulation
cu	carry-under
d	downcomer
f	feedwater
l	liquid
v	vapour
Do	Dodewaard

Physical Modelling of a Rapid Boron Dilution Transient.

N.G. Andersson, B. Hemström,
R. Karlsson
Vattenfall Utveckling AB
S-810 70 Älvkarleby
Sweden
tel : +462683500 fax : +462683670

S. Jacobson
Vattenfall AB, Ringhals
S-430 22 Väröbacka
Sweden
tel : +46340667075 fax : +46340667305

ABSTRACT

The analysis of boron dilution accidents in pressurised water reactors has traditionally assumed that mixing is instantaneous and complete everywhere, eliminating in this way the possibility of concentration inhomogeneities. Situations can nevertheless arise where a volume of coolant with a low boron concentration may eventually enter the core and generate a severe reactivity transient. The work presented in this paper deals with a category of Rapid Boron Dilution Events characterised by a rapid start of a Reactor Coolant Pump (RCP) with a plug of relatively unborated water present in the RCS pipe. Model tests have been made at Vattenfall Utveckling AB in a simplified 1:5 scale model of a Westinghouse PWR. Conductivity measurements are used to determine dimensionless boron concentration. The main purpose of this experimental work is to define an experimental benchmark against which a mathematical model can be tested. The final goal is to be able to numerically predict Boron Dilution Transients. This work has been performed as a part of a Co-operative Agreement with Electricité de France (EDF).

INTRODUCTION

The analysis of boron dilution accidents in pressurised water reactors has traditionally assumed that the boron concentration field will remain uniform and homogeneous in the entire reactor coolant system during the dilution transient, i. e. instantaneous and complete mixing is assumed everywhere, eliminating in this way the possibility of concentration inhomogeneity. However, situations can arise where a volume of coolant with a low boron concentration may enter the core and generate a severe reactivity transient. Such situations have been analysed by Jacobson [1] and were probably first presented in Jacobson [5].

The work presented in this paper deals with a category of Rapid Boron Dilution Events characterised by a rapid start of a Reactor Coolant Pump (RCP) with a plug of relatively unborated water present in the RCS pipe. This scenario is assumed to occur after a Steam Generator (SG) maintenance. As a result of a SG tube leak (most likely caused by improperly completed SG maintenance), secondary water enters the RCS and collects in the RCP suction piping, in SG outlet plenum and perhaps in the SG tubes. The existence of this pocket is assumed to be undetectable by boron normal sampling of the reactor coolant being circulated, and assumed to be undetected (although detectable) by mass balance. Subsequent start of the RCP sweeps the clean water into the core.

Model tests have been made at Vattenfall Utveckling AB in a 1:5 scale model of a Westinghouse PWR. Figure 1 and Figure 2 give a general view of the model. The model is simplified compared to the actual PWR, in that the core and the structures in the lower plenum are not being modelled. The two idle loops are closed.

A mathematical model has been developed by Jacobson [1]. The main purpose of the experimental work is to define an experimental benchmark against which the mathematical model can be tested. The final goal is to be able to numerically predict Boron Dilution Transients.

The plug of unborated water is modelled by means of a salt-water solution and the borated water by means of tap-water. The unborated water is defined to have a dimensionless boron concentration equal to 0.0 and the borated water a dimensionless boron concentration equal to 1.0. Dimensionless boron concentrations for mixtures of the two solutions are obtained through

conductivity measurements. This is possible since conductivity is a linear function of salinity to a high degree of accuracy. The non-linearity is quantified below.

Salt behaves as a passive tracer and equation 1 therefore gives an exact expression for dimensionless boron concentration:

$$c=(s-s_u)/(s_b-s_u) \tag{1}$$

c = dimensionless boron concentration
su = salinity of unborated water (‰ or g/kg water)
sb = salinity of borated water (‰)

If conductivity can be expressed as a linear function of salinity, dimensionless boron concentration can be obtained through conductivity measurements using equation 2:

$$c=(\gamma-\gamma_u)/(\gamma_b-\gamma_u) \tag{2}$$

c = dimensionless boron concentration
γ_u = conductivity of unborated water (1/Ωm)
γ_b = conductivity of borated water (1/Ωm)

An expression for how the conductivity varies with salinity and temperature is given in equation 3:

$$\gamma = 9.7862\cdot10^{-2}\cdot s - 1.5664\cdot10^{-3}\cdot s^2 + 3.602\cdot10^{-3}\cdot s\cdot T + 2.332\cdot10^{-5}\cdot s^2\cdot T$$

γ = conductivity (1/Ωm)(3)
s = salinity (‰) 0 ‰ < s < 10 ‰
T = temperature (°C) 10°C < T < 30°C

The terms in equation 3 that are quadratic with s are small compared to the terms that are linear with s. The relative importance of the quadratic terms are greatest for high salinities. The highest salinity used in the tests is 2.27‰. The corresponding temperature was 19.4°C. The error that is made when calculating dimensionless boron concentration from equation 2 is largest for a true dimensionless boron concentration of 0.5, the calculated value being 0.003 dimensionless boron concentration units too low.

Another deviation from linearity in equation 3 is introduced if the temperature of the salt-water and the tap-water isn't the same. For the temperatures used in the tests the calculated dimensionless boron concentration is between -0.003 and 0.015 dimensionless boron concentration units too high, the quadratic error included.

Both these errors can be compensated for in the evaluation of the data. This has not been done, accepting the relatively small error.

Conductivities are measured at a plane halfway between the top of the bottom plate and the bottom of the core.

MEASUREMENT TECHNIQUE

A relatively well established technique has been used for measuring conductivity. The measurement technique is described in more detail in Andersson [2].

The measurement technique is based on measuring conductivity by means of two electrodes, one which is the sensing electrode positioned at the measuring point and the other which has, relative to the sensing electrode, a much larger surface and is also very far away from the measurement point. The sensing electrode consists of a 0.1 mm diameter platinum wire surrounded

by a several cm long and 5 mm wide cylinder of araldite. One end of the cylinder is conically shaped and the platinum wire sticks out approximately 0.05 mm from the tip. The electrodes are connected through a resistor to a carrier frequency oscillator with a frequency of 7.5 kHz. Alternating voltage is necessary in order to avoid electrolysis phenomena.

If an electrolyte with varying conductivity is flowing between the two electrodes, the resistance between the two electrodes will also vary, and the 7.5 kHz voltage signal at the resistor will be amplitude modulated. The variations in amplitude of the modulated signal give a measure of the variations in conductivity in a small region around the sensing electrode. The probe sensing volume (definition in Tinoco, Hemström & Andersson [3], page 14) is equivalent to a sphere with a diameter of around 0.6-1.1 mm. An approximate estimate of the frequency response of the probes was obtained by immersing the probes from air to a NaCl-solution. The rise time was measured using an oscilloscope to approximately 1 to 2 ms.

The modulated signal is amplified, demodulated, offset compensated and filtered in order to obtain a DC signal which is a measure of and varies with the conductivity. The filtering of the signal is done with a fourth order Butterworth low pass filter with limit frequency 1500 Hz. Several probes close to one another do not disturb each other.

In order to calibrate the conductivity probes, both electrodes were inserted in beakers containing ten different NaCl-solutions ranging from 0.022 $1/\Omega m$ to 0.61 $1/\Omega m$. The true conductivity was measured using a separate conductivity-measurement instrument, a "P Series conductivity meter (CM-11P)" from TOA Electronics Ltd. Calibration curves based on an analytical form were then adjusted to the data to give functional relationships between conductivity and voltage for each individual probe.

The initial calibration curves were later corrected based on conductivity measurements in direct conjunction with the tests. There are two reasons for correcting the initial calibration curves:

1. Several days had gone between the initial calibration and the calibration linked with the tests. During this period of time some probes had got a slightly different calibration curve due to fouling.

2. The calibration curves describing the relationship between conductivity and voltage do not have a form that correlates perfectly to the measured values.

Two different solutions are used for the in-situ calibration:

I. Salt-water with a conductivity around 0.37 $1/\Omega m$, which is close to the conductivity used to model the unborated water.

II. Tap-water with a conductivity around 0.04 $1/\Omega m$, which is close to the conductivity used to model the borated water.

The calibration curves were therefore linearly corrected to give most accurate results for an approximate minimum boron concentration of 0.75, which was considered to be the most proper choice.
Figure 3 gives the maximum error of the conductivity measurement technique after these final adjustments of the calibration curves. The ordinate shows the ratio between the conductivity measured by the probe (using the corrected calibration curves) and the true conductivity measured by the reference instrument. This ratio should, of course, ideally be exactly equal to 1. The main reason for this not being the case is the misfit of the calibration curves discussed above. In Figure 3 this phenomenon shows up as a deviation between X-d symbols (with or without a square) and +-ed symbols (with or without a square). As the calibration curves have been corrected so as to give best accuracy for conductivities around the approximate minimum boron concentration of 0.75, the X-ed symbols (e.g. "tap-water conductivity" corresponding to a boron concentration close to 1.0) are closer to 1.0 than the +-ed symbols ("salt-water conductivity" corresponding to a boron concentration close to 0.0). As the vast majority of the measured boron

concentration values lies between 1.0 and 0.75 the inaccuracy of the measurements can be estimated to be the difference between the X-ed symbols (boron concentration = 1.0) and 1.0 (dimensionless boron concentration = 0.75). This leads to an error of typically +2% and a maximum error of +4% in conductivity. The latter leads to an error in measured dimensionless boron concentration of [-0.02 , +0.03] dimensionless boron concentration units, the non-linearity errors included. Exceptions are probes 2, 3 and 4, who show larger errors. These probes do not, however, lie in regions of low minimum dimensionless boron concentrations. All 61 probes were used in the further evaluation of the results.

MODEL AND EXPERIMENTAL PROCEDURE

The model scale of 1:5 was chosen as the best compromise between the physical phenomena to be modelled and the costs involved. A schematic sketch of the model is shown i Figure 1. Figure 2 shows a section of the model.

Tap-water is stored in a 15 m^3 steel tank. In earlier tests tap-water was stored in a concrete basin also used for other models. This resulted in very dirty water and consequently led to disturbances on the signals from the conductivity probes. The steel tank now provides much cleaner tap-water to the model.

A model test starts with filling the whole system with tap water. A salt-water solution is then prepared in the salt-water tank. The pipe section between the valves V4 and V5 is then evacuated and filled with salt water from the tank. The pump is started and runs against a closed motor-valve (V3) placed further upstream from the salt-water plug. The valves V4 and V5 are then manually opened during a period of a few seconds. Immediately afterwards the motor-operated valve will start opening and the flow through the model starts to increase. When preparing the salt water solution the density of the salt water was modified using ethanol in order to get approximately the same density as for the tap water. The interfaces between the salt water plug and the tap water thereby become more stable during the few seconds between the opening the valves V4 and V5 and the start of opening of the motor-operated valve. The maximum difference in density in the tests was approximately 0.6 kg/m^3. The adequate volume of ethanol was calculated and the resulting densities of the salt-water-ethanol solution and the tap water were checked with an areometer. The maximum error in the determination of density was estimated to be 0.5 kg/m^3. The time between start of opening the valves V4 and V5 and the start of opening the motor-operated valve was approximately 12 seconds. The diameter of the pipe is 100 mm. Based on these data one could estimate the distance that the salt water front has moved:

$$s_f = U_f \cdot t_f = \frac{1}{2} \cdot \left(\frac{\Delta\rho}{\rho_1} \cdot gH \right)^{\frac{1}{2}} \cdot t_f \qquad (4)$$

sf = distance that the salt water front has moved during tf (m)
tf = time between start of opening of valves V4 and V5 and start of opening of motor-operated valve = 12 s.
Uf = velocity of salt-water front (m/s)
$\Delta\rho$ = density difference between salt water and tap water (error estimate included) = 1.1 kg/m^3
$\rho 1$ = density of the heaviest fluid $\approx$ 1000 kg/m^3
g = acceleration of gravity = 9.81 m/s^2
H = diameter of pipe = 0.100 m.

Equation 4 gives s_f = 0.20 m, or 2 pipe diameters. This could be compared to the total length of the salt water plug, which is 3.6 m or 24 pipe diameters. Consequently, the erosion of the salt-water plug can not penetrate very deeply into the salt-water plug.

Natural convection effects for the flow in the vessel are negligible.

The water leaving the reactor vessel leaves the system through valve V7, with valve V8 closed.

RESULTS

The specific case modelled is a Rapid Boron Dilution Transient due to sweeping by the RCP of a full scale volume of 8 m^3 (model volume is 63.6 l) unborated water. Five tests have been made with a flow increase from zero to full flow conditions during 5 seconds (see Figure 4). The full scale maximum flow rate is 6 m^3/s (model maximum flow rate is 48 l/s). Consequently, the velocities in the model are in average five times lower than the full-scale velocities. The transit time for the plug is therefore approximately the same in the model as in full-scale. The initial position of the frontal edge of the salt water plug is about 10 m (model distance = 2 m) upstream of the inlet to the downcomer of the reactor vessel. The two loops, simulating the loops with idle RCPs are closed during the whole transient.

The full flow Reynolds number based on the horizontal geometry of the downcomer is 37000. For steady flow, the critical Reynolds number is about 10^4. Alvarez et.al. [6] give a value of 10^5 for the upper limit of the critical Reynolds number for accelerating flow. Only flow visualisations can give better knowledge of critical Reynolds number. This has not yet been done.

Conductivities are measured at a plane halfway between the top of the bottom plate and the bottom of the core. A total number of 61 probes were installed in a triangular arrangement and equally spaced over the plane. The distance between the probes is 7.5 cm (model scale).

Figure 5 (upper curve) shows the measured ensemble- and spatially-averaged dimensionless boron concentration over the measurement section. This curve can also be interpreted as the typical (or average) response at the measuring plane. One can see that the front of the salt water plug reaches the measurement section after about 5.5 seconds. The mean dimensionless boron concentration at the measurement section then decreases rapidly to reach its minimum value of approximately 0.79 after 9 seconds. A substantial mixing has thus occurred before the plug reaches the core. The following increase of dimensionless boron concentration is slower.

Figure 5 also shows dimensionless boron concentration for the probe with the lowest measured minimum dimensionless boron concentration (lower curve) that occur during the transient. One can see that the lowest measured ensemble averaged dimensionless boron concentration was 0.63, which occurred 7.1 seconds after the start of the transient. The lowest instantaneous dimensionless boron concentration measured was 0.47.

The ensemble averaged minimum dimensionless boron concentrations that occur during the transient are shown in Figure 6 together with the positions of the probes. One can see that the lowest minimum values are found at positions at about half the radius of the vessel. High minimum concentrations are found close to the inlet and on the opposite side from the inlet. The pattern is somewhat twisted to the right in comparison with the symmetry line through the inlet. One reason for non-symmetry is most probably that the outlet from the vessel is 60 degrees to the left, as seen from the inlet (see Figure 1). This could lead to a tendency for the flow field, and consequently for the dimensionless boron concentration field, to be pulled towards the outlet.

Figure 7 shows the dimensionless boron concentration field after 6.5 seconds, e.g. 1 second after the first traces of unborated water has reached the measurement plane. This figure thus gives a picture of the first affected areas. One can see a very symmetric pattern relative to the symmetry line through the inlet. There is a strong positive correlation between the position of these first affected areas and the areas of the lowest minimum concentration (see Figure 6). The symmetric pattern is also a good indication on the quality of the measurement technique.

CONCLUSIONS

Results from model tests on a Rapid Boron Dilution Event characterised by a rapid start of a Reactor Coolant Pump (RCP) with a plug of relatively unborated water present in the RCS pipe have been presented. The conductivity measuring technique used to determine the dimensionless boron concentration has been shown to give a maximum error of [-0.02 , +0.03] dimensionless boron concentration units in regions of low boron concentration.

A substantial mixing occurs before the plug reaches the core. The lowest measured ensemble averaged dimensionless boron concentration at the core inlet that was measured during the transient was 0.63. As a comparison, a typical PWR operated in a 12 month fuel cycle has an initial boron concentration of 2000 ppm. The experiments thus indicate that the lowest boron concentration at the core inlet would be 1260 ppm. This in turn would indicate that the mixing at the reactor is sufficient to prevent criticality and that no power excursion would occur. It is, however, at this stage of the project not clear to what extent scale effects and the fact that the core, the structures in the lower plenum and the idle loops are not being modelled affect the dilution.

REFERENCES

[1] Jacobson, S. "Risk evaluation of Local Dilution Transients in a Pressurized Water Reactor.", Linköping University (1992).

[2] Andersson N.G. "Vidareutveckling av konduktivitetsmätningsutrustning. Teoretisk genomgång av mätmetodik." Report no. VU-S 94:B12. Vattenfall Utveckling AB (1994).

[3] Tinoco H., Hemström B. & Andersson N.G. "Physical modelling of a Rapid Boron Dilution Transient". Report no. VU-S 93:B21. Vattenfall Utveckling AB (1993).

[4] Hemström B. & Andersson N.G. "Physical modelling of a Rapid Boron Dilution Transient. The EDF Case". Report no. VU-S 94:B16. Vattenfall Utveckling AB (1994).

[5] Jacobson, "Possibility to Get Prompt Criticality in Conjunction with RCP Start". Swedish State Power Board letter to Westinghouse/Bryssel, R4-SVWE-739, December 1982.

[6] Alvarez, D., Daubert, O., Janvier, L. & Schneider, J. P., "Three dimensional calculations and experimental investigations of the primary coolant flow in a 900 MW PWR vessel", in proceedings of NURETH 5, Salt Lake City, USA, 1992.

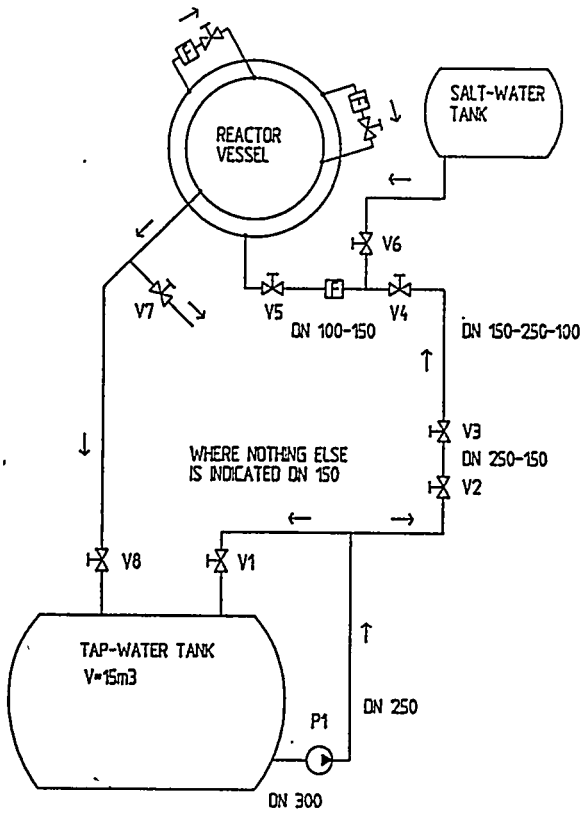

Figure 1. Schematic sketch of the model.

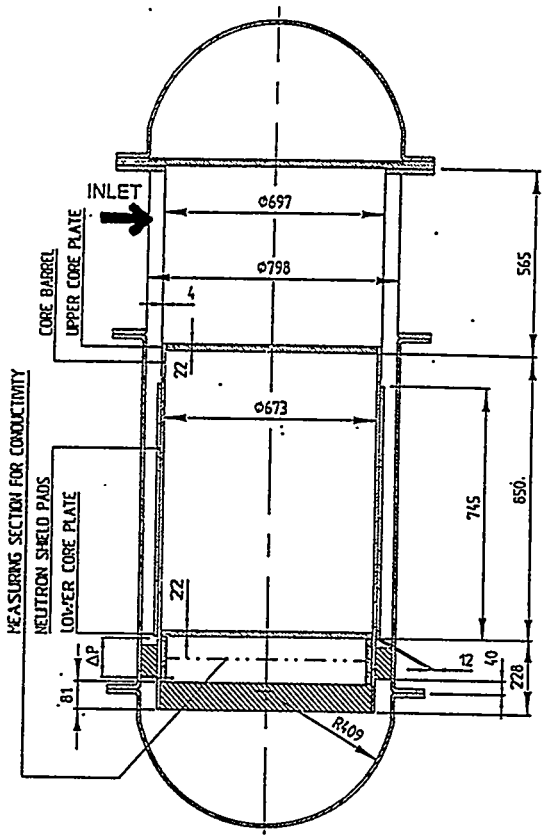

Figure 2. A section of the reactor vessel model.

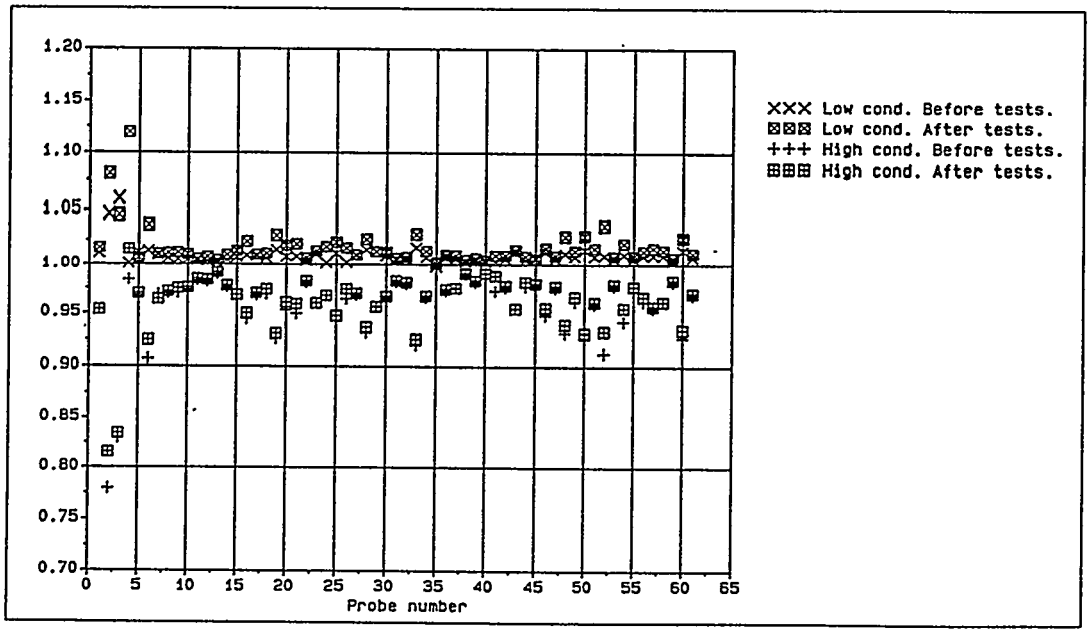

Figure 3. Error diagram for probes. Conductivity measured by probes divided by true conductivity.

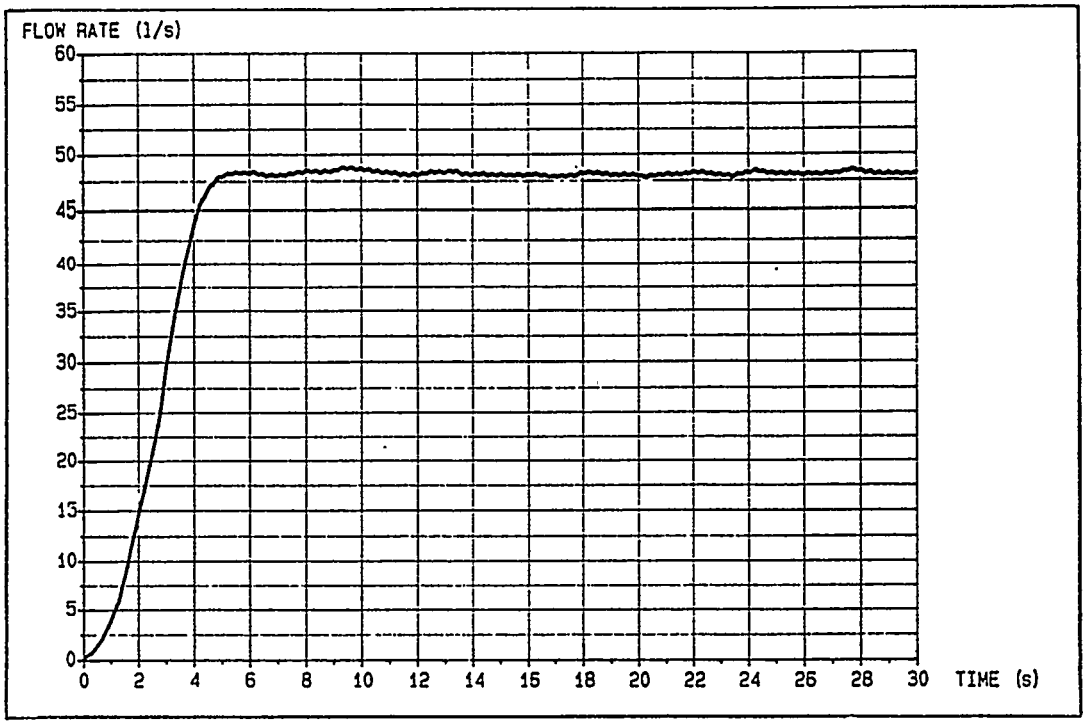

Figure 4. Flow rate as a function of time.

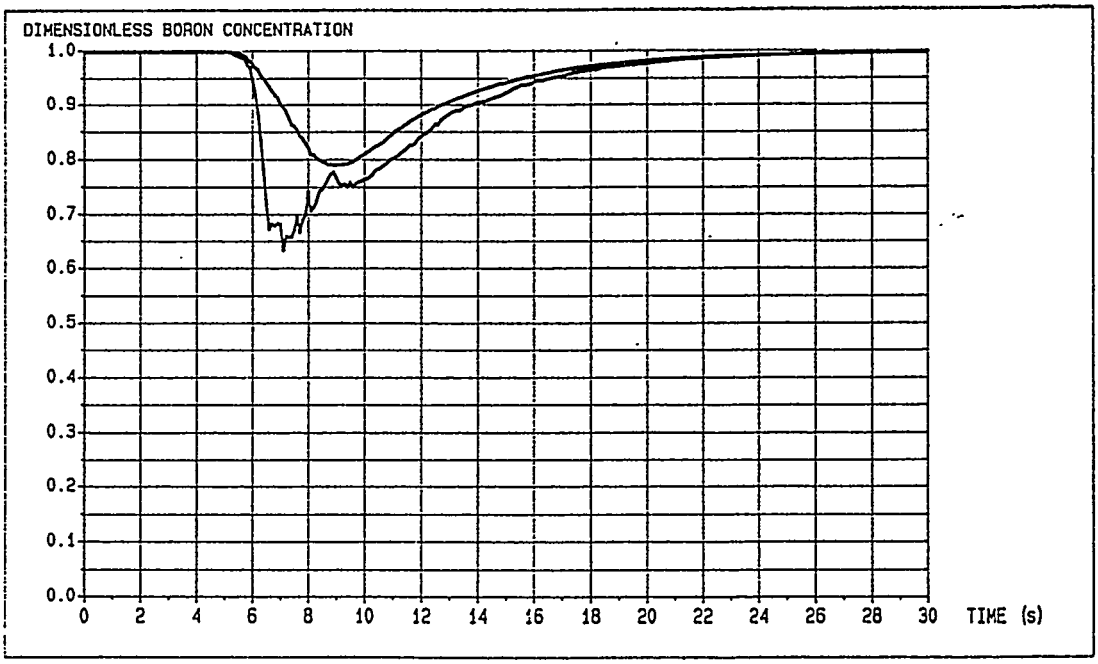

Figure 5. Ensemble- and spatially-averaged dimensionless boron concentration (upper curve) and ensemble averaged dimensionless boron concentration for the probe with the lowest measured minimum dimensionless boron concentration (lower curve) at measurement plane.

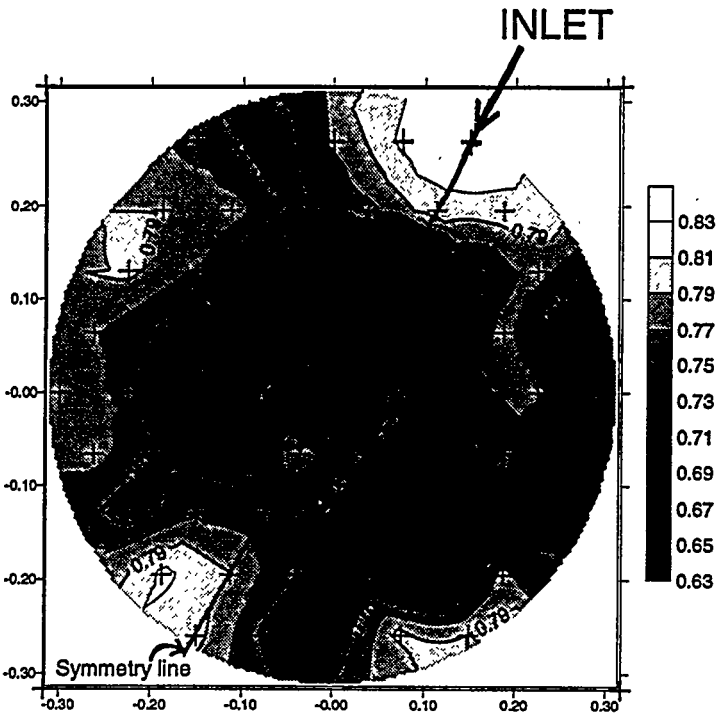

Figure 6. Ensemble averaged minimum dimensionless boron concentration at measurement plane.

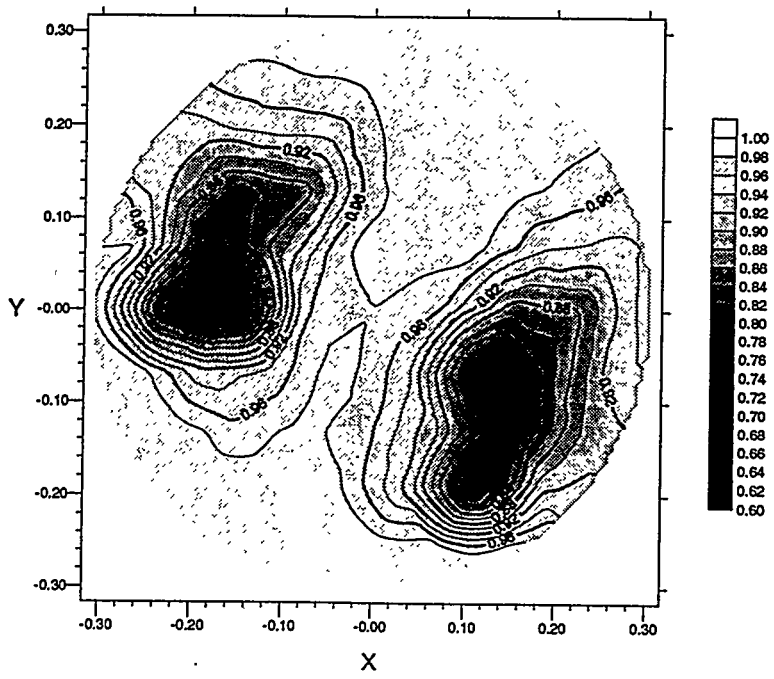

Figure 7. Ensemble averaged dimensionless boron concentration at the measurement plane 6.5 seconds after the start of the transient.

FURTHER EVALUATION OF THE CSNI SEPARATE EFFECT TEST ACTIVITY

F. D'Auria Univ. of Pisa (Italy)
S. N. Aksan PSI (Switzerland)
H. Glaeser GRS (Germany)
A. Sjoberg Studsvik (Sweden)
R. Pochard CEA (France)
J. Lillington AEA (United Kingdom)

Abstract

An internationally agreed Separate Effect Test (SET) Validation Matrix for the thermalhydraulic system codes has been established by a subgroup of the Task Group on Thermalhydraulic System Behaviour as requested by OECD/NEA Committee on the Safety of Nuclear Installations (CSNI) Principal Working Group No. 2 on Coolant System Behaviour. The construction of such matrix constituted an attempt to collect together in a systematic way the best sets of openly available test data to select for code validation.

As a final result, 67 phenomena have been identified and characterized, roughly 200 facilities have been considered and more than 1000 experiments have been selected as useful for the validation of the codes.

The objective of the present paper is to provide additional evaluation of the obtained data base and to supply an a-posteriori judgement in relation to a) the data base adequacy, b) the phenomenon, and c) the need for additional experiments. This has been provided independently by each of the authors.

The main conclusions are that large amounts of data are available for certain popular phenomena e.g. heat transfer, but data are severely lacking in more esoteric areas e.g. for characterizing phenomena such as parallel channel instability and boron mixing and transport.

1. INTRODUCTION

An activity has been recently completed under the frame of OECD Committee on the Safety of Nuclear Installations (CSNI) Principal Working Group No. 2 on Coolant System Behaviour with the aim to collect together the best sets of openly available test data for code validation and improvement. The wide range of experiments that have been carried out world-wide in the field of thermalhydraulics constitute the origin of the data. The activity is fully documented in two reports issued by CSNI, refs. [1], [2]; further pubblications include some details of the activities (refs. [3] to [6]).

The methodology developed during the process of establishing the Separate Effect Test (SET) validation matrix includes six main steps as provided in refs. [1] and [2] and is given as items below:

1. Identification of phenomena relevant to Loss of Coolant Accidents (LOCA) and thermalhydraulic transients in Light Water Reactors (LWR);
2. Characterization of phenomena, in terms of a short description of each phenomenon, its relevance to nuclear reactor safety, information on measurement ability, instrumentation and data base; in addition, the present state of knowledge and the predictive capabilities of the codes are discussed for each phenomenon;
3. Establishment of a catalogue of information sheets on the experimental facilities, as a basis for the selection of the facilities and of specific experiments;

4. Formation of a separate effects test facility cross-reference matrix by the classification of the facilities in terms of the phenomena they address;
5 Identification of the relevant experimental parameter ranges in relation to each facility that addresses a phenomenon and selection of relevant facilities related to each phenomenon;
6. Establishment of a matrix of experiments (the SET matrix) suitable for the developmental assessment of thermalhydraulic transient system computer codes, by selecting individual tests from the selected facilities, relevant to each phenomenon.

The scope and conclusions of this paper are restricted to present generation western LWRs.

2. A SHORT SUMMARY OF THE SET MATRIX RELATED ACTIVITY

The general framework of the activities that brought about the development of the SET matrix, was the follow up of wide ranging programs carried out by CSNI and by US NRC that are documented in the "Compendium" of thermalhydraulic researches [7], the State of the Art Report on Thermalhydraulics of Emergency Systems [8] and the Integral Test Facility Code Validation matrix [9].

The limitations of the basic thermalhydraulic equations and of the numerical methods utilized for obtaining solutions require extensive and systematic code validations. This should be done for a suitable range of parameters recognizing that it is unrealistic to obtain data measured in Nuclear Plants. Experiments performed in Basic, Separate Effect and Integral Test facilities are therefore necessary.

2.1 Identification of phenomena

The thermalhydraulic scenarios foreseeable in the plants for the case of off-normal conditions within the Design Basis were taken as the reference for arriving at the list of phenomena. Time trends of relevant quantities measured in experimental simulators or predicted by the codes, were useful in carrying out this activity.

Classes of phenomena (e.g. Small Break LOCA), phenomenological windows in each class (e.g. subcooled blowdown) and single thermalhydraulics aspects (e.g. dryout, two-phase critical flow, etc.) were used to get the list of the 67 phenomena reported in Tab. 1.

The "basic phenomena" 1-9 (for further details, see ref. [6]) in the list, impact on the evolution of all the other listed phenomena. Furthermore, some phenomena may be dependent upon each other, for example spray effect and condensation.

2.2 Characterization of the phenomena

The internationally available literature including textbooks, conference and journal papers and the mentioned refs. [6] - [8], contain detailed descriptions of the phenomena. However, these cannot be considered as systematic and comprehensive of the different aspects. Summaries relevant to each of the 67 phenomena are provided in the reports [1] and [2] under the headings:

- description;
- relevance to nuclear reactor safety;
- measurement ability, instrumentation and data base;
- present state of knowledge - predictive capability.

In particular, it should be emphasized that measurement ability and predictive capabilities of phenomena are interconnected. Furthermore, phenomena more relevant in terms of reactor safety have been studied more deeply than phenomena having less relevance.

0	BASIC PHENOMENA	1	Evaporation due to Depressurization
		2	Evaporation due to Heat Input
		3	Condensation due to Pressurization
		4	Condensation due to Heat Removal
		5	Interfacial Friction in Vertical Flow
		6	Interfacial Friction in Horizontal Flow
		7	Wall to Fluid Friction
		8	Pressure Drops at Geometric Discontinuities
		9	Pressure Wave Propagation
1	CRITICAL FLOW	1	Breaks
		2	Valves
		3	Pipes
2	PHASE SEPARATION/VERTICAL FLOW WITH AND WITHOUT MIXTURE LEVEL	1	Pipes/Plena
		2	Core
		3	Downcomwer
3	STRATIFICATION IN HORIZONTAL FLOW	1	Pipes
4	PHASE SEPARATION AT BRANCHES	1	Branches
5	ENTRAINMENT/DEENTRAINMENT	1	Core
		2	Upper Plenum
		3	Downcomer
		4	Steam Generator Tube
		5	Steam Generator Mixing Chamber (PWR)
		6	Hot Leg with ECCI (PWR)
6	LIQUID-VAPOUR MIXING WITH CONDENSATION	1	Core
		2	Downcomer
		3	Upper Plenum
		4	Lower Plenum
		5	Steam Generator Mixing Chambre (PWR)
		6	ECCI in Hot and Cold Leg (PWR)
7	CONDENSATION IN STRATIFIED CONDITIONS	1	Pressuriser (PWR)
		2	Steam Generator Primary Side (PWR)
		3	Steam Generator Secondary Side (PWR)
		4	Horizontal Pipes
8	SPRAY EFFECTS	1	Core (BWR)
		2	Pressuriser (PWR)
		3	Once-Through Steam Generator Secondary Side (PWR)
9	COUNTERCURRENT FLOW/ COUNTERCURRENT FLOW LIMITATION	1	Upper Tie Plate
		2	Channel Inlet Orifices (BWR)
		3	Hot and Cold Leg
		4	Steam Generator Tube (PWR)
		5	Downcomer
		6	Surgeline (PWR)
10	GLOBAL MULTIDIMENSIONAL FLUID TEMPERATURE, VOID AND FLOW DISTRIBUTION	1	Upper Plenum
		2	Core
		3	Downcomer
		4	Steam Generator Secondary Side
11	HEAT TRANSFER:		
	NATURAL OR FORCED CONVECTION	1	Core, Steam Generator, Structures
	SUBCOOLED/NUCLEATE BOILING	2	Core, Steam Generator, Structures
	DNB/DRYOUT	3	Core, Steam Generator, Structures
	POST CRITICAL HEAT FLUX	4	Core, Steam Generator, Structures
	RADIATION	5	Core
	CONDENSATION	6	Steam Generator, Structures
12	QUENCH FRONT PROPAGATION/REWET	1	Fuel Rods
		2	Channel Walls and Water Rods (BWR)
13	LOWER PLENUM FLASHING		
14	GUIDE TUBE FLASHING (BWR)		
15	ONE AND TWO PHASE IMPELLER-PUMP BEHAVIOUR		
16	ONE AND TWO PHASE JET-PUMP BEHAVIOUR (BWR)		
17	SEPARATOR BEHAVIOUR		
18	STEAM DRYER BEHAVIOUR		
19	ACCUMULATOR BEHAVIOUR		
20	LOOP SEAL FILLING AND CLEARANCE (PWR)		
21	ECC BYPASS/DOWNCOMER PENETRATION		
22	PARALLEL CHANNEL INSTABILITIES (BWR)		
23	BORON MIXING AND TRANSPORT		
24	NONCONDENSABLE GAS EFFECT (PWR)		
25	LOWER PLENUM ENTRAINMENT		

Table 1 - List of phenomena

2.3 Catalogue of information sheets

In 1989, under the coordination of the CSNI Task Group on Thermalhydraulic System Behaviour, a letter was sent to various organizations owning or operating test facilities known to the Group Members. Information was requested in relation to: objectives of the facilities, geometry, experimental conditions and parameter ranges, measurements, available documentation, use of the data, special features of the tests and main investigated phenomena. On this basis, a list of 187 SET facilities which have or have been operated in 12 OECD countries, has been compiled: a specific "Information Sheet" was prepared for most of the facilities. This is the document ref. [2].

2.4 Test facility cross reference matrix

The subsequent step consisted in homogenising the collected information, specifically the facilities objectives and the relation to the 67 phenomena. This resulted in the Separate Effect Test Facility Cross Reference Matrix, ref. [1]. An example of this is given in Tab. 2. A judgement of the suitability of the facility is also given.

2.5 Relevant parameter ranges

The ranges of relevant parameters (e.g. pressure) were identified by considering the operating conditions of the facilities: the expected variation of a parameter during foreseeable plant conditions was not taken into account. Facility identification, reasons behind the keyword selected and notes, were included in the 67 tables: one of this, i.e. Tab. 5.4 in ref. [1], is shown in Tab. 3 in this paper.

2.6 Separate Effect Test (SET) Matrix

The last step of the activity led to the proposal of a suitable list of experiments deemed necessary for a complete code assessment process. Again, 67 tables were prepared including experiment identification, a few relevant boundary and initial conditions values and additional specific bibliographical information: criteria were fixed for the choice of the experiments, ref. [1]. An example is reported as Tab. 4 (this is a part of Tab. 6.5.1 in ref. [1]).

Selection criteria were agreed to limit the number of experiments in the matrix; furthermore, no tests were found in relation to some phenomena (e.g spray effect in Once Through Steam Generator). Notwithstanding this, the total amount of selected tests is larger than 1000. Further details are included in a companion paper, ref. [6].

3. EVALUATION OF THE RESULTING DATA BASE

A statistical evaluation of the data was done in ref. [5]. Figures and tables such as Fig. 1 and Tab. 5 were obtained. The numbers of selected tests for the various phenomena from Fig. 1 show a large spread. Steady state tests (results usually characterized by a few values) and transient tests (characterized by time trends) are both distinguished. It can be inferred from Tab. 5, that no test was selected (available) for 8 of the phenomena.

A global re-evaluation of the activity was performed looking at the possible practical applications or interests arising from the achieved results. However the scope of the work did not extend to the code validation area.

The main conclusion from the considered data base consists in the need for new experiments. Obviously, new experiments improve of knowledge. The question is whether these are necessary for the safety of nuclear power plants. Recommendations must be tempered by costs considerations.

Phenomena			Separate Effects Test Facilities																					
LEGEND x suitable for model validation ° limited suitability for model validation - not suitable for model validation							3. France																	
			MOBY-DICK	SUPER MOBY-DICK	CANON and SUPER CANON (Horiz.)	VERTICAL CANON		TAPIOCA (Vertical)	DADINE (Vertical Tube, Inside)	PERICLES Retangular	PERICLES Cylindrical	PATRICIA GV 1	PATRICE GV2	ERSEC Tube (Inside)	ERSEC Rod Bundle	OMEGA Tube (Inside)	OMEGA Rod Bundle	ECTHOR Loop Seal (Air/Water)	COSI	SUPER MOBY-DICK Tee	PIERO (Air/Water)	EPOPEE	EVA
		Facility No.	1	2	3	4	5	6	7	8	9	10	11	12	13	14	15	16	17	18	19	20	21
		Info. Sheet available	a	a	a	a		a	a	a	a	a	a	a	a	a	a	a	a	a	a		a
0	BASIC PHENOMENA	1 Evaporation due to Depressurization	x	x	x	x		x	-	-	-	-	-	-	-	o	o	-	-	-	-	-	-
		2 Evaporation due to Heat Input	-	-	-	-		-	o	-	-	-	-	o	o	o	o	-	-	-	-	-	-
		3 Condensation due to Pressurization	-	-	-	-		-	-	-	-	-	-	-	-	-	-	-	-	-	-	-	-
		4 Condensation due to Heat Removal	-	-	-	-		-	-	-	-	o	-	-	-	-	-	-	o	-	-	-	-
		5 Interfacial Friction in Vertical Flow	-	-	-	o		o	x	-	-	-	o	-	-	-	o	o	o	-	-	-	-
		6 Interfacial Friction in Horizontal Flow	-	-	o	-		-	-	-	-	-	-	-	-	-	-	-	o	o	-	-	-
		7 Wall to Fluid Friction	x	x	x	-		-	-	-	-	-	-	-	-	-	-	-	-	-	x	-	-
		8 Press. Drops at Geometr. Discontinuities	-	x	-	o		o	-	-	-	-	-	-	-	-	-	-	-	-	x	-	-
		9 Pressure Wave Propagation																					
1	CRITICAL FLOW	1 Breaks	-	x	x	x		x	-	-	-	-	-	-	-	x	x	-	-	x	-	-	-
		2 Valves	-	-	-	-		-	-	-	-	-	-	-	-	-	-	-	-	-	-	-	-
		3 Pipes	x	x	-	-		-	-	-	-	-	-	-	-	-	-	-	-	-	-	-	-
2	PHASE SEPARATION/VERTICAL FLOW WITH AND WITHOUT MIXTURE LEVEL	1 Pipes/Plena	-	-	-	x		x	o	-	-	o	x	-	-	-	-	-	-	-	o	-	-
		2 Core	-	-	-	-		-	-	x	x	-	-	-	-	-	-	-	-	-	-	-	-
		3 Downcomer	-	-	-	-		-	-	-	-	-	-	-	-	-	-	-	-	-	-	-	-
3	STRATIFICATION IN HORIZONTAL FLOW	1 Pipes	-	-	-	-		-	-	-	-	-	-	-	-	-	-	o	o	x	-	-	-
4	PHASE SEPARATION AT BRANCHES	1 Branches	-	-	-	-		-	-	-	-	-	-	-	-	-	-	-	-	x	-	-	-
5	ENTRAINMENT/DEENTRAINMENT	1 Core	-	-	-	-		-	o	x	x	-	-	-	x	-	x	-	-	-	-	-	-
		2 Upper Plenum	-	-	-	-		-	-	o	x	-	-	-	-	-	-	-	-	-	-	-	-
		3 Downcomer	-	-	-	-		-	-	-	-	-	-	-	-	-	-	-	-	-	-	-	-
		4 SG Tube	-	-	-	-		-	-	-	-	x	-	-	-	-	-	-	-	-	-	-	-
		5 SG Mixing Chamber (PWR)	-	-	-	-		-	-	-	-	-	-	-	-	-	-	-	-	-	-	-	-
		6 Hot Leg with ECCI (PWR)	-	-	-	-		-	-	-	-	-	-	-	-	-	-	-	-	-	-	-	-

Table 2 - Separate effects test facility cross reference matrix

FACILITY IDENTIFICATION			KEYWORDS	RELEVANT PARAMETERS RANGES				REASONS FOR SELECTION OR NOTES
No.	Status in the matrix	Name		P MPa	d/D (-)	G kg/s m2	X (-)	
1.4	x a	HEADER TEST FACILITY (CANDU REACTORS)	-several branch junctions -candu geometry	up to 5.	0.05/0.3	around 1000	-	7 8
3.18	x a	SUPER MOBY DICK - TEE	-stratified flow -vertical upwards/downward -horizontal	2.	0.02 + 0.13	up to 16000	0.+1.	1 2 5
4.16	x a	T-JUNCTION TEST FACILITY (KfK)	-different branch orientation and diameter	up to 10.	0.08 + 1.	up to 50(+)	-	(+) Kg/s 2 3 7 8
6.3	x a	T-BREAK TF (AIR/WATER) JAERI	-stratified flow -square duct -air-water	up to 0.7	(0.01 + 0.02) 0.19	3.3(+) 0.55(++)	-	(+) gas superficial velocity (++)liquid superficial velocity
11.35	x a	TPFL/INEL TEE CRITICAL FLOW	-large facility -multipurpose research	up to 6.	0.034/0.28	420(+) 25(++)	-	(+) Kg/s - liquid (++) " - steam 3 5

Comments

- Qualified data from integral facilities can be very usefull especially in relation to transient conditions, with time varying upstream conditions.
- Transient situations are lacking in this data base.

Table 3 - Example of table for facility selection: Phenomenon No. 4 - Phase separation at branches

FACILITIES IDENTIFIER		10.1	10.2	11.3
Main Parameters				
P (MPa)	Initial flow vel. (cm/s)			
0.12	0.			
0.2	0.			
0.2	0.			
0.21	2.0			
0.21	4.0			
0.2	30.0			
0.3	30.0			
0.3	Natural reflood			
0.2	0.		561-2	
0.52			551-2	
1.02	Boil-off		555-4	
2.02			555-6	
4.03			557-8	
0.27	1.5			34006
	2.5			31504
	7.6			31302
	15.5			31701
0.41	2.6			32013

References:

10.1 - Summary list of the tests performed during the ACHILLES experimental programme 1987 - 1991" ACHILLES Workshop, Winfrith, U.K., November 1991
P. Dore and M.K. Denham: "ACHILLES unballooned cluster experiments part 5: Best estimate experiments" AEEW-R-2412, 1992

10.2 - M.G. Croxford, P.C. Hall: "Analysis of the THETIS boil-down experiments using RELAP5/Mod2". NUREG/IA-0014, July 1989.

11.23 - M.J. Loftus et al.: "PWR FLECHT-SEASET unblocked bundle, forced gravity reflood task data report". NUREG/CR-1532 (EPRI-NP-1459) Vol. 1 and 2, June 1980.

Additional Information:

10.1 - ACHILLES test No. A1B105 is the CSNI-ISP-25

Table 4 - Example of table for test selection: Entrainment/De-Entrainment in Core (part 3 of 4)

NUMBER OF PHENOMENA	NUMBER OF TEST
8	0
2	1
2	2
7	3
4	4 to 5
5	6 to 10
11	10 to 20
18	20 to 50
10	>50

Table 5 - Phenomena covered by a given number of tests

To this aim, a list of consistent questions was distributed to the authors of refs. [1] and [2], considering each of the 67 phenomena:

a) is the data base adequate for scaling?: i.e. is the experimentally available range of parameters, although far from the range expected in a plant, such to allow comparisons at different values of parameters (e.g. geometrical dimensions, pressure, etc.)?
   a1) what is the pressure range spanned by the experimental data?: this can be considered a part of the answer to the above item; in fact the expected range of pressure of interest in nuclear reactor safety can be fixed, in a general sense, as 0.1 - 16. MPa;

b) is it possible to use measured data in Integral Test Facilities to characterize the concerned phenomenon?

c) is the phenomenon relevant to reactor safety?: this is the same question previously answered and included in sect. 2.2.

The results are summarized in Tab. 6: in particular the columns 1-6 include quantities obtained from refs. [1] and [2], while columns 7-11 provide the answer to the questions.

The agreed levels of judgements and the various adopted symbols are indicated at the bottom of the table. Purposely, no attempt was made, so far, to homogenize the answers independently given by the various authors or to justify the differences in the judgements.

New researches on basic phenomena (items 0.1 - 0.6 in Tab. 6) should be regarded as necessary if improved knowledge is required for any of the subsequent phenomena; this consideration also reflects the lack of agreement for these cases.

From the analysis of the table it seems clear that there is no need for additional data in areas such as two-phase critical flow or heat transfer (phenomena 1 and 11 in the table).

Contradictory evaluations appear in relation to the need for additional experiments for phenomena such as entrainment (e.g. 5.3 to 5.6), direct contact condensation (e.g. 6.1, 6.2, 6.4 and 6.5) and separator behaviour (e.g. 17), etc.

Need for new data is unanimously requested in the cases of parallel channel instabilities (e.g. 22) and boron mixing and transport (e.g. 23).

		1	2	3	4	5	6	7	8	9	10	11
Nr.	PHENOMENON	NUMBER OF FACILITIES SUITABLE FOR MODEL VALIDATION	NUMBER OF FACILITIES PARTLY SUITABLE FOR MODEL VALIDATION	NUMBER OF FACILITIES MENTIONED FOR THE SET MATRIX	NUMBER OF FACILITIES RECOMMENDED IN CHAPT. 5	NUMBER OF FACILITIES SELECT. WITH IDENT. TESTS FOR THE SET MATRIX	NUMBER OF TESTS SELECT. FOR THE SET MATRIX	OVERALL RANGE OF PRESSURE OF THE FACILITIES (MPa)	IS DATA BASE ADEQUATE FOR SCALING? (1)	POSSIBILITY TO USE ITF DATA FOR CHARACTERIZING THE PHENOMENA (2)	RELEVANCE TO NUCLEAR REACTOR SAFETY (3)	NEED OF ADDITIONAL EXPERIMENTAL DATA (4)
0.1	Basic phenomena: evaporation due to depressurization	12	7	10	5	5	23	0.1-15.	-	* N	* Y	-
0.2	Basic phenomena: evaporation due to heat input	4	17	1	1	1	14	1.2-8.7	-	* N	* Y	-
0.3	Basic phenomena: condensation due to pressurisation	2	1	2	2	1	5	0.3-15.	-	o N	* Y	-
0.4	Basic phenomena: condensation due to heat removal	6	5	3	3	3	31	0.03-11.2	-	o N	* Y	-
0.5	Basic phenomena: interfacial friction in vertical flow	12	31	4	3	2	12	0.1-0.8	-	o N	* Y	-
0.6	Basic phenomena: interfacial friction in horizontal flow	4	9	10	3	1	6	0.1-15.	-	o N	* Y	-
0.7	Basic phenomena: wall to fluid friction	10	7	9	4	3	59	0.1-15.	-	o L	o Y	-
0.8	Basic phenomena: pressure drops at geometric discontinuities	5	11	4	2	2	27	0.2-12.	-	o L	* Y	-
0.9	Basic phenomena: pressure wave propagation	/	/	/	/	/	/	/	/	/	/	/
1.1	Critical flow in breaks	20	4	17	9	4	22	0.1-31.	* Y	o Y	* Y	o N
1.2	Critical flow in valves	5	0	6	2	2	28	4.-19.	-	-	* Y	o N
1.3	Critical flow in pipes	8	0	7	5	3	97	0.1-12.0	* Y	-	* Y	* N
2.1	Phase separation/vertical flow with and without mixture level in pipes/plena	12	8	13	8	3	11	0.1-15.	o A	-	* Y	* N
2.2	Phase separation/vertical flow with and without mixture level in core	23	1	12	11	5	30	0.1-12.	o A	o L	* Y	* N
2.3	Phase separation/vertical flow with and without mixture level in downcomer	3	2	3	3	3	36	0.1-1.1	o A	-	* Y	-
3	Stratification in horizontal flow	17	3	16	4	4	29	0.1-12.	o Y	-	* Y	o N
4	Phase separation at branches	6	2	5	4	3	62	0.7-10.	-	-	* Y	-
5.1	Entrainment/deentrainment in core	16	7	16	11	8	67	0.1-15.	o Y	-	* Y	* N
5.2	Entrainment/deentrainment in upper plenum	7	3	6	4	2	12	0.2-6.	o A	* L	* Y	* N
5.3	Entrainment/deentrainment in downcomer	1	0	1	1	1	4	2.	-	* L	* Y	-
5.4	Entrainment/deentrainment in steam generator tube	3	1	3	2	1	3	3.5-8.	o Y	-	* Y	-
5.5	Entrainment/deentrainment in steam generator mixing chamber (PWR)	0	1	1	1	1	3	/	-	L	o Y	-
5.6	Entrainment/deentrainment in hot leg with ECCI (PWR)	2	0	3	1	1	5	1.5	o A	o L	o Y	-

(1) (Y) = Yes; (A) = Analysis needed before concluding; (P) = Plant data are necessary; (E) = Experiments are necessary for scaling; (N) = No, on the basis of the considered data base.

(2) (Y) = Yes, (N) = No; (L) = in a Limited way.

(3) (Y) = Yes, the phenomenon is relevant; (N) = No, the phenomenon is not relevant.

(4) (Y) = Yes, additional experimental data are needed; (N) = No, experimental data are not needed; (-) = No, recommendation is given.

* Full agreement of experts judgements

o Majority agreement of expert judgements (> 4)

\- No agreement

Table 6 - Evaluation of SET Matrix related activity (part 1)

		1	2	3	4	5	6	7	8	9	10	11
Nr.	PHENOMENON	NUMBER OF FACILITIES SUITABLE FOR MODEL VALIDATION	NUMBER OF FACILITIES PARTLY SUITABLE FOR MODEL VALIDATION	NUMBER OF FACILITIES MENTIONED FOR THE SET MATRIX	NUMBER OF FACILITIES RECOMMENDED IN CHAPT. 5	NUMBER OF FACILITIES SELECT. WITH IDENT. TESTS FOR THE SET MATRIX	NUMBER OF TESTS SELECT. FOR THE SET MATRIX	OVERALL RANGE OF PRESSURE OF THE FACILITIES (MPa)	IS DATA BASE ADEQUATE FOR SCALING? (1)	POSSIBILITY TO USE ITF DATA FOR CHARACTERIZING THE PHENOMENA (2)	RELEVANCE TO NUCLEAR REACTOR SAFETY (3)	NEED OF ADDITIONAL EXPERIMENTAL DATA (4)
6.1	Liquid-vapour mixing with condensation in the core	0	2	2	1	1	14	0.1-2.0	-	* L	* Y	-
6.2	Liquid-vapour mixing with condensation in the downcomer	1	0	1	1	1	3	0.3-1.1	-	* L	* Y	-
6.3	Liquid-vapour mixing with condensation in the upper plenum	6	3	7	4	3	8	0.1-1.5	o A	* L	* Y	o N
6.4	Liquid-vapour mixing with condensation in lower plenum	0	1	1	1	1	3	2.0	-	* L	o Y	-
6.5	Liquid-vapour mixing with condensation in steam generator mixing chamber (PWR)	0	0	0	0	0	0	/	-	* L	o N	-
6.6	Liquid-vapour mixing with condensation of ECCI in hot and cold leg (PWR)	4	2	4	3	3	25	0.4-7.	* Y	-	* Y	* N
7.1	Condensation in stratified conditions in pressurizer (PWR)	3	0	3	3	1	5	0.1-15.	-	* L	o Y	o N
7.2	Condensation in stratified conditions in steam generator primary side (PWR)	1	0	1	1	1	3	4.-7.	-	* L	* Y	-
7.3	Condensation in stratified conditions in steam generator secondary side (PWR)	1	0	1	1	1	17	1.-7.	-	* L	o Y	-
7.4	Condensation in stratified conditions in horizontal pipes	5	2	4	4	3	32	0.1-7.	-	o L	o Y	* N
8.1	Spray effects in core (BWR)	6	0	6	4	2	2	0.1-2.	-	* L	* Y	* N
8.2	Spray effects in pressurizer (PWR)	3	1	3	2	1	2	12.-15.	-	* L	o N	* N
8.3	Spray effects in once-through steam generator secondary side	0	0	0	0	0	0	/	-	* L	-	-
9.1	Countercurrent flow/countercurrent flow limitation at the upper tie plate	12	5	3	3	3	16	0.1-2.0	o A	o L	* Y	o N
9.2	Countercurrent flow/countercurrent flow limitation at channel inlet orifices (BWR)	1	1	2	1	1	3	1.0	-	o L	o Y	-
9.3	Countercurrent flow/countercurrent flow limitation in the hot and cold legs	4	5	5	1	1	3	0.1-1.5	o A	* L	* Y	* N
9.4	Countercurrent flow/countercurrent flow limitation in steam generator tube (PWR)	5	1	6	2	1	72	0.15-7.	o A	-	* Y	o N
9.5	Countercurrent flow/countercurrent flow limitation in the downcomer	3	0	3	2	3	40	0.1-1.1	o A	* L	* Y	* N
9.6	Countercurrent flow/countercurrent flow limitation in surgeline (PWR)	1	3	3	1	1	49	0.1-7.	-	o L	* Y	-

(1) (Y) = Yes; (A) = Analysis needed before concluding; (P) = Plant data are necessary; (E) = Experiments are necessary for scaling; (N) = No, on the basis of the considered data base.

(2) (Y) = Yes, (N) = No; (L) = in a Limited way.

(3) (Y) = Yes, the phenomenon is relevant; (N) = No, the phenomenon is not relevant.

(4) (Y) = Yes, additional experimental data are needed; (N) = No, experimental data are not needed; (-) = No, recommendation is given.

* Full agreement of experts judgements

o Majority agreement of expert judgements (> 4)

\- No agreement

Table 6 - Evaluation of SET Matrix related activity (part 2)

		1	2	3	4	5	6	7	8	9	10	11
Nr.	PHENOMENON	NUMBER OF FACILITIES SUITABLE FOR MODEL VALIDATION	NUMBER OF FACILITIES PARTLY SUITABLE FOR MODEL VALIDATION	NUMBER OF FACILITIES MENTIONED FOR THE SET MATRIX	NUMBER OF FACILITIES RECOMMENDED IN CHAPT. 5	NUMBER OF FACILITIES SELECT. WITH IDENT. TESTS FOR THE SET MATRIX	NUMBER OF TESTS SELECT. FOR THE SET MATRIX	OVERALL RANGE OF PRESSURE OF THE FACILITIES (MPa)	IS DATA BASE ADEQUATE FOR SCALING? (1)	POSSIBILITY TO USE ITF DATA FOR CHARACTERIZING THE PHENOMENA (2)	RELEVANCE TO NUCLEAR REACTOR SAFETY (3)	NEED OF ADDITIONAL EXPERIMENTAL DATA (4)
10.1	Global multidimensional fluid temperature, void and flow distribution in the upper plenum	5	3	5	2	2	8	0.2-8.8	* Y	* L	* Y	* N
10.2	Global multidimensional fluid temperature, void and flow distribution in the core	10	1	6	6	6	36	0.1-4.0	o A	* L	* Y	* N
10.3	Global multidimensional fluid temperature, void and flow distribution in the downcomer	11	2	8	8	3	40	0.1-10.7	* Y	* L	* Y	* N
10.4	Global multidimensional fluid temperature, void and flow distribution in steam generator secondary side	0	0	0	0	0	0	/	o N	* L	-	-
11.1	Heat transfer: natural or forced convenction in the core, in the steam generator and at structures	18	2	11	11	4	25	0.1-8.0	* Y	o Y	* Y	* N
11.2	Heat transfer: subcooled/nucleate boiling in the core, in the steam generator and at structures	17	0	17	9	5	75	0.1-28.	* Y	o Y	* Y	* N
11.3	Heat transfer: DNB/dryout in the core, in the steam generator and at structures	29	4	28	17	7	52	0.1-28.	* Y	o L	* Y	* N
11.4	Heat transfer: post-CHF in the core, in the steam generator and at structures	36	5	35	19	15	120	0.1-28.	* Y	o L	* Y	* N
11.5	Heat transfer: radiation in the core	5	2	6	4	3	12	0.1-2.0	o A	o L	* Y	* N
11.6	Heat transfer: condensation in the steam generator tubes and on structures	7	2	9	2	2	9	0.1-15.5	o A	o L	* Y	* N
12.1	Quench front propagation/rewet, fuel rods	27	9	27	15	10	71	0.1-12.	o A	o Y	* Y	-
12.2	Quench front propagation/rewet, channel walls and water rods (BWR)	6	4	9	4	2	22	0.1-2.	o A	o L	* Y	* N
13	Lower plenum flashing	4	6	5	4	3	15	2.-16.	o A	o Y	* Y	* N
14	Guide tube flashing (BWR)	1	1	2	0	0	0	1.	-	-	-	o N
15	One and two phase impeller pump behaviour	7	0	2	2	2	150	0.8-2.9	o A	o L	* Y	-
16	One and two phase jet pump behaviour	1	0	1	1	0	0	8.2	-	o L	* Y	-
17	Separator behaviour	3	1	4	1	1	14	7.-8.	-	o L	o Y	-
18	Steam dryer behaviour	0	0	0	0	0	0	/	-	o N	-	-
19	Accumulator behaviour	0	1	1	0	0	0	/	-	o Y	* Y	-
20	Loop seal filling and clearance (PWR)	4	0	4	3	3	0	0.1-2.	o A	* Y	* Y	* N
21	ECC bypass/downcomer penetration	3	0	2	2	2	41	0.1-1.8	* Y	* Y	* Y	* N
22	Parallel channel instabilities (BWR)	3	2	5	3	1	1	0.1-0.5	-	o L	* Y	* Y
23	Boron mixing and transport	2	1	3	3	2	12	0.5	-	o L	* Y	* Y
24	Non condensable gas effect (PWR)	7	3	6	6	4	18	0.2-7.	o A	o L	* Y	-
25	Lower plenum entrainment	1	1	2	1	1	7	/	-	o L	o Y	-

(1) (Y) = Yes; (A) = Analysis needed before concluding; (P) = Plant data are necessary; (E) = Experiments are necessary for scaling; (N) = No, on the basis of the considered data base.

(2) (Y) = Yes, (N) = No; (L) = in a Limited way.

(3) (Y) = Yes, the phenomenon is relevant; (N) = No, the phenomenon is not relevant.

(4) (Y) = Yes, additional experimental data are needed; (N) = No, experimental data are not needed; (-) = No, recommendation is given.

* Full agreement of experts judgements

o Majority agreement of expert judgements (> 4)

\- No agreement

Table 6 - Evaluation of SET Matrix related activity (part 3)

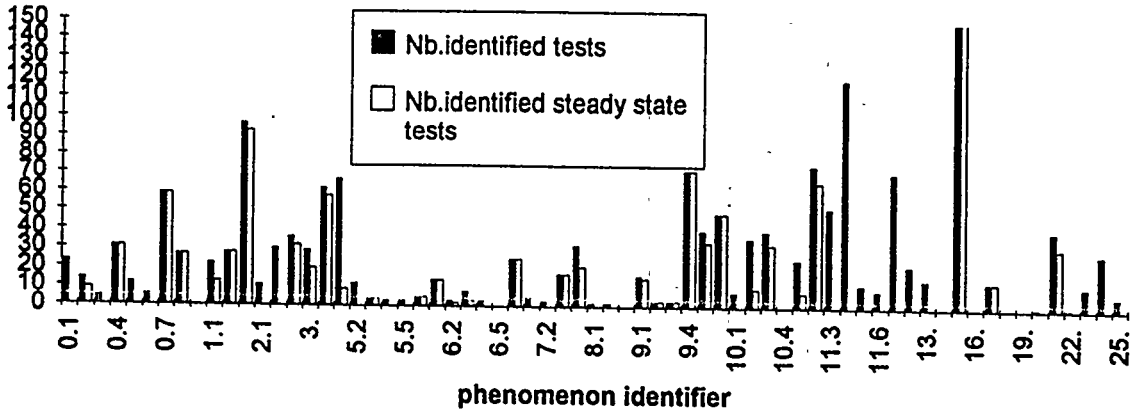

Figure 1 - Summaryof identified tests per phenomenon

4. CONCLUSIONS

A wide ranging evaluation has been carried out making reference to experimental programs in the OECD countries. This led to classification and characterization of the thermalhydraulic phenomena relevant in nuclear reactor technology and to fix a reference list of experiments to be considered for a comprehensive system code validation program. The identification of more than 1000 tests performed in, approximately, 100 test facilities, covering 67 phenomena of interest, resulted in the Separate Effects Test (SET) matrix and is the most important outcome of the activity. Furthermore, it was found that a large amount of data are available for some "popular" phenomena, e.g. heat transfer, while tests are lacking in more "exotic" areas e.g. direct contact condensation. A re-evaluation of the whole activity by the same authors who worked together during a four-years period to produce the SET matrix, was recently conducted on the basis of a consistent set of questions independently answered. The main results are as follows:

- experimental activities in relation to what are called "basic phenomena" are recommended not only for academic purposes but also to better understand thermalhydraulic evolutions of more complex phenomena;
- new data are not considered necessary for improving reactor safety in areas like two-phase critical flows or heat transfer;
- data are required for characterizing phenomena such as parallel channel instability and boron mixing and transport;
- in relation to 23 out of the 58 phenomena (i.e. 67 phenomena excluding the "basic" ones), no agreement was reached among the authors, although no attempt was made to homogenize the individual judgement level.

Additional outcomes can be drawn in forthcoming activities starting from the wide data base collected so far: e.g. ranking of phenomena, consideration of range of parameters expected in the plant and scenarios in Integral Test Facilities. Furthermore, CSNI recently proposed to reach an agreement on recommendations on the data basis for future needs.

REFERENCES

[1] Aksan S.N., D'Auria, F., Glaeser H., Pochard R., Richards C., Sjoberg A.
"Separate Effects Test Matrix for Thermalhydraulic Code Validation: Phenomena Characterisation and Selection of Facilities and Tests - Vol. I", OECD-CSNI Report OCDE/GD (94) 82, Paris (F), September 1993

[2] Aksan S.N., D'Auria, F., Glaeser H., Pochard R., Richards C., Sjoberg A.
"Separate Effects Test Matrix for Thermalhydraulic Code Validation: Facility and Experiment Characteristics - Vol. II", OECD-CSNI OCDE/GD (94) 83, Paris (F), September 1993

[3] Aksan S.N., D'Auria F., Glaeser H., Pochard R., Richards C., Sjoberg A.
"CSNI Separate Effect Tests Validation Matrix: General Description and Methodology", Int. Conf. on New Trends in Nuclear System Thermohydraulics - Pisa (I), May 30 - June 2 1994

[4] D'Auria F., Aksan S.N., Glaeser H., Lillington J., Pochard R., Richards C., Sjoberg A.
"Thermalhydraulic Phenomena in the CSNI Separate Effect Validation Matrix", Int. Conf. on New Trends in Nuclear System Thermohydraulics - Pisa (I), May 30 - June 2 1994

[5] Pochard R., Richards C., Aksan S.N., D'Auria F., Glaeser H., Sjoberg A.
"Evaluation of the Separate Effect Tests (SETs) Matrix Data Base for Validation of Thermalhydraulics Codes", Int. Conf. on New Trends in Nuclear System Thermohydraulics - Pisa (I), May 30 - June 2 1994

[6] Aksan N., D'Auria F., Glaeser H., Pochard R., Richards C., Sjoberg A.
"Overview of CSNI Separate Effects Test Validation Matrix", NURETH-7 Meet. Saratoga Springs (USA) - September 10-15, 1995

[7] US-NRC
"Compendium of ECCS research for realistic LOCA analysis", NUREG-1230

[8] CSNI Group of Experts
"State of the Art Report (SOAR) on Thermal-Hydraulics of Emergency Core Cooling in Light Water Reactors", OECD-NEA-CSNI Report No. 161

[9] CSNI Group of Experts
"CSNI Code Validation Matrix of Thermal-Hydraulic Codes for LWR LOCA and Transients", OECD-NEA-CSNI Report No. 132

WATER HAMMER PHENOMENA OCCURRING IN NUCLEAR POWER INSTALLATIONS WHILE FILLING HORIZONTAL PIPE CONTAINING SATURATED STEAM WITH LIQUID

Yu.F. SELIVANOV, P.L. KIRILLOV and A.D. YEFANOV

The State Scientific Center - The Institute of Physics and Power Engineering, Obninsk, Russia

The potentiality of the water hammer occurrence in nuclear reactor loop components has been considered under the conditions of filling a steam-containing pipeline leg involving horizontal and vertical sections with liquid subcooled to the saturation temperature. As a result of free discharging from the tank, the liquid enters the horizontal pipeline. When the liquid front runs an obstacle like a pipeline turn, the condition meeting the liquid slug formation in the pipeline is fulfilled. The pressure drop being occurred in steam flowing along the pipeline causes the liquid slug to move to the pipeline inlet. When the liquid slug decelerates, a water hammer occurs. This mechanism of water hammer occurrence is tested by experiments. The regimes of the occurrence of multiple considerable water hammers were identified.

The experience of the exploitation of water cooled nuclear power installations showed that accident situations or incorrect actions of the operating personnel usually resulted in strong water hammer events with destructive sequences in NPP loops [1]. The analysis of the situation preceding water hammers enabled one to infer that the main portion of them refers to condensation water hammers. The nature of that kind of water hammers is related to the two-phase state of coolant circulating round the loops and, simultaneously, to the occurrence of conditions for a high-rate condensation of steam phase.

To prevent the water hammer occurrence or mitigate its destructive consequences, certain engineering arrangements and design decisions are needed. To develop these, the knowledge of the mechanisms and conditions of the water hammer occurrence in structural NPP components is necessary.

Based on the rough classification of water hammers by the mechanism of their occurrence [1,2], one may infer that the cases with liquid entering the pipelines filled with steam are characterized by the largest number of water hammers. The mechanisms of water hammer occurrence differ depending on the pipeline orientation in space, their length and the availability of turns, elbows and blind pipelines [3]. In horizontally oriented pipelines, the mechanism of the water hammer occurrence is associated with the potentiality of the steam-accelerated liquid slug formation.

For a water hammer to occur, at least two conditions need be coupled:
- a certain liquid flow pattern at which the conditions are developed, giving rise to liquid waves overlapping the whole pipe cross-section (the formation of liquid slugs); and
- the onset of a pressure drop in steam on the both sides of the slug, as a result of which the acceleration of the formated slug takes place, followed by water hammer occurring due to its further deceleration.

One of the causes of the liquid slug formation is associated with the interaction of the flow of liquid partially filling the pipeline cross-section with obstacles (pipeline elbows or end plugs) in its path. The liquid can enter the pipe in two ways: by pumping (with the occurrence of a "hydraulic jump") or as a result of free discharge from the tank.

Let us consider the case of free discharge of liquid from the tank and define the potentiality of the liquid slug occurrence based on the solution of the following hydrodynamic problem. To simplify the problem, the height of the tank is assumed to be equal to the pipe diameter. The tank is separated from the pipe by a baffle. As a result, the problem is formulated as follows. The channel of a length L_0 is separated by the baffle in two portions. The left portion of the channel with a length L is initially filled with liquid on the height h_0, the right portion of the channel is restricted by a vertical wall. At a certain moment of time, the baffle is removed. It is necessary to identify the velocity and height of the liquid flow. The liquid is assumed to be perfect and the flow - one-dimensional. Letting x to denote the horizontal axis with the origin being matched to the left end of the pipe, τ - the time, h - the liquid flow height, ρ and g to denote the liquid density and gravitational acceleration, respectively, and U - the liquid velocity, write down the balance equation for mass and impulse, describing this flow, in terms of:

$$\frac{\partial(\rho h)}{\partial \tau} + \frac{\partial(\rho U h)}{\partial x} = 0 , \qquad (1)$$

$$\frac{\partial(\rho U h)}{\partial \tau} + \frac{\partial}{\partial x}(\rho U^2 h + \frac{\rho g h^2}{2}) = 0 . \qquad (2)$$

Having replaced x with the Lagrangian mass variable $s = \int_0^x \rho h dx$, the length scale h_0: $h = h_0 H$, where H is the dimensionless height of liquid, we obtain instead of the set of equations (1)-(2) the following set:

$$\frac{1}{h_0}\frac{\partial}{\partial\tau}\left(\frac{1}{\rho H}\right) = \frac{\partial U}{\partial s} ,$$

$$\frac{\partial U}{\partial\tau} = -\frac{gh_0^2}{2}\frac{\partial}{\partial s}(\rho H^2) .$$

The introduction of the variable s substantially simplifies the giving of boundary conditions, since the region of the definition of the variable s is unchanged in time:

$0 \le s \le M$, where $M = \int_0^L \rho H dx$. The initial and boundary conditions are:

$U(s,0) = 0$, $H(s,0) = 1$, $U(0,\tau) = 0$, $H(M,\tau) = 0$.

The scheme having justified itself in calculating one-dimensional gas flows is chosen as the difference scheme approximating the presented differential equations.

The set of differential equations was solved by iteration at each time step. As the calculations demonstrate, the water splash exceeding the channel height appears after the liquid flow comes up to the turn of a pipeline (Fig. 1).

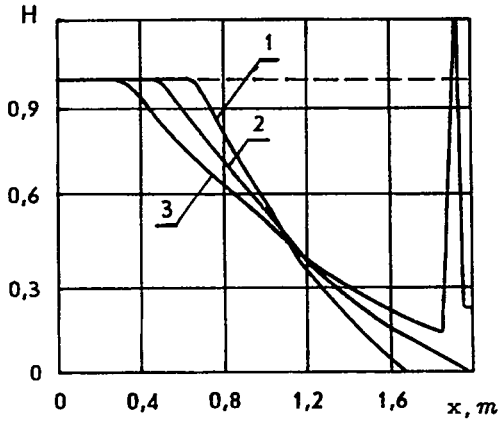

Fig. 1. The distribution of the dimensionless height of the liquid height along the channel length at different time moments, h_0 = 40 mm, L_0 = 2.0 m, L = 1.11 m, 1: τ = 0.7 s, 2: τ = 1.0 s, 3: τ = 1.3 s.

In this way, the condition required for a liquid slug to occur is met. This condition is suitable for blind pipelines and horizontally arranged pipeline legs. However, this condition is insufficient for a liquid slug to occur in vertical legs. Besides the requirement to the wave height, it is necessary here to fulfill one more condition under which the wave spans the channel over its

whole cross-section and which is ignored in the current calculation model. Spanning is possible provided that a condensate layer of sufficient height is present in the steam-filled pipelines.

The second necessary condition of the water hammer occurrence can be satisfied given that the liquid temperature at the pipeline inlet is below the saturation temperature. As the liquid flows along the pipeline, it is heated up at the expense of heat being generated at the steam condensation and due to heat transfer to pipeline walls. The difference in the steam condensate rate caused by the liquid heating-up results in a steam pressure difference on the both sides of the formated slug which first accelerates and then is followed by water hammer occurring due to its deceleration.

The expected mechanism of the water hammer occurrence for the given tubular channel geometry was checked by experiments.

The test facility represents a closed circulation loop incorporating a test section, centrifugal pump, electric heater, steam generator, separator, mixer, cooler, control and closing valves, etc. The test section shown schematically in Fig. 2 is a 2 m long, 40 mm - i.d. tube made of stainless steel. The tube is

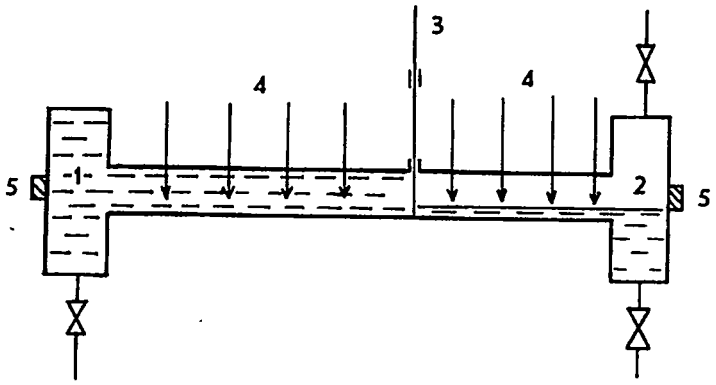

Fig. 2. The schematic of the test section; 1: liquid zone, 2: steam zone, 3: fast-response baffle, 4: temperature transmitters, 5: pressure transducers.

sectioned in two portions by a quick-response baffle. One portion of the tube together with the collector totally 1.11 m long was the liquid reservoir. The second portion of the tube together with the collector totally 0.89 m long serves as a steam chamber. The test section is equipped with Chr - Al thermocouples with a variable depth of insertion, standard pressure gauges, two pressure transducers of type "Sapphire - 22 DI" and fast pressure transducers of type DD-10. As it was established, the DD-10 transducers showed a considerable dependence on temperature readings. In order to minimize the temperature error of measurements in the course of testing, the DD-10 transducer indications were compared with the readings obtained by means of transducers of type "Sapphire" under the steady-state conditions, and the necessary correction was introduced into the calibration performance of the DD-10 transducers.

The procedure of tests dealt with the water hammer study under the liquid-steam interaction conditions is as follows: filling the liquid reservoir with liquid (water) at required temperature, preheating and filling the steam zone with steam entering the test section from the separator, setting the necessary level of steam collector filling with condensate, opening the fast-response baffle.

The reference liquid level was established in the steam zone at the expense of the condensate accumulation. The generated initial liquid level enabled one to vary the liquid flow conditions in the channel and the size of reflected liquid wave.

The experiments on the investigation of the water hammer occurrence conditions and water hammer magnitude were carried out for different operating variables: pressure and, correspondingly, temperature of the saturated steam in the steam zone of the test section, water temperature in the liquid zone of the test section, the initial level of filling the steam zone of the test section with liquid (condensate).

The pressure value of the saturated steam was governed by the pressure level over the loop and restricted by the strength capabilities of the test section. Taking into account potential magnitudes of water hammers, the upper level of the steam pressure was about 6 bar.

The water temperature in the liquid zone of the test section was varied by means of a heater set in the loop, with delivering, if necessary, a portion of water via the cooler. The water pressure was chosen such that the fast-response baffle separating the test section only provided a significant pressure drop on the both sides of the baffle (about 2 bar), operated reliably. The water level automatically set in the course of arranging the steam path through the test section was taken as the base to generate the necessary initial liquid level. The use of one of potential steam exits from the test section causes the liquid level to be set at a height being twice as low as the height of the test cross-section. The liquid level was determined by means of a special metering device. Water hammers were observed to occur when the liquid level in the steam zone rose to the 1/2 of the tube cross-section height.

The calculations performed according to the above technique demonstrated that the liquid flow reached the turn of the tube in 1.05 sec after the baffle had been opened. This magnitude may be considered a tentative reference value defining the time interval between the moments of the baffle opening and water hammer occurrence.

The typical results of the pressure variation in the liquid collector are shown in Fig. 3.

As it was expected, the pressure wave appearing at the deceleration of accelerated liquid slug, propagated in the liquid phase. This is confirmed by the fact that only transmitters set in the liquid collector make record of water hammer. As for the steam collector, slight variations in pressure were observed there, which were tentatively induced by the deceleration of the liquid entering the steam zone when it ran into the wall and some steam pressure oscillations accompanying the liquid slug flow.

Water hammers occurred approximately in equal time intervals being 1.5 - 2 s at a pressure of 3.4 bar and 1.6 - 1.8 s at a pressure of 5.4 bar.

Fig. 4 illustrates basic regularities being observed during testing:

- water hammers differ in magnitude;
- water hammers last over a long period of time.

- the most considerable water hammer is not necessarily the first;
- water hammers last over a long period of time.

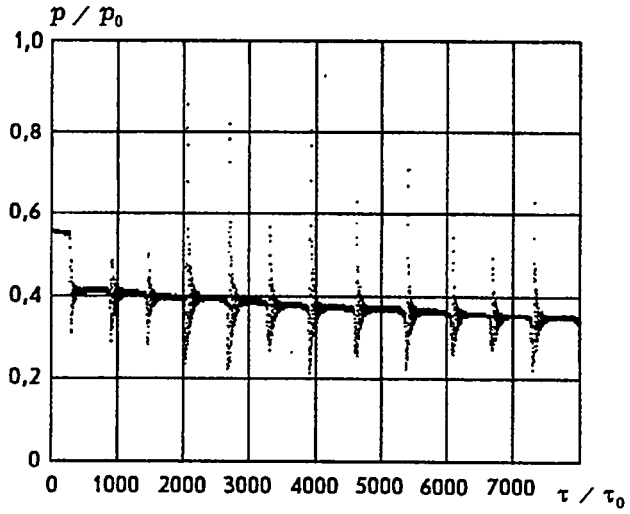

Fig. 3. Water hammers indicated in the liquid collector when subcooled liquid issues into steam; initial steam pressure is 3.4 bar; liquid temperature is 33.0 °C, p_0 = 8.0 bar and τ_0 = 2.69 ms.

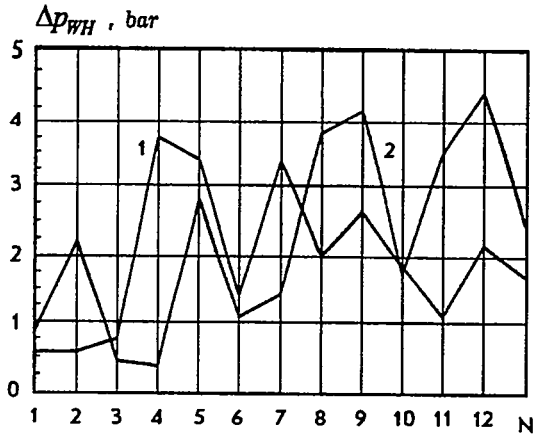

Fig. 4. The distribution of water hammers magnitudes in the course of their occurrence; 1: initial steam pressure is 3.4 bar, initial liquid temperature is 33.0 °C; 2: initial steam pressure is 5.4 bar, initial liquid temperature is 27.0 °C.

These phenomena can be explained by the fact that the water hammer magnitude is determined by both the section length along which the slug is accelerated and the pressure drop at (both sides of the slug) being the driving force. These two factors affect the water hammer magnitude in different ways.

Eventually, the section length where the liquid slug accelerates increases owing to the water discharge; at the same time, the rate of the steam condensation decreases owing to liquid heating-up, causing the reduction of the driving pressure drop. The predominance of one or another effect results in the water hammer magnitude. In the course of experiments, a regularity related to the magnitude of the first (in the course) water hammer was noted. At rather high initial liquid level in the steam zone, being 1/2 of the tube cross-section height or a few millimeters in excess of this level, considerable water hammers occurred just upon the baffle had been opened.

If the initial level of the liquid was lower than the half of the tube cross-section height, then the first water hammers were insignificant. However, their magnitude increased in time owing to the increase of the amount of liquid in the steam zone and thus the fulfillment of conditions under which the tube cross-section is overlapped with a liquid slug.

Each water hammer was preceded by considerable pressure reduction in the liquid zone. This phenomenon seems to be caused by the steam condensation in a closed steam space appearing in the course of the liquid slug formation. In defining the present pressure reduction, one can assess the pressure drop value accelerating the liquid slug. The largest pressure drops were 1.3 bar for a pressure about 3.4 bar and 2.4 bar for a pressure about 5.4 bar.

One of the parameters defining the water hammer magnitude is the liquid temperature at the pipe inlet. The distribution of maximum water hammers by sizes for each test as a function of the liquid subcooling degree (the difference between the saturated steam temperature and liquid temperature) for two steam pressure levels is shown in Fig. 5. It is evident that the most

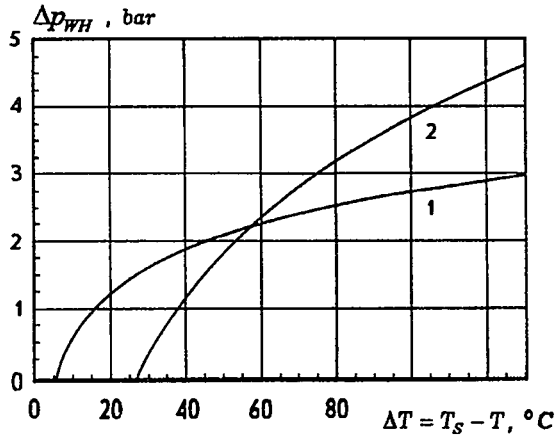

Fig. 5. The magnitude of maximum water hammers as a function of liquid entering the pipe;
1: initial steam pressure is 3.4 bar;
2: initial steam pressure is 5.4 bar.

considerable water hammers occur at the maximum liquid subcooling. For a steam pressure level of 3.4 bar, the highest pressure jump 3.7 bar (during the water hammer occurrence) corresponded to a subcooling of 105.5 °C, whereas for the pressure level of 5.4 bar, with increasing the pressure (at a water

hammer) by 4.5 bar, subcooling of 122.0 °C was typical. As the degree of subcooling decreases, the magnitudes of maximum water hammers are significantly decreased. This is related to decreasing in the steam condensation rate on the liquid flow surface because the process of the liquid slug formation seems to be weakly dependent on temperature.

References

[1] Y. Chou and P.Griffith, "Avoiding steam - bubble - collapse-induced water hammer in piping systems," EPRY Report, EPRY NP-6447 (1989).

[2] H.H. Safwat, A.H. Arastu and S.M. Husaini, "Systematic methodology for diagnosis of water hammer in LWR power plants," Nucl. Engrg. Des. 122, 365-376 (1990).

[3] Y. Chou and P.Griffith, "Admitting cold water into steam filled pipes without water hammer due to steam bubble collapse," Nucl. Engrg. Des. 121, 367-378 (1990).

[4] А.А. Самарский и Ю.П. Попов, Разностные схемы газовой динамики, Наука, Moscow (1975) (in Russian).

NATURAL CIRCULATION ANALYSIS FOR THE ADVANCED NEUTRON SOURCE REACTOR REFUELING PROCESS II[1]

R. F. Tucker, Srikanth Dasardhi, and Y. Elkassabgi
Texas A&M University-Kingsville
Kingsville, Texas

G. L. Yoder
Oak Ridge National Laboratory[2]
P.O. Box 2009
Oak Ridge, Tennessee

ABSTRACT

During the refueling process of the Advanced Neutron Source Reactor (ANSR), the spent fuel elements must be moved from the primary coolant loop (containing D_2O), through a heavy water pool, and finally into a light water spent fuel storage area. The present refueling scheme utilizes remote refueling equipment to move the spent fuel elements through a D_2O filled stack and tunnel into a temporary storage canal. A transfer lock is used to move the spent fuel elements from the D_2O-filled interim storage canal to a light water pool. Each spent fuel element must be cooled during this process, using either natural circulation or forced convection. This paper presents a summary of the numerical techniques used to analyze natural circulation cooling of the ANSR fuel elements as well as selected results of the calculations. Details of the analysis indicate that coolant velocities below 10 cm/s exist in the coolant channels under single phase natural circulation conditions. Also, boiling does not occur within the channels if power levels are below a few hundred kW when the core transitions to natural circulation conditions.

Nomenclature

a	=	constant used in incipient boiling correlation pressure correction factor (0.95071362)
A_c	=	channel cross-sectional area normal to flow direction
A_{side}	=	(channel gap)·(element height)
b	=	constant used in incipient boiling correlation pressure correction factor (0.40980412)
c	=	constant used in incipient boiling correlation pressure correction factor (0.3303747)

[2]Managed by Martin Marietta Energy Systems, Inc., under contract DE-AC05-84OR21400 with the U.S. Department of Energy.

Nomenclature (Con't)

C_p	=	constant specific heat
d	=	constant used in incipient boiling correlation pressure correction factor (-0.1605523)
D_e	=	hydraulic diameter
e	=	constant used in incipient boiling correlation pressure correction factor (-0.13561859)
f	=	Fanning friction factor
f'	=	constant used in incipient boiling correlation pressure correction factor (0.01459134)
F_{D_2O}	=	correction factor for Bergles-Rohsenow incipient boiling correlation
g	=	constant used in incipient boiling correlation pressure correction factor (0.012468927)
Gz	=	(Re Pr D_e) / X
h	=	heat transfer coefficient
k	=	thermal conductivity
L	=	channel height
m	=	dynamic viscosity
Nu	=	Nusselt number (h D_e/k)
Pr	=	Prandtl number (μ C_p/k)
q	=	heat flux
R	=	radial or spanwise distance normal to direction of flow
Re	=	Reynolds Number (ρ V D_e/μ)
V	=	axial coolant velocity
X	=	axial distance in the direction of flow
μ	=	dynamic viscosity
ρ	=	density

Subscripts:

amb	=	ambient
b	=	bulk
c	=	cross section
D_2O	=	heavy water
e	=	exit
i	=	axial direction index
IB	=	incipient boiling
in	=	inlet
j	=	radial direction index
s	=	saturation
w	=	wall

INTRODUCTION

The Advanced Neutron Source Reactor (ANSR), presently in the advanced conceptual design stage, will become the world's most advanced research reactor for performing neutron scattering research. The reactor, which is being designed at the Oak Ridge National Laboratory, has three major technical goals: 1) to provide irradiation facilities at least as good as those at the existing High Flux Isotope Reactor (HFIR), 2) to provide isotope production capabilities at least as good as those at HFIR, and 3) to provide the world's highest continuous neutron flux for performing neutron beam experiments. A very compact, high-power core is being designed to achieve these goals.

Heavy water moderates and cools the highly enriched uranium silicide fuel (U_3Si_2) in the reactor core. A 0.762 mm thickness (maximum fuel meat thickness) of U_3Si_2 is sandwiched between 6061 Aluminum cladding, making each fuel plate 1.27 mm thick. The fuel is graded both axially and radially within the fuel plates by varying the thickness of the fuel meat. This allows tailoring of the power distribution within each of two fuel elements and improves the thermal hydraulic performance of the core. The fuel elements are made up of 684 involute-shaped fuel plates, and are constructed by welding each plate to inner and outer cylindrical side plates. The involute shape provides a constant coolant channel gap of 1.27 mm over the span of the plates (87.4 mm for the inner element and 70.3 mm for the outer element). The two fuel elements are separated axially and radially to improve the neutron flux levels and to provide a separate coolant flow to the inlet of each fuel element (see Figure 1).

During normal operation, heavy water flowing upward through the fuel elements at a velocity of 25 m/s cools the reactor core. The cooling design incorporates four separate cooling loops (three of them active at any one time, and the remaining one inactive), each containing main and emergency heat exchangers, and a main coolant circulation pump. The configuration of these loops and components promote natural circulation for decay heat removal (e.g., heat exchangers are placed high in the loop, the core is placed low in the loop, etc.). Each main circulation pump is also equipped with a pony motor that can provide 10% of nominal flow. The pony motors have battery systems that can supply power for up to 30 minutes under emergency conditions. Under normal shutdown conditions, the pony motors operate until the primary coolant system is opened. Beyond this point in time, natural circulation within the primary system is sufficient to cool the core at decay heat levels.

A full irradiation cycle lasts 17 days with four additional days presently allocated for the refueling process. Thirty hours after shutdown, the primary coolant system is opened to begin the refueling procedure. Each fuel element will be moved separately from its location in the primary coolant loop and eventually placed in a light water fuel storage pool. This process will be performed using remotely operated refueling equipment. Figure 2 shows the refueling path. The region marked as 1 in the figure is filled with heavy water, and will be open to the primary system during the refueling process. An absorber will be installed in each fuel element as it is removed from its original position (labeled A) in the primary coolant loop. The refueling equipment will move each element from position A to position B through a refueling stack and transfer tunnel. After a 42 day cool-down period, each element will be placed in a heavy water/light water transfer

lock. The lock, initially filled with detritiated heavy water, opens to the transfer tunnel to accept an element. It will then be resealed and flushed with light water. At this point, the element can be moved to the light water fuel storage pool until it is removed for reprocessing.

Even though decay heat levels are only a few percent of normal operating power, the elements produce several hundred kilowatts of heat that must be removed. The preferred method is via natural circulation. This paper investigates natural circulation cooling of the spent fuel element in an infinite heavy water pool.

ANALYSIS AND RESULTS

The analysis for the refueling process of the ANSR was performed using a revised version of the computer code NATCON (Smith and Woodruff, 1988). The NATCON code analyzes the steady-state natural convection thermal-hydraulics of plate-type fuel as used in many research reactor designs. The code calculates the coolant flow rate, the axial temperature distributions within the coolant, and the fuel plate surface and centerline temperature. Flow is driven by density differences between the coolant and the surrounding constant-temperature coolant pool. The flow velocity is determined by equating the coolant buoyancy and viscous forces. The code was validated using two reactors as an example. The results are outlined in Smith and Woodruff (1988). The structure of the code was changed to enable it to account for radial as well as axial variations in the power density distribution. Earlier versions of the code (Elkassabgi et al., 1993) were capable of analyzing only axial variations in the power density distribution. Lateral fluid interaction between channels is now accounted for explicitly, using a discretized approximation. Significant enhancement of the code's predictive capabilities was also achieved by altering and extending both the Nusselt number and friction factor relationships.. In addition, physical property subroutines for light water were replaced by heavy water subroutines. Since light and heavy water thermophysical properties normally differ by less than 10%, it is expected that thermal-hydraulic correlations (such as heat transfer coefficients, friction factors, etc.) developed for light water will be appropriate for heavy water as well. Figure 3.a shows the grid layout for the numerical nodes. These also correspond to locations where the local fuel plate power densities are known. The flow channel is divided into 24 sub-channels. For each sub-channel there are 69 axial nodes. The frictional (including minor losses at the inlet and exit of the channel) and buoyant forces in the flow channel are calculated using the following equations:

$$friction\ force = \left[\frac{(\rho V)_{in}^2}{2}\right] A_c \left[\frac{1}{2\rho_{in}} + \sum_{i=1}^{n}\left(\frac{f\Delta X_i}{\rho_i D_e}\right) + \frac{1}{\rho_{out}}\right] + \mu_b A_{side}\left[\frac{V_{i,j} - V_{i,j+1}}{R_{i,j} - R_{i,j+1}}\right] + \mu_b A_{side}\left[\frac{V_{i,j} - V_{i,j-1}}{R_{i,j} - R_{i,j-1}}\right] \quad (1)$$

and

$$buoyancy\ force = \left(\overline{\rho}_c - \rho_{amb}\right) A_c L_c g \quad (2)$$

where $\bar{\rho}_c = \frac{1}{L_c}\left[\int_0^{L_c} \rho_c(x)dx\right]$

Figure (3.b) shows the energy balance for a sub-channel.

The convective heat flux from the fuel plate surface is evaluated using a Nusselt number correlation for upward vertical flow in a heated rectangular channel developed by Sudo, et. al. (1985).

$$\mathrm{Nu} = \begin{cases} 2.0\ (\mathrm{Gz})^{0.3} & \text{for } 40 \le \mathrm{Gz} \\ 6.0 & \text{for } 16 \le \mathrm{Gz} \le 40 \end{cases} \tag{3}$$

The above correlation replaced the numerical data referenced in Kays (1980) in the original code. Equation (3) takes into consideration thermal and hydrodynamic entry length effects. The friction factor correlations used to evaluate the frictional forces in equation (1) were based on Eckert and Irvine (1957) in the original code. These were replaced by the following correlations:

(i) For fully developed laminar flow the Shah and London (1978) correlation was adopted ($\mathrm{Re} < 2140$)

$$f = \left(\frac{23.53}{\mathrm{Re}_b}\right)\left(\frac{\mu_b}{\mu_w}\right)^{-0.32} \tag{4}$$

where the viscosity ratio term is due to Bonilla (1958).

(ii) For transitional flow, an interpolation between laminar and turbulent friction factors is used ($2140 < \mathrm{Re} < 4240$)

$$f = 0.011\left(\frac{\mu_b}{\mu_w}\right)^{-0.32} \tag{5}$$

(iii) For turbulent flow the following correlation is adapted ($4240 < \mathrm{Re} < 10^6$)

$$f = \left\{\frac{0.279}{\left[1.82\log(\mathrm{Re}_b) - 1.64\right]^2}\right\}\left\{\frac{7 - \left(\frac{\mu_b}{\mu_w}\right)}{6}\right\} \tag{6}$$

This expression is based on the Filonenko (1954) and Petukhov (1970) correlations. The inlet and exit pressure losses were calculated as half a dynamic head and one dynamic head respectively.

Uncertainties that affect calculation of the bulk coolant temperature and the local flow conditions were also included in the analysis. Hot spot factors of 1.62 (when analyzing the average channel) and 1.23 (when analyzing the hot channel) were used. An additional uncertainty of 10% was also applied to the temperature rise of the hot channel. These factors and channels were chosen to reflect some "smearing" of the power distribution expected after shutdown due to the increased importance of gamma heating. A friction factor uncertainty of 1.10 was also included.

For the present calculations, incipient boiling was used as the thermal design limit and was calculated using the Bergles and Rohsenow (1964) correlation:

$$q_{IB} = F_{D_2O} \times 1.7978 \times 10^{-6} \, P^{1.156} \left[1.8\left(T_w - T_s\right)\right]^{\left(\frac{2.8285}{P^{0.0234}}\right)} \tag{7}$$

where F_{D_2O} is a correction factor for applying the Bergles and Rohsenow correlation to heavy water (P is in MPa, T is in degrees Kelvin, and q_{IB} is in kW/m^2). This factor is pressure dependent and its value is correlated as (Yoder, et. al. 1994):

$$F_{D_2O} = \left(a + c \cdot P + e \cdot P^2 + g \cdot P^3\right) / \left(1 + b \cdot P + d \cdot P^2 + f \cdot P^3\right) \tag{8}$$

Values for the correlating coefficients a through g are given in the nomenclature. Since many details of the refueling process have yet to be determined, a parametric study was performed. Three parameters were examined: the effect of location within the pool [i.e., the pool depth where the element is located (defined from the top surface of the pool liquid to the bottom of the element)], the effect of coolant temperature, and the effect of adding a chimney above the core to improve natural circulation performance. The present analysis assumes no obstruction to the flow either at the bottom or top of the coolant channel and that the fuel element is submerged in an infinite coolant pool. Since the ANSR consists of two separate spent fuel elements, each of which will be separately cooled by pool water, the maximum power (the power where one point in the core is at the incipient boiling limit) for each spent fuel element was calculated based on the beginning of cycle (BOC) power distribution for the lower element and the end of cycle (EOC) power distribution for the upper element. These conditions are the limiting distributions for each element.

Figure 4 shows the incipient boiling power (total core power) for an average channel that will limit the lower element at BOC as a function of the coolant pool temperature and depth. The thermal power limit is almost a linear function of the initial coolant temperature for a fixed coolant depth. The thermal power limit decreases as the coolant bulk temperature approaches the saturation temperature. An increase in coolant depth, on the other hand, causes an increase in local static pressure that raises the incipient boiling limit.

Figure 5 shows the core inlet coolant velocity for the conditions of Figure 4. Initially, the velocities show a slight increase as the pool bulk temperature rises (35°C to 60°C), they then drop with further temperature increases.

Figure 6 shows the radial variation in margin to incipient boiling temperature (defined as the difference between the surface temperature and that required to initiate boiling) for both the discrete solution as well as the average solution (one which assumes a uniform radial power density, based on radially averaged conditions, at each axial position). The graph shows the outer portion of the channel to be more restrictive because of higher power densities in these areas.

Figures 7 and 8 show the inlet and exit coolant velocities as a function of radial location for the lower fuel element. The average solution for those axial locations is also presented. Results indicate higher coolant velocities for the average solution than for the discrete solution. This occurs because the uncertainties used in the average channel solution and the discrete solution are not the same (as previously discussed). Figure 9 shows the effect of adding a chimney to the lower element. The chimney was assumed to be an extension of the outside boundary of the element, where the density of the bulk liquid remained constant at the average core exit value. The addition of a chimney increased the buoyancy forces available to drive the flow, and caused an increase in coolant velocity, an enhanced heat transfer coefficient, and greater limiting power. Results for the upper fuel element were similar to those discussed above. However, the lower element limits overall core power.

SUMMARY

In order to refuel the ANSR reactor within the desired 4-day shutdown period between fuel cycles, some means of removing several hundred kilowatts of decay heat is needed. One means is to rely on natural circulation cooling to provide the desired amount of heat rejection capability. Calculations using a modified version of the computer code NATCON show that very low coolant velocities (a few cm/s) can be expected under natural circulation conditions.

In conclusion, a new, revised version of the NATCON computer code is available for steady-state analysis of research reactors cooled by natural convection. The revised code can now accommodate a two-dimensional power density distribution. The predictive correlations for the friction and heat transfer calculations are also more accurate, and thermophysical correlations for heavy water have been included.

REFERENCES

A. E. Bergles and W. M. Rohsenow, "The Determination of Forced Convection Surface-Boiling Heat Transfer," *ASME Journal of Heat Transfer*, Vol. 86, pp. 365-372, 1964.

C. F. Bonilla, "Fluid Flow in Reactor Systems," p. 9-35, *Nuclear Engineering Handbook*, H. Etherington (ED.), 1st Ed., McGraw-Hill, 1958.

E. R. G. Eckert and T. F. Irvine, Jr., *Incompressible Friction Factor, Transition and Hydrodynamic Entrance Length Studies of Ducts with Triangular and Rectangular Cross Sections,* WADC Tech. Report 58-85, 1957.

Y. Elkassabgi, G. L. Yoder, and W. R. Gambill, "Thermal-Hydraulic Analysis of the Advanced Neutron Source Reactor Refueling Process," *Nuclear Technology*, Journal of the American Nuclear Society, Vol. 105, PP 411-420, March 1994.

G. K. Filonenko, "Hydraulic Resistance in Pipes," *Teploenergetika,* 1, No. 4, pp. 40-44, 1954.

W. M. Kays and M. E. Crawford, Convective Heat and Mass Transfer, 2nd Edition, McGraw Hill publishing company, pp.114-117, 1980.

H. A. McLain, *HFIR Fuel Element Steady State Heat Transfer Analysis Revised Version,* ORNL-TM-1904, December 1967.

B. S. Petukhov, "Heat Transfer and Friction in Turbulent Pipe Flow with Variable Physical Properties," in *Advances in Heat Transfer*, Vol. 6, pp. 504-564, Academic Press, 1970.

R. K. Shah and A. L. London, "Laminar Flow Forced Convection in Ducts," *Advances in Heat Transfer,* Supplement 1, Chapter VII, Rectangular Ducts, pp. 199-201, Academic Press, 1978.

M. Siman-Tov, W. R. Gambill, W. R. Nelson, A. E. Ruggles, G. L. Yoder, "Thermal-Hydraulic Correlations for the Advanced Neutron Source Reactor Fuel Element Design and Analysis," Proc. American Society of Mechanical Engineers Winter Meeting, Atlanta, Georgia, December 1-6, 1991.

R. S. Smith and W. L. Woodruff, *A Computer Code, NATCON, for the Analysis of Steady-state Thermal-Hydraulics and Safety Margins in Plate-Type Research Reactors Cooled by Natural Convection,* ANL/RERTR/TN-12, Argonne National Laboratory, December 1988.

Y. Sudo, K. Miyata, H. Ikawa and M. Kaminaga, "Experimental Study of Differences in Single-or Narrow Rectangular Channel," *Journal of Nuclear Science and Technology,* 22[3], pp. 202-212, March 1985.

G. L. Yoder, Jr., et. al., *Steady-State Thermal-Hydraulic Design Analysis of the Advanced Neutron Source Reactor*, ORNL/TM-12398, May 1994.

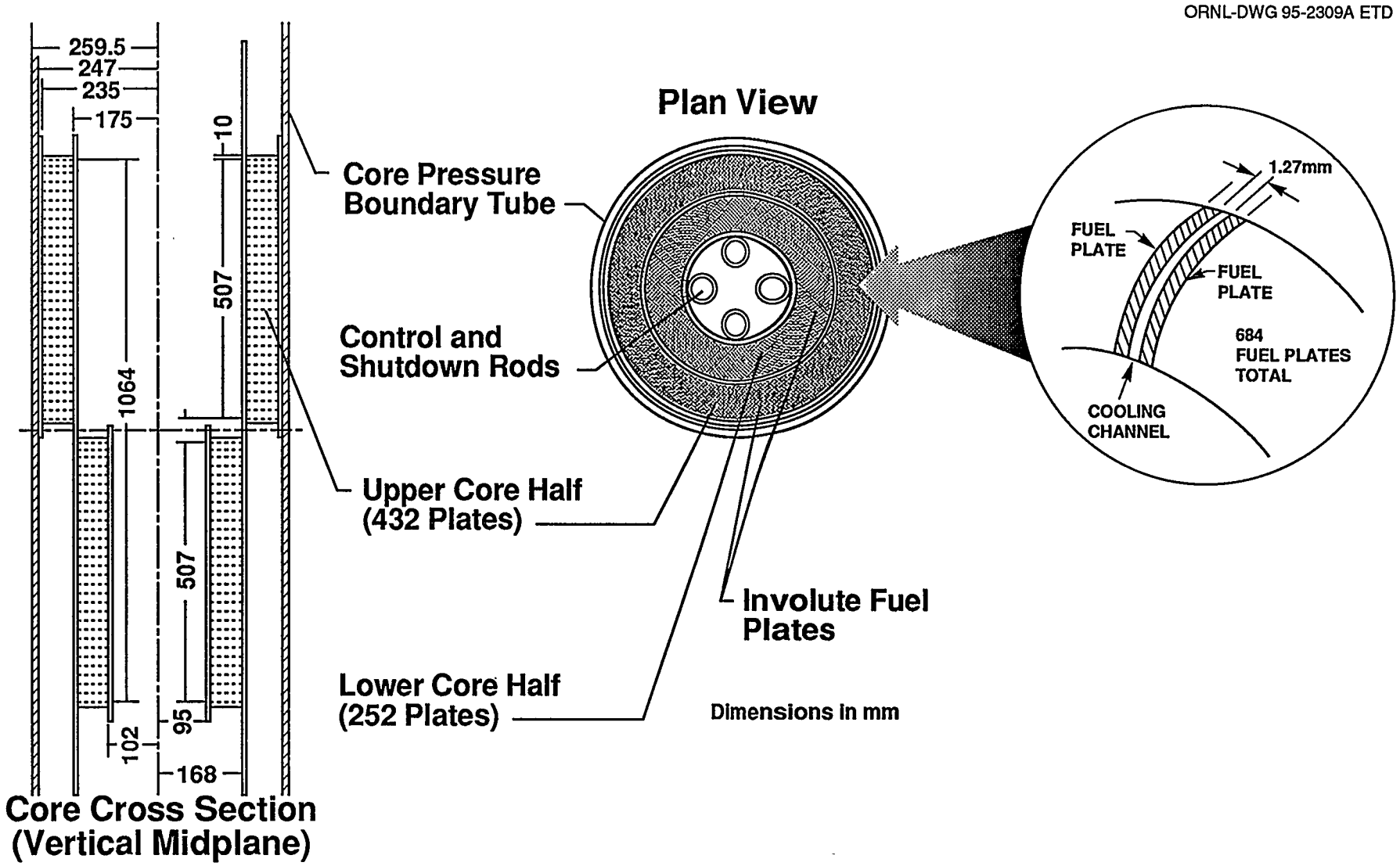

Figure 1. Schematic of ANS core region

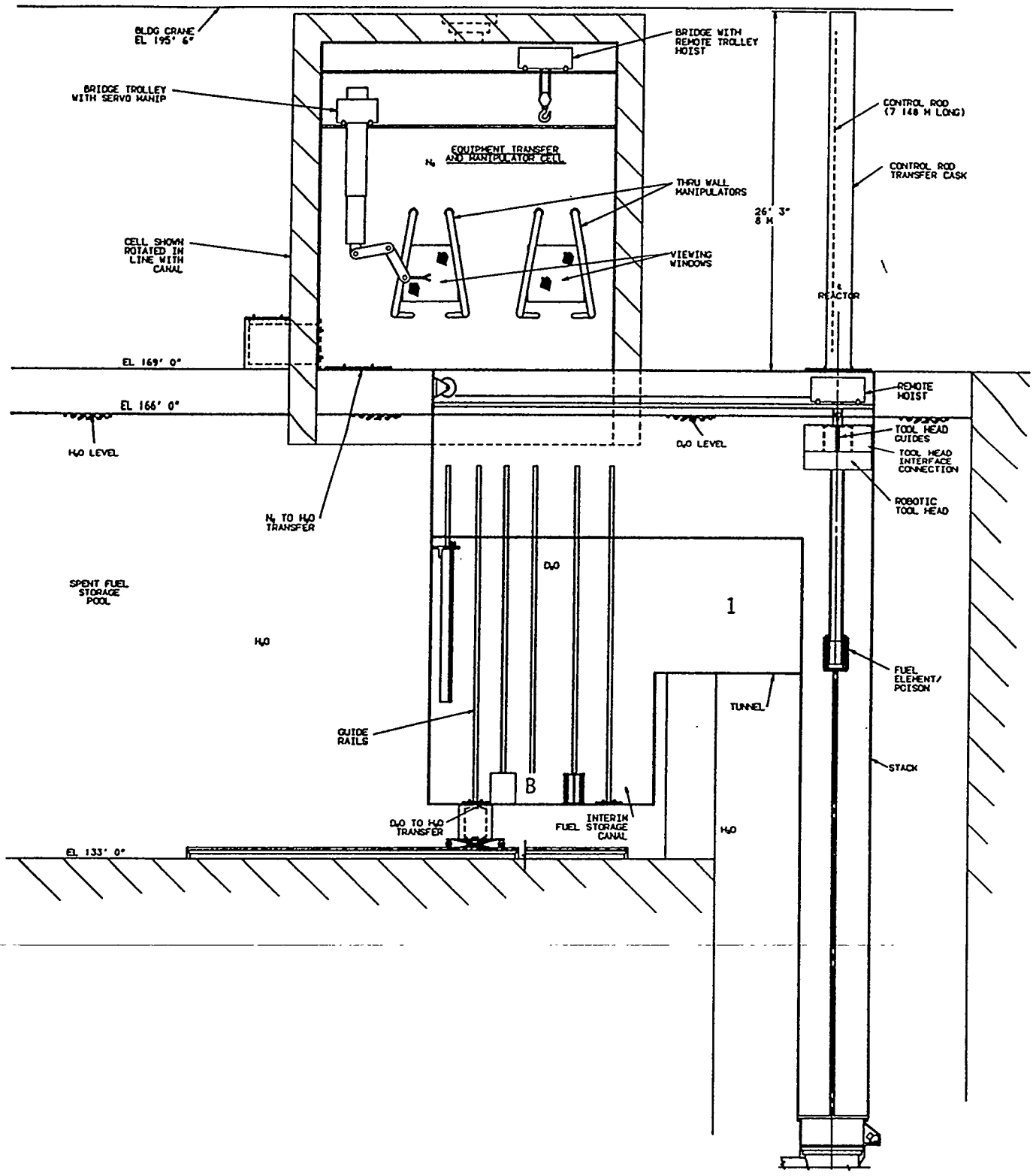

Figure 2. ANS refueling path.

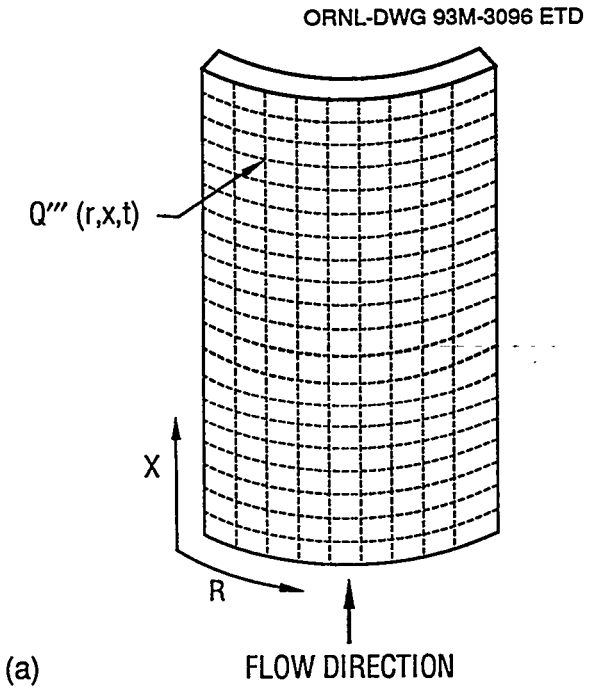

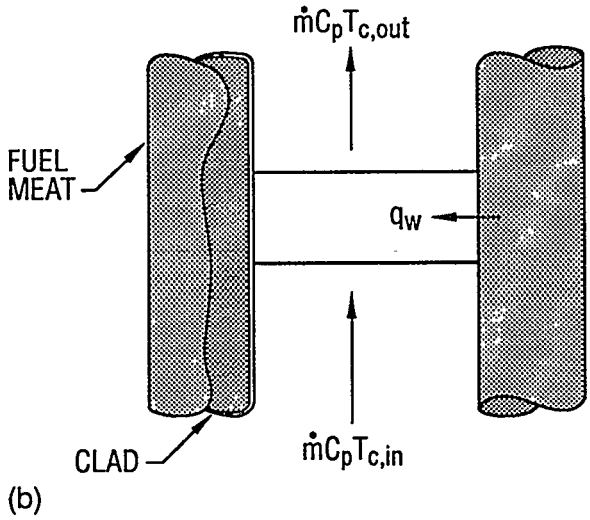

Figure 3. Grid used to analyze ANS refueling process

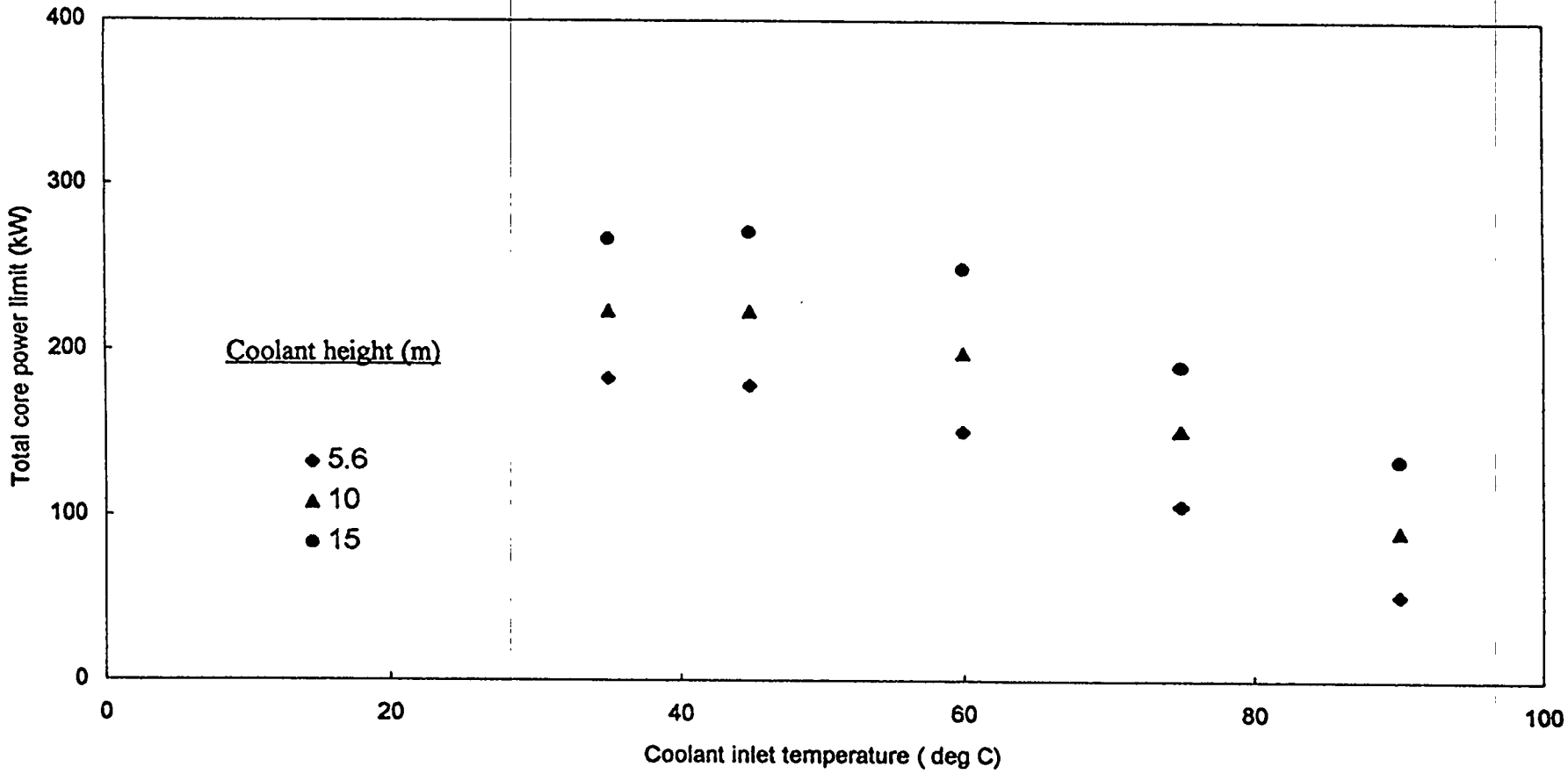

Figure 4. Effect of inlet coolant temperature on the thermal power limit for the lower element.

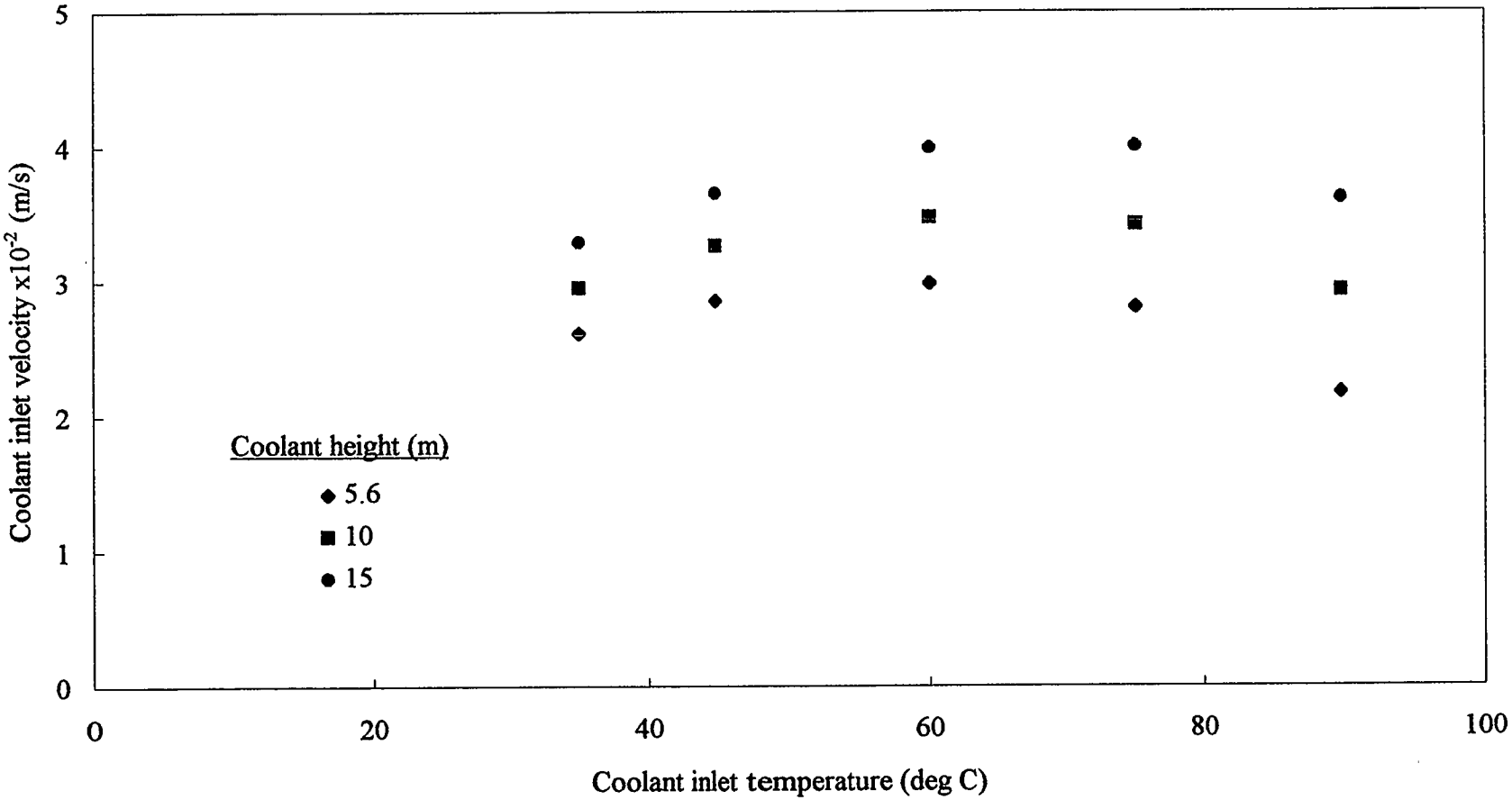

Figure 5. The effect of coolant temeprature on the natural-circulation-induced inlet coolant velocity for lower element.

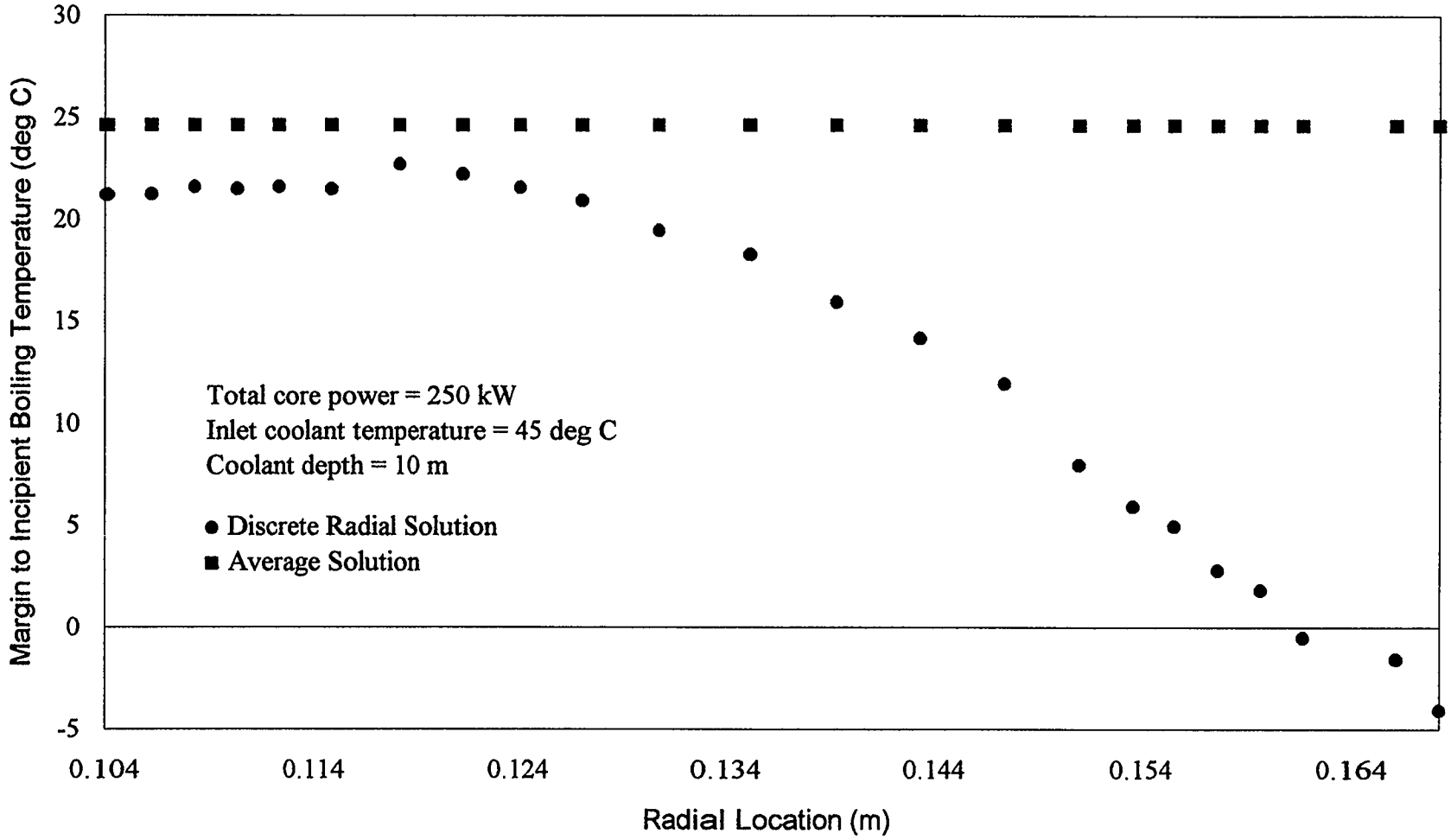

Figure 6. The radial distribution of Margin to Incipient Boiling Temperature in the lower half-core.

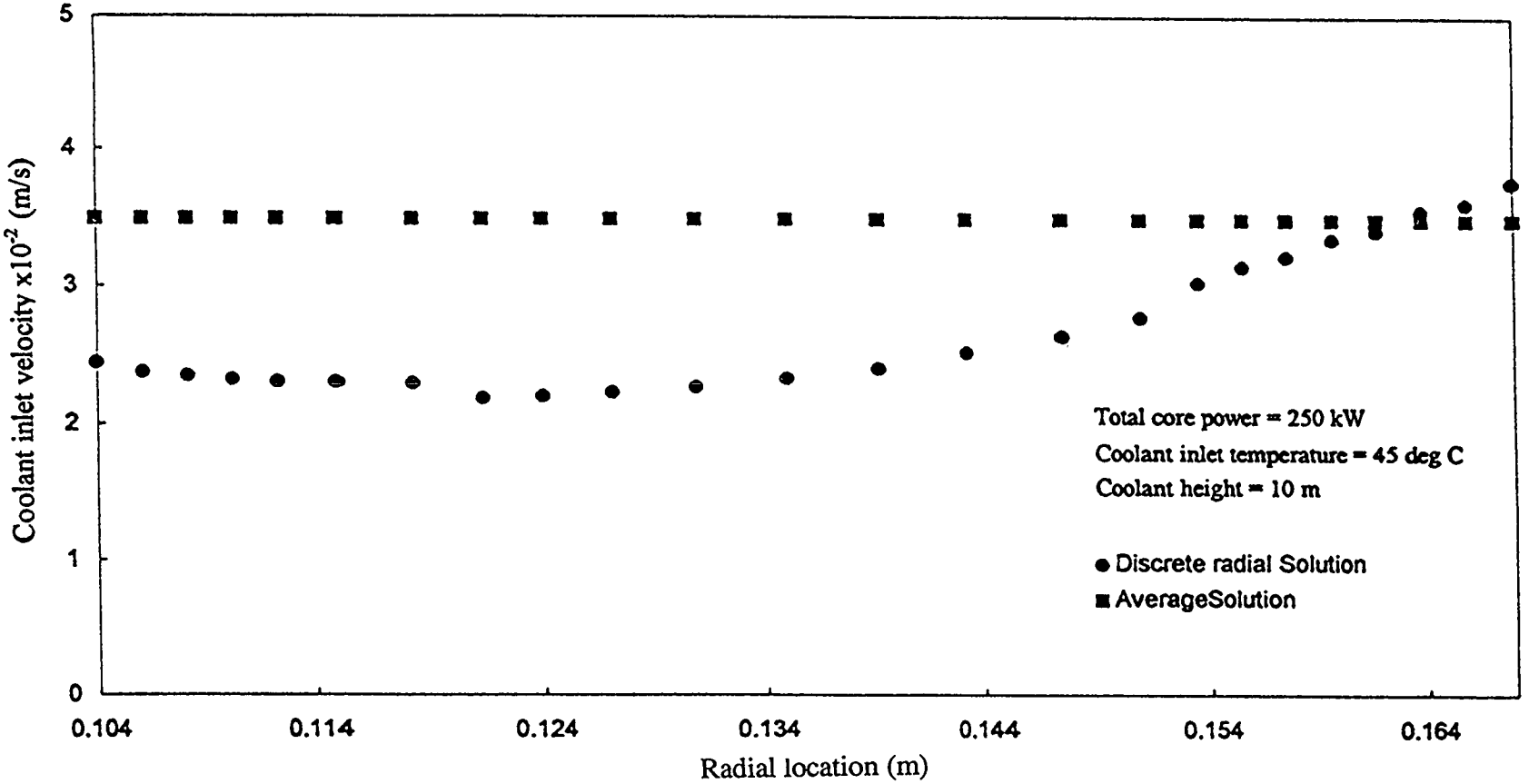

Figure 7. The radial distribution of coolant velocity in the lower element.

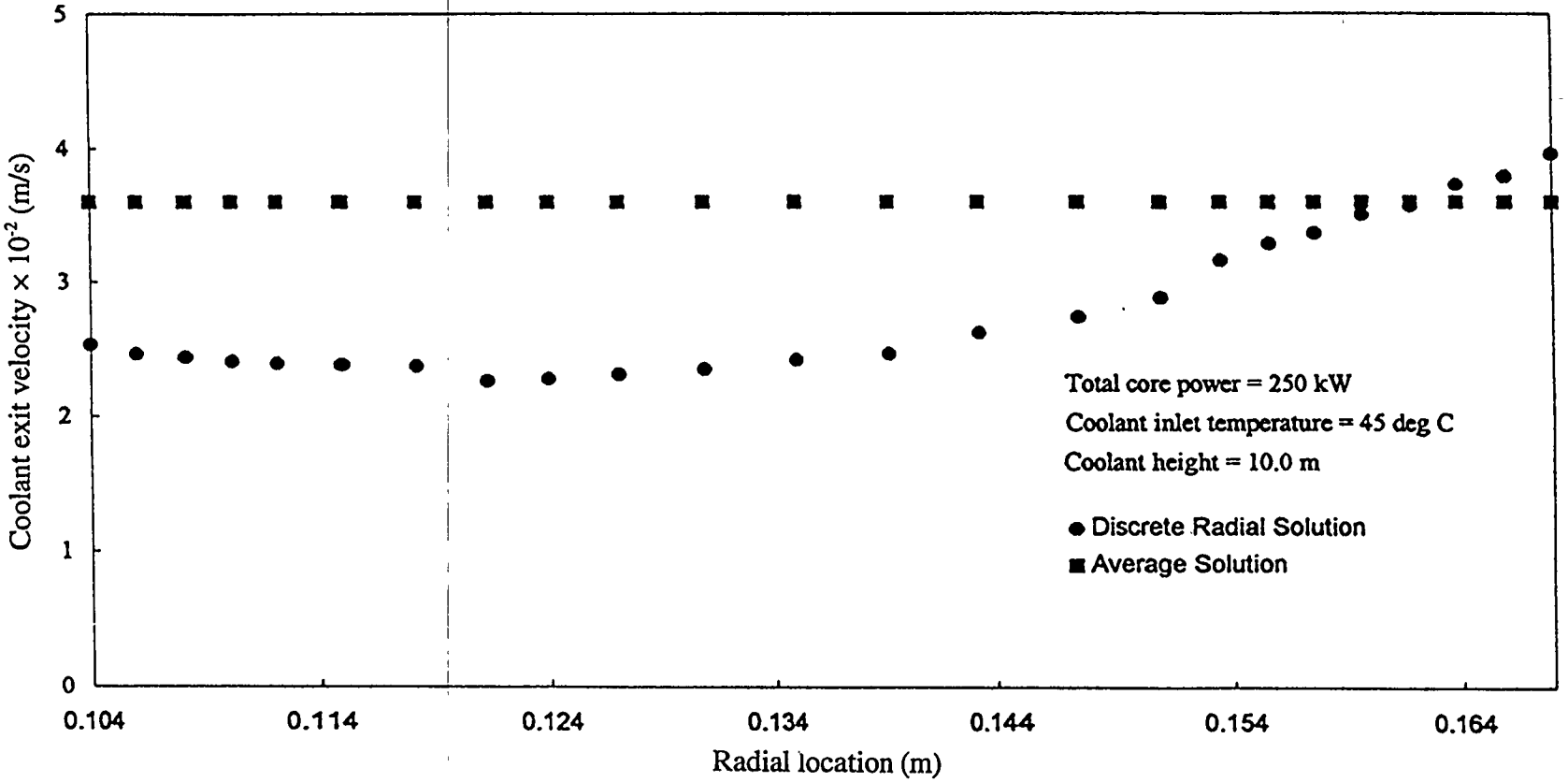

Figure 8. The radial distribution of the coolant exit velocity of the lower element.

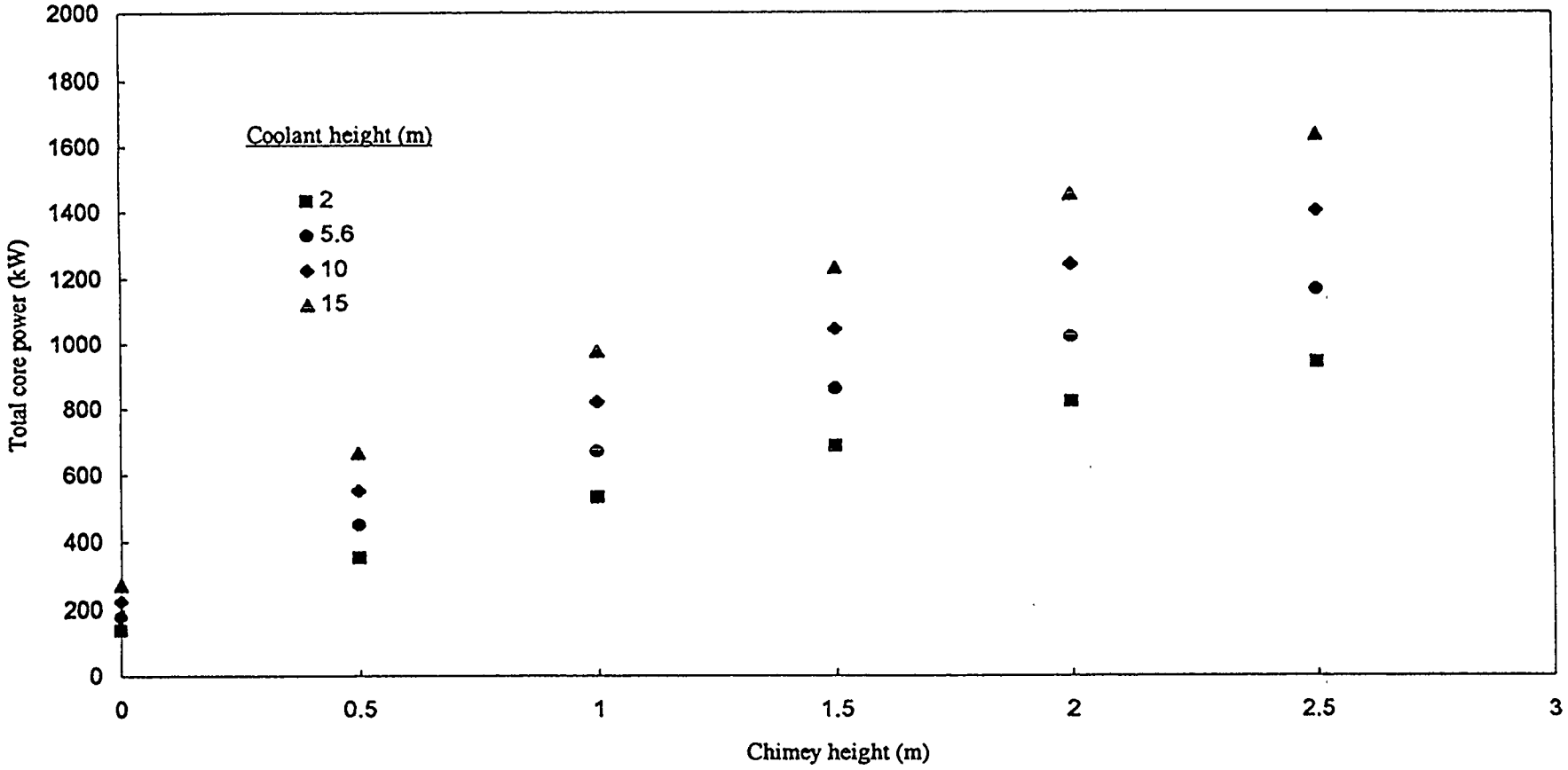

Figure 9. Effect of chimney on the thermal power limit of the lower element.

Cold Source Vessel Development for the Advanced Neutron Source

P. T. Williams and A. T. Lucas
Oak Ridge National Laboratory, Oak Ridge, Tennessee, USA

ABSTRACT

The Advanced Neutron Source (ANS), in its conceptual design phase at Oak Ridge National Laboratory (ORNL), will be a user-oriented neutron research facility that will produce the most intense flux of neutrons in the world. Among its many scientific applications, the production of cold neutrons is a significant research mission for the ANS. The cold neutrons come from two independent cold sources positioned near the reactor core. Contained by an aluminum alloy vessel, each cold source is a 410 mm diameter sphere of liquid deuterium that functions both as a neutron moderator and a cryogenic coolant. With nuclear heating of the containment vessel and internal baffling, steady-state operation requires close control of the liquid deuterium flow near the vessel's inner surface. Preliminary thermal-hydraulic analyses supporting the cold source design are being performed with multi-dimensional computational fluid dynamics simulations of the liquid deuterium flow and heat transfer. This paper presents the starting phase of a challenging program and describes the cold source conceptual design, the thermal-hydraulic feasibility studies of the containment vessel, and the future computational and experimental studies that will be used to verify the final design.

INTRODUCTION

The Advanced Neutron Source (ANS), now in its conceptual design phase at the Oak Ridge National Laboratory (ORNL), is being planned as a user-oriented neutron research facility that will produce the most intense flux of thermal and subthermal neutrons in the world [1]. Representing a significant research mission of the ANS, the production of cold neutron beams is one of many scientific applications for the 330 MW(f) reactor that provides the source of neutrons.

In the ANS conceptual design, cold neutrons are derived from two independent cold sources placed near the reactor core. Each cold source is a 410 mm diameter sphere of liquid deuterium contained by an aluminum alloy vessel. The liquid deuterium serves both as a neutron moderator and a single-phase cryogenic coolant for the containment vessel. For each cold source, neutron and gamma bombardment produces a heat load of approximately 15 kW in the liquid deuterium and an additional 15 kW in the vessel. The objective is to keep the pressurized cryogen, circulating through the cold source, free from boiling under normal operation and maintain a minimum temperature as low as practicable with a liquid flow rate of 6.5 L/s (~1.0 kg/s). The temperature of the liquid deuterium supplied to the vessel is 20 K (1.3 K above the triple point); the deuterium exit temperature is 25 K (2 K below the saturation temperature for a minimum system pressure of 0.25 MPa). Because of these rather narrow margins to the phase change temperatures, careful control of all parameters is vitally important. Consistent control of the cryogen velocity over the entire inner surface of the vessel is necessary because of the requirement to remove 15 kW of heat from the vessel. This control is achieved by internal baffling, designed to add as low a mass as possible to minimize the heat load. Experimental flow visualization tests using a surrogate

fluid and transparent candidate cold source vessel designs will provide valuable general indications of internal flow behavior. Thermal-hydraulic analyses will also be performed using two- and three-dimensional numerical simulations. Since published data are limited over the range of interest, an experimental program for the measurement of thermophysical property and heat transfer data is planned to support the computational thermal-hydraulic design studies. It will be essential to ultimately consider two-phase flow as part of the analysis of certain normal and abnormal operational transients. Final verification of the selected design will be provided by setting up a full-scale test loop with realistic heat loads and liquid deuterium flows. Throughout these design-verification tests, the outer surface temperature of the vessel will be monitored by a phosphor-thermometry technique, available at ORNL, to identify possible hot-spot regions.

This paper describes the cold source design concept and the results of initial supporting thermal-hydraulic feasibility studies.

COLD SOURCE CONCEPTUAL DESIGN

Many current cold source designs operate as a closed-loop gravity-driven thermosyphon in which the moderator material (e.g., hydrogen or a hydrogen-bearing cryogen) condenses in a heat exchanger, flows by gravity as a subcooled liquid to the moderator vessel, boils in the moderator vessel due to neutronic heating, and returns finally to the condenser as a superheated vapor. There are variants on this principle in which boiling occurs only in the vapor-return piping due to a sufficiently large driving head in the condenser drain line. These systems are practical only with low power applications. Reliability is the primary advantage of thermosyphon systems, since they require no mechanical pumps or control valves and are typically self-adjusting to a range of operating loads.

The high heat loads applied to the ANS cold source, however, presented severe design difficulties for a thermosyphon system. To minimize pressure losses, a large vapor-return line would have been required, occupying otherwise heavy water moderator space resulting in reduced cold-neutron yields and increased shielding problems. Therefore a decision was taken to use a flooded single-phase system in which liquid deuterium, pressurized to 0.4 MPa, is circulated in a closed-loop by a mechanical cryogenic pump. Since operation of the cold source and, therefore, the reactor is dependant on this circulator, it is important to provide redundancy in the design. A second circulator unit will be installed to obtain the necessary redundancy.

Figure 1 shows the proposed operating envelope superimposed on the vapor pressure curve for deuterium. A deuterium flowrate of 6.5 L/s (~1.0 kg/s) results in a temperature rise of 5 K across the moderator vessel, bringing the maximum temperature of the liquid to within 2 K of its saturation temperature (27 K) at the minimum design pressure of 0.25 MPa (see Table 1). The liquid deuterium flows in a closed loop with a storage vessel designed to accommodate expansion when the system is warm. The additional storage volume allows the system to remain at an overall maximum pressure of 0.4 MPa at all times.

Cooldown will always occur with the reactor off, and the remaining heat load on the cold source will amount to no more than 1 kW. The cryogenic circulators will not be used during cooldown, so the loop is designed to promote natural convection. Initially, it might be necessary to circulate the warm deuterium gas until its density has increased enough to promote adequate natural convection. The liquefaction phase of startup requires natural convection to avoid vapor-locking the cryogenic circulator

impellers.

Heat transfer must be strictly controlled throughout the cooldown phase to remove the enthalpy of the metal components of the loop and limit the cooldown time to about 24 hours. During normal operation when the reactor is at full power and is heating the cold source, the circulating liquid must remove 15 kW from the deuterium itself and a further 15 kW from the vessel walls to maintain temperature control. It is therefore essential to have adequate heat transfer within the cold source vessel. The necessary forced-convection heat-transfer coefficients will be established through internal baffles that provide sufficiently high liquid deuterium velocities next to the inner surface of the containment vessel walls. Figure 2 shows an arrangement in which an inner beryllium baffle shell creates a spherical annulus through which the full liquid flow is forced before circulating through the interior of the cold source sphere. The flow in the cold source interior is strongly 3-dimensional due to the rectangular geometry of the reentrant cavity that partially blocks the interior flow.

The ANS operating cycle, determined by the anticipated burn-up rate of the reactor fuel and fuel inventory, is currently estimated at 21 days. During the four days required for reactor refuelling, the cold source vessel must be heated to 373 K and recooled to operating conditions. This high temperature is required to anneal the vessel material, thereby redistributing clusters of silicon produced by nuclear transmutation. The heat to raise the vessel temperature will be provided by residual reactor energy immediately following shut down. To prevent overheating of the vessel, cooled deuterium gas will be circulated through the cold source. Additional feasibility studies of this operation are planned.

THERMAL-HYDRAULIC MODEL DESCRIPTION

During the conceptual design phase of the cold source, the thermal-hydraulic studies have focused on determining the feasibility of using single-phase forced convection to remove the 30 kW of heat generated by neutron and gamma bombardment of the containment vessel and liquid deuterium during normal steady-state operation. The necessary forced-convection heat transfer at the inner surface of the containment vessel is accomplished by directing the recirculating liquid deuterium, as it first enters the cold source, through a spherical annulus formed by an internal beryllium baffle and the aluminum containment vessel wall. This annulus was modeled, using the computational fluid dynamics (CFD) computer program CFDS-FLOW3D [2], with a hemispheric 2-dimensional axisymmetric geometry for the half of the cold source sphere near the reactor. The model included internal heat generation and conduction within the 1.5 mm thick aluminum shell and the 1 mm thick beryllium inner baffle, as well as internal heat generation, turbulent flow, and heat transfer within the 2 mm wide liquid deuterium annular flow field. A schematic of the model is shown in Fig. 3 where the computational domain includes the 38 mm ID inlet pipe, the aluminum containment vessel, the beryllium baffle, the spherical annulus, and the outlet transition into the interior of the cold source. The cold source interior was not explicitly included in the model, but its influence on heat transfer in the annulus was approximated with a constant heat transfer coefficient and cold source interior D_2 temperature, T_∞, applied to the inner wall of the baffle.

For a design volumetric flowrate of 6.5 L/s, the Reynolds number, Re, of the liquid deuterium in the annulus varies from a maximum of approximately 2.5×10^5 near the inlet and outlet transitions to a minimum of approximately 5×10^4 at the equator. This Reynolds number range (where $\mathrm{Re} \equiv G_b D_h/\mu$ is based on the local mass flux, $G_b = \dot{m} / [\pi \cos\theta\,(205^2 - 203^2)]$ where $\dot{m}$ is the total mass flowrate and θ is defined in Fig. 3, and the hydraulic diameter of the annulus, $D_h = (D_o - D_i) = 4$ mm) is representative of

fully-developed turbulent flow in interior channels. Deviations from fully-developed velocity and temperature profiles should be expected, however, in channel transition regions.

The turbulent flow of a liquid cryogen with internal heat generation is governed by the physical principles of conservation of mass, momentum, and energy. An appropriate mathematical form for this conservation law system is the coupled set of nonlinear partial differential equations called the Reynolds-averaged Navier-Stokes equations for an incompressible (constant density) fluid [2]. Using index notation, steady-state forms for the conservation of mass, momentum, and energy are the continuity equation

$$\frac{\partial U_j}{\partial x_j} = 0 \quad , \tag{1}$$

the momentum equations,

$$\frac{\partial}{\partial x_j}\left[\rho U_i U_j - \mu\left(\frac{\partial U_i}{\partial x_j} + \frac{\partial U_j}{\partial x_i}\right) + \rho\overline{u_i' u_j'}\right] + \nabla p = 0 \quad , \tag{2}$$

and the energy equation,

$$\frac{\partial}{\partial x_j}\left(\rho U_j H - \rho\alpha\frac{\partial H}{\partial x_j} + \rho\overline{u_j' h'}\right) - S_H = 0 \quad , \tag{3}$$

where ρ, μ, and α are the density, molecular dynamic viscosity, and molecular thermal diffusivity, respectively, of the fluid; U_i is the time-averaged velocity vector resolution of the mean flow field; H is the time-averaged static enthalpy; p is the *motion* pressure (equal to the thermostatic pressure minus the hydrostatic pressure), and S_H represents any distributed volumetric heat sources. Repeated indices imply summation over the computational domain, $\mathbb{R}^n$. In CFDS-FLOW3D, Eqs. (1)-(3) are discretized using a nonstaggered finite volume method, and steady-state solutions for the discrete equation set are calculated using the SIMPLEC [3] algorithm.

Arising from the time-averaging of the convection terms in the original instantaneous conservation law system, statistical double correlations appear in Eqs. (2) and (3) that characterize the effects of turbulence on the transport of momentum (Reynolds stresses, $\rho\overline{u_i' u_j'}$), and thermal energy (turbulent heat fluxes, $\rho\overline{u_i' h'}$) in the mean flow field. Transport equations for each of these double correlations can be derived, but these new equations unfortunately contain additional unknown higher-order correlations; therefore, Eqs. (1)-(3) do not represent a closed set. An exact closure for these correlations does not exist. The result is the classic *turbulence closure problem*, and approximate closure is the task of turbulence models.

For engineering calculations, the most commonly used turbulence models are based upon the Boussinesq eddy-viscosity approximation, where the Reynolds stresses are modeled by a constitutive relation having a form similar to the Stokes viscosity law for Newtonian fluids,

$$-\rho\overline{u_i' u_j'} = -\frac{2}{3}\rho\kappa\delta_{ij} + \mu_T\left(\frac{\partial U_i}{\partial x_j} + \frac{\partial U_j}{\partial x_i}\right) \quad , \tag{4}$$

where κ is the turbulent kinetic energy per unit mass ($\kappa \equiv \frac{\overline{u_i' u_i'}}{2}$), δ_{ij} is the Kronecker delta, and μ_T is the

eddy viscosity. Similar *eddy diffusivity* hypotheses, coupled with Reynolds-analogy approximations, result in constitutive relations for the turbulent heat flux

$$-\rho\overline{u_i'h'} = \Gamma_H \frac{\partial H}{\partial x_i} = \frac{\mu_T}{\sigma_H}\frac{\partial H}{\partial x_i} \quad , \tag{5}$$

where Γ_H is the thermal eddy diffusivity, and σ_H is the turbulent Prandtl number. Equations (4)-(5) represent defining relations for the eddy viscosity and eddy diffusivities. A method for calculating these quantities remains to be identified to obtain closure.

From dimensional arguments, turbulence models based on the Boussinesq approximation, Eq. (4), assume that the eddy viscosity is proportional to the product of length and velocity scales that are characteristic of the turbulence. The two-equation κ-ϵ (ϵ is the isotropic turbulence dissipation rate) turbulence model uses the Prandtl-Kolmogorov equation,

$$\mu_T = C_\mu \rho \frac{\kappa^2}{\epsilon} \quad , \tag{6}$$

where C_μ is an empirically-derived constant, to relate κ and ϵ to the eddy viscosity, μ_T. The velocity scale is $\sqrt{\kappa}$, and the characteristic length scale is $\kappa^{3/2}/\epsilon$. Transport equations for κ and ϵ are solved to complete the approximate turbulence closure,

$$\frac{\partial \rho U_j \kappa}{\partial x_j} - \frac{\partial}{\partial x_j}\left[\left(\mu + \frac{\mu_T}{\sigma_\kappa}\right)\frac{\partial \kappa}{\partial x_j}\right] - (\mu + \mu_T)\frac{\partial U_i}{\partial x_j}\left(\frac{\partial U_i}{\partial x_j} + \frac{\partial U_j}{\partial x_i}\right) + \rho\epsilon = 0 \quad , \tag{7}$$

$$\frac{\partial \rho U_j \epsilon}{\partial x_j} - \frac{\partial}{\partial x_j}\left[\left(\mu + \frac{\mu_T}{\sigma_\epsilon}\right)\frac{\partial \epsilon}{\partial x_j}\right] - C_1\frac{\epsilon}{\kappa}(\mu + \mu_T)\frac{\partial U_i}{\partial x_j}\left(\frac{\partial U_i}{\partial x_j} + \frac{\partial U_j}{\partial x_i}\right) + C_2\rho\frac{\epsilon^2}{\kappa} = 0 \quad , \tag{8}$$

where σ_κ, σ_ϵ, C_1, and C_2 are empirically-derived constants. In the standard high-Reynolds number κ-ϵ model, the computational domain does not extend all the way to solid walls. So-called *wall functions*, derived from the logarithmic "law-of-the-wall" velocity profile, are employed to simulate the effect of the no-slip wall boundary condition on the flow field adjacent to the wall. Related *heat flux wall functions* are also available for the energy equation to calculate the heat transfer between the flow domain and solid boundaries [4].

The Boussinesq approximation, Eq. (4), assumes that the eddy viscosity is isotropic, i.e., the eddy viscosity is the same for all components of the Reynolds stress tensor. This assumption prevents eddy-viscosity turbulence models from predicting certain turbulence-induced secondary flows. One approach to calculating approximations for the Reynolds stresses and turbulent heat fluxes that does not involve the eddy viscosity hypothesis is to derive transport differential equations for the individual components of the Reynolds stresses, using modeled terms to approximate the higher-order correlations to obtain

$$\frac{\partial}{\partial x_k}\left(\rho\overline{u_i'u_j'}U_k\right) - \frac{\partial}{\partial x_k}\left[\rho\frac{C_s}{\sigma_{DS}}\frac{\kappa}{\epsilon}\overline{u_i'u_l'}\frac{\partial\overline{u_k'u_j'}}{\partial x_l}\right] - P_{ij} - \Phi_{ij} + \frac{2}{3}\rho\epsilon\delta_{ij} = 0 \quad , \tag{9}$$

where P_{ij} is the shear-stress-production tensor,

$$P_{ij} = -\rho\left(\overline{u_i'u_k'}\frac{\partial U_j}{\partial x_k} + \frac{\partial U_i}{\partial x_k}\overline{u_k'u_j'}\right) \quad , \tag{10}$$

and Φ_{ij} is the pressure-strain tensor,

$$\Phi_{ij} \equiv -\rho C_{1s}\frac{\epsilon}{\kappa}\left(\overline{u_i'u_j'} - \frac{2}{3}\kappa\delta_{ij}\right) - C_{2s}\left(P_{ij} - \frac{1}{3}P_{kk}\delta_{ij}\right) \tag{11}$$

In addition to the differential transport equations for the Reynolds stress tensor components and the dissipation rate ϵ, the differential Reynolds-flux turbulence model (DFM) solves a transport equation for the Reynolds turbulent heat flux, $\rho\,\overline{u_i'h'}$, the statistical double correlation between the velocity fluctuations and the fluctuating instantaneous static enthalpy, h' ,

$$\frac{\partial}{\partial x_j}\left(\rho\,\overline{u_i'h'}\,U_j\right) - \frac{\partial}{\partial x_k}\left(\rho\frac{C_s}{\sigma_{DF}}\frac{\kappa}{\epsilon}\overline{u_i'u_j'}\frac{\partial\overline{u_k'h'}}{\partial x_j}\right) - P_{Fi} - \pi_i = 0 \quad , \tag{12}$$

where P_{Fi} is the mean-field-production vector,

$$P_{Fi} \equiv -\rho\left(\overline{u_i'u_j'}\frac{\partial H}{\partial x_j} + \frac{\partial U_i}{\partial x_j}\overline{u_j'h'}\right) \quad , \tag{13}$$

and π_i is a pressure-scalar gradient term,

$$\pi_i = -\rho C_{1F}\frac{\epsilon}{\kappa}\overline{u_i'h'} - \rho C_{2F}\frac{\partial U_i}{\partial x_j}\overline{u_j'h'} \quad . \tag{14}$$

The model constants in Eqs. (9)-(14), σ_{DS}, σ_{DF}, C_s, C_{1s}, C_{2s}, C_{1F}, and C_{2F}, are assigned default values as discussed in [2], and wall functions are applied to connect the computational domain to solid wall boundaries. Additional wall-reflection terms are included in the pressure-scalar gradient vector π_i as discussed by Clarke and Wilkes [5]. Both the two-equation κ-ϵ model and the DFM were used in the sensitivity studies discussed in the next section.

Thermophysical properties (thermal conductivity, density, and specific heat) for aluminum and beryllium were taken from Touloukian [6] for the cryogenic temperature range of interest, 20-30 K. The results of an extensive literature survey of property data (dynamic viscosity, density, specific heat, and thermal conductivity) for liquid deuterium by Bass [7] were also used in the model development.

RESULTS AND DISCUSSION

An initial meshing study was carried out to determine the spanwise resolution required to obtain essentially grid-independent solutions. For a deuterium mass flowrate of 1.02 kg/s, inlet temperature of 20 K, and a uniform nuclear heating rate of 10.94 kW in the aluminum vessel hemisphere, steady-state solutions using spanwise discretizations across the annulus of 5, 10, and 15 finite volumes showed only small differences in the pressure drop and temperature distributions for the 10 and 15 volume cross-channel cases. Therefore, all subsequent cases employed 15 finite volumes distributed uniformly across the annulus. The flow path within the annulus was discretized with 200 columns of cross-channel rows

nonuniformly graded to concentrate the mesh near the inlet and outlet transition regions. Different gradings were also tested to determine a grid-independent configuration.

The results of thirteen steady-state solutions are summarized in Table 2 where the test matrix includes variations in mass flowrate, nuclear heat generation, heat transfer links to the cold source interior, and annulus geometry. Of primary interest are the calculated pressure drop from the 38 mm ID inlet to the outlet of the model (at the point of entry into the cold source interior), temperatures of the liquid deuterium, and the wall-temperature distributions in the aluminum containment vessel (the outer wall of the annulus) and in the beryllium baffle (the inner wall of the annulus). Both the DFM and κ-ϵ turbulence models were used for the initial test cases, and the DFM consistently predicted maximum wall temperatures approximately 0.2 K higher than the κ-ϵ turbulence model. No significant differences in pressure drop or flow field velocity distributions were observed between the two models. The greater detail available in the DFM may prove to be more important in the 3-dimensional models planned for future studies. All of the results presented in Table 2 were calculated using the DFM.

Pressure drops of from 0.107 to 0.154 MPa were calculated in the first three cases. A significant contributor to the pressure drop in these cases was a flow separation around a sharp reentrant corner in the transition of the flow from the 38 mm ID inlet line to the 2 mm annulus. The flow separation was removed by adding a curvature (7 mm radius) to the outer wall geometry in this region, thus emphasizing the importance of smooth transitions in the piping design. For the remaining cases the pressure drops in the liquid deuterium were approximately 0.08 MPa for the design flow rate of 1.02 kg/s (0.51 kg/s in the model) and 0.11 MPa for a 20% higher flow rate of 1.224 kg/s (0.612 kg/s in the model) in Case 6. Cases 4 through 9 demonstrated the sensitivity of the model to nuclear heating levels and distribution, liquid deuterium mass flow rate, and convection heat transfer at the inner wall of the beryllium baffle. The angle θ referred to under the column heading "Heat Flux Distribution" is the angle with respect to the horizontal, where $\theta = 0$ is the point on the cold source surface nearest to the reactor, see Fig. 3. Cases 10 and 11 checked the sensitivity of the model when the annulus width was increased to 3 mm for uniform and distributed nuclear heating, respectively. The increased cross-sectional flow area reduced the pressure drop to 0.04 MPa.

For all of the simulations studied, the liquid deuterium remained subcooled over the complete flow path through the annulus. In calculating wall superheat ($T_{wall} - T_{sat}$), the saturation temperature, T_{sat}, for each case was determined from the minimum calculated pressure equal to 0.4 MPa (the design supply pressure at the inlet to the cold source) minus the total ΔP. Since most of the pressure loss occurred in the transition between the 38 mm ID inlet line and the annulus, the outlet pressure was close to (but always less than) the local pressure at the point of maximum wall superheat. Localized regions of wall superheat ranging from 1 to 3 K were observed in the 2 mm wide annulus. Increasing the annulus width to 3 mm produced maximum wall-superheat values up to 5 K. The calculated temperature distributions for the beryllium inner shell were below the saturation temperature of liquid deuterium for all thirteen test cases.

Case 12 represents the current baseline calculation and includes the most recent nuclear heating estimates for the aluminum containment vessel (10.69 kW for the reactor-side hemisphere) and beryllium baffle (2.74 kW). The nuclear heating within the containment vessel was distributed as a function of distance from the reactor with a cosine function so that the peak heat load occurred at the equator, and the integrated load over the near-reactor-side hemisphere was 10.69 kW. This distribution is conservative in the sense that it over-estimates the peak heat loads at the equator where the liquid deuterium velocities are minimum. The nuclear heating of the beryllium baffle was distributed uniformly over the shell.

Figure 4 shows the computed temperature distribution for Case 12. The maximum vessel temperature of 30.7 K and maximum superheat of 2.3 K occurred at approximately 8 degrees below the equator. The first liquid deuterium node next to the maximum wall temperature node has a subcooled temperature of 23.7 K. Across the channel at the beryllium baffle, the liquid deuterium temperature near the wall is 21.8 K with a corresponding 22.9 K wall temperature for the beryllium baffle. The temperature gradient across the beryllium baffle is approximately 0.1 K. Smoothly varying levels of wall superheat were calculated along the aluminum vessel between latitudinal angles 23 degrees above and 40 degrees below the equatorial plane. Outside of this region, the annulus wall temperatures were below the saturation temperature. With the flow converging at the annulus exit, a jet is formed as the liquid deuterium enters the interior of the cold source.

Although the model was not able to predict vapor generation explicitly, sufficient information was available from the simulation to perform some preliminary calculations. The theoretical analysis of Frost and Dzakowic [8] presents a method of calculating the minimum required wall superheat for the initiation of vapor-bubble nucleation. For the heat fluxes, annulus geometry, and fluid properties in the baseline case (Case 12), bubble nucleation is expected to occur for wall-superheat temperatures greater than approximately 0.4 K. Since the calculated maximum wall superheat is 2.3 K, incipient nucleate boiling is probable. As heat conducts from the wall into the bubble, vapor continues to be generated, and the bubble continues to grow until it breaks away from the wall. The size of the bubble at departure can be estimated by the theoretical model of Levy [9] based upon a force balance between the drag imposed on the bubble by the bulk flow and the surface tension of the liquid/vapor interface contacting the wall. For a baseline velocity of 2.65 m/s at the equator, the bubble size at departure is approximately 0.024 mm. This small bubble size is an encouraging result, since it indicates that incipient nucleation will not produce bubbles that extend across a significant portion of the annulus width. However, it is still a design goal to have subcooled walls along the complete flow path. One approach is to increase the liquid deuterium velocities in critical regions by selectively decreasing the flow cross-sectional area.

In Figure 5, the inner baffle has been divided into three sections with the upper and lower section providing a uniform 2 mm gap near the inlet and outlet of the annulus. The geometry of the containment vessel remains the same as the baseline case. The central section of the baffle is replaced by a non-spherical shell in the form of a "bulge" that creates a variable annulus width smoothly changing from 2 mm to 1 mm at the equator and then back to 2 mm. The temperature distribution calculated in Case 13 for this configuration produced subcooled wall temperatures in the region immediately above and below the equatorial plane. Wall superheat was still observed downstream of the equator, as in Case 12. The results of Case 13 offer encouragement that, by additional modifications to the annulus geometry, a completely subcooled annulus design can be developed.

CONCLUSIONS

The preliminary thermal-hydraulic computational studies for the ANS cold source vessel design have been aimed at demonstrating the feasibility of achieving the necessary heat transfer at the vessel walls without producing a significant net vapor generation. Any practical engineering design is the result of optimization and arriving at the best considered compromise. The scale of this problem and the need for accurate results, presents a considerable challenge. However, the modeling to date is relatively basic, and accordingly some fundamental assumptions have been made. As the model complexity increases, three dimensional effects, caused by nonuniform heating, and the presence of an internal cavity will be considered. Also, the effects of temperature gradients within the inner chamber will be investigated.

Manufacturing difficulties and the ability to maintain the annulus geometry after temperature excursions and high levels of radiation might force the design of a more complex baffle configuration. This design effort will be the subject of future work extending the results of the analyses described herein with integrated 3-dimensional numerical models of the cold source interior.

Physical testing is planned to supplement the computer modeling. Initially surrogate fluids will be used to examine the merits of alternative configurations. All designs however must seriously limit the mass of material used as this directly affects the overall heat load. The final design will be validated using full-scale experimental tests to which realistic heat loads will be applied with an authentic flow of liquid deuterium. Heat will be applied to the vessel walls by induction coils providing 15 kW of heat to represent nuclear heat generation in the vessel. After the liquid deuterium exits the annulus, a further 15 kW will be added by an external heater before the flow reenters the interior of the cold source sphere. During this test, the outer surface of the vessel will be scanned to identify any high temperature regions which would indicate poor heat transfer. A further test will use a full-scale loop, built to the correct geometry, to demonstrate the ability of the system design to fill and subcool the loop in its final configuration. A refrigerator capacity of only about 2 kW will be sufficient to simulate realistic cooldown conditions.

REFERENCES

[1] C. D. West, "The U. S. Advanced Neutron Source," *Advanced Neutron Sources 1988, Proc. 10th Meeting of the Int. Collaboration on Advanced Neutron Sources (ICANS X)*, **97**, 643-654 (1988).

[2] *CFDS-FLOW3D Release 3.2 User's Manual*, AEA Industrial Technology, Harwell, Oxfordshire, UK.

[3] J. P. van Doormaal and G. D. Raithby, "Enhancements of the SIMPLE method for predicting incompressible fluid flows," *Numerical Heat Transfer* **7**, 147-163 (1984).

[4] B. E. Launder and D. B. Spalding, "The numerical computation of turbulent flows," *Computer Methods in Applied Mechanics and Engineering* **3**, 269-289 (1974).

[5] D. S. Clarke and N. S. Wilkes, "The calculation of turbulent flow in complex geometries using a Differential Flux Model," AEA-InTec-0216, Harwell, Oxfordshire, UK, 1991.

[6] Y. S. Touloukian, et al., *Thermophysical Properties of Matter*, IFI/Plenum, New York (1970).

[7] C. R. Bass, "Thermal-hydraulic characterization of a cryogenic neutron cold-source," Ph.D. dissertation, University of Virginia (1994).

[8] W. Frost and G. S. Dzakowic, "An extension of the method of predicting incipient boiling on commercially finished surfaces," Paper presented at the ASME-AIChE Heat Transfer Conference, Seattle, WA, 67-HT-61 (August, 1967).

[9] S. Levy, "Forced convection subcooled boiling prediction of vapour volumetric fraction," *Int. J. Heat Mass Transfer* **10**, 951-965 (1967).

Table 1. Engineering Design Conditions for ANS Cold Source.

MODERATOR/CRYOGEN COOLANT	LIQUID DEUTERIUM, D_2
MAXIMUM SYSTEM PRESSURE	0.4 MPa
MINIMUM SYSTEM PRESSURE	0.25 MPa
MINIMUM TEMPERATURE	20 K
MAXIMUM TEMPERATURE	25 K
SATURATION TEMPERATURE @ 0.25 MPa	27 K
SATURATION TEMPERATURE @ 0.4 MPa	29 K
D_2 TRIPLE POINT	18.7 K
D_2 CRITICAL TEMPERATURE	38.3 K
D_2 CRITICAL PRESSURE	1.62 MPa
DESIGN MASS FLOWRATE	1.02 kg/s

Table 2. ANS Cold Source 2D Axisymmetric Model of Spherical Annulus - Reactor-Side Hemisphere
CASE SUMMARY

Case	Liquid D_2			Aluminum Outer Shell and Annulus						Beryllium Shell-Inner Surface		
	Mass Flow [1]	ΔT [2]	max. ΔP	Heat to Hemi-sphere	Heat Flux Distribution	at max. Al. shell temperature location				at max. Al shell temperature location		
						T_{wall}	$\Delta T_{super.}$ [3]	$T_{f,outer}$	$T_{f,inner}$	h	T_∞	T_{Be}
	kg/s	K	MPa	kW	kW/m²	K	K	K	K	W/m²-K	K	K
1	0.51	3.6	0.10675	10.94	41.6	29.4	1.5	23.4	21.7	0	25	21.7
2	0.51	3.6	0.10675	10.94	52.8 cosθ	30.8	2.9	23.6	21.5	0	25	21.5
3	0.612	3.0	0.15375	10.94	52.8 cosθ	29.6	2.5	23.2	21.3	0	25	21.3
Curvature (7 mm radius) added to junction between supply line and annulus for all of the following cases.												
4	0.51	3.6	0.07615	10.94	41.6	29.4	1.0	23.5	21.8	150	25	22.0
5	0.51	3.6	0.07615	10.94	52.8 cosθ	30.8	2.4	23.6	21.6	150	25	21.7
6	0.612	3.0	0.10917	10.94	52.8 cosθ	29.6	1.8	23.1	21.3	150	25	21.5
7	0.51	4.7	0.07615	10.94	52.8 cosθ	31.3	3.0	24.4	23.0	∞	25	25.0
8	0.51	2.5	0.07615	7.5	29.5	27.0	0.0	22.5	21.3	150	25	21.5
9	0.51	2.5	0.07615	7.5	29.5	27.0	0.0	22.5	21.4	150	22.5	21.4
The following two cases have a 3 mm gap.												
10	0.51	3.6	0.036	10.94	41.6	32.0	3.1	23.9	21.5	150	25	21.5
11	0.51	3.6	0.036	10.94	52.8 cosθ	33.7	4.8	24.2	21.3	150	25	21.3
Baseline Case: The following case has the conduction effects in the Al and Be shells included; a uniform internal heat generation of 1.37 kW has been added to the Be hemisphere (2.74kW total).												
12	0.51	3.9	0.07615	10.69	51.6 cosθ	30.7	2.3	23.7	21.8	150	25	22.9
The following case has the same heat loads as 12; but the geometry has been modified to include a bulge in the Be shell. This bulge gives a 1mm gap width at the equator.												
13	0.51	3.9	0.07615	10.69	51.6 cosθ	30.6	2.2	24.6	22.6	150	25	22.6

[1] This is the mass flow through the hemisphere model or ½ of the total liquid deuterium flow through the cold source.
[2] ΔT is the temperature rise of the liquid deuterium as it passes through the annulus.
[3] Wall superheat is calculated using a saturation temperature based upon the minimum pressure in the annulus. The inlet pressure is 0.4 MPa.

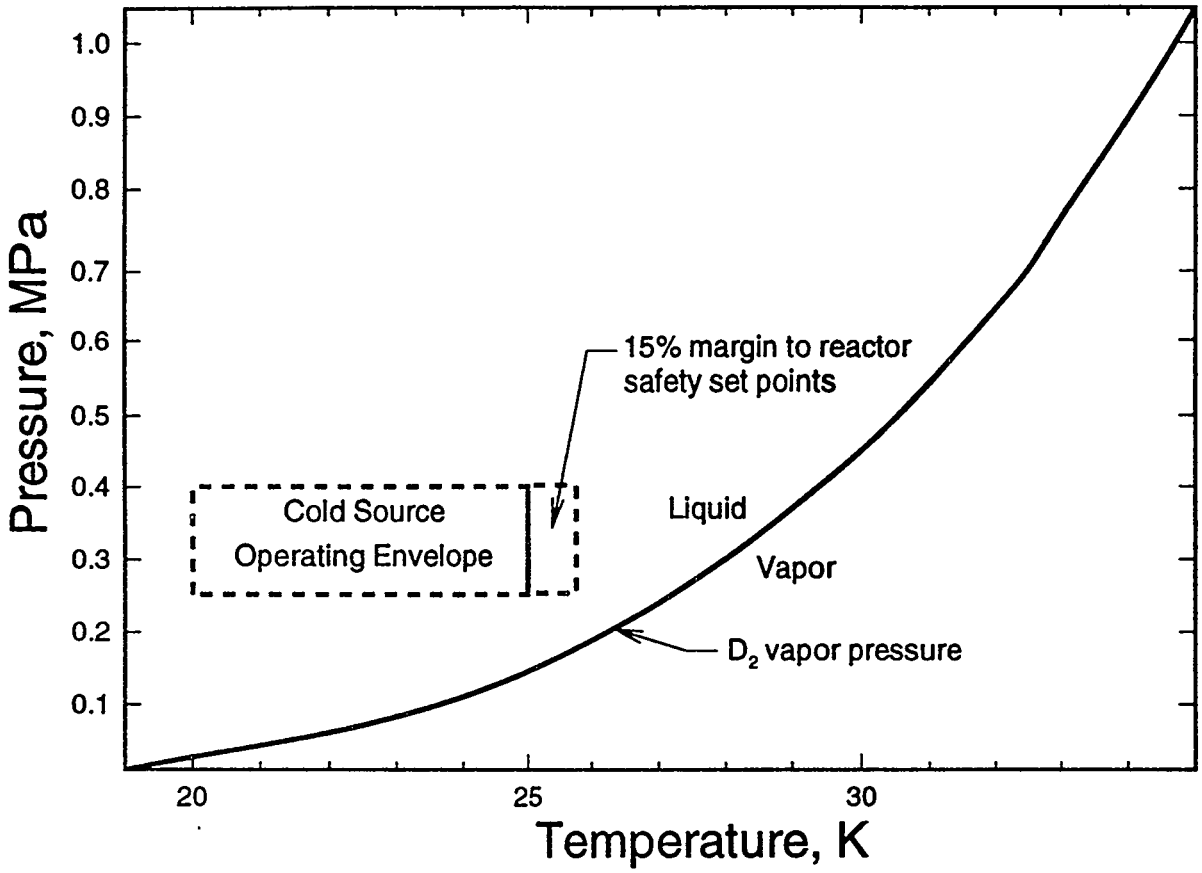

Figure 1 - Cold source pressure v. temperature operating envelope.

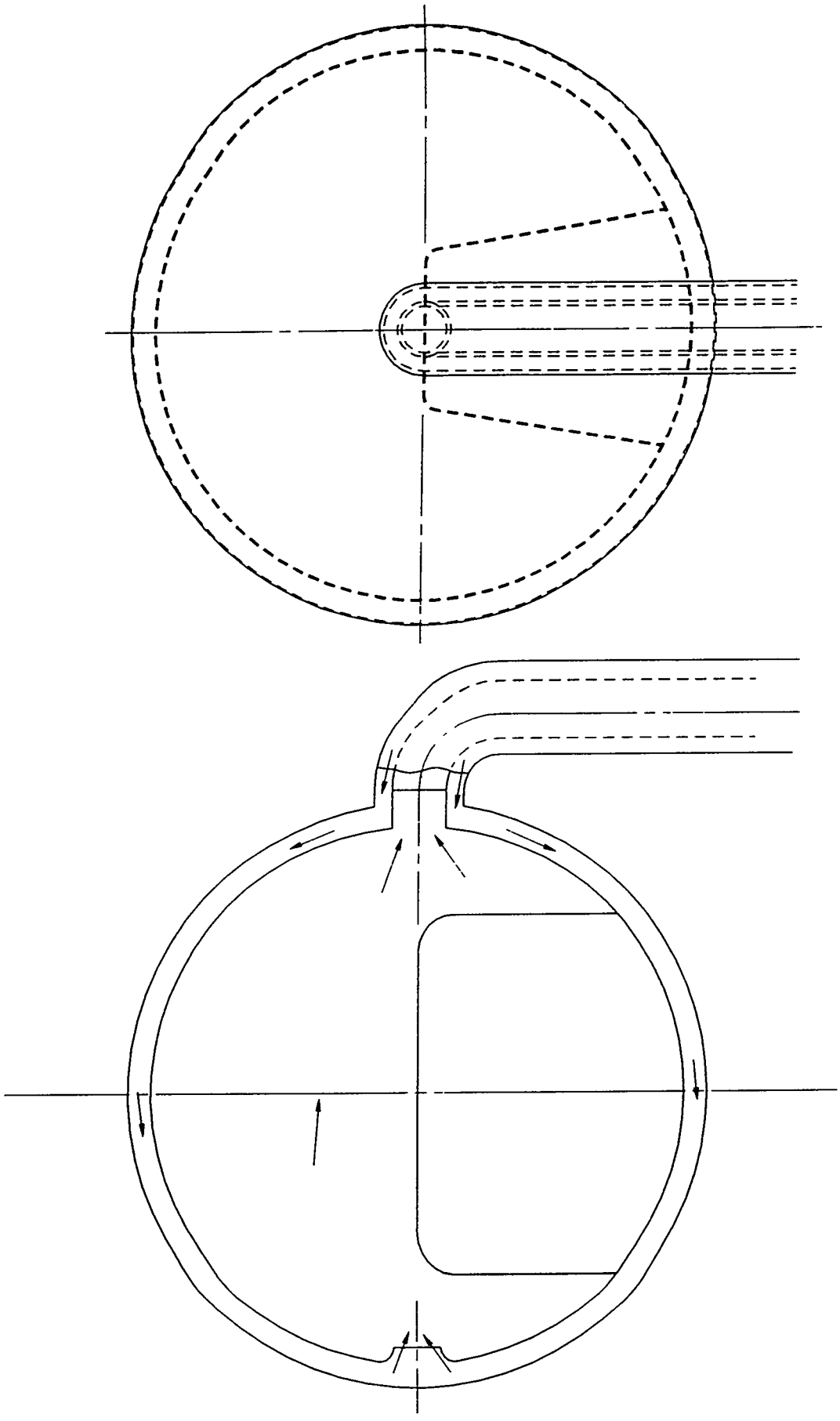

ANS MODERATOR VESSEL
CONCEPTUAL DESIGN

FIG.2

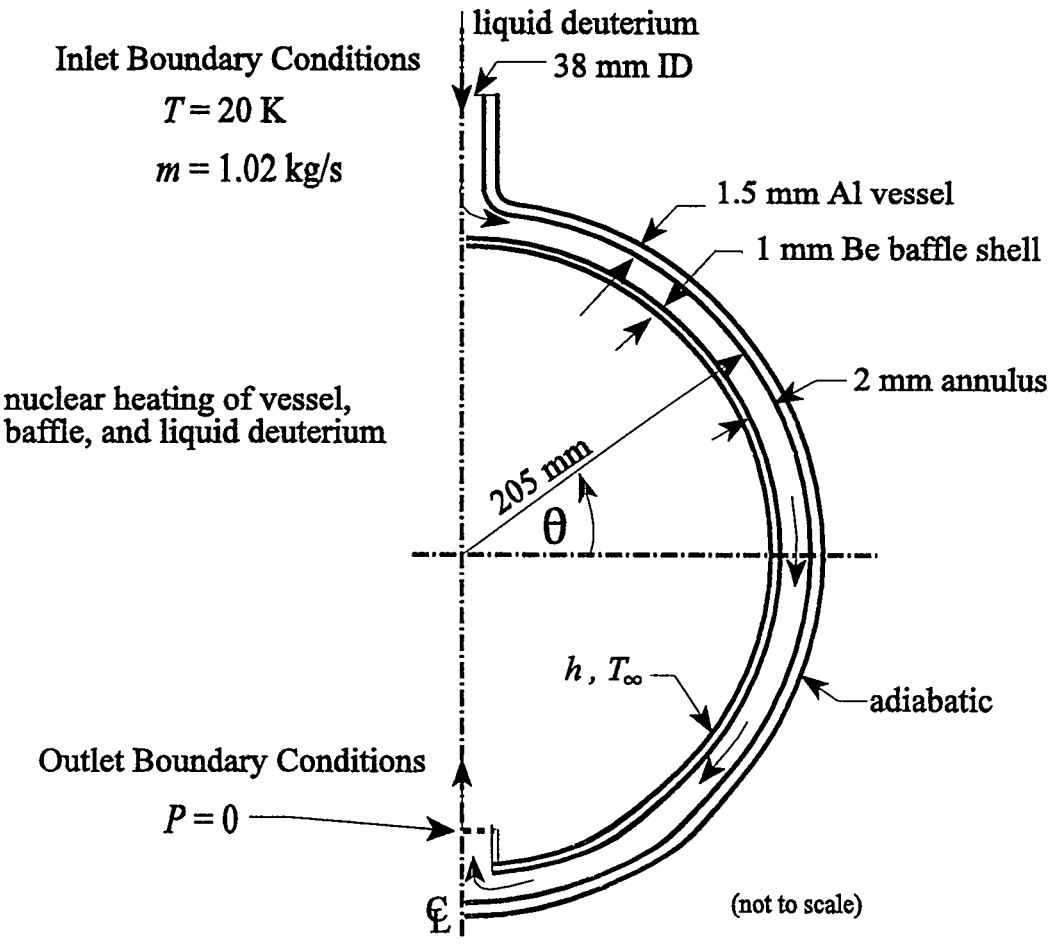

Figure 3. Schematic of 2D axisymmetric cold source model.

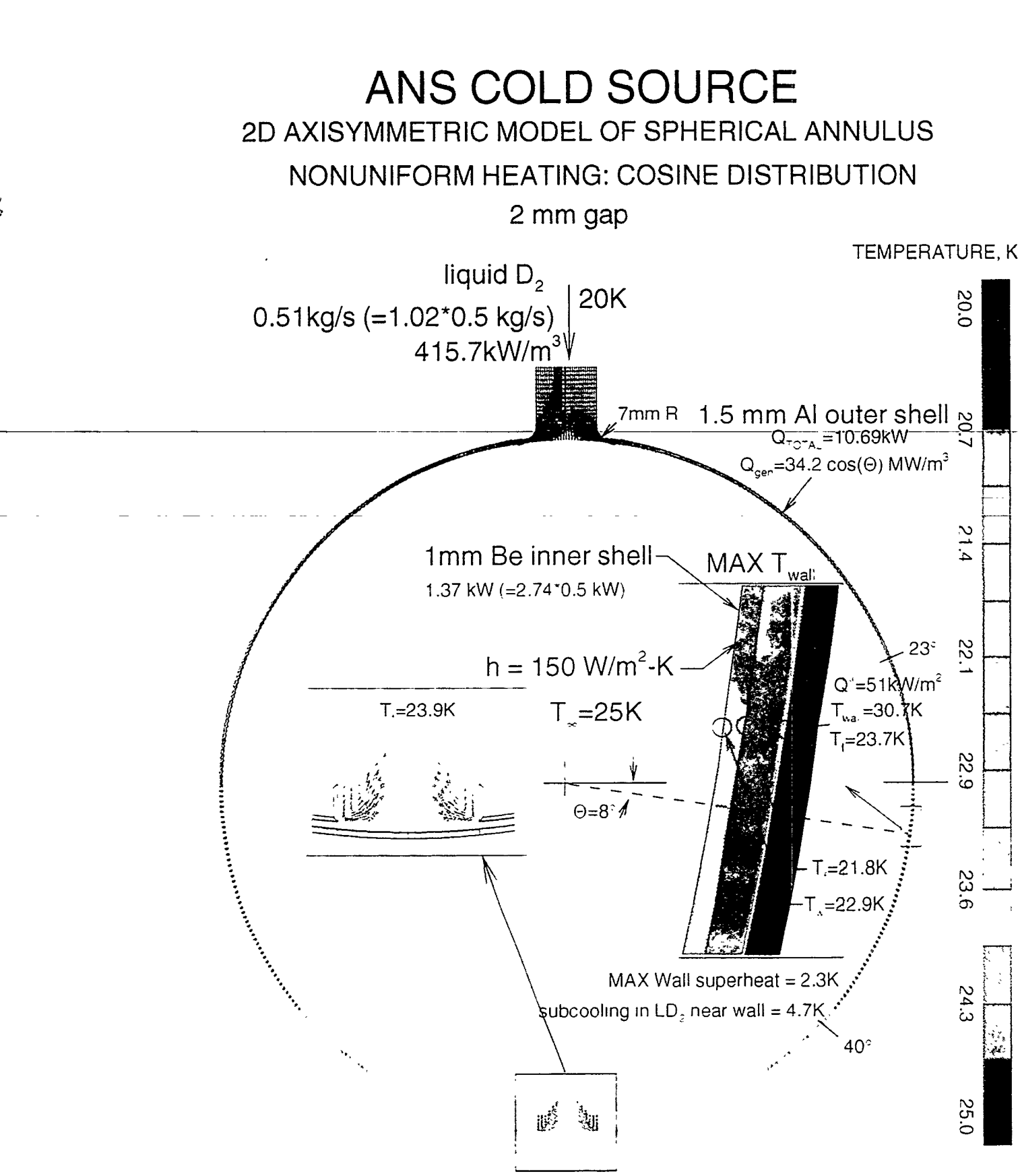

Figure 4. Temperatures for baseline Case No. 12.

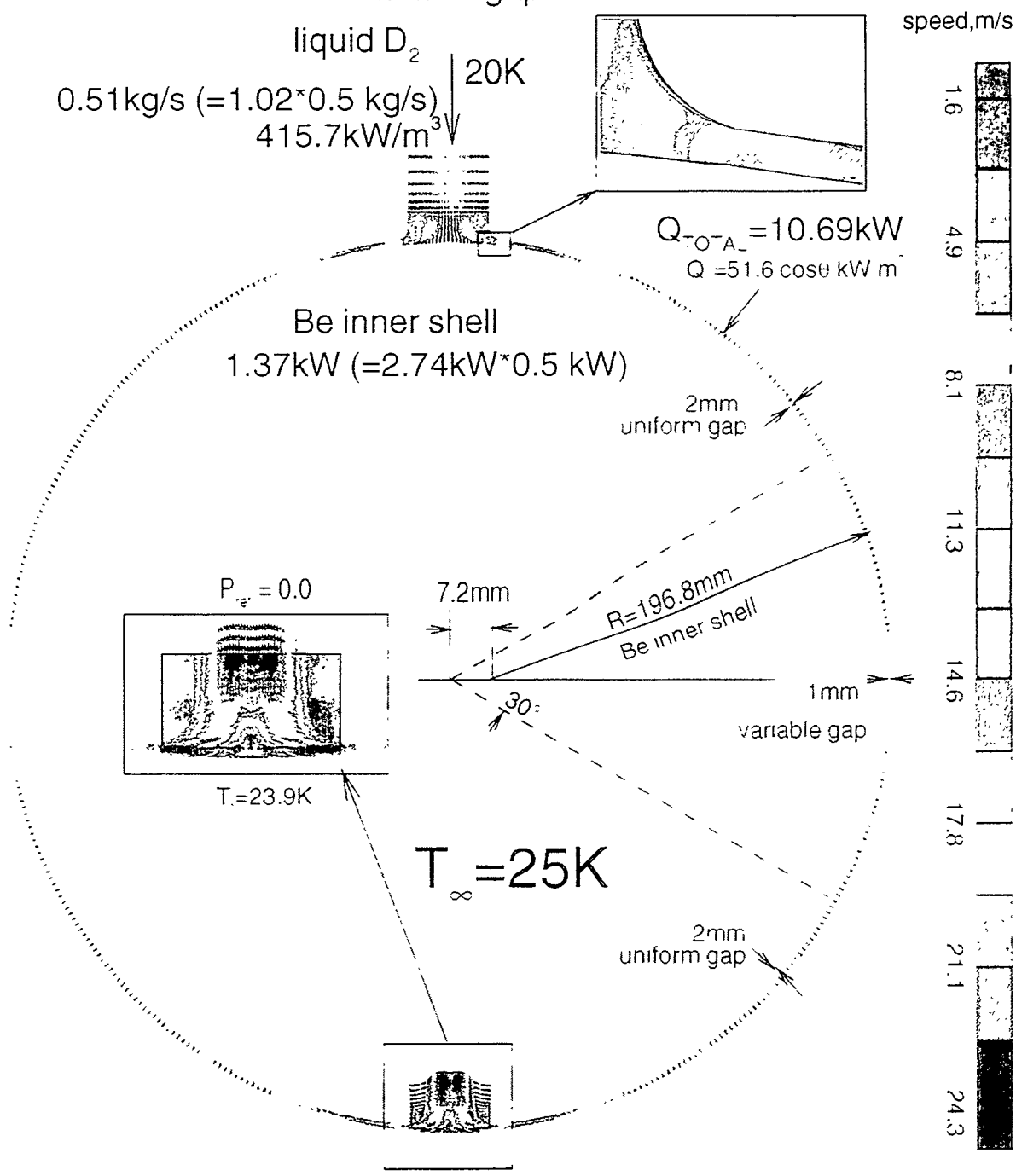

Figure 5. Case No. 13 - variable gap width.

Modeling and Analysis of Thermal-Hydraulic Response of Uranium-Aluminum Reactor Fuel Plates Under Transient Heatup Conditions

S. Navarro-Valenti, S.H. Kim, V. Georgevich, R.P. Taleyarkhan,
Oak Ridge National Laboratory, Oak Ridge, TN.

T. Fuketa, K. Soyama, K. Ishijima and T. Kodaira
Japan Atomic Energy Research Institute, Tokai, Japan.

ABSTRACT

The purpose of this paper is to describe the analysis performed to predict the thermal behavior of fuel miniplates under rapid transient heatup conditions. The possibility of explosive boiling was considered, and it was concluded that the heating rates are not large enough for explosive boiling to occur. However, transient boiling effects were pronounced. Because of the complexity of transient pool boiling and the unavailability of experimental data for the situations studied, an approximation was made that predicted the data very well within the uncertainties present. If pool boiling from the miniplates had been assumed to be steady during the heating pulse, the experimental data would have been greatly overestimated. This fact demonstrates the importance of considering the transient nature of heat transfer in the analysis of reactivity excursion accidents. An additional contribution of the present work is that it provided data on highly subcooled steady nucleate boiling from the cooling portion of the thermocouple traces.

INTRODUCTION

The Advanced Neutron Source (ANS) is a user facility currently in the design stage at the Oak Ridge National Laboratory (ORNL). ANS is planned to be a 330-MW research reactor using uranium-silicide cermet fuel in a plate-type configuration. A defense-in-depth philosophy has been adopted for the facility. In response to this commitment, ANS Project management initiated severe accident analysis and related technology development early in the design phase. This was done to aid in designing a robust containment for retention and controlled release of radionuclides in the event of a severe accident. It also provides a means for satisfying on- and off-site regulatory requirements, accident-related dose exposures, and containment response and source-term best estimate analyses for the level-2 and -3 probabilistic risk analyses that will be produced.

As part of the safety evaluation of ANS from the standpoint of damage initiation and propagation, it is necessary to understand the behavior of fuel plates under transient heatup conditions. Effects to be studied are the onset of blistering, bowing, cracking, melting, chemical interactions, and material dispersion leading to steam explosions. For beyond design-basis accidents, damaging transient heatup conditions for ANS-type research reactors may occur due to rapid energy deposition the onset of film boiling due to hypothetical flow blockage or reactivity insertion accidents.

For the past several years, the Japan Atomic Energy Research Institute (JAERI) has been developing a data base of information related to uranium silicide-fueled plate performance under rapid power deposition conditions. Data have been obtained for fuel plate performance subjected to rapid neutron power bursts in JAERI's Nuclear Safety Research Reactor (NSRR). Tests are conducted with a single fuel plate in a relatively large pool of water, and also with a plate-cluster geometry (wherein narrow gap spacing effects are simulated). The range of temperatures cover heatup to melting and superheating past the phase change boundaries.

The purpose of this paper is to present the model developed to analyze the thermal behavior of the fuel miniplates under pulse irradiation conditions.

DESCRIPTION OF THE EXPERIMENT

The tests were performed in the NSRR which is a modified TRIGA annular core-pulsed reactor with large pulsing capability and a 0.22-m-diam dry irradiation space located at the center of the reactor core to accommodate the test specimens. The pulsing operation is performed by withdrawal of the transient rods from the core. The maximum pulse of 4.7$ (3.41% Δk) produces a peak reactor power of 21,000 MW and a core energy release of 117 MJ with a minimum reactor period of 1.13 ms. Details on the reactor configuration and on the experimental data taken for Japanese Material Test Reactor (JMTR) fuel miniplates are given by Yanagisawa et. al. [1].

The ANS fuel miniplates consist of a uranium silicide-aluminum mixture located in the center (70 mm long, 25 mm wide and .77 mm thick), surrounded by an aluminum 6061 cladding. The miniplates are 130 mm long, 35 mm wide, and 1.27 mm thick. The fuel plates were subjected to a power pulse and the temperature of the surface of the cladding was measured. The instrumentation available consists of five Pt/Pt-Rh 13% intrinsic thermocouples spot-welded to the surface of the cladding and one thermocouple to measure the temperature of the coolant. The location of the thermocouples is shown in Figure 2.

Typical thermocouple traces obtained for ANS fuel miniplates are shown in Fig. 1a. The reactor power and the cumulative reactor energy as functions of time are shown in Fig. 1b. As shown in Fig. 1b, the reactor power increases monotonically to a peak and then decreases monotonically. The thermocouple traces have a similar behavior, but the peak is reached with some time lag related to the time that it takes the thermal wave to travel from the fuel to the surface of the cladding. At later times, during the cooling period of the plates, the reactor power remains almost constant and at a very low level, and the cumulative reactor energy increases very slowly.

The total energy deposited in the plates was determined by performing gamma scans of the plates at selected times after they were irradiated. These values were confirmed with neutronic calculations. It should be noted that the prompt energy deposited in the plate causes the rapid increase in temperature. This energy was estimated by JAERI's researchers using a point kinetics code and experimentally [2].

Five tests have been performed with single plate configurations. For four of them temperature measurements were obtained. The cases were chosen to be able to determine the temperature for the onset of cracking of cladding and fuel dispersion. Table 1 contains a description of each of these tests. It includes the homogeneity status (i.e., distribution of fuel particles in plate), the energy deposited in the plates during the pulse, the maximum cladding temperature, and a description of the plate after the test.

Table 1 Description of Experimental Tests

Test No.	Fuel homogeneity	Energy deposited (kJ)	Peak temperature (°C)	Observation
518-1	Inadequate	3.3	410	Cracking
518-2	Inadequate	5.2	700	Melting
518-3	Adequate	3.5	N/A	No failure
518-4	Adequate	2.5	210	No failure
518-5	Adequate	5.66	600	Melting

DESCRIPTION OF THE MODEL

A detailed three-dimensional heat conduction model for the ANS fuel miniplates was developed. For this purpose, the heat conduction code HEATING 7 [3] was used. A transient, spatially uniform heat source was introduced to simulate the heating process. The temporal dependence of the heat source is the same as the reactor power temporal behavior.

The fuel miniplate was divided into 8 nodes in the thickness direction, 17 nodes in the length direction, and 17 nodes in the direction of the width. A schematic diagram of the fuel plate nodalization is shown in Fig. 2. The fuel was assumed to be homogeneously distributed. The properties of the materials were modeled as functions of temperature and included in HEATING 7 in the form of tables. The melting of pure aluminum in the fuel section was modeled (as occurring at a fixed temperature), and the melting of the alloyed aluminum cladding (Al6061) was approximated by dividing the solidus-liquidus region into 4 equal, discrete phase changes.

To model the boundary conditions, it is necessary to determine the heat transfer coefficient as a function of the wall and coolant temperatures for a very broad range of wall temperatures. Since the water is at room temperature (approximately 20°C), we are dealing with highly subcooled pool boiling (80°C subcooling).

During the pulse irradiation period, given the very rapid heating of the plate (~10^{4}°C/s), the possibility of explosive boiling of the coolant was considered. Explosive boiling occurs when the fluid reaches the homogeneous nucleation temperature before the surface is completely covered by bubbles (i.e., the presence of active nucleation sites on the surface does not prevent the increase of the temperature to the homogenous nucleation point).

We can estimate the criteria for the occurrence of explosive boiling as follows. It will be assumed that the liquid is saturated initially and that the rate of heating of the liquid adjacent to the surface of the plate is the same as that of the plate itself. Thus, the instantaneous liquid temperature asuming a constant heating rate, will be given by:

$$T_l - T_{sat} = \dot{T}_l t \qquad (1)$$

The fraction of the surface that is covered by bubbles for a given bubble number density (number of bubbles per unit area) is given by:

$$f = \pi R^2 N \qquad (2)$$

The growth of bubbles early in the boiling process is predicted by the Rayleigh equation [4]. Thus, the radius will be:

$$R \approx t\sqrt{\frac{2[P_{sat}(T_l) - P_\infty]}{3\rho_l}} \qquad (3)$$

For explosive boiling to occur, the liquid must reach the spontaneous nucleation temperature (T_{sn}) before the surface is covered with vapor (i.e., before f=1). Thus, the criterion for explosive boiling would be given as:

$$\dot{T} \geq \left(\frac{2\pi}{3}\right)^{1/2} \sqrt{\left[\frac{N[P_{sat}(T_{sn}) - P_{\infty}]}{\rho_l}\right]} (T_{sn} - T_{sat}) \qquad (4)$$

From the data obtained by Gaertner and Westwater [5] and Sultan and Judd[6] for a surface heat flux of the order of 10^6 W/m^2 we know that N is at least equal to 10^6 sites/m^2. Blander et. al.[7] measured the spontaneous nucleation temperature of water of 250°C. Substituting these values in Eq. (4), we will conclude that explosive boiling can only occur if the rate at which temperature increases is greater than 1.35 x 10^7°C/s. Even if we assume that explosive boiling occurs at only 130°C, the temperature rise required would be 5.7 x 10^5°C/s. The change in temperature as a function of time in the NSRR is of the order of 10^4°C/s, which is clearly smaller than the criterion for explosive boiling to occur.

Thus, we can conclude that the heat transfer phenomena occurring in the tests are not explosive in nature. However, the heating rates are high enough that the boundary layer does not have enough time to respond to the heating rates of the surface. Such a transient pool boiling phenomenon needs to be considered to be able to model the thermal behavior of the fuel plates.

We can divide the overall heatup transient into three different regions:

Region I. Transient heating of the plate before the onset of nucleate boiling
Region II. Transient boiling during the heatup period of the plate (including nucleate and film boiling)
Region III. Transient cooling of the plate after the power level has become small and constant (including nucleate and film boiling)

Analysis of Region I

Since no boiling occurs in this region, the transient heat transfer problem can be addressed by solving simultaneously the transient energy equation of the coolant and the plate. Because the heating periods of the transients are very small, the increasing rate of the surface temperature is too rapid for natural convection to contribute appreciably to the heat transfer before boiling commences. Goldstein and Briggs [8] developed a model to predict the time necessary for natural convection to develop over a vertical surface. This time is given by:

$$t_{NC} = \left[\frac{Lk}{0.058\dot{q}''g\beta\alpha^{0.5}}\right]^{2/5} \qquad (5)$$

If we apply this equation to the conditions of the NSRR tests, the time necessary to develop natural convection would be of the order of 1 s, which is clearly much greater than the transient heating time period of the NSRR tests.

Thus, in this region, water can be treated like an infinite solid. The heat conduction equation in the coolant was solved using HEATING 7. This solution was utilized up to the onset of nucleate boiling.

Incipience of boiling in transient pool boiling was studied by Sakurai and Shiotsu [9]. Their experimental results indicate that the incipience of boiling depends on the heating period and the water subcooling. For a subcooling of 75°C and a period of 12 ms, the incipience will occur at 121°C; for a period of 8 ms, at 125°C; and for 5 ms, at 130°C. These data were used in the model

to determine the onset of nucleate boiling. Sakurai and Shioutsu [9] also observed that the incipience of boiling occurs near the intersection between the solution of the transient conduction equation in the water and the steady boiling curve.

Analysis of Region II

It has been observed in the past by Kawamura et. al. [10] that for very rapid heating transients, there is not enough time for the boundary layer to respond to the heating rate of the surface. Thus, the boiling phenomena that occur are different from a steady situation. Hall and Harrison [11] observed transient heat transfer fluxes that exceeded by a factor of up to ten the maximum heat fluxes for steady pool boiling. It has also been observed that the heat transfer coefficient depends on the period of heating, the peak heating rate, the wall superheat, and the coolant subcooling.

Kawamura et. al. [10] reported pool boiling curves for a subcooling of 40°C, a square secant heating pulse shape, and eight different peak powers. For nucleate boiling, the heat flux increased with increasing surface temperature superheat and reached a maximum value. This is called the transient Departure from Nucleate Boiling (DNB) point. The heat flux maintains a fairly high level even after the DNB point. In addition, the boiling curves depend on the peak power. In the NSRR experiments, each test has a different period and peak power. Thus, to model the heat transfer coefficient accurately, we would need to know the boiling curve for each pair of values of period and power peak for an 80°C subcooling. Given that this information is not available in the literature and that the scope of this work is not to develop a heat transfer correlation for transient boiling, an approximation to the heat transfer rate has been developed.

The maximum heat transfer rate for transient nucleate boiling at different subcoolings and average periods was reported by Kawamura et. al. [10], who defined the average period for a given pulse shape as:

$$\tau = \frac{\int_0^t q''(\zeta)d\zeta}{q''(t)} \qquad (6)$$

This period is constant for an exponential pulse. The average periods for each of the NSRR tests were obtained using this definition and are given in Table 2. For these periods and a subcooling of 80°C, the DNB heat transfer rate can be obtained by extrapolating Kawamura's data [10]. Table 2 contains the DNB heat transfer rate for each of the ANS tests.

Table 2 Average Period, Transient DNB Heat Flux and Multiplier for NSRR Tests

Case	Period (ms)	$q''_{DNB\,tr}$	$q''_{DNB\,tr}/q''_{DNB\,st}$
518-4	12	21	3.4
518-1	8.3	18	4.0
518-2	6.0	26	4.8
518-5	5.4	29	5.4

The heat transfer rate for transient boiling (excluding film boiling) in the tests was approximated by multiplying the steady heat transfer coefficient by the ratio of the DNB transient heat transfer

rate to the maximum steady heat transfer rate. This means that the shape of the transient pool boiling curve (for nucleate and transition boiling) has been approximated to the shape of the steady pool boiling curve. Even though we expect the transient pool boiling curve to be different from the steady pool boiling curve, and to be dependent on the peak power, the approximation performed here is good enough to produce reasonable predictions of the experimental data obtained at JAERI.

As shown in Table 2, the average periods for NSRR tests are in the range of 12 to 5.4 ms with a corresponding ratio of transient to steady DNB heat transfer rate varying from 3.8 to 5.4. Thus, the transient nucleate boiling heat transfer rate was approximated as 3.8 to 5.4 times the steady heat transfer rate for these tests.

It has been reported [12] that the behavior of heat transfer during transient film boiling follows the same behavior as for steady film boiling. Thus, film boiling was modeled using the steady state values that will be discussed in the description of modeling of region III (in the next section).

Analysis of Region III

After the reactor power pulse, the reactor power becomes small and remains approximately constant during the cooling period of the plate. Thus, the question arises as to the time that it takes for a quasi-steady heat transfer rate to develop.

Sakurai et. al. [12] observed that the transient cooling process follows the steady-state nucleate boiling curve. However, the time frame of their transient was one order of magnitude larger than the one present in the NSRR tests and therefore, can not be directly applied to the NSRR tests. These data do provide guidance on modeling of transient cooldown phase heat transfer. This observation was used in conjunction with a more direct approach.

To obtain information on the heat transfer rates present in Region III, the cooling portion of the curve was used to determine the steady heat transfer coefficient. If we model the plate as one node (i.e., utilize a lumped parameter approach), the energy equation for Region III will be given by:

$$m_m c_{p_m} \frac{dT_m}{dt} = \dot{q}'''V - hA(T_m - T_\infty) \qquad (7)$$

Thus, the heat transfer coefficient will be given by:

$$h = \frac{\dot{q}'''V - m_m c_{p_m} \frac{dT_m}{dt}}{A(T_m - T_\infty)} \qquad (8)$$

where c_{p_m} is the mass averaged specific heat, given as:

$$c_{p_m} = \frac{m_f c_{p_f} + m_c c_{p_c}}{m_m} \qquad (9)$$

The heat transfer rate from the surface of the miniplate to the coolant is given as:

$$\dot{q}'' = h(T_w - T_\infty) \qquad (10)$$

The results obtained using Eq. (10) are compared with the steady, highly subcooled heat transfer rate data available in the literature in Fig. 3. As shown in this figure, the heat transfer rates obtained are in the range of values of the steady state heat transfer coefficients. As mentioned in the description of the model for Region II, transient boiling heat transfer rates for the period and subcooling ranges in NSRR experiments are several times larger than steady boiling heat transfer rates. Thus, these results for Region III demonstrate that the heat transfer rates will follow a quasi-steady pool boiling curve.

The results obtained from the NSRR data agree very well with the results obtained by Ohnishi et. al. [13]. Their data were obtained using fuel rods; thus, geometry does not seem to have great effect on the heat transfer rate in this case. Ohnishi et. al. [13] did not obtain data for the region of nucleate boiling, but only for transition and film boiling. The data obtained in the NSRR tests with ANS plates include only heat transfer rates for temperatures lower than the solidus temperature of Al 6061.

Thus, for temperatures lower than the melting point of the aluminum, the heat transfer coefficient obtained from the data will be used. For larger temperatures, the data of Ohnishi et. al. [13] will be utilized.

As also demonstrated by Bradfield [14], for steady-state heat transfer, the coolant subcooling has great influence on the heat transfer coefficient and on the critical heat flux. Several authors have studied highly subcooled steady pool boiling [13,14,15,16]. However, to the knowledge of the authors, there are no data available for a vertical plate geometry. Thus, an additional contribution of the present work is to provide data highly subcooled steady nucleate and transition pool boiling from a vertical plate.

RESULTS

From the results obtained using the three-dimensional model it can be noted that, the temperature difference between the center of the fueled region and the surface of the cladding (in the direction of the thickness) is of the order of 10%. The temperature at the interface between the fueled and unfueled regions (in the direction of the length and width) was noted to be generally about 20% smaller than the temperature at the thermocouple 5 (TC5) location. In addition, the temperature difference between the different locations of the thermocouples is less than 1% (since we assumed homogenously distributed fuel). Considering the above, and for the sake of clarity, the location of TC5 (at center of thermocouple cluster) has been chosen to display predicted results and to compare them with the experimental data in the discussion that follows.

To illustrate the importance of recognizing the transient nature of pool boiling in Region II, case 518-4 was modeled using a steady state heat transfer coefficient for Region II. The results that are obtained are shown in Fig. 4. As presented, the temperature traces are overpredicted by ~100% if the fact that transient boiling is occurring during the heatup period is not recognized.

The error due to the fin effect of the thermocouples was estimated using a three dimensional model of the thermocouple spot welded to a portion of the fuel miniplate. The results obtained indicate that an error of the order of 10% can be expected because of this effect.

The results obtained for case 518-4 using the approximation for the heat transfer coefficient in Region II and the model described in the preceding section are shown in Fig. 5. As presented in the figure, the predictions obtained for Region II using the approximation for the heat transfer

coefficient produces results that only slightly overpredict (+12%) the experimental data for the peak temperature. However, this variation is well within the overall uncertainties of the measurements. In addition, the cooling portion of the curve is predicted very well within the uncertainty of the data. This means that the steady heat transfer coefficient values that are being used in Region III of the experiment correctly represent the data.

Figure 6 contains the predictions for test 518-1. In this case, the predictions are in very good agreement with the experimental data. The variation between the thermocouple readings for this test is greater than in test 518-4. This is caused by the inhomogeneities present in fuel miniplates used for tests 518-1 and 518-2.

The predictions obtained for test 518-2 are presented in Fig. 7. Melting of the aluminum is predicted, and the predictions are within the range of experimental values. In this case, the analysis of the plates after the test indicated that the center region of the plate had completely melted (corresponding to TC 5). As observed in Fig. 7, there are strong variations in the thermocouple readings for this test. This is partly due to inhomogeneities present in the first two miniplates. In addition, after melting occurs, the possibility exists that the thermocouples will relocate or penetrate deeper into the thickness of the miniplate. Thus, thermocouple 5 could be measuring the temperature of the fuel section instead of the cladding after melting has occurred. This aspect was confirmed via post-irradiation destructive examination of the ANS miniplates.

The results for test 518-5 are shown in Fig. 8. In this case, more melting than in case 518-2 was predicted and experimentally observed. The results obtained are in the range of variation of the experimental data. However, it seems that one of the thermocouples malfunctioned after melting occurred.

SUMMARY AND CONCLUSIONS

To understand the structural behavior subsequent to transient heating of ANS fuel miniplates, it is necessary to model the thermal behavior. A three-dimensional model of the fuel miniplates has been developed. This model includes the heat transfer analysis of highly subcooled nucleate and film boiling. Given the large heating rates present in these tests, the possibility of the occurrence of explosive boiling was considered. It was concluded that no explosive boiling will occur under the heating rates existent in the NSRR tests.

The heat deposition rates in NSRR do cause transient pool boiling to occur during the time frame of the reactor pulse. Thus, the transient was divided into three temporal regions:

Region I. Heating of the plate before the onset of nucleate boiling
Region II. Heating of the plate with transient nucleate and film pool boiling
Region III. Cooling of the plate after power has become small and fairly constant

It was determined that for the time frame of the transients occurring in NSRR tests, no significant natural convection would develop. Thus, the coolant was treated as an infinite solid for temperatures lower than the onset of nucleate boiling during the heating of the plate (Region I).

Due to the complex behavior of transient boiling and to the unavailability of experimental data in the literature for our specific situation, an approximation to the transient heat transfer coefficient in Region II was performed. The results obtained using this approximation predicted the experimental data very well, within the uncertainties of the data. If a steady state heat transfer coefficient in this region is used, the experimental data are greatly overpredicted. Thus, the importance of considering the transient nature of heat transfer in Region II was demonstrated. In addition, an approximate approach to model this region has been proposed and implemented.

By determining the heat transfer rates to the coolant from the cooling portion of the tests (after the reactor power has tapered off), and comparing it to the steady heat transfer rates for highly subcooled pool boiling, it was concluded that the heat transfer rate occurring in Region III follows the steady pool boiling curve. The exact time at which transient heat flux becomes quasi-steady is not known. Thus, the transition was assumed to occur at the moment the power tapers off.

To the knowledge of the authors, there are no data available in the literature for nucleate boiling in the conditions present in these tests. Thus, an additional contribution of this work consists on providing data for highly subcooled nucleate and transition boiling from a vertical plate.

Acknowledgements

The authors acknowledge the consulting advice provided by M. Epstein of Fauske & Associates, Inc., Chicago, IL, dealing with explosive boiling and steady state highly subcooled boiling.

LIST OF SYMBOLS

A	Cross sectional area (0.07 m x 0.025 m) [m^2]
c_p	Specific heat [J/kgK]
f	Fraction of surface covered by bubbles
g	Gravity acceleration [m/s^2]
h	Heat transfer coefficient [W/Km^2]
k	Thermal conductivity [W/Km]
L	Length of heated section of plate (0.07 m) [m]
m	Mass of fuel plate [kg]
N	Number density of bubbles [$1/m^2$]
P	Pressure [Pa]
q"	Heat flux to coolant [W/m^2]
q"'	Volumetric heat generation in plate [W/m^3]
R	Radius of bubble [m]
T	Temperature [°C]
t	Time [s]
V	Volume [m^3]

Greek symbols

α	Thermal diffusivity of coolant [m^2/s]
β	Coefficient of thermal expansion [1/K]
ρ	Density [kg/m^3]
τ	Average period of pulse defined by Eq. (6) [s]
ζ	Dummy variable

Indexes

NC	Nucleate boiling onset
DNB	Departure from nucleate boiling
c	Cladding
f	Fuel
l	Liquid coolant
m	Miniplate considered as one node
sat	Saturated
sn	Spontaneous nucleation
st	Steady
tr	Transient
w	Surface of the cladding

REFERENCES

[1] Yanagisawa,K , Fujishiro, T., Kazuhiko, S., Ichikawa, H. and Kodaira, T., "Dimensional Stability of Low Enriched Uranium Silicide Plate-Type Fuel for Research Reactors at Transient Conditions", J. Nucl. Sci. Tech. 29., 233-243 (1992).

[2] Ohnishi, N. and Inabe, T., "Evaluation of Effective Energy Deposition in Test Fuel During Power Burst Experiment in NSRR" J. Nucl. Sci. Tech., 19, 528-542 (1982).

[3] Childs, K.W., "Heating 7.2b Multidimensional, Finite-Difference Heat Conduction Analysis", RSIC Peripheral Shielding Routine Collection. ORNL/TM-12262 (1993).

[4] Hsu, Y-Y, Graham, R. W., "Transport Processes in Boiling and Two-Phase Systems", Mc. Graw-Hill, p. 18 (1976).

[5] Gaertner, R. F. and Westwater, J. W., "Population of Active Sites in Nucleate Boiling Heat Transfer", Chem. Engr. Prog. Symp. Series 56, 39-48 (1960).

[6] Sultan, M., and Judd, R. L., "Spatial Distribution of Active Sites and Bubble Flux Density", J. Heat Transfer, 100, 56-62 (1978).

[7] Blander, M., Hengstenberg, D., and Katz, J. L., "Bubble Nucleation in n-Pentane, n -Hexane, n-Pentane +Hexadecane Mixtures and Water", J. Physical Chemistry 75, 3613-3619 (1971).

[8] Goldstein, J. and Briggs, D. G. "Natural Convection from Vertical Surfaces", Trans. ASME, J. Heat Transfer 86, No. 4 (1964).

[9] Sakurai, A. and Shiotsu, M., "Transient Pool Boiling Heat Transfer", Trans. ASME, J. Heat Transfer 99, 554-560 (1964).

[10] Kawamura, H., Fujio, T., Akiyama, M., "Heat Transfer and DNB Heat Flux in Transient Boiling". 4th. Intl. Heat Transfer Conference, Versailles (1970).

[11] Hall, W.B., Harrison, W.C., "Transient Boiling of Water at Atmospheric Pressure", 3rd. Intl. Heat Transfer Conference, Chicago, vol. 3 (1966).

[12] Sakurai, A., Shiotsu, M., Hata, K., "Transient Boiling Caused by Vapor Film Collapse at Minimum Heat Flux in Film Boiling", Nucl. Engrg. Des. 99, 167-175 (1987).

[13] Ohnishi, N.,Ishijima, K., Tanzawa, S., "A Study of Subcooled Film-Boiling Heat Transfer Under Reactivity-Initiated Accident Conditions in Ligth Water Reactors", Nucl. Sci. Engrg 88, 331-341 (1984).

[14] Bradfield, W.S., "On the Effect of Subcooling on Wall Superheat in Pool Boiling", J. Heat Transfer 89, 269-270 (1967).

[15] Siviour, J.B., Ede, A.J., "Heat Transfer in Subcooled Pool Film Boiling", 4th Intl. Heat Transfer Conference, Versailles (1970).

[16] Lauer, H. and Hufschmidt, W., "Heat Tranfer and Surface Rewet During Quenching", Two-Phase Flows and Heat Transfer, Proc. NATO Advanced Study Institute, Vol. 2, 1310, Hemisphere Publishing Corp. (1977).

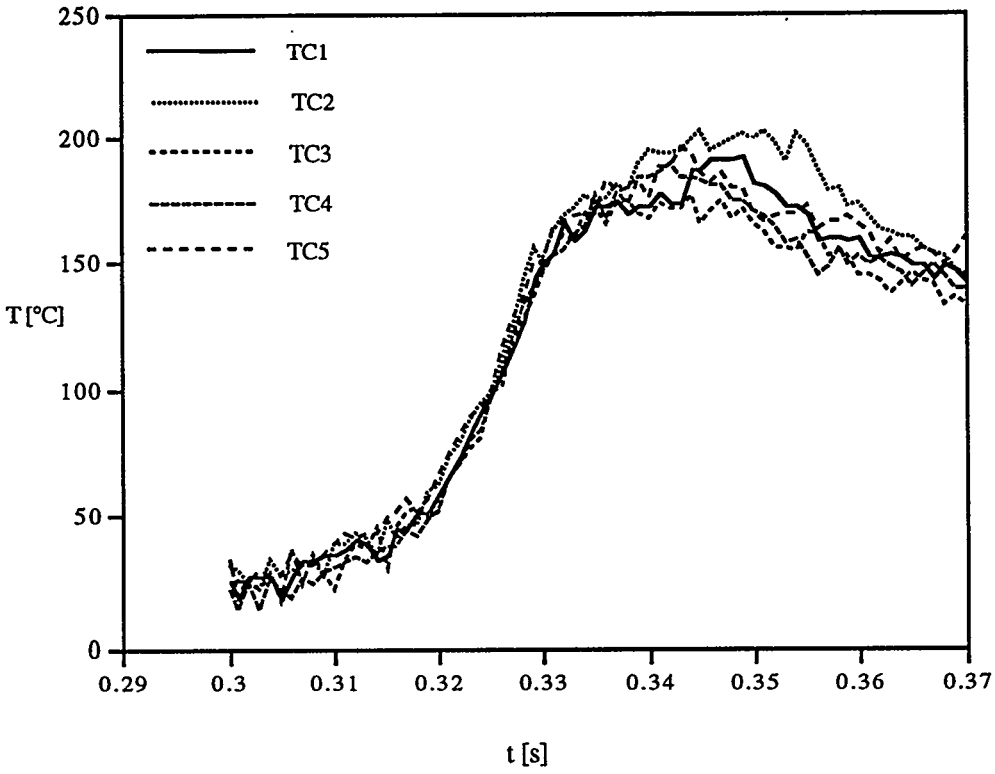

Fig. 1a Typical Thermocouple Traces from NSRR.

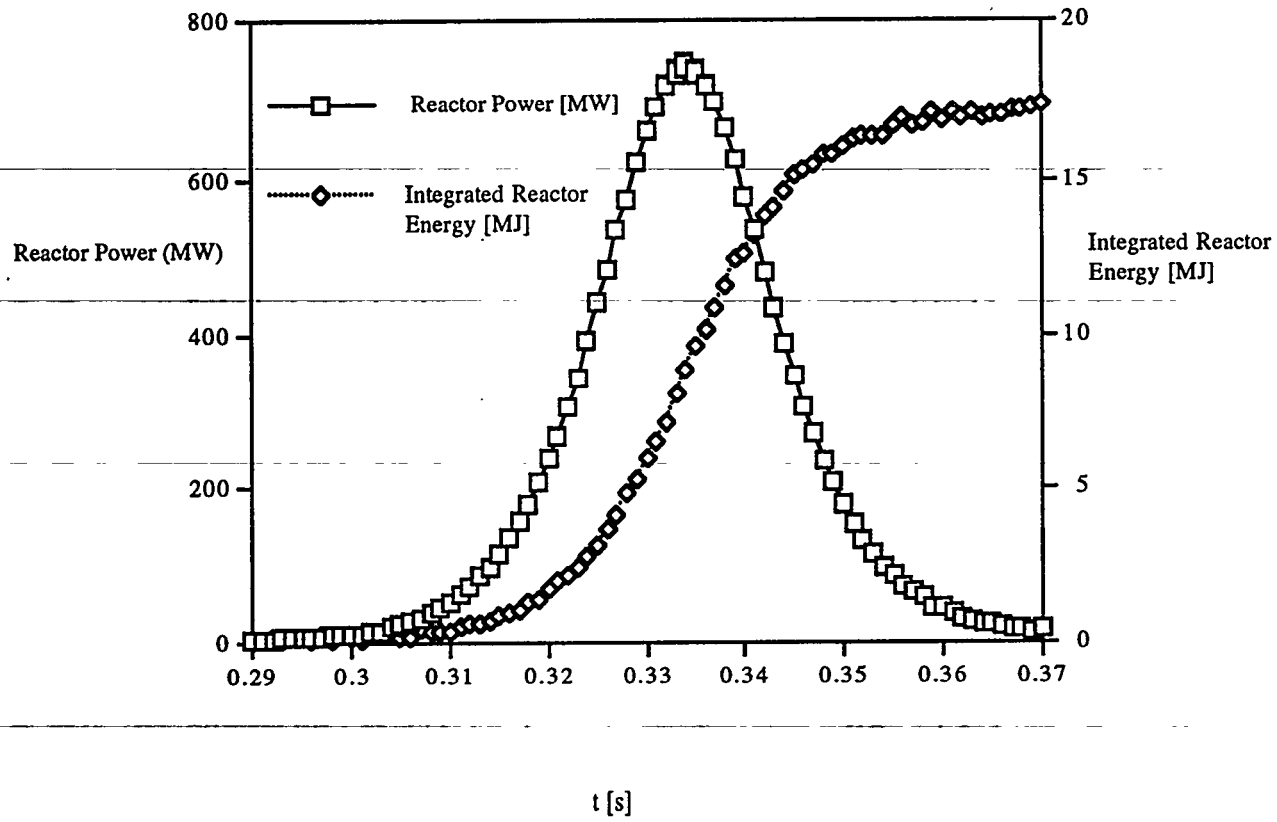

Fig. 1b Typical Data for Reactor Power and Integrated Reactor Energy from NSRR.

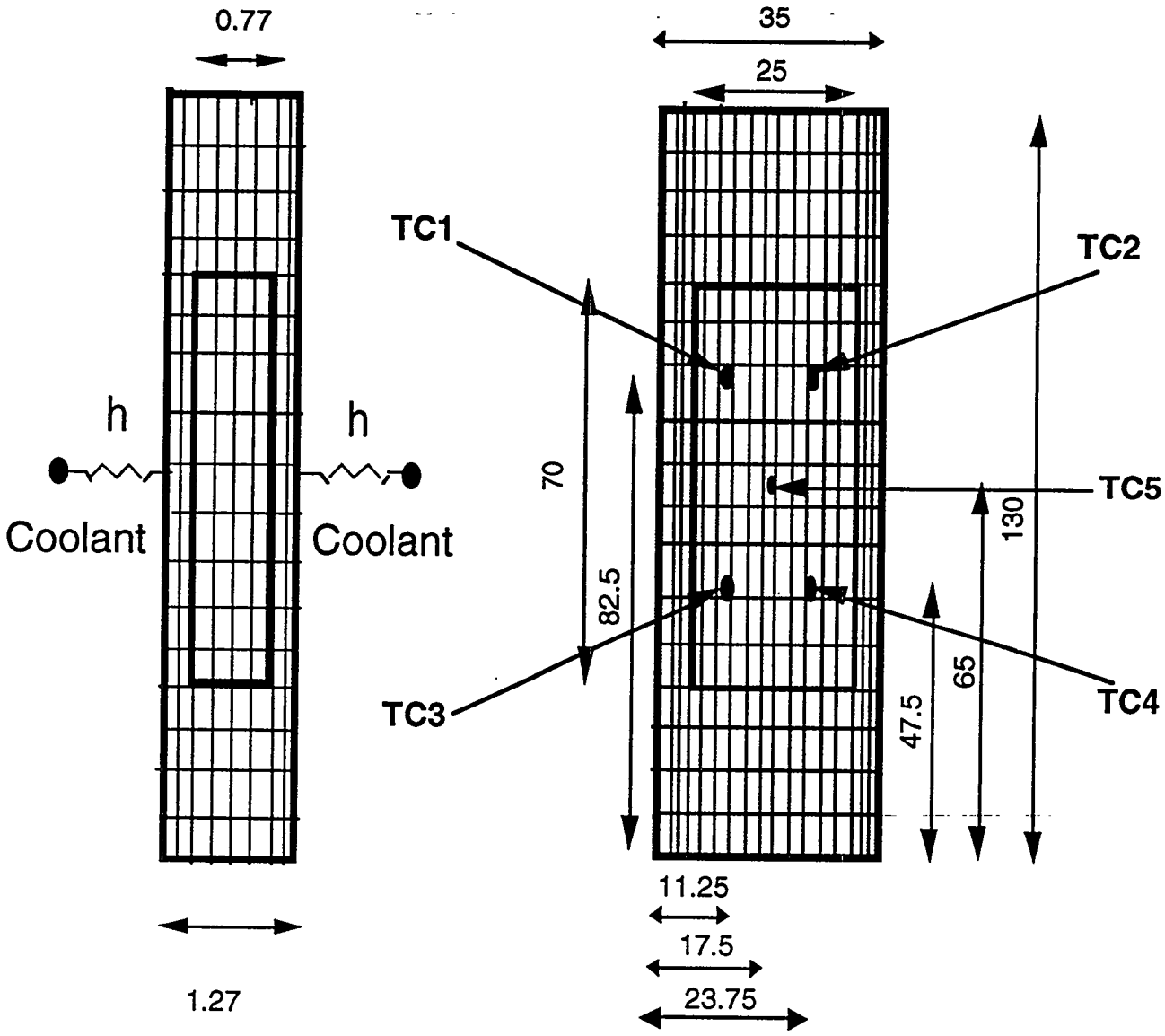

Fig. 2 Schematic Diagram of Fuel Plate Nodalization.

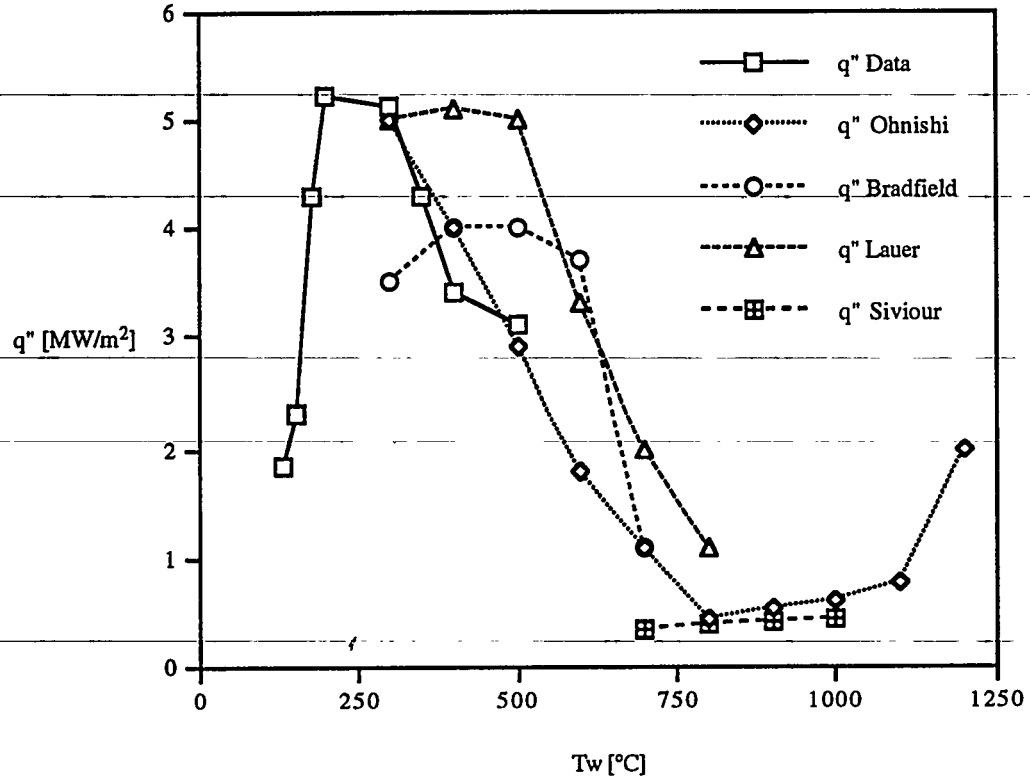

Fig. 3 Comparison of Heat Transfer Coefficient from Cooling Region of Data with Steady Heat Transfer Coefficients by Other Authors.

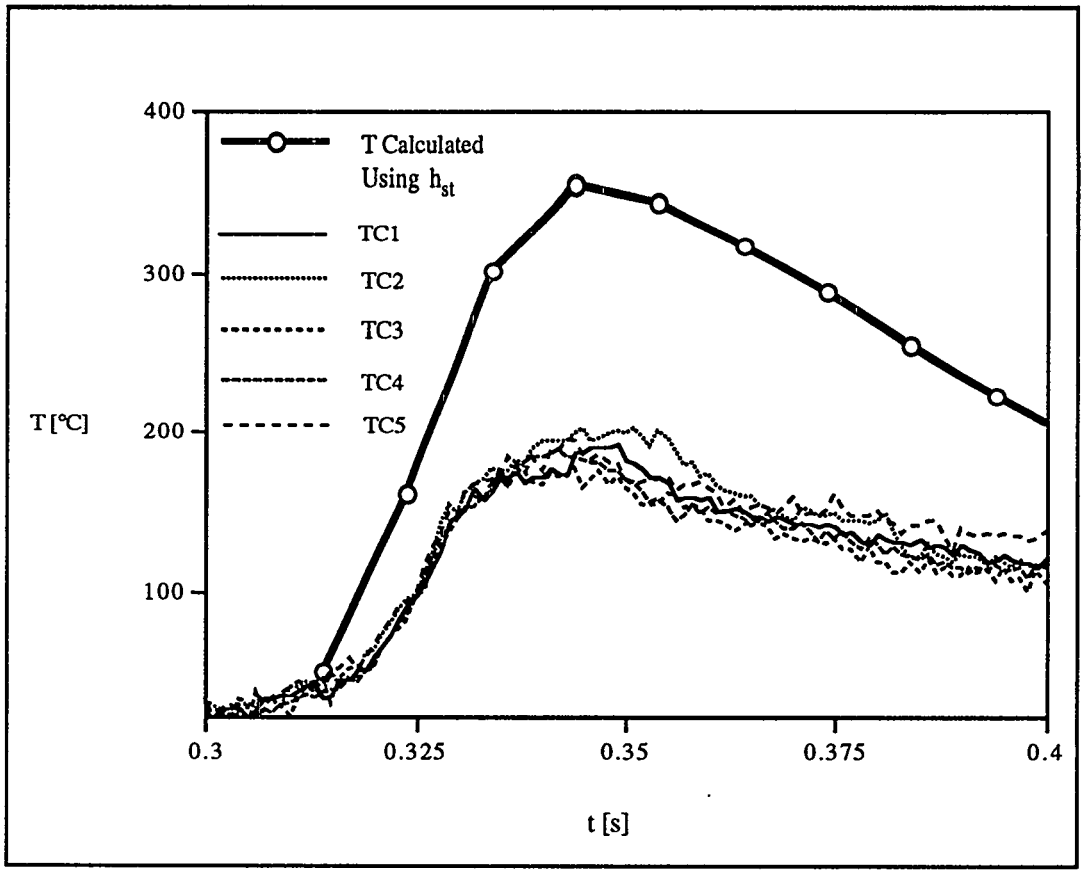

Fig. 4 Predictions and Experimental Data for Case 518-4 Assuming Steady Pool Boiling in Region II.

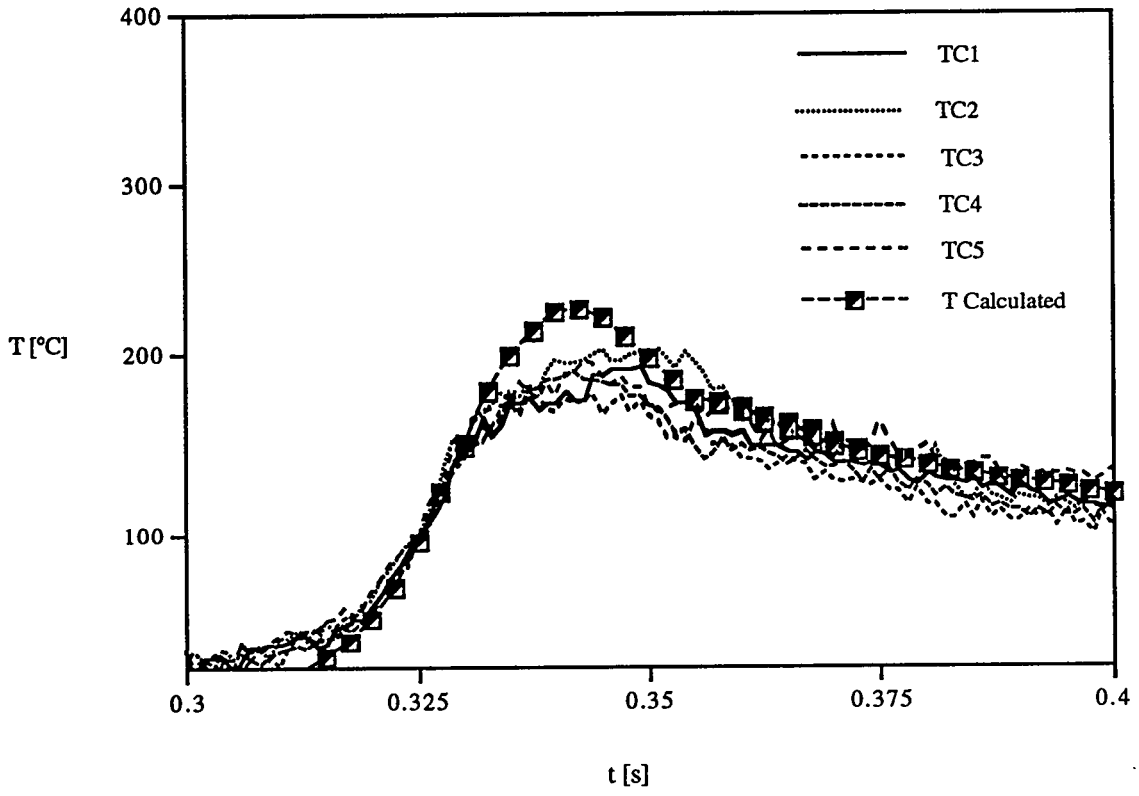

Fig. 5 Predictions and Experimental Data for Case 518-4.

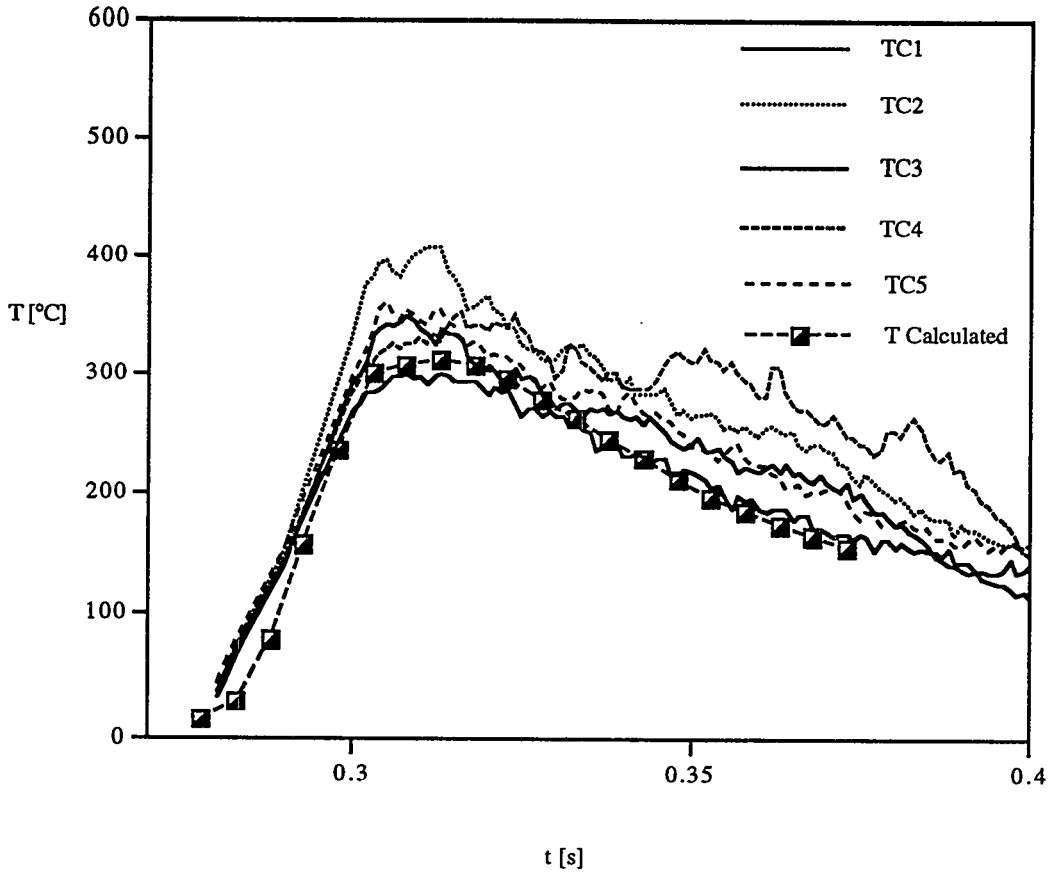

Fig. 6 Predictions and Experimental Data for Case 518-1.

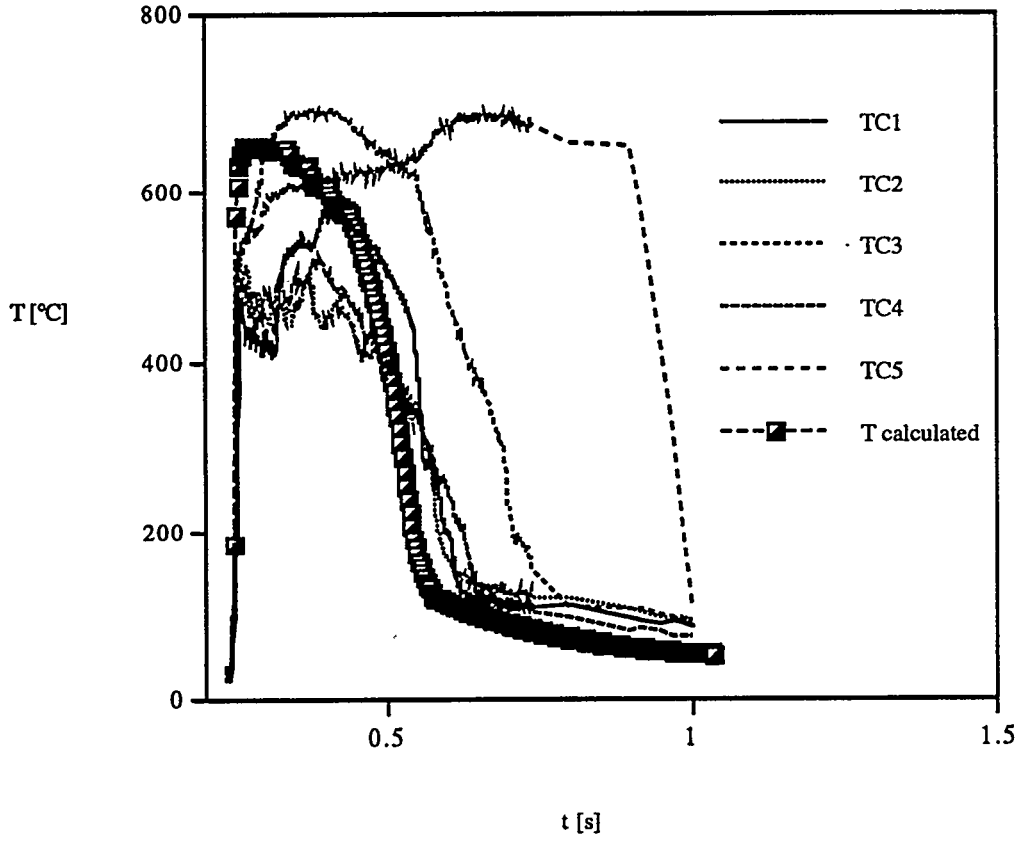

Figure 7. Predictions and Experimental Data for Case 518-2.

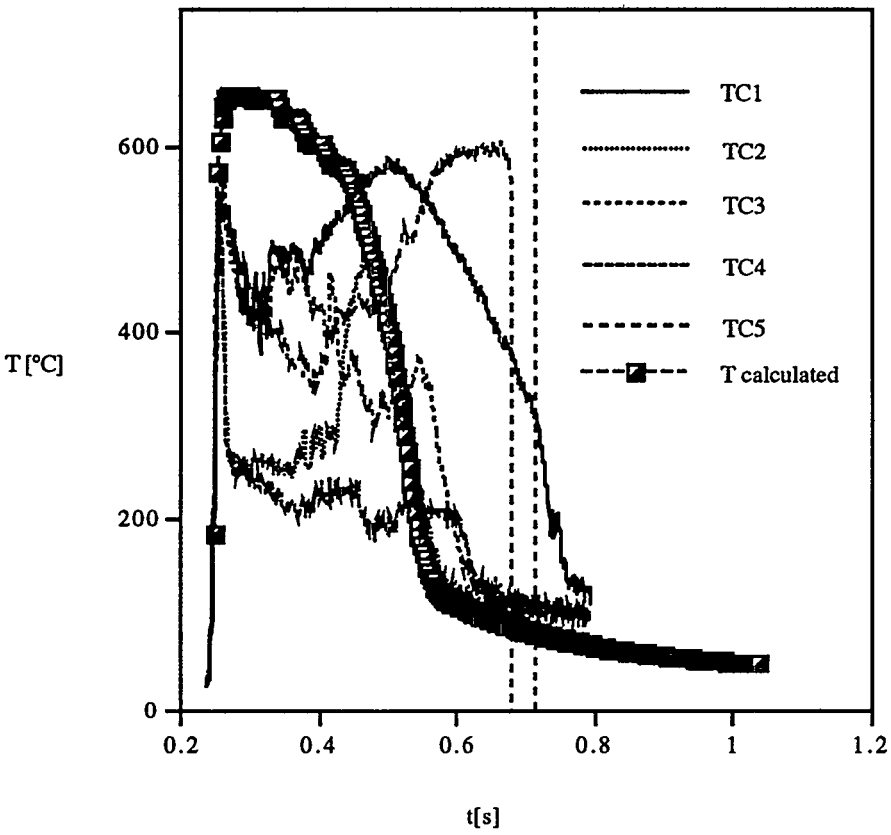

Fig. 8 Predictions and Experimental Data for Case 518-5.

Study on Severe Accident Fuel Dispersion Behavior in the Advanced Neutron Source Reactor at Oak Ridge National Laboratory*

S.H. Kim, R.P. Taleyarkhan, S. Navarro-Valenti, and V. Georgevich
Engineering Technology Division
Oak Ridge National Laboratory
Oak Ridge, TN 37831-8045

J.Y. Xiang
Wabash College
Crawfordsville, IN 47933

Abstract

Core flow blockage events have been determined to represent a leading contributor to core damage initiation risk in the Advanced Neutron Source (ANS) reactor. During such an accident, insufficient cooling of the fuel in a few adjacent blocked coolant channels out of several hundred channels, could also result in core heatup and melting under full coolant flow condition in other coolant channels. Coolant inertia forces acting on the melt surface would likely break up the melt into small particles. Under thermal-hydraulic conditions of ANS coolant channel, micro-fine melt particles are expected. Heat transfer between melt particle and coolant, which affects the particle breakup characteristics, was studied. The study indicates that the thermal effect on melt fragmentation seems to be negligible because the time corresponding to the breakup due to hydrodynamic forces is much shorter than the time for the melt surface to solidify. The study included modeling and analyses to predict transient behavior and transport of debris particles throughout the coolant system. The transient model accounts for the surface forces acting on the particle that results from the pressure variation on the surface, inertia, virtual mass, viscous force due to the relative motion of the particle in the coolant, gravitation, and resistance due to inhomogenous coolant velocity radially across piping due to possible turbulent coolant motions. The results indicate that debris particles would reside longest in heat exchangers because of lower coolant velocity there. Also they are entrained and move together in a cloud.

Introduction

The Advanced Neutron Source (ANS) is to be a multipurpose neutron research center and is currently in the advanced conceptual design stage at the Oak Ridge National Laboratory (ORNL). Major areas of research will include condensed matter physics, materials science, isotope production, and fundamental physics [1, 2]. The ANS is planned to be a 303-MW(t) heavy-water-cooled and moderated research reactor housed in a large, double-walled containment dome and surrounded by thermal neutron beam experimental facilities. The reactor uses U_3Si_2–Al cermet fuel in a plate-type configuration. Cooling systems are designed with many safety features, including large heat sinks sufficient for decay heat removal; passive inventory control by accumulators, pools, and flooded cells; a layout that maximizes natural circulation capabilities; and fast, redundant shutdown systems. A defense-in-depth philosophy has been adopted. In response to this commitment, ANS project management initiated severe accident analyses and related technology development early in the design phase. This was done to aid in designing a sufficiently robust containment for retention and controlled release of

* Prepared by the Oak Ridge National Laboratory, Oak Ridge, TN 37831 operated by Martin Marietta Energy Systems Inc., for the US Department of Energy under Contract No. DE-AC05-840R21400

radionuclides in the event of an accident. It also provides a means for satisfying on- and off-site regulatory requirements, accident-related dose exposures, containment response, and source-term best-estimate analysis for Level-2 and -3 Probabilistic Risk Analyses (PRAs) that will be produced. Moreover, it will provide the best possible understanding of the ANS under severe accident conditions and, consequently, provide insights for development of strategies and design philosophies for accident mitigation, management, and emergency preparedness efforts [3].

Past scoping studies have indicated the possibility of core debris recriticality in reactor coolant system (RCS) piping sections, under dispersed configuration [4]. Clearly, in order to provide the basis for closure of this concern and the incorporation of suitable design fixes, the likelihood of such dispersed configurations needs to be quantified. This requires an ability to describe the various material motions and characterization of the various energetic phenomena as they are affected by phase change and/or fission gas release.

In this paper, the modeling and analysis framework for evaluation of ANS core debris dispersion phenomena are described. For an accident initiated by a core flow blockage event, several mathematical models have been developed for characterizing debris particles, statistical distribution of particle size, dispersion, and transport into the coolant stream. These models are presented along with analyses results conducted to date.

ANS System Description

The ANS is currently in the conceptual design stage. As such, design features of the containment and reactor systems are evolving, based on insights from ongoing studies. Table 1 summarizes the current principal design features of the ANS from a severe accident perspective compared with the High Flux Isotope Reactor (HFIR) and a commercial light-water reactor (LWR). Specifically, the ANS reactor will use uranium silicide fuel in an aluminum matrix with plate-type geometry and a total core mass of 100 kg. The power density of the ANS will be only about 2 times higher than that of the HFIR, but about 50 to 100 times higher than that of a large LWR. Because of such radical differences, high-power-density research reactors may give rise to significantly different severe accident issues. Such features have led to increased attention being given to phenomenological considerations dealing with steam explosions, recriticality, core-concrete interactions, core-melt progression, and fission-product release. However, compared to power reactor scenarios, overall containment loads from hydrogen generation and deflagration are relatively small for the ANS.

Table 1 Severe accident characteristics of the ANS and other reactor systems

Parameter	Commercial LWR	HFIR	ANS
Power, MW(t)	2600	100 [a]	303
Fuel	UO_2	U_3O_8–Al	U_3Si_2–Al
Enrichment (m/o)	2–5	93	93 [b]
Fuel cladding	Zircaloy	Al	Al
Coolant/moderator	H_2O	H_2O	D_2O
Coolant outlet temperature, K	590	342	365
Average power density, MW/L	<0.1	2.0	4.5
Clad melting temperature, K	2123	853	853
Hydrogen generation potential, kg	850	10	12

[a] Now operating at a reduced power of 85 MW.

[b] 1992 baseline (reduced enrichment now being considered)

The reactor core is enclosed within a core pressure boundary tube and enveloped in a reflector vessel, which is immersed in a large pool of water. Each element of the core is constructed with a series of involute fuel plates arranged in an annular array. The involute design provides uniform coolant gaps at all spanwise positions. The 1.27-mm-thick fuel plate consists of 0.254-mm-thick 6061 aluminum cladding material, sandwiching a 0.762-mm mixture of uranium silicide (U_3Si_2) and aluminum. Each coolant gap is also 1.27 mm in width and has a span of 70.29 or 87.35 mm (upper or lower core, respectively). Fuel plates are welded to inner and outer cylindrical side plates with each element having 507 mm of fueled length. Unheated 10-mm leading and trailing edges complete the fuel plate design.

Particle Entrainment During a Severe Fuel Damage Event

Accident progression to the onset of core melting due to flow blockage is described in a companion paper [5]. Once a fuel plate becomes molten, structural change is expected to occur due to the presence of the unstable interfaces. Generally, the interaction at an interface between two media of different densities results in wave formation. Stability of this interface largely depends on surface tension and coolant inertia forces ($\sigma/\delta_l \sim \rho u^2$). In most cases of interest, a characteristic length, δ_l, can be related to the critical wave length as

$$\delta_l \sim \sqrt{\frac{\sigma}{g\,\Delta\rho}} \tag{1}$$

where $\Delta\rho$ is a density difference of two contacting media. Therefore, a critical flow velocity at which the interface becomes unstable, u_e, can be written [6]

$$u_e = \zeta \left[\frac{\sigma_p\, g\,(\rho_p - \rho_c)}{\rho_c^2}\right]^{0.25} \tag{2}$$

where the subscripts, p, c denote the molten fuel plate and coolant medium, respectively, and ρ_c is the density of the continuous phase for a given stable regime (e.g., coolant). At a liquid water-vapor interface, the first waves to appear are small ripples. Higher vapor velocities lead to an increase in the amplitude of these ripples, and soon three-dimensional disturbances are generated. For a two-phase system of liquid water and vapor, it was observed experimentally that the water liquid film abruptly broke up and was entrained by the vapor at the critical vapor velocity, corresponding to the stability number (ζ) of around 3.7 [7]. There is uncertainty in applying this stability number for a liquid-liquid interface. However, it provides us with an idea about the critical velocity at which the fuel entrainment would occur.

Using Eq. (2) for the ANS, the critical coolant velocity for the fuel entrainment can be obtained as 1.3 m/s (based on ρ_c = 1000 kg/m^3, ρ_p = 2700 kg/m^3, σ_p = 0.868 N/m). If the coolant is saturated steam, then 13 m/s is the velocity obtained based on ρ_c = 12 kg/m^3 at 2.5 MPa.

To further examine the coolant condition (in a single channel where significant boiling is assumed to occur under a hypothetical severe accident), its velocity is evaluated as a function of channel inlet velocity assuming constant pressure and homogeneous two-

phase flow. By neglecting internal heat generation and viscous dissipation, the local steam velocity at any axial position, z, is given by [8]

$$u_g(t) = \frac{G_i(t)}{\rho_c} + \Omega[z - \lambda(t)] \tag{3}$$

the parameter, Ω, represents the speed at which phase change takes place and is expressed as

$$\Omega \equiv \frac{2\dot{q}'' w v_{fg}}{h_{fg} A_{x-s}} \tag{4}$$

The boiling boundary, λ(t), is given by

$$\lambda(t) = \frac{G_i(t) A_{x-s} \Delta h_{sub}}{2\dot{q}'' w} \tag{5}$$

Figure 1 illustrates fluid velocity at the channel exit (0.507 m) as a function of fluid inlet velocity for various heat fluxes. As the inlet velocity increases, the exit velocity decreases because of increased boiling boundary length. The exit velocity eventually reaches the same value as the inlet velocity when no bulk boiling occurs in the channel (due to the assumption of constant pressure). In reality, since we have several hundred channels in parallel, the occurrence of significant boiling in any one channel would cause parallel channel flow instability [5], which results in flow from the channel with boiling to be diverted into other non-boiling channels. Nevertheless, as seen in the figure, fluid velocity in the coolant channel is sufficiently high to entrain the fuel melt whether or not it boils.

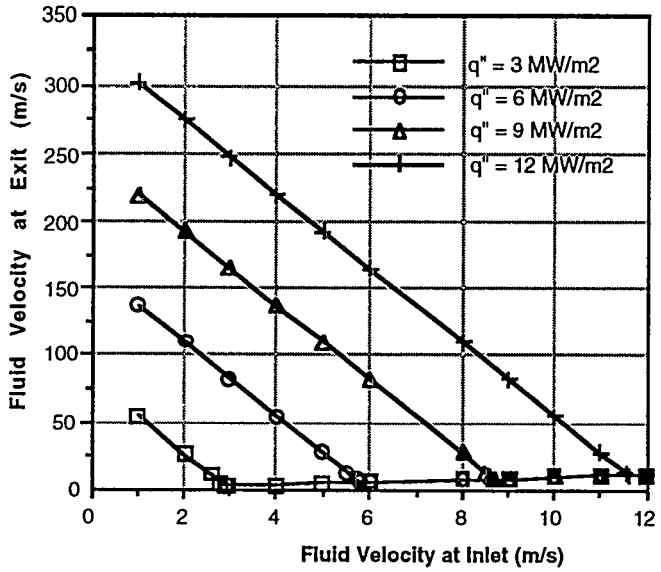

Fig. 1 Fluid velocity at channel exit versus inlet velocity under hypothetical, fixed inlet flow conditions

Melt Particle Breakup

Initial particle size

The characteristic length, defined in Eq. (1), is based on an instability at the interface induced by the density difference of two contacting media. For aluminum, Eq. (1) gives values of 5 to 7 mm depending on vapor or liquid phase of continuing fluid medium. This number is substantially larger than the physical thickness of a fuel plate (e.g., 1.27 mm) and of the coolant gap. Initial breakup of the melted plate is thought to be governed by Kelvin-Helmholtz (KH) instability. A wave is developed at the interface of two media moving at different velocities. An intact (melted) plate with coolant (either vapor or liquid) flowing at a relatively high velocity in ANS conditions is a configuration similar to melt jet penetrating through a stagnant (or slowly moving) water pool. Extensive research has been performed in the past to predict this jet penetration problem. A general agreement is that at the interface between melted jet and water, KH instability determines the jet breakup behavior. Kocamustafaogullari derived the maximum stable particle size based on classical KH instability theory for molten drops, and his predictions were compared reasonably well against breakup data collected by several other researchers for various gas-liquid and liquid-liquid systems [9]. According to his predictions and data collected, the maximum stable particle size varies in the range of 5 to 10 mm for a gas-liquid system and of 6 to 150 mm for a liquid-liquid system. Initial particle sizes must have been larger than these maximum particle sizes. As indicated above, however, initial breakup will be limited by the physical size of the melted plate. Furthermore, any wave growth at the melt-coolant interface must be limited by the physical size of the coolant gap, which is 1.27 mm. Therefore, in our study, we assume that the initial melt particle is 1.27-mm-diameter, which is the plate thickness, instead of expending further efforts to study details of interfacial stability problems.

Particle size distribution

Based on Wolfe's extensive data collected for Bis drops (d_0 = 1.6 mm, 2.7 mm), Pilch described particle size variations as a log-normal distribution given as [10]

$$f\left(\frac{d}{d_o}\right) = \frac{1}{\sqrt{2\pi}}\frac{1}{\beta}\frac{d_o}{d}\exp\left\{-\frac{1}{2\beta^2}\left[\ln\left(\frac{d}{d_o}\right) - \gamma\right]^2\right\} \qquad (6)$$

where β and γ can be determined as a function of the Weber number, from Wolfe's data as

$$\beta = -0.0879\ln(We) + 1.38 \qquad \text{and} \qquad \gamma = \ln(-0.168\,We^{-0.5}) \qquad (7)$$

The normalized number distribution in Eq. (6) is defined as the fractional number of fragments per drop per normalized size range. Our molten debris consists of aluminum mixed with uranium silicide, and thus a statistical distribution of particle size might be different from the Wolfe's data. Furthermore, a chemical reaction between aluminum and uranium silicide at the temperature above aluminum melting temperature may change material properties due to eutectic formation. Such a change in material properties has not been known yet. For the current study, therefore, it was decided to use the Wolfe's data for particle size distribution. In future, we can probably collect our own data for our material, and formulate similar expressions for β and γ, as given in Eq. (7). For our

condition, assuming 2700 kg/m^3 for debris density, 20 m/s for liquid coolant velocity, and 1.27 mm for initial particle diameter, the Weber number is estimated as 585. Listed in Table 2 is the resulting particle distribution discretized into five bins.

Table 2 Discretized Particle Distribution

Bin	Size range, diam. (m)	Number fraction	Mass fraction
1	10^{-8} to 5 x 10^{-6}	0.47923	0.10999
2	5 x 10^{-6} to 7 x 10^{-6}	0.2232	0.23645
3	7 x 10^{-6} to 9 x 10^{-6}	0.1832	0.34797
4	9 x 10^{-6} to 10^{-5}	0.07699	0.1973
5	10^{-5} to 10^{-4}	0.03748	0.10829

Effect of melt solidification on melt breakup

While the melt (or melted plate) undergoes breakup, the particles will transfer heat to its surrounding medium. Under certain conditions, the particle breakup process may be limited by solidification of particles. Such a thermal effect is assessed by comparing the time for the melt to become solidified against the time for melt breakup to occur.

The melt particles will start to solidify if heat generation becomes less than heat losses. A solid crust will form at the particle surface and grow inward. As it grows, this crust shell becomes stronger; at the same time it will be exposed to increased stress because of pressure buildup due to heat generation inside of the crust shell. At a certain threshold shell thickness, the crust will break up, and the internal melt will be exposed to hydrodynamic forces for further breakup. The time for this thermal process (t_t) can be characterized into two periods. One is the time taken for the temperature of the melt particle surface to decrease to its solidification temperature (t_{ts}), and the other is the time taken for the crust shell to break up due to internal pressure buildup (t_{tb}). The effect of this thermal process can be assessed by comparing this time against the time for the melt breakup due to hydrodynamic forces (t_h). If $t_{ts} >> t_h$, evaluation of t_{tb} is not necessary, and we can conclude that hydrodynamics dominate over thermal process for melt particle breakup.

To evaluate t_{ts}, transient heat conduction equation for a sphere is written as

$$\frac{1}{\alpha}\frac{\partial\theta}{\partial t} = \frac{1}{r^2}\frac{\partial}{\partial r}\left(r^2\frac{\partial\theta}{\partial r}\right) + \frac{\dot{q}'''}{k} \tag{8}$$

where $\theta = T - T_\infty$, and T_∞ is the surrounding bulk temperature. With boundary and initial conditions as the following,

$$\left.\frac{\partial\theta}{\partial r}\right|_{r=0} = 0, \quad -k\left.\frac{\partial\theta}{\partial r}\right|_{r=R} = h\theta, \quad \theta|_{t=0} = T_o - T_\infty \equiv \theta_o \tag{9}$$

Equation (8) can be solved to give temperature distribution in a melt particle as

$$\theta(r,t) = \frac{1}{r}\sum_{n=1}^{\infty} k_n \sin(\lambda_n r)\, e^{-\alpha\lambda_n^2 t} + \frac{\dot{q}'''}{6k}(R^2 - r^2) + \frac{\dot{q}'''R}{3h} \tag{10}$$

where the constant k_n is determined as a function of the eigenvalue, λ_n. Table 3 lists the four eigenvalues for various particle diameters with 740 W/m^2-K of convective heat transfer coefficient and 190 W/m-K of thermal conductivity. The first term on the right-hand side of Eq. (10) becomes zero for n = 1 ($\lambda_1 = 0$). For n = 3,4,..., this term becomes too small to compare with that for n = 2, due to the large eigenvalues in the exponential term.

Table 3 Eigenvalues for Various Particle Diameters (d)

n	d = 4 x 10^{-4} m	d = 8 x 10^{-4} m	d = 1.27 x 10^{-3} m
1	0	0	0
2	241.6	170.8	135.6
3	22,467	11,234	7,077
4	38,626	19,313	12,166

When the melt starts to experience solidification at its surface, therefore, its corresponding time can be approximated from Eq. (10) as

$$t_{ts} \approx -\frac{1}{\alpha\lambda_2^2} \ln\left[\frac{R\left(\theta_m - \frac{\dot{q}'''R}{3h}\right)}{k_2 \sin(\lambda_2 R)}\right] \quad , \qquad where\ \theta_m = T_{melt} - T_\infty \qquad (11)$$

Hydrodynamic breakup time (t_h) is defined as the time when the melt particles are no longer subject to further breakup. The normalized breakup time was correlated by Pilch, based on experimental data collected by several investigators for a gas-liquid system, and given as [10]

$$\tau_h = a(We - 12)^b \qquad (12)$$

Hydrodynamic breakup time is defined from normalized breakup time as

$$t_h = \tau_h \frac{d_o}{u_c - u_p}\left(\frac{\rho_c}{\rho_p}\right)^{0.5} \qquad (13)$$

The constants a and b in Eq. (12) are listed in Table 4.

Table 4 Constants for Pilch's Correlation for Melt Breakup Time for Gas-Liquid System

Range	a	b
12 ≤ We < 18	6	- 0.25
18 ≤ We < 45	2.45	0.25
45 ≤ We < 351	14.1	- 0.25
351 ≤ We < 2670	0.766	0.25
2670 ≤ We	5.5	0

There are not enough data available to draw a general conclusion for the breakup time for the liquid-liquid system. Baines' study of the breakup of mercury drops in water revealed a normalized breakup time for the liquid-liquid system, τ_b, of 4 to 5, which is comparable to that for a gas-liquid system [11] . On the other hand, Theofanous reported a significantly lower breakup time for a mercury-water system (e.g., 2 to 5 times faster) [12]. However, if the breakup time from Eq. (12) is estimated to be smaller than the solidification time, t_s, we can still draw a reasonable conclusion that the hydrodynamics govern the melt break-up process.

With 1.27 mm of initial diameter, the breakup time given by Eqs. (12) and (13) is estimated to be 0.145 ms. Melt solidification time is illustrated in Fig. 2, as a function of particle size for various levels of power generation and 10 K initial super heat above the particle melting temperature. One can easily see that the particle breakup due to hydrodynamic process occurs much earlier, even before the melt surface starts to become solidified. This leads to the conclusion that the particle breakup process is mainly governed by hydrodynamic process, at least in the fuel melting accidents in the ANS, which we currently consider.

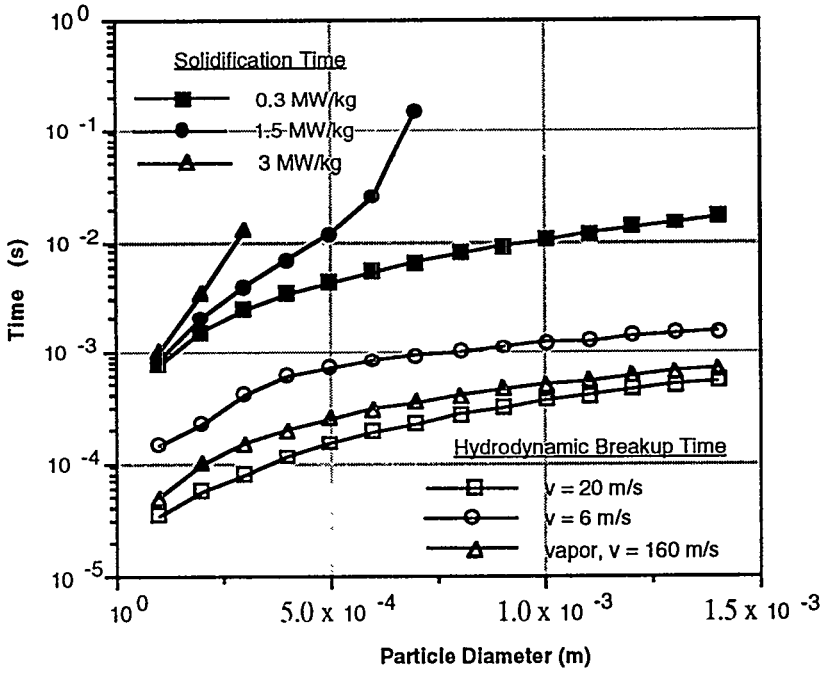

Fig. 2 Melt particle solidification time

Particle Dispersion Throughout RCS

It is desirable to know how debris particles originating from the core region in a severe accident would be dispersed throughout the coolant system at different velocities. To conduct this evaluation, the entire coolant system was nodalized into several control volumes, as seen in Fig. 3. Particle density of size bin-i in control volume-j, $n_{i,j}$ can then be expressed as

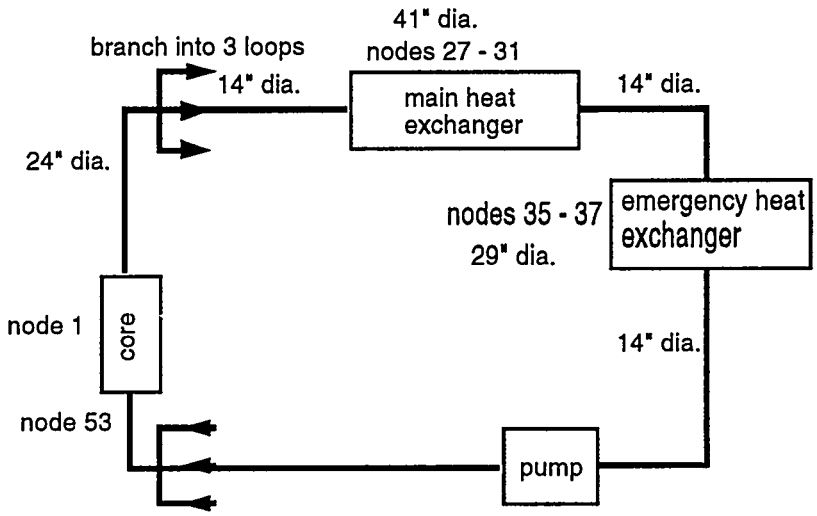

Fig. 3 Schematic nodalization of ANS RCS

$$\frac{dn_{i,j}}{dt} = \frac{1}{V_j}\left[n_{i,j}\, u_{i,j}\, A_j\right]_{out}^{in} + s_{i,j} \tag{14}$$

where the bracket, $[\ ]_{out}^{in}$, represents inflow subtracted by outflow and where donor cell properties are used for flow properties, including particle velocity and particle density.

It is realized that the motion of particles in the coolant stream is certainly nonuniform, and always changing both in direction and magnitude of velocity. However, to obtain an overall perspective and to capture the essential physics of the transport processes, a one-dimensional approximation was made. The transient rectilinear motion of a spherical particle in a turbulent flow, with nonzero mean velocity, can be given as [13,14]

$$\begin{aligned}\frac{\pi d^3\rho_p}{6}\frac{du_p}{dt} = {} & \frac{\pi d^3\rho_c}{6}\frac{du_c}{dt} + \frac{1}{2}\frac{\pi d^3\rho_c}{6}\left(\frac{du_c}{dt} - \frac{du_p}{dt}\right) + 3\pi\nu_c\rho_c d\left(u_c - u_p\right) \\ & + \frac{\pi d^3}{6}\left(\rho_c - \rho_p\right)g\delta - \frac{5\pi d^3\rho_c}{16R}u_c\left(u_c - u_p\right)\end{aligned} \tag{15}$$

where ν is the kinematic viscosity and subscripts p and c are particle and coolant fluid, respectively. The first term on the right-hand side of Eq. (15) is the surface force acting on the particle that results from the pressure variation on the surface, which is a function of the pressure field in the entraining coolant. The second term is for the inertia of the virtual mass (entrained with relative motion of the particle in the coolant) and is equivalent to an increase in particle mass equal to half the mass of the coolant displaced. The third term describes the viscous force (e.g., Stokes' linear resistance) due to the relative motion of the particle in the coolant. The fourth term is the gravitational force, and δ in this term is the directional cosine. The last term describes a resistance due to inhomogeneous coolant motion caused by turbulence. According to Tchen [14], coolant motion in the radial direction in pipe flow induces additional resistance to the particle movement and is expressed as

$$F = \frac{\pi}{4}\rho_c d^3\left(u_c - u_p\right)\frac{\partial u_c}{\partial r} \tag{16}$$

For turbulent flow in a round pipe, the coolant velocity profile can be approximated as [15]

$$u_c(r) = u_{c,\max}\left(1 - \frac{r}{R}\right)^{\frac{1}{7}} \tag{17}$$

Averaging the derivative of Eq. (17) with respect to r for $u_{c,max} = 5u_c/4$ yields

$$\left\langle \frac{\partial u_c}{\partial r} \right\rangle = \frac{1}{R}\int_0^R \frac{\partial u_c}{\partial r}\, dr = -\frac{5}{4}\frac{u_c}{R} \tag{18}$$

Therefore, Eq. (16) averaged over a pipe cross-sectional area is expressed as the last term in Eq. (15).

Interactions between particles, and between particles and pipe (or structure) wall, are not included in Eq. (15) because particle sizes under consideration are small enough to neglect particle collision. The coolant velocity is assumed to be constant with time in our calculations and is taken from a separate RELAP calculation (i.e., 25 m/s in core and 6~7 m/s in other regions of reactor coolant loop). This implies the absence of any significant influence of debris particles on the bulk coolant flow. This postulate was based on the significantly larger inertia of the bulk coolant flow relative to inertia of debris particles.

Results and Analysis

A preliminary calculation has been performed to observe the debris particle dispersion throughout the primary RCS. The entire coolant system was nodalized into 53 control volumes. Each control volume was set at about 2 m in length. The effective core diameter (e.g., control volume 1) was determined from the rate of coolant flowing through the core (1,994 kg/s) and the coolant density of 1,000 kg/m^3. Among the four coolant loops, three loops are normally on-line, with the fourth loop on a standby basis. The control volumes 16 through 52 represent one of the three loops. One main heat exchanger and one emergency heat exchanger are in each coolant loop. The primary coolant is to flow through the shell side of each heat exchanger. Main and emergency heat exchangers are represented by five and three control volumes, respectively; that is, control volumes 27 through 31 for main heat exchanger and 35 through 37 for emergency heat exchanger, as seen in Fig. 3. The control volume length and coolant velocity for the heat exchangers were obtained to correctly evaluate the residence time of the coolant in heat exchangers. For the given coolant velocity (e.g., 0.78 m/s for main heat exchangers, and 1.57 m/s for emergency heat exchangers) and mass flow rate, the diameter of each heat exchanger was calculated as 1.04 m (41 in.) and 0.73 m (28.9 in.) for main and emergency heat exchangers, respectively.

Only the first control volume representing the reactor core generates debris particles. For a test case, the debris particles were generated at the rate of 667.67 kg/s for 0.15 s, which results in 100 kg of debris particles. This 667.67 kg/s was based on a constant melting of the core; that is 303 MW of power divided by 0.397 MJ/kg of latent heat of fusion of aluminum. Actually it gives 755.67 kg/s and 0.1323 s of melting period to generate 100 kg of debris particles. However, the melting rate was adjusted to be 667.67 kg/s during 0.15 s of melting period. The statistical distribution of the particle size is given in Table 2. Note that the largest particle size would be (as in Table 2) 10^{-4} m, which is even smaller than the mesh size of the strainer in the cold leg. Therefore, it is conservatively

assumed that the effect of the strainer for capturing the core debris particles is negligible. Variation in particle size turns out not to affect the debris dispersion behavior very much because the high coolant velocity leads the particle to approach the terminal velocity (e.g., coolant velocity) very quickly. It was usually observed that the particles reach the coolant velocity within the first control volume where they are introduced. Core debris is a mixture of solid uranium silicide particles dispersed in molten aluminum. Because uranium silicide is heavier than aluminum (e.g., 12.8 g/ml for U_3Si_2 vs 2.7 g/ml for Al), it is possible for U_3Si_2 particles to be segregated. To examine this possibility, calculations were performed as if all the particles are U_3Si_2. The resulting particle distribution throughout the coolant system was compared with that for the case with all aluminum particles. The differences were almost negligible because the particles reach the equilibrium velocity so quickly in the fast-moving coolant that we consider here. Therefore, the description of results and the analysis are provided for the dispersion of aluminum particles.

Figures 4 through 7 demonstrate the results in terms of debris mass and also the temporal variation of debris mass at a few selected locations. Debris mass distributions at several different times are shown in Figures 4 (a) and (b). It is seen that the heat exchangers are the locations where the particles reside longest. One must note that debris mass in one actual coolant loop is to be one-third of the value shown in the figures for nodes from 16 through 52. Also, it needs to be pointed out that a particle takes about 27 s to traverse an entire coolant loop, as evident in Figure 4 (b) for the debris mass at 30, 35 and 40 s. Figure 5 shows the same results for an earlier time period, from 0.5 s through 5 s. It is clearly seen that the debris mass at the moving front diminishes as the particles disperse farther. Debris mass is also shown in Figure 6 for 0.05 s through 0.5 s. It is seen that the debris particle mass in the control volume 1 (core) increases during debris particle generation (0.15 s). In this calculation, one should note that the intact core mass is not included as a part of debris mass in the control volume 1, which is the core. Upon completing debris particle production, core debris mass decreases as seen in the figure. However, debris mass in the next volume (CV-2) keeps increasing to about 90 kg for a time because the particle takes about 0.28 s to travel through the control volume as evident from the fact that the particle starts showing up in the third volume at 0.3 s in the figure (this time difference, 0.28 s vs 0.3 s is due to the finite size of time step). Figures 7 (a) and (b) show the temporal variation of debris mass at control volumes 2,3,4, and two heat exchanger volumes. It is seen that at the coolant downstream out of the core, maximum debris mass is predicted to be about 90 kg. This means that the entire core moves almost together under the assumed conditions of debris particle generation and introduction into the fast-moving coolant. However, it shows that the debris particles disperse throughout the coolant loop volumes as they move. The entire debris mass (100 kg) is seen to stay in the main heat exchanger at around 14 s. But, one must recall that we have three heat exchangers holding this 100 kg of core mass. Therefore, the main heat exchanger in each coolant loop would hold one-third of 100 kg of debris mass if debris at the branch node 16 is equally distributed among the three loops. To check the sensitivity of nodalization on the debris mass, the control volume 2 was further divided into two volumes. The results indicate that the control volume nodalization does not seem to be very sensitive in debris dispersion, while it may be possible to have locally higher debris concentration in some instances.

Summary and Conclusion

In this paper, models for debris particle dispersion have been developed and presented. Along with particle dispersion, debris breakup behavior was also characterized. The transient model for particle dispersion and transport accounts for the surface forces acting on the particle that results from the pressure variation on the surface, inertia, virtual mass,

viscous force due to the relative motion of the particle in the coolant, gravitation, and resistance due to inhomogenous coolant velocity radially across piping due to possible turbulent coolant motions. Numerical calculations were performed for debris dispersion throughout the primary coolant system.

Coolant inertia force acting on the melt surface will likely break up the melt into small particles. Under the expected thermal-hydraulic conditions in an ANS coolant channel, micro-fine melt particles are predicted. Heat transfer between melt particles and coolant, which affects the particle breakup characteristics, was studied. The study indicated that the thermal effect on melt fragmentation seems to be negligible because the time corresponding to the breakup due to hydrodynamic forces is much shorter than the time for the melt surface to solidify. For the specific case analyzed, the results of particle dispersion calculations indicate that debris particles would reside longest in heat exchangers because of the lower coolant velocity there. Also, core debris tends to move together upon melting and entrainment. Recriticality concern will be studied in future, with respect to debris particle dispersion in RCS.

The current model for the debris dispersion does not account for the interaction between particles, or for interaction between particles and structure walls, which may slow down particle dispersion in some degree. However, further work to include particle interaction modeling does not seem to be necessary at this stage because its effect is thought to be small. Also missed in the current model is the feedback to the coolant. The coolant velocity must be affected by existence of debris in its stream. The current model, however, assumes that the coolant velocity stays constant, unaltered by debris particles in it stream. In addition, missed is the model for the particle entrapment in local pockets where the bulk coolant velocity is nearly zero.

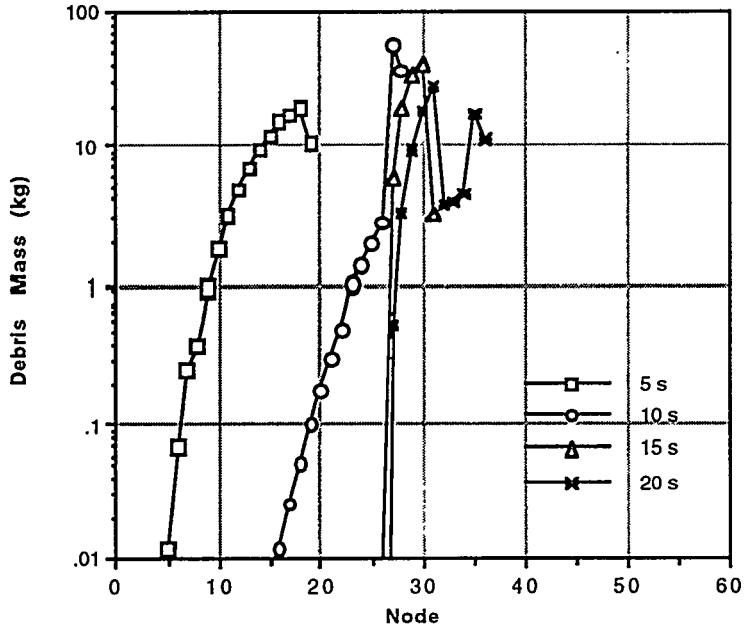

Fig. 4(a) Distribution of debris mass upon 100% core disruption

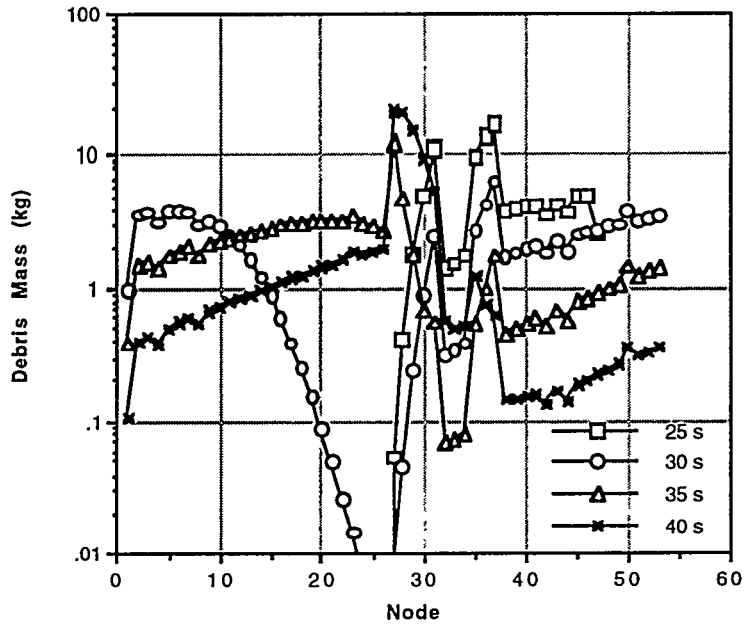

Fig. 4(b) Distribution of debris mass upon 100% core disruption

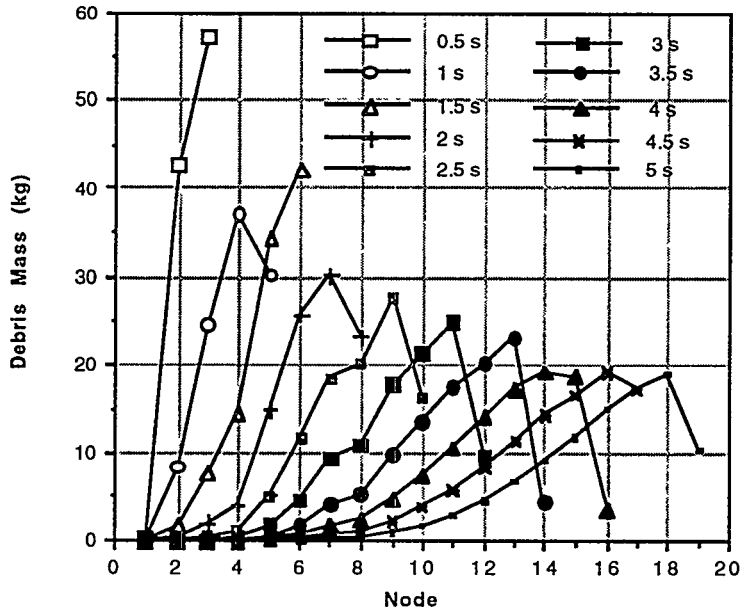

Fig. 5 Debris particle distribution from 0.5 to 5.0 s

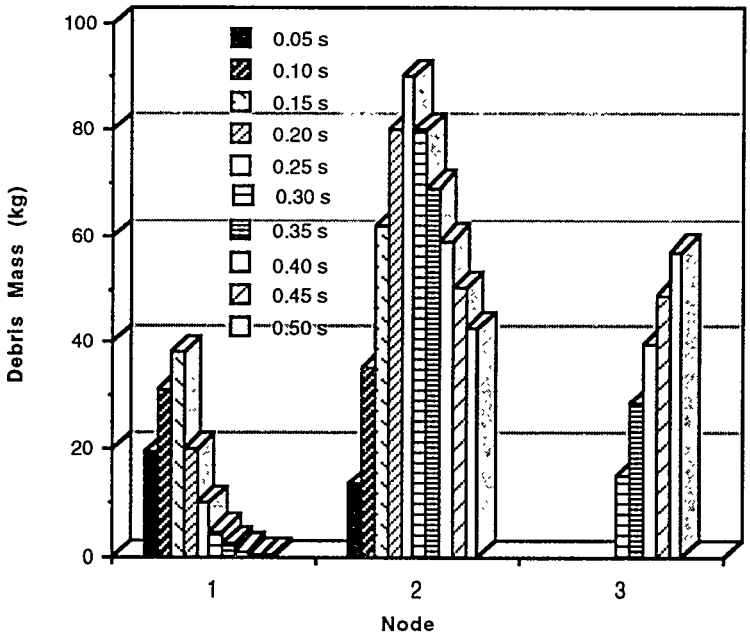

Fig. 6 Debris particle distribution from 0.05 to 0.50 s

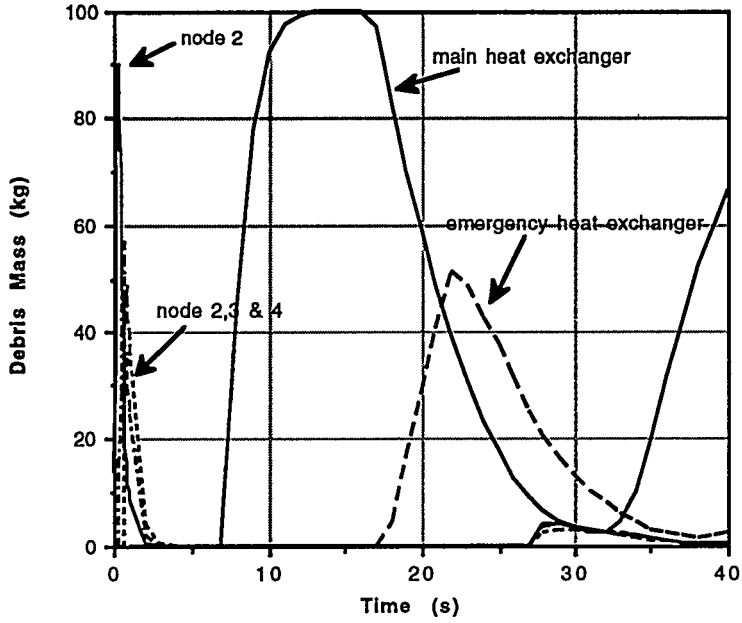

Fig. 7(a) Time variation of debris mass at selected locations

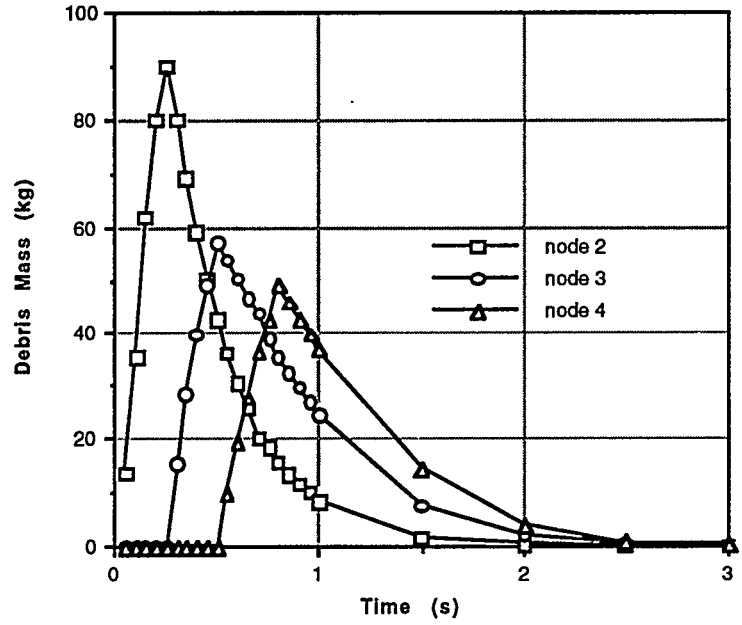

Fig. 7(b) Time variation of debris mass at core downstream

Nomenclature

A_j	cross-sectional flow area of control volume j
A_{x-s}	cross-sectional area
d	particle diameter
d_o	initial particle diameter
G_i	mass flux at channel inlet
g	gravitational acceleration
h	convective heat transfer coefficient
h_{fg}	heat of vaporization of water
k	thermal conductivity
n_{ij}	number density of particle bin i in control volume j
q''	heat flux
q'''	volumetric heat generation
R	pipe radius or effective radius of control volume
s_{ij}	rate of volumetric particle source of bin i in control volume j
t_h	particle break-up time due to hydrodanamic process
t_t	particle break-up time due to thermal process
t_{ts}	time taken for the particle surface to be solidified
t_{tb}	time taken for the solidified particle shell to be broken up
u	velocity
u_{ij}	particle velocity of bin i in control volume j
v_{fg}	difference of specific volumes (= v_g - v_f)
V_j	volume of control volume j
w	channel width
We	Weber number ($=\rho u^2 d_o/\sigma$)
z	channel length
Δh_{sub}	inlet subcooling of coolant channel
α	thermal diffusivity
β & γ	experimentally determined coefficients for particle distribution
δ	directional cosine
δ_l	characteristic length
λ	boiling boundary
λ_n	eigen value
ν	kinematic viscosity
ρ	material density
σ	surface tension
ζ	stability number
Ω	phase change speed

References

[1] C. D. West, "The Advanced Neutron Source: A New Reactor-Based Facility for Neutron Research," Trans. Amer. Nuc. Soc. 61, 375 (June 1990).

[2] C. D. West, "Advanced Neutron Source Plant Design Requirements," ORNL/TM-11625, (May 1992).

[3] R. P. Taleyarkhan, and S. H. Kim, "Severe Accident Risk Minimization Studies for the Advanced Neutron Source at the Oak Ridge National Laboratory," Proc. of the 5th International Workshop on Containment Integrity, Washington, D.C. (May 1992).

[4] S.H. Kim et al., "Modeling and Analysis of Core Debris Recriticality During Hypothetical Severe Accidents in the Advanced Neutron Source Reactor," Proc. of the Second International Conference on Nuclear Engineering (ICONE-2), San Francisco, CA (March 1993).

[5] S.H. Kim et al., "Modeling and Analysis Framework for Core Damage Propagation During Flow-Blockage Initiated Accidents in the Advanced Neutron Source Reactor at Oak Ridge National Laboratory," Proc. of the 7th International Meeting on Nuclear Hydraulics (NURETH-7), Saratoga Springs, NY (September 1995).

[6] G.B. Wallis, One-Dimensional Two-Phase Flow, McGraw-Hill Book Co. (1969).

[7] M. Ishii and M.A. Grolmes, "Inception Criteria for Droplet Entrainment in Two-phase Cocurrent Film Flow," AIChE Journal, 21(2), 308 (March 1975).

[8] R .T. Lahey,Jr., and F.J. Moody, The Thermal-Hydraulics of a Boiling Water Nuclear Reactor, an ANS monograph (1977).

[9] G. Kocamustafaogullari, I.Y. Chen, and M. Ishii, "Unified Theory for Predicting Maximum Fluid Particle Size for Drops and Bubbles," NUREG/CR-4028 (October 1984).

[10] M. Pilch, C.A. Erdman, and A.B. Reynolds, "Acceleration Induced Fragmentation of Liquid Drops," NUREG/CR-2247 (August 1981).

[11] M. Baines and N.E. Buttery, "Differential Velocity Fragmentation in Liquid-Liquid Systems," RD/B/N4643, Berkley Nuclear Laboratories (September 1979).

[12] T.G. Theofanous et al., "LWR and HTGR Coolant Dynamics: The Containment of Severe Accidents," NUREG/CR-3306 (July 1983).

[13] N.P. Cheremisinoff, and R. Gupta, Handbook of Fluids in Motion, Ann Arbor Science (1983).

[14] C.-M. Tchen, "Mean Value and Correlation Problems Connected with the Motion of Small Particles Suspended in a Turbulent Fluid," Mededeling No. 51 Uit Het Laboratorium Voor Aero-En Hydrodynamica Der Technische Hogeschool Te Delft, Martinus Nijhoff (1947) .

[15] R.B. Bird et al., Transport Phenomena, John Wiley & Sons (1960).

THE PHEBUS FP THERMAL-HYDRAULIC ANALYSIS WITH MELCOR

Kikuo Akagane,Yoshihiro Kiso
Nuclear Power Engineering Corporation
3-17-1 Toranomon Minato-ku
Tokyo 105 JAPAN
Tel: 3-5470-5461
Fax: 3-5470-5466

Takanori Fukahori
Hitachi Engineering Co., Ltd.
3-2-1 Saiwai-cho
Hitachi-shi Ibaraki-ken
JAPAN
Tel: 0294-21-1111 (4066)
Fax: 0294-53-1398

Mamoru Yoshino
Nuclear Engineering Limited
1-3-7 Tosabori Nishi-ku
Osaka 550 JAPAN
Tel: 3-5470-5461
Fax: 3-5470-5466

ABSTRACT

The severe accident analysis code MELCOR, version 1.8.2,has been applied for thermal-hydraulic pre-test analysis of the first test of the Phebus FP program (test FPT-0) to study the best test parameters and the applicability of the code. The Phebus FP program is an in-pile test program which has been planned by the French Commissariat a L'Energie Atomique and the Commission of the European Union. The experiments are being conducted by an international collaboration to study the release and transport of fission products (FPs) under conditions assumed to be the most representative of those that would occur in a severe accident.

The Phebus FP test apparatus simulates a test bundle of an in-pile section, the circuit including the steam generator U-tubes and the containment. The FPT-0 test was designed to simulate the heat-up and subsequent fuel bundle degradation after a loss of coolant severe accident, using fresh fuel.

Two options for fuel degradation models in MELCOR have been applied to fuel degradation behavior. The first model assumes that fuel debris will be formed immediately after the fuel support fails by cladding relocation due to the candling process. The other is the uncollapsed bare fuel pellets option, improved in this present study, in which the fuel pellets remain standing in a columnar shape until the fuel reaches its melting point, even if the cladding has been relocated by candling. The latter option model has been improved to simulate UO_2 melting and relocation by candling.

Bundle power is linearly increased by nuclear heating by the time that oxidation runaway begins and continues until the cladding melting temperature is reached. When the first debris formation option is used, fuel debris is formed immediately after oxidation runaway due to loss of support by cladding relocation, causing particulate debris relocation to lower cells. In this case, fuel relocation is induced only by eutectic formation with the zircaloy cladding. On the other hand, when the bare fuel option is used, fuel reaches the melting temperature followed by fuel candling and blockage formation in the bundle lower section.

The fuel degradation models of MELCOR have shown that the early phase of fuel degradation is well-predicted if either the bare fuel pellets columns remain standing or the pellets collapse without fuel melting after the cladding relocation. Improved bare fuel model seems preferable for simulating further degradation phenomena according to previous experiments and TIM-2 experience.

The thermal-hydraulic behaviors in the circuit and containment of Phebus FP are discussed herein. Flow velocities in the Phebus FP circuit are high in order to produce turbulent flow in a small diameter test pipe. The MELCOR calculation has shown that the length of the hot leg and steam generator are adequate to attain steam temperatures of 700℃ and 150℃ in the respective outlets. The containment atmosphere temperature and humidity derived by once through integral system calculation show that objective test conditions would be satisfied in the Phebus FP experiment.

For the code validation, post-test analysis would be expected for the Phebus FP experiment.

INTRODUCTION

In order to evaluate the behavior of fission products released from a core at a nuclear power light water reactor during a severe accident, the Phebus FP program is under way at CADARACHE(FRANCE) as an international project (Delchambre and von der Hardt[1]). In this program, the fission products released from the core are injected via a steam current into a containment vessel which is 1/5000 in volume of the actual plant.

The Phebus FP program is unique in that it is the first in the world to study the transport of real fission products from their release in the fuel to their behavior in the circuit and containment.

Thermal-hydraulics is key in order to provide representative conditions of severe reactor accidents to observe their effect on the aerosol behavior and fission products chemistry. MELCOR is a fully integrated computer code that models all phases of the progression of severe accidents in light water reactor nuclear power plants (Summers [2] , Madni and Eltawila [3]) . It is being developed for the NRC by SNL and seems to be a suitable tool for integral experimental analysis from fuel bundle to the containment such as Phebus FP.

Many calculations with various codes, models and assumptions are needed to promote the experimental planning in advance in order to verify that the objectives are fulfilled. In this point of view, MELCOR seems a suitable tool for this objective.

In NUPEC (Nuclear Power Engineering corp.) ,

MELCOR has been applied for thermal-hydraulic pre-test analysis of the first test of the Phebus FP program (test FPT-0) to study the applicability of the code for analysis of fuel bundle degradation

phenomena and to confirm that the targeted constant test conditions can be attained in the circuit and containment. This paper presents the Phebus FPT-0 pre-test analysis by MELCOR version 1.8.2.

1. THE OUTLINE OF THE PHEBUS FP TEST

1.1 The Phebus Test Facility

Figure 1 shows illustration of Phebus FP test facility. It is made up of three main parts, ie., the bundle, the experimental circuit, and the containment vessel. The FPT0 test was designed to simulate the heat-up and subsequent fuel bundle degradation after a loss of coolant severe accident, using the in-pile test facility.

The main object of Phebus FP is to investigate the release of fission products and other materials from a degrading rod bundle, their transport through a model primary circuit and their deposition in a containment vessel.

Twenty PWR type fuel rods (1 m in height) and Ag-In-Cd (SIC) control rod are held in the bundle (Figure 2). The circuit consists of a hot line (12m in length) from the top of the test train (fuel bundle section) to the steam generator (8m in length). The steam generator followed by a horizontal line (5m in length) inserted into the containment (10㎥ in volume).

A long pipe of hot line is imposed by the distance between the driver core pool and the safety vessel housing all the components of the experimental facility. Therefore, a large section of this line had to be designed to provide the minimum FP/aerosol retention. This was achieved by maintaining the pipe wall temperature 700 ℃ by an electric heater and optimizing the pipe inner diameter to 30 mm. The secondary side of the steam generator is cooled to 150℃ by organic liquid to avoid steam condensation. The cold leg is also kept at a constant temperature of 150℃.

The containment vessel is a 1/1500 model in volume of an actual PWR containment. The containment has a unique structure in which the condensers are installed at the top of the vessel to give the same condensing surface area to volume ratio as in real plants. The temperature of the condensers and containment sump are maintained at 90℃. On the other hand, the containment wall temperature is kept higher, at 110℃, to reduce the amount of vapor and aerosol deposition to the minimum amount.

1.2 Test Procedure of FPT-0 Fuel Bundle Transient Phase

The fuel bundle transient has been calculated to simulate the fuel heat-up and subsequent bundle degradation under controlled rate of steam cooling and nuclear heating (Figure 3). The total duration of 18000 seconds of the bundle transient consists of two phases of 9000 seconds. The first phase is devoted to the thermal calibration of the bundle to keep the bundle temperature constant in three stages, while the second one is the temperature transient and degradation part of the test. Each phase divided into various periods according to the variations of the mass flow rate injected to the bundle inlet and the power driven to the fuel rods. The injected fluid is pure steam at a temperature of 165℃ and an initial pressure of approximately 0.2 MPa.

For all the circuit test duration, the circuitt system is maintained at the above mentioned temperatures. Fission product and aerosol depletion through several mechanisms will be explored. Before the fuel transient starts, the containment atomsphere arrives to steady state during 24 hour pre-conditioning by fixing the containment wall and sump temperature. During the bundle degradation, fission product and aerosols will be

released to the containment through the circuit. In this phase, incoming aerosols are removed by settling and by diffusiophoresis on the cooling parts of the condensers.

2. KEY PARAMETERS AND MODELS OF MELCOR FOR PHEBUS FP THERMAL-HYDRAULIC ANALYSIS

Fuel degradation models are most dominant parameters which are supposed to be sensitive and complicated to simulate the Phebus FP thermalhydraulic behavior by MELCOR 1.8.2. MELCOR calculates oxidation of both Zircaloy and steel by solid state diffusion through the oxide layer using standard parabolic kinetics, with appropriate rate constant expressions and limited by steam availability. For Zircaloy, the rate constant is evaluated from the correlation by Urbanic and Heidrich.

Eutectic reactions can be treated between Zircaloy cladding-Uranium oxide and SIC-steel cladding-Zircaloy guide tube. If the enthalpy of the molten mixture exceeds its liquidus enthalpy, then the mixture will begin to dissolve certain solids if they are present in the same core cell.

In the cladding relocation criteria, molten material hold-up by the oxide shell has been implemented. Molten material is held up within a component when the oxide thickness is greater than a user defined critical value (0.1 mm), if the component temperature is less than a critical value (default: 2500K), and if no candling from the component in that cell has taken place.

Mass relocation by candling of molten core materials, the formation of flow blockages by refrozen by candling materials and formation of particulate debris from intact core componets are modeled by MELCOR. There are two options for fuel degradation behavior. The first model assumes that fuel debris will be formed immediately after the fuel support fails due to cladding relocation by the candling process. The other is the uncollapsed bare fuel pellets option, in which the fuel pellets remain standing in a columnar shape until Uranium oxide reaches its melting point even if the cladding has been relocated by candling.

Figure 4 shows the conceptual diagram of two models. Concerning the subroutines corresponding to the bare fuel model, original MELCOR 1.8.2 version has been updated in this work to correctly melt and relocate the Uranium oxide at the melting point.

3. MELCOR NODALIZATION FOR PHEBUS FP

Figure 5 shows the MELCOR noding diagram for the FPT-0 test, for a through analysis from the fuel bundle section to the containment. There are 19 control volumes (lower plenum, fuel bundle, upper plenum, 4 hot line, 3 steam generator primary side, 3 steam generator secordary side, 4 cold line and 2 containment vessel) and 16 flow paths interconnecting them. The fuel bundle is nodalized into two radial rings and 11 axial cells in which cell n03 to n12 are the fuel region and cell n13 is the fission gas plenum section. The core volume is surrounded by the heat structure of the Zirconia shroud. The shroud is nodalized axially to match the core cells and radially into several layers.

The circuit walls and containment structures are modeled by heat structures. The internal surface of the circuit, steam generator and containment are modeled by convective heat transfer. Constant temperature is given at the outer surface of hot line, cold line containment and condenser tube inside surface. The sump is modeled in the bottom of the containment

4. THERMAL-HYDRAULIC ANALYSIS FOR THE FUEL TRANSIENT PHASE

4.1 Fuel bundle behavior

Fuel temperature histories are shown in Figure 6 to Figure 9. Three steps of temperature plateaus up to 9000 seconds are controlled to calibrate the thermocouples with pre-test estimation prior to the fuel transient. The increase of the temperature during 3 plateaus leads to a maximum temperature of 1200K at mid-plane level. Bundle power is linearly increased from 9000 seconds until 16000 seconds up to 90 KW (Figure 3). Between 9000 seconds and 10000 seconds, the increase of nuclear power leads to a fuel heat-up. The steam flow rate increase up to 3g/s till 10000 seconds and continues to 12000 seconds. From 12000 seconds to 14000 seconds, the steam flowrate decrease to 1.5g /s to simulate steam starvation caused by core uncovery (Figure 3).

Oxidation runaway begins around 10000 seconds and continues until the cladding temperature reaches its

melting point. Oxidation heat escalates the solid phase oxygen diffusion to further accelerate exothermic oxidation reaction. Zircaloy oxidation reaches 73% in the mid-plane of outer layer at 11000 seconds. Sudden drop off to 0° K means material melt and relocation downward.

Figure 10 shows the produced hydrogen till the reactor shutdown which shows the oxidation is almost saturated at 14000 seconds. When the bare fuel option is used, produced hydrogen is slightly less than that of the debris option due to formation of conglomerate debris that inhibit further oxidation.

When stainless steel cladding of the control rod reaches its melting point of 1700K in 10500 seconds (Figure 8 and Figure 9), melt relocation of SIC material occured since the SIC already reached to its melting point of 1075 K during the third plateau but remained enclosed in the stainless steel cladding. Most of all SIC materials (90%) relocate to the lower plenum by 12200 seconds (Figure 8 and Figure 9).

When the debris formation option is used, fuel debris is formed after 10500 seconds due to loss of support by cladding relocation, causing debris relocation to lower cells. In this case, intact fuel melting is induced only by eutectic formation with zircaloy cladding. Fuel pellets from all levels generate UO_2 debris Finally, 96% of UO_2 is transformed to the particulate debris without fuel melting at 16000 seconds (Figure 11).

On the other hand, fuel reaches the melting temperaturee when the bare fuel option is used. At 13000 seconds, the initial fuel melting occurred due to reach the melting point 3113 K at mid-plane in inner ring (Figure 7). The zone where melting occurs is enlarged by the increase of the nuclear power. Due to the power increase in the inner ring by control rod disappearance before the power escalation, melting of the inner ring occurred. Then this cause the coolability increase in the outer ring. At the end of the transient, completely disappeared fuel region is located between the levels 0.3 m and 0.9 m in inner ring (Figure 11).

Candling of molten materials leads to the refreezing in the lower part of the bundle. Refreezing of the flowing down mixture leads to a flow area reduction in the lower part of the bundle. During the relocation of materials, total flow area in inside ring is completely blocked between level 0.2 m and 0.3 m at 13000 seconds.

4.2 Circuit and containment

The temperature of steam flow along the circuit has been predicted by MELCOR and shows as a parameter of time (Figure 12) . The times chosen for the plots correspond to the first plateau (at 2000 seconds), second plateau (at 4000 seconds), fuel oxidation phase (at 11000 seconds) and fuel melting phase (at 15000 seconds). The flow temperature results show the large gradients which exist above the bundle and entry in the steam generator tube. Flow velocities show maximum value of 17 m/s at the entrance to the steam generator tube. This high flow rates correspond to objectives of adjustment Reynold number and minimal deposition in the circuit to shorten the residence time. The hot leg temperature is 700℃ except above bundle plenum, the cold leg and half of the steam generator tube is 150℃ which shows the temperature control in the circuit meets the objective conditions.

Twenty four hours before the start of the bundle transient, control of containment inside wall and sump water temperatures is started to increase to the objective test conditions during the preparatory phase. Containment conditions at the start of bundle transient is the steady state after 24 hours preparatory phase. These values are obtained in advance for the isolated containment. Calculated humidity ratio, atmosphere temperature and pressure are 59 %, 104℃ and 0.199 MPa respectively.

The atmosphere temperature during the transient phase lies between 104℃ and 112℃ (Figure 13) depending on the steam inlet flow rate into the containment. The humidity ratio lies between 60% and 80% (Figure 14) corresponding to atmosphere temperature. Figure 15 shows steam condensation rate on the containment wall and inner structures. Almost all steam condensed on the condenser surface and condensation on other surfaces is negligible. This shows the containment wall is almost free from fission product deposition since little steam condensation occurs on the wall.

DISCUSSION

The present version of MELCOR 1.8.2 does not model the cladding rupture due to internal pressure. In course of the situation toward severe accident, cladding rupture due to internal pressure escalation is not important since the time from cladding rupture to melt is very short. Temperature is the only failure criteria for cladding. This means that cladding failure may occur earlier in the Phebus FP test than in MELCOR predictions. During the third plateau, SIC materials melted in steel cladding. This would be a cause of cladding rupture inducing SIC vapor release into the coolant channel earlier in the actual accident scenario than in the

calculations. MELCOR calculation has shown that candling and flow channel blockage are well modeled.

The Phebus SFD test (Gonnier, Repetto and Geoffroy [4]) shows that uncollapsed bare fuel may exist in the early phase of bundle degradation. However rubble bed formation before massive melting has been hypothesized to have occurred in TMI-2 accident (Broughton et al. [5]) . The fuel degradation models of MELCOR have shown that the early phase of fuel degradation is well-predicted if either the bare fuel pellets columns remain standing until fuel candling is induced or the pellets collapse without fuel melting after the cladding relocation to form rubble bed (I.K. Modni and F. Eltawila [3]). However, in order to simulate further degradation phenomena, models for debris bed formation via bare fuel and molten fuel candling process may be needed in MELCOR.

MELCOR calculations have shown that zirconia shroud does not reach to its melting temperature during the test. Although zirconia will withstand heating, there is still remaining the possibility of its damage by chemical interaction with metallic components in debris since this process does not seem adequately modeled in MELCOR.

The circuit calculation shows that the length of the hot leg and steam generator are adequate to attain steam temperature of 700℃ and 150℃ in the respective outlets. For the containment, steam condensation and humidity requirements derived by once through integral system calculation would be satisfied in Phebus FP experiment. MELCOR calculation shows that the test objective conditions will be satisfied as shown in a summarized table (Table 1) .

CONCLUSIONS AND FUTURE WORK

The fuel bundle degradation model of MELCOR 1.8.2 has been improved by incorporating the UO_2 candling and relocation criteria. Original version and improved version were applied to Phebus FP pre-test analysis. According to the empirical phenomena by Phebus SFD and TMI-2, this improved model would be more realistic compared with original debris formation model. Although the Phebus FPT0 has been performed, many samples are under analyses and not yet available. Phebus FPT-0 results would provide useful data for code validation and improvement especially in fuel degradation behaviors.

Generally, MELCOR shows the capability of simulating the thermal-hydraulic behavior of total system of Phebus FP test facility through the fuel bundle, circuit and containment. It can be concluded that the use of the MELCOR code for Phebus FP experimental analysis will provide the code validation and user defined parameter values for code application in near future.

ACKNOWLEDGMENTS

The authors would like to offer special thanks to Mr. A.M. Arnaud at CEA/IPSN/Cadarache, Mr. P. von der Hardt at CEC/JRC/Cadarache and Mr. A.V. Jones at CEC/JRC/Ispra for allowing this paper publication.

The authors wish to acknowledge to the following people and organizations for providing us the boundary condition data for Phebus FP pre-test calculation:

Mr. I. Shepherd, CEC/JRC/Ispra
Mr. F. Serre and Mr. G. Repetto,
CEA/IPSN/Cadarache
Mr. H. Scheurer, CEC/JRC/Cadarache

The financial support by the Japanese Ministry of International Trade and Industries (MITI) is also acknowledged.

REFERENCES

[1] Ph. DELCHAMBER, P. VON. DER HARDT, Phebus FP Test Facility, The Phebus Fission Product Project, edited by W. KRISCHER and M.C. RUBINSTEIN, Elsevier Applied Science. (1991)

[2] R.M. SUMMERS, MELCOR Development for Existing and Advanced Reactors, NUREG/CP-0132 (Oct. 1993)

[3] I.K. MADNI, F. ELTAWILA, Independent Assessment of MELCOR as a Severe Accident Thermal-hydraulic/Source Term Analysis Tool, Proc. of the International Conference on New Trends in Nuclear System Thermohydraulics (1994).

[4] G. GONNIER, G. REPETTO, G. GEOFFROY, Phebus Severe Fuel Damage Program Main Experimental Results and Instrumentation Behavior, Elsevier Applied Science. (1991)

[5] J.M. Broughton, P. Kuan, Incomplete D.A. Petti, E.L. Tolman, A. Scenario of The Three Mile Island Unit 2 Accident, Nuclear Technology (Aug. 1989)

Item	Test objective conditions	MECLOR calculation
Circuit		
Hot line outlet gas temperature	700℃	700℃
Steam generator outlet gas temperature	150℃	150℃
Containment (steam injection phase)		
Steam condensation on vessel wall	vessel wall is neutral against to steam condensation	negligible
Relative humidity	intermediate	60%~83%

Table1 Comparison with Phebus FPT-0 Test Thermalhydraulic Conditions and MELCOR Calculation

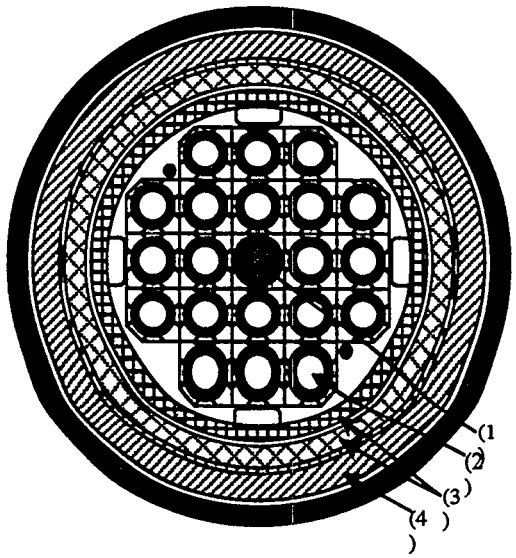

(1)SIC rod; (2)Fuel pins; (3)ZrO2shroud; (4)Inconel tube

Figure2 Fuel Bundle Cross Section

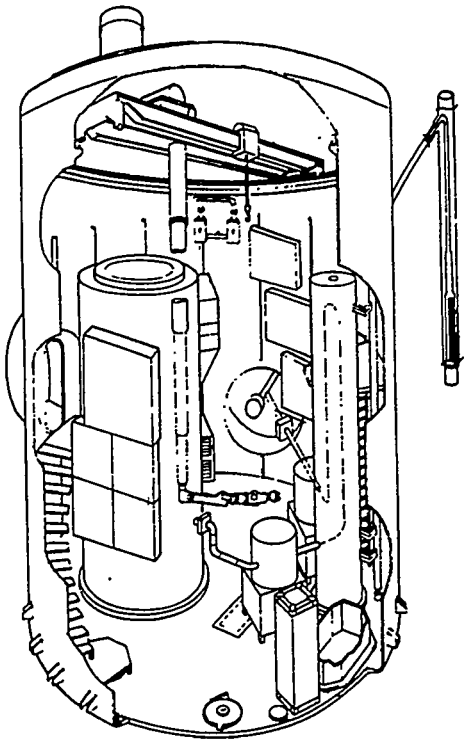

Figure 1 Phebus FP Test Facility

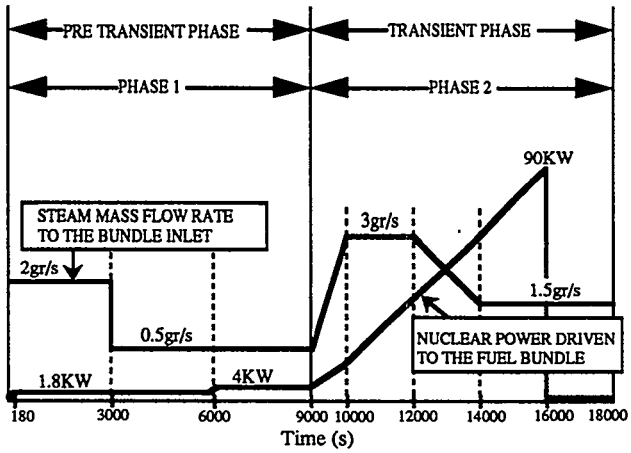

Figure 3 Scenario Scheduled for FPT0 Test

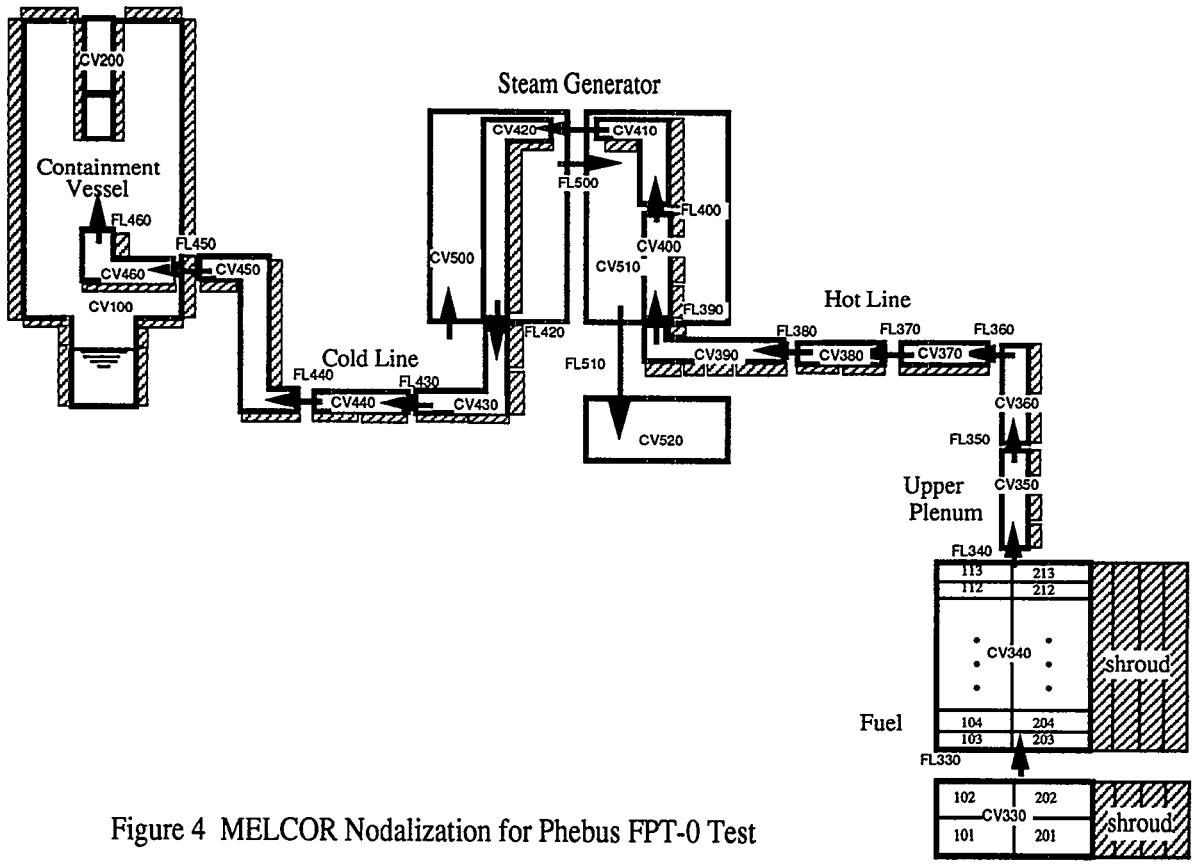

Figure 4 MELCOR Nodalization for Phebus FPT-0 Test

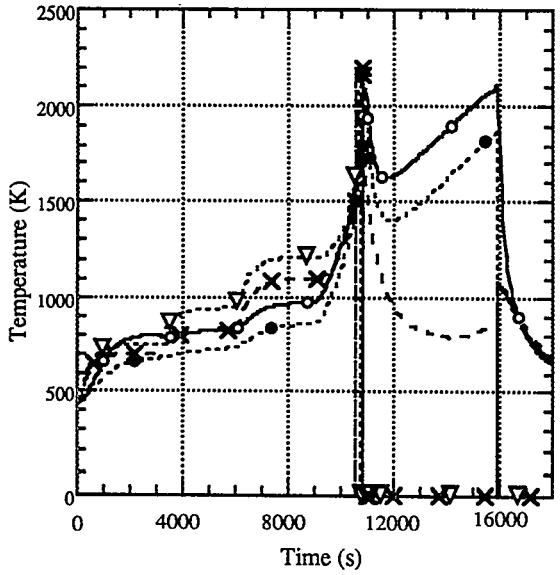

elevation		inner ring	outer ring
0.3-0.4m	UO2	----▽----	- -X- -
0.3-0.4m	debris	- - - - -	———
0.9-1.0m	UO2	—o—	----●----

Figure 5 Fuel Temperature (debris model)

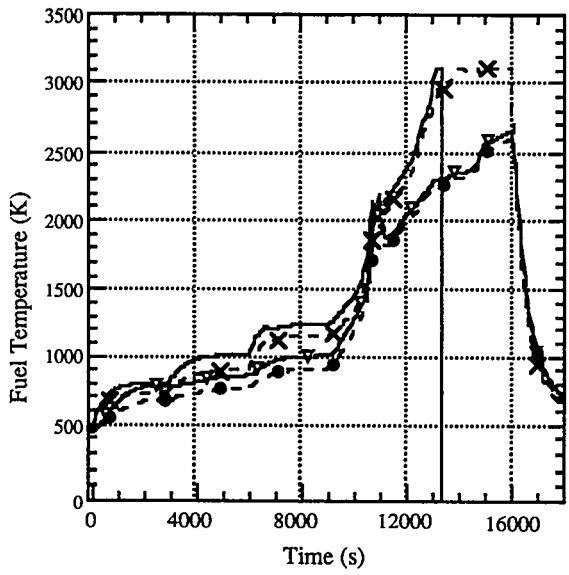

elevation		inner ring	outer ring
0.4-0.5m	UO2	———	- -X- -
0.9-1.0m	UO2	—▽—	- -●- -

Figure 6 Fuel Temperature(bare fuel model)

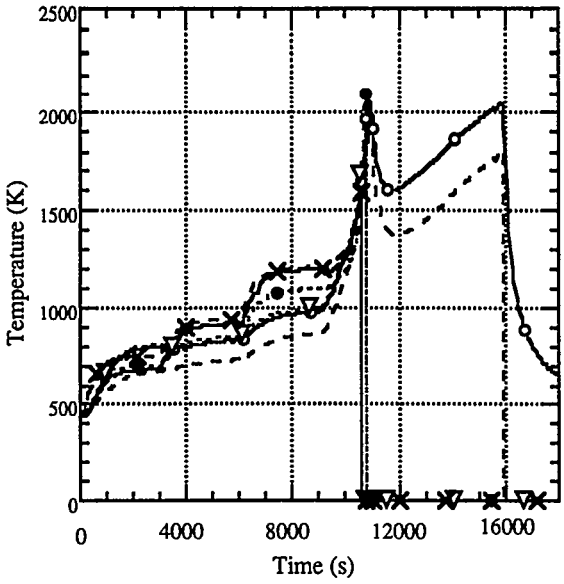

elevation		inner ring	outer ring
0.3-0.4m	Zr		
0.3-0.4m	Steel		
0.9-1.0m	Zr		
0.9-1.0m	Steel		

Figure 7 Cladding Temperature (debris model)

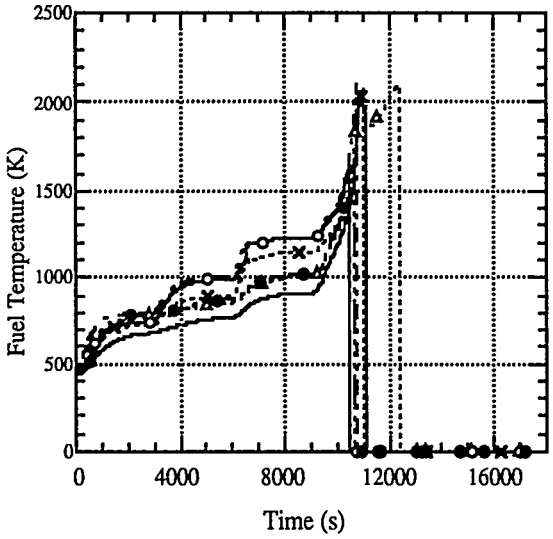

elevation		inner ring	outer ring
0.4-0.5m	Zr		
0.4-0.5m	Steel		
0.9-1.0m	Zr		
0.9-1.0m	Steel		

Figure 8 Cladding Temperature(bare fuel model)

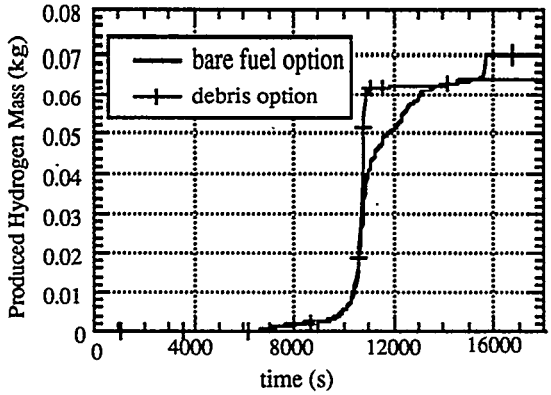

Figure 9 Hydrogen Production by Zircaloy Oxidation

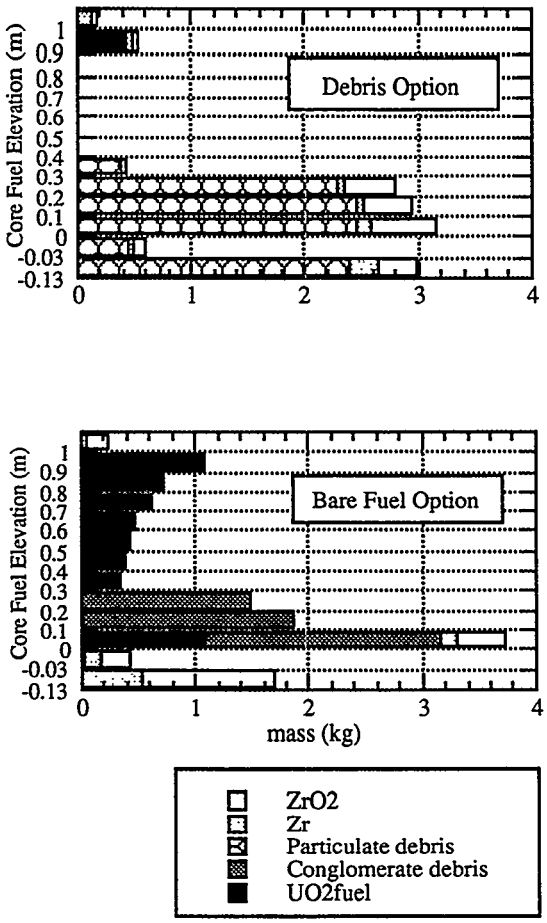

figure 10 Fuel Material Relocation in Final State

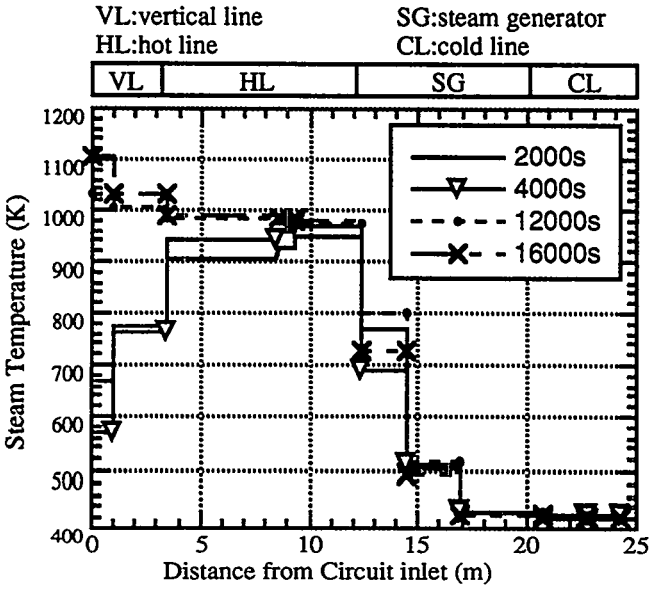

Figure 11 Steam Temperature in Circuit

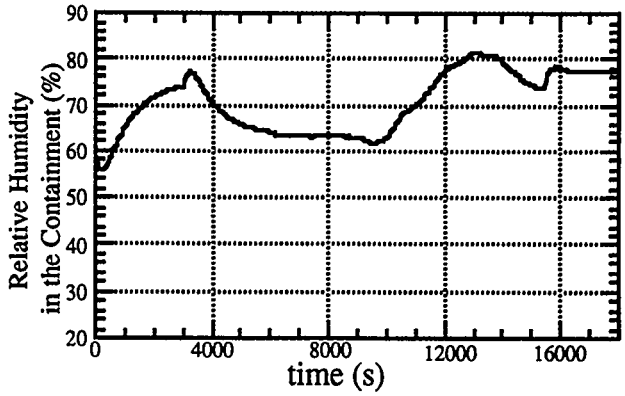

Figure 13 Relative Humidity in Containment

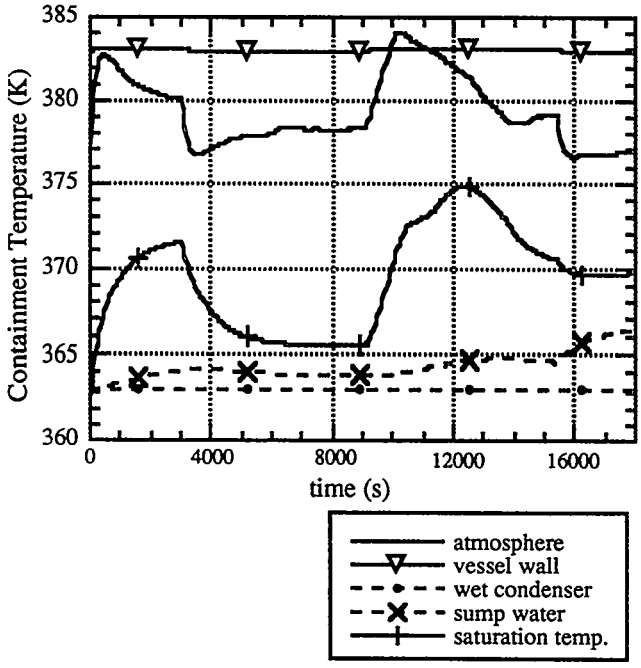

Figure 12 Containment Temperature

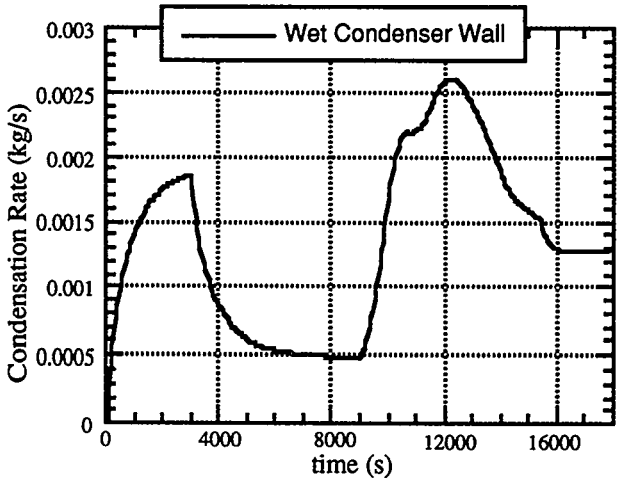

Figure 14 Steam Condensation Rate inside Containment

FLOW EXCURSION TIME SCALES IN THE ADVANCED NEUTRON SOURCE REACTOR

C. D. Sulfredge

Oak Ridge National Laboratory[1]
Martin Marietta Energy Systems, Inc.
Bldg. 9204-1, MS-8045
Oak Ridge, TN 37831-8045

ABSTRACT

Flow excursion transients give rise to a key thermal limit for the proposed Advanced Neutron Source (ANS) reactor because its core involves many parallel flow channels with a common pressure drop. Since one can envision certain accident scenarios in which the thermal limits set by flow excursion correlations might be exceeded for brief intervals, a key objective is to determine how long a flow excursion would take to bring about a system failure that could lead to fuel damage. The anticipated time scale for flow excursions has been examined by subdividing the process into its component phenomena: bubble formation, flow deceleration, and fuel plate heat-up. Models were developed to estimate the time required for each individual stage. Accident scenarios involving sudden reduction in core flow or core exit pressure have been examined, and the models compared with RELAP5 output for the ANS geometry. For a high-performance reactor like the ANS, flow excursion time scales were predicted to be in the millisecond range, so that even very brief transients might lead to fuel damage. These results have been useful for determining the significance of momentary flow excursion events calculated for accident situations in the ANS reactor. In addition, the methods presented are applicable for evaluating the timing of flow excursion transients in other facilities as well.

Nomenclature

b	Channel gap (m)	q"	Heat flux (W/m^2)
c_p	Specific heat (J/kgK)	r	Radius (m)
D_H	Hydraulic diameter (m)	R^+	Normalized bubble radius
$\dot{E}_{gen}$	Internal heat generation rate (W)	s	Channel span (m)
f	Moody friction factor	t	Time (s)
g	Acceleration due to gravity (=9.81 m/s^2)	t^+	Normalized time
G	Coolant mass flux (kg/m^2s)	T	Temperature (K)
h	Convective heat transfer coefficient (W/m^2K)	V	Velocity (m/s)
h_{fg}	Enthalpy of vaporization (J/kg)	x(z)	Thermodynamic flow quality
Ja	Jakob number $[(T_w - T_{sat}) c_p \rho_l/(h_{fg}\rho_v)]$	x'(z)	Flow vapor mass fraction.
k	Thermal conductivity (W/mK)	Y_b	Actual bubble radius at detachment (m)
L	Channel length (m)	Y_b^+	Normalized bubble size at detachment
P	Pressure (Pa)	z	Axial coordinate (m)

Greek Symbols

$\alpha(z)$	Flow void fraction
α_l	Liquid thermal diffusivity (m^2/s)
ϵ	Surface roughness (m)
μ	Dynamic viscosity (Ns/m^2)
ρ	Mass density (kg/m^3)
σ	Surface tension (N/m)
τ	Surface shear stress (N/m^2)
ϕ^2	Two-phase friction multiplier

Subscripts

b	Bubble
c	Cavity
CHF	Critical heat flux
e	Channel exit
f	Friction
i	Channel inlet
l	Liquid
sat	Saturation conditions
v	Vapor
w	Wall surface
1ϕ	One-phase
2ϕ	Two-phase

INTRODUCTION

The Advanced Neutron Source (ANS) reactor is currently being designed to generate the world's highest steady-state thermal neutron fluxes for use in scattering experiments. As a result, the ANS reactor core operates with a very high power density, and thus with a very high heat flux from the fuel plates. The current reference design for the core uses aluminum-clad fuel plates packed in an involute geometry to form parallel flow channels between common upper and lower plenums. To achieve the desired power density, a narrow channel gap of 1.27 mm is planned, together with a 507-mm heated length and a nominal coolant velocity of 25 m/s. The nominal average and peak heat fluxes are approximately 6 and 12 MW/m^2, respectively. Such a parallel-plate core is potentially vulnerable to fuel damage resulting from excursive flow instability, which represents the most restrictive thermal limit for the ANS under many accident scenarios [1].

Flow excursion instability was first investigated by Ledinegg [2], and differs from a true critical heat flux (CHF) failure because the mass flow rate in the affected channel is not constant. The mechanism of flow excursion is most easily visualized in terms of supply and demand curves for the channel pressure drop as a function of flow rate. As illustrated in Fig. 1, the demand curve representing the pressure difference necessary to force coolant through a particular heated channel has a characteristic "S" shape. At very high coolant velocities, the flow will be entirely single-phase liquid, while extremely low flow rates would give rise to single-phase vapor flow in the channel. Both these situations have typical positively-sloped demand curves in which the flow rate is directly related to pressure drop. When the coolant velocity approaches intermediate values where two-phase flow appears, the channel demand characteristic begins to deviate from the single-phase liquid and vapor curves. The region of the demand curve with significant two-phase flow present is marked by a negative slope, as seen in Fig. 1. Two-phase effects first appear in a single- phase liquid flow at the point of incipient boiling (IB) and become pronounced with the onset of significant voiding (OSV) in the fluid. In contrast to the demand pressure drop for each channel, which depends on the flow through it, the supply pressure differential available to drive the flow is only a function of the pressure in the common inlet and outlet plenums. The plenum pressure drop will be identical for all the parallel channels, and is only slightly affected by boiling or flow excursion in the most limiting channel. Hence, the supply curve in Fig. 1 is shown by a horizontal line. Steady-state operation is possible only at points corresponding to an intersection of this supply line with the channel demand curve.

Interaction between the demand and supply curves leads to the phenomenon of flow excursion in a parallel-channel system. Under normal operating conditions in the ANS, the supply pressure drop is given by the upper line, so that the coolant flow is entirely single phase at the operating point A. If the nominal supply pressure drop in Fig. 1 were somehow reduced, point A would move down the demand curve until it reached the minimum. Any further decrease in the supply pressure drop to a position such as ΔP_{Supply} (2) would leave no operating intersection available except point B in the single-phase vapor flow regime. Ledinegg showed that this situation would force the flow to redistribute itself to adjacent parallel channels, so that mass flow in the channel with the highest heat flux would be sharply reduced. A critical heat flux condition would then occur in the affected channel because of flow starvation well before the system reached point B, leading to fuel damage in at least a portion of the reactor core. The difference between the supply and demand curves indicated in Fig. 1 represents a pressure "defect" that decelerates the flow during an excursion. The thermal-hydraulic conditions leading to flow excursion can arise from either a decrease in the available supply pressure drop or from an upward shift of the demand curve minimum due to system depressurization. In a system of parallel channels, accident scenarios usually indicate fuel damage resulting from excursive instability and flow redistribution rather than a true CHF situation at nominal flow rate.

One of the correlations presently being used by the ANS Project to predict the onset of flow instability was developed by Costa [3] in 1967. Safety margins are defined in terms of a flow excursion limit ratio

$$Thermal\ Limit\ Ratio = \frac{q''_{Costa}}{q''_{actual}} \tag{1}$$

Thus, as long as the thermal limit ratio remains greater than 1 during a projected accident scenario, no fuel damage should occur. Although the Costa correlation allows one to estimate the conditions that lead to flow excursion, it says nothing about the time scale of the transient leading up to failure. In fact, none of the flow excursion correlations available addresses the transient nature of the problem. This lack of knowledge causes particular problems when analyzing a high-performance research reactor such as the ANS. Figure 2, taken from an ANS progress report [4], shows the RELAP5 MOD3 simulation of a 127-mm diameter pipe break near the ANS primary system vessel adaptor weld (PSVAW), with the flow excursion limit ratio plotted as a function of time. Early in the transient at t = 8.8 ms and again at t = 32.5 ms, the flow excursion limit is exceeded as a result of depressurization because of acoustic waves propagating from the point of fracture. The first such period lasts for only 2 ms and the second lasts for 4 ms. Whether these brief intervals actually allow a flow excursion to take place and cause any fuel plate damage remains unresolved by RELAP5. An independent model for each stage of the flow excursion process is also desirable for comparison with the RELAP5 results. This paper will examine the transient nature of flow excursion in detail and evaluate the time scale required for a flow excursion to develop under ANS conditions.

MODELING THE STAGES OF FLOW EXCURSION

The anticipated time scale of flow excursion in the ANS has been examined by recognizing that a flow excursion is actually the net result of several distinct processes. Once conditions necessary to initiate an excursion failure are present, vapor bubble nucleation and growth to detachment size must take place. The resulting two-phase flow then has to be decelerated until a critical heat flux condition occurs. Finally, the thermal inertia of the ANS fuel plates themselves must be taken into account to see how much time elapses

between a CHF film-boiling condition and irreversible fuel melting. Depending on the surface characteristics of the ANS fuel plates, the creation of vapor bubbles may also be delayed by the need to form a metastable, superheated liquid prior to nucleation. Models have been developed to estimate the time required for each of these individual stages.

Bubble Formation Time

To estimate the time required for vapor formation, models for both the bubble size at detachment and the bubble growth rate on a heated surface must be available. The normalized bubble detachment size, Y_b^+, can be found from the work of Levy [5]:

$$Y_b^+ = 0.015\ (\sigma D_H\ \rho_l\ )^{1/2}\ \frac{1}{\mu_l} \tag{2}$$

where σ is the liquid surface tension and D_H is the channel hydraulic diameter. The expected bubble radius when it leaves the wall can then be calculated from Y_b^+ using the relationships

$$Y_b = Y_b^+\ (\tau_w\ /\rho_l\ )^{1/2}\ \frac{\rho_l}{\mu_l}$$

$$\textit{where}\ \tau_w = \frac{f}{8}\ \frac{G^2}{\rho_l}\ \ \textit{and}\ f = 0.0055\left(\ 1 + \left[20000\left(\frac{\epsilon}{D_H}\right) + \frac{10^6}{GD_H\ /\mu_l}\right]^{1/3}\right) \tag{3}$$

In all these equations, G represents the mass flux in the flow channel and f stands for the Moody friction factor. Once Y_b has been calculated, a model for bubble growth can be invoked to solve for the growth time necessary to attain this radius. A useful relation for bubble radius as a function of time is given by the model of Mikic, et al. [6]:

$$R^+ = \frac{2}{3}\left[(t^+ + 1)^{3/2} - (t^+)^{3/2} - 1\right] \tag{4}$$

where $R^+ = \dfrac{r_b}{(B^2/A)}$ is a dimensionless bubble radius and $t^+ = \dfrac{t}{(B^2/A^2)}$ is a normalized time for bubble growth. The parameters A and B are evaluated using

$$A = \left[\frac{\pi}{7}\,\frac{(T_w - T_{sat})\,h_{fg}\,\rho_v}{T_{sat}\,\rho_l}\right]^{1/2}$$

$$B = \left[\frac{12}{\pi}\,Ja^2\,\alpha_l\right]^{1/2} \tag{5}$$

for bubble growth on a surface of temperature T_w where $Ja = \dfrac{(T_w - T_{sat})\,c_p\rho_l}{h_{fg}\,\rho_v}$ is the Jakob number relating the latent and sensible heats. This solution for the bubble growth time to detachment is valid in both the early inertia-controlled stage of bubble growth and later on when heat diffusion is the limiting factor.

Flow Deceleration Delay

After nucleation and bubble growth to detachment, the time required to slow the two-phase flow in the channel must be addressed. This portion of the transient can be modeled by applying the integral momentum equation to a control volume located inside the cooling channel. Figure 3 shows a schematic of the control volume used to analyze two-phase flow in a channel of span s, gap b, and overall length L under the assumption of one-dimensional flow with uniform velocity and temperature at any cross-section. Neglecting the influence of gravity, which is very minor compared to forced flow effects at ANS flow rates, the forces acting on the control volume are the inlet and exit pressures plus single- and two-phase shear forces along the walls. Applying the integral momentum equation then yields

$$\frac{dV_i\,(t)}{dt} = \frac{1}{\rho_i sbL}\,[\;(P_i - P_e)sb - 2(s+b)\,\tau_{1\phi}(t)\,L_{1\phi}(t) - \int_{L_{1\phi}}^{L} 2(s+b)\tau_{2\phi}(t,z)\,dz - \rho_i V_i(t)sb[V_e(t) - V_i(t)]\;] \tag{6}$$

which is a differential equation for the inlet flow velocity as a function of time. The first term on the right hand side represents the supply pressure drop available to drive the flow, with $P_i(t)$ and $P_e(t)$ taken to be specified time-dependent boundary conditions that are obtained from the plenum pressures after allowing for inlet and exit losses. The next two terms represent shear forces integrated along the channel in the single-phase regime up to $z = L_{1\phi}(t)$ and in the two-phase region between $L_{1\phi}(t)$ and L. The last term on the right is a momentum term arising from acceleration of the flow due to heat input. Invoking the continuity equation gives $V_e(t) = V_i(t)\,\rho_i/\rho_e$ for the exit velocity if one neglects any transient accumulation of mass inside the channel. This idealization assumes the vapor mass fraction remains relatively low and the liquid phase is sufficiently incompressible that channel mass inflow and outflow are essentially equal at any time during the transient.

Equation (6) provides a way to reconstruct the channel demand and supply curves analytically and track changes in inlet velocity brought about by flow redistribution as a flow excursion proceeds. To carry out the calculations, several more correlations are necessary. First, one must have some relationship for determining the onset of significant voiding that initiates two-phase flow at $z = L_{l\phi}$. The OSV correlation selected for this analysis is the one proposed by Saha and Zuber [7]:

$$T_{sat} - T_{bulk} = 0.0022 \left[\frac{q''D_h}{k_l}\right] \qquad Pe < 70000$$

$$or\ T_{sat} - T_{bulk} = 153.8 \left[\frac{q''}{G\ c_p}\right] \qquad Pe > 70000 \tag{7}$$

for local conditions at the OSV point. In these equations, q'' is the local heat flux, k_l the fluid conductivity, and $Pe = \dfrac{G\ D_H\ c_p}{k_l} = RePr$ is the Peclet number. Combined with an energy balance, Eq. (7) allows the single-phase flow length $L_{l\phi}$ to be calculated directly.

After the boundary is established between single-phase and two-phase flow at $L_{l\phi}$, the shear terms must be dealt with. The single-phase flow can be readily modeled based on the Filonenko friction factor correlation and the Petukhov expression for the forced-convection heat transfer coefficient on the surface of the fuel plates that are currently used in the ANS Project [8]. Unfortunately analyzing the two-phase portion of the channel is not nearly as clear cut. A relatively simple drift flux model developed by Levy [5] was selected to predict the void fraction and two-phase friction multiplier in this region. According to the Levy model, the mass fraction of vapor in the flow, $x'(z)$, is related to the "true" thermodynamic quality $x(z)$ by

$$x'(z) = x\ (z) - x\ (L_{1\phi})\ \exp\left[\frac{x\ (z)}{x\ (L_{1\phi})} - 1\right] \tag{8}$$

where $x(z) = c_p\ [T(z) - T_{sat}(P_z)]/h_{fg}\ (T_{sat})$ is determined from an energy balance. The associated void fraction in Levy's model, $\alpha(z)$, can then be found from

$$\alpha(z) = x'(z) \left[\frac{C_o(\rho_l - \rho_v)}{\rho_l}\ x'(z) + \left[C_o + \frac{\overline{u_{gj}}}{V_i}\right]\frac{\rho_v}{\rho_l}\right]^{-1}$$

$$where\ C_o = 1.13\ and\ \overline{u_{gj}} = 1.18 \left[\frac{\sigma\ g\ (\rho_l - \rho_v)}{\rho_l^2}\right]^{1/4} \tag{9}$$

Levy also gave the two-phase friction multiplier, ϕ^2 as [9]

$$\phi^2 = \frac{\left[1 - x'(z)\right]^{1.75}}{\left[1 - \alpha(z)\right]^2} \tag{10}$$

which represents the increase in wall shear relative to an equivalent single-phase flow. Hence

$$-\frac{dP}{dz}\Big|_{f,2\phi} = -\frac{dP}{dz}\Big|_{f,1\phi}\ \phi^2 \tag{11}$$

where the frictional pressure drop, $\frac{dP}{dz}\Big|_{f,1\phi}$, for the single phase flow is determined using the Filonenko correlation discussed earlier.

One more correlation is still needed for integration of Eq. (6). To see how far the excursion should be allowed to proceed, one must have an expression predicting when CHF and the switch to film boiling in the channel will take place. The CHF correlation currently being used by the ANS Project is the Gambill/Weatherhead relation [8]:

$$q''_{CHF} = h\left[T_w - T_{bulk}\right] + 0.18 h_{fg}\rho_v\left[\sigma g\ (\rho_l - \rho_v)/\rho_v^2\right]^{0.25} \times\left[1 + (\rho_l/\rho_v)^{0.75}\ c_p(T_{sat} - T_{bulk})/(9.8 h_{fg})\right] \tag{12a}$$

$$and\ T_w = [\ 47.7 - 0.127\ T_{sat}\ ]\left(\frac{q''_{CHF}}{3154.6}\right)^{0.25} + T_{sat} \tag{12b}$$

where q''_{CHF} is the critical heat flux, h is the forced-convection heat transfer coefficient predicted by Petukhov, and T_w is the channel wall surface temperature. Since Eq. (12b) is a dimensional correlation, the heat flux needs to be expressed in kilowatts and all temperatures must be in Celsius for the results to be valid. The Gambill/Weatherhead equation can then be solved for $V_{i,CHF}$, the channel inlet flow velocity below which flow starvation causes a CHF failure at the exit.

To generate the solution of Eq. (6), a FORTRAN computer code called FLOWEXC was written that employs 4th-order Runge-Kutta integration to obtain $V_i(t)$. The code FLOWEXC incorporates all the thermal hydraulic correlations already described, plus a set of relations compiled by Crabtree and Siman-Tov [10] to evaluate the thermophysical properties of light or heavy water as functions of temperature. Once $L_{1\phi}$ is obtained at each time step by iterating to find the axial location where the Saha-Zuber correlation is satisfied, all components of the momentum equation are evaluated and a new inlet flow velocity is calculated using the Runge-Kutta method. The transient calculations then continue until $V_i(t) \leq V_{i,CHF}$ from Gambill/Weatherhead. The flow deceleration delay for a flow excursion will be defined as the time between rounding the minimum of the

demand curve, when the system first enters an unstable flow regime, and the point when FLOWEXC determines $V_{i,CHF}$ has been reached in the channel.

The transient code FLOWEXC was initially benchmarked by simulating a steady-state flow excursion experiment conducted in the thermal hydraulic test loop (THTL) here at the Oak Ridge National Laboratory. Designed to collect thermal-hydraulic data for the ANS, the THTL features prototypic heat fluxes and flow velocities comparable to those planned for the reactor [11]. Figures 4-6 show some results obtained using FLOWEXC to analyze THTL experiment FE331A, which had $T_i = 45\,°C$, a constant heat flux of 12.2 MW/m^2, and a fixed channel exit pressure of 1.7 MPa. An initial supply pressure perturbation of 0.05 MPa below the demand curve minimum was imposed by reducing P_i to 2.23 MPa to bring about a flow excursion. The program FLOWEXC allows one to view the separate effects of single-phase friction, two-phase friction, and the acceleration momentum term on the overall demand curve. In Fig. 4 the individual components of the demand curve pressure drop are plotted versus velocity, which decreases with time throughout the transient. It is clear from the overall demand curve shown in Fig. 4 that the momentum term is the dominant factor influencing the shape of the demand curve to the left of the minimum point. In contrast to the rapid growth of the momentum term in two-phase flow, single-phase friction declined almost linearly throughout the transient, and two-phase friction was always relatively small. One should also note the change in slope predicted for the single-phase friction term at a velocity of about 17.9 m/s, which is due to reduction in $L_{1\phi}$ once two-phase flow appears at the channel exit. In addition to the demand components, Fig. 4 contains a plot of the pressure defect curve during the excursion, which has the same shape as the overall demand curve shifted downward by the imposed supply pressure drop.

Figure 5 illustrates the contributions to the demand curve pressure drop of the single-phase and two-phase sections of the THTL channel. The single-phase contribution declined throughout the transient as the inlet flow velocity decreased. However this reduced pressure drop due to the single-phase flow was more than offset by an increasing pressure drop in the two-phase flow near the exit. Thus the pressure defect between supply and demand continues to increase, and the flow excursion proceeds at an accelerating pace as the two-phase flow section lengthens. The growing segment of the THTL channel that experiences two-phase flow is also evident in Fig. 6, which plots the ratios of single-phase flow length and incipient boiling location length to total channel length. For this calculation, FLOWEXC was modified to include the Bergles-Rohsenow correlation [12] for IB on the channel surface. Like RELAP5, FLOWEXC interprets the Saha-Zuber OSV point as the start of two-phase flow. Any multiphase effects between the IB and OSV points are neglected. For the THTL run simulated, the single-phase length ratio ranged from 1.0 down to 0.96, and the IB location length ratio went from 0.70 to 0.63.

Using the input data from THTL Case FE331A, FLOWEXC calculated a flow deceleration delay of 5.4 ms between rounding the demand curve minimum and CHF. This is consistent with the FE331A test, which indicated a very rapid transient, but the THTL instrumentation is currently inadequate to measure a precise time value. The numerically-generated minimum of the demand curve also occurred at a flow velocity of about 17.75 m/s, quite close to the steady-state experimental value of 17.0 m/s. Thus the pressure drop and void fraction models included in FLOWEXC appear to fit the data relatively well. One other qualitative characteristic of flow excursions was also evident from simulating the THTL experiment: Most of the flow excursion time prior to CHF is spent near the minimum of the demand curve. Once the flow velocity in the channel becomes appreciably less than that corresponding to the local minimum in the pressure drop, the difference between the supply and demand increases rapidly until failure. Since this pressure defect provides the driving potential for flow excursion, the transient moves much quicker away from the minimum.

Metastable Liquid Effects

Another physical phenomenon that tends to impose a delay in flow excursion transients is the need to form a metastable, superheated liquid prior to nucleation of vapor bubbles. Clearly the onset of net vapor generation, which leads to flow excursion, cannot occur until sufficient superheat has built up for nucleation to begin. A key feature in any model for heterogeneous vapor nucleation is the size distribution of cavities available at the heated surface. For a particular cavity to be capable of nucleating vapor bubbles, the wall temperature must be enough above T_{sat} for a bubble to be in thermomechanical equilibrium with the fluid in the thermal boundary layer. The equilibrium equations generally predict a range of active cavity sizes that becomes narrower as the superheat declines. Below some threshold value of the superheat, the active cavity range goes to zero and no bubbles can be nucleated. Currently the ANS fuel plates are expected to have an average surface roughness of about 0.5×10^{-6} m, which gives some indication of the likely cavity size range. Thus sufficient superheat to initiate nucleation from cavities in this size range must be available prior to OSV.

Several models are available for predicting when cavities of any size are capable of becoming active nucleation sites. At present, the Bergles-Rohsenow correlation is being used in the ANS Project to indicate incipient boiling conditions [8]. Bergles and Rohsenow solved for the IB point by applying a graphical technique to the equations of thermomechanical equilibrium; hence this method is not suitable for calculating the range of active cavity sizes if the superheat is increased. However, the Hsu [13] and Davis-Anderson [14] models for incipient boiling can be manipulated to yield both criteria that a cavity must satisfy to become activated and predictions for the range of active cavity dimensions at higher wall superheats.

Since flow excursions can result from a reduction in either the channel flow rate or channel exit pressure, it is convenient to have two different forms of the IB criterion. When the supply pressure drop falls, the onset of nucleation will be due to rising T_w as the flow is reduced while P_e remains unchanged, so incipient boiling is best presented in terms of a minimum wall temperature for nucleation. Exit depressurization transients, on the other hand, have T_w relatively constant, so the IB condition should be expressed as the value of P_e (or T_{sat} at the exit) above which nucleation is impossible. Using Davis-Anderson, the required equations are

$$T_{w,min} = T_{sat} + \left[\frac{8\sigma T_{sat}\, q''_w}{k_l\, h_{fg}\, \rho_v}\right]^{1/2}$$

or

$$T_{sat,max} = T_w + \frac{4\, q''_w\, \sigma}{k_l\, h_{fg}\, \rho_v} - \left[\frac{8\, q''_w\, \sigma}{k_l\, h_{fg}\, \rho_v}\left(T_w + \frac{2\, q''_w\, \sigma}{k_l\, h_{fg}\, \rho_v}\right)\right]^{1/2} \qquad (13)$$

and the cavity size range that is active at higher superheats is given by

$$r_c = \frac{1}{2}\left[\frac{(T_w - T_{sat})\, k_l}{q''_w} \pm \left[\left(\frac{(T_w - T_{sat})\, k_l}{q''_w}\right)^2 - \frac{8\, \sigma\, k_l\, T_{sat}}{h_{fg}\, \rho_v\, q''_w}\right]^{1/2}\right] \qquad (14)$$

Hsu's model yields the analogous formulas

$$T_{w,min} = T_{sat} + \frac{6.4\ \sigma\ T_{sat}\ h}{h_{fg}\ \rho_v\ k_l} + \left[\frac{6.4\ \sigma\ T_{sat}\ h}{h_{fg}\ \rho_v\ k_l}\left[2(T_{sat} - T_\infty) + \frac{6.4\ \sigma\ T_{sat}\ h}{h_{fg}\ \rho_v\ k_l}\right]\right]^{1/2}$$

or

$$T_{sat,max} = T_w + \frac{6.4\ \sigma\ h\ (T_w - T_\infty)}{k_l\ h_{fg}\ \rho_v} - \left[\frac{12.8\ \sigma\ h\ (T_w - T_\infty)}{k_l\ h_{fg}\ \rho_v}\left[T_w + \frac{3.2\ \sigma\ h\ (T_w - T_\infty)}{k_l\ h_{fg}\ \rho_v}\right]\right]^{1/2} \tag{15}$$

for the IB requirements and

$$r_c = \frac{k_l}{4h}\left[\left(1 - \frac{T_{sat} - T_\infty}{T_w - T_\infty}\right) \pm \left[\left(1 - \frac{T_{sat} - T_\infty}{T_w - T_\infty}\right)^2 - \frac{12.8\ \sigma\ T_{sat}\ h}{\rho_v\ h_{fg}\ k_l\ (T_w - T_\infty)}\right]^{1/2}\right] \tag{16}$$

for the active cavity size range. The primary difference between the two models arises because of slight variations in the assumed shape of the embryo bubble. These equations will be used to test the thermal-hydraulic conditions predicted by FLOWEXC at IB and OSV to see whether enough wall superheat is available for activation of cavities in the expected ANS size range. If metastable liquid effects can delay the nucleation of vapor bubbles past the expected OSV point, then the time scale for flow excursion must be lengthened accordingly until more superheat can develop.

Fuel Plate Heat-Up Time

The last phase of a flow excursion transient will involve heat-up of the fuel plates toward the melting point as a result of inadequate cooling near the channel exit. Weatherhead's correlation for T_w [Eq. (12b)] allows one to calculate the minimum temperature needed for CHF at the exit. Once this wall temperature has been exceeded, a rapid fuel plate heat-up leading to damage becomes unavoidable unless the exit pressure increases significantly. To obtain a conservative initial estimate of the role of thermal inertia, the adiabatic heating rate, $\frac{dT}{dt}$, for a fuel plate can be determined from the equation

$$(m_{fuel}\ c_{p,fuel} + m_{cladding}\ c_{p,cladding})\ \frac{dT}{dt} = \dot{E}_{gen} \tag{17}$$

where $\dot{E}_{gen}$ is the internal heat generation rate within the plate. Thus it is possible to obtain a characteristic minimum time required for heat release inside a fuel plate to bring about any temperature increase necessary for CHF to take place.

COMPARISON WITH RELAP5 MOD3 RESULTS

Three RELAP5 flow excursion cases in the ANS geometry were selected for analysis using the transient models developed in the preceding section. Both declining core flow and core exit depressurization scenarios have been examined, with all calculations starting from full ANS power levels. In the first RELAP case, the supply pressure drop across a flow channel was ramped linearly from its nominal value down to zero over a period of 100 seconds to start the excursion, while the exit pressure remained fixed. Another simulation involved reducing the channel exit pressure linearly to atmospheric over a period of 100 seconds with flow rate held constant. The first of these cases corresponds to a flow excursion generated by movement down the channel demand curve to the minimum point, and the second simulates an excursion resulting from an upward shift of the demand curve at lower pressures. The last case analyzed was the 127-mm PSVAW break scenario discussed in connection with Fig. 2, where flow excursion limits were briefly exceeded. To reproduce the channel flow characteristics indicated by RELAP5, the channel inlet and exit pressures as functions of time were extracted from the RELAP run and submitted to FLOWEXC as boundary conditions. Figure 7 shows these pressure histories, with the sharp minima that caused the Costa limit to be exceeded at 8.8 ms and 32.5 ms clearly evident.

For all three of these transient cases, the first stage of flow excursion involves forming vapor bubbles of detachment size. Table 1 summarizes the results from applying the bubble growth models developed earlier to the Saha-Zuber OSV conditions for each case. The calculated bubble radius at detachment from the wall ranged from 4.73×10^{-6}m for the PSVAW break simulation up to 8.97×10^{-6}m for the declining flow transient, leading to growth times between 0.421 and 1.76 microseconds. Longer times were associated with the declining flow case because the more subcooled exit conditions slowed bubble growth, and the bubbles also had to be larger before the reduced flow velocity could strip them off the wall. However the flow excursion delay due to bubble nucleation and growth appears to be insignificant under conditions typical of the ANS.

The flow deceleration delays for the reduced-flow and loss-of-exit-pressure scenarios allow the most direct comparisons between the transient models developed in this paper and those from RELAP5. To estimate the fluid deceleration time scale for a flow excursion, one must plot the demand curve reconstructed by either RELAP or FLOWEXC and then measure the elapsed time between the minimum point and critical heat flux conditions. Figures 8 and 9 illustrate the demand curves output by RELAP5 for one nodalization of each case. In Fig. 8, 50 nodes were used axially along the ANS channel to do the declining flow transient, while Fig. 9 presents the demand curve for an exit depressurization based on 95 axial nodes. Both sets of calculations were done using FLOWEXC as well as several different RELAP5 nodalizations, and the results are given in Table 2. All the reduced-flow transients exhibited a negatively sloped demand pressure drop prior to the onset of flow instability at the minimum point, while OSV had already occurred somewhat earlier in the transient. On the other hand, the exit depressurization situations started out from a fixed flow rate and channel pressure drop until the instability. Here OSV essentially coincided with the minimum point because the formation of vapor is due to virtually instantaneous flashing at low pressure.

Examination of Table 2 shows several interesting features of these transients. Clearly a fine axial nodalization is very important to model such problems with RELAP. For both decreasing flow and core exit depressurization situations, the calculated flow deceleration delay decreased significantly as the original 5-node model was refined. The transient time needed to bring about OSV was also reduced with each finer nodalization. This earlier appearance of OSV is easily understood when one remembers that RELAP5 only calculates pressures at cell centers. A finer node spacing means the center of the last cell will be closer in pressure to the exit plenum; thus less reduction in P_e is necessary to bring this cell to OSV conditions.

Predicted deceleration delays for the declining flow transient ranged from 0.33 to 0.38 s with the fine-nodalization RELAP runs. These numbers compare reasonably well with the 0.16 s estimate obtained from FLOWEXC. For the exit depressurization simulations, the shortest flow deceleration time scale calculated with RELAP was 8.3 s, which is much longer than the FLOWEXC value of 0.4 ms. This discrepancy apparently reflects different models for the strength of vapor generation in the two codes. However most of the experimental evidence available points to times much closer to the FLOWEXC value for depressurization flow excursions [15].

No attempt was made to plot the demand curves generated by RELAP and FLOWEXC when simulating the 127-mm PSVAW break because they would have been distorted by the rapid pressure variations. Instead, the main question in this case was simply whether the fluid deceleration delay provided sufficient time for the system to "ride over" the depressurization spikes at t = 8.8 ms and 32.5 ms without experiencing a flow excursion, even though the Costa condition was violated. The RELAP5 run indicated no OSV or flow excursion under these conditions. On the other hand FLOWEXC experienced OSV 8.0 ms into the transient and suffered a CHF failure at t = 8.2 ms, before P_e even reached its first minimum value. This situation probably reflects the same difference between the two codes that was evident with the earlier depressurization transient. In addition, FLOWEXC used a slightly different technique from that found in RELAP5 when evaluating the coolant bulk temperature. This change also makes the transient progress faster than predicted by RELAP.

Table 3 contains the results from applying the Hsu and Davis-Anderson models for incipient boiling to the reduced flow transient, the core exit depressurization, and the PSVAW break simulation. With the reduced flow transient, the IB condition is presented in terms of a minimum wall temperature for nucleation, while the two depressurization cases express it in terms of a maximum exit pressure. Both models indicate IB would occur later than predicted by Bergles-Rohsenow, but the nucleation criteria were always satisfied prior to the Saha-Zuber OSV point except for the Hsu model analysis of the exit depressurization run. Furthermore, the active cavity range predictions of both models under OSV conditions nicely span the average surface roughness expected with ANS fuel plates for either reduced flow or the PSVAW break situation. For exit depressurization at OSV, the Davis-Anderson active cavity span was slightly larger than the mean ANS roughness but in the same general size range, while the Hsu nucleation criterion was not quite satisfied. In general, it appears metastable liquid effects may delay incipient boiling somewhat, but IB is unlikely to be extended past the OSV point enough to inhibit a flow excursion during any of the three transients studied.

The last time scale for flow excursion in the ANS is derived from heat-up of the fuel plates themselves. Results of these calculations for all three test cases are included in Table 4. The table shows the initial single-phase convection wall temperature at the channel exit for each case, and gives the minimum wall temperature necessary for CHF at the exit from Weatherhead's correlation. All these numbers are based on the thermal-hydraulic conditions at the end of the FLOWEXC transient. Once the plate adiabatic heating rate has been determined, it is then possible to estimate the minimum time needed to reach CHF. As seen in Table 4, the CHF wall temperatures at failure for both exit depressurization and the PSVAW break run are slightly less than the corresponding initial wall temperatures. This fact reflects the drop in T_{CHF} as the exit pressure falls during the transient. No fuel heat-up delay seems to be available under such conditions. For the reduced flow case, a minimum delay of 9.01 ms is necessary to reach T_{CHF}, but this characteristic time is still much shorter than the 0.160 s time already predicted by FLOWEXC for flow deceleration. Apparently adiabatic thermal inertia effects can do little to extend the flow excursion times calculated from deceleration of the coolant in the ANS reactor core.

All the analysis performed so far to supplement RELAP5 runs for the ANS Project has emphasized the high speed of flow excursion transients under the thermal-hydraulic conditions present in the ANS core. At present, it does not appear that the ANS conceptual design can survive the acoustic expansion waves propagating through the coolant from an instantaneous pipe break without suffering some fuel damage due to flow excursion. Work continues on refining the transient models developed for each stage of a flow excursion and improving the agreement with complementary RELAP5 simulations. It is also planned to carry out some transient experiments here at ORNL, so that each stage of flow excursion can be observed in real time. Hopefully this work will lead to increased understanding of flow excursion transients and how they would progress during accident scenarios in the ANS reactor or any system involving similar geometry and power densities.

CONCLUSIONS

1. Time scales for flow excursion transients can be obtained by separating the transient into its component phenomena and modeling them individually.

2. Deceleration of the coolant flow provides the dominant time delay during a flow excursion under ANS conditions. As a result, most of the transient prior to fuel damage is spent near the minimum in the demand curve.

3. Fuel plate heat-up time is most evident in reduced flow transients, while the influence of a metastable liquid phase is largely confined to depressurization cases. However neither effect adds appreciably to flow deceleration delays in the ANS.

4. A fine axial nodalization is necessary to obtain a realistic flow excursion simulation in RELAP5. Even so, RELAP's vapor generation rate seems too slow for exit depressurization cases.

5. For high performance, parallel-channel reactors like the ANS, flow excursion time scales are often in the millisecond range, especially when the exit plenum pressure drops suddenly. Apparently even a very brief excursion scenario might lead to fuel damage.

ACKNOWLEDGEMENT

This paper is based on research supported by the ANS Project office at ORNL. The assistance of Lara James, David Morris, Moshe Siman-Tov, Grady Yoder, and other contributors who helped make the work possible is greatly appreciated.

REFERENCES

1. R. M. Harrington, et al., "Advanced Neutron Source Conceptual Safety Analysis Report," Chapter 15, Oak Ridge National Laboratory (1992).

2. M. Ledinegg, "Instability of Flow During Natural and Forced Circulation," *Die Warme*, **61**, 891-898 (1938).

3. J. Costa, "Measurement of the Momentum Pressure Drop and Study of the Appearance of Vapor and Change in the Void Fraction in Subcooled Boiling at Low Pressure," *Proc. of Meeting of the European Group Double-Phase*, Winfrith (1967). Translated from French as ORNL/TR-90/21.

4. G. L. Yoder, et al., "ANS Transient Thermal Hydraulic Task Monthly Progress Report for December 1993," Memo to R. M. Harrington and K. F. Rosenbalm of ORNL (1994).

5. S. Levy, "Forced Convection Subcooled Boiling — Prediction of Vapor Volumetric Fraction," *Int. J. Heat and Mass Transfer*, **10**, 951-965 (1967).

6. B. B. Mikic, W. M. Rohsenow, and P. Griffith, "On Bubble Growth Rates," *Int. J. Heat and Mass Transfer*, **13**, 657-666 (1970).

7. P. Saha and N. Zuber, "Point of Net Vapor Generation and Vapor Void Fraction in Subcooled Boiling," *Proc. 5th Int. Heat Transfer Conference*, Tokyo, **4**, 175-179 (1974).

8. M. Siman-Tov, W. R. Gambill, W. R. Nelson, A. E. Ruggles and G. L. Yoder, "Thermal-Hydraulic Correlations for the Advanced Neutron Source Reactor Fuel Element Design and Analysis," *Proc. 1991 ASME Winter Annual Meeting*, Atlanta (1991).

9. J. G. Collier, *Convective Boiling and Condensation*, McGraw Hill, New York (1981).

10. A. Crabtree and M. Siman-Tov, "Thermophysical Properties of Saturated Light and Heavy Water for Advanced Neutron Source Applications," ORNL/TM-12322 (1993).

11. D. K. Felde, et al., "Advanced Neutron Source Reactor Thermal-Hydraulic Test Loop Facility Description," ORNL/TM-12397 (1994).

12. A. E. Bergles and W. M. Rohsenow, "The Determination of Forced-Convection Surface-Boiling Heat Transfer," *ASME J. of Heat Transfer*, **86**, 365-372 (1964).

13. Y. Y. Hsu, "On the Size Range of Active Nucleation Cavities on a Heating Surface," *ASME J. of Heat Transfer*, **84**, 207-213 (1962).

14. E. J. Davis and G. H. Anderson, "The Incipience of Nucleate Boiling in Forced Convection Flow," *AIChE J.*, **12**, 4, 774-780 (1966).

15. C. A. Wemple, et al., "Advanced Neutron Source Idaho National Engineering Laboratory Monthly Report for January 1993," Memo to D. L. Selby of ORNL (1993).

Table 1. Summary of bubble growth times to detachment

	Normalized detachment radius	Actual radius at detachment (μm)	Normalized bubble growth time	Actual bubble growth time (μs)
Declining flow transient case	29.27	8.973	10.512	1.76
Exit depressurization case	22.39	4.780	0.0719	0.62
127-mm PSVAW break case (hot-stripe heat fluxes)	23.68	4.729	0.0622	0.42

Table 2. Flow deceleration delays for declining flow and exit depressurization

	Model adopted	Transient time to OSV (s)	Transient time to demand curve minimum (s)	Flow deceleration delay beyond minimum point (s)
Declining flow transient case	RELAP 5-cell	29.0	29.85	1.0
	RELAP 20-cell	27.10	29.63	0.33
	RELAP 50-cell	27.05	29.45	0.38
	FLOWEXC	—	—	0.16
Declining core exit pressure case	RELAP 5-cell	66.7	66.7	19.3
	RELAP 20-cell	59.3	59.3	9.7
	RELAP 95-cell	57.4	57.4	8.3
	FLOWEXC	—	—	0.0004

Table 3. Summary of activated cavity size ranges at OSV

	Nucleation condition needed for IB		Cavity radius range at OSV	
	Hsu model	Davis-Anderson model	Hsu model	Davis-Anderson model
Declining flow case	$T_w > 225.5°C$	$T_w > 219.1°C$	7.600×10^{-8} m to 1.533×10^{-6} m	9.321×10^{-8} m to 3.125×10^{-6} m
Exit depressurization case	$P_e < 0.291$ MPa	$P_e < 0.348$ MPa	—	7.741×10^{-7} m to 1.830×10^{-6} m
127-mm PSVAW Break Case (hot-stripe heat fluxes)	$P_e < 0.539$ MPa	$P_e < 0.649$ MPa	2.526×10^{-7} m to 1.078×10^{-6} m	2.867×10^{-7} m to 2.375×10^{-6} m

Table 4. Summary of fuel plate heat-up information

	Initial wall temp. (°C)	CHF wall temp. (°C)	Adiabatic heating rate (°C/s)	Minimum heating time (ms)
Declining flow case	164.5	228.8	7138	9.01
Exit depressurization case	164.5	161.1	7264	—
127 mm PSVAW break case (hot-stripe heat fluxes)	186.6	181.0	7451	—

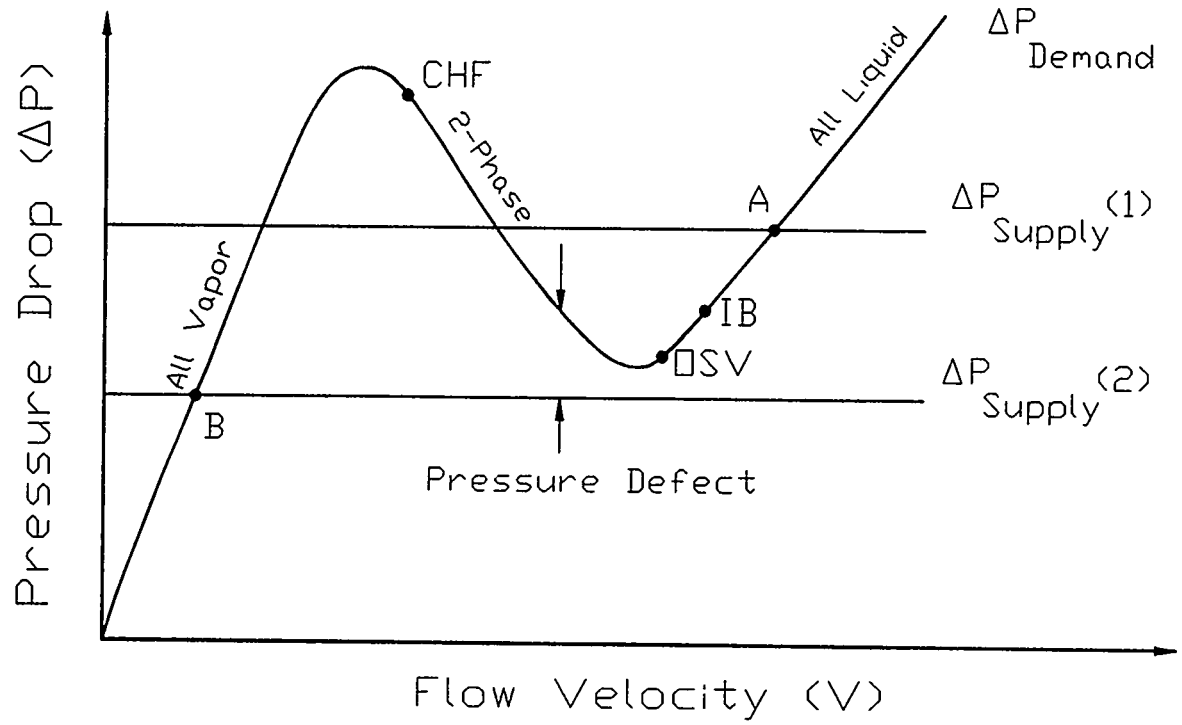

Figure 1. Supply and demand curves showing the mechanism of flow excursion in a system of parallel channels.

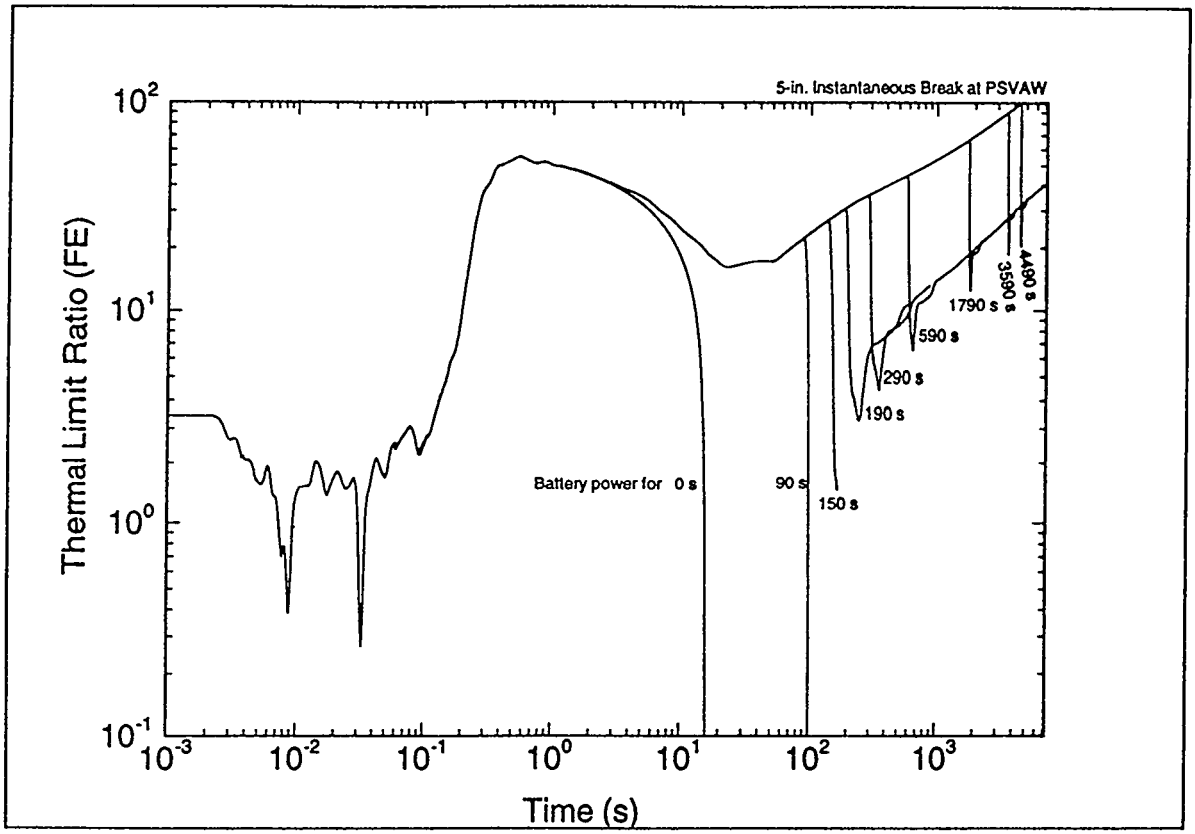

Figure 2. Flow excursion thermal limit ratio for various battery lifetimes during an instantaneous 127-mm break at the PSVAW.

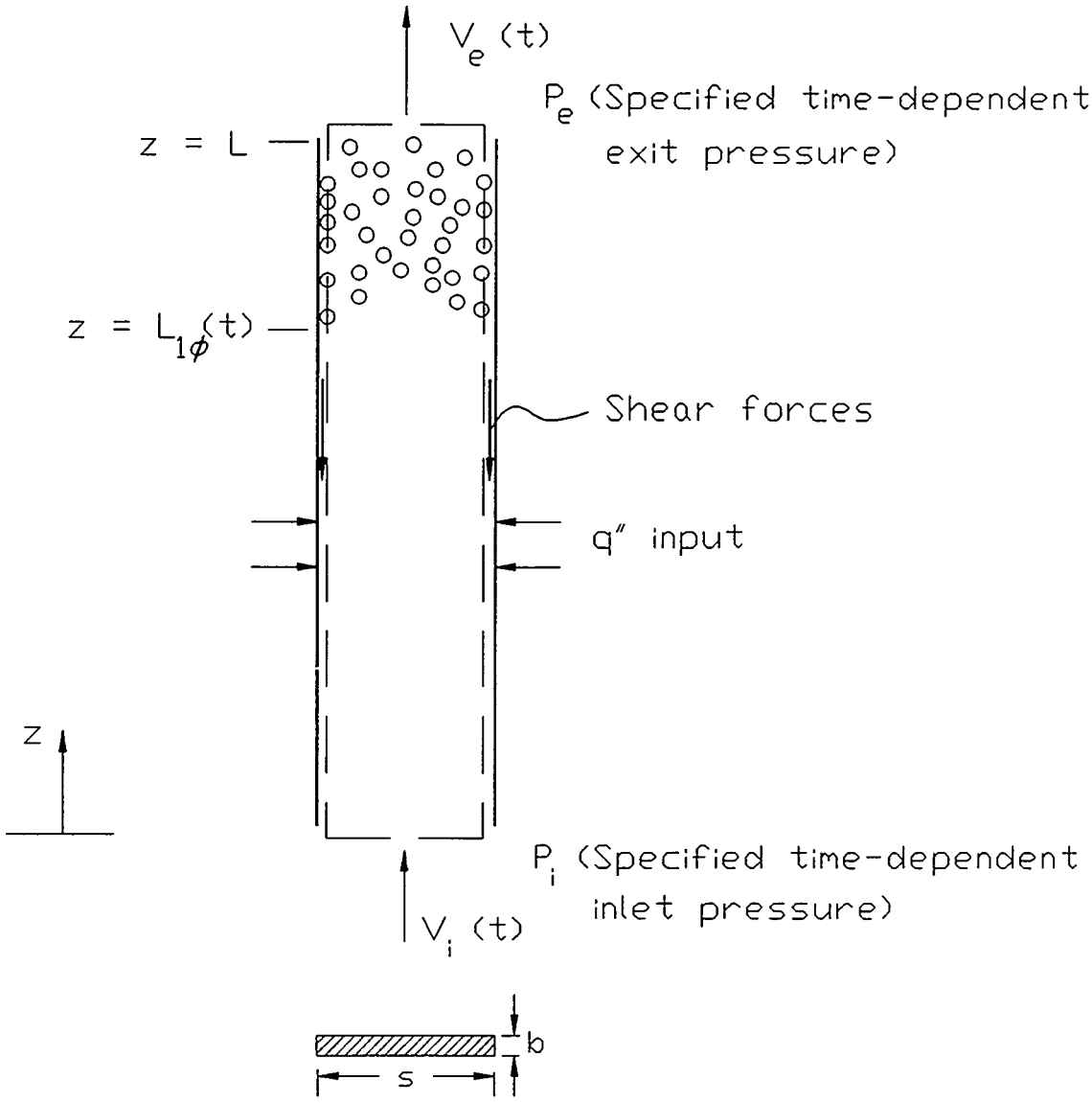

Figure 3. Schematic of an ANS coolant channel for applying the integral momentum equation.

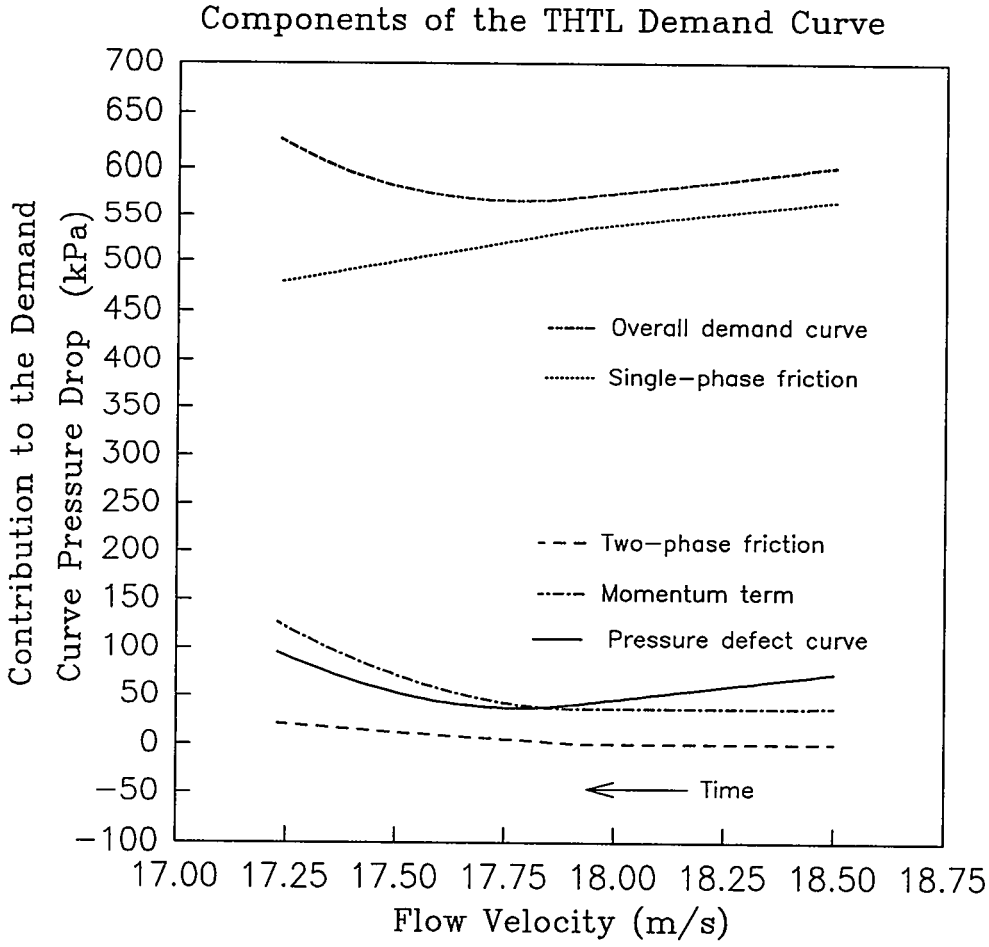

Figure 4. Contribution of the individual force components to the overall demand curve for flow excursion test FE331A in the THTL as calculated by FLOWEXC.

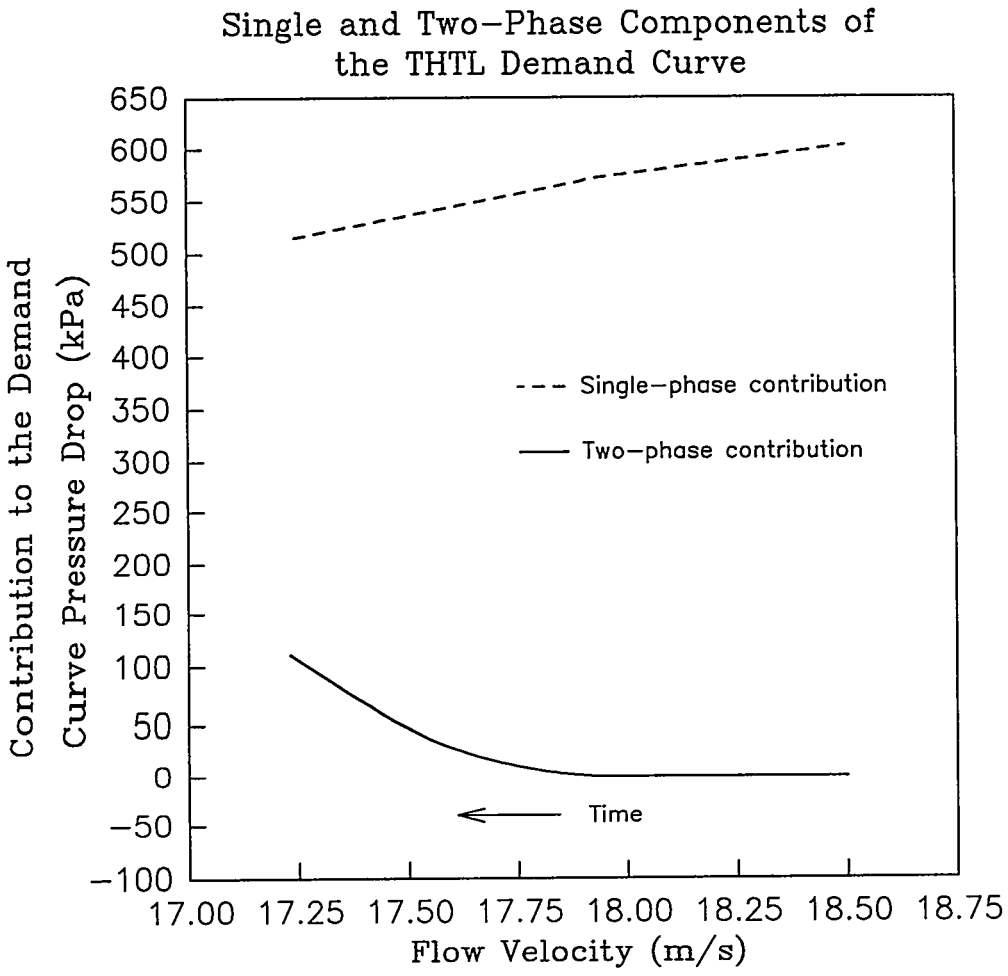

Figure 5. Single-phase flow and two-phase flow contributions to the overall demand curve during an excursion in the THTL as calculated by FLOWEXC.

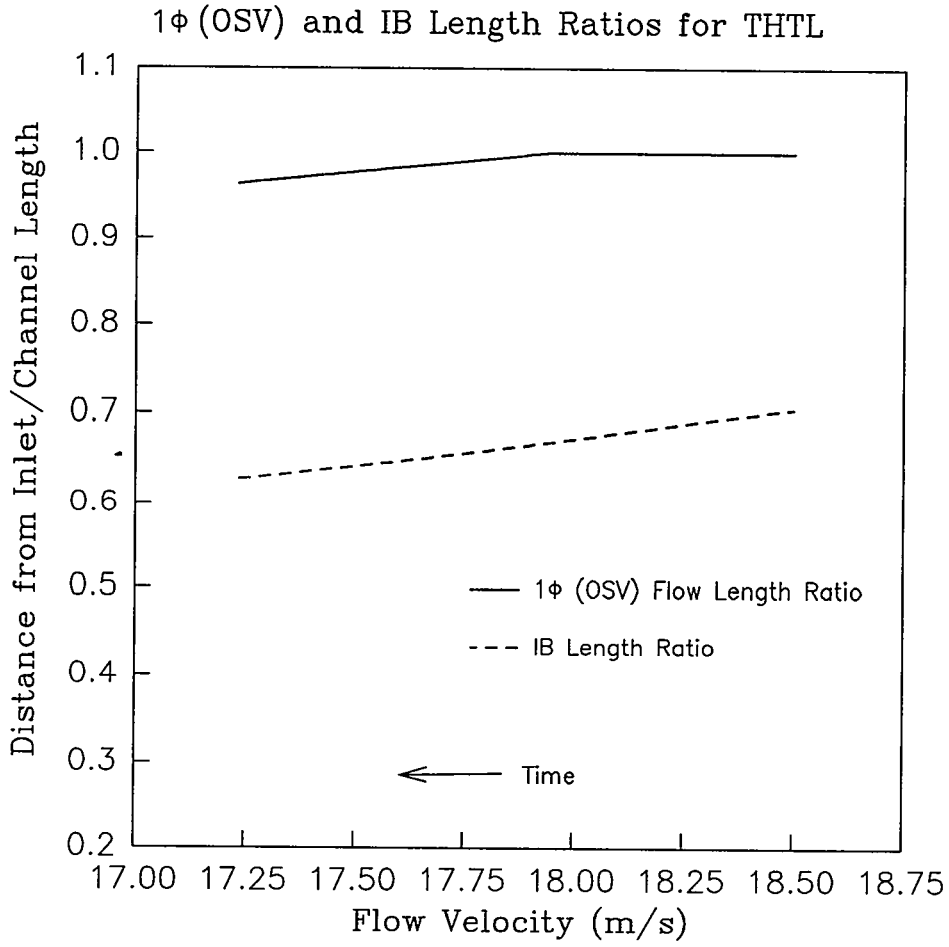

Figure 6. Single-phase flow and incipient boiling length ratios for a flow excursion in the THTL as calculated by FLOWEXC.

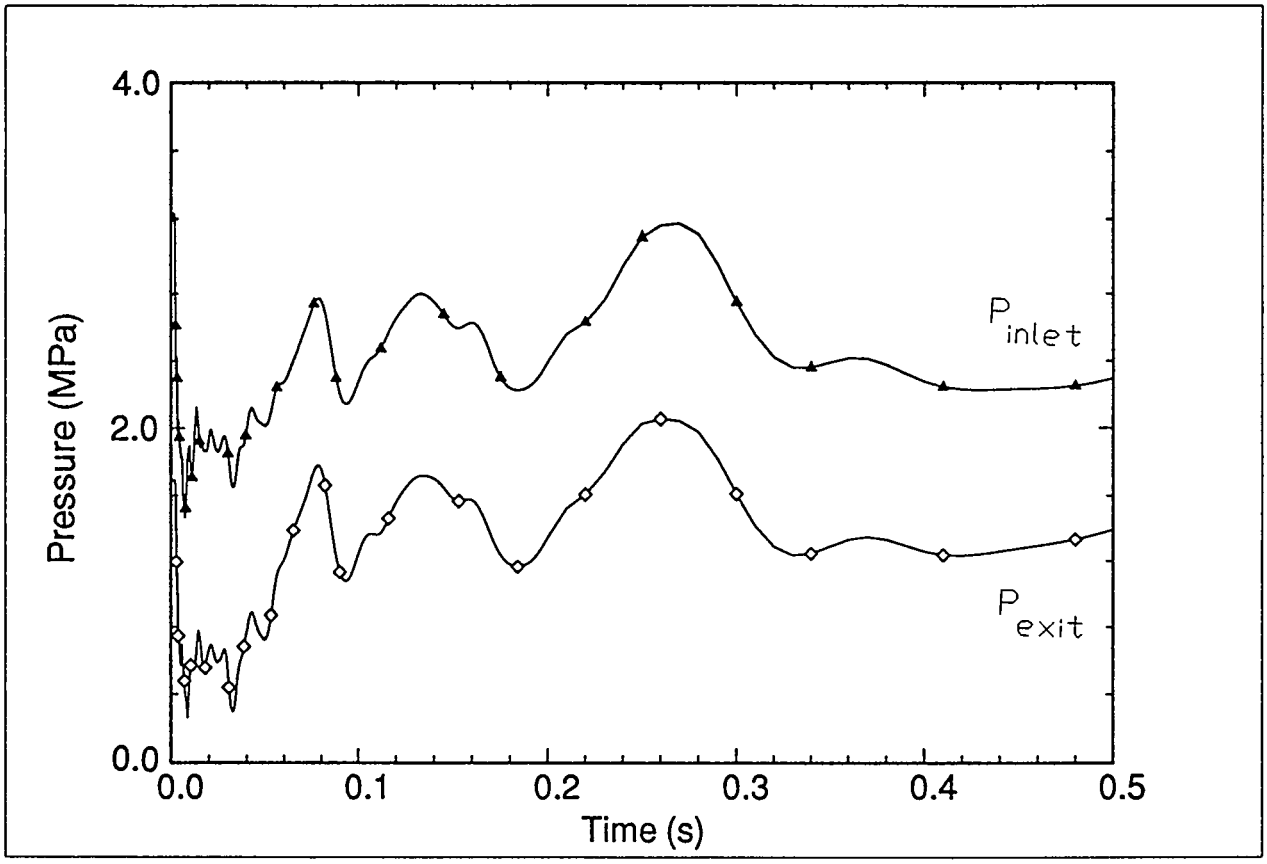

Figure 7. Time history of the channel inlet and exit pressures used as FLOWEXC boundary conditions for the PSVAW break case.

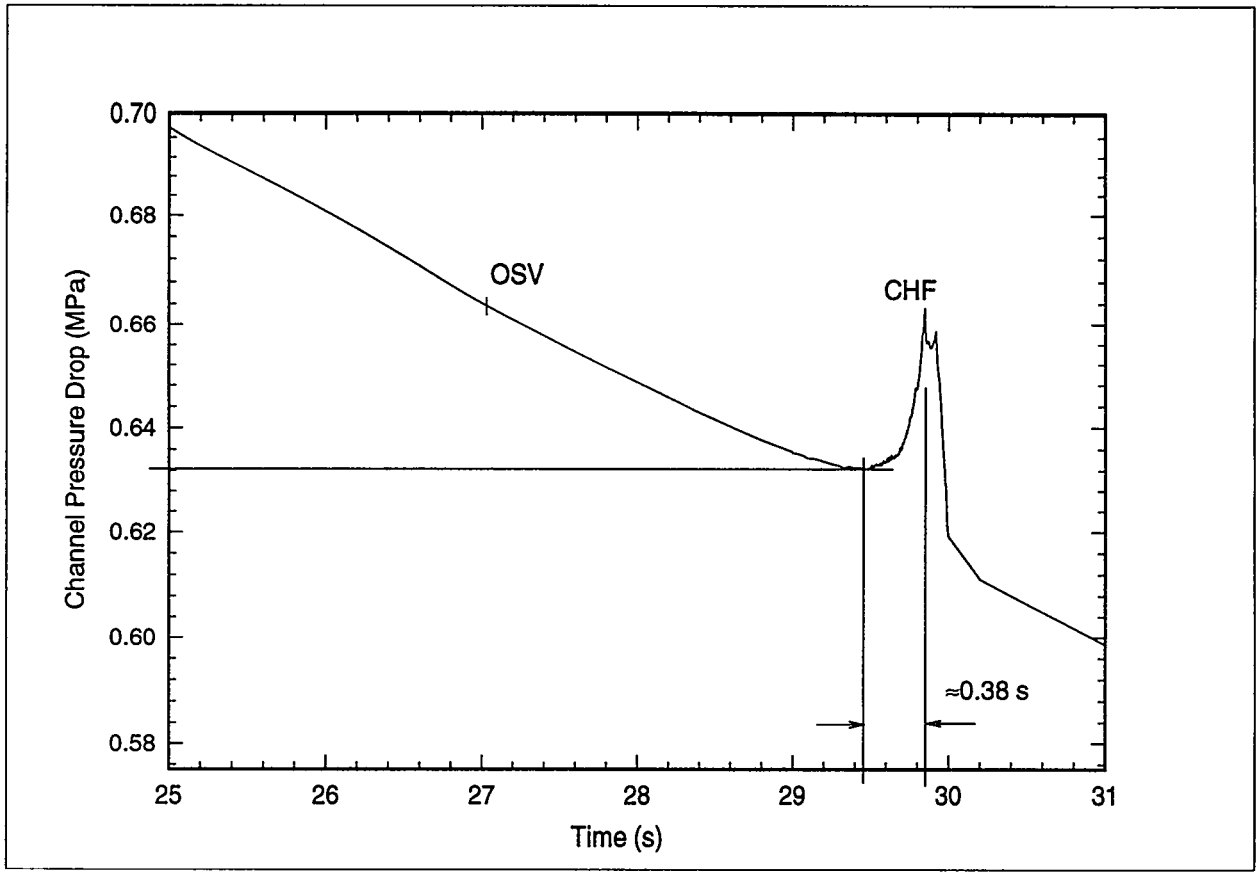

Figure 8. Channel demand pressure drop for the reduced flow transient case using 50 axial nodes in RELAP5.

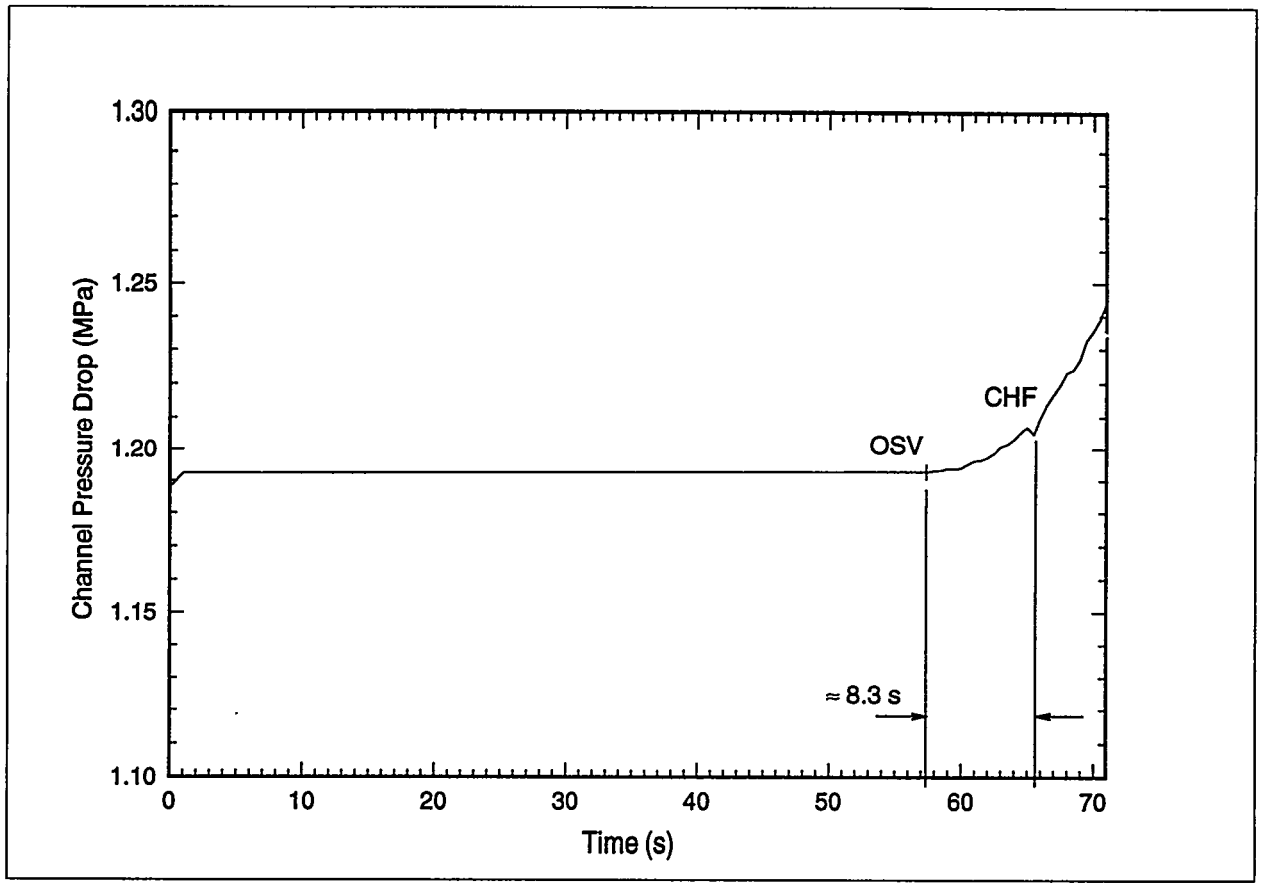

Figure 9. Channel demand pressure drop for the exit depressurization transient case using 95 axial nodes in RELAP5.

Thermal-Hydraulics of Wave Propagation and Pressure Distribution Under Hypothetical Steam Explosion Conditions in the ANS Reactor*

by

R. P. Taleyarkhan, V. Georgevich, S. N-Valenti, S. H. Kim
Oak Ridge National Laboratory, Oak Ridge, TN 37831-8045, U.S.A

ABSTRACT

This paper describes salient aspects of the modeling and analysis framework for evaluation of dynamic loads, wave propagation, and pressure distributions (under hypothetical steam explosion conditions) around key structural boundaries of the Advanced Neutron Source (ANS) reactor core region. A staged approach was followed, using simple thermodynamic models for bounding loads and the CTH code for evaluating realistic estimates in a staged multidimensional framework. Effects of nodalization, melt dispersal into coolant during explosion, single versus multidirectional dissipation, energy level of melt, and rate of energy deposition into coolant were studied. The importance of capturing multidimensional effects that simultaneously account for fluid-structural interactions was demonstrated. As opposed to using bounding loads from thermodynamic evaluations, it was revealed that the ANS reactor system will not be vulnerable to vertically generated missiles that threaten containment if realistic estimates of energetics are used (from CTH calculations for thermally generated steam explosions without significant aluminum ignition).

1. INTRODUCTION

The Advanced Neutron Source [1] is to be a multipurpose neutron research center, currently in the design stage at the Oak Ridge National Laboratory (ORNL). ANS is planned to be a 330-MW heavy-water cooled and moderated research reactor surrounded by neutron beam experimental facilities, and housed in a large, double-walled containment. The reactor uses U_3Si_2-Al cermet fuel in a plate-type configuration. Cooling systems are designed with many safety features, including large heat sinks sufficient for decay heat removal; passive inventory control by accumulators, pools, and flooded cells; a layout that maximizes natural circulation capabilities; and fast, redundant shutdown systems. A defense-in-depth philosophy has been adopted. In response to this commitment, ANS project management initiated severe accident analyses and related technology development early in the design phase.

Among several possible scenarios of core damage accidents in ANS, primary emphasis has been placed on analyzing core damage accidents initiated by blockage of one or more coolant channels at the inlet. The Level-1 Probabilistic Risk Assessment (PRA) of ANS indicates that this initiating event represents the largest contributor (>90%) to the overall core damage frequency. As part of an effort toward issue closure, a study was undertaken to evaluate system vulnerabilities from dynamic loads resulting from ensuing flow blockage-induced energetic fuel-coolant-interactions (FCIs) or steam explosions in the core region. Front-end work related to evaluation of melting and propagation is presented in a companion paper by Kim et

al. [2]. The purpose of this paper is to describe the modeling and analysis approach followed, along with pertinent analyses conducted to date, to evaluate pressurization and wave propagation aspects under steam explosion conditions initiated by a core flow-blockage accident in the ANS reactor core. Resulting transient loadings on key components around the ANS core region from energetic FCI events initiated by core flow blockage are to be used as a key component for deriving insights and plans for closure of concerns (such as generation of containment-threatening missiles and failure of vulnerable components leading to bypass).

2. DESCRIPTION OF ANS SYSTEM DESIGN

ANS is in an advanced conceptual design stage. As such, design features of the containment and reactor systems are evolving, based on insights from ongoing studies. Specifically, the 330-MW(f) ANS reactor will use ~20 kg of highly enriched uranium-silicide fuel in an aluminum matrix, rolled into plate form. The core consists of several hundred fuel plates of involute shape that are welded between annular rings. Total (conceptual design) core mass and volume are ~100 kg and 68 L, respectively. The core is enclosed within a pressure vessel (also called core-pressure-boundary-tube, or CPBT). The CPBT is surrounded by a heavy water-filled reflector tank. The reflector tank encompasses several beam tubes leading into experiment rooms. The entire reactor system is immersed in a large pool of water. The ~95,000 m^3 primary containment consists of a steel shell housed in a reinforced concrete, secondary containment wall. Annulus flow is exhausted through filter banks. The base or conceptual ANS containment and key component locations are shown in Fig. 1.

3. MODELING AND PROBLEM FORMULATION

A systematic assessment was conducted of the ANS conceptual design to evaluate potential vulnerabilities related to missile generation and rupture of key components around the core region. This study indicated that the top portion of the CPBT (see Fig. 1) a short distance above the core, may result in a potential missile upon failure. The missile was determined to be the closure elbow and water in the fuel transfer channel above it. For the horizontal directions, it was determined that failure of the many beam tubes (shown schematically in Fig. 1) in the reflector tank may lead to potential missiles and radionuclide bypass pathways. Component dynamic failure envelopes, that will indicate the necessary combinations of pressure pulse magnitude and time duration necessary for component failure, are under development. These failure envelopes need to be combined with knowledge of thermal-hydraulics of wave propagation and dynamic loading histories along the CPBT and in various regions of the reflector tank.

The evaluation of dynamic loads in the ANS core was done in a staged manner taking front-end information on core melting and superheat from studies reported in a companion paper by Kim et al. [2]. In this staged approach, we first evaluated steam explosion dynamics from thermodynamic considerations using the models and approaches of Board-Hall (BH) and Hicks-Menzies (HM) [3,4].. These approaches provide point estimates of the maximum possible levels of pressurization and thermal-to-mechanical energy conversion and, thus, provide a useful check for more refined calculations of energetics. These models were used over a wide range of coolant-debris mixture void fractions and melt temperatures. Some preliminary conclusions could then be drawn for judging propensity for containment-threatening missile generation. If the system can tolerate such bounding loads, no

further analysis is necessary. For the present situation, this approach was found to be unsatisfactory and too bounding.

The thermodynamic estimates, while providing useful initial estimates for gaging the magnitude of the overall loading function (and the risk thereof), do not provide answers on multidimensional aspects and also do not address aspects dealing with focusing, dissipation in water and structural media, fluid-structural interactions, etc. To provide such clarification requires a sophisticated wave propagation and interaction analysis framework, for which we employed the CTH code system [5]. CTH provides the capacity to analyze in one- two- and three-dimensions shock wave transport and multi-material motion phenomena allowing one to address fluid-structural interaction aspects also. The code system models multidimensional, multi-material, large deformation, strong shock physics in cylindrical, spherical and rectangular coordinates. A two-step numerical solution scheme is used with these meshes. The first step is a Lagrangian step in which the cells distort to follow the material motion. The second step is a remesh step in which distorted cells are mapped back to the Eulerian mesh. The finite difference analogs of the Lagrangian equations of mass, momentum and energy conservation are employed with continuous rezoning to construct Eulerian differencing. Models are included for material strength, fracture, distended materials, high explosives and a variety of boundary conditions. CTH capabilities have undergone extensive benchmarking and validation. The code has also been used for several reactor safety studies [6,7,8].

As mentioned above, significant improvements can be achieved over HM- and BH-type bounding model predictions by taking axial dependencies into account, even assuming reflective boundaries. An improvement over this would be to consider what fraction of mechanical energy can leave through the walls of the CPBT to the reflector tank, even without CPBT rupture. Such a postulated evaluation process would tend to give realistic bounding loads at the location of the closure elbow for investigating vulnerabilities in the vertical direction.

For judging vulnerabilities in the lateral direction it is necessary to consider the possibility of the CPBT rupturing. Thereafter, wave propagation and dynamic pressurization in the reflector tank should be possible to evaluate in a realistically bounding sense, if a break of a reasonable size (varied parametrically, if necessary) is postulated in the CPBT around the explosion zone.

On the basis of the above perspectives, three cases were developed for performing CTH modeling and analyses over a range of energy deposition levels in the core region. The three cases are shown in Fig. 2. As seen, Case A is the case wherein the situation is analyzed in a one dimensional (1-D) sense to provide a first-cut improvement over the static, zero dimension calculations with HM and BH models to obtain maximum possible spatially-dependent loads along the CPBT. Case B is the same as Case A, except that the CPBT and reflector tank volumes are added. Case C is the same as Case B except for the CPBT, which is postulated to be ruptured.

For the multidimensional CTH calculations, due to the significantly longer computation time required, a base case had to be developed to limit the total number of cases analyzed for this study. Several postulates and assumptions had to be made, which are described herein. To begin with, it was postulated that during a steam explosion molten debris from various parts of the core would be ejected over a 1-m length of the CPBT, also approximately representing the axial length, or average circumference, of the conceptual ANS core. This postulate could lead to smearing out the pressure buildup but is considered reasonable since a propagating steam

explosion of a melting core under full-flow and power conditions would very likely involve some degree of melt dispersal (the characteristics of which have not yet been quantified mechanistically). Again, with propagation velocities ranging from ~700 to 1000 m/s, separate calculations with FCIMOD.ORNL [7,9] (for transient breakup and pressure buildup) and others reported in a companion paper [10] indicate that the time duration for energy deposition should be ~1 ms. Such a fast time interval precludes any appreciable water mass from leaving the explosion (or melt dispersal) region before all the energy is deposited. Nevertheless, such an effect of mass exiting from the explosion volume is taken into account in the CTH calculations. It is further assumed that energy deposition in the explosion zone occurs uniformly. It is realized that dividing the energy deposition zone into smaller regions complicates the problem but might also assist in better simulation of a varying density explosion zone. This aspect will be investigated, as needed, during later studies.

For evaluation of realistically bounding loads in the horizontal direction with CPBT rupture, a rupture length had to be assumed. Based on the postulate that flow-blockage induced melting and subsequent steam explosions would occur from melting of one of the two axially offset fuel core elements (each with several hundred plates and lengths of ~0.5 m), it was assumed that the rupture length of the CPBT would be in the 0.5 m range (see Case C in Fig. 2).

Due to very high aspect ratios involved for resolving components and regions of the CPBT and reflector tank (e.g., CPBT thickness is < 20 mm compared to length scales of ~8 m), conducting coupled best-estimate fluid-structural interaction calculations involving details of CPBT rupture, etc., would require nodalization in excess of 1500 x 1500 nodes, even for 2-D calculations. This was far beyond the RISC/6000 workstation machine capability, and a single run, even if it were feasible, would take several months of cpu time. To circumvent this difficulty and to provide reasonable estimates of thermal-hydraulics of wave propagation and dynamic loadings for the vertical and horizontal directions in a separate-effects fashion, a much thicker than normal CPBT was modeled to allow node sizes of ~40-80 mm. It is realized that such a prescription introduced to prevent CPBT rupture will also lead to larger than actual absorption of shock-wave energy into the material of CPBT. However, this approximation was necessary to permit practical evaluations for cases with and without CPBT rupture, when considered separately. Again, in the spirit of evaluating realistically bounding loads in a piece-wise fashion for the vertical and horizontal directions, reflective boundaries were prescribed for the vertical and horizontal edges. Several components (such as beam tubes and instrument lines) in the reflector tank were not represented to permit practical evaluations to be conducted. Not representing structures in the reflector tank at this stage would tend to provide higher pressure values due to not considering energy absorption into structural components. However, this is offset by the reduction in volume of water, which these components would have displaced, that would lead to increased pressurization.

Based on the above, a test matrix of calculations was developed and is shown in Table 1. As noted therein, much of the parametric calculations were conducted with the 1-D representation before embarking upon time-consuming 2-D simulations. Various situations analyzed include effects of nodalization, time span for energy deposition, core volume fractions over which thermal energy transfer occurs, and the effect of transmitting boundaries (to study the bounding condition wherein boundary rupture may allow for water or mass ejection, thereby relieving system pressure buildup). Upon gaining insights from 1-D calculations (Cases A), 2-D cases (viz., Cases B and C) were executed with base nodalization with whole-core volume fraction for thermal energy input over a range of values, a 1-ms time span of energy insertion, and

reflective boundaries at the extreme axial and radial directions. Energy input was varied from 800 MJ (representing complete aluminum ignition of the ~30 kg core mass that is predicted [2] to melt and superheat) to a low value of 18 MJ (representing 10% of the core mass thermal energy component that is predicted to melt). This range was chosen to give an idea on thresholds below which steam explosion loads would be tolerable from the standpoint of safety and risk goals. The results of these evaluations (supplemented with additional work as necessary) provide a framework to determine what, if any, focused analytical-cum-experimental work is necessary or what design modifications may be possible to introduce in order to absorb loads in an efficient manner and allow ANS severe-accident safety goals to be met.

4. RESULTS AND DISCUSSION

The melt progression analyses (reported in a companion paper) predicts a core melt energy level of ~180 MJ, a value that increases to ~800 MJ if we assume chemical ignition of all the aluminum during the energetic FCI event. Using information on melt masses and superheats from a companion paper on core melting and damage propagation, we conducted steam explosion energetics calculations using the thermodynamic HM and BH models to obtain upper bounds on pressurization and thermal-to-mechanical energy conservation. This preliminary analysis indicated the theoretical possibilities of thermal-to-mechanical energy conversion ratios near 50% and pressures in the several thousand MPa range. For a worst-case situation in which energy needed to break bolts is not accounted and no lateral energy dissipation is assumed, the energy conversion ratio needed to lead to a containment-threatening missile was estimated to be ~5.5% with 180-MJ thermal energy, and ~1.2% for 800-MJ thermal energy, respectively. The missile in this case, is the ~600 kg closure elbow and the ~30,000 kg fuel transfer channel water (slug) above it. For preliminary analysis, it is conservatively assumed that containment failure occurs if this ~30,600 kg missile reaches and contacts the containment liner. Clearly, applying the thermodynamic models in a simplistic manner (without accounting for lateral and axial dissipation) can lead to unacceptably bounding results and provide the motivation for conducting CTH evaluations for obtaining realistic loadings. These results are presented in step-wise fashion for Cases A through C, respectively.

4.1 1-D CTH model results (Case A)

The impacts of nodalization and time span for thermal energy input in a 1-m-long explosion zone were first tested. The base nodalization scheme used 80-mm-length nodes. Reducing node sizes to 40 mm did not result in any appreciable changes in pressure histories and, in essence, confirmed the adequacy of the node sizes used. Sample results of pressure traces with time for three axial locations are shown in Fig. 3. As seen, the pressure in the explosion zone (L1) increases to ~200 MPa, whereas the pressure at L3 (close to the closure elbow in the CPBT) is much higher at a level of ~425 MPa and lasts for ~2 ms. The result of increasing the time span (t) for thermal energy deposition gave rise to impulses at L3 that are very similar (~400 kPa-s), but only up to a point. Beyond 2.5 ms, forward and reflection wave patterns overlap significantly since it takes only ~1.5 ms for acoustic propagation from center of the explosion zone to the top and back. This is clearly evident from Fig. 4, where the energy deposition time was increased to 3 ms. The true impact of the importance of knowing precisely such energy deposition time frames will evidently rest on the nature of the structural failure envelopes.

Further 1-D calculations were also done to evaluate the effect of energy deposition over a smaller coolant volume (viz., less melt dispersal into the coolant before the

onset of an explosion). These are Cases A.4 through A.6 in Table 1 and Table 2. Salient results concerning pressure buildup and average density changes in the explosion zone (L1) and at the top of CPBT (L3) of these analyses are shown in Table 2 and Fig. 5. As can be noted from these results, the impact of energy deposition (viz., mass of coolant in the explosion zone) can have a significant effect on the pressure and thermal-hydraulics of the situation. Peak pressure buildup rises rapidly with decreasing explosion zone size, but tends to level off. Work done by the explosion zone against the surroundings was estimated for the duration of the initial pressure pulse (by multiplying the explosion zone pressure times the fractional change in explosion zone water volume). This analysis reveals a work output ranging from ~4.5 MJ for Case A.1, which increases to ~9.5 MJ for Case A.4, and then decreases to ~4.5 MJ for Case A.6. These translate into thermodynamic efficiencies varying between 2% and, 5%. These values are an order of magnitude lower than the corresponding efficiencies computed with the HM and BH models, and underscore the benefits to be gained from CTH-type analyses.

Table 2 also lists values for pressure buildup for Case A.7 (which is identical to Case A.6 except that transmitting boundary conditions are used to represent the possible situation in which structural rupture has occurred and mass is permitted to leave). This situation tends to represent a semi-infinite condition in which a close-to infinite pool of water is represented above the top of the CPBT. As seen, the lack of a reflecting boundary under these thermal-hydraulic conditions leads to a considerable reduction in pressure buildup and reflection pulses at the potentially vulnerable location L3.

4.2 2-D Cases B.1 to B.5 (Intact CPBT with Reflector Tank)

Cases B.1 to B.5 provide a useful reference for values of pressure buildup in the vertical direction (with some lateral dissipation from wave energies transferred through the intact, albeit much thicker CPBT) and in the reflector tank regions even in the absence of CPBT rupture. Values from Case B.1 can be directly compared with those from Case A.1 (where no lateral dissipation was allowed) to judge the benefits gained from multidimensional assessments. Sample results of pressurization for selected locations for 180 MJ and 800 MJ levels of thermal energy deposition (Cases B.1 and B.2) are shown in Figs. 6 to 7. Further results for all five cases are tabulated in Table 3. When results for Cases B.1 and A.1 are compared, for the same total energy deposition (of 180 MJ), a fairly significant decrease occurs in peak pressure buildup (and impulse) both in the explosion zone and at the top of the CPBT. Clearly, energy transferred to the CPBT and reflector tank regions can play a role, even when the CPBT is intact. Pressure spikes in the reflector tank region are modest in comparison, and are largely short duration pulses. A noteworthy point is revealed upon comparing Case B.2 results with Case B.1 results for pressure buildup at top of CPBT (point L3). Although the total energy deposition level is 4.5 times larger, the resulting peak pressure at L3 is only 2.6 times larger. Therefore, one may not a priori scale pressure buildup linearly. This is even more important when comparing impulses at L3. Comparing corresponding impulses, we obtain an impulse of ~475 kPa-s for Case B.2 (800 MJ) and an impulse value close to it of ~350 kPa-s for Case B.1 (180 MJ). This is clearly an important effect, which indicates that higher energy levels by themselves do not necessarily lead to scaled values of impulses.

It is seen from Table 3 that work output increases from ~0.4% for the 18-MJ energy insertion case to ~2.5% for the base case with 180 MJ energy insertion, to ~7% for the 600-MJ energy insertion case and then increases only slightly to ~7.3% for the 800-

MJ energy insertion case. Coolant fractional density changes in the explosion zone follow the same trends as seen for the conversion ratio variations.

4.3 2-D Cases C.1 to C.5 (Ruptured CPBT with Reflector Tank)

As opposed to the previous cases described, Cases C.1 to C.5 provide information on the thermal-hydraulics of pressure buildup and wave propagation for the situation in which the CPBT may have ruptured from the initial pressure buildup in the core region. Results presented should be used with due caution since the actual rupturing process is not modeled, which, if included, should increase pressure buildup predictions for the vertical direction and reduce the pressure buildup values for the horizontal direction locations in the reflector tank. Sample results of computations for Cases C.1 (for 180 MJ) and C.2 (for 800 MJ) are given in Figs. 8 and 9. Further results for all five cases are tabulated in Table 4. Comparing results of the ruptured CPBT cases with results of corresponding cases with intact CPBT, a significant reduction is seen in pressure and impulse buildup for the 180-MJ energy insertion cases. At point L1, the peak pressure reduces from 200-MPa to ~50-MPa, and at L3 the peak pressure reduces from ~350-MPa to ~125-MPa. However, as expected, pressure buildup in the reflector tank jumps up significantly compared with that in the intact CPBT case.

In comparison with the intact CPBT cases, comparing the 180-MJ and 800-MJ cases (viz., Cases C.1 and C.2) we note a very different trend in terms of ratio of pressure or impulse at L3 at energies of 800-MJ and 180-MJ, respectively. For the intact CPBT cases a significant dependence of this ratio was not noted on deposited energy level. For the cases with ruptured CPBT, the ratio of pressure at L3 for 800 MJ to that for 180 MJ is ~4.5. The corresponding impulse values at L3 are higher by a factor of 8. Despite the higher overall pressures for the intact CPBT case, the impulse at L3 for the intact and ruptured CPBT cases become similar as the energy deposition level increases to 800 MJ.

When the same approach is used to evaluate mechanical work in the explosion zone (as done for 1-D and 2-D with intact CPBT calculations), it is seen from Table 4 that work output increases from ~0.25% for the 18-MJ energy insertion case to ~1.4% for the base case with 180-MJ energy insertion, to ~5% for the 600-MJ energy insertion case and then starts decreasing to reach about 4% for the 800-MJ energy insertion case. Coolant fractional density changes in the explosion zone increase rapidly (and somewhat linearly) at first from 5% for the 18-MJ insertion case, reaching about 35% for the base case with 180 MJ energy insertion, to ~90% for the 600-MJ energy insertion case, and then levels off to about 95% for the case with 800-MJ energy insertion.

Compared with Case A situations, corresponding coolant density changes in the explosion region are far greater for Case B situations. This is attributable to combined effects of reduced pressure buildup and enhanced lateral dissipation of energy. However, corresponding work output in the explosion zone is much lower than for the intact CPBT cases and confirms the importance of inertial constraint (which is much larger for Cases B than for Cases C).

Clearly, even though some trends are discernible, the dynamics of the situations for the intact vs. ruptured CPBT can be expected to be considerably different and should be investigated on a case-by-case basis.

5. SUMMARY & CONCLUSIONS

To summarize, this paper has described salient aspects of the modeling and analysis framework for evaluation of dynamic loads, wave propagation, and pressure distributions (under steam explosion conditions) around key structural boundaries of the ANS reactor core region. The analyses for energetics were centered on the melt energy contents evaluated from a core melt propagation study described in a companion paper. The melt energy content used as a baseline was 180-MJ of thermal energy, assuming no aluminum ignition during the energetic FCI event.

A staged approach was followed, using simple thermodynamic models for bounding loads and the CTH code system for evaluating realistic estimates in a staged multidimensional framework. The approach using HM- and BH-type thermodynamic models, which incorporate no time and spatial dependencies, gave rise to intolerable values for thermal-to-mechanical energy conversion. Several CTH models were developed in a staged manner. The 1-D model was used to ascertain adequacy of nodalization and to evaluate the impact of uncertain parameters (viz., time span for energy deposition, and degree of melt dispersal into coolant during explosion). It was revealed that for small variations about the best-estimate value of time span for energy deposition, no significant impact occurs on impulses delivered at the top of the CPBT. That is, despite the lower values of peak pressure buildup, the increase in pulse width compensates for the reduction in pressure. Beyond the value of 2.5 ms (associated with acoustic wave transport in the specific geometry being analyzed), considerable wave overlapping occurs between incident and reflective pressure fronts leading to rapid equilibration. The impact of coolant mass available in the explosion zone was quite pronounced in that the mechanical work resulting in the explosion zone varies non linearly (displaying a bell-shaped curve) with available coolant mass for the given amount of thermal energy. Even though the magnitude and dependence on coolant-to-fuel mixing volumes are different, these trends are consistent with past observations and results from thermodynamic modeling approaches. Peak value for thermal-to-mechanical energy conversion ratio obtained was ~4%, which is lower by an order of magnitude than that produced using HM and BH-type models. When the 1-D work output values for the 180-MJ thermal energy content were used, coupled with conservatively bounding assumptions for structural failure of the closure elbow, it was judged that no vulnerability exists for the ANS containment from vertically generated missiles.

Multidirectional dissipation aspects were studied for relevance and comparison with 1-D approximations using two CTH model representations of the CPBT and reflector tank regions. The first model considered the impact of an intact CPBT. When compared with the 1-D case, it was found that significant reductions in impulse loading at the top of the CPBT can result as a consequence of lateral dissipation of energy into the CPBT and reflector tank even without rupture. Variations of peak pressure and impulses transferred revealed a nonlinear dependence on the energy deposition level. The second model considered the possibility of a ruptured CPBT and gave rise to much lower pressure buildup in the vertical direction, but, as expected, significant impulsive pressures were observed in the reflector tank. The characteristics of mechanical work output, and the thermal-hydraulic behavior in the explosion zone for these two limiting configurations were significantly different. Work output was generally greater for the intact CPBT case, even though coolant density reductions were much higher for the ruptured CPBT case (attributable to reduced pressures and inertial constraint). The results of this modeling framework and analyses will be used in conjunction with dynamic failure

envelopes for various components, to determine appropriate courses of action related to closure of concerns on flow-blockage-induced energetic FCIs.

REFERENCES

1. C. D. West, "The Advanced Neutron Source: A New Reactor Based Facility for Neutron Research," Transactions of the American Nuclear Society, Vol. 61 (June 1990).

2. S. H. Kim et al., "Modeling and Analysis Framework for Core Damage Propagation During Flow-Blockage Initiated Accidents in the Advanced Neutron Source Reactor at Oak Ridge National Laboratory," Proceedings of NURETH-7, Saratoga Springs, New York (September 1995).

3. S. J. Board and R. W. Hall, "Propagation of Thermal Explosions Part 2: A Theoretical Model," Central Electricity Generating Board Report RD/B/N3249, 1974.

4. E. P. Hicks and D. P. Menzies, "Theoretical Studies on Fast Reactor Maximum Accidents," Argonne National Laboratory Report, ANL-7120, 1965.

5. J. M. McGlaun and S. L. Thompson, "CTH: A Three-Dimensional Shock-Wave Physics Code,"International Journal of Impact Engineering," 10, 251-360 (1990).

6. R. K. Byers, "CSQ Calculations of H2 Detonations in the Zion and Sequoyah Nuclear Plants," NUREG/CR-2385, July 1982.

7. R. P. Taleyarkhan et al., "Analysis and Modeling of Flow-Blockage Induced Steam Explosion Events in the High Flux Isotope Reactor," Nuclear Safety Journal, Vol.35-1, 58-73, (January-June, 1994).

8. R. P. Taleyarkhan et al., "Modeling and Analysis of Hydrogen Detonation Events in the Advanced Neutron Source Reactor Containment," Proceedings of Containment Design and Operation Conference, Toronto, October 1994.

9. V. Georgevich, R. P. Taleyarkhan and C. W. Nestor, "Modeling and Analysis of Steam Explosion Energetics in Uranium-Aluminum Fueled Reactors," Proceedings of the Intl. Topical Meeting on Probabilistic Safety Assessment (PSA'93), Clearwater Beach, Florida, 1993.

10. S. H. Kim et al., "Study on Fuel Dispersion Behavior in Advanced Neutron Source Reactor at Oak Ridge National Laboratory," Proceedings of NURETH-7, Saratoga Springs, New York (September 1995).

Table 1. CTH cases considered for FCI Studies in CPBT and reflector tank regions

Case ID	Representation	Energy Deposited(MJ)	Remarks
A.1[a]	1-D	180	40-mm and 80-mm node sizes; Energy inserted over 1 ms
A.2[a]	1-D	180	80-mm node sizes; energy inserted over 2 ms
A.3[a]	1-D	180	80-mm node sizes; energy inserted over 3 ms
A.4	1-D	180	Same as Case A.1; explosion zone length reduced from 1-m to 0.5-m
A.5	1-D	180	Same as Case A.1; explosion zone length reduced from 1-m to 0.25-m
A.6	1-D	180	Same as Case A.1; explosion zone length reduced from 1-m to 0.08-m
A.7	1-D	180	Same as Case A.1; boundaries changed from reflecting to transmitting
B.1[a]	2-D (intact CPBT)	180	80-mm nodes; energy over 1 ms
B.2[a]	2-D (intact CPBT)	800	80-mm nodes; energy over 1 ms
B.3[a]	2-D (intact CPBT)	600	80-mm nodes; energy over 1 ms
B.4[a]	2-D (intact CPBT)	100	80-mm nodes; energy over 1 ms
B.5[a]	2-D (intact CPBT)	18	80-mm nodes; energy over 1 ms
C.1[a]	2-D (ruptured CPBT)	180	80-mm nodes; energy over 1 ms
C.2[a]	2-D (ruptured CPBT)	800	80-mm nodes; energy over 1 ms
C.3[a]	2-D (ruptured CPBT)	600	80-mm nodes; energy over 1 ms
C.4[a]	2-D (ruptured CPBT)	100	80-mm nodes; energy over 1 ms
C.5[a]	2-D (ruptured CPBT)	18	80-mm nodes; energy over 1 ms

a - Explosion length = 1-m; reflecting boundaries.

Table 2. Summary of results for 1-D Cases

Case	Peak pressure at L1 (MPa)*	Peak pressure at L3 (MPa)	Avg. pressure at L1 (MPa)*	Fractional density change	Explosion zone length (m)	Conversion ratio (%)
A.1	210	425	110	0.23	1	2.53
A.4	320	675	220	0.48	0.5	5.28
A.5	400	925	275	0.7	0.25	4.81
A.6	400	1000	350	0.9	0.08	2.52
A.7	400	400	275	0.9	0.08	1.98

Table 3. Summary of results for 2-D cases with intact CPBT

Case	Peak pressure at L1 (MPa)*	Peak pressure at L3 (MPa)	Peak pressure at L8 (MPa)*	Avg. pressure at L1 (MPa)*	Fractional density change	Energy deposited (MJ)	Conversion ratio (%)
B.1	200	325	3.5	110	0.23	180	2.53
B.2	625	900	70	463	0.7	800	7.28
B.3	500	750	45	394	0.6	600	7.09
B.4	100	170	1.5	74	0.14	100	1.86
B.5	17	22	0.8	11	0.035	18	0.39

Table 4. Summary of results for 2-D cases with ruptured CPBT

Case	Peak pressure at L1 (MPa)*	Peak pressure at L3 (MPa)	Peak pressure at L9 (MPa)*	Avg. pressure at L1 (MPa)*	Fractional density change	Energy deposited (MJ)	Conversion ratio (%)
B.1	50	112	20	40	0.35	180	1.40
B.2	350	550	220	175	0.95	800	3.74
B.3	300	480	170	179	0.9	600	4.83
B.4	29	50	10	16	0.3	100	0.88
B.5	7.5	9.5	2	5	0.05	18	0.25

(*) - values quoted correspond to energy deposition time frame.

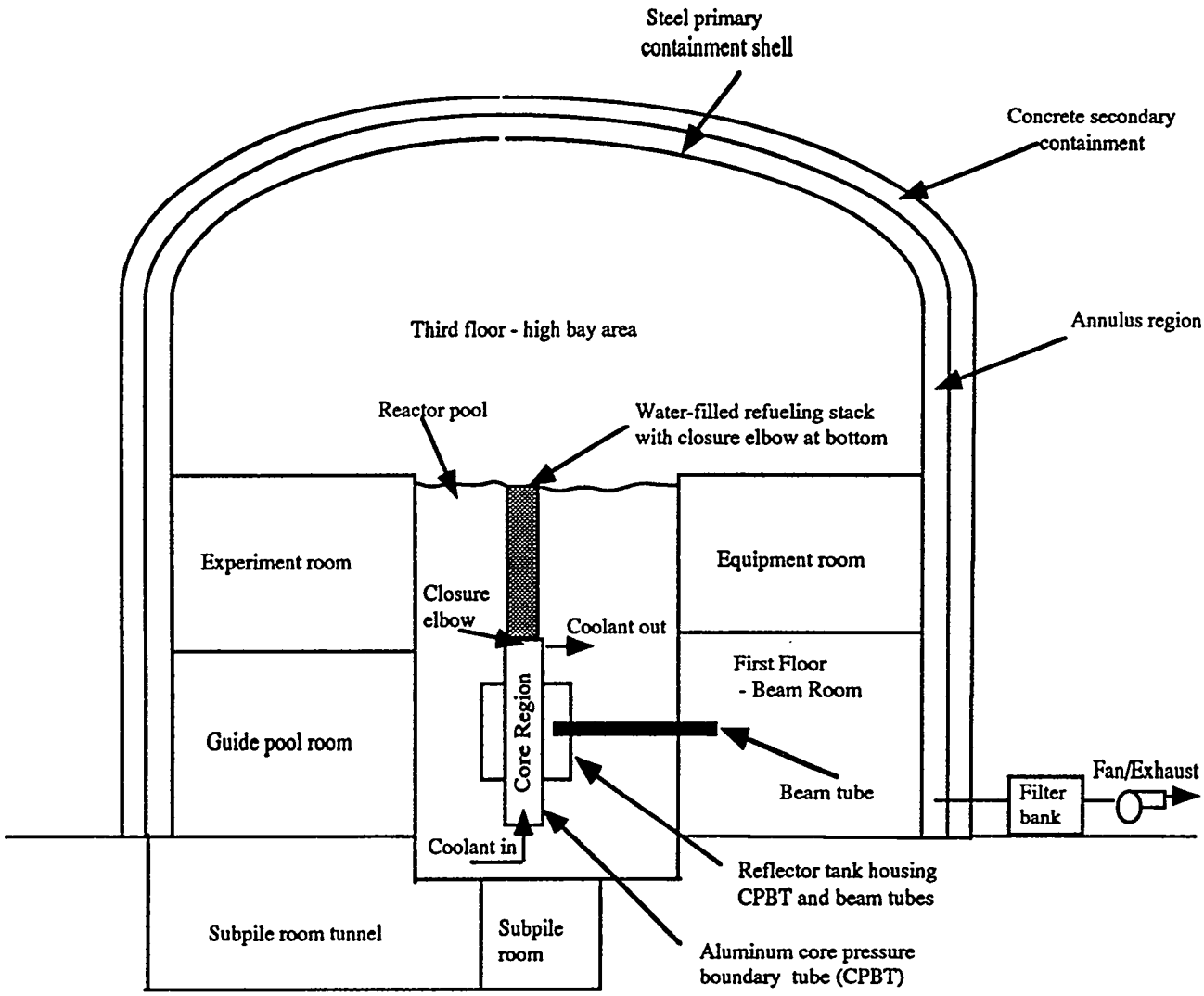

Fig. 1. Schematic representation of ANS conceptual containment design.

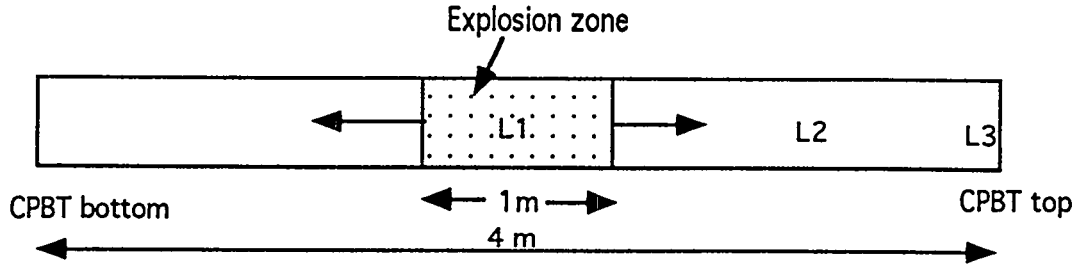

Fig. 2a. Case A, 1-D simulation of CPBT wave transport.

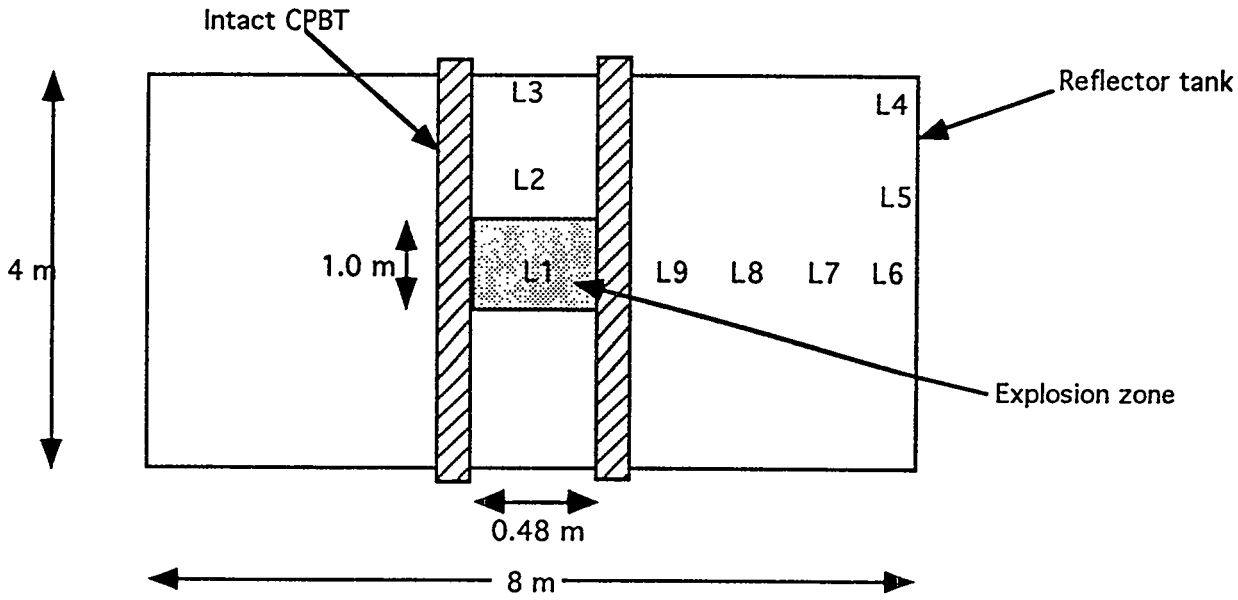

Fig. 2b. Case B, 2-D simulation with intact CPBT.

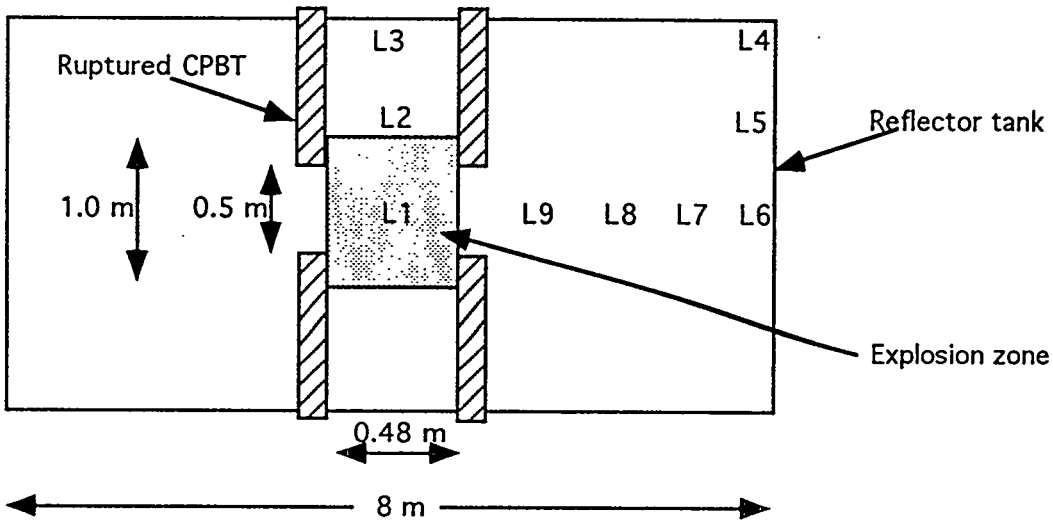

Fig. 2c. Case C, 2-D simulation with ruptured CPBT.

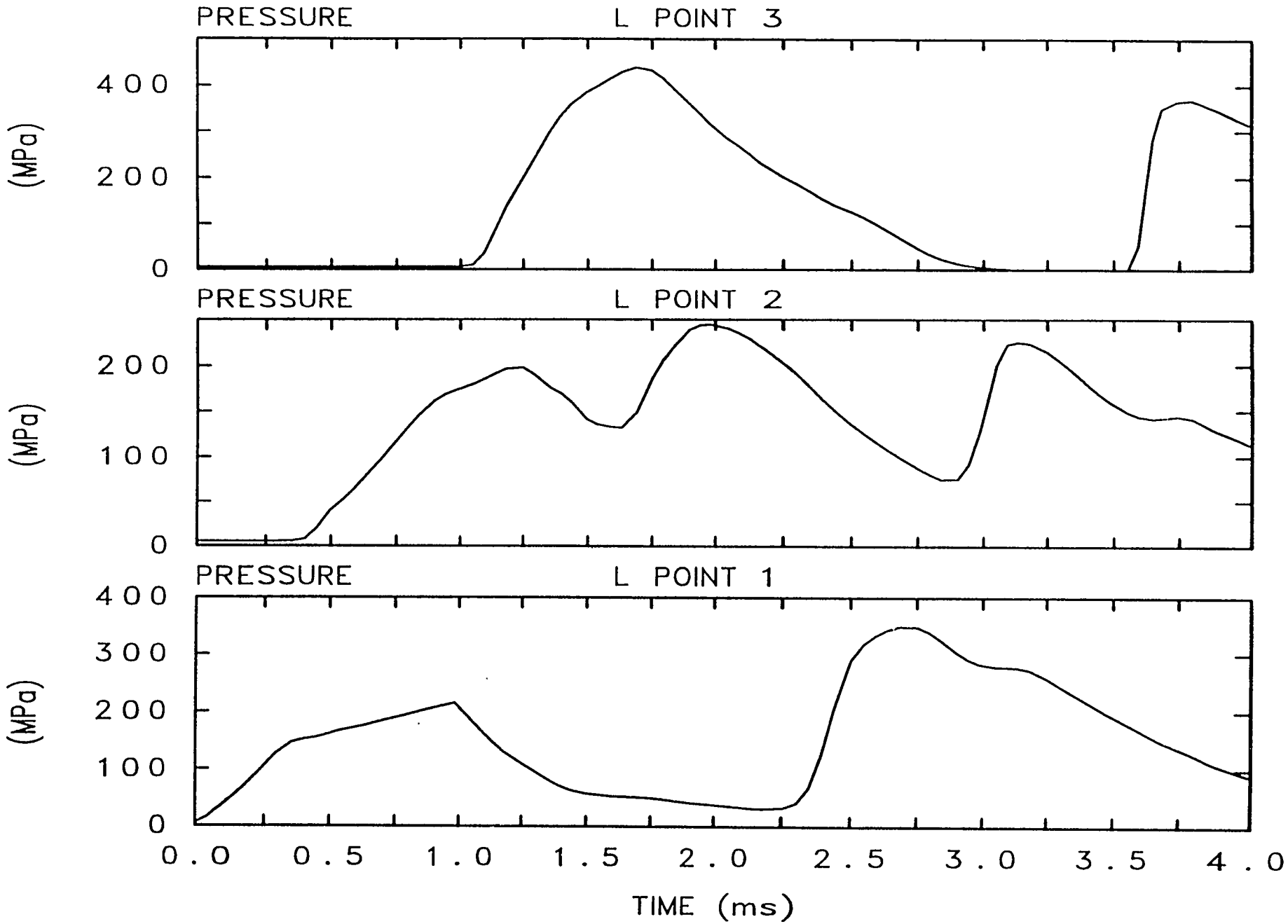

Fig. 3(a). Transient pressure variation at various locations for Case A.1 (Energy insertion= 180-MJ over 1 ms; 1-D simulation).

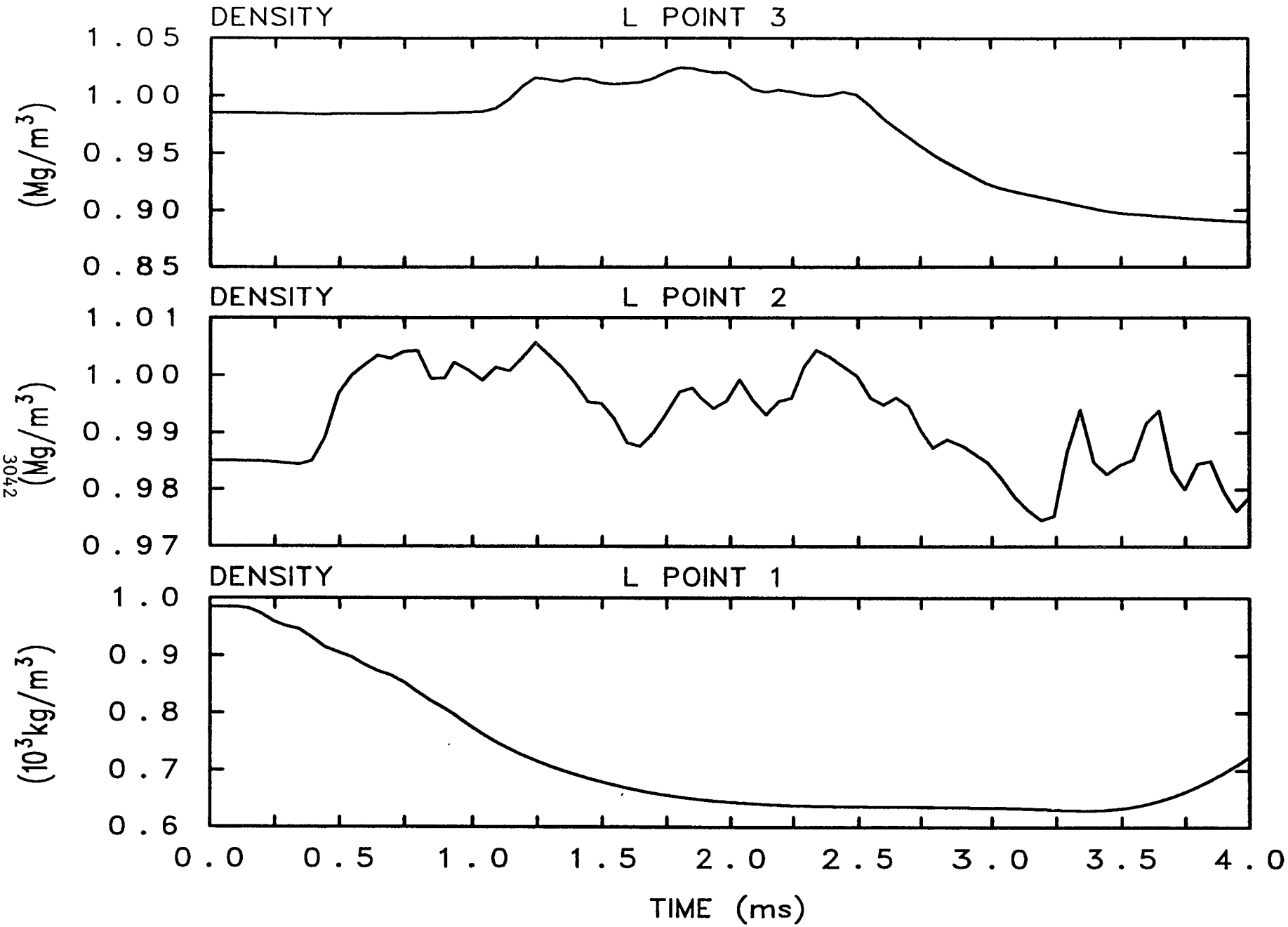

Fig. 3(b). Transient density variation at various locations for Case A.1 (Energy insertion= 180-MJ over 1 ms; 1-D simulation).

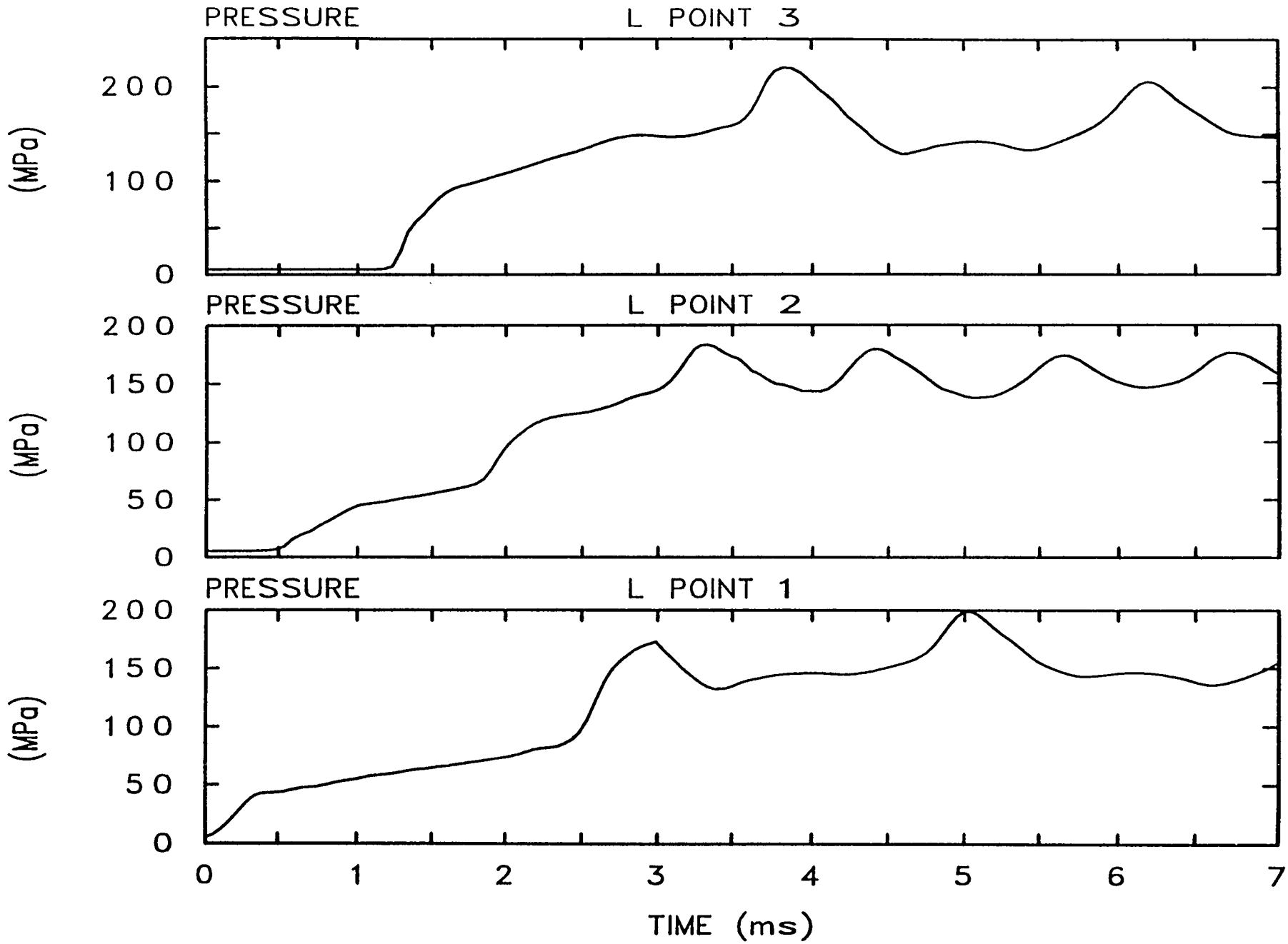

Fig. 4. Transient pressure variation at various locations for Case A.3 (Energy insertion= 180-MJ over 3 ms; 1-D simulation).

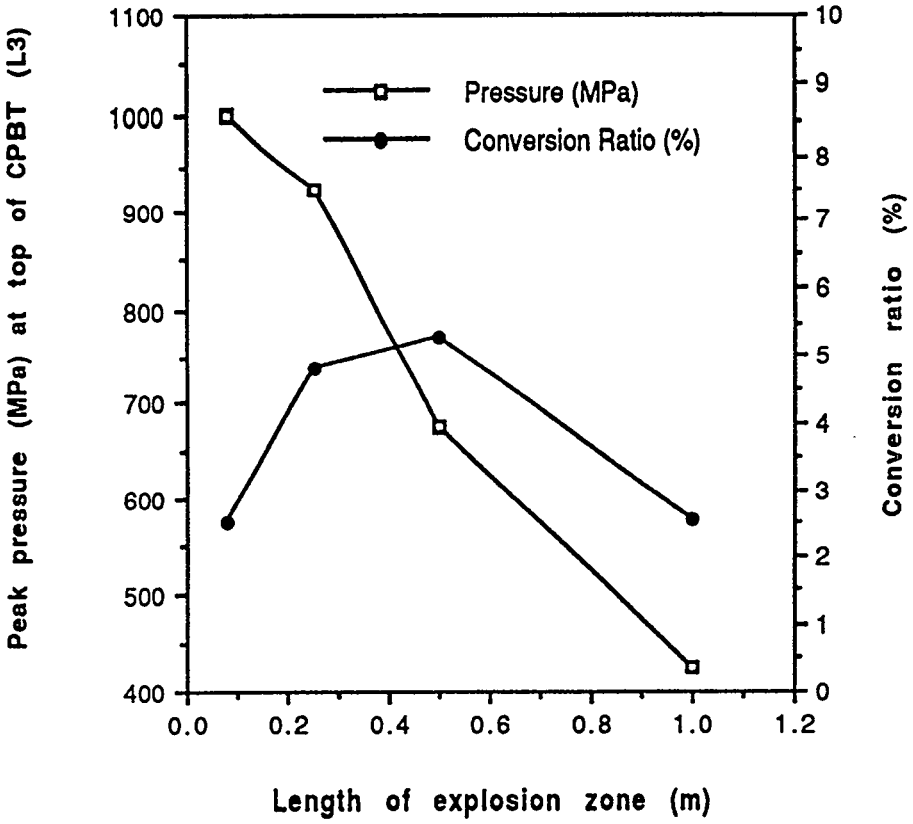

Fig. 5. Peak pressure at top of CPBT and conversion ratio variation with length of explosion zone (1-D CTH results)

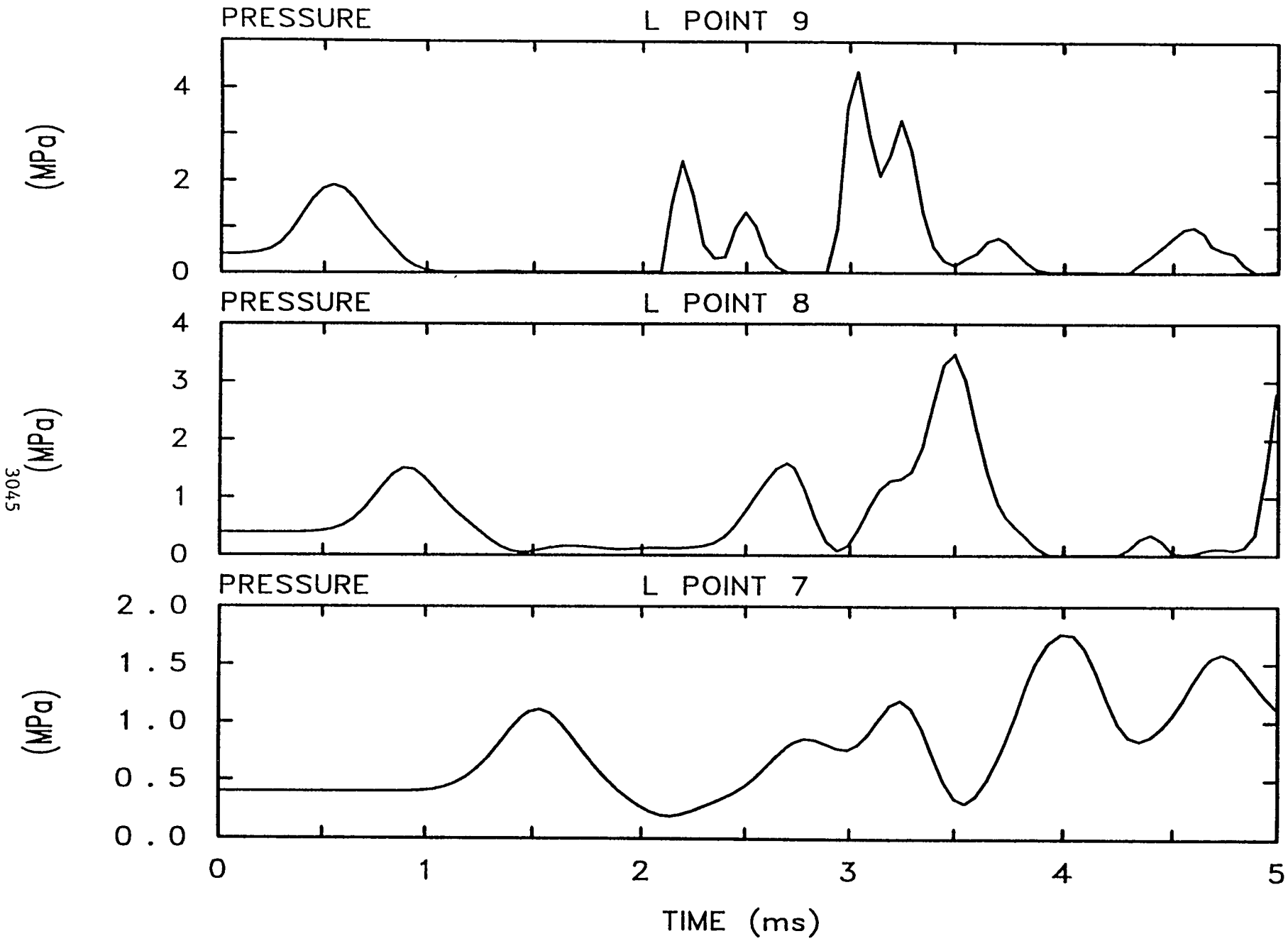

Fig. 6 (b). Transient pressure variation at various locations for Case B.1 (Energy insertion= 180-MJ; 2-D simulation with intact CPBT).

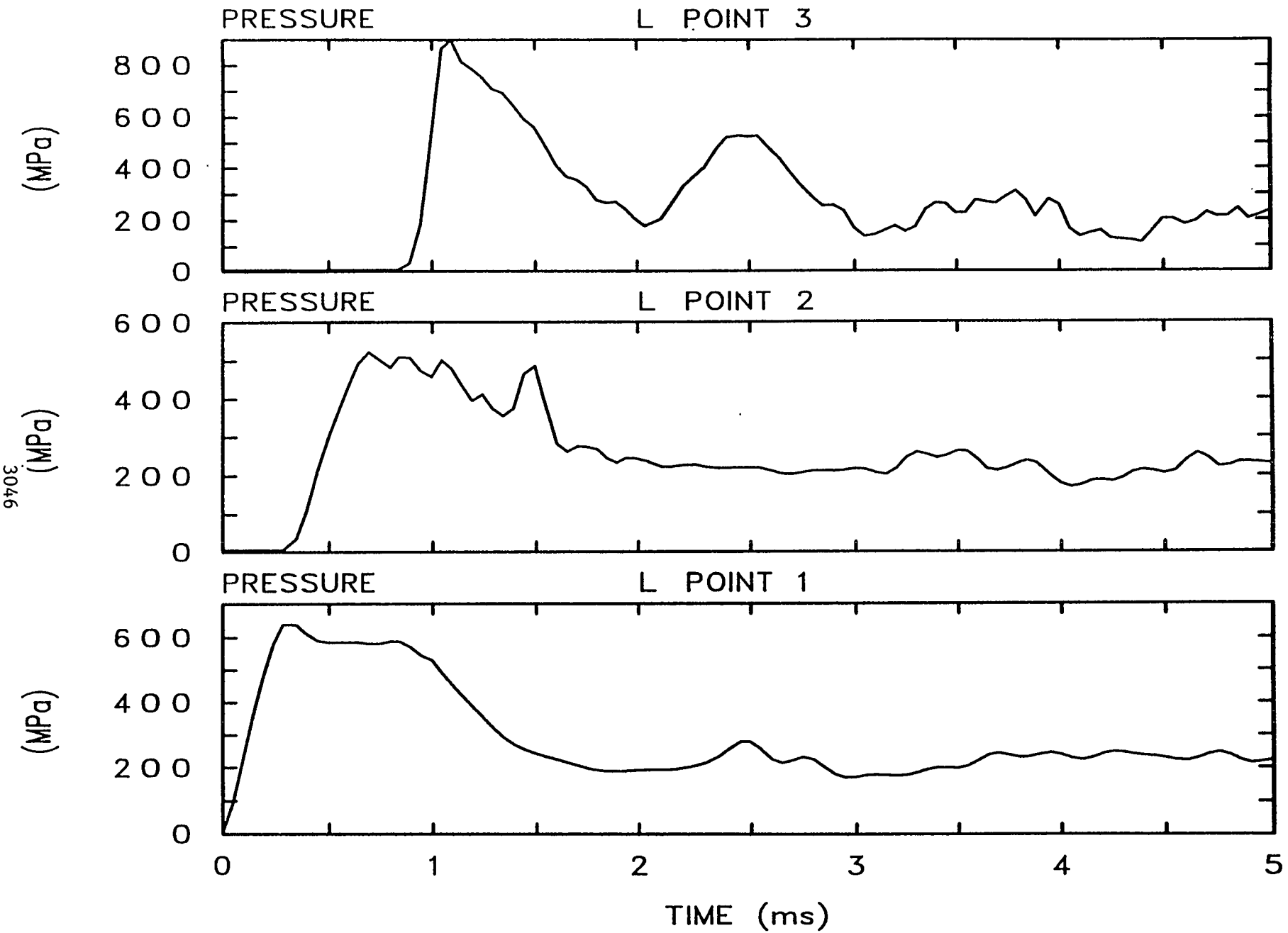

3046

Fig. 7 (a). Transient pressure variation at various locations for Case B.2 (Energy insertion= 800-MJ; 2-D simulation with intact CPBT).

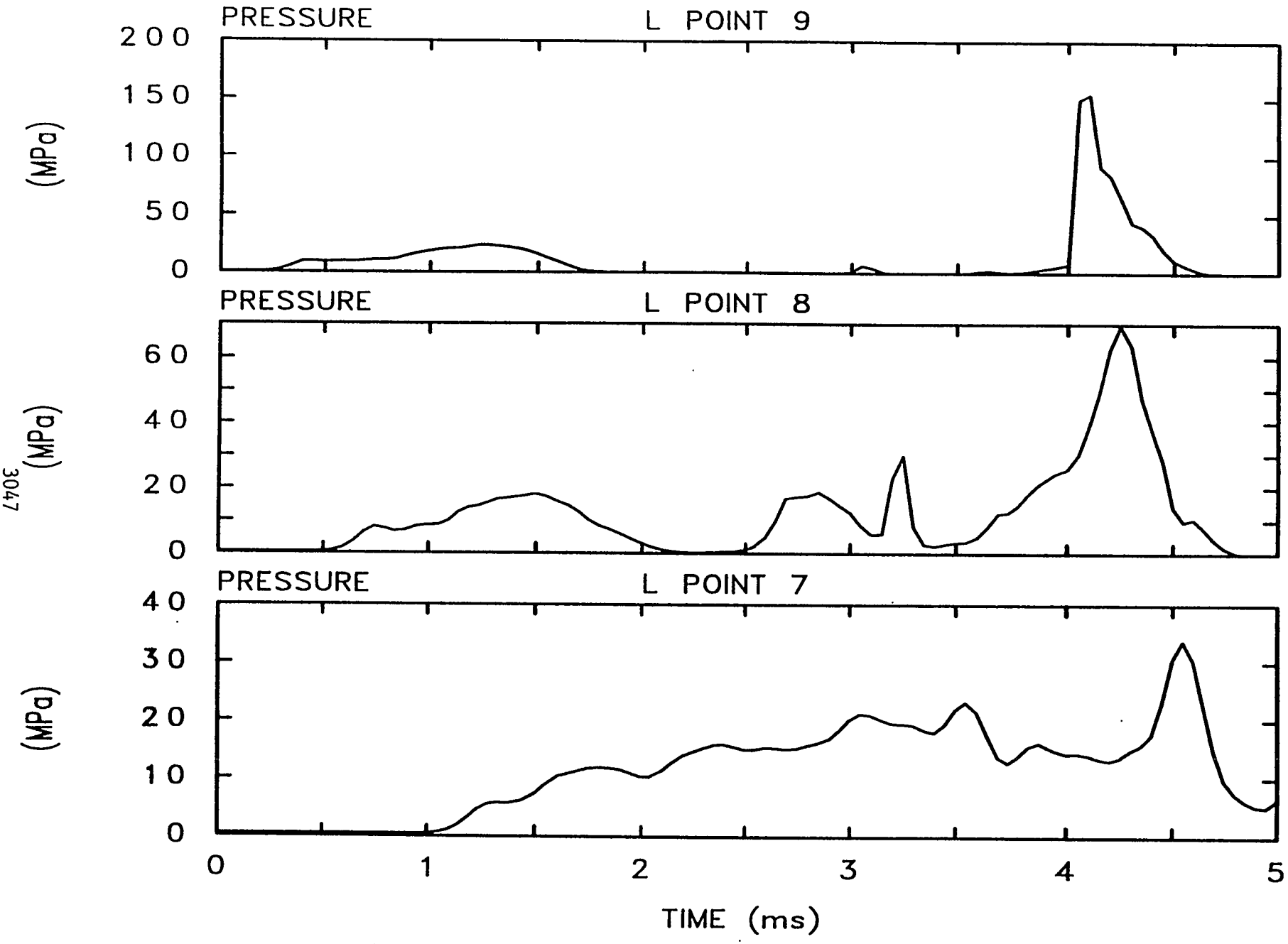

Fig. 7 (b). Transient pressure variation at various locations for Case B.2 (Energy insertion= 800-MJ; 2-D simulation with intact CPBT).

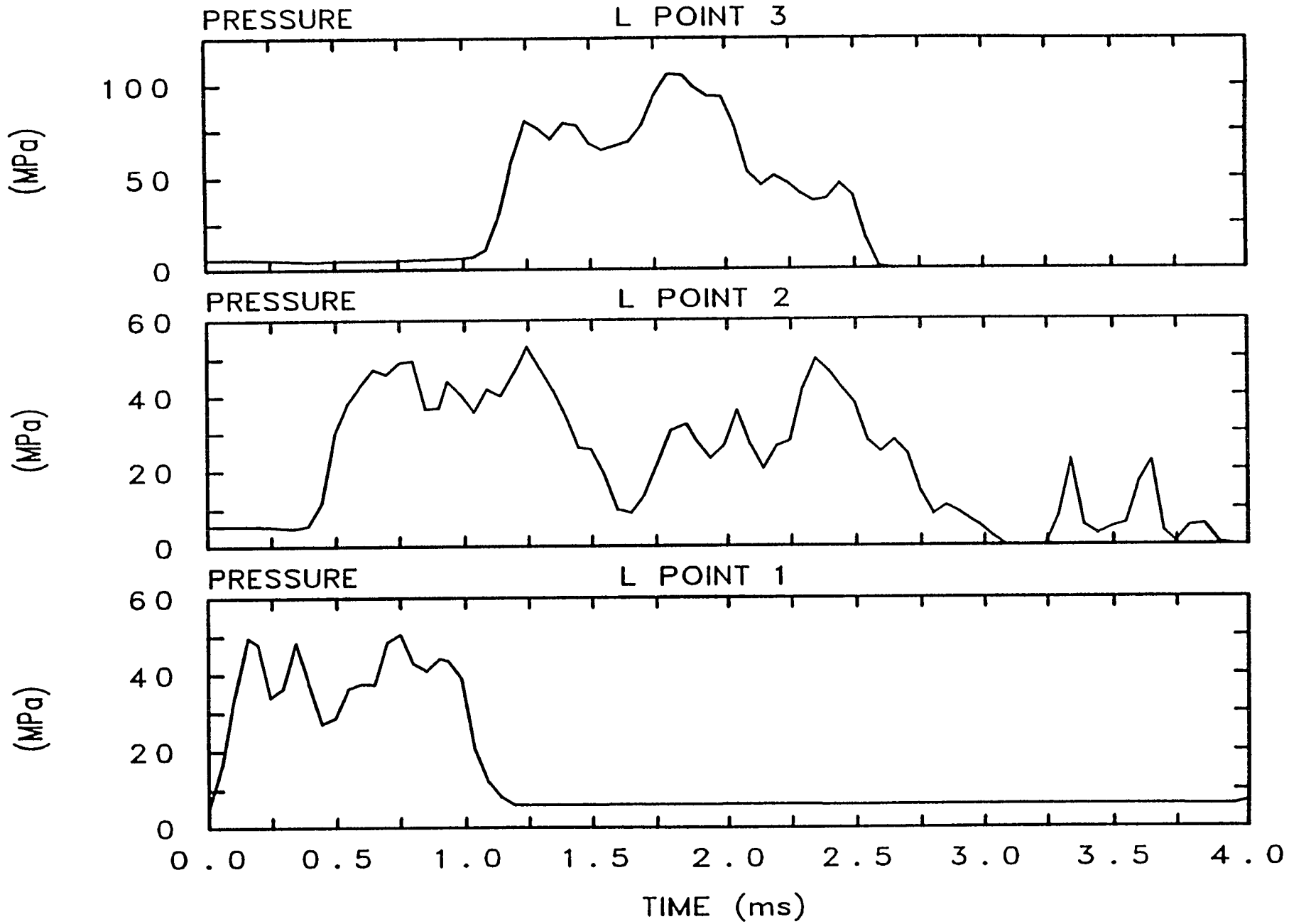

Fig. 8 (a). Transient pressure variation at various locations for Case B.1 (Energy insertion= 180-MJ; 2-D simulation with ruptured CPBT).

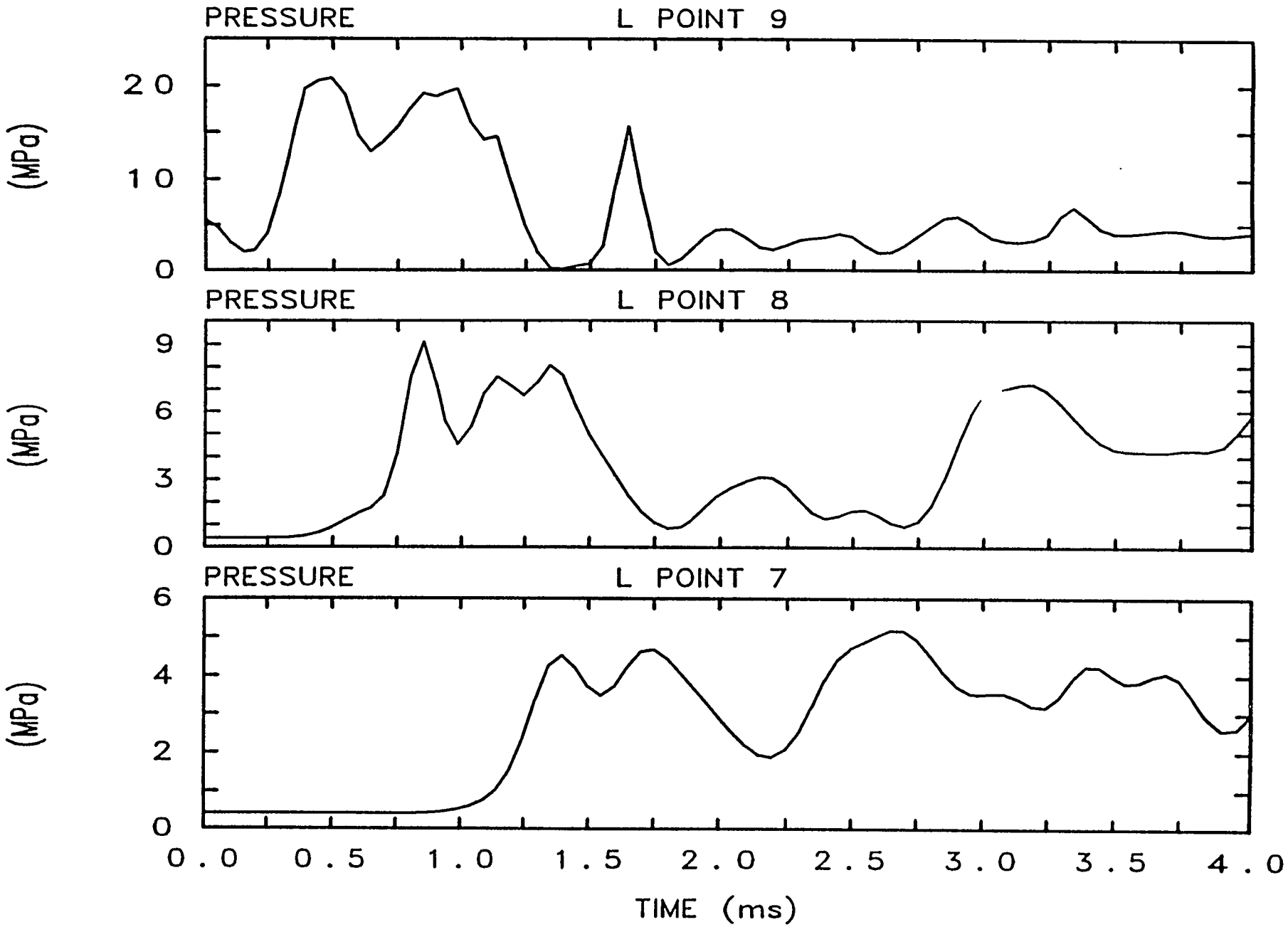

Fig. 8 (b). Transient pressure variation at various locations for Case B.1 (Energy insertion= 180-MJ; 2-D simulation with ruptured CPBT).

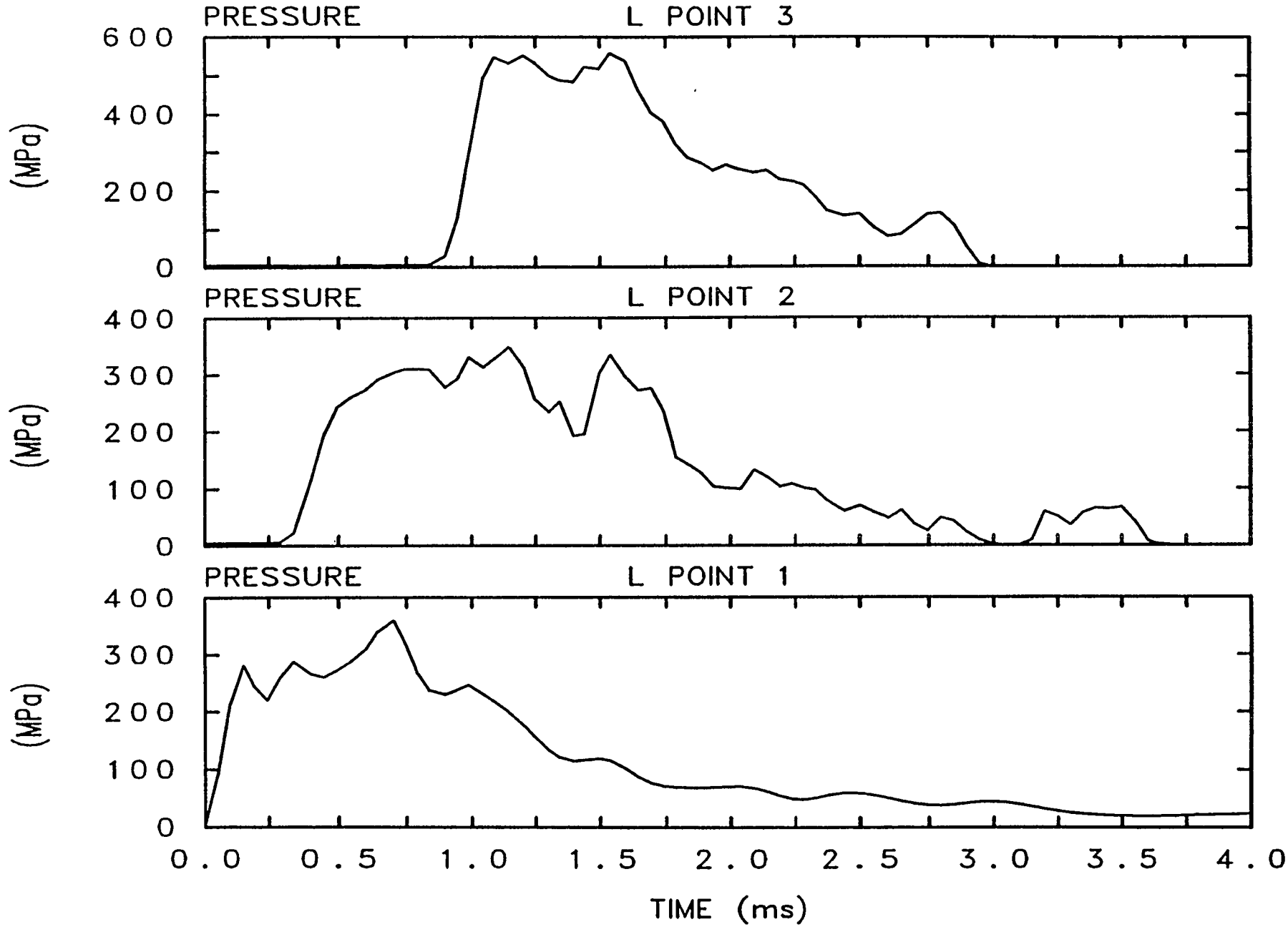

Fig. 9 (a). Transient pressure variation at various locations for Case B.2 (Energy insertion= 800-MJ; 2-D simulation with ruptured CPBT).

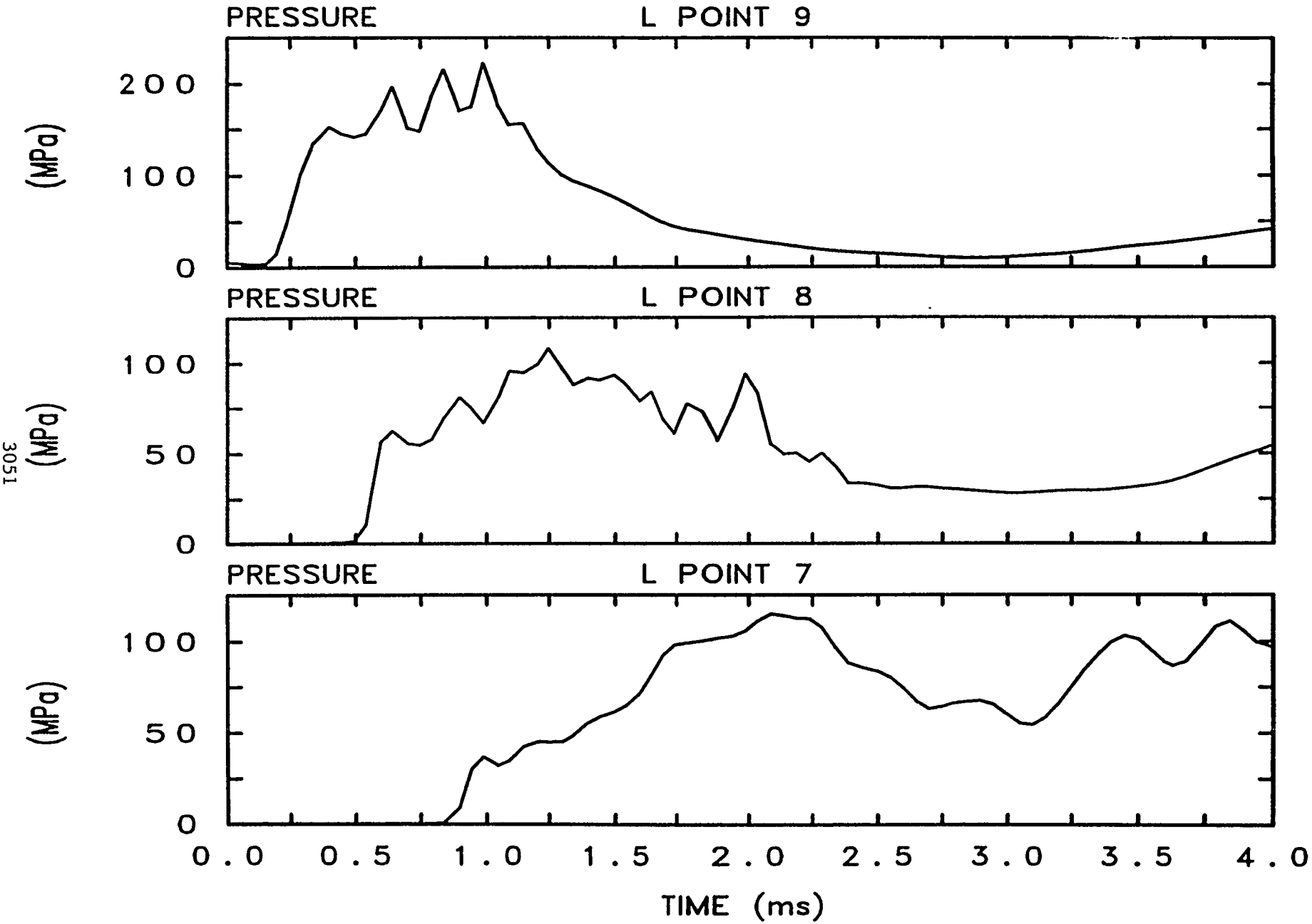

Fig. 9 (b). Transient pressure variation at various locations for Case B.2 (Energy insertion= 800-MJ; 2-D simulation with ruptured CPBT).

Modeling and Analysis Framework for Core Damage Propagation During Flow-Blockage-Initiated Accidents in the Advanced Neutron Source Reactor at Oak Ridge National Laboratory*

S.H. Kim, R.P. Taleyarkhan, S. Navarro-Valenti, and V. Georgevich
Engineering Technology Division
Oak Ridge National Laboratory
Oak Ridge, TN 37831-8045

Abstract

This paper describes modeling and analysis to evaluate the extent of core damage during flow blockage events in the Advanced Neutron Source (ANS) reactor planned to be built at the Oak Ridge National Laboratory (ORNL). Damage propagation is postulated to occur from thermal conduction between damaged and undamaged plates due to direct thermal contact. Such direct thermal contact may occur because of fuel plate swelling during fission product vapor release or plate buckling. Complex phenomena of damage propagation were modeled using a one-dimensional heat transfer model. A scoping study was conducted to learn what parameters are important for core damage propagation, and to obtain initial estimates of core melt mass for addressing recriticality and steam explosion events. The study included investigating the effects of the plate contact area, the convective heat transfer coefficient, thermal conductivity upon fuel swelling, and the initial temperature of the plate being contacted by the damaged plate. Also, the side support plates were modeled to account for their effects on damage propagation. The results provide useful insights into how various uncertain parameters affect damage propagation.

Introduction

The Advanced Neutron Source (ANS) is to be a multipurpose neutron research center and is currently in an advanced conceptual design stage at the Oak Ridge National Laboratory (ORNL). Major areas of research will include condensed matter physics, materials science, isotope production, and fundamental physics [1, 2]. The ANS is planned to be a 303-MW(t) heavy-water-cooled and moderated research reactor housed in a large, double-walled containment dome and surrounded by thermal neutron beam experimental facilities. The reactor uses U_3Si_2–Al cermet fuel in a plate-type configuration. Cooling systems are designed with many safety features, including large heat sinks sufficient for decay heat removal; passive inventory control by accumulators, pools, and flooded cells; a layout that maximizes natural circulation capabilities; and fast, redundant shutdown systems. A defense-in-depth philosophy has been adopted. In response to this commitment, ANS project management initiated severe accident analyses and related technology development early in the design phase. This was done to aid in designing a sufficiently robust containment for retention and controlled release of radionuclides in the event of an accident. It also provides a means for satisfying on- and off-site regulatory requirements, accident-related dose exposures, containment response, and source-term best-estimate analyses for Level-2 and -3 Probabilistic Risk Analyses (PRAs) that will be produced. Moreover, it will provide the best possible understanding of the ANS under severe accident conditions and, consequently, provide insights for development of strategies and design philosophies for accident mitigation, management, and emergency preparedness efforts [3].

* Prepared by the Oak Ridge National Laboratory, Oak Ridge, TN 37831 operated by Martin Marietta Energy Systems Inc., for the US Department of Energy under Contract No. DE-AC05-840R21400

The preliminary Level 1 PRA of the ANS has indicated core damage initiation to be dominated by core flow blockage events. From a safety perspective, to investigate energetics of fuel-coolant interactions (FCIs), it is necessary to quantify the degree of core damage propagation, once initiated. This paper describes the overall framework for capturing in-core damage propagation and presents an initial model to analyze it during a postulated severe accident in the ANS reactor core. Among several possible scenarios of core damage accidents, primary emphasis has been currently placed on analyzing core damage accidents initiated by blockage of one or more coolant channels at the inlet (Fig. 1).

ANS System Description

The ANS is currently in an advanced conceptual design stage. As such, design features of the containment and reactor systems are evolving, based on insights from on-going studies. Table 1 summarizes the current principal design features of the ANS from a severe accident perspective compared with the High-Flux Isotope Reactor (HFIR) and a commercial light-water reactor (LWR). The ANS is to use uranium silicide fuel in an aluminum matrix with plate-type geometry and a total core mass of 100 kg. The power density of the ANS will be only about 2 times higher than that of the HFIR, but about 50 to 100 times higher than that of a large LWR. Because of such radical differences, high-power-density research reactors may give rise to significantly different severe accident issues. Such features have led to increased attention being given to phenomenological considerations dealing with steam explosions, recriticality, core-concrete interactions, core-melt progression, and fission-product release. However, compared to power reactor scenarios, overall containment loads from hydrogen generation and deflagration are relatively small for the ANS.

The reactor core is enclosed within a core pressure boundary tube and enveloped in a reflector vessel, which is immersed in a large pool of water. Each element of the core is constructed with a series of involute fuel plates arranged in an annular array. The involute design provides uniform coolant gaps at all spanwise positions. The fuel plate is 1.27-mm thick and consists of 0.254-mm thick 6061 aluminum cladding material sandwiching a 0.762-mm mixture of uranium silicide (U_3Si_2) and aluminum. Each coolant gap is also 1.27 mm in width and has a span of 70.29 and 87.35 mm for upper and lower core elements, respectively. Fuel plates are welded to inner and outer cylindrical side plates with each element having 507 mm of fueled length. Unfueled 10-mm leading and trailing edges are added to the fuel plates.

Table 1 Severe Accident Characteristics of the ANS and Other Reactor Systems

Parameter	Commercial LWR	HFIR	ANS
Power, MW(t)	2600	100 [a]	303
Fuel	UO_2	U_3O_8–Al	U_3Si_2–Al
Enrichment (m/o)	2–5	93	93 [b]
Fuel cladding	Zircaloy	Al	Al
Coolant/moderator	H_2O	H_2O	D_2O
Coolant outlet temperature, K	590	342	365
Average power density, MW/L	<0.1	2.0	4.5
Clad melting temperature, K	2123	853	853
Hydrogen generation potential, kg	850	10	12

[a] Now operating at a reduced power of 85 MW.

[b] 1992 baseline (reduced enrichment now being considered)

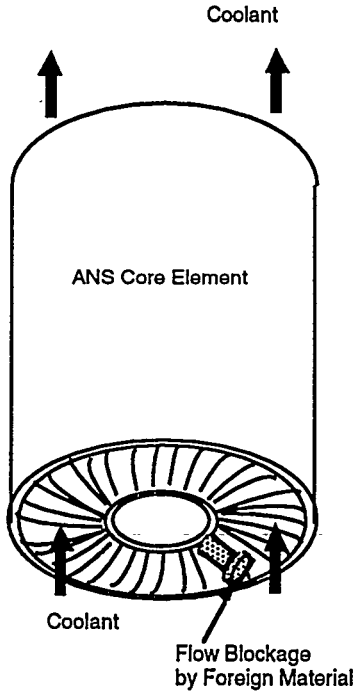

Fig. 1 Schematics of postulated flow blockage in ANS core element.

Core Damage Propagation Initiated by Flow Blockage Events

As mentioned above, the preliminary Level 1 PRA of the ANS [4] reveals flow blockage as the most probable initiating event leading to core damage. The median core damage frequency (CDF) for the event was estimated to be less than 10^{-4} per reactor year. The study divided the event into four categories, as shown in Table 2. The PRA conservatively assumed that any debris items of dimension > 5 mm could initiate damage, and that about half of the potential debris sources would be larger than 10 mm. Hence, partial blockage accounts for a major portion of the risk.

For each initiating event, core damage progression may be somewhat different. However, in analyzing the phenomena, the overall progression of the flow blockage event is not much different from one initiating event to the others.

Table 2 Summary of Core Damage Frequency of Flow Blockage Event

Initiating Event [a]	Median Annual CDF	Percentage of Total CDF
L1 Flow Blockage	1×10^{-5}	17
L2 Flow Blockage	5×10^{-5}	56
L3 Flow Blockage	2×10^{-7}	0.2
L4 Flow Blockage	2×10^{-5}	26

[a] L1 is the event caused by debris generated in the space from the core to the inlet strainer,
L2 is the event caused by debris generated in the space from the inlet strainer to the core,
L3 is the event caused by an external debris,
L4 is the event caused by debris due to fuel manufacturing defect.

Core damage propagation can be characterized into several modes depending on the likelihood of fuel melt removal. Figure 2 depicts a summarized core damage propagation mode. As seen in the figure, core melt may either be removed (relocated) or stay at the location where the fuel plate melts. The likelihood of melt removal has not been addressed yet.

As demonstrated in a companion paper described by S.H. Kim, et. al. [5], core melt can be removed via entrainment by high velocity coolant. Coolant inertia plays a major role in sweeping fuel debris away into the coolant stream. Another possible removal mechanism is associated with a sudden expansion of water entrapped in the melt. During the process of core melting, the melt can be possibly mixed with coolant water. Such a mixture can flow along the coolant stream in a similar mode to melt entrainment. However, water entrapped in the melt globule can vaporize quickly. Consequently, an increased channel pressure may result in blowing the melt debris out of the core assembly. In this case, the debris particles, whose velocity is high enough to overcome the pressure imposed by in-coming coolant, can be dispersed into the coolant upstream as well as downstream. Also, fuel melt could candle down toward the core bottom if the inlet coolant flow is not sufficiently large.

Molten portions of fuel might also stay inside the core assembly without being removed. During normal operation, a pressure drop of about 1.5 MPa is imposed across coolant channels from inlet to exit. At the same time, however, along with significant structural deformations between the unfueled inlet and exit sections of the core, it is possible for the coolant with significant voids to be superheated and pressurized quickly in a (fully or partially) blocked channel high enough to compensate or overcome the nominal pressure drop across the channel. In this case, the melt may not be removed from its originating place. Consequently, the course of damage propagation will change if the melt contacts the adjacent fuel plate. If no contact is made, the damage can propagate to the next plate through convection and radiation of heat from the melted plate. This case is possible only when the magnitude of fuel swelling is limited or none. There are several modes in which fuel melt can contact its neighboring plate . Plate bowing due to thermal and/or mechanical stress is a possible cause of local plate contact. With a rapid evolution of fission product vapor in the fuel matrix, molten fuel could swell sufficiently to fill the coolant gap and connect with the neighboring plate. Also, debris expansion because of internal pressurization of coolant channel can cause bridging to the next plate.

As explained above, the possibility of in-core melt propagation cannot be ruled out. The current study has focused on the damage propagation mode without fuel melt removal to make conservative estimates for energetic FCI calculations. However, the effect of melt removal on the extent of damage propagation is also addressed. Fuel at the end of the cycle is assumed to contain substantial amounts of volatile fission products. Direct thermal contact between fuel plates upon fuel plate swelling, as fission product vapor is released, is a conservative assumption for enhanced damage (melting) propagation.

Several initiating events can cause the coolant channel blockage, and substantial efforts are being made by the ANS project to characterize the blockage, including evaluation of thermal-hydraulic parameters for such an event. In any case, once a coolant channel is sufficiently blocked, the affected fuel plates will experience a loss or reduction of heat removal. These plates will necessarily heat up to a temperature for fuel swelling to begin due to the rapid release of fission product vapors in addition to the temperature-induced volumetric expansion. Upon being contacted by such a hot damaged plate, a neighboring plate will start to heat up, become deformed, and eventually attack its neighboring plate. Such fuel damage would propagate until an overall balance between heat generation and cooling is met. Such a heat balance may be established either by drop in fission energy

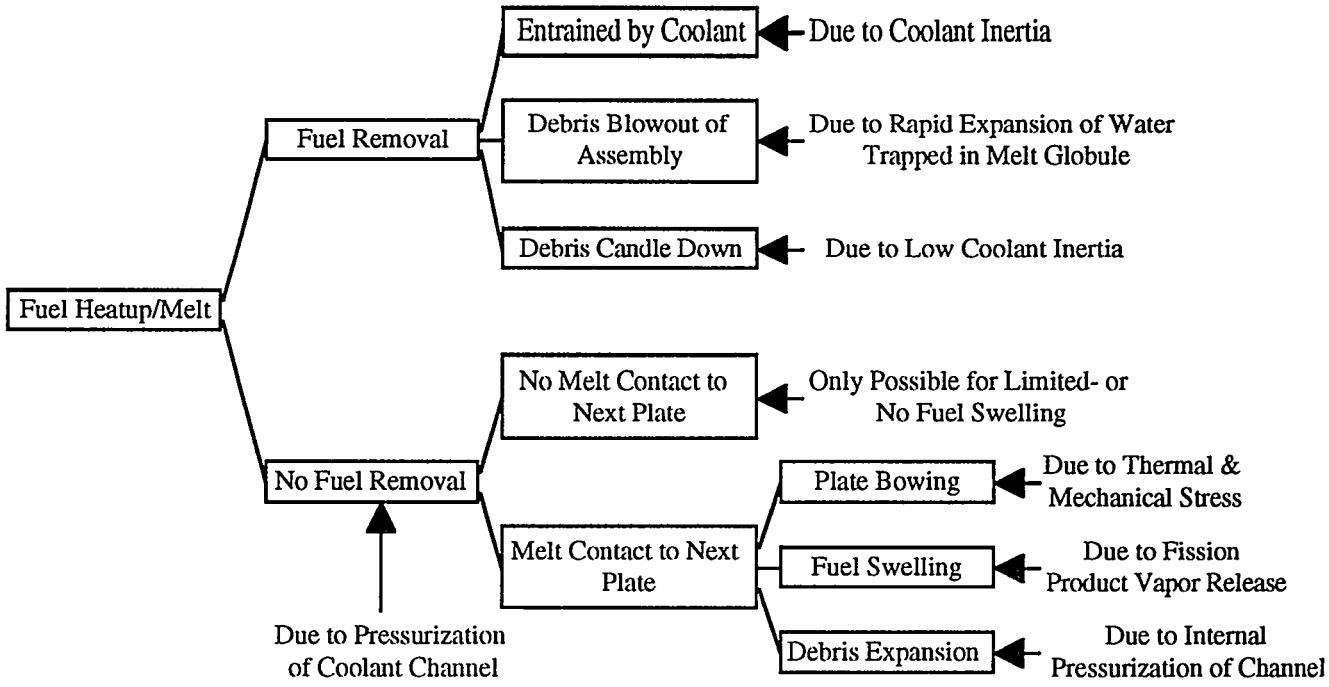

Fig. 2 Core damage propagation mode for flow blockage event.

following a successful reactor scram or by sufficient coolant flow provided for the plate cooling. Various configurations for the blockage are possible. Since a front-end condition for the blockage is still under investigation, however, the blockage is assumed in a way to lead to the most conservative consequences (assuming absence of localized steam explosion loads). In the current study, both coolant channels of the plate under consideration (e.g., left and right sides of the plate) are assumed to be blocked with a magnitude to reduce the coolant flow to a low enough level to cause plate damage. A constant heat transfer in other coolant channels is assumed and changed as a parameter to study the effect of heat transfer coefficient on plate damage propagation. Results of this study will be used to evaluate maximum possible energetic loads due to FCIs (described in a companion paper by R.P. Taleyarkhan, et al.[6]). Therefore, temperature of the plate melt as well as its mass involved in the damage propagation need to be evaluated.

Limited work was attempted in the past for understanding damage propagation in ANS-type core under flow blockage conditions [7,8,9]. This work was attempted for HFIR conditions and did not account for much of the essential physics of core melt propagation. For example, Cole et al. arbitrarily bounded the extent of damage propagation based upon the HFIR control system response to a $1 reactivity change in the core from voiding resulting from an unspecified core flow blockage [7]. Kirkpatrick utilized a simplistic lumped parameter approach wherein temperature gradients within melted plates are not considered, and the melt temperature is not permitted to rise above aluminum melting [8]. Freels utilized RELAP5 to investigate melt propagation, once again, disregarding effects such as fuel plate temperature rise beyond melting temperature of aluminum (viz., melt superheat), thermal gradients within the melted agglomerate of fuel plates, upflow of coolant, and thermal heat transfer to the side plates [9]. These models also do not permit sensitivity studies to evaluate effects of foamed fuel thermal conductivity changes, effects of variable contact areas of foams and undamaged fuel plates, etc. As such, although limited insights were drawn, these models are devoid of the essential physics of core

damage propagation-related melting-freezing thermal hydraulics, fuel behavior, as also the unique neutronic (i.e., void-reactivity coupling) behavior of the ANS core. Therefore, the above-mentioned models of Cole, Kirkpatrick and Freels were not considered suitable for ANS core damage propagation studies.

Several assumptions employed for the current study are described below.

Assumptions

- The core assembly is assumed to be represented by one-dimensional multiple layers of rectangular plates separated by coolant channels. It is evident that the plate melting/relocation and damage propagation have multi-dimensional aspects. However, for initial scoping estimates, such a one-dimensional treatment should provide a conservative estimation of the plate damage propagation, assuming that the core material, once it is damaged/melted, does not transport to other places, nor can it be disrupted by any external forces like coolant flow. In reality, unless the coolant channel is completely blocked, a damaged plate may possibly be swept by a high velocity coolant, and further damage propagation may be prevented. One other possible scenario is that the damaged plate mixed with coolant may trigger a local steam explosion that affects the integrity of its neighboring plates. This local steam explosion may be strong enough to disrupt the plates in neighboring channels, and/or fragments blocking other coolant channels will lead to possibly another local steam explosion. If a local steam explosion does not occur and the damaged plate mass stays there, then a thermal wave will keep propagating to heat-up the next plate. At some point of the propagation, more mass that is much hotter may be involved in a more extensive steam explosion. Currently, however, it is assumed that such a local steam explosion does not occur until the damage propagation is complete. Here, the term "propagation completion" means the end of the transient calculation due to a successful reactor scram. Even after the reactor scram, fission product decay heat will be available as a heat source. However, it is evident that such an amount is not sufficient to sustain rapid plate melting and propagation. Therefore, a transient calculation has been performed only until successful reactor scram. Initial estimates indicate that this time frame is about 4 s.

- Uniform material properties are assumed such as thermal conductivity, specific heat, and no thermal expansion (i.e., constant density). Although these properties change as a function of temperature (e.g., 10~20% for temperature range we are interested in), we assume they are constant. For future development of more detailed mechanistic models, we plan to include temperature dependency of these properties. Also, uniform constant heat generation is assumed. Data used for the calculations are given below.

κ (thermal conductivity)	=	190	W/m-K
c_p (specific heat capacity)	=	1000	J/kg-K
Q (rate of heat generation)	=	303	MW
m (total fuel/aluminum mass)	=	100	kg
Δz (channel length)	=	0.507	m
δ (plate/coolant channel thickness)	=	1.27	mm
w (plate width)	=	87.7	mm
T_{mlt} (melting temperature)	=	853	K
h_{mlt} (latent heat of fusion)	=	397	kJ/kg
T_{vap} (vaporization temperature)	=	2767	K
h_{vap} (heat of vaporization)	=	10.8	MJ/kg
T_{init} (plate initial temperature)	=	388	K

A_{cont} = f_{cont} w Δz (where f_{cont} is the fraction of surface area between nodes that intimately contact during fuel foaming)

Total number of fuel plates = 684 (432 and 252 plates for upper and lower core elements, respectively)

- Fuel meat and clad are assumed to be perfectly mixed and represented by one average material with the density of 2,589 kg/m^3. This density is evaluated based on 100 kg of core mass occupied by the volume of 684 plates with 0.507 m of plate length, 1.27 mm of plate thickness and 87.7 mm of plate width.

- Plate material is assumed to have one melting temperature (e.g., 853 K) and one vaporization temperature (e.g., 2767 K). Thus, once a phase change occurs, its temperature remains constant until the phase change is complete.

- Constant reactor power is assumed during damage propagation; that is, reactivity feedback effects are neglected.

- Instead of calculating parameters to determine coolant characteristics such as coolant temperature, pressure, void fraction, and heat transfer coefficients, we assume a constant heat transfer coefficient and coolant temperature throughout the transient.

- It was assumed that the plates are not deflected due to external forces such as pressure difference between inner and outer surfaces of the affected plate.

- In a blocked channel, there is no heat sink, and thus no heat transfer is permitted from the plate surface to this coolant channel; that is, instantaneous flashing of the coolant is assumed if the channel is blocked.

- When a fuel plate reaches its melting temperature, it immediately slumps against its neighbor to the outside and blocks the coolant channel. This is assumed to be due to plate swelling caused by coalescence of fission product vapors from the fuel matrix near its melting temperature. A preliminary study shows that the fuel swelling magnitude at the end of the cycle upon fuel melting is large enough to fill the coolant gap. Any portion of the plate filling the coolant channel is assumed to be at its melting temperature. Mass of swelled nodes is reduced to one half of the original mass to ensure mass conservation.

- It was assumed that the vaporized fuel plates remain in their original locations or regions. It is realized that at this high temperature, the results become suspect. However, we already do not consider several possible physical processes to determine not only plate thermal state but also the structural behavior, mainly caused by exothermic chemical reaction between aluminum and water (i.e., ignition). This assumption is recognized as being bounding in nature, and was made to allow this scoping study to proceed.

Model Description for Thermal State Evaluation

A transient one-dimensional heat conduction equation describes heat transfer in fuel plates in the thickness direction, and is given by

$$\frac{\partial}{\partial t}\left(\rho\, c_p T\right) = \kappa \frac{\partial^2 T}{\partial x^2} + q''' \qquad (1)$$

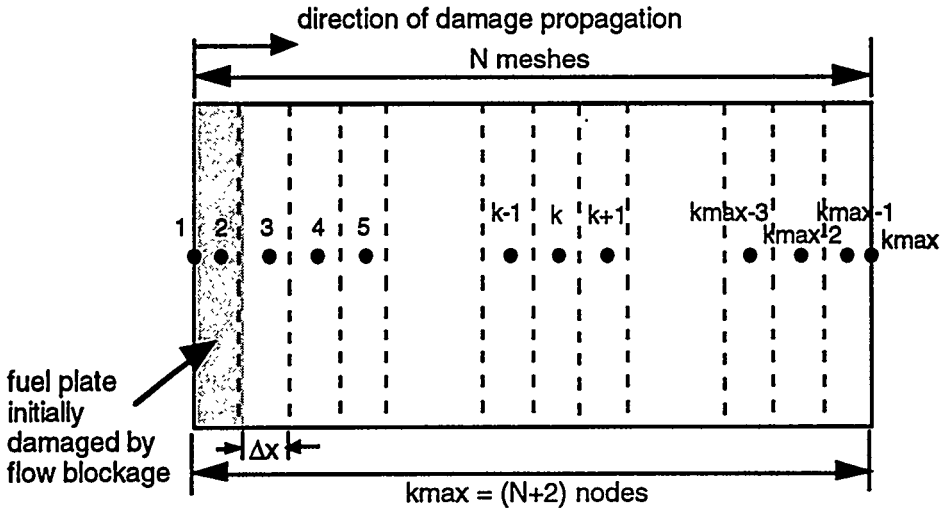

Fig. 3 Nodalization for a multiple plate system.

The numerical procedure for solving Eq. (1) involves coupled, implicit difference algorithms that apply a quasi-linearization technique, as appropriate, to ensure a stable solution of the resulting algebraic equations [10]. Numerical estimates of heatup characteristics for the plates are obtained by means of implicit finite-difference approximations to the governing conservation equation, Eq. (1).

Each set of plates under consideration is uniformly subdivided into N meshes. A nodal point is designated at the center of each mesh. In addition, to evaluate plate surface phenomena, a node with zero mass is assigned at each boundary. Therefore, a set of plate system will have (N+2) nodes. The number of plates under consideration changes as damaged plates increase. Figure 3 illustrates nodalization.

For an arbitrary node k of mass m_k and temperature T_k, the difference approximation to Eq. (1) over a time interval t-Δt to t is taken as

$$\frac{(mc_p)_k}{\Delta t}\left(T_k - T_k^*\right) = C_{k-1,k}\left(T_{k-1} - T_k\right) + C_{k,k+1}\left(T_{k+1} - T_k\right) + Q_k \qquad (2)$$

A superscript ' * ' denotes a value evaluated at the previous time step. Equation (2) is rearranged as successive back-substitution for nodes k= kmax-1,kmax-2,....., 1 (the details are given in Appendix I), resulting in the final form for T_k as

$$T_k = D_k^* T_{f,L} + E_k^* T_{f,R} + F_k^* \qquad (3)$$

Equation (3) with appropriate boundary conditions describes the temperature distribution of plates. It is apparent that from Eq. (3), D_k^* and E_k^* must be zero and F_k^* becomes the same as the melting or vaporization temperature of node-k if the k^{th} node undergoes phase change as melting/freezing or vaporization/condensation.

Each node may be heated up to its melting point or the melt may undergo freezing because of net heat loss to neighboring plates and/or bulk coolant. When a nodal

temperature first crosses the melting point (over- or under-shooting in the temperature is expected due to a finite size of a time step), the nodal temperature is reset to the melting temperature, and the excess energy is used to calculate the mass of material that changes phase. Therefore, the amount of the melt in node k when T_k first crosses the melting temperature (i.e., overshoots) is evaluated as

$$m_{m,k} = \frac{\left(m c_p\right)_k \left(T_k - T_{m,k}\right)}{\lambda_k} \tag{4}$$

where $T_{m,k}$ and λ_k are the melting temperature and the latent heat of fusion of the k^{th} node, respectively. In subsequent time steps, the amount of the melt in node k is evaluated as

$$m_{m,k} = m^*_{m,k} + \frac{Q_k \Delta t}{\lambda_k} \tag{5}$$

where $m^*_{m,k}$ is the molten mass at the previous time step.

Once the k^{th} node becomes completely molten, its temperature starts to increase until it reaches the temperature for the next phase change (e.g., vaporization/condensation). Such a temperature change is again described by Eq. (3), and subsequent vaporization/condensation can be described by a similar expression as in Eqs. (4) and (5).

Since the numerical algorithm employed in the current study utilizes a fully implicit finite difference representation of Eq. (1), the solution is unconditionally stable and expected to yield a truncation error of $O[\Delta t, (\Delta x)^2]$. Our difference representation for this marching problem provides an acceptable solution to Eq. (1) because it meets the conditions of consistency and stability [11]. To examine modeling and coding errors, extensive validation and verification work was performed. It included a comparison between the results from our finite difference formulation and analytical calculations. Also included was a comparison between our results and those obtained from the well-known HEATING7 code [12]. All the cases that we examined revealed that the current formulation is quite acceptable with 3 nodal points for a single plate and time step less than 1 s. This is also true even for a very stiff problem such as sudden contact of hot melt with a cold plate. For a sample comparison against results from HEATING7, our model predicted very close results even with much more coarse nodalization (e.g., 1 node in our formulation versus 10 nodes in HEATING7 representation) and with larger time step (e.g., 0.1 s in our formulation versus 0.01 s in HEATING7).

Heat Conduction to Side Plates

Fuel plates in the ANS core span between supporting cylinders. Heat conduction to side plates may delay the damage propagation. If the side plate fails, additional flow blockage may be provided due to transport of fragments originating from the lower assembly to the upper assembly. The geometry assumed for the calculations is given in Fig. 4.

A side plate is nodalized into the same mesh size as a connected fuel plate; that is, if each plate is nodalized into three meshes, three meshes are provided for a section of the side plate connected to the fuel plate and another three for a section facing the coolant channel. Heat transfer between the side plate meshes was neglected because it is

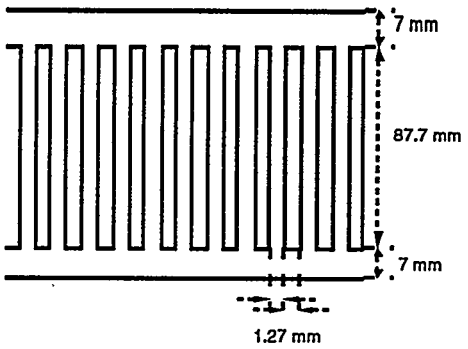

Fig. 4 Assumed geometry of fuel assembly (top view).

expected much smaller to compare with that between the fuel plate and the side plate. Also, neglected was heat loss to the surrounding coolant because the side plate is expected to be covered by the steam blanket quickly once it heats up. Therefore, the nodal temperature of the side plate is given by

$$T_{k,c} = T^*_{k,c} + \frac{q''_k A_c \Delta t}{\rho_c (\Delta x\, z\, L)_c\, c_{p,c}} \tag{6}$$

where

subscript c = side plate

$T^*_{k,c}$ = temperature of node-k at the previous time,

ρ_c = density (2,700 kg/m^3),
Δx = mesh thickness,
z = mesh width (7 mm),
L = cylinder length (0.507 m),
$c_{p,c}$ = specific heat capacity (1,000 J/kg-K),
A_c = thermal conduction area (Δx L),
Δt = time step, and

q''_k is heat flux coming in from fuel plate given by

$$q''_k = \frac{\kappa}{\delta_c}\left(T_k - T_{k,c}\right) \tag{7}$$

where

κ = thermal conductivity (190 W/m-K)
δ_c = thermal conduction layer
[e.g., (z + 0.5*fuel plate width)/2 = 25.4 mm]
T_k = fuel plate temperature of node-k

When it is heated up to the melting temperature (853 K), the mesh undergoes phase change as the fuel plate does. In reality, the size of the inner cylinder is different from that of the outer cylinder. However, as seen in Fig. 4, the geometry of the cylinder including the fuel plate is assumed to be rectangular. Therefore, a representative side plate is the same for both inner and outer cylinders. For these initial calculations, therefore, only one (averaged) side plate is included.

Computations and Analysis

Case Without Side Plates

A scenario for fuel plate melting and propagation is depicted in Fig. 5. In these calculations, no side plates were assumed. As seen in the figure, the plate in blocked channels undergoes heatup. When the plate temperature reaches 853 K, which is the solidus temperature of AL-6061, a rapid release of fission product vapors in a fuel matrix leads to a volumetric expansion of the plate (swelling) [13]. This expanded plate will fill the adjacent coolant gap and directly contact the next plate. When expanded, the nodal mass of the swelled plate is assumed to be reduced to half of its initial mass. Here, for convenience, let us call the swelled plate plate-1, and a new intact plate being touched by the swelled plate is called plate-2.

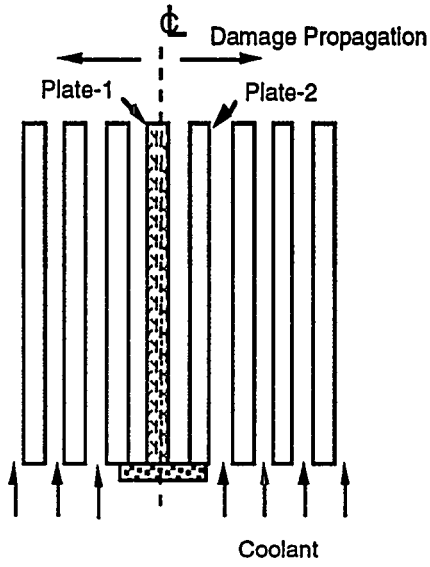

Fig. 5 Initiation of plate damage propagation.

When contacted by the hot swelled plate material, the initial temperature of plate-2 will not be same as that of plate-1 before the event was initiated. This is because plate-2 must have been heated up by convection and radiation from plate-1 before the contact. Also, if flow to this coolant channel were already affected by onset of flow excursion instability, the temperature of plate-2 should already have increased due to lack of sufficient cooling. However, at this stage the transient variation has not been modeled. Instead, a parametric analysis was done to gage the relative impact by changing the initial temperature of plate-2. One value used for the calculations was selected to be the initial temperature of plate-1 (e.g., 388 K). The other value was selected as an average of the plate-1 initial temperature and the plate melting temperature (e.g., 620.5 K).

Another uncertain parameter is the thermal conductivity of the plate. Once the plate swells, its volume is assumed to increase by a factor of two so as to fill the coolant space. Therefore, the void volume in the plate is bounded at 50%. The volume of U_3Si_2 fuel in the plate is about 11%. Under the condition of the plate expansion, the fuel particle volume will be half of 11%. Therefore, total volumetric fraction of the void and fuel will be about 56% (i.e., 50% + 11% / 2). According to the Ref. [14], thermal conductivity of such a configuration for U_3Si_2 fuel is about 20 W/m-K at 60 ^oC. Furthermore, Ref. [14] states that the fission gas bubbles will reduce the thermal conductivity further. Therefore,

a parametric study has been performed using the constant value of 190 W/m-K all the way through the transient and with a reduced value of 10 W/m-K upon plate swelling.

The thermal conduction area is another uncertain parameter. Upon the plate swelling and mixing with voids in the coolant channel, the effective thermal conduction area will be reduced to about one-half. This is because we assume that the molten plate swells to also occupy the coolant space, the volume of which is the same as that of the plate. Hence, an effective contact area between plates will be likely reduced to ~50% since the melted plate upon swelling due to fission product gas agglomeration fills a volume that is twice the original plate volume. However, the effective heat conduction area also needs to account for heat conduction through the voids filling with hot gas (e.g., volatile fission products). Therefore, the calculations have been performed using two different thermal conduction areas between nodes in the swelled region: one for no change of the area from its initial value, and the other for the area reduced in half.

The next uncertain parameter is the convective heat transfer coefficient at unblocked coolant side of plate-2. As mentioned above, configurations for the coolant channel blockage are complex. For example, only a single channel might be completely or partially blocked, or multiple channels might also be completely or partially blocked. Because all the coolant channels are in parallel and connected with the same inlet and outlet plenums, channel blockage will possibly cause a flow excursion if a pressure drop in some channels is different from that of others caused by a significant void generation. Therefore, such a dynamic nature of the coolant thermal-hydraulics needs to be analyzed to correctly define heat transfer between plates and coolant. If a coolant channel experiences flow excursion, heat transfer from the heated plate surface to the coolant will be significantly affected. In the absence of a detailed study, the convective heat transfer coefficient at plate-2 is also varied as a parameter to investigate the plate damage propagation. Considering a possible extensive flow excursion and corresponding flashing in the affected channels, it may be conservative to choose a value corresponding to zero heat transfer to the coolant.

The reactor protection system takes a finite time (~4 s) to detect abnormality resulting from presence of fission products in the coolant downstream, and also respond to shut down the reactor. A transient time of 4 s, therefore, was selected as the time frame for plate damage propagation. Full reactor operating power (e.g., 303 MW(t)) is assumed during this period. Calculations were not extended further beyond 4 s since the ANS system has been designed to have enough capability to remove fission product decay heat by natural circulation mode after reactor shutdown.

Figures 6 through 8 show selected results of the calculations with the parametric variations described above. Table 3 also lists the number of fuel plates involved in damage propagation. As seen in Fig. 6, the plate damage propagation strongly depends on each of the parameters we examined. The case of no heat transfer to the coolant with full conduction area and high initial contact temperature (in the figure, this case is shown as T=620, k=190, a=1) yields the largest number of damaged plates (e.g., 202). With a reduced thermal contact area of 50% (in the figure, T=620, k=190, Fa=0.5) , the number of damaged plates comes down to 174. Also, Fig. 6 shows that thermal conductivity affects the damage propagation. As the conductivity is lowered, the damage propagation becomes slower. Good estimation of the initial temperature of plate-2 is also important in precisely determining the damage propagation. Figure 6 also shows that the fuel plate damage does not propagate further if sufficient cooling can be provided for plate-2. With a heat transfer coefficient of 52 kW/m^2-K, none of the cases shows damage propagation. The average heat transfer coefficient at fuel plate surface is expected to be around 100

kW/m^2K during normal operating conditions. According to the data collected from experiments performed at the Flow Blockage Test Facility (FBTF), this heat transfer coefficient drops to ~20-40 kW/m^2K for 25% edge blockage, and ~50 kW/m^2K for 35% center blockage [15]. The heat transfer coefficient of 52 kW/m^2K evaluated by the current model for limiting the damage propagation, needs to be investigated further.

Figure 7 shows nodal temperature variations as a function of time for the case of no heat loss to the coolant with full contact area and high initial temperature of plate-2 (for which 600 nodes correspond to about 100 plates). It is seen that in about 1.2 s of the transient, inner nodes start vaporizing. A large number of nodes in melted plates experience vaporization during the transient. Such a condition could likely initiate an energetic FCI (as described in a paper by V. Georgevich, et al. [16]). This phenomenon, nevertheless, is conservatively neglected from consideration in the present work. However, none of the nodes at the end of the calculations is completely vaporized. Average fraction of the vaporized mass is shown in Fig. 8. This fraction was averaged over the entire damaged plates at the end of the transient. The fraction, as seen in the figure, seems to depend only on convective heat transfer at plate-2. All the cases show a similar vaporization fraction. Even the case of the slower damage propagation (e.g., T=388, k=10, Fa=0.5) shows a similar fraction. However, that case reveals a higher vaporization fraction in inner nodes.

Table 3 Number of Damaged Plates Predicted by the Code Calculations

h (W/m^2K) [a]	388-10-0.5 [b]	388-190-1 [b]	620-10-0.5 [b]	620-190-1 [b]	620-190-0.5 [b]
0.00×10^0	64	123	116	202	174
5.00×10^3	56	112	98	182	154
1.00×10^4	48	102	78	158	132
1.50×10^4	40	92	58	134	110
2.00×10^4	30	82	38	102	80
4.00×10^4	12	64	12	74	54
5.00×10^4	2	48	2	56	44
5.04×10^4		46		54	
5.08×10^4		46		52	
5.12×10^4		42		50	
5.16×10^4		40		46	
5.18×10^4		34		42	
5.20×10^4		2		2	2

a Convective heat transfer coefficient

b Case description:

Case	T	k	Fa
388-10-0.5	388	10	0.5
388-190-1	388	190	1
620-10-0.5	620	10	0.5
620-190-1	620	190	1
620-190-0.5	620	190	0.5

where T is initial temperature of plate-2 (K), k is thermal conductivity of swelled plates (W/m-K), and Fa is fractional contact area upon fuel swelling.

Case With Side Plates

The case "620-190-1" was used as a base for this calculation. This case assumes that the second plate temperature is 620.5 K before it contacts slumping fuel plate melt, the thermal conductivity is 190 W/m-K, and a full thermal contact area exists between plates. This case represents a worst case that conservatively estimates 202 plates to be damaged during 4 s of the transient period. This case has been repeated here along with the model of side plates. The number of damaged fuel plates was estimated as 202, which is the same as the original case without accounting for the side plates. However, average mass fraction of vaporized fuel plate was reduced from 0.32 to 0.28, which is equivalent to 11.6 MJ. This amount of energy is transferred to heat up and melt the side plates.

Other results are depicted in Figs. 9 and 10. Figure 9 shows temperature variations along the nodes at the end of the calculations (e.g., 4 s). Node-0 corresponds to the location where the damage started propagation. As seen, the side plate is heated up substantially. The number of cylinder nodes experiencing melting is about 450 nodes, which is equivalent to 7.3 kg total, accounting for symmetry of the propagation and duplex cylinders. Figure 10 shows the molten mass fraction of each node at the end of the calculations.

Effect of Fuel Melt Removal on Damage Propagation

One of most crucial assumptions employed in above calculations is that the molten fuel cannot be relocated or removed from its originating location. In reality, there might be other situations involved with fuel relocation or dispersal. In those cases, it is

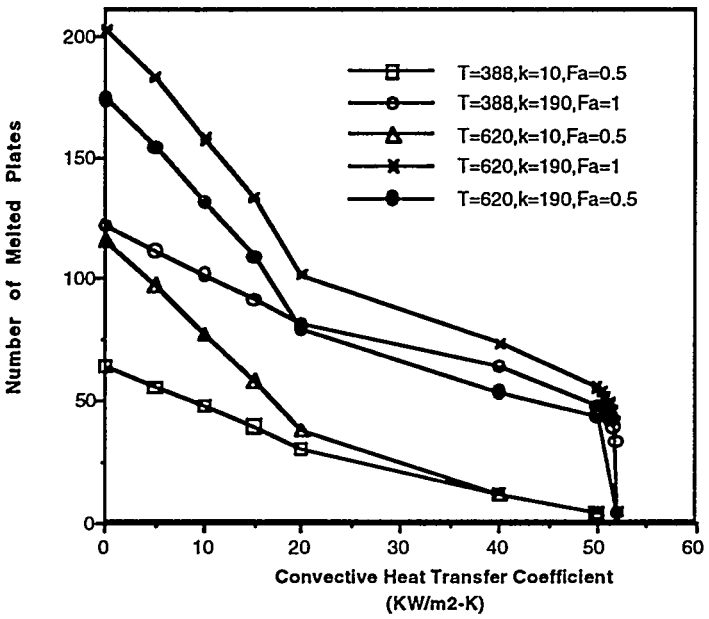

Fig. 6 Propagation of ANS core plate damage.

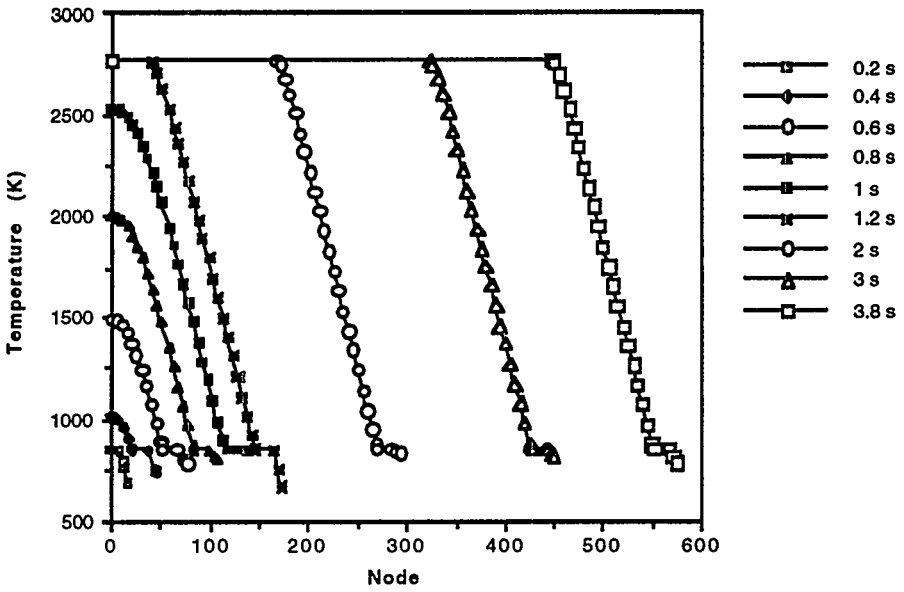

Fig. 7 Nodal temperature distribution at various time moments of the case T=620, k=190, Fa=1, h=0 (six nodes correspond to one plate).

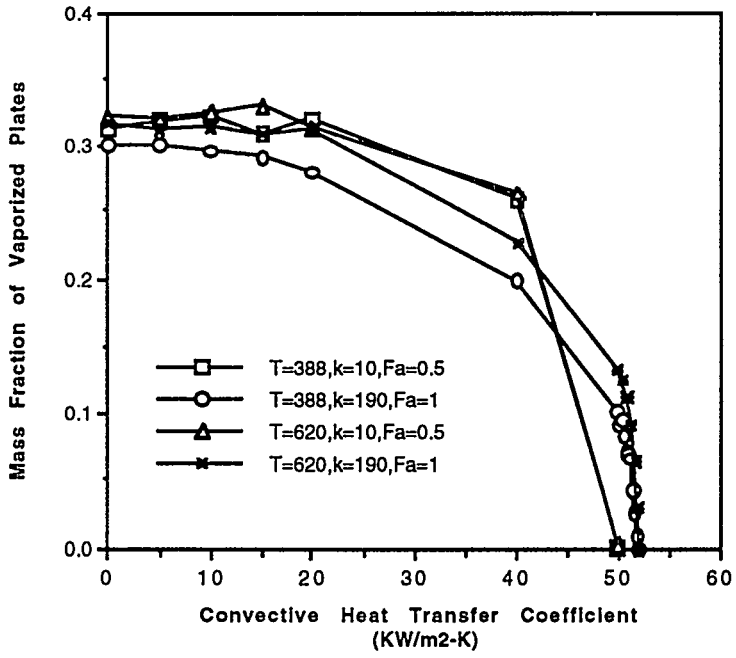

Fig. 8 Average mass fraction of vaporized plates.

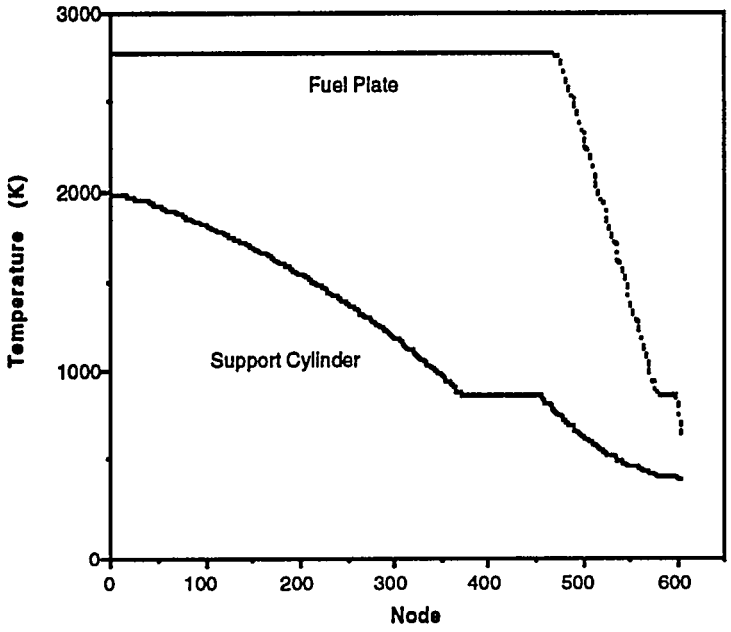

Fig. 9 Variation of node temperatures at the end of the calculations (six nodes correspond to one plate).

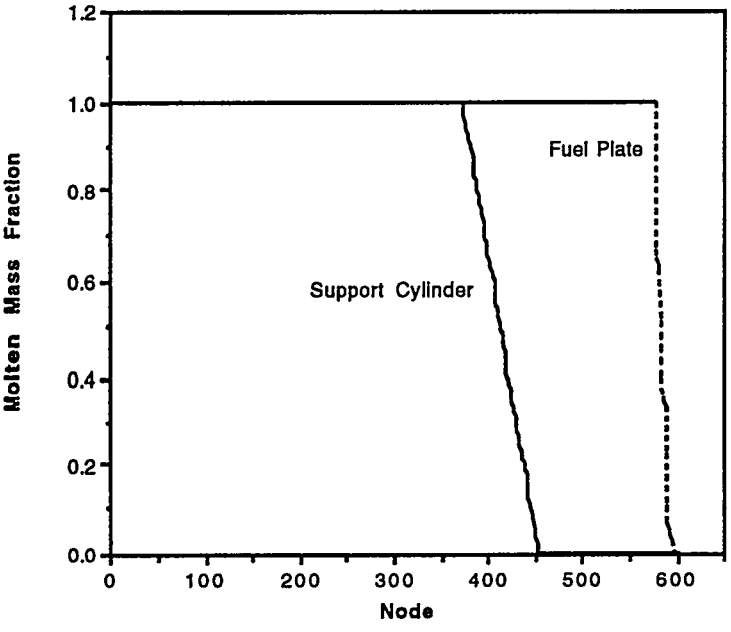

Fig. 10 Variation of molten mass fraction at the end of the calculations

not appropriate to assume that there is no fuel relocation/dispersal. Therefore, a parametric study has been performed to investigate the effect of molten fuel relocation/dispersal. The molten fuel (actually node) is forced to disappear once its temperature reaches a certain limit; one case with 1500 K, and the other with 863 K. A fuel melt temperature of 1500 K was selected as a fuel melt disappearance threshold, because that temperature is high enough to trigger the onset of aluminum ignition, as evidenced in past experiments [17]. 863 K was selected as the temperature at which molten fuel will either be swept upwards by the coolant or relocates downwards. This temperature is ~10K above aluminum melting temperature. Once the node at which the temperature increases above this threshold value disappears, we have to specify a new boundary condition to the inner node that was previously connected to the missing node. At this new boundary, the inner node may obtain more heat or lose heat depending on the situation. If extensive fuel ignition occurs, more energy will be added to the system under consideration through this boundary. If the relocation is due to coolant inertia, the system may loose heat to the coolant. For the current study, due to lack of knowledge on how this relocated node behaves, we assumed an adiabatic condition for this boundary. This assumption may not be too far from reality if we exclude the possibility of fuel ignition, since convective heat transfer in this channel is believed to be negligible. This is because the plate surface in this channel might be instantaneously covered by a vapor blanket upon coolant contact with the hot plate surface, along with reduced coolant velocity due to increased coolant channel flow area. For heat transfer at the damage propagation front, the same values of thermal conductivity and contact area between plates were used as for case 620-190-1 with no-melt removal. Results show that for both cases, the amount of damaged fuel was predicted to remain the same; that is 202 fuel plates. With an assumption of adiabatic boundary conditions, the heat flux at the damage propagation front was evaluated to be the same as that for the no-melt removal case. Therefore, damage propagation is predicted to proceed at the same speed, resulting in the same amount of fuel damage.

Summary and Conclusions

One-dimensional heat transfer calculations have been performed to investigate fuel plate damage propagation in the ANS reactor during a hypothetical coolant blockage event. The results provide useful insights into how various uncertain parameters affect the damage propagation. For the case with no heat transfer to the coolant, high thermal conductivity and high initial temperature for plate-2, and full thermal contact area of the swelled plates (e.g., the case is described in Fig. 6 as T=620, k=190, Fa=1), 202 plates, equivalent to about 30 kg of aluminum (202 plates x 0.1462 kg), are predicted as damaged at the end of 4 s. Also, it was found that the plate damage does not propagate if a 52 kW/m^2-K or larger heat transfer coefficient is provided to cool plate-2. The inclusion of side plates does not change the calculated number of damaged fuel plates. Instead, the energy content of those plates is reduced from about 180 MJ to 168.4 MJ. The difference (e.g., 11.6 MJ) has been transferred to the side plates. The mass of the side plates experiencing melting is estimated as 7.3 kg. This amount could contribute an additional chemical energy source of up to 130 MJ. A substantial portion of the side plates heated up to a temperature well beyond melting. Finally, it is cautioned that, if the plate damage was initiated in the lower fuel element, failure of the side plate may generate fragments that block the coolant channels of a downstream fuel element.

The present model represents an initial attempt at evaluating the highly complex aspects of ANS core damage propagation initiated by flow blockage. Shortcomings such as not accounting for fluid-structure interactions, core debris expulsion due to pressure buildup, plate rippling and buckling upon heatup, multidimensional effects, and absence of nuclear

reactivity feedback will be addressed as necessary during the issue closure process wherein the ROAAM-type approach is being employed [18]. Nevertheless, the present model provides useful information on gauging the potential for core damage propagation in the absence of dynamic loads and sweepoff and evaluating the direction for further development and model enhancements.

Appendix I Nodal Temperature Evaluation*

For the surface node (massless) k=1, Eq. (2) becomes

$$C_{01}(T_0 - T_1) + C_{12}(T_2 - T_1) + Q_1 = 0 \tag{I.1}$$

At the surface, oxidation of the plate surface or radiation heat transfer may contribute to form Q_1 in Eq. (I.1). In a current modeling consideration, however, we assume that no energy generation is involved on the surfaces so that Q_1 becomes zero. Equation (I.1) can be rewritten for $T_0 = T_{f,L}$ (fluid temperature of flow channel on the left boundary of the plate)

$$T_1 = A_1 T_2 + B_1 + D_1 T_{f,L} \tag{I.2}$$

where constants in Eq. (I.2) are given as

$$\begin{aligned} A_1 &= \frac{C_{12}}{U_1} \\ B_1 &= \frac{Q_1}{U_1} = 0 \\ D_1 &= \frac{C_{01}}{U_1} \\ U_1 &= C_{01} + C_{12} \\ Q_1 &= 0 \\ C_{01} &= h_L A_{01} = h_L w \Delta z \\ C_{12} &= \frac{\kappa_2 A_{12}}{(\Delta x/2)} = \frac{2 \kappa w \Delta z}{\Delta x} \end{aligned} \tag{I.3}$$

where h_L is the convective heat transfer coefficient at this surface.

For interior nodes (k = 2, 3, ..., kmax-1), successive substitution of similar expressions into Eq. (2) gives

$$T_k = A_k T_{k+1} + B_k^* + D_k T_{f,L} \tag{I.4}$$

where

---

* The numerical solution is obtained from Ref. [7] and was originally based on an unpublished work performed by V. Denny.

$$
\begin{aligned}
A_k &= \frac{C_{k,k+1}}{U_k} \\
B_k^* &= \frac{1}{U_k}\left\{Q_k + \frac{(m\,c_p)_k\,T_k^*}{\Delta t} + C_{k-1,k}\,B_{k-1}^*\right\} \\
D_k &= \frac{C_{k-1,k}\,D_{k-1}}{U_k} \\
U_k &= \frac{(m\,c_p)_k}{\Delta t} + C_{k-1,k}\left(1 - A_{k-1}\right) + C_{k,k+1} \\
Q_k &= Q_{\text{internal},k} \\
C_{k-1,k} &= \frac{\kappa_{k-1}\,\kappa_k\,A_{k-1,k}}{\kappa_{k-1}\left(\frac{\Delta x_{k-1}}{2}\right) + \kappa_k\left(\frac{\Delta x_k}{2}\right)} = \frac{\kappa\,w\,\Delta z}{\Delta x}
\end{aligned}
\tag{I.5}
$$

At the surface (massless) node k=kmax, $T_{kmax+1} = T_{f,R}$, giving

$$
T_{k\,\max} = A_{k\,\max}\,T_{f,R} + B_{k\,\max}^* + D_{k\,\max}\,T_{f,L} \tag{I.6}
$$

To generalize the solution, Eq. (I.6) is rewritten as

$$
T_{k\,\max} = D_{k\,\max}\,T_{f,L} + E_{k\,\max}\,T_{f,R} + F_{k\,\max}^* \tag{I.7}
$$

where

$$
\begin{aligned}
D_{k\,\max} &= \frac{C_{k\,\max-1,k\,\max}\,D_{k\,\max-1}}{U_{k\,\max}} \\
E_{k\,\max} &= \frac{C_{k\,\max,k\,\max+1}}{U_{k\,\max}} \\
F_{k\,\max}^* &= \frac{Q_{k\,\max} + C_{k\,\max-1,k\,\max}\,B_{k\,\max-1}^*}{U_{k\,\max}^*} \\
U_{k\,\max} &= C_{k\,\max-1,k\,\max}\left(1 - A_{k\,\max-1}\right) + C_{k\,\max,k\,\max+1} \\
Q_{k\,\max} &= 0 \\
C_{k\,\max-1,k\,\max} &= \frac{\kappa_{k\,\max}\,A_{k\,\max-1,k\,\max}}{(\Delta x/2)} = \frac{2\,\kappa\,w\,\Delta z}{\Delta x} \\
C_{k\,\max,k\,\max+1} &= h_R\,A_{k\,\max,k\,\max+1} = h_R\,w\,\Delta z
\end{aligned}
\tag{I.8}
$$

where h_R is the convective heat transfer coefficient at this surface.

Back substitution of Eq. (I.7) into Eq. (I.4) for k = kmax-1, kmax-2, ..., 1, then gives the final form for the assembly nodal temperature distribution:

$$
\begin{aligned}
T_k &= \left(A_k\,D_{k+1} + D_k\right)T_{f,L} + A_k\,E_{k+1}\,T_{f,R} + A_k\,F_{k+1}^* + B_k^* \\
&= D_k\,T_{f,L} + E_k\,T_{f,R} + F_k^*
\end{aligned}
\tag{I.9}
$$

References

[1] C. D. West, "The Advanced Neutron Source: A New Reactor-Based Facility for Neutron Research," Trans. Amer. Nuc. Soc. 61, 375 (June 1990).

[2] C. D. West, "Advanced Neutron Source Plant Design Requirements," ORNL/TM-11625 (May 1992).

[3] R. P. Taleyarkhan and S. H. Kim, "Severe Accident Risk Minimization Studies for the Advanced Neutron Source at the Oak Ridge National Laboratory," Proc. of the 5th International Workshop on Containment Integrity, Washington, D.C. (May 1992).

[4] C. Ramsey, "Probabilistic Risk Assessment of the Conceptual Design for the Advanced Neutron Source Reactor," ORNL/TM-12501 Draft (1993).

[5] S.H. Kim, et. al, "Study on Severe Accident Fuel Dispersion Behavior in the Advanced Neutron Source Reactor at Oak Ridge National Laboratory," Proc. of the 7th International Meeting on Nuclear Reactor Thermal-Hydraulics (NURETH-7) Saratoga Springs, NY (September 1995).

[6] R.P. Taleyarkhan, et. al., "Thermal-Hydraulics of Wave Propagation and Pressure Distribution Under Steam Explosion Conditions in the Advanced Neutron Source Reactor," Proc. of the 7th International Meeting on Nuclear Reactor Thermal-Hydraulics (NURETH-7) Saratoga Springs, NY (September 1995).

[7] F.T. Binford, T.E. Cole and E.N. Cramer, "The High Flux Isotope Reactor Accident Analysis," ORNL-3573, Oak Ridge National Laboratory (April 1967).

[8] J.R. Kirkpatrick, "Estimate of Propagation of Melting in HFIR Fuel Plates Initiated by Blockage of Two Adjacent Channels," HFIR-CTD-91-JRK-15-2, Oak Ridge National Laboratory (May 1991)

[9] J. Freels, "Estimate of HFIR Core Damage Following a Core Blockage Based on RELAP5/Mod2.5/v3t with HFIR CHF Extensions," C-HFIR-92-023, Oak Ridge National Laboratory (June 1992)

[10] S.H. Kim, et. al., "A Parametric Model for Analyses of Melt Progression in U-Al Assemblies," Proc. of ANS Topical Meeting on the Safety, Status and Future of Non-Commercial Reactors and Irradiation Facilities, Boise, ID (October 1990).

[11] D.A. Anderson, J.C. Tannehill and R.H. Pletcher, "Computational Fluid Mechanics and Heat Transfer," McGraw-Hill Book Company (1984)

[12] K.W. Childs, "HEATING 7.2 User's Manual," ORNL/TM-12262, Oak Ridge National Laboratory (February 1993)

[13] R.P. Taleyarkhan, "Analysis and Modeling of Fission Product Release from Heated Uranium-Aluminum Plate Type Reactor Fuels," Nuclear Safety, Vol. 33-1 (1992).

[14] J.L. Snelgrove, et. al., "The Use of U_3Si_2 Dispersed in Aluminum in Plate-Type Fuel Elements for Research and Test Reactors," ANL/RERTR/TM-11, Argonne National Laboratory (October 1987).

[15] D.L. Selby, R.H. Harrington and P.B. Thompson, "Advanced Neutron Source (ANS) Project Progress Report, FY1994," ORNL-6821, Oak Ridge National Laboratory (January 1995).

[16] V. Georgevich, et. al., "Thermally Induced Dispersion Mechanisms for the U3Si2 Cermet Plate Type Fuel Under Rapid Transient Energy Deposition," Proc. of the 1995 National Heat Transfer Conference, Portland, OR (1995).

[17] L.S. Nelson, "Steam Explosions of Single Drops of Pure and Alloyed Molten Aluminum," Proc. of CSNI-FCI Specialist Meeting, Santa Barbara, CA (January 1993).

[18] T.G. Theofanous and H. Yan, "ROAAM: A Risk-Oriented Accident Analysis Methodology," Proc. of the International Conference on Probabilistic Safety Assessment and Management (PSAM), Beverly Hills, CA (February 1991).

TURBULENT MIXED CONVECTION IN VERTICAL AND INCLINED FLAT CHANNELS WITH AIDING FLOWS

P. Poškas, J. Vilemas, J. E. Adomaitis, G. Bartkus

Lithuanian Energy Institute

Abstract

This paper presents an experimental study of turbulent mixed convection heat transfer for aiding flows in a vertical ($\varphi = 90°$), inclined ($\varphi = 60°, 30°$), and horizontal ($\varphi = 0°$) flat channels with symmetrical heating and a ratio of height h to width b of about 1:10 and with length about 4 m ($x/2h$ about 44). The study covered Re from 4×10^3 to 5×10^4 and Gr_q from 5×10^7 to 3×10^{10}. For the upper wall, a region of impaired heat transfer was found for all angular positions (from vertical to horizontal) and for bottom wall the augmentation of heat transfer in comparison to forced convection was revealed in the region of $\varphi = 0°–60°$. Different characteristic buoyancy parameters were found for regions of impaired and enhanced heat transfer. General relations are suggested to predict the heat transfer for fully-developed-flow conditions and different angular positions.

1. Introduction

The development of the new generation of nuclear reactors with passive cooling systems requires very detailed studies of mixed and natural convection peculiarities for channels with different cross-sectional shapes. The assurance of proper safety for nuclear reactors demands a substantial understanding of the effect of buoyancy on the heat transfer in different channels, as the effect can reach significant levels in emergency operation and in the shut-down behaviour of nuclear reactors.

. We reported in NURETH-6 experimental results for turbulent heat transfer in a flat horizontal channel with stable and unstable stratification in the flow [1]. The present paper covers our experiments with symmetrical heating in vertical and inclined flat channels for aiding flows (a case where the buoyancy forces act in the flow direction). There being no secondary flows due to free convection in turbulent flat channel flows, the arrangement opens the way to evaluating the effect of buoyancy on the turbulent transport and consequently on the heat transfer rates for the different orientation of the channels in space.

So far turbulent mixed convection has been mostly studied in pipes. The available results on the heat transfer in vertical pipes were reviewed by Petukhov and Polyakov [2] and by Jackson et al. [3]. Further investigations were reported by Vilemas et al. [4]. Different authors revealed enhanced heat transfer in opposing turbulent flows. In aiding flows laminarization of the flow and impaired heat transfer were observed in the low-buoyancy range, but more intensive turbulent transport and enhanced heat transfer were observed at higher levels of buoyancy. In long channels with strong effects of buoyancy, typical maxima and minima of the wall temperature were observed, corresponding to minima and maxima in the heat transfer rate.

A number of different expressions of buoyancy parameter have been suggested for the heat transfer predictions in vertical tubes with aiding flows in different fluids. Jackson and Hall [5] related the behaviour of relative heat transfer to a buoyancy parameter expressed as $Gr_\rho / Re^{2.7}\overline{Pr}^{0.5}$. Later this parameter was modified by Jackson and Rouai [6] to $Gr_q / Re^{3.425}Pr^{0.8}$. Petukhov and Polyakov [2] introduced another expression of buoyancy parameter $Gr_q / Re^4 Pr$. The most common expression is $Gr_q / 4Re^3 Pr$, used successfully by Connor and Car [7] to correlate data for aiding flows of air, water and mercury in the region of heat transfer recovery (increasing heat transfer).

The studies on mixed convection in vertical flat channels are not numerous and they lead to contradictory conclusions. Swanson and Catton [8] found the same effects of buoyancy in flat channels under symmetrical bilateral heating as in pipes. Axcell and Winstanley [9] studied mixed convection heat transfer in flat channels of air-cooled transformers. The authors found enhanced heat transfer rates in opposing flows while for aiding flows the initially impaired heat transfer rates later exceeded those for forced convection. Sudo et al. [10] studied the effect of channel gap size on mixed-convection heat transfer in water flows in vertical rectangular channels heated from both sides. The experiments were carried out for both aiding and opposing flow conditions. In both cases mixed-convection heat transfer was higher than for pure forced or free convection. It was shown by Poškas et al. [11] that in vertical flat channels with aiding flows heat transfer data could be correlated more successfully using different buoyancy parameters in the region of impaired heat transfer and in the region of heat transfer recovery.

We do not know any experimental investigations of turbulent mixed convection in inclined flat channels. This paper presents an experimental study of the buoyancy effect on turbulent heat transfer in symmetrically heated vertical and inclined flat channels in a wide range of Gr_q-to-Re ratio. The study revealed a different effect of buoyancy for the different orientation modes.

2. Experimental details

Our experiments were performed in an open wind channel. Purified air was supplied under 20 MPa to pressure chambers and through a reducer to a low pressure receiver under 1.5 MPa. From there, through one of the three parallel lines with matched orifice plates of different clear areas (for flow rate measurements), the air was supplied to the test section after which it was vented to the atmosphere through a throttle valve.

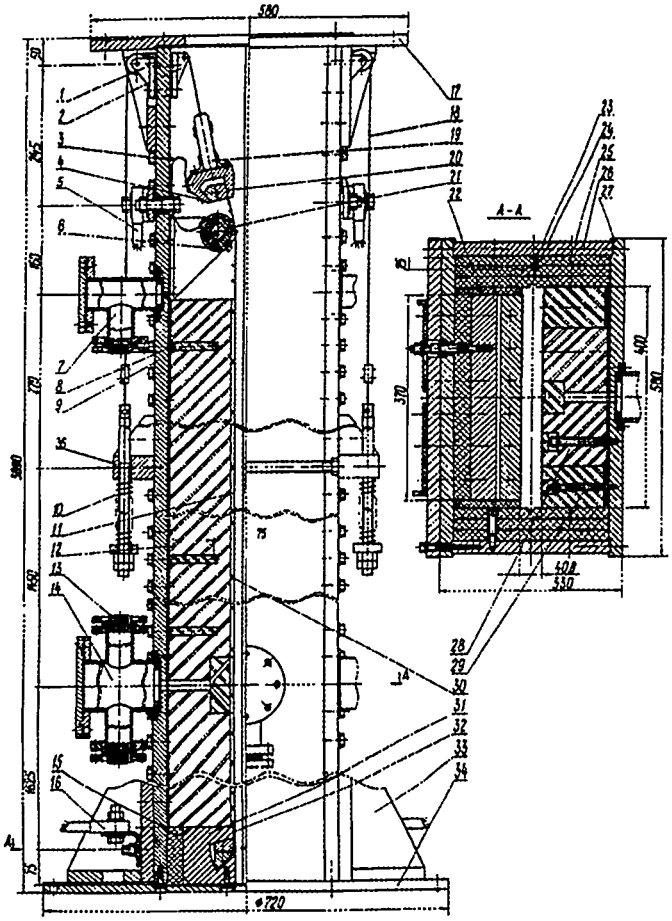

Fig. 1. Test section: 1, 2, directing rolls; 3, flexible copper leads; 4, 6, 8, 24, 30, 32, thermocouples; 5, 16, copper conductors; 7, 14, seals; 9, 23, stoppers; 10, springs; 11, heated surface (stainless steel calorimeter foil); 12, 15, 22, textile-reinforced plastic pieces; 13, sealed joint; 17, 33, 34, fixing flanges; 18, steel cords; 19, insulators; 20, 31, brass contacts; 21, rotating brass contacts; 25, 28, 29, asbestos and cement–asbestos strips; 26, lateral duralumin plates; 27, central duralumin plates; 35, spring units.

We studied mixed convection in a flat-channel test section with a height-to-width ratio h/b of about 1/10, and length about 3.6 m (x/d about 44) (Fig. 1). The channel was 400 mm wide and 40.8 mm high. The test section was preceded by a hydrodynamic stabilizer 2.4 m long (x/d about 29). It was

placed inside a case 0.6 m in diameter and 2.7 m long, with air-supply penetrations and a set of grids. The test section contained two central (27) and two lateral (26) duralumin plates (see Fig. 1). Its mid part was insulated by 120 mm thick asbestos strips (28, 29) on the central plates (27) and by 60 mm thick cement–asbestos strips (25) on the lateral plates (26). The calorimetric heated surfaces (11) of the central two plates were made of stainless steel foil 0.38 mm thick and 370 mm wide, and were fixed at the inlet to brass contacts (31). These were fastened by brass screws to copper conductors (16) through textile-reinforced plastic pieces (15, 22). At the outlet the foils (11) were fixed in a similar way by rotating brass contacts (21) to motion-free upper brass contacts (20). Flexible copper leads (3) were extended through the contacts (20, 21) and the copper conductor (5). Upper contacts (20) were connected via insulators (19) and steel cords (18) to springs (10) each of a 200 kg/cm^2 tension force. This arrangement provides proper compensation for thermal expansion of the calorimeter foil and a reliable contact between the foil (11) and the insulator (28).

The temperature of the calorimeter test surface (11) was measured by chromel–alumel thermocouples (30) of a 0.3 mm diameter wire, which were fixed to the inverse surface of the test foil. Longitudinal voltage drops in the heated foil were measured by the same thermocouples. Each of the electrically heated calorimeter surfaces had 25 thermocouples fixed at the center. Heat loss was measured by two thermocouples (8) in each of the six more cross-sections in the insulation layers (28) of the central plates (27) and by two thermocouples (24) in eight more cross-sections in the insulation layers (25) of the lateral plates (26). The thermocouples (8) and (24) were separated by 75 mm and 25 mm respectively.

To cover higher values of Gr_q or higher effects of buoyancy, the pressure of the air flow was varied from 0.1 to 1 MPa. This was achieved by sealing the whole test section in a pressurized vessel of 0.87 m diameter, 7.2 m long and of weight about 2000 kgf; the volume was about 4 m^3. It consisted of two flange-sealed parts. The stabilization part of the pressurized vessel had penetrations for inlet air and for the leads of thermocouples which measured the fluid temperature. The test-section part of the pressurized vessel had penetrations for outlet air and for the leads and seals of thermocouples, which measured the temperatures of the heated foil surfaces, of the insulation layers, and of the outlet air, as well as for inlet–outlet pieces of the heating mains. The vessel was equipped with two safety valves and a manometer, as well as a turning gear which allowed to change the inclination angle of the test section to the horizontal line.

Our experiments were performed at 4 positions of the flat channel. The horizontal position is at $\varphi = 0°$. The test section also was turned up into positions with inclination angles of 30° and 60°. The vertical position corresponds to strong aiding flows and is at $\varphi = 90°$.

The effect of buoyancy on the heat transfer was evaluated for the boundary condition q_w = constant; the maximum wall–fluid temperature difference was 150 K. The series of tests in a two-side-heated channel was performed at $q_{w1} = q_{w2}$. Bulk flow temperature and hydraulic diameter $d=2h$ were used as reference parameters. The test covered turbulent mixed convection at Re from 4×10^3 to 5×10^4 and Gr_q up to 3×10^{10}.

The inside surface temperature of the calorimeter foil was determined from the measured outside surface temperature and the temperature drop across the foil. The bulk flow temperature of the air was found from local enthalpy (by known flow temperature at the inlet and heat flux to the flow). Convective heat flux was evaluated from the heat balance and included both the heat loss in the insulating layer and the axial heat loss in the foil, and the heat loss by radiation. The heat flux density at the insulation layer was determined by a separate experiment. To exclude free convection, the channel was packed with asbestos pellets. The calorimeter foil was heated by electric current, and the only sink for the heat emitted by the test surface in the center of the channel was across the insulation layer. This heat loss was determined by a relation for conduction in a flat plate from the difference of temperatures measured by thermocouples on the opposite sides of the insulation layer. Numerical heat loss values were approximated by second-order polynomials for each test wall, and the solution was used to find heat loss values at the test points on the calorimeter during the main experiments.

3. Results and discussion

Fig. 2 presents heat transfer from the upper and the bottom walls along the channel. Its inclination angles were varied, but nearly constant pressure of the air (about 0.4 MPa), Re (about

7000) and a high Gr_q (about 10^{10}) were maintained throughout the experiment. Note the lowest heat transfer from the upper wall in the horizontal position ($\varphi = 0°$), and its consistent increase with an increase of the inclination angle (φ = 30°, 60°, and 90°). Similar to aiding flows in pipes with significant effects of buoyancy, in a vertical flat channel (φ = 90°) typical minima ($x/d \approx 7$) and maxima ($x/d \approx 17$) of the heat transfer are observed. They are related to highly complicated longitudinal processes of laminarization and turbularization. Similar maxima and minima of the heat transfer were observed in nearly vertical positions of the channel ($\varphi = 60°$). A specific feature is, that for similar parameters of buoyancy the points of minimum or maximum heat transfer are closest to the flow inlet in vertical channels. This is an indication of the most pronounced effect of buoyancy on increase of turbulence and is supported by the higher value of Nu. See in Fig. 2, that for smaller angles of inclination (φ = 30°), longitudinal variations of the heat transfer are leveled out and disappear altogether in the horizontal channel.

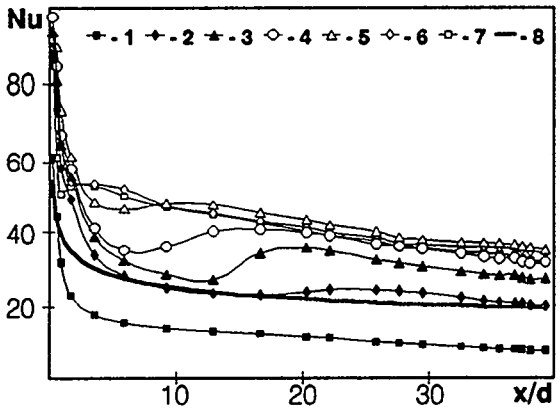

Fig. 2. Longitudinal distribution of the local heat transfer in a flat channel on upper (blackened symbols) and bottom (open symbols) walls at Re ≈ 7000 for P = 0.4 MPa and $Gr_q \approx 10^{10}$ for the following inclination angles: 1 and 7, 0°; 2 and 6, 30°; 3 and 5, 60°; 4, 90°; 8, prediction by Eqs. (1)–(5) for pure forced convection.

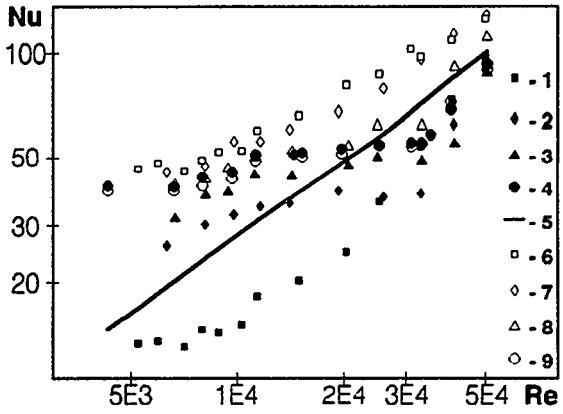

Fig. 3. The behaviour of heat transfer as a function of Re in a flat channel on upper (blackened symbols) and bottom (open symbols) walls for P = 0.7 MPa at x/d = 38 for the following inclination angles: 1 and 6, 0°; 2 and 7, 30°; 3 and 8, 60°; 4 and 9, 90°; 5, prediction by Eqs. (1)–(5) for pure forced convection.

The behaviour of heat transfer from the bottom wall is loosely related to the inclination angle, Fig. 2, in sufficiently large x/d distances, but its level is higher than in the forced convection case. We shall see later that for φ from 0° to 60° the tendency persists under arbitrary effects of buoyancy. A significant decrease of the heat transfer was observed in a certain range of buoyancy with the approach to the vertical position.

See in Fig. 2, that for x/d over 20 or 25, heat transfer rates become fully developed in arbitrary modes of the flow. The further decrease of Nu is related to the longitudinal variation of buoyancy. We consider below only fully developed heat transfer for variable Re and with different values of buoyancy parameters.

Fig. 3 relates heat transfer rates from the upper and the bottom walls to Re for different angles of inclination but for fixed air pressure and x/d value. Here again the closest correlation is between the heat transfer from the upper wall and the angle of inclination. Because of the stable stratification in horizontal channels, the rate of this heat transfer is always below the pure-forced-convection value. Heat transfer rates increase sharply with the deviation from the horizontal position, so that at $\varphi = 30°$ in the range of low Re they are higher than for forced convection. With a further increase of the inclination angle the value of Nu increases, too. Anyway, both at $\varphi = 60°$ and $\varphi = 90°$ there exists a certain upper range of Re where the heat transfer is below the forced-convection value. Because of the unstable stratification of the flow, heat transfer from the bottom wall is both at $\varphi = 30°$ and at $\varphi = 60°$ higher, than under forced convection. On the other hand, with the approach to φ = 90° also a range of Re was observed, where Nu was lower, than under forced convection.

Now for convenience we consider the heat transfer in a more general approach, by evaluating relative heat transfer with different characteristic buoyancy parameters.

Let us first normalize the Nu for mixed convection with the standard Nu_T for turbulent pure-forced-convection heat transfer. Forced convection heat transfer in a flat channel was determined by the technique suggested by Vilemas at al. [12]:

$$Nu_T / Nu_{\psi=1} = 1 - 0.744\left\{1 - \exp\left[-K_f\left(af + n_\mu \Phi K_f\right)\right]\right\} \tag{1}$$

where $a = -0.53 n_\rho - \frac{1}{3} n_\lambda - \frac{1}{4} n_c$,

$f = 1 - \exp(-0.1\tilde{x})$,

$\Phi = \frac{1.25(0.01\tilde{x})^2}{1 + (0.01\tilde{x})^2}$,

$\tilde{x} = \frac{x}{d}$,

$K_f = \frac{q_w d}{\lambda_f T_f Nu_{\psi=1}}$,

$n_\rho, n_\lambda, n_c, n_\mu$ are power indices for exponential relations of the temperature-dependent fluid-physical properties.

The equations include heat transfer for constant fluid physical properties $Nu_{\psi=1}$ which was determined by the technique of Petukhov and Roizen [13]. For bilateral heating the relation is

$$Nu_{\psi=1} = \frac{Nu}{1 + \Theta Nu} \tag{2}$$

where Θ stands for dimensionless adiabatic temperature of the wall

$$\Theta = -16.06\,Re^{-0.87}\,Pr^{-1.05} \tag{3}$$

and Nu for Petukhov and Roizen [14] description of one-side heating:

$$Nu / Nu_{t,\infty} = \left(1 - f(Pr)\right)\left[0.86 + 0.8(x/d)^{-0.4}\right] \tag{4}$$

where $f(Pr) = 0.45/(2.4 + Pr)$.

The $Nu_{t,\infty}$ term gives the heat transfer in the stabilized part of the channel determined by the technique of Petukhov and Polyakov [2] for the low range of Re

$$Nu_{t,\infty} = \frac{Re\,Pr\frac{\xi}{8}}{1 + \frac{900}{Re} + 12.7\sqrt{\frac{\xi}{8}}\left(Pr^{2/3} - 1\right)}, \tag{5}$$

here ξ is friction factor after Blasius: $\xi = 0.316\,Re^{-0.25}$.

The above descriptions include also variations of fluid physical properties. Our experiments covered moderate rates of heating, but corrections from 5 to 7% were necessary in certain cases.

Fig. 4 presents relative heat transfer from the two walls in the vertical position. Note a satisfactory agreement of the test points for the two walls in this limiting case. Our analysis included

different buoyancy parameters from $Bo_1 = Gr_q / Re^4 Pr$ to $Bo_2 = Gr_q / Re^{2.5} Pr$ and well-known $Bo = Gr_q / Re^{3.425} Pr^{0.8}$ parameter was suggested as the characteristic buoyancy parameter for the regions of impaired heat transfer of vertical channels. Some growth of the power index of Re was noticed with a deviation from the vertical position, but for correlation of data at different inclination angles $Bo = Gr_q / Re^{3.425} Pr^{0.8}$ parameter was used. Fig. 4 shows that this parameter correlates date rather well in the region of impaired heat transfer for variable pressures. The test points are more widely scattered over pressures in regions of recovered heat transfer. As we can see, the data for impaired heat transfer region are in good agreement with correlation for vertical tube of Jackson and Rouai [6]:

$$\frac{Nu}{Nu_T} = \left(\left| 1 - 8.3 \times 10^4 \, Bo \left(\frac{Nu}{Nu_T} \right)^{-2} \right| \right)^{0.46} . \qquad (6)$$

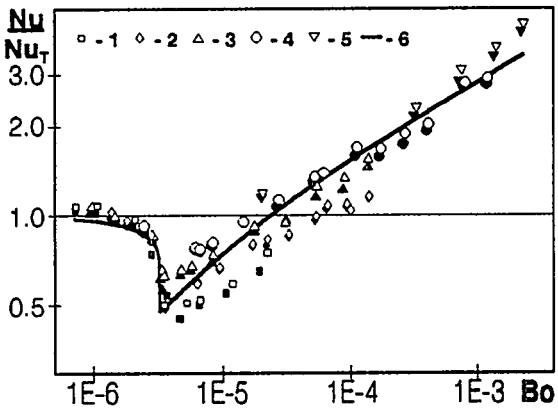

Fig. 4. Relative heat transfer from the first (blackened symbols) and the second (open symbols) walls of a vertical flat channel at x/d = 38 for the following P values: 1, 0.1 MPa; 2, 0.2 MPa; 3, 0.4 MPa; 4, 0.7 MPa; 5, 1 MPa; 6, prediction by Eq. (6).

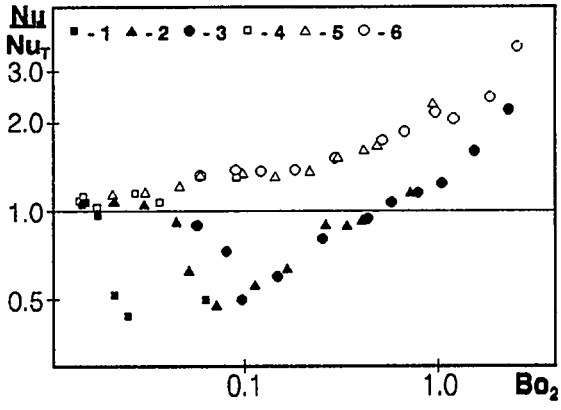

Fig. 5. Relative heat transfer from the upper (blackened symbols) and bottom (open symbols) walls of the flat channel for x/d = 38 at inclination angle φ = 30° for the following P values: 1 and 4, 0.1 MPa; 2 and 5, 0.4 MPa; 3 and 6, 0.7 MPa.

From another analysis a close correlation of the test points of variable pressures was found with the $Bo_2 = Gr_q / Re^{2.5} Pr$ buoyancy parameter, Fig. 5, in the region of recovering heat transfer for the upper wall. The scatter was very wide for regions of impaired heat transfer. This buoyancy parameter gives a rather good correlation of the test points in the region of augmented heat transfer, Fig. 5, bottom wall. As the result, two characteristic buoyancy parameters were used in the interpretation: $Bo = Gr_q / Re^{3.425} Pr^{0.8}$ for regions of impaired heat transfer and $Bo_2 = Gr_q / Re^{2.5} Pr$ for regions of recovered and augmented heat transfer.

Fig. 6 presents data for regions of impaired heat transfer from the upper wall for different angles of inclination. It is evident that maximum decrease of the heat transfer is not related to the angle of inclination. The lowest rate of the heat transfer constitutes 45% of the forced-convection value in all cases, but the buoyancy parameter value related to the lowest heat transfer (for lack of a better name lets call it a "critical value") is closely dependent on the spatial position of the channel. This is especially true for nearly horizontal positions, in nearly vertical positions this variation of the critical value of buoyancy parameter is less pronounced. Table 1 presents this critical values Bo_{cr} for different angles of inclination.

Table 1. Critical values of buoyancy parameter

INCLINATION ANGLE φ, °	CRITICAL VALUE Bo_{cr}	INCLINATION ANGLE φ, °	CRITICAL VALUE Bo_{cr}
0	1.3×10^{-5}	60	4.3×10^{-6}
30	5.5×10^{-6}	90	4.0×10^{-6}

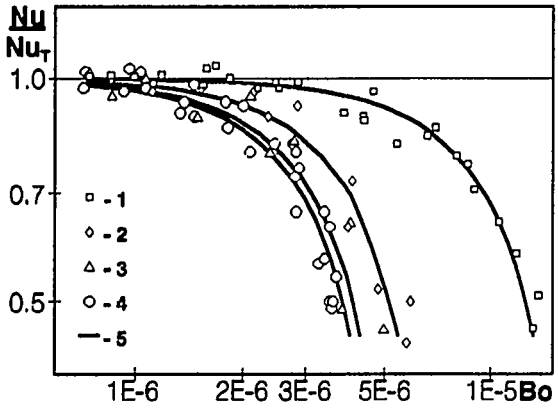

Fig. 6. Relative heat transfer from the upper wall of the flat channel in the region of impaired heat transfer at x/d = 38 for the following inclination angles: 1, 0°; 2, 30°; 3, 60°; 4, 90°; 5, prediction by Eq. (7).

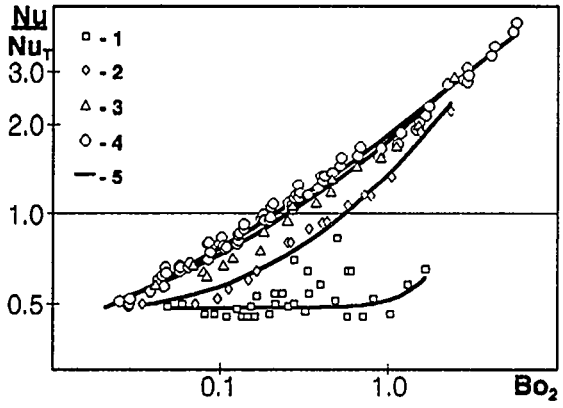

Fig. 7. Relative heat transfer from the upper wall of the flat channel in the region of heat transfer recovery at x/d = 38 for the following inclination angles: 1, 0°; 2, 30°; 3, 60°; 4, 90°; 5, prediction by Eq. (8).

Judging from Fig. 6, the effect of buoyancy is most pronounced in vertical channels, where critical values Bo_{cr} are the smallest. The effect is weakest in horizontal channels, that is, where stable stratification of the flow is involved. In spite of this, maximum reduction rates of the heat transfer from forced-convection values are similar in all cases. The following relation describes the heat transfer in this region within 14%:

$$\frac{Nu}{Nu_T} = 1 - 10^{10} c_1 Bo^{1.91} \qquad (7)$$

where $c_1 = 0.115 + \sin\varphi$.

Fig. 7 contains data on the heat transfer from the upper wall in the region of its recovery. Note the abrupt increase of the heat transfer in the vertical position. With a deviation from this position the heat transfer is recovered in a more and more slow manner with increase of buoyancy parameter. Data for φ from 30° to 90° where approximated within 7% by

$$\frac{Nu}{Nu_T} = 0.247(c_2 + c_3 Bo_2^{n_1}) \qquad (8)$$

where $c_2 = 1.96^{\cos\varphi}$,

$c_3 = 0.127 + 6.42(\sin\varphi)^{0.815}$,

$n_1 = 2.8 - 2.3(\sin\varphi)^{0.25}$.

Heat transfer for inclination angles from 0° to 30° can also be approximated by this Eq.(8) but with lower accuracy (within 13%). Further experiments must be performed for closer approximations of the heat transfer in this range.

Relative heat transfer from the bottom wall is related to the same $Gr_q / Re^{2.5} Pr$ buoyancy parameter in Fig. 8. Observe the augmentation of the relative heat transfer in the unstable stratification case for φ from 0° (horizontal channel) to 60°. An important decrease of the heat transfer seems natural for the vertical position, while buoyancy parameter is rather small. Here wide scatter of the test points over different pressures comes from the poor performance of the $Gr_q / Re^{2.5} Pr$ buoyancy parameter. As it was shown on Fig. 4, $Gr_q / Re^{3.425} Pr^{0.8}$ parameter must be used in this region. The test points were approximated within 6% for φ from 0° to 60° by

$$\frac{Nu}{Nu_T} = 1 + c_4 Bo_2^{n_2}, \tag{9}$$

where $c_4 = 1.22 - \dfrac{0.022}{(\cos\varphi)^{4.33}}$,

$$n_2 = 0.59 + \frac{0.01}{(\cos\varphi)^{4.62}}.$$

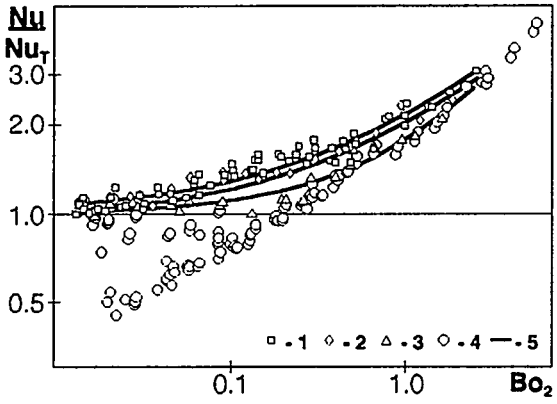

Fig. 8. Relative heat transfer from the bottom wall of the flat channel at x/d = 38 for the following inclination angles: 1, 0°; 2, 30°; 3, 60°; 4, 90°; 5, prediction by Eq. (9).

The behaviour of the heat transfer rates for φ from 60° to 90° calls for further studies because heat transfer decrease below the forced-convection values are to be expected not only in the vertical position, but also in the approaching positions.

4. Conclusion

Experiments on turbulent mixed convection heat transfer in a flat channel for different angles of its inclination lead to the following conclusions:

(1) A qualitative similarity of the heat transfer behaviour from the upper wall is observed in arbitrary angles of inclination. For the small influence of buoyancy mixed-convection heat transfer is lower than the forced-convection rate at the same Re. With increase of buoyancy parameter heat transfer recovers and becomes even higher than the pure-forced-convection level.

(2) Heat transfer from the bottom wall is weakly dependent on the inclination angles in the region from φ = 0° to φ = 60° and due to unstable stratification of the flow is higher than forced-convection rate. With the approach to the vertical position the behaviour is similar to that on the upper wall: the heat transfer rate is first reduced, and recovered afterwards.

(3) Characteristic buoyancy parameters and general relations (Eqs. (7)–(9)) are suggested for turbulent mixed-convection heat transfer in the specific ranges of the inclination angles and parameters covered.

Nomenclature

b	width (m)
Bo	buoyancy parameter $Gr_q / Re^{3.425} Pr^{0.8}$
Bo_1	buoyancy parameter $Gr_q / Re^4 Pr$
Bo_2	buoyancy parameter $Gr_q / Re^{2.5} Pr$
c_p	specific heat capacity at constant pressure ($J kg^{-1}K^{-1}$)
d	hydraulic diameter $2h$ (m)
g	acceleration of gravity ($m s^{-2}$)
Gr_q	Grashof number based on wall heat flux $\beta g q_w d^4 / \lambda \nu^2$
Gr_ρ	Grashof number based on density gradient $g\rho(\rho - \bar{\rho})d^3 / \mu^2$
h	height (m)
Nu	Nusselt number $q_w d / (T_w - T_f)\lambda$
p	pressure (Pa)
Pr	Prandtl number $\mu c_p / \lambda$
$\overline{Pr}$	Prandtl number based on integrated specific heat capacity $\mu \bar{c}_p / \lambda$
q	heat flux ($W m^{-2}$)
Re	Reynolds number du / ν
T	temperature (K)
u	velocity ($m s^{-1}$)
x	longitudinal coordinate (m)

Greek letters

β	volume expansion coefficient ($1K^{-1}$)
λ	thermal conductivity ($W m^{-1}K^{-1}$)
μ	dynamic viscosity ($kg m^{-1}s^{-1}$)
ν	kinematic viscosity ($m^2 s^{-1}$)
ξ	friction factor
ρ	mass density ($kg m^{-3}$)
φ	inclination angle (degrees)
Ψ	temperature factor T_w / T_f

Subscripts

cr	critical
f	in the flow, bulk
T	for pure forced convection conditions
t	in the tube
w	at the wall
Ψ=1	at constant physical properties
∞	in the fully-developed-heat-transfer region
$(\bar{})$	averaging

Other symbols are defined in the text.

References

[1] J.Vilemas, P.Poškas, and J.E.Adomaitis, "Turbulent heat transfer in a flat channel with stable and unstable stratification in the flow", Nucl. Engrg. Des. 149, 261-268 (1994).

[2] B.S. Petukhov and A.F. Polyakov, Teploobmen pri Smeshannoy Turbulentnoy Konvektsii (Heat Transfer in Turbulent Mixed Convection), Nauka, Moscow (1986).

[3] J.D. Jackson, M.A. Cotton, and B.P. Axcell, "Studies of mixed convection in vertical tubes", Int. J. Heat Fluid Flow 10, 2-15 (1989).

[4] J.V.Vilemas, P.S.Poškas, and V.E.Kaupas, "Local heat transfer in a vertical gas-cooled tube with turbulent mixed convection and different heat fluxes", Int. J. Heat Mass Transfer 35, 2421-2428 (1992).

[5] J.D. Jackson and W.B. Hall, "Influences of buoyancy on heat transfer to fluids flowing in vertical tubes under turbulent conditions", Turbulent Forced Convection in Channels and Bundles, Advanced Study Institute, London, 2, 613-640 (1979).

[6] J.D.Jackson and N.M.Rouai, "Experimental investigation of heat transfer to water flowing in a vertical tube with strong influence of free convection", Turbulent Convection, Proc. Anglo-Soviet Seminar, 1-23 (1990).

[7] M.A. Connor and A.D. Carr, "Heat transfer in vertical tubes under conditions of mixed free and forced convection", Proc. 6th Int. Heat Transfer Conf., 1, 43-48 (1978).

[8] L.Swanson and I.Catton, "Surface renewal theory for turbulent mixed convection in vertical ducts", Int. J. Heat Mass Transfer 30, 2271-2279 (1987).

[9] B.P.Axcell and R.Winstanley, "Experimental investigation of mixed convection heat transfer in the passage between vertical plane surfaces", Turbulent Convection, Proc. Anglo-Soviet Seminar, 183-203 (1990).

[10] Y.Sudo, M.Kaminaga, and K.Minazoe, "Experimental study of the effects of channel gap size on mixed convection heat transfer characteristics in vertical rectangular channels heated from both sides", Nucl. Engrg. Des. 120, 135-146 (1990).

[11] P.Poškas, J.E.Adomaitis, J.Vilemas, and G.Bartkus, "Development of turbulent heat transfer over the length of vertical flat channel under a strong influence of buoyancy", Proc. Tenth Int. Heat Transfer Conf., 5, 555-560 (1994).

[12] J.Vilemas, B.Čėsna, and V.Survila, Heat Transfer in Gas-Cooled Annular Channels, Hemisphere, New York City, New York (1987).

[13] B.S. Petukhov and L.I. Roizen, "Teploobmen v trubakh koltsevogo sechenya" ("Heat transfer in annuli"), Inzh. Fiz. Zh. 6, 3-11 (1963).

[14] B.S. Petukhov and L.I. Roizen, "Obobshchennye zavisimosti dlia teplootdachi v trubakh koltsevogo sechenya" ("Correlations for heat transfer in annuli"), Teplofiz. Vys. Temp. 12, 565-569 (1974)..

Mixing Phenomena of Interest to Boron Dilution During Small Break LOCAs in PWRs*

H. P. Nourbakhsh and Z. Cheng
Department of Advanced Technology
Brookhaven National Laboratory
Upton, NY 11973-5000
Tel. (516)282-5405

ABSTRACT

This paper presents the results of a study of mixing phenomena related to boron dilution during small break loss of coolant accidents (LOCAs) in pressurized water reactors (PWRs). Boron free condensate can accumulate in the cold leg loop seals when the reactor is operating in a reflux/boiler-condenser mode. A problem may occur when subsequent change in flow conditions such as loop seal clearing or re-establishment of natural circulation flow drive the diluted water in the loop seals into the reactor core without sufficient mixing with the highly borated water in the reactor downcomer and lower plenum. The resulting low boron concentration coolant entering the core may cause a power excursion leading to fuel failure. The mixing processes associated with a slow moving stream of diluted water through the loop seal to the core are examined in this paper. Bounding calculations for boron concentration of coolant entering the core during a small break LOCA in a typical Westinghouse-designed four-loop plant are also presented.

1. INTRODUCTION

A small-break LOCA is characterized by slow reactor coolant system (RCS) depressurization rates and low fluid velocities within the RCS as compared to a design basis large-break LOCA. Because of the slow depressurization rate, various phase change/separation phenomena dominate the thermal hydraulic characteristics of small-break LOCAs. One aspect of this behavior which has been recognized more recently [1] is the existence of an inherent boron dilution mechanism in the course of small-break LOCAs that involves decay heat removal by phase-separating natural circulation (i.e., reflux/boiler condenser mode operation). The steam that is generated in the core is largely devoid of boric acid. Due to subsequent condensation in the steam generators, a portion of boron-free condensate can run down the downflow side of the steam generator tubes and accumulate in the loop seals between the steam generator outlet plena and the reactor coolant pumps (RCPs). A subsequent change in flow such as loop seal clearing or re-establishment of natural circulation flow, may provide an effective mechanism to drive the slug of diluted water into the core. However, the buoyancy and turbulent mixing process between the loop seal and the core may sufficiently increase the boron concentration of the diluted stream to prevent a power excursion leading to fuel failure.

The mixing processes associated with a slow moving stream of diluted water through the loop seal to the core are examined in this paper. The quantitative aspects of different mixing mechanisms and a simplified, yet physically based, methodology for their integration into an overall prediction of dilution boundary will be presented. Bounding case analyses of the boron concentration in the coolant entering the core due to loop seal clearing or re-establishment of natural circulation flow in a typical Westinghouse designed 4-loop plant (see Figure 1) will be also provided.

*This work was performed under the auspices of the U. S. Nuclear Regulatory Commission, Office of Nuclear Regulatory Research.

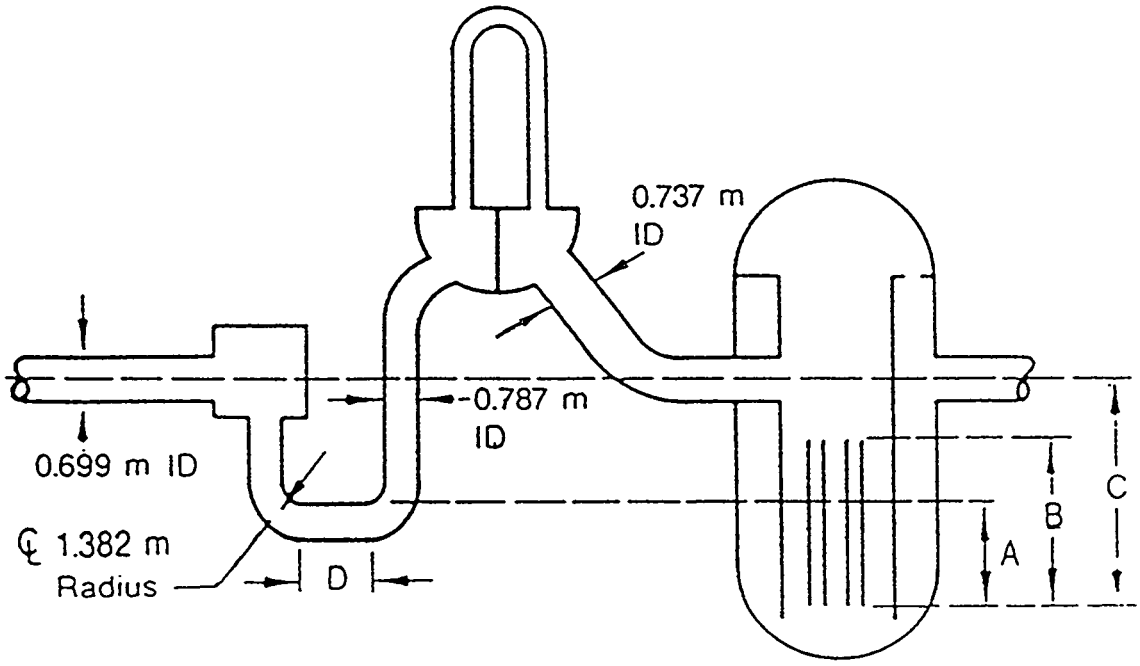

Dimension A = 2.507 m
Dimension B = 3.658 m
Dimension C = 5.256 m
Dimension D = 1.097 m

Full Core Power = 3410 MW(t)
Core Flow Area = 5.029 m^2
Lower Plenum Volume = 18.4 m^3
Downcomer Volume = 16.8 m^3
Pump Volume = 2 m^3

Figure 1 Pertinent Data for a Typical Westinghouse Design Four-Loop Plant (RESAR-3S)

2. MIXING PROCESSES AND PHENOMENA

2.1 Mixing in the Loop Seals

During reflux condensation the loop mean flow rate is virtually null. The safety injection of cold and highly borated water into a stagnant loop leads to stratification accompanied by counter-current flows and a global recirculating flow pattern with flow rates significantly higher than the net flow through the system. This keeps a major portion of the system volume including the loop seals (vertical leg below the pump and bottom horizontal leg), the downcomer (excluding the region above the cold leg) and the lower plenum in a well mixed condition. The ensuing flow regime was first established analytically by Theofanous and Nourbakhsh [2,3] as part of the work supporting an NRC sponsored study related to Pressurized Thermal Shock (PTS). This work predicted overcooling transients due to high pressure safety injection into a stagnant loop of a PWR. The physical situation may be described with the help of Figure 2. A "cold stream" originates with the safety injection buoyant jet at the point of injection, continues toward both ends of the cold leg, and decays away as the resulting buoyant jets fall into the downcomer and pump/loop-seal regions. A "hot stream" flows counter to this "cold stream" supplying the flow necessary for mixing (entrainment) at each location. This mixing is most intensive in certain locations identified as mixing regions (MRs). The quantitative aspects of this behavior may be found in the regional mixing model [2-4]. This model has been successfully employed to interpret all available thermal mixing experimental data obtained from the system simulation tests performed in support of the PTS study [3-5].

Similar thermal stratification and mixing behavior may even exist in the presence of very low loop mean flow. In the presence of thermal stratification and effective natural recirculating flows, the dilution transient can be represented by a simple global boron mass conservation equation:

$$\rho V\frac{dC_m}{dt} = q_{SI}(C_{SI} - Cm) + q_L(C_L - C_m) \quad (1)$$

Where ρ is the density (the effect of density variation is neglected); V is the system volume; C_m, C_{SI} and C_L are boron concentrations of flow entering the core, safety injection and loop flow (entering the bottom horizontal leg of the loop seal), respectively; and q_{SI} and q_L are the safety injection and loop flows, respectively. It should be noted that the volume V includes the cold leg, pump, lower plenum, downcomer (excluding the portion above the cold leg) and the vertical leg below the pump and bottom horizontal leg of the loop seal. The downcomer and lower plenum volumes should be partitioned equally among the available loops.

Equation 1 can be integrated analytically to:

$$C_m = \frac{C_{SI}+RC_L}{1+R} + \left[C_o - \frac{C_{SI}+RC_L}{1+R}\right] e^{\frac{-(1+R)t}{\tau}} \quad (2)$$

where

$$\tau = \frac{\rho V}{q_{SI}} \quad (3)$$

and

$$R = \frac{q_L}{q_{SI}} \quad (4)$$

Assuming that initially, the system is filled with borated water with a boron concentration of 1500 ppm, the time variation of boron concentration, C_m, due to the loop flow of unborated water (C_L = 0) for q_{SI} = 7 kg/s, C_{SI} = 2200 ppm and different values of R is illustrated in Figure 3. For example at a pressure of 8 MPa and with the assumption that three steam generators stay active, q_L = 7 kg/s and $R \approx 1$ [6]. With a flow ratio of R = 1, the boron concentration would be more than 1100 ppm.

2.2 Mixing at the Safety Injection Point

For a well mixed condition there must be sufficient loop flow not only to break up the safety injection plume (jet) but also to produce stable flow into the downcomer. Nourbakhsh and Theofanous [7] used the boundary of stability and developed a criterion for the existence of perfect mixing in the presence of loop flow, their stratification/mixing boundary can be expressed by:

$$Fr_{SI,CL} = \left[1 + \frac{Q_L}{Q_{SI}}\right]^{-7/5} \quad (5)$$

where Q_{SI} and Q_L are the volumetric flow rates of the safety injection and the loop, respectively. The Froude number, $Fr_{SI,CL}$ is defined as:

$$Fr_{SI,CL} = \frac{Q_{SI}}{A_{CL}}\left\{gD_{CL}\frac{(\rho_{SI} - \rho_L)}{\rho_{SI}}\right\}^{-1/2} \quad (6)$$

where A_{CL} and D_{CL} are the flow area and the diameter of cold leg, respectively.

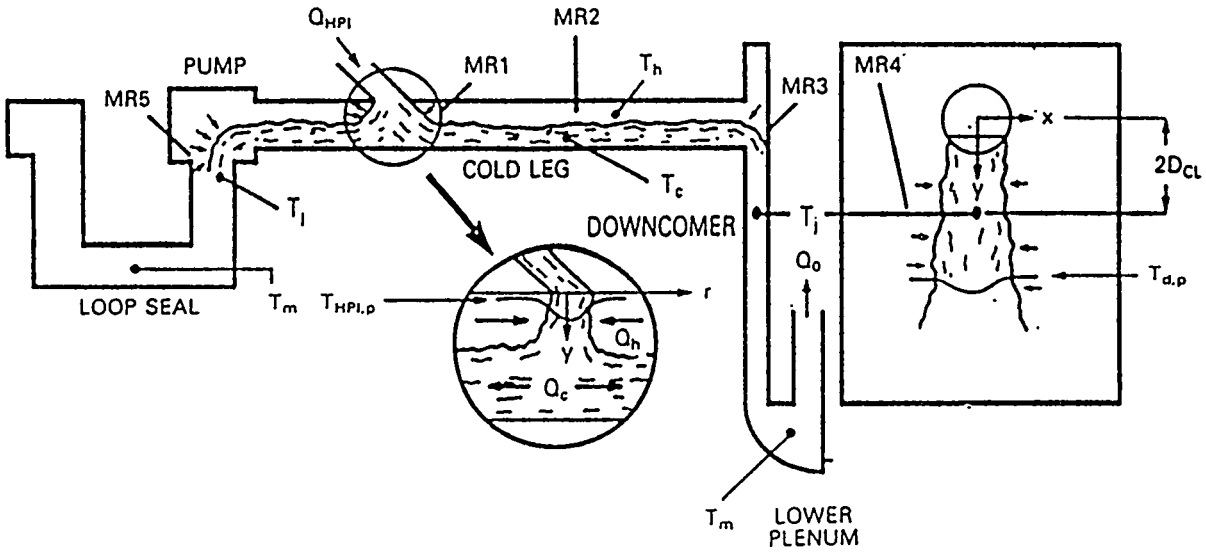

Figure 2. Conceptual Definition of Flow Regime and Regional Mixing Model

This stratification criterion should be considered as providing a high estimate of the flow ratio, R, necessary for ignoring stratification. For perfect mixing, the concentration of diluted flow stream after mixing with the safety injection flow, C_{pm} can be easily quantified by the boron mass balance at the mixing point:

$$C_{pm} = \frac{C_{SI} + RC_L}{1+R} \qquad (7)$$

Typically, natural circulation flows are in the 110 to 250 kg/s range. For a RCS pressure of 4.2 MPa, the safety injection flow is ~ 10 kg/s. In terms of stratification criterion (Eq. 5) parameters, these values correspond to $Fr_{SI,CL} \approx 0.02$ and $R = 15$, indicating perfect mixing except for the lower range of natural circulation flow.

2.3 Mixing in the Downcomer

A highly complicated three-dimensional mixing pattern occurs at the cold leg-downcomer junction. This contribution to mixing is conservatively neglected and the dilute stream exiting the cold-leg is assumed to form smoothly into a planar plume within the downcomer. Under low loop flow conditions, the diluted stream entering the downcomer would be colder due to mixing with the safety injection, than the downcomer coolant. The resulting positively buoyant planar jets decay rapidly, enhancing the mixing and global flow recirculation. However, in the presence of relatively high natural circulation loop flow, the temperature of condensate, even after the mixing with the safety injection flow, would be higher than the downcomer temperature and thus the inlet flow into the downcomer would constitute a negatively buoyant jet (Inverted Fountain). A schematic of both positively and negatively buoyant jets is illustrated in Figure 4.

Except for limited data on maximum penetration distance [8], there have been no experimental or analytical studies on the behavior of negatively buoyant planar jets reported in the open literature. In order to be able to quantify the mixing of a negatively buoyant planar jet of the diluted water with the highly borated downcomer ambient, an extensive analytical study of negatively buoyant jets was performed as a part of the present work [6]. The jet model of Chen and Rodi [9] was adopted for this purpose. The model utilizes the standard equations for natural convection boundary layer type flows with a vertically oriented buoyant force and a K-ϵ-$\bar{T}^2$ differential turbulence model to evaluate the transport terms in the equations.

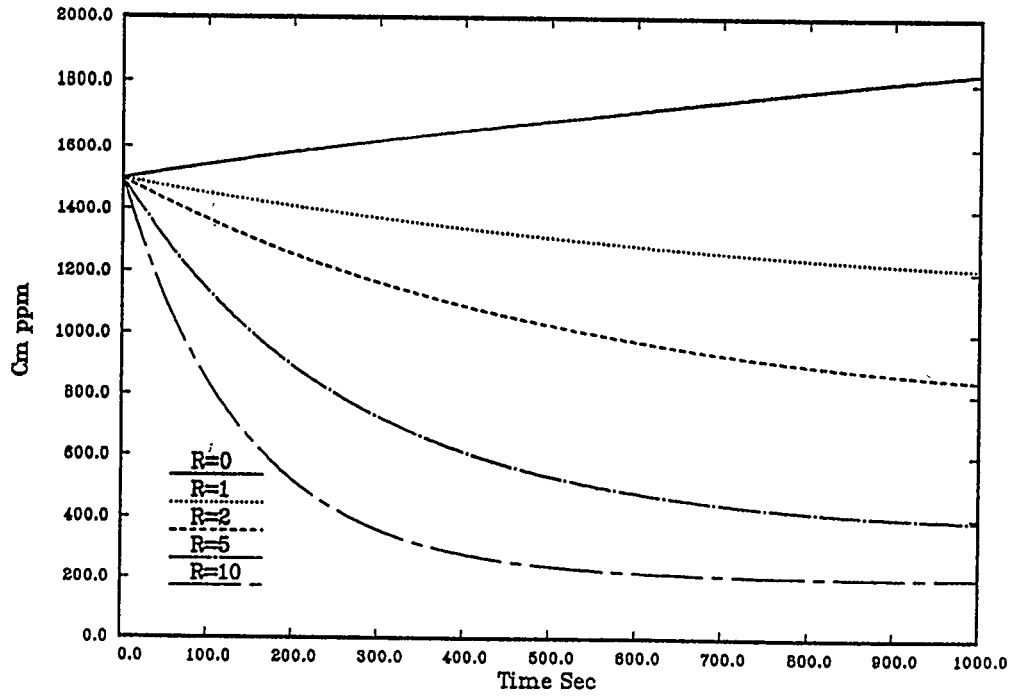

Figure 3. Dilution Transient Under Stratified and Recirculating Flow Regime

The integration was carried out using the Patankar-Spalding method [10]. In order to achieve high computational efficiency this method invokes a coordinate transformation, which utilizes a normalized Von Mises variable; and thus instead of the y coordinate, a nondimensional stream function is used in the transverse coordinate.

Results for the range of small Froude numbers of interest here are presented in Figures 5 through 8. It should be noted that the nondimensional axial and transverse direction X^*, Y^*, Froude number, Fr, nondimensional temperature (or concentration), T^*, and nondimensional velocity U^* are defined as follows:

$$X^* = \frac{x}{2B_o} \tag{8}$$

$$Y^* = \frac{Y}{2B_o} \tag{9}$$

$$T^* = \frac{T-T_a}{T_o-T_a} = \frac{C-C_a}{C_o-C_a} \tag{10}$$

$$U^* = \frac{U}{U_o} \tag{11}$$

$$Fr = \frac{U_o}{\sqrt{2B_o g(\rho_a-\rho_o)/\rho_o}} \tag{12}$$

The results of the turbulent jet model illustrate that at low Froude number, the negatively buoyant planar jets spread rapidly in the lateral dimension with much lower entrainment or mixing as compared to positively buoyant planar jets. For example a negatively buoyant planar jet with a Froude number of 1.5 deaccelerates to less than 50% of its initial velocity, without any significant entrainment or mixing, within less than one initial width of the jet ($X^*<1$). In a negatively buoyant jet, due to the buoyancy force which acts against the flow direction, the flow penetrates to a finite distance in the ambient environment before reversal occurs. It should be noted that the present Parabolic turbulent jet model neglects the effect of return flow. Furthermore, the validity of boundary layer assumptions is questionable near the stagnation point where the axial velocity approaches zero and significant lateral spreading of the jet occurs.

The turbulent jet model was also utilized to predict the maximum penetration distance for negatively buoyant planar jets. If the source is small compared with the maximum penetration distance, the flow will depend only on the buoyancy flux, F_o, and momentum flux, M_o, at the jet source. In this case the flow will not depend explicitly on the volume flux, Q_o. Following an approach similar to the one used by Turner for the

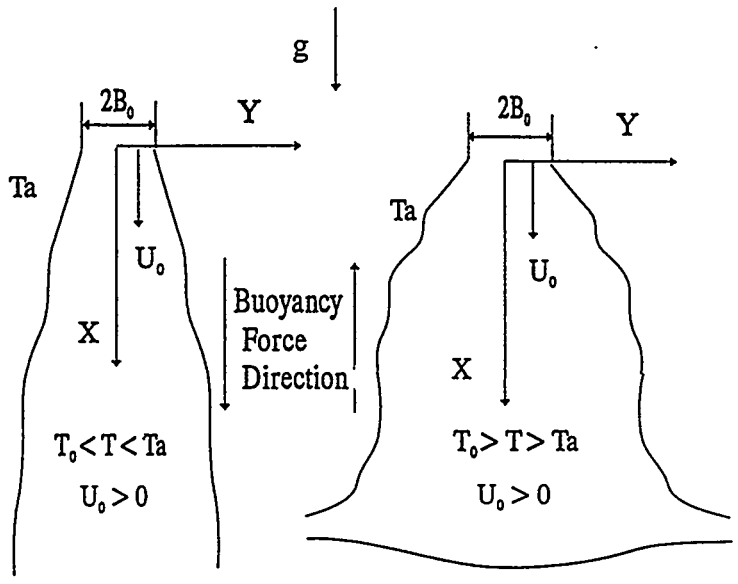

(a) Positively buoyant jet (b) Negatively buoyant jet

Figure 4. Schematic of a Positively and a Negatively Buoyant Jet

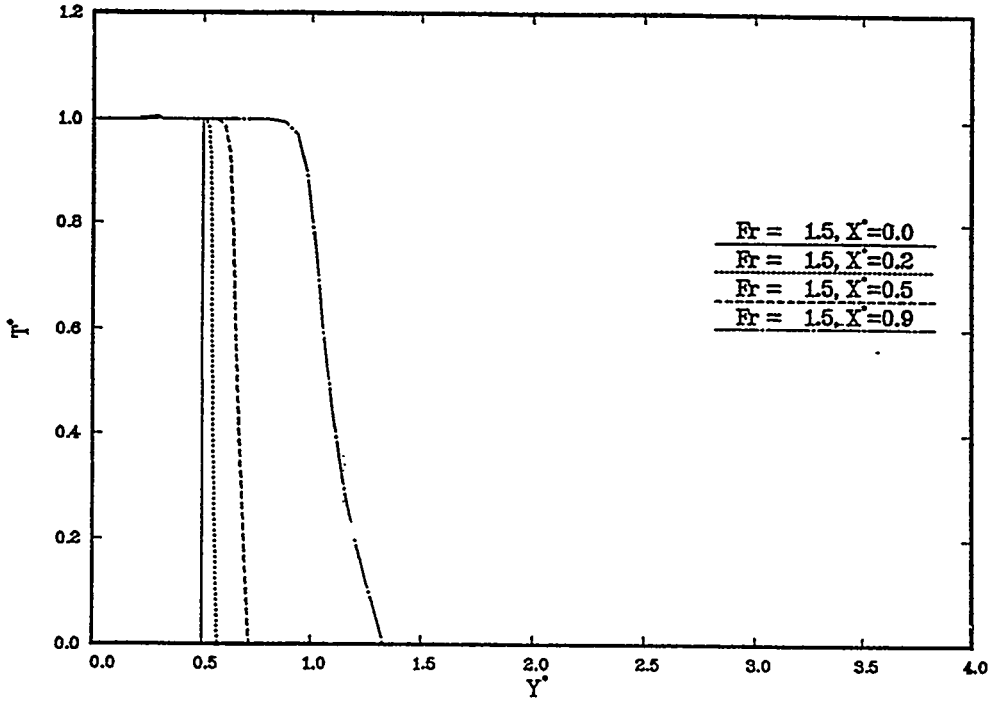

Figure 5. Calculated Results of Temperature (or Concentration) Profiles for a Negatively Buoyant Planar Jet (Fr = 1.5)

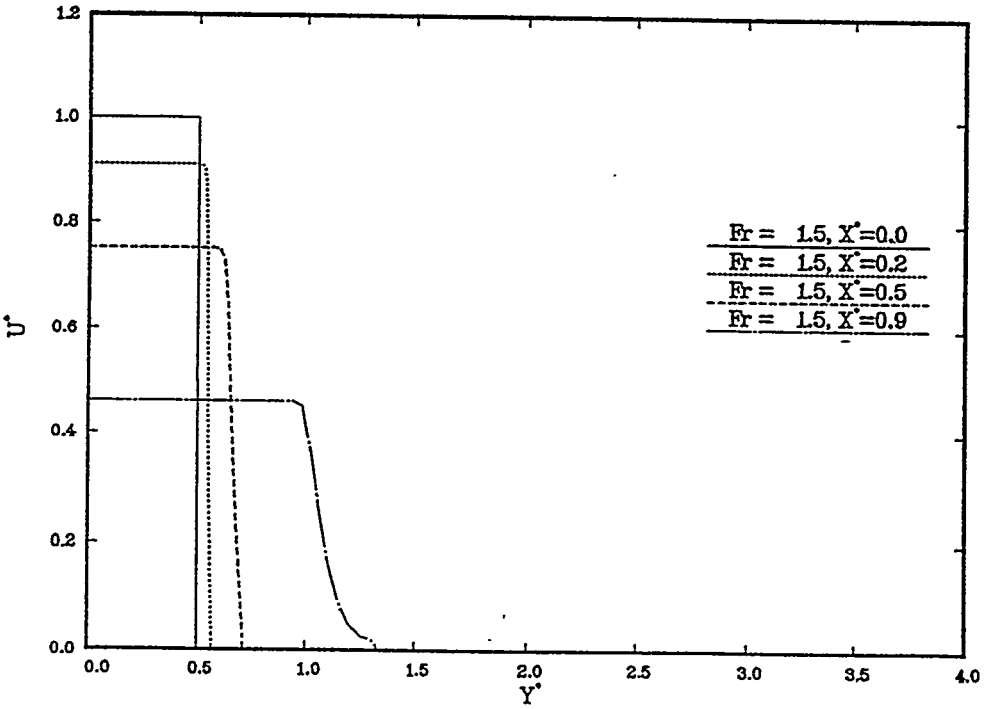

Figure 6. Calculated Results of Velocity Profiles for a Negatively Buoyant Planar Jet (Fr = 1.5)

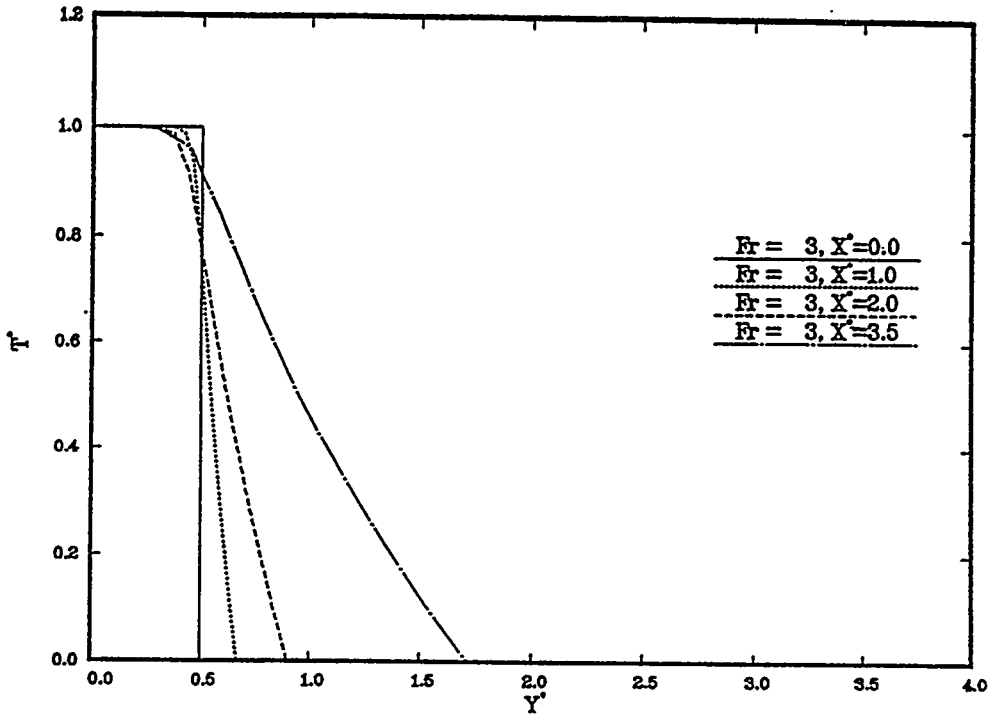

Figure 7. Calculated Results of Temperature (or Concentration) Profiles for a Negatively Buoyant Planar Jet (Fr = 3)

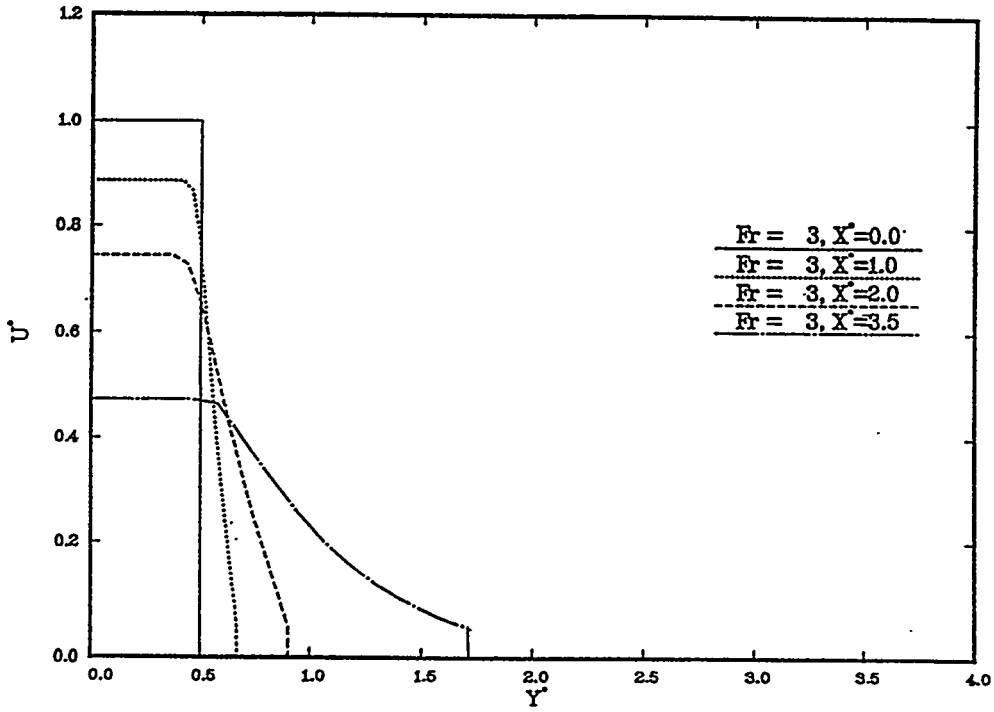

Figure 8. Calculated Results of Velocity Profiles for a Negatively Buoyant Planar Jet (Fr = 3)

case of a circular fountain [11], the maximum penetration distance of a negatively buoyant planar jet, H_{max}, can be defined by the dimensional consistency requirement as:

$$H_{\max} = \text{constant} \times \left[\frac{M_o}{\rho_o}\right] \left[\frac{F_o}{\rho_o}\right]^{-2/3} \quad (13)$$

where

$$M_o = 2B_o\rho_o U_o^2 \quad (14)$$

$$F_o = 2B_o\rho_o U_o g(\rho_a - \rho_o)/\rho_a \quad (15)$$

Combined with the definition of the densimetric Froude number, (Eq. 12), the maximum penetration distance (Eq. 13) can be expressed by:

$$\frac{H_{\max}}{2B_o} = \text{constant} \times F_r^{4/3} \quad (16)$$

The proportionality constant evaluated by the turbulent jet model predictions is 2.42 as shown in Figure 9. Due to computational difficulty, it was not possible to predict the maximum penetration distance for low Froude number jets ($Fr<3$). Assuming that at low Froude number the flow depends on momentum flux and volume flux only, based on the dimensional consistency requirement, the maximum penetration distance, $H_{max}/2B_o$, should be a constant. This is also supported by the experimental data reported by Goldman and Jaluria [8] which indicate a finite value of penetration distance as the Froude number decreases to a very low value. Thus the maximum penetration distance can be correlated by:

$$\frac{H_{\max}}{2Bo} = 2.42\ Fr^{4/3} \text{ for } Fr > 2 \quad (17)$$

A comparison of the present correlation with the data reported by Goldman and Jaluria is also presented in Figure 9.

Assuming that the ambient to the negatively buoyant planar jet in the downcomer behaves as though it is well mixed, the global boron mass conservation equation can be expressed as:

$$\rho V_a \frac{dC_a}{dt} = q_{ent}(C_{mj} - C_a) \quad (18)$$

$$C_{mj} = \frac{C_o + \frac{q_{ent}}{q_o} C_a}{1 + \frac{q_{ent}}{q_o}} \quad (19)$$

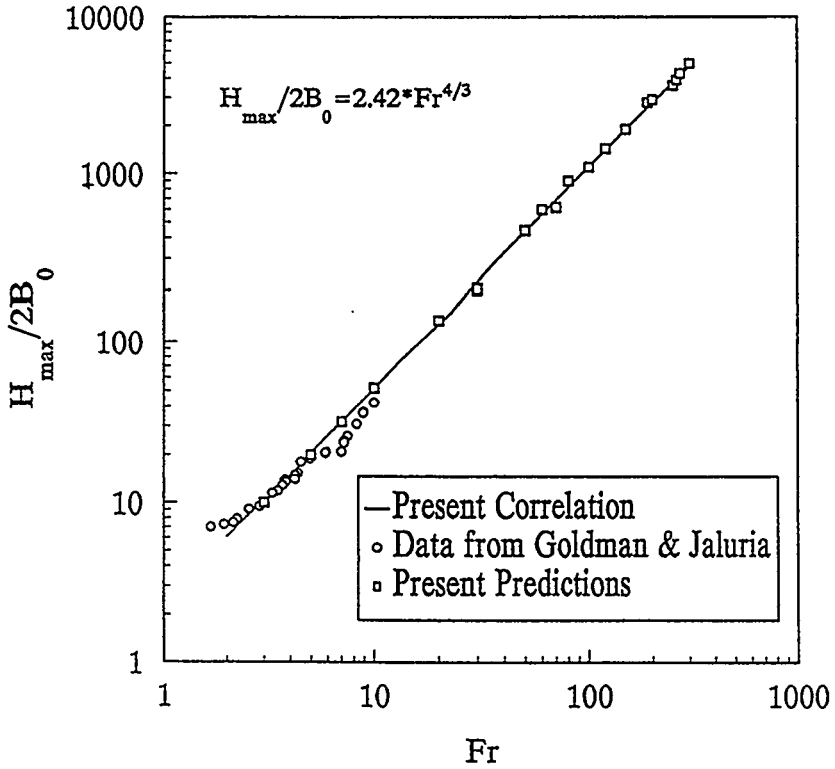

Figure 9. Comparison of Predicted Maximum Penetration Distance of Negatively Buoyant Vertical Planar Jets with Experimental Data

Where ρ is the density (effect of density variation is neglected); C_o, C_a and C_{mj}; are boron concentrations of flow entering the downcomer, the ambient, and mean jet flow entering the lower plenum; respectively; V_a is the volume of ambient; and q_o and q_{ent} are the inlet flow to downcomer and entrainment flow into planar jet, respectively. It should be noted in the case of symmetric flow of diluted water from different loops, the low Froude number negatively buoyant jets entering the downcomer grow rapidly in lateral direction and thus would occupy the whole downcomer circumference before reaching to lower plenum. In this case the volume of ambient would be reduced accordingly.

Equations 18 and 19 can be integrated analytically to:

$$\frac{C_a - C_o}{C_a^o - C_o} = e^{-\frac{\alpha}{1+\alpha}\frac{q_o}{\rho V_a}t} \tag{20}$$

$$\frac{C_{mj} - C_o}{C_a^o - C_o} = \frac{\alpha}{1+\alpha} e^{-\frac{\alpha}{1+\alpha}\frac{q_o}{\rho V_a}t} \tag{21}$$

where

$$\alpha = \frac{q_{ent}}{q_o} \tag{22}$$

The numerical values of α are obtained from the results of jet model.

2.4 Mixing In The Lower Plenum

The diluted stream of water leaving the downcomer will experience some mixing with the highly borated water of the lower plenum before entering the core.

In the presence of thermal stratification (very low loop flow), due to entrainment, the positively buoyant planar wall jet entering the lower plenum carries a flow which is at least one order of magnitude higher than the safety injection flow. Thus the highly borated water in the lower plenum is drawn continuously to the downcomer and cold leg resulting in a very intensive mixing and recirculation in the lower plenum. Indeed the results of thermal mixing experiments related to pressurized thermal shock [5] (under stagnated flow condition) indicate no thermal stratification in the lower plenum (i.e., a well mixed lower plenum).

Under the relatively high natural circulation loop flow (even in the presence of stratification), the loop flow accommodates a significant portion of entrainment and thus there may not be significant recirculation (if any) from the lower plenum back to downcomer. However, the negatively buoyant wall jet of diluted water entering the lower plenum will penetrate to some finite depth before it reaches to a stagnation point and then reverses direction upward toward the core region. The highly borated ambient water in the lower plenum will be entrained into this flow, resulting in a higher boron concentration in the flow entering the core compared with that entering the lower plenum. The detailed quantification of mixing in the lower plenum is beyond the scope of the present study. Some bounding calculations to show the impact of lower plenum mixing are presented in the following section.

3. BOUNDING ANALYSES

Many thermal hydraulic aspects of boron dilution, except the mixing effects, can be analyzed by using system codes such as TRAC and RELAP. The mixing processes underway from the loop seal to the core involve multidimensional one-phase flow effects which typically are not modelled in system codes. Furthermore, these codes exhibit far too much numerical diffusion to be useful for tracking a relatively sharp concentration gradient around the system [1]. Simulation of dilution transients using one of the system codes to provide the thermal hydraulic conditions needed for both the mixing analysis and the reactor physics calculations is beyond the scope of the present study.

The boron dilution necessary to cause fuel damage depends on many factors including the initial shutdown margin, the doppler feedback, the delayed neutron fraction, the neutron lifetime and the speed at which the slug of diluted water moves through the core. The consequence analysis to predict the effect of dilution on fuel integrity is beyond the scope of the present study. However, it should be noted that the results of neutronics calculations [13], based on an approximate synthesis method, obtained within the context of externally caused rapid boron dilution (with an insurge slug velocity corresponding to 13% of rated flow) indicate that a slug with a concentration of 750 ppm entering the core region with an initial 1500 ppm concentration, could result in an excursion that breaches reactivity insertion accident (RIA) criteria.

In this section bounding calculations for boron concentration of coolant entering the core due to subsequent change in flow conditions such as loop seal clearing or re-establishment of natural circulation flow in a typical Westinghouse design 4-loop plant (RESAR-3S) are presented.

3.1 Boron Dilution Due to Loop Seal Clearing

Loop seal clearing has been suggested as a potential mechanism for driving an accumulated slug of diluted water from the loop seals into the core [1]. The experimental evidence on loop seal clearing [12] indicate that the loop seals are cleared only after the liquid level in the vertical leg below the steam generator outlet plenum reaches the top of the bottom horizontal section. During this period of gradual reduction of liquid level in the vertical leg the loop flow entering the bottom horizontal leg of the loop seals is relatively low. As discussed in section 2 (under low loop flow conditions) the safety injection of cold, highly borated water into the cold leg leads to stratification accompanied by counter-current flows and recirculation. For example at a pressure of 8.MPa, and with the assumption that three steam generators stay active, the safety injection flow, q_{SI}, is 7 kg/s. The flow of condensate entering the bottom horizontal leg, q_L, based on condensation rate and the TRAC results of loop seal level change for a 3 in. break reported in Reference 14, is estimated to be $\approx$11.9 kg/s. Under these conditions $Fr_{SI,CL} = 0.013$ and $R \approx 1.7$, indicating flow stratification. Thus the resulting boron concentration of flow entering the core, C_m, can be estimated by using Equation (2) (see also Figure 3). Assuming that initially the system is filled with borated water with a boron concentration of 1500 ppm, the boron concentration after 350 seconds (based on the time duration of level reduction before loop seal clearing reported in Reference 14) is more than 1200 ppm.

3.2 Boron Dilution Due to Re-establishment of Natural Circulation Flow

The re-establishment of natural circulation flow may occur during the refill phase of small break LOCAs (SBLOCAs) as long as the secondary heat sink is available. The magnitude and timing of the natural circulation flow depends on plant geometry, break size and location, emergency core cooling system (ECCS) capacities, equipment failure criteria and operational actions, all of which differ considerably in various designs. In the absence of detailed system code simulation results during the refill phase of small break LOCAs, bounding estimates of the needed thermal-hydraulic conditions for mixing calculations was used to predict the dilution boundary.

If the RCS refill and re-establishment of natural circulation proceed at low pressure (a characteristic of relatively large SBLOCAs) high flow of cold, highly borated water injected into the cold legs, via accumulators or low pressure safety injection system, mixes with the natural circulation flow of unborated water. This leads to a significant increase in boron concentration of the resulting flow before entering the core region. For example for a typical Westinghouse designed 4-loop plant, the low pressure safety injection flow is on the order of 115 kg/s per loop. The natural circulation flow by conservatively assuming 2% core decay power is about 4% of the nominal flow or 175 kg/s per loop [6]. Neglecting the potential for thermal stratification and conservatively assuming perfect mixing, the boron concentration of the resulting flow entering the downcomer estimated by using Equation (7) is 872 ppm. Even without considering any mixing in the downcomer and lower plenum, this level of boron concentration does not result in a power excursion leading to fuel failure.

For the present bounding analyses, it was also assumed that the re-establishment of natural circulation occurs at a RCS pressure higher than accumulator injection setpoint (a characteristic of relatively smaller SBLOCAs). Assuming an RCS pressure of 4.8 MPa ($\approx$700 psia) and a bounding estimate of single phase natural circulation flow of 225 kg/s per loop, the boron concentration of flow after mixing with the safety injection of 12 kg/s (perfect mixing condition) is $\approx$111 ppm. The resulting flow of 237 kg/s into downcomer was assumed to form a planar jet with an initial Froude number of $\approx$1.5. Using the mixing models presented in section 2, with $Va \approx 0.3$ m^3 and $\alpha \approx 0.08$, the transient boron concentration entering the core was calculated for a total condensate volume of 4 m^3 per loop. Calculations were performed under two limiting conditions of mixing in the lower plenum as shown in Figure 10.

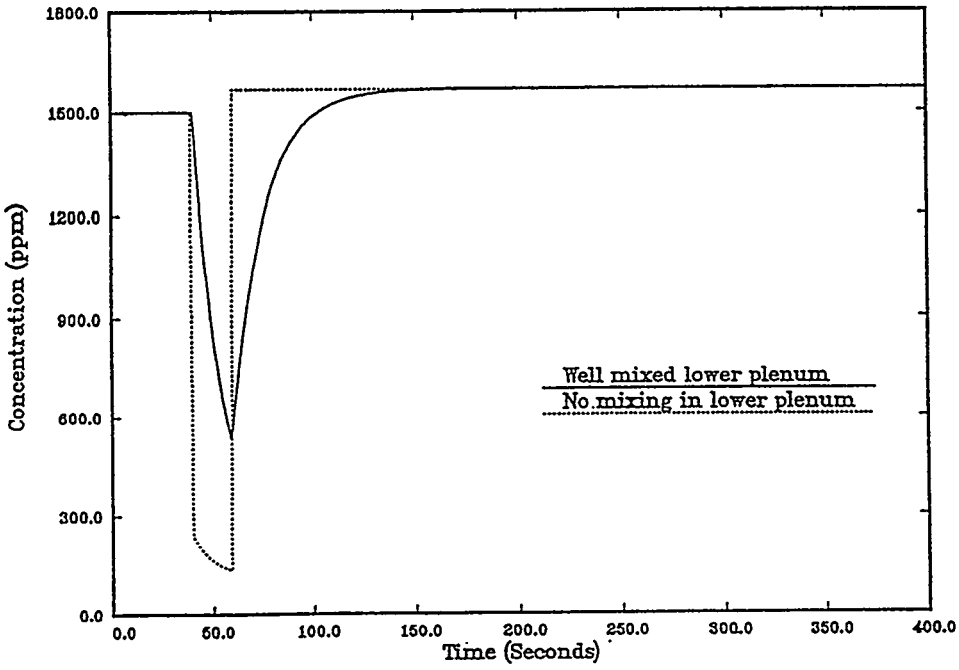

Figure 10. Transient Boron Concentration Entering the Core

4 SUMMARY AND CONCLUSIONS

The mixing processes associated with a slow moving stream of diluted water through the loop seals to the core were examined. The quantitative aspects of different mixing mechanisms and a simplified, yet physically based, methodology for their integration into an overall prediction of the dilution boundary were presented. Bounding analyses for the concentration of boron in the coolant entering the core due to loop seal clearing or re-establishment of natural circulation flow for a typical Westinghouse designed 4-loop plant were also presented.

Experimental studies on loop seal clearing indicate that the loop seals are cleared only after the liquid level in the vertical leg below the steam generator outlet plenum reaches the top of the bottom horizontal section. During this period of gradual reduction of liquid level in the vertical leg, the safety injection of cold and highly borated water into the cold leg leads to stratification accompanied by counter-current flow and recirculation. An illustrative prediction for a typical Westinghouse-designed, 4-loop plant indicates that the boron concentration of flow entering the core does not fall below 1200 ppm when the initial boron concentration in the vessel is 1500 ppm.

If the RCS refill and re-establishment of natural circulation flow proceeds at low pressure (a characteristic of relatively large SBLOCAs), the loop flow of unborated water mixes with the highly borated water injected into the cold leg via accumulators and the low pressure safety injection system. This leads to a significant increase in boron concentration of the resulting flow before it enters the core region.

For the present scoping analyses, it was also assumed that the re-establishment of natural circulation flow occurs at a RCS pressure higher than the accumulator injection setpoint (a characteristic of relatively smaller SBLOCAs). For the bounding cases considered, the boron concentration of the loop flow after mixing with the high-pressure injection (HPI) is 111 ppm. The resulting low Froude number negatively buoyant jets entering the downcomer (assuming symmetric flow of diluted water from different loops) grow rapidly in the lateral direction without significant mixing (and will occupy the entire downcomer circumference before reaching the lower plenum. Sensitivity calculations indicate the importance of quantification of mixing in the lower plenum for a more realistic prediction of boron concentration entering the core region.

For the purpose of more realistic assessment of the boron dilution and relevant mixing processes, the thermal-hydraulic conditions during the refill phase of small break LOCAs and the effects of secondary side depressurization on primary inventory recovery and re-establishment of natural circulation should be further evaluated. The detailed quantification of mixing in lower plenum is also desirable.

ACKNOWLEDGEMENTS

The authors wish to extend their appreciation to Dr. D. Ebert of U. S. Nuclear Regulatory Commission and Professor A. Baretta of Pennsylvania State University for their support and encouragement.

NOMENCLATURE

Latin Letters

A	area
B	initial half width of a planar jet
C	concentration
D	diameter
F_o	buoyancy flux at the jet source
Fr	Froude number
g	gravitational acceleration
H	height
M_o	momentum flux at the jet source
Q	volumetric flow rate
q	mass flow rate
R	flow ratio (See Eq. 4)
T	temperature
t	time
U	velocity
V	volume
X	coordinate in axial direction
Y	coordinate in transverse direction

Greek Letter

α	nondimensional entrainment flow (see Eq. 22)
ρ	density
τ	mixing time constant under no loop flow condition (see Eq. 3)

Subscripts

o	initial
α	ambient
CL	cold leg
ent	entrainment
L	loop
m	mixed mean
max	maximum
SI	safety injection

REFERENCES

1. J. Havärinen, "An Inherent Boron Dilution Mechanism in Pressurized Water Reactors," The 5th International Topical Meeting on Reactor Thermal Hydraulics, NURETH-5, Salt Lake City, USA, 1992.

2. T. G. Theofanous and H. P. Nourbakhsh, "PWR Downcomer Fluid Temperature Transients Due to High Pressure Injection at Stagnated Loop Flow," Proceeding of Joint NRC/ANS Meeting on Basic Thermal Hydraulic Mechanisms in LWR Analysis, Bethesda, MD, 1982, NUREG/CP-0043, pp. 583-613.

3. H. P. Nourbakhsh and T. G. Theofanous, "Decay of Buoyancy Driven Stratified Layers with Application to Pressurized Thermal Shock, Part I: The Regional Mixing Model," Nuclear Eng. & Design, (in Press).

4. T. G. Theofanous, H. P. Nourbakhsh, P. Gherson and K. Iyer, "Decoy of Buoyancy Driven Stratified Layers with Application to Pressurized Thermal Shock," NUREG/CR-3700, 1984.

5. T. G. Theofanous and H. Yan, "A Unified Interpretation of One-Fifth to Full-Scale Thermal Mixing Experiments Related to Pressurized Thermal Shock," NUREG/CR-5677, 1991.

6. H. P. Nourbakhsh and Z. Cheng, "Potential for Boron Dilution During Small Break LOCAs in PWRs," Brookhaven National Laboratory Report, 1994.

7. H. P. Nourbakhsh and T. G. Theofanous, "A Criterion for Predicting Thermal Stratification Due to High-Pressure Injection in a Circulating Reactor Loop," Nuclear Science & Engineering, Vol. 94, pp. 77-79, September 1986.

8. D. Goldman and Y. Jaluria, "Effect of Opposing Buoyancy on the Flow in Free and Wall Jets," J. Fluid Mech., Vol. 166, pp. 41-56, 1986.

9. C. J. Chen and W. Rodi, "A Mathematical Model for Stratified Turbulent Flows and Its Application to Buoyant Jets," XVIth Congress, International Association for Hydraulic Research, San Paulo, 1975.

10. S. V. Patankar and D. B. Spalding, "A Finite Difference Procedure for Solving the Equations of the Two Dimensional Boundary Layer," Int. J. of Heat & Mass Transfer, Vol. 10, pp. 1389-1411, 1968.

11. J. S. Turner, "Jets and Plumes with Negative and Reversing Buoyancy," J. Fluid Mech., Vol. 26, pp. 779-792, 1966.

12. N. Lee, "Discussion on Loop Seal Behavior During Cold Leg Small Break LOCAs of a PWR," Nuclear Engineering and Design, Vol. 99, pp. 453-458, 1987.

13. D. J. Diamond, P. Kohut, H. Nourbakhsh, K. Valtonen, and P. Secker, "Probability and Consequences of Rapid Boron Dilution in a PWR," NUREG/CR-5819, BNL-NUREG-52313, 1992.

14. C. D. Fletcher and M. Kulberg, "Break Spectrum Analysis for Small Break Loss of Coolant Accidents in a RESAR-35 Plant" NUREG/CR-4384, INEL, March, 1986.

NUMERICAL BORON MIXING STUDIES FOR LOVIISA NUCLEAR POWER PLANT

Peter Gango
IVO International Ltd
01019 IVO, Finland

ABSTRACT

A program has been started for studying numerically boron mixing in the downcomer of Loviisa NPP (VVER-440). Mixing during the transport of a diluted slug from the loop to the core might serve as an inherent protection mechanism against severe reactivity accidents in inhomogenous boron dilution scenarios for PWRs. The commercial general purpose Computational Fluid Dynamics (CFD) code PHOENICS is used for solving the governing fluid flow equations in the downcomer geometry of VVER-440. So far numerical analyses have been performed for steady state operation conditions and two different pump driven transients. The steady state analyses focused on model development and validation against existing experimental data. The two pump driven transient scenarios reported are based on slug transport during the start of the sixth and first loop respectively. The results from the two transients show that mixing is case and plant specific; the high and open downcomer geometry of VVER-440 seems to be advantageous from mixing point of view. In addition the analyzing work for the "first pump start" scenario brought up some considerations about flow distribution in the existing experimental facilities.

1 INTRODUCTION

Inhomogenous boron dilution has recently become one of the most important issues in PWR safety. It has been found out that certain operational or accidental conditions might induce formation of slugs with low boron concentration in the primary circuit loops of a PWR [1,2,3]. If such a slug is transported unmixed to the core there is a risk for a reactivity accident. This transport may occur during a Reactor Coolant Pump (RCP) start or reestablishment of natural circulation. However, in many scenarios the boron content of the diluted slug is supposed to increase during the transport due to mixing in the downcomer. Thus mixing serves as an inherent protection mechanism, which diminishes the risk and might eliminate it completely.

At present there are two possible methods available for studying mixing in the downcomer of a PWR; scaled down model experiments and numerical simulation. The scaling principles for forced flow conditions allow relatively small scale models to be used (1/5), but in natural circulation conditions large and expensive test facilities are needed for a proper scaling. The rapid development of computers has made it possible to make use of CFD in studying large 3D problems. However, in nuclear applications the numerical models require experimental validation to be accepted as tools for solving crucial problems, even if commercial widely used codes were used. Therefore at present the most common procedure for studying mixing of boron in a PWR downcomer is a combined experimental and numerical approach [3,4]. Small scale model experiments are used for code validation purposes and in the cases were scaling problems exist, the scaling is done by the numerical model.

This paper describes the current approach applied at Loviisa NPP for studying boron mixing in the downcomer of the reactor. Loviisa NPP is owned and operated by Imatran Voima Oy and consists of two Russian VVER-440 type reactor units, 445 MWe each. The primary circuit lay-out is shown in figure 1 and the pressure vessel and its internals in figure 2. The total coolant volume of the primary circuit is about 200 m^3 (pressurizer not included). The six primary loops have a volume of 16 m^3 each. The volumes of the downcomer and the lower plenum are 20 m^3 and 27 m^3 respectively. The large coolant volumes in the downcomer and in the lower plenum compared to the loop volume (ratio 3:1) show that a considerable mixing potential exists. This favorable geometrical feature is specific to the VVER-440 design; a typical volume ratio for western PWRs is 1:1.

2 THE MIXING PROCESS

The mixing of boron in the downcomer occurs by convection, that is by the combined process of advection and diffusion. The general conservation equation for a scalar C in a flow field can be written as

$$\frac{\partial \rho C}{\partial t} + u_i \frac{\partial \rho C}{\partial x_i} = \frac{\partial}{\partial x_i}\left(D \frac{\partial \rho C}{\partial x_i}\right) + S \,, \qquad (1)$$

where D is the diffusion coefficient, S the source term and subscript i refers to cartesian co-ordinate direction. Although the advection and diffusion terms are treated separately in the equation the mixing process itself is a complex combination of the phenomena. In turbulent flows the local concentration gradients are smoothened out by turbulence and finally by molecular diffusion. In typical downcomer flow conditions (operation with pumps or natural circulation) the molecular effects are neglible from the large scale mixing point of view.

In modeling of the mixing process most commonly the effect of turbulence on mixing is implemented in the diffusion coefficient. This effective diffusion coefficient is highly dependent on flow conditions. In CFD usually the local diffusion coefficient is calculated with a given turbulent Schmidt number from an eddy viscosity field produced by the turbulence model used. In more advanced turbulence models the eddy viscosity concept and the turbulent diffusion coefficient are not used, instead direction dependent turbulent fluxes are calculated [5].

3 NUMERICAL APPROACH

In our numerical modeling approach the PHOENICS code is used for solving the governing fluid flow equations. In the developed model the time dependent, Reynolds averaged elliptic Navier-Stokes equations for uncompressible, isothermal flow are solved by using implicit time integration. The body-fitted co-ordinate option in the code is made use of to reproduce the complex geometry of the downcomer [6].

The "traditional" first order upwind discretisation method for the advection terms in the equations is known to produce artificial smoothing or numerical diffusion in coarse grid solutions. The role of numerical diffusion in boron mixing can be controlled by densing the calculational grid, but the current computer capacity sets limits to the usage of this procedure. To diminish the undesired effect of numerical mixing, built-in higher order discretisation scheme options in PHOENICS were taken in use. Second or third order

discretisation was used for all momentum equations and scalar equations including the turbulence quantities. The usage of higher order discretisation schemes, however, does not completely solve the problem of numerical diffusion. The role of numerics in the solution must be found by grid independency studies and time step variation. The numerical effects have to be small or insignificant to prevent false conclusions about the efficiency of mixing.

At this stage only the built-in standard k-ε model has been used for turbulence modeling. The k-ε model is known to have weaknesses, but the simple structure compared to more advanced models makes its usage attractive. The most severe uncertainties concerning the usage of k-ε turbulence model in the mixing studies come from the behavior in rapidly accelerating flows and from the well known difficulties in modeling buoyancy induced turbulence.

4 CONSIDERATIONS ON EXPERIMENTS AND MODEL VALIDATION

Model experiments for studying mixing of diluted slugs in the downcomer of PWRs are being performed at least in Sweden, France and Russia. Interestingly enough, all these model experiments have the same scaling factor 1/5. Full scale mixing experiments in natural circulation conditions were performed as a part of the UPTF-TRAM program in Germany.

At the moment many of the studies seem to be concentrated on the scenario "first pump start in diluted loop". In this scenario the diluted slug is transported from the loop to the core by starting a main circulation pump. The flow in the starting loop accelerates rapidly. Flow is distributed to counter flow in the open non-operating loops and to the core. The distribution ratio of the flows during start-up is determined by friction, but also by acceleration effects due to the different inertias of the flow paths. In the beginning of the transient, acceleration effects determine the distribution. Later on, when velocities increase, the friction effects take over. The proper flow distribution is important to reproduce a correct slug behavior and flow field in the downcomer. Due to the importance of the inertias for the flow distribution, geometrical similarity of the whole primary circuit should be maintained in model experiments. Alternative measures that produce the correct distribution can be considered, of course. Some of the current experimental facilities do not reproduce the correct distribution due to incomplete design of loop geometry. The distribution is set by valves, which are adjusted only for the steady state condition. Thus, the result from these experiments serve only as reference data for numerical model validation.

A rough validation of the flow field calculated by our numerical model was

performed against model experiments in steady state flow conditions with a different number of operating loops. The purpose of the original model experiments were to study the hydraulic performance of the downcomer and the elliptic bottom of VVER-440. The qualitative behavior of the calculated velocity profiles was seen to be correct, but unfortunately detailed comparison of the results is not possible [7].

Another rough validation of steady state calculations was done against measured temperature fields in the real reactor operating at full flow rate in all six loops. The measurements were performed at Loviisa 2 and they show a strongly sectorized flow field in the downcomer, which indicates limited mixing between the flows of different loops [8]. Similar results have been obtained for the VVER-440 reactors at Paks (Hungary) [9]. Figure 3a shows the measured mixing factors at Loviisa 2 and 3b the corresponding calculational results. The results of the numerical calculations behave correctly, but the model seems to underestimate mixing. The reasons for the underestimation are assumed to be found both in the numerical model and in the measurements. Firstly, the calculated data is collected in the lower support plate of the the fuel extension protection tubes. This means that mixing occuring in the protection tube unit (volume $\approx$17 m^3) is completely neglected in the model. Secondly, the mixing coefficients given by the measurements are considered not to be very accurate because of the measurement techique used.

It is assumed that model validation in natural and mixed convection conditions needs more effort than the forced convection cases. The standard k-ε turbulence model is known to have difficulties in describing buoyancy induced turbulence. In our approach the buoyancy extended numerical models will be validated against mixing experiments performed for studying Pressurized Thermal Shocks (PTS) caused by cold High Pressure emergency coolant Injection (HPI). A comprehensive series of such experiments for VVER-440 geometry was performed at Imatran Voima Oy in the mid 80s [10].

5 STUDIED CASES

In the following the results of two pump driven forced convection cases are reported. From mixing point of view the two cases are completely different and they demonstrate the influence of studied scenario and applied boundary conditions.

5.1 Sixth loop start by opening the main gate valve

5.1.1 Description of case

The VVER-440 reactors are equipped with Main Gate Valves (MGV), which enable operation of the plant with isolated loops. The scenario is based on the assumption that the reactor is operating with five loops and the sixth loop is taken in use by starting the pump against the MGV and then opening the valve. If diluted coolant is present in the loop, it will be transported to the core. This measure is not in accordance with current procedures and the case is considered as a residual risk scenario.

The flow in the starting loop increases as the valve opens. The opening of the valve lasts about 1 minute, which means that the original content of the whole loop is injected to the downcomer before full flow rate is reached. The injection of the hot leg ends at about 30 seconds. With increasing flow the loop occupies a larger sector of the downcomer. In this sectorized flow pattern mixing occurs almost only at the boundaries to neighbour loops. Therefore proper mixing is expected only in the beginning of the transient when the sector is narrow.

In the studied case the diluted slug is assumed to fill the hot leg of the starting loop (3 m^3). In the steam generator the shape of the slug ends are changed due to different flow path lengths. Two different plug shapes were studied, one with stepwise fronts and the other with smoothened fronts due to mixing in the steam generator. Here only the results from the smoothened pulse case are reported in detail.

5.1.2 Grid and boundaries

The computational grid for the case is shown in figure 4. The grid consists of 70000 active cells. Cold leg piping is included corresponding to a length of two pipe diameters. The number of cells and grid lay-out used in the final simulations are based on introductory studies concerning grid density and setting of the boundary conditions. The outlet boundary is set in the protection tube unit for the fuel extensions about 0.5 m below core inlet. The uniform flow field in the protection tube unit made it possible to collect core inlet data already at the level of the lower support plate of the protection tubes. By this procedure we could eliminate additional numerical effects to affect the results. Thus the real mixing in the protection tube unit is not taken into account either.

The mass flow boundaries at loop inlets were set according to the precalculated

flow rate behavior shown in figure 5. The different parts of the loop are marked in the figure. At model outlet (core inlet) fixed pressure conditions were set. Wall friction in the cells next to solid boundaries was treated with the standard logarithmic wall function approach. Porosity factors and the corresponding sources of friction pressure loss were used to model the perforated plates in the bottom area and the flow conductors in the upper part of the downcomer.

The scalar representing the boron content of the slug is treated in normalized form by setting the original boron concentration deficit of the slug equal to unity. Therefore in the results at core inlet, the value of the scalar gives directly a mixing factor to be used for different original boron concentrations of the slug. The concentration profiles at model inlet for the two pulse shapes are shown in figure 6.

5.1.3 Results

The results confirmed the assumption of poor mixing in sectorized flow conditions. The propagation of the slug in the downcomer is illustrated in figure 7 and the corresponding core inlet concentrations in figure 8. Figure 9 shows the propagation of the slug in the protection tube unit. In the square pulse case totally unmixed parts of the slug were found at core inlet. In the second case with the smoothened pulse the peak value had decreased by 10 %.

The influence of numerics was studied especially with the square pulse. The results from a comparison of different discretisation schemes are shown in figure 10. The performance of different schemes was also separately tested before [11]. Accordingly, the schemes Monotonic Second Order Upwind (MSOU), Quadratic Upstream Interpolation for Convective Kinematics (QUICK) and Monotonic High Accuracy Upwind (MHAU) were chosen for further testing. The higher order schemes give far more accurate results than the first order upwind scheme (UDS). In the figure a reference curve is plotted for a scalar (MSOU -discretisation), were the diffusion term of equation 1 was not activated. The sensitivity for chosen time step length is shown in figure 11. Decreasing the time step length from 0.05 s to 0.025 s does not increase the peak values, but sharpens the fronts. Consequently the shorter time step was used in the smoothened pulse case.

5.2 First pump start in open loop

5.2.1 Description of case

The second pump driven scenario is based on the transient caused by the first pump start in a diluted open loop. All MGVs are assumed initially to be open and the loops to be stagnant. The flow in the starting loop accelerates fast; in Loviisa NPP the starting time of the pump in hot shutdown conditions is 13 seconds. In the other open loops counter flows develop. Initially the diluted slug is assumed to occupy the whole volume of the loop (16 m^3). Therefore the slug injection starts immediately when the transient begins and ends at 13.5 seconds, which is just after the full flow rate has been achieved. The acceleration is assumed to be linear.

5.2.2 Grid and boundaries

The computational grid used in the second pump driven scenario had almost the same lay-out as in the first case. Somewhat less cells were used to speed up the calculation, in this case the grid consisted of 63000 active cells. All other boundaries except the inlets and the outlets were set equal to the first scenario.

The only flow boundary condition given for performing the calculation was the linearly increasing flow in the starting loop. The model outlets at the non-operating loop ends and at core inlet were set by fixing the pressure to a common value for describing the pressure in the upper plenum of the reactor. However, this procedure required additional modelling of the primary circuit components that were not included in the model, that is primary piping, steam generators and the core. Their effect was modelled as acceleration pressure differences in the cells before the model outlet cells. The friction pressure losses in the parts not inluded were modelled in the same cells. The setting of the flow boundaries would be much easier with given flows in each loop and the core measured in the real reactor or in a correctly scaled model.

5.2.3 Results

The results of the calculations show that very complex flow patterns develop in the downcomer in this scenario. The injection is distributed into two main jets, one on each side of the downcomer. In addition several secondary flows are seen in various parts of the

downcomer. Especially strong swirling occurs in the areas close to the non-operating loop nozzles and below the injection loop. Figure 12 shows the final steady state flow conditions in the downcomer.

The flow distribution during the transient is shown in figure 13. In the beginning the flow is directed almost totally to the core. Later on the distribution stabilizes at the steady state value, an overshoot in the distribution curve is seen before the final stabilizing.

The complex flow field promotes strong mixing of the slug in the downcomer. The slug behavior is shown in figures 14 - 17. Although the slug divides into several parts a clearly distinguishable main front propagates towards the core at the opposite side of the downcomer (compared to the injection loop YA11). Parts of this main front enters the core unmixed. However, the unmixed regions are local and they arrive at core inlet at different points of time. Figure 16 shows the importance of activating higher order discretisation in the scalar equation, the results with the first order upwind scheme show considerable numerical smoothing. The resulting slug mass flows in the model are shown in figure 18.

It must be pointed out that the slug size in the studied case was set equal to the volume of the whole loop. The results confirm that the large and high downcomer of VVER-440 compared to loop size is beneficial for mixing. Additionally the open structure of the downcomer (no hot leg penetrations, no thermal shields) connected to effective flow resistances in the elliptic bottom enables development of an advantageous flow field. Though it seems that the content of the whole loop can not be properly mixed, we can conclude that smaller slugs certainly will experience efficient mixing in this scenario. Sensitivity studies concerning grid density, model lay-out, boundary conditions and slug size are going on.

6 FURTHER WORK

Further work for studying boron mixing in Loviisa NPP will consist of a validation of a buoyancy extended numerical model against PTS -experiments. The validation process will be followed by a comprehensive study of different scenarios with natural circulation restart in the diluted loop in shut-down or accidental conditions. In these cases the HPI and the density differences are expected to produce complex flow patterns that promote mixing and might completely prevent the unmixed transport of the slug to the core. Experimental evidence on such flow fields is seen in the PTS experiments. The biggest problem of these scenarios will be the setting of boundary conditions; they can be obtained either from simple assumptions and hand calculations, or for example from RELAP -analyses. Inevitably a wide series of simulations will be needed to study the different scenarios. Further

work on the pump driven cases is not considered necessary at this stage. Separate experimental studies are needed only if the numerical results are not satisfactory and/or the threshold to severe reactivity accidents is too narrow for important scenarios.

7 CONCLUSIONS

In the inhomogenous boron dilution problem mixing serves as an inherent protection mechanism. According to the numerical studies for Loviisa NPP reported in this paper mixing is highly case and plant dependent. In the first pump driven scenario "sixth loop start" mixing was reported not to be very efficient. However, the second studied scenario "first pump start" indicated quite efficient mixing even with a slug size corresponding to the volume of the whole loop.

The performed analyses show that CFD is becoming a general purpose tool for complicated single-phase problems in nuclear reactor thermal-hydraulics. At the moment the largest obstacle for a real break-through is the lack of reported experimental and validation data. In the nuclear CFD applications model validation is especially important for safety reasons.

REFERENCES

[1] Jacobson, S. Some local dilution transients in a pressurized water reactor. Linköping University, Diploma thesis no. 171, Sweden, March 1989.

[2] Hyvärinen, J. An inherent boron dilution mechanism in pressurized water reactors. Fifth International Topical Mtg. on Reactor Thermal Hydraulics (NURETH-5), Salt Lake City, September 1992.

[3] Alvarez, D. et al. Three dimensional calculations and experimental investigations of primary coolant flow in a 900 MW PWR vessel. Fifth International Topical Mtg. on Reactor Thermal Hydraulics (NURETH-5), Salt Lake City, September 1992, Vol. II, pp. 586-592.

[4] Jacobson, S. Risk evaluation of local dilution transients in a pressurized water reactor. Linköping University, Studies in Science and Technology, Dissertations No. 275, 1992.

[5] Rodi, W. The simulation of turbulence in practical flow calculation. In: Proceedings of Basel World CFD User Days 1992. Basel 24-28 May 1992.

[6] Spalding, D.B. PHOENICS Beginner's Guide.

[7] Investigation of the reactor hydrodynamic characteristics on models. GKAE report by OKB Gidropress, 1976, originally in Russian (proprietary).

[8] Tsimbalov, S.A et al. Coolant temperature distribution at VVER-440 core inlet. Atomnaya Energiya, Vol 52, No. 5, pp. 304 - 308, May 1982.

[9] Elter, J. et al. Opredelenie koefficientov peremešivanija neobhodimyh dlja vosstanovlenija polja vhodnyh temperatur (Determination of mixing coefficients for calculation of temperature distribution at core inlet). In: Teplofizika 88, Teplotehničeskaja bezopasnost' jadernyh reaktorov VVER, Svornik dokladov iz seminara SEV, Warzava, September 1988, Vol. 1 (in Russian).

[10] Tuomisto, H. Thermal-hydraulics of the Loviisa reactor pressure vessel overcooling transients. Imatran Voima Oy Research Reports, IVO-A-01/87, Helsinki, 1987.

[11] Gango, P. Loviisa 1, Development of CFD -model for the reactor downcomer. IVO International Ltd, working report LO1-K859-136, 12 September 1994 (in Finnish).

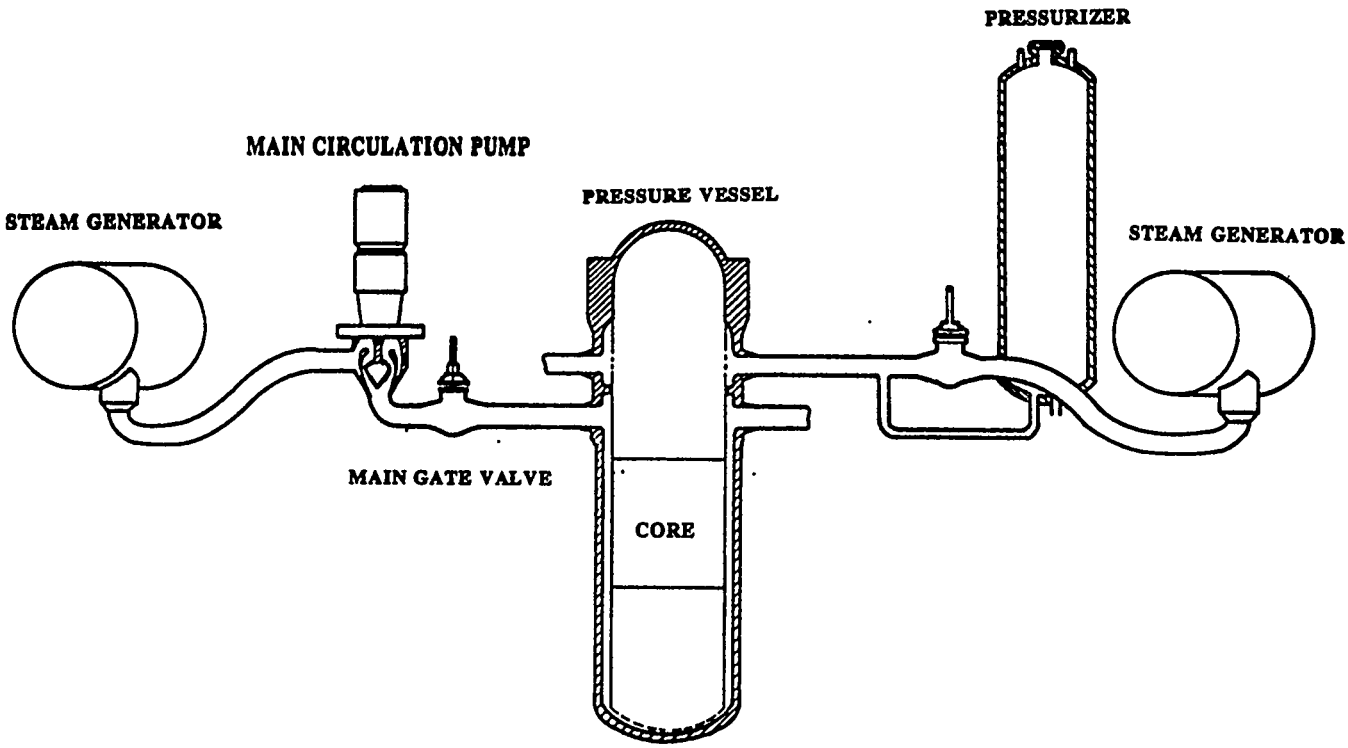

Figure 1. Loviisa 1 primary circuit lay-out

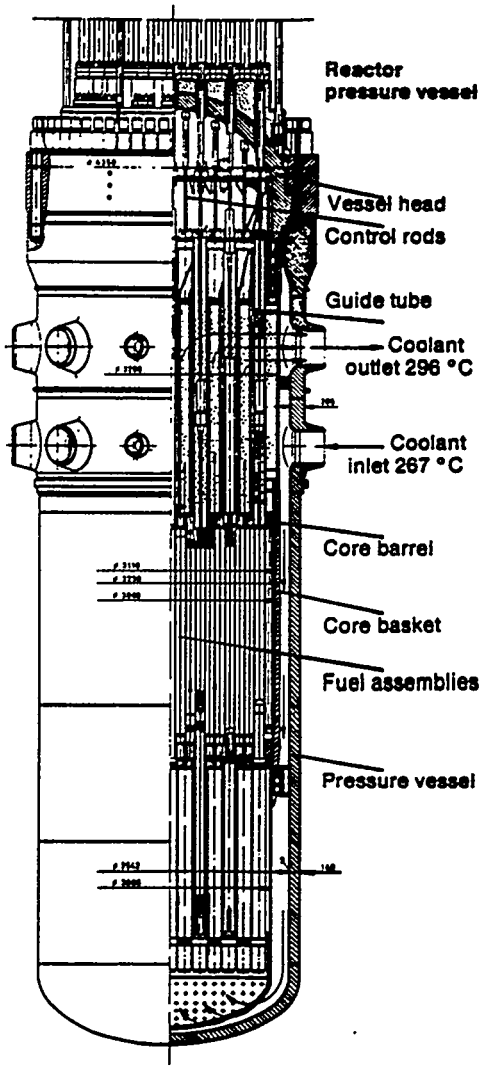

Figure 2. Loviisa 1 pressure vessel and internals

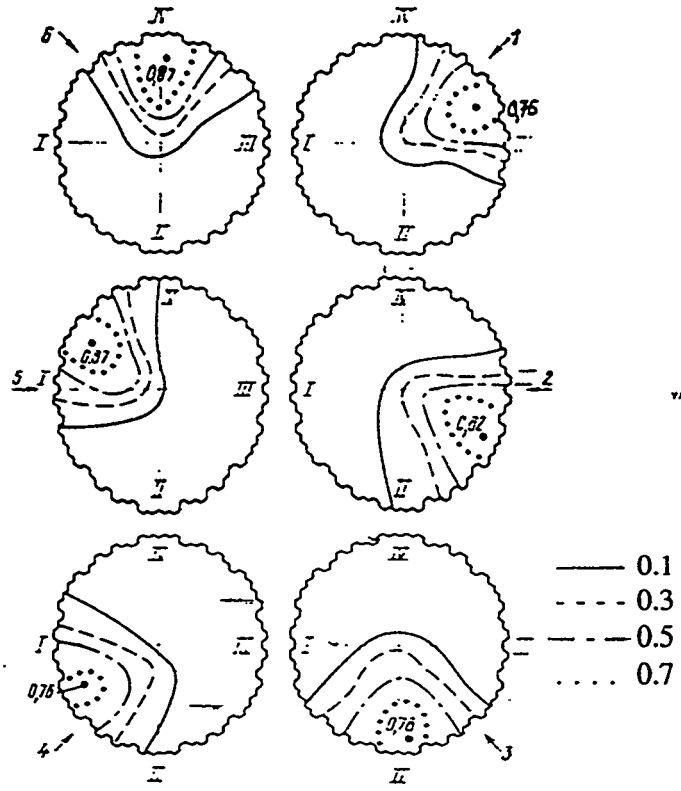

Figure 3a. Measured mixing factors at Loviisa 2 core inlet [8]

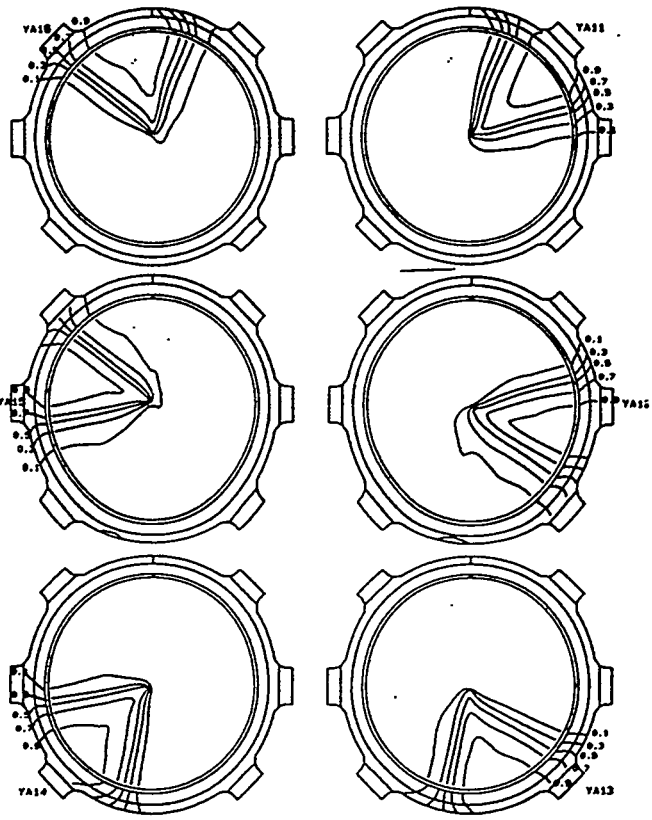

Figure 3b. Calculated mixing factors at core inlet

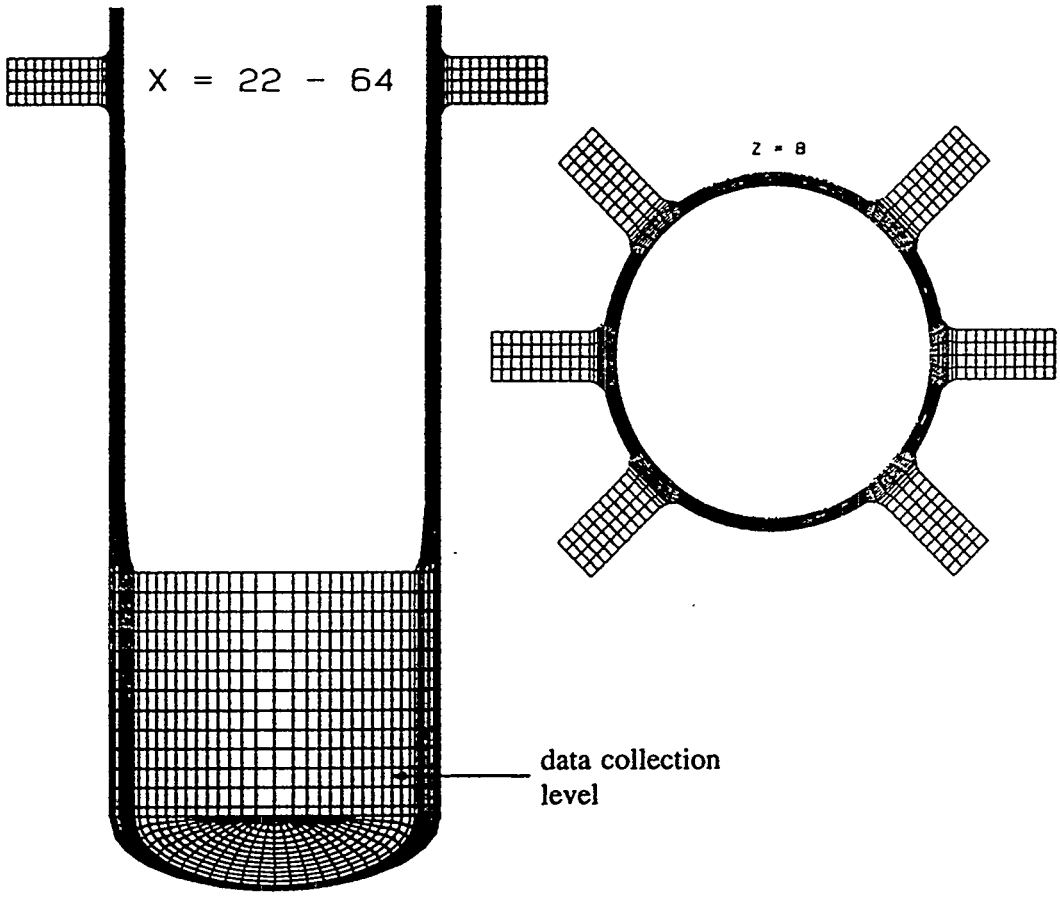

Figure 4. Computational grid, sixth loop start

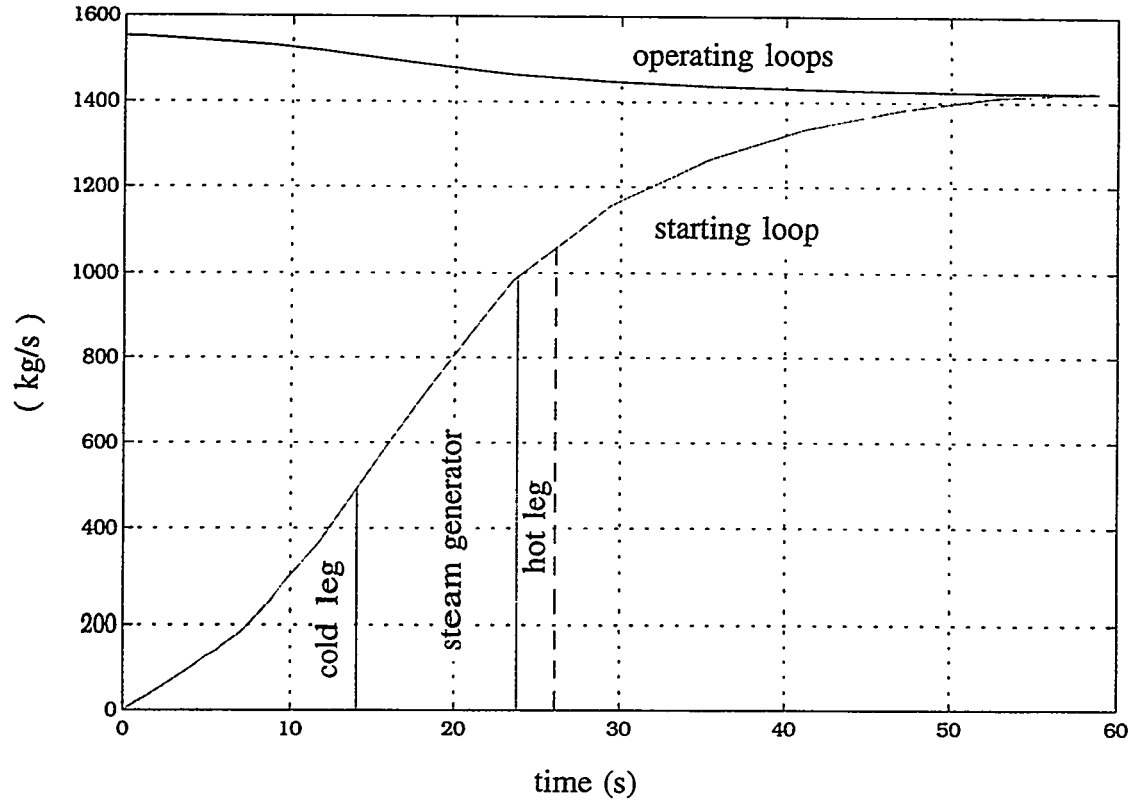

Figure 5. Flow rates in the loops, inlet boundary conditions, sixth loop start

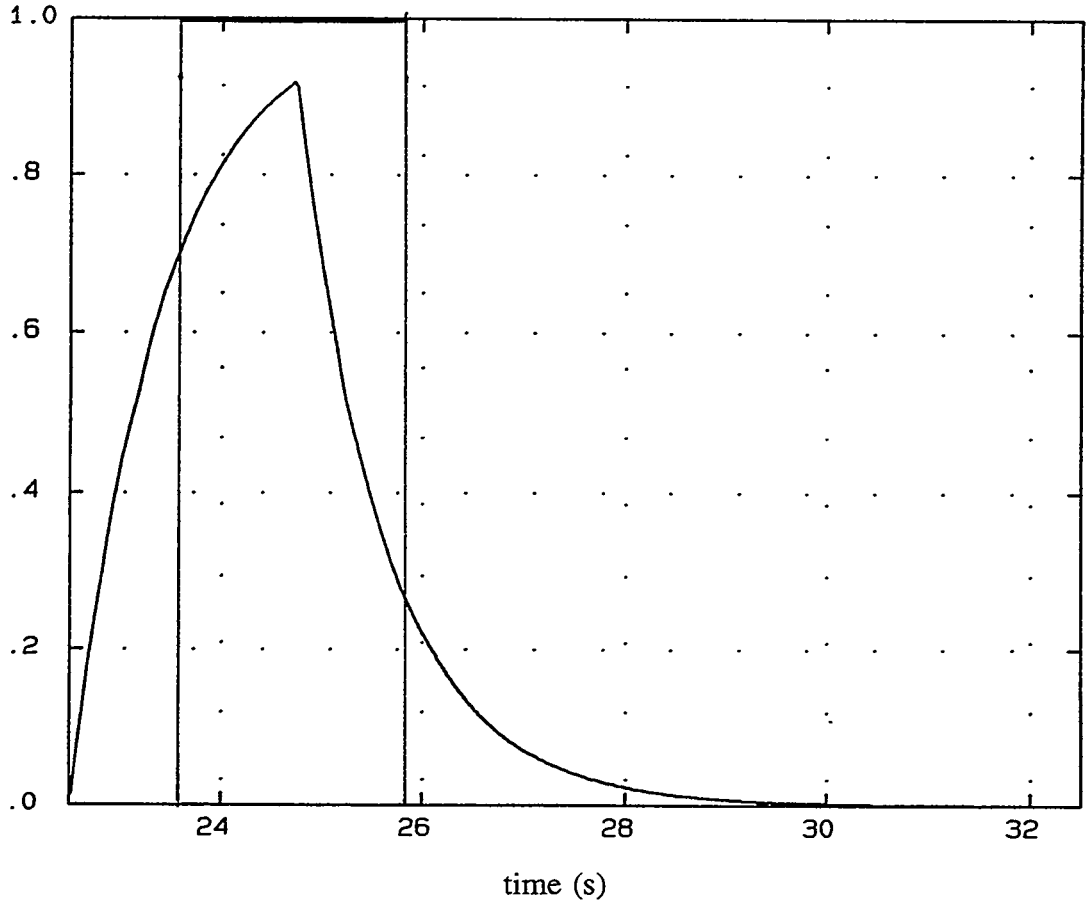

Figure 6. Concentration profiles at inlet, sixth loop start

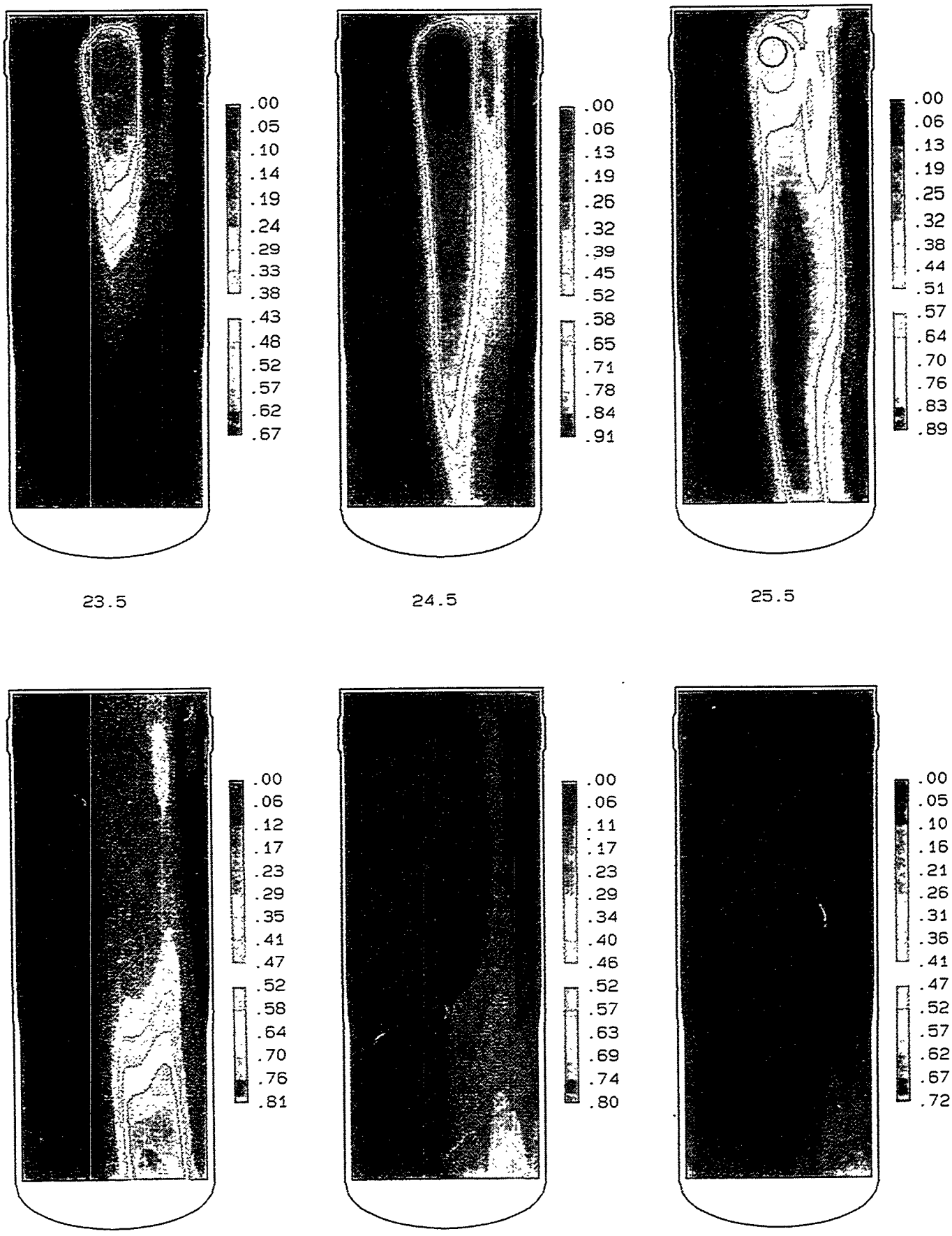

Figure 7. Slug propagation in the downcomer, sixth loop start

Figure 8. Concentration fields in lower support plate, sixth loop start

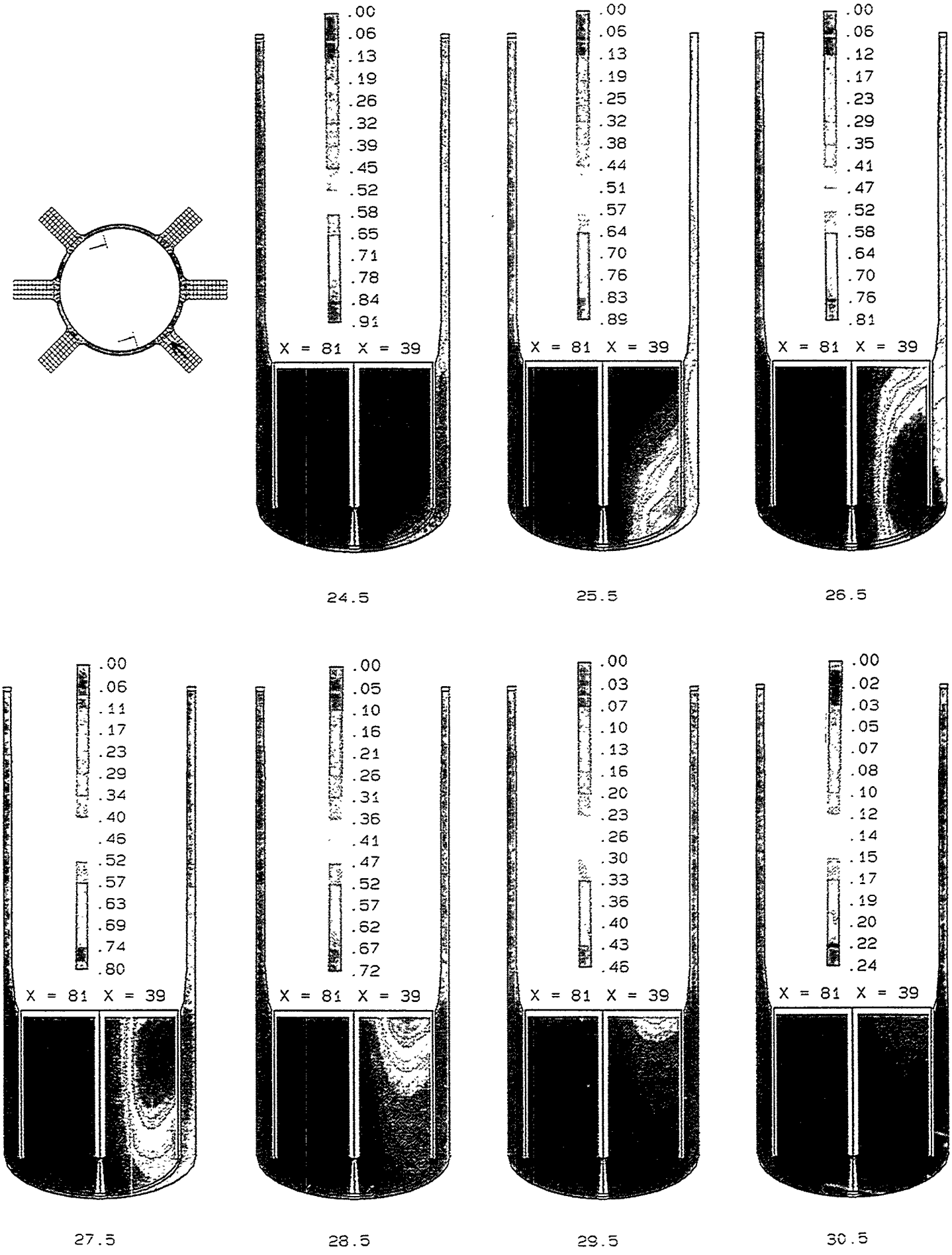

Figure 9. Slug propagation in the protection tube unit, sixth loop start

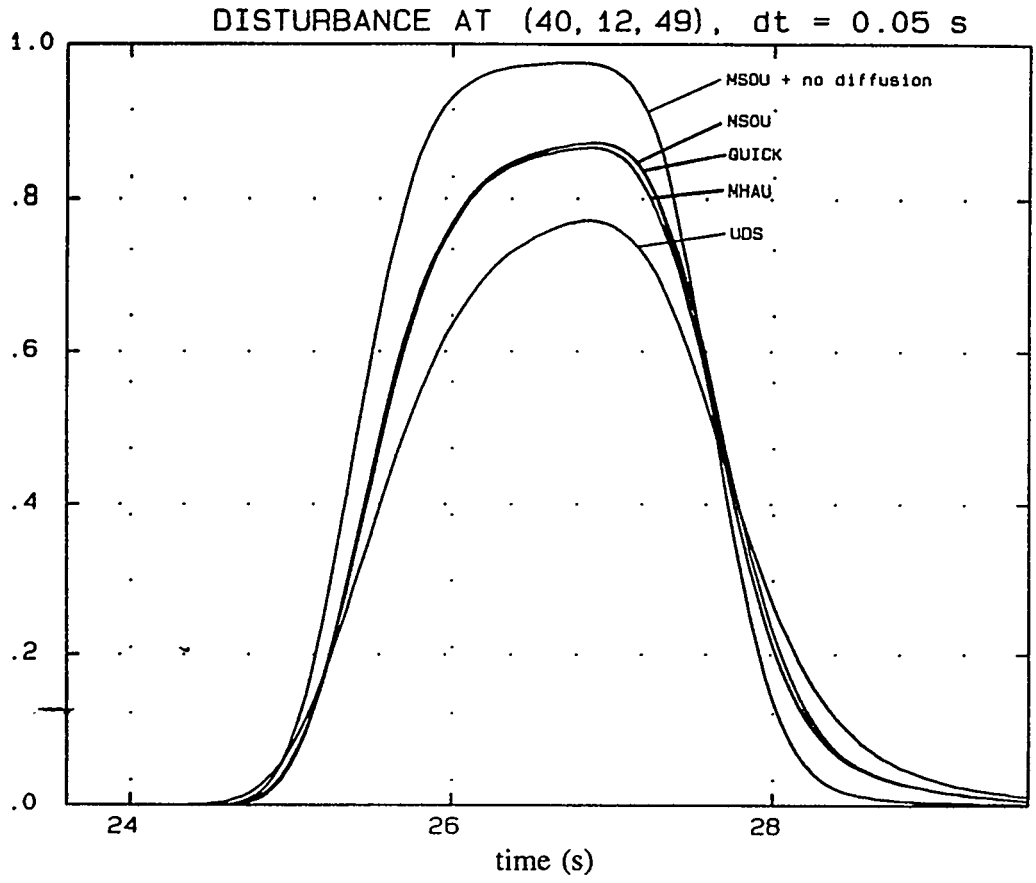

Figure 10. Comparison of different discretisation scheme spot values, sixth loop start

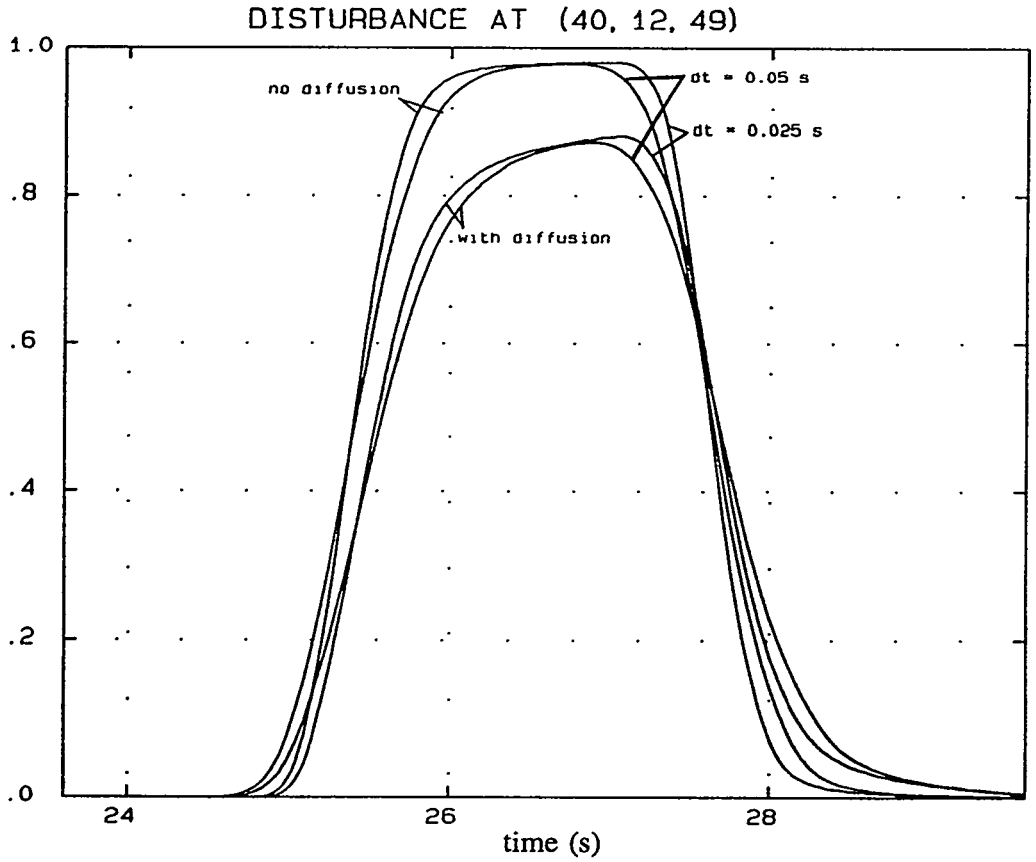

Figure 11. Spot values for two different time-step length, sixth loop start

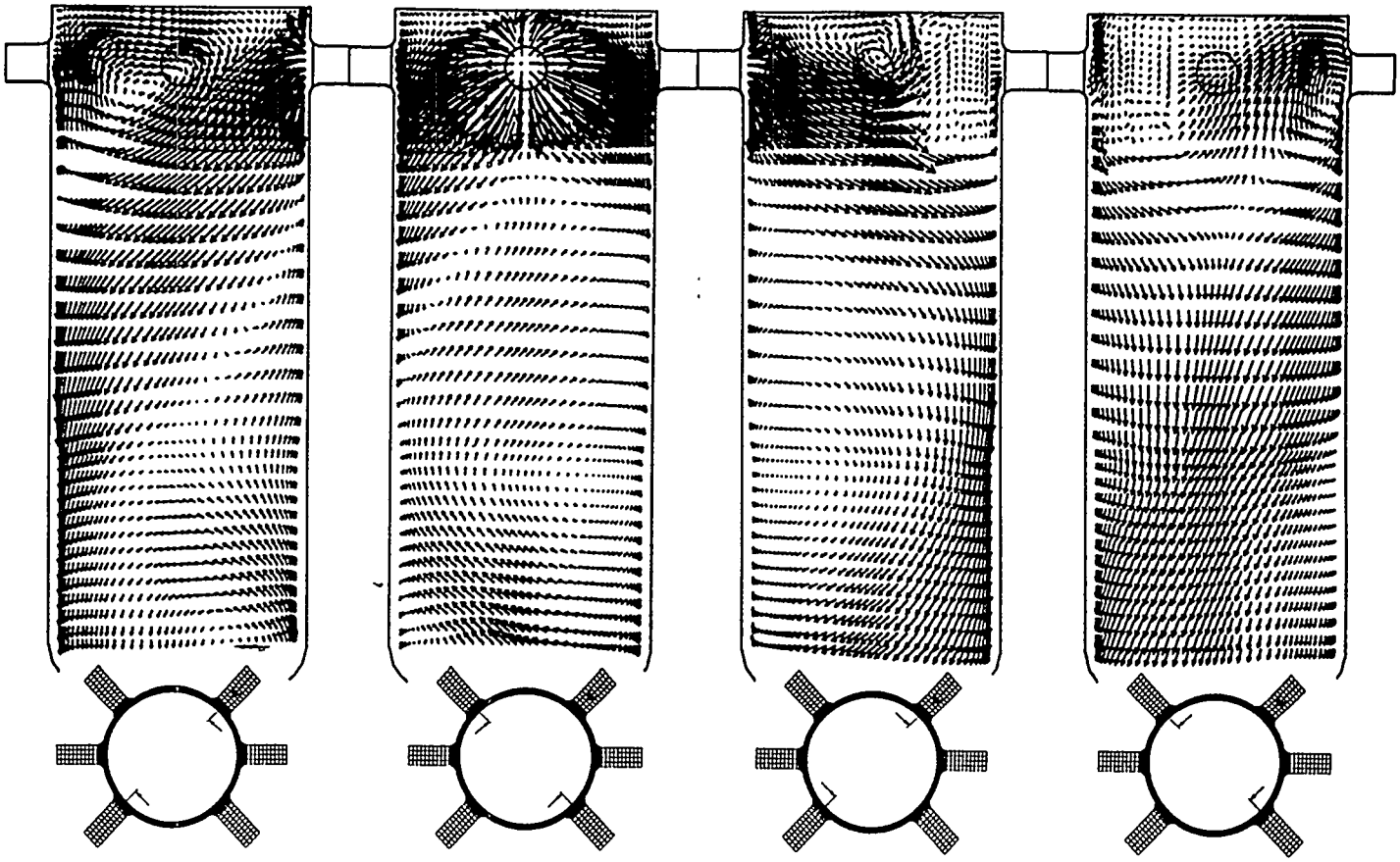

Figure 12. Steady state flow field in the downcomer, first loop start

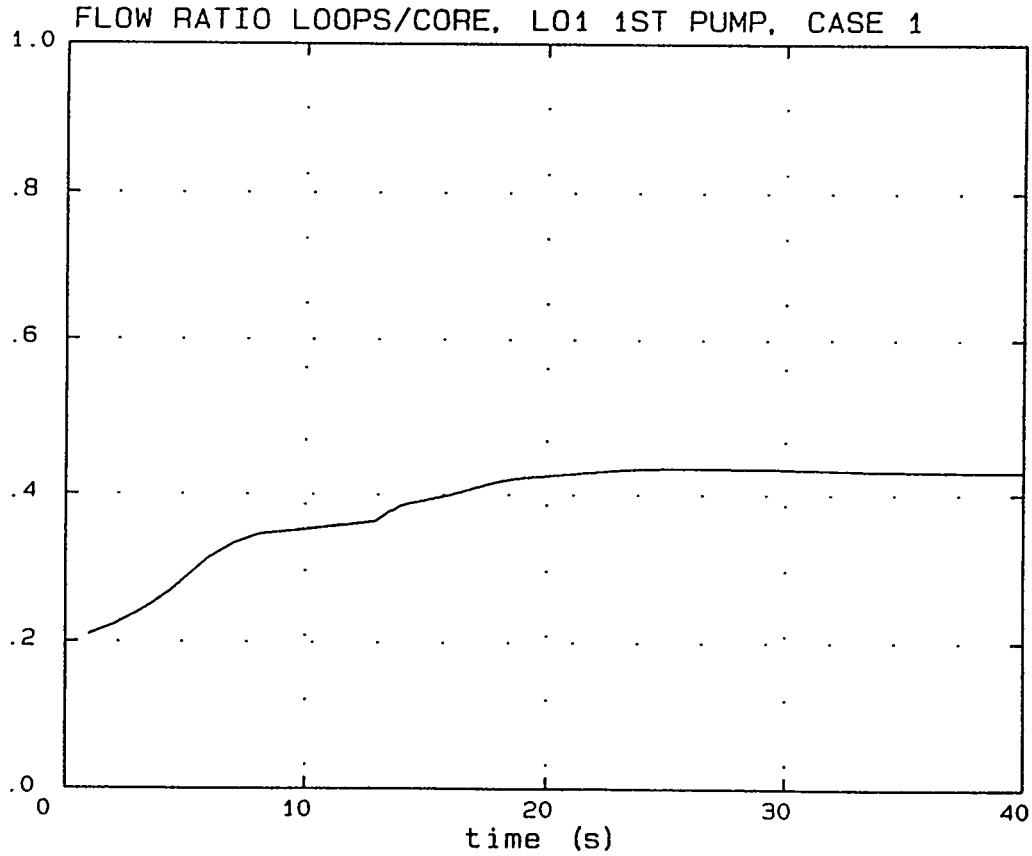

Figure 13. Ratio of flow to loops versus core during transient, first loop start

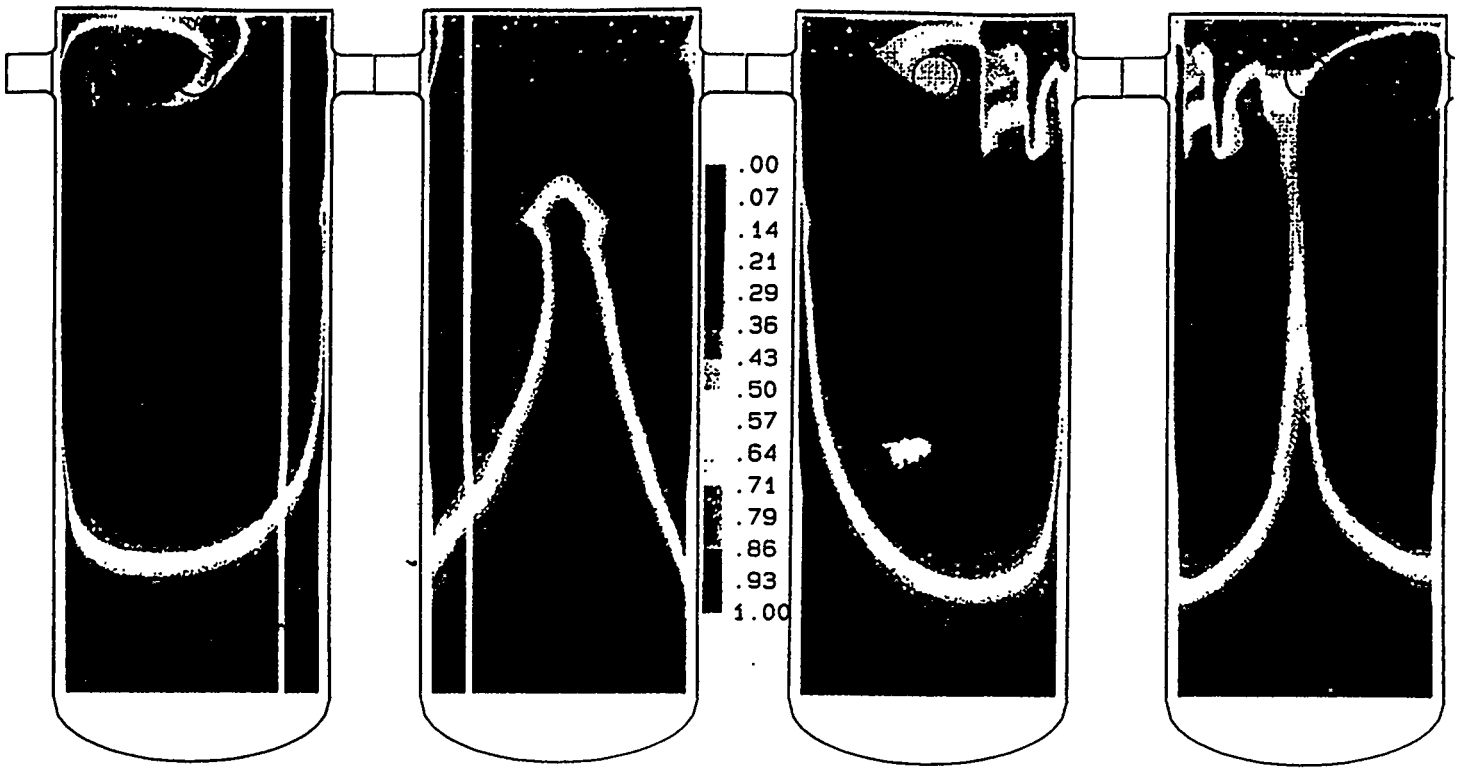

LO1. FIRST PUMP START. CASE 11. t=12.0s

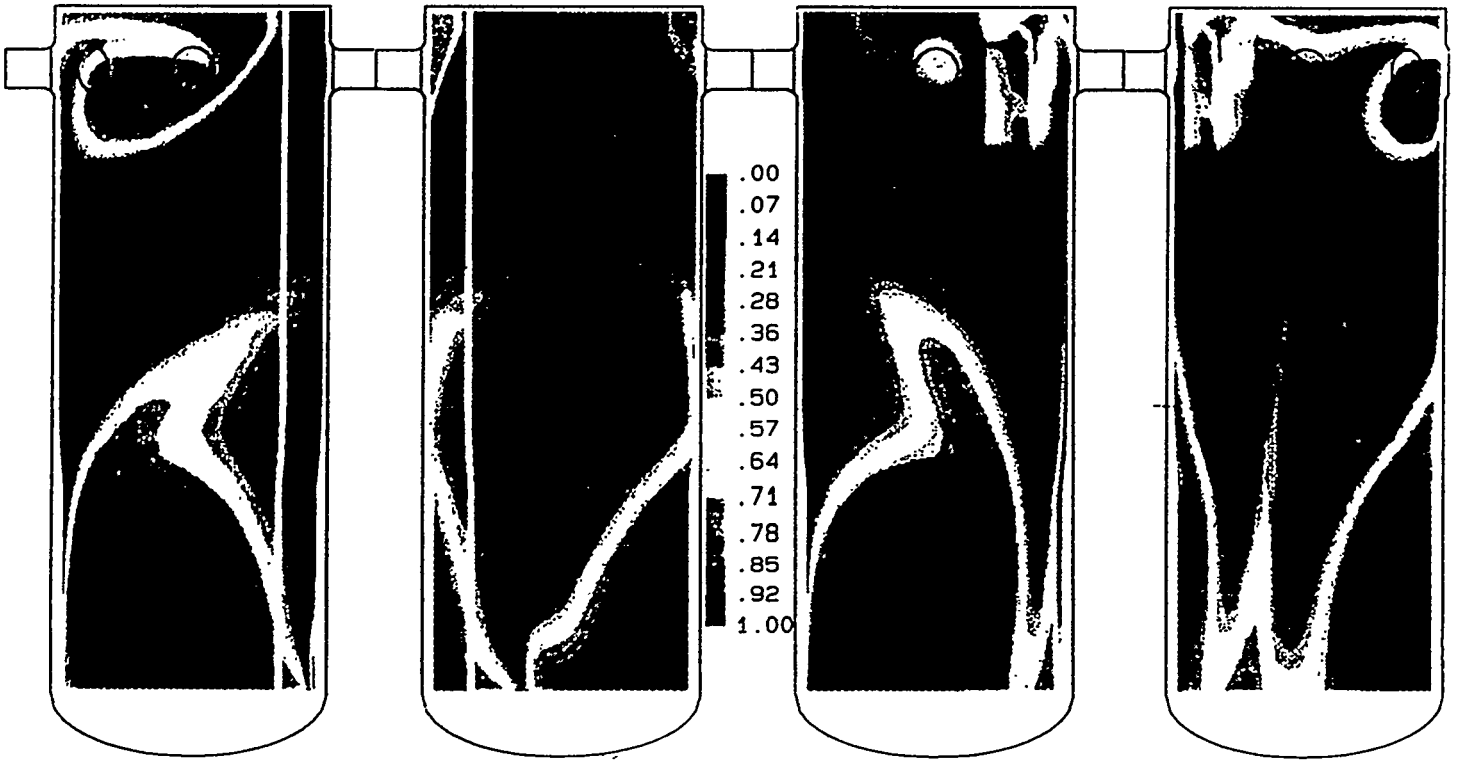

LO1. FIRST PUMP START. CASE 11. t=16.5s

Figure 14. Slug field in the downcomer at two moments, first loop start

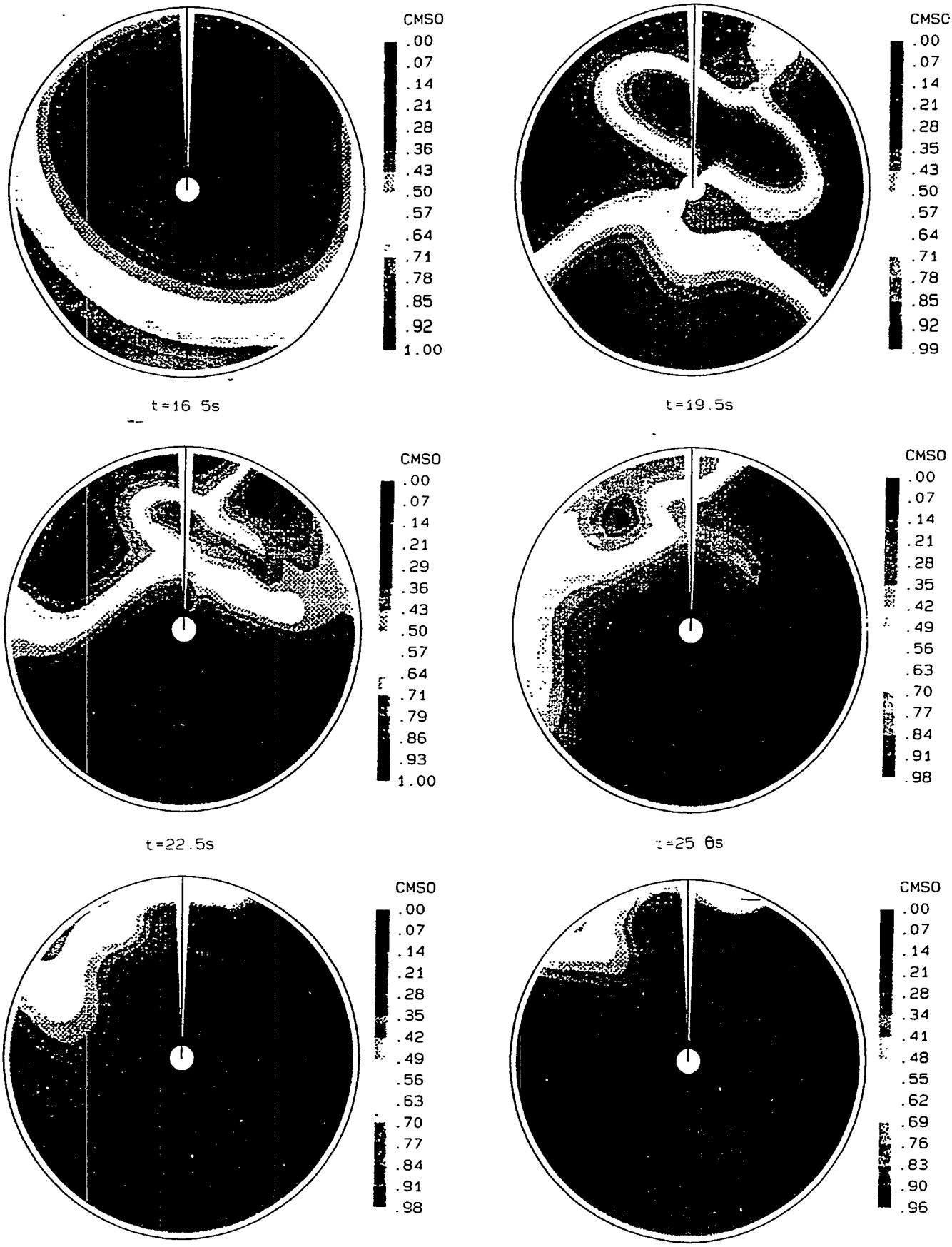

Figure 15. Concentration fields in lower support plate, first pump start

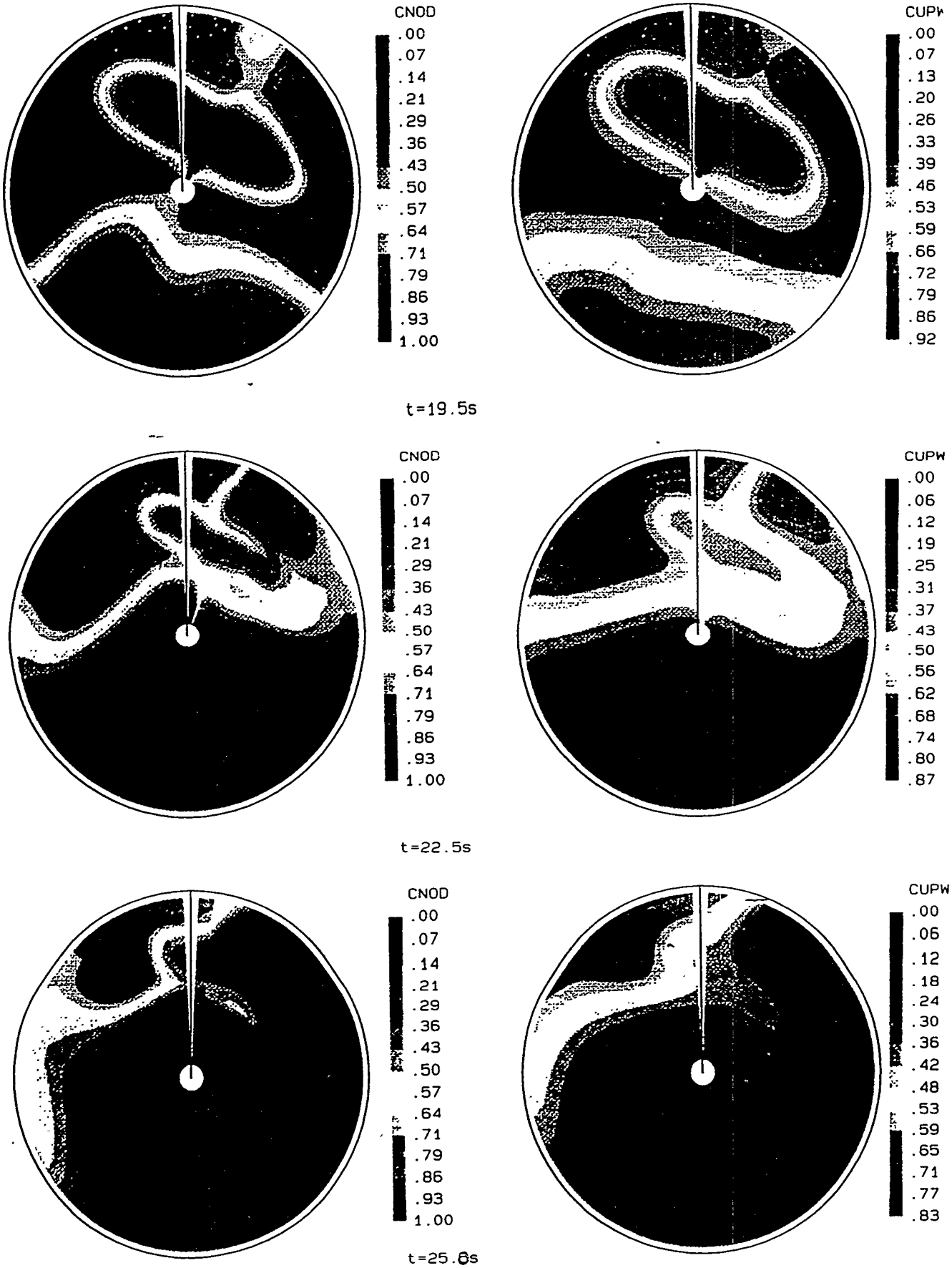

Figure 16. Concentration fields in lower support plate, first pump start, left: second order + no diffusion, right: first order + diffusion

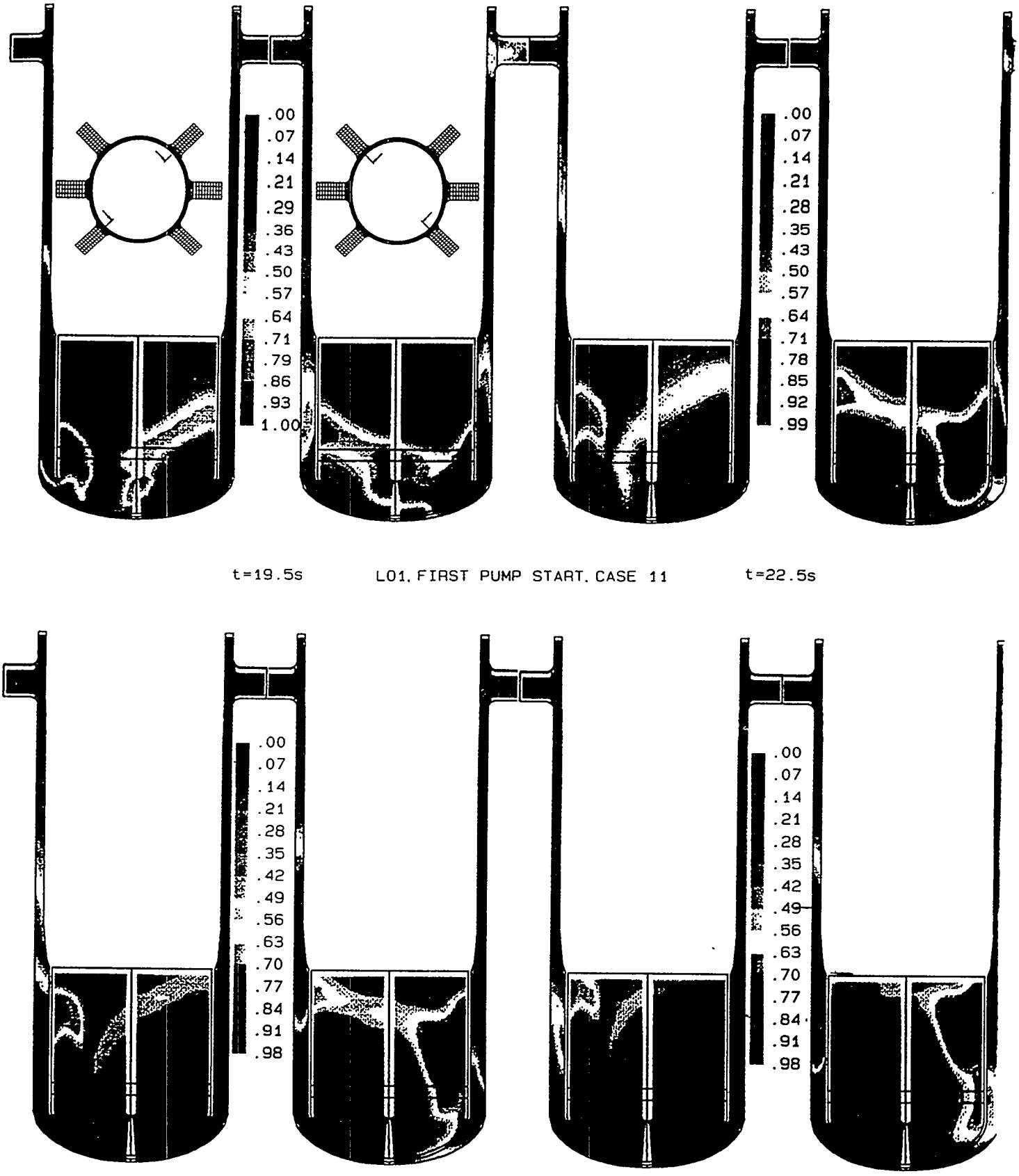

Figure 17. Slug propagation in the protection tube unit, first pump start

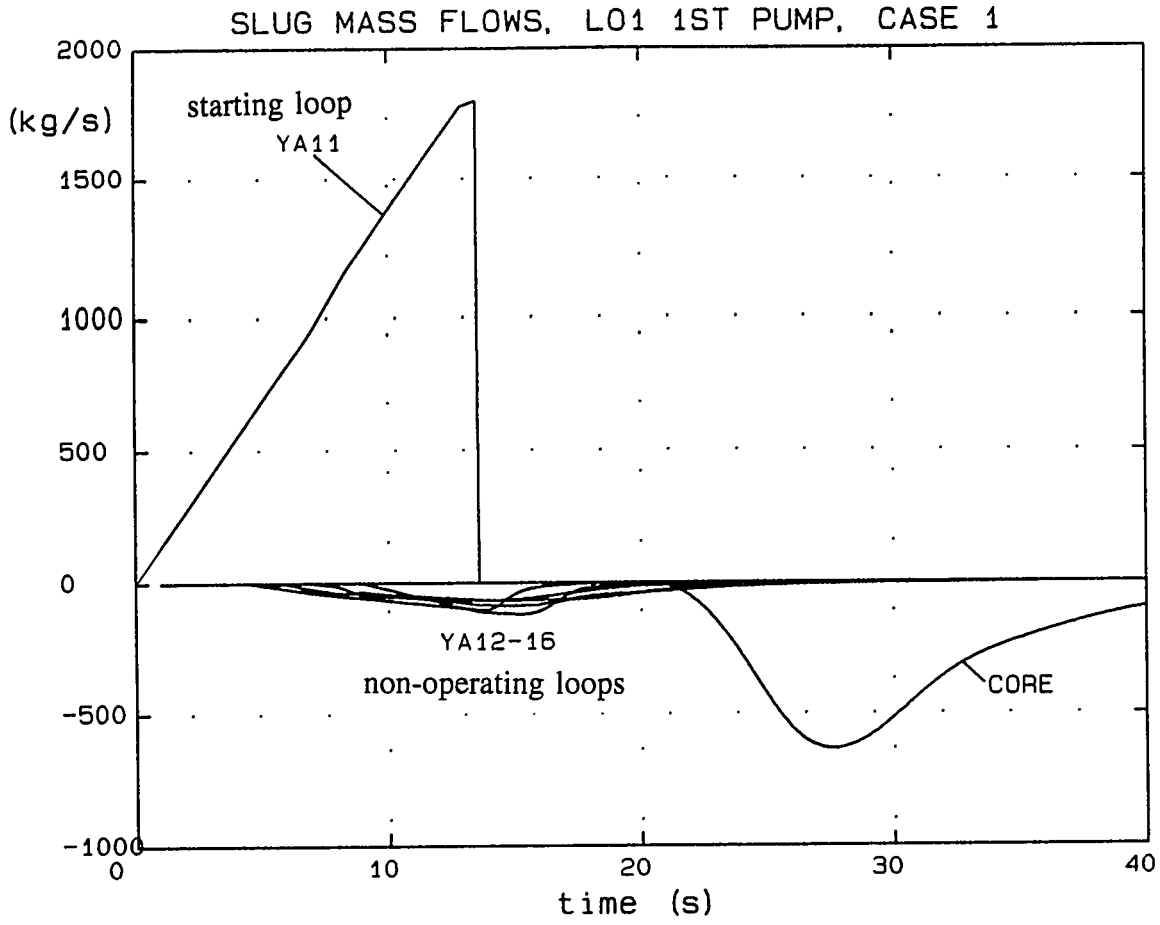

Figure 18. Slug mass flows in the model during the transient, first pump start

TURBULENCE PREDICTION IN TWO-DIMENSIONAL BUNDLE FLOWS USING LARGE EDDY SIMULATION

Wael A. Ibrahim
Yassin A. Hassan

Department of Nuclear Engineering
Texas A&M University
College Station, Texas 77843-3133
Phone: (409) 845-7090
FAX: (409) 845-6443

ABSTRACT

Turbulent flow is characterized by random fluctuations in the fluid velocity and by intense mixing of the fluid. Due to velocity fluctuations, a wide range of eddies exists in the flow field. Because these eddies carry mass, momentum, and energy, this enhanced mixing can sometimes lead to serious problems, such as tube vibrations in many engineering systems that include fluid-tube bundle combinations. Nuclear fuel bundles and PWR steam generators are existing examples in nuclear power plants. Fluid-induced vibration problems are often discovered during the operation of such systems because some of the fluid-tube interaction characteristics are not fully understood. Large Eddy Simulation, incorporated in a three dimensional computer code, became one of the promising techniques to estimate flow turbulence, predict and prevent of long-term tube fretting affecting PWR steam generators. The present turbulence investigation is a step towards more understanding of fluid-tube interaction characteristics by comparing the calculations with the available experimental data. In this study, simulation of flow across tube bundles with various pitch-to-diameter ratios were performed. Power spectral densities were used for comparison with experimental data. Correlations, calculations of different length scales in the flow domain and other important turbulent-related parameters were calculated. Finally, important characteristics of turbulent flow field were presented with the aid of flow visualization with tracers impeded in the flow field.

INTRODUCTION

When a fluid flows across a tube array, a fraction of its energy is transmitted to the tubes, resulting in tube vibration. Because of the tube's flexibility, the hydrodynamic load causes it to deflect, an effect which is balanced by an elastic restoring force. If the hydrodynamic load fluctuates, the tube vibrates under the influence of the fluctuating load, resulting in fretting wear. The flow field is defined here as the velocity of the fluid as a function of position and time. The complexity of the flow pattern over tubes makes it practically unthinkable to obtain exact data concerning the flow forces and the nature of flow-induced tube vibrations. These are all needed for analytical calculations. Hence, engineering approaches to turbulent flow used to be based mainly on a combination of theory and experiment. With the current strides of computer technology, practical numerical approaches to turbulence modeling are feasible. Large Eddy Simulation (LES) [1], in this study, is applied to practical engineering problems such as the flow across bundle of steam generator tubes.

In large eddy simulation, it is mainly the large scale eddies that transport momentum in a turbulent flow field. Therefore, it is the large scale motion that has to be accurately calculated to estimate the velocity and pressure distributions of that flow field. Large scale turbulent motion is strongly dependent upon the boundary conditions. The mean flow will have a preferred direction which is imposed on the twisting motion of the large scale eddies. This large scale turbulent motion has intensity and length scales that are different for the respective directions (anisotropic turbulence). As the large scale turbulent motion cascades to the smaller scales (large eddies make small eddies), the direction sensitivity is lost and the small scale dissipative motion approaches an isotropic condition (no direction sensitivity).

In the present study, the large eddy simulation is combined with the computer code GUST [2] to simulate flows across tube bundles with two different pitch-to diameter ratios. GUST is a FORTRAN computer code for LES of incompressible, isothermal flow turbulence in complex three-dimensional flow geometries. GUST solves the unsteady, space-averaged Navier-Stokes equations. The GUST code computes the development and transport of large eddies, while simply modeling the effects of the smaller eddies. The results of a GUST simulation are time histories of velocity and pressure fluctuations at each finite mesh.

THEORY

In 1963, meteorologists proposed a turbulence modeling technique in which the averaging is performed over space instead of time [3]. This early work has evolved into LES. The idea of the LES came from the limitation of direct simulation and the experimental evidence that large eddies are flow dependent and responsible for most of the production of the turbulent energy while the small eddies are more universal and are mainly responsible for dissipation of the turbulent energy. Table 1. provides more comparisons between the two different scales [4].

Table 1. Differences between Large Eddies and Fine-Scale Eddies

Large Eddies	Fine-Scale Turbulence
produced by mean flow	produced by large eddies
depend on boundaries	universal
ordered	random
require deterministic description	can be modeled
inhomogeneous	homogeneous
anisotropic	isotropic
long-living	short-living
diffusive	dissipative
difficult to model	easier to model

The momentum equation takes the following form for uniform-density Newtonian fluids in the absence of an external force:

$$\frac{\partial U_i}{\partial t} + \frac{\partial U_j U_i}{\partial x_j} = -\frac{1}{\rho}\frac{\partial P}{\partial x_i} + \nu \frac{\partial^2 U_i}{\partial x_j \partial x_j} \qquad (1)$$

here, U_i is the component of instantaneous velocity in the x_i direction, P is the instantaneous static pressure, and ν is the kinematic viscosity. It should be noticed that there are four unknowns (U_i, P) in three equations. In order to form a complete set of

equations for fluid motion, the three equations of motion are coupled with the equation of mass conservation (continuity equation):

$$\frac{\partial U_i}{\partial x_i} = 0. \tag{2}$$

These equations are second-order, non-linear, partial differential equations. In their complete form, they have not been solved exactly. There are two main reasons why it is difficult, if not impossible, to obtain exact solutions. First, the equations are nonlinear (in fact, they are quadratic) in U_i. Secondly, there is no separate equation for P.

In LES, each flow variable, f, is decomposed into an 'average' component, $\bar{f}$ and a 'fluctuating' component, f', such that,

$$f = \bar{f} + f'. \tag{3}$$

By the virtue of LES features, no model is needed to resolve the large scale motions. However, modeling the effect of the small eddies is required. In homogeneous turbulence, sub-grid scale (SGS) (dissipating) eddies are of order $Re^{3/4}$ times smaller than grid-scale (GS) (energy-containing) eddies. A numerical simulation of turbulence requires the inclusion of the effect of this range of spatial scales on the allowable time step. This poor scaling with the Reynolds number is the reason for interest in the LES method, in which effects on scales smaller than those resolvable numerically are modeled, usually by an eddy viscosity model. The LES solves space filtered Navier-Stokes equations for large GS eddies instead of solving the original Navier-Stokes equations. It introduces a simple model for small SGS eddies to close the system of equations. The filtering operation eliminates the rapidly fluctuating components from the filtered variables. An approximation or modeling is required for the SGS eddies. For homogeneous flows, Leonard [5] defined the GS component $\overline{U}(\vec{x},t)$ as the convolution of $U(\vec{x}',t)$ with a filter function $G(\vec{x} - \vec{x}')$. The filtering operation can be written as:

$$\overline{U}(\vec{x},t) = \int_v G(\vec{x} - \vec{x}')\, U(\vec{x}',t)\, d\vec{x}'. \tag{4}$$

The filter function $G(\vec{x} - \vec{x}')$ can be expressed as:

$$G(\vec{x} - \vec{x}') = \prod_{i=1}^{3} G_i(x_i - x_i'), \tag{5}$$

where $G_i(x_i - x_i')$ is a one-dimensional filter and $\vec{x} = (x_1,x_2,x_3) = (x,y,z)$, is a Cartesian position vector. For the box filter (top hat), the filter function $G_i(x_i - x_i')$ is given by [6]:

$$\begin{aligned} G_i(x_i - x_i') &= \frac{1}{\Delta_i} \quad \text{for} \quad |x_i - x_i'| \le \frac{\Delta_i}{2} \\ &= 0 \quad \text{for} \quad |x_i - x_i'| > \frac{\Delta_i}{2}. \end{aligned} \qquad i=1,2,3 \tag{6}$$

where Δ_i is the 'filter width' in the i-th direction. Space and time derivatives commute with the filtering operation for 'uniform' filters only. Substituting equations (3) and (4) into the original Navier-Stokes equation and applying the filtering operation, yields the following filtered equation:

$$\frac{\partial \overline{U_i}}{\partial t} + \frac{\partial \overline{\overline{U_j}\,\overline{U_i}}}{\partial x_j} = -\frac{1}{\rho}\frac{\partial \overline{P}}{\partial x_i} + \nu \frac{\partial^2 \overline{U_i}}{\partial x_j \partial x_j} - \frac{\partial R_{ij}}{\partial x_j}, \tag{7}$$

where Reynolds stress term R_{ij} is:

$$R_{ij} = \overline{u_i'\,\overline{U_j}} + \overline{\overline{U_i}\,u_j'} + \overline{u_i'\,u_j'}. \tag{8}$$

Furthermore, R_{ij} can be divided into traceless and diagonal components. Since the diagonal part represents a normal stress, it can be added to the pressure term i.e.,

$$\begin{aligned} R_{ij} &= R_{ij} - \frac{1}{3}R_{kk} + \frac{1}{3}R_{kk}, \\ &= \tau_{ij} + \frac{1}{3}R_{kk}. \end{aligned} \tag{9}$$

$$P = \overline{P} + \frac{1}{3}R_{kk}. \tag{10}$$

The above filtered equation can be rewritten as:

$$\frac{\partial \overline{U_i}}{\partial t} + \frac{\partial \overline{\overline{U_j}\,\overline{U_i}}}{\partial x_j} = -\frac{1}{\rho}\frac{\partial P}{\partial x_i} + \nu \frac{\partial^2 \overline{U_i}}{\partial x_j \partial x_j} - \frac{\partial \tau_{ij}}{\partial x_j}. \tag{11}$$

In the above equation all terms are expressed with GS variables only, except τ_{ij}, which includes SGS terms. The fact that equation (11) is not closed is not only due to the presence of the SGS term, but also it has an integro-differential characteristics since the double filtering in the advection term is an integration by definition [7]. To close the system of equations we need modeling for Reynolds stress τ_{ij}. As Re increases, the fraction of the total field that is unresolved also increases, the model is required to represent a larger range of turbulence scales, and the accuracy of the simulation becomes more sensitive to the quality of the SGS model.

According to the eddy viscosity concept, the Reynolds equation (equation 11) becomes

$$\begin{aligned} \frac{\partial \overline{U_i}}{\partial t} + \frac{\partial \overline{\overline{U_j}\,\overline{U_i}}}{\partial x_j} &= -\frac{1}{\rho}\frac{\partial \overline{P}}{\partial x_i} + \frac{\partial}{\partial x_j}\left(\nu \frac{\partial \overline{U_i}}{\partial x_j} + \nu_\tau\left(\frac{\partial \overline{U_i}}{\partial x_j} + \frac{\partial \overline{U_j}}{\partial x_i}\right)\right), \\ \frac{\partial \overline{U_i}}{\partial t} + \frac{\partial \overline{\overline{U_j}\,\overline{U_i}}}{\partial x_j} &= -\frac{1}{\rho}\frac{\partial \overline{P}}{\partial x_i} + \frac{\partial}{\partial x_j}\left((\nu + \nu_\tau)\frac{\partial \overline{U_i}}{\partial x_j} + \nu_\tau\left(\frac{\partial \overline{U_j}}{\partial x_i}\right)\right). \end{aligned} \tag{12}$$

Equation (12) can be used for turbulent and laminar flows without changing the mathematical form of the equation. This convenience of the eddy viscosity concept allows the same solution procedure for turbulent and laminar flows. Now, the problem of the eddy viscosity model is how to calculate the eddy viscosity ν_τ.

Smagorinsky's eddy viscosity model is the simplest and most widely used as a sub-grid scale model. Smagorinsky [3] based his model on the 'eddy viscosity' concept. He used the following approximations as in the conventional time averaging method,

$$\overline{\overline{U_i}\,\overline{U_j}} = \overline{U_i}\,\overline{U_j}\,, \tag{13}$$

$$\overline{\overline{U_i}\,u_j'} = 0, \tag{14}$$

and,

$$\overline{u_i'\,\overline{U_j}} = 0. \tag{15}$$

Then the same form of the Reynolds stress term as in the time averaged model can be obtained,

$$\tau_{ij} = \overline{u_i'\,u_j'}\,. \tag{16}$$

In the above expression, τ_{ij} is called SGS Reynolds stress. This term is a tensor and consists of correlation of the fluctuating velocities. These correlations come from space averaging of the convective acceleration term. The Reynolds stresses are considered as apparent turbulent friction because they represent the high energy dissipation rate in the flow field due to the eddy motion. The energy dissipation rate is high due to the eddies moving high speed flow into low speed regions and vise versa, (enhanced mixing). The space averaged equations do not give a closed form solution due to the unknown $\overline{u_i'u_j'}$ values. These unknown values must be supplied to the space averaged equations by a turbulence model. The spatial gradient of the $\overline{u_i'u_j'}$ can be interpreted as a stress on an element of fluid due turbulence. Based on the observation that the SGS tensor is symmetric and traceless and from the fact that, the simplest tensor functional of the velocity field that has these properties is the rate of strain tensor, S_{ij}, so it is normal to assume proportionality between the two. It is common for the Reynolds terms to be related to an effective viscosity (eddy viscosity) due to turbulent motion. Turbulence increases friction, hence increases viscous effects.

$$\tau_{ij} = -\nu_\tau\left(\frac{\partial\overline{U_i}}{\partial x_j} + \frac{\partial\overline{U_j}}{\partial x_i}\right). \tag{17}$$

In the above equation, ν_τ is the turbulent or eddy viscosity, which, in contrast to the molecular viscosity ν, is not a fluid property but depends strongly on the flow field. Smagorinsky proposed the following expression for ν_τ:

$$\nu_\tau = (C_s \Delta)^2 \left(\frac{\partial \overline{U_i}}{\partial x_j} \left(\frac{\partial \overline{U_j}}{\partial x_i} + \frac{\partial \overline{U_i}}{\partial x_j} \right) \right)^{1/2} \tag{18}$$

where, C_s, is the Smagorinsky constant and Δ is a filter width (typically two times of mesh spacing). Values of C_s ranging from 0.10 to 0.20 are usually used [7]. C_s controls the intensity of the turbulence fluctuations. The main advantage of this model that it can simulate homogeneous turbulence (averaged quantities are independent of position) reasonably well. Also, Smagorinsky's model works well in predicting the decay of isotropic turbulence [8].

The LES code, GUST, adopts Smagorinsky's model as a SGS model with C_s equal to 0.15. Complex geometries are represented in GUST using partially blocked cells. The no-slip boundary condition imposed on solid walls implies a zero fluid velocity near a wall. In highly turbulent flows, a finite difference calculation does not capture the thin boundary layer near a wall unless the cell structure is sufficiently fine. Therefore, some modeling is required to approximate near wall effect. GUST assumes a linear relationship between the velocity adjacent to the wall (U_w) and shear stress (τ_w) given by:

$$\tau_w = \overline{\tau_w} \frac{U_w}{\overline{U_w}} , \tag{19}$$

where $\overline{U_w}$ and $\overline{\tau_w}$ are unknown time mean values. A relationship between $\overline{U_w}$ and $\overline{\tau_w}$ is used based on experimental data [9]:

$$\overline{U_w} = \frac{1}{\kappa} u^* \ln \left(\frac{\delta}{k} \right) , \tag{20}$$

where,

$$u^* = \sqrt{\frac{\overline{\tau_w}}{\rho}} , \tag{21}$$

and κ is the von Karman constant ($\sim$ 0.4), k is the surface roughness scale, and δ is the separation between $\overline{U_w}$ and the wall. Typical values of $\overline{U_w}$, δ , and k are chosen for each GUST calculation [2].

GUST uses a Factorized Implicit Solution Technique (FIST) to solve the space-averaged Navier-Stokes equations. The FIST is a finite difference algorithm to advance a multidimensional solution field in time in an implicit manner, without having to solve large systems of coupled algebraic equations at each time step. The implicit nature of FIST allows use of time steps that are large enough to significantly reduce computer costs without losing temporal accuracy. The FIST algorithm is stable at large time steps (up to a Courant number of five). FIST uses an energy conserving differencing scheme for advection terms in the momentum equations and thus ensures that mechanical energy is not destroyed due to numerical dissipation, hence, posses minimal numerical (artificial) diffusion [2]. The Incomplete Cholesky-decomposition Conjugate Gradient of order zero (ICCG0) iterative solution technique is used to solve the Poisson equation [7].

RESULTS

In this study, two experimental sets are simulated. The first set [10] utilized a square

pitch tube array with a pitch-to-diameter ratio (P/D) of 1.4, subjected to three turbulence intensity levels. The free stream velocity was varied to produce a Reynolds number from $1x10^4$ to $1x10^5$. The Reynolds number is based on tube diameter and gap velocity. Figure 1 shows the tube bundle nodalization. The tubes used are geometrically typical of many steam generator designs. The magnitudes of the turbulence intensity generated in the experiment are typical of those found in the flow inlets of steam generators. Tests are conducted on a four row bundle of twenty stainless steel tubes. Each tube is 1.5824 cm diameter and is exposed to flow over a 30.48 cm span. A 0.1 msec time step (Courant number of 2.8) was used in the simulation with 282x122 meshes. In the first stage of the simulation, the same domain dimensions without the presence of the tubes were used. An input velocity of 1.524 m/s with turbulence intensity of 11% was used as an input boundary condition at the inlet region (flow direction) and periodic boundary conditions were used in the transverse direction. The reason for performing two stages is the unknown fluctuating velocity field at the entrance region. The first stage gives a reasonable turbulence structure at the entrance of the tube bundle. This is acceptable since the fluctuations are short lived and arise periodically [11]. In the second stage, the saved output velocity time histories were used as an input for the flow domain with the presence of the tubes. Forty meshes/pitch were used in both directions. The simulation was run for 1900 cycles after achieving steady state. Each 100 cycles of computation required about 7 hours of CPU time on the Cray-YMP.

The second set [12] performed utilizing experimental setup which involved the study of the fluctuating forces induced by water cross flow on tube rows with (P/D) of 1.5 and 3 with mass flux range from 375 to 4125 $Kg/(m^2s)$. Figure 2 shows the tube bundle nodalization. The simulation involved P/D of 1.5 with 30 mm tube diameters. The same number of cycles and time step as in the first simulation were used in this simulation. Mesh nodalization of 30 meshes/pitch in j-th (flow) direction and 45 meshes/pitch in i-th (transverse) direction resulted in 152x182. Each 100 cycles of computation required about 5 hours of CPU time on the Cray-YMP. The same technique of using two stages as in the first simulation was used. In the first stage, input velocity boundary conditions of 0.5 and 0.75 m/s each with 7% turbulence intensity in the flow direction and wall (no slip) boundary conditions in the transverse directions were used.

An important measure of flow turbulence is the 'correlation function'. The Lagrangian (temporal) autocorrelation over a time T is defined to be length of time (past history) that is related to a given event:

$$R(\tau) = \frac{\overline{u'(t)\,u'(t+\tau)}}{\overline{u'(t)\,u'(t)}} \qquad \text{or} \qquad R(\tau) = \lim_{T\to\infty} \frac{1}{T}\int_{t=0}^{t=T} u'(t)\,u'(t+\tau)\,dt \tag{22}$$

Nondimensional Dimensional

Physically, $R(\tau)$ represents the average of the product of the fluctuating velocity, u', values at a given time and at a time Δt later. $R(\tau)$ gives information about whether, and for how long, the instantaneous value of u' depends on its previous values. It is a measure of the degree of resemblance of u' with itself as time passes. Knowledge of u' for a sufficiently long time allows prediction with sufficient confidence its value at a later time by 'extrapolation'. On the other hand, when $R(\tau)$ goes to zero, the temporal similarity of u' with itself disappears. Autocorrelation is a function of the direction of the turbulent

velocity component. The form of the autocorrelation curve provides information about the mean eddy size of the turbulence. The curvature of the autocorrelation curve near time zero describes the micro scale of the turbulence [13]. The smaller the radius of curvature of the curve then the smaller the micro time scale of the turbulence [13]. Correlation curves can also be obtained as a function of the time delay to give the correlation between the velocities at consecutive points.

$$R_{12}(\tau) = \frac{1}{T}\int_{t=0}^{t=T} u_1'(t)\, u_2'(t+\tau)\, dt\,, \tag{23}$$

R_{12} gives the correlations of the velocities in the flow direction. The individual correlation curves peak at a given value of the time delay. The peaking of the correlation curves is associated with the convection of the excitation forces and a 'convection velocity' is defined as [14]:

$$U_c = \frac{l}{t_m}\,, \tag{24}$$

where, l is the distance between the positions of u_1 and u_2, and t_m is the time delay corresponding to the peak of the curve. From equation (24), U_c can be calculated. The convection velocity represents the speed at which the fluid excitation force is transported downstream. For isotropic turbulence, ($R_{u'v'}$=0.0), if a peak exits, it is an indication of presence of coherence structure; thus, as peak increases coherence increases.

Of primary concern in turbulence measurements is how the energy spectrum, or the power spectral density (PSD), of the eddies are distributed by size. The PSD of the velocity profile, E(n), is defined to be [15],

$$\overline{u'^2} = \int_{-\infty}^{\infty} E(n)\, dn\,. \tag{25}$$

The PSD is numerically equal to the square of the Fourier transform of u'(t).

$$E(n) = \frac{4\pi^2 |\, a(n)\,|^2}{T}\,, \tag{26}$$

where T is the time period over which the integration is performed. The Fourier transformation will initially give a two-sided power spectrum for which positive and negative values are identical. In this investigation, the PSD is defined to be a one-sided spectrum, where E(n) is the sum of the power at positive and negative n. The PSD is frequently normalized such that the area under the curve is unity. The PSD of the fluctuating force coefficients is normalized by multiplying it by the average gap velocity and the reciprocal of the tube diameter. For the fast Fourier transform (FFT) the required number of data points should be a power of two. The power spectral density is computed by utilizing last 1024 cycles of whole 1900 cycles. By doing this, initial instability can be excluded.

Auto and Cross Correlation Plots

For the first simulation, figures 3 and 4 show the streamwise velocity correlations (R_{uu}) with the lag time at transverse location (i=22) (figure 1). The correlation of a velocity point with itself is the Lagrangian autocorrelation. Figure 3 shows the correlations between the first velocity point (u1) and the successive inter-tube (gap) velocity points. Figure 4 shows the correlations between u1 and the successive free velocity points. Figures 5 and 6 show R_{uu} with the lag time at transverse location (i=62). The previous figures have the same general features, such that the individual correlation curves peaks at a given value of time delay. The peaking of the curves is associated with the convection of the excitation forces and other turbulent features in such direction. Also, the peaks get lowered as the flow advances until reaching the lowest peak which is corresponding to the correlation between the first velocity point, u1, and the last velocity point in this direction. The excitation force is transported in the streamwise direction starting with a value about 8 m/sec (equation (24)) and ending with a value about 2 m/sec.

Power Spectral Density Plots

For the second simulation, figures 7 and 8 show a comparison between calculated and measured [12] normalized drag and lift coefficient power spectral densities vs. Strouhal Number (St),respectively. Strouhal Number is defined as frequency (f) times tube diameter (D) over gap velocity (Vr). The gap velocity is equal to free stream velocity times the ratio (P/(P-D)). Two different values of the free stream velocity were used (V=0.75 and 0.5 m/s). Except for the low frequency region (St > 0.3), the slopes of the calculated curves are close to the measured data (~ -3.5). The two peaks of the calculated curves (St ~ 0.4) are close to the peak of the measured data (St ~ 0.37), i.e., the simulation results agree well with the experimental data capturing the vortex shedding peak. Also the two figures show the agreement between the calculations and the experimental results in the cascade region. However, there is an order of magnitude difference between the numerical and experimental results in the comparison related to the normalized lift coefficient PSD (figure 8). Figure 7 shows that the PSD curve for (V=0.75 m/s) fits well with the experimental results, where an order of magnitude difference is noticeable in the case of (V=0.5 m/s). Table 2. shows the two free stream velocities (V) used in the calculations, the corresponding gap velocities (Vr); and Reynolds numbers (Re), and the resulted Kolmogorov length scale (η); and Taylor length scale (λ) [16]. The grid size in the simulation is on the order of 10 times larger than the Taylor length scale and ~ 100 times greater than the Kolmogorov length scale. Considering the uncertainty involved in the length scale predictions, the grid size should give reasonably geometry resolution for an accurate simulation.

Table 2. Length Scale Calculations

V (m/s)	Vr (m/s)	Re	η (mm)	λ (mm)	dx & dy (mm)
0.50	1.50	4.5×10^4	~ 0.010	~ 0.1	1.0
0.75	2.25	6.7×10^4	~ 0.008	~ 0.1	1.0

In general, the PSD curves predict the main features of the turbulence eddies. The upper size limit of the eddies is determined by the size of the flow field geometry. The small eddy sizes are dependent on the viscous forces which are in turn are dependent on the viscosity of the fluid. Turbulence by nature is dissipative due to the viscosity μ. Viscosity

acts to pull up energy from the flow by draining energy from the turbulence eddies [16]. The eddy sizes range (difference between the smallest and largest eddy) will increase with Reynolds number. The shape of the probability distribution of this range of eddy sizes may also change as the Reynolds number increases. The largest eddies exhibit fluctuations at low frequencies whereas the smallest eddies exhibit fluctuations at high frequencies.

Flow Visualization

One of the common techniques to describe a flow field is flow visualization. A flow visualization is a technique to make visible the motion of fluid or changes in the fluid due to motion. As such, it generally qualifies a flow (nature of the flow field) rather than quantifies it. As an important technique, flow visualization can be used to understand and relate physical properties and check results from turbulence models (average flow direction). Flow visualization can be useful in determining if a flow field is anisotropic, thus, indicating the type of turbulence model necessary to solve the flow. The output velocity time history from GUST for the first simulation was used to generate figures 9 to 12. In order to capture more important phenomena like flow switching, flow tracers "seeds" were used to describe the flow more qualitatively. Basically, total of 120 seeds were inserted at j=30 as a start (see figures 1 and 9). For each seed and with the available information from the neighbor velocity components (i- and j-directions) and the time step used in the original GUST simulation, a new position is calculated. 500 frames were created and used later to generate an animation of the flow field for the last 500 cycles "time steps" out of 1900 cycles. Only 4 frames were chosen here to describe the flow field. In each of figures 9 to 12 two images are shown. The one on the left hand side combines both the flow field and the tracers, while the one on the right hand side shows the tracers more clearly. Figure 9 shows the first frame with the initial position of the flow tracers. This frame represents cycle number 1501. Gap velocity of about 5 m/s is shown between the inter tubes (equivalent to 100 on the scale) which agrees with what was calculated before (gap velocity of 5.334 m/s). Figure 10 shows frame number 125 with the tracers being carried by the flow to the corresponding new positions as they are about to enter the tube bundle. Figure 11 shows frame number 250. The tracers are passing the third row of tubes and more switching at the exit region is noticeable. More refined details about the flow are noticed at the exit (we believe that they are due to small eddy effects rather than due to numerical diffusion). Finally, figure 12 shows frame number 325. The tracers show the switching behavior of the flow as it is exiting the bundle domain. At the exit region, flow recirculation and switching is noticed with maximum velocity of 9 m/s.

CONCLUSIONS

In this investigation, the large eddy simulation technique utilizing Smagorinsky's eddy viscosity model, has been used to predict and then study the turbulent characteristics of flow within tube bundles of geometry similar to that of actual heat exchanger bundles. Two-dimensional simulations were used to simulate a square pitch tube array with different pitch-to diameter ratios (P/D= 1.4 and 1.5). The code predictions have been compared against the available experimental results using PSD's of the lift and drag coefficients. An overall consistent and favorable comparisons with previous experimental results were obtained. Agreement between the data obtained and the experimental findings have illustrated the general characteristics of flow across a tube array. As the flow passes through each row of tubes, the fluid is subjected to resistance, the effect of which is to convert some of the fluid pressure energy to turbulent energy. In the first row, the transformation of energy occurs in a more orderly manner. As the flow reaches the interior tubes, unsteadiness of the flow increases, hence, a randomness of the flow and its pressure

fluctuations exist in the flow field. The discrepancies between the experimental data and the simulation results could be due to experimental uncertainty or the effects of numerical resolution. Finally, flow visualization was used both to qualify and quantify the flow field. Recirculation and switching phenomena were observed and the predictions of the flow field velocities agreed with the calculations. These switching effectscause tube vibration leading to eventual tube wear.

NOMENCLATURE

C_s = Smagorinsky's constant
D = tube diameter (cm)
dx = mesh size in i-th direction
dy = mesh size in j-th direction
EPRI = Electrical Power Research Institute
FFT = Fast Fourier Transform
FIST = Factorized Implicit Solution Technique
GS = grid-scale
$G(\vec{x})$ = filter function
$G_i(x_i')$ = one dimensional filter function in i-direction
i, j, k = rectangular spatial dimension components (x, y, z)
k = surface roughness
LES = Large Eddy Simulation
P = static pressure (N/m^2), pitch (cm)
P/D = pitch-to-diameter ratio
PSD = power spectral density
$R(\tau)$ = Lagrangian autocorrelation
R_{ij} = Reynolds stress term
Re = Reynolds number
R_{uu} = cross correlation of velocity points in the streamwise direction
SGS = sub-grid scale
S_t = Strouhal number
t = time (sec)
T = time interval (sec)
t_m = time delay corresponding to the correlation curve peak
U = instantaneous velocity
U_w = velocity adjacent to the wall
$\overline{U}$ = mean velocity, filtered velocity
$\overline{\overline{U}}$ = double filtered velocity
U_c = convection velocity
u' = fluctuating velocity
$\overline{u'}$ = mean of fluctuating velocity
$\overline{u'^2}$ = variance of fluctuating velocity
V = free stream velocity m/s
Vr = gap velocity m/s

Symbols

δ = laminar sub-layer thickness
Δ = mesh spacing, filter width

Δ_f = filter width
Δt = time-step size
η = Kolmogorov length scale
κ = von Karman constant
λ = Taylor length scale
μ = laminar viscosity
ν = kinematic viscosity
ν_τ = turbulent (eddy) viscosity
∂ = partial differential increment
ρ = density
τ = time lag
τ_{ij} = Reynolds stress term
τ_w = wall shear stress

Superscripts

$\bar{}$ = spatial or temporal average
$'$ = spatial or temporal fluctuating component
: = from-to
~ = in the order of, approximately

REFERENCES

[1] Y.A. Hassan, "Large Eddy Simulation on Supercomputers," EPRI Report, EPRI NP-7041 (1990).
[2] R. Chilukuri, "GUST: A Computer Program for Large Eddy Simulation of Incompressible Isothermal Flow Turbulence," Theory Manual, EPRI Project, EPRI S309-2 (1987).
[3] J. Smagorinsky, " General Circulation Experiments with Primitive Equations," Monthly Weather Review 91, 216-241 (1963).
[4] U. Schumann and R. Friedrich, " Direct and Large Eddy Simulation of Turbulence, " Notes on Numerical Fluid Mechanics 15, 88-104 (1986).
[5] A. Leonard," Energy Cascade in Large-eddy Simulations of Turbulent Fluid Flows," Advances in Geophysics A 18, 237-248 (1974).
[6] A. Findikakis and R.L. Street, "Mathematical Description of Turbulent Flows," Journal of the Hydraulics Division ASCE 108, 887-903 (1982).
[7] S.Y. Lee, "A Study and Improvement of Large Eddy Simulation (LES) for Practical Application," Doctor of Philosophy Dissertation, Texas A&M University (1992).
[8] J.H. Ferziger, "Large Eddy Simulation: The Next Five Years," Computer Methods in Applied Sciences and Engineering VI, 587 (1984).
[9] J.W. Deardorff, "A Numerical Study of Three-Dimensional Turbulent Channel Flow of Large Reynolds Numbers," Journal of Fluid Engineering 41, 453-480 (1970).
[10] J.E. Johnson and J.C. Simonis, "Experimental Determination of Turbulent Buffeting Effects in Tube Bundles". EPRI Report, EPRI NP-5540 (1988b).
[11] L. Schmitt and R. Friedrich, " Large-eddy simulation of turbulent boundary layer flow: Proc. 5th GAMM-Conf. on Num. Meth. Fluid Mechanics, 7, 299-306.(1984).
[12] C. Taylor, M. Pettigrew, F. Axisa, and B. Villard, "Experimental Determination of Single and Two-Phase Cross-Flow Induced Forces on Tube Rows," Flow Induced

Vibration 104, 31-39 (1986).
[13] S.S. Chen and J.A. Jendrzejczyk, "Fluid Excitation Forces Acting on a Square Tube Array," Journal of Fluid Engineering 109, 415-423 (1987).
[14] S.S. Chen and J.A. Jendrzejczyk, "Fluid Excitation Forces Acting on a Tube Array," ANL Report, ANL-85-55 (1985).
[15] J.O. Hinze, Turbulence, 2nd. ed., McGraw-Hill, New York, New York (1975).
[16] W. Rodi, Turbulence Models and Their Application in Hydraulics, 2nd. ed., Institute fur Hydromechanik, University of Karlsruhe, Federal republic of Germany (1984).

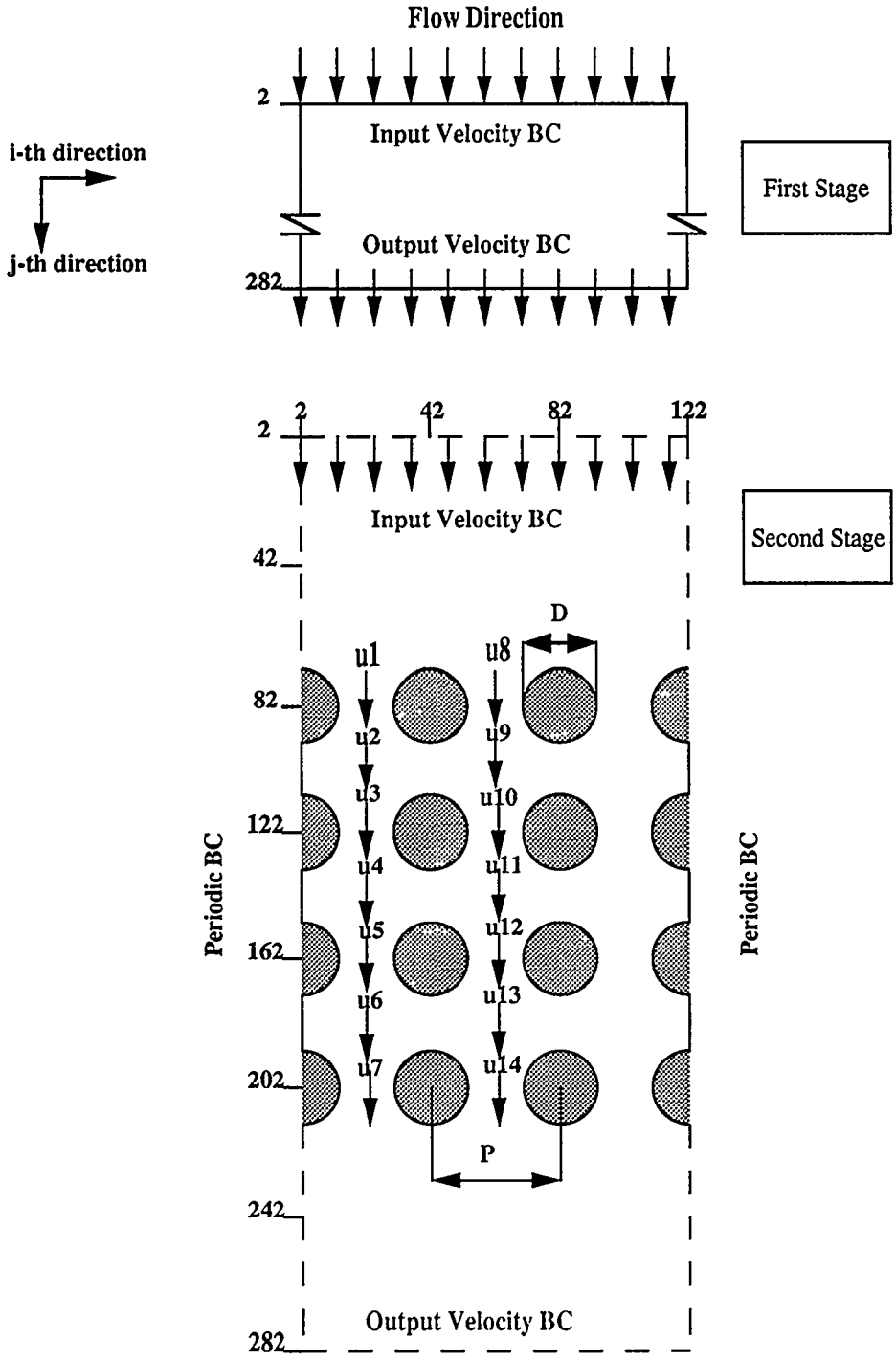

Figure 1. Two Dimensional Square Pitch Tube Bundle Nodalization

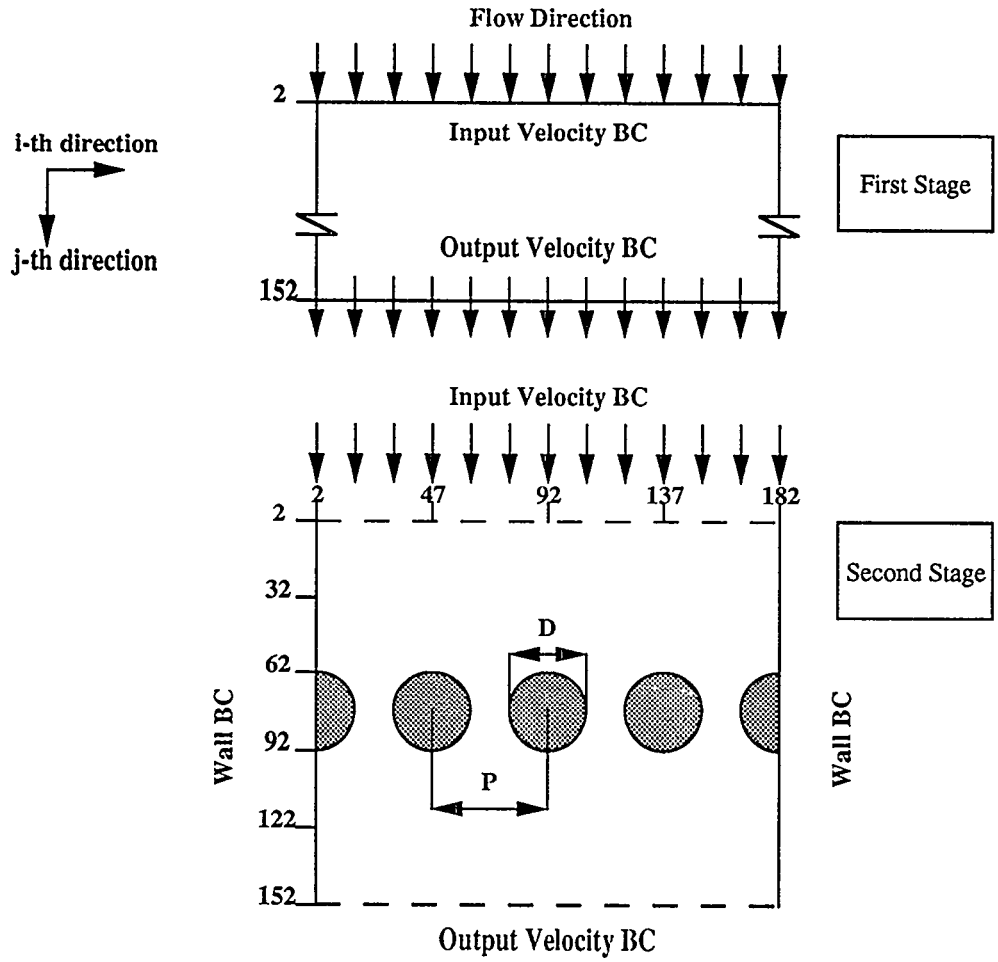

Figure 2. Two Dimensional Tube Row Nodalization

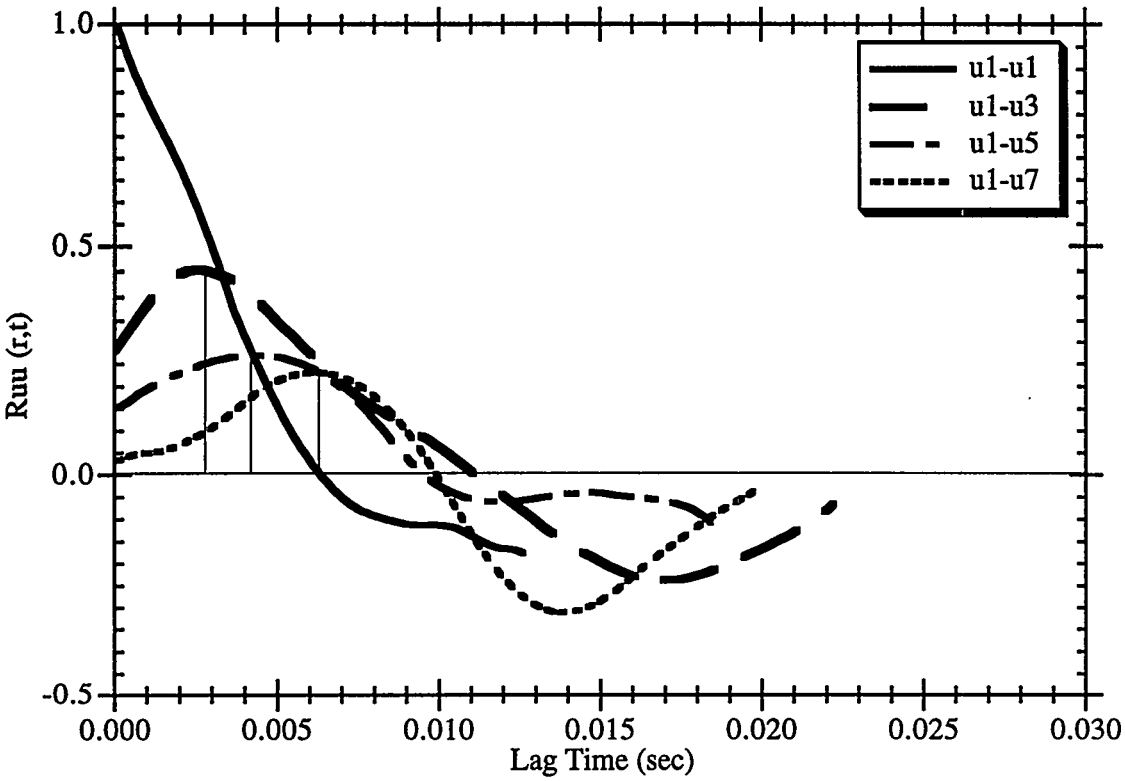

Figure 3. Streamwise Velocity Correlation (u1:u7)

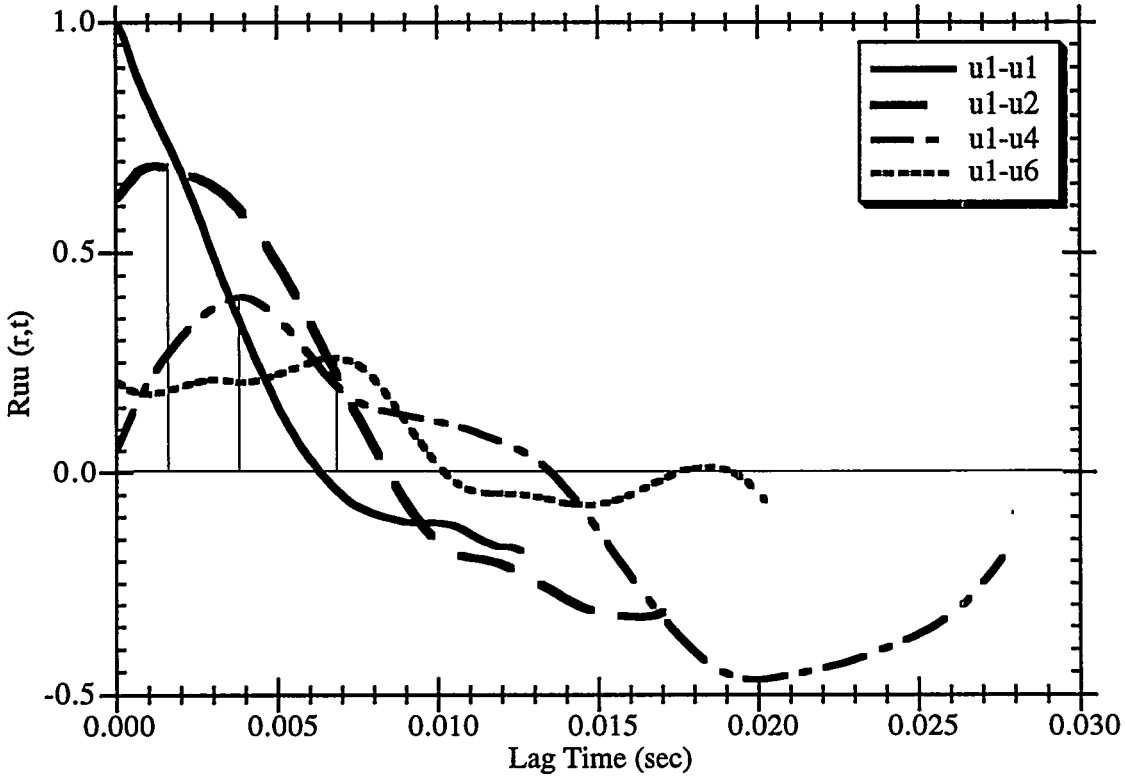

Figure 4. Streamwise Velocity Correlation (u1:u6)

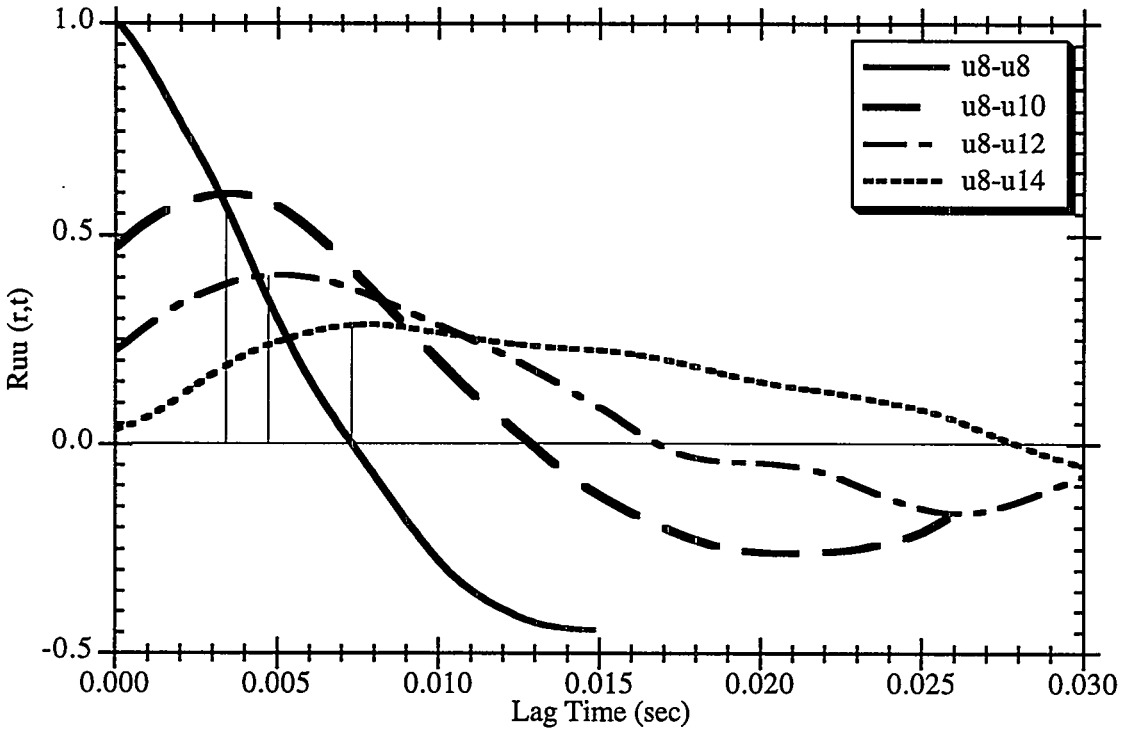

Figure 5. Streamwise Velocity Correlation (u8:u14)

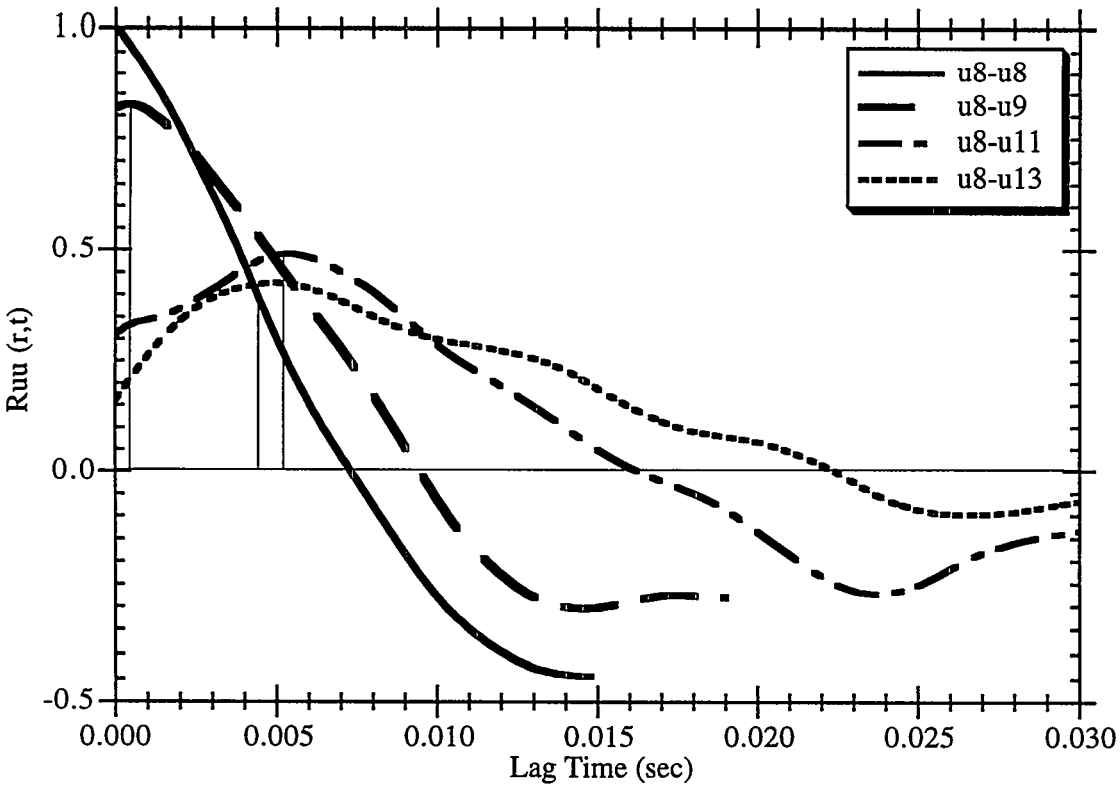

Figure 6. Streamwise Velocity Correlation (u8:u13)

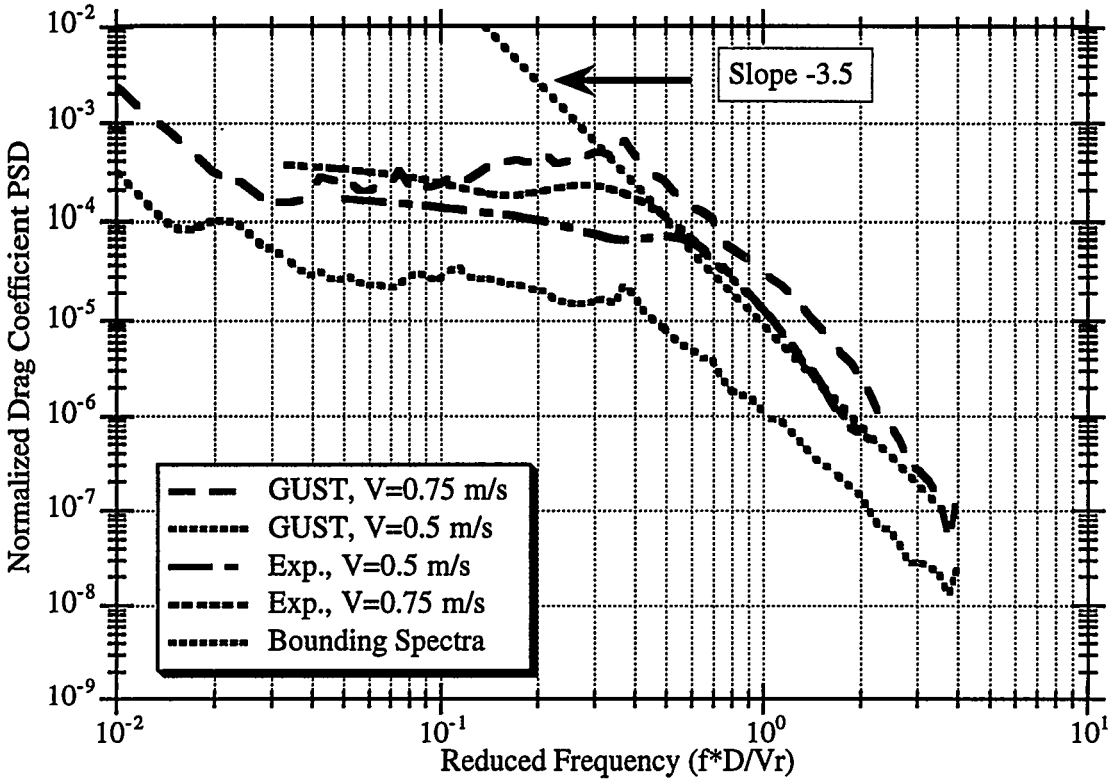

Figure 7. Normalized Drag Coefficient PSD Vs. Strouhal Number

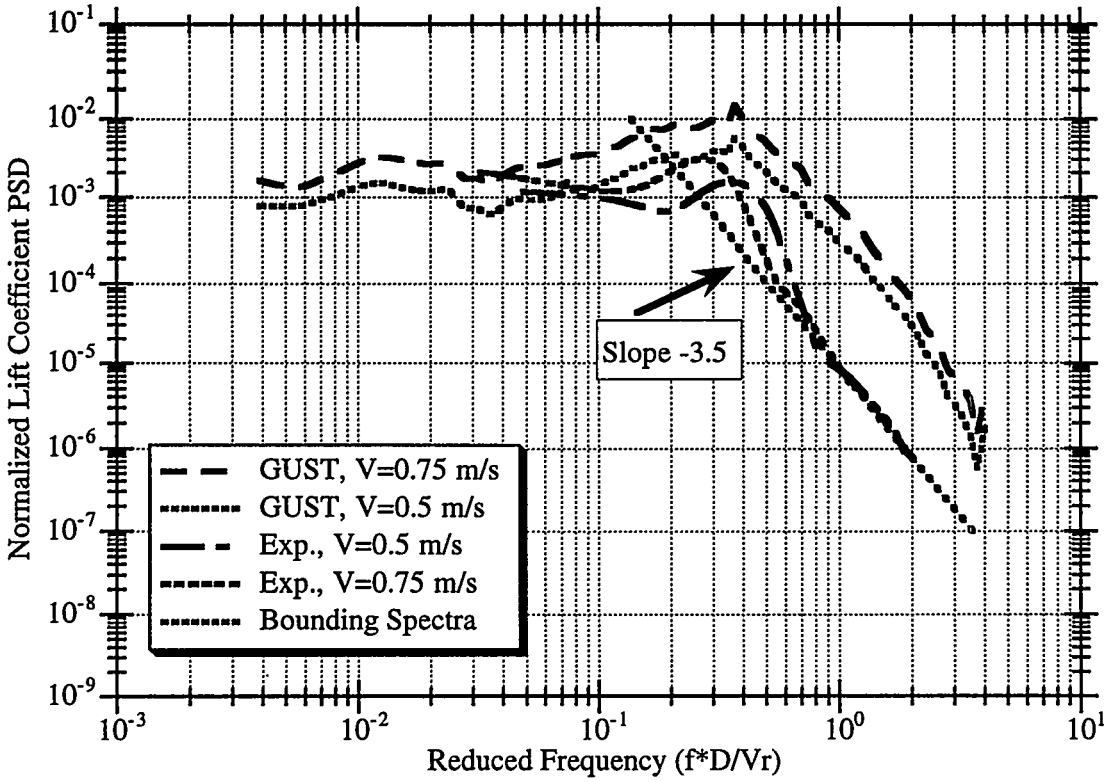

Figure 8. Normalized Lift Coefficient PSD Vs. Strouhal Number

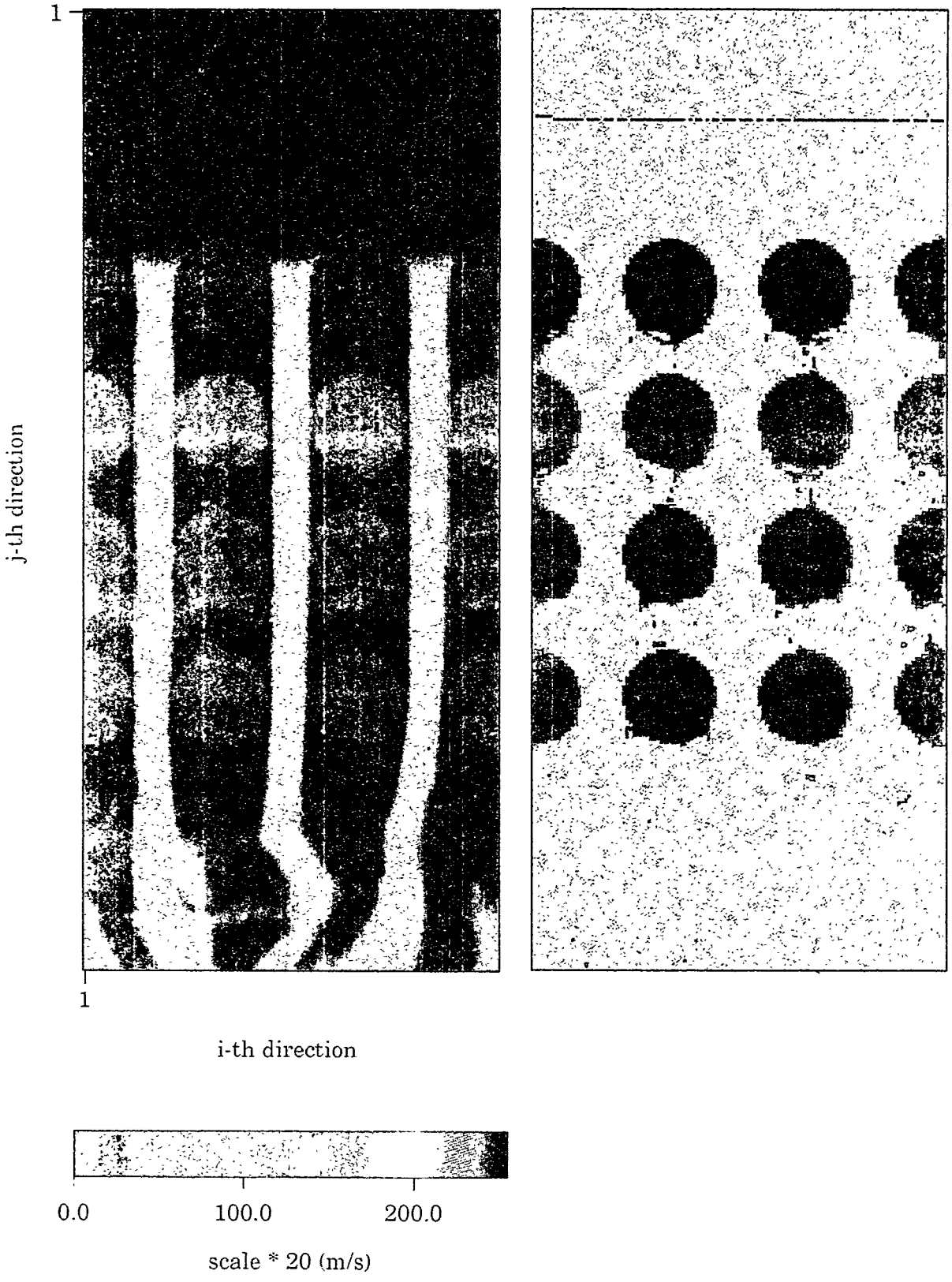

Figure 9. Frame Number 1

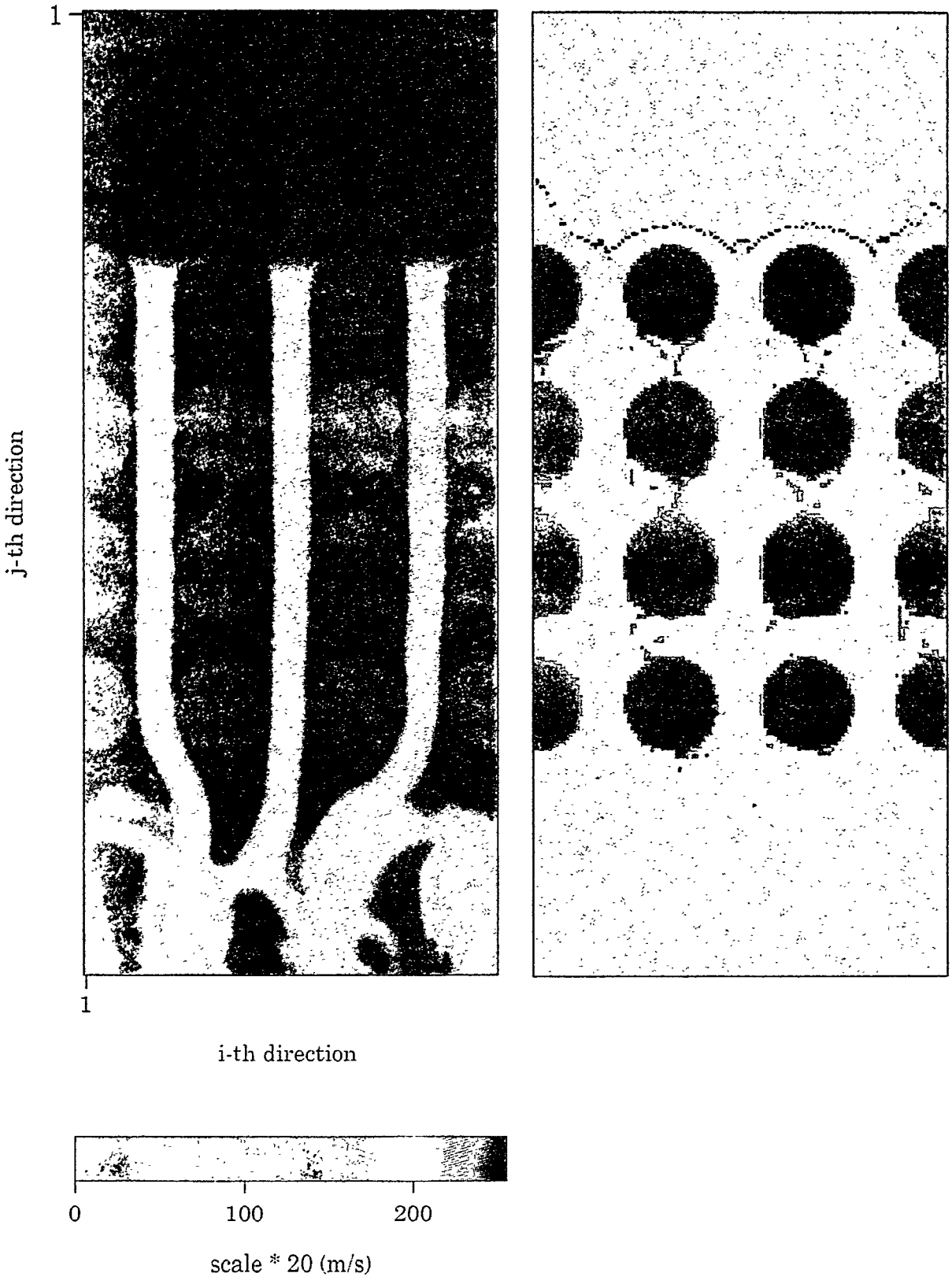

Figure 10. Frame Number 125

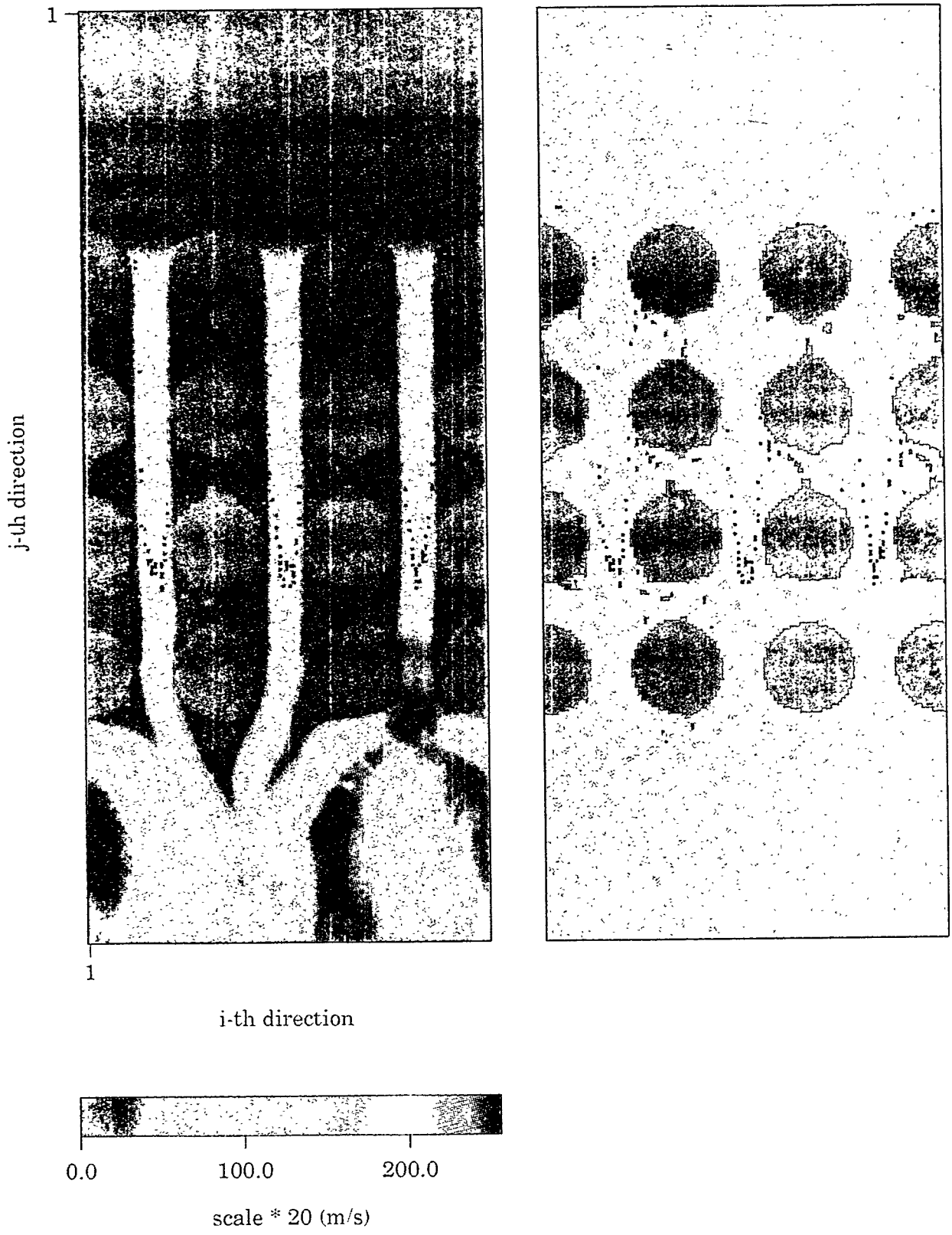

Figure 11. Frame Number 250

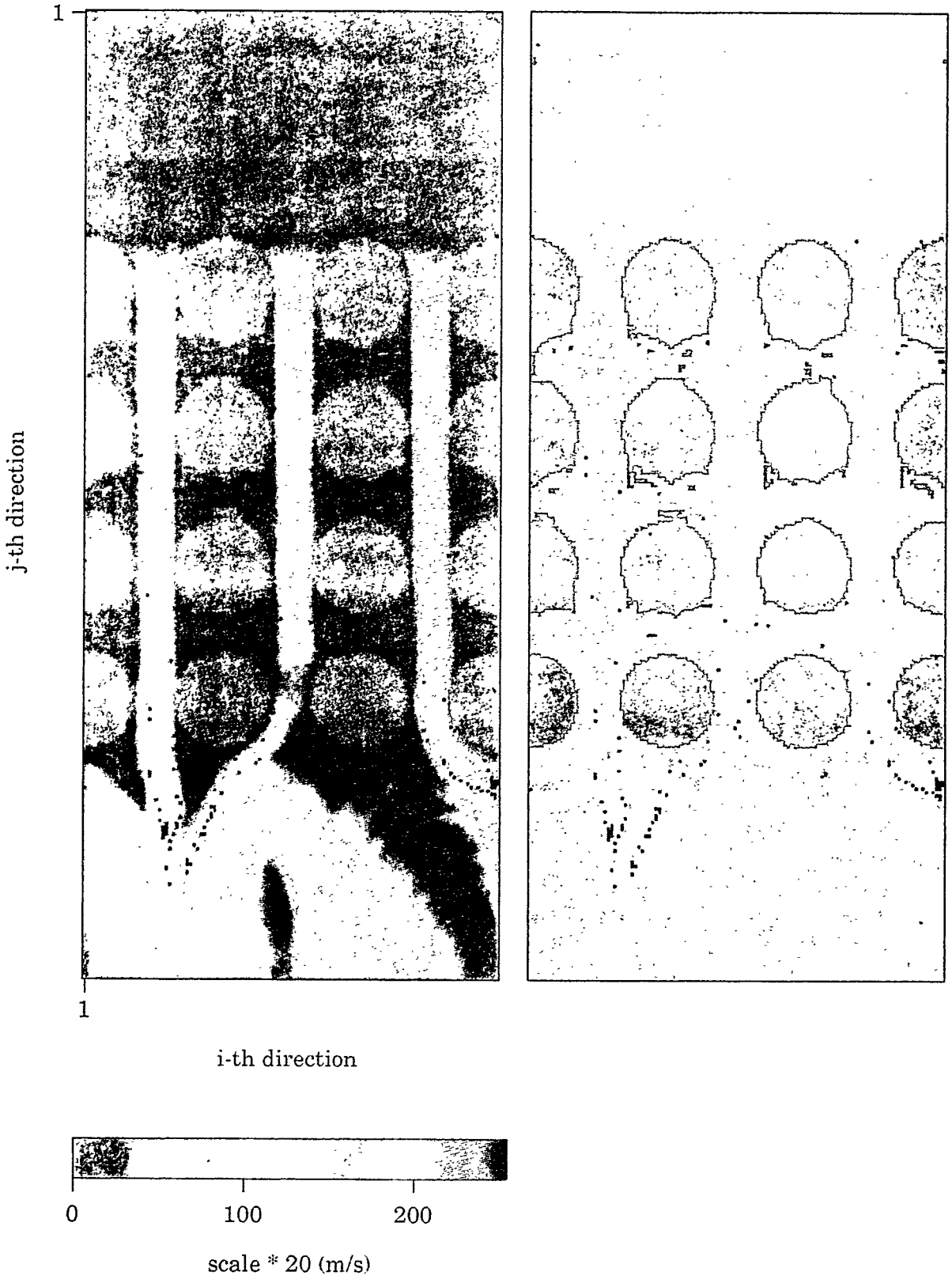

Figure 12. Frame Number 325

Statistical Parameter Characteristics of Gas-Phase Fluctuations for Gas-Liquid Intermittent Flow

G.Matsui, H.Monji and M.Takaguchi
Institute of Engineering Mechanics
University of Tsukuba
Tsukuba 305, Japan

ABSTRACT

This study deals with theoretical analysis on the general behavior of statistical parameters of gas-phase fluctuations and comparison of statistical parameter characteristics for the real void fraction fluctuations measured with those for the wave form modified the real fluctuations. In order to investigate the details of the relation between the behavior of the statistical parameters in real intermittent flow and analytical results obtained from information on the real flow, the distributions of statistical parameters for general fundamental wave form of gas-phase fluctuations are discussed in detail. By modifying the real gas-phase fluctuations to a trapezoidal wave, the experimental results can be directly compared with the analytical results. The analytical results for intermittent flow show that the wave form parameter, and the total amplitude of void fraction fluctuations, affects strongly on the statistical parameter characteristics. The comparison with experiment using nitrogen gas-water intermittent flow suggests that the parameters of skewness and excess may be better as indicators of flow pattern. That is, the macroscopic nature of intermittent flow can be grasped by the skewness and the excess, and the detailed flow structure may be described by the mean and the standard deviation.

INTRODUCTION

A flow pattern is considered as one of the basic and inherent parameters such as void fraction and slip ratio describing gas-liquid two-phase flow. Nevertheless, the flow pattern is not a quantitative parameter. However, some recent experiments and analyses have been developed under way to aim at the quantitative indication of the flow pattern [1]-[15].

Pervious experimental results [9]-[13] of flow pattern identification using PDF of differential pressure fluctuations corresponding to gas-phase fluctuations show that the statistical parameters (the mean, m, the standard deviation, σ, the skewness, γ_1, the excess, γ_2) exhibit the following peculiar behaviors of flow pattern in the parameter spaces; (1) It is feasible that a flow pattern is identified by the characteristics of the parameters. (2) The experimental data of (γ_1, γ_2) distribute on and around a parabolic line for plug or slug flows, and concentrate around the origin for bubble flow. (3) The experimental data of (m, σ) concentrate in a very small standard deviation region for stratified flow.

The peculiar distributions of the statistical parameters in their planes were analyzed using the fundamental gas-phase fluctuations formed with reference to the measured signals of fluctuations [14], [15]. The functional relations between m and σ, and between γ_1 and γ_2 were derived to explain the peculiar distributions of the parameters on their spaces. It was found that the flow pattern is characterized by the fundamental wave form of fluctuations such as a rectangular wave for intermittent flow and a triangle wave for bubble flow.

In the previous work [14], [15], the distributions of the statistical parameters were theoretically explained based on typical fundamental gas-phase fluctuations. However, because the real gas-phase fluctuations do not generally form an ideal and simple wave form similar to typical ones used in the theoretical analysis, the wave form parameters of the real fluctuations cannot be directly obtained. Accordingly, the statistical parameter characteristics for the real fluctuations cannot be directly discussed on the detail of flow pattern using only the real fluctuations. Hence, it is necessary to investigate in detail the relation between the flow pattern or gas-phase structure and the distributions of the statistical parameters by determining a wave form through modification of real fluctuations in order to treat analytically the real fluctuations.

In the present study, the behavior of the statistical parameters are more generally investigated by extending the analytical results for the typical wave form of intermittent flow. Furthermore, the relation between the flow pattern or gas-phase structure and the behavior of statistical parameters of the real gas phase fluctuations, measured by the constant current method for plug and slug flows, is compared with the analytical results for the wave form which modified the real fluctuations without a lack of flow pattern characteristics .

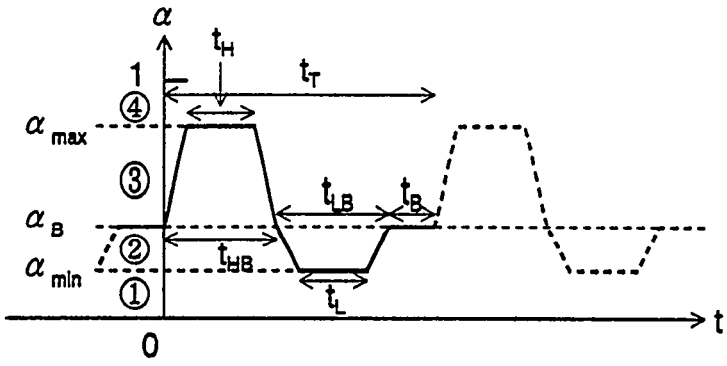

Fig.1 Fundamental wave form for analysis.

THEORETICAL ANALYSIS

Fundamental Wave Form

In previous work [14], [15], the flow pattern characteristics of real gas-liquid two-phase flow in a pipe have been analyzed supposing that the gas-phase fluctuations have a typical fundamental wave form. Figure 1 shows the fundamental wave form of gas-phase structure or the void fraction fluctuations for analysis. The fundamental wave form is composed of a trapezoidal part which are formed by a higher part (t_{HB}, $\alpha_{max} \geq \alpha \geq \alpha_B$) and a lower part ($t_{LB}$, $\alpha_B \geq \alpha \geq \alpha_{min}$), and a DC or base part (t_B, α_B) for a fundamental period (t_T). Steady two-phase flow has gas-phase (or void fraction) fluctuations obtained by repeating the fundamental wave. The variation of the fundamental wave form can easily represent some typical flow patterns. Here, when the wave form parameters, $f_H = t_H / t_{HB}$ and $f_L = t_L / t_{LB}$, are given, a wave form is determined, where $0 \leq f_H, f_L \leq 1$. At $f_H = f_L = 0$, the wave is triangular, and at $f_H = f_L = 1$, the wave is rectangular.

The duration times, t_{HB}, t_{LB} and t_B are normalized with t_T; $\tau_{HB} = t_{HB}/t_T$, $\tau_{LB} = t_{LB}/t_T$, $\tau_B = t_B/t_T$, where $\tau_{HB} + \tau_{LB} + \tau_B = 1$.

The statistical parameter characteristics can be revealed by analysis based on the fundamental wave forms for various flow patterns.

Statistical Parameter Characteristics for Intermittent Flow

Here intermittent flow with a more general wave form is considered comparing it with the previous case for a trapezoidal wave symmetric with respect to the base void fraction, α_B. That is slug or plug flow with void fraction fluctuations of trapezoidal waves not symmetric with respect to α_B, or at $\alpha_G - \alpha_B \neq \alpha_B - \alpha_L$, $\tau_B = 0$ or $\tau_{HB} + \tau_{LB} + \tau_B = 1$, and $f_H = f_L = f$. Thus, the wave form of the fundamental fluctuations becomes generally trapezoidal.

We have the following relation between m and σ;

$$\sigma^2 + \left[m - \left\{ \frac{2(1+2f)}{3(1+f)} \left(\frac{\alpha_G + \alpha_L}{2} - \frac{1-f}{2(1+2f)} \alpha_B \right) \right\} \right]^2 = \left\{ \frac{2(1+2f)}{3(1+f)} \right\}^2 \left\{ \left(\frac{\alpha_G - \alpha_L}{2} \right)^2 - \frac{(1-f)(5+7f)}{4(1+2f)^2} (\alpha_G - \alpha_B)(\alpha_B - \alpha_L) \right\}, \quad m, \sigma \geq 0, \qquad (1)$$

where α_G denotes the void fraction of gas slug ($= \alpha_{max}$) and α_L denotes the void fraction of liquid slug ($= \alpha_{min}$), respectively. The half circle (m, σ), expressed by Eq.(1), reduces generally to an arc because of the following restriction,

$$0 < \tau_{HB}, \tau_{LB} < 1. \quad (2)$$

When α_G and α_L are constant, the points of (m, σ) lie on a half circle (at f = 1) or an arc (at f < 1) in m -σ plane as shown in Figs. 2 to 5. The circle of Eq.(1) passes the origin for plug flow, because the void fraction of liquid plug is zero. Therefore, the points of (m, σ) in plug flow is located nearer the origin than those in slug flow.

Figures 2 to 5 show the effect of the wave form parameter or duration ratio, f, the base void fraction, α_B, and both the maximum and the minimum void fractions, α_G and α_L, on a half circle or an arc in Eq.(1). The arrows in the figures indicate the moving direction of the point (m, σ) for increasing τ_{HB} ($0<\tau_{HB}<1$). The numerical results show the following characteristics in the m - σ plane;

- The arc is reduced but the center shifts a little toward the right with decreasing f, as shown in Fig.2. This suggests that the wave form parameter, f, affects strongly the existence region of (m, σ), because the fundamental wave form depends on f.
- The region of arc changes but the center shifts slightly with increasing α_B, as shown in Fig.3. This suggests that

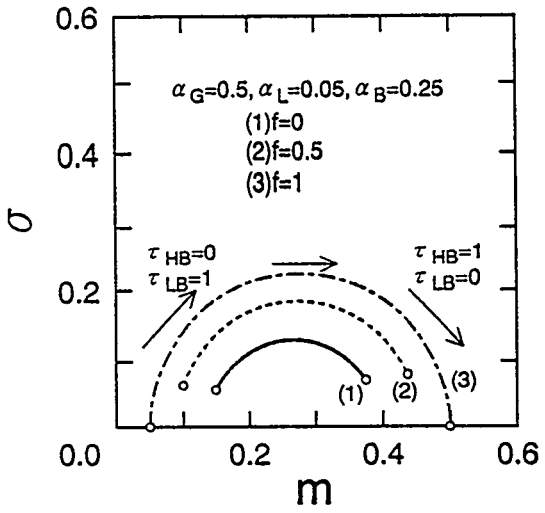

Fig.2 Effect of the wave form parameter, f on a half circle or an arc expressed by Eq.(1) in m-σ plane.

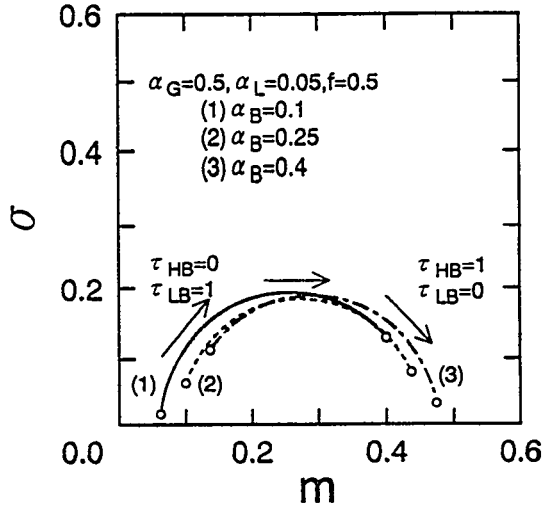

Fig.3 Effect of the base void fraction, α_B in m-σ plane.

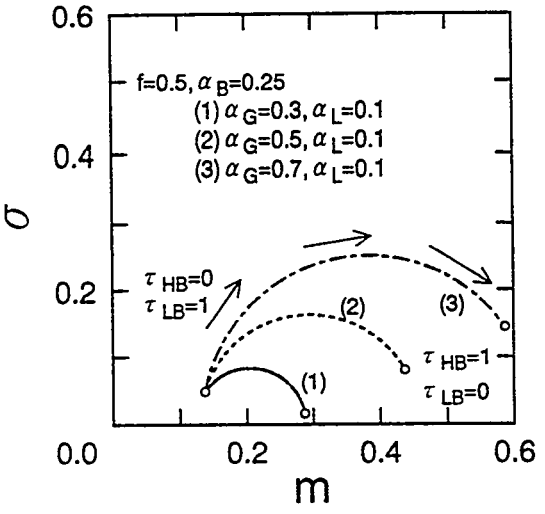

Fig.4 Effect of the total amplitude, $(\alpha_G - \alpha_L)$ in m-σ plane.

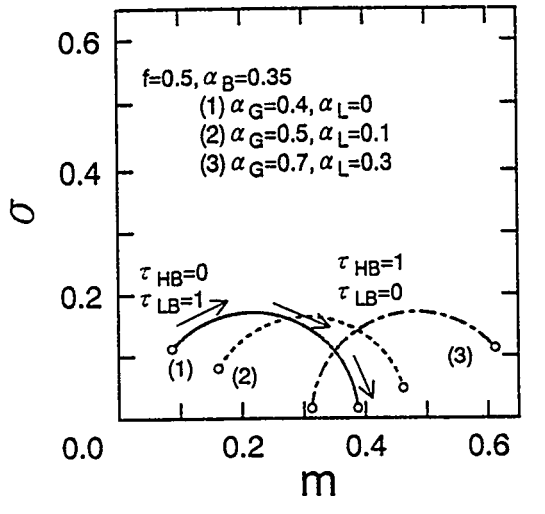

Fig.5 Effect of α_G and α_L in m-σ plane.

the existence region of (m, σ) depends little on α_B.

- The arc becomes big and the center shifts toward the mean increasing direction with increasing ($\alpha_G - \alpha_L$), as shown in Fig.4. In the case of $\alpha_G - \alpha_B = constant$ as shown in Fig.5, the arc do not become big but the center shifts toward the mean increasing direction. This suggests that the existence region of (m, σ) depends on the total amplitude of trapezoidal wave, $(\alpha_G - \alpha_L)$ and $(\alpha_G + \alpha_L)/2$.

For a symmetrical trapezoidal wave form at $\alpha_G - \alpha_B = \alpha_B - \alpha_L$, the relation between γ_1 and γ_2 is shown in Fig.6. The arrows in the figure indicate the moving direction of the point (γ_1, γ_2) for increasing τ_{HB} $(0<\tau_{HB}<1)$. The numerical results namely curved lines are not a parabola except the case of f = 1.

On the other hand, at $\alpha_G - \alpha_B \neq \alpha_B - \alpha_L$, the curved lines become asymmetrical with regard to the γ_2-axis as shown in Figs.7 to 10 corresponding to Figs.2 to 5, respectively. The arrows in the figures indicate the moving direction of the point (γ_1, γ_2) for increasing τ_{HB} $(0 < t_{HB} < 1)$. The numerical results show the following characteristics in the γ_1-γ_2 plane;

- The curved lines reduce in the left half plane with decreasing *f*, but the curved lines extend in the right half plane comparing with the symmetrical case of $\alpha_G - \alpha_B = \alpha_B - \alpha_L$. In addition, the minimum value of γ_2 increases with

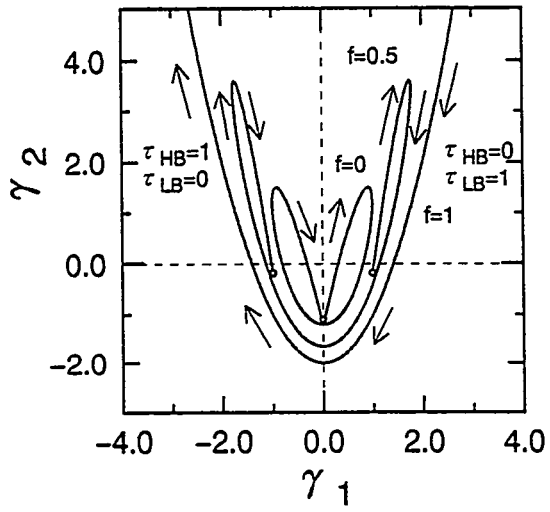

Fig.6 Relations between γ_1 and γ_2 for a trapezoidal wave form in γ_1-γ_2 plane. $(\alpha_G - \alpha_B = \alpha_B - \alpha_L)$.

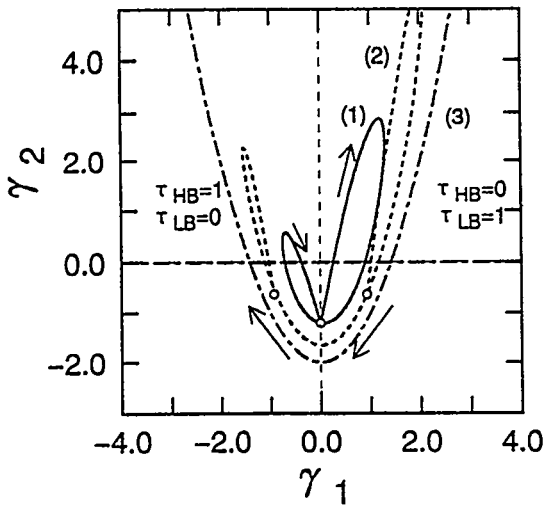

Fig.7 Effect of the wave form parameter, *f* on a curve line in γ_1-γ_2 plane . $(\alpha_B = 0.25,\ \alpha_G = 0.5,\ \alpha_L = 0.05)$. (1) f = 0 (2) f = 0.5 (3) f = 1 .

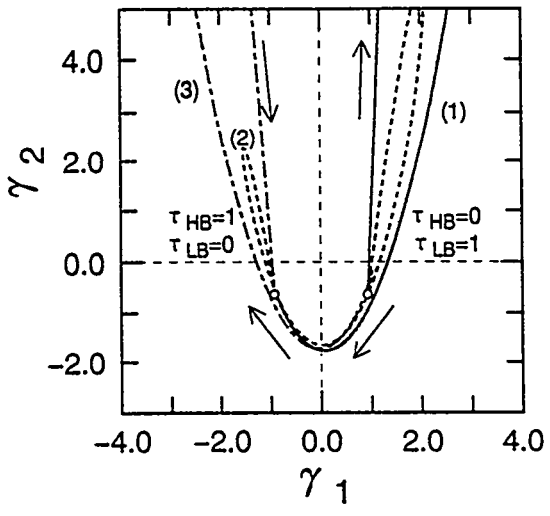

Fig.8 Effect of the base void fraction, α_B in γ_1-γ_2 plane. $(\alpha_G = 0.5,\ \alpha_L = 0.05,\ f = 0.5)$. (1) $\alpha_B = 0.1$ (2) $\alpha_B = 0.25$ (3) $\alpha_B = 0.4$.

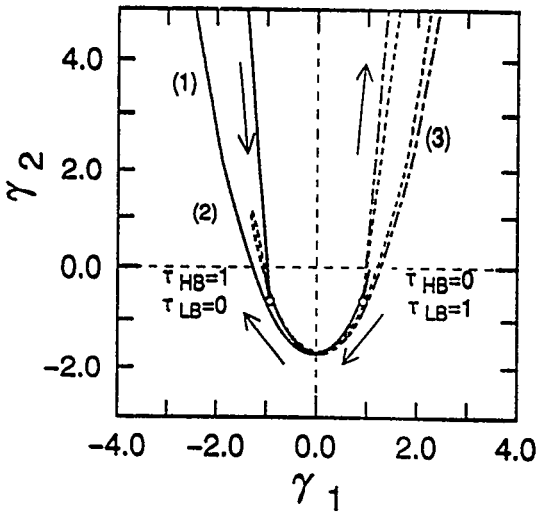

Fig.9 Effect of the total amplitude, $(\alpha_G - \alpha_L)$ in γ_1-γ_2 plane. ($\alpha_B = 0.25$, f =0.5). (1) $\alpha_G = 0.3$, $\alpha_L = 0.1$ (2) $\alpha_G = 0.5$, $\alpha_L = 0.1$ (3) $\alpha_G = 0.7$, $\alpha_L = 0.1$.

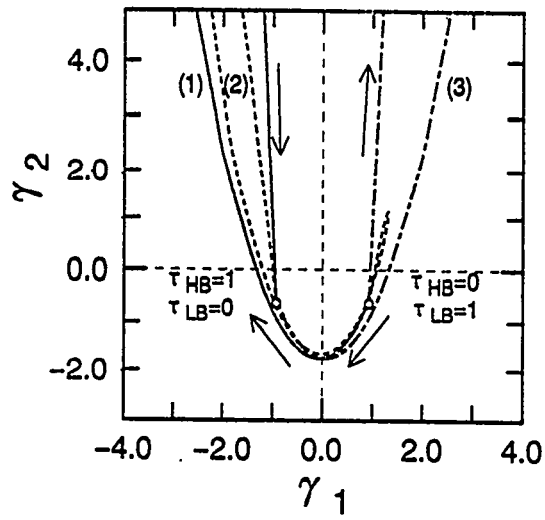

Fig.10 Effect of α_G and α_L in γ_1-γ_2 plane. ($\alpha_B = 0.25$, f =0.5). (1) $\alpha_G = 0.4$, $\alpha_L = 0$ (2) $\alpha_G = 0.5$, $\alpha_L = 0.1$ (3) $\alpha_G = 0.7$, $\alpha_L = 0.3$.

decreasing *f*. This suggests that *f* changes remarkably the existence region of (γ_1, γ_2), as well as in the m-σ plane.

- The curved lines reduce in the left half plane but extend in the right half plane with increasing ($\alpha_G - \alpha_B$) or decreasing ($\alpha_B - \alpha_L$). This suggests that the existence region of (γ_1, γ_2) depends a little on α_B in the meaning of a distribution around a parabolic line. However, the existence region depends on the total amplitude, $(\alpha_G - \alpha_L)$, and $(\alpha_G + \alpha_L)/2$, as well as in the m-σ plane.

COMPARISON WITH EXPERIMENT

Experimental Apparatus and Instrumentation

A schematic diagram of the experimental apparatus and its test section is shown in Fig.11. The apparatus was a single channel closed loop. Liquid flowed into a gas-liquid separator through a flowmeter, a mixer and a horizontal test section from the separator. Gas flowed into the mixer through a gas flowmeter from a gas-cylinder to make two-phase flow in the test section. After that the gas flowed into the separator. The test section was constructed using a transparent plastic tube of 20 mm i.d.. Ring-type electrodes of width 5.5 mm were fitted in the pipe wall of the test section 1.6 m downstream of the mixer.

Nitrogen gas (or air) and water were used as working fluids. The water flowrate was measured by a turbine-type flowmeter and the gas flow rate was measured by a float-type flowmeter. Void fraction was detected at the test section by a constant current method.

The void fraction was sampled by a 12-bit A/D converter with the conversion time of 10 μs, and fed into a personal computer for data processing. The sampling time interval was 10 ms and the number of sampling point was 20,480 per each void fraction signal.

The experiments were carried out in the range of the liquid and gas superficial velocities, $U_L = 0.26 - 0.80$ m/s and $U_G = 0.02 - 1.6$ m/s. The flow pattern was observed by sight, photographs, and video images. Measurements were carried out in the flow pattern region especially from plug flow to slug flow under the conditions of the constant liquid flowrate and several gas flowrates changed. Void fluctuation signals through a low pass filter were sampled 20,480 points at 10 ms intervals.

The statistical parameters, *m*, σ, γ_1, and γ_2 were calculated from the signals measured. In addition, based on the signal wave form or fundamental wave form modified from the real void fraction fluctuations, the relation between the statistical parameters of modified fluctuations were also calculated.

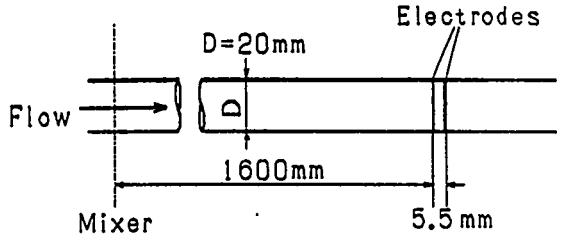

Test section

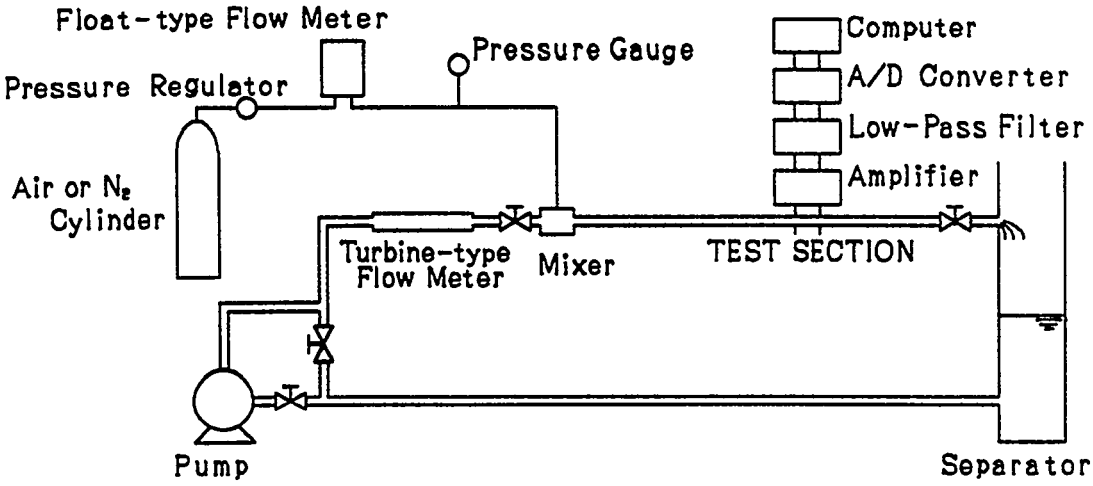

Experimental apparatus

Fig.11 Schematic diagram of experimental apparatus.

Experimental Results and Discussion

Figure 12 shows examples of the void fraction fluctuations of plug and slug flows. The dotted lines in the figures indicate the measured signals and the solid lines in the figures, the modified ones. The measured signals were modified to eliminate small amplitude fluctuations compared with the difference between the maximum and the minimum values and to simplify slow fluctuations to a constant value. The signals in each experimental example are arranged in order of increase of the gas superficial velocity. The real void fraction fluctuations measured were modified to treat analytically the statistical parameter characteristics, based on the knowledge of theoretical results obtained by the method above.

The experimental data, namely the statistical parameters obtained from the real void fraction fluctuations, and the analytical results based on the modified void fraction wave form are plotted in Fig.13 (a) to (c) corresponding to Fig.12 (a) to (c). Figure 13 show characteristics in the m-σ plane and in the γ_1-γ_2 plane. The solid lines in the figures represent the results calculated based on the all modified signals in each example, the dotted lines in the figures represent the fitted arcs or curved lines obtained based on a fundamental wave form determined to approximate some experimental data points with an arc, and the dash-dotted lines in the figure represent the results calculated based on the modified signals corresponding to the data used for the approximation. These lines are drawn only within the range of the normalized duration time of higher part, τ_{HB} estimated from the measured signals. The number of data point in Fig. 13 is corresponding to the signals shown in Fig.12.

It may be expected that the data on the statistical parameters lie on an arc calculated by the modified signal, when the void fraction does not depend on the gas flowrate. However, the arcs (m, σ) obtained from the modified signals don't agree quantitatively with the experimental data, but the curved lines in the γ_1-γ_2 plane agree well with the data. On the other hand, the dotted curved lines in the γ_1-γ_2 plane also agree well with the data even under the conditions for the fitted arcs. This suggests that the parameters, γ_1 and γ_2 may be better than the parameters, m and σ as the indicators of flow pattern, that is, the macroscopic nature or essence of intermittent flow can be grasped by γ_1 and γ_2. However, the detailed flow structure may be described by m and σ, because of strong dependency on the wave form parameter, f. In other words, the microscopic nature of the flow may be obtained, if the real fluctuations

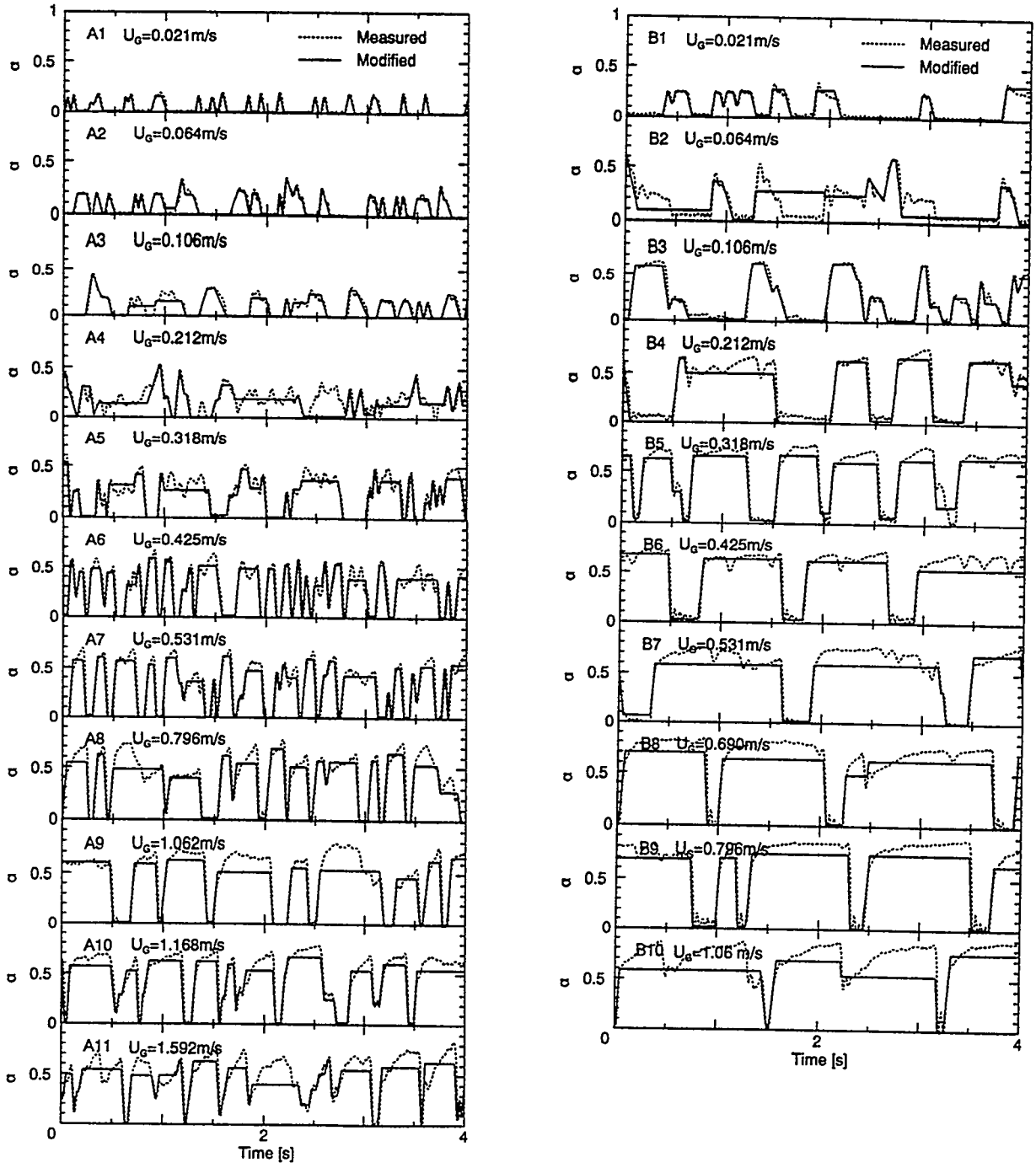

(a) Example (A): U_L = 0.58 m/s, U_G= 0.02 - 1.59 m/s. (b) Example (B): U_L = 0.27 m/s, U_G= 0.02 - 1.06 m/s.

Fig.12 Examples of void fraction signals.

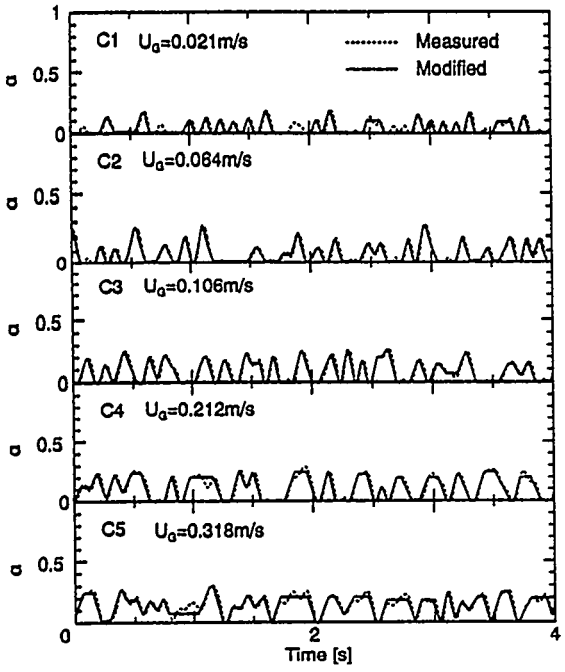

(c) Example (C): U_L = 0.67 m/s, U_G= 0.02 - 0.32 m/s

Fig.12 Examples of void fraction signals.

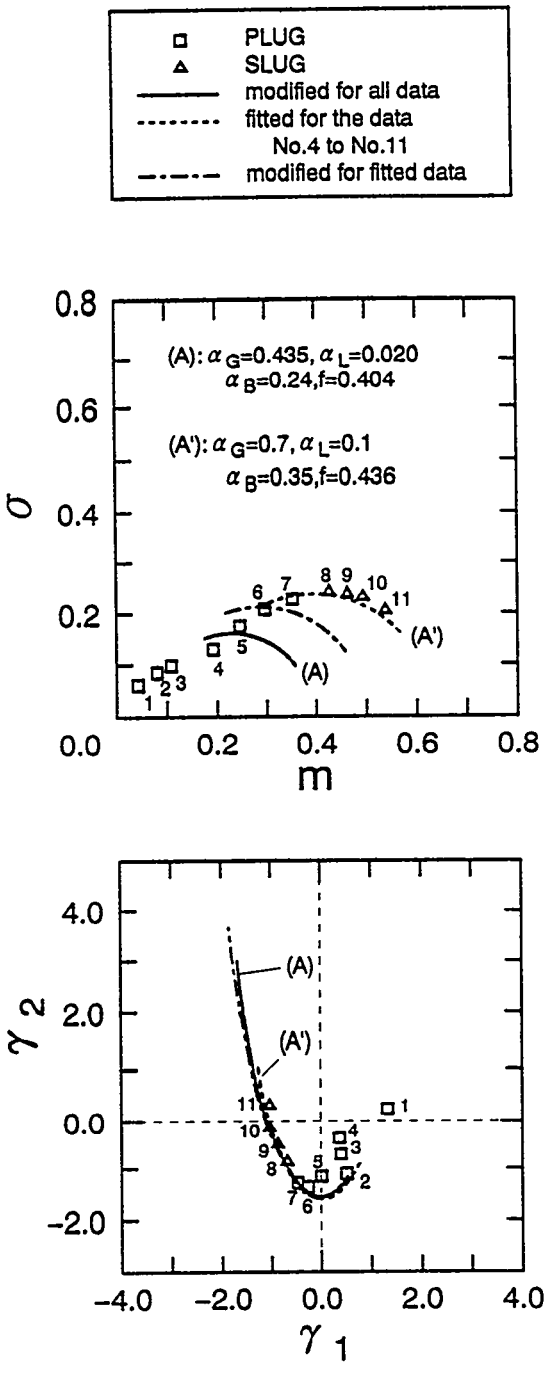

(a) Example (A): U_L = 0.58 m/s, U_G= 0.02 - 1.59 m/s.

Fig.13 Flow characteristics in statistical parameter planes.

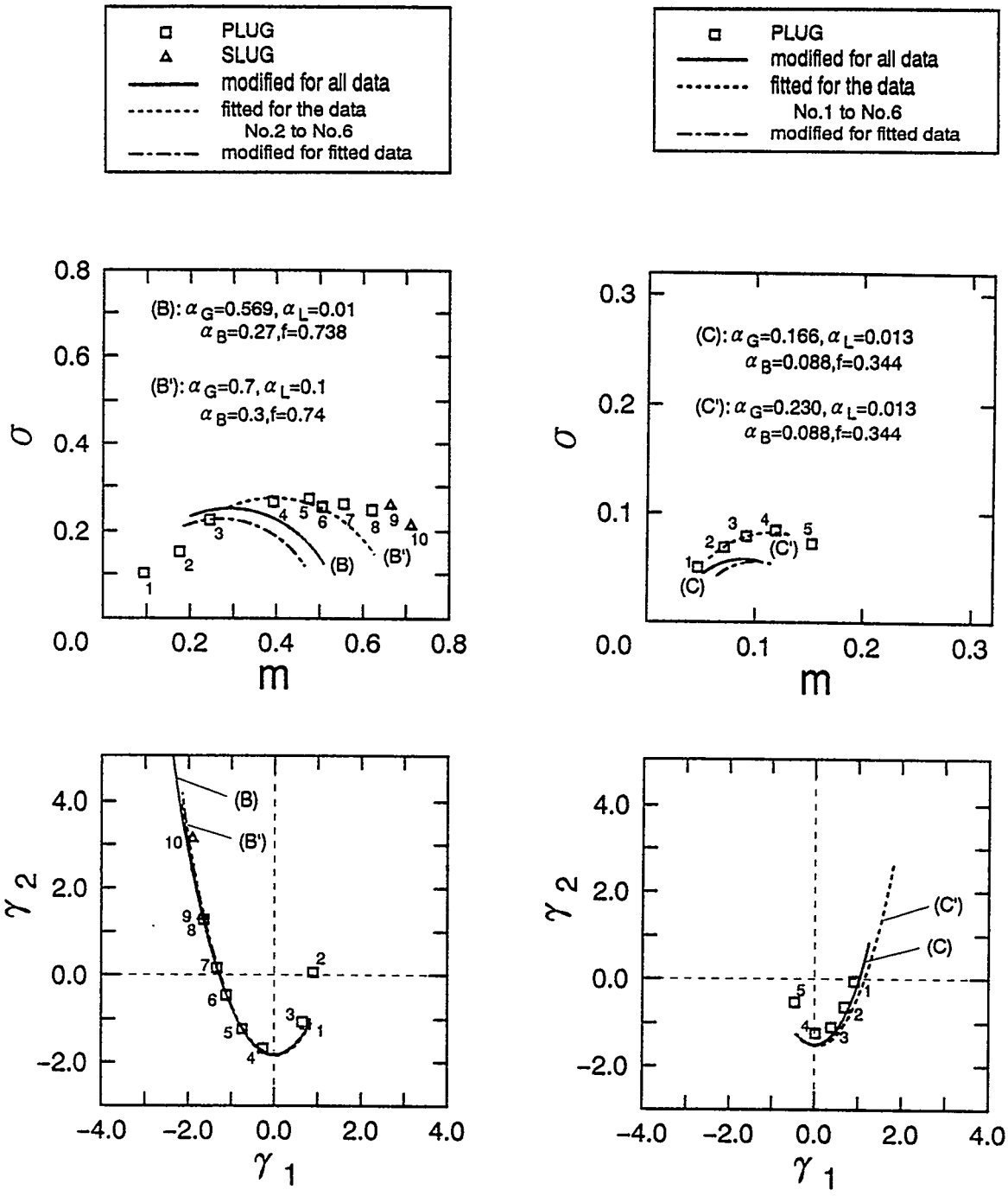

(b) Example (B): U_L = 0.27 m/s, U_G= 0.02 - 1.06 m/s.

(c) Example (C): U_L = 0.67 m/s, U_G= 0.02 - 0.32 m/s.

Fig.13 Flow characteristics in statistical parameter planes.

were modified to the adequate fundamental wave form. In the small gas flowrate region of Examples (A) and (B), the tendency of experimental data is different from the arcs in the m - σ plane and the curved lines in the γ_1-γ_2 plane. This suggests the assumption of $f_H = f_L = f$ may not be valid for these flows, and that a further study for flow pattern recognition may be necessary if these flows are judged not to be intermittent flow.

CONCLUSION

The detailed behavior of the statistical parameters of the gas-phase fluctuations in the parameter planes was investigated for plug and slug flows analytically and experimentally. The analytical results showed that the points (m, σ) lie on a half circle or an arc when the void fractions in both liquid and gas slugs do not depend on the gas flowrate, and that the center and radius are influenced by both the shape and the total amplitude of the gas-phase fluctuations. The curved lines (γ_1, γ_2) are also influenced by those factors.

Experiments were carried out using nitrogen gas-water two-phase flow. The behavior of statistical parameters was analyzed based on the void fraction signals measured by the constant current method. Furthermore, the relation between the measured gas-phase structure and the behavior of the statistical parameters was compared with the analytical results for the modified fluctuations. The results show that the arcs (m, σ) do not agree quantitatively with the experimental data but the behavior of parameters, m and σ was qualitatively explained by the analytical results. On the other hand, the curved lines (γ_1, γ_2) agree well with the experimental data. This suggests that the parameters, γ_1 and γ_2 may be better than the parameters, *m* and σ as the indicators of flow pattern. However, the detailed flow structure may be described by *m* and σ, because of strong dependency on the wave form parameter.

NOMENCLATURE

m	mean
f	wave form parameter (ratio of duration time of maximum amplitude to that of higher or lower part)
U_G	gas superficial velocity
U_L	liquid superficial velocity

Greek symbols

α	void fraction
γ_1	coefficient of skewness
γ_2	coefficient of excess
σ	standard deviation
τ	normalized time ($= t / t_T$).

Subscripts

B	base line
G	gas plug or slug
H	maximum void fraction part
HB	higher void fraction part
L	minimum void fraction part, or liquid plug or slug
LB	lower void fraction part
T	period

REFERENCES

[1] M.G. Hubbard and A.E. Dukler, "The characterization of flow regimes for horizontal two-phase flow", Proc. Heat Transfer and Fluid Mechanics Institute, Stanford Press, 100-121(1966).

[2] O.C. Jones and N. Zuber, "The interrelation between void fraction fluctuations and flow patterns in two-phase flow", Int. J. Multiphase Flow 2, 273-306(1975).

[3] J. Weisman, D. Duncan, J. Gibson and T. Crowford, "Effects of fluid properties and pipe diameter on two-phase flow patterns in horizontal lines", Int. J. Multiphase Flow 5, 437-462(1977).

[4] G.Matsui and S. Arimoto, "Flow pattern estimation of gas-liquid two-phase mixture in a perpendicular pipe", ICHMT-1978 Int. Seminar on Momentum, Heat and Mass Transfer in Two-Phase Energy and

Chemical System, (1978).
[5] P. Kehler, "Use of PNA techniques for two-phase flow characterization", Transient Two-Phase Flow (Proc. Third CSNI Specialist Meeting), Hemisphere, 39-50(1981).
[6] G. Matsui, "Identification of flow regimes in vertical gas-liquid two-phase flow using differential pressure fluctuations", Int. J. Multiphase Flow 10, 711-720(1984).
[7] A.M.C. Chan, "A single-beam multi-detector gamma densitometer for void fraction and phase distribution measurements in transient two-phase flows", Measuring Techniques in Gas-Liquid Two-Phase Flows, Springer-Verag, 281-304(1984).
[8] R.W. Albrecht, R.G. Bass, R.D. Crowe, D.J. Dailey and D.F. Hollenbach, "Noise techniques for dynamic two-phase flow characterization", Proc. Japan-US Seminar on Two-Phase Flow Dynamics, B-9(1984).
[9] G. Matsui, "Identification of flow patterns in horizontal gas-liquid two-phase flow using differential pressure fluctuations", Preprints, Int. Symp. on Fluid Control and Measurement, Pergamon Press, Tokyo, 819-824(1985).
[10] G. Matsui, "Automatic Identification of Flow Regimes in Vertical Two-Phase Flow Using Differential Pressure Fluctuations", Nuclear Engineering and Design 95, 221-231(1986).
[11] G.Matsui, T.Aizawa and A.Morita, "Statistical properties of differential pressure fluctuations and flow patterns in horizontal gas-liquid two-phase flow (differential pressure between the top and the bottom of a tube cross-section), Trans. JSME(B), 52, 2337-2344(1986) .
[12] G. Matsui, T. Aizawa and T. Kumazawa, "Statistical characteristics of differential pressure fluctuations and flow patterns of gas-liquid two-phase flow in a inclined pipe", Proc. 1987 ASME-JSME Thermal Engineering Joint Conf., 5, 397-402(1987).
[13] G.Matsui and T.Aoki, "Identification method of flow patterns in gas-liquid two-phase flow", Proc. of Tenth Symposium on Efficiency Use of Energy and Direct Electrical Power Generation, 260-269(1988).
[14] H. Monji, T. Sugiyama and G. Matsui, "Statistical Parameter Characteristics of Gas-Phase Fluctuations in Gas-Liquid Two-Phase Flow", Proc. Japan-U.S. Seminar on Two-Phase Flow Dynamics, 269-276(1992).
[15] G.Matsui and H.Monji, "Statistical Parameter Characteristics of Gas-Phase Fluctuations in Gas-Liquid Two-Phase Flow", Proc. German-Japanese Symposium on Multi-Phase Flow (Supplement), KfK 5411, 41-52(1994).

3-D Flow Analyses for Design of Nuclear Fuel Spacer

Zeses Karoutas
ABB Combustion Engineering, 1000 Prospect Hill Road, Windsor, Connecticut 06095-0500, U.S.A.

Chun-Yuan Gu
ABB Corporate Research, S-721 78 Västerås, Sweden

Bertil Schölin
ABB Atom AB, S-721 63 Västerås, Sweden

Abstract

The Computational Fluid Dynamics (CFD) code, CFDS-FLOW3D, was used to develop improved fuel designs for PWR cores. It was used primarily to understand the fluid dynamics of grid spacers, the mass transfer between subchannels caused by spacers and in the long term to develop two-phase models which enable prediction of critical heat flux in PWR fuel.

A single subchannel of one grid span was modeled. In this model different spacer designs with mixing devices were analyzed. A special treatment of the boundary condition was developed making use of flow symmetry to model the mass transfer between different subchannels and minimize the size of the computational model. This reduced the computational model to a fraction of a subchannel using traditional periodic boundary conditions. The Navier-Stokes equation was solved for the liquid and the flow turbulence was modeled by k-ε turbulence model. The spacer and mixing device were treated as infinite thin surfaces in the model and a zero velocity condition and turbulent wall function were applied on each side of the thin surfaces. This approach simulated the swirl from the mixing devices well, but had the drawback of not predicting pressure drop accurately since the wake behind the plates and the acceleration effect of the spacers were ignored.

CFDS-FLOW3D models with mixing devices were applied in the single-phase flow regime. Velocity profiles from the CFDS-FLOW3D models were compared to Laser Doppler Velocimeter measurements taken from the flow field downstream of spacers in a full scale, cold water test loop. The predicted axial and lateral velocity profiles were in good agreement with the measurements. The evaluation of the performance of different spacer devices was made by comparing the swirl ratio downstream of the grid spacers. In future efforts it is planned to evaluate heat transfer coefficient downstream of the spacer, to implement two-phase flow models, and to model the superheated boundary layer on the surface of the fuel rod for predicting DNB.

1. INTRODUCTION

The Computational Fluid Dynamics (CFD) code, CFDS-FLOW3D[1] was used to develop improved fuel designs by ABB for PWR cores. It was used primarily to understand the fluid dynamics of grid spacers, the mass transfer between subchannels caused by spacers and in the long term to develop two-phase flow models which enable prediction of Critical Heat Flux in PWR fuel.

2. PWR APPLICATIONS FOR NUCLEAR FUEL SUBCHANNELS

2.1 Governing Equations

The primary flow in a PWR is mainly single phase flow. The water is heated by the fuel rods, and a complex flow pattern can be present due to the mixing process within the subchannels.

The Reynolds Averaged Navier-Stokes equations with the k-ε turbulence model were utilized in the analyses. These equations which include the conservation of mass, momentum, and energy are expressed as:

$$\frac{\partial}{\partial t}(\rho_l) + \nabla \bullet (\rho_l \vec{u}_l) = 0 \tag{1}$$

$$\frac{\partial}{\partial t}(\rho_l \vec{u}_l) + \nabla \bullet \left(\rho_l \vec{u}_l \otimes \vec{u}_l - \mu_l \left(\nabla \vec{u}_l + (\nabla \vec{u}_l)^T\right)\right) = -\nabla p \tag{2}$$

$$\frac{D}{Dt}(\rho_l h_l) - \nabla \bullet (\lambda_l \nabla h_l) = q \tag{3}$$

where, ρ, $\vec{u}$, p and h are the density ,velocity, pressure and enthalpy of the water respectively. The heat flux into the water is given by q. The subscript l denotes the liquid phase.

In the PWR, the water flow is highly turbulent. It is not possible to resolve all scales in time and space by the numerical simulation. The common approach in engineering analyses is to resolve the mean (averaged) flow field, and to model the fluctuating flow. A widely used model is the k–ε turbulence model. Here, k stands for turbulent kinetic energy, and ε stands for the dissipation rate, Launder, Spalding, (1974)[2].

The effective viscosity in the governing equations (1-3) has been redefined as,

$$\mu_l = \mu_{l,\lambda} + \mu_{l,t} \tag{4.a}$$

Where,

$$\mu_{l,t} = C_\mu \frac{k^2}{\varepsilon} \tag{4.b}$$

$\mu_{l,\lambda}$ is laminar viscosity and

C_μ is a model constant

The partial differential equations are solved by the CFDS-FLOW3D code, which uses a finite volume approach with multi-block structure.

2.2 Modeling of Subchannels with Mixing Devices

A single subchannel of one grid span was modeled in the CFDS-FLOW3D code by ABB Corporate Research for PWR applications. In this model, different spacer designs with mixing devices were analyzed in the single-phase flow regime. Two different mixing devices shown in Figures 2-1 and 2-2 were selected for modeling, based on different flow patterns generated by the mixing devices. The split vane design shown in Figure 2-1 generates a swirling flow pattern in the subchannel and the squeezed tube design in Figure 2-2 generates a swirling flow pattern around the fuel rod. In Figure 2-1 two vanes are placed on top of the spacer and bent in opposite directions to promote a swirling flow pattern in the subchannel. In Figure 2-2 a circular tube placed in the spacer is squeezed at the top to swirl flow around the fuel rod. Figures 2-1 and 2-2 also show a larger array of the spacers to demonstrate flow patterns in adjacent channels. In the axial geometry of the split vane model, the simulation starts 45 mm upstream of the leading edge of the spacer and the total length of the model is 570 mm. For the squeezed tube model the simulation starts at 50 mm upstream of spacer and the total length is 600 mm.

To model the diversion of flow between subchannels and minimize the size of the computational model, a special treatment of the boundary condition was developed making use of flow symmetry. This reduces the computational model to a fraction of a subchannel (1/2 for split vane and 1/4 for squeezed tube) using traditional periodic boundary conditions. Simply described, what is coming out through one part of the boundary is going in through another part of the boundary in the computational domain. The boundary conditions are shown in Figures 2-3a and 2-3b for the split-vane and squeezed tube spacer models.

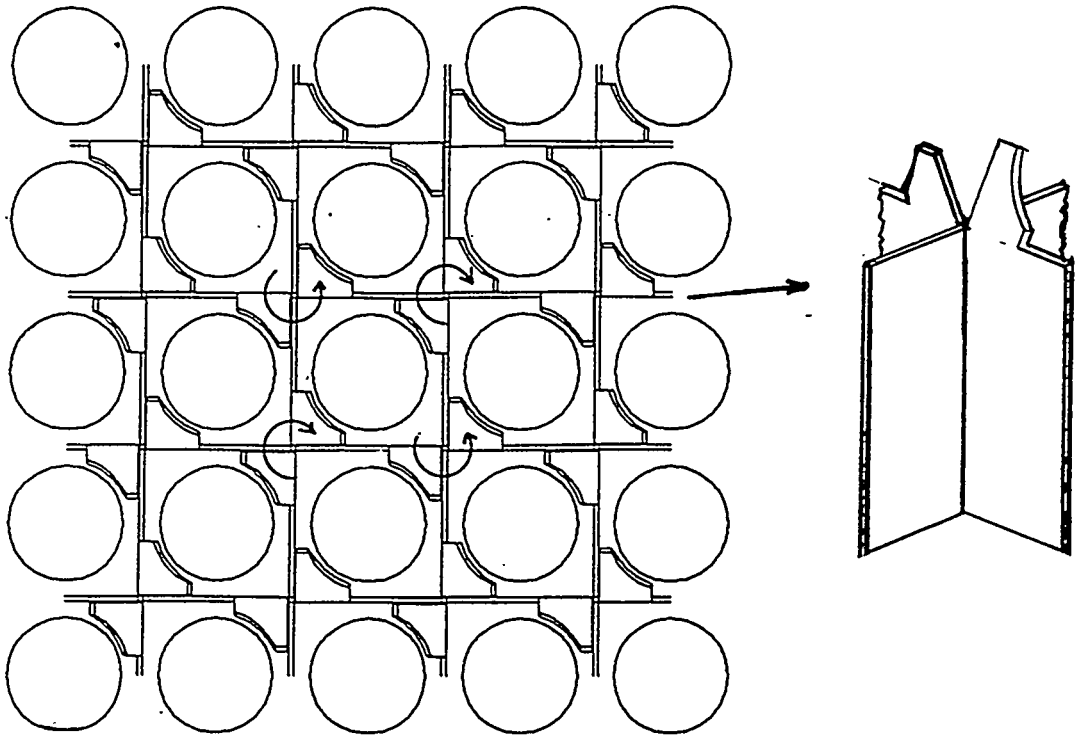

Figure 2-1 Split Vane Mixing Device

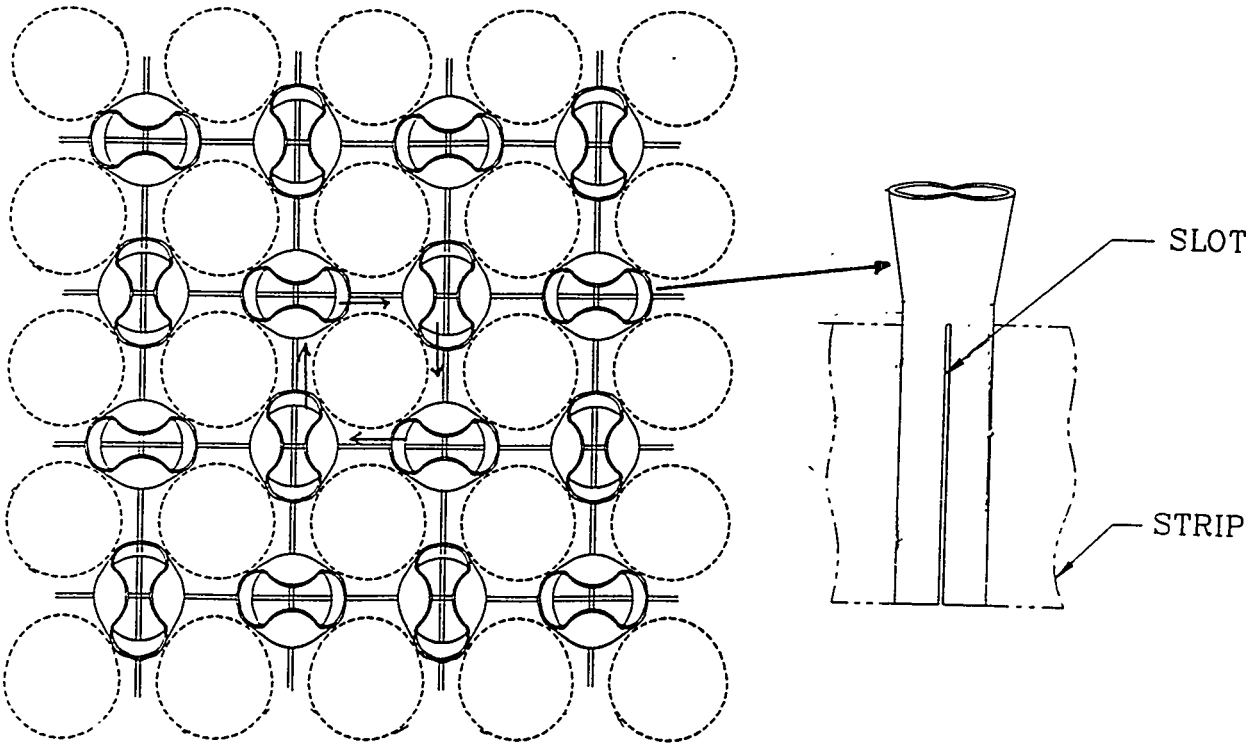

Figure 2-2 Squeezed Tube Mixing Device

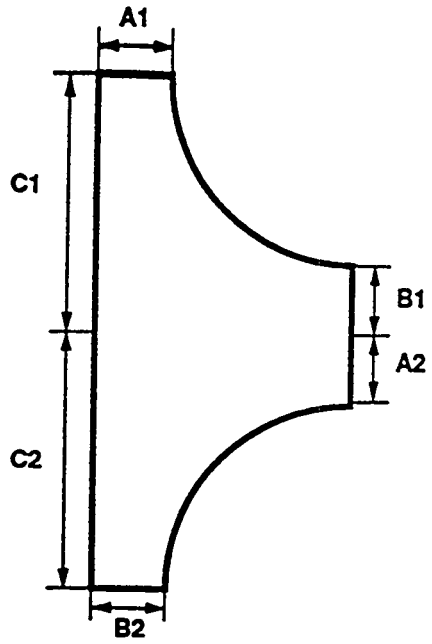

Figure 2-3a Split Vane - Boundaries with the Same Letter Are Connected

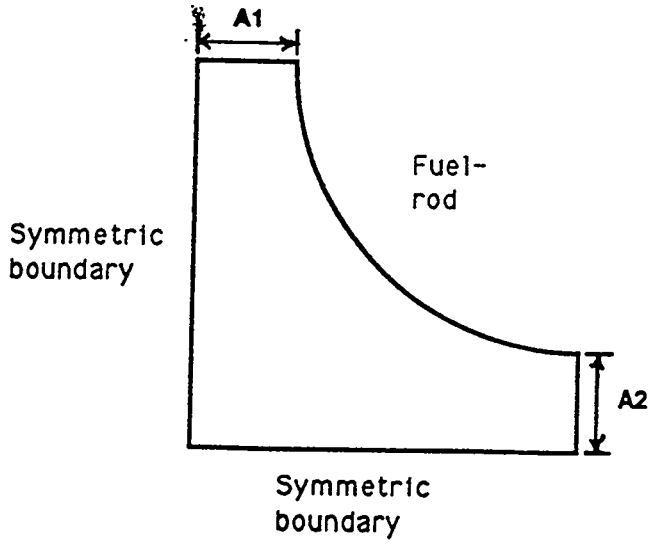

Figure 2-3b Squeezed Tube - Boundaries

The spacer and the mixing device was modeled with the thin surfaces option in CFDS-FLOW3D. For example, the mixing vane has no thickness and it is placed between two computational cells. This way of modeling thin details makes the grid generation much easier and it allows a more coarse grid since no cells must be as thin as the thin detail. To verify this assumption the thickness of the squeezed tube was modeled and compared to a model assuming a thin surface. A few other variations were modeled with the squeezed tube design. These variations are summarized below for all spacer designs:

Design A: Split Vane

Design B: Squeezed Tube, continues straight up 9.6 mm above grid without squeezing

Design C: Squeezed Tube, same as Design B without 9.6 mm straight section

Design D: Squeezed Tube, Same as Design C but tube is squeezed more to increase flow diversion

Design D Solid: Squeezed Tube, Same as Design D but thickness of tube is modeled (No thin surface, but solid)

The computational grid for the split vane model was 16x32x262 cells and the axial length of the cells varied from 0.58 mm at the mixing vane to 2.5 mm near the end of the model. The computational grid for the squeezed tube grid was 16x16x258 cells and the axial length varied from 0.74 mm at the squeezed tubes to 2.71 mm at the end. The size of the model was selected to keep the same mesh spacing for both cases. One problem with this kind of simulation is the very long subchannel combined with a small cross section. The fine grid of computational cells in the cross section should have enough detail to resolve the flow field, therefore a detailed computational grid was needed. The cross section grids for Designs A and B are shown in Figures 2-4 to 2-7 for illustration.

The inlet profiles used in the simulations were taken from a model without a spacer. The inlet boundary condition was a top hat profile with mean inlet velocity 6.79 m/s. Side boundary conditions were symmetric at all four sides and a usual outlet boundary (Neuman boundary condition) was used. Velocities, turbulent kinetic energy and turbulent dissipation rate were transferred from the outlet in the no spacer case to the inlet in the main simulations with the spacers. A pressure boundary was also used at the outlet with constant pressure in the cross section for the model with spacers.

The standard κ–ε turbulence model of Launder, Spalding, (1974)[2] was used in the simulations. The κ–ε model is known to not accurately model high swirling flow. Fortunately the swirl magnitude was not large and good agreement was obtained between predictions and measurements as discussed in Section 2.4.

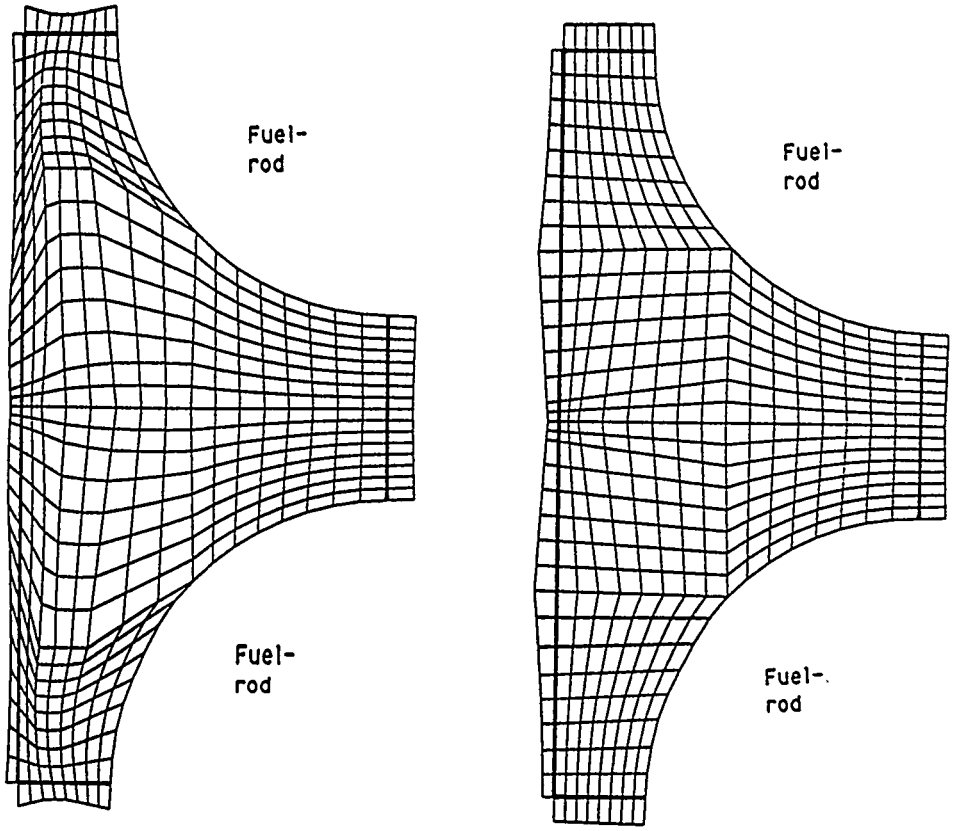

Top of Split Vane *Away from Split Vane*

Figure 2-4 FLOW3D Computational Grid - Split Vane

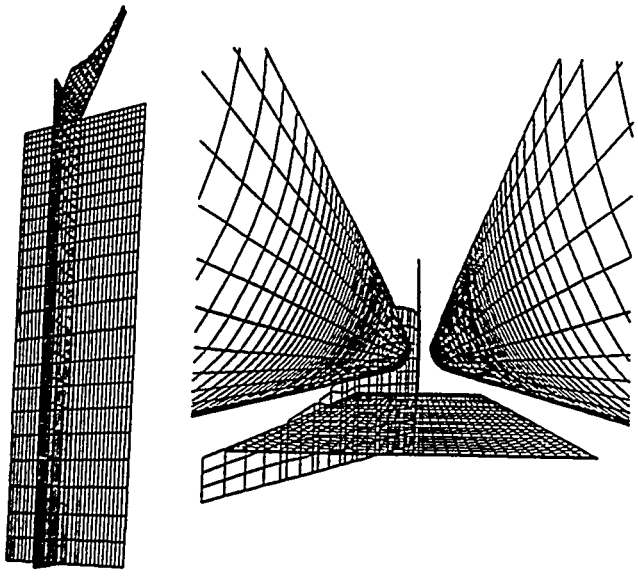

Figure 2-5 Computational Grid at Surfaces Around Spacer and Split Vane

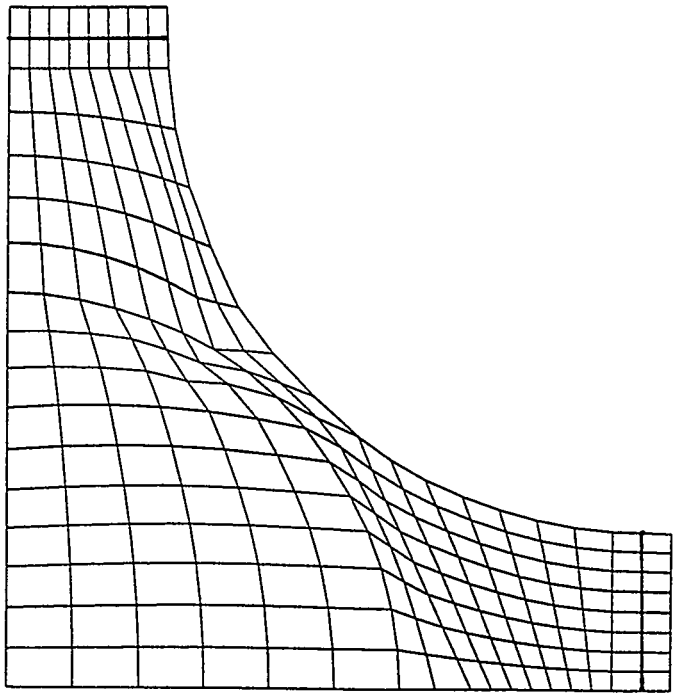

Figure 2-6 FLOW3D Computational Grid - Before Squeezed Tube

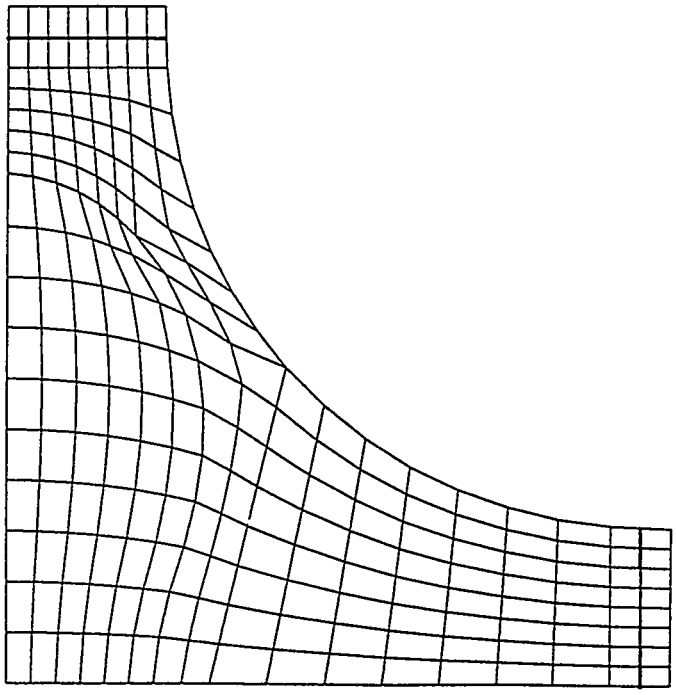

Figure 2-7 FLOW3D Computational Grid - After Squeezed Tube

No problems occurred in obtaining a solution in the CFDS-FLOW3D simulations. Standard relaxation methods were used and each iteration took approximately 25 CPU seconds on a IBM RS6000. The calculation was terminated when the level of residuals for all equations were reduced by a factor 10^4 to 10^5. No grid refinement was performed due to the limitation of workstation capacity. The size of the model for the split vane was about 130,000 cells. Higher order upwind differencing scheme was used in the calculations. It is believed that the mesh size was fine enough to be consistent with other assumptions made, such as use of thin surfaces and turbulent wall function, etc.. Approximately 3000 to 5000 iterations were needed to obtain a converged solution.

2.3 Laser Doppler Velocimeter Measurements

Laser Doppler Velocimeter (LDV) measurements were performed by ABB Combustion Engineering in a full scale cold water loop for a 5x5 rod array test section. These measurements were made at various axial elevations downstream of several grid designs with and without mixing devices. Pressure drop measurements were also performed. The radial and axial geometry of the 5x5 test section are shown in Figures 2-8 and 2-9, respectively. The test bundles were placed in a shroud with square cross section made up of two plexiglas panels and two metal panels. LDV measurements were taken in two paths traversing the full width of the test section in increments of 1.27 mm at the center line between rods. These measurements were made at seven axial distances downstream from the top of the grid:

Level	Distance from top of grid
A	12.7 mm
B	25.4 mm
C	50.8 mm
D	101.6 mm
E	190.5 mm
F	317.5 mm
G	463.5 mm

The tests we performed at the following operating conditions:

Average Test Section Velocity	6.79 m/s
Water Temperature	26.67 °C
Water Pressure	4.83 bar

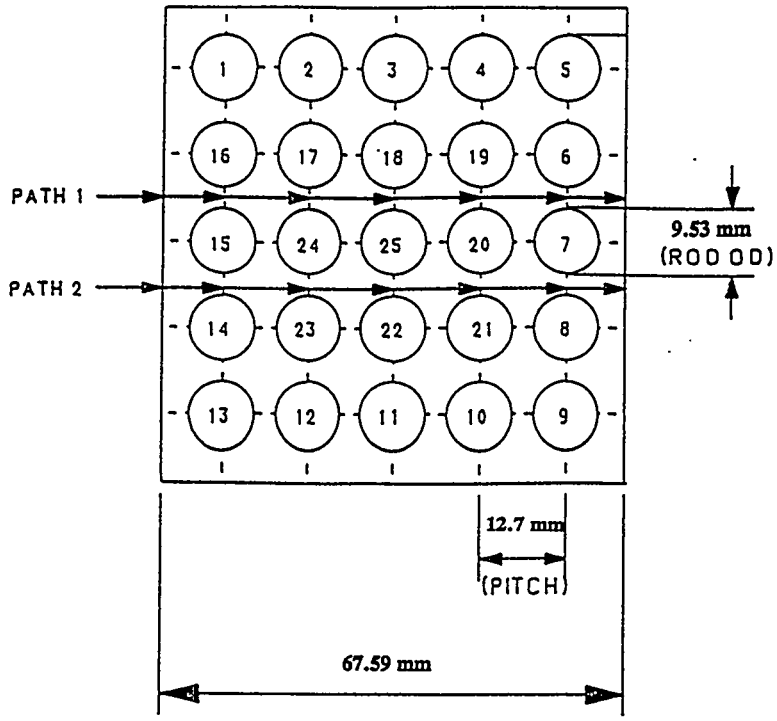

Figure 2-8 5X5 Radial Geometry

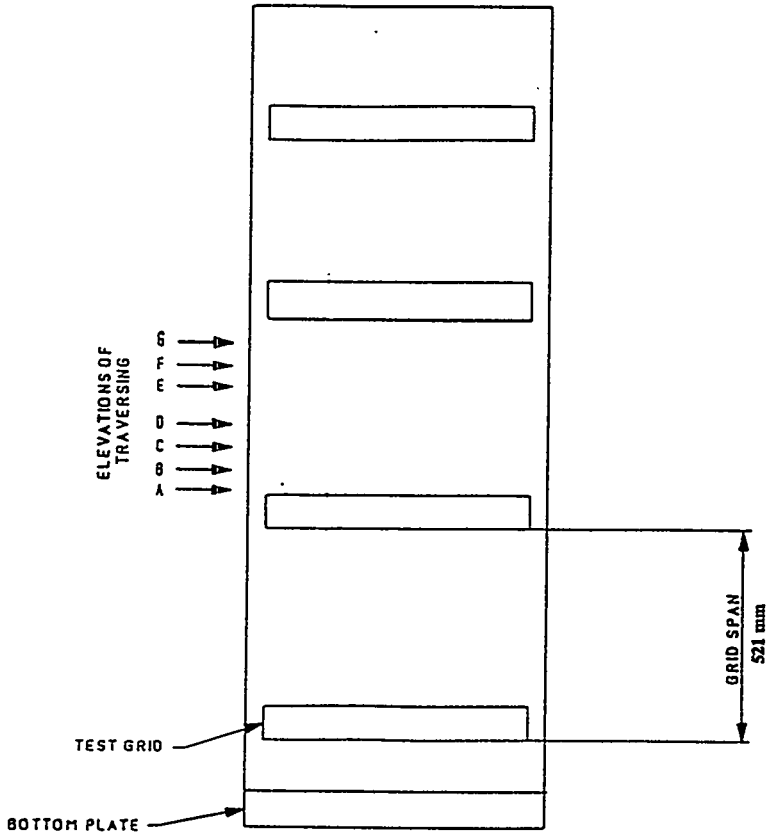

Figure 2-9 5X5 Axial Geometry

A two dimensional table-mounted 2 watt Argon-Ion laser with optical components, a one inch diameter fiber optics probe, signal processor and a computer system, were used to make the LDV measurements. The probe was coupled to the laser by a ten meter long fiber optics cable. The use of the probe allowed for ease of positioning at the different axial levels downstream of the grid. The focal length of the two incident beams leaving the probe was fixed at 135 mm in air and the measurement volume size was approximately 0.14 mm wide and 2.7 mm in length. The probe was held in a rotatable assembly which was mounted on to a micrometer driven X-Y position device. The LDV probe was a backscatter-based device so optical access was needed from only one side of the test section.

The water in the model was seeded with 12 μm metallic coated spherical particles in order to achieve a good count rate and high signal to noise ratio. One to two grams of material were added to approximately 100 gallons of water in the recirculating test loop. Although these particles were not exactly neutrally buoyant, they were recommended for their high reflectivity, and ability to accurately follow the fluid flow at the measured velocities.

Axial and lateral velocity measurements were taken at each location in the path by measuring the change in frequency of the scattered light leaving the measurement volume. The measurement volume was created by splitting the original laser beam into two beams of identical size and intensity, and crossing them through the use of focusing lenses. The measurement volume is the region where two beams intersect. When a particle in the flow passes through this region, the particle scatters the light. The scattered light contains the Doppler frequency, which is different from the frequency of the original laser light.

Two sets of beams were used to measure the axial and lateral velocities. Axial velocity measurements were made across the full width of the model with a set of beams in the vertical orientation and the lateral velocity measurements were made with a set of beams in the horizontal orientation. The lateral velocity measurements were limited to a shorter distance (approximately 2/3s of shroud width) due to limited penetration of the incident laser beams in the narrow gap of the rods. The lateral velocity of the fluid normal to the surface of the probe also could not be obtained. Therefore flow interchange occurring in the gaps between rods were not measured. The velocity mean, standard deviation, and turbulence intensity information were determined from the test data. The uncertainty in the velocity measurements due to errors in data processing, seeding, laser beam geometry and the electronic processor was determined to be within a range of .1% to .5%.

2.4 Results and Comparisons

CFDS-FLOW3D predictions were made for the split-vane mixing device. Figure 2-10 shows that the split-vane produced a swirl in the subchannel as expected. Predictions were compared to axial and lateral velocity measurements in Figures 2-11 and 2-12 respectively. The axial or lateral velocity was normalized to the axial bulk velocity in the test section and plotted versus dimensionless distance, where dimensionless distance (x/L) was measured across the width of two channels as shown in Figure 2-11 and 2-12. The results of the comparison show qualitatively good agreement however there are some differences worth noting.

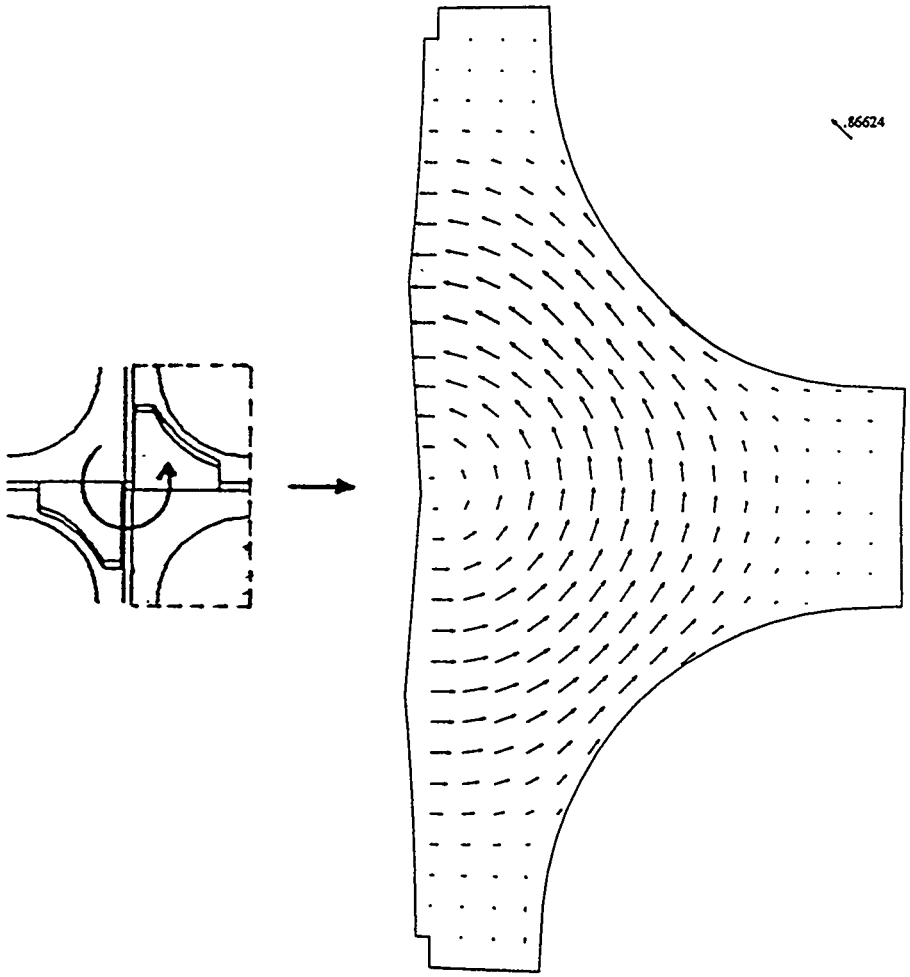

Figure 2-10 Split Vane Swirl in Subchannel

Close to the spacer and the mixing vane, the measured axial velocities in Figure 2-11 have higher differences between maximum and minimum values relative to predictions, due to the thickness of the spacer strip and the rod support features of the grid (arches and springs). In the CFDS-FLOW3D model these grid features were not modeled.

Further downstream the predicted axial velocities have a more developed pipe flow (parabolic shape) than the measurements show. This may be due to not modeling the next spacer at the outlet of the FLOW3D model. Modeling the next spacer could produce a damping effect on the center line subchannel velocity so there may be better agreement with measurements. The next spacer was not simulated to minimize the size and execution of the model.

Lateral velocities produced by the split vanes showed good agreement in paths 1A to 1G in Figure 2-12. Path 1B which is 25.4 mm downstream of the spacer showed the biggest difference between measurements and predictions. The reason for this difference is not clearly understood however it may be due to inaccurate modeling of mixing between adjacent subchannels due to the use of special side boundary conditions described in Section 2-2 for reducing the size of the computational model.

A swirl ratio was calculated to compare data from the measuring path to predictions. The swirl ratio was defined in the following way:

$$F = \frac{1}{L}\int \frac{|V_{lat}|}{V_{axial}} dx \qquad (5.a)$$

L	Length of integral path
V_{lat}	Lateral velocity at measurement location, perpendicular to the integral path
V_{axial}	Axial velocity at measurement location

The integral was evaluated along the measuring path in the cross section and evaluated at all measuring heights. This swirl ratio was compared to the prediction as a function of the dimensionless distance from the top of the spacer. The dimensionless distance is defined as the axial distance from the top of the spacer (z) divided by the hydraulic diameter (D_h) of the subchannel. A comparison of the measured and predicted swirl factors shown in Figure 2-13 indicate good agreement. It is believed that increasing this swirl ratio and its persistence downstream of spacer can improve DNB performance.

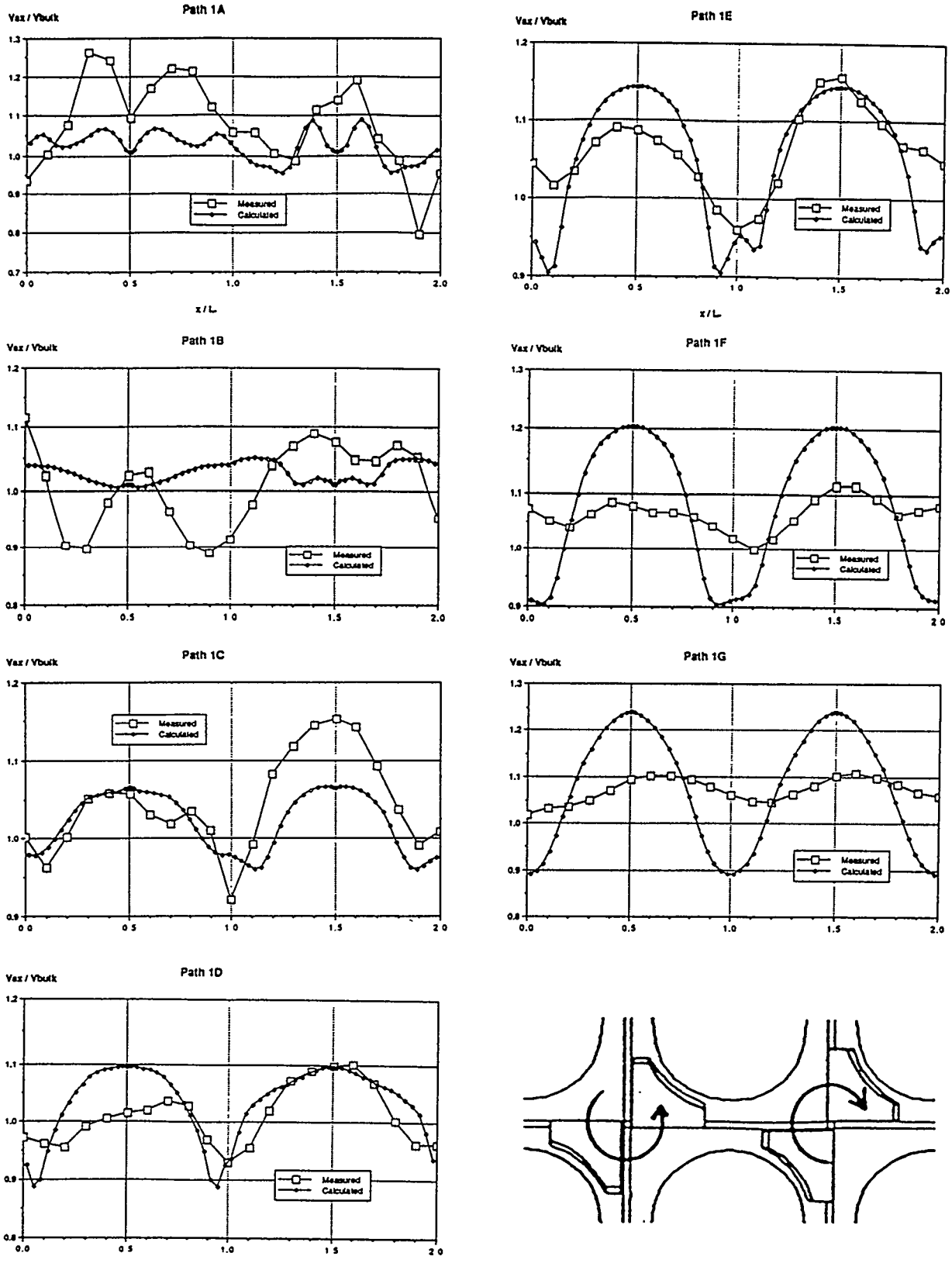

Figure 2-11 Axial Velocity Comparison for Split Vane

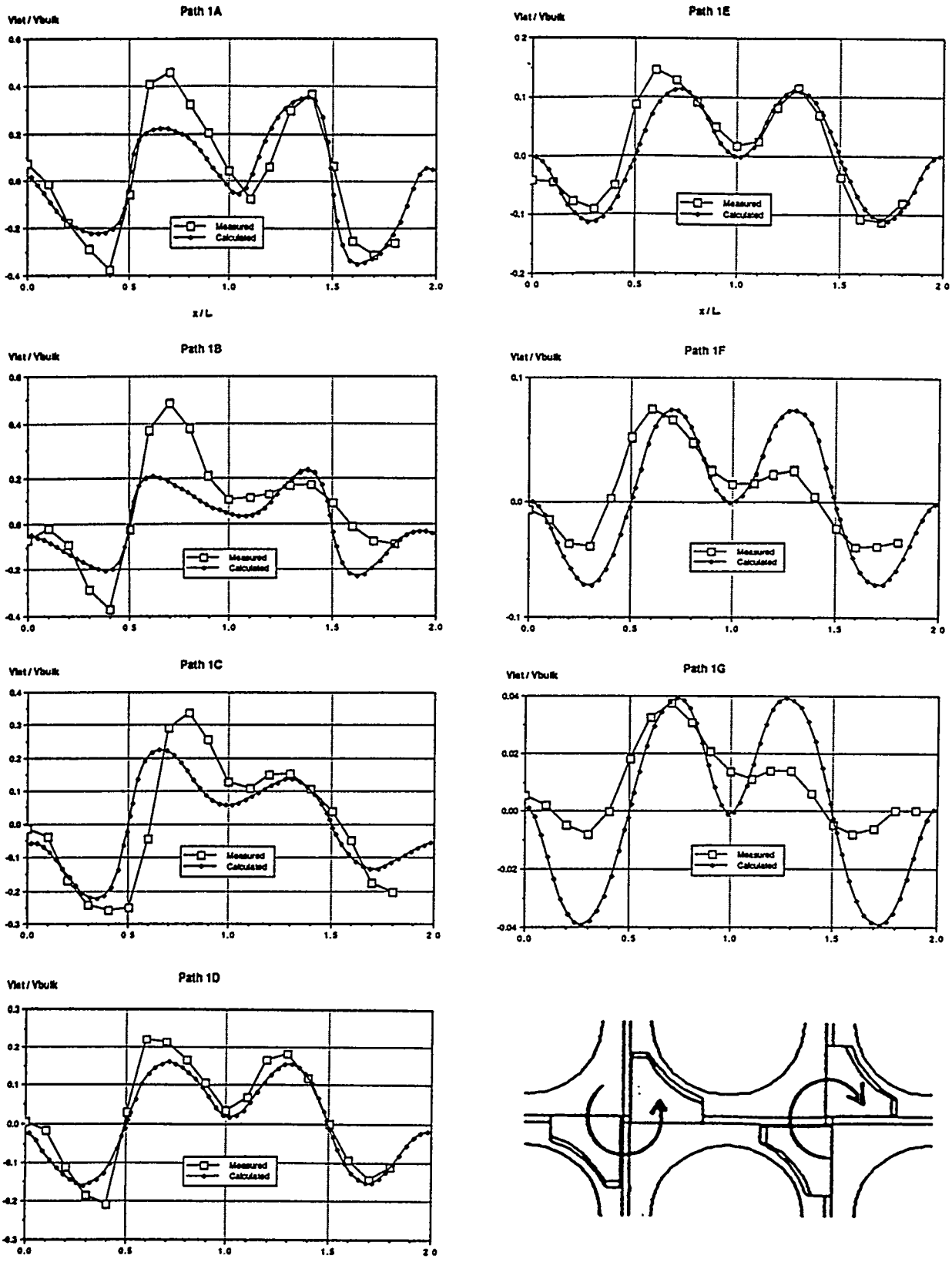

Figure 2-12 Lateral Velocity Comparison for Split Vane

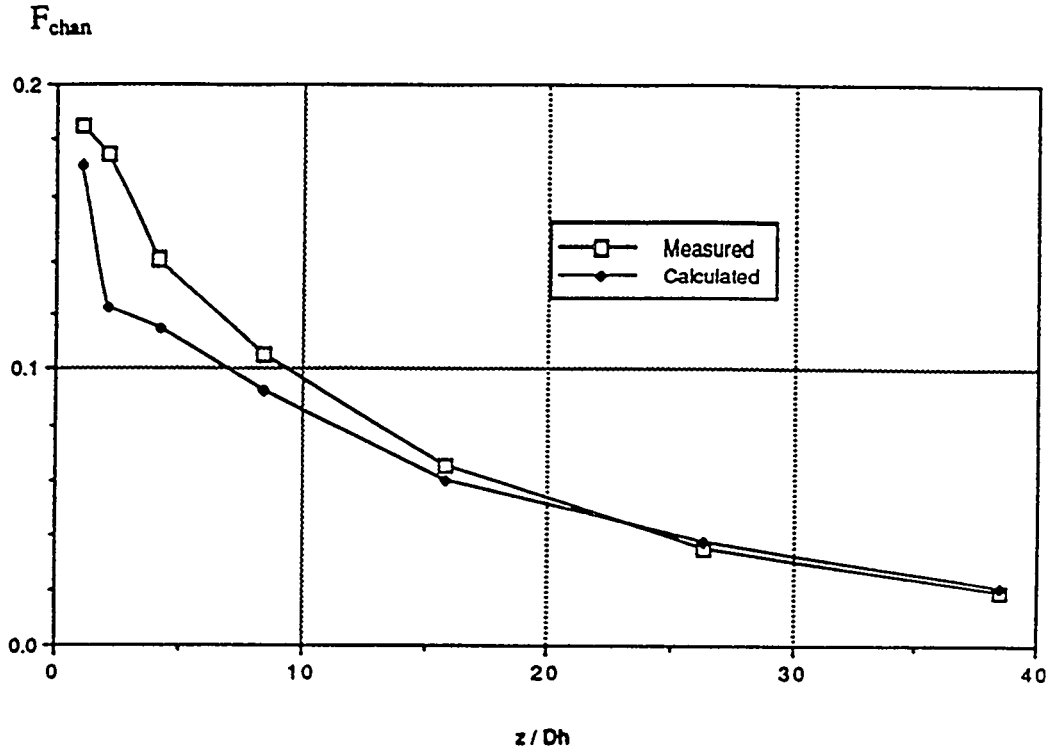

Figure 2-13 Swirl Ratio in Subchannel for Split Vane

The squeezed tube mixing device swirled flow around the rod instead of the subchannel, as shown in Figure 2-14. Axial velocity comparisons and the measuring path for the squeeze tube, mixing designs B, C, and D are shown in Figures 2-16 and 2-17, respectively. Lateral velocity comparisons were not made because LDV equipment did not have the capability to measure the lateral velocities in the gaps between rods. The results of the comparisons indicate that the velocities in the simulations are in general higher, but the shape of the curves show rather good agreement. The lower measured velocities may be due to an increased bypass flow on the periphery of the shroud associated with this spacer device. At x/L=.5 and 1.5 (center of tubes) the predictions in Figure 2-16 show larger axial velocities compared to measured values close to the spacer. This increase in velocity may be due to the assumption of using thin surfaces in the tube of the CFDS-FLOW3D model. The use of thin surfaces to simulate the spacer strips reduces the hydraulic resistance in the tube so more flow exits the tubes. Figure 2-17 shows that the solid modeling of the spacer strips and the tube instead of using thin surfaces, fits the measurements better near the spacer. Further downstream there is no difference between the solid and thin surface models.

A swirl ratio was also calculated for the squeezed tube designs however this ratio was based on swirl around the rod instead of the subchannel. The swirl ratio was defined as:

$$F = \frac{1}{g}\int \frac{|V_{lat}|}{V_{bulk}} dx \qquad (5.b)$$

g	Length of integration path, i.e. gap between two fuel rods.
V_{lat}	Lateral velocity at measurement location, perpendicular to the integral path
V_{bulk}	Axial bulk velocity

The integral was evaluated along a path between two neighboring fuel rods. These predicted swirl ratios are summarized in Figure 2-15 for all squeezed tube designs and for the split-vane design. The swirl ratio for the split-vane design was also evaluated similarly in the gap region. Based on the curves in Figure 2-15 the swirl ratio for design D was twice as large as designs B and C since the squeezing of the tube was increased significantly for design D. The swirl ratio for the split-vane showed little swirl around the rod as compared to the squeezed tube mixing devices since the split-vane mainly generated a swirl in the subchannel. It was unclear which swirl pattern, around the rod or in the subchannel, would be better for increasing DNB performance.

The predicted pressure drop was also compared for different spacer designs in Figures 2-18 and 2-19. Figure 2-18 shows the area weighted mean pressure in the cross sections along the subchannel for each design. The axial distance (z) is normalized to the hydraulic diameter (D_h) of the subchannel. At the top of the spacer (z/D_h) is zero. Figure 2-19 shows the mean pressure versus distance closer to the spacer. The predicted pressure drop in the vicinity of the spacer is strongly affected by using solid modeling instead of thin surfaces in the CFDS-FLOW3D model. The wake behind the spacer and acceleration effects are ignored by using thin surfaces. To obtain an accurate calculation of pressure drop of the spacer, solid modeling must be used, however, a relative comparison can still be made with the same modeling method.

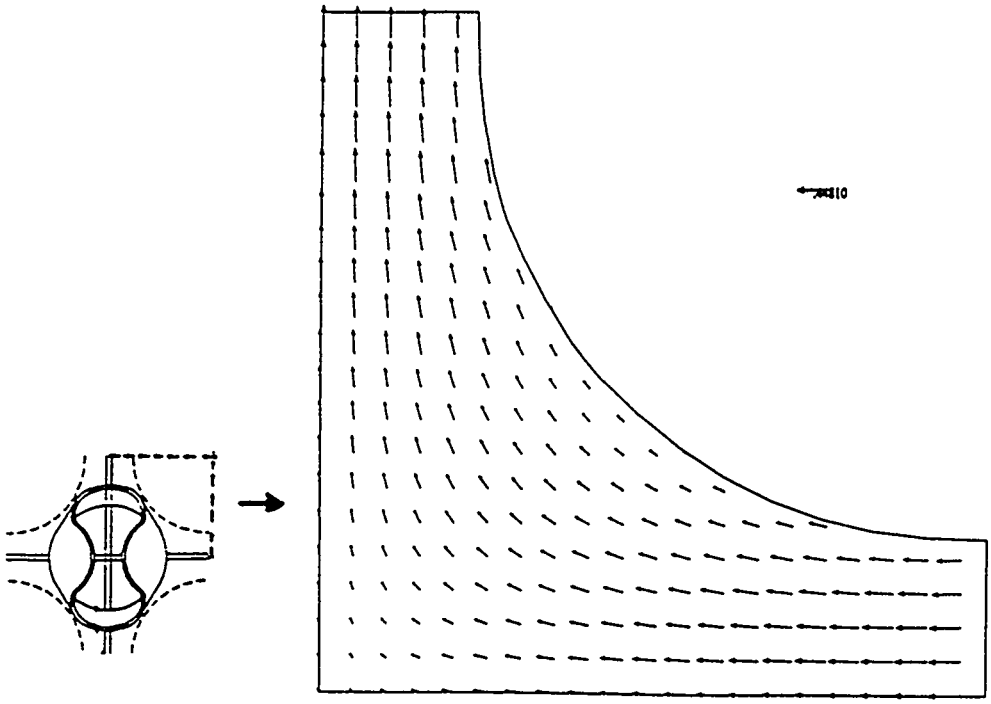

Figure 2-14 Squeezed Tube Swirl Around Rod

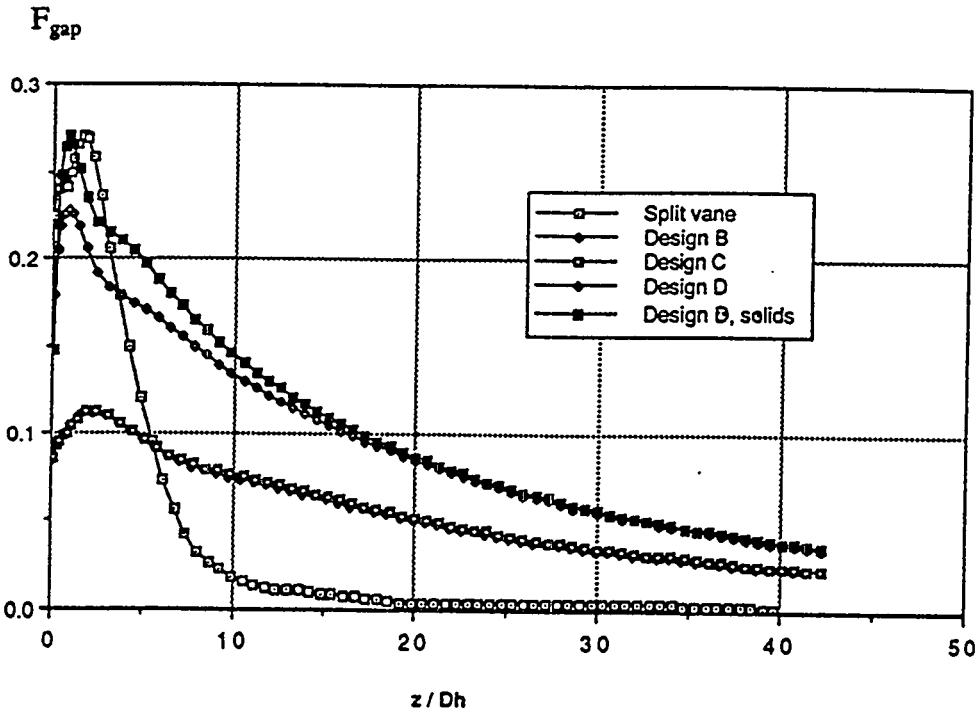

Figure 2-15 Swirl Ratio Around Rod for Split Vane and Squeezed Tube

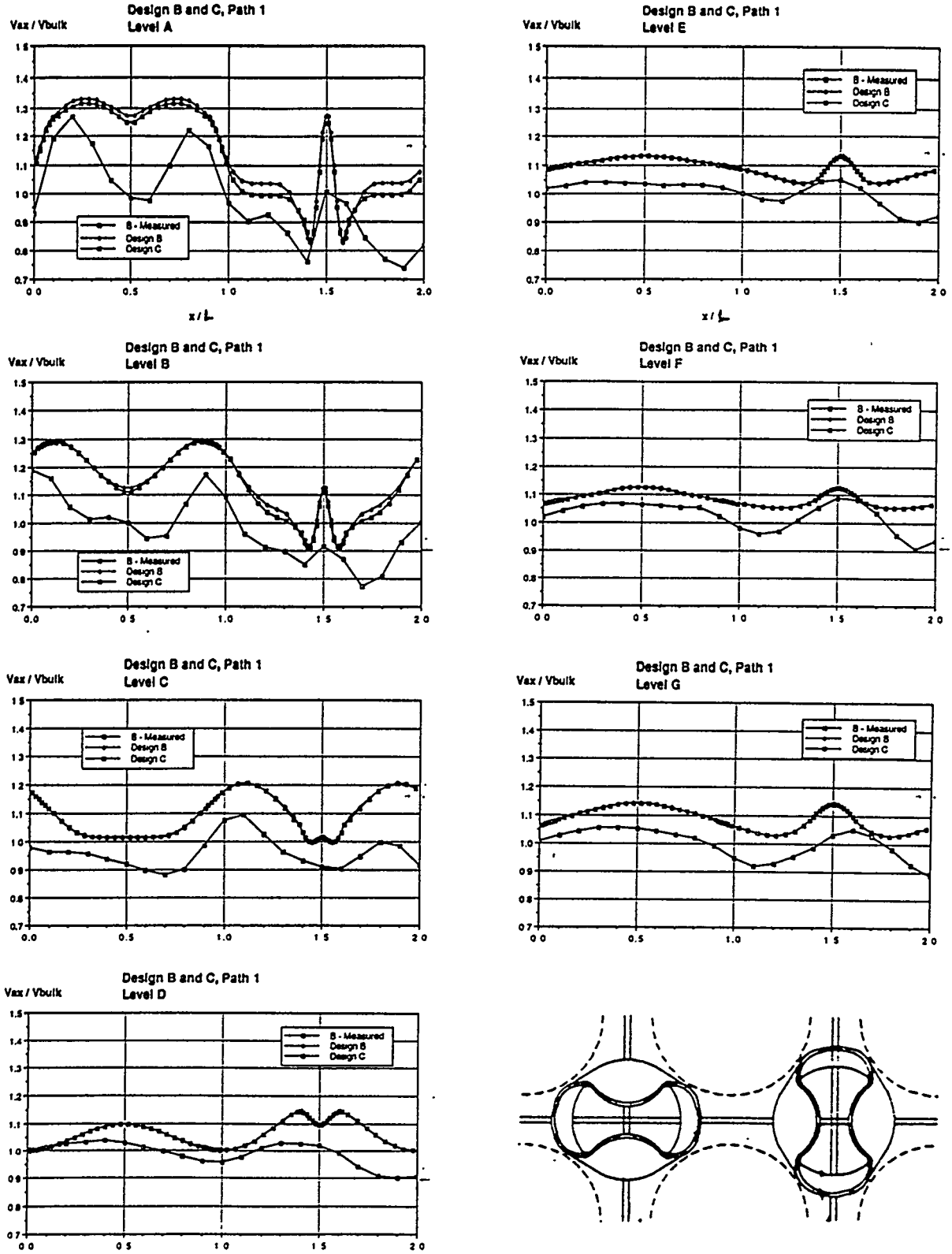

Figure 2-16 Axial Velocity Comparison for Squeezed Tube Designs B and C

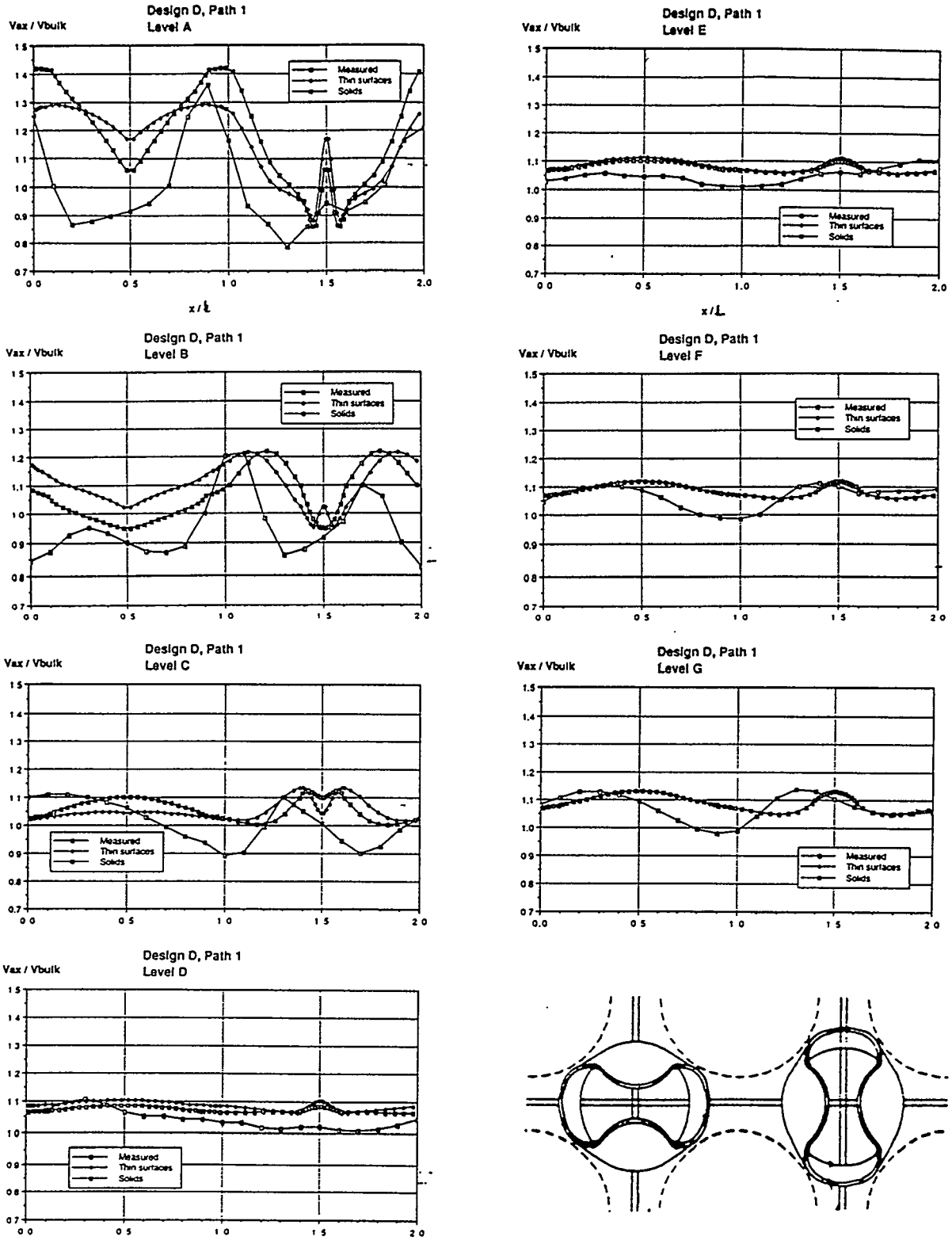

Figure 2-17 Axial Velocity Comparisons for Squeezed Tube Design D

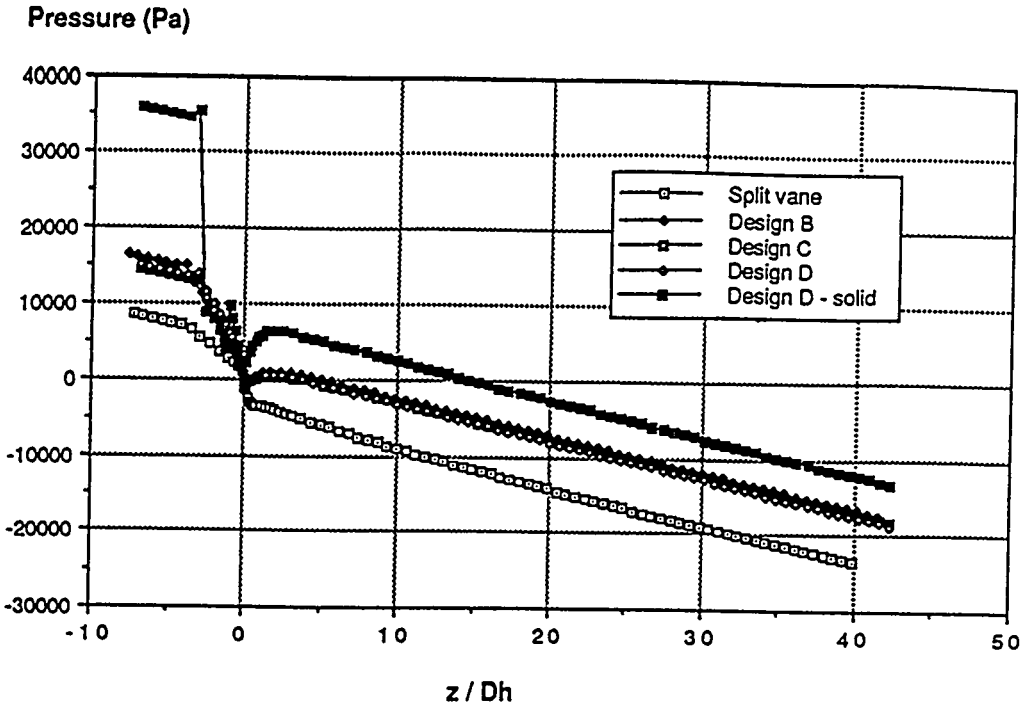

Figure 2-18 Mean Pressure Along Subchannel

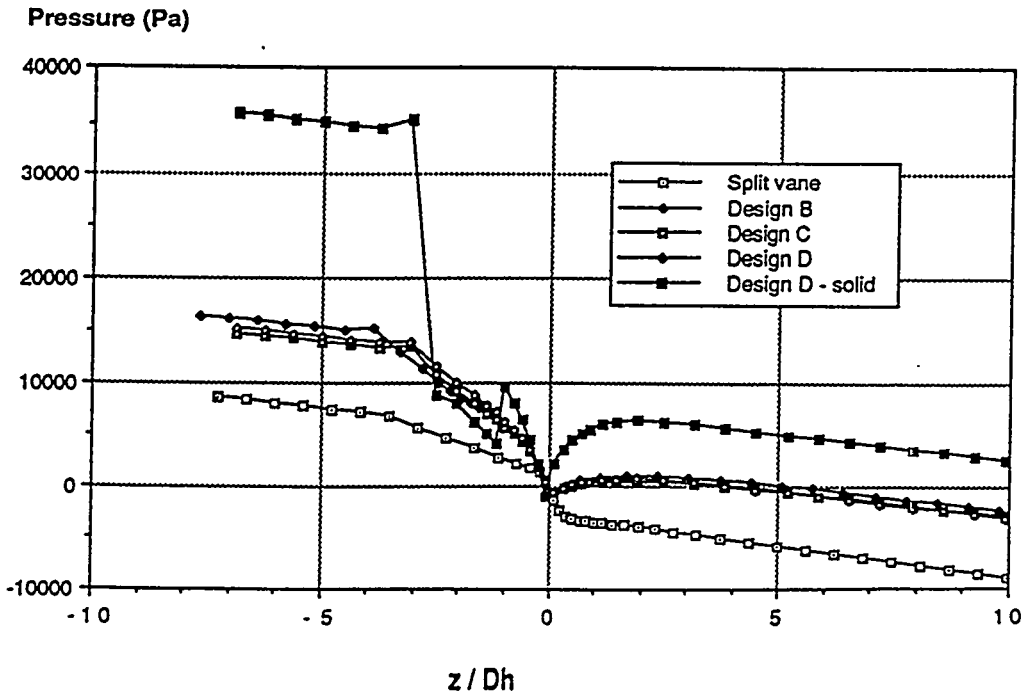

Figure 2-19 Mean Pressure Along Subchannel Around Spacer

3. SUMMARY

The relatively good comparison between CFDS-FLOW3D predictions and LDV measurements indicate that CFD tools can be helpful in optimizing grid design relative to T-H performance and in performing more detailed subchannel analysis downstream of spacers. The swirl ratio may also be a qualitative indicator of the spacer design impact on DNB performance. A better understanding on how swirling flow patterns in subchannels and around fuel rods improves DNB performance in different flow regimes is needed. The detailed flow simulation can help provide some physical understanding of these flow mechanisms however experimental data will be needed to verify them.

4. REFERENCES

[1] FLOW3D Users Guide, Release 2.3, AEA Industrial Technology, Harwell Laboratory, Oxfordshire, UK.

[2] Lander B.E. and Spalding D.B., *The Numerical Computation of Turbulent Flows*, **Computational Methods in Applied Mechanics and Engineering 3 (1974) 269-289.**

Bubble Behaviour and Mean Diameter in Subcooled Flow Boiling

O. Zeitoun and M. Shoukri

Mechanical Engineering Department, McMaster University
Hamilton, Ontario, L8S 4L7, CANADA

Abstract

Bubble behaviour and mean bubble diameter in subcooled upward flow boiling in a vertical annular channel were investigated under low pressure and mass flux conditions. A high speed video system was used to visualize the subcooled flow boiling phenomenon. The high speed photographic results indicated that, contrary to the common understanding, bubbles tend to detach from the heating surface upstream of the net vapour generation point. Digital image processing technique was used to measure the mean bubble diameter along the subcooled flow boiling region. Data on the axial area-averaged void fraction distributions were also obtained using a single beam gamma densitometer. Effects of the liquid subcooling, applied heat flux and mass flux on the mean bubble size were investigated. A correlation for the mean bubble diameter as a function of the local subcooling, heat flux and mass flux was obtained.

1. Introduction

One of the most important thermal non-equilibrium two-phase flow phenomena is that of forced convective subcooled boiling. The enormous surface heat flux which can be achieved without using high heating surface temperature is the main advantage of the nucleate boiling regime. Subcooled flow boiling is encountered in many applications; nuclear reactors, boilers, refrigeration systems and heat exchangers.

The subcooled flow boiling along a heated channel is commonly divided, as introduced by Griffith et al. (1958), into two regions; a highly subcooled region, where the void fraction is

very low, and a slightly subcooled region, where the void fraction increases significantly. The transition between these two regions is called the net vapour generation (NVG), or the onset of significant void (OSV), point. The NVG point was related directly, or indirectly, to bubble behaviour. The highly subcooled region is also commonly called the wall voidage region, implying that the vapour bubbles are located at the wall since the liquid bulk is highly subcooled. Understanding the local flow field at the NVG point is important since it marks the location at which significant increase in void fraction along the boiling channel is encountered. Griffith et al. (1958) speculated that this transition point is reached when the heating surface is fully covered with attached bubbles. Others, including Bowring (1962), Levy (1967), Rogers et al. (1987), Rogers and Li (1992) and Lee and Bankoff (1992), associated the NVG point with the first bubble detachment from the heating wall. In another approach, Dix (1970) and Serizawa (1979) attributed the NVG phenomenon to bubble ejection from a bubbly layer in the vicinity of the heating surface.

Until recently, most research efforts in this area focused on high pressure flow boiling, because of its relevance to power reactors, and lacked detailed information on local bubble behaviour and size along the boiling channel. Recently, Bibeau (1993), Shoukri et al. (1991), Stangl and Mayinger (1990), Dimmick and Selander (1990), Bibeau et al. (1990) reported void fraction measurements in subcooled flow boiling. They found that the void fraction profile upstream of the NVG point tended to be flat and formed a plateau longer than that associated with the high pressure case.

The present work is driven by the need to understand the physical phenomena associated with low pressure subcooled flow boiling and the need for information on bubble size, velocity and interfacial area for numerical modelling of subcooled flow boiling in low pressure pool-type reactors.

2. Experimental Arrangements

2.1. Experimental Facility

A schematic of the test loop is presented in Figure 1. The low pressure circulating loop consisted mainly of a holding tank, in which distilled-degassed water temperature was controlled by an immersed electric heater and a cooling coil, a circulating pump, a preheater and the test section. The test section contains a heated section, where vapour bubbles are formed, followed by an unheated section, where the vapour bubbles are condensed. The water at the test section outlet was pumped back to the holding tank where its temperature was regulated. Detailed description of the facility used in this study was reported in Zeitoun et al. (1994a and 1994b).

The test section was a vertical concentric annular test section. The inner tube, which was a 12.7 mm outside diameter, consisted of three axial sections. The middle section of the inner tube was a 30.6 cm long, thin-walled stainless-steel tube (0.25 mm thickness) that was electrically heated. This heated section was preceded and followed by 34 cm long, and 50 cm long, thick-walled copper tubes, respectively. The entire inner tube was connected to a 55 kW DC power supply. Accordingly, heat was generated uniformly in the middle section of the inner

tube. The outer tube was a 25.4 mm inner diameter plexiglass tube that permits visual observation. The flow that entered the annulus developed through the first unheated section of the annular test section. Voids, which were generated in the heated section, collapsed in the downstream unheated section. This arrangement was found to be convenient to separately examine vapour generation and condensation. The present study was carried out in the heated section to investigate bubble behaviour and size in subcooled flow boiling. A square cross section plexiglass shield was put around the outer tube and filled with water during photography to reduce light reflection and refraction. Any minor change in the inlet temperature to the heating region was compensated for by readjusting the preheater.

2.2 Measurements and Instrumentation

Experiments were carried out at different levels of mass flux, heat flux and inlet subcooling. The test conditions are listed in Table 1. A high speed video system was used to collect visual information to study bubble behaviour upstream, near and downstream of the NVG point. A digital image processing technique was used to analyze the high speed video information and to measure bubble size distributions along the subcooled boiling region. The measurements and instrumentation used are discussed here briefly. More details were reported by Zeitoun et al. (1994a and 1994b).

The high speed video system, Kodak Ektapro EM Motion Analyzer, was used to visualize the flow at two centimetres intervals along the subcooled flow boiling region. The camera, and the light sources were mounted on a traversing table to enable the flow along the test section to be visualized at the same locations where the void fractions were measured. Two procedures were followed to collect the visual information. Firstly, the camera was focused on the annular gap where it was found appropriate to investigate bubble detachment, sliding and ejection. In the second procedure, the camera was focused on the heater surface itself. This procedure was found convenient to examine bubble population density, bubble interactions and bubble size along the heating surface. Digital image processing technology was used to measure bubble size. Measured distances in the field of view were estimated to be accurate within ± 0.05 mm.

A single beam gamma densitometer was used for void fraction measurements. It consisted of a 75 mCi Cobalt 57 sealed line source and a cubic NaI (Tl) scintillator. As shown by Zietoun et al. (1994a, 1994b), the uncertainty of the area-averaged void fraction measurements was in the range of $\pm$ 4% of the calibrated range of $0.02 < \alpha < 0.3$.

Other measurements included the flow rate, using a bank of rotameters with an estimated error of $\pm$ 2%, test section inlet and outlet temperature using calibrated platinum resistance temperature detectors, as well as the liquid subcooling along the test section using J-type calibrated thermocouples. The uncertainty in the temperature measurements was estimated by Zeitoun (1994) to be $\pm$ 0.2°C.

3. Bubble Behaviour

3.1 Background

It is well accepted that a bubble is generally initiated from a small gas filled cavity or crack on a solid surface, when the heating surface is heated to a sufficiently high temperature. Many theories have been established to describe the bubble growth process in nucleate pool boiling. Fewer studies focussed on bubble dynamics in flow nucleate boiling. Koumoutses et al. (1968) and Zeng et al. (1993b) investigated bubble departure in horizontal flow boiling, while Gunther (1951), Abdelmessih et al. (1972), Akiyama and Tachibana (1974), Cooper et al. (1983) and Bibeau (1993) reported experimental investigations of bubble dynamics in vertical upward flow boiling. Ünal (1976) and Meister (1979) carried out theoretical analysis of bubble growth and collapse in highly subcooled flow boiling. However, they did not include bubble detachment in their analysis, i.e. they considered that the bubble grew and collapsed on the heating surface. In their analysis, the bubble continued to receive heat energy from the heating surface during the condensation period.

In the case of subcooled flow boiling, there are two types of bubble detachment from the heating surface. As the bubble grows on a heating surface, it reaches a certain size when it starts to slide along the heating surface (parallel detachment) and the growth continues until it leaves the surface (normal detachment, ejection or lift off). High speed photographic results reported by Bibeau (1993), for subcooled flow boiling at low pressures, showed that parallel detachment occurred very early after nucleation. It also showed that the bubble continued growing while sliding along the heating surface until it reached a maximum size after which the bubble size decreased as the condensation rate exceed the evaporation. The normal detachment occurred during bubble condensation and sliding along the heating surface. The bubble collapsed completely as it moved through the subcooled bulk. The normal detachment of a bubble was seen as the phenomenon which determines the end of the evaporating process associated with this bubble.

Bubbles detach in the two directions due to the forces acting on them. Modelling these forces is a very difficult task because of the link between these forces and the thermal bubble growth-collapse process. Formulation of these forces was investigated for pool boiling by Beer (1973) and Zeng et al. (1993a) and for forced flow boiling along a horizontal surface by and Koumoutses (1968) and Zing et al. (1993b). For upward flow boiling, the forces acting in the axial direction are buoyancy, drag, surface tension and inertia of the surrounding liquid. Forces acting in the normal direction are surface tension, excess pressure force, capillary pressure force, lift, drag and the inertia of the surrounding liquid.

3.2 Visual Observations

Some visual observations derived from the high speed photography are presented. Figure 2 shows typical bubble growth-collapse photographs along the subcooled flow boiling region for run B4, (see Table 1). In this figure, the heater edge appears at the right side of the image and the wall of the plexiglass tube and a one-millimetre reference tube appear at the left side. The measured axial void fraction profiles for this run is shown in Figure 6. The location of the

NVG point was defined, as in the literature, by the point at which the void fraction started to increase significantly. The photographs shown in Figure 3 show the change of bubble size and population upstream, near, and downstream of the NVG point. Some individual bubbles are identified to show the bubble cycle as it nucleates, grows and slides along the heating surface, detaches and collapses in the subcooled liquid bulk.

Upstream of the NVG point, the photographs show that after nucleation, the bubbles grow while attached to, or slowly sliding along, the heating surface until they lift off. After detachment, the bubbles condense very rapidly in the subcooled bulk. The photographs confirm that bubbles consistently detach from the heating surface upstream of the NVG point and accordingly, at least under the present test conditions, bubble detachment is not the cause of the NVG phenomenon. Moreover, the concept of a bubbly layer from which a bubble ejected to mark the occurrence of NVG, Dix (1971) and Serizawa (1979), cannot be supported by the present observations. The reason can be attributed to the relatively large bubbles observed under this low pressure flow boiling conditions. The bubbles may be contained in a relatively large envelope along the heating section, as compared to the high pressure case, and this envelope may become thicker due to the decrease in subcooling along the heated section. For high pressure and high mass flow rate, where the bubbles tend to be very small, the bubbly layer may be encountered. The present observations are in agreement with recent low pressure results of Bibeau (1993).

The effect of the decreasing subcooling along the heated section on the bubble size and period, i.e. growth-collapse time, can also be demonstrated by Figure 2, where three bubbles at three different elevations, below, near and after the NVG point are identified. The first at $z = 3$ cm, where the void fraction and the subcooling were 3% and 22.6°C, respectively. The second at $z = 13$ cm, where the void fraction and subcooling were 3% and 14.8°C, respectively. The third at $z = 23$ cm, where the void fraction and subcooling were 8% and 7°C, respectively. Analyzing these photographs showed that the maximum bubble diameter measured was: 1.0 mm at $z = 3$ cm, 2.25 cm at $z = 13$ cm and 3.25 mm at $z = 23$ cm and the bubble total growth-collapse time increased; 7, 11 and 22 ms, respectively. Of significance here is the trend, rather than the exact values, because of the sensitivity of the nucleation process to nucleation site size and bubble interaction. The effect of the subcooling will be investigated in detail during the analysis of the mean bubble size.

In the second flow visualization method, the high speed video camera was focused on the heater surface itself. This procedure was found convenient to examine bubble population density, bubble interactions and bubble size along the heating surface. Figure 3 shows typical bubble behaviour along the test section for the same run number B4. The measured void fraction and the location of the NVG point of these runs are shown in Figure 6. As shown in the photographs, the bubble size increased as the subcooling decreased along the test section. The main reason for the size increase along the heating section is the decrease in the condensation at the subcooled water-bubble interface. In subcooled boiling, the bubble grows on the heating surface under two opposing mechanisms; evaporation at the heating surface and at the superheated liquid-bubble interface and condensation at the subcooled water-vapour interface. The final bubble size and life duration are mainly dependent on the relative importance of these mechanisms. The bubble population density increases also as the subcooling decreases. The

increase in the bubble population may be caused by longer bubble life and by the increase of the nucleation site density.

Two distinct regions were observed along the heating section, which can be seen in Figure 3. In the region before the NVG point, the bubbles behave as individual bubbles, or discrete bubbles. Bubble interactions or coalescence is not a major mechanism in this region. Bubble coalescence intensifies in the region after the NVG point and is caused by the increase in bubble size, bubble density and bubble growth-collapse period. This is clearly associated with reduction in the relative importance of condensation at the bubble interface due to the decrease in liquid subcooling. It appears that this behaviour is associated with the NVG phenomenon and a detailed discussion of this phenomenon will be presented in future papers. As the bubble coalescence intensifies in the downstream of the NVG point, bigger bubbles are formed. The increase in bubble size decreases the interfacial area concentration, for a given void fraction, causing a reduction in the condensation rate per unit volume of the channel. Consequently, the relative effect of condensation is reduced and noticeable increase of void fraction is observed along the channel. Near the end of the heater, the coalescence intensifies significantly and the flow regime changes from bubbly flow to churn flow.

4. Bubble Size in Subcooled Flow Boiling

4.1 Background

One of the parameters required to estimate the interfacial transport of mass, momentum and energy is the bubble size, or interfacial area concentration. Despite the importance of the bubble size in two-fluid formulation of subcooled flow boiling, no measurement was reported in the literature for mean bubble diameter in subcooled flow boiling. A few investigators, Gunther (1951), Abdelmessih et al. (1972) and Bibeau (1993), reported measurements for bubble growth-collapse history in subcooled flow boiling. Ünal (1976) and Meister (1978) theoretically investigated the bubble growth-collapse in subcooled flow boiling. Ünal (1976) analyzed the growth and collapse of an attached hemispherical bubble. The bubble grew on the heating surface under the influence of microlayer evaporation beneath the bubble base and the condensation at the curved surface. The condensation at the interface was calculated using Levenspiel's model (1959) of bubble condensation. The detachment effects were excluded from the analysis as it was assumed that the bubble remained attached to the heating surface during the growth-collapse cycle. This will, in fact, cause a longer collapse time due to the continuous evaporation during the total bubble life. Based on this analysis, the following relationship was obtained for the maximum bubble diameter, which was considered by the authors to be the bubble detachment diameter,

$$D_{max} = \frac{2.42\times10^{-5}\ P^{0.709}\ \left(q - h_{sp}\ (T_s - T_l)\right)^{1/3}\ k\ \gamma_u}{2\ C_u^{1/3}\ \rho_g\ h_{fg}\ (\pi\ a)^{1/2}\ (b_u\ \phi_u)^{1/2}} \qquad (1)$$

where:

$$\gamma_u = \sqrt{k_s \rho_s C_{ps} / k_l p_l C_p}$$

$$C_u = \frac{h_{fg} \mu [C_p/(0.013 h_{fg} Pr^{1.7})]^3}{(\sigma/g \Delta\rho)^{1/2}}$$

$$b_u = (T_s - T_l)/2 (1 - \rho_g/\rho_l) \qquad (2)$$

$$\phi_u = (U_l/0.61)^{0.47} \quad \text{for } U_l > 0.61 \text{ m/s}$$

or

$$\phi_u = 1 \quad \text{for } U_l \leq 0.61$$

where k_s, ρ_s and C_{ps} are the thermal conductivity, density and specific heat of heater material. The effect of pressure on D_{max} appears both explicitly and implicitly, through its effect on the thermo-physical properties, in the above equation. The equation correctly predicts a net decrease in the maximum bubble diameter with increasing pressure. For bubble departure diameter, Ünal (1976) recommended the use of Equation (1) in flow boiling. However, it should be noted that the high speed photographic results of Bibeau (1993) showed that bubble detachment occurred after reaching the maximum diameter, not at the maximum diameter.

Based on data from literature, Serizawa (1979) introduced the following empirical relationship for bubble detachment diameter D_d,

$$D_d = \psi_s \exp\left[-k_1 (T_s - T_l) - k_2 q\right] \qquad (3)$$

where k_1, k_2 and ψ_s are empirical functions of mass flux, heat flux, test section geometry and fluid properties.

Bibeau (1993) reported that Farajisarir (1993) analyzed his high speed photographic results and obtained the following correlation for the maximum bubble diameter,

$$\frac{D_{max}\,\sigma}{\rho_l\, a^2} = 10.02 \times 10^9\, Ja_w^{-1.65} \left[\frac{T_w - T_l}{T_w - T_s}\right]^{-1.65} \qquad (4)$$

where Ja_w is the Jakob number based on the heating surface superheat. Examination of this correlation shows that the maximum bubble diameter is proportional to $(T_w - T_l)^{-1.65}$. This parameter, in fact, includes the effect of the wall superheat and bulk subcooling. It implicitly assumes that the effect of liquid subcooling and wall superheat can simply be added to form a single parameter.

In formulating a two-fluid model for subcooled flow boiling, there is a need to estimate the mean bubble diameter in subcooled flow boiling. No correlations are available for this purpose. Current models use available correlations, which mostly reflects an estimate of the maximum bubble diameter or the bubble diameter at detachment.

4.2 Mean Bubble Diameter Measurements

The high speed video and digital image processing systems were used to obtain data on bubble size in subcooled flow boiling at two centimetre intervals along the heated section for the ten experimental runs listed in Table 1. The digital image processing technique was used to analyze the high speed photographic images stored on the video tape, to measure the bubble size. The volume, and the surface area of each bubble, was calculated by measuring two diameters. The measured diameters were the maximum diameter and that perpendicular to the maximum diameter. The cross sectional area was assumed to be an ellipse and the two measured diameters were considered the maximum and the minimum dimensions of that ellipse. The bubble volume and surface area were calculated by rotating this cross section around the maximum diameter. It was endeavoured to measure the maximum number of bubbles from each frame.

At each axial location, a total of about 350 bubbles were analyzed. The bubble volume v_b and surface area a_b were calculated as discussed above. For each bubble, the Sauter bubble diameter, $d_s = 6\ v_b/a_b$, was calculated. Typical histograms representing the individual Sauter bubble diameter, versus its frequency of occurrence, are shown in Figure 4. The average bubble surface area and volume at each location were calculated as follows:

$$A_b = \frac{1}{n_b} \sum_{j=1}^{n_b} a_{b_j} \tag{5}$$

$$V_b = \frac{1}{n_b} \sum_{j=1}^{n_b} v_{b_j} \tag{6}$$

where n_b is the number of the measured bubbles. The mean Sauter bubble diameter at any given axial location was defined by:

$$D_s = \frac{6.0\ V_b}{A_b} \tag{7}$$

Zietoun (1994b) estimated the uncertainty in determining the bubble diameter to be in the range of $\pm$ 6%.

4.3 Data Analysis

Since the objective of this work was to obtain the average bubble diameter relevant to the various interfacial parameters, e.g. area concentration, heat transfer, etc., which are required for two-fluid modelling, the sample used included all bubbles present in the field of view, i.e. detached and attached to the wall.

Typical mean Sauter bubble diameter distribution is shown in Figure 5. As shown in the figure, the bubble diameter gradually increases in the region upstream of the NVG point due to the decrease in the condensation, caused by the reduction in the subcooling, at the subcooled water-

bubble interface. The bubble diameter appears to increase at a higher rate in the region downstream of the NVG point. This was caused by two factors; the decrease in the subcooling, and consequently the condensation, and bubble coalescence.

It is important to note the similarity between the bubble size and the measured void fraction in the region before, and after, the NVG point. D_s^3 was plotted as well as the void fraction along the heated section as shown in Figure 6. The interesting finding, based on these figures, is the strong link between bubble size and void fraction. The parameter D_s^3 and the void fraction show similar trends before and after the NVG point. The rate of increase of both along the test section appears to increase at the point of NVG.

To examine the effect of mass and heat flux on the bubble size, the measured mean bubble diameter was plotted versus Jakob number (subcooling). The local subcooling was obtained by interpolation between the four liquid subcooling measurements taken along the heated section. It was interesting to note that the local subcooling was in agreement with the values calculated by a simple heat balance:

$$\theta_l = \theta_{in} - \frac{q\, P_h\, z}{A\, G\, C_p} \tag{8}$$

In subcooled flow boiling almost all the wall heat flux is used to heat up the liquid either directly or indirectly through vapour condensation. The effect of the mass flux is shown in Figure 7 while the effect of heat flux is shown in Figure 8. As shown, increasing the mass flux decreases the bubble size, in the high Jakob number region before the NVG point. As the subcooling decreases, i.e. the Jakob number decreases, the above trend is reversed, i.e. increasing the mass flux tends to increase the bubble size. In this low Jakob number region, where the bubble number density is high, increasing the mass flux increases the bubble absolute velocity which enhance bubble coalescence. Increasing the heat flux, as shown in Figure 8, tends to increase the bubble size. This may be caused by the increase in the driving force of the bubble growth process, i.e. the wall superheat.

The authors are not aware of existing correlations for the mean bubble diameter in subcooled flow boiling. Serizawa (1979) presented a correlation for bubble size at detachment, Ünal's (1976) and Farajisarir (1993) (as reported in Bibeau, 1993) presented correlations for the maximum bubble diameter, which represents an upper limit for the bubble diameter. The predictions of these correlations are superimposed on the present data in Figure 9. As shown in the figures, the prediction of Ünal's model (1976) of the maximum bubble diameter is lower than the measured mean bubble diameter. However, the trend of the predicted maximum bubble along the heating section is qualitatively similar to the measured mean bubble diameter. The maximum bubble size predicted by Farajisarir (1993) (as reported in Bibeau, 1993) is mostly higher than the measured mean bubble diameter as one would expect. It should be noted that Farajisarir's correlation for the maximum bubble diameter was based on small bubbles less than 2 mm in diameter.

4.4 Proposed Correlation

Many methods were tried to correlate the present data of the mean bubble diameter. In these analyses, a dimensionless form with the correct limits was considered. It was found appropriate to correlate the present data by the following formula:

$$\frac{D_s}{\sqrt{\sigma / g\Delta\rho}} = \frac{0.0683\ (\rho_l/\rho_g)^{1.326}}{Re^{0.324}\left[Ja + \frac{149.2\ (\rho_l/\rho_g)^{1.326}}{Bo^{0.487}\ Re^{1.6}}\right]} \tag{9}$$

The comparison between the present data and the proposed correlation is shown in Figure 10. This correlation has a correlation coefficient of 90% and is capable of predicting the present data within $\pm$ 15%. The mean bubble diameters, calculated from the above equation, are imposed on Figure 5.

5. Conclusions

An experimental investigation into the bubble behaviour in low pressure subcooled flow boiling in a vertical annulus was undertaken. Using a high speed video camera bubble behaviour was examined for different levels of mass flux, heat flux and inlet subcooling. The high speed photographic results confirmed the fact that the bubble departure was not the reason of the NVG phenomenon. It was found that the bubble growth-collapse cycle is similar, regarding parallel and normal detachment, along the subcooled boiling regions, i.e. upstream and downstream of the NVG point. But, the mean bubble size, and life duration, increased as the subcooling was decreased. The bubble coalescence was intensified downstream of the NVG point. The increase in bubble size due to decrease in condensation and bubble coalescence was the main reason for the significant increase in void fraction along the heated channel. Effects of local subcooling, mass flux and heat flux on the mean bubble diameter were investigated. A new correlation for the mean bubble diameter, in terms of the flow Reynolds number, Boiling number, local Jakob number and fluid properties, was obtained. The proposed correlation has a correlation coefficient of 90% and can predict the present data within $\pm$ 15%.

6. Acknowledgement

The work presented herein was funded by a joint grant from Atomic Energy of Canada Ltd. (AECL) and the Natural Science and Engineering Research Council (NSERC). The support and input of Dr. V. Chatoorgoon from AECL is greatly appreciated.

Nomenclature

A	Flow area.	m^2
a	Liquid thermal diffusivity	m^2/s

a_b	Bubble surface area	m^2
A_b	Mean bubble surface area	m^2
Bo	Boiling number, $q/G\ h_{fg}$	
C_p	Liquid specific heat	J/kg K
D_h	Channel hydraulic diameter	m
d_s	Sauter bubble diameter	m
D_s	Mean Sauter bubble diameter	m
G	Mass flux	kg/m^2 s
h_{fg}	Latent heat	J/kg
h_{sp}	Single-phase convective heat transfer coefficient	w/m^2
Ja	Jakob number based on liquid subcooling, $\rho_l\ C_p\ (T_s-T_l)/\rho_g\ h_{fg}$	
Ja_w	Jakob number based on the superheat at the heating surface, $\rho_l\ C_p\ (T_w-T_s)/\rho_g\ h_{fg}$	
k	Liquid thermal conductivity	W/m K
P	Pressure	Pa
P_h	Heater perimeter	m
Pr	Liquid Prandtl number	
q	Applied heat flux	W/m^2
Re	Flow Reynolds number, $G\ D_h/\mu$	
T	Temperature	°C
v_b	Bubble volume	m^3
V_b	Average bubble volume	m^3
z	Axial location in z-direction	m

Greek Symbols

α	Area-averaged void fraction.	
μ	Liquid viscosity	Pa s
ρ	Density	kg/m^3
σ	Surface tension	N/m
Θ	$\Theta = T_s-T$	°C
$\Delta\rho$	$\rho_l-\rho_g$	kg/m^3

Subscripts

l	Liquid
g	Vapour
s	Saturation
in	Inlet
w	Wall

References

A.H. Abdelmessih, F.C. Hooper and S. Nangia, "Flow effects on bubble growth and collapse in surface boiling", Int J. Heat and Mass Transfer, Vol. 15, pp. 115-125 (1972).

M. Akiyama and F. Tachibana, "Motion of vapour bubbles in subcooled heated channel", Bulletin of the JSME, Vol. 104, pp. 241-247 (1974).

H. Beer, P. Burow and R. Best, "Bubble growth, bubble dynamics, and heat transfer in nucleate boiling, viewed with a laser interferometer", in: Heat Transfer in Boiling, ed. E. Hahne and U. Grigull, Hemisphere Publishing corporation, Ch. 2, pp. 21-52 (1977).

E.L. Bibeau, "Void growth in subcooled flow boiling for circular and finned geometries for low values of pressure and velocity", Ph.D. Thesis, The University of British Columbia (1993).

E.L. Bibeau and M. Salcudean, "The effect of flow direction on void growth at low velocities and low pressure", Int. Comm. Heat Mass Transfer, Vol. 17, pp. 19-25 (1990).

R.W. Bowring, "Physical model based on bubble detachment and calculation of steam voidage in the subcooled region of a heated channel", HPR-10, Institute for Atomenergi, Halden (1962).

M.G. Cooper, K. Mori and C.R. Stone, "Behaviour of vapour bubbles growing at a wall with forced flow", Int. J. Heat and Mass Transfer, Vol. 26, pp. 1489-1507 (1983).

G.R. Dimmick and W.N. Selander, "A dynamic model for predicting subcooled void: Experimental results and model development", EUROTHERM Seminar # 16 (1990).

G.E. Dix, "Vapour void fraction for forced convection with subcooled boiling at low flow rates", General Electric Report No. NEDO-10491 (1970).

P. Griffith, J.A. Clark and W.M. Rohsenow, "Void volumes in subcooled boiling", ASME Paper 58-HT-19, U.S. National Heat Transfer Conf., Chicago (1958).

F.C. Gunther, "Photographic study of surface-boiling heat transfer to water with forced convection", Transaction of ASME, pp. 115-123 (1951).

N. Koumoutsos, R. Moissis and A. Spyridonos, "A study of bubble departure in forced-convection boiling", J. Heat Transfer, pp. 223-230 (1968).

S.C. Lee and S.G. Bankoff, "Prediction of the onset of significant void in down flow subcooled nucleate boiling" HTD-Vol 197, Two-Phase Flow and Heat Transfer, ASME, pp. 93-100 (1992).

O. Levenspiel, "Collapse of steam bubbles in water", Industrial and Engineering Chemistry, Vol. 51 (1959).

S. Levy, "Forced convection subcooled boiling: Prediction of vapour volumetric fraction", Int. J. Heat Mass Transfer, Vol. 10, pp 951-965 (1967).

G. Meister, "Vapour bubble growth and recondensation in subcooled boiling flow", Nuclear Engineering and Design, Vol. 54, pp. 97-114 (1979).

J.T. Rogers and J. Li, "Prediction of the onset of significant void in flow boiling of water", HTD-Vol. 217, Fundamentals of Subcooled Flow Boiling, ASME, pp. 41-52 (1992).

J.T. Rogers, M. Salcudean, Z. Abdullah, D. McLeod and D. Poirier, "The onset of significant void in up-flow boiling of water at low pressure and low velocities", Int. J. Heat Mass Transfer, Vol. 30, No. 11, pp. 2247-2260 (1987).

A. Serizawa, "A study of forced convection subcooled flow boiling", Two-Phase Momentum, Heat and Mass Transfer in Chemical Processes and Energy Engineering Systems, ed. Drust, F., Tsiklauri, G. V. and Afgan, N. H., Vol. I, pp. 231-242 (1979).

M. Shoukri, R.L. Judd, B. Donevski and G.R. Dimmick, "Experiments on subcooled flow boiling and condensation in vertical annular channels", in: Phase-Interface Phenomena in Multiphase Flow, Ed. Hewitt, G.F., Mayinger, F. and Rizinic, J.R., Hemisphere Pub. Corp., pp. 413-422 (1991).

G. Stangl and F. Mayinger, "Void fraction measurement in subcooled forced convection boiling with Refrigerant 12", Experimental Heat Transfer, Vol. 3, pp. 323-340 (1990).

H.C. Ünal, "Maximum bubble diameter, maximum bubble-growth time and bubble-growth rate during the subcooled nucleate flow boiling of water up to 17.7 MN/m^2", Int. J. Heat Mass Transfer, Vol. 19, pp. 643-649 (1976).

O. Zeitoun, M. Shoukri and V. Chatoorgoon, "Measurement of interfacial area concentration in subcooled liquid-vapour flow", Nuc. Eng. and Design, 152, pp. 243-255 (1994a).

O. Zeitoun, "Subcooled flow boiling and condensation", Ph.D. Thesis, McMaster University (1994b).

L.Z. Zeng, J.F. Klausner and R. Mei, "A unified model for the prediction of bubble detachment diameters in boiling systems – I. Pool boiling", Int. J. Heat and Mass Transfer, Vol. 36, pp. 2261-2270 (1993a).

L.Z. Zeng, J.F. Klausner, D.M. Bernhard and R. Mei, "A unified model for the prediction of bubble detachment diameters in boiling systems – II. Flow boiling", Int. J. Heat and Mass Transfer, Vol. 36, pp. 2271-2279 (1993b).

Table 1 Test Conditions

Run No.	q kW/m^2	G kg/m^2s	P bar	θ_{in} °C
B1	286.68	156.15	1.37	14.9
B2	286.5	258.16	1.22	11.6
B3	487.88	252.78	1.17	16.6
B4	478.44	152.5	1.19	24.7
B5	508.0	264.34	1.5	16.8
B6	496.5	151.4	1.56	21.7
B7	705.5	411.7	1.5	22.5
B8	596.0	263.8	1.2	20.1
B9	593.2	152.6	1.22	31.1
B10	603.24	403.0	1.68	19.1

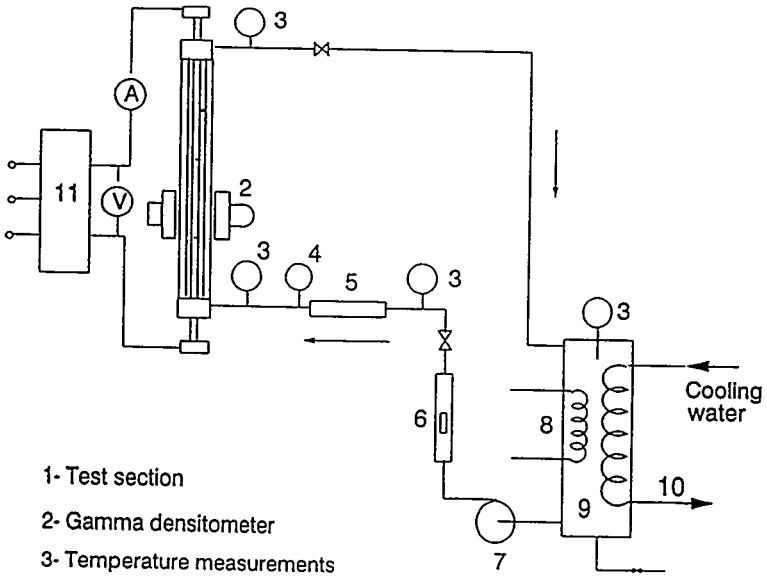

1- Test section
2- Gamma densitometer
3- Temperature measurements
4- Pressure measurements
5- Preheater
6- Flowmeter
7- Pump
8- Tank heater
9- Holding tank
10- Tank cooler
11- DC power supply

Figure 1: Test loop

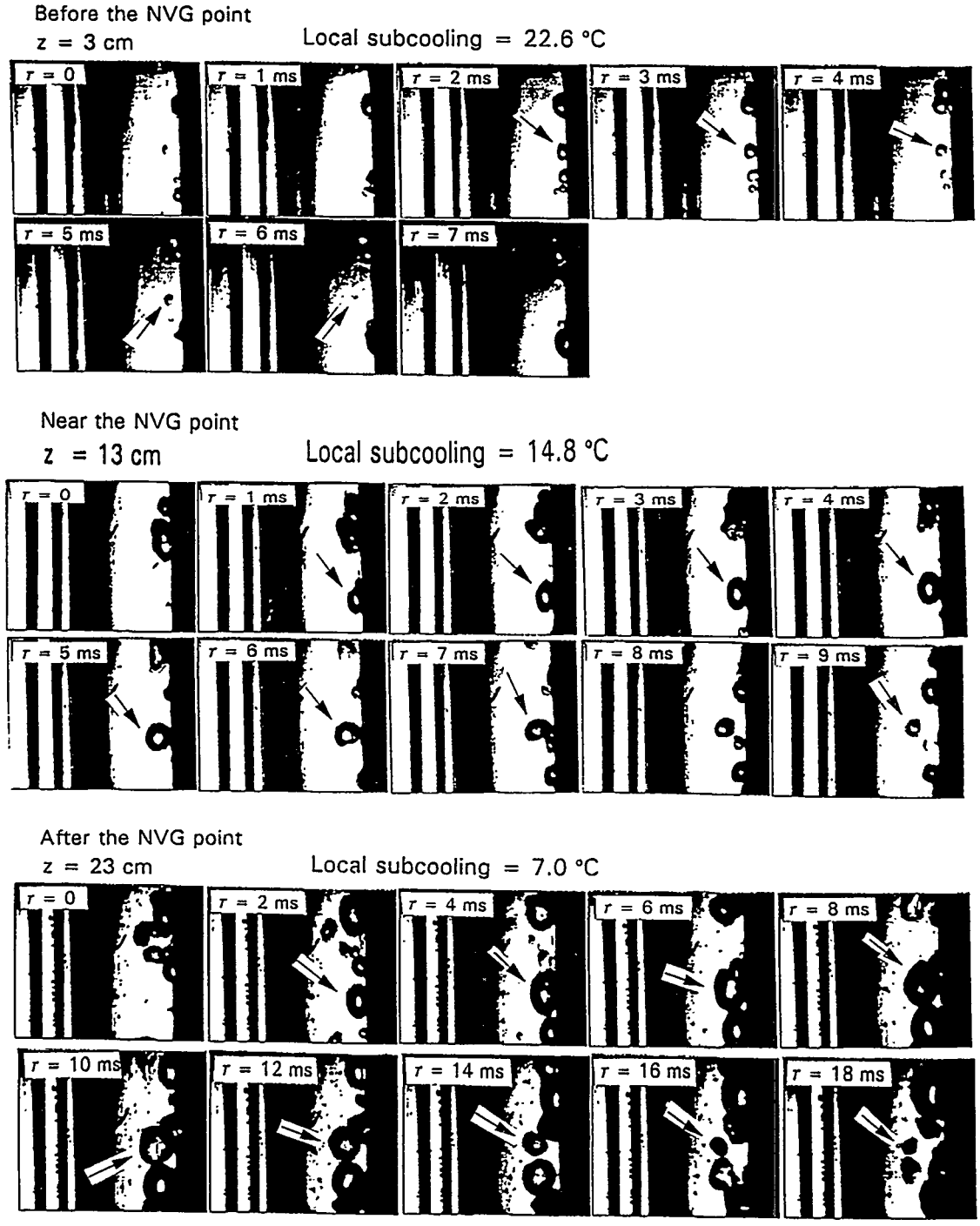

Figure 2: Bubble growth-collapse cycle before, near and after the NVG point for run no. B4 ($q = 478.4$ kW/m^2, $G = 152.5$ kg/m^2.s, inlet subcooling = 24.7 °C)

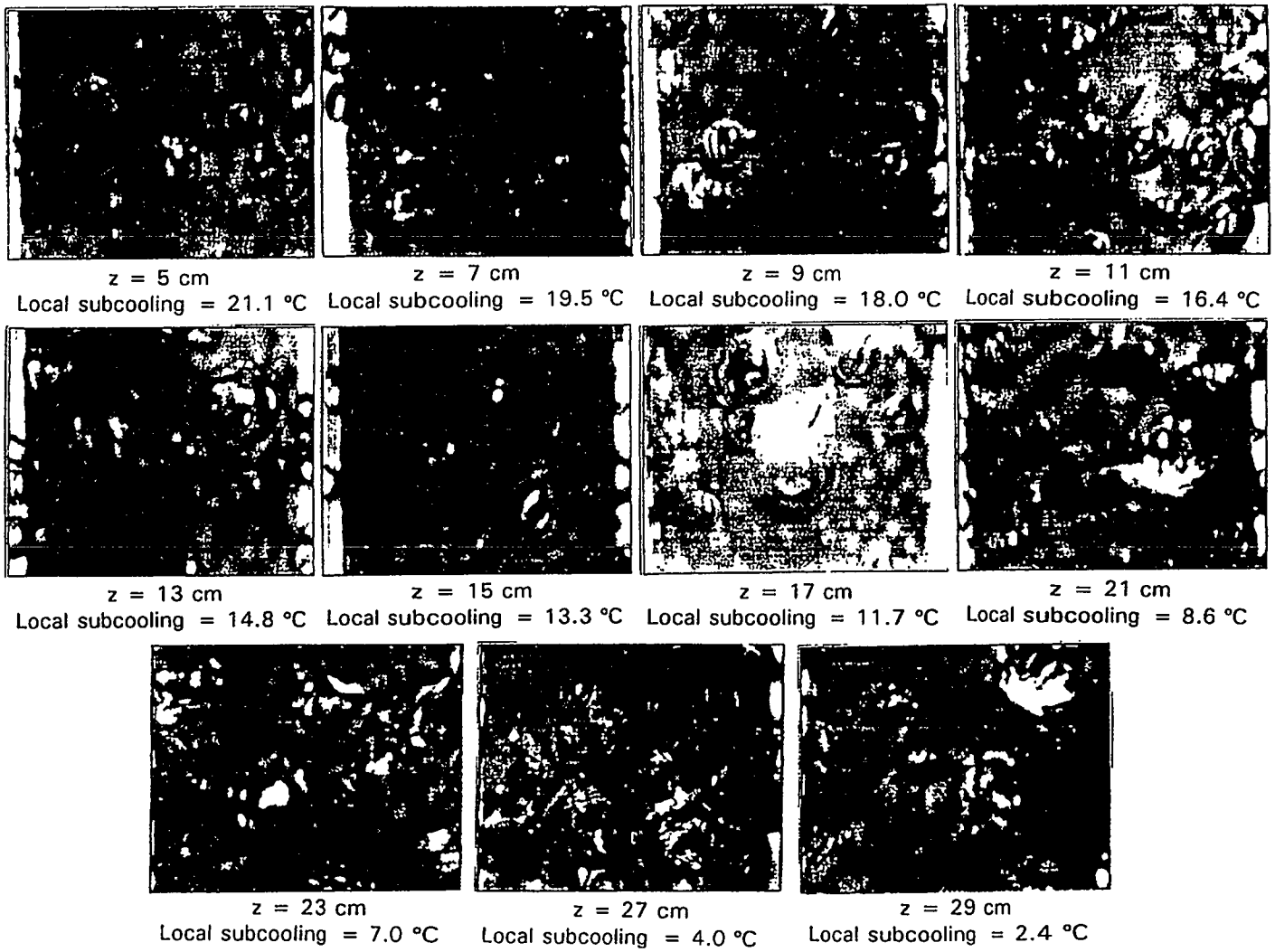

Figure 3: Bubble Behaviour along subcooled flow boiling region for run no. B4 ($q = 478.4$ kW/m^2, $G = 152.5$ kg/m^2.s, inlet subcooling $= 24.7$ °C)

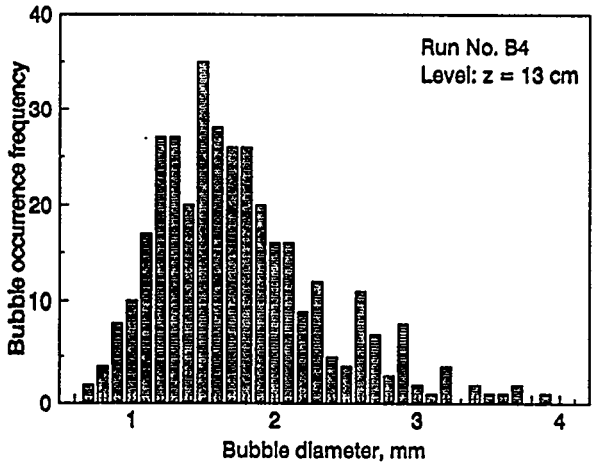

Figure 4: Typical histogram of bubble occurrence frequency versus individual Sauter bubble diameter

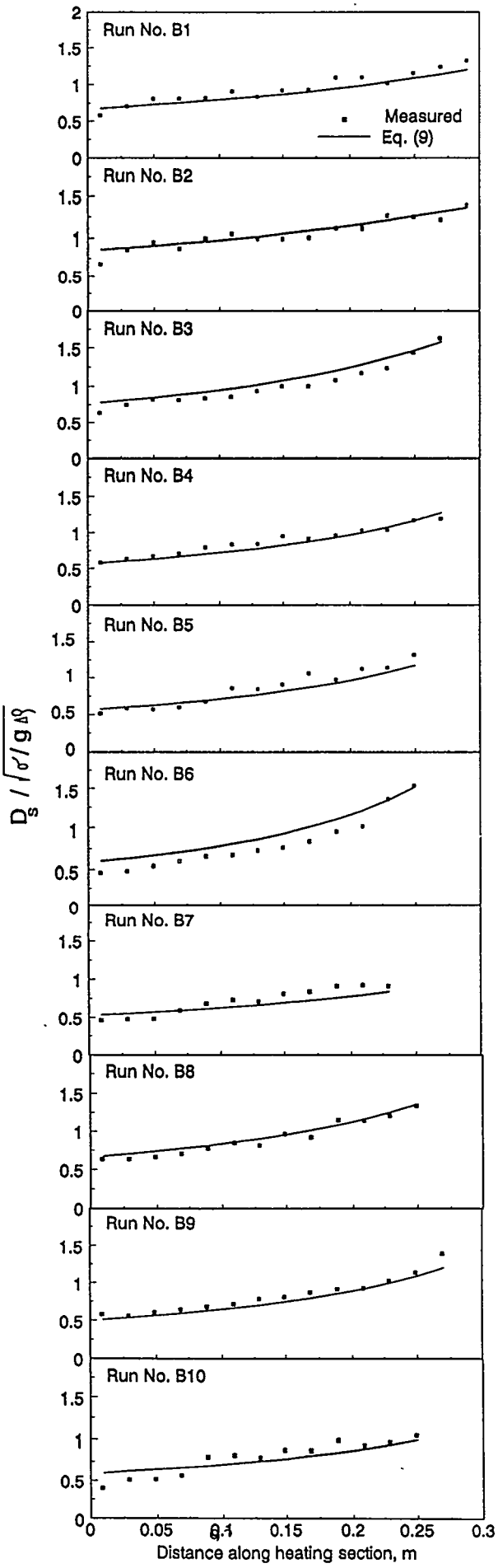

Figure 5: Measured mean Sauter bubble Diameter

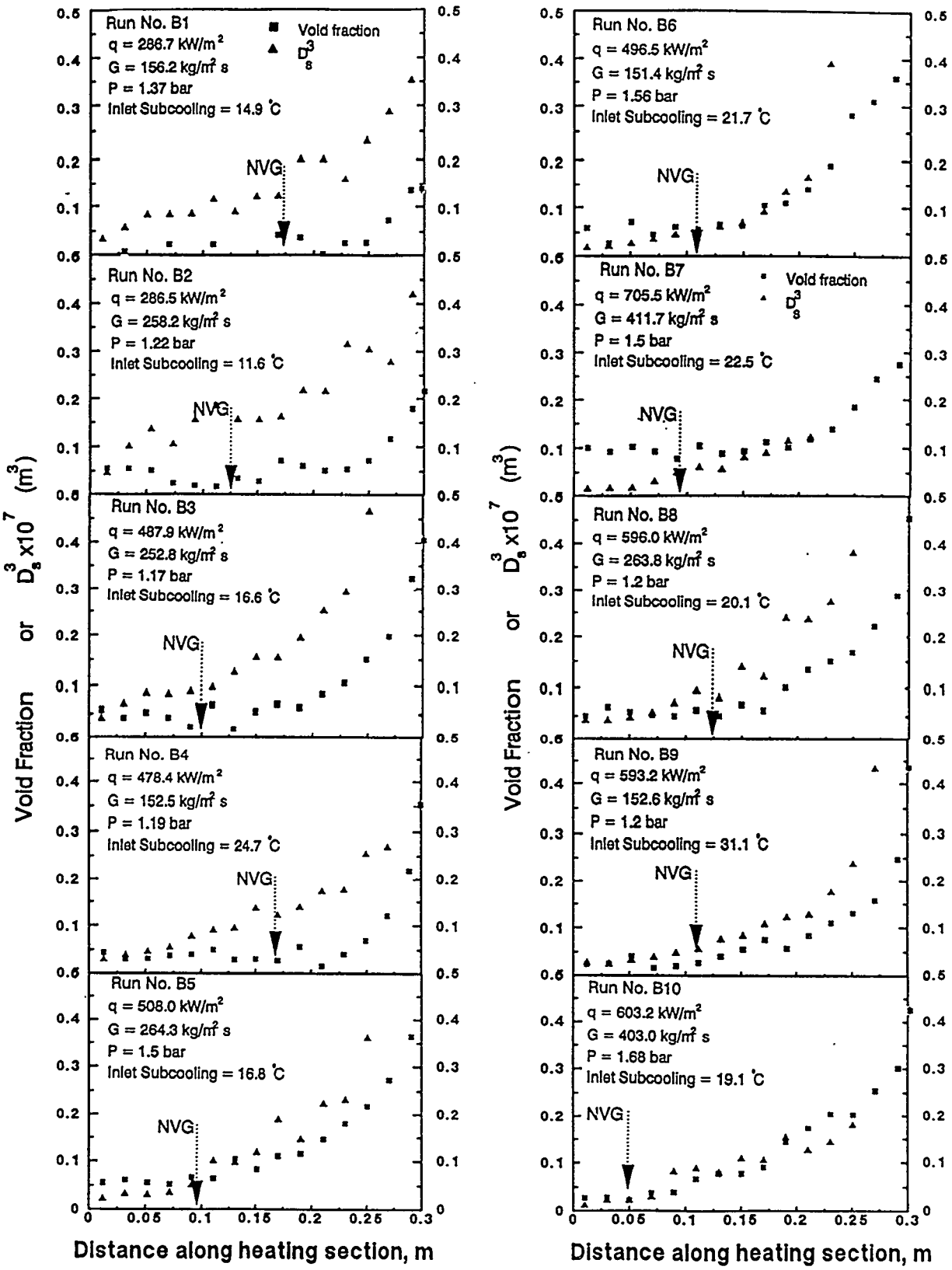

Figure 6: Relation between bubble size and void fraction

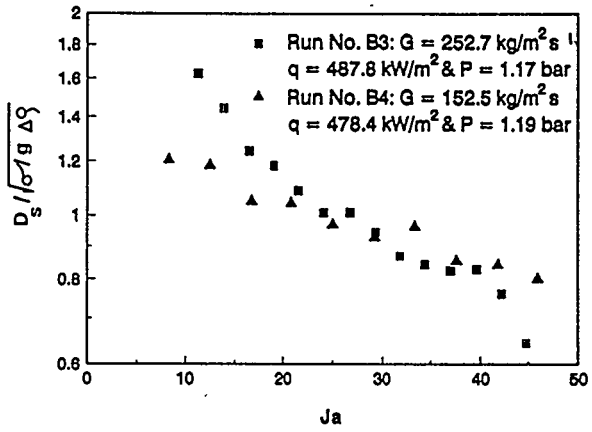

Figure 7: Effect of mass flux on mean bubble diameter

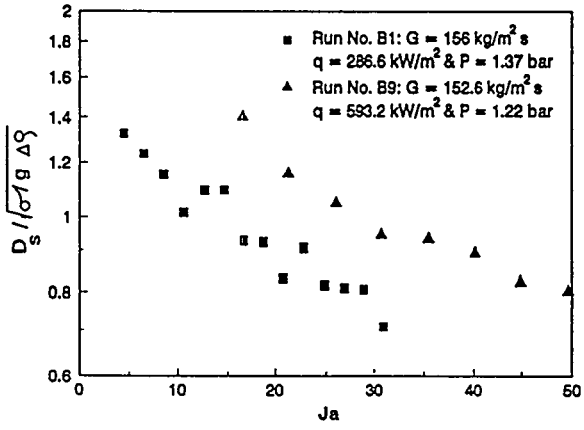

Figure 8: Effect of applied heat flux on mean bubble diameter

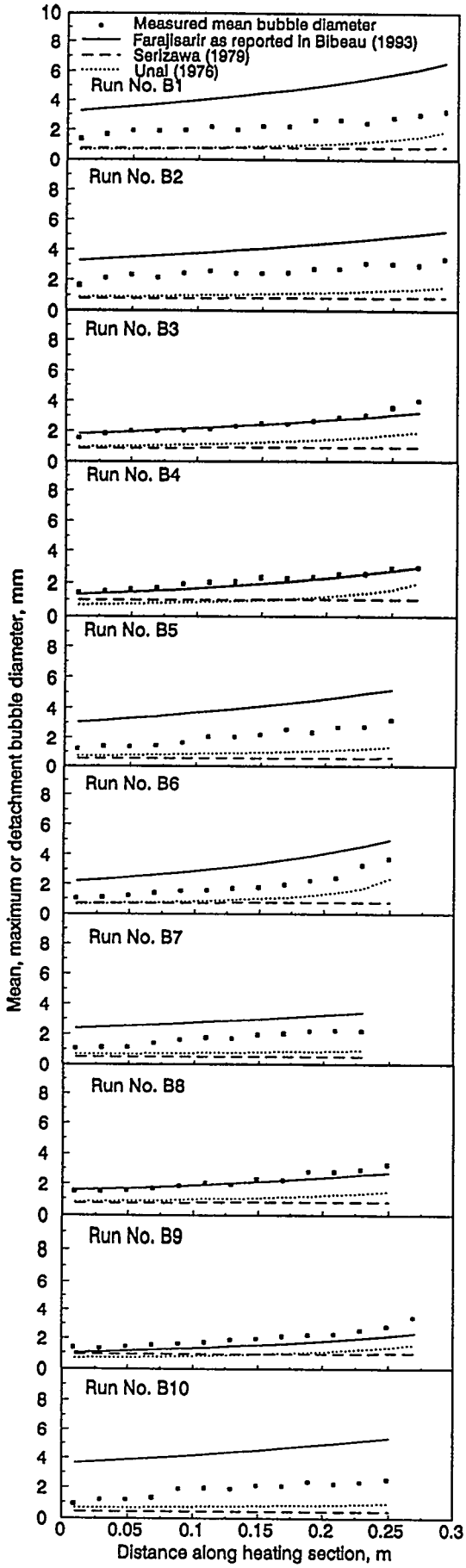

Figure 9: Comparison between measured mean bubble diameter and existing models of maximum and detachment bubble diameter

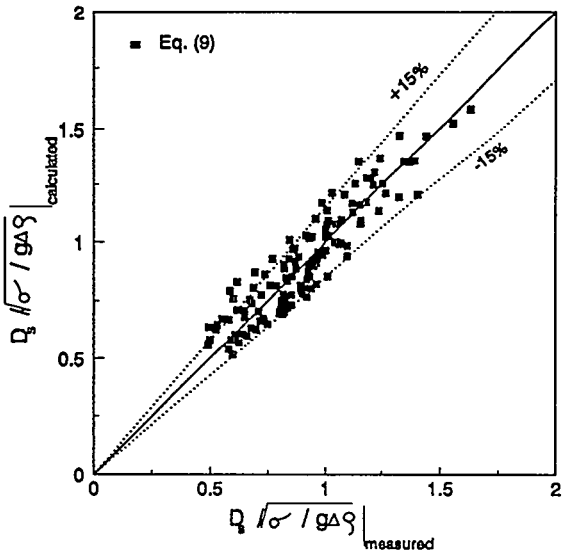

Figure 10: Comparison between proposed correlation and measured mean bubble diameter

Correlation of Critical Heat Flux Data for Uniform Tubes

T. Jafri, T.J. Dougherty, and B.W. Yang

Heat Transfer Research Facility
Columbia University
New York, NY 10027

ABSTRACT

A data base of more than 10,000 critical heat flux (CHF) data points has been compiled and analyzed. Two regimes of CHF are observed which will be referred to as the high CHF regime and the low CHF regime. In the high CHF regime, for pressures less than 110 bar, CHF (q_c) is a determined by local conditions and is adequately represented by $q_c = (1.2/D^{1/2})\exp[-\gamma(GX_t)^{1/2}]$ where the parameter γ is an increasing function of pressure only, X_t the true mass fraction of steam, and all units are metric but the heat flux is in MWm^{-2}.

A simple kinetic model has been developed to estimate X_t as a function of G, X, X_i, and X_0, where X_i is the inlet quality and X_0 represents the quality at the Onset of Significant Vaporization (OSV) which is estimated from the Saha-Zuber (S-Z) correlation. This model is based on a rate equation for vaporization suggested by, and consistent with, the S-Z correlation and contains no adjustable parameters. When $X_i < X_0$ (both negative), X_t is independent of X_i and is a function of local variables only. For $X_i > X_0$, X_t depends on X_i, a nonlocal variable, and, in this case, CHF, although determined by local conditions, obeys a nonlocal correlation. This model appears to be satisfactory for pressures less than 110 bar, where the S-Z correlation is known to be reliable. Above 110 bar the method of calculating X_0, and consequently X_t, appears to fail, so this approach can not be applied to high pressure CHF data.

Above 35 bar, the bulk of the available data lies in the high CHF regime while, at pressures less than 35 bar, almost all of the available data lie in the low CHF regime and appear to be nonlocal. The two-parameter, nonlocal correlation

$$q_s/q_c = d + 0.346[1 - \exp[-4.40(X_0 - X_i)]]$$

correlates the low pressure data reasonably well. This expression fits the data with a standard deviation of 5.52% and predicts q_c with a standard deviation of 10.1% (note that X_0 depends on q_c). The variable $q_s = \lambda GX_iD/4L$ is the heat flux to produce an exit quality of zero (saturation heat flux), and d is a dimensionless variable defined as D/4LS, where S is the value of the Stanton number at OSV, as predicted by the Saha-Zuber correlation, and is a function of Peclet number. Efforts are being made to improve this correlation and to extend it to higher pressures.

1. INTRODUCTION

The object of the work presented in this paper was to obtain relatively simple but meaningfull correlations for critical heat flux (CHF) for water in uniform tubes. For a uniform tube, CHF data is available as a function of five independent variables, $q_c = f(P,G,T_i,L,D)$ where T_i is the inlet temperature and P is the exit pressure. A data base of approximately 10,000 data points for CHF in uniform tubes was compiled from the available world literature (Jafri [1]). The range of variables covered was as follows.

Mass Velocity (G)	250 - 7500 kg/m^2/s
Pressure (P)	2.0 - 196 bar
Inlet quality (X_i)	(-1.20) - (-0.00)
Equilibrium exit quality X(L)	(-0.80) - (1.00)
Length (L)	0.15 - 5.00 m
Diameter (D)	1.0 - 37.5 mm

Not all possible combinations of these variables occur in this data base, and accurate correlations were not obtained for the complete ranges of all of these variables. In a uniform tubes, the only case considered here, CHF normally occurs at the end of the tube. The thermodynamic equilibrium quality, X, is defined by $X = [h - h_s]/[h_g - h_s] = (h - h_s)/\lambda$. A CHF correlation that depends only upon the local variables D, P, G, and X, is called a local correlation. Since only uniform tubes are considered here, P and X refer to the values at the tube exit (end of heated length); i.e., at the location of CHF. In the few situations where X does not refer to the exit quality, the meaning should be clear from the context.

The value of X is obtained by heat balance

$$q = G(h - h_i)D/4L = \lambda G(X - X_i)D/4L = q_s + \lambda GXD/4L \qquad (1)$$

where the nonlocal variable, q_s, is defined as

$$q_s = G(h_s - h_i)D/4L = -\lambda GX_iD/4L \qquad (2)$$

and represents the heat flux required to produce an exit quality of zero. Low pressure CHF data obtained in this laboratory [2, 3], for both vertical upflow and downflow, was found to correlate approximately linearly with q_s; i.e.,

$$q_c = mq_s + b \qquad (3)$$

Further investigation showed that this simple equation fits a substantial body of data over a wide range of variables with suprising accuracy. Using equation (1) to eliminate q_s from equation (3), we obtain,

$$q_c = A - B\lambda GX \qquad (4)$$

where the symbols A and B are defined as follows,

$$A = b/(1 - m) \qquad (5)$$

$$B = (D/4L)m/(1 - m) \qquad (6)$$

For a local correlation the coefficients A and B should be independent of length, which implies a specific dependence on length for the coefficents b and m. A negative value for the coefficient B (positive slope in GX plot) would imply upstream burnout unless B decreases in magnitude with increasing heated length. Equation (6) shows that for B to be positive and the slope of q_c

versus GX to be negative, the slope m of the q_c versus q_s curve should be less than one. Thus if B is negative (m > 1) the correlation must be nonlocal (assuming that upstream burnout never occurs in uniform tubes) while a positive value of B (m < 1) is compatible with a local correlation (a necessary, but not sufficient, condition). Much of the CHF data was found to obey such a local correlation. The desire to understand the significance of these simple facts was one of two factors that motivated this investigation.

Although equations (3) and (4) are mathematically equivalent, equation (4) reveals the local or nonlocal character of the data more directly but equation (3) is, in some ways, more suited to quantitative data analysis since it relates q_c to independent experimental variables; i.e., variables which are independent of heat flux. On the other hand, since the parameters in equation (4) are independent of length for a local correlation, plotting versus GX gives a better overview of data for different length tubes. Generally, data for a single tube does not provide a global picture of CHF. In the present work, emphasis is placed on correlations which provide a uniform approximation to the data (global view) and, because of.the very nonuniform distribution of the data, very rarely are correlations sought by methods such as least square fitting of the data to a correlation. To employ mechanical methods, such as least squares, it would be necessary to assign appropriate weights to the data. The approach utilized here is complicated by the dimensionality of the problem and it is necessary to reduce the dimensionality by seeking appropriate combinations of variables. Even if this is successfully accomplished, a great many data plots must be prepared and examined, and this undertaking would have been difficult, if not impossible, without a modern computers and appropriate software.

The appearance of the product GX suggests that steam mass flux is a fundamental variable. If so, a more logical variable would be $G(X - X_o)$, where X_o is the quality at the onset of significant void generation (OSV).

$$q_c = \alpha - \beta\lambda G(X - X_o) \qquad (7)$$

Saha and Zuber [4] compiled OSV data for water, refrigerants, and ammonia in tubes, channels, and annuli. For water the pressures ranged up to 100 bar. They found that the data obeyed the simple correlation

$$S = q/G(h_s - h_o) = S_1/p \qquad (8)$$

where S represents the value of the Stanton number, St, at OSV, and $S_1 = 0.0065$, and p = Pe/70000 for Pe < 70,000, and p = 1 for Pe > 70,000. In the Peclet number, $Pe = DGC_p/k$, the properties k and c_p, are the thermal conductivity and heat capacity of the liquid, respectively, evaluated at saturation, although it would be more accurate to use the temperature at OSV (calculated by iteration). The S-Z correlation is a local correlation and is not restricted to uniform tubes, but can be applied as well to annuli, channels, and nonuniform tubes. Thus, much of what follows can be generalized to cover these situations, although CHF in annuli and channels presents additional complications related to surface curvature. The desire to understand the meaning of the Saha-Zuber correlation, which is truly remarkable in its simplicity, generality and mathematical form, was the second factor that motivated the work presented here.

The Saha-Zuber (S-Z) correlation can be written as

$$q = -S\lambda GX_o \qquad (9)$$

Solving equation (9) for X_0 and substituting the result into equation (7) yields

$$q_c = (\alpha - \beta\lambda GX)/(1 + \beta/S) \quad (10)$$

The parameters A and B are related to α and β as follows,

$$A = \alpha/(1 + \beta/S) \quad (11)$$

$$B = \beta/(1 + \beta/S) \quad (12)$$

From equation (12) we observe that for β to be a positive number B must be less than S, the Stanton number at OSV. We might expect that the parameter α, which represents the value of CHF at OSV where the fluid is essentially a liquid, to be relatively insensitive to pressure. For almost all of the CHF data that obey a local correlation, the Peclet number is greater than 70000 and $S = S_1 = 0.0065$. The fact that equations (4) and (10) have the same form reinforced the belief that these relations have some fundamental significance and suggested that better results could be obtained if the true mass fraction of steam could be estimated.

2. ESTIMATION OF TRUE MASS FRACTION

A reasonable form for the rate of vapor generation that is consistent with the Saha-Zuber correlation is

$$d(\lambda M_V) = Y(h_l(z) - h_0)\pi D dz \quad (13)$$

where $h_l(z)$ is the enthalpy of the liquid at a distance z from the inlet, h_0 is the enthalpy at OSV, M_V is the mass flow rate of vapor, D is the tube diameter, and Y = SG. When $h_l(z)$ is at the saturation value, all of the heat input goes into vaporization and equation (13) becomes the S-Z correlation for h_0. The meaning of equation (13) becomes clearer if we define the vaporization heat flux as

$$q_V = d(\lambda M_V)/d(\pi D z) = Y(h_l(z) - h_0) \quad (14)$$

and the heat flux to raise the enthalpy of the liquid as

$$q_l = q - q_V = Y(h_S - h_0) - Y(h_l(z) - h_0) = Y(h_S - h_l) \quad (15)$$

where q has been expressed in terms of h_0 by means of the S-Z relation. Thus we see that the present formulation is equivalent to a relation for heat transfer to the liquid phase with an enthalpy driving force of $h_S - h_0$. This might be pictured as heat being transferred to the liquid by the vapor formed at the wall. Past the point of incipient boiling, the wall temperature is often not much higher than the saturation temperature so heat transfer by direct conduction to the liquid can also be considered as included, at least approximately. Since the S-Z correlation is reasonably successful in predicting OSV for pressures less than 100 bar, possible modifications, which might very well be necessary, will not be considered at this time. At high pressure and high flow rates and inlet subcoolings (high CHF values) CHF often occurs at exit qualities less than the quality at which OSV is predicted to occur by the S-Z correlation.

The heat transfer coefficient, Y, depends on the Peclet number. In the low Peclet number region the rate of heat transfer is controlled by thermal conduction and is independent of mass velocity and depends on the thermal properties of the liquid, while in the higher Peclet number region, which can be regarded as the region of forced convection heat transfer, the rate of heat transfer is proportional to the mass velocity and is independent of the properties of the liquid.

Assuming that the enthalpy of the vapor, h_v, is constant at the saturation value at the exit pressure, and neglecting kinetic energy changes, the overall mass and energy balance yields

$$dQ = q\pi Ddz = d[h_l M_l + h_v M_v] = M_l dh_l + (h_v - h_l)dM_v \qquad (16)$$

where M_v and M_l represent the mass flow rate of vapor and liquid, respectively and their sum is the total mass flow rate, M, a constant. The equilibrium quality, X(z), is related to the variable z by the energy balance

$$q\pi Ddz = \lambda M dX(z) \qquad (17)$$

Thus equations (13) and (16) can be written, respectively, in the form

$$dX_t/dX = (Y/q)(h_l - h_o) = (h_l - h_o)/(h_s - h_o) \qquad (18)$$

$$(1 - X_t)dh_l/dX + (h_v - h_l)dX_t/dX = \lambda \qquad (19)$$

where X_t represents the true mass fraction of steam, M_v/M. Equation (19) can be immediately integrated once to yield

$$(1 - X_t)h_l + h_v X_t = \lambda X + C$$

Let X_b denote the quality at which significant vaporization actually begins. Thus $X_b = X_o$ if $X_o > X_i$ and $X_b = X_i$ if $X_o < X_i$. From the initial condition $X_t = 0$ when $X = X_b$, the constant of integration is found to be h_s.

$$(1 - X_t)h_l + h_v X_t = \lambda X + h_s = h \qquad (20)$$

This result is obvious and could have been obtained directly from the definition of h.

Using equation (20) to eliminate h_l in equation (18) yields

$$(1 - X_t)dX_t/dX + X_t(h_v - h_o)/(h_s - h_o) = 1 + \lambda X/(h_s - h_o) \qquad (21)$$

Let $Z = 1 - X_t$ and recall that $h_o - h_s = \lambda X_o$, then

$$ZdZ/dX - (1 - Z)(h_v - h_s + \lambda X_o)/\lambda X_o = -1 + X/X_o$$

or

$$ZdZ/dX + Z(1 - 1/X_o) = -(1 - X)/X_o$$

Letting $s = 1 - X$ and $Z = sF$ yields

$$sFdF/ds + FF - (1 - 1/X_o)F = 1/X_o$$

Let $t = \ln s$.

$$FdF/dt + FF - (1 - 1/X_o)F = 1/X_o \qquad (22)$$

Separating variables and integrating by partial fractions gives

$$X_o/(1 + X_o)\ln(F - 1) + 1/(1 + X_o)\ln(F + 1/X_o) = -\ln s + C$$

where $F = (1 - X_t)/(1 - X)$ and $s = 1 - X$. For $X = X_b$, $X_t = 0$, $s = 1 - X_b$ and $F = 1/(1 - X_b)$. Thus, the exact analytical solution found from this model is the transcendental equation

$$X_o\ln[(1-X_b)(F-1)/X_b] + \ln[(X_oF+1)/(X_o/(1-X_b)+1)] = (1+X_o)\ln[(1-X_b)/(1-X)]$$

which can be written in the simpler form

$$X_o\ln[(X-X_t)/X_b] + \ln[(1-X+X_o-X_oX_t)/(1-X_b + X_o)] = 0 \qquad (23)$$

If $X_i > 0$, X_t is assumed to be simply the equilibrium quality, X.

Note that For $X_o > X_i$, $X_b = X_o$ and this result simplifies to

$$X_o\ln[(X-X_t)/X_o] + \ln[1 - X + X_o - X_oX_t)] = 0 \qquad (24)$$

In this case, X_t is determined by X and X_o and is independent of inlet conditions, or equivalently, the tube length; i.e., it is a function of local variables only. In physical terms, the portion of the heater tube upstream of the OSV point serves only as a preheater to heat the liquid to the point of OSV. In the other case, where the inlet quality is above the OSV quality,

significant vapor generation occurs immediately at the beginning of the heated length and, in that case, the value of X_t depends explicitly on X_i, the quality at the inlet, yielding a nonlocal relation for X_t. Thus we see that, even if CHF is determined by the local value of X_t, the correlation with experimental variables can be nonlocal. In other words, even if CHF is determined by local conditions the CHF correlation can be nonlocal.

A form of equation (24) which is sometimes useful for computation, is

$$-(1 + X_0)\ln(1 - y) = X_0\ln(1 + V/X_0) + \ln(1 + X_0V) \qquad (25)$$

where y and V are the normalized variables

$$y = (X - X_0)/(1- X_0) \qquad V = (y - X_t)/(1 - y) \qquad (26)$$

This form also exhibits an interesting symmetry property since equation (25) is unchanged by replacing X_0 by $1/X_0$.

As X approaches one, X_t approaches X. An approximate result for small values of X_t (X - X_0 small) is

$$X_t = -(X - X_0)^2/2X_0 \qquad (27)$$

Recall that X_0 is negative. Substitution for X_0 from the S-Z correlation gives,

$$X - X_0 = (2q_cX_t /\lambda GS)^{1/2} \qquad (28)$$

Multiplying both sides with mass velocity G we obtain,

$$G(X-X_0) = (2q_c/\lambda S)^{1/2}(GX_t)^{1/2} \qquad (29)$$

This shows that $G(X-X_0)$ is a function of GX_t, the steam mass flux. For small values of X_t, q_c can be replaced by α, the value of q_c when X equals X_0. Therefore, for small values of X_t, $G(X-X_0)$ is directly proportional to the square root of steam mass flux, and a linear dependence of CHF on GX (or q_s) implies a square root dependence on steam mass flux. Substituting equation (29) into equation (7), we obtain,

$$q_c = \alpha - \beta\lambda G(X-X_0) = \alpha - \beta(2\alpha/S)^{1/2}(\lambda GX_t)^{1/2} \qquad (30)$$

Analysis of the experimental data suggests that, for a wide range of conditions, the actual dependence of CHF on steam mass flux is compatible with the simple exponential function

$$q_c = \alpha\exp[-\gamma(GX_t)^{1/2}] \qquad (31)$$

For small X_t, this is equivalent to equation (30) which yields

$$\gamma = \beta(2\lambda/S\alpha)^{1/2} \qquad (32)$$

The above analysis is based on the assumption that the steam enthalpy is constant at the saturation value corresponding to the pressure at the point at which CHF occurs, in this case, the exit pressure. Thus, the difference in pressure between the OSV point and the CHF point can not be too great. This limitation might not be very serious since the difference between the values of X and X_t is usually small when X is significantly greater than X_0.

In the following sections, we attempt to analyze a large body of data using the concepts and formulas presented above. In the process new phenomena, requiring additional concepts, emerge. The material presented represents only a portion of the data analyzed, which has been chosen to illustrate the main points of this paper. More details are given in the Ph. D. thesis of T. Jafri [1].

3. DATA ANALYSIS

For various practical reasons, it is convenient to divide the data into three pressure regimes, which will be denoted as low, medium, and high pressure. Low pressure will refer to pressures below 35 bar (ca. 500 psia), high pressure to pressures above 110 bar (ca. 1500 psia), and medium pressure to pressures of 35 to 110 bar (ca. 500 to 1500 psia). This should not be taken to imply that there is any fundamental difference in the mechanisms of CHF in these different pressure regimes. The medium pressure regime will be considered first, principally because of the relatively large and complete body of data available in this regime, but also because the S-Z correlation is known to be valid at these pressures.

3A. Analysis of Medium Pressure Data

In the medium pressure (35-110 bar) range, many data points are available for a wide range of diameters, lengths and flow rates, particularly at 69 bar (1000 psia). Figure 1 shows a plot of $D^{1/2}q_c$ versus $(GX_t)^{1/2}$ for almost all of the data of Table 6 (69 bar) of the Thompson-Macbeth compilation [6]. No data has been excluded unless there was some independent reason (e.g., poor heat balance, complete lack of consistency with related data, etc.) for suspecting the validity of the data. This data is adequately represented by the equation

$$D^{1/2}q_c = 1.2\exp[-0.12(GX_tP/P_c)^{1/2}] = 1.2\exp[-0.067(GX_t)^{1/2}] \qquad (33)$$

Figure 2 shows the corresponding plot of the Soviet data [7], (see also Collier [5], pp 262-264) for the range of pressures from 29.5 to 98 bar. A problem in the analysis of this Soviet data was the lack of information regarding inlet conditions and tube length. Therefore X_t was calculated assuming that X_o was always greater than X_i and that X_i was always negative. These sets of data exhibit a peculiar "S" shaped curve with an inflection point. These inflection points correspond to $X = 0$, although this latter fact is not evident from this figure.

Figure 3 shows a similar plot for pressures from 34 to 103 bar of data from the Thompson-Macbeth compilation. A portion of this data lies substantially below the exponential curve and obeys a nonlocal correlation [14]. The points which lie substantially above this curve pertain to very high mass velocities and very small values of X_t. In these cases the value of GX_t is sensitive to small errors in X_t. In extreme cases, high mass velocity and high inlet subcooling, the value of the equilibrium exit quality is below the value calculated for OSV from the S-Z correlation, so the calculated values of X_t are not meaningful. This last phenomenom becomes more common at higher pressures. Plotted in Figure 4 is the Lee-Obertelli data [9] for pressures of 86 to 124 bar. Additional data from these and other [10, 11] sources has been analyzed but can not be presented in this limited space. Again, the simple exponential function provides a reasonable approximation to the data, most of which lies close to the curve.

In Figure 5, the Swedish CHF data of Becker et al. [8], from report number KTH-NEL-14, (referred to hereafter as KTH) for a 10 mm ID, 2 m long tube is plotted versus $(GX_tP/Pc)^{0.5}$ for pressures of 50-120 bar. This data exhibits both local and nonlocal behavior, the nonlocal being in the lower CHF range where the slopes are positive. In Figure 6, data from the same

source (KTH) is plotted versus q_s for pressures of 50-180 bar. Only portions of the available data have been plotted to conserve space and avoid excessive clutter in the figures. In this figure, the nonlocal data increases much more rapidly with q_s than the local data. Also note the linearity of large portions of these plots.

How well does the correlation represented by equation (33) represent the data and how accurately does it predict CHF? Figure 7 shows the values of q_c calculated from equation (33) for the data shown in Figure 1 plotted versus the observed values. Several points should be made here. The value of the parameter in the exponent was taken as 0.068 instead of 0.067, since 0.068 actually fits the data at this pressure (69 bar) more accurately and with zero average error and a standard deviation of 18.4%. More importantly, some of the nonlocal data points were omitted. In Figure 1, one can see some of these nonlocal CHF points (most evident is the 10.8 mm ID data - small diamonds) where the data have broken away from the main trend and are forming small positively sloped lines. A total of 29 points out of 792 points have thus been omitted. Because of the scatter in the points we have tried to be very conservative in omitting any data and some of the high points shown in Figure 7 very likely are nonlocal data points. In these plots, X_t has been calculated from the experimental data which includes the observed CHF values. We must now consider the problem of prediction of both X_t and q_c by solution of equations (23) and (33).

Figures 8 and 9 show the predicted values of X_t and q_c, respectively, versus the observed values. In the case of X_t, by observed value we mean the value calculated from the observed data. A minor miracle occurs here since the predicted values of q_c are better than the calculated values (standard deviation 16.0%). Furthermore, another piece of good fortune enables us to improve even further on this prediction. When X is calculated from the predicted value of q_c, it occasionally happens that X is greater than the predicted value of X_t, which is physically unreasonable, and suggests that the predicted value of X be replaced by its upper bound, the predicted value of X_t. From this new value of X an improved estimate of q_c (standard deviation 12.2%) can be calculated from the heat balance. Figure 9 shows these "corrected" predictions of q_c plotted versus the observed values.

3B. Analysis of High Pressure Data

A portion of the high pressure data has already been shown in the Figure 6 plotted versus q_c. Figure 10 shows some additional data for a pressure of approximately 140 bar plotted versus GX. Not all of the USSR data points are shown since the range of that data extends well beyond the limits of this figure (in both directions) and the omitted portion does not add any new insights. Again we note that the part of the data which is local lies predominantly in the subcooled region where the plot is reasonably linear. The transition to a nonlocal correlation is observed for all data except the USSR data which has some peculiar behavior near zero quality. This data is a composite of data for many different size tubes, which would obscure the transition to nonlocal behavior.

At, or above, 110 bar (1500 psia), the estimation of X_t by the method presented in this paper encounters a basic difficulty since the exit quality, X, is sometimes less than X_o, as

calculated by the S-Z correlation. Furthermore, the data no longer collapses to a single universal function at a given pressure. The S-Z correlation has not been tested at these pressures and might be invalid in this region. It is also possible that GX_t is not the principal factor determining CHF in this pressure range, but this can not be ascertained at this time. The distinction between liquid and vapor diminishes as the pressure approaches the critical pressure so we must expect that, at some point, the steam mass flux will cease to be a dominant factor.

Examination of numerous plots of q_c versus GX or q_s does not reveal any marked changes as pressure is increased leading us to believe that there is no fundamental change in the mechanisms of CHF in the high pressure region and that the principal problem lies in the inadequacies of our estimation of X_t from the S-Z correlation. To resolve this question requires OSV data for high pressures and/or measured values of X_t at CHF.

3C. Analysis of Low Pressure Data

Figure 11 shows the CHF data obtained in the laboratory [2,3] and some of the low pressure Swedish data [Becker, 12] from Table 1 of the report AE177 plotted versus $(GX_t)^{1/2}$. Only portions of the Swedish data have been plotted to avoid making the figure too cluttered with points. The range of pressures for the Swedish data was 2 to 35 bar and for the HTRF data from 2 to 10 bar. There is clearly insufficient low pressure local data to obtain a reasonable fit but the solid curve represents a rough eyeball estimate. The value of the parameter in the exponent, 0.05, corresponds to the value of $0.12(P/P_c)^{1/2}$ for a pressure of 30 bar. For the low pressure data, less than 35 bar, the pressure dependence found at medium pressure can not possibly hold, and it appears that there is very little explicit pressure dependence in this region. This conclusion is tentative and more data is required to draw firm conclusions.

Figure 12 shows the HTRF data and the Swedish data for a 13.06 mm I.D. plotted vs. q_s. The Swedish and HTRF data complement each other. Initially the slope is greater than one, then the curve turns giving a slope less than one. The HTRF data presumably lies principally in the local regime. Since this data is for only one tube length, this conclusion can not be stated as established fact. In addition, this data appears to have little explicit pressure dependence, but this is difficult to determine precisely with so little data and such a small pressure range.

All of the low pressure Swedish data points (AE177) are plotted in Figure 13 versus GXD/4L. The bulk of this data obeys a nonlocal correlation. From a total of 1218 data points, 898 points, for which $1.2q_c$ was less than the values predicted by the high CHF (local) correlation, were analyzed and the equation

$$q_s/q_c = d + 0.358(1 - \exp[-4.40(X_o - X_i)]) \qquad (34)$$

was found to fit this data with a standard deviation of 5.52% and to predict q_c with a standard deviation of 10.1%. Figure 14 shows the low pressure data plotted based on equation (34). The dimensionless variable d is defined as D/4LS (recall that S is a function of Peclet number). Efforts are being made to improve this correlation and to extend it to higher pressures.

4. CHF DEPENDENCE ON G, X, AND q_s

The simple looking correlation given in equation (33) is actually a very complicated function of the normal experimental variables G, X_i,D, L and P. Figure 15 illustrates the type of dependence on these variables implied by this equation for a 10 mm I.D. tube at a pressure of 69 bar and for the simple case of local conditions ($X_o > X_i$). This figure exhibits many familiar features of CHF data. Some of the curves cross at an exit quality very close to zero. For water at these conditions the Peclet number is less than 70,000 when G is less than 773, which is the explanation of the qualitative difference between the curves for G = 500 and G = 1000 and which is also the reason that the curves for G = 200 and G = 500 intersect at q_c = 12 MW/m^2 (the value at X_t =0; i.e., X = X_O). Note that, for the points at the top of this figure, the exit qualities are equal to X_O which is independent of G for Peclet numbers less than 70,000.

A second point of some interest is the linear relation that is often observed between q_c and q_s. Figure 16 shows a plot of q_c values calculated from the correlation versus q_s for a 10 mm I.D. tube and four different lengths at a pressure of 69 bar, for inlet qualities greater than -1.2. The straight lines represent the least squares fit of this "data" and the slopes and intercepts are shown in the legend. Thus, we see that such (approximately) linear relations are compatible with the correlation presented here and that we should not be surprised to find them. One final point relates the numerical values of the slopes and intercepts, which we can use to calculate values of α, β, and γ. The results are shown in Table 1 below and we see that there is a systematic discrepancy between the values obtained by fitting with q_s and with GX_t.

L, mm	slope, m	intercept, b	α	β	γ
250	0.239	3.907	9.92	0.00606	0.0414
500	0.416	2.924	11.09	0.00789	0.0511
1000	0.573	2.091	10.74	0.00695	0.0470
2000	0.686	1.497	8.21	0.00470	0.0335

Table 1. Values of parameters α, β, γ calculated from slopes and intercepts of q_c vs. q_s plot generated the GX_t correlation for a 10 mm I.D. tube at 69 bar. (α =12.0, γ = 0.068).

5. SUMMARY

After this lengthy analysis of the data, it might prove helpful to summarize the principal results obtained so far and to indicate the course of current work.

A. A method has been presented to estimate the mass fraction of steam. This method was inspired by the Saha-Zuber correlation for OSV and has no greater range of validity than that correlation. Although the present work does not completely establish the validity of this method, we feel that it does indicate that the basic concept contains a large measure of truth and warrants more extensive investigation and extension to other problems of two phase flow; e.g. heat transfer, CHF, and pressure drop calculations and correlations for nonuniform tubes, channels, and annuli. Some of these investigations have already begun. This method for

estimating the mass fraction of steam gives numerical results not much different from some empirical expressions (e.g., Kroger and Zuber [15]) that have been proposed and which agree reasonably well with void fraction measurements.

B. CHF divides into two major regimes: a high CHF regime; and a low CHF regime. In the higher range of CHF values much of the data follows the simple exponential function

$$D^{1/2}q_c = 1.2\exp[-\gamma(GX_t)^{1/2}]$$

where γ is approximately proportional to $P^{1/2}$ for medium pressure and apparently only weakly dependent on pressure in the low pressure region. Thus CHF is determined by local conditions but this correlation is local only if OSV occurs inside the tube ($X_0 > X_i$). At high pressures, the calculation of X_0 by the Saha-Zuber correlation is probably wrong and likewise the calculation of X_t which is based upon the S-Z correlation. At some sufficiently high pressure the variable GX_t is not expected to be the dominant variable. Direct measurement of X_t at CHF is needed.

C. In the lower range of CHF values, CHF appears to be nonlocal. Furthermore, in contrast to the situation in the high CHF regime, the Peclet number for a substantial portion of this data is less than 70,000. Attempts to correlate this data are in progress and the results will be presented in a separate paper. Most of the available data for pressures below 35 bar is in the low CHF regime and is nonlocal. A fairly good (898 data points, standard deviation 10.1%) two-parameter correlation for this data has been obtained and applied to CHF study in natural circulation loops at low pressure [16]. Efforts are being made to improve this correlation and to extend it to higher pressures.

D. Besides distinguishing between the high and low regimes of CHF mentioned above, it necessary to discriminate between data with Peclet number above 70,000 and data with Peclet number below 70,000. Of course, other sub regions might, and probably do, exist. It is further necessary to discriminate among inlet qualities which are less than the quality at OSV, between OSV and saturation, and above saturation.

E. One ambiguous point remains. Since q_c has two branches, a high branch and a low branch, for the prediction of CHF it is necessary to determine which branch is the appropriate one. Two computations are necessary since a value for q_c is required to calculate the values of X_t, and X. The appropriate value of CHF should be the lower of the two values. This point requires more careful investigation once a more accurate correlation for the low CHF regime is obtained.

6. REFERENCES

[1] T. Jafri, "Interpretation and Analysis of the Vertical Round Tube Critical Heat Flux Data", Ph.D. Thesis Columbia University (1993).

[2] T.J. Dougherty, G. D. Reddy, and B.W. Yang., "Flow Excursion Experimental Program. Single Tube Tests, Critical Heat Flux Program", Report No. CU-HTRF-T8-92-03, September 1992.

[3] T.J. Dougherty and B.W. Yang, "Onset of Flow Instability (OFI) and Critical Heat Flux (CHF) Experiments", Report No. CU-HTRF-92-06, December 1992.

[4] P. Saha and N. Zuber, "Point of Net Vapor Generation and Vapor Void Fraction in Subcooled Boiling", Proc. 5th Int. Heat Transfer Conf., Tokyo, Paper B4.7 (1974).

[5] J. G. Collier and J.R. Thome, "Convective Boiling and Condensation (3rd. ed.)." Clarendon Press, Oxford (1994).

[6] B. Thompson and R.V. Macbeth, "Boiling Water Heat Transfer Burnout in Uniformly Heated Round Tubes: A Compilation of World Data with Accurate Correlations." AEEW-R 356 (1964).

[7] Working Party of the Heat and Mass Transfer Section of Scientific Council of the USSR Academy of Sciences. "Tubular Data for Calculating Burnout when Boiling Water in Uniformly Heated Round Tubes." Teploenergetika, 23 (9), 90-92 (1976), or in Thermal Engineering, 77-79, Sept. (1977).

[8] K.M. Becker, "Round Tube Burnout Data for Flow of Boiling Water at Pressures between 30 and 200 Bar." Royal Institute of Technology, Laboratory of Nuclear Engineering, Sweden (1971).

[9] D.H. Lee, "An Experimental Investigation of Forced Convection Burnout in High Pressure Water." Pt. IV, AEEW-R 479 (1966).

[10] DeBortoli et al., "Forced Convection Heat Transfer Burnout Studies for Water in Rectangular Channels and Round Tubes at Pressures above 500 Psia." USAEC Report WAPD-188, (1958).

[11] J. Griffel, "Forced Convection Boiling Burnout For Water in Uniformly Heated Tubular Test Sections." USAEC Report NYO-187-7, TID-4500, May (1965).

[12] K.M. Becker et al., "Burnout Data for Flow of Boiling Water in Vertical Round Ducts, Annuli, and Rod Clusters", Aktiebolaget Atomenergi Report AE177, Sweden (1965).

[13] K.M. Becker, "An Analytical and Experimental Study of Burnout Conditions in Vertical Round Ducts." A.B. Atomenergie Report AE 178, Sweden (1965).

[14] E.D. Waters, et al. "Experimental Observations of Upstream Boiling Burnout" HW 73902 (Rev). Hanford Atomic Products Operation, Richland, WA, November (1962).

[15] P.G. Kroger and N. Zuber, "An aAnalysis of the effects of Various Parameters on the Average Void Fractions in Subcooled Boiling." Int. J. Heat Mass Transfer, 11, 211-233 (1968).

[16] T.J. Dougherty and B.W. Yang, "Flow Instability and CHF in Natural Circulation Loops at Low Pressure ", National Heat Transfer Conference, Portland, Oregon, August 5-8, (1995).

7. NOMENCLATURE

Symbol	Description	Metric Units
A	intercept, q_c vs. GX correlation	MW/m^2
B	slope, q_c vs. GX correlation	none
D	tube inside diameter	m
F	= Z/s = $(1 - X_t)/(1 - X)$	none
G	mass velocity	$kg/m^2/s$
L	heated length of tube	m
M	mass flow rate	kg/s
P	exit pressure	bar
Q	heat input	MW
S	Stanton number at OSV	none
S_1	= 0.0065, value of S for Pe>70000	none
T	temperature	^oC
V	= $(y - X_t)/(1 - y)$	none
X	thermodynamic quality	none
X_t	true mass fraction of steam	none
Y	S-Z heat transfer coefficient	$kg/m^2/s$
Z	$1 - X_t$	none
b	intercept, q_c vs. q_s correlation	MW/m^2
c_p	heat capacity, constant pressure	$kJ/kg/^oC$
d	= D/4LS	none
h	specific enthalpy	kJ/kg
k	thermal conductivity	$kW/m/^oC$
m	slope in q_c vs. q_s correlation	none
p	minimum(1, Pe/70000)	none
q	heat flux	MW/m^2
q_c	critical heat flux	MW/m^2
q_s	heat flux for saturation at exit	MW/m^2
s	= 1 - X	none
t	= ln s	none
y	= $(X - X_o)/(1 - X_o)$	none
z	distance along tube from inlet	m
α	parameter in CHF correlation	MW/m^2
β	parameter, CHF correlation	none
γ	parameter, CHF correlation	$(kg/m^2/s)^{-1/2}$
λ	heat of vaporization	kJ/kg
μ	viscosity	kg/m/s
ρ	density	kg/m^3
Nu	Nusselt number, Nu = $qD/k\Delta T$	none
Pe	Peclet number, Pe = DGc_p/k	none
Re	Reynolds number, $[DG/\mu]$	none
St	Stanton number, $[q''/G\Delta h]$	none

Subscript	Description
b	beginning of vaporization
c	critical condition
f	fluid
g	gas
h	heat transfer
i	inlet
l	liquid
o	onset of significant vaporization
s	saturation
t	true (as in true mass fraction X_t)
v	vapor
1	value at p =1

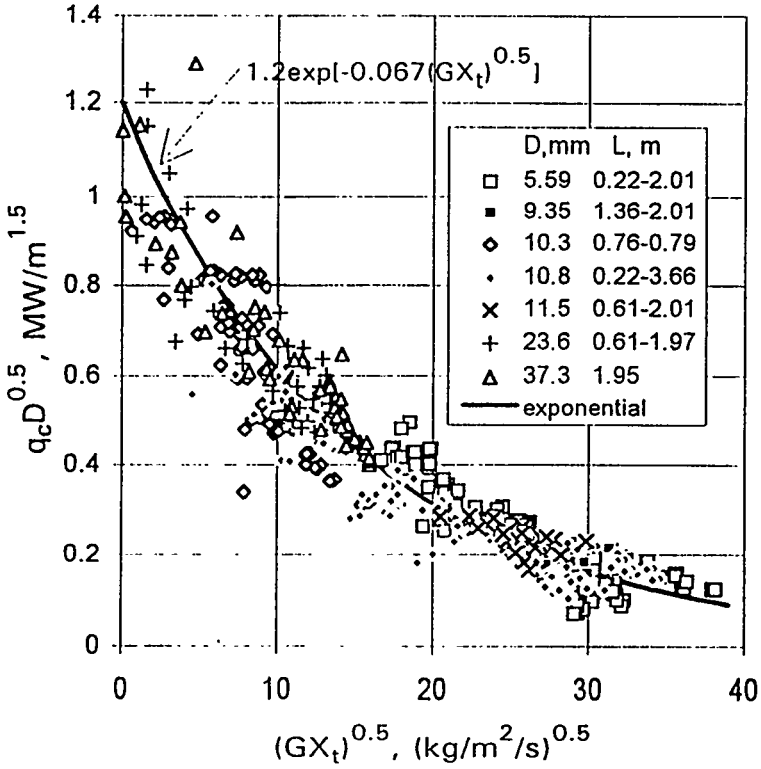

Figure 1. Data from Table 6 of Thompson Macbeth Compilation
Pressure = 69 bar (1000 psia).

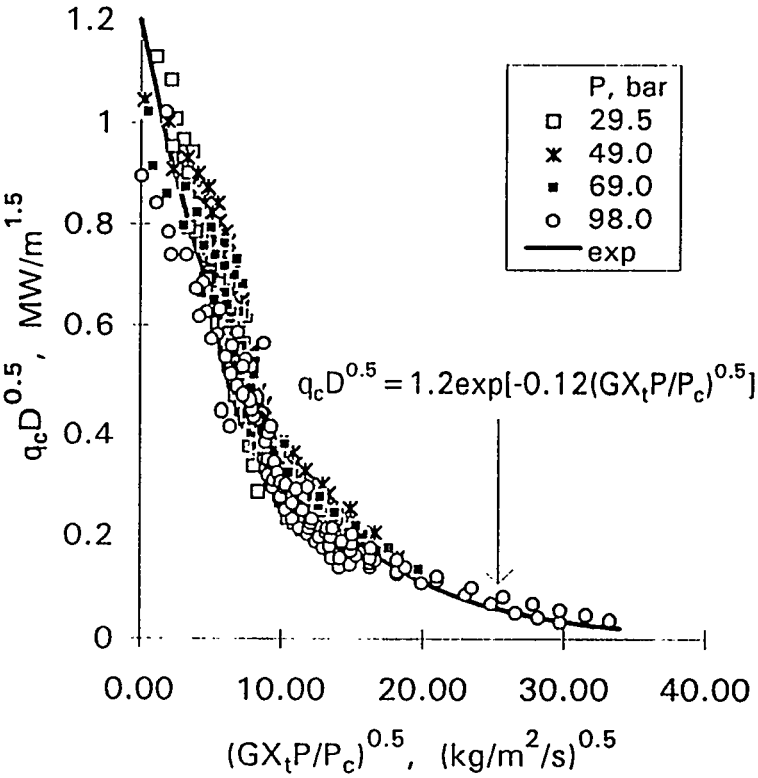

Figure 2. Medium Pressure USSR CHF Data
for 8mm ID tube.

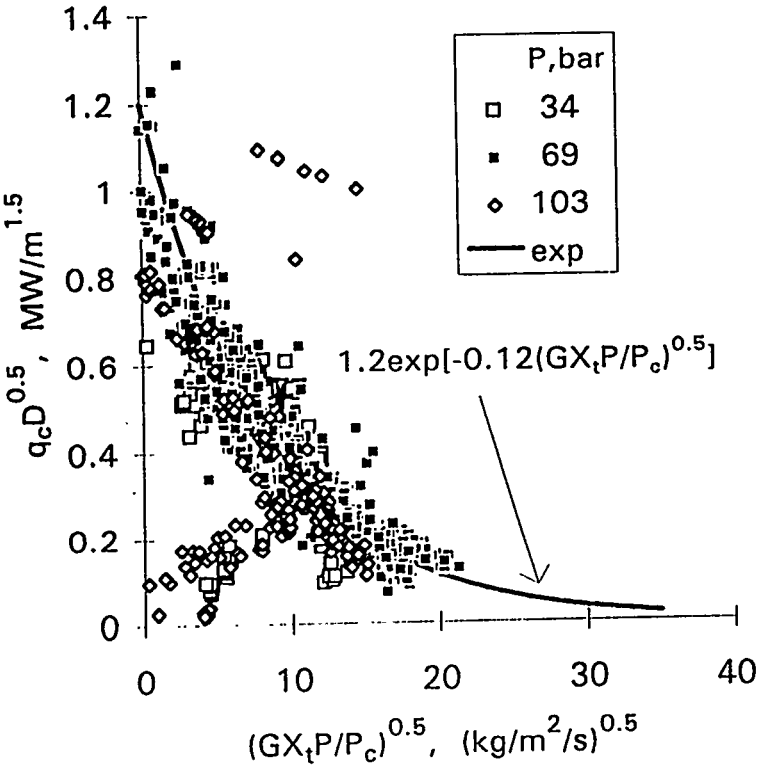

Figure 3. Data from Thompson-Macbeth compilation.

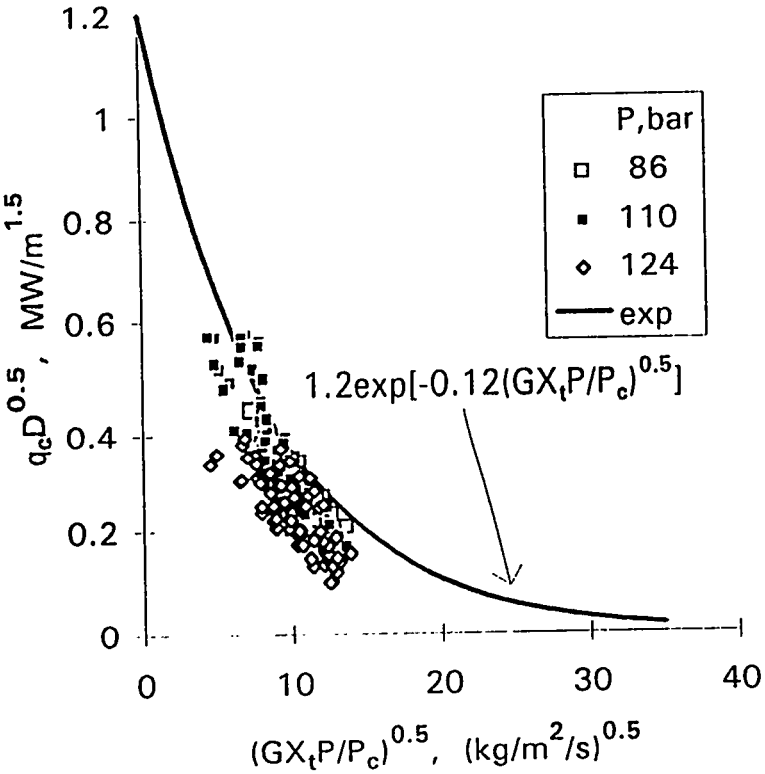

Figure 4. Data from Lee-Obertelli.

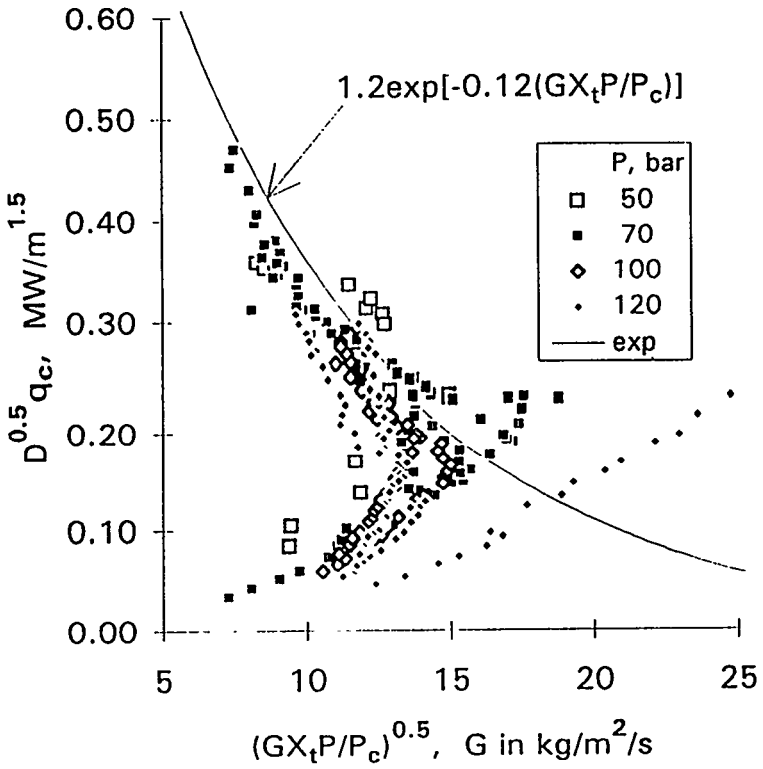

Figure 5. Swedish CHF data (KTH) for 2 m length, 10 mm ID .

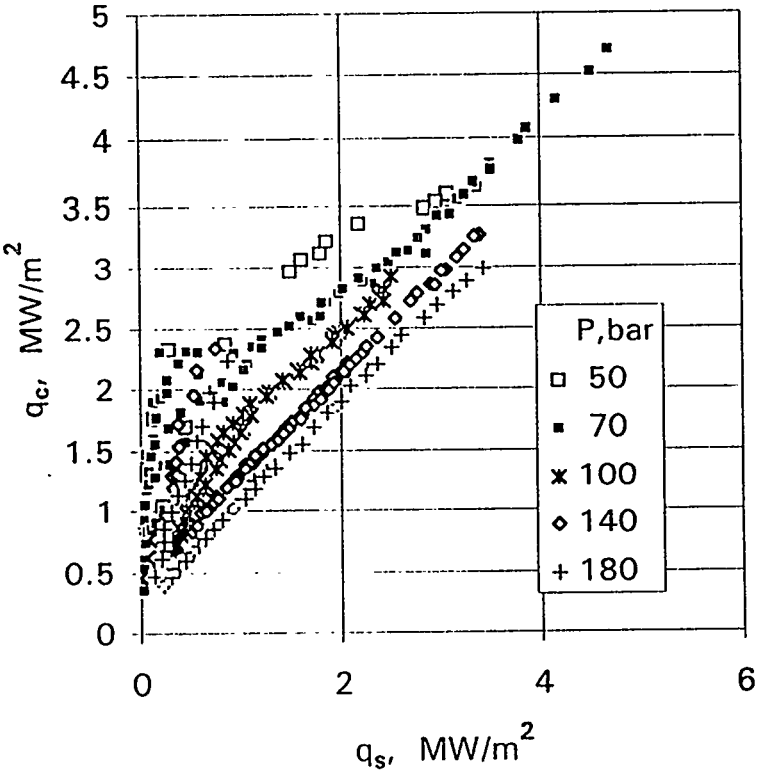

Figure 6. Swedish CHF data (KTH) for 2 m length, 10 mm ID

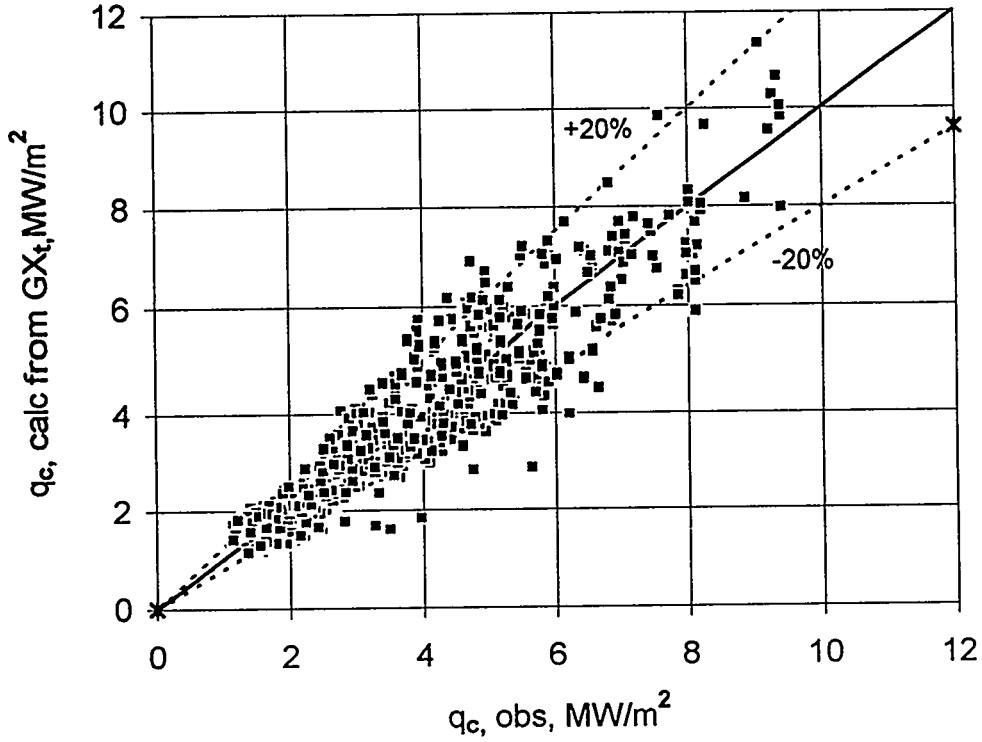

Figure 7. Calculated values of CHF vs. observed values for data from Thompson-Macbeth compilation Table 6 at 69 bar.

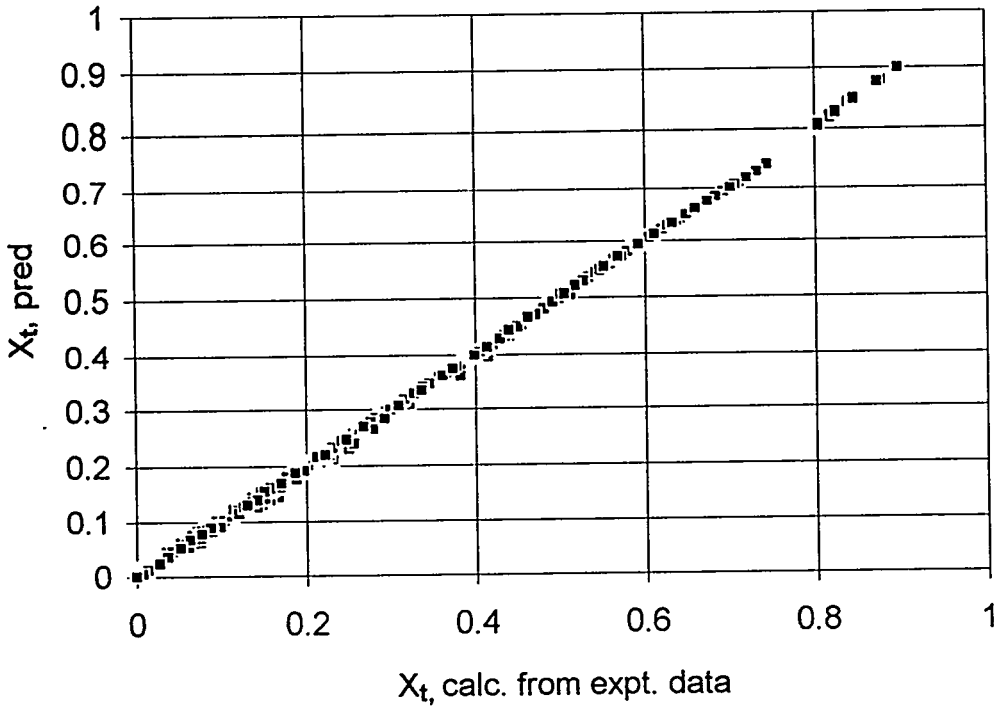

Figure 8. Data from Thompson-Macbeth compilation Table 6 at 69 bar

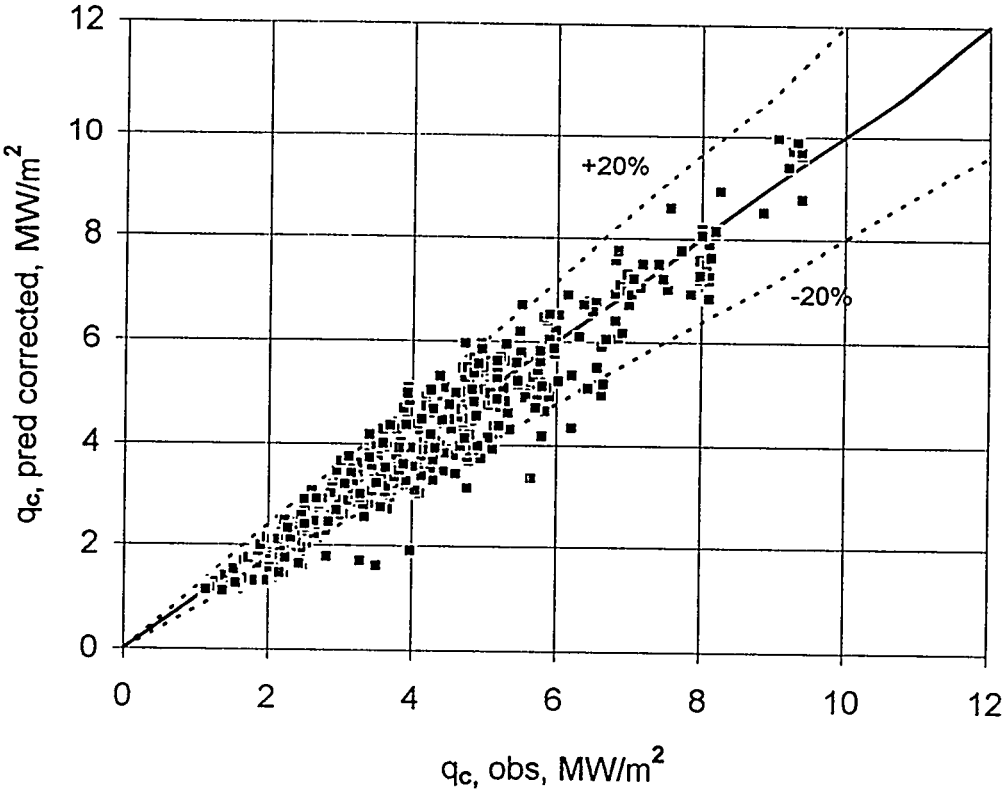

Figure 9. Comparison of predicted (corrected) values of CHF vs. observed values for data from Thompson-Macbeth compilation Table 6 at 69 bar.

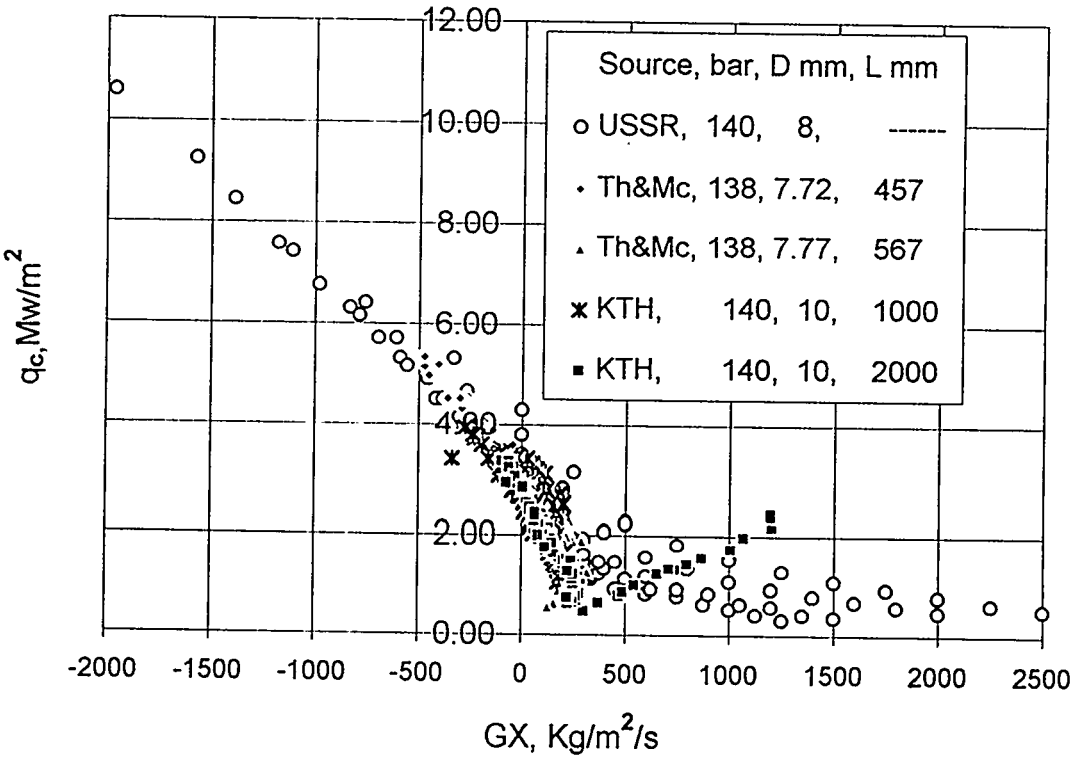

Figure 10. Some high pressure CHF data vs. GX.

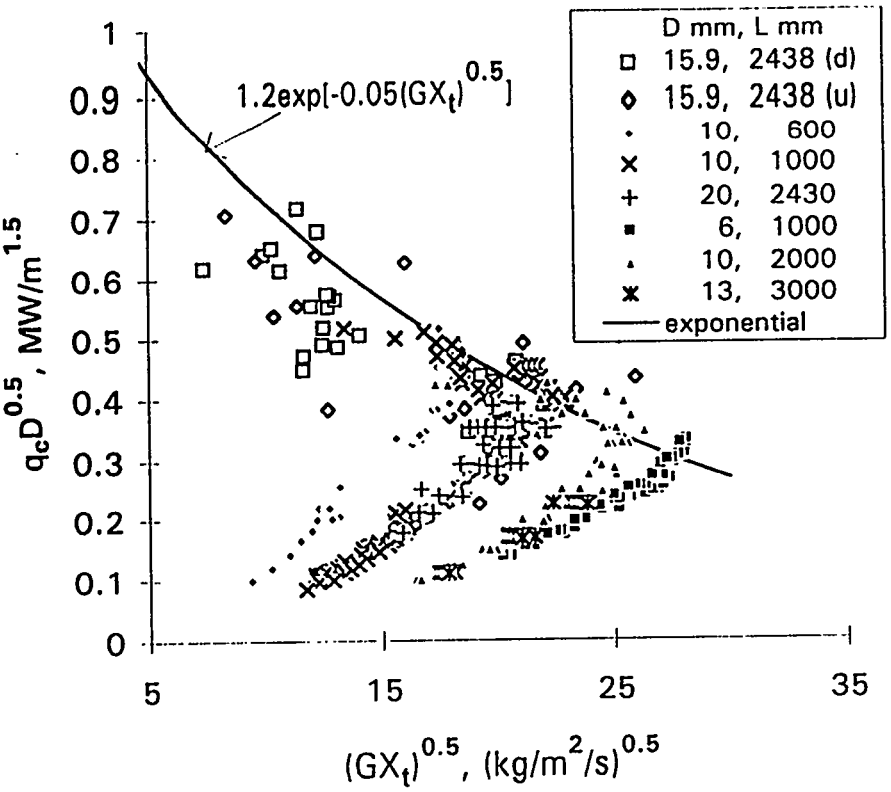

Figure 11. HTRF and Swedish (AE177) low pressure CHF data.

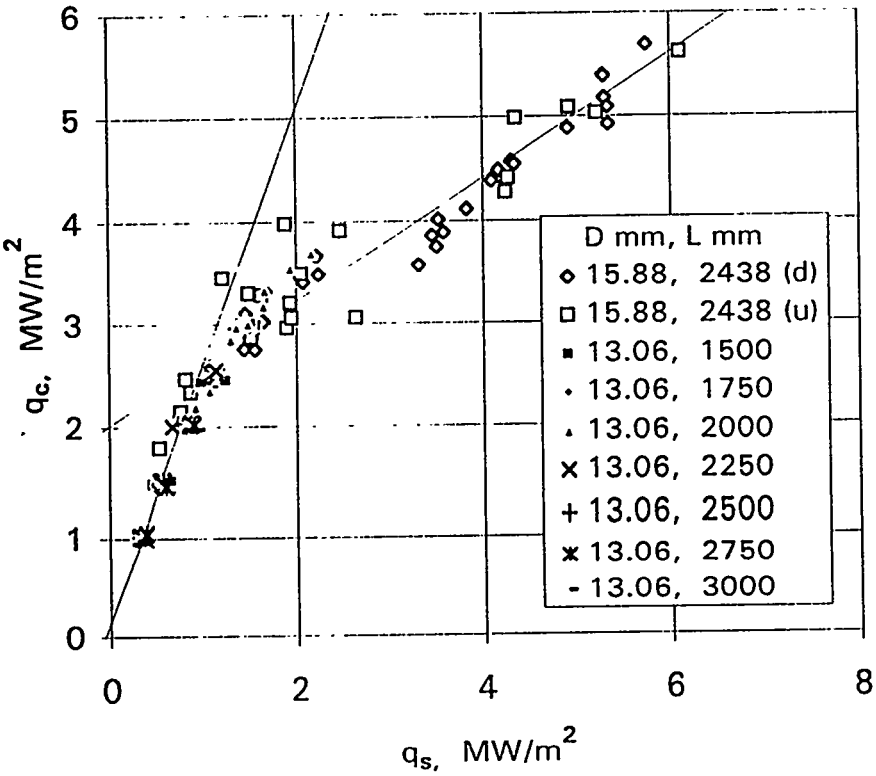

Figure 12. Low pressure Swedish (Table 1, AE177) and HTRF upflow (u) and down flow (d) CHF data vs. qs.

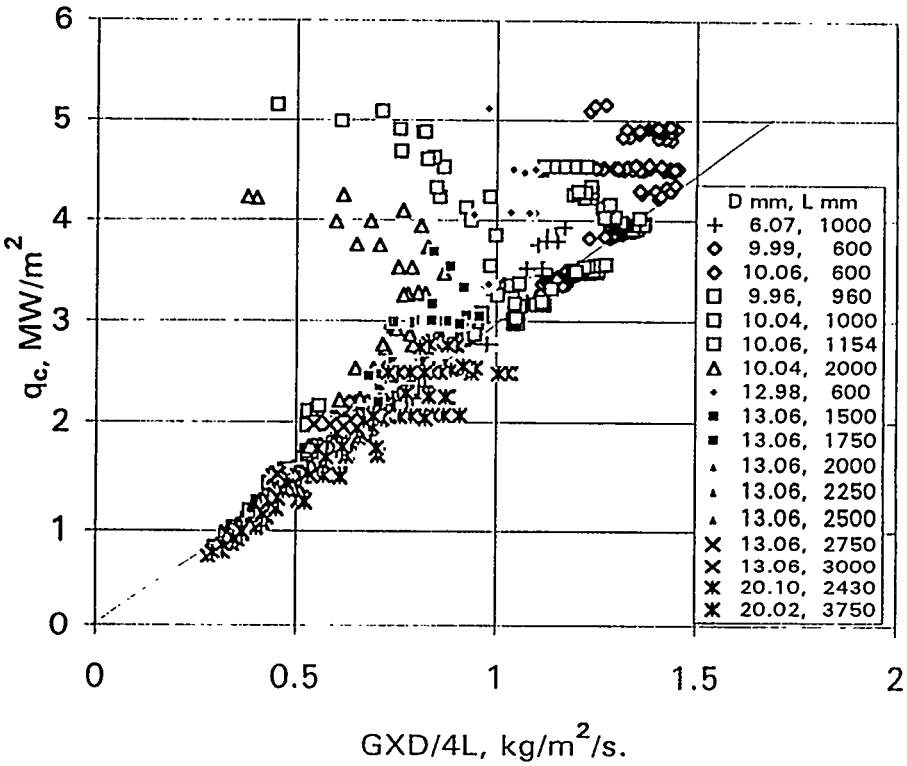

Figure 13. Low Pressure Swedish CHF data from Table 1 of AE177 plotted vs. GXD/4L.

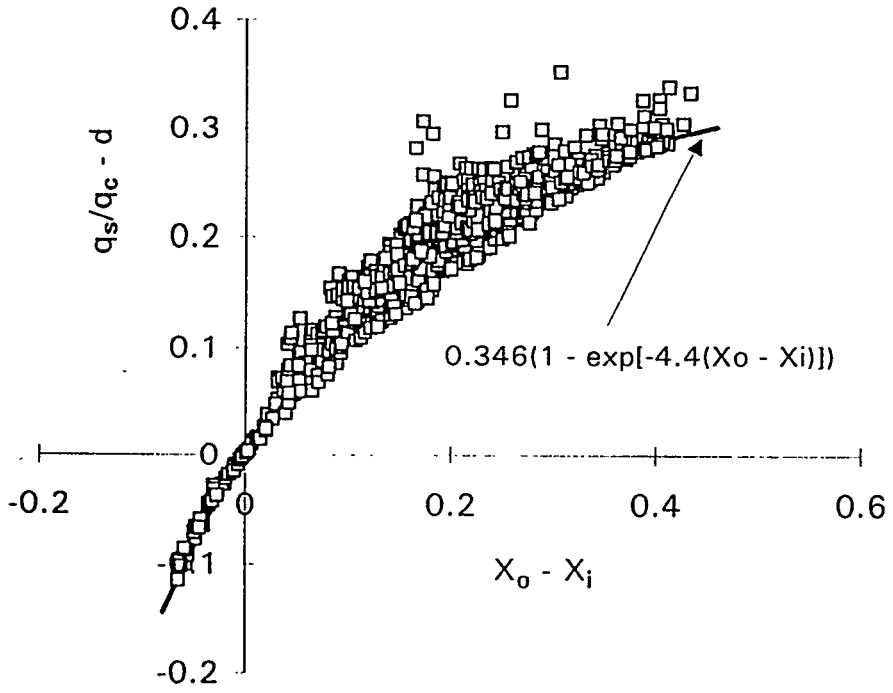

Figure 14. CHF Correlation for low pressure, low CHF region.

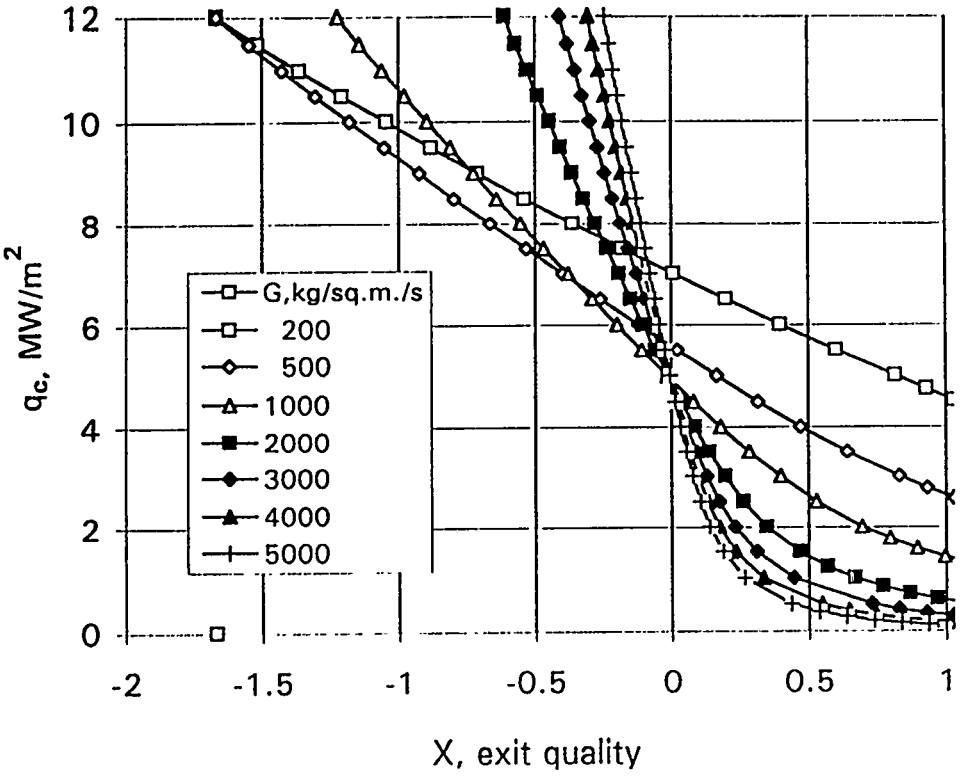

Figure 15. CHF as a function of G and X calculated from local correlation experimental fit for a 10 mm ID tube at 69 bar.

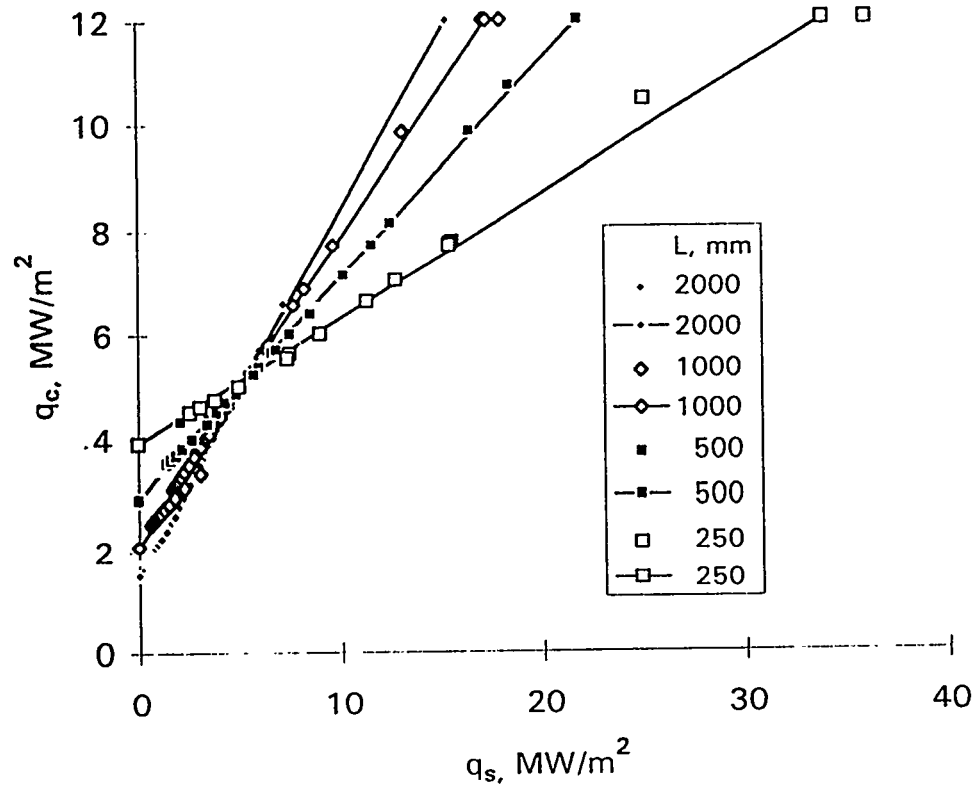

Figure 16. CHF calculated from exponential fit vs. qs.
Values with very high subcooling (Xi < -1.0) excluded.
for 10 mm ID tube at 69 bar

A Model of Film Boiling in the Presence of Electric Fields

P. M. Carrica, V. Masson and A. Clausse
Centro Atómico Bariloche and Instituto Balseiro
8400 – Bariloche – Argentina

P. Di Marco and W. Grassi
Dipartimento di Energetica, Università di Pisa
via Diotisalvi 2, 56126 Pisa – Italy

Abstract

Recently it was found that, when a strong electric field is applied around a heated wire, two distinct film boiling heat transfer regimes are observed. In this paper, a semi-empirical model is derived to analyze the pool boiling process in the presence of non uniform electric field. The model takes into account the dielectrophoretic force acting on the bubbles as they grow and the effect of the electric field on the most dangerous wavelength. It is shown how the transition between the two film boiling regimes is possible for high strength electric fields. The threshold voltage for transition, transition heat fluxes and hysteresis values are compared with experimental outcomes showing a satisfactory agreement.

1. Introduction

The phenomenon of the boiling transition, leading to a substantial degradation of the heat transfer performance, is of paramount importance for process boiling heat transfer as well as for nuclear safety. Models to predict it in various conditions have been developed starting from 1950. However, despite the big amount of work on this topic, the fundamental mechanisms leading to the transition are still subject of discussion within the scientific community, and the entire phenomenon is not yet well understood. Therefore, the authors deem that any new fact extending the knowledge on this subject must be very conscientiously considered, since any advancement in the modelling and the understanding of the boiling transitions is also a considerable progress in nuclear safety.

The present work moves from the study of pool boiling in the presence of an electric field. It has been widely reported that boiling heat transfer can be strongly improved by imposing an external electric field [1]. The main observed effects are substantial increase of peak heat flux, enhancement of film boiling heat transfer and reduction of bubble departure size [2,3]. Several promising techniques, based on EHD effect, are currently under development for active heat transfer enhancement [4], although their application to nuclear technology is by no means problematic.

Recent experiments have revealed that, when a strong electric field is applied around a heated wire, two distinct film boiling heat transfer regimes are observed [5]. These film boiling regimes are separated by a sudden transition, similar to the first boiling crisis, i.e. the one leading to the departure from nucleate boiling. This outcome will be considered in the paper, since it may lead to reconsider the entire phenomenon of the boiling transitions in a new perspective. After a description of the experimental results, a simple model is developed to attempt to explain the phenomenon.

2. Overview of the Experimental Results

2.1. Experimental Apparatus

The experimental setup (see Fig.1) consisted of a test section placed inside a horizontal cylindrical vessel of stainless steel, 175 mm internal diameter, with appropriate windows for visualization and instrumentation for control and measurement of pressure and temperature. The working fluid was R–113 ($C_2Cl_3F_3$) at atmospheric pressure. Saturation temperature was achieved using a 300 W electric preheater, and a copper finned condenser, cooled by tap water, condensed the vapor back to the pool. The pressure was controlled by means of a reflux condenser open to the atmosphere.

Steady–state experiments were carried out using horizontal platinum wires of 0.2 and 0.3 mm diameter and 46 mm length. The electric field was generated imposing 0 to 15 kV DC to a 60 mm diameter, 8-wire cylindrical cage surrounding the heater, and grounding the negative electrode to the heater itself. This configuration yielded a cylindrical field in the surrounding (within 10 mm) of the heater, as confirmed by computer analysis [5]. The length of the cage was 240 mm to avoid side-end effects on the heater.

The heat flux was calculated from the power given to the heater and the heater area. The temperature in the heater was derived using the standard method of detection of the resistance of the platinum wire.

2.2. Uncertainty Assessment

Using the standard error propagation procedure, the errors in wire overheating and heat flux measurements can be evaluated, starting from the ones in current, voltage and reference resistance [5]. The resulting maximum random uncertainties in heat flux and overheating are

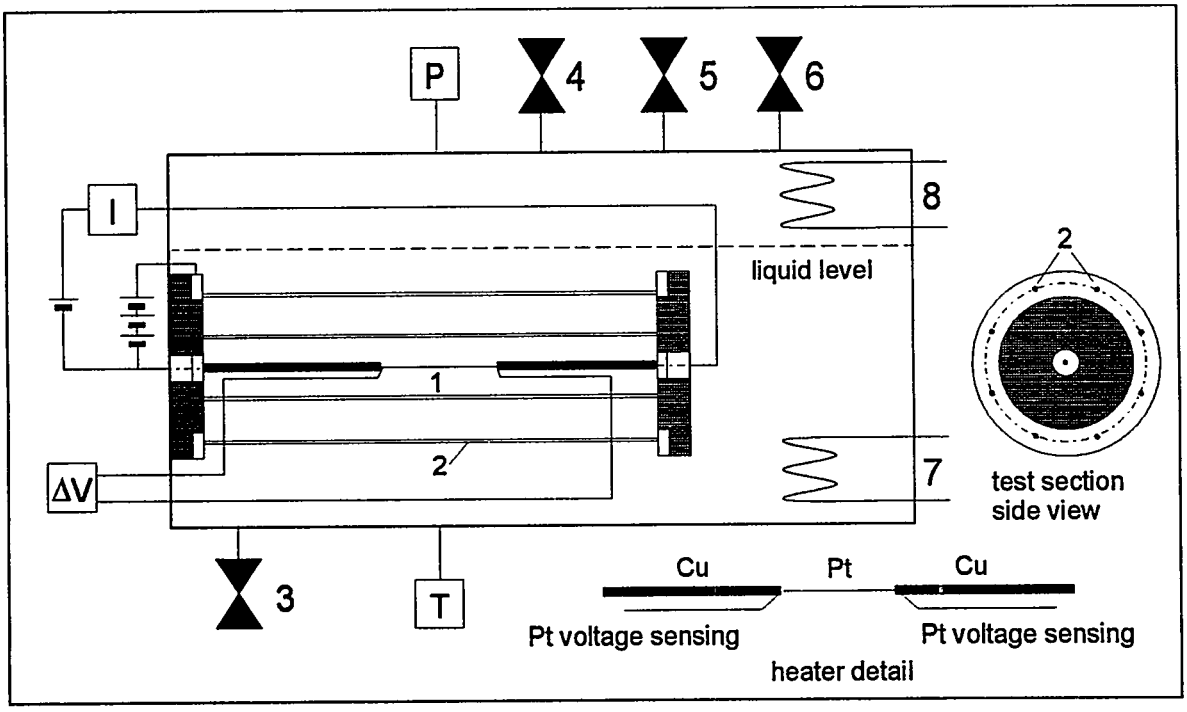

Figure 1: Sketch of the experimental apparatus: 1) heater; 2) high voltage cage wires; 3) drain valve; 4) fill valve; 5) to reflux condenser; 6) to vacuum line; 7) preheater; 8) condenser.

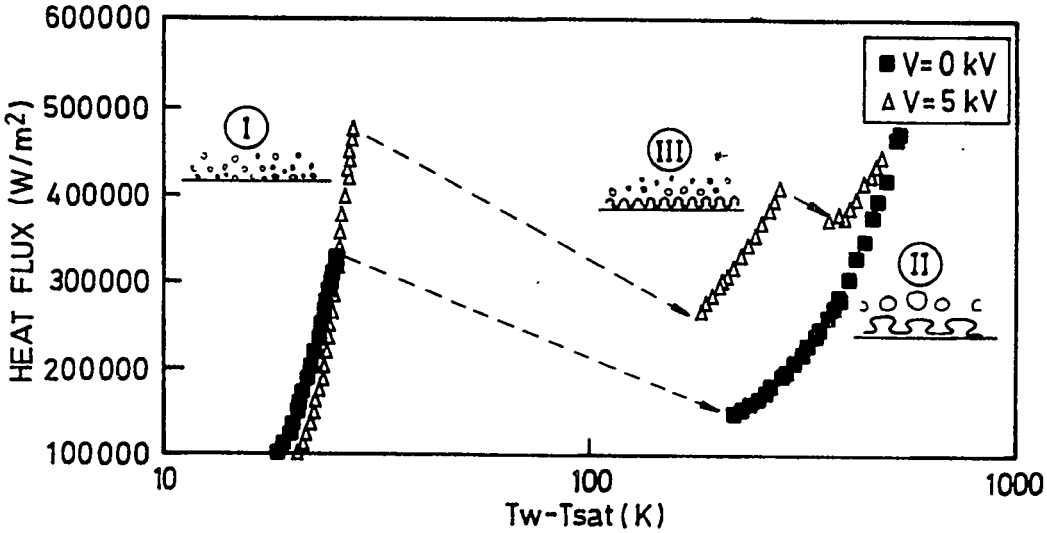

Figure 2: Complete experimental boiling curves for a 0.2 mm diameter wire with and without an imposed electric field (after Carrica *et al.* [5]).

$\delta_{\Delta T} = 2.5$ % and $\delta_{q''} = 0.5$ %.

A fixed error in the heat flux is originated by the uncertainty in the evaluation of the heat transfer area (mainly due to the one in wire diameter), and is less than 4%.

A further fixed error is originated by the heat losses due to conduction through the clamped ends of the wire, which leads to overestimate the heat flux and underestimate the temperature in the central zone of the wire. An evaluation of this error is reported in [5]. In the present experiments, the fixed error in the determination of the temperature due to this effect is estimated to range from 10 % to 20 % for 7.5 kV and from 13 % to 22 % for 0 kV. The error in heat flux is from 0.5 to 0.7 times the one in temperature.

2.3. Experimental Results

In Fig.2 the complete boiling curves for a 0.2 mm diameter horizontal heater wire immersed in saturated R–113 are shown, for 0 and 5 kV applied voltages [5]. In the nucleate boiling regime (I) the heat transfer curves are slightly different [6], although the peak heat flux increases about 60 % for 5 kV. In this region the two–phase flow pattern is the typical bubble plume of nucleate boiling. At the peak heat flux, the system without electric field jumps to the film boiling regime (II), while the 5 kV curve jumps to the film boiling regime (III). In both these regimes, the flow pattern is the characteristic one of film boiling, with bubbles detaching at regular intervals from a vapour blanket surrounding the heater. However, in regime (III) the bubbles detach from the film with a much smaller size than in regime (II). A new transition, from regime (III) to regime (II), can be observed for the 5 kV curve at about 0.4 MW/m^2. At high overheatings the boiling curves relative to 0 kV and 5 kV are almost coincident.

The measurements carried out with a 0.3 mm wire diameter heater showed the same qualitative trend observed in the thinner wire [5]. The weak dependence of the second film boiling regime on the electric field was confirmed.

3. Theoretical Model

In order to explain the existence of the double transition detected in the experiments, a simple model of pool film boiling on wires in the presence of a cylindrical electrostatic field will be derived in the following. For simplicity, the following assumptions are made:

Bubbles detaching from the film are spherical.
Before departure, the bubbles are attached to the film tangentially, as shown in Fig.3a.
The dielectrophoretic force over the bubbles is calculated using the electric field gradient at the center of the bubbles.
Bubbles are assumed to detach when the growth velocity of the radius, dr_b/dt, is equal to the rise velocity of the bubble, u.
Under these assumptions, the model is restricted to determine equations for dr_b/dt and u.

3.1. Electric Field

Consider a heater wire of radius R_i and a cylindrical shell of radius R_e, as shown in Fig.3b. The external shell is subject to a potential V_o and the wire is grounded. If the fluid can be modelled as an insulating medium and the side-end effects are negligible, the electric field in cylindrical geometry is related to the applied voltage V_o as

$$\vec{E} = \frac{V_0}{\ln(R_e/R_i)} \frac{\vec{r}}{r^2} \tag{1}$$

If vapor (with a different electric permittivity from the liquid) surrounds the heater up to a radius b, the electric field on the liquid side of the vapor–liquid interface can be calculated as

$$\vec{E}_b = \frac{V_0 \vec{r}/r}{b\left(\ln(R_e/b) + \frac{\varepsilon_f}{\varepsilon_g}\ln(b/R_i)\right)} \tag{2}$$

and the corresponding potential in b is

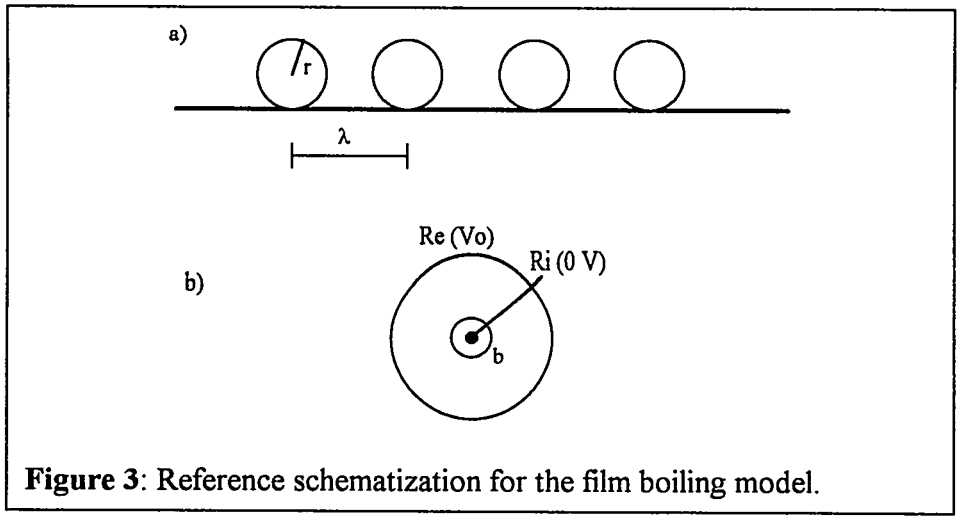

Figure 3: Reference schematization for the film boiling model.

$$V_b = \frac{V_0 \frac{\varepsilon_f}{\varepsilon_g} \ln(b/R_i)}{\ln(R_e/b) + \frac{\varepsilon_f}{\varepsilon_g} \ln(b/R_i)} \tag{3}$$

The electric field at any point between b and R_e can be calculated from

$$\vec{E} = \frac{V_0 - V_b}{\ln(R_e/b)} \frac{\vec{r}}{r^2} \tag{4}$$

3.2. Bubble Velocity

To calculate the bubble velocity it is necessary to calculate the forces over the bubbles. The force balance equation over a spherical bubble can be written as [7]

$$\rho_g \frac{d}{dt}(u v) = (\rho_f - \rho_g) g v + F_e - P\sigma - D - \frac{1}{2}\rho_f \frac{d}{dt}(u v) \tag{5}$$

where the inertial, gravitational, dielectrophoretic, surface tension, drag and virtual mass [8] terms are written from left to right. Assuming that the bubble acceleration and the surface tension terms are much smaller than the others, we can rewrite Eq.(5) as

$$(\rho_f - \rho_g) g v + F_e = \frac{1}{2}\rho_f C_d \pi r^2 u^2 + \left(\frac{1}{2}\rho_f + \rho_g\right) u \frac{dv}{dt} \tag{6}$$

For simplicity, the drag has been modelled as the one for an insulated bubble in an infinite medium. A value of C_d= 8/3 [9] has been assumed.

The dielectrophoretic force is assumed to be the relevant electrostatic force acting on the bubbles. This is true when the working liquid is highly insulating [10]. The dielectrophoretic force can be calculated for a dielectric sphere in an electric field [11]

$$\vec{F}_e = 2\pi r_b^3 \frac{\varepsilon_g - \varepsilon_f}{\varepsilon_g + 2\varepsilon_f} \varepsilon_0 \varepsilon_f \vec{\nabla}(E^2) \tag{7}$$

and tends to push the bubbles, of lower dielectric permittivity, towards the zone of weaker electric fields. Since bubbles detach mainly from the upper part of the wire, it can be assumed that dielectrophoretic force has the same direction as gravity force (which is not true in the lower part of the heater wire), and both forces can be lumped defining the effective gravity as

$$g_{eff} = g + \frac{1.5}{\rho_f - \rho_g} \frac{\varepsilon_g - \varepsilon_f}{\varepsilon_g + 2\varepsilon_f} \varepsilon_0 \varepsilon_f \left|\vec{\nabla}(E^2)\right| \tag{8}$$

The effective gravity is calculated at the center of the bubble, yielding:

$$g_{eff} = g + \frac{3}{\rho_f - \rho_g} \frac{\varepsilon_g - \varepsilon_f}{\varepsilon_g + 2\varepsilon_f} \varepsilon_0 \varepsilon_f \frac{(V_0 - V_b)^2}{\ln^2(R_e/b)\,(R_i + r_b)^3} \tag{9}$$

Combining Eqs. (9) and (6), and neglecting the gas density with respect to the liquid density, the bubble velocity can be calculated

$$u = -\frac{2}{C_d}\frac{dr_b}{dt} + 2\sqrt{\frac{2g_{eff}r_b}{3C_d} + \frac{1}{C_d^2}\left(\frac{dr_b}{dt}\right)^2} \tag{10}$$

3.3. Bubble Growth Rate

In film boiling, each bubble is assumed to be fed by the vapor generated at a length , the fastest growing wavelength, which is a function of the electric field. On the other hand, the electric field is affected by the bubbles near the heater. The fact that electric field is not uniform causes a variation of the wavelength as the bubble grows. The value of the electric field which determines the most dangerous wavelength is assumed to correspond to a certain radius between the film thickness and the bubble top. For the purpose of this analysis, the electric field will be evaluated at $b = R_i + k r_b$, k being some constant less than one.

To the sake of simplicity, the results related to a plane interface separating two layers of infinite thickness [1], [12], will be adopted in the following. Besides, it will be assumed that there is a uniform shell of vapor surrounding the heater from R_i to b.

The most dangerous wavelength in film boiling without electric field can be calculated from [13]

$$\lambda_d = 2\pi\sqrt{\frac{3\sigma}{(\rho_f - \rho_g)g}} \tag{11}$$

In presence of an electric field the most dangerous wavelength is modified to take into account the additional instability mechanism caused by the electric forces [2]

$$\lambda = \lambda_d \frac{\sqrt{3}}{E_l^* + \sqrt{E_l^{*2} + 3}} \tag{12}$$

The electric influence number E_l^* is given by[12]

$$E_l^* = \frac{\varepsilon_{eq} E^2}{\sqrt{(\rho_l - \rho_g)\sigma g}} \tag{13}$$

In Eq. (13) ε_{eq} is the equivalent electric permittivity for DC fields, and can be written as [12]

$$\varepsilon_{eq} = \frac{\varepsilon_0 \varepsilon_f (\varepsilon_f - \varepsilon_g)^2}{\varepsilon_g (\varepsilon_f + \varepsilon_g)} \tag{14}$$

The bubble growth velocity can be calculated from

$$\frac{dv}{dt} = \Gamma' \lambda \tag{15}$$

where Γ' is the linear volumetric generation rate of vapor, given by

$$\Gamma' = \frac{q'' 2\pi R_i}{\rho_g h_{fg}} \tag{16}$$

The variation of λ (due to the variations in the electric field induced by the growing bubble) can be modelled as

$$\lambda = \lambda_0 + \Delta\lambda = \lambda_0 + \frac{v}{\Gamma' \lambda_0} \frac{d\lambda}{dt} \tag{17}$$

where λ_0 is the oscillation wavelength evaluated adopting the value of E in the single-phase fluid (Eq.1). Hence

$$\frac{dv}{dt} = \Gamma' \lambda_0 + \frac{v}{\lambda_0} \frac{d\lambda}{dt} \tag{18}$$

Relating bubble volume with bubble radius, Eq.(18) yields

$$2 r_b^2 \frac{dr_b}{dt} = \frac{\Gamma' \lambda_0}{2\pi} + \frac{2 r_b^3}{3\lambda_0} \frac{d\lambda}{dr_b} \frac{dr_b}{dt} \tag{19}$$

The variation of the wavelength with the bubble radius is calculated from

$$\frac{d\lambda}{dr_b} = \frac{d\lambda}{dE_l^*} \frac{dE_l^*}{dE} \frac{dE}{dr_b} \tag{20}$$

where

$$\frac{d\lambda}{dE_l^*} = -\frac{\lambda}{\sqrt{E_l^{*2} + 3}} \tag{21}$$

$$\frac{dE_l^*}{dE} = \frac{2E_l^*}{E} \tag{22}$$

$$\frac{dE}{dr_b} = -\frac{kE}{b}\left[1 + \frac{\varepsilon_f - \varepsilon_g}{\varepsilon_g \ln(R_e/b) + \varepsilon_f \ln(b/R_i)}\right] \tag{23}$$

Combining Eqs.(19) to (23) yields:

$$\frac{dr_b}{dt} = \frac{\Gamma' \lambda_0}{4\pi r_b^2}\left(1 - \frac{2k}{3\sqrt{E_l^{*2} + 3}} \frac{E_l^* r_b}{b}\left[1 + \frac{\varepsilon_f - \varepsilon_g}{\varepsilon_g \ln(R_e/b) + \varepsilon_f \ln(b/R_i)}\right]\right)^{-1} \tag{24}$$

4. Model Results

The values of R_i and R_e are 0.1 and 30 mm, respectively. The coefficient k In Eq.(24) was adjusted to fit the experimental value of the transition between the small bubbles regime (III) to the large bubbles one (II) in film boiling for 7.5 kV. The resulting value is k = 0.24, which means to consider the value of the electric field (see the beginning of section 3.3) in a reasonable position very close to the heater

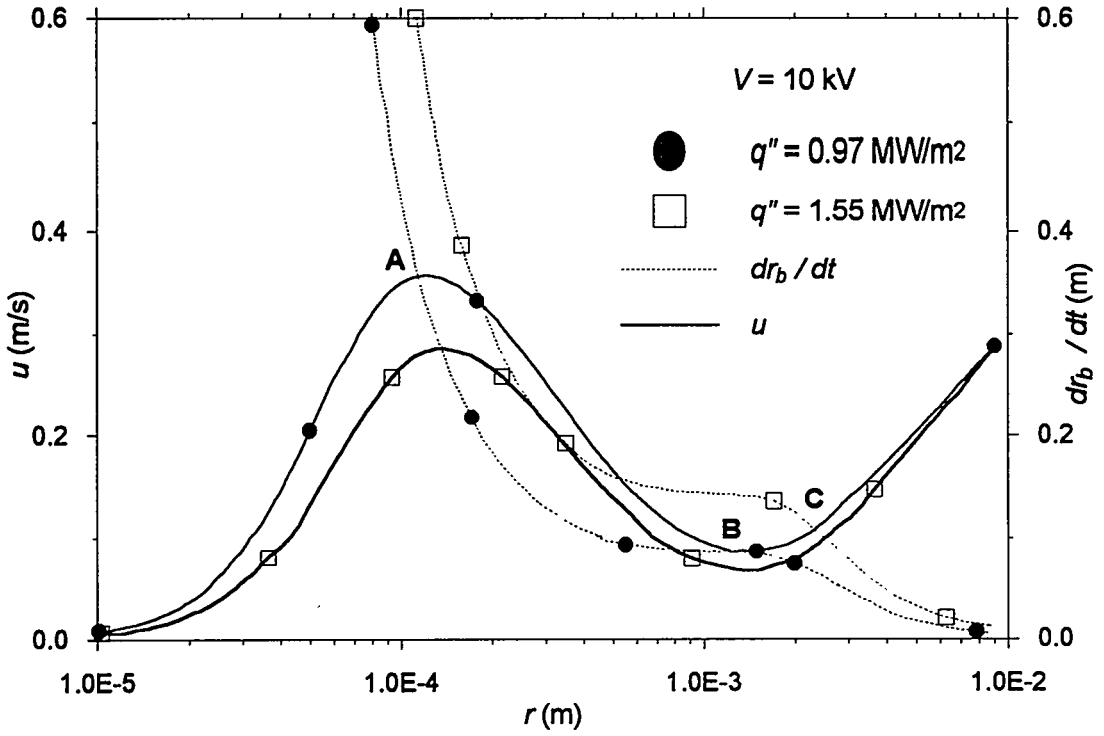

Figure 4: Transition curves (u from Eq.10 and dr_b/dt from Eq.24) for an applied voltage of 10 kV. Points A and C correspond to the stable solution for q''=0.97 MW/m^2 and q''=1.55 MW/m^2, respectively

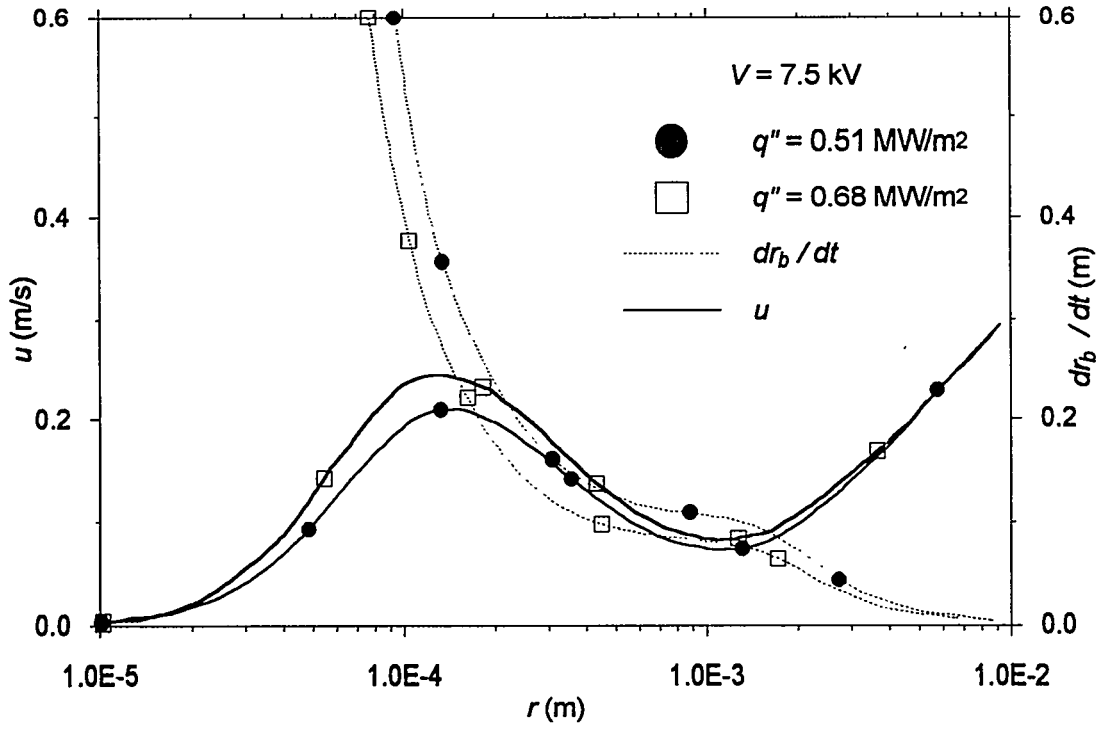

Figure 5: Transition curves (u from Eq.10 and dr_b/dt from Eq.24) for an applied voltage of 7.5 kV.

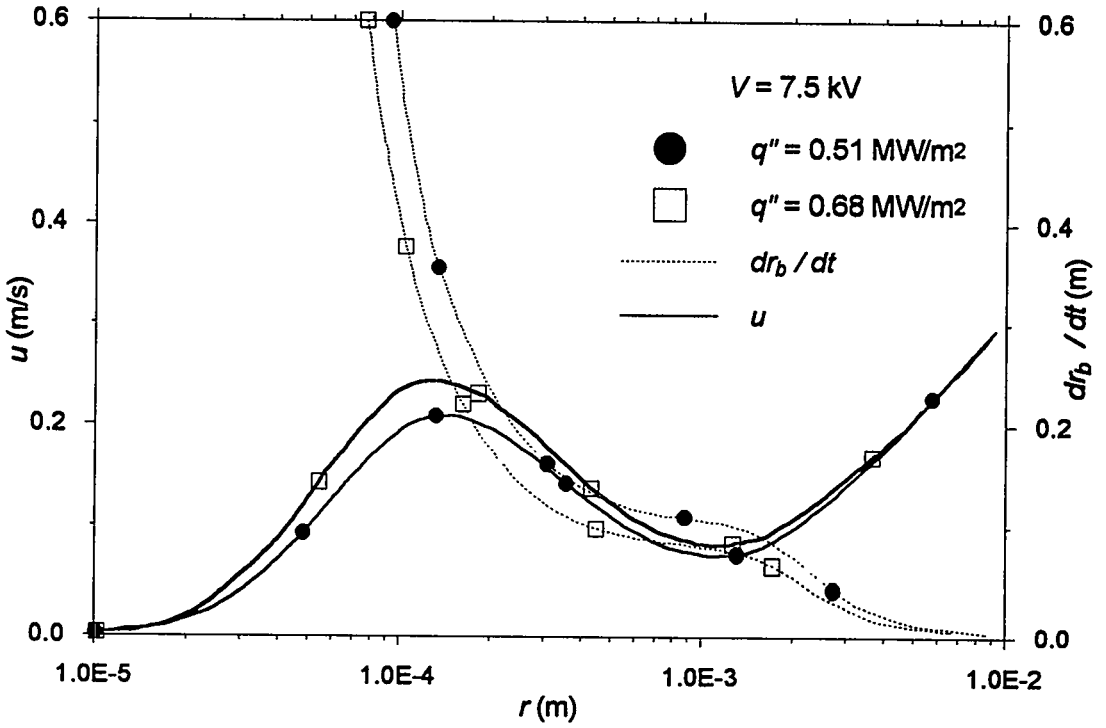

Figure 6: Transition curves (u from Eq.10 and dr_b/dt from Eq.24) for an applied voltage of 0 kV.

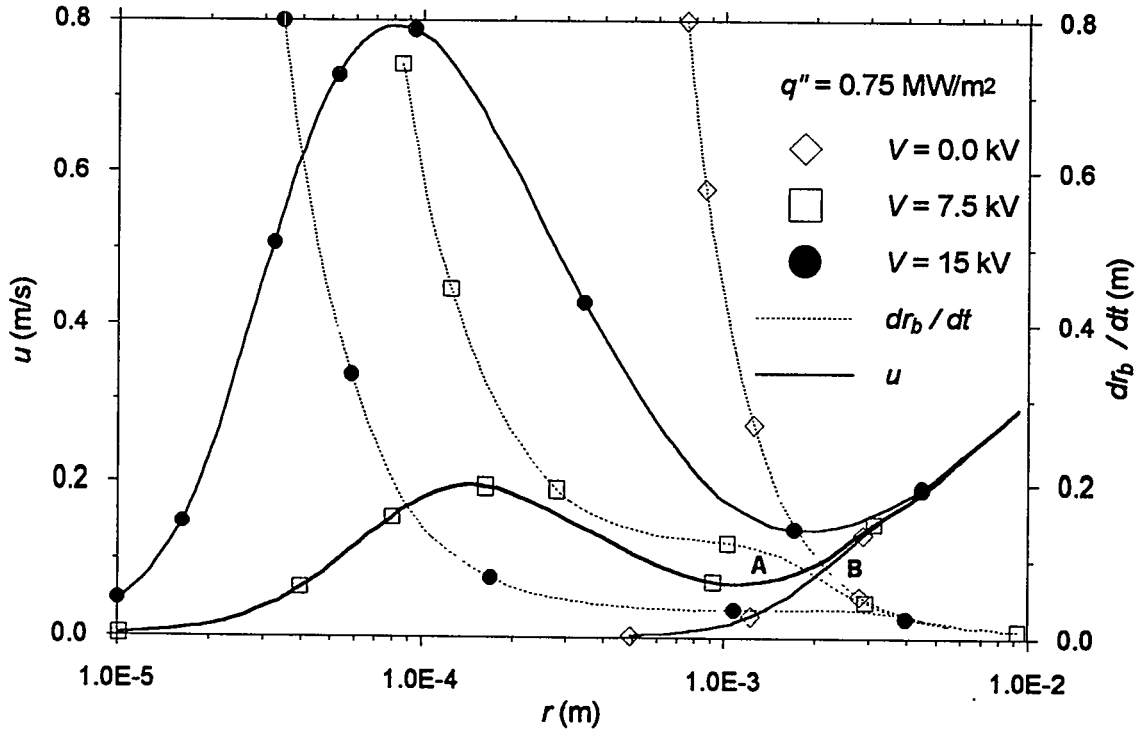

Figure 7: Transition curves (u from Eq.10 and dr_b/dt from Eq.24) at q''=0.75 MW/m^2 for different applied voltages. Points A and B correspond to the stable solution in film boiling regime II, for V=0 kV and V=7.5 kV, respectively.

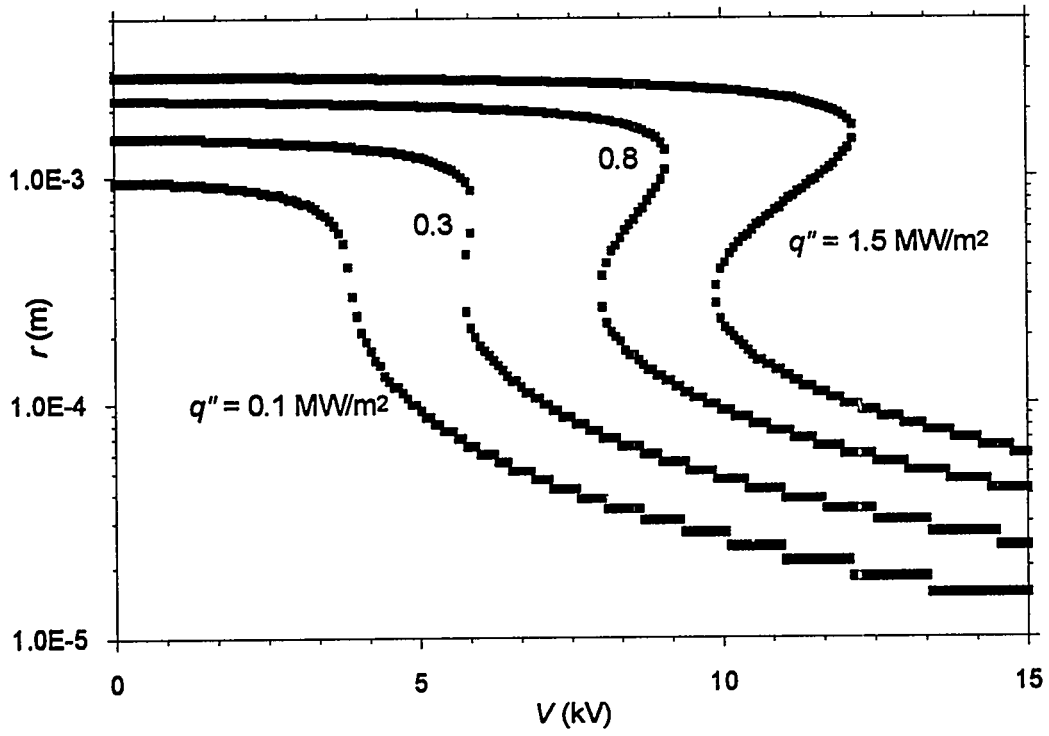

Figure 8: Detachment size of bubbles as a function of applied voltage for different heat fluxes.

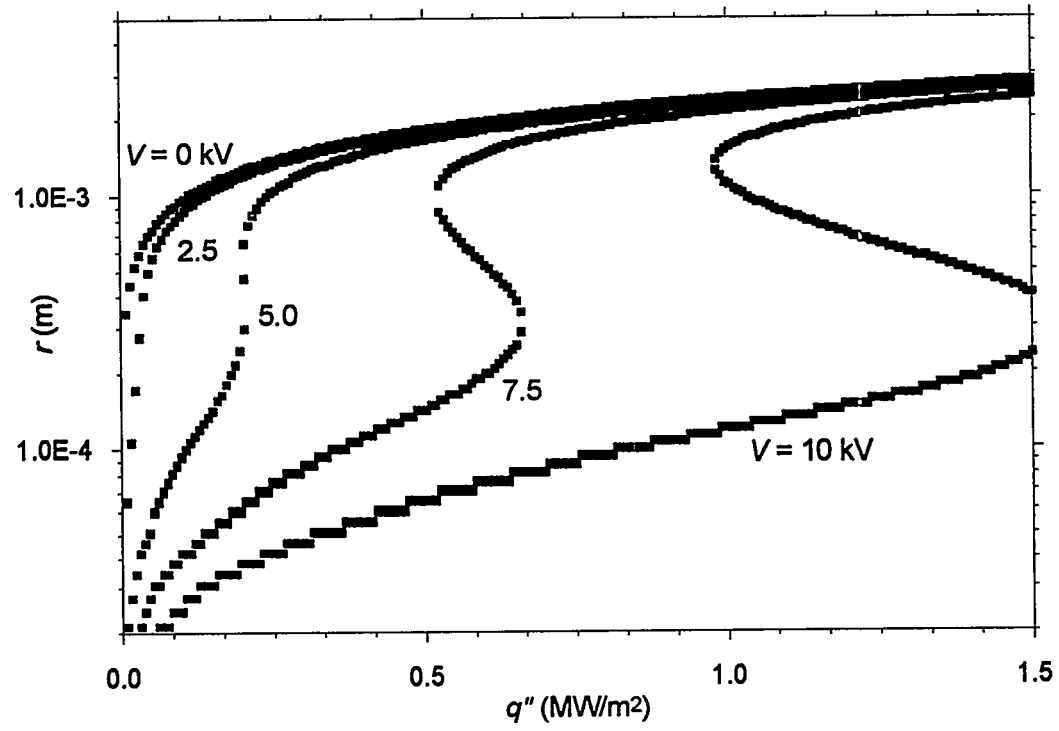

Figure 9: Detachment size of bubbles as a function of heat flux for different applied voltages.

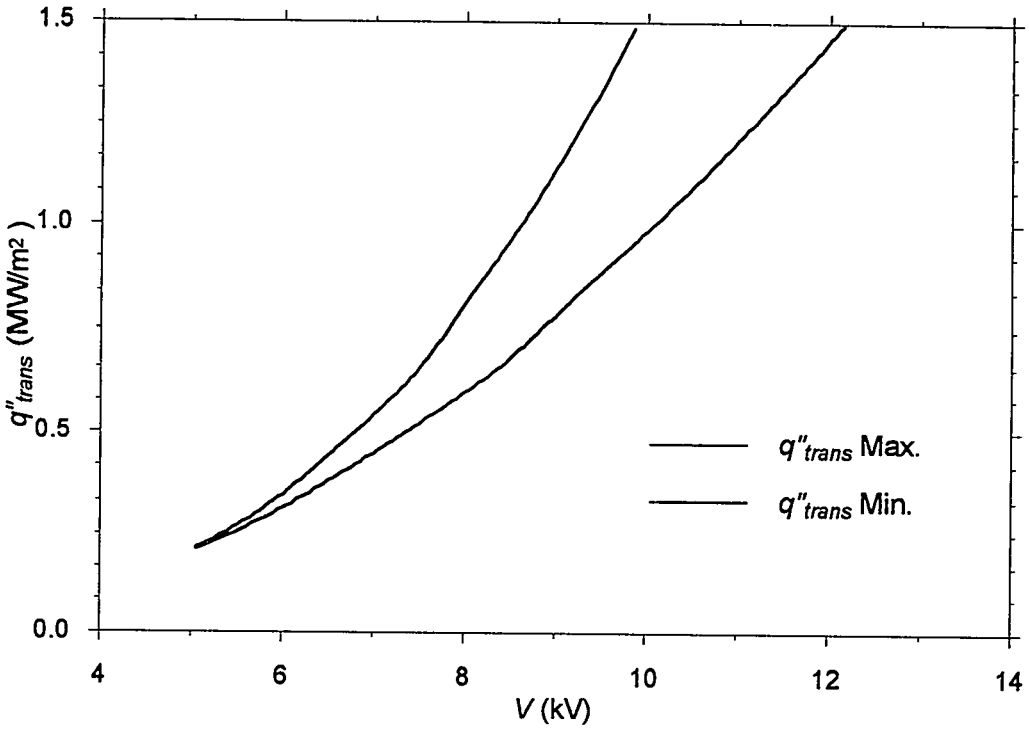

Figure 10: Maximum and minimum transition heat flux as a function of applied voltage. The curves correspond to the values of q'' for transition from small to large bubbles regime and vice-versa, respectively.

Eqs.(10) and (24) are shown in Fig.4 as a function of bubble radius for an applied voltage of 10 kV. As stated in the initial hypotheses (section 3), bubbles are assumed to detach when their growth rate, dr_b/dt (Eq.24) is equal to the rise velocity, u (Eq.10). At 0.97 MW/m^2 two detachment sizes are possible, (points A and B in Fig.4) but the system is stable in the small detachment size (point A), so no transition occurs. When the heat flux reaches 1.55 MW/m^2 the small detachment size solution disappears, and the system experiences a sudden transition to a much bigger detachment size (corresponding to point C). Starting from the regime of large bubbles and decreasing power, a reversal behavior occurs. When the heat flux is reduced to 0.97 MW/m^2 the system experiences a transition and the only detachment size is the small one.

Eqs.(10) and (24) for applied voltages of 7.5 and 0 kV are shown in Figs.5 and 6 respectively. In Fig.6 there is only one stable solution for every value of heat flux, and no transition can occur.

Fig.7 shows the theoretical curves corresponding to Eqs.(10) and (24) for different voltages with the same heat flux. It can be seen that the bubble departure size is almost constant in the large bubbles film boiling regime (points A, B), as observed experimentally. This in turn causes very little variation in the heat transfer coefficient with the applied voltage in this range. On the other hand, in the small bubbles regime the bubble detachment size is strongly dependent on the applied voltage.

The described trends are evidenced in Figs.8 and 9 which show respectively the departure radius as a function of the voltage for different heat fluxes and as a function of the heat flux for different voltages. From Fig.9 it can be seen that, for applied voltages higher than a critical value, the curves present a multivalued region, which is the origin of the regime transition.

It is interesting to recognize the similitude of the curves shown in Figs.8 and 9 with the Van der Waals isotherms of a fluid changing phase. Actually, a correspondence can be established between both processes, where V and q'' play a role similar to that of pressure and temperature in the equation of state. The effect of the electric field on the film boiling process can be viewed from this perspective as a critical phenomenon correspondent to a first order transition. A "pseudo-critical" point can be determined for the value of V for which the curves cease to be multivalued versus q''. Below this value of V, no transition can exist. This "pseudo-critical point" for the described experiment [5] corresponds to

$$q''_{crit} = 0.2 \text{ MW/m}^2$$

$$V_{crit} = 4.9 \text{ kV}$$

$$r_{crit} = 0.4 \text{ mm}$$

In our case, two transition curves can be drawn in the V-q'' plane, indicating the values of q'' for which the transition occurs in jumping from small to large bubble regime (labelled as Min. in Fig.10) and vice versa (labelled as Max.).The curves, as expected, converge at the pseudo-critical point. The transition disappears for applied voltages lower than 4.9 kV, and the heat flux difference between both transitions increases with the applied voltage. This trend has been also verified experimentally [5].

5. Conclusions

A recent experimental campaign revealed that in the presence of strong electric field, a further boiling transition between two different film boiling regimes can be detected. It has the same features as the classical one (from nucleate to film boiling, which is anyway present), i.e. is characterized by a sudden jump from a regime to the other and exhibits hysteresis.

After a description of the main experimental outcomes, a simple semi-empirical model has been derived in the paper to explain the presence of two film boiling regimes. According to it, this feature is essentially produced by the interdependence of the electric force and the film oscillation wavelength. Although the model is very simple and it still needs an empirical constant, to be adjusted on experimental data, it is able to explain the main trends observed experimentally: there is a critical voltage threshold above which two film boiling regimes are observed, the bubble detachment size in the large bubbles regime is almost independent of the applied voltage and the heat flux at the transition between the two film boiling regimes increases with applied voltage.

The fact that, in some instances, a double crisis can be detected in boiling systems may lead to reconsider the entire item in a new perspective. In particular, the possibility that several different mechanisms may lead to a boiling transition appears more sounded.

6. References

[1] P. Di Marco & W. Grassi, "Saturated Pool Boiling Enhancement by Means of an Electric Field", *J. Enhanced Heat Transfer*, *1*, 99–114 (1993)

[2] R. L. Johnson, "Effect of an Electric Field in Boiling Heat Transfer", *AIAA J.*, *6*, 1456–1460 (1968)

[3] T. B. Jones, "Electrohydrodynamically Enhanced Heat Transfer in Liquids–a Review", *Advances in Heat Transfer, 14*, 107–148 (1978)

[4] J. Ogata & A. Yabe, "Basic Study on the Enhancement of Nucleate Boiling Heat Transfer by Applying Electric Fields", *Int. J. Heat Mass Transfer*, Vol.36, pp.775-782 (1993).

[5] P. M. Carrica, P. Di Marco & W. Grassi, "Electric Field Effects on Film Boiling on a Wire", accepted for publication in *Experimental Heat Transfer* (1995)

[6] P. M. Carrica, P. Di Marco & W. Grassi, "Effect of an Electric Field on Nucleate Pool Boiling and Critical Heat Flux: Overview of the Results of an Experimental Study", *Proc. of IV Joint ASME/JSME Thermal Eng. Conference, 2*, Lahaina, Maui, HI, USA, March 19-24, (1995)

[7] P. M. Carrica & A. Clausse, "A Mathematical Model of Local Boiling Nonlinear Dynamics and Crisis", *Latin American Appl. Res., 24*, 77–87 (1994)

[8] D. Drew, L. Cheng & R. T. Lahey, "The Analysis of Virtual Mass Effects on Two–Phase Flows", *Int. J. Multiphase Flow, 5*, 233–242 (1979)

[9] G.B. Wallis, *One Dimensional Two-Phase Flow*, McGraw-Hill, Ch.IX (1969).

[10] J. Berghmans, "Prediction of the Effect of Electric Field on the Most Unstable Wavelength During Film Boiling on Small Wires", *J. of Electrostatics, 5*, 275–272 (1978)

[11] N. F. Baboi, N. K. Bologa & A. A. Klyukanov, "Some Features of Ebullition in an Electric Field", *Appl. Elec. Phenomena (USSR), 20*, 57–70 (1968)

[12] P. Di Marco & W. Grassi, Gas–Liquid Interface Stability in Presence of an Imposed Electric Field", *Proc. of the 12th UIT Nat. Heat Transfer Conf.*, L'Aquila (I) June 23–24 (1994)

[13] H. Lamb, *Hydrodynamics*, Dover, NYC (1945)

7. Nomenclature

b	mean radius at the vapor–liquid interface	[m]
C_d	drag coefficient	[Dimensionless]
E	electric field	[V/m]
E_l^*	electric influence number	[Dimensionless]
F_e	dielectrophoretic force	[N]
g	gravity acceleration	[m/s^2]
h_{fg}	heat of phase change	[J/kg]
q''	heat flux	[W/m^2]
r	radius	[m]
r_b	bubble radius	[m]
R_e	radius of the external electrode	[m]
R_i	radius of the internal electrode (wire radius)	[m]
t	time	[s]
u	bubble velocity	[m/s]

v	bubble volume	[m^3]
V	potential, applied voltage	[V]
Γ'	linear vapor volumetric generation rate	[m^3/m s]
δ	relative uncertainty in measurements	[Dimensionless]
	relative permittivity	[Dimensionless]
ε_0	absolute vacuum permittivity	[F/m]
λ_d	most dangerous wavelength (no field)	[m]
	most dangerous wavelength (with field)	[m]
	density	[kg/m^3]
	surface tension	[N/m]

subscripts

b	at radius *b*
crit	critical
eff	effective
eq	equivalent
f	liquid
g	gas
trans	transition
0	at outer electrode

A SIMPLE DELAY MODEL FOR TWO-PHASE FLOW DYNAMICS

A. Clausse, D.F. Delmastro and L.E. Juanicó
Centro Atómico Bariloche, 8400 Bariloche, Argentina

Abstract

A model based in delay equations for density-wave oscillations is presented. High Froude numbers and moderate ones were considered. The equations were numerically analyzed and compared with more sophisticated models. The influence of the gravity term was studied. Different kinds of behavior were found, particularly sub-critical and super-critical Hopf bifurcations. Moreover the present approach can be used to better understand the complicated dynamics of boiling flows systems.

1. Introduction

The phenomenon of density-wave instabilities in boiling channels has been extensively studied during the last 30 years [1]. These oscillations may be encountered for certain operating conditions of boiling system, in which they become unstable due to lags in the phasing of the pressure-drop feedback mechanisms. Perturbations at the inlet of the channel move with the fluid, yielding transport delays in the local changes of state variables. Given the appropriate set of operating conditions, these delays may lead to self-excitation.

The most common manifestations of density-wave instabilities are self-sustained oscillations of the flow variables. The amplitudes of these oscillations can be very large, and can lead to flow reversals (that is, negative inlet velocities). It may also happen that these oscillations can cause the system to reach the point of excursive instability [2].

Density-wave instabilities in boiling system, besides being scientifically interesting, have serious practical implications for many industries. Boiling water nuclear reactors (BWRs), steam generators, phase-change heat exchangers and various chemical-process equipment, are potential candidates to experience density-wave instability.

The classical tool which has been used to study the problem of density-wave instability in boiling systems is the linear frequency-domain analysis. Rather accurate and reliable models are now available for the stability analysis of complicated systems, such as BWRs [3,4].

The study of the nonlinear behaviour of density-wave instabilities has attracted considerable interest recently. Hopf-bifurcation techniques have been used to study the amplitude and frequency of oscillations [5]. In addition, numerical time-domain analyses were performed [6], where a chaotic attractor was found for periodically forced flows.

On the other hand, not much research work has been focused on the influence of the gravitational term in the stability of two-phase boiling flows[7]. The gravitational effect would be of interest for new reactors designed to work by natural circulation.

In this paper a simple model of density-wave oscillations based in delay equations is presented. The present aprroach consider gravity neglactable system as much as non neglectable ones. Solutions are compared with results from more sophisticated models, showing good agreement. Different kinds of behavior were found, particularly sub-critical and super-critical Hopf bifurcations.

2. Boiling channel model

Let us consider the boiling channel shown in Fig.1. The liquid enters at constant subcooled temperature and is heated up uniformly along the channel. At certain location the fluid reaches its saturation temperature and starts to boil, exiting the channel as a two-phase mixture.

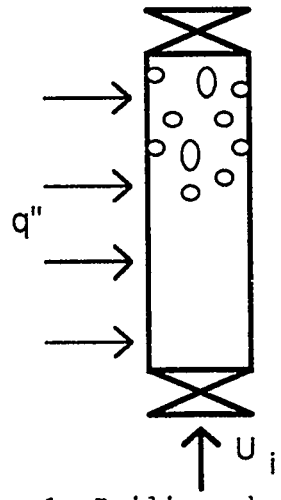

Fig. 1. Boiling channel

The following assumptions have been made in the modeling of the two-phase flow :

- The flow is homogeneous (that is, no phasic slip occurs).
- The system pressure is constant.
- The heat flux is constant in space and time.
- Both phases are incompressible.
- The phases are in thermodynamic equilibrium.
- Viscous dissipation and internal heat generation are neglected in the energy equation.
- Friction losses are concentred at the inlet and the exit of the channel.

In the hypotheses above, the one-dimensional conservation equations of mass and energy can be written as:

$$\frac{\partial \rho}{\partial t} + \frac{\partial (\rho u)}{\partial z} = 0 \tag{1a}$$

$$\frac{\partial (\rho h)}{\partial t} + \frac{\partial (\rho h u)}{\partial z} = q \tag{1b}$$

Moreover, enthalpy and density are related by the following equation of state:

$$\rho = \rho_f \quad \text{for } h \leq h_f \tag{2a}$$

$$\rho = \left[v_f + \frac{(h - h_f)}{h_{fg}} v_{fg} \right]^{-1} \quad \text{for } h > h_f \tag{2b}$$

Combining Eqs.(1b) and (2b) for the two-phase region gives:

$$\frac{\partial u}{\partial z} = q \frac{v_{fg}}{h_{fg}} \equiv \Omega \tag{3a}$$

Similarly in the single phase region, we have:

$$\frac{\partial u}{\partial z} = 0 \tag{3b}$$

Integrating Eqs.(3) along the channel leads to:

$$u_e = u_i + \Omega(L-\lambda) \tag{4}$$

Where the subcooled length, λ(t), is defined by

$$\lambda(t) = \int_{t-\upsilon}^{t} u_i(t')\,dt' \tag{5}$$

Here ν is the time needed by a fluid particle at the inlet of the channel to reach saturation temperature:

$$\nu = \frac{\Delta h_{sub}\ \rho_f}{q} \tag{6}$$

For low frequencies the subcooled lenght can be written as:

$$\lambda(t) = \int_{t-\upsilon}^{t} u_i(t')\,dt' = \nu u(t-t_1) \tag{7}$$

In Eqn.(7), t_1 is a delay time such that $0 < t_1 < \nu$.
Assuming a quasi-static balance of forces in the momentum equation the external pressure head is then balanced by the friction, gravity and acceleration forces, that is

$$(k_i - 1)\rho_f u_i^2 + (k_e + 1)\rho_e u_e^2 + \frac{M_{ch} g}{A_{xs}} = \Delta p \tag{8}$$

Following the quasi-static approximation it can be assumed that the exit flow follows the history of the inlet flow [8] that is:

$$\rho_e(t)u_e(t) = \rho_f u_i(t-t_2) \tag{9}$$

where t_2 is a certain transport delay which will be considered constant. Assuming an enthalpy linear profile along the two-phase region, the exit density, ρ_e, the boiling boundary, λ, and the channel mass, Mch, are related [9] by:

$$M_{ch} = A_{xs}\rho_f\left[\lambda + \frac{(L-\lambda)\ln(\rho_f/\rho_e)}{(\rho_f/\rho_e - 1)}\right] \tag{10}$$

Combining Eqs.(4),(7),(9) and (10) gives:

$$M_{ch} = A_{xs}\rho_f \left[\nu u(t-t_1) + \frac{(L-\nu u(t-t_1))\,u(t-t_2)\;ln\left(\frac{u(t)+\Omega(L-\nu\hat{u}(t-t_1))}{\hat{u}(t-t_2)}\right)}{u(t)+\Omega(L-\nu u(t-t_1))-u(t-t_2)} \right] \qquad (11)$$

Eqs.(8) and (11) may be combined in a delay equation relating the values of the inlet velocity, u_i, at three different times: t, t-t_1 and t-t_2, according to:

$$(k_i-1)\rho_f u_i^2(t) \;+\; (k_e+1)\rho_f u_i(t-t_2)\,[u_i(t) - \Omega\,\nu\,u_i(t-t_1) + \Omega L] \;+$$

$$+ \;A_{xs}\rho_f \left[\nu u(t-t_1) + \frac{(L-\nu u(t-t_1))\,u(t-t_2)\;ln\left(\frac{u(t)+\Omega(L-\nu\hat{u}(t-t_1))}{\hat{u}(t-t_2)}\right)}{u(t)+\Omega(L-\nu u(t-t_1))-u(t-t_2)} \right] \;=\; \Delta p \qquad (12)$$

Putting Eqn.(12) in a nondimensional form, using the following reference values:

$L_{ref} = L_{ch}$,
$u_{ref} = \Omega L_{ref}$,
$\rho_{ref} = \rho_f$,
$M_{ref} = A_{xs} L \rho_f$

we obtain:

$$(k_i-1)\hat{u}_i^2(t) + (k_e+1)\hat{u}_i(t-t_2)\,[\,\hat{u}_i(t) - N_{sub}\;\hat{u}_i(t-t_1) + 1] \;+$$

$$+ \;N_{sub}\,\hat{u}(t-t_1) + \frac{(1-N_{sub}\,\hat{u}(t-t_1))\,\hat{u}(t-t_2)\;ln\left(\frac{\hat{u}(t)+N_{sub}(1-N_{sub}\,\hat{u}(t-t_1))}{\hat{u}(t-t_2)}\right)}{\hat{u}(t)+N_{sub}(1-N_{sub}\,\hat{u}(t-t_1))-\hat{u}(t-t_2)} \;= Eu \qquad (13)$$

where the ^ superscript means dimensionless and the Euler, Froude and subcooling number are defined as:

$$Eu = \frac{\Delta p}{\rho_f\,u_r^2} \qquad Fr = \frac{u_{ref}^2}{gL} \qquad N_{sub} = \nu\Omega = \frac{\Delta h_{sub}\;\nu_{fg}}{h_{fg}\;\nu_f}.$$

3. A Two-Dimensional Mapping of Density-Wave Instabilities

An interesting result can be reached considering $t_1 = t_2$ = .

$$_i + 1 \;\hat{}_n^{\,2} + \;\; _e - 1 \;\hat{}_{n-2} \;\hat{}_n - N_{sub}\;\hat{}_{n-1} + 1$$

$$+\frac{1}{Fr}\left[N_{sub}\,\hat{u}_{n-1} + \frac{(\;-N_{sub}\,\hat{u}_{n-1})\,\hat{u}_{n-2}\;ln\left(\frac{\hat{u}_n + N_{sub}(\;-N_{sub}\,\hat{u}_{n-1})}{\hat{u}_{n-2}}\right)}{\hat{u}_n + N_{sub}(\;-N_{sub}\,\hat{u}_{n-1}) - \hat{u}_{n-2}} \right] \;=\; Eu \qquad (14)$$

where:

$$\hat{u}_n = \hat{u}_i(t),$$
$$\hat{u}_{n-1} = \hat{u}_i(t-\tau),$$
$$\hat{u}_{n-2} = \hat{u}_i(t-2\tau).$$

This is reasonable if the two-phase residence time, *i.e.* the time that a particle needs to travel along the boiling region, is smaller than ν.

3.1 High Froude Numbers.

For high Froude numbers the gravity term can be neglected. For this case, simple solutions can be obtained in the linear stability analysis.

3.1.1 Fixed Points.

The fixed points of the two-dimensional map given by Eqn.(14), can be obtained by making $\hat{u}_n = \hat{u}_{n-1} = \hat{u}_{n-2} = \hat{u}_0$, that is:

$$\hat{u}_0 = \frac{u_0}{\Omega L_{ch}} = \frac{1}{N_{pch}} = \frac{-(k_e+1) \pm \sqrt{(k_e+1)^2 + 4Eu(k_i - 1 + k_e(1-N_{sub}))}}{2(k_i - 1 + (k_e - 1)(1-N_{sub}))} \tag{15}$$

where N_{pch} is well known in the literature as the "phase change number".

This equation gives different kind of solutions depending on the subcooling number.

If

$$N_{sub} < \frac{k_i + k_e}{k_e + 1} \tag{16}$$

there are two real fixed points, one positive and one negative.

If

$$\frac{k_i + k_e}{k_e + 1} < N_{sub} < \frac{k_i + k_e}{k_e + 1} + \frac{k_e + 1}{4Eu} \tag{17}$$

there are two positive real solutions.

If

$$N_{sub} > \frac{k_i + k_e}{k_e + 1} + \frac{k_e + 1}{4Eu} \tag{18}$$

there are not real solutions.

3.1.2 Linear Stability.

Linearizing Eqn.(14) , about a fixed point, $\hat{u}_0$, leads to the following characteristic equation (written in ξ variable) :

$$\left(\frac{2k_i + k_e - 1}{k_e + 1}\right)\xi^2 - N_{sub}\,\xi + (1 + N_{pch} - N_{sub}) = 0 \tag{19}$$

If the eigenvalues (η,ζ) are both inside the unit circle in the complex plane the system is stable. If one of the eigenvalues is real and exceeds 1, the fixed point is a saddle node, repelling along one direction in the plane $(\hat{u}_n , \hat{u}_{n-1})$. When one of the eigenvalues is a real negative less than -1 a flip bifurcation occurs. On the other hand, if the eigenvalues are

complex conjugate they can cross the complex unit cycle at an angle ø (different from 0 or π). This is called a secondary Hopf bifurcation or Niemark instability [10].

Defining the parameter:

$$k = \frac{2k_i + k_e - 1}{k_e + 1} \tag{20}$$

We can express the solutions of Eqn. (19) in terms of k, N_{sub} and N_{pch} as follows :

$$x_{1,2} = \frac{1}{2k}\left[N_{sub} \pm \sqrt{N_{sub}^2 - 4(1+N_{pch}-N_{sub})k}\right] \tag{21}$$

Complex eigenvalues exist if:

$$N_{pch} > \frac{N_{sub}^2}{4k} + N_{sub} - 1 \tag{22}$$

In that case, a Niemark instability occurs if the module of the eigenvalues exceeds 1, which occurs for:

$$N_{pch} > N_{sub} + k - 1 \tag{23}$$

On the other hand, if the eigenvalues are real, a saddle point exist when the largest eigenvalue exceed 1, that is:

$$N_{pch} < 2N_{sub} - k - 1 \tag{24}$$

If the smallest eigenvalue is less than -1 a flip bifurcation occurs. However, N_{sub}, k and $(N_{pch}-N_{sub})$ are always positive in the range of physical values. Therefore, from Eqn.(21) the eigenvalues are always greater than zero, and consequently a flip bifurcation cannot exist.

The stability criteria, given by Eqns.(22),(23) and (24), are illustrated in the two-parametric plane $(N_{sub}, N_{pch}-N_{sub})$ showed in Fig.2. We can see in it, stable regions with real (a) or complex (b) eigenvalues, the Niemark instability region (c) and the saddle excursion region (d).

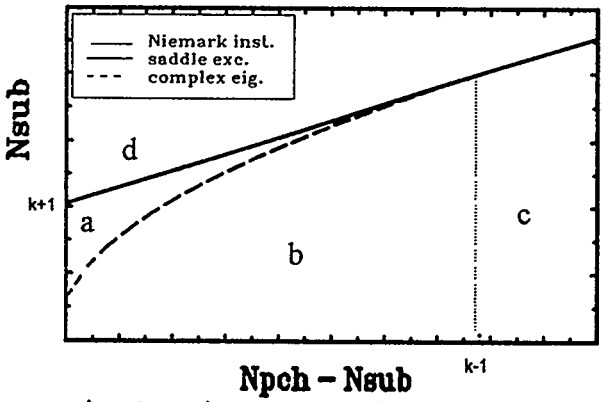

Fig.2: Linear stability map.

3.1.3 The Ledinegg Excursion.

Let us consider the stability of the fixed point with the minus sing, $\hat{u}_0^-$. Replacing Eqn. (17) in Eqn. (15) gives that there exist valid solutions of $\hat{u}_0^-$ in the range:

$$0 < N_{pch} < 2N_{sub} - k - 1 \tag{25}$$

The upper limit of Eqn.(25) is exactly the same as the condition for saddle excursion, Eqn. (24). Therefore the point $\hat{u}_0^-$ is always unstable and causes an excursive instability, usually known as the Ledinegg instability[2].

3.1.4 Density-Wave Instability.

Let us consider the stability of the fixed point of Eqn.(14) with the plus sign, $\hat{u}_0^+$. There are always positive solutions provided that:

$$N_{sub} > \frac{k_i + k_e}{k_e + 1} + \frac{k_e + 1}{4\,Eu} \tag{26}$$

Combining Eqn. (26) with Eqn.(15) and (20) leads to :

$$N_{pch} > 2N_{sub} - k - 1 \tag{27}$$

By comparing Eqn. (24) and Eqn. (27) we can see that the point $\hat{u}_0^+$ can never be a saddle point. The range of stable values of $N_{pch} - N_{sub}$ are limited by the equation :

$$N_{pch} - N_{sub} = k \tag{28}$$

The system goes to a Niemark bifurcation when N_{pch} - N_{sub} exceeds k-1 (remarked as the c region in Fig. 2). This instability has an oscillatory character, reflected in density waves traveling along the channel, which gives the name to the phenomena.

3.1.5 Stability Comparison.

Comparing the lineal stability map for this simple delay model with the complete differential model [11] and Ishii's criterion [12] we found good agreement for a wide range of subcooling numbers. Fig. 3 shows lineal stability maps obtained with each model.

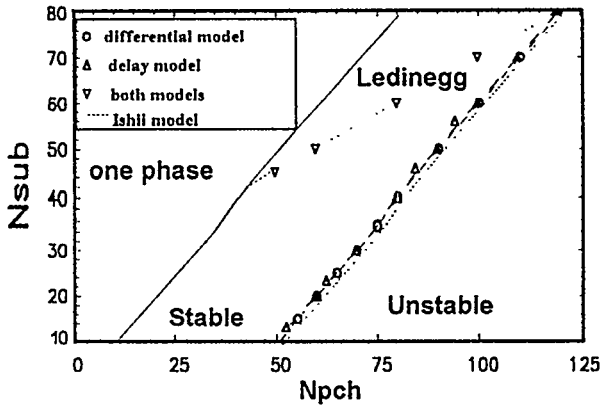

Fig. 3 Stability comparison

For low subcooling numbers, the delay model is too conservative, but it should be noted that in this region t_1 is much less than t_2, which invalidate the model hypothesis.

3.1.6 Non-Linear Behavior.

The iterative Eqn.(14) can be used to study the dynamical system response under unstable conditions. Two different kind of behavior for density-wave instability were found depending on the subcooling number. For high subcooling numbers a supercritical Hopf bifurcation appears. Fig. 4 illustrates a series of limit cycles appearing in the presence of a Niemark instability in the unstable region of the Fig. 3. The "nose" appearing in

the right side of the cycle for large amplitudes is due to the presence of the Ledinegg saddle point[8].

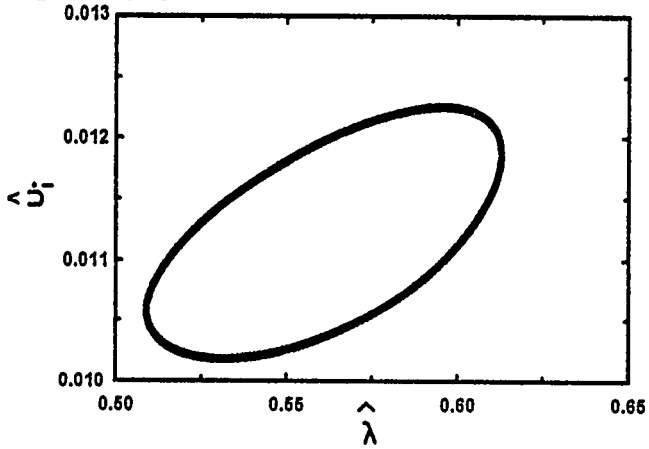

Fig. 4a Limit cycle ($N_{sub} = 50$, $N_{pch} = 89.1$, $K_i = 40$, $K_e = 1$)

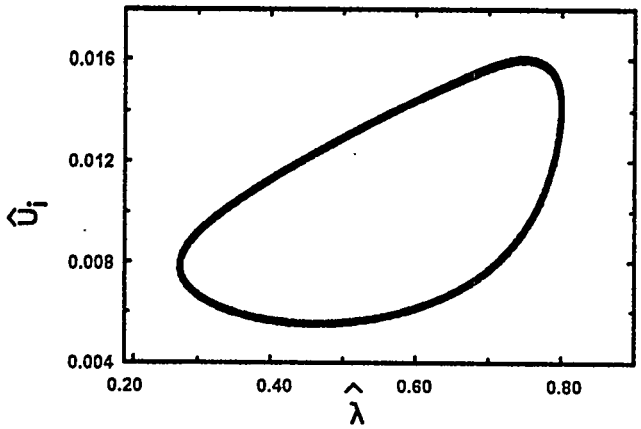

Fig.4b Limit cycle ($N_{sub} = 50$, $N_{pch} = 91.1$, Ki = 40, Ke = 1)

On the other hand, for low subcooling numbers a subcritical Hopf bifurcation appears. Figure 5 shows this kind of behavior. As can be seen for a small perturbation the system is stable but for a big one the oscillations diverge.

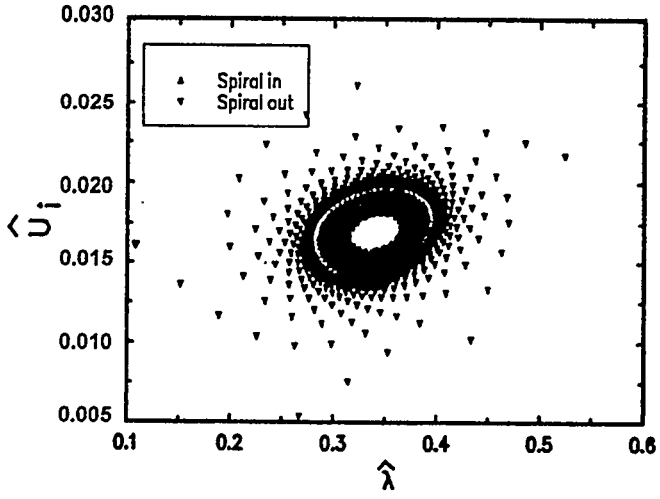

Fig. 5 Sub critical Hopf bifurcation, simple model
($N_{sub} = 20$, $N_{pch} = 58.8$, Ki = 40, Ke = 1)

A more sophisticated model [5] was used to check the present results. Good agreement was found as can be seen in Fig. 6, where the same situation of Fig. 5 was studied.

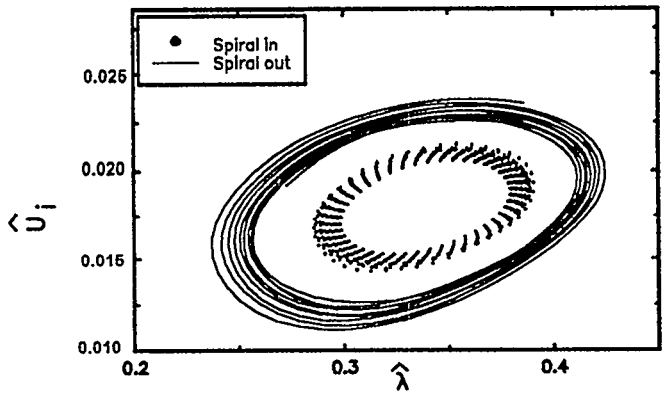

Fig. 6 Subcritical Hopf bifurcation, differential model .

For both kind of bifurcations, the amplitude of the limit cycles was studied. For the subcritical region the locus of the unstable limit cycles is shown in Fig 7. While for a perturbation inside of this conical region the system converges to the fixed point, for another outside that region, the system diverges.

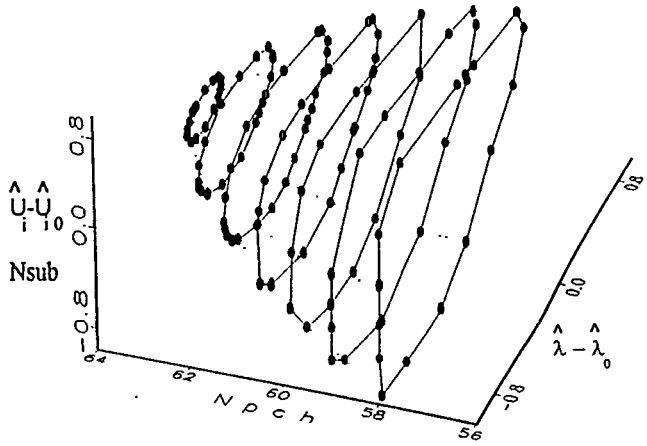

Fig 7: Stability surface of a subcritical bifurcation. ($N_{sub} = 25$, $K_i = 40$, $K_e = 1$).

For the supercritical behavior the locus of stables limit cycles are shown in Fig 8. Either for a perturbation inside or outside of this conical surface, the system evolve to a stable limit cycle.

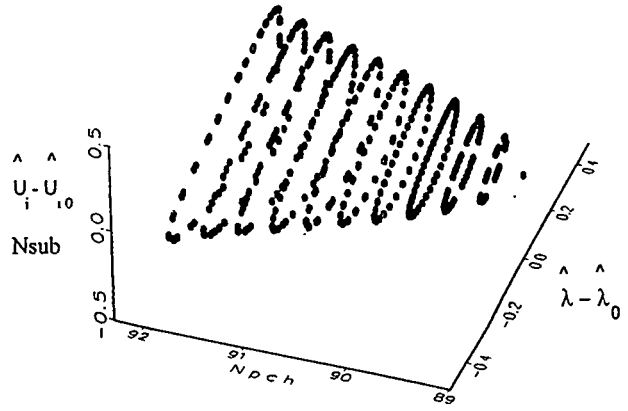

Fig. 8: Stables limit cycles locus. ($N_{sub} = 25$, $K_i = 40$, $K_e = 1$).

3.2 Moderate Froude Numbers.
3.2.1 Linear Stability.

Linearizing Eq.(14) about a fixed point, $\hat{u}_0$, similarly as the previous subsection, but considering now the mass term, an expression for the density-waves linear stability boundary for moderate Froude numbers can be obtained:

$$2K_i + \frac{1}{N_{sub}\, Fr\, \alpha} = K_e (N_{pch} - N_{sub}) + \frac{\ln(\alpha\, N_{pch}) - 1}{N_{sub}\, Fr} Npch + \frac{2\ln(\alpha\, N_{pch})}{N_{sub}\, Fr\, \beta} \qquad (29)$$

where:

$$\alpha = N_{pch}^{-1} + N_{sub}(1 - N_{sub}\, N_{pch}^{-1}) \qquad \text{and} \qquad \beta = \alpha - N_{pch}^{-1}$$

One of the most important gravity property, is it unstabilizing effect over the density-waves limit as much as the mass term increases. Fig. 9 shows these results for different Fr values. Comparing this particular behavior with differential model [11], we founded qualitative agreement for high subcoolings as can be seen in Fig 9. On the other hand, an stabilizing effect over the Ledinegg limit was found.

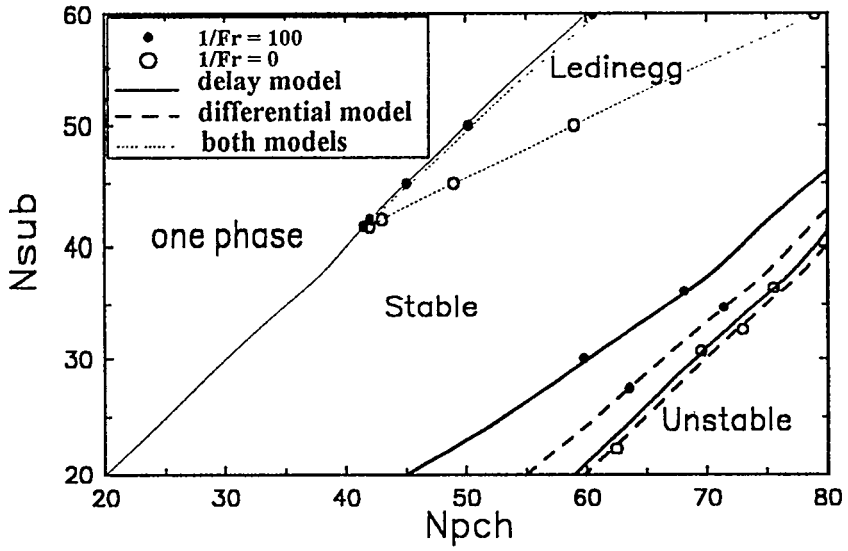

Fig. 9: Map of density-wave boundary for different gravity influence in both model.

3.2.2 Nonlinear Behavior.

Another interesting result due to gravity effect, is the change of the limit cycles shape. This change appears as a clockwise rotation of the limit cycles axes when the gravity term is increased, in good agreement with complex model. Figs. 10 show this behavior.

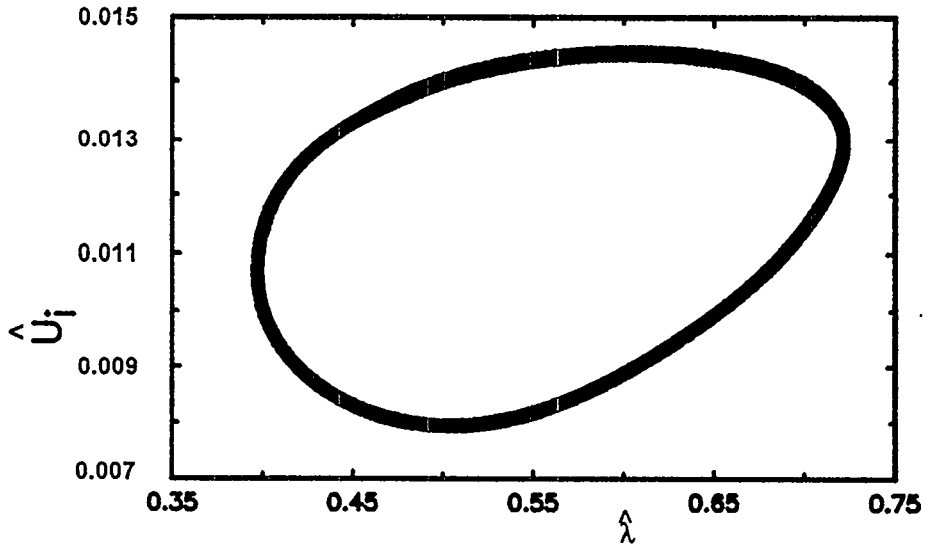

Fig. 10a Limit cycle for simple model (Nsub = 50, Npch = 88, Fr = 0.04 Ki = 40, Ke = 1)

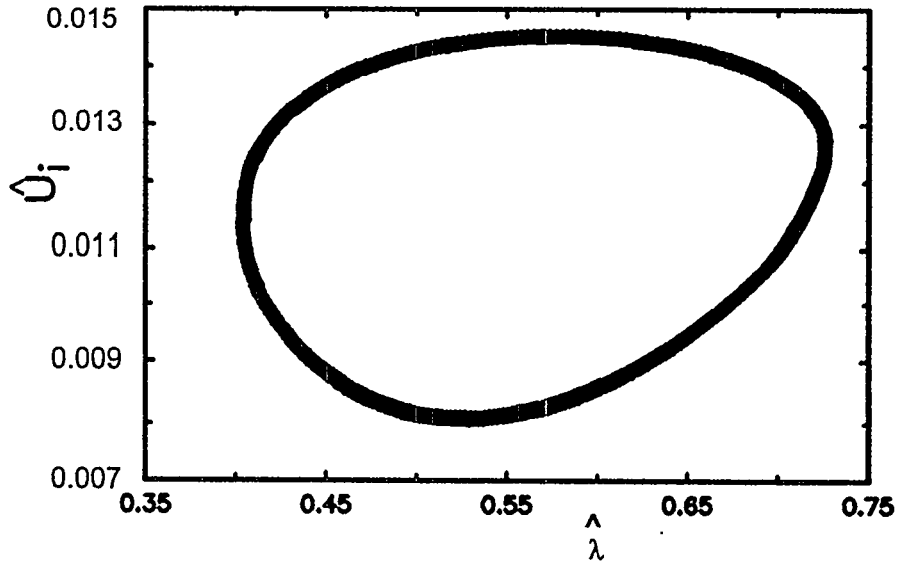

Fig. 10b Limit cycle for simple model (Nsub = 50, Npch = 87.1, Fr = 0.025, Ki = 40, Ke = 1)

For the subcritical Hopf bifurcations these limit cycles are unstables, while for the supercritical ones, these are stables. It was also found that decreasing the Froude number, *i.e.* increasing the gravity term, the Hopf bifurcations change from super-critical to sub-critical at higher subcooling numbers. These results were compared with the ones obtained by using more sophisticated models, showing qualitative good agreement.

4. Conclusions

A simple delay model based in a two-dimensional mapping was studied. The approach is useful to contribute to the understanding of density-wave instabilities. Moreover, significative computational time saving (compared with complete differential models) is an attractive quality of this simple model.

Regarding its performance, the model shows qualitative agreement with the differential treatment of the equations. For the linear stability analysis, simple expressions and good agreement were observed, for high subcoolings. Sub-critical and super-critical Hopf bifurcations were observed. This feature is similar to the behavior predicted by more complicated models.

The gravity term was modeled. Gravity influence for a wide range of Froude numbers was studied. It was found that increasing the gravity effect, i.e. decreasing the Froude number, has an unstabilizing effect

over the density-waves limit. On the other hand, stabilizing effect over the Ledinegg limit was found. Also related with the gravity influence, variations on the nonlinear behavior were found.

The assumptions used in this work seem to be reasonable for forced convection systems. However more studies are necessary in order to represent natural convection ones.

5. Nomenclature

Eu Euler number,
Fr Froude number,
h specific enthalpy,
h_{fg} $h_g - h_f$,
k concentred friction constant,
L_{ch} heated channel lenght,
M_{ch} mass channel,
N_{pch} phase change number,
N_{sub} subcooling number,
p pressure,
q volumetric power,
t time,
u velocity,
v specific volume,
v_{fg} $v_g - v_f$,
z space coordinate.
λ boiling boundary position,
ρ density,
ν liquid phase particle time,
τ two-phase particle time,
Ω $q\, v_{fg}/h_{fg}$.

Subscripts

e exit,
f liquid (saturation),
g vapor,
i inlet,
n number of time step,
o steady state,
ref reference.

Other

^ non-dimensional.

6. References

[1] Lahey R.T., Jr. and D.A. Drew, "An Assessment of the Literature Related to LWR Instability Modes", NUREG Report, NUREG/CR- 1414,(1980).
[2] Lahey R.T., Jr. and F.J. Moody, "The Thermal hydraulics of a Boiling Water Nuclear Reactor", ANS Monograph, (1977).
[3] Peng S.J., M. Z. Podowsky and R.T. Lahey Jr., "BWR Linear stability analysis", Nuclear Engineering and Design, 93 25-37 (1986).
[4] Xiao M., X.J. Chen, M.Y. Zhang, T.N. Verizoglu and S. Kokac, "A multivariable linear investigation of two-phase flow instabilities in parallel boiling channels under high pressure", Int. J. Multiphase Flow, 19, 65-77 (1993).

[5] Achard J.L., Drew D.A .and Lahey Jr. R.T., "The analysis of nonlinear density-wave oscillations in boiling channels", J. Fluid Mech., 155 , 213-232 (1985).
[6] Rizwan-Uddin and Dorning J.J., "A chaotic Attractor in a Periodically Forced Two-Phase Flow System", Nucl. Sci. Eng., 100, 393-404 (1988).
[7]] Achard J.L., Drew D.A .and Lahey Jr. R.T., "The effect of gravity and friction om the stability of boiling flow in a channel", Chem. Eng. Commun. 11 59-79 (1981).
[8] Lahey R.T. Jr., . Clausse A and P. Dimarco,"Chaos and non-linear dynamics of density-wave instabilities in a boiling channel". In Salim B. Yilmaz, editor, Heat Transfer-Philadelphia, 256-261 (1989).
[9] Delmastro D.F. and A. Clausse , "Modelado por medio de elementos finitos moviles de la dinámica de flujos en ebullición", Métodos numéricos para cálculo y diseño en ingeniería, 463-471 (1992).
[10] Thompson J.M.T. and H.B. Stewart, "Nonlinear Dynamics and Chaos", John Wiley & Sons (1986).
[11] Delmastro D.F., Clausse A .and Converti J., "The influence of gravity on the stability of boiling flows", Nuclear Engrg. Des. 127, 129-139 (1991).
[12] Tong L.S. and Weisman J. "Thermal analysis of pressurized water reactors". In The American Nuclear Society, 227-228 (1979).

AUTHORS INDEX

NRC FORM 335 (2-89) NRCM 1102, 3201, 3202

U.S. NUCLEAR REGULATORY COMMISSION

BIBLIOGRAPHIC DATA SHEET

(See instructions on the reverse)

1. REPORT NUMBER (Assigned by NRC, Add Vol., Supp., Rev., and Addendum Numbers, if any.)
NUREG/CP-0142
Vol. 4

2. TITLE AND SUBTITLE
Proceedings of the 7th International Meeting on Nuclear Reactor Thermal-Hydraulics
NURETH-7
Sessions 17 - 24

3. DATE REPORT PUBLISHED
MONTH: September | YEAR: 1995

4. FIN OR GRANT NUMBER

5. AUTHOR(S)
Compiled by R. C. Block and F. Feiner, Northeastern New York Chapter, American Nuclear Society

6. TYPE OF REPORT
Conference Proceedings

7. PERIOD COVERED *(Inclusive Dates)*

8. PERFORMING ORGANIZATION – NAME AND ADDRESS *(If NRC, provide Division, Office or Region, U.S. Nuclear Regulatory Commission, and mailing address; if contractor, provide name and mailing address.)*
Compiled by Northeastern New York Chapter, American Nuclear Society

9. SPONSORING ORGANIZATION – NAME AND ADDRESS *(If NRC, type "Same as above"; if contractor, provide NRC Division, Office or Region, U.S. Nuclear Regulatory Commission, and mailing address.)*

American Nuclear Society
555 N. Kensington Avenue
La Grange Park, IL 60525

American Institute of Chemical Engineers
345 East 47th Street
New York, NY 10017-2392

American Society of Mechanical Engineers
345 East 47th Street
New York, NY 10017-2392

Canadian Nuclear Society
144 Front Street West
Suire 725
Toronto, Ontario, Canada M5J2L7

European Nuclear Society
Secretariat: Monbijoustrasse 5
P.O. Box 5032
CH-3001 Berne, Switzerland

Atomic Energy Society of Japan
No. 1-13, 1-chome
Shimbashi, Minato-ku
Tokyo 105, Japan

Japan Society of Multiphase Flow
Prof. Akimi Serizawa
Department of Nuclear Engineering
Yoshida, Sakyo, Kycto 606-01
Japan

Division of Systems Technology
Office of Nuclear Regulatory Researc..
U.S. Nuclear Regulatory Commission
Washington, DC 20555-0001

10. SUPPLEMENTARY NOTES

11. ABSTRACT *(200 words or less)*

This volume includes papers presented at the 7th International Meeting on Nuclear Reactor Thermal-Hydraulics (NURETH-7) September 10-15, 1995 at Saratoga Springs, N.Y. The following subjects are discussed: progress in analytical and experimental work on the fundamentals of nuclear thermal-hydraulics, the development of advanced mathematical and numerical methods, and the application of advancements in the field in the development of novel reactor concepts. Also combined issues of thermal-hydraulics and reactor/power-plant safety, core neutronics and/or radiation.

12. KEY WORDS/DESCRIPTORS *(List words or phrases that will assist researchers in locating the report.)*
thermal-hydraulics, reactor/power-plant safety, core neutronics and/or radiation

13. AVAILABILITY STATEMENT
unlimited

14. SECURITY CLASSIFICATION
(This Page)
unclassified
(This Report)
unclassified

15. NUMBER OF PAGES

16. PRICE